Transactions of the ASME

The Journal of Engineering for Gas Turbines and Power (ISSN 0022-0825) is published quarterly for $100 per year by The American Society of Mechanical Engineers, 345 East 47th Street, New York, NY 10017. Second class postage paid at New York, NY and additional mailing offices. POSTMASTER: Send address change to The Journal of Engineering for Gas Turbines and Power, c/o The AMERICAN SOCIETY OF MECHANICAL ENGINEERS, 22 Law Drive, Box 2300, Fairfield, NJ 07007-2300.

CHANGES OF ADDRESS must be received at Society headquarters seven weeks before they are to be effective. Please send old label and new address.

PRICES: To members, $24.00, annually; to nonmembers, $100.00. Add $6.00 for postage to countries outside the United States and Canada.

INDEXED by the Engineering Index, Inc.

Journal of Engineering for Gas Turbines and Power

Published Quarterly by The American Society of Mechanical Engineers

Volume 107 • Number 2 • APRIL 1985

TECHNICAL PAPERS

(Contents Continued)

Recent Progress in the Understanding of Basic Aspects of Secondary Flows in Turbine Blade Passages

C. H. Sieverding
von Karman Institute
for Fluid Dynamics,
Chaussee de Waterloo, 72
B-1640 Rhode Saint Genese,
Belgium

The present paper is an attempt to summarize the results of experimental secondary flow research over the past decade in order to give a full picture of our present knowledge and uncertainties of basic secondary flow aspects. The paper gives a detailed description of secondary flow vortex structures and their effect on endwall boundary layer characteristics and loss growth through straight turbine blade passages.

Introduction

In a discussion of a paper in 1954 by Turner [1] on endwall boundary layers in a turbine nozzle cascade, Kraft said, "It is certainly to be hoped that more work of this nature will be undertaken and published. In view of the difficulty of the undertaking, it cannot be expected that a technically useful explanation of this phenomenon (i.e., secondary flows) will be furnished quickly. However, if a number of capable experimenters expend some effort along this line, the time should come when the effect of the various parameters, especially that of the profile contours, will be fully understood." His hopes seem at least partially to have been realized in 1970 when Dunham stated in the conclusion of his paper "A review of cascade data on secondary losses in turbines" [2] that ". . . the flow pattern associated with secondary losses is adequately understood, but the magnitude of the losses not." His belief in further improvements on secondary loss correlations was apparently not very strong, since he suggested that the most practical way of advancing the state-of-the-art would be a fresh approach using three-dimensional boundary layer theory, supported by detailed measurements. This recommendation was not made in vain, since several experimental research programs on secondary flows were started in the early seventies with the particular aim to provide the information needed to develop appropriate flow models for the theoretical analysis. These investigations led to detailed interpretations of hitherto neglected flow features like horseshoe vortices and three-dimensional separation and reattachment lines. Referring to this work, Tall [3] did not hesitate to declare in 1976: "It certainly dispels any remaining notion that secondary flows in cascades are understood."

The present paper is an attempt to summarize the results of the many valuable experimental secondary flow investigations carried out over the last 10 to 12 years in order to give a full picture of our present knowledge and uncertainties of basic secondary flow aspects. Whenever necessary, of course, reference is made to previous work.

Vortex Structure

Classical Secondary Flow Model. The classical secondary flow vortex system as depicted in Fig. 1 was described for the first time by Hawthorne in 1955 [4]. The vortex system presents the components of vorticity in the direction of flow when a flow with inlet vorticity is deflected through a cascade. The so-called passage vortex presents the distribution of secondary circulation, which occurs due to the distortion of the vortex filaments of the inlet boundary layer passing with the flow through a curved passage. The vortex sheet at the trailing edge is composed of:

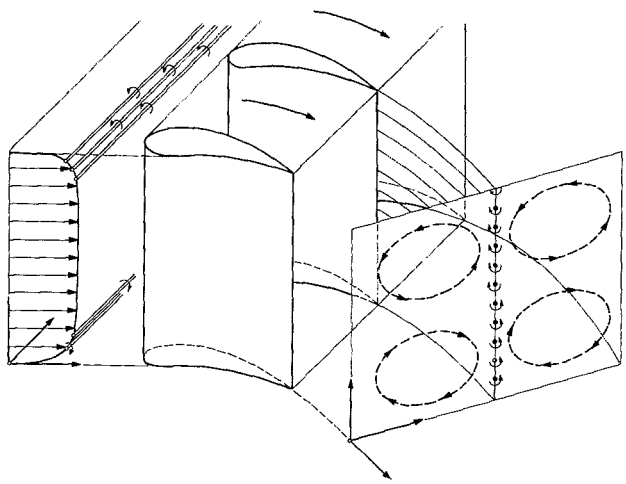

Fig. 1 Classical secondary flow model of Hawthorne

Contributed by the Gas Turbine Division of THE AMERICAN SOCIETY OF MECHANICAL ENGINEERS and presented at the 29th International Gas Turbine Conference and Exhibit, Amsterdam, The Netherlands, June 4-7, 1984. Manuscript received at ASME Headquarters January 5, 1984. Paper No. 84-GT-78.

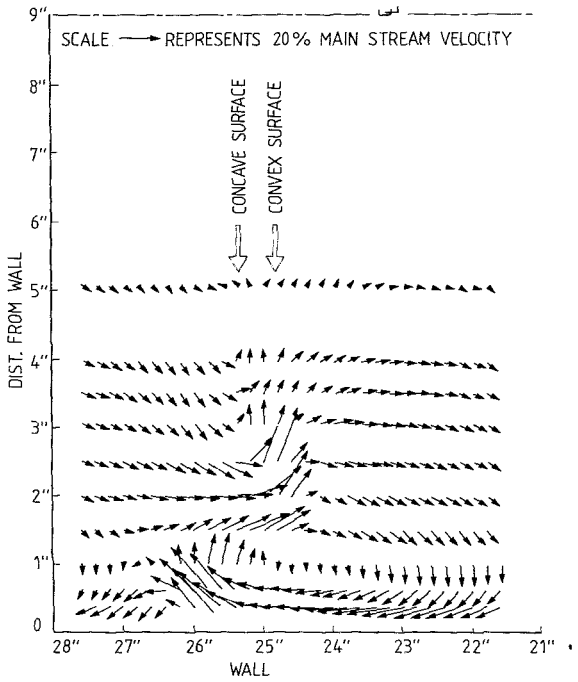

Fig. 2 Secondary velocity vectors downstream of impulse blade (from Armstrong [6])

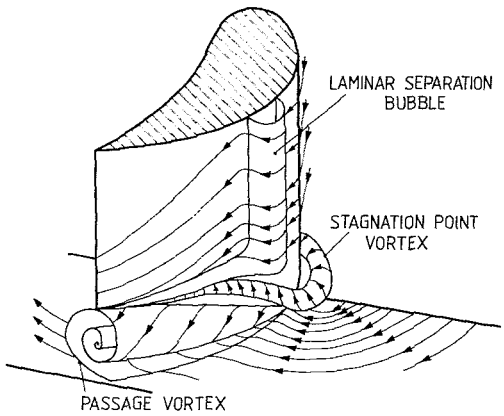

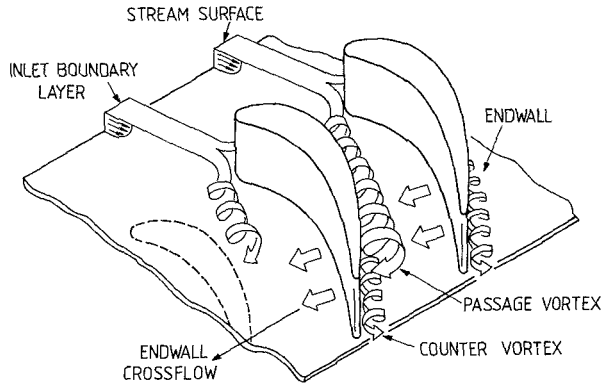

Fig. 3 Endwall flow models by Klein and Langston

(*a*) The trailing filament vortices, which arise due to the stretching of the inlet vortex filaments when passing through the cascade with different velocities between suction side and pressure side

(*b*) The trailing shed vorticity, which is due to the spanwise change of the blade circulation

The sense of rotation of the trailing filament and trailing shed vorticities is opposite to that of the passage vortex. Smoke visualizations by Herzig et al. [5] in 1954 demonstrated clearly the existence of the passage vortex, while secondary velocity vector plots by Armstrong in 1957 [6] from measurements behind an impulse blade present evidence of both the passage vortex and blade shed circulation (Fig. 2). The resemblance with the theoretical model is, however, poor.

Horseshoe Vortex. The rolling up of the endwall boundary layer in front of a cylinder on a flat plate into a vortical motion, called a horseshoe vortex due to its particular shape when flowing on both sides past the cylinder, is a well-known phenomenon. Its significance to the flow in turbine bladings has been recognized only very recently.

Oil flow visualizations by Fritsche in 1955 [7] show evidence of the horseshoe vortex in accelerating cascades, but to the author's knowledge, it is Klein in 1966 [8] who mentions first the existence of what he calls a stagnation point vortex. Without any further comments, Klein presents a cascade vortex model with both the passage and horseshoe vortices (Fig. 3(*a*)). This flow phenomenon attracted little interest from the scientific turbomachinery community until the early seventies, apart from exceptions such as Bölcs [9], who demonstrated in 1969 in a water table test the equivalence of the near-wall patterns round a cylinder and round the leading edge of a turbine blade.

In the early seventies both aerodynamicists and heat transfer people started to show an increasing interest in the leading edge vortex. In an experimental study of the heat transfer on large-scale turbine endwalls by Blair in 1973 [10], increased heat transfer rates were shown to occur near the leading edges of the pressure and suction surfaces and the author attributed this to the distortion of the endwall boundary layer by the leading edge vortex. The aerodynamicists discovered an interest in the leading edge vortex as a result of a new approach to secondary flow research. Contrary to the hitherto prevailing control volume approach in which the flow survey is limited to measurement

Nomenclature

b = spanwise extension of secondary flow region
C = chord
g = pitch
H = blade height or boundary layer shape factor ($H = \delta^*/\theta$)
P = pressure
Re = Reynolds number based on chord and downstream velocity
S = distance across blade passage
V = velocity
V_m = mean velocity (between upstream and downstream)
x = axial direction
z = spanwise direction
α = flow angle
δ = boundary layer thickness
δ^* = displacement thickness
ϵ = deviation angle
θ = momentum thickness

Subscripts

1 = inlet
2 = outlet
ax = axial
Fs = free stream
n = normal to streamwise direction
S = streamwise direction

of the up- and downstream flow conditions, the new approach consisted in looking at the secondary problem as an endwall boundary layer problem, which required a detailed study of the evolution of the flow throughout the cascade. The papers of Langston et al. [11], presented in 1976, and of Sjolander [12], in 1975, are pioneering works for the detailed analysis of secondary flow patterns in turbine cascades in general and of the role of the leading-edge horseshoe vortex in particular. The cascade vortex model (Fig. 3(*b*)) derived from the measurements in [11] (three-dimensional pressure probe measurements and visualizations of limiting streamlines by ink traces) is presented by Langston [13] in a later paper. The main differences between the models of Klein and Langston are twofold:

(*a*) Langston clearly postulates that the pressure side leg of the leading edge horseshoe vortex, H_p, which has the same sense of rotation as the passage vortex, merges with and becomes part of the passage vortex.

(*b*) Langston sees the suction side leg of the leading edge horseshoe vortex, H_s (called counter vortex in Fig. 3(*b*)), which rotates in the opposite sense to the passage vortex, continuing in the suction side endwall corner, while the presentation of Klein suggests that this vortex is gradually dissipated in contact with the passage vortex.

In 1977, Marchal and Sieverding [14] introduced the light sheet technique in secondary flow research, which allowed them to take sectional views of the flow in selected planes of the blade passage. The authors agree with Langston that the leading edge vortex, H_p, and the passage vortex seem to merge to form a single vortex, but contrary to Langston, they present smoke visualizations showing the counter-rotating vortex, H_s, in the trailing edge plane on the midspan side of the passage vortex rather than in the corner. However, a clear description of the merging process between the H_p branch of the leading edge vortex and the passage vortex and of the interaction between the H_s branch of the leading edge vortex and the passage vortex cannot yet be given.

More details on the horseshoe vortex were obtained by Gaugler and Russell in 1980 [15]. By injecting neutrally buoyant helium filled soap bubbles into the upstream boundary layer of a cascade, they were able to visualize the corkscrew flow path of streamlines caught in the horseshoe vortex. The streamwise stretching of the rotational motion of these streamlines is put into evidence.

Description of the Synchronous Evolution of Horseshoe and Passage Vortices. An essential piece of information about the evolution of horseshoe and passage vortices through cascade passages was contributed by Moore and Smith in 1983 [16], who measured the flow trajectories by ethylene detection in the exit plane of a replica of Langston's cascade. The authors found that ethylene injected at the location of the suction side branch of the horseshoe vortex near the blade leading edge was convected around the passage vortex core while ethylene injected into the pressure side branch of the horseshoe vortex was found in the center of the passage vortex.

A more detailed explanation of the synchronous evolution of horseshoe and passage vortices is finally given in late 1983 by Sieverding and Van den Bosch [17]. The authors used a colored smoke wire technique to visualize the evolution of entire stream surfaces through cascades. Based on photographs and direct observations, they presented the flow model in Fig. 4. It shows the shape of two stream surfaces, SS_1 and SS_2; SS_1 starting upstream inside the endwall boundary layer and SS_2 outside the endwall boundary layer at different axial positions in the blade passage. Approaching the leading edge the lateral extremities of stream surface SS_1 start to roll up into the two counterrotating branches of the horseshoe vortex, H_p and H_s, the main part of the stream

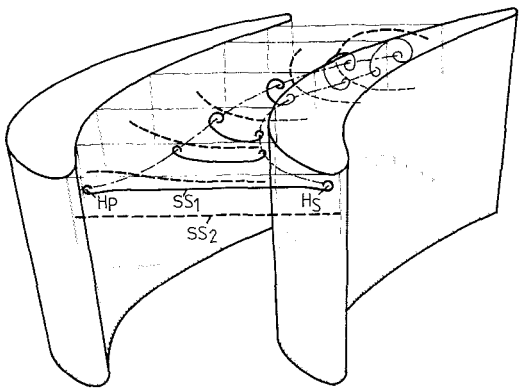

Fig. 4 Synchronous evolution of horseshoe and passage vortices after Sieverding and Van den Bosch [17]

surface being nearly undisturbed. Behind the leading edge plane the whole stream surface starts slowly to rotate. All parts of the stream surface, including the vortices H_p and H_s, take part in this vortical motion which gradually develops into what is called a passage vortex. The flow visualizations show that the pressure side branch of the horseshoe vortex, H_p, follows basically a smooth curve through the passage without any noticeable vortical motion, which would indeed suggest that its core coincides with that of the passage vortex, while the suction side branch of the horseshoe vortex, H_s, wraps itself around the passage vortex core which confirms the results of Moore and Smith in their ethylene detection tests. The position of the H_s vortex depends on the rotational speed of the passage vortex, which in turn depends on the cascade geometry and the overall flow conditions. This explains why Marchal and Sieverding locate the H_s vortex on the midspan side of the passage vortex, while Moore and Smith can detect it on the endwall side. The counter vortex of Langston right in the endwall suction side corner is believed to be of different origin as seen in the next section.

Except in the entrance region, nobody has succeeded so far in using pressure probes to trace the flow path of the H_s vortex through the cascade. The reason for this is different in the front and rear parts of the passage. In the accelerating front part the vortex moves away from the endwall but stays close to the suction surface. Its small size combined with a strong stretching in the streamwise direction makes it difficult to detect it. In the rear decelerating part it grows in size, but it has lost its intensity in contact with the passage vortex due to the dissipating action of the shear forces.

Moore and Ransmayr [18] investigated the effect of the leading edge geometry on secondary flows by replacing the standard cylindrical leading edge of their cascade by a wedge-shaped leading edge. They found that neither the static pressure nor the overall losses were significantly affected by this modification. This result demands two comments: (*i*) It seems logical to assume that the addition of a sharp leading edge to a simple round cylinder will suppress the formation of the leading edge vortex. However, in the case of a cascade, the stagnation streamline is curved and the incidence angle to the sharp nose will probably be different from zero. The flow "sees" in fact a blunt leading edge. Hence the size of the leading edge vortex will greatly depend on the incidence angle. (*ii*) Figure 4 suggests that the reduction or elimination of the leading edge horseshoe vortices will indeed have little effect on the shape and position of the passage vortex. However, the rotational speed of the particles near the vortex center might be affected by the strength of the horseshoe vortex H_p.

Corner Vortex. Here we want to refer to a vortex that rotates in the opposite sense to the passage vortex and is located invariably right in the endwall/suction side corner.

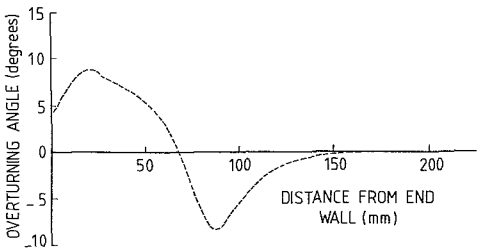

Fig. 5 Reduction of overturning near the endwall due to presence of corner vortex (extracted from Gregory-Smith and Graves [19])

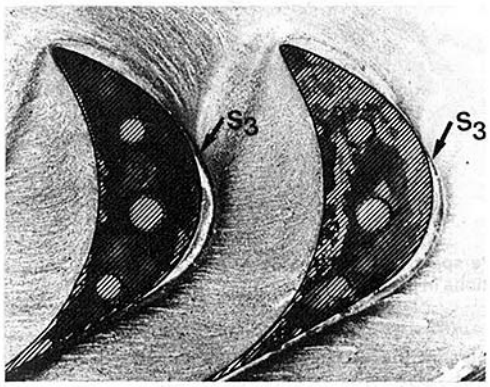

Fig. 6 Endwall limiting streamlines indicating generation of corner vortex in an impulse blade passage (from Belik [20])

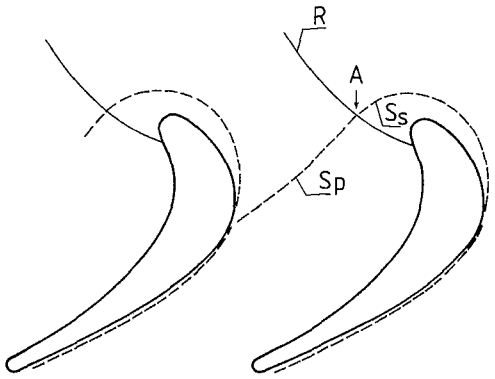

Fig. 7 Endwall three-dimensional separation and reattachment lines after Langston [11]

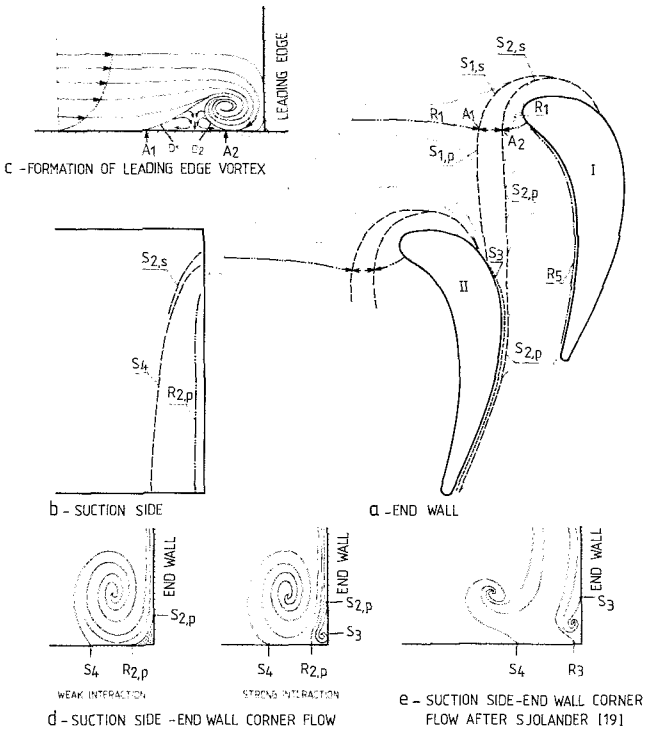

Fig. 8 General presentation of endwall flow characteristics

Because of its relatively small size, it is difficult to visualize, but its existence is often put into evidence in the spanwise angle distribution behind highly loaded cascades by a characteristic reduction of the overturning near the endwall, as shown in Fig. 5 extracted from a recent paper (1983) by Gregory-Smith and Graves [19]. To trace the corner vortex back to its origin is more difficult, but the oil flow visualization in Fig. 6 from Belik in 1975 [20], showing the limiting streamlines in a very high turning impulse type cascade, is enlightening. The overturning at the endwall is such that the limiting streamlines interfere almost at a right angle with the blade suction surface near the position of maximum surface curvature. It is certainly not too far-fetched to compare this interaction with that causing the boundary layer ahead of the leading edge to roll up into a vortical motion. Without going further into the analysis of limiting streamlines (see following chapter) let us note: (*a*) that the line S_3 in Fig. 6 presents a three-dimensional separation line that is characteristic of the existence of a vortex turning in the opposite direction of the passage vortex; and (*b*) that this separation line starts near the point where the crossflow interferes the first time with the suction surface. Similar, but in general, less violent situations occur in most cascades with significant crossflows (see oil flow visualizations by Marchal and Sieverding [14] and by Moore [21]).

Effect of Vortex Structures on Endwall Boundary Layer

Limiting Streamlines. The visualization of limiting streamlines by coating the blade and endwall surfaces with a mixture of oil and T_i0_2-powder before starting the wind tunnel has been widely used. However, the high viscosity of this mixture presents a certain drawback when using it at low speed. Tests at both low and high speed by Marchal and Sieverding [14] showed substantial improvements in the visualization of the limiting streamlines at high speed. Langston et al. [11] used ink traces probably for the same reason, but here, the spatial resolution is less satisfactory since the ink traces must not be allowed to mix with each other. Recently, Langston and Boyle (1982) developed a new ink dot technique giving more accurate surface streamlines [22].

Figure 7 presents schematically the results of the analysis by Langston et al. [11] of the ink traces of the limiting streamlines in the cascade. The flow field is divided into distinct regions through the three-dimensional separation lines S and the reattachment line R (stagnation streamline) with the separation saddle point A at their intersection. The horseshoe and passage vortices form behind the separation line S: the pressure side branch of the horseshoe vortex, H_p, and the passage vortex behind S_p (starting from A) and the suction side branch of the horseshoe vortex, H_s, behind S_s. The passage vortex separates from the blade suction surface along line S_4 (position like in Fig. 8).

The oil flow visualization by Belik in Fig. 6 and others by Sjolander [12], Marchal and Sieverding [14], Moore [21], and Gotthardt [23], as well as the smoke visualizations in [14], indicate that the endwall limiting streamline patterns might be much more complicated. An attempt is made to present this

schematically in Fig. 8. There are two major separation lines ahead of the leading edge. The secondary separation line S_2 corresponds to the "lift off" line of the horseshoe vortex, while the separation line S_1 is due to the boundary layer separation ahead of the horseshoe vortex. The secondary separation line is in general easier to detect in cascade endwall flow visualizations than the primary line, which is often rather weak. The observation of both separation lines in cascades is in accordance with flow visualizations around cylinders mounted on a flat plate by Belik [24], Peake et al. [26], and East and Hoxey [27]. Smoke visualizations using the light sheet technique [14] confirm the existence of a low-energy region between the two separation lines near the leading edge. Based on this experimental evidence, one may postulate the existence of two dividing stream surfaces, D_1 and D_2, along which low momentum material is fed into the stagnant separation bubble (see Fig. 8(*c*) and two saddle points A_1 and A_2 rather than one as in Fig. 7). Sjolander [12] found this separation bubble also in his endwall boundary layer measurements (see next section). More tests are needed to investigate how the distances of the two separation streamlines S_1 and S_2 from the leading edge and the lateral extension of the stagnant separation bubble depend on the endwall boundary layer characteristics, the shape of the leading edge and the incidence angle. A change of the incidence angle causes the stagnation streamline to shift around the leading edge with the result that the leading edge appears more or less blunt to the incoming flow (Langston et al. [11], Stastny [25]).

At the intersection of the near wall streamlines, contained between separation streamlines $S_{1,p}$ and $S_{2,p}$, with the suction surface of blade II, one of two things may happen. Depending on the blade loading the interaction may be of the strong or weak type (high or low angle of attack of streamlines with respect to blade surface). In the case of a strong interaction (e.g., Fig. 6 or cascade of Moore [21]), a corner vortex is created under similar conditions as at the leading edge. This results in the formation of a separation line S_3 originating in the intersection point of the separation line, $S_{1,p}$ with the suction surface (see Fig. 6). The separation line $S_{2,p}$ continues parallel to the line S_3 towards the cascade exit plane (Fig. 8(*a*)). In the case of a weak interaction (e.g., nozzle blades in [14] and [23]), the oil flow visualizations show only the separation line $S_{2,p}$ running along the suction side endwall corner. Figure 8(*d*) shows schematically the suction side corner flow for both types of interaction in a plane normal to the rear suction surface. For comparison, Fig. 8(*e*) shows also the interpretation of the corner flow patterns by Sjolander [12]. His patterns are overall similar to those of the strong interaction type in Fig. 8(*d*). The different shape of the passage vortices is unimportant. What matters is that Sjolander indicates a separation line S_3, which in his flow visualization clearly originates in the region of the intersection of the separation lines $S_{1,p}$ and $S_{2,p}$ with the suction side surface, as shown in Fig. 8(*a*). On the contrary, the separation line $S_{2,p}$ was not observed downstream of this region. As a result, Sjolander's interpretation of the position of the separation line S_3 on the rear suction surface differs from that of the present author. Corresponding to the separation line $S_{2,p}$ in Figs. 8(*a*) and 8(*d*), there is a reattachment line $R_{2,p}$ on the blade surface near the endwall (Fig. 8(*b*)). This line was clearly observed in [14] and [23]. Further away from the endwall appears the three-dimensional separation line S_4 of the passage vortex (Fig. 8(*b*)).

The evolution of the separation lines $S_{1,s}$ and $S_{2,s}$ is dictated by the strong flow acceleration on the front part of the blade suction side and the transverse pressure gradient. The primary separation line $S_{1,s}$ rapidly joins the secondary separation line $S_{2,s}$, which intersects the suction surface after a short distance

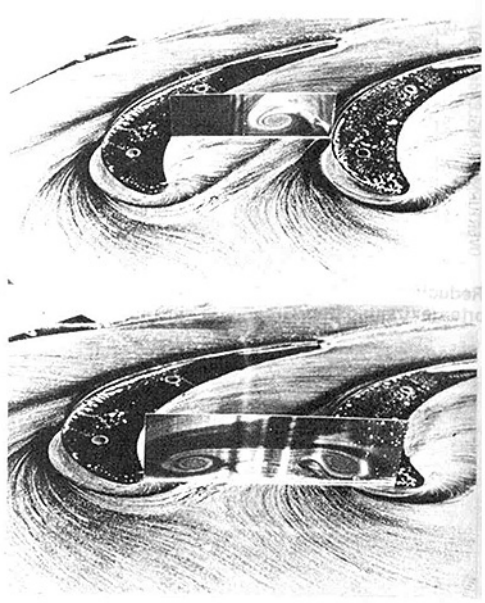

Fig. 9 Perspective view of endwall limiting streamlines and smoke visualizations in a plane normal to the endwall

indicating that the suction side branch of the horseshoe vortex has shifted away from the endwall on to the suction side. The trace of this vortex, i.e., its three-dimensional separation line, can be followed on the suction surface until the vortex eventually moves away from it into the passage under the influence of the rotational motion of the passage vortex to which it is linked as seen in Fig. 4.

Finally, Fig. 8(*a*) shows a reattachment line R_5, which gives evidence of a pressure side endwall corner vortex, the importance of which probably increases with increasing positive inlet flow angle. Its origin is found in a downwash motion observed on the front part of the pressure side. This downwash seems to be in general small, except in the rotor blade flow visualizations in [14] which were made at 15 deg positive incidence. The pressure side corner vortex rotates in the same sense as the suction side corner vortex and thus contributes to reduce the downstream overturning angle near the endwall.

The relation between vortices and endwall limiting lines is best demonstrated in Fig. 9 (cascade: $\alpha_1 = 45$ deg, $\alpha_2 = -69$ deg, $g/C = 0.69$), which shows two photographic montages of a combination of oil flow and smoke visualization pictures, the latter being placed normal to the first. The good agreement between the smoke and the oil flow visualizations is somewhat surprising since the Reynolds numbers for the tests differed by a factor of 20 (smoke visualization: $\mathrm{Re} = 0.6 \times 10^5$, oil flow visualization: $\mathrm{Re} = 1.2 \times 10^6$). However, tests by Peake et al. [26] for both laminar and turbulent endwall flows around oval cylinders indicate that the changes in the endwall streamlines are quantitative rather than qualitative in nature. In particular, the existence of both the primary and secondary separation lines ahead of the cylinder was not affected. Nevertheless, it should be mentioned that in laminar flow more than one vortex may occur. A similar phenomenon also occurred occasionally in the smoke tests by Marchal and Sieverding.

Endwall Boundary Layer Characteristics. One of the most important tasks of current secondary flow research is to provide test cases for viscous flow calculations. This implies the provision of information on the nature of endwall boundary layer: the type of boundary layer profile, separation regions, wall shear stresses, and turbulence throughout the blade passage. Before the mid 1970s, Senoo [28] was apparently the only investigator to carry out boundary layer

measurements within a turbine blade passage. He studied the flow in a high turning nozzle cascade. He concluded that the endwall boundary layer in the throat is laminar no matter what the state and thickness of the upstream boundary layer and ascribed this to the steep favorable gradient.

Flow surveys including detailed endwall boundary layer traverses inside the cascade passages have become more frequent since the mid 1970s. Examples of such experiments with collateral inlet boundary layers are those by Langston et al. [11], Marchal and Sieverding [14], Bario-Leboeuf-Papailiou [29], Bailey [30], and Gregory-Smith and Graves [19] in straight cascades and Sjolander [12] and Sieverding-Boletis-Van Hove [31] in annular cascades. Only a few results have been presented in the form of endwall velocity profiles. In most cases, the authors have preferred to present their results as total and static pressure coefficient loss contour plots. All tests are done at low speed with Reynolds numbers in the range Re = 2.5×10^5 to 10^6. The state of the inlet boundary layer was in most cases turbulent and in a few cases transitional (range of shape factors from $H = 1.3$ to 1.7). The inlet free-stream turbulence level was in general of the order of 0.5 to 1 percent (in one case 3 percent).

The boundary layer profiles are in general presented under the form of streamwise and crossflow velocity profiles, except for Sjolander who plots total pressure deficit coefficients and yaw angles. A short description of the most characteristic velocity profiles which may occur in a turbine blade passage is given below. For their positioning in the cascade the reader is referred to Fig. 8(*a*).

- Upstream Flow Field: The upstream effect of the cascade imposes a positive crossflow component on the incoming pressure size streamlines and a negative component on the incoming suction side streamlines (positive direction: from pressure side to suction side), see Fig. 10(*a*) [31]. The streamwise component conserves a two-dimensional character.
- Passage Entrance Field up to the Primary Separation Line: The crossflow components are reinforced. The streamwise component remains essentially two-dimensional in character. The strong convergence in the suction side leading edge region (ahead of the separation lines $S_{1,s}$ and $S_{2,s}$) causes a local thickening of the boundary layer. This effect is rapidly reduced through the action of the strong streamwise acceleration of the flow in this region.
- Region Between Separation Lines $S_{1,p}$ and $S_{2,p}$: Only Sjolander [12], refers specifically to boundary layer measurements in this region. One of his traverses is positioned approximately halfway between the separation lines $S_{1,p}$ and $S_{2,p}$, at lateral distance from A_1A_2 (saddle points defined in Fig. 8) approximately equal to the distance $A_1 \rightarrow A_2$. He concludes that the stagnation separation bubble still has a radial extension of about one-fifth of the boundary layer thickness at this point.
- Downstream of Separation Line $S_{2,p}$: The vortical motion of the horseshoe and/or passage vortices convects fluid from the outer boundary layer or even from the free-stream toward the endwall and reenergizes the near endwall layers. To which degree and over what part of the passage this happens depends on the intensity of the passage vortex. A new boundary layer is growing. This effect is most apparent from the streamwise velocity component as schematically shown in Fig. 10(*b*). In addition to this, the passage vortex imposes the characteristic over- and underturning on the crossflow profile of the endwall flow. The resulting profile varies significantly from the pressure side to the suction side, changing from a single crossflow profile at the pressure side to a crossover crossflow profile. Near the suction side the crossover crossflow profile may be further complicated by (*a*) the influence of an initially significant negative crossflow component at the passage entrance as shown by Sieverding et al. [31] and (*b*) a suction side corner vortex like that apparent in the profiles measured by Langston [13]. The foregoing described profiles are presented in Fig. 10(*c*). Langston found that the crossflow behavior of the profiles (*a*) and (*b*) in Fig. 10(*c*) could be correlated in the form of polar plots by the expression

$$\frac{V_n}{V_s} = \tan((\epsilon_w - az)e^{-\gamma z})$$

The constants ϵ_w, a, and γ (ϵ_w represents the yaw angle deviation with respect to free-stream conditions of the wall, a is a measure for the wall distance at which ϵ changes sign, and γ is related to the maximum underturning) have to be determined experimentally. Since both the strength and position of the passage vortex depend on the blade loading and the inlet endwall boundary layer thickness (to mention the most important parameters), it will be difficult to find a general correlation for these constants. Crossflow profiles of types (*c*) and (*d*) in Fig. 10(*c*) are clearly excluded at once from any approach based on experimental correlations.

The convection of high energy fluid to the endwall through the action of the horseshoe and passage vortices results in an increase of the skin friction and wall shear stresses as stated by Belik [32], who measured the variation of the wall shear stresses along the centerline of two high turning nozzle cascades (~70 deg turning) using thin film gauges. He finds a strong increase of the shear stresses with the flow path length, the maximum stresses occurring near the point of maximum streamwise pressure gradient. Measurements of endwall boundary layer noise confirm that this position corresponds closely to the start of a laminar boundary layer. Except for Belik and Senoo [28], all investigators find the viscous layer behind the separation line $S_{2,p}$ too small for it to be possible to ascertain the state of the boundary layer.

So far only few data have been published on turbulence measurements and unfortunately they are rather contradictory. In an investigation of the flow through a single large-scale turbine vane passage with an inlet turbulence level varying from a root mean square value of 0.7 percent at midspan to 6 percent near the wall, Bailey [30] states that turbulent stresses are insignificant in large regions of the passage vortex, suggesting that a laminar flow calculation procedure may provide a reasonably accurate prediction of the secondary flow structure far from the wall. Gregory-Smith and Graves [19] found, for an upstream free-stream turbulence of 3 percent, peak turbulence intensities of 30 percent in the vortex core. The authors concluded that some

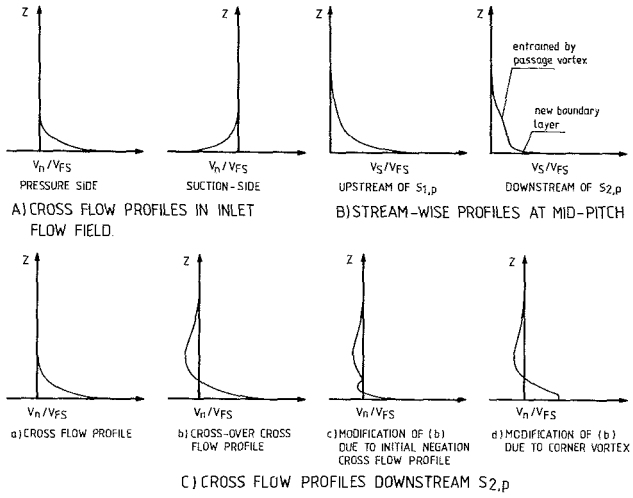

Fig. 10 Various types of endwall boundary layer profiles

of the total pressure loss through the cascade appears as an increase in turbulent kinetic energy before being dissipated by viscous action. Unfortunately, the authors did not quote the turbulence increase through their rather thick inlet endwall boundary layer. Langston et al. [11] present turbulence measurements in the trailing edge plane, but no data within the high loss core in the endwall suction side region. The one traverse located just at the edge of the loss core gives a slight hint that the turbulence intensity might actually increase in the loss core.

Origin, Growth and Spatial Distribution of Losses

Generation and Redistribution of Low Momentum Flow in Cascades. Analysis of the vortex structures and their effects on the endwall boundary layer gives a fairly clear idea about the factors contributing to the generation and spatial distribution of low momentum flow through turbine cascades. The most important loss contributions are summarized below:

(*a*) Natural increase of the inlet endwall boundary layer up to the separation lines

(*b*) Stagnant separation bubble in the leading edge region between the two separation lines

(*c*) Growth of new boundary layer behind the separation line $S_{2,p}$

(*d*) Corner losses in both pressure side and suction side endwall corners, the latter being the most important

(*e*) Shear stress effects along all three-dimensional separation lines

(*f*) Losses due to the shear action of the passage vortex on the blade suction side and the mixing process between the crossflow and the blade flow along the three-dimensional separation line S_4

(*g*) Dissipation of all vortices and complete mixing of the nonuniform outlet flow field downstream of the cascade

Gregory-Smith calculated secondary losses by taking into account only the losses due to the new boundary layer (with a two-dimensional boundary layer method) and the secondary kinetic energy (as presented by classical secondary flow theory), which was considered to be lost entirely. Adding to this, the losses due to the inlet boundary layer, he found fair agreement with experimental data in at least two cascades [33, 19]. Calculations of the kinetic energy of the measured secondary flow motion in the trailing edge plane of a rotor blade ($\alpha_1 = 30$ deg, $\alpha_2 = -60$ deg, $H/C = 0.83$) tested at VKI showed that the ratio of secondary to total kinetic energy varied from 0.6 percent for an inlet boundary layer with $\delta^*/C = 0.011$ to 1.2 percent for $\delta^*/C = 0.028$ with a distribution of 55 percent for the spanwise secondary velocity component and 45 percent for the component normal to the streamwise direction. It is probably correct to say that the assumption that the entire secondary kinetic energy is lost is exaggerated and partially accounts for other losses, such as corner losses and mixing losses along the separation line S_4.

The pitch- and spanwise distribution of secondary losses under the influence of the secondary flow vortex structures is one of the most characteristic aspects of secondary flows. The limiting streamlines indicate that the inlet low momentum boundary layer material in the immediate vicinity of the endwall is directly deflected to the blade suction side along the separation line $S_{1,p}$ except in front of the leading edge. Here part of it is fed into the stagnation separation bubble from where it is directed between the two separation lines $S_{1,p}$ and $S_{2,p}$ also towards the suction surface. The particles in the remaining part of the inlet boundary layer can take very different paths. If they get involved with the horseshoe vortex, either they migrate to the passage vortex center or are convected around the passage vortex core, depending on whether they are part of the pressure or suction side part of the horseshoe vortex. Inlet boundary layer material which is not involved in the leading edge vortex and which makes its way across the region between the two separation lines $S_{1,p}$ and $S_{2,p}$ will be either entrained by the passage vortex along the secondary separation line without necessarily migrating to the vortex center or it is turned behind the separation line towards the endwall, where it takes part in the formation of the new boundary layer. The motion of low momentum boundary layer material toward the blade suction side continues downstream of the the second separation line, including even parts of the pressure surface boundary layer. All endwall boundary layer material that has been pushed throughout the passage onto the blade surface is driven together with parts of the regular blade surface boundary layer to the separation line S_4 as indicated by the limiting streamlines in Fig. 11. However, not all of the boundary layer material that has moved across the passage migrates to the suction surface; some of it continues in the suction side endwall corner and may appear downstream as a nonnegligible local loss core from which low momentum material is continuously fed into the main stream [19]. Apart from the remaining boundary layers on the endwalls, there are three characteristic types of loss concentrations that may be found in the trailing edge plane:

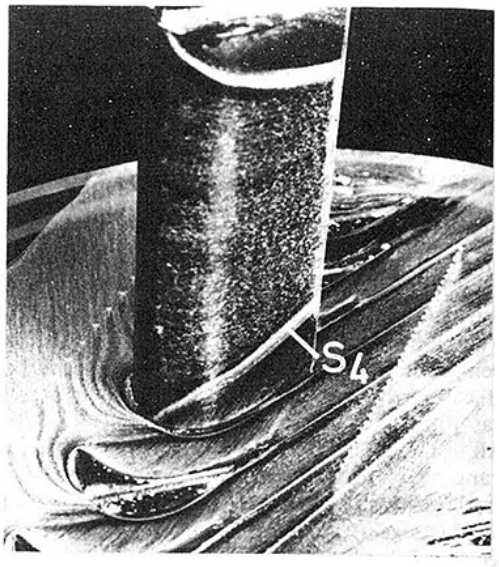

Fig. 11 Limiting streamlines indicating transport of endwall boundary layer material onto blade suction side (from ANSALDO)

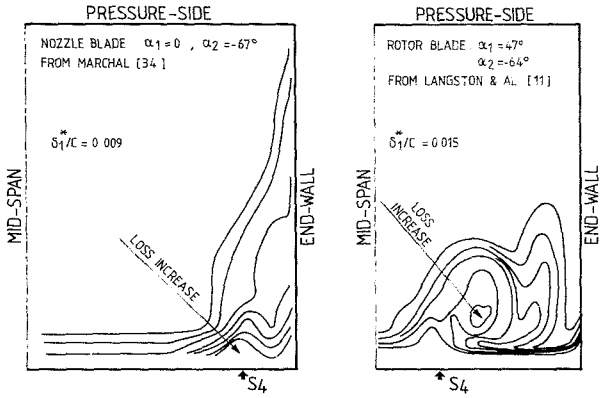

Fig. 12 Influence of cascade geometry on loss contour plots in trailing edge plane

(*a*) Corner loss

(*b*) Loss core associated with passage vortex (a coincidence of the center of the loss core with the center of the passage vortex is, however, fortuitous, see [19])

(*c*) Loss core along passage vortex separation line S_4.

Depending on the inlet boundary layer thickness and blade loading, these loss cores are more or less superimposed. Two examples are given in Fig. 12.

The position of the passage vortex in the trailing edge plane is obviously of primary importance for the loss distribution. The following general tendencies have been observed:

(*a*) Increasing the inlet flow angle α_1 at constant α_2 and δ_1^*/C results in a shift of the passage vortex center toward the blade suction side. This pitchwise shift is accompanied by a spanwise displacement (see nozzle blades [14, 23] and high turning rotor blade sections [11, 14, 19, 29]).

(*b*) A variation from a thick to a thin inlet boundary layer causes a decrease of the distance separating the vortex center from the endwall and a shift of the vortex towards the blade suction side ([30, 34] and from pressure measurements of Graziani et al. in [41]).

(*c*) A decrease of the aspect ratio below the critical value (mutual interference of secondary flow regions from both blades ends) moves the passage vortex closer to the endwall. (Bailey [30]). This could partially explain the nonlinear variation of secondary losses at low aspect ratios.

(*d*) A variation of the outlet Mach number (in the subsonic range) does not seem to affect significantly the position of the passage vortex (tests on nozzle blade by Sieverding and Wilputte [42] from $M_2 = 0.1$ to 0.8).

Loss Growth Through Cascade. Various authors have presented the growth of the pitch- and spanwise-averaged losses within their cascades. Gregory-Smith and Graves [19] find a fairly steady growth of the losses throughout their cascade. On the contrary, Langston [11] and Marchal and Sieverding [14] conclude that the losses remain fairly constant up to the axial position of the maximum suction side velocity and then grow rapidly from there to the trailing edge. The growth is attributed to the interaction of the endwall crossflow with the suction side boundary layer and to the overall effect of the rear suction side flow deceleration on the entire secondary flow behavior. It is interesting to note that the calculation of the loss growth through Langston's cascade by Hah [43] with a Navier-Stokes computer code shows almost constant losses up to 30 percent of the axial chord followed by a rapid increase of the losses up to the trailing edge.

Figure 13 presents the loss growth inside the blade passage for three different cascades measured by Marchal [34]. By approximating the loss increase for each cascade by a straight line, he was able to correlate the slope of the curves with a parameter, a, representing the maximum pressure difference across the blade passage, divided by the corresponding distance between pressure and suction sides and non-dimensionalized by the mean kinetic energy of the main flow

$$a = \frac{C_{ax}}{S} \cdot \frac{\Delta P_{\max}}{\frac{1}{2}\rho \cdot V_m^2}$$

Taking into account the distance of the minimum suction side pressure from the leading edge plane, $x_{\min}$, Marchal further proposed a quality factor

$$Q = \left(1 - \frac{X_{\min}}{S}\right)\left(\frac{C_{ax}}{S} \cdot \frac{\Delta P_{\max}}{\frac{1}{2}\rho V_m^2}\right)^{1.25}$$

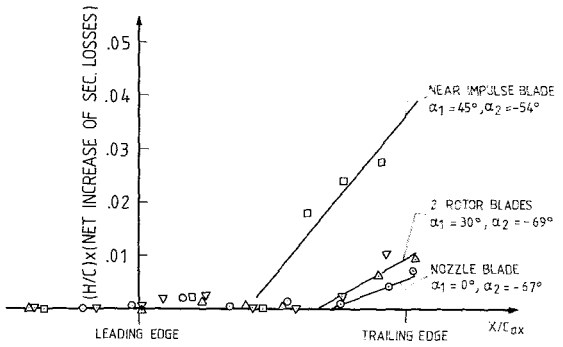

Fig. 13 Loss growth through cascade (from Marchal [34])

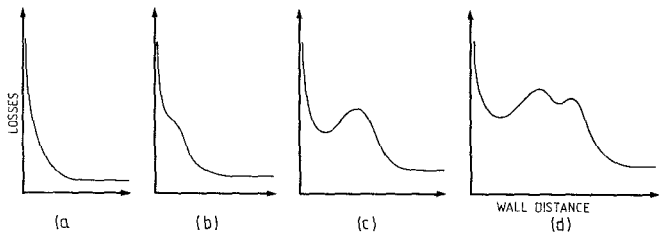

Fig. 14 Various types of spanwise loss distributions

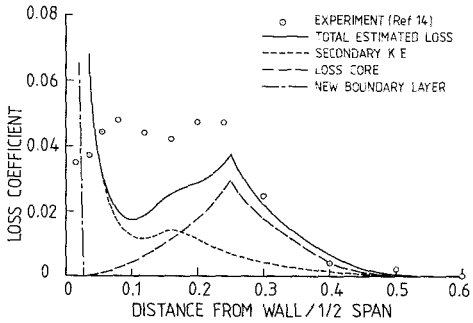

Fig. 15 Prediction of spanwise loss distribution by Gregory-Smith [33]

which allows a qualitative evaluation of the effect of blade design on secondary losses. This factor has been used to analyze the performance of blades with the same overall load but different load distributions. An increase of Q indicates an increase of secondary losses. In the particular case of two bladings tested at VKI, a front loaded blade A and a rear loaded blade B (designed for $\alpha_1 = 30$ deg, $\alpha_2 = -69$ deg, $g/C_{ax} = 0.87$), the quality factor $Q_A = Q_B = 1.44$ explained why the modification of the blade geometry did not affect the secondary losses.

Downstream Spanwise Loss Distribution. The downstream spanwise loss distribution is naturally closely related to the position of the passage vortex. However, the actual shape does not only depend on the blade loading (Groschup [35], Marchal [34]) but also on the inlet boundary layer (Wolf [37], Came [36]) and the downstream distance (Armstrong [6], Wolf [37], Gregory-Smith and Graves [19]). The most frequent types of distribution are shown in Fig. 14. Everything else being the same the loss distribution will change from left to right with increasing loading. The bump in the loss distribution in Fig. 14(*b*), and the loss cores occurring well away from the endwall in 14(*c*) and 14(*d*) are evident results of the displacement action of the passage vortex on the endwall boundary layer as described before. A change from pattern (*b*) to (*c*) may also occur as a result of a strong thinning of the inlet boundary layer [36, 37]. The appearance of a double peak as shown in Fig. 14(*d*) can have

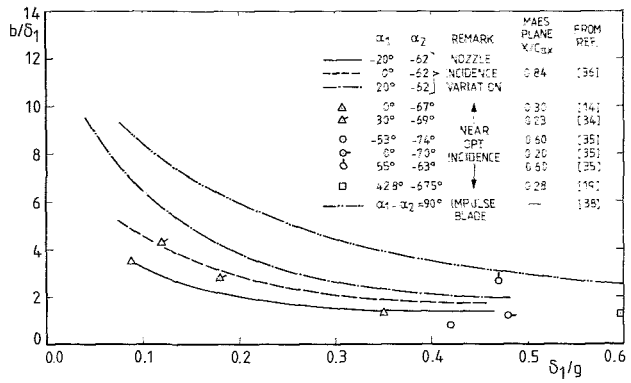

Fig. 16 Dependence of extension of secondary loss region on inlet boundary layer thickness

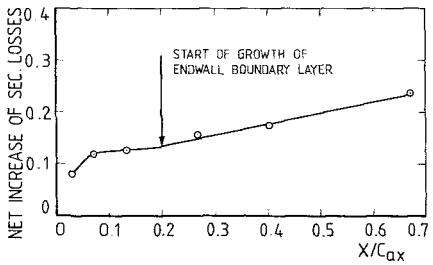

Fig. 17 Example of growth of secondary losses downstream of cascade (from Gotthardt [23])

two reasons: the existence of important losses along the suction side separation line S_4 next to the loss core associated with the passage vortex (see [19]) or the splitting of the main loss core by the shearing action of the passage and trailing edge vortices as shown by Armstrong [6].

The best physical approach to spanwise modeling is probably that of Gregory-Smith [33], which is illustrated in Fig. 15. The sharp peak of the loss core which represents the kinetic energy deficit is due to the assumption of a triangular distribution of these losses. A distribution function of the type e^{-z} as proposed by Groschup [35] would probably further improve the model. Since the model is based partially on classical secondary flow theory the extension of the secondary flow region is naturally taken equal to the inlet boundary layer thickness. This is, however, not at all the general case. Figure 16 presents data on the relation: extension of secondary loss zone b with respect to the inlet boundary layer thickness δ_1 by Wolf [38], Came [36], Groschup [35], Marchal [34] and Gregory-Smith [19]. In cases where the beginning of the secondary loss region was not clearly defined, it was arbitrarily decided to put it at a wall distance, where the losses reached 1.1 times the value of the profile losses. In spite of the fact that the downstream measurement plane varied considerably between the various investigators (see Fig. 16), several conclusions can be drawn:

(*a*) Except for thick boundary layer and low turning blades, the ratio b/δ_1 is always greater than 1.

(*b*) The relation $b=f(\delta_1)$ is not linear; the rate at which b/δ_1 changes decreases rapidly to reach asymptotically a constant value for large values of δ_1/g.

(*c*) The ratio b/δ_1 increases with blade loading at constant δ_1/g.

Downstream Growth of Losses. The fact that the endwall losses continue to rise with increasing downstream distance due to the action of wall shear stresses makes an exact definition of secondary losses difficult. The situation is further complicated by the fact that the low momentum material produced by the wall shear stresses does not necessarily appear under the form of a normal boundary layer profile at the endwall, but is often fed into the main flow for some downstream distances [19, 23, 38]. This is reflected in the spanwise loss distribution by the absence of a "normal" wall loss profile whch has been assumed to exist in all loss distributions in Fig. 13. Under these circumstances the spanwise loss distribution pattern might, for instance, change from a single loss maximum to two in Fig. 14(*c*) and from a double peak in Fig. 14(*d*) to a triple. Tests by Wolf [38] on a cascade with $\alpha_1 = 32$ deg, $\alpha_2 = -58$ deg and $g/C = 0.8$ show that this feeding process continues up to a downstream distance $X/C_{ax} = 0.8$, preventing up to there the development of a full endwall boundary layer. For bigger downstream distances, the secondary losses start to rise rapidly. Tests on a nozzle blade by Gotthardt [23], Fig. 17, indicate the same characteristic change of the secondary loss evolution to occur at $X/C_{ax}=0.2$ (the figure presents the net increase of all secondary losses occurring downstream of the trailing edge plane).

The way in which the losses mix out is entirely unclear. There is not a single test which shows the complete downstream mixing process. Obviously the passage and trailing edge vortices play a significant role but their mutual interference is not clear. The fact that the passage vortex changes its position with respect to the trailing edge vortex as a function of the loading should play an important role for the downstream mixing.

In a real machine the increase of secondary losses due to wall shear stresses is interrupted when the flow enters the following blade row. To ensure the applicability of secondary loss data from straight cascades to a turbine stage, it is therefore advisable to select the downstream traverse plane at a distance corresponding to the distance between the blade rows. Such an approach was taken by Groschup [35]. In the absence of a direct application to a particular turbine, an axial distance equal to the throat seems to be adequate in most cases, since according to Dejc and Trojanovsky [39] this distance presents an optimum value for the axial interspace between two blade rows. The tests by Came [36] and Wolf [38] are made at about twice this distance. In any case, secondary loss data should also include mixing losses occurring downstream of the measurement plane. An idea of the order of magnitude may be obtained from the extreme case of Woods [40] who measured the flow conditions behind a low aspect ratio impulse cascade of 135 deg turning and $g/C = 0.59$ at a downstream distance of only 5 percent of the axial chord. Applying the momentum theorem to the flow between the measurement station and the uniform flow far downstream, the author calculates an increase for the sum of profile plus secondary losses of about 15 percent for an aspect ratio $H/C = 1.0$. As pointed out by Woods, the calculation does not take into account the shear stress integral in the measurement plane.

Conclusions

The experimental research on secondary flows over the last decade has resulted in a fairly detailed description of the complex endwall flow patterns in turbine blade passages. More information will be needed concerning the turbulent structure of the endwall flow and the mixing processes on both the blade suction side and downstream of the cascade. However, the aim of basic secondary flow research is not only to provide a complete flow description, but also to evaluate the significance of the various flow aspects. This applies in particular to the leading edge vortices and their associated three-dimensional separation lines. It is absolutely essential to know whether they are only of local or of overall significance, since this conditions to a large extent the choice of the appropriate endwall flow analysis method. From a limited

number of experiments, it appears that the importance of leading edge effects is closely related to the incidence angle. This leads us to secondary flows at off design conditions, an area which has been given too little attention up to now.

References

1 Turner, J. R., "An Investigation of the Endwall Boundary Layer of a Turbine-Nozzle Cascade," ASME *Transactions*, Nov. 1957.

2 Dunham, J., "A Review of Cascade Data on Secondary Losses in Turbines," *J. Mech. Engrg. Sci.*, Vol. 12, 1970.

3 Tall, W. A., "Understanding Turbine Secondary Flow," *Secondary Flows in Turbomachines*, AGARD CP 214, 1977.

4 Hawthorne, W. R., "Rotational Flow Through Cascades," *J. Mech. & Appl. Math.*, Vol. 3, 1955.

5 Herzig, H. Z., Hansen, A. G., and Costello, G. R., "Visualization Study of Secondary Flow in Cascades," NACA TN 1163, 1954.

6 Armstrong, NcD., "The Secondary Low in a Cascade of Turbine Blades," ARC R&M 2979, 1955.

7 Fritsche, A., "Strömungsvorgänge in Schaufelgittern," *Techn. Rundschau Sulzer*, No. 3, 1955.

8 Klein, A., "Untersuchungen über den Einfluss der Zuström-grenzschicht auf die Sekundärströmung in den Beschaufelungen von Axialturbinen," *Forsch. Ing.*, Bd 32, Nr 6, 1966; (English translation: Investigation of the Entry Boundary Layer on the Secondary Flows in the Blading of Axial Turbines, BHRA T 1004, 1966).

9 Bölcs, A., "Flow Investigations in a Water Channel at Subsonic and Supersonic Velocities," *Escher Wyss News*, Vol. 42, No. 1, 1969.

10 Blair, M. F., "An Experimental Study of Heat Transfer and Film Cooling on Large-Scale Turbine Endwalls," ASME *Journal of Heat Transfer*, Vol. 96, No. 4, Nov. 1974, pp. 524–529.

11 Langston, L. S., Nice, M. L., and Hooper, R. M., "Three-Dimensional Flow Within a Turbine Blade Passage," ASME JOURNAL OF ENGINEERING FOR POWER, Vol. 99, No. 1, Jan. 1977, pp. 21–28.

12 Sjolander, S. A., "The Endwall Boundary Layer in an Annular Cascade to Turbine Nozzle Guide Vanes," Carleton U., Canada, TR ME/A 75–4.

13 Langston, L. S., "Crossflows in a Turbine Cascade Passage," ASME JOURNAL OF ENGINEERING FOR POWER, Vol. 102, No. 4, Oct. 1980, pp. 866–874.

14 Marchal, P., and Sieverding, C. H., "Secondary Flows Within Turbomachinery Bladings," *Secondary Flows in Turbomachines*, AGARD CP 214, 1977.

15 Gaugler, R. E., and Russell, L. M., "Streakline Flow Visualization Study of a Horseshoe Vortex in a Large-Scale, Two-Dimensional Turbine Stator Cascade," ASME Paper No. 80-GT-4.

16 Moore, J., and Smith, B. L., "Flow in a Turbine Cascade. Part 2: Measurement of Flow Trajectories by Ethylene Detection," ASME Paper No. 83-GT-69.

17 Sieverding, C. H., and Van den Bosch, P., "The Use of Coloured Smoke to Visualize Secondary Flows in a Turbine-Blade Cascade," *Journal of Fluid Mechanics*, Vol. 134, Sept. 1983, pp. 85–89.

18 Moore, J., and Ransmayr, A., "Flow in a Turbine Cascade, Part 1: Losses and Leading Edge Effects," ASME Paper No. 83-GT-68.

19 Gregory-Smith, D. G., and Graves, C. P., "Secondary Flows and Losses in a Turbine Cascade," *Viscous Effects in Turbomachines*, AGARD CP 351, 1983.

20 Belik, L., "Secondary Losses in Turbine Blade Cascade With Low Aspect Ratio and Large Deflection," *Proc. 6th Conf. on Steam Turbines of Large-Power Output*, Plzen, Czechoslovakia, Sept. 1975.

21 Moore, J., "Flow Trajectories, Mixing and Entropy Fluxes in a Turbine Cascade," *Viscous Effects in Turbomachines*, AGARD CP 351, 1983.

22 Langston, L. S., and Boyle, M. T., "A New Surface Streamline Flow Visualization Technique," *J. Fluid Mechanics*, Vol. 125, Dec. 1982, pp. 53–57.

23 Gotthardt, H., "Theoretische und experimentelle Untersuchungen an ebenen Turbinengittern mit Pfeilung und V-Stellung," dissertation, TU Braunschweig, Germany, 1983.

24 Belik, L., "The Secondary Flows Around a Cylinder Mounted on a Flat Plate," *Aer. Qua.*, Vol. XXIV, pt. 1, Feb. 1973, pp. 47–54.

25 Stastny, H., "Visualization of Some Phenomena Connected with Nonpotentiality of the Flow in Steam Turbines," *Int. Symp. on Flow Visualization*, Bochum, Germany, Sept. 1980, pp. 261–266.

26 Peake, D. J., Galway, R. D., and Rainbird, W. J., "The Three-Dimensional Separation of a Plane, Incompressible, Laminar Boundary Layer Produced by a Rankine Oval Mounted Normal to a Flat Plate," NRC LR 446, 1965.

27 East, L. F., and Hoxey, R. P., "Low-Speed Three-Dimensional Turbulent Boundary Layer Data, Part 1," RAE TR 69041, 1969.

28 Senoo, Y., "The Boundary Layer on the Endwall of a Turbine Nozzle Cascade," ASME JOURNAL OF ENGINEERING FOR POWER, Vol. 80, 1958.

29 Bario, F., Leboeuf, F., and Papailiou, K. D., "Study of Secondary Flows in Blade Cascades of Turbomachines," ASME JOURNAL OF ENGINEERING FOR POWER, Vol. 104, No. 2, April 1982, pp. 497–509.

30 Bailey, D. A., "Study of Mean and Turbulent Velocity Fields in a Large-Scale Turbine-Vane Passage," ASME JOURNAL OF ENGINEERING FOR POWER, Vol. 102, No. 1, Jan. 1980, pp. 88–97.

31 Sieverding, C. H., Boletis, E., and Van Hove, W., "Experimental Study of the Three-Dimensional Flow Field in an Annular Turbine Nozzle Guide Vane," ASME Paper No. 83-GT-120; (also VKI Preprint 1982–38).

32 Belik, L., "Three-Dimensional and Relaminarization Effects in Turbine Blade Cascades–An Experimental Study," JSME-ASME Joint Gas Turbine Conf., Paper 37, 1977.

33 Gregory-Smith, D. G., "Secondary Flows and Losses in Axial Flow Turbines," ASME JOURNAL OF ENGINEERING FOR POWER, Vol. 104, No. 4, Oct. 1982, pp. 819–822.

34 Marchal, P., "Etude des écoulements secondaires en grille d'aubes de détente," Ph.D. thesis, U. Libre de Bruxelles, 1980.

35 Groschup, G., "Strömungstechnische Untersuchung Einer Axialturbinenstufe in Vergleich zum Verhalten der Ebenen Gitter Ihrer Beschaufelung," dissertation TU Hannover, Germany, 1977.

36 Came, P. M., "Secondary Loss Measurements in a Cascade of Turbine Blades," Inst. Mech. Engrs, C33/73.

37 Wolf, H., "Ein Beitrag Zum Problem der Sekundärströmung in Schaufelgitttern," *Wiss. Z. Techn.*, Hochschule Dresden Bd 7, Heft 4, 1958/59.

38 Wolf, H., "Die Randverluste in geraden Schaufelgitter," *Wiss. Z. Techn.*, Hochschule Dresden, Bd 10, Heft 2, 1961.

39 Dejc, M. E., and Trojanovskij, B. M., "Untersuchung und Berechnung axialer Turbinenstufen," Berlin, VEB Verlag Technik, 1973.

40 Woods, J. R., "An Investigation of Secondary Flow Phenomena and Associated Losses in a High Deflection Turbine Cascade," Ph.D. thesis, Naval Post Graduate School, 1972.

41 Graziani, R. A., Blair, M. F., Taylor, J. R., and Mayle, R. E., "An Experimental Study of Endwall and Airfoil Surface Heat Transfer in a Large-Scale Turbine Blade Cascade," ASME JOURNAL OF ENGINEERING FOR POWER, Vol. 102, No. 2, Apr. 1980, pp. 257–267.

42 Sieverding, C. H., and Wilputte, P., "Influence of Mach Number and Endwall Cooling on Secondary Flows in a Straight Nozzle Cascade," ASME JOURNAL OF ENGINEERING FOR POWER, Vol. 103, No. 2, Apr. 1981, pp. 257–264; (also VKI Preprint 1980–02).

43 Hah, C., "A Navier-Stokes Analysis of Three-Dimensional Turbulent Flows Inside Turbine Blade Rows at Design and Off-Design Conditions," ASME Paper No. 83-GT-40.

D. G. Holmes

S. S. Tong

General Electric Company,
Corporate Research and Development Center,
Schenectady, N.Y. 12301

A Three-Dimensional Euler Solver for Turbomachinery Blade Rows

This paper describes a three-dimensional Euler solver for turbomachinery blade rows. The algorithm used is based on the explicit, four-step, finite volume method advocated by Jameson. Some of the issues addressed include the spatial interpolation scheme compatible with the wall boundary condition; the appropriate interpolation scheme for correctly interpolating a uniform absolute flow in a rotating coordinate system; smoothing techniques that assure global conservation; and code vectorization. The Euler solver has been tested on turbine nozzles, turbine rotors, centrifugal compressor rotors, transonic fans, and propellers, in all cases without any modification to the code or any parameter adjustment.

1 Introduction

This paper describes a fully operational Euler code for three-dimensional turbomachinery blade rows and propellers. The algorithm is based on the scheme described by Jameson et al. [1].

The Euler equations are discretized in space using a straightforward finite volume scheme that is equivalent to central spatial differencing on a regular, rectangular grid. The discretized equations are marched forward in time to a steady state using an explicit, four-step Runge-Kutta scheme. The four-step time marching is stable out to a Courant number of $2\sqrt{2}$ and tolerates the use of local time step limits. As with any central difference scheme, the algorithm is susceptible to wiggles, and some smoothing is needed to suppress the wiggles. Smoothing is also needed to capture shocks. Both smoothing tasks are fulfilled by a blend of second and fourth order smoothing, with the coefficient of the second order smoothing proportional to the second spatial difference of the pressure.

This Jameson scheme has several advantages: 1) Flexibility in algorithm modification and coding; the spatial interpolation, time marching and smoothing are handled independently, and can be modified independently. 2) The overall scheme is fully conservative. Conservative equations are solved with a conservative interpolation scheme, and the added smoothing is cast in a conservative form. The calculated mass flows into and out of the blade row match to within the accumulated roundoff error; the net momentum flux into the blade row exactly balances the net pressure force on the blade row; the net energy flux into the blade row exactly balances the power absorbed by the blade row. 3) The smoothing is brought out into the open and under the user's control, rather than buried in, say, an upwind spatial interpolation scheme. The user is able to adjust the smoothing to the lowest possible level consistent with stability and freedom from wiggles, in order to obtain solutions very little corrupted by numerical diffusion. 4) The scheme is very systematic, and thus easy to code and very vectorizable.

In the following discussion of the algorithm, the only features of the algorithm that are discussed at length are those that are unique to the turbomachinery blade row application, or are changes in the algorithm incorporated by the author. For a clear introduction to the algorithm the reader is referred to the paper of Jameson et al. [1].

Sample solutions are shown for a high turning turbine nozzle and a turbine rotor. Both solutions were obtained with the same code, and without any tuning of the code or parameter adjustments. Solutions have also been obtained for centrifugal compressor rotors, axial compressor blade rows, transonic fans, and propellers.

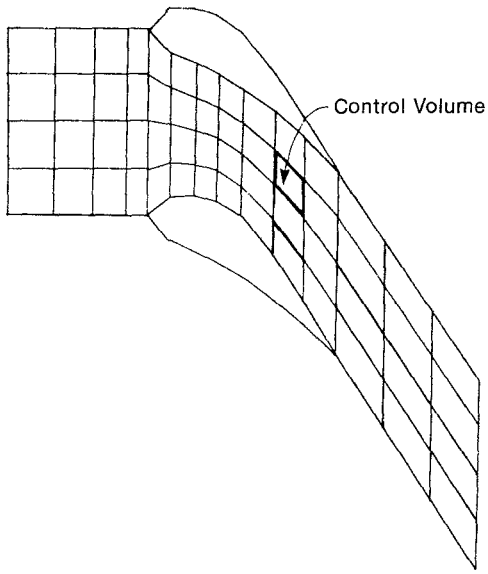

Fig. 1 The finite volume discretization

Contributed by the Gas Turbine Division of THE AMERICAN SOCIETY OF MECHANICAL ENGINEERS and presented at the 29th International Gas Turbine Conference and Exhibit, Amsterdam, The Netherlands, June 4-7, 1984. Manuscript received at ASME Headquarters, January 5, 1984. Paper No. 84-GT-79.

2 Algorithm Description

The Equations of Motion. We solve for the absolute flow variables, ρ, ρv and ρe, in a Cartesian reference frame which may be rotating with a uniform angular velocity Ω about the z-axis. The equations may also be formulated in terms of the relative flow variables, however, using the absolute flow variables gives much better results for propellers where the absolute far-field flow is uniform but the relative flow is nonuniform. The use of Cartesian, rather than cylindrical polar coordinates simplifies the interior algorithm, but complicates the inlet, outlet and periodic boundary condition algorithms. There are, however, many more interior points than boundary points. The equations of motion can be written

$$\frac{\partial U}{\partial t}+\frac{\partial F}{\partial x}+\frac{\partial G}{\partial y}+\frac{\partial H}{\partial z}=E \tag{1}$$

where:

$$U=\begin{bmatrix}\rho\\ \rho v_x\\ \rho v_y\\ \rho v_z\\ \rho e\end{bmatrix} \qquad E=\begin{bmatrix}0\\ \Omega\rho v_y\\ -\Omega\rho v_x\\ 0\\ 0\end{bmatrix}$$

$$F=\begin{bmatrix}\rho w_x\\ \rho w_x v_x+p\\ \rho w_x v_y\\ \rho w_x v_z\\ \rho w_x h+u_x p\end{bmatrix} \quad G=\begin{bmatrix}\rho w_y\\ \rho w_y v_x\\ \rho w_y v_y+p\\ \rho w_y v_z\\ \rho w_y h+u_y p\end{bmatrix} \tag{2}$$

$$H=\begin{bmatrix}\rho w_z\\ \rho w_z v_x\\ \rho w_z v_y\\ \rho w_z v_z+p\\ \rho w_z h\end{bmatrix}$$

where ρ is the density, p the pressure, e is the total internal energy, h is the total enthalpy, (v_x, v_y, v_z) is the absolute velocity, and (w_x, w_y, w_z) is the relative velocity, given by

$$\begin{aligned} w_x &= v_x-u_x\\ w_y &= v_y-u_y\\ w_z &= v_z \end{aligned} \tag{3}$$

and the "whirl" velocities u_x and u_y are

$$\begin{aligned} u_x &= -\Omega y\\ u_y &= \Omega x. \end{aligned} \tag{4}$$

Spatial Interpolation. The computational grid is formed from three intersecting families of grid lines. The points of intersection of the three families of grid lines define the vertices of the hexahedral control volumes (Fig. 1). The control volumes form a nonoverlapping, contiguous set of cells filling the whole computational domain. The flow variables are not defined on the grid points, which are the vertices of the control volumes, but on the control volumes themselves. The flow variables can be thought of as being defined as "average" values with a cell, or as values at a point at the center of a cell. The time marching algorithm makes no reference to the coordinates of the cell centers, so perhaps the interpretation of the flow variables as cell average values is more correct.

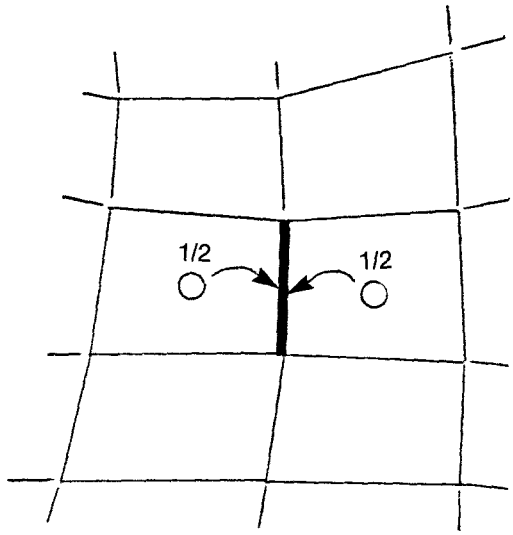

Fig. 2 Equal weight interpolation from control volumes to a face

In the finite volume scheme, volume integrals of $\partial F/\partial x$, etc., are converted into surface integrals, so that

$$I=\int_V\left[\frac{\partial F}{\partial x}+\frac{\partial G}{\partial y}+\frac{\partial H}{\partial z}\right]dV=\int_A\left[FdA_x+GdA_y+HdA_z\right] \tag{5}$$

where $d\mathbf{A}=(dA_x, dA_y, dA_z)$ is the vector element of the cell surface, positive inward. The quantity I is physically interpretable as the integrated or net flux of mass, momentum or energy into the control volume. For the continuity equation, I becomes

$$\dot{m}=\int_A \rho\mathbf{w}\cdot d\mathbf{A} \tag{6}$$

For the momentum equations, I becomes

$$\mathbf{Q}+\mathbf{P}=\int_A \rho v\mathbf{w}\cdot d\mathbf{A}+\int_A p d\mathbf{A} \tag{7}$$

where we have separated out the momentum flux $\mathbf{Q}$ and the pressure force $\mathbf{P}$.

For the energy equation, I becomes:

$$T+W=\int_A \rho h\mathbf{w}\cdot d\mathbf{A}+\int_A p\mathbf{u}\cdot d\mathbf{A} \tag{8}$$

where we have separated out the energy flux T and the "whirl work" W. If the finite volume interpolation scheme is implemented using equation (5), we require that the flux vectors F, G, and H be estimated on each face. The estimate is made by interpolating flow variables, with equal weight, from the two cells that share the face (Fig. 2). The interpolation can be done in two ways:

$$\text{(i) } F_{\text{face}}=\frac{1}{2}\left[F(U_A)+F(U_B)\right] \tag{9}$$

$$\text{(ii) } F_{\text{face}}=F\left[\frac{1}{2}\left(U_A+U_B\right)\right]. \tag{10}$$

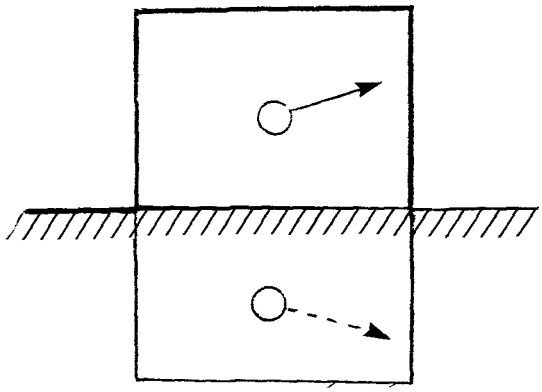

Fig. 3 Implementing the wall boundary condition using a phantom control volume

In the first scheme the flux vectors are evaluated at the cells and then interpolated to the faces. In the second scheme the flow variables U are interpolated to the faces, where the flux vectors are then computed.

Numerical experiments show that scheme (i) can be unstable near those solid wall grid boundaries where the surface curvature is high and that even when it is stable it produces large stagnation pressure errors near the walls. A possible explanation can be made with reference to Fig. 3. At the face lying in the wall boundary, we require that there be no mass, momentum or energy fluxes through the wall, and that the only contributions made by the face to the integrals over the cell surface come from the pressure terms in the momentum and energy equations. One way of enforcing this requirement is define a "phantom" cell on the other side of the face, and to define flow variables U at this cell so that the wall boundary fluxes of mass, momentum and energy are zero. In general, there is no set of flow variables U at the phantom cell that can give zero fluxes using scheme (i). Only when the velocity at the interior cell adjacent to the wall is exactly parallel to the wall can flow variables at the phantom cell be defined to give zero fluxes. If the cells are very small, or, equivalently, the curvature is very low, the velocity at the interior cell becomes closely parallel to the wall, and the scheme becomes stable.

For scheme (ii), on the other hand, it is always possible to define U at the phantom boundary cell so as to give zero fluxes. Scheme (ii) is always stable, but is more expensive than scheme (i), as it requires three times as many evaluations of F, G, and H from U as scheme (i).

Two other schemes have been tried. Both are stable, and with a computational cost similar to scheme (i). Both schemes are inspired, not by the formal style of equation (5), but by the more physical expressions in equations (6) through (8). In scheme (iii), the volume flux through a face is estimated as:

$$\dot{q} = \frac{1}{2}(\mathbf{w}_A + \mathbf{w}_B)\cdot\mathbf{A} \tag{11}$$

where $\mathbf{A}$ is the vector face area. All convective fluxes are now computed using this volume flux. The mass flux is:

$$\dot{m} = \frac{1}{2}\dot{q}(\rho_A + \rho_B) \tag{12}$$

The momentum flux is:

$$\mathbf{Q} = \frac{1}{2}\dot{q}[(\rho\mathbf{v})_A + (\rho\mathbf{v})_B] \tag{13}$$

The pressure force is:

$$\mathbf{P} = \frac{1}{2}(p_A + p_B)\mathbf{A} \tag{14}$$

The energy flux is:

$$T = \frac{1}{2}\dot{q}[(\rho h)_A + (\rho h)_B] \tag{15}$$

(The interpolation for the whirl work will be described later.)

This scheme is the one used by Jameson, although it takes a careful reading of his papers to realize it. Suitable flow variables U can be devised at the phantom boundary cell to give zero volume flux $\dot{q}$, and thus zero fluxes $\dot{m}$, $\mathbf{Q}$ and T. Once again, this perhaps helps explain the stability of the scheme.

A final scheme, scheme (iv), is almost the same as (iii), but calculates the mass flux, rather than the volume flux:

$$\dot{m} = \frac{1}{2}[(\rho\mathbf{w})_A + (\rho\mathbf{w})_B]\cdot\mathbf{A}. \tag{16}$$

The momentum flux $\mathbf{Q}$ is then:

$$\mathbf{Q} = \frac{1}{2}\dot{m}(\mathbf{v}_A + \mathbf{v}_B) \tag{17}$$

and the energy flux T is:

$$T = \frac{1}{2}\dot{m}(h_A + h_B) \tag{18}$$

This scheme differs from scheme (iii) in that it produces somewhat more wiggly solutions. The reason for the poorer behavior is unknown.

Scheme (iii) is currently the preferred scheme. Other schemes are possible, and should be tried. In view of the variations in stability, cost and wiggle generation among these four schemes, there may yet be an even better scheme to be found.

It should be pointed out that the chosen finite volume approach, which interpolates from cells to faces, performs rather poorly when the grid has variable spacing between the grid lines. The essential task of the scheme can be seen as the evaluation first derivatives such as $\partial F/\partial x$. On a uniform mesh, with all control volumes identical (although they may be sheared into parallelepipeds), one can show that $\partial F/\partial x$ can be calculated correctly for F a *quadratic* function of the coordinates (x, y, z). Shearing the grid, so that the grid lines are not orthogonal, does not change the *order* of the truncation error associated with the estimation of $\partial F/\partial x$, although it does increase the *magnitude* of the truncation error. On a nonuniform mesh, with varying sizes and shapes of control volumes, the accuracy of the scheme drops precipitously, and the interpolation scheme only evaluates $\partial F/\partial x$ correctly when F is a *constant* (and $\partial F/\partial x$ is zero). This property of correctly evaluating the derivative of a constant, regardless of grid distortion, is an essential and useful property of any finite volume scheme, but one wishes for more than this minimal accuracy under grid distortion. Note that a scheme such as Ni's [2], where the flow variables are defined at the control volume vertices, does a lot better on a nonuniform grid. Ni's scheme can evaluate the derivative of F correctly on a nonuniform grid when F is a *linear* function of the coordinates (x, y, z).

The ability to interpolate a uniform flow correctly, regardless of grid nonuniformity, becomes essential in analyzing propeller flows, where the far-field flow is uniform, and the grid may be highly nonuniform. But propeller solutions must be obtained in a coordinate system rotating with the propeller, and the resulting whirl velocity $\mathbf{u}$ is not uniform in the far field. The terms involving the whirl velocity must be handled separately, and in a special way. The volume flux through a face is:

$$\dot{q} = \int_A \mathbf{v}\cdot d\mathbf{A} - \int_A \mathbf{u}\cdot d\mathbf{A} \tag{19}$$

and this can be approximated as

$$\dot{q} = \frac{1}{2}(v_A + v_B)\cdot\mathbf{A} - \int_A \mathbf{u}\cdot d\mathbf{A}$$

$$= \frac{1}{2}(v_A + v_B)\cdot\mathbf{A} + \Omega\int_A y dA_x - \Omega\int_A x dA_y \qquad (20)$$

i.e., the absolute volume flux is handled in the usual way, but the whirl volume flux is left in integral form. This integral of the whirl volume flux is a purely geometrical quantity, and can be evaluated exactly. Thus, no approximation is involved in the evaluation of terms involving **u**, the only variable that persists in its nonuniformity in the far field.

The added terms involving **u** in the energy equation are treated in exactly the same way. The whirl work becomes

$$W = \frac{1}{2}(p_A + p_B)\int_A \mathbf{u}\cdot d\mathbf{A}$$

$$= \frac{1}{2}(p_A + p_B)\left[-\Omega\int_A y dA_x + \Omega\int_A x dA_y\right]. \qquad (21)$$

Without these special treatments of the flux terms involving **u**, it is impossible to obtain decent propeller solutions, with smooth far-field flows.

The Time Step Limit. Grids for turbomachinery blade row calculations tend to have regions of high grid distortion. It is important to be able to calculate tight upper bounds on the permissible time steps in such regions of high distortion. Accordingly, an analysis of the time step limit on a distorted three-dimensional grid has been done, using the technique described by Richtmeyer and Morton [3]. The analysis assumes small perturbations of a uniform flow on a uniform grid which is composed of an array of identical parallelepipeds. If (x, y, z) are the Cartesian coordinates associated with the distorted grid, and (ξ, ζ, η) are the coordinates of the transformed, cubical grid, we define quantities like:

$$A_x^\xi = \frac{\partial y}{\partial \zeta}\cdot\frac{\partial z}{\partial \eta} - \frac{\partial z}{\partial \zeta}\cdot\frac{\partial y}{\partial \eta},$$

$$A_y^\xi = \frac{\partial z}{\partial \zeta}\cdot\frac{\partial x}{\partial \eta} - \frac{\partial x}{\partial \zeta}\cdot\frac{\partial z}{\partial \eta}, \text{etc.} \qquad (22)$$

In this uniform mesh, $\mathbf{A}^\xi = (A_x^\xi, A_y^\xi, A_z^\xi)$ is the (vector) area of the control volume faces pierced by the ξ-coordinate lines. We define the relative contravariant velocities as:

$$w^\xi = \mathbf{w}\cdot\mathbf{A}^\xi, w^\zeta = \mathbf{w}\cdot\mathbf{A}^\zeta, w^\eta = \mathbf{w}\cdot\mathbf{A}^\eta \qquad (23)$$

and a quantity $\tilde{A}$ as:

$$\tilde{A} = [\mathbf{A}^\xi\cdot\mathbf{A}^\xi + \mathbf{A}^\zeta\cdot\mathbf{A}^\zeta + \mathbf{A}^\eta\cdot\mathbf{A}^\eta + 2(|\mathbf{A}^\xi\cdot\mathbf{A}^\zeta| + |\mathbf{A}^\zeta\cdot\mathbf{A}^\eta| + |\mathbf{A}^\eta\cdot\mathbf{A}^\xi|)]^{1/2}. \qquad (24)$$

The time step limit is:

$$\Delta t \le \frac{\lambda V}{|w^\xi| + |w^\zeta| + |w^\eta| + \tilde{A}c} \qquad (25)$$

where V is the volume of the control volume, c is the local sound speed, and λ is the limiting CFL number.

This time step limit has proved to be reliable and to be a fairly tight bound. The practical boundary between stability and instability appears to be very close to the theoretical limit of $2\sqrt{2}$. No difficulties have ever been encountered in using local time steps, with the time step at each control volume set to a specified local CFL number. On a real, nonuniform mesh, quantities such as $\mathbf{A}^\xi$ are calculated as the average of the two face areas on either side of the control volume.

The quantity $\tilde{A}$ is interesting. If the time step analysis is carried through in two dimensions, the quantity analogous to $\tilde{A}$ is the length of the longest diagonal of the cell. The obvious three-dimensional analog would be the area of the largest shadow cast by the volume. One can show that $\tilde{A}$ is indeed the largest shadow for the cases where the volume is a cube or a thin lamina. To prove that $\tilde{A}$ is the largest shadow for the general case would be an enjoyable task for anyone with a bent for analytical geometry.

The Cell Volume. There has been some discussion of the correct way to calculate the volume of a distorted control volume (see, for example, Kordulla and Venokur [4]). We make two further minor contributions to this discussion. The first is that since, according to equation (25), when local time stepping is used the time step is proportional to the volume, and the changes in the flow variables at each step are proportional to the time step divided by the volume, the value assigned to the volume is irrelevant. The only situation in which the volume appears directly in the algorithm is in the rotor case, where right-hand side terms like $\Omega\rho v_y$ are multiplied by the time step, but not divided by the volume.

In rotor cases, then, we need to know the cell volume. We propose as our second contribution, yet another formula for the volume. For each face, take the cross product of the two diagonals; dot this with the vector from any point to the center of the face (defined as the average of the four corner points) – the sum of these six scalars is the volume of the cell. This formula has several advantages. It does not involve an arbitrary partitioning of hexahedral volume into tetrahedra. The formula has been shown, by numerical experiments, to give identical results to a much more complex "exact" formula involving an integral over the hexahedral volume seen as a tri-linear isoparametric mapping of the volume on to a unit cube. And finally, the volumes of a group of cells are calculated without gaps or overlaps at the cell boundaries.

Smoothing. The smoothing algorithm follows closely the prescription of Jameson. In each grid direction the smoothing operators, both second and fourth order, are implemented as differences between, respectively, first and third difference operators. The first and third difference operators are defined on the control volume faces on either side of the cell and can be thought of as fictitious smoothing fluxes. A smoothing flux defined on a face is shared by the two cells adjacent to the face. The whole smoothing process is thus conservative. The fictitious smoothing fluxes on the six surfaces of a single cell may perturb the real, physical flux balance for the cell, but for a large block of cells, the smoothing fluxes at the interior faces cancel out, and the only perturbation to the physical flux balance for the block of cells comes from the smoothing fluxes on the exterior faces of the block. Local regions of high smoothing, as in a shock, may produce large local physical flux imbalances, but not global flux imbalances. The mass flux, for example, may be perturbed strongly in passing through a shock, but downstream of the shock the mass flux will recover its upstream value. This global conservation property of the smoothing algorithm is a valuable feature of the overall algorithm.

It is not obvious how the smoothing fluxes should be defined on the grid boundaries. Three possible approaches are:

(i) Set all smoothing fluxes to zero on the boundaries. This results in complete global conservation, but gives strong, one-sided smoothing at the cells on the grid boundaries.

(ii) Set smoothing fluxes at boundary cell faces equal to the fluxes at the adjacent interior faces. This gives zero smoothing at the cells on the grid boundaries, but may give global conservation errors.

(iii) Use extrapolated, fictitious flow variables at phantom cells exterior to the grid to compute the boundary smoothing fluxes. This approach may also produce global conservation errors.

We have adopted approach (i) i.e., use zero boundary

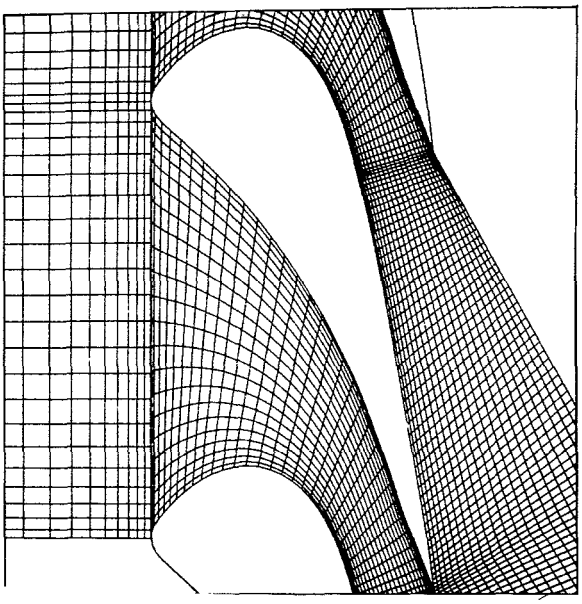

Fig. 4 Computational grid, VKI turbine nozzle

smoothing fluxes. This gives global conservation and the effects of one-sided smoothing at the solid walls are not obviously detrimental. (At the inlet and outlet the flow is usually fairly uniform, so the one-sided smoothing is innocuous.) At the periodic boundaries there is no need to zero the smoothing fluxes; the periodicity condition gives enough information for the computation of the correct fluxes.

Boundary Conditions. The wall boundary condition is adopted from Jameson. Since all convective fluxes are zero at the wall, the only quantities we need to know at the wall are the whirl volume flux and the pressure. The whirl volume flux is known from the grid geometry. The pressure is obtained from the normal momentum equation, as in Jameson's paper. His formulation has to be extended to three dimensions, and terms allowing for the centripetal and Coriolis acceleration components normal to the wall must be included.

The inlet and outlet boundary conditions are adopted from Denton [5]. At the inlet, four conditions are specified. Two conditions are fixed stagnation pressure and fixed stagnation enthalpy. The other two are either the two independent direction cosines of the absolute or relative flow angles, or the two components of tangential velocity. The one flow variable that must be extrapolated from the interior is the pressure. The pressure extrapolation is lagged using the simple relaxation procedure proposed by Denton. At the outlet the pressure is specified, and four flow variables must be extrapolated – the three components of velocity and the internal energy. The specified spanwise pressure distribution at the outlet may optionally be adjusted to preserve radial equilibrium as the calculation proceeds.

For propeller problems the inlet boundary conditions are replaced by the free stream inlet boundary conditions proposed by Jameson. For propeller problems there is also an outer free stream boundary. This boundary is sloped sightly so that the flow at this boundary is always an inflow, and an inflow condition can be used. For propeller problems at the outlet the outlet boundary condition described above is used. The radial equilibrium option is used because of the possibility that high swirl in the propeller slipstream would prevent a return to the free stream pressure. Radial equilibrium is enforced relative to the free stream pressure at the outer free stream boundary.

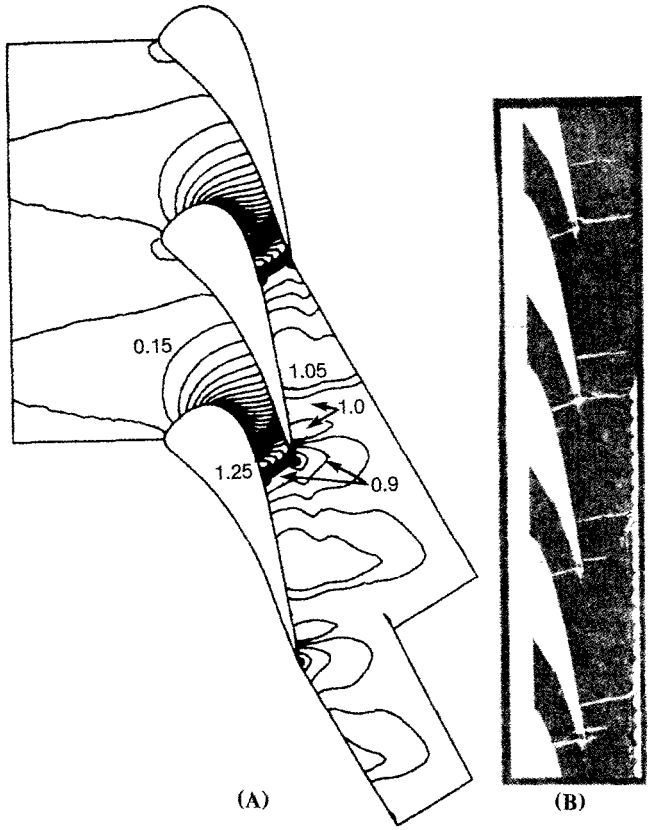

Fig. 5 Computed Mach number contours (A), and Schlieren photograph of the flow (B), for the VKI turbine nozzle

3 Test Cases

Out of the wide variety of test cases that have been run, two are reported here. They are a high turning transonic turbine nozzle from the von Karman Institute, and the low Mach number turbine rotor reported by Dring.

VKI Nozzle. In a 1981 Lecture Series at the von Karman Institute in Brussels [6], participants were challenged to calculate the flow through a high turning transonic turbine nozzle for which experimental data had been obtained. The seven Euler solutions that were submitted were all two dimensional and all blind in that the calculations were performed in ignorance of the experimental data. The solution we show here was not one of the submitted solutions. It was made after the lecture series and with the benefit of the experimental data to compare with the calculated solution.

The grid used in the calculation is shown in Fig. 4. It is an H-grid, and as the calculation is only two dimensional, it is rather generous (144 × 22 cells). The blunt trailing edge of the blade is modeled as a wedge, simulating the recirculation zone aft of the blunt trailing edge. This is probably the best way to handle the blunt trailing with an inviscid code. Ideally, the wedge should carry no net pressure load, though this might take several cycles of calculation and wedge adjustment to achieve.

Figure 5 shows the calculated Mach number contours along with a Schlieren photograph of the flow, for an isentropic exit Mach number of unity. The calculation has clearly captured the entire system of three shocks that the flow passes through. Figure 6 shows the agreement is good between the calculated and measured isentropic Mach number distributions around the blade.

The calculations shown here are better, we believe, than any of the calculations submitted at the lecture series. The ex-

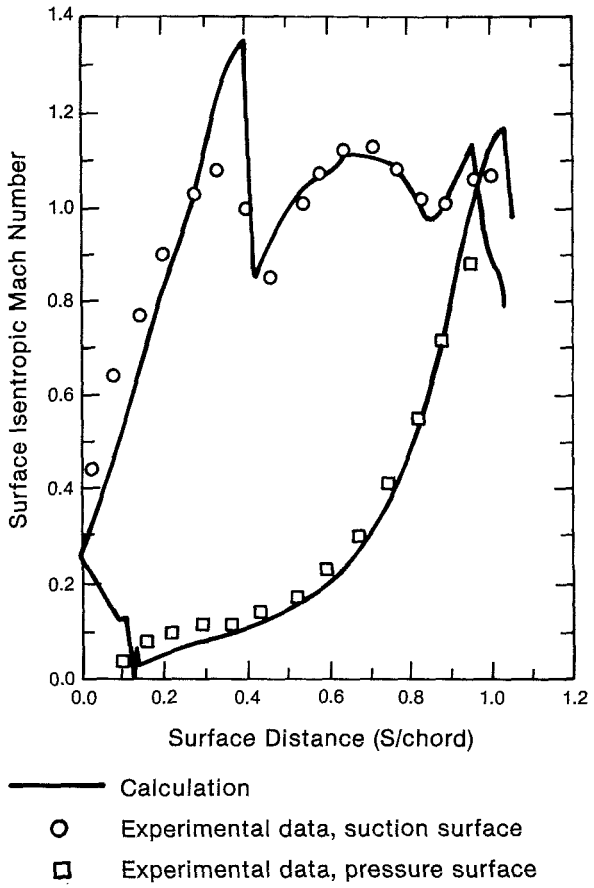

Fig. 6 Calculated and measured isentropic Mach number distribution along the blade surface, VKI turbine nozzle. (S/chord >1.0 indicates point inside the trailing edge wedge).

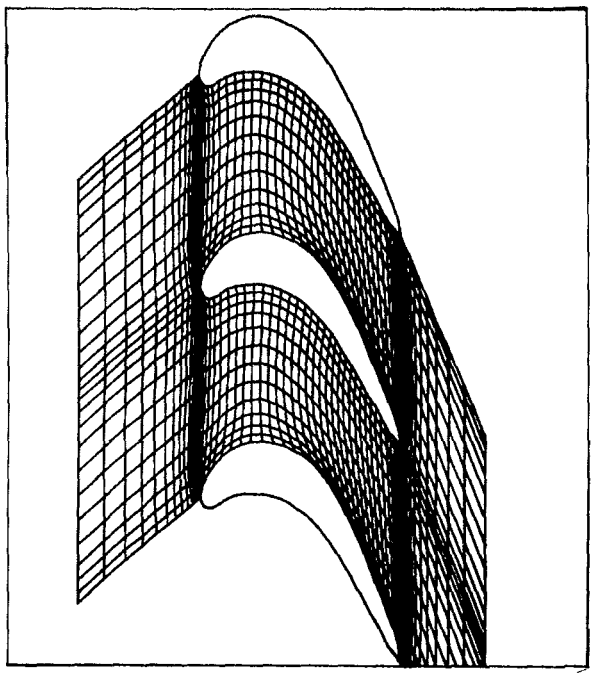

Fig. 7 The computational grid for the dring rotor, on a surface midway between hub and tip

cellent performance of the code on this problem cannot entirely be attributed to the quality of the code! Much of the solution quality comes from use of a wedge trailing edge model and from the grid. The grid is notable for its quantity

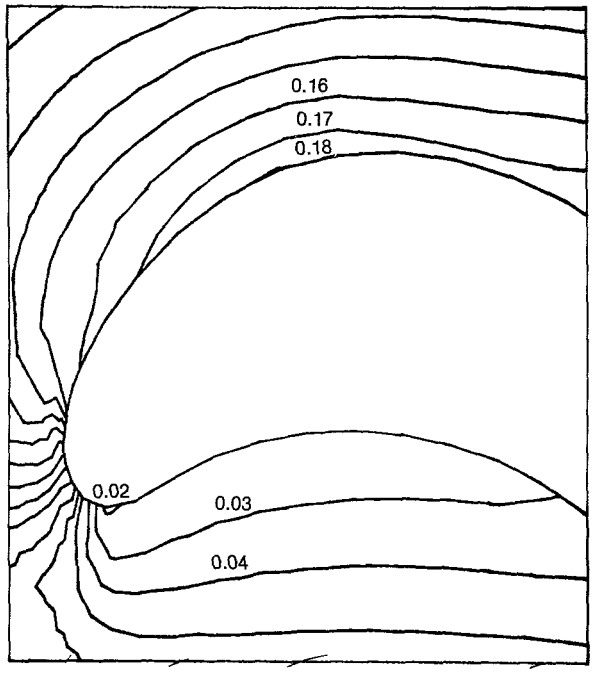

Fig. 8 Relative Mach number contours calculated on the grid surface shown in Fig. 7

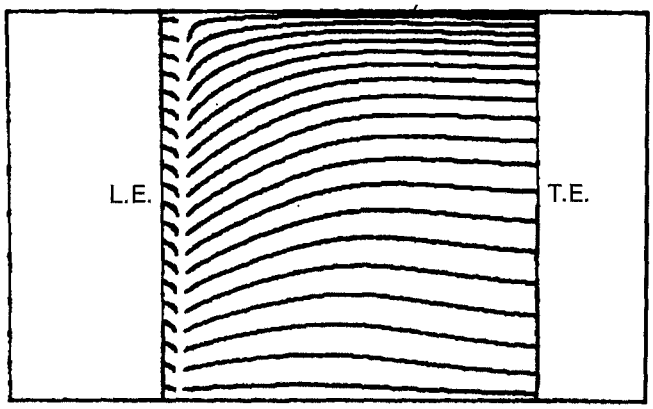

Fig. 9 Calculated blade pressure surface streamlines for the Dring rotor

(about three times as many grid points as in the submitted solutions) and its quality (a careful distribution of grid points, especially at the leading and trailing edges). An even better solution would result from the use of a combined H- and C-grid, as advocated by Ghia and Ghia [7].

The Turbine Rotor Test Case. The second test case is a turbine rotor blade row tested by Dring [8]. This case was of interest because of the strong radial flows observed by Dring on the pressure surface of the blade, and his assertion that this radial flow was a purely inviscid, relative eddy effect. If it is, the radial flows should show up in a Euler solution. The computational grid on a blade-to-blade grid surface is shown in Fig. 7. The blunt leading edge is modeled correctly without a cusp; the blunt trailing edge is replaced by a short wedge, simulating the recirculating flow zone downstream of the trailing edge.

The peak relative Mach number for this blade row is only about 0.2 so that the flow is virtually incompressible. The convergence of the Euler code was thus slow. Figure 8 shows calculated contours of relative Mach number on the same grid surface as shown in Fig. 7. The reason for the strong radial

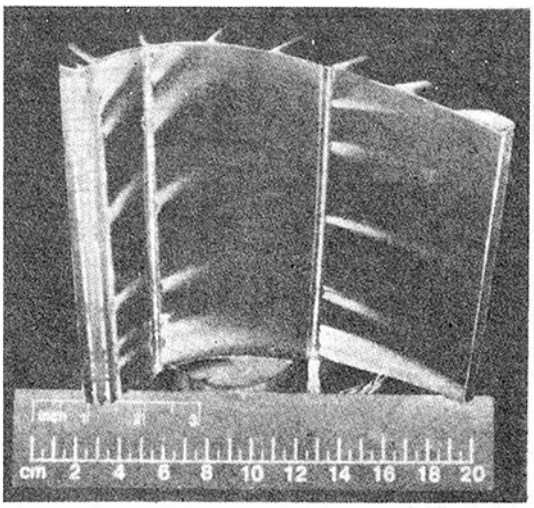

Fig. 10 Observed blade pressure surface streamlines for the Dring rotor

flow is apparent. A pool of virtually stagnant fluid (Mach number 0.03 or less) lies on the pressure surface aft of the leading edge. This stagnant fluid will be driven radially out by the centrifugal force field. Figure 9 shows calculated blade surface streamlines on the pressure surface. The strong radial flow is evident. Figure 10, taken from Dring, shows the striking resemblance of the blade surface streamlines observed experimentally.

Strong radial flows are not unique to this low Mach number rotor. Equally strong radial flows have been observed in other turbine rotor cases at engine operating conditions.

4 Discussion

Overall, the code based on the Jameson algorithm performs well. The program has run on a wide variety of turbomachinery flow problems from centrifugal compressor rotors to propellers, without any customization of the code or parameter adjustment. Whenever convergence problems have occurred, they have always been traced to bad grids and have vanished when the grid was improved.

The combination of the four-step time stepping scheme and the blended second and fourth order smoothing produces an algorithm with a high arithmetic count per unit operation, where a unit operation is defined as updating one control volume by one complete time step. The high arithmetic count is to some extent counteracted by the higher CFL limit made possible by the four-step scheme. Although the arithmetic count is high, the arithmetic is very systematic, and totally vectorizable. On a Cray One supercomputer, most loops vectorize with extremely long vector lengths and no loop fails to vectorize over at least one grid index. As a result the code runs extremely quickly, requiring less than 30 μs per basic operation on the Cray One. This is 300$\times$ the speed of the code on a Vax 11/780 super-minicomputer. A typical run time is about 10 min on a Cray One, for a 15,000 grid point case.

The H-grid, although it is probably the best "all-purpose" grid for turbomachinery flows, can perform poorly in some problems. High turning turbine nozzles give rise to severe grid shear with H-grids; and solving propeller problems with H-grids results in an excessive and wasteful meshing of the far field. Real benefits would be achieved by recoding to enable the program to accept a variety of grid topologies.

Acknowledgments

The authors would like to thank Anthony Jameson for his advice and criticism; Frank Hackert, who provided one of the two grids used in the test cases published here; Claus Sieverding, who provided the photograph in Fig. 5; and Kervyn Mach, who provided the photograph in Fig. 10.

References

1 Jameson, A., Schmidt, W., and Turkel, E., "Numerical Solutions of the Euler Equations by Finite Volume Methods Using Runge-Kutta Time-Stepping Schemes," AIAA Paper 81-1259, 1981.

2 Ni, R. H., "A Multiple-Grid Scheme for Solving the Euler Equations," *AIAA Journal*, Vol. 20, No. 11, 1982, pp. 1565–1571.

3 Richtmeyer, R. D., and Morton, K. W., *Difference Methods for Initial Value Problems*, Wiley, N.Y., 1967.

4 Kordulla, W., and Vinokur, M., "Efficient Computation of Volume in Flow Predictions," *AIAA Journal*, Vol. 21, No. 6, 1983, p. 917–918.

5 Denton, J. D., "A Time-Marching Method for Two- and Three-Dimensional Blade to Blade Flow," ARC R. and M. 3775, 1975.

6 *Workshop on Two- and Thee-Dimensional Flow Calculations in Turbine Bladings*, von Karman Institute, Apr. 1982.

7 Ghia, U., Ghia, K. N., and Ramamurti, R., "Hybrid C-H Grids for Turbomachinery Cascades," *Advances in Grid Generation*, ASME publication, 1983.

8 Dring, R. P., "The Relative Eddy in Axial Turbine Rotor Passages," ASME Paper 83-GT-22, 1983.

Assessment of Three-Dimensional Inviscid Codes and Loss Calculations for Turbine Aerodynamic Computations

L. A. Povinelli
NASA Lewis Research Center
Cleveland, Ohio 44135

An assessment of several three-dimensional inviscid turbine aerodynamic computer codes and loss models used at the NASA Lewis Research Center is presented. Five flow situations are examined, for which both experimental data and computational results are available. The five flows form a basis for the evalution of the computational procedures. It was concluded that stator flows may be calculated with a high degree of accuracy, whereas rotor flow fields are less accurately determined. Exploitation of contouring, leaning, bowing, and sweeping will require a three-dimensional viscous analysis technique.

Introduction

The design and analysis of turbines requires increasingly more analytical sophistication. This increase in sophistication is required because turbine design is becoming more complex as newer features such as endwall contouring, and leaning, bowing, and sweeping of the vanes and blades are used. These newer design features in combination with lower blade aspect ratios will lead to more complicated flows within turbine stages. Along with those flows, there will be an increasing uncertainty in the heat transfer to the endwalls and to the vane and blade surfaces. A greater fundamental knowledge of the flow will be required for effective design, including such items as boundary layer state and location of transition and the effect of turbulence on both transition and heat transfer. Interactions between the stator and rotor flow fields is also an important area that requires far greater understanding. The proper representation of the initial conditions entering the turbine, i.e., the effects of the combustor exit distortions, must also be understood as well as modeled. If these complex phenomena are to be modeled and computed, it will be necessary to develop three-dimensional viscous codes. A substantial amount of effort will be required for the development, assessment, refinement, and application of such codes. However, the potential returns in term of increased aerodynamic performance and improved heat transfer predictions make the effort worthwhile.

The current approach to the design and analysis of turbines is to rely on inviscid computations coupled with a boundary layer calculation and an assortment of loss correlations. By and large, turbomachinery designers have learned how to design and analyze turbines using that approach coupled with a great deal of intuitive judgment.

The scope of this paper is limited to the evaluation or assessment of the design procedure described above. For purposes of assessment, attention is focused on flow field computations using the inviscid computer codes, TSONIC, TSONIC/MERIDL [1, 2] and the DENTON code [3, 4]. The results from an integral boundary layer code, BLAYER [5], as well as profile, mixing, and endwall losses using Stewart's analysis [6] are also evaluated. Secondary flow losses, incidence losses, and tip clearance losses as determined from various loss correlations [7, 8] are evaluated as well. Comparisons are presented of the computed results with experimental data obtained from two-dimensional [9] and annular cascades [10–12], a large warm core turbine [13], and a small axial turbine [8]. The method or approach used to carry out the assessment of the computations is presented in the following section.

Method/Approach

The approach used in this paper is to examine a number of experimental studies for which selected aerodynamic parameters have also been computed, and to arrive at conclusions regarding our current predictive capability. Five experiments and corresponding computations will be examined in sequence. A brief description of each study will be presented, including, as appropriate, the design approach, the experimental measurements, the inviscid flow computations, the boundary layer loss calculation, and the calculations from correlations for secondary flow, incidence, and tip clearance losses. Each of the five studies were examined as to the adequacy of the computational scheme to predict the experimental data. On the basis of the com-

Contributed by the Gas Turbine Division of THE AMERICAN SOCIETY OF MECHANICAL ENGINEERS and presented at the 29th International Gas Turbine Conference and Exhibit, Amsterdam, The Netherlands, June 4–7, 1984. Manuscript received at ASME Headquarters January 12, 1984. Paper No. 84-GT-187.

Table 1 Vane design parameters

Aftermix flow angle, α, degrees	Aftermix velocity ratio, $(V/V_{cr})_2$	Trailing-edge blockage factor, b	Axial solidity factor, σ_x	Zwiefel loading factor, Ψ
67.0	0.778	0.111	0.929	0.774
74.9	.843	.079	.716	.701
75.0	.833	.122	.630	.792
77.5	.810	.124	.537	.790
79.6	.795	.076	.439	.813

parison, an evaluation or assessment of the predictive capability of the computer code will be presented. In addition, potential difficulties associated with the computational method will be identified. Specific examples will also be discussed regarding the needs for additional code verification.

The five flow examples chosen for study involved an examination of:

- Kinetic energy loss coefficients in two-dimensional cascade flow [9]
- Axial and tangential velocities and flow angles in an annular cascade [10, 11]
- Rotor temperature and flow angle with nonuniform inlet flow [13]
- Contoured endwall stator losses [12, 14]
- Small axial stage stator and rotor losses [8]

These examples will be discussed in sequential fashion in the following section.

Results

Rectangular Cascade Flow [9].

Vane Design. The first assessment was carried out for a series of stators having turning angles from 74 to 79.6 deg. The vanes were tested in a two-dimensional cascade in order to determine aerodynamic losses. The vane design parameters are shown in Table 1. The velocity diagram for each vane was selected using a meanline turbine design calculation and a common set of inlet conditions that are representative of an advanced high bypass ratio turbofan engine. The design stator exit velocity ratio was selected so that the absolute stator exit velocity was equal to the relative rotor exit velocity. In this way, the stage kinetic energy was minimized and the losses held to a minimum. Data for a more conservative 67-deg vane are also included for comparison.

Surface Velocity Distributions. TSONIC, which is a finite difference inviscid streamfunction solution on the vane-to-vane surface [1], was used to obtain the theoretical vane surface velocity distributions. The stream sheet thickness values used in the computation were modified to account for the effects of boundary layer growth and contraction on the endwalls of the cascade tunnel and the test section. A 1 percent total pressure loss from vane inlet to exit was assumed.

A comparison of the experimental and theoretical velocity distributions is shown in Fig. 1. Excellent agreement was obtained on the pressure side for all the vanes. The agreement on the suction surface is not as good, particularly with the higher exit angle vanes. The maximum deviation occurs with the 79.6-deg vane, where the theoretical value is about 10 percent higher than the data. In general, the difference between the theoretical and experimental suction surface velocity increased with vane exit angle.

Kinetic Energy Loss Coefficients. The computed velocity distributions were used as input for an integral method boundary layer code [5], BLAYER. The BLAYER code provided boundary layer parameters for an aerodynamic loss calculation [6]. Laminar to turbulent transition was imposed where laminar instability was predicted by the code (momentum thickness Reynolds number of 200–300). The experimental loss values were determined in the following way. Flow angle and pressure survey data were used to calculate velocity, mass flow, and axial and tangential components of momentum as a function of the probe position. Integration of these quantities yielded overall values of the foregoing quantities at the survey plane. The aftermix kinetic energy loss coefficient was calculated at the hypothetical aftermix station where flow conditions were assumed to be uniform. The procedure for making these calculations can be found in Appendix B of [15]. The experimental and theoretical losses are shown in Fig. 2 at the design ideal aftermix critical velocity ratio for each vane.

Two additional computations of the losses were made. The first computation was performed in order to eliminate the effect of a variable trailing edge thickness. The experimental loss data were adjusted to a common 0.1-cm trailing edge thickness, using the suggestion of [16], wherein 10 percent blockage yields 1 percent loss. The theoretical losses were also recalculated on the basis of a 0.1 cm thickness. The results are shown in Fig. 3(*a*). The second additional calculation was made using the experimental velocity distributions rather than the theoretical distributions. The results are shown in Fig.

Nomenclature

b = trailing edge blockage factor, $t/s \cos \alpha$
c_x = vane axial chord, cm
e = kinetic energy loss coefficient, $1 - (V/V_{id})^2$
p,P = absolute pressure, N/cm^2
R = radial position
R_x = rotor reaction, ΔP rotor/ΔP stage
s = vane pitch, cm
t = trailing edge thickness, cm
T = temperature, K
V,U = velocity, m/s
V_1, V_2 = velocity components (see Fig. 5)
w = mass flow rate per unit vane span, kg/s-cm
Z = axial position
α = flow angle or absolute swirl angle, deg
θ = angular position (Fig. 6)
η = efficiency
σ_x = axial solidity factor, c_x/s
ψ = Zweifel loading factor
ϕ = flow angle (see Fig. 5)

Subscripts

cr = critical condition
id = ideal process
m = mean
s = vane surface
1 = stator inlet
2 = stator aftermix station
2.5 = station 0.52 cm downstream of vane trailing edge
$3M$ = aftermix station

Superscripts

$'$ = total state condition
$-$ = mean

3(*b*). Both of the figures show an improvement in agreement between theoretical and experimental values.

Assessment of Analysis. The quasi-three-dimensional inviscid analysis exhibited excellent prediction capability for the pressure side of all vanes, but overpredicted the suction surface velocity near the trailing edge, especially for the higher angle vanes. These theoretical velocity distributions were subsequently used to determine boundary layer parameters and loss coefficients. The difference in the theoretical and experimental loss coefficient varied from nearly 0 (74.9 deg vane in Fig. 2(*b*)) to about 25 percent (75 and 79.6 deg vanes in Fig. 2(*c*) and 2(*e*)). The larger value of 25 percent represents an absolute loss coefficient value of about 3/4 of 1 percent. It is concluded, therefore, that the use of the quasi-three-dimensional inviscid and boundary layer analysis for the prediction of the kinetic energy loss coefficients for high turning angle vanes is accurate to within 3/4 of a point.

Correction of the data and analysis for trailing edge effects (Fig. 3(*a*)) indicates that the computational approach described does not model the flow accurately in the base region. In addition, the improved agreement resulting from the use of the experimental velocities (Fig. 3(*b*)) indicates that a source of error exists prior to the boundary layer loss calculation. Availability of a viscous analysis that treats the entire flow field simultaneously, as opposed to combining an inviscid solver with a boundary layer computation, would provide a more direct computational approach for loss determination. Regardless of these considerations, it should be emphasized that the mixing and profile loss calculation for two-dimensional high turning angle vanes is accurate to within 3/4 of 1 point.

Annular Cascade Flow [10, 11].

Cascade Experiment. The second assessment was made for the case of flow through an annular cascade having stator vanes with 67 deg of turning, as described in the previous section. A laser system was used to obtain velocity and flow angle data. The experimental stator ring assembly with the window opening on the shroud surface is shown in Fig. 4. At a fixed point in the flow field, two components of velocity were measured so that magnitude and direction could be calculated. The orientation of the resultant velocity V and the flow angle α is illustrated in Fig. 5. Laser survey measurements were made at 11 axial locations within the vane passage and at an axial location 1/2 axial chord downstream of the trailing edge, as shown in Fig. 6. At a given axial plane, measurements were taken for one or more fixed radial positions at 1/3-deg increments across the passage, Fig. 6.

Flow Velocities and Angles. The velocity of the air flowing through the vane passage was calculated by using the inviscid two-dimensional computer programs MERIDL and TSONIC described in [1] and [2], respectively. The MERIDL program calculates the flow on the hub-to-tip midchannel stream surface that is subsequently used in the TSONIC program to obtain a solution on a number of blade-to-blade stream surfaces from hub-to-tip. A quasi-three-dimensional solution is obtained by requiring that, for each of the

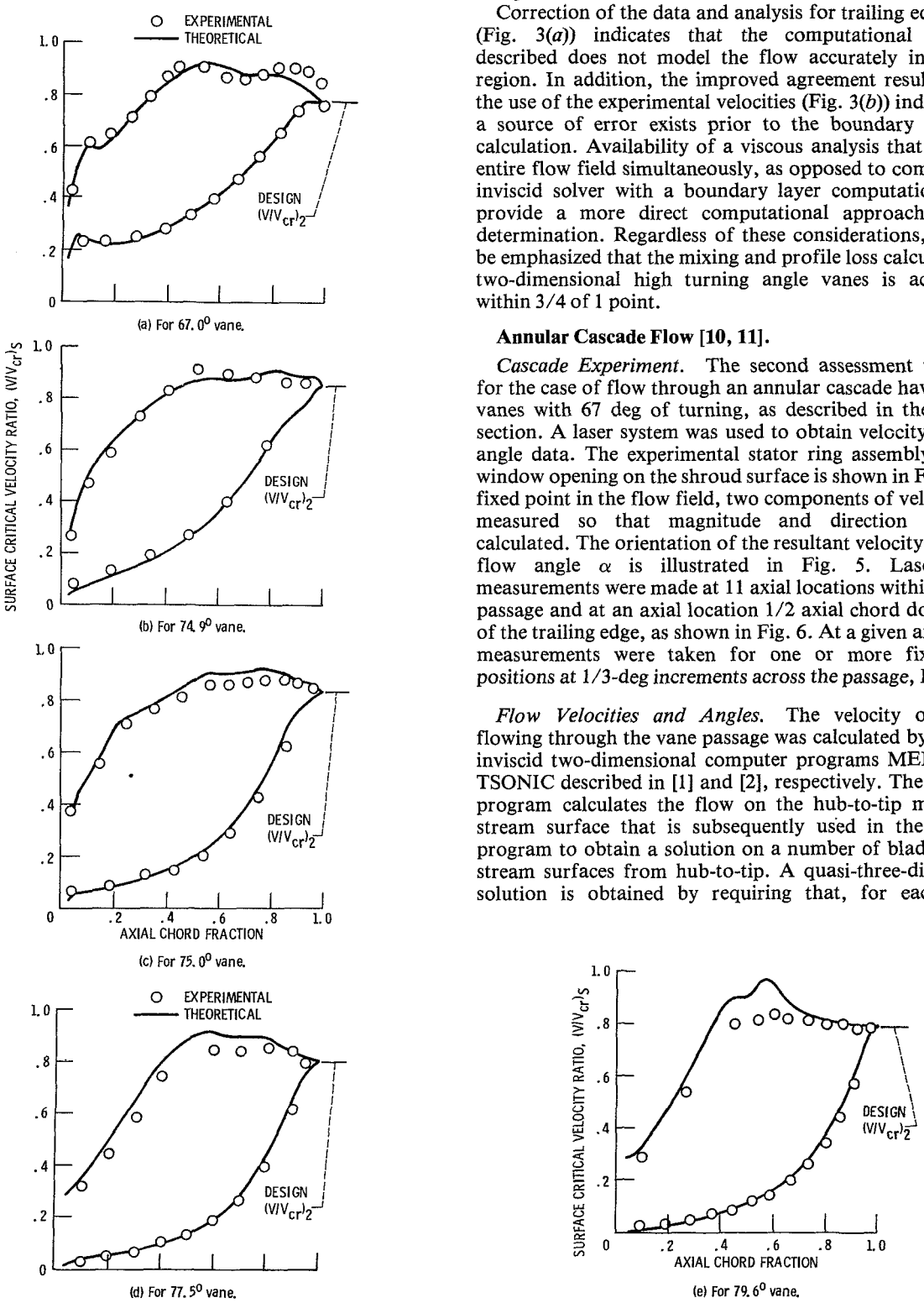

Fig. 1 Surface velocity distribution

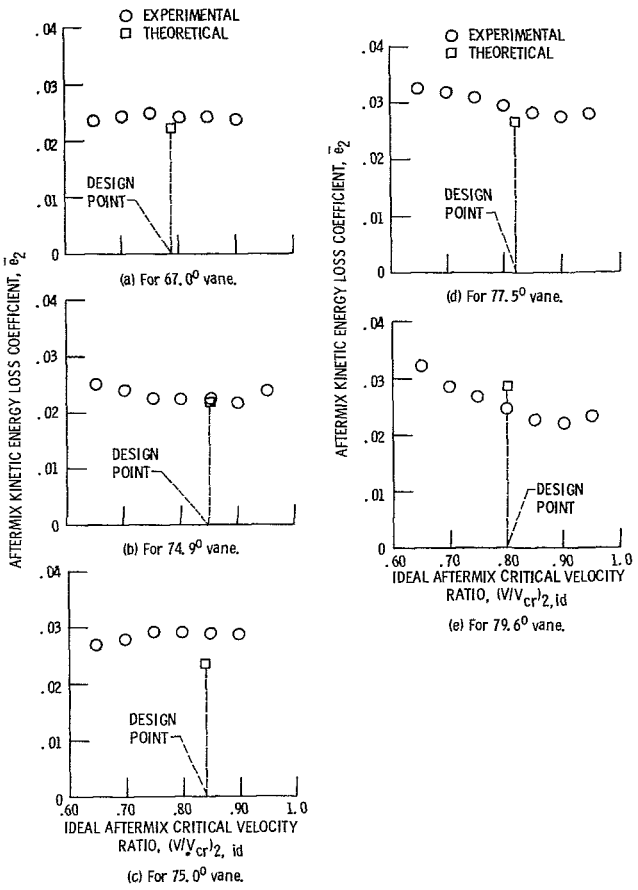

Fig. 2 Kinetic energy losses

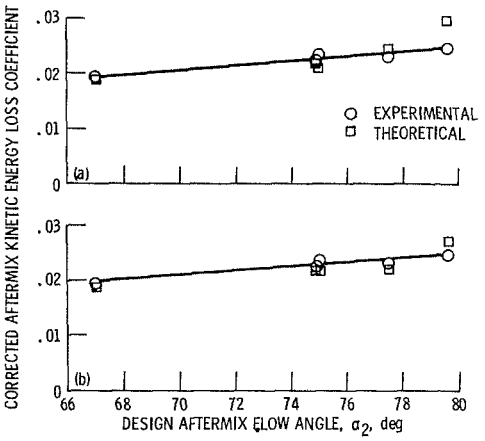

Fig. 3 Comparison of experimental losses corrected to 0.100-cm trailing edge thickness with theoretical losses calculated using 0.100-cm trailing edge thickness and experimental surface velocity distributions

TSONIC solutions, the pressure and suction-surface static pressures be equal near the vane trailing edge. This condition is obtained by slightly changing the downstream whirl distribution for the MERIDL program, repeating the TSONIC solutions, and iterating until the preceding static-pressure equality is satisfied to within some tolerance limit. This procedure [17] requires the user to make the downstream whirl distribution changes. Flow velocities and angles were also computed using the DENTON code [3, 4], which is a time-marching finite volume solution of the Euler equations. At the downstream boundary, the static pressure is specified

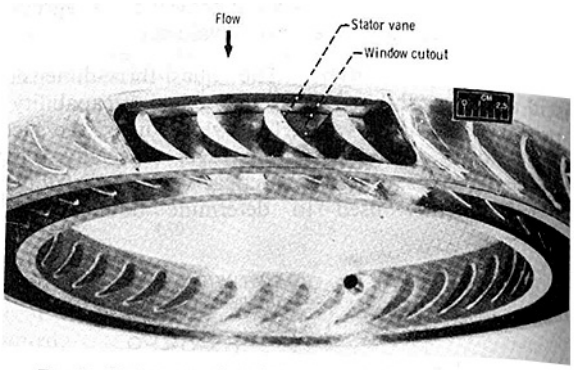

Fig. 4 Stator vane ring showing cutout for laser window

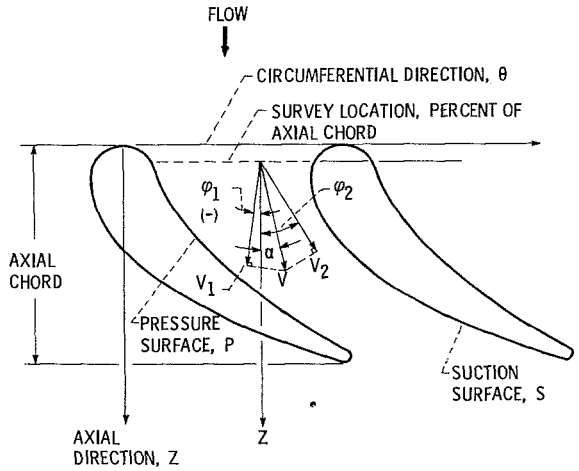

Fig. 5 Nomenclature and orientation of velocity component measurements for laser anemometer surveys

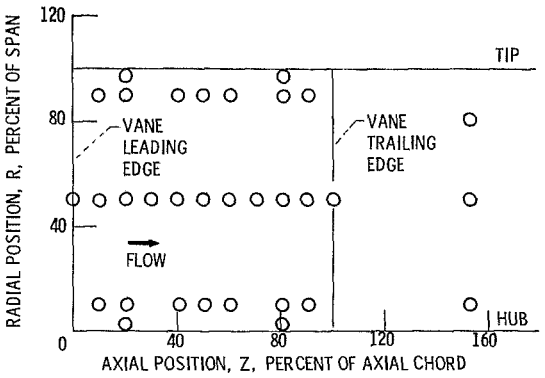

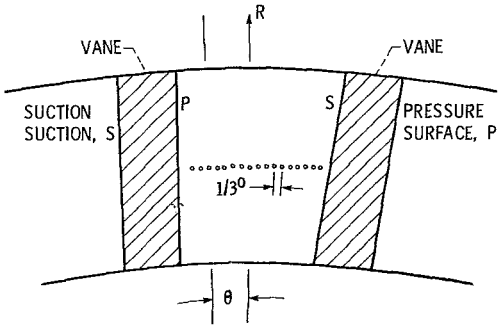

Fig. 6 Laser survey measurement locations

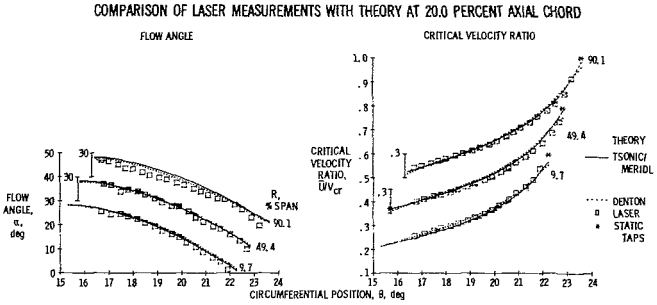

Fig. 7 Comparison of laser measurements with theory at 20.0 percent axial chord

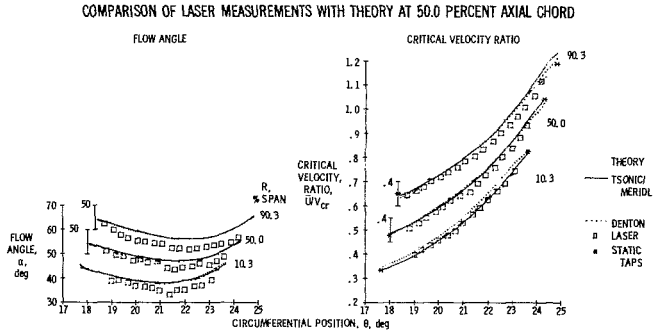

Fig. 8 Comparison of laser measurements with theory at 50.0 percent axial chord

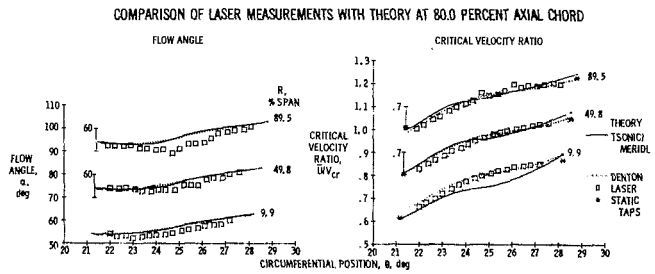

Fig. 9 Comparison of laser measurements with theory at 80.0 percent axial chord

at the hub, and the spanwise pressure variation is calculated by the program assuming zero meridional streamline curvature (simple radial equilibrium).

Cusps are located at the vane leading and trailing edges in order to minimize discontinuities in the grid slope. The cusps carry no load and, therefore, periodicity is automatically satisfied by the DENTON program. A comparison of the theoretical and experimental flow angles and velocities are presented in Figs. 7, 8, and 9 for constant axial positions of 20, 50, and 80 percent of axial chord. The results are shown for 10, 50, and 90 percent of span. The theoretical results shown were obtained from the quasi-three-dimensional inviscid TSONIC/MERIDL code and the three-dimensional DENTON code. At 20 percent axial chord, Fig. 7, the TSONIC/MERIDL comparison is generally good. At the 50 percent chord position, TSONIC/MERIDL slightly overpredicts the velocity at the 50 and 90 percent span positions. At 80 percent chord, TSONIC/MERIDL underpredicts the velocity near the hub, then tends to overpredict at the midspan and vane tip locations near the pressure side, whereas the DENTON results accurately predict the velocities at the three span positions. The flow angles generally are slightly overpredicted by both codes over the entire region.

The experimental accuracy of the measurements was determined using a parameter estimation technique and comparisons were made with the computed results. The velocity magnitudes using TSONIC/MERIDL and DENTON at 20 percent axial chord were found to fall outside the measurement uncertainty band by 1.0 and 0.4 percent, whereas the flow angles fell inside the band. The uncertainty band for the measurements was approximately 1.0 percent for the seed particle measurement and less than 2.0 percent for seed particle lag. The corresponding flow angle uncertainties were 1.4 deg and less than 1 deg. At 50 percent axial chord, the corresponding values were 2.0 and 0.7 percent for the velocities, and 0.1 deg for the flow angles. At 80 percent axial chord, the percentages for the velocities were 2.0 and 0.4 and for the flow angles were 0.1 and 0.2 deg.

Assessment. Inspection of the overall results shows that both of the inviscid codes accurately predict two components (axial and tangential) of velocity and the corresponding flow angle through a 67 deg annular stator cascade. Velocity magnitudes are predicted to within 2 percent and flow angles to within 0.2 deg of the uncertainty band. The largest differences occur near the endwall and toward the vane exit, where viscous and secondary flow effects are the largest. A more critical assessment of the computer codes will be made when the radial component of the velocity is measured. Also the inviscid codes will be put to a more stringent test when applied to the prediction of the flow field in higher turning angle stators (i.e., 75 to 80 deg), where stronger secondary flows will be generated. Some evidence that the DENTON code will not model regions of strong secondary flows is presented in [18] and [19]. The results of [18] and [19] are not surprising in view of the fact that the secondary flows due to viscous effects (i.e., endwall boundary layer and vane leading edge interaction) is not accounted for in the inviscid codes. However, until such time as the aforementioned assessments are performed, it is concluded that the inviscid codes described accurately predict the two components of velocity and the flow angle in a stator.

Nonuniform Turbine Inlet Temperature Flow [13].

Turbine Design. The third assessment was made for a 20-in. rotor diameter low aspect ratio turbine stage with nonuniform radial temperature distribution at the stator entrance. Figure 10 shows the turbine inlet temperature distributions with and without the Combustor Exit Radial Temperature Simulator (CERTS). The corresponding inlet total pressure distributions are shown in Fig. 11. The stators vanes were designed for 75 deg of turning and were similar to that described in section 1, entitled "Rectangular Cascade Flow." Total temperatures, flow angles, and pressures were measured at inlet and exit planes.

Secondary Flow and Temperatures. The inviscid rotational code developed by Denton was also used to obtain the analytical results. The code is a three-dimensional, time-marching solver of the unsteady Euler equations in finite-volume form for fixed or rotating turbomachinery blade rows [3, 4]. Good resolution of the blade profiles was obtained by using nonuniform grid generation. The grid used for the stator vane channel was 19 (pitch) × 19 (span) × 58 (axial). The corresponding grid dimensions for the rotor blade channel were 10 × 19 × 68. Computational time was reduced by using a two-level multigrid technique. The code was run for the stator with the measured inlet temperature and pressure profiles from the experiment, both with and without CERTS, as are shown in Figs. 10 and 11. The stator exit velocity was matched to the experimental data by specifying appropriate static pressures at the stator exit hub and tip. The computed results at the stator exit were then circumferentially averaged using mass flow weighting and used as inlet conditions for the rotor. The rotor exit velocity was matched to the experimental data by specifying appropriate static pressures at the rotor exit hub and tip. The computed results

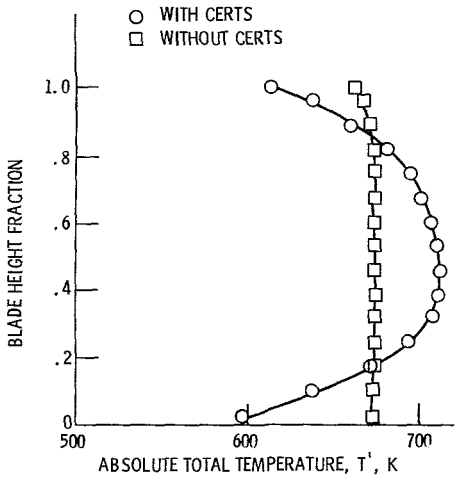

Fig. 10 Stator inlet temperature profiles

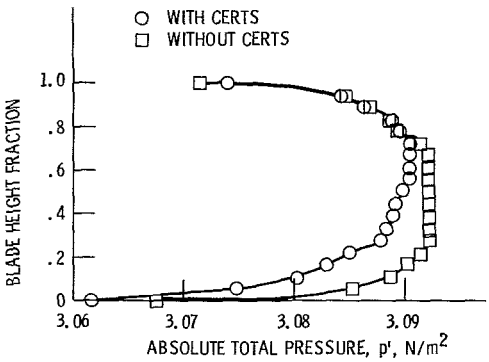

Fig. 11 Stator inlet pressure profiles

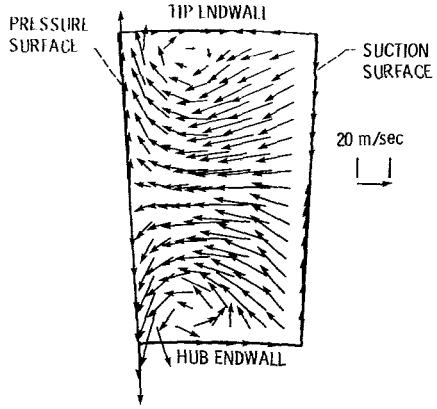

Fig. 12 Computed relative secondary flow vectors at rotor blade midchord

at the rotor exit were also circumferentially averaged to allow comparison with the experimental survey results obtained from probes in the stationary frame.

The secondary flow pattern computed with the Denton code is shown in Fig. 12 for the midchord position of the rotor. The flow movement, from suction to pressure surface, causes a redistribution of the inlet temperature profile. The hot flow at the midspan position shifts toward the endwalls at the pressure surface and the cooler endwall fluid moves toward the midspan region at the suction surface.

Figure 13 compares the analytical and experimental rotor exit temperature profiles with and without CERTS. The results indicate that the CERTS temperature profile is mixed out at the exit survey plane, although the analytical profile indicates a lack of mixing (see Fig. 13). The slight temperature drop in the experimental data at the tip endwall is attributed to heat transfer through the casing. The computed profile without the simulator, Fig. 13, shows close agreement with the data with the exception at the tip endwall.

Rotor Flow Angles. The rotor exit angles are shown in Fig. 14. For the test with the simulator, close agreement is observed at the hub, while large differences are seen at midspan and tip. The difference at the tip is believed to be due to increased clearance due to the use of coolant air with the simulator (0.5 percent clearance without CERTS versus 1.1 percent with CERTS). The flow angles without the simulator, Fig. 14, show close agreement at the tip. However, the midspan flow shows a substantial difference between theory and experiment. A significant amount of underturning occurs at the midspan of the rotor.

Assessment. In contrast to the good agreement shown in the previous section between computed and measured flow angles for the annular cascade, the predicted flow angle from the rotor is in severe disagreement with the measured data. The experimental rotor exit flow angles had 11 to 14 deg less turning than predicted by the DENTON code. The occurrence of this severe underturning is believed to be partly due to the low aspect ratio of the blades, which give rise to strong secondary flow over a large portion of the span. As noted previously, it may not be possible to compute the strong secondary flow fields with the DENTON code. This is because only the rotational portion of the secondary flow is computed, whereas the viscous contributions (i.e., vortex formation) is not accounted for in an Euler code. An additional factor contributing to the discrepancy between the experimental and measured flow angles may be the interaction between the stator and rotor secondary flow fields which is not accounted for in the analysis. The computed results at the stator exit had to be circumferentially mass averaged and then used as inlet conditions for the rotor. The rotor inlet flow field used for the DENTON computations, therefore, does not correspond to the physical flow field.

The discrepancy noted in the flow angles of the present flow example suggests that the inviscid rotational code is unable to predict the strong secondary flows present in a rotor passage, and that a three-dimensional viscous code may be required in order to accurately predict rotor flow fields.

Contoured Endwall Stator Flow [12, 14, 17].

Endwall Design. The fourth assessment was carried out on the effect of stator endwall contouring on flow losses in a small annular cascade. Two different contoured endwall stator geometries were designed and tested for comparison with a cylindrical geometry. The same vane profile shape [12] was used for all three configurations. The three geometries are shown in Fig. 15: a cylindrical, an S-shape, and a conical geometry. The vane surface velocities for the three stators are shown in Fig. 16. These were obtained by using the MERIDL/TSONIC codes [1, 2]. For those cases where supersonic flow occurred, Wood's modification was used [20]. At the hub and mean positions, the surface velocities were slightly lower for the two contoured stators, a result of the increased inlet passage height. At the tip, when configuration A turns the flow radially inward, the surface velocities decreased, followed by a large overshoot in the suction surface velocity. The computed pressure distributions along the suction surfaces of the three stator configurations are shown in Fig. 17. It may be seen in Fig. 17(*a*) that the pressure gradient from the leading edge to about 70 percent chord will drive the flow from hub to tip. Near the stator exit, the pressure becomes lower near the hub, and the low

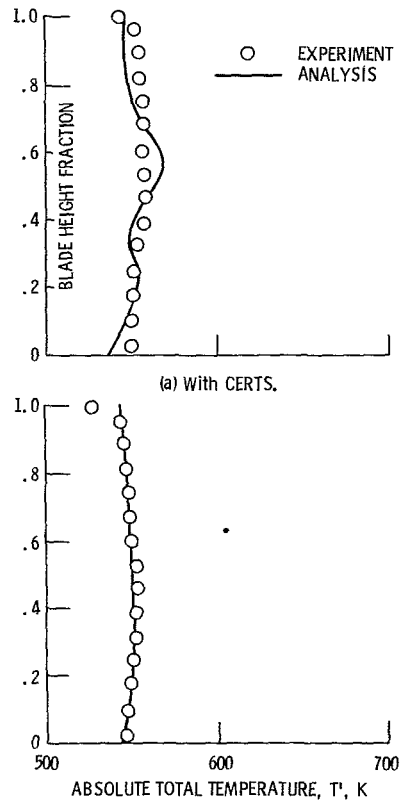

Fig. 13 Rotor exit temperature profiles

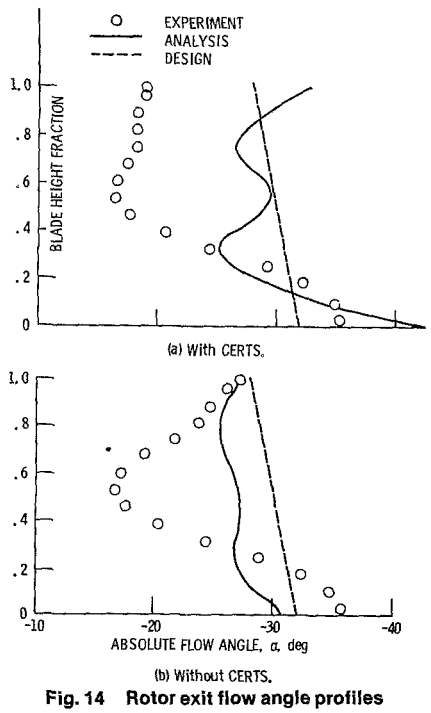

Fig. 14 Rotor exit flow angle profiles

momentum fluid along the tip wall would migrate to the hub wall. Contoured stator A, Fig. 17(*b*), has a pressure distribution which would prevent migration of low momentum fluid from the hub beyond midspan. At about 80 percent of the axial chord, a low-pressure region occurs near the tip, trapping low momentum fluid in that location. Stator contour B, Fig. 17(*c*), has less severe pressure gradients and hence there is not a strong driving force to move low-

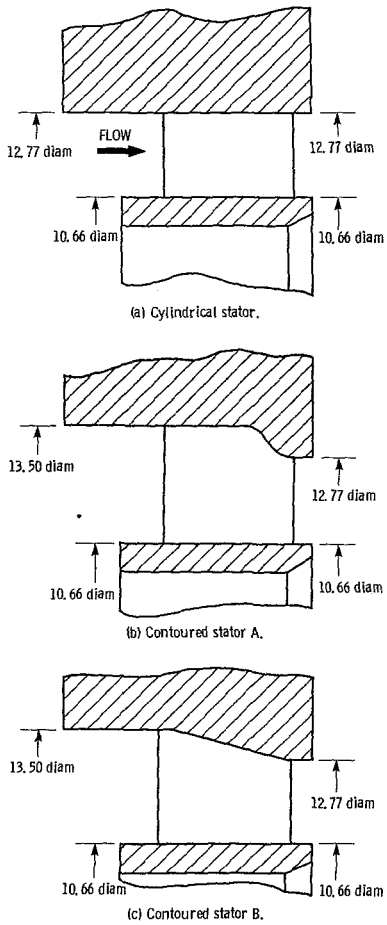

Fig. 15 Schematic cross-sectional view of three stator configurations tested (dimensions are in cm)

momentum fluid to either the hub or tip regions. From these data, it appears that a significant effect of endwall contouring is to reduce the radial migration of low-momentum fluid.

Kinetic Energy Loss Coefficient. The stator kinetic energy loss coefficient was calculated from flow angle and total pressure surveys. The calculation was based on the determination of complete mixing at a hypothetical downstream station as described in the section entitled "Rectangular Cascade Flow." The losses, computed in this fashion, are shown in Fig. 18 for the three geometries at the design stator pressure ratio of 1.8 and also for 1.35. The data show that the cylindrical stator had lower losses near the tip and higher losses near the hub than the two contoured stator configurations. It appears that the effect of contouring is to change the radial distribution of loss. For the two contoured stator configurations, the loss region remained near the tip instead of migrating radially inward toward the hub as was the case for the cylindrical stator. These experimental observations are in agreement with the conclusions drawn from the computed suction surface pressure distributions shown in Fig. 17 and discussed in the previous section. The overall kinetic energy loss coefficients were approximately 0.5 percent lower for the two contoured geometries than was the cylindrical.

MERIDL/TSONIC and BLAYER were used to calculate the aftermix kinetic energy loss coefficients for both the vane profile and the endwalls. The profile loss included the friction loss along the suction and pressure surfaces, and the mixing loss. The endwall loss was the total friction loss along the hub and tip endwalls up to the axial measuring station.

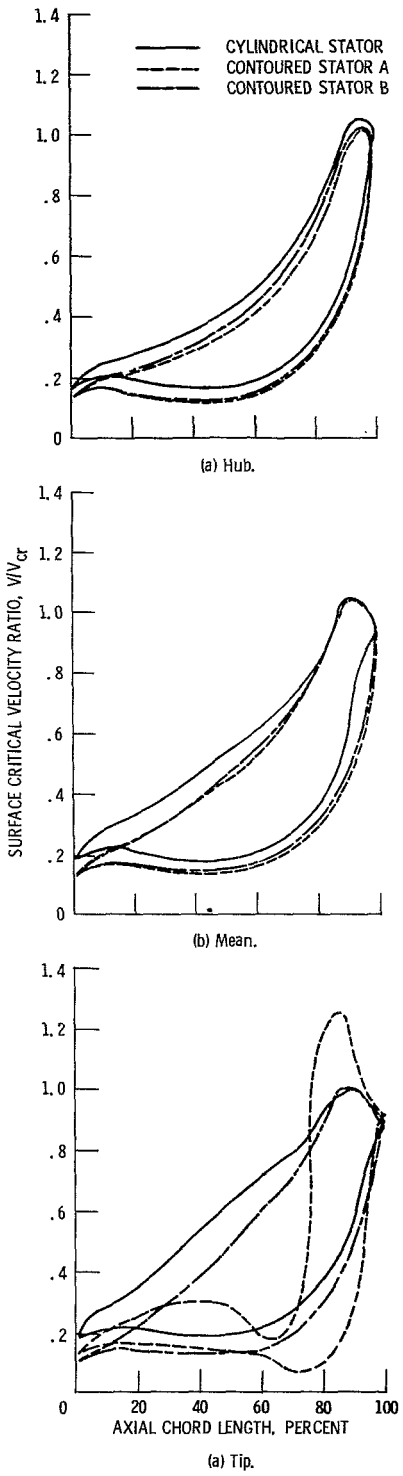

Fig. 16 Design blade surface velocity distributions for the three stator configurations

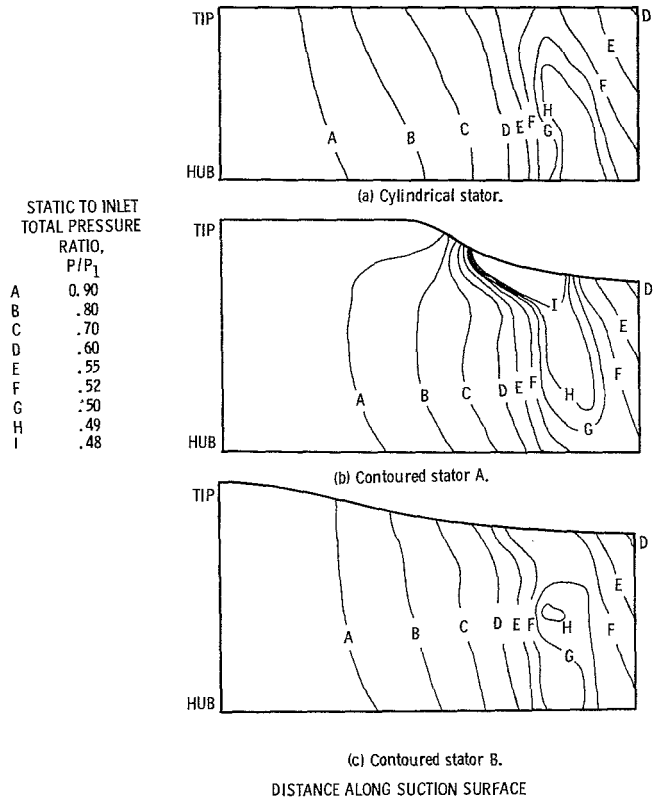

Fig. 17 Comparison of analytical pressure distributions along suction surfaces of the three stator configurations

The experimental values of typical kinetic energy loss coefficients at design equivalent speed and stage pressure ratio are compared with the computed values in the upper portion of Table 2. The computed results include the secondary losses as well as an incidence loss. The correlation of Morris and Hoare [7] was used for the secondary loss calculation with one modification, i.e., only the inlet displacement thickness term was used since the BLAYER calculation already accounted for the downstream boundary layer losses. The comparison in Table 2 shows that the calculated losses were 0.005 and 0.004 lower for stator contours A and B than the cylindrical contour. In addition, the measured loss coefficients were 0.003 lower for stators A and B than the cylindrical stator. The computed loss coefficients were in error by only 1.8, 5.8, and 3.8 percent, respectively, relative to the measurements, for the cylindrical, contour A and contour B stators. The difference in stator pressure ratio for the three configurations was due to variations in the stator-rotor throat area ratios. This effect is addressed in the following section on Small Axial Stage Flow.

Assessment. The aftermixed kinetic energy loss coefficient calculated from MERIDL/TSONIC with BLAYER and the secondary flow losses using the correlation of Morris and Hoare yielded values which agreed closely with the overall measured stator loss. Both the analysis and experiment showed that the reduction in loss with contouring was small for the lightly loaded configurations used in this study. A more meaningful case would involve a highly loaded stator configuration in which the radial and cross channel gradients, and hence, the secondary flows, would be greater. Most of the loss reduction with the contoured stators was attributed to a reduction in boundary layer growth along the vanes and endwall surfaces.

On the basis of the comparisons between the computed results and the experimental data, the combined inviscid-correlative approach (or coupled analysis) appears to have the potential of accurately predicting stator performance. The difficulty with this analytical approach is that the accuracy of the individual loss calculations is not amenable to verification. Profile and mixing losses, endwall friction losses, secondary flow losses, and incidence losses for the stator rings cannot be experimentally determined on an individual basis. The only measure of success is the comparison of overall experimental loss with the sum of the individual calculated losses. In addition, since the reduction in the loss

Table 2 Calculated and measured stator and rotor losses

	Cylindrical Stator	Contoured Stator A	Contoured Stator B
CALCULATED STATOR LOSSES ($\bar{e}$):			
Profile and mixing	0.029	0.027	0.026
Endwall friction	.018	.017	.016
Secondary	.006	.005	.008
Incidence	.001	.000	.000
Total	0.054	0.049	0.050
$\Delta\eta$'stage	.035	.027	.031
Total-to-Static pressure ratio across stator	2.01	1.82	1.91
MEASURED STATOR $\bar{e}$	.055	.052	.052
CALCULATED ROTOR LOSSES ($\bar{e}$):			
Profile and mixing	.034	.031	.031
Hub endwall friction	.008	.006	.007
Secondary	.022	.017	.020
Incidence	.024	.007	.014
Tip Clearance	.086	.083	.085
Disk windage	.002	.002	.002
Total	.176	.146	.159
$\Delta\eta$'stage	.104	.101	.101
Total-to-Static pressure ratio across rotor	1.87	2.06	1.95
EXHAUST DUCT LOSS, $\Delta\eta$'stage	.005	.007	.005
OVERALL STAGE EFFICIENCY	.856	.865	.863
R_x	.271	.355	.315
stage pressure ratio	2.77	2.77	2.77
MEASURED STAGE EFFICIENCY	.845	.851	.853

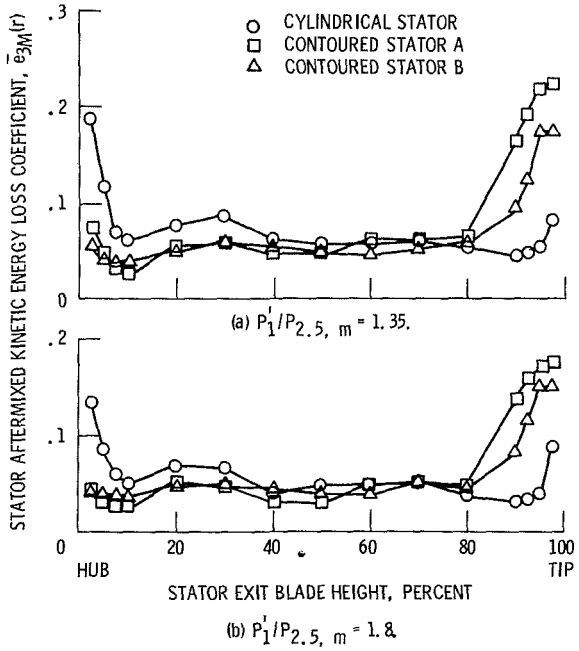

Fig. 18 Radial variation of stator kinetic energy loss coefficient

coefficient appears to be associated with a redistribution of losses across the passages, one would expect that a reliable computational approach must be capable of treating the secondary flows that occur in a turbine passage. The analytical approach requires a formulation which treats the secondary flow generated by vane leading edges as well as by passage turning.

In spite of the considerations discussed, it is noted that the computed stator losses are in excellent agreement with the experimental data. Until further assessment is carried out, it is concluded that the three-dimensional inviscid approach coupled with an integral boundary layer and loss correlations provides a highly accurate technique for computing losses in a stator row.

Small Axial Stage Flow [8].

Geometric Configuration. The three stator configurations described in the preceding section, "Contoured Endwall Stator," were tested with a common rotor to determine the effect of contouring on overall stage performance. It is currently believed that contouring reduces the radial and cross-channel pressure gradients and reduces boundary layer growth, thus inhibiting the movement of low momentum fluid and reducing loss. Further testing was carried out using a small (12.8-cm-dia) axial flow turbine.

Loss and Efficiency Calculation. The losses for the three configurations were calculated using MERIDL/TSONIC, BLAYER, and Morris and Hoare's correlation as described previously and in [8]. The analysis used the experimental values of turbine inlet temperature, pressure, mass flow, wall displacement, and stator pressure ratio. Table 2 shows the breakdown of the individual losses calculated for both the stator and the rotor. As seen in the previous section (Contoured Endwall Stator Flow), the calculated total stator kinetic energy loss coefficients were within 0.003 of the measured values. Inspection of the rotor losses shows that there is a substantial reduction in the calculated total rotor

kinetic energy loss coefficient for the two contoured stators relative to the cylindrical geometry. When the rotor loss coefficient is converted into stage efficiency loss [8], the values are nearly constant for all three stator configurations (i.e., 0.104, 0.101, 0.101). This effect is due to the fact that the two contoured stages have higher rotor pressure ratios. (Loss computations were also made for stator configurations A and B with rotated vanes so that the same stator and rotor pressure ratios were achieved as with the cylindrical geometry. The results caused only minor changes to the values in Table 2 and had no effect on the conclusions.) Addition of the computed stator and rotor losses yields overall stage efficiencies of 0.856, 0.865, and 0.863 for the cylindrical, stator A and stator B configurations, respectively. The corresponding measured values of the stage efficiencies were 0.845, 0.851, and 0.853.

Assessment. Using the detailed data presented in Table 2 it is possible to compare the calculated efficiency losses ($\Delta\eta'$) with those measured for the three geometric configurations. This was done by converting the measured stator kinetic energy loss coefficient to a stage efficiency loss using the expression in [8]. For the case of the cylindrical contour, the measured values $\bar{e}$ of 0.055 converts to a $\Delta\eta'$ value of 0.036. The computed value of the efficiency loss (0.035) is within 2.8 percent of the measured value. For contour A, the difference between calculated and measured $\Delta\eta'$ is 6.9 percent; and for stator B, the value is zero. As observed earlier, the ability to compute stator losses with a combined inviscid, boundary-layer-correlative approach for these geometries appears to be excellent. Since the rotor efficiency loss cannot be measured separately, the efficiency losses for the stator and exhaust duct were summed and deducted from the measured stage efficiency loss. That is: $\Delta\eta'_{\text{rotor}} = \Delta\eta'_{\text{stage}} - (\Delta\eta'_{\text{stator}} + \Delta\eta'_{\text{exhaust duct}})$. Hence for the cylindrical geometry, the sum of the measured stator efficiency loss (0.036) and the duct efficiency loss (0.005) were subtracted from the measured stage efficiency loss (0.155) to yield a "measured" rotor efficiency loss (0.114). The computed value of the rotor efficiency loss for the cylindrical configuration (0.104) shows a difference of 8.8 percent relative to the measured value. Likewise, the difference between the computed and measured rotor efficiency loss for contour A was 10.6 percent and for contour B was 9 percent. These results for the stator and rotor indicate that improvements in the computation of turbine efficiency require greater accuracy in the rotor passage. In view of the spanwise redistribution of low-momentum fluid and the associated transverse flows that occur as the flow leaves the contoured stator passage and enters the rotor passage, a three-dimensional viscous analysis may be required to improve the accuracy of the rotor flow field calculation.

It is noted that the results discussed above were obtained with high solidity stator blading, accompanied by light loading and well accelerated flow. The ability of the analysis to predict the losses in lower solidity blading with higher loading is not yet assessed.

Conclusions

Comparisons between measured and computed aerodynamic parameters have been examined in an effort to evaluate current computational capabilities. Specifically, the ability of the inviscid TSONIC code, an integral boundary layer code (BLAYER) and a mixing loss model by Stewart to compute the kinetic energy loss coefficients for a series of two-dimensional high turning angle vanes was examined. It was concluded that the computational procedure was accurate to within 3/4 of 1 point in loss coefficient. It was further concluded that improvements in the computation could result from improved flow modeling in the trailing edge region. Improvement is also desirable in the computation of the suction surface velocity distribution.

The second evaluation was carried out for annular cascade flow for which experimental laser measurements of two velocity components and flow angle were available. These data were compared with the results of the quasi-three-dimensional inviscid TSONIC/MERIDL code and the three-dimensional inviscid DENTON code. It was concluded that both of these codes accurately predicted the axial and tangential velocity components and the corresponding flow angle through a 67 deg turning vane. Additional evaluation of the two codes needs to be carried out for the radial velocity component and for higher turning angle vanes with significantly larger secondary flows.

A third assessment was performed to measure the ability of the DENTON code to predict the temperature and flow angles downstream of a single stage turbine operated with and without a radial variation in entrance temperature. The three-dimensional inviscid DENTON code gave reasonable agreement with the rotor exit temperature profiles but was in poor agreement with the rotor exit flow angle distributions. The computation does not predict the significant underturning at the midspan rotor position that is measured experimentally. It was concluded that the strong secondary flows present in the low aspect blades may not be sufficiently well modeled in the code. In addition, the inviscid rotational approach is unable to account for realistic rotor inlet conditions (note that the rotor inlet flow had to be circumferentially mass averaged) and stator-rotor interaction. Development of a three-dimensional viscous analysis for the rotor flow fields appears necessary.

A fourth evaluation was performed regarding the ability of TSONIC/MERIDL, BLAYER and a series of loss correlations to predict the losses in contoured stator rings. Comparison of the calculated stator kinetic energy loss coefficients with the measured values show excellent agreement. Further assessment of the computational approach is required for more highly loaded stator configurations than those available for comparison. A difficulty with the present approach is that individual loss comparisons cannot be performed for annular configurations. This situation creates a problem in attempting to evaluate the benefits of contouring versus leaning versus bowing versus sweeping. Significant deviations from two-dimensionality will give rise to cross-channel variations and influence the ability to predict secondary flow phenomena accurately.

The final assessment was on the application of the TSONIC/MERIDL, BLAYER, and loss correlations to a small axial stage with contoured endwalls. This comparison made use of the results previously described for the contoured stators by the addition of a common rotor. The computed rotor losses were compared to the experimental measurements. It was concluded that additional improvements are needed for the rotor flow field computations.

In summary, the ability to compute losses and flow fields within two-dimensional and annular cascade passages has evolved to a high degree of accuracy, with some exception. In contrast, the ability to predict the flow field and the losses occurring in the rotor is much less accurate. In view of the highly complex nature of the flow field that may occur in a turbine passage and a strong desire to exploit novel stator and rotor geometries, development of an accurate three-dimensional viscous code is necessary.

References

1 Katsanis, T., "FORTRAN Program for Calculating Transonic Velocities on a Blade-to-Blade Stream Surface of a Turbomachine," NASA TN D-5427, 1969.

2 Katsanis, T., and McNally, W. D., "Revised FORTRAN Program for Calculating Velocities and Streamlines on the Hub-Shroud Midchannel Stream

Surface of an Axial-, Radial-, or Mixed-Flow Turbomachine or Annular Duct," *I—User's Manual*, NASA TN D-8430, 1977.

3 Denton, J. D., and Singh, U. K., "Time-Marching Methods for Turbomachinery Flow Calculation. Part I—Basic Principles and 20 Applications; II—Three-Dimensional Flows," Application of Numerical Methods to Flow Calculations in Turbomachine, VKI Lecture Series 1979-7, 1979.

4 Denton, J. D., "An Improved Time-Marching Method for Turbomachinery Flow Calculation," ASME Paper 82-GS-239, Apr. 1982.

5 McNally, W. D., "FORTRAN Program for Calculating Compressible Laminar and Turbulent Boundary Layers in Arbitrary Pressure Gradients," NASA TN D-5681, 1970.

6 Stewart, W. L., "Analysis of Two-Dimensional Compressible Flow Loss Characteristics Downstream of Turbomachine Blade Rows in Terms of Boundary Layer Characteristics," NASA TN-3515, 1955.

7 Morris, A. W. H., and Hoare, R. G., "Secondary Loss Measurements in a Cascade of Turbine Blades with Meridional Wall Profiling," ASME Paper No. 75-WA/GT-13, Nov. 1975.

8 Haas, J. E., and Boyle, R. J., "Analytical and Experimental Investigation of Stator Endwall Contouring in a Small Axial-Flow Turbine, Part II: Stage Performance," Proposed NASA technical paper.

9 Schwab, J. R., "Aerodynamic Performance of High Turning Core Turbine Vanes in a Two-Dimensional Cascade," NASA TM-82894, 1982.

10 Goldman, L. J., and Seasholtz, R. G., "Laser Anemometer Measurements in an Annular Cascade of Core Turbine Vanes and Comparison with Theory," NASA TP-2018, 1982.

11 Goldman, L. J., and Seaholtz, R. G., "Comparison of Laser Anemometer Measurements and Theory in an Annular Turbine Cascade with Experimental Accuracy Determined by Parameter Estimation," *Engineering Applications of Laser Velocimetry*, edited by H. W. Coleman and P. A. Pfund, ASME, 1982.

12 Haas, J. E., "Analytical and Experimental Investigation of Stator Endwall Contouring in a Small Axial Flow Turbine. I: Stator Performance," NASA TP-2023, 1982.

13 Schwab, J. R., Stabe, R. G., and Whitney, W. J., "Analytical and Experimental Study of Flow Through an Axial Turbine Stage With a Nonuniform Inlet Radial Temperature Profile," AIAA Paper 83-1175, June 1983.

14 Boyle, R. J., and Haas, J. E., "Comparison of Experimental and Analytic Performance for Contoured Endwall Stators," NASA TM-82877, AVRADCOM TR 82-C-12, June 1982.

15 Goldman, L. J., and McLallin, K. L., "Cold-Air Annular-Cascade Investigation of Aerodynamic Performance of Cooled Turbine Vanes. I: Facility Description and Base (Solid) Vane Performance," NASA TM X-3006, 1974.

16 Prust, H. W. Jr., Moffitt, T. P., and Bider, B., "Effect of Variable Stator Area on Performance of a Single-Stage Turbine Suitable for Air Cooling. V: Stator Detailed Losses with 70-Percent Design Area," NASA TM X-1696, 1968.

17 Boyle, R. J., Rohlik, H. E., and Goldman, L. J., "Analytic Investigation of Effect of Endwall Contouring on Stator Performance," NASA TP-1943, 1981.

18 Schwab, J. R., and Povinelli, L. A., "Comparison of Secondary Flows Predicted by a Viscous Code and an Inviscid Code with Experimental Data for a Turning Duct," in: *Computation of Internal Flows: Methods and Applications*, FED, Vol. 14, Feb. 1984.

19 Dawes, W. N., and Richards, P. H., "A Comparison of Experimental and Numerical Results Obtained for the Secondary Flow in a Large Turbine Cascade," *Journal of Physics Design: Applied Physics*, Vol. 16, No. 4, Apr. 14, 1983, pp. 539–551.

20 Wood, J. R., "Improved Method for Calculating Transonic Velocities on Blade-to-Blade Stream Surfaces of a Turbomachine," NASA TP-1772, 1981.

Surface of an Axial-, Radial-, or Mixed-Flow Turbomachine or Annular Duct," *I—User's Manual*, NASA TN D-8430, 1977.

3 Denton, J. D., and Singh, U. K., "Time-Marching Methods for Turbomachinery Flow Calculation. Part I—Basic Principles and 20 Applications; II—Three-Dimensional Flows," Application of Numerical Methods to Flow Calculations in Turbomachine, VKI Lecture Series 1979-7, 1979.

4 Denton, J. D., "An Improved Time-Marching Method for Turbomachinery Flow Calculation," ASME Paper 82-GS-239, Apr. 1982.

5 McNally, W. D., "FORTRAN Program for Calculating Compressible Laminar and Turbulent Boundary Layers in Arbitrary Pressure Gradients," NASA TN D-5681, 1970.

6 Stewart, W. L., "Analysis of Two-Dimensional Compressible Flow Loss Characteristics Downstream of Turbomachine Blade Rows in Terms of Boundary Layer Characteristics," NASA TN-3515, 1955.

7 Morris, A. W. H., and Hoare, R. G., "Secondary Loss Measurements in a Cascade of Turbine Blades with Meridional Wall Profiling," ASME Paper No. 75-WA/GT-13, Nov. 1975.

8 Haas, J. E., and Boyle, R. J., "Analytical and Experimental Investigation of Stator Endwall Contouring in a Small Axial-Flow Turbine, Part II: Stage Performance," Proposed NASA technical paper.

9 Schwab, J. R., "Aerodynamic Performance of High Turning Core Turbine Vanes in a Two-Dimensional Cascade," NASA TM-82894, 1982.

10 Goldman, L. J., and Seasholtz, R. G., "Laser Anemometer Measurements in an Annular Cascade of Core Turbine Vanes and Comparison with Theory," NASA TP-2018, 1982.

11 Goldman, L. J., and Seaholtz, R. G., "Comparison of Laser Anemometer Measurements and Theory in an Annular Turbine Cascade with Experimental Accuracy Determined by Parameter Estimation," *Engineering Applications of Laser Velocimetry*, edited by H. W. Coleman and P. A. Pfund, ASME, 1982.

12 Haas, J. E., "Analytical and Experimental Investigation of Stator Endwall Contouring in a Small Axial Flow Turbine. I: Stator Performance," NASA TP-2023, 1982.

13 Schwab, J. R., Stabe, R. G., and Whitney, W. J., "Analytical and Experimental Study of Flow Through an Axial Turbine Stage With a Nonuniform Inlet Radial Temperature Profile," AIAA Paper 83-1175, June 1983.

14 Boyle, R. J., and Haas, J. E., "Comparison of Experimental and Analytic Performance for Contoured Endwall Stators," NASA TM-82877, AVRADCOM TR 82-C-12, June 1982.

15 Goldman, L. J., and McLallin, K. L., "Cold-Air Annular-Cascade Investigation of Aerodynamic Performance of Cooled Turbine Vanes. I: Facility Description and Base (Solid) Vane Performance," NASA TM X-3006, 1974.

16 Prust, H. W. Jr., Moffitt, T. P., and Bider, B., "Effect of Variable Stator Area on Performance of a Single-Stage Turbine Suitable for Air Cooling. V: Stator Detailed Losses with 70-Percent Design Area," NASA TM X-1696, 1968.

17 Boyle, R. J., Rohlik, H. E., and Goldman, L. J., "Analytic Investigation of Effect of Endwall Contouring on Stator Performance," NASA TP-1943, 1981.

18 Schwab, J. R., and Povinelli, L. A., "Comparison of Secondary Flows Predicted by a Viscous Code and an Inviscid Code with Experimental Data for a Turning Duct," in: *Computation of Internal Flows: Methods and Applications*, FED, Vol. 14, Feb. 1984.

19 Dawes, W. N., and Richards, P. H., "A Comparison of Experimental and Numerical Results Obtained for the Secondary Flow in a Large Turbine Cascade," *Journal of Physics Design: Applied Physics*, Vol. 16, No. 4, Apr. 14, 1983, pp. 539–551.

20 Wood, J. R., "Improved Method for Calculating Transonic Velocities on Blade-to-Blade Stream Surfaces of a Turbomachine," NASA TP-1772, 1981.

DISCUSSION

J. W. Kurzrock[1]

The author has written a concise summary of the computational/experimental techniques that are presently being used at NASA Lewis to evaluate subsonic/transonic turbine stage performance. The references cited indicate that extensive analytical and experimental research has been conducted in the area of turbine aerodynamic design. In particular, stators and contoured stators have been investigated for total-to-static pressure ratios in the range of 1.20–2.1. Reaction rotors have been considered for a total-to-static pressure range of 1.87–2.06.

The aftermix or mixed-out uniform exit conditions have been used to compare the analytical and experimental kinetic energy loss coefficients. I also advocate the use of the uniform flow exit condition to assess the vane/blade losses for numerical computation or experimental surveys, since the loss becomes independent of the experimental survey or numerical computation location [21, 22]. The results cited by the author indicate good agreement between the predicted and experimental mixed-out kinetic energy loss coefficients.

The annular stators or contoured stators, and the reaction turbine rotors, also require loss estimates for the secondary flow that occurs because of the interaction of the endwall inlet boundary layer with the blunt leading edge of the vanes. A horseshoe vortex is formed, which eventually becomes part of the passage vortex [23]. Note that the secondary losses listed for the small axial turbine stage (Table 2) represent 1/3 of the total loss for the stator but only 1/8 of the loss for the rotor. The stator and rotor had aspect ratios of 0.5 [8] but the Zweifel loading coefficient was 0.47 for the stator and 0.84 for the rotor. The secondary loss for the stator would have been expected to be much greater if the stator loading were higher. The incidence loss represents about 1/2 of the total rotor loss. I am interested in the method used to calculate the incidence and tip clearance losses for the rotor.

The annular cascade flow field compared the laser experimental data with three flow field prediction codes. The solidity of this stator was 1.35 and the aspect ratio was 0.69 [10]. The Zweifel loading coefficient is calculated to be 0.77. The numerical computations codes indicate satisfactory agreement with the laser flow field surveys with the exception of the Dodge code. The author should comment on the significant deviations between the Dodge code and the laser flow surveys. Were the Dodge and Denton [3, 4] codes used with inlet boundary layer simulation to aid in predicting secondary flow due to end wall boundary layer? The computational time and grid sizes used for these predictive codes would be of interest to turbine designers.

References

21 Kurzrock, J. W., and Novick, A. S., "Transonic Flow Around Rotor Blade Elements," ASME *Journal of Fluids Engineering*, Vol. 97, No. 4, Dec. 1975, pp. 598–605.

22 Kurzrock, J. W., and Novick, A. S., "Transonic Flow Around Compressor Rotor Blade Elements, Vol. I: Analysis," AFAPL-TR-73-69, Aug. 1973.

23 Gaugler, R. E., and Russell, L. M., "Comparison of Visualized Turbine Endwall Secondary Flows and Measured Heat Transfer Patterns," ASME JOURNAL OF ENGINEERING FOR GAS TURBINES AND POWER, Vol. 106, No. 1, Jan. 1984, pp. 168–172.

J. D. Denton[2]

I would like to ask Dr. Povinelli how the inlet boundary conditions were obtained for the turbine rotor calculations shown in Figs. 13 and 14 of the paper. The secondary flow in the rotor, illustrated in Fig. 12, is completely determined by

[1] Principal Research Engineer, Sundstrand Aviation Operations, P. O. Box 7002, Rockford, IL 61125

[2] Whittle Laboratory, Cambridge, England

the distribution of total pressure input to the rotor and it is hard to see how the true distribution, which is circumferentially nonuniform and unsteady in the rotor relative frame, can be simulated in a calculation of this type. A further minor point is that it would have been more meaningful to plot the distribution of relative rather than absolute flow angle in Fig. 14. This would have shown a much smaller discrepancy between analysis and experiment.

Author's Closure

In response to Professor Denton's comment, the stator exit velocity was matched to the experimental data by specifying appropriate static pressures at the stator exit hub and tip. The computed results at the stator exit were then circumferentially averaged using mass flow weighting and then used as inlet conditions for the rotor. The rotor exit velocity was matched to the experimental data by specifying appropriate static pressures at the rotor exit hub and tip. The computed results at the rotor exit were also circumferentially averaged to allow comparison with the experimental survey results. The rotor inlet flow used for the Denton computations, therefore, did not include any circumferential nonuniformities or unsteadiness relative to the rotor. The computed secondary flow in the rotor is at best only an approximation of the flow distribution.

Quasi-Three-Dimensional and Full Three-Dimensional Rotational Flow Calculations in Turbomachines

Wang Qinghuan

Zhu Genxing

Wu Chung-Hua

Institute of Engineering Thermophysics, Academia Sinica, Beijing, China

Progress in the development of quasi-three-dimensional and full three-dimensional numerical solutions for steady subsonic rotational flow through turbomachines is presented. An iterative calculation between the flow on a mean hub-to-tip S_2 stream surface and a number of blade-to-blade S_1 stream surfaces gives the quasi-three-dimensional solution, which is very easily extended to give full three-dimensional solution by merely calculating a few more S_2 surface flows and relaxing the restriction that S_1 surfaces are surfaces of revolution. A new S_2-S_1 iteration scheme has been developed and employed in the present code. The governing equations on the S_1 and S_2 surfaces are expressed in terms of general nonorthogonal curvilinear coordinates so that they are body-fitted without any coordinate transformation and are solved by either matrix method or line-relaxation method. An automatic computing system is used, which first computes the quasi-three-dimensional flow for blade design and then computes the full three-dimensional flow for the blade row just designed. The results obtained by applying this computing system to the design and determination of full three-dimensional flow field of a two-stage axial compressor and a high subsonic compressor stator are obtained and shows clearly the amount of the twist of the general S_1 surfaces and the difference in the flow field between the quasi-three-dimensional and full three-dimensional solutions.

Introduction

Since its publication, the general three-dimensional flow theory developed by Wu [1] has been used as the basis for many turbomachine design and analysis calculations. In addition to the relaxation, matrix, and mean-streamline series expansion method employed in the early days [2, 3], several other methods have been developed to calculate the flow on the hub-to-tip S_2 surfaces and blade-to-blade S_1 surfaces (for example, references [4–8]).

During the last few years, due to the need for more accurate design of turbomachines, the individual S_1 and S_2 flow codes have been combined to give more accurate three-dimensional design and analysis calculation. When it is assumed that the S_1 surface is a surface of revolution, iterative calculation between the flow on a single S_2 surface, which is preferably the mean S_2 surface located somewhere in the middle of the blade passage, and the flow on a number of S_1 surfaces may give a good approximate three-dimensional flow [9–13]. In cases where the assumption on the S_1 surface is not good enough, design or analysis calculation should take the twist of the S_1 surface into consideration.

Progress in the development of new efficient computing codes for individual calculation of the flow on S_1 and S_2 surfaces has been made in the Institute of Engineering Thermophysics, CAS. They are based on the original work of Wu [1]. Since then, the governing equations have been expressed with respect to general nonorthogonal curvilinear coordinates and corresponding nonorthogonal velocity components [14]. This coordinate system has the advantage that the coordinate lines can be chosen to coincide with the blade surface, wall surface, leading and trailing edge, and even the shock front, so that boundary conditions can be expressed easily and satisfied accurately. The individual S_1 and S_2 computer codes programmed with the use of this general coordinate system [15] have been recently combined together to form an automatic computing system, which is able to perform a number of selected functions. It is especially adopted to design turbomachine blades on a quasi-three-dimensional basis and to perform an analysis calculation on a full three-dimensional basis for the blade just designed.

A description of this three-dimensional computing system will be described in the following sections with emphasis on the calculation of the flow on the twisted S_1 surface, the determination of appropriate far upstream inlet and downstream exit conditions for S_1 calculation of an embedded blade row in a multiblade row machine, the automatic transfer of calculated results from one surface to the next, and its versatility for pure S_2, quasi-three-dimensional and full three-dimensional calculations.

Examples are given to illustrate the effectiveness of this

Contributed by the Gas Turbine Division of THE AMERICAN SOCIETY OF MECHANICAL ENGINEERS and presented at the 29th International Gas Turbine Conference and Exhibit, Amsterdam, The Netherlands, June 4–7, 1984. Manuscript received at ASME Headquarters, January 12, 1984. Paper No. 84-GT-185.

system. The calculated twist of the S_1 surfaces and the difference between quasi-three-dimensional and full three-dimensional solutions are clearly seen.

Quasi-Three-Dimensional Design and Analysis Code

1. Computing Scheme. The scheme of calculation will first be explained for quasi-three-dimensional design application. It proceeds as follows:

1 S_{2m} Stream Surface Calculation Including all Blade Rows of the Turbomachine:

The flow path in the meridional plane is obtained by a separate simplified-radial-equilibrium type of calculation. The variation of $V_\theta r$ of the fluid, isentropic efficiency of rotor, stagnation-pressure loss of stator, rotational speed, flow-blockage coefficient, and fluid state at machine inlet are specified by the designer.

The result of calculation, which includes the variations of Ψ, V, T, ρ, p, streamline distribution and distance between streamlines is stored in common blocks of the code for use in the next calculation.

2 Determination of the Far-Field Inlet and Exit Boundary Conditions and the Stream Surface Shape for S_1 Calculation of an Embedded Blade Row:

In order to calculate the S_1 flow of an embedded blade row in a multiblade row machine, all blade rows upstream and downstream of that blade row have to be taken out and proper far-field inlet and exit boundary conditions and stream surface shape, which will give the same value of flow variables at the gap stations G-G and F-F shown in Fig. 1, should be provided. In the present code, the method suggested in [16] is adopted. The known gas state at the gap station G-G and F-F is used as the inlet boundary condition for a backward and a forward S_2 calculation. The flow condition obtained at the inlet station I-I and exit station E-E, the streamline shape between I-I and G-G, and between F-F and E-E will be used as the input for the S_1 calculation in the next step.

3 Blade Geometry:

The blade section coordinates are obtained by one of the following blade construction subroutines:

(*a*) 65-series blade profile
(*b*) DCA blade profile
(*c*) Specified blade thickness distribution

In all three subroutines, the blade sections are laid out on conical surfaces.

4 Calculation of Flow on a Number of S_1 Surfaces of Revolution:

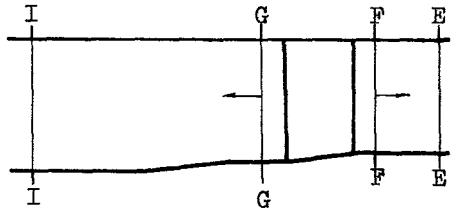

Fig. 1 Determination of flow condition upstream and downstream of the isolated blade row

This calculation gives the velocity distribution around the blade profile, which can be used to judge whether the flow field is satisfactory or not. In addition, the necessary information for the next cycle of iteration, namely the distributions of $V_\theta r$ and the thickness of the S_{2m} stream filament are to be determined in this calculation.

5 Stacking of Blade Sections:

In order to meet the strength requirement, the stacking line deviates slightly from a radial line. The amount of deviation in terms of a displacement in the axial coordinate away from the center of gravity of the hub section of the rotor and an angular displacement in the circumferential direction is specified by the designer. After stacking of the blade sections, the shape and position of the leading edge and trailing edge of the blade row have been changed. These new meridional coordinates will be used in the next cycle of calculation.

6 Check of Convergence:

The iterative calculation between the flow on S_1 and S_2 surface continues until the convergence criterion is satisfied at all grid

$$\left| \frac{Ms_1 - Ms_2}{Ms_2} \right|_{\max} < \epsilon$$

points. Here, subscript s_1 and s_2 denote the value on the intersecting streamline obtained in the S_1 and S_2 calculation, respectively. ϵ is the accuracy of convergence which is specified by the user. Machine calculation stops automatically when this criterion is satisfied. The user can then evaluate the result and modify the design if necessary. When a satisfactory solution is obtained, the blade coordinates on a number of planes perpendicular to a radial line are obtained by interpolation. They are used to construct contour plates to check fabricated blade profiles.

The S_1 and S_2 computing codes described in the preceding paragraphs can also be used for analysis problems. One may estimate the distribution of $V_\theta r$ and start with a S_{2m}

Nomenclature

a_{ij} = basic metric tensor
B = angular thickness of S_2 filament
H = absolute stagnation enthalpy per unit mass of gas
I = relative stagnation rothalpy per unit mass of gas
l = meridional coordinate for S_1 surface of revolution
Ni = the covariant component of unit vector normal to the stream surface
p = gas pressure
P = cascade spacing
$\dot{q}$ = heat transfer to gas per unit mass per unit time
r,φ,z = cylindrical coordinates
s = entropy of gas per unit mass
S_{2m} = mean S_2 surface
t = circumferential thickness of blade (or time)
T = temperature
$\mathbf{V}$ = absolute velocity of gas
$V_\theta r$ = angular momentum
$\mathbf{W}$ = relative velocity of gas
W^i = physical component of relative velocity along the x^i direction
x^i = general nonorthogonal curvilinear coordinates
β = angle between the $\mathbf{w}$ and its component on the meridional plane
ϵ = convergence accuracy
θ_{ij} = angle included by coordinate lines
Π' = viscous force tensor
ρ = static density of gas
σ = angle between Z and l
τ = normal thickness of S_1 (or S_2) stream filament
$\Delta\varphi$ = included angle corresponding to one pitch
Φ = dissipation function
Ψ = stream function
$\partial/\partial x^i$ = derivative of a flow variable following motion on stream surface with respect to the coordinate x^i on the meridional plane
$\partial/\partial x^i$ = ordinary derivative of a flow variable
ω = rotational speed

calculation, or one may estimate the location and shape of meridional streamlines and start with a number of S_1 calculations. Of course, in the latter case, the blade construction subroutine and stacking procedure will be bypassed.

2. Basic Equations. The basic aerothermodynamic equations for relative flow of a real gas passing through a turbomachine blade row rotating at constant angluar speed, ω, were given by Wu in references [17] and [18]. They are

Continuity:

$$\frac{\partial \rho}{\partial t} + \nabla \cdot (\rho \mathbf{W}) = 0 \tag{1a}$$

Motion:

$$-\frac{1}{\rho}\nabla p + \frac{1}{\rho}\nabla \Pi' = \frac{d'\mathbf{W}}{dt} - \omega^2 \mathbf{r} + 2\omega \times \mathbf{W} \tag{2a}$$

1st Law of Thermodynamics:

$$\frac{dI}{dt} = \frac{1}{\rho}\frac{\partial p}{\partial t} + \dot{q} + \frac{1}{\rho}\nabla \cdot (\Pi' \mathbf{W}) \tag{3a}$$

2nd Law of Thermodynamics:

$$T\frac{ds}{dt} = \dot{q} + \frac{\Phi}{\rho} \tag{4a}$$

where the first term on the right-hand side of equation (2) denotes the acceleration of relative flow.

Because the gas viscosity is the source of losses in turbomachines, its effect on gas flow cannot be entirely neglected in the design of turbomachines. But up to now it is not possible to calculate all the viscous terms in the equations. An approximate engineering method first suggested in [17] and [19] and now widely used is also used in the present code. Instead of equation (4); the increase of entropy in the flow process is estimated from experimental value of rotor efficiency and stator stagnation-pressure-loss coefficient. The entropy gradient value so obtained is then used in the following form of equation of motion for steady relative flow of nonviscous fluid

$$\mathbf{W} \times [\nabla \times \mathbf{V}] \approx \nabla I - T\nabla s \tag{2b}$$

In essence, this engineering model means that only the accumulated effect of upstream viscous action in increasing the entropy is considered in the flow calculation while the local viscous stresses are neglected in equations (2) and (3).

For the three-dimensional flow calculation which employs iterative calculations between the flow on S_1 and S_2 surfaces, it is important to use a consistent value of the gas state at a grid point common to the two surfaces. In our code system, entropy increase in the flow is empirically evaluated in the S_2 calculation. The radial entropy gradient so obtained decreases the flow velocity toward the inner and outer walls, as shown in Fig. 2. This radial velocity profile is of course closer to the actual flow than an isentropic velocity profile. In order to be consistent, the same value of entropy at a grid point in the S_2 calculation is also used in S_1 calculation.

Thus, the following set of basic equations is employed for S_1 and S_2 calculations in the present code:

$$\nabla \cdot (\rho \mathbf{W}) = 0 \tag{1b}$$

$$\mathbf{W} \times (\nabla \times \mathbf{V}) \approx \nabla I - T\nabla s \tag{2c}$$

$$\frac{d\mathbf{I}}{dt} \approx 0 \tag{3b}$$

$$\frac{ds}{dt} > 0 \tag{4b}$$

If it is preferred, an isentropic inviscid solution can be easily obtained by putting the value of rotor efficiency and stator stagnation-pressure-loss in the input of the code to be 100 percent and zero, respectively.

3. Principal Equation on S_1 and S_2 Stream Surface. General nonorthogonal curvilinear coordinates and corresponding nonorthogonal velocity components are

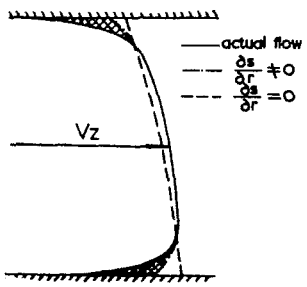

Fig. 2 Velocity distribution in radial direction

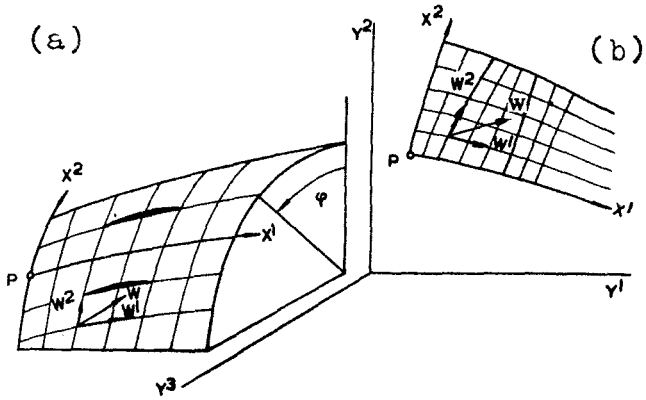

Fig. 3 Nonorthogonal curvilinear coordinates and nonorthogonal velocity components used for S_1 and S_2 stream surfaces

employed in the present code. It has the advantage that coordinate lines can be chosen to coincide with the blade surface, the hub and casing wall, and the leading and trailing edge of blades, so that the boundary condition can be accurately satisfied and that the code is applicable to any arbitrary geometrical configuration. For S_2 surface flow, nonorthogonal coordinates x^1 and x^2 are placed on the meridional plane (see Fig. 3(*b*)) and the bold symbol $\underline{\partial}/\underline{\partial}$ is used to denote the derivative of a flow variable on the S_2 surface with respect to the coordinates on the meridional plane.

The principal equation for S_2 surface flow is [14, 15]

$$\frac{1}{a_{11}}\frac{\underline{\partial}^2\Psi}{\underline{\partial}(x^1)^2} - 2\frac{\cos\theta_{12}}{\sqrt{a_{11}a_{22}}}\frac{\underline{\partial}^2\Psi}{\underline{\partial}x^1\underline{\partial}x^2} + \frac{1}{a_{22}}\frac{\underline{\partial}^2\Psi}{\underline{\partial}(x^2)^2} + \frac{J}{\sqrt{a_{11}}}\frac{\underline{\partial}\Psi}{\underline{\partial}x^1} + \frac{K}{\sqrt{a_{22}}}\frac{\underline{\partial}\Psi}{\underline{\partial}x^2} = M \tag{5}$$

where

$$J = -\frac{\underline{\partial}\ln(\sqrt{a_{11}/a_{22}}\,r\sin\theta_{12})}{\sqrt{a_{11}}\,\underline{\partial}x^1} + \frac{\cos\theta_{12}}{\sqrt{a_{22}}}\frac{\underline{\partial}\ln r}{\underline{\partial}x^2} + \frac{1}{\sin\theta_{12}\sqrt{a_{22}}}\frac{\underline{\partial}\theta_{12}}{\underline{\partial}x^2}$$

$$K = -\frac{\underline{\partial}\ln(\sqrt{a_{22}/a_{11}}\,r\sin\theta_{12})}{\sqrt{a_{22}}\,\underline{\partial}x^2} + \frac{\cos\theta_{12}}{\sqrt{a_{11}}}\frac{\underline{\partial}\ln r}{\underline{\partial}x^1} + \frac{1}{\sin\theta_{12}\sqrt{a_{11}}}\frac{\underline{\partial}\theta_{12}}{\underline{\partial}x^1}$$

$$M = \left(\frac{1}{\sqrt{a_{11}}}\frac{\underline{\partial}\ln\rho}{\underline{\partial}x^1} - \frac{\cos\theta_{12}}{\sqrt{a_{22}}}\frac{\underline{\partial}\ln\rho}{\underline{\partial}x^2}\right)\frac{1}{\sqrt{a_{11}}}\frac{\underline{\partial}\Psi}{\underline{\partial}x^1} + \left(\frac{1}{\sqrt{a_{22}}}\frac{\underline{\partial}\ln\rho}{\underline{\partial}x^2} - \frac{\cos\theta_{12}}{\sqrt{a_{11}}}\frac{\underline{\partial}\ln\rho}{\underline{\partial}x^1}\right)\frac{1}{\sqrt{a_{22}}}\frac{\underline{\partial}\Psi}{\underline{\partial}x^2}$$

$$+\frac{\tau\sin\theta_{12}}{\sqrt{a_{11}a_{22}}}\rho C$$

$$C = \frac{\sqrt{a_{11}}}{W^1}\left[-\frac{W\varphi}{r}\frac{\partial(V_\theta r)}{\partial x^2}+\frac{\partial \mathbf{I}}{\partial x^2}-T\frac{\partial s}{\partial x^2}-f_2\right]$$

f_2 is the covariant component of the **F** which is the same **F** of [1]

Where $a_{\alpha\beta}$ is the covariant metric tensor of a surface:

$$a_{\alpha\beta}=\frac{\partial y^k}{\partial x^\alpha}\frac{\partial y^k}{\partial x^\beta}=\mathbf{e}_\alpha\cdot\mathbf{e}_\beta=a_{\beta\alpha}$$

$\mathbf{e}_i$ is the base vector directed tangentially to the x^i coordinate curve. y^k is the usual orthogonal Cartesian coordinates of a point P.

For quasi-three-dimensional calculation, nonorthogonal coordinates x^1 and x^2 are taken on the S_1 surface of revolution (see Fig. 3(*a*)). The principal equation for S_1 surface flow is [14, 15]

$$\frac{1}{a_{11}}\frac{\partial^2\Psi}{\partial(x^1)^2}-2\frac{\cos\theta_{12}}{\sqrt{a_{11}a_{22}}}\frac{\partial^2\Psi}{\partial x^1\partial x^2}+\frac{1}{a_{22}}\frac{\partial^2\Psi}{\partial(x^2)^2}+\frac{J}{\sqrt{a_{11}}}\frac{\partial\Psi}{\partial x^1}+\frac{K}{\sqrt{a_{22}}}\frac{\partial\Psi}{\partial x^2}=M \tag{6}$$

where

$$J = -\frac{\partial\ln(\sqrt{a_{11}/a_{22}}\tau\sin\theta_{12})}{\sqrt{a_{11}}\partial x^1}+\frac{\cos\theta_{12}\partial\ln\tau}{\sqrt{a_{22}}\partial x^2}+\frac{1}{\sin\theta_{12}\sqrt{a_{22}}}\frac{\partial\theta_{12}}{\partial x^2}$$

$$K = -\frac{\partial\ln(\sqrt{a_{22}/a_{11}}\tau\sin\theta_{12})}{\sqrt{a_{22}}\partial x^2}+\frac{\cos\theta_{12}\partial\ln\tau}{\sqrt{a_{11}}\partial x^1}+\frac{1}{\sin\theta_{12}\sqrt{a_{11}}}\frac{\partial\theta_{12}}{\partial x^1}$$

$$M = \left(\frac{1}{\sqrt{a_{11}}}\frac{\partial\ln\rho}{\partial x^1}-\frac{\cos\theta_{12}}{\sqrt{a_{22}}}\frac{\partial\ln\rho}{\partial x^2}\right)\frac{1}{\sqrt{a_{11}}}\frac{\partial\Psi}{\partial x^1}+\left(\frac{1}{\sqrt{a_{22}}}\frac{\partial\ln\rho}{\partial x^2}-\frac{\cos\theta_{12}}{\sqrt{a_{11}}}\frac{\partial\ln\rho}{\partial x^1}\right)\frac{1}{\sqrt{a_{22}}}\frac{\partial\Psi}{\partial x^2}-2\omega^3\tau\rho\sin^2\theta_{12}$$

It is to be noted that when the S_1 surface is a surface of revolution, $\omega^3=\omega\sin\sigma$.

Equations (5) and (6) can be solved either by matrix method or by relaxation method. The present code system utilizes the S_1 code solved by the matrix method [20] and the S_2 code solved by the relaxation method [21], which have been well developed and readily available in the IETP, CAS.

In the present code system, for S_2 calculations, the grid is set up on the meridional plane. Eleven grid lines in x^2 direction and maximum 80 grid lines in x^1 direction can be taken. The hub and casing of a turbomachine as well as the leading edge and the trailing edge of a blade can be used as grid lines. For S_1 calculations, the grid is set up on the stream surface. Seven or 9 grid lines in x^2 direction are used during the initial stage of calculation, but it is increased to 15 grid lines in the few iterations near convergence, in order to increase the accuracy of the computation. Maximum 70 grid lines in x^1 direction can be taken. In practical calculations, the grid lines specified within the range of a blade row is finer than that in the expanded parts upstream and downstream of the blade row.

Full Three-Dimensional Calculation

An important feature of the present automatic computing system is that after a quasi-three-dimensional design is completed, a followup full three-dimensional analysis calculation can be very easily carried out in the following manner: The result obtained in the step (4) of the quasi-three-dimensional calculation is used to form a number of S_2 surfaces (see Fig. 4). The flow on these S_2 surfaces is calculated by the same code used to compute the S_{2m} flow in the quasi-three-dimensional design calculation.

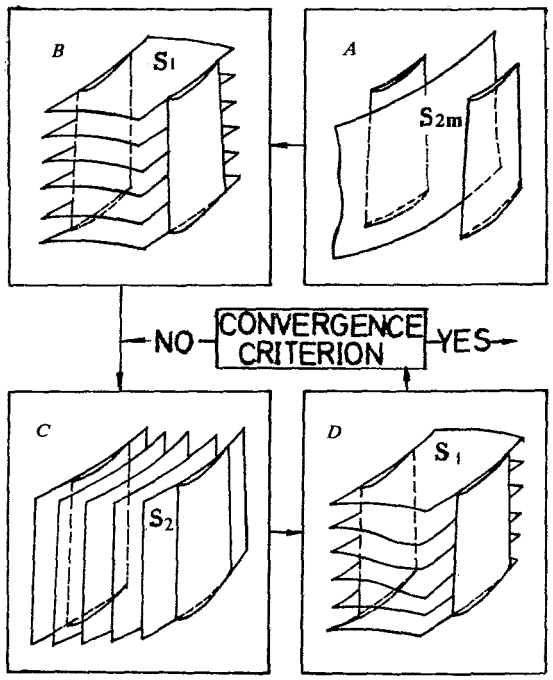

Fig. 4 Full three-dimensional solution

The results obtained in the S_2 calculation, in turn, are used to form a number of general S_1 surfaces, which are not surfaces of revolution (see Fig. 4(*d*)). A full three-dimensional solution is then obtained by iterative calculation between the flow on a number of S_2 surfaces (see Fig. 4(*c*)) and a number of S_1 surfaces (see Fig. 4(*d*)).

When an S_2 surface is chosen to coincide with either the suction or pressure surface of the blade, the S_2 code is able to calculate the value of $V_\theta r$ along the blade surface by the use of the components of the unit vector normal to the blade surface as follows

$$W_\varphi=-\left(\frac{N_1}{N_\varphi}W^1+\frac{N_2}{N_\varphi}W^2\right)\sin\theta_{12} \tag{7}$$

$$V_\theta r=\left[W^1\frac{1}{\sqrt{a_{11}}}\left(\frac{\partial\varphi}{\partial x^1}\right)+W^2\frac{1}{\sqrt{a_{22}}}\left(\frac{\partial\varphi}{\partial x^2}\right)+\omega\right]r^2 \tag{8}$$

For flow calculation on general S_1 surfaces, one of the following two alternatives may be chosen:

1 General coordinates x^1 and x^2 are placed on a cylindrical surface. The derivatives in the equation are that of the flow variable on the S_1 surface with respect to the coordinate on the cylindrical surface and are denoted by the special derivative in bold sign as is the case of S_2 surface flow.

2 General coordinates x^1 and x^2 are placed on the S_1 stream surface. The corresponding principal equation is

$$\frac{1}{a_{11}}\frac{\partial^2\Psi}{\partial(x^1)^2}-2\frac{\cos\theta_{12}}{\sqrt{a_{11}a_{22}}}\frac{\partial^2\Psi}{\partial x^1\partial x^2}+\frac{1}{a_{22}}\frac{\partial^2\Psi}{\partial(x^2)^2}+\frac{J}{\sqrt{a_{11}}}\frac{\partial\Psi}{\partial x^1}+\frac{K}{\sqrt{a_{22}}}\frac{\partial\Psi}{\partial x^2}=M \tag{9}$$

where

$$J = -\frac{\partial \ln(\sqrt{a_{11}/a_{22}}\tau \sin\theta_{12})}{\sqrt{a_{11}}\partial x^1} + \frac{\cos\theta_{12}\partial \ln\tau}{\sqrt{a_{22}}\partial x^2} + \frac{1}{\sin\theta_{12}\sqrt{a_{22}}}\frac{\partial\theta_{12}}{\partial x^2}$$

$$K = -\frac{\partial \ln(\sqrt{a_{22}/a_{11}}\tau \sin\theta_{12})}{\sqrt{a_{22}}\partial x^2} + \frac{\cos\theta_{12}\partial \ln\tau}{\sqrt{a_{11}}\partial x^1} + \frac{1}{\sin\theta_{12}\sqrt{a_{11}}}\frac{\partial\theta_{12}}{\partial x^1}$$

$$M = \left(\frac{1}{\sqrt{a_{11}}}\frac{\partial \ln\rho}{\partial x^1} - \frac{\cos\theta_{12}}{\sqrt{a_{22}}}\frac{\partial \ln\rho}{\partial x^2}\right)\frac{1}{\sqrt{a_{11}}}\frac{\partial\Psi}{\partial x^1} + \left(\frac{1}{\sqrt{a_{22}}}\frac{\partial \ln\rho}{\partial x^2} - \frac{\cos\theta_{12}}{\sqrt{a_{11}}}\frac{\partial \ln\rho}{\partial x^1}\right)\frac{1}{\sqrt{a_{22}}}\frac{\partial\Psi}{\partial x^2} - 2\omega^3\tau\rho\sin^2\theta_{12}$$

It may be noted that this choice of x^1 and x^2 coordinates is preferred to the preceding one, because it may be used to compute the flow on general S_1 surface in a centrifugal or mixed-flow turbomachines. It is to be noted that when S_1 surface is a surface of revolution

$$\omega^3 = \omega\sin\sigma \tag{10}$$

and equation (9) reduces to equation (6) in the quasi-three-dimensional calculation.

Actually, the present computing system contains only a computing code for general S_1 and a computing code for general S_2 surface flow. The general S_1 code can be used for S_1 surface-of-revolution calculation in the quasi-three-dimensional solution.

Numerical Examples and Discussions

1. Example 1. The quasi-three-dimensional code has been used to design a two-stage axial-compressor. The flow passage is divided into five sections as shown in Fig. 5. This compressor is designed for a mass flow rate of 88 kg/s, rotating speed of rotor of 8000 revs/min, and a tip-relative Mach number of the first rotor of 0.75.

In Fig. 6, curve A shows the convergence history for the first stator and curve B, that for the complete first stage. Actually, curve B reflects the convergence history of the rotor, because the calculation indicated that the iterative error of the rotor is always higher than that of the stator. The two curves show that the degree of convergence increases monotonically and smoothly and the convergence is so fast that only 5 or 6 cycles of iteration are needed to reach an acceptable convergence criterion. This fact indicates that the quasi-three-dimensional solution based on the stream-function equation, which is expressed with respect to nonorthogonal curvilinear coordinates and nonorthogonal velocity components, is quite suitable for use in the engineering design of turbomachine blades.

Curve C in Fig. 6 indicates the convergence history of the same stator, but the preparatory calculation of S_1 stream surface (that is, the far-field S_{2m} calculation for the isolated blade row) was omitted, and arbitrary values are taken at the inlet and exit stations I-I and E-E. As a result, the convergence accuracy was reduced.

Curve D indicates the convergence history of the first stage when the entropy gradient was omitted in the S_1 calculation. The importance of using the same thermodynamic state of the gas at the grid points of the intersecting streamline of the S_1 and S_2 surface is thus apparent.

The variation of $V_\theta r$ throughout the blade row and its

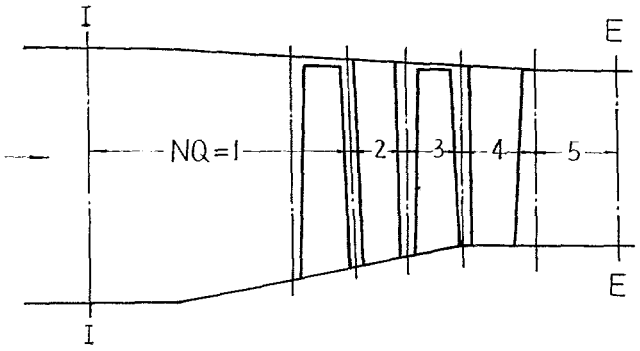

Fig. 5 Flow path

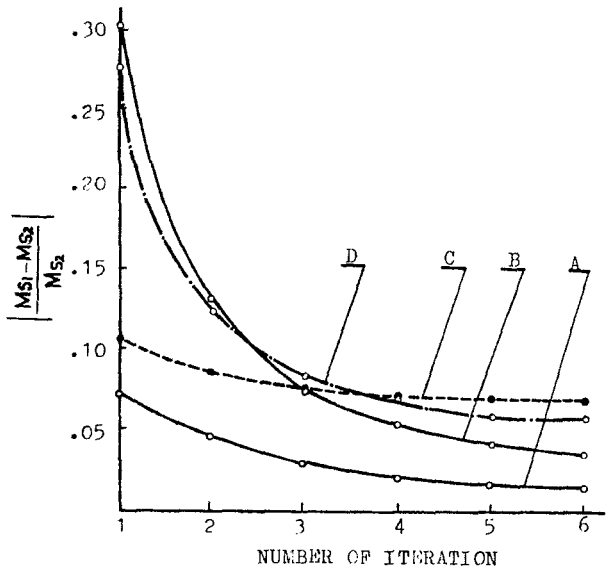

Fig. 6 History of convergence for quasi-three-dimensional calculation

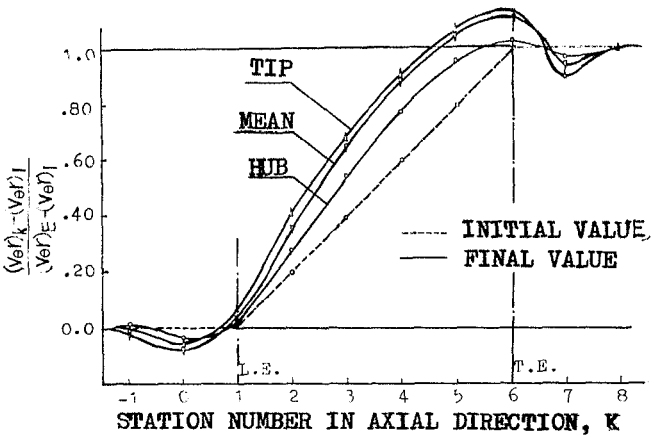

Fig. 7 Distribution of $V_\theta r$ in stator of first stage

difference between the initial and final value are shown in Fig. 7. It is seen that the latter is quite large.

Figure 7 indicates that the quasi-three-dimensional design method, obtained by iterative solution between the flow on a single S_2 surface and a number of S_1 surfaces, is better than a two-dimensional design. The calculation of the flow on an S_1 surface plays an important role in the quasi-three-dimensional code.

Mach number distribution around the blade surface at mean radius is shown in Fig. 8.

2. Example 2. The automatic computing system presented herein has been used to design a high subsonic

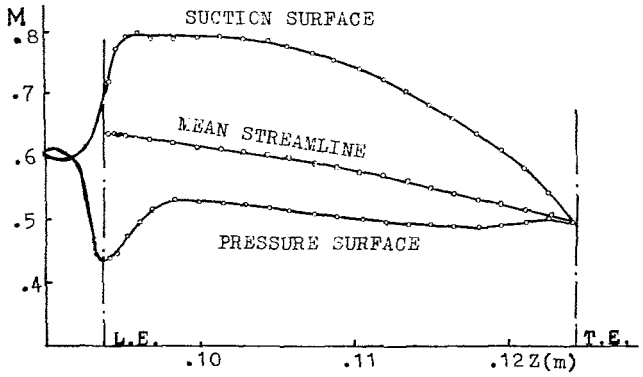

Fig. 8 Mach number distribution around the stator of first stage (midspan section)

stator of a single stage transonic fan. After completion of the blade design on the basis of a quasi-three-dimensional calculation, a full three-dimensional analysis was immediately carried out. The quasi-three-dimensional design took 5 cycles of iteration, whereas the full three-dimensional analysis took only 3 cycles of iteration.

The difference between the two solutions is indicated by the twist of the S_1 surface, in other words, by the deviation of S_1 surface from surface of revolution. Figure 9(*a*) shows the amount of deviation for the S_1 surface no. 3 and no. 5 of Fig. 9(*b*), at a number of stations along the flow direction. It is apparent that the deviation of surface no. 3, which is located nearly at midspan, is larger than that of no. 5. The deviation measured by the difference in radius, Δr, is less than one percent of the radius r. Figure 9(*b*) also shows twist of S_1 stream surfaces near the leading edge and the trailing edge of the stator.

The difference in the streamline distribution, the variation of $V_\theta r$ along the intersecting streamline of S_1 and S_2 surfaces, and the variation of the angular thickness of S_{2m} filament as determined in the S_1 calculation, respectively, are shown in Fig. 10(*a*), 10(*b*), 10(*c*), respectively, and are seen to be small. Yet these small differences are sufficient to cause a significant difference on the Mach number distribution over the blade surface (see Fig. 11).

It is interesting to note that the peak Mach number on the suction surface obtained in the full three-dimensional solution is higher than that obtained in the quasi-three-dimensional

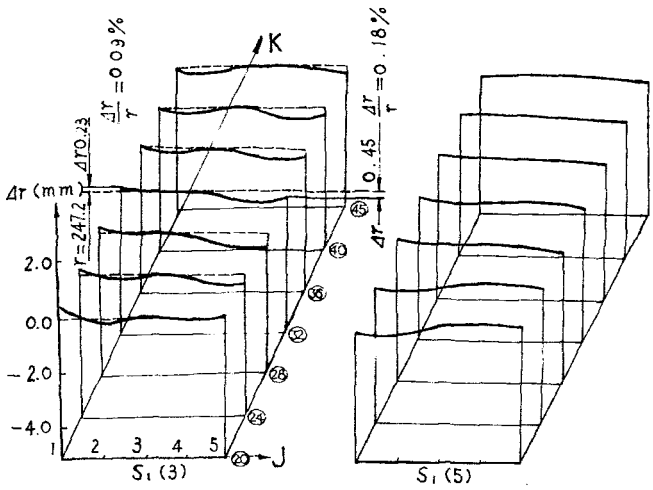

Fig. 9(*a*) Deviation of general S_1 surface from surface of revolution (*magnified ten times*)

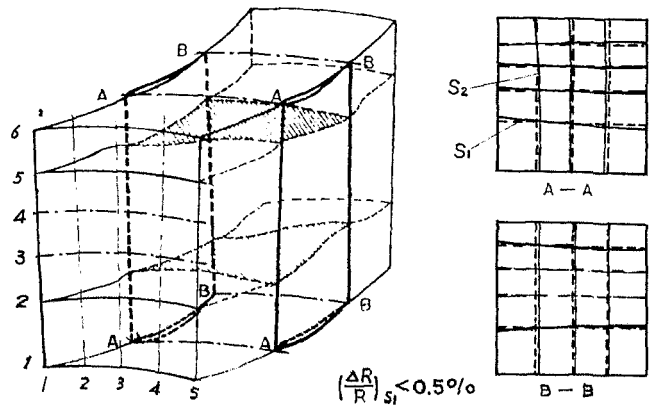

Fig. 9(*b*) Deviation of general S_1 surface from surface of revolution (schematic)

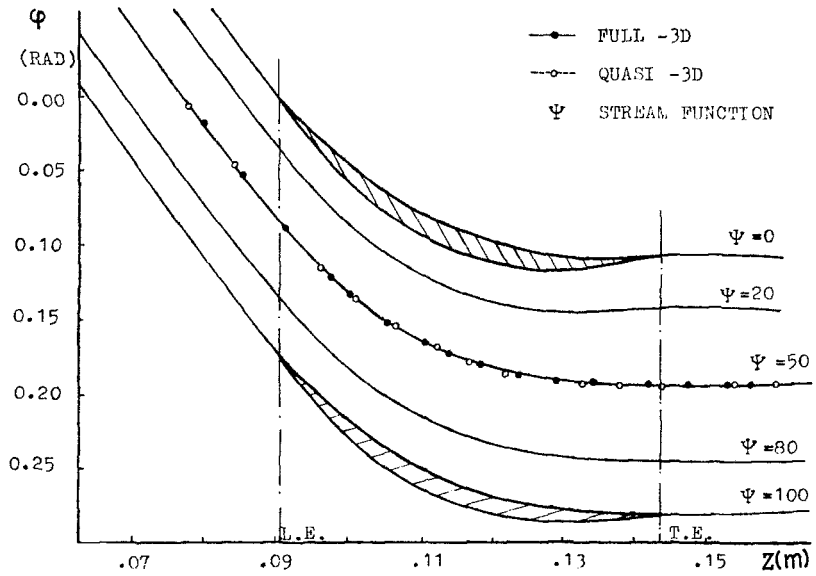

Fig. 10(*a*) The streamlines on S_1 stream surface (midspan section)

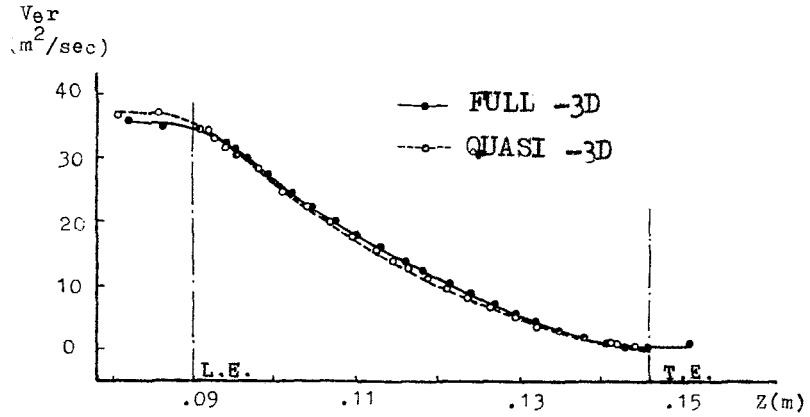

Fig. 10(*b*) Variation of $V_{\theta}r$ on mean streamline (midspan section)

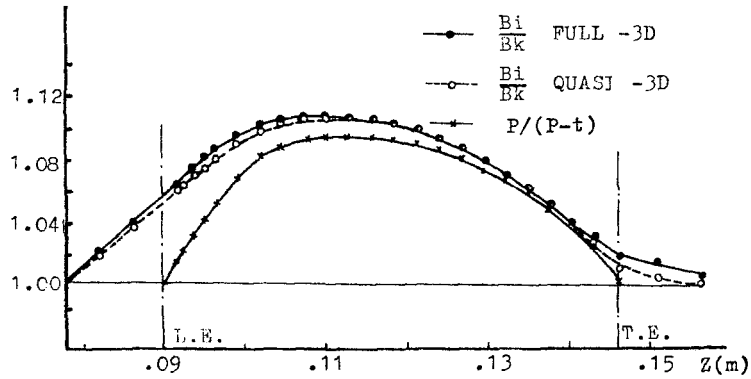

Fig. 10(c) Variation of *Bi/Bk* and *P/(P−t)* on mean streamline (midspan section)

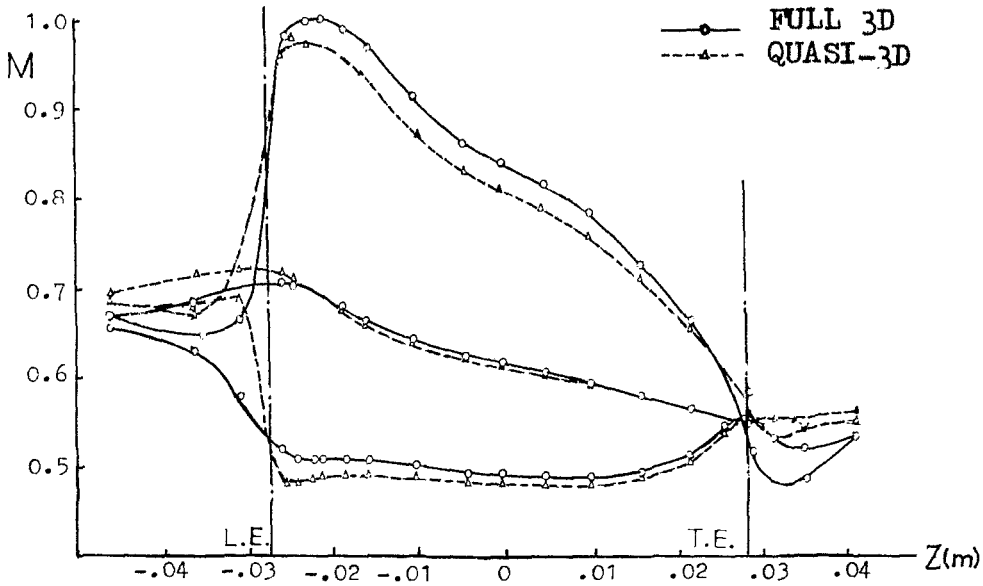

Fig. 11 Mach number distribution over blade surface (midspan section)

solution. In this case, the full three-dimensional peak Mach number exceeds the sonic value slightly.

Concluding Remarks

Two quasi-three-dimensional calculations made for a two stage axial compressor and a high subsonic stator of a single-stage transonic fan took only five cycles of iteration with a satisfactory accuracy of convergence. It shows that the quasi-three-dimensional blade design method obtained by iterative calculation between the flow on a number of S_1 surfaces of revolution and a single S_{2m} surface is a practical engineering method. The success of the present code may be attributed, in part, to the use of the new $S_1 - S_2$ iterative model.

Because the full three-dimensional analysis calculation is based on an iterative calculation of the flow on a number of general S_1 surfaces and a number of general S_2 surfaces, the same codes in the quasi-three-dimensional calculation can be used for this purpose, only difference being that calculation is carried out on more S_2 surfaces in the full three-dimensional

solution. This is the main advantage of the present method of solving full three-dimensional method. Moreover, the deviation of the S_1 surface from a surface of revolution is readily available in the full three-dimensional calculation and directly indicates the amount of secondary flow involved in that particular blade design.

References

1 Wu, C.-H., "A General Theory of Three-Dimensional Flow in Subsonic and Supersonic Turbomachines of Axial-, Radial-, and Mixed-Flow Types," ASME Paper No. 50-A-79, 1950 (Trans. ASME, Nov. 1952), or NACA TN 2604, 1952.

2 Wu, C.-H., "Matrix and Relaxation Solutions that Determine Subsonic Through-Flow in an Axial-Flow Gas Turbine," NACA TN 2750, 1950.

3 Wu, C.-H., and Brown, C. A., "Method of Analysis for Compressible Flow Past Arbitrary Turbomachine Blades on General Surface of Revolution," NACA TN 2470, 1951.

4 Novak, R. A., "Streamline Curvature Computing Procedures for Fluid-Flow Problems," ASME JOURNAL OF ENGINEERING FOR POWER, 1967.

5 Marsh, H., "A Digital Computer Program for the Through Flow Fluid Mechanics in an Arbitrary Turbomachine, Using a Matrix Method," ARC R&M 3509, 1968.

6 Frost, D. H., and Smith, D. J. L., "A Streamline Curvature Computer Program for Analyzing the Subsonic Compressible Flow Past a Cascade of Aerofoils," NGTE Report R. 327, ARC Paper No. 35346, 1973.

7 Smith, D. J. L., "Computer Solutions of Wu's Equations for Compressible Flow Through Turbomachines," NASA SP-304, *Fluid Mechanics Acoustics and Design of Turbomachinery*, Part I, 1974, pp. 43–74.

8 Hirsch, C., "Finite Element Method for Throughflow Calculations," AGARD-CP-195, 1976.

9 Bosman, C., and El-Shaarawi, M. A. I., "Quasi-Three-Dimensional Numerical Solution of Flow in Turbomachines," ASME Paper No. 76-FE-23, 1976.

10 Novak, R. A., and Hearsey, R. M., "A Nearly Three Dimensional Intrablade Computing System for Turbomachinery," ASME *Journal of Fluids Engineering*, Mar. 1977.

11 Academia Sinica, Shenyang Aeroengine Company, "Theory, Method and Application of Three-Dimensional Flow Design of Transonic Axial-Flow Compressor," *Journal of Engineering Thermophysics*, Vol. 1, No. 1, 1980 (in Chinese).

12 McDonald, P. W., Bolt, C. R., Dunker, R. J., and Weyer, H. B., "A Comparison Between Measured and Computed Flow Field in a Transonic Compressor Rotor," ASME Paper No. 80-GT-7, 1980.

13 Zhu, G., Ge, M., and Wu, C.-H., "Three-Dimensional Subsonic Flow Through a Stator by Use of a Central S_2 Stream Surface and Several S_1 Surfaces of Revolution," *Journal of Engineering Thermophysics*, Vol. 4, No. 2, 1983 (in Chinese).

14 Wu, C.-H., "Three-Dimensional Turbomachine Flow Equations Expressed with Respect to Non-Orthogonal Curvilinear Coordinates and Methods of Solution," Lecture Notes, China University of Science and Technology, 1975, or *Proceedings of 3rd ISABE*, 1976, pp. 233–252.

15 Wu, W.-Q., Zhu, R.-G., and Liu, C.-E., "Computational Design of Turbomachine Blades," *J. Aircraft*, Vol. 17, No. 5, May 1980.

16 Wu, C.-H., and Zhu, G., "Determination of the Appropriate Upstream and Downstream Conditions in Rotating Cascade Experiment and Calculation of Arbitrary S_1 Stream Surface for an Embedded Blade Row," *Journal of Engineering Thermophysics*, Vol. 4, No. 1, 1983 (in Chinese).

17 Wu, C.-H., and Wolfenstein, L., "Application of Radial-Equilibrium-Condition to Axial-Flow Compressor and Turbine Design," NACA TR 955, 1950.

18 Wu, C.-H., "Fundamental Aerothermodynamic Equations for Stationary and Moving Coordinate Systems: Action of Viscous Forces and Physical Significance of Viscous Terms," *Journal of Mechanical Engineering*, Vol. 13, No. 4, Dec. 1965 (in Chinese) or *Engineering Thermophysics in China*, Vol. 1, No. 1, 1980, Rumford Pub. Co., U.S.A.

19 Members of the Compressor and Turbine Research Division, "Aerodynamic Design of Axial-Flow Compressors," NACA RM E56B03, 1956.

20 Wu, W.-Q., and Liu, C.-E., "Flow-Field Matrix Solution for Direct Problem of Flow Along S_1 Relative Stream Surface Employing Non-Orthogonal Curvilinear Coordinates and Corresponding Non-Orthogonal Velocity Components," *Journal of Engineering Thermophysics*, Vol. 1, No. 1, 1980 (in Chinese).

21 Zhu, R.-G., "Flow-Field Line-Relaxation Solution for Inverse Problem of Flow Along S_2 Relative Stream Surface Employing Non-Orthogonal Curvilinear Coordinates and Corresponding Non-Orthogonal Velocity Components," *Journal of Engineering Thermophysics*, Vol. 1, No. 1, 1980 (in Chinese).

solution. This is the main advantage of the present method of solving full three-dimensional method. Moreover, the deviation of the S_1 surface from a surface of revolution is readily available in the full three-dimensional calculation and directly indicates the amount of secondary flow involved in that particular blade design.

References

1 Wu, C.-H., "A General Theory of Three-Dimensional Flow in Subsonic and Supersonic Turbomachines of Axial-, Radial-, and Mixed-Flow Types," ASME Paper No. 50-A-79, 1950 (Trans. ASME, Nov. 1952), or NACA TN 2604, 1952.

2 Wu, C.-H., "Matrix and Relaxation Solutions that Determine Subsonic Through-Flow in an Axial-Flow Gas Turbine," NACA TN 2750, 1950.

3 Wu, C.-H., and Brown, C. A., "Method of Analysis for Compressible Flow Past Arbitrary Turbomachine Blades on General Surface of Revolution," NACA TN 2470, 1951.

4 Novak, R. A., "Streamline Curvature Computing Procedures for Fluid-Flow Problems," ASME JOURNAL OF ENGINEERING FOR POWER, 1967.

5 Marsh, H., "A Digital Computer Program for the Through Flow Fluid Mechanics in an Arbitrary Turbomachine, Using a Matrix Method," ARC R&M 3509, 1968.

6 Frost, D. H., and Smith, D. J. L., "A Streamline Curvature Computer Program for Analyzing the Subsonic Compressible Flow Past a Cascade of Aerofoils," NGTE Report R. 327, ARC Paper No. 35346, 1973.

7 Smith, D. J. L., "Computer Solutions of Wu's Equations for Compressible Flow Through Turbomachines," NASA SP-304, *Fluid Mechanics Acoustics and Design of Turbomachinery*, Part I, 1974, pp. 43–74.

8 Hirsch, C., "Finite Element Method for Throughflow Calculations," AGARD-CP-195, 1976.

9 Bosman, C., and El-Shaarawi, M. A. I., "Quasi-Three-Dimensional Numerical Solution of Flow in Turbomachines," ASME Paper No. 76-FE-23, 1976.

10 Novak, R. A., and Hearsey, R. M., "A Nearly Three Dimensional Intrablade Computing System for Turbomachinery," ASME *Journal of Fluids Engineering*, Mar. 1977.

11 Academia Sinica, Shenyang Aeroengine Company, "Theory, Method and Application of Three-Dimensional Flow Design of Transonic Axial-Flow Compressor," *Journal of Engineering Thermophysics*, Vol. 1, No. 1, 1980 (in Chinese).

12 McDonald, P. W., Bolt, C. R., Dunker, R. J., and Weyer, H. B., "A Comparison Between Measured and Computed Flow Field in a Transonic Compressor Rotor," ASME Paper No. 80-GT-7, 1980.

13 Zhu, G., Ge, M., and Wu, C.-H., "Three-Dimensional Subsonic Flow Through a Stator by Use of a Central S_2 Stream Surface and Several S_1 Surfaces of Revolution," *Journal of Engineering Thermophysics*, Vol. 4, No. 2, 1983 (in Chinese).

14 Wu, C.-H., "Three-Dimensional Turbomachine Flow Equations Expressed with Respect to Non-Orthogonal Curvilinear Coordinates and Methods of Solution," Lecture Notes, China University of Science and Technology, 1975, or *Proceedings of 3rd ISABE*, 1976, pp. 233–252.

15 Wu, W.-Q., Zhu, R.-G., and Liu, C.-E., "Computational Design of Turbomachine Blades," *J. Aircraft*, Vol. 17, No. 5, May 1980.

16 Wu, C.-H., and Zhu, G., "Determination of the Appropriate Upstream and Downstream Conditions in Rotating Cascade Experiment and Calculation of Arbitrary S_1 Stream Surface for an Embedded Blade Row," *Journal of Engineering Thermophysics*, Vol. 4, No. 1, 1983 (in Chinese).

17 Wu, C.-H., and Wolfenstein, L., "Application of Radial-Equilibrium-Condition to Axial-Flow Compressor and Turbine Design," NACA TR 955, 1950.

18 Wu, C.-H., "Fundamental Aerothermodynamic Equations for Stationary and Moving Coordinate Systems: Action of Viscous Forces and Physical Significance of Viscous Terms," *Journal of Mechanical Engineering*, Vol. 13, No. 4, Dec. 1965 (in Chinese) or *Engineering Thermophysics in China*, Vol. 1, No. 1, 1980, Rumford Pub. Co., U.S.A.

19 Members of the Compressor and Turbine Research Division, "Aerodynamic Design of Axial-Flow Compressors," NACA RM E56B03, 1956.

20 Wu, W.-Q., and Liu, C.-E., "Flow-Field Matrix Solution for Direct Problem of Flow Along S_1 Relative Stream Surface Employing Non-Orthogonal Curvilinear Coordinates and Corresponding Non-Orthogonal Velocity Components," *Journal of Engineering Thermophysics*, Vol. 1, No. 1, 1980 (in Chinese).

21 Zhu, R.-G., "Flow-Field Line-Relaxation Solution for Inverse Problem of Flow Along S_2 Relative Stream Surface Employing Non-Orthogonal Curvilinear Coordinates and Corresponding Non-Orthogonal Velocity Components," *Journal of Engineering Thermophysics*, Vol. 1, No. 1, 1980 (in Chinese).

DISCUSSION

I. K. Jennions[1]

Firstly I would like to take this opportunity to congratulate Professor Wu and his colleagues on their recent publication of so many interesting papers; we look forward to developments of the S_1/S_2 approach. The present paper puts the original ideas of Wu [1] into practice to form both quasi-three-dimensional and fully three-dimensional numerical solution procedures, which are demonstrated on two examples.

With all quasi-three-dimensional solution procedures involving the use of an S_2 surface one has the question of how the surface is defined, and also what approximations are inherent with the approach. The authors have chosen their S_2 surface to be a streamsurface defined by the locus of the $\psi = 50$ S_1 streamlines. Other authors have defined their S_2 surface as a mean cambersurface [22], or the locus of S_1 mass-averaged streamlines [9]. It is not clear considering these choices how the S_2 surface should be defined and what effect this definition would have on the answers. A technique that avoids this problem is passage averaging [23, 24, 25], where the through-flow solution is calculated for the mean flow properties and no S_2 surface needs to be introduced. What is also not clear is the way in which the present paper defines and uses B_i, and consequently any assumption that may be made in the continuity equation. A discussion from the authors as to the choice of S_2 surface and the assumptions that are made in their method would be most welcome.

Example 1 is the design of a two-stage axial compressor for which the losses are taken from a previous experiment on a similar machine. The objective of a design, once the primary goals of pressure ratio, etc., have been met, is to perform the process efficiently. This involves understanding loss mechanisms and changing the design to increase efficiency. The example does not address this question and would be more easily understood as an analysis of an existing machine.

For the same example, Fig. 6 shows some confusion between convergence of the iterative scheme and consistency between the S_1 and S_2 solutions, which can be illustrated as follows. Convergence is most easily defined as being achieved when a chosen parameter of the system does not change by a significant amount from one iteration to the next. This parameter could be the streamtube contraction through the row, the blade exit angle, or the Mach number. For a quasi-three-dimensional calculation on a turbine rotor, performed in a similar way to that described in [26], Fig. 12 shows the change in rotor exit angle with iteration. The exit angle is calculated in the blade-to-blade program using a Kutta condition on the trailing edge. The angle is then transferred to the through-flow program for the next iteration. Convergence, as defined by the change in the exit angle from one iteration to the next, is seen to be rapid. This, however, does not ensure consistency between the through-flow and blade-to-blade solutions, a measure of which can be obtained from Fig. 13. Here the maximum value of $|(Ms_1 - Ms_2)/Ms_2|$ is 0.016, where it is stressed that this is a more severe test case (>100 deg turning) than that presented by the authors. All quasi-3D methods will possess a residual value of $|(Ms_1 - Ms_2)/Ms_2|$ due to passing averaged variables from one program to another with the inevitable interpolations. What one needs to achieve is consistency between the solutions to an acceptable level for design purposes.

[1]Principal Theoretical Scientist, Theoretical Science Group, Rolls-Royce Ltd., P.O. Box 31, Derby DE2 8BJ, England

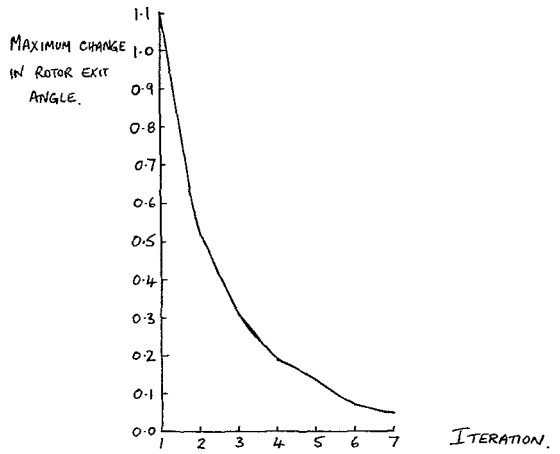

Fig. 12 Change in rotor exit angle with iteration

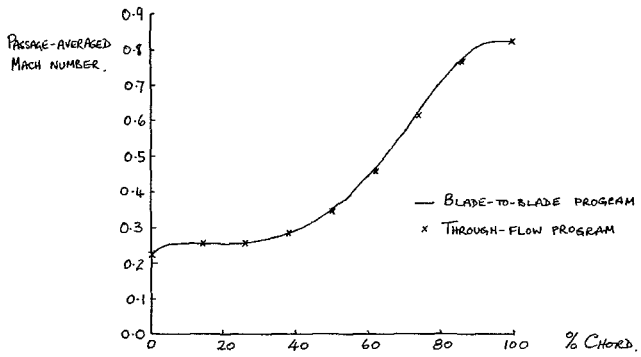

Fig. 13 Midheight section Mach numbers

Finally, it is not obvious from the paper how the authors treat conditions just downstream of the trailing edge for the fully three-dimensional solution. On a twisted S_1 surface the normal repeat condition cannot be applied as the suction and pressure surfaces are at different radial heights. If the repeat condition were to be applied properly then the S_1 calculations could not be performed in isolation. One possible treatment would be to solve for the flow with the blade in the center of the solution domain with the repeat condition applied between blade midpassage locations.

References

22 Senoo, Y., and Nakase, Y., "An Analysis of Flow Through a Mixed Flow Impeller," ASME JOURNAL OF ENGINEERING FOR POWER, 1972, pp. 43–50.

23 Smith, L. H., Jr., "The Radial Equilibrium Equation of Turbomachinery," ASME JOURNAL OF ENGINEERING FOR POWER, Jan. 1966, pp. 1–12.

24 Hirsch, C., and Warzee, G., "An Integrated Quasi-3D Finite Element Calculation Program for Turbomachinery Flows," ASME JOURNAL OF ENGINEERING FOR POWER, 1979, pp. 141–148.

25 Jennions, I. K., and Stow, P., "A Quasi-Three-Dimensional Turbomachinery Blade Design System: Part I—Through-Flow Analysis," ASME JOURNAL OF ENGINEERING FOR GAS TURBINES AND POWER, Vol. 107, No. 2, Apr. 1985, pp. 301–307.

26 Jennions, I. K., and Stow, P., "A Quasi-Three-Dimensional Turbomachinery Blade Design System: Part II—Computerized System," ASME JOURNAL OF ENGINEERING FOR GAS TURBINES AND POWER, Vol. 107, No. 2, Apr. 1985, pp. 308–316.

T. Katsanis[2] and E. McFarland[2]

The authors are to be congratulated for preparing a fine paper. In the interest of brevity, our discussion will be confined to raising questions about specific details.

The distinction between the matrix method and the relaxation method is not clear, since the relaxation method is used to solve matrix equations. Would you clarify this distinction?

The explanation of the flow calculation on a general S_1 surface does not appear complete. When the S_1 surface is a surface of revolution, periodic boundary conditions are used upstream and downstream of the blade row. However, when the S_1 surface is not a surface of revolution, the flow is not periodic on the surface upstream and downstream of the blade row. How is this problem handled?

In a three-dimensional flow, S_1 and S_2 surfaces become highly distorted, and may even be doubled back over themselves. It does not seem practical to use this scheme for a fully three-dimensional flow. In any event, the question remains as to how close a solution obtained by this method would come to a solution obtained by a three-dimensional Euler code such as Denton's.

A discussion by the authors of the limitations of their three-dimensional method would be appreciated. It is quesionable, for instance, whether the method could calculate a flow with a strong passage vortex.

Work similar to this has been done previously using the finite element method, and reported in [27].

References

27 Krimerman and Adler, "The Complete Three-Dimensional Calculation of the Compressible Flow Field in Turbo Impellers," *Journal of Mechanical Engineering Science*, Vol. 20, 1978.

[2]NASA-Lewis Research Center, Cleveland, Ohio

Note: The Author's Closure to the discussion by I. K. Jennions appears on p. 553.

(*continued from p. 285*)

Author's Closure

1 The Definition and Role of Central (Mean) S_2 Surface in the Quasi-3D Solution Procedure

1 Firstly, I would like very much to emphasize that, since the first publication of Wu's work on 3D turbomachine flow, in his 2D flow solution along an S_1 or S_2 surface and his theory of 3d Solution based on the iterative solution between flows on S_1 and S_2 surfaces, he always works definitely on calculation for a number of physical surfaces (either S_1 or S_2 surfaces). The definitions of S_1 and S_2 surface were clearly given in his first publication [28] and remain unchanged throughout his later development and all his computer codes.

2 Secondly, depending on particular situations, the shape of the S_1 or S_2 surface may either be given at the beginning of calculation or obtained at the end of the solution of the other surface flow. For instance, in S_1 calculation, usually the geometry of the S_1 stream sheet (i.e., the shape of the central stream surface plus the thickness variation of the sheet) is given and calculation is made to obtain the flow in the stream sheet (i.e., along its central stream surface).

On the other hand, the conception of the S_2 surface is especially useful for the optimum design of hub and casing contours and 3D blade design. For this type of application, the shape of the hub/tip shape and the variations of $V_\theta r$ of gas flow along central S_2 surface[3] and of its thickness[4] are specified by the designer and calculation is made to obtain the complete flow variation along the central S_2 surface and also the shape of this central S_2 surface (please see Figs. 3, 4, 5, 9 of [28], Fig. 15 of [29], and Figs. 1, 4 of [30]). Perhaps I should mention that this latter feature of Wu's S_2 solution was often overlooked by some readers. It seems to us that the phrase "quasi-3D solution" has been used by different people with different meanings. Some people seem to call his solution based on one S_2 surface flow and several S_1 surface flows a "quasi-3D solution." We use this phrase to refer to the converged solution of iterative calculation between the central S_2 surface flow and several S_1 surface flows. We believe this latter usage is the right one. The former one should be called "approximate quasi-3D solution."

Of course, in the quasi-3D solution, S_1 surfaces are usually approximately taken to be surfaces of revolution.

Therefore, in our quasi-3D blade design solution, the following procedure is taken:

1 Calculation of the central S_2 surface (called S_{2m} surface or central S_2 surface) for a prescribed design variation of hub-tip contours, $V_\theta r$, and stream sheet thickness is carried out. From the solution, the shape of the central S_2 surface and the streamline variation on the surface and the corresponding lines on the meridional plane are obtained. These latter lines are revolved around the axis of the turbomachine to form S_1 surfaces of revolution.

2 Certain blade sections are chosen on several S_1 surfaces and direct-problem solutions are obtained. (The blade section may also be designed by some method such as the mean-streamline method [31]). The variations of $V_\theta r$ and S_2 stream sheet thickness for the mean streamlines of these S_1 surfaces serves as new input values for the second calculation of the S_{2m} or central S_2 surface.

3 The above process is repeated until converged solution is obtained.

[3] In the sense that this S_2 surface lies in the central part of the blade passage

[4] In the first approximation, this is estimated by the blade thickness variation (with correction at the leading and trailing edges)

2 Full 3D Solution (Direct Problem)

In the method presented in the original paper, the blade designed by the quasi-3D solution described in the preceding section is followed right away by a full 3D direct solution. In the latter calculation, corresponding streamlines obtained in the several S_1 surface-of-revolution solution give the shapes of several S_2 surfaces, including the ones which coincide with the blade suction and pressure surface, respectively. In turn, the corresponding streamlines obtained in the several S_2 solutions give the geometry of several general (i.e., twisted and not surface of revolution any more) S_1 surfaces.

Converged solution of the iterative calculation between these two families of flow surfaces gives the full 3D solution.

It may be emphasized again that we in China always follow this original concept of S_1 and S_2 flow surfaces as first put forth in [28]. There is no ambiguity in the definition of either S_1 or S_2 surface, there is no approximation involved in the employment of S_2 surface, and there is no need for obtaining some kind of circumferentially averaged flow properties or passage-averaging procedure. Indeed we feel a kind of disappointment that this clear-cut application of physically real S_{2m} or "central" S_2 surface concept as originally put forth in [28] was overlooked or not well understood by quite a number of readers in other countries.

3 Consideration of Flow Losses in Blade Design

The present paper does not include the physical analysis of flow losses, or a method to reduce losses, but rather a way to include in the blade design process the overall effect of various kinds of losses, which are likely to exist in the type of blades to be designed, in order that the blade designed in this way will give the required performance (not only pressure ratio but also efficiency).

The paper does present a new finding in the 3D design calculation: In the S_1 calculation, entropy values consistent with those in the S_2 calculation must be used.

4 Convergence of the Iterative Process

The physical meaning of the convergence criterion

$$\left| \frac{(Ms_1 - Ms_2)}{Ms_2} \right| < \epsilon$$

we used to indicate the convergence of iterative process between S_1 and S_2 stream flow calculations is clear. In fact, the crux of Wu's theory of two families of stream surfaces is to simplify a 3D flow solution into two 2D solutions on S_1 and S_2 stream surfaces. Therefore, the result of convergence has to be given by the final equality of solutions at the same position obtained from S_1 and S_2 calculation, respectively. This is the reason that we choose this convergence criterion. Furthermore, the convergence processes of many computations we performed have shown that convergences of other flow variables, such as the streamsheet contraction in passing through the blade row, the blade exit angle, or the Mach number, had also been achieved, so long as the criterion mentioned above was fulfilled.

5 Boundary Condition Downstream of Blade Trailing Edge

The boundary condition just downstream of the trailing edge for the full 3D solution can only be approximately treated in the inviscid solution because the existence of trailing vortex cannot be considered in the inviscid model. But the twist of the S_1 stream surface is adequately considered in the full 3D solution. Just upstream of the blade leading edge and

just downstream of the trailing edge, the Dirichlet boundary condition was used in the computer code. The values of stream function on the two boundary lines of the flow domain were directly given in the calculation. Far upstream and downstream of the blade, the periodic condition is considered, i.e., identical values of any parameters have been maintained at the corresponding positions on the two boundary lines of the flow domain downstream of the trailing edge or upstream of the leading edge. (These corresponding positions have the same axial and radial coordinates.)

References

28 Wu Chung-Hua, "A General Theory of Three-Dimensional Flow in Subsonic and Supersonic Turbomachines of Axial, Radial, and Mixed-Flow Types," *Trans. ASME*, Nov. 1952; NACA TN 2604, 1952.

29 Wu Chung-Hua, "Matrix and Relaxation Solutions That Determine Subsonic Through-Flow in an Axial-Flow Gas Turbine," NACA TN 2750, 1950.

30 Wu Chung-Hua, "Subsonic Flow of Air Through a Single-Stage and a Seven-Stage Compressor," NACA TN 2961, 1953.

31 R. Cai, "A Summary of Developments of the Mean-Streamline Method in China," ASME JOURNAL OF ENGINEERING FOR GAS TURBINES AND POWER, Vol. 106, No. 2, Apr. 1984, pp. 300–305.

Calculation of the Three-Dimensional, Steady, Inviscid Flow in a Transonic Axial Turbine Stage

T. Arts
von Karman Institute for Fluid Dynamics,
B-1640 Rhode Saint Genèse, Belgium

The aim of this paper is to develop an approach to compute the three-dimensional, rotational, adiabatic, inviscid flow of a perfect gas in a transonic axial turbine stage. The time-dependent Euler equations, expressed in a cylindrical coordinate system, are solved using a time-marching method and a finite volume approach. The absolute flow is calculated in the stator, whereas the relative flow is computed in the rotor. A time-averaged blade row interaction is assumed. The method is applied to a transonic single-stage turbine. The calculated results agree well with the measured performance and three-dimensional aspects of the flow appear clearly.

Introduction

In the past twelve years, considerable improvement has been obtained in the calculation of flows in turbomachinery [1]. This progress is especially exemplified by the important development of time-marching techniques combined with a finite volume approach for the computation of inviscid, transonic flows in cascades. The aim of this paper is to present a method to compute the three-dimensional, rotational, adiabatic, inviscid flow of a perfect gas in a transonic axial turbine stage. As will be explained in the next section, the flow is assumed to be time-averaged rather than periodically unsteady.

Fully three-dimensional solutions are important because they do not impose any kind of geometrical restriction on the flow pattern. Moreover, the influence of high spanwise gradients or complex meridional geometry can be verified directly, e.g., through the axial asymmetry of the stream surfaces or the presence of intense local radial flows. Stage calculations are attractive, because they allow study of the mutual influence between two successive blade rows. They provide, for example, realistic entrance flow conditions to the rotor or take into account the upstream effect on the stator flow of choking in the rotor.

A three-dimensional program for a single fixed blade row has been developed at VKI and has proved its capabilities for low subsonic flows [2]. The objective of this paper is to show how it can be generalized to an axial turbine stage. In the present application, the code deals with transonic flow and with fixed and rotating passages. The mutual influence between stator and rotor is obtained by repeatedly updating the interrow boundary conditions. The purpose is not to develop a brand-new method showing very low calculation times and very high accuracy, but to apply an existing technique to the case of a turbine stage calculation in order to verify its capabilities and limitations.

Principle of Stage Calculation

The flow through two successive blade rows in relative motion is basically unsteady. For a two-dimensional geometry, some authors [3, 4] have tried to model this situation by assuming a periodic behavior of all flow unknowns. Depending on the relative number of vanes and blades, the rotor sees periodically the same entrance flow pattern. But due to substantial CPU times and large memory requirements, this approach cannot reasonably be extended to three-dimensional configurations.

The alternative approach [5, 6] is to accept the assumption of a time-averaged flow; upstream of each blade row, along the span, the tangential variation of all flow properties is set to zero, providing a mean or steady interaction between fixed and rotating blade rows. We have put this basic idea in concrete form by performing simultaneously two interconnected three-dimensional blade row calculations: one in the stator and one in the rotor. The main difference from a conventional cascade flow calculation as in [2] is that the boundary conditions of the present problem, downstream of the stator and upstream of the rotor, are not known as they are part of the solution. The mean interaction between vanes and blades is achieved by repeatedly adapting these interrow boundary conditions to the evolution of the flow pattern until stabilization and correspondence of mass flow in both blade rows is achieved.

Contributed by the Gas Turbine Division of THE AMERICAN SOCIETY OF MECHANICAL ENGINEERS and presented at the 29th International Gas Turbine Conference and Exhibit, Amsterdam, The Netherlands, June 4–7, 1984. Manuscript received at ASME Headquarters January 5, 1984. Paper No. 84-GT-76.

System of Partial Differential Equations

The partial differential system to solve is the time-dependent Euler system of equations. For turbomachinery flow calculations, these are generally expressed in a cylindrical system of coordinates (r, θ, z). In the stator, absolute velocities and a fixed frame of reference are considered, whereas in the rotor it was decided to work with relative velocities and a coordinate system rotating at the blade angular velocity Ω around the z-axis, coinciding with the machine axis.

In the stator, the equations are nondimensionalized by a characteristic length and by the stage inlet total thermodynamic conditions. In the rotor, the equations are nondimensionalized by the same length but by the rotor inlet relative total thermodynamic conditions, iteratively determined as will be shown later. The system is written in the following quasi-conservative form, valid for both vanes ($\Omega = 0$) and blades

$$\frac{\partial \sigma}{\partial t} + \frac{1}{r}\frac{\partial}{\partial r}(r\mathbf{f}) + \frac{1}{r}\frac{\partial}{\partial \theta}(\mathbf{g}) + \frac{\partial}{\partial z}(\mathbf{h}) + \mathbf{b} = 0 \qquad (1)$$

$$\sigma = \begin{pmatrix} \rho \\ \rho w_r \\ \rho w_\theta \\ \rho w_z \\ \rho e \end{pmatrix} \quad \mathbf{f} = \begin{pmatrix} \rho w_r \\ \rho w_r^2 + p \\ \rho w_r w_\theta \\ \rho w_r w_z \\ \rho w_r \left(e + \frac{p}{\rho}\right) \end{pmatrix}$$

$$\mathbf{g} = \begin{pmatrix} \rho w_\theta \\ \rho w_r w_\theta \\ \rho w_\theta^2 + p \\ \rho w_\theta w_z \\ \rho w_\theta \left(e + \frac{p}{\rho}\right) \end{pmatrix} \quad \mathbf{h} = \begin{pmatrix} \rho w_z \\ \rho w_r w_z \\ \rho w_z w_\theta \\ \rho w_z^2 + p \\ \rho w_r \left(e + \frac{p}{\rho}\right) \end{pmatrix}$$

$$\mathbf{b} = \begin{pmatrix} 0 \\ -\rho w_\theta^2/r - p/r - \rho r\Omega^2 - 2\rho\Omega w_\theta \\ +\rho w_r w_\theta/r + 2\rho\Omega w_r \\ 0 \\ 0 \end{pmatrix}$$

It can be seen that this system is hyperbolic with respect to time for any flow regime. The use of the quasi-conservative form is essential to provide a correct treatment of shock waves by a shock capturing technique. Using the perfect gas law and the definition of total absolute or relative energy, (1) is completed by the following relation

$$p = (\kappa - 1)\left(\rho e - \frac{\rho w^2}{2} + \rho\Omega^2 \frac{r^2}{2}\right) \qquad (2)$$

Discretization of the Flow Domain

Stator and rotor flow domains are discretized independently. Each of them is made up of one blade passage and extends upstream and downstream, approximately in the flow direction, over a distance of the order of a characteristic dimension of the blade row. These extensions are defined to minimize the effect of pitchwise uniform inlet and outlet boundary conditions on the flow distribution inside each passage. Experience shows that rather short extensions can be used without affecting the solution in the passage, providing a sufficient number of grid points are used. This implies that a dense mesh is generally used in the downstream part of the stator and in the upstream part of the rotor as the area covered by these two contiguous regions should remain as close as possible to the physical gap existing between vanes and blades. As the grid should not be unreasonably dense in this gap, and hence the stability time step too low, affecting the convergence, the gap might artificially be increased.

As was done in [2], each flow domain is discretized using three kinds of surfaces. The *streamwise surfaces* (Fig. 1(*a*)) are variably spaced along the spanwise direction and are limited by the hub and the tip of the blade row. The *bladewise surfaces* (Fig. 1(*b*)) are evenly spaced along the tangential direction and are limited by the suction side of one blade and the pressure side of the adjacent one.

The *spanwise surfaces* (Fig. 1(*c*)) are variably spaced along the axial direction, depending on the required precision, the expected density gradients, or any special requirements, e.g., upstream of the rotor, and are limited by the inlet and outlet planes.

The choice of the control volume is based on a detailed analysis of consistency and order of accuracy of the discretization procedure [14, 7]. The computational molecule is made up of two almost regular polyhedra, defined by the streamwise, bladewise, and spanwise surfaces. The position of the discretization nodes is defined in Fig. 2 and was chosen to obtain the best compromise between a limited number of nodes per molecule and the least severe consistency condition. As seen in [7], an unconditionally two-dimensional consistent discretization would already require 6 nodes per molecule and would even be more time consuming in a three-dimensional

Nomenclature

c_{ax} = axial chord
e = total energy $\left(e = c_v T + \frac{w^2}{2} - \frac{\Omega^2 r^2}{2}\right)$
M = Mach number
$\mathbf{n}$ = unit vector normal to a surface
p = pressure
r, Θ, z = cylindrical coordinates
t = time
Δt = time increment
T = temperature
V = volume or absolute velocity
w = velocity (absolute in stator and relative in rotor)
α, β = pitchwise flow angles (absolute, relative)
γ = spanwise flow angle
ξ = numerical viscosity coefficient
ρ = density
κ = ratio of specific heats
Ω = angular velocity of the blades

Subscripts

r, θ, z, l, k, i = coordinate indices
0 = total condition
cr = critical condition
1 = inlet of stage
2 = outlet of stator, inlet of rotor
3 = outlet of stage
* = updating time index (corrected viscosity)
A = absolute
R = relative

Superscripts

— = pitchwise averaged quantity

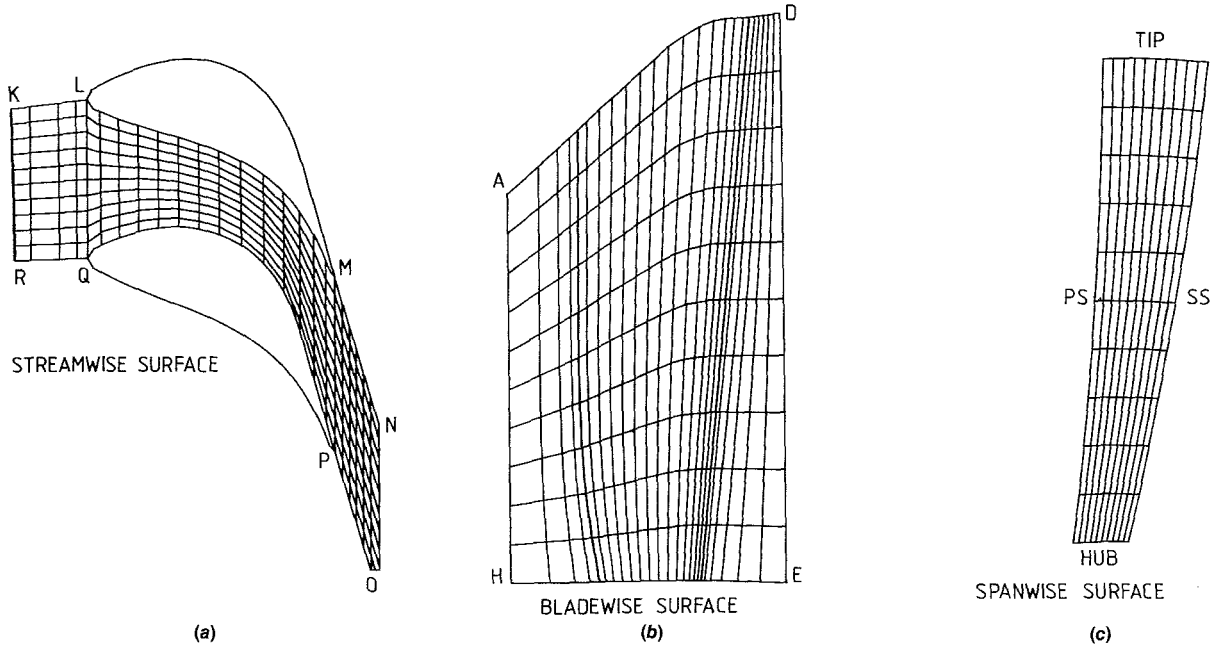

Fig. 1 Grid

geometry. The unknowns in the central node (i, k, l) are computed from the corresponding values in the six surrounding nodes. Due to the position of the mesh points, halfway between streamwise and bladewise surfaces, the values of the unknowns along the impermeable wall boundaries (suction and pressure side, hub and tip) are obtained from extrapolation of the corresponding unknowns calculated inside the passage.

Numerical Procedure

Finite Volume Discretization. Let us consider a small control volume V ($dV = rdrd\theta dz$) over which we integrate (1)

$$\iiint_V \frac{1}{r}\frac{\partial}{\partial r}(r\mathbf{f})rdrd\theta dz + \iiint_V \frac{1}{r}\frac{\partial}{\partial \theta}(\mathbf{g})rdrd\theta dz + \iiint_V \frac{\partial}{\partial z}(\mathbf{h})rdrd\theta dz = \iiint_V -\left(\frac{\partial \sigma}{\partial t}+\mathbf{b}\right)dV \quad (3)$$

Let $\mathbf{n}\,(=n_r\mathbf{1}_r+n_\theta\mathbf{1}_\theta+n_z\mathbf{1}_z)$ be the outward going normal to the boundary S of V. Applying the divergence theorem, (3) becomes

$$\iint_S \mathbf{f}n_r rd\theta dz + \iint_S \mathbf{g}n_\theta drdz + \iint_S \mathbf{h}n_z rd\theta dr = \left[-\frac{\partial \sigma}{\partial t}-\mathbf{b}\right]\cdot V \quad (4)$$

As V is limited by six almost regular surfaces forming S, and assuming the convective flux terms to be constant over these surfaces, (4) may be approximated by

$$\sum_{m=1}^{6}\mathbf{f}_m\iint_{S_m} n_r dS + \sum_{m=1}^{6}\mathbf{g}_m\iint_{S_m} n_\theta dS + \sum_{m=1}^{6}\mathbf{h}_m\iint_{S_m} n_z dS = \left[-\frac{\partial \sigma}{\partial t}-\mathbf{b}\right]\mathbf{V} \quad (5)$$

$$\sum_{m=1}^{6} S_m = S \quad (6)$$

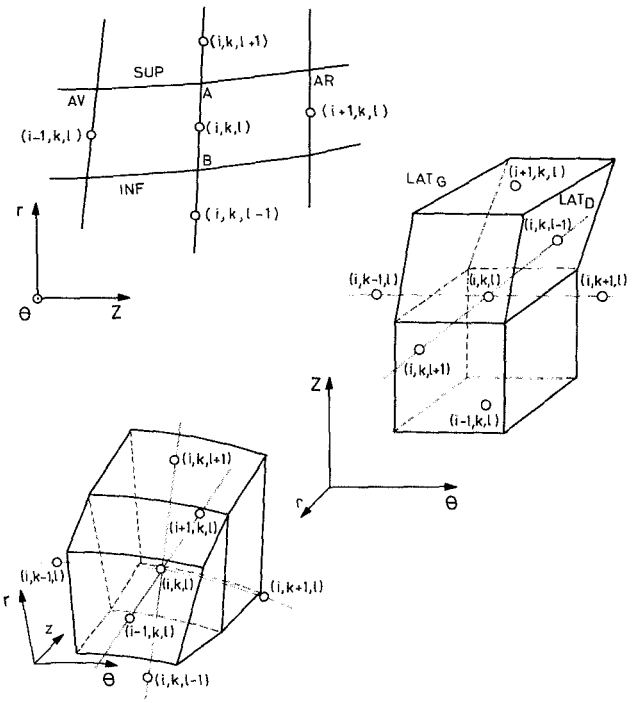

Fig. 2 Control volume

The left-hand side of (5) expresses the value of net transport by convection through S of the different unknowns defined in (1). Each control element is mapped into a cube with unit length using an isoparametric transformation in order to determine the measure of its volume and of the area of the different surface projections in the r-, θ- and z-directions. The detailed expressions of these quantities are given in [8]. The same analysis as the one performed in [7] shows that the discretized form (5), applied to the present type of control volume, is only conditionally consistent with (1). Moreover, it is generally first-order accurate with respect to the central node. The consistency condition is to allow only second-order variations between the areas of successive spanwise surfaces,

whereas the accuracy is mostly influenced by streamwise and bladewise surface slope variations. Therefore, consistency errors and poor accuracy become really significant in the case of important grid distortions inside a control volume, which are avoided in most of the computational domain.

Corrected Viscosity Scheme. The time derivative in (1) is discretized with the corrected viscosity scheme developed by McDonald [9]. This numerical scheme has been used intensively for two-dimensional [7, 10, 11] and three-dimensional [2, 8] flow calculations and has shown very good convergence, stability and accuracy properties. Applied to three-dimensional flows, one gets

$$\sigma_{i,k,l}^{t+\Delta t} = -\frac{\Delta t}{V}(\text{Net transport by convection})^t - \Delta t \mathbf{b}_{i,k,l}^t + \frac{1}{6}(\sigma_{i-1,k,l}^{t+\Delta t} + \sigma_{i+1,k,l}^t + \sigma_{i,k-1,l}^t + \sigma_{i,k+1,l}^t + \sigma_{i,k,l-1}^t + \sigma_{i,k,l+1}^t) - \frac{\xi}{6}(\sigma_{i-1,k,l}^* + \sigma_{i+1,k,l}^* + \sigma_{i,k-1,l}^* + \sigma_{i,k+1,l}^* + \sigma_{i,k,l-1}^* + \sigma_{i,k,l+1}^* - 6\sigma_{i,k,l}^*) \quad (7)$$

According to the principles of the corrected viscosity scheme [12], the terms superscripted by an asterisk are updated every Nv ($=15 \ldots 25$) iterations. This regular adjustment is introduced to correct the important smoothing generated by the second factor of the RHS of (7), equivalent to a second derivative of σ and hence to a viscouslike term. ξ is a numerical coefficient close to 1, used to provide the most effective correction. It is calculated as a function of the local density gradient in order to ensure the necessary damping near a flow discontinuity, e.g., a shock wave. In this way, the latter can be captured quite precisely. Δt is the time increment, determined from the CFL stability condition, since this numerical scheme is fully explicit. It is only first-order accurate in time [10], providing a completely artificial time history of the calculation.

Boundary Conditions

In order to have a well-posed problem, (1) must be completed with a set of boundary conditions. Along KL, RQ, MN, and PO (Fig. 1), a periodicity condition is enforced. Mass, momentum, and energy fluxes across KL are equal, in absolute value, to the corresponding transport across RQ. The same reasoning is applied along MN and PO. Along AD, HE, LM, and QP, an impermeability condition must be fulfilled. As a flux notation is explicitly used in (6), the condition is enforced by setting to zero the mass and energy flux components through the boundary considered, while the momentum flux reduces to a force contribution, provided by the local pressure.

In the inlet plane of the stage, the given physical boundary conditions are the absolute flow angles α_1 and γ_1 and the absolute pressure and temperature p_{01} and T_{01}. Their spanwise distribution is specified, whereas their pitchwise distribution is assumed to be uniform. This set of conditions is most generally used for turbomachinery flow calculations. To solve numerically the system of equations in the inlet plane, an additional relation must be added: the axial momentum equation is solved in a half-control volume (or 1 polyhedron) for each node of the plane. In the outlet plane of the stage, the static pressure p_3, uniform in the pitchwise direction, is specified at the hub. The spanwise distribution is obtained from a radial equilibrium calculation performed at each time step by integrating the steady, pitchwise-averaged, radial momentum equation

$$\int_r^{r+dr} \frac{\partial p}{\partial r}\,dr = \int_r^{r+dr} \left(\frac{\overline{\rho w_\theta^2}}{r} - \frac{\overline{\rho w_r^2}}{r} + \overline{\rho} r\Omega^2 + 2\Omega\overline{\rho w_\theta} - \frac{\partial}{\partial r}(\overline{\rho w_r^2}) - \frac{\partial}{\partial z}(\overline{\rho w_z w_r})\right) dr \quad (8)$$

The data pressure is fixed at the hub only to facilitate the integration procedure; obviously, it can be given anywhere else. As additional conditions, the continuity and the three momentum equations are solved in a half-control volume (or 1 polyhedron) for each node of the outlet plane. The set of additional conditions presented herein is one of the numerous possibilities presented in [8]. Its definite advantage is to guarantee stability and convergence for any case.

As the solution procedure is based on a repeated interaction between two three-dimensional blade row calculations, boundary conditions must also be specified in the outlet plane of the stator and in the inlet plane of the rotor. Each of these conditions is physically equivalent to providing information coming from outside the computational domain. Hence, the conditions to be applied in the inlet plane of the rotor (β_2, γ_2, p_{02R}, T_{02R}) will be computed from vane flow quantities whereas the conditions at the outlet of the stator (p_{2A}) will be determined from blade flow parameters. As these conditions are obviously not known at the beginning of the calculation, their spanwise distribution is repeatedly updated, the two blade row calculations running simultaneously. The following relations are used

$$p_{2_A} = \left((\kappa-1)\rho E_R - \frac{\kappa-1}{2}\frac{\rho w_{r_R}^2 + \rho w_{\theta_R}^2 + \rho w_{z_R}^2}{\rho}\right)_{\text{inlet rotor}}$$

$$T_{02_R} = \left(\frac{\kappa-1}{\kappa}\frac{\rho E_A + p}{\rho}\right)_{\text{outlet stator}}$$

$$p_{02_R} = \left[p\left(\frac{T_{02_R}}{p/\rho}\right)^{\frac{\kappa}{\kappa-1}}\right]_{\text{outlet stator}}$$

$$\beta_2 = \left[tg^{-1}\left(\frac{w_{\theta_A} - \Omega r}{w_{z_A}}\right)\right]_{\text{outlet stator}}$$

$$\gamma_2 = \left[tg^{-1}\left(\frac{w_{r_A}}{w_{z_A}}\right)\right]_{\text{outlet stator}}$$

This procedure, implemented in the code, does not require any human intervention. The numerical boundary conditions already described complete these two sets of interrow physical boundary conditions.

Single-Stage Turbine With High Work Output

Calculations were performed on a single-stage turbine with high work output, which has been investigated by Moffit et al. at NASA Lewis [13]. The stator is fabricated with untwisted vanes of constant mean section profile (Fig. 3). The blades are twisted about 9 deg from hub to tip (Fig. 4). The aspect ratios of the vanes and the blades are respectively 1.0 and 1.11, whereas the hub/tip ratio is 0.85 and the interrow spacing is 1/2 height of the blades. The stage has 36 vanes and 64 blades. A schematic cross section of the turbine (Fig. 5) shows the measuring stations: 1 (inlet of the stage), 2 (between stator and rotor), and 3 (outlet of the stage). A complete description of geometry, test conditions, and measurements is presented in [13]. Unfortunately, the present application does not fully display the capabilities of the method; detailed measurements in complex meridional geometries are not available so far. This example is one of the very few transonic turbine stage test cases to be adequately documented.

Due to a lack of information about the inlet boundary layer, the entrance conditions to the stage were uniform span-

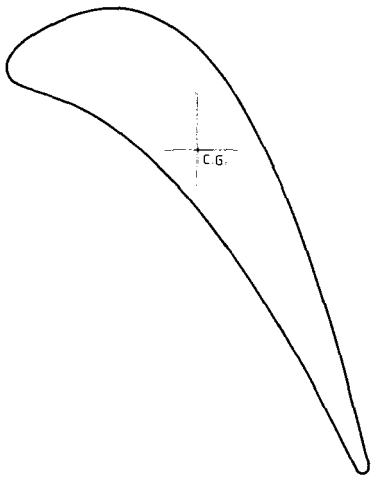

Fig. 3 Stator

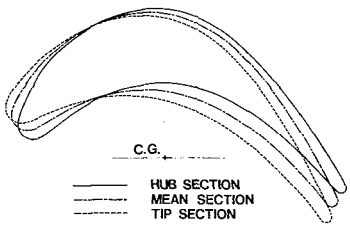

Fig. 4 Rotor

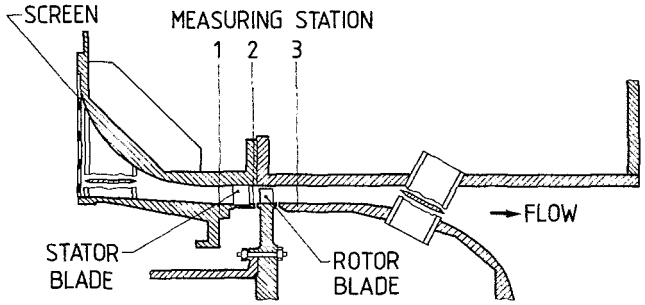

Fig. 5 Meridional geometry

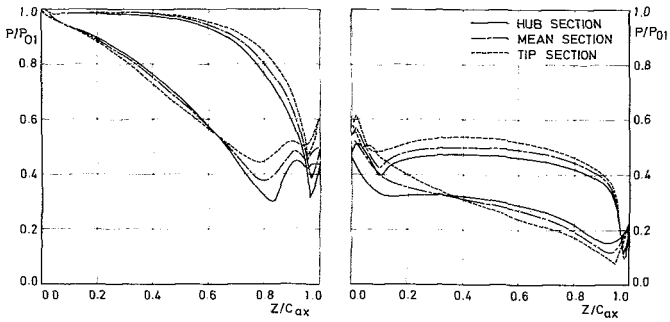

Fig. 6 Pressure distribution

and pitchwise velocity and absolute temperature and pressure profiles. Nevertheless, the code can take into account the existence of any nonuniform spanwise distribution. The overall pressure ratio (p_3/p_{01}) was fixed at the hub to the value of 0.225, corresponding to the nominal regime. The corrected rotational speed is 8081 rev/min (for sea level equivalent conditions) and the ratio of specific heats is $\kappa = 1.4$.

The numerical results presented in this paper were obtained for both vanes and blades with a grid of 49 spanwise (29 between leading and trailing edge), 11 streamwise and 11 bladewise surfaces (49 × 10 × 10 control volumes in each blade row). The streamwise and bladewise surfaces were equally spaced, which was not the case for the spanwise surfaces. A detailed two-dimensional calculation at midspan is presented in [8].

According to the conclusions of [7] and due to the high memory requirements, the convergence was checked using the pitchwise mass-averaged blade-to-blade flow angles α_2 and β_3, both stabilized within ±0.15 deg. The stabilization of the interrow boundary conditions calculation was verified using the static pressure variation over one time step downstream of the stator, which was reduced to 0.1 percent and the relative difference in mass flow through stator and rotor, which was equal to 1 percent when the calculation was stopped. Using a VAX 11/780 computer, the necessary CPU time per grid point and per time step was $2. \times 10^{-3}$s. 4000 time steps were performed, resulting in about 21 h of CPU time. The complete calculation was performed using a single grid. As shown in [2, 8], a grid refinement technique decreases the total CPU time but does not change fundamentally the accuracy of the results. A research program is currently under way at VKI to improve the method using a multigrid approach.

Mass Flow. As noted in [13] and as will be seen from the velocity distributions, the flow chokes in the stator. The measured mass flow at choking conditions is 3.856 kg/s. A mean value equal to 3.95 kg/s was obtained from the present calculation. The overestimation of 2.4 percent is principally due to the fact that no boundary layer and no losses are considered in this approach.

Velocity Diagrams at Midspan. The next table summarizes the comparison between the flow quantities defining the velocity triangles at midspan as given by measurements and by the present computational method. All values correspond to turbine inlet conditions of US standard sea level air.

		Measurements	3D calculation
W_{2A}	(m/s)	325.6	318.4
α_2	(°)	72.25	72.72
W_{2R}	(m/s)	149.1	145.7
β_2	(°)	48.26	48.02
W_{3A}	(m/s)	197.8	193.6
α_3	(°)	−22.60	−18.9
W_{3R}	(m/s)	330.0	319.3
β_3	(°)	−56.40	−54.98

At station 2, the velocity triangle is quite well predicted. The computed values of absolute and relative velocities vary about 2 percent from the measured ones, whereas the calculated absolute and relative flow angles differ respectively by about 0.5 and 0.2 deg from the experiments. At station 3, the relative variation in velocity is about 2 . . . 3 percent, whereas the differences in relative and absolute flow angles are respectively 1.4 and 3.7 deg. A possible explanation for this higher difference is a slight error in our estimate of the stage pressure ratio; this parameter is in fact not numerically given in [13] but was deduced graphically. A change in p_3 will not influence the mass flow because of choking, but can modify the absolute flow angle value.

Blade Surface Static Pressure and Velocity Distributions. The computed static pressure distributions along the suction and pressure sides at hub, midspan, and tip, are shown in Fig. 6. The local static pressure is nondimensionalized by the stage inlet total pressure. The pressure drop in the stator at hub, midspan, and tip amounts respectively to 74, 65, and 53 percent of the pressure drop over the stage. Looking at the pressure side distributions, the classical overexpansion around the trailing edge obtained with

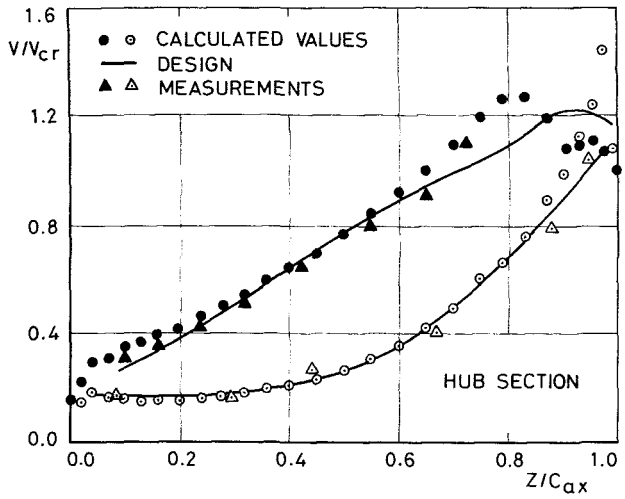

Fig. 7

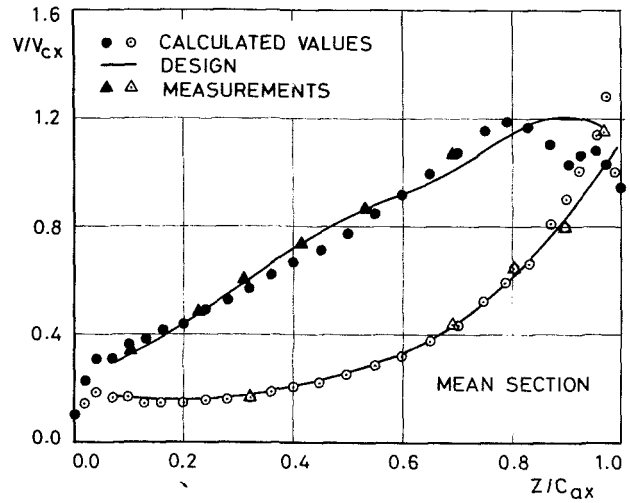

Fig. 8

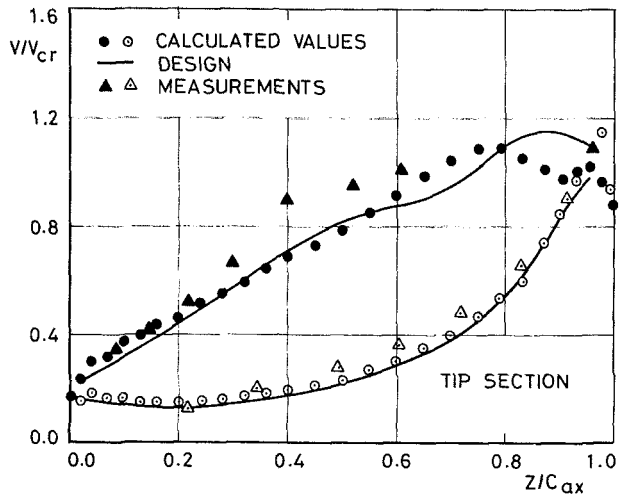

Fig. 9

Velocity distribution in the stator

inviscid calculations is observed. According to the measurements, a nearly uniform spanwise pressure distribution is computed at measurement station 3; the maximum calculated deviation with respect to the measured value is 0.13 percent.

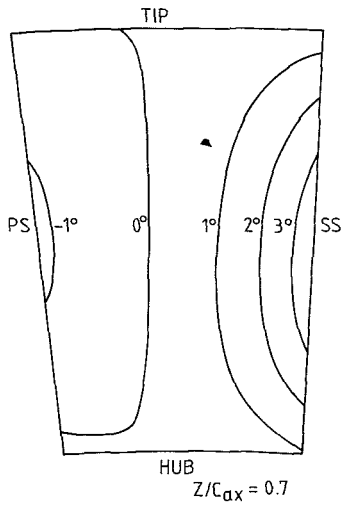

Fig. 10 Stator

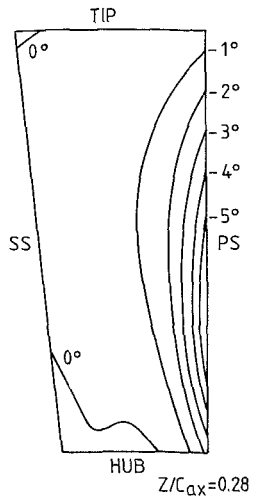

Fig. 11 Rotor

Meridional angle contour plots

Experimental velocity distributions were obtained in [13] from static taps along the vane suction and pressure sides at hub, midspan, and tip. They are compared to the computed results (Figs. 7–9) using the local velocity over critical velocity ratio. The comparison is fairly good in the hub and midspan region (Figs. 7 and 8). Along the suction side, the computed and measured values agree quite well with the design values up to $z/c_{ax} \simeq 0.65$. Further downstream, the measured stronger acceleration due to the convex shape of the blade profile in this region is also well predicted. Along the pressure side, the agreement is also good. Some discrepancies were observed along the suction side in the tip region (Fig. 9). As in the two preceding cases, the computed velocity distribution agrees quite well with the designed one up to $z/c_x \simeq 0.60$, whereas the measured acceleration is stronger between 30 and 40 percent of c_{ax}. No physical explanation of this phenomenon has been found.

Three-Dimensional Aspect of the Flow. The ability of the method to compute real three-dimensional effects appears clearly in the following examples (Figs. 10 and 11). These figures represent constant meridional flow angle contours in a given spanwise surface. In the stator, at $z/c_{ax} = 0.700$ (Fig. 10), a deviation of the streamlines towards the tip is observed going from pressure to suction side. On the contrary, the opposed phenomenon is observed in the rotor at $z/c_{ax} =$

0.280 (Fig. 11); the streamlines are deviated towards the hub of the blade row going from suction to pressure side. These results show the limitations of the axisymmetric stream surface assumption used in quasi-three-dimensional calculations. As mentioned previously, the γ values at a boundary are obtained from extrapolation. This explains why at tip and hub one does not exactly find the $\gamma=0$ line. In a mesh made up of only 11 stream surfaces, the extrapolation procedure could lead to errors, especially in a region of large angle gradients.

Conclusions

The calculated results show the capabilities and limitations of the present method to describe a three-dimensional flow in a transonic axial turbine stage using a time-averaged blade row interaction and an inviscid flow model. Using these assumptions, the mass flow and the overall aerodynamic characteristics of both blade rows are well predicted. The comparison between computed and measured vane velocity distributions is fairly good. Real three-dimensional effects, such as a lack of stream surface axial symmetry, are clearly seen from the calculated results. The definite advantage of this approach over an isolated blade row calculation is that the interrow boundary conditions adapt themselves automatically to the flow pattern, no experimental data being "built in" to the calculation.

References

1 McNally, W. D., and Sockol, P. M., "Computational Methods for Internal Flows With Emphasis on Turbomachinery," NASA TM 82 764, Nov. 1981.

2 Van Hove, W., "Calculation of Three-Dimensional, Inviscid, Rotational Flow in Axial Turbine Blade Rows," ASME Paper 83-GT-119, VKI Preprint 1982-35.

3 Erdos, J. I., and Alzner, E., "Computation of Unsteady Transonic Flows Through Rotating and Stationary Cascades," NASA CR 2900, December 1977.

4 Mitchell, N. A., "A Time-Marching Method for Unsteady Two-Dimensional Flow in a Blade Passage," *Int. J. Heat and Fluid Flow*, Vol. 2, No. 4, 1980, pp. 205–220.

5 Denton, J. D., and Singh, U. K., "Time-Marching Methods for Turbomachinery Calculations," *Application of Numerical Methods to Flow Calculations in Turbomachines*, VKI LS 1979-07.

6 Singh, U. K., "A Computation and Comparison With Measurements of Transonic Flow in an Axial Compressor Stage With Shock and Boundary Layer Interaction," ASME JOURNAL OF ENGINEERING FOR POWER, Vol. 104, No. 4, Apr. 1982, pp. 510–515.

7 Arts, T., "Cascade Flow Calculations Using a Finite Volume Method," *Numerical Methods for Flows in Turbomachinery Bladings*, VKI LS 1982-05.

8 Arts, T., "Etude de l'ecoulement tridimensionnel dans un étage de turbine transsonique," Ph.D. thesis, U. Catholique de Louvain, Oct. 1982.

9 McDonald, P. W., "The Computation of Transonic Flow Through Two-Dimensional Gas Turbine Cascades," ASME Paper 71-GT-89.

10 Couston, M., "Méthode de calcul de l'écoulement inter-aubes pseudo-tridimensionnel en régime transsonique," Ph.D. thesis, U. Libre de Bruxelles, 1976.

11 Lehthaus, F., "Anwendung eines Zeit-Schritt-Verfahrens zur Berechnung der transsonischen Durchströmung ebener Turbinengitter und experimentelle Überprüfung," DFVLR 25177 A 01, February 1977.

12 Couston, M., McDonald, P. W., and Smolderen, J. J., "The Damping Surface Technique for Time-Dependent Solutions to Fluid Dynamic Problems," VKI TN 109, 1975.

13 Moffitt, T. P., et al., "Design and Cold-Air Test of Single-Stage Uncooled Core Turbine With High Work Output," NASA TP 1680, June 1980.

14 Richtmyer, R. D., and Morton, K. W., *Difference Methods for Initial-Value Problems*, Interscience, 1967.

A Simple Method for Solving Three-Dimensional Inverse Problems of Turbomachine Flow and the Annular Constraint Condition

Zhao Xiao-lu
Research Associate.

Sun Chun-lin
Research Associate.

Wu Chung-Hua
Professor and Director.

Institute of Engineering Thermophysics,
Chinese Academy of Sciences,
Beijing, People's Republic of China

In 1950, Wu [1] suggested that the three-dimensional inverse (design) problem of turbomachine flow may be solved approximately by a Taylor series expansion in the circumferential direction based on the known flow variation over an S_2 stream surface in the midchannel of the blade passage. This idea has been realized recently. A new coordinate transformation has been developed. The coordinate surfaces are coincident with the S_2 stream surfaces. This transformation leads to a new method to calculate the aerodynamic equations of three-dimensional flow. By the use of this transformation, a high-order expansion is realized to determine the shape of the blade surfaces from the fluid state on the S_{2m} stream surface directly. Computation in this manner soon leads to the discovery that theoretically the distribution of flow parameter (usually $V_\theta r$) on S_{2m} prescribed by the designer should satisfy a constraint condition, which guarantees that the S_1 stream surfaces along the hub and shroud obtained from circumferential extension of the S_{2m} surface are surfaces of revolution. An approximate method is suggested to meet this condition.

Introduction

In 1950, a general theory of three-dimensional compressible flow in turbomachines based on the flow on two intersecting families of relative stream surfaces was presented [1]. The basic computation is that of the flow variation on the blade-to-blade S_1 stream surface or hub-to-tip S_2 stream surface (Fig. 1). Early computation methods [2–4] have been further developed and improved by expressing the basic equations in terms of nonorthogonal curvilinear coordinate system and corresponding nonorthogonal velocity components.

In general a complete three-dimensional solution is to be obtained by an iterative procedure between the two basic computations of S_1 and S_2. In cases, where the S_1 stream surfaces may be taken as surfaces of revolution, only one S_2 surface, which is usually chosen in the middle of the flow channel formed two neighbouring blades, is needed. The flow on the S_1 surfaces of revolution, which are generated by the streamlines on the S_{2m} surface, may be solved accurately by the field method (for example, [3–7]), or by the approximate, but much quicker, mean-streamline, series-expansion method (for example, early work [9, 10] and recent improvement [11–13]). The solution thus obtained is called quasi-three-dimensional solution.

In cases where the assumption that S_1 surfaces are surfaces of revolution is not good enough, it is necessary to compute flow on general S_1 surfaces and a number of general S_2 surfaces, and solution for axial compressor by finite difference method and for centrifugal compressor by finite element method have been obtained according to this procedure. More solutions obtained by this method would define whether the area within quasi three-dimensional flow is accurate enough for engineering application. Full three-dimensional solution of turbomachine flow may also be

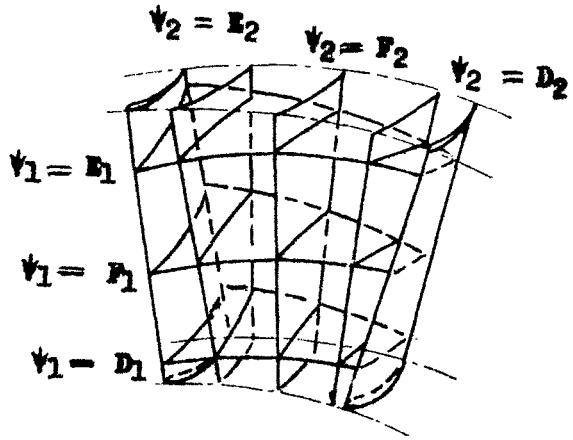

Fig. 1 Two isospace families in three-dimensional space

Contributed by the Gas Turbine Division of THE AMERICAN SOCIETY OF MECHANICAL ENGINEERS and presented at the 29th International Gas Turbine Conference and Exhibit, Amsterdam, The Netherlands, June 4–7, 1984. Manuscript received at ASME Headquarters January 18, 1984. Paper No. 84-GT-198.

obtained without assuming that S_1 surfaces are surfaces of revolution namely determination by the use of Taylor series expansions, and the circumferential derivatives in the series are calculated from known values on the S_{2m} surface.

This procedure is different from the two-dimensional, mean-streamline, series-expansion method in two important respects. First, the circumference derivatives are to be calculated from flow variation along one coordinate line other than in the circumferential coordinate line but also from the flow variation along the fluid coordinate as well. Second, the successive S_2 surfaces in the circumferential directions cannot be determined simply by a mass balance on the surface of revolution as in the two-dimension case. This type of three-dimensional solution was first obtained in [19, 20]. A three-dimensional flow field can be obtained very quickly.

Being an approximate method, the method may be limited to a range of value of flow configuration and design parameters. It should be very useful in analyzing the nature of three-dimensional flow corresponding to certain flow parameters and geometrical configurations, and especially, in a preliminary three-dimensional design blades of turbomachines.

Determination of the Shape of S_{2m} and the Flow Along S_{2m}

The S_{2m} calculation is the same as that in a quasi three-dimensional design procedure. The hub and casing wall contours and the projection of the S_{2m} surface are specified by the designer. The variation of the angular momentum of the fluid about the machine axis ($V_\theta r$) along the S_{2m} surface and the circumferential thickness of the S_{2m} surface are also specified by the designer. (The latter is to be obtained empirically from a desirable thickness distribution of the blade to be designed). Calculation of S_{2m} flow gives the shape of the S_{2m} surface, the streamline distribution on the S_{2m} surface, and the variation of all flow properties on the S_{2m}.

The Partial Derives of Flow Quantities in Nonorthogonal Curvilinear Coordinates

The flow properties at a point in the flow passage can be obtained from the known values on the S_{2m} surface by Taylor series expansion as follows

$$q(\varphi)=q(\varphi_m)+(\varphi-\varphi_m)q'(\varphi_m)+\frac{(\varphi-\varphi_m)^2}{2}q''(\varphi_m)+\ldots \tag{1}$$

In [5], the vorticities and continuity equations were expressed as follows

$$\xi^1=\frac{1}{\sqrt{a}}\left[\frac{\partial(V_\theta r)}{\partial x^2}-\frac{\partial w_2}{\partial\varphi}\right]$$

$$\xi^2=\frac{1}{\sqrt{a}}\left[\frac{\partial w_1}{\partial\varphi}-\frac{\partial(V_\theta r)}{\partial x^1}\right] \tag{2}$$

$$\xi^3=\frac{1}{\sqrt{a}}\left[\frac{\partial w_2}{\partial x^1}-\frac{\partial w_1}{\partial x^2}\right]$$

$$\nabla\cdot(\rho W)=0 \tag{3}$$

When the flow is isentropic and irrotational, the first and second derivative of W^1, W^2, W_φ, ρ with respect to φ can be obtained in a manner similar to that used in [1] as follows (for details, see Appendix A):

$$\begin{bmatrix} \sqrt{a_{22}}\cos\theta_{12} & \sqrt{a_{22}} & r\dfrac{\partial\varphi}{\partial x^2} \\ \sqrt{a_{11}} & \sqrt{a_{11}}\cos\theta_{12} & r\dfrac{\partial\varphi}{\partial x^1} \\ \dfrac{1}{\sqrt{a_{11}}}\dfrac{\partial\varphi}{\partial x^1} & \dfrac{1}{\sqrt{a_{22}}}\dfrac{\partial\varphi}{\partial x^2} & \dfrac{1}{r} \end{bmatrix}\cdot\begin{bmatrix} \dfrac{\partial W^1}{\partial\varphi} \\ \dfrac{\partial W^2}{\partial\varphi} \\ \dfrac{\partial W_\varphi}{\partial\varphi} \end{bmatrix}=\begin{bmatrix} \dfrac{\partial(V_\theta r)}{\partial x^2} \\ \dfrac{\partial(V_\theta r)}{\partial x^1} \\ C \end{bmatrix} \tag{4}$$

where

$$C=\left[\frac{\partial}{\partial x^1}(r\rho W^1\sqrt{a_{22}}\sin\theta_{12})+\frac{\partial}{\partial x^2}(r\rho W^2\sqrt{a_{11}}\sin\theta_{12})\right]\cdot\frac{1}{r\rho\sqrt{a_{11}}} \tag{5}$$

Nomenclature

a_{ij} = basic metric tensor
a = Jacobian composed of a_{ij}
B = integrating factor in the continuity equation for S_2 stream surfaces
C = nonzero term on the right-hand side of the continuity equation for S_2 stream surface
$D_1, E_1, \ldots$ = values of stream function's on isospace of S_1 family
$D_2, E_2, \ldots$ = values of stream function's on isospace of S_2 family
h = enthalpy per unit mass of fluid
I = relative stagnation rothalpy, $(h-U^2/2)+W^2/2$
J = station along x^1 coordinate lines
K = station along x^2 coordinate lines
L = distance along streamline
q = any fluid quantity
r,φ,z = relative cylindrical coordinates
$V_\theta r$ = angular momentum of fluid about axis of rotation
W = relative velocity
w^i = contravariant component of W
w_i = covariant component of W
W^i = physical component of W tangent to x^i
t = time
x^1, x^2, x^3 = general nonorthogonal coordinates
κ = ratio of specific heats
θ_{ij} = angle included by the coordinate lines x^i and x^j
ξ = absolute vorticity, $\nabla\times V$
ξ,η,ψ = nonorthogonal coordinate system
ρ = gas density
ψ = stream function
ω = angular velocity of blade

Subscripts

c = casing
h = hub
i = inlet
m = mean (midchannel)
n = component in the direction normal to hub or casing
p = pressure surface of blade
s = suction surface of blade

Superscripts

ν = number of S_2 sheets in S_2 family

$$\frac{\partial \rho}{\partial \varphi} = \frac{\rho}{(\kappa-1)h}\left[\frac{\partial I}{\partial \varphi} - \frac{\partial}{\partial \varphi}\{[(\rho W^1)^2 + (\rho W^2)^2 - 2(\rho W^1)(\rho W^2)\cos\theta_{12}] + (\rho W_\varphi)^2\}\right] \quad (6)$$

The Annular Constraint

It is shown in [21], when the integrability condition is considered in blade design, the flow variation a designer is free to specify is stream filament thickness, in addition to the variation of the thickness only one aerothermodynamic relation on the S_{2m} may be specified, which is usually the variation of $V_\theta r$.

New computations by equation (1) immediately show that the aerothermodynamic flow quantities must satisfy a constraint condition in order to guarantee that the S_1 stream surfaces obtained on the casing and hub wall are surfaces of revolution. The velocity component normal to hub or shroud (W_n) should be equal to 0 to satisfy the solid wall boundary condition. As the same as other fluid properties, the W_n should be obtained from the known values on the S_{2m} surface by Taylor series expansion

$$W_n(\varphi)_{hC} = W_n(\varphi_m) + (\varphi-\varphi_m)\frac{\partial W_n}{\partial \varphi}(\varphi_m) + \frac{(\varphi-\varphi_m)^2}{2}\frac{\partial^2 W_n}{\partial(\varphi)^2}(\varphi_m) \quad (7)$$

On the S_{2m} surface

$$W_n(\varphi_m)_{n,S} \equiv 0. \quad (8)$$

Thus all orders of partial derivatives of W_n on S_{2m} with respect to φ at the hub and casing should be equal to 0, satisfying the solid wall condition. As a first-order approximation, the first partial derivative should be equal to zero. In nonorthogonal curvilinear coordinate this relation is

$$\left.\frac{\partial W^2}{\partial \varphi}\right|_{r_c, r_s} = 0 \quad (9)$$

By adjusting the variation of $V_\theta r$ on S_{2m} in the vicinity of hub and casing wall, the values of $\partial(V_\theta r)/\partial x^2$ can easily be modified to satisfy equations (6). This method obtained through our numerical calculations is similar to the conclusion reached in [22]. Table shows variations of $\partial W^2/\partial\varphi$ and $V_\theta r$ at the hub and casing boundaries on S_{2m} in our numerical calculation.

Determination of the Blade Shape

Determination of the blade shape is the key part of this three-dimensional, mean-streamsurface method. The blade shape cannot be determined only by the mass flow relation on a surface of revolution as in the two-dimensional mean-streamline method. The following function proposed in [23] is used in [24] to describe the flow on the two intersecting families of S_1 and S_2 surfaces in a three-dimensional turbomachine flow passage (see Fig. 1).

$$\nabla\psi_1 \times \nabla\psi_2 = \rho W \quad (10)$$

$$\psi_1 = \psi_1(x^1, x^2, x^3) = D_1, E_1 \ldots$$
$$\psi_2 = \psi_2(x^1, x^2, x^3) = D_2, E_2 \ldots \quad (11)$$

where $D_1, E_1, \ldots\ldots D_2, E_2, \ldots\ldots$ are values of stream

$\partial W^2/\partial\varphi$ before adjustment

m/s

K/J	0	1	2	3	4	5	6	7
11	131.3	114.9	2.5	−6.0	−28.9	−42.0	−12.1	251.0
10	77.5	81.1	4.8	−6.1	−17.3	−13.3	−9.6	181.9
2	34.8	32.4	199.2	163.9	145.4	112.2	30.5	−288.8
1	−39.6	15.0	216.5	173.6	170.5	127.9	31.3	−252.7

$\partial W^2/\partial\varphi$ after adjustment

m/s

K/J	0	1	2	3	4	5	6	7
11	0.03	0.04	0.05	0.01	−0.04	−0.03	0.06	0.08
10	33.5	41.2	−21.0	−15.0	−16.6	−10.0	−8.0	0.7
2	26.8	−2.8	66.1	68.7	72.4	69.7	29.2	5.3
1	−1.1	−3.2	−3.5	−2.3	0.2	2.4	1.4	−0.1

$V_{\theta r}$ before adjustment

m²/s

K/J	0	1	2	3	4	5	6	7
11	39.5	37.5	26.9	16.6	8.0	2.1	−0.6	0.0
10	37.6	35.6	25.8	16.0	7.9	2.0	−0.6	0.0
2	35.0	35.9	22.8	13.9	6.9	1.3	−0.5	0.0
1	35.0	36.6	22.5	13.3	6.4	0.8	−0.7	0.0

$V_{\theta r}$ after adjustment

m²/s

K/J	0	1	2	3	4	5	6	7
11	38.0	36.2	26.7	16.6	8.3	2.5	−0.6	0.0
10	37.6	35.6	25.8	16.0	7.9	2.3	−0.7	0.0
2	35.0	35.9	22.8	13.9	6.9	1.3	−0.5	0.0
1	35.6	36.1	23.7	14.6	8.1	2.5	0.2	0.2

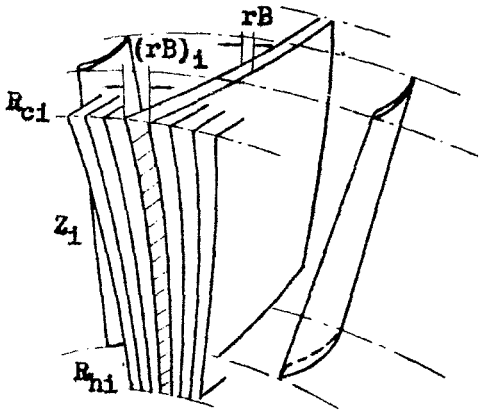

Fig. 2 Family of S_2 surface and intersection with inlet plane Z_i

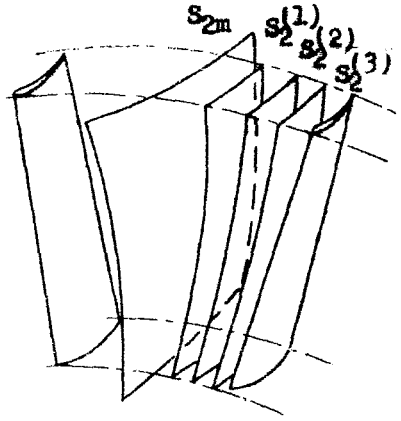

Fig. 3 Family of S_2 surface formed progressively from S_{2m}

functions on these stream surfaces. In the three-dimensional space, the distribution of these streamsurfaces is restricted by the boundaries of the flow passage as follows:

1 Hub and casing walls are two stream surfaces of the S_1 family.

2 Pressure and suction surfaces of the blade are two stream surfaces of the S_2 family.

From the known S_{2m} surface a family of S_2 surfaces will be formed (see next section). In this family, two surfaces are the pressure surface and suction surface of two neighbouring blades, respectively, and S_{2m} divides the total mass flow through the channel into suitable proportions.

Forming S_2 Family by Progressing Circumferentially from S_{2m}

Similar to the two-dimensional mean-streamline method, the φ coordinate of S_2 surface can be obtained by the use of a series expansion from S_{2m} as follows

$$\Delta\varphi=\varphi-\varphi_m=(\psi_2-\psi_2)_m\left(\frac{\partial\varphi}{\partial\psi_2}\right)_m + \frac{1}{2}(\psi_2-\psi_{2m}^2)\left(\frac{\partial^2\varphi}{\partial\varphi_2^2}\right)_m+\cdots\cdots \quad (12)$$

where φ is the circumferential coordinate of any S_2 surface and ψ_2 is the value of stream function of that S_2 surface.

The integrating factor B of [1] is now expressed as follows (see Fig. 2)

$$B/B_i=\Delta\varphi/\Delta\varphi_i \quad (13)$$

$$\frac{D\ln B}{Dt}=w^2\frac{\partial\ln B}{\partial x^2}+w^1\frac{\partial\ln B}{\partial x^1}=C \quad (14)$$

The inlet plane Z_i is usually sufficiently far upstream of the blade row, where the flow can be considered to be uniform. The intersection of the family of S_2 surface with this Z_i-plane is a family of curves. The variation of the stream function of two adjacent S_2 surfaces is the mass flow passing through the small area between the two adjacent curves (shaded area in Fig. 2). Then the variation of ψ_2 can be determined in the inlet plane Z_i as follows

$$\Delta\psi_2=(\rho W\Delta A)_i=[\rho W(r_c^2-r_n^2)\Delta\varphi]_i \quad (15)$$

From equations (8) and (10)

$$B/B_i=\Delta\varphi/\Delta\varphi_i=\Delta\varphi/\Delta\psi_i \quad (16)$$

When $\Delta\psi_2$ approaches 0 as a limit, B/B_i becomes the first derivative of φ with respect to ψ_2. Using first-order expansion, the ψ of S_2 surface can be determined step by step as follows

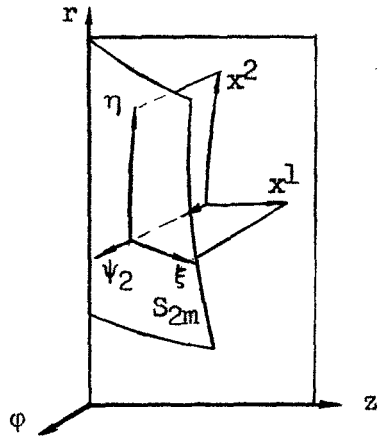

Fig. 4 Transformation of coordinates

$$\Delta\varphi=\varphi^{\nu+1}-\varphi^{\nu}=(\psi_2^{\nu+1}-\psi_2^{\nu})\left(\frac{\partial\varphi}{\partial\psi_2}\right)^{\nu}+(\psi_1^{\nu+1}-\psi_2^{\nu})(B/B_i)^{\nu} \quad (17)$$

When the φ-coordinate of $(\nu+1)$th S_2 surface is obtained, the fluid properties W^1, W^2, and ρ on the $S_2^{[\nu+1]}$ surface can be determined by power series from S_{2m}

$$W^1(\varphi)=W^1(\varphi_m)+(\varphi-\varphi_m)\frac{\partial W^1}{\partial\varphi}(\varphi_m) + \frac{(\varphi-\varphi_m)^2}{2}\frac{\partial^2 W^1}{\partial(\varphi)^2}(\varphi_m) \quad (18)$$

etc. Subsequently, equation (14) gives $(B/B_i)^{[\nu+1]}$ and the position of the next S_2 surface can be determined. This method may be called streamsurface extension method. A more accurate method is introduced in the next section.

Coordinate Transformation and Direct Expansion Method

In computation of the flow along the S_{2m} stream, the meridional plane is usually taken as the coordinate surface. The coordinate system is (x^1, x^2, φ). The coordinate transformation is as follows

$$\xi=x(r,z)$$
$$\eta=x(r,z) \quad (19)$$
$$\psi_2=\psi_2(r,\varphi,z)$$

The surfaces of revolution obtained by rotating around z-axis with the x^1 and x^2 curves, and the S_{2m} stream surfaces are the new coordinate surfaces. The following relations may be obtained directly

$$\frac{\partial q}{\partial x^1}=\frac{\partial q}{\partial\xi}\quad\frac{\partial q}{\partial x^2}=\frac{\partial q}{\partial\eta} \quad (20)$$

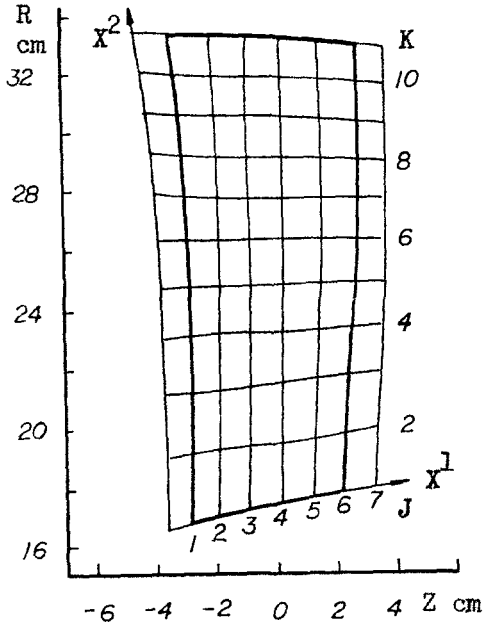

Fig. 5 Meridional projection of S_{2m}

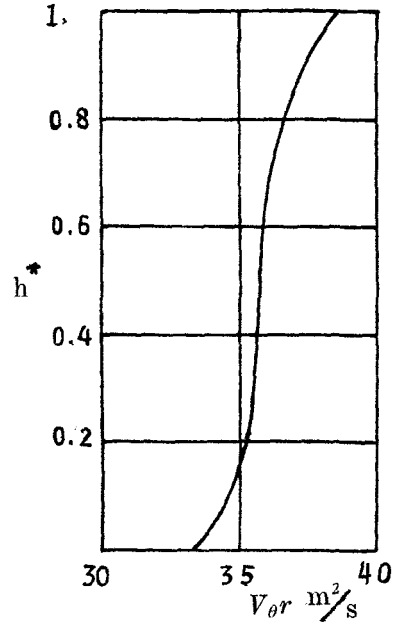

Fig. 6 Distribution of $V_\theta r$ in front of the stator

$$\frac{\partial}{\partial\psi_2}\left(\frac{\partial q}{\partial x^1}\right)=\frac{\partial}{\partial x^1}\left(\frac{\partial q}{\partial\psi_2}\right)\frac{\partial}{\partial\psi_2}\left(\frac{\partial q}{\partial x^2}\right)$$

$$=\frac{\partial}{\partial x^2}\left(\frac{\partial q}{\partial\psi_2}\right) \tag{21}$$

$$W^1=W^{\mathrm{I}},W^2=W^{\mathrm{II}},W^{\mathrm{III}}=0 \tag{22}$$

where a bold partial derivative sign is used to denote the partial derivative of a quantity following the motion along S_{2m} with respect to x^1 or x^2 on the meridional plane. The w^1, w^2, w^{I}, w^{II} are used to represent the contravariant components of W in (x^1, x^2, φ) or (ξ, η, ψ_2) system, respectively. The derivatives of W^1, W^2, W_φ, and ψ_1 with respect to ψ_2 can be obtained. The details are shown in Appendix B. Differentiating the relation (14) with respect to ψ_2 and combining with relations (21) determines the first derivative of the angular thickness B with respect to ψ_2

$$\frac{D}{Dt}\left(\frac{\partial\ln B}{\partial\psi_2}\right)=\frac{-1}{\rho}\left\{\frac{1}{r\sqrt{a}}\left[\frac{\partial}{\partial x^1}\left(\sqrt{a_{22}}\sin\theta_{12}r\frac{\partial(W^1\rho)}{\partial\psi_2}\right)\right.\right.$$

$$\left.+\frac{\partial}{\partial x^2}\left(\sqrt{a_{11}}\sin\theta_{12}r\frac{\partial(W^2\rho)}{\partial\psi}\right)\right]+\frac{\partial(\rho W^1)}{\partial\psi_2}\frac{\partial\ln B}{\partial x^1}\frac{1}{\sqrt{a_{11}}}$$

$$\left.+\frac{\partial(\rho W^2)}{\partial\psi_2}\frac{\partial\ln B}{\partial x^2}\frac{1}{\sqrt{a_{22}}}\right\} \tag{23}$$

The φ coordinate of any S_2 surface, especially those of the suction or pressure surface of the two neighboring blades, can be obtained directly from S_{2m} by a power series expansion

$$\varphi=\varphi_m+(\psi_2-\psi_{2m})B_m+\frac{1}{2}(\psi_2-\psi_{2m})^2\left(\frac{\partial B}{\partial\psi_2}\right)_m$$

$$+\frac{1}{6}(\psi_2-\psi_{2m})^3\left(\frac{\partial^2 B}{\partial\psi_2^2}\right)_m \tag{24}$$

The fluid properties W^1, W^2, and ρ on the suction or pressure surface can then be obtained by Taylor series

$$W^1(\psi_{2s})=W^1(\psi_{2m})+(\psi_{2s}-\psi_{2m})\frac{\partial W^1}{\partial\psi_2}(\psi_{2m})$$

$$+\frac{1}{2}(\psi_{2s}-\psi_{2m})^2\frac{\partial^2 W^1}{\partial\psi_2^2}(\psi_{2m}) \tag{25}$$

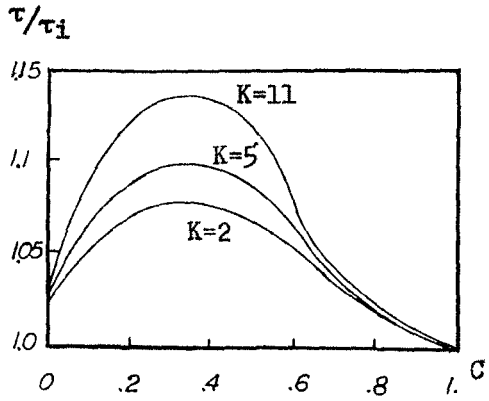

Fig. 7 Distribution of thickness

The distribution of S_1 stream function ψ_1 in the flow passage can also be obtained by Taylor series, determines the shape of S_1 surfaces. This direct expansion method is more accurate than the streamsurface extension method described in the preceding section.

Illustrative Example

FORTRAN IV programs based on the two methods presented herein have been coded to study the three-dimensional flow in axial turbomachines. The blade shape, the distribution of S_1 and S_2 surfaces, and the fluid properties in the flow passage can be obtained in less than a minute on a UNIVAC-1100 computer.

Example 1. The stator of a single-stage CAS research compressor reported in [16]. The mass flow is 61 kg/s, the rotor tip M is 1.4, the stage total-pressure ratio is 1.5. The hub-tip ratio at stator inlet is 0.49, the number of stator blades is 37. The projection of S_{2m} and its streamline distribution on the meridional plane is shown in Fig. 5. The specified radial variation of $V_\theta r$ in front of the stator is shown in Fig. 6. Figure 7 shows the blade thickness distribution specified. The blade shape and distribution of velocity on the $k=7$ coordinate surface obtained by the two methods are shown in Fig. 8. The difference between the two is small. A comparison of Mach number distribution with that obtained

in the full three-dimensional solution [17] is shown in Fig. 9. Except near the leading edge, the result obtained from the present method is close to that of the three-dimensional solution. The relative twist of S_1 surfaces at the suction surface ($J=4$) is shown in Fig. 10. Rm is the value of R on the S_{2m} surface of the same S_1 surface. (R is the local value to the point $J=4$, $k=1, \ldots 11$.) It is seen that largest $\Delta R/R$ occurs a short distance from the hub wall and the maximum difference between the present solution and the full three-dimensional solution also occurs there. It may be noted that the maximum relative twist is rather small, being less than 1 percent.

Example 2. A turbine rotor. The mass flow is 2.2 kg/s, the expansion ratio is 1.4, the rotor speed is 16,000 rpm, the number of blades is 60, and the hub-tip ratio is 0.66. The meridional projection of S_{2m} and its distribution of streamline are shown in Fig. 11. The blade shape and the circumferential variation of velocity on $k=3$ coordinate surface obtained in the direct expansion method are shown in Fig. 12. The intersections of the $J=3$, 4, 5 coordinate surfaces with the S_1 surface and S_2 surface are shown in Fig. 13. The direction of twist of the S_1 surface is basically consistent with the conclusion reached in [22]; i.e., under most conditions, the S_1 surfaces twist upward at the suction surface in the turbine stator and inward in the turbine rotor. As this turbine is designed for radially nonuniform work output so that the twist involved is relatively large, but is still under 2 percent.

Concluding Remarks

1 In prescribing a desired flow variation on the midchannel hub to tip S_{2m} streamsurface in three-dimensional blade design, it should be noted that prescribed variation should satisfy a constraint condition in order that the resulting blade to blade S_1 flow surfaces along the hub and casing walls are surfaces of revolution.

2 A new coordinate transformation, in which the S_2 stream-surface is taken as a coordinate surfaces, leads to a new method for calculating partial derivatives of flow variables with respect to the stream function of S_2 surface. High-order derivatives can be obtained, and consequently high-order series expansion can be used to compute the three-dimensional flow field.

3 This three-dimensional mean-streamsurface series expansion method is different from the two-dimensional mean-streamline series expansion method in that the known flow variations along two general curvilinear coordinates on the mean streamsurface are now used to compute the circumferential derivatives of the flow variables. Based on the three-dimensional flow field obtained by series expansion, the blade shape corresponding to a mass flow rate passing through the three-dimensional blade channel can be determined. The blade to blade surfaces obtained in the solution between (and not including) the hub wall and casing wall are general S_1 streamsurfaces, and twists of these S_1 surfaces are readily available in the calculation.

4 Two illustrative examples indicate that the method for solving the inverse problem of three-dimensional flow by the use of the present method is a feasible quick approximate engineering method. The nature and magnitude of the twist of S_1 surface obtained in a high-subsonic, axial-flow compressor and a high-subsonic, axial-flow turbine are determined in the computation.

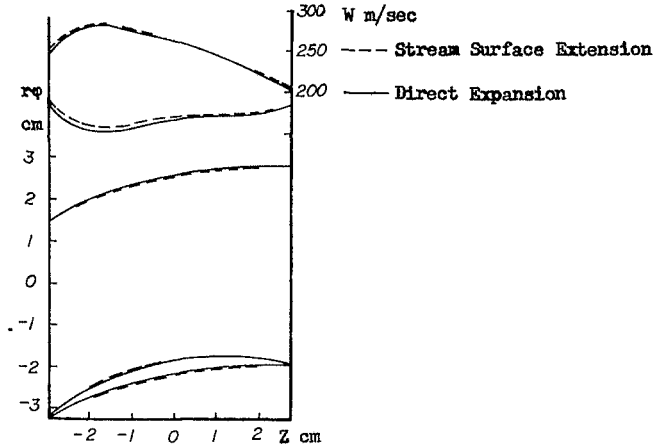

Fig. 8 Blade shape and distribution of W on $K=7$ coordinate surface

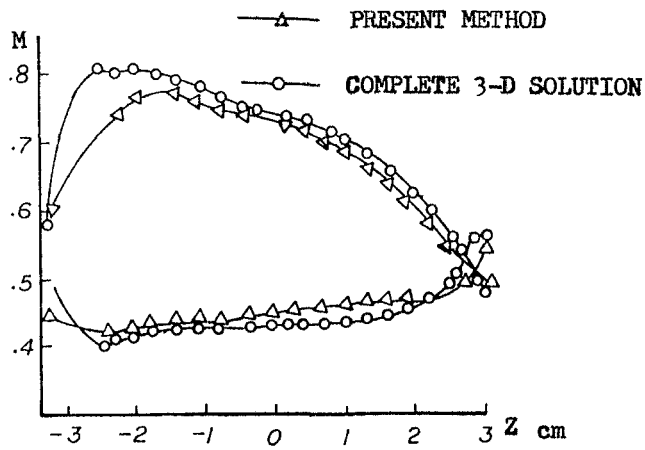

Fig. 9 Distribution Mach number on $k=9$ S_1 surface

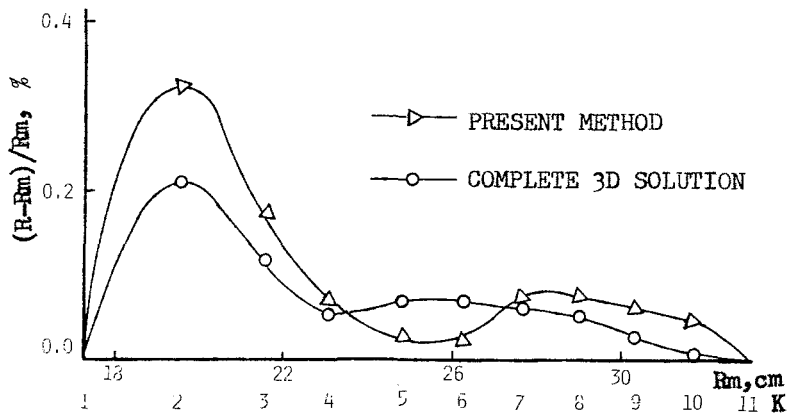

Fig. 10 The relative twist quantity on the $J=3$ suction surface

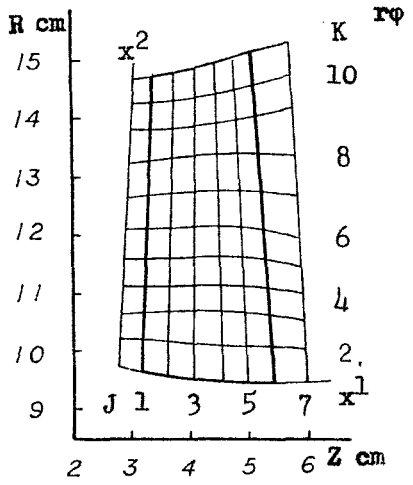

Fig. 11 Meridional projection of S_{2m}

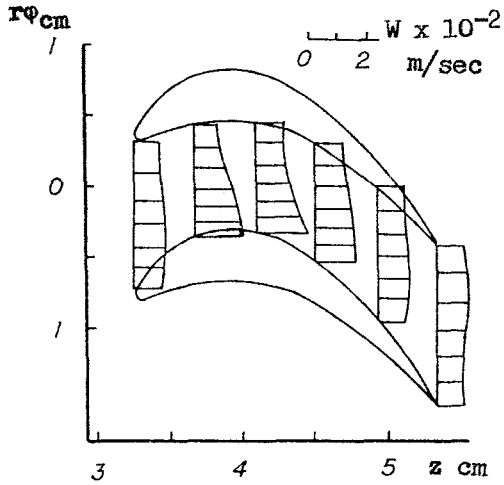

Fig. 12 The distribution of W on $k = 3$ coordinate surface

5 This simple, quick, approximate three-dimensional method should be useful to evaluate the nature and order of magnitude of the departure of blade-to-blade S_1 surface from surface of revolution and in different geometrical configurations and design specifications, the accuracy of quasi-three-dimensional solution as compared to full three-dimensional solution, and for three-dimensional blade design, especially where a certain three-dimensional distribution of blade thickness is desired. It may also be used as a three-dimensional analysis method by successively correcting the mean-streamsurface flow. This correction is similar to the successive correction of the mean-streamline shape in the two-dimensional analysis method.

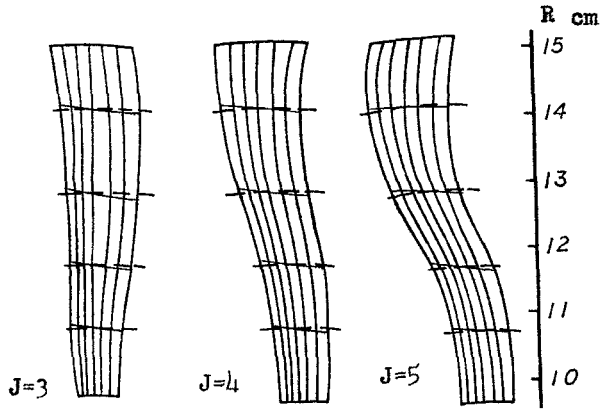

Fig. 13 Intersection of S_1, S_2 surfaces with $J = 3$, 4, 5 coordinate surfaces

References

1 Wu Chung-Hua, "A General Theory of Three-Dimensional Flow in Subsonic and Supersonic Turbomachines of Axial-, Radial-, and Mixed-Flow Types," ASME Paper No. 50-A-79, 1950, ASME *Trans.*, Nov. 1952.

2 Wu Chung-Hua, and Brown, C. A., "Method of Analysis for Compressible Flow Past Arbitrary Turbomachine Blades on General Surface of Revolution," NACA TN 2407, 1951.

3 Wu Chung-Hua, "Subsonic Flow of Air Through a Single-Stage and A Seven-Stage Compressor," NACA TN 2961, 1953.

4 Wu Chung-Hua, "Matrix and Relaxation Solution that Determine Subsonic Through-Flow in an Axial-Flow Gas Turbine," NACA TN 2750, 1950.

5 Wu Chung-Hua, "Three-Dimensional Turbomachine Flow Equations Expressed with Respect to Non-Orthogonal Curvilinear Coordinates and Methods of Solution," Lecture Notes, China University of Science and Technology, 1975; also *Proceedings of 3rd I.S.A.B.E.*, 1976.

6 Wu, W. Q., and Liu, C. E., "Flow-Field Matrix Solution for Direct Problem of Flow Along S_1 Relative Stream Surface Employing Non-Orthogonal Curvilinear Coordinates and Corresponding Non-Orthogonal Velocity Components," *J. of Engineering Thermophysics* (in Chinese), Vol. 1, No. 1, 1980.

7 Zhu, R. G., "Flow-Field Line-Relaxation Solution for Inverse Problem of Flow Along S_2 Relative Stream Surface Employing Non-Orthogonal Curvilinear Coordinates and Corresponding Non-Orthogonal Velocity Components," *J. of Engineering Thermophysics* (in Chinese), Vol. 1, No. 1, 1980.

8 Wu, W., Chu, Y., and Lin, C., "Computer Programs of Flow Calculations on Relative Stream Surfaces S_1 and S_2 Employing Non-Orthogonal Velocity Components and Their Applications to the Design of Turbomachine Blades Based on Three-Dimensional Flow," *Proceedings of 4th I.S.A.B.E.*, Apr., 1979.

9 Wu Chung-Hua, and Brown, C. A., "A Method of Designing Turbomachine Blades with a Desirable Thickness Distribution, for Compressible Flow Along an Arbitrary Stream Filament of Revolution," NACA TN 2455, 1951.

10 Wu Chung-Hua, and Brown, C. A., "An Approximate Method of Determining the Subsonic Flow in an Arbitrary Stream Filament of Revolution Cut by Arbitrary Turbomachine Blades," NACA TN 2702, 1952.

11 Wang, Z., and Cai, R., "MSLM with High-Order Derivatives for Calculating Cascades Laying on Arbitrary Revolution Surface," *J. of Engineering Thermophysics*, (in Chinese), Vol. 4, 1983, pp. 347–350.

12 Cai, R., "A Summary of Development of the Mean-Stream-Line Method in China," ASME 83-GT-11, 1983.

13 Novak, R. A., and Haymann-Haber, G., "A Mixed-Flow Cascade Passage Design Procedure Based on a Power Series Expansion," ASME 82-GT-121, 1982.

14 Novak, R. A., and Hearsey, R. M., "A Nearly Three-Dimensional Intrablade Computing Systems for Turbomachinery," *J. of Fluids Engineering*, Mar. 1977.

15 Bosman, C., and El-Shaarawi, M., "Quasi-Three-Dimensional Numerical Solution Flow in Turbomachines," *J. of Fluids Engineering*, Mar. 1977.

16 Acadima Sinica, Shenyang Aeroengine Factory, "Theory, Method and Application of Three-Dimensional Flow Design of Transonic Axial-Flow Compressor," *J. of Engineering Thermophysics* (in Chinese), Vol. 1, No. 1, 1980.

17 Wang, Q. H., Wu, W. Q., Zhu, G. X., and Li, W. H., "Complete Three-Dimensional Flow Solved by S_1 and S_2 Families of Stream Surfaces in Axial-Compressor," *J. of Engineering Thermophysics* (in Chinese), Vol. 4, No. 4, 1983.

18 Krimermen, Y., and Adler, D., "The Complete Three-Dimensional Calculation of the Compressible Flow Field in Turbo-Impellers," *J. of Mechanical Engineering Science*, Vol. 20, No. 3, 1978.

19 Zhao, X., "A Method for Solving Inverse Problem of Three-Dimensional Turbomachine Flow-the Mean Stream Surface Method, and the Annular Constraint Condition (in Chinese), M.S. thesis, Institute of Engineering Thermophysics, 1981.

20 Sun, C., "A New Method for Series Expansion from S_{2m} Surface (in Chinese), M.S. thesis, Institute of Engineering Thermophysics, 1983.

21 Wu Chung-Hua, and Wolfenstein, L., "Application of Radial-Equilibrium Condition to Axial-Flow Compressor and Turbine Design," NACA Rep. 955, 1950.

22 Cai, R. X., "Constraint on Design Parameters and Twist of S_1 Surfaces in Turbomachines," *Scientia Sinica* (series A), Vol. 26, No. 4, 1983.

23 Giese, J. H., "Stream Function for Three-Dimensional Flows," *J. Math. Phys.*, Vol. 30, 1951, pp. 31–35.

24 Wu, W. Q., "Streamfunction Equations of Three-Dimensional Flow in Turbomachine-Unified Equations Governing Fluid Flow on S_1 and S_2 Relative Stream Surfaces," *J. of Mechanical Engineering* (in Chinese), Vol. 15, No. 1, 1979.

APPENDIX A

Consider now a unit vector normal to the S_{2m} surface

$$\mathbf{n}=n_i\mathbf{e}^i \tag{A1}$$

The orthogonal relation is expressed by

$$n_i\mathbf{e}^i\cdot dx^i\mathbf{e}_i=n_1dx^1+n_2dx^2+n_\varphi d\varphi=0 \tag{A2}$$

The derivative of a fluid quantity on S_{2m} with respect to x^1 and x^2 is

$$\frac{\partial}{\partial x^1}=\frac{\partial}{\partial x^1}+\frac{\partial}{\partial\varphi}\frac{\partial\varphi}{\partial x^1}=\frac{\partial}{\partial x^1}-\frac{n_1}{n_\varphi}\frac{\partial}{\partial\varphi} \tag{A3}$$

$$\frac{\partial}{\partial x^2}=\frac{\partial}{\partial x^2}+\frac{\partial}{\partial\varphi}\frac{\partial\varphi}{\partial x^2}=\frac{\partial}{\partial x^2}-\frac{n_2}{n_\varphi}\frac{\partial}{\partial\varphi} \tag{A4}$$

n is, of course, perpendicular to the relative velocity W

$$n\cdot W=0 \tag{A5}$$

When the flow is irrotational the substitution of equations (A3, A4) into equations (2) gives

$$\sqrt{a_{11}}\cos\theta_{12}\frac{\partial W^1}{\partial\varphi}+\sqrt{a_{11}}\frac{\partial W^2}{\partial\varphi}+\frac{\partial\varphi}{\partial x^2}r\frac{\partial W_\varphi}{\partial\varphi}=\frac{\partial(V_\theta r)}{\partial x^2} \tag{A6}$$

$$\sqrt{a_{11}}\frac{\partial W^1}{\partial\varphi}+\sqrt{a_{11}}\cos\theta_{12}\frac{\partial W^2}{\partial\varphi}+\frac{\partial\varphi}{\partial x^2}r\frac{\partial W_\varphi}{\partial\varphi}=\frac{\partial(V_\theta r)}{\partial x^1} \tag{A7}$$

When equations (A3, A4, A5) are used, equations (3) can be written as

$$-\frac{1}{\sqrt{a_{11}}}\frac{\partial\varphi}{\partial x^1}\frac{\partial W^1}{\partial\varphi}-\frac{1}{\sqrt{a_{22}}}\frac{\partial\varphi}{\partial x^2}\frac{\partial W^2}{\partial\varphi}+\frac{1}{r}\frac{\partial W_\varphi}{\partial\varphi}=C \tag{A8}$$

Differentiating equations (A6–A8) with respect to φ and combining with equations (A2–A4) give the second derivatives of W^1, W^2, W_φ as

$$\begin{bmatrix}\sqrt{a_{22}}\cos\theta_{12} & \sqrt{a_{22}} & r\frac{\partial\varphi}{\partial x^2}\\ \sqrt{a_{11}} & \sqrt{a_{11}}\cos\theta_{12} & r\frac{\partial\varphi}{\partial x^1}\\ \frac{1}{\sqrt{a_{11}}}\frac{\partial\varphi}{\partial x^1} & \frac{1}{\sqrt{a_{22}}}\frac{\partial\varphi}{\partial x^2} & \frac{1}{r}\end{bmatrix}\cdot\begin{bmatrix}\frac{\partial W^1}{\partial\varphi}\\ \frac{\partial W^2}{\partial\varphi}\\ \frac{\partial W_\varphi}{\partial\varphi}\end{bmatrix}=\begin{bmatrix}\frac{\partial}{\partial x^2}r\frac{\partial W_\varphi}{\partial\varphi}\\ \frac{\partial}{\partial x^1}r\frac{\partial W_\varphi}{\partial\varphi}\\ D\end{bmatrix} \tag{A9}$$

where

$$D=-\frac{1}{\sqrt{a}r\rho}\left\{\frac{\partial}{\partial x^1}\left[\sqrt{a}r\rho\left(W^1\frac{\partial\ln\rho}{\partial\varphi}+\frac{\partial W^1}{\partial\varphi}\right)\right]+\frac{\partial}{\partial x^2}\left(\sqrt{a}r\rho\frac{\partial W^2}{\partial\varphi}\right)\right\}-2\frac{\partial\ln\rho}{\partial\varphi}C$$

APPENDIX B

Substituting

$$\frac{\partial q}{\partial\varphi}=\frac{\partial q}{\partial\psi_2}\frac{\partial\psi_2}{\partial\varphi}=\frac{1}{B}\frac{\partial q}{\partial\psi_2}$$

into vorticity and continuity equation gives the derivatives of W^1, W^2, W_φ

$$\begin{bmatrix}\sqrt{a_{22}}\cos\theta_{12} & \sqrt{a_{22}} & r\frac{\partial\varphi}{\partial x^2}\\ \sqrt{a_{11}} & \sqrt{a_{11}}\cos\theta_{12} & r\frac{\partial\varphi}{\partial x^1}\\ \frac{1}{\sqrt{a_{11}}}\frac{\partial\varphi}{\partial x^1} & \frac{1}{\sqrt{a_{22}}}\frac{\partial\varphi}{\partial x^2} & \frac{1}{r}\end{bmatrix}\cdot\begin{bmatrix}\frac{\partial W^1}{\partial\psi_2}\\ \frac{\partial W^2}{\partial\psi_2}\\ \frac{\partial W_\varphi}{\partial\psi_2}\end{bmatrix}=\begin{bmatrix}\frac{\partial(V_{\theta r})}{\partial x^2}B\\ \frac{\partial(V_{\theta r})}{\partial x^1}B\\ C'\end{bmatrix} \tag{B1}$$

$$C'=\frac{W^1}{\sqrt{a_{11}}}\cdot\frac{\partial B}{\partial x}+\frac{W^2}{\sqrt{a_{22}}}\cdot\frac{\partial B}{\partial x} \tag{B2}$$

$$\frac{\partial\rho}{\partial\psi_2}=\frac{\rho}{\kappa-1h}\left[\frac{\partial I}{\partial\psi_2}-\frac{\partial}{\partial\psi_2}\{[(\rho W^1)^2+(\rho W^2)^2-2(\rho W^1)(\rho W^2)\cos\theta_{12}]+(\rho W_\varphi)^2\}\right] \tag{B3}$$

The second derivatives of W^1, W^2, W_φ, ρ can be obtained in a similar way. From equations (10)

$$\frac{1}{\sqrt{g}}\left(\frac{\partial\psi_1}{\partial x^2}\frac{\partial\psi_2}{\partial\psi_2}-\frac{\partial\psi_2}{\partial x^2}\frac{\partial\psi_1}{\partial\psi_2}\right)=\rho W^1$$

$$\frac{1}{\sqrt{g}}\left(\frac{\partial\psi_1}{\partial\psi_2}\frac{\partial\psi_2}{\partial x^1}-\frac{\partial\psi_1}{\partial x^1}\frac{\partial\psi_2}{\partial\psi_2}\right)=\rho W^2 \tag{B4}$$

$$\frac{1}{\sqrt{g}}\left(\frac{\partial\psi_1}{\partial x^1}\frac{\partial\psi_2}{\partial x^2}-\frac{\partial\psi_1}{\partial x^2}\frac{\partial\psi_2}{\partial x^1}\right)=\rho W^3$$

Because

$$\frac{\partial\psi_2}{\partial x^1}\equiv0,\quad\frac{\partial\psi_2}{\partial x^2}\equiv0,\quad\frac{\partial\psi_2}{\partial\psi_2}\equiv1$$

Equation (B4) can then be written as:

$$\frac{\partial\psi_1}{\partial x^1}=-\sqrt{g}\rho W^2 \tag{B5}$$

Differentiating equation (B5) with respect to ψ_2, the first, second, or high-order derivatives of ψ_1 can be obtained

$$\frac{\partial}{\partial\psi_2}\left(\frac{\partial\psi_1}{\partial x^1}\right)=\frac{\partial}{\partial x^1}\left(\frac{\partial\psi_1}{\partial\psi_2}\right)=\frac{\partial}{\partial\psi_2}(\sqrt{g}\rho W^2) \tag{B6}$$

$$\frac{\partial\psi_1}{\partial\psi_2}=\int_{x_i}^{x'}-\frac{\partial}{\partial\psi_2}(\sqrt{g}\rho W^2)dx' \tag{B7}$$

etc.

Differentiating equations (23) with respect to ψ_2 and combining with equations (21), the second derivative of B is obtained.

$$\frac{D}{Dt}\left(\frac{\partial^2\ln B}{\partial\psi_2^2}\right)=$$

$$-\frac{1}{\rho}\left\{\frac{1}{r\sqrt{a}_{11}\sqrt{a}_{22}\sin\theta_{12}}\left[\frac{\partial}{\partial x^1}\left(r\sqrt{a}_{22}\sin\theta_{12}\frac{\partial^2(\rho W^1)}{\partial\psi_2^2}\right)+\frac{\partial}{\partial x^2}\left(r\sqrt{a}_{11}\sin\theta_{12}\frac{\partial^2(\rho W^2)}{\partial\psi_2^2}\right)\right]+\frac{\partial^2(\rho W^1)}{\partial\psi_2^2}\frac{\partial\ln B}{\partial\psi_2}/\sqrt{a}_{11}\right.$$

$$+\frac{\partial^2(\rho W^2)}{\partial\psi_2^2}\frac{\partial\ln B}{\partial\psi_2}/\sqrt{a}_{22}+2\frac{\partial}{\partial x^1}\left(\frac{\partial\ln B}{\partial\psi_2}\right)\frac{\partial(\rho W^1)}{\partial\psi_2}/\sqrt{a}_{11}$$

$$\left.+2\frac{\partial}{\partial x^2}\left(\frac{\partial\ln B}{\partial\psi}\right)\frac{\partial(\rho W^2)}{\partial\psi_2}/\sqrt{a}_{22}\right. \tag{B8}$$

High-order derivatives can be obtained by similar manner.

A Quasi-Three-Dimensional Turbomachinery Blade Design System: Part I—Throughflow Analysis

I. K. Jennions
Principal Theoretical Scientist.

P. Stow
Head of Theoretical Science.

Theoretical Science Group,
Rolls-Royce Limited,
Derby DE2 8BJ, England

The purpose of this work has been to develop a quasi-three-dimensional blade design and analysis system incorporating fully linked throughflow, blade-to-blade and blade section stacking programs. In Part I of the paper, the throughflow analysis is developed. This is based on a rigorous passage averaging technique to derive throughflow equations valid inside a blade row. The advantages of this approach are that the meridional streamsurface does not have to be of a prescribed shape, and by introducing density weighted averages the continuity equation is of an exact form. Included in the equations are the effects of blade blockage, blade forces, blade-to-blade variations and loss. The solution of the equations is developed for the well-known streamline curvature method, and the contributions from these extra effects on the radial equilibrium equation are discussed. Part II of the paper incorporates the analysis into a quasi-three-dimensional computing system and demonstrates its operational feasibility.

Introduction

If one considers the flow in a compressor or turbine, there are rotating and stationary blade rows that change in their orientation and cross sectional geometry from hub to tip. There are boundary layers on the annulus walls and the blade surfaces, wakes from the trailing edges of blades, overtip leakage flows, cooling flows ejected over the surfaces of turbine blades etc. The flow is unsteady, compressible, three-dimensional and viscous, and the solution of the full equations of motion with the true boundary conditions represents a formidable task. In the past few years, fully three-dimensional methods have been developed and are now in use for turbomachinery blade design. However, even for steady flow it is likely that for some years to come methods for solving three-dimensional problems will be of such a speed that only isolated blade rows, or at best single stages, can be computed in the design times available. In order to incorporate three-dimensional effects early in the design cycle a quasi-three-dimensional design system has been developed. This is efficient and economical, both in man and machine time, and is capable of describing some of the more fundamental aspects of three-dimensional flows. As such it can make a significant contribution to a blade design system.

Most throughflow calculation procedures can be traced back to the general theory of Wu [1]. In his theory, the steady flow solution is calculated on two families of intersecting streamsurfaces: a family of blade-to-blade streamsurfaces (S_1 surfaces) and a family of throughflow streamsurfaces (S_2 surfaces). Calculations are peformed on each family of streamsurfaces, but contain linkage terms to the other family. The solution is obtained in an iterative manner and is fully three-dimensional. Krimerman and Adler [2] have performed such a calculation, but in general this procedure has not been adopted. The most common technique is to use only one S_2 surface through the blade row, together with a number of S_1 surfaces. With this approach the S_1 surfaces are taken as surfaces of revolution and the method is referred to as quasi-three-dimensional.

The flow on the S_1 surfaces can be computed using a variety of techniques, e.g., streamline curvature [3], time marching [4] and finite element [5]. Information from the throughflow calculation is used to define the S_1 blade-to-blade surfaces in terms of streamline radius and streamtube height and to provide flow boundary conditions for blade design. In order to obtain accurate streamline shapes through the blade row, intra blade computing stations are necessary, and so an analysis to account for the blade force and geometry effects has to be produced. It is this analysis that is central to all quasi-three-dimensional methods. Four numerical solution techniques have been used in quasi-three-dimensional schemes; these are: the streamline curvature method, the matrix solution procedure, and the more recent finite element and time marching methods.

Contributed by the Gas Turbine Division of THE AMERICAN SOCIETY OF MECHANICAL ENGINEERS and presented at the 29th International Gas Turbine Conference and Exhibit, Amsterdam, The Netherlands, June 4–7, 1984. Manuscript received at ASME Headquarters December 19, 1983. Paper No. 84-GT-26.

The streamline curvature technique has been developed in papers by Smith [6], Silvester and Hetherington [7], Novak [8] and Frost [9], with quasi-three-dimensional applications reported by Senoo and Nakase [10] and Novak and Hearsey [11]. Senoo and Nakase defined their S_2 surface to coincide with the blade mean camberline and demonstrated their method on a centrifugal impeller. For axial flow turbines, Novak and Hearsey showed that this definition could not be expected to give reliable results. Instead they chose their S_2 surface to be generated by S_1 streamlines that divide the passage into equal mass flows. The work includes the specific mass flow ratio (B), a quantity analogous to the local coefficient of discharge along each S_1 surface, which is used in the throughflow continuity equation. B was shown to change rapidly with meridional distance and was not unity immediately upstream and downstream of the blade, regions where the throughflow program must treat the flow as axisymmetric ($B=1$).

In the matrix solution procedure, the throughflow equations are written in terms of a stream function. The resulting stream function equation is then put into finite difference form and solved by a matrix inversion technique. Marsh [12] presents the method for the throughflow problem, while Bosman and El Shaarawi [13] have incorporated the technique into a quasi-three-dimensional solution. Their method defines the S_2 surface by S_1 mass averaged streamlines that do not coincide with any actual S_1 streamlines but are taken to be representative of them all.

The finite element methods presented by Hirsch and Warzee [14] and Habashi and Youngson [15] are very similar to the matrix method, using a stream function as the dependent variable but adopting a finite element rather than a finite difference solution technique. Hirsch and Warzee employ a passage averaging technique similar to that used by Smith [6], but extend it by using mass averaged quantities to reduce the interaction terms between the S_1 surfaces and the meridional flow. Their quasi-three-dimensional system is integrated into a single program, and is therefore aimed at analysis type calculations.

Denton has shown the feasibility of using a time marching method for solving both the throughflow [16] and the blade-to-blade [4] problems. A quasi-three-dimensional application incorporating both solution procedures has been reported by Spurr [17]. This involved the calculation of the transonic flow (in the meridional plane) in an annular cascade, and hence was ideally suited to a time marching approach.

The present paper describes a rigorous passage averaging technique similar to that used by Hirsch, which is used to derive the throughflow equations valid inside a blade row for use with an existing streamline curvature method. Passage averaging avoids any indeterminacy associated with defining the S_2 surface, a problem that has continually been the subject of debate as illustrated by the various alternative approaches that have been adopted [11, 13]. The passage averaged throughflow equations contain the effects of the blade force, blade geometry, and perturbations on the mean flow, which are supplied from blade-to-blade and section stacking programs. The modular approach adopted in this quasi-three-dimensional design system is discussed fully in Part II of this paper [18].

The first section of the current paper describes the streamline curvature method as it relates to the present work. The governing equations are then passage averaged. Finally the radial equilibrium equation is formed and the new terms appearing in the analysis simplified. The major definitions and consequences of passage averaging may be found in the Appendix.

Description of the Streamline Curvature Method

The streamline curvature method has been described in some detail by Silvester and Hetherington [7] and Frost [9]. It is based on successive refinements of streamline paths through the flow domain by considering the radial equilibrium of the gas on each of the calculating stations shown in Fig. 1. This equilibrium can be described by a radial equilibrium equation (REE), which is a first order differential equation relating the static pressure gradient to the streamline geometry, whirl angle, etc. The streamlines provide the axial linking between calculating stations and are approximated by a curve fit through points of equal mass flow. The solution proceeds by guessing the midspan static pressure from which the REE can be solved and the mass flow through the station calculated. The midspan pressure is then adjusted until the desired mass flow through the station is attained, and the streamlines updated using the new flow variables. The whole procedure is repeated on each calculating station from inlet to exit successively until changes in the flow variables are small.

Governing Equations

The steady three-dimensional flow through a turbomachine is governed by the equations of mass conservation, momentum, energy, and state. In a coordinate system rotating with the blade at a constant angular velocity Ω the continuity equation is

$$\nabla(\rho \mathbf{W}) = 0 \tag{1}$$

and the inviscid momentum equations are written as

$$(\mathbf{W}.\nabla)\mathbf{W} = -\frac{1}{\rho}\nabla p + \Omega^2\mathbf{R} - 2\Omega\times\mathbf{W} + \mathbf{F}_\tau \tag{2}$$

Nomenclature

B = blade blockage term
C_p = specific heat at constant pressure
F_B = blade force
F_τ = dissipative body force
I = rothalpy
m = direction along a meridional streamline
$\dot{m}$ = mass flow rate
N = number of blades
p = static pressure
P = perturbation term
R = radius from machine axis; gas constant
s = entropy; true streamwise direction
t = static temperature
$\mathbf{W}$ = relative velocity vector
x = distance along machine axis
β = relative whirl angle
δ = radial blade lean
λ = hade angle
θ = circumferential direction
ρ = density
ψ = stream function
Ω = angular velocity of the blade row
σ = axial blade lean

Superscripts

$-$ = passage average
$\sim$ = density weighted average
$/$ = perturbation about a passage average
$//$ = perturbation about a density weighted average

Subscripts

c = mean cambersurface
H = hub
p = pressure surface
R = radial component
s = suction surface
T = tip
x = axial component
θ = circumferential component
ψ = along a streamline

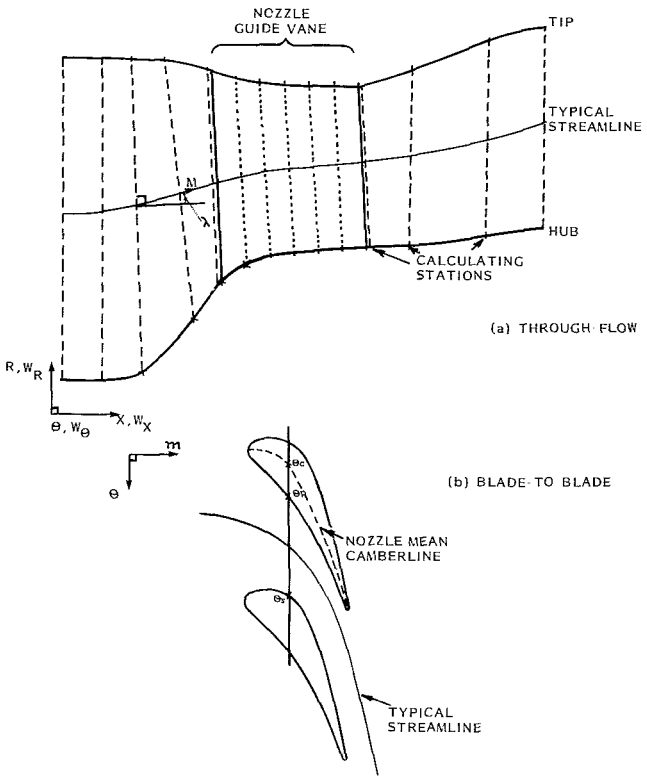

Fig. 1 Geometry definitions

where $\mathbf{W}$ is the relative velocity vector and $\mathbf{F}_\tau$ is a dissipative body force term. This $\mathbf{F}_\tau$ term was discussed by Horlock [19] and later by Wennerstrom [20]; it accounts for entropy increases in adiabatic flows and is related to the entropy field in a later section. In an (x, R, θ) cylindrical polar coordinate system, equations (1) and (2) are

$$\frac{\partial}{\partial x}(R\rho W_x)+\frac{\partial}{\partial R}(R\rho W_R)+\frac{\partial}{\partial \theta}(\rho W_\theta)=0 \tag{3}$$

$$\frac{\partial}{\partial x}(R\rho W_x^2)+\frac{\partial}{\partial R}(R\rho W_R W_x)+\frac{\partial}{\partial \theta}(\rho W_\theta W_x) = -R\frac{\partial p}{\partial x}+R\rho F_{\tau x} \tag{4}$$

$$\frac{\partial}{\partial x}(R\rho W_x W_R)+\frac{\partial}{\partial R}(R\rho W_R^2)+\frac{\partial}{\partial \theta}(\rho W_\theta W_R)-\rho(W_\theta+\Omega R)^2 = -R\frac{\partial p}{\partial R}+R\rho F_{\tau R} \tag{5}$$

$$\frac{\partial}{\partial x}(R\rho W_x W_\theta)+\frac{\partial}{\partial R}(R\rho W_R W_\theta)+\frac{\partial}{\partial \theta}(\rho W_\theta^2)+\rho W_R(W_\theta+2\Omega R)=-\frac{\partial p}{\partial \theta}+R\rho F_{\tau\theta} \tag{6}$$

The energy equation is written in its customary form for adiabatic flow as

$$\mathbf{W}.\nabla I=0 \tag{7}$$

i.e., the rothalpy (I) defined by

$$I=C_p t+\frac{1}{2}(W_x^2+W_\theta^2+W_R^2)-\frac{\Omega^2R^2}{2} \tag{8}$$

is constant along a streamline. Finally the equation of state for a perfect gas is written as

$$\rho=p/Rt \tag{9}$$

Passage Averaged Equations

In this work, equations (3–6) are averaged across the blade passage. Two types of average are defined: a passage average denoted by an overbar and a density weighted average denoted by a tilde. Their use for the terms encountered in the analysis is developed in the Appendix. It is therefore sufficient to quote the resulting averaged equations, starting with the continuity equation

$$\frac{\partial}{\partial x}(BR\bar{\rho}\tilde{W}_x)+\frac{\partial}{\partial R}(BR\bar{\rho}\tilde{W}_R)=0 \tag{10}$$

in which B is the blade blockage term defined by

$$B=\frac{N(\theta_s-\theta_p)}{2\pi} \tag{11}$$

Equation (10) is an exact form of the continuity equation with a simple physical interpretation for B: it is the non-dimensional circumferential spacing between the blades. This can be contrasted with other approaches [11] where integrating factors are introduced to take account of the different means used. The form of equation (10) is important in a streamline curvature method as we can now define a stream function by

$$\delta\psi=\int_R^{R+\delta R} BR\bar{\rho}\tilde{W}_x dR \tag{12}$$

from which the total mass flow through any radial calculating station can be seen to be

$$\dot{m}=2\pi\int_{R_H}^{R_T} BR\bar{\rho}\tilde{W}_x dR \tag{13}$$

The averaged momentum equations are

$$\tilde{W}_x\frac{\partial \tilde{W}_x}{\partial x}\bigg|_\psi=-\frac{1}{\bar{\rho}}\frac{\partial \bar{p}}{\partial x}+F_{Bx}+\tilde{F}_{\tau x}+P_x \tag{14}$$

$$\tilde{W}_x\frac{\partial \tilde{W}_R}{\partial x}\bigg|_\psi-\frac{(\tilde{W}_\theta+\Omega R)^2}{R}=-\frac{1}{\bar{\rho}}\frac{\partial \bar{p}}{\partial R}+F_{BR}+\tilde{F}_{\tau R}+P_R \tag{15}$$

and

$$\frac{\tilde{W}_x}{R}\frac{\partial}{\partial x}[(\tilde{W}_\theta+\Omega R)R]\bigg|_\psi=F_{B\theta}+\tilde{F}_{\tau\theta}+P_\theta \tag{16}$$

in which differentiation along a streamline is defined by

$$\frac{\partial}{\partial x}\bigg|_\psi=\frac{\partial}{\partial x}+\tan\lambda\frac{\partial}{\partial R} \tag{17}$$

and the hade[1] angle (λ) is given by

$$\tan\lambda=\tilde{W}_R/\tilde{W}_x \tag{18}$$

The deviation from axisymmetric duct flow

$$\left(\frac{\partial}{\partial\theta}=0,\quad \frac{\partial s}{\partial m}=0\right)$$

can be seen in the last three terms in each of equations (14–16). The first of these is the blade force term and is related to the pressure difference across the blade and the blade geometry by

$$F_{Bx}=\frac{N}{2\pi B\bar{\rho}}\left(p_s'\frac{\partial\theta_s}{\partial x}-p_p'\frac{\partial\theta_p}{\partial x}\right) \tag{19}$$

$$F_{BR}=\frac{N}{2\pi B\bar{\rho}}\left(p_s'\frac{\partial\theta_s}{\partial R}-p_p'\frac{\partial\theta_p}{\partial R}\right) \tag{20}$$

and

$$F_{B\theta}=\frac{N}{2\pi B\bar{\rho}R}(p_p'-p_s') \tag{21}$$

[1] Rolls-Royce terminology

The second is the consistent loss term, while the third term involves the perturbation terms which are given by

$$P_x = -\frac{1}{BR\bar{\rho}}\left[\frac{\partial}{\partial x}\left(BR\overline{\rho W_x''^2}\right) + \frac{\partial}{\partial R}\left(BR\overline{\rho W_x'' W_R''}\right)\right] \tag{22}$$

$$P_R = -\frac{1}{BR\bar{\rho}}\left[\frac{\partial}{\partial x}\left(BR\overline{\rho W_x'' W_R''}\right) + \frac{\partial}{\partial R}\left(BR\overline{\rho W_R''^2}\right)\right] + \frac{\widetilde{W_\theta''^2}}{R} \tag{23}$$

$$P_\theta = \frac{1}{BR\bar{\rho}}\left[\frac{\partial}{\partial x}\left(BR\overline{\rho W_x'' W_\theta''}\right) + \frac{\partial}{\partial R}\left(BR\overline{\rho W_R'' W_\theta''}\right)\right] + \frac{\widetilde{W_R'' W_\theta''}}{R} \tag{24}$$

The evaulation of the blade force, loss and perturbation terms will be discussed after the REE has been derived.

Radial Equilibrium Equation

In early formulations of the streamline curvature method applied to duct flows, the REE was derived in such a way that the only axial derivatives in the equation involved streamline hade and curvature. When flow inside a blade row is considered, this is not necessarily the most appropriate approach. In the work presented here, we have elected to form a REE from the averaged R and x momentum equations only, in order to avoid numerical singularities and maintain both simplicity and a clear physical interpretation of the terms involved.

In general, the REE would be formulated in a local coordinate system along a curved calculating station, but in order to clarify the analysis, the REE for purely radial stations is derived here. Defining the relative whirl angle (β) by

$$\tan\beta = \tilde{W}_R / \tilde{W}_x \tag{25}$$

we can combine equations (14) and (15) to give the desired REE as

$$\frac{\sec^2\lambda}{\bar{\rho}}\frac{\partial \bar{p}}{\partial R} = -\tilde{W}_x^2\frac{\partial \tan\lambda}{\partial x}\bigg|_\psi + \frac{(\tilde{W}_x\tan\beta + \Omega R)^2}{R} + \frac{\tan\lambda}{\bar{\rho}}\frac{\partial \bar{p}}{\partial x}\bigg|_\psi$$

I II III

$$(F_{BR} - F_{Bx}\tan\lambda) + (\tilde{F}_{\tau R} - \tilde{F}_{\tau x}\tan\lambda) + (P_R - P_x\tan\lambda) \tag{26}$$

IV V VI

The terms contributing to the radial pressure gradient can be identified as follows.

- I Streamline curvature in the meridional plane
- II Centrifuging of the fluid
- III Axial pressure gradient
- IV Blade force
- V Dissipative body force
- VI Perturbation (non axisymmetric) effects

In the next few sections we will examine how to evaluate the last three of these terms.

Blade Force Terms

Expressions for the blade force components have been presented in equations (19-21). We could form these terms from information obtained from the blade-to-blade and geometry programs in the proposed system, but this would result in a redundant circumferential momentum equation. Instead, we choose to relate the R and x components to the θ component, which is determined directly from the change in angular momentum. A convenient way to do this is to select the mean cambersurface and relate it to the suction and pressure surface θ coordinates by

$$\theta_p = \theta_c + \pi/N(1-B) \tag{27}$$

and

$$\theta_s = \theta_c + \pi/N(1+B) \tag{28}$$

Differentiating these expressions, substituting them into equation (20) and simplifying the result using equation (21) produces

$$F_{BR} = -F_{B\theta}\tan\delta + \frac{1}{2\bar{\rho}B}\frac{\partial B}{\partial R}(p_s' + p_p') \tag{29}$$

in which the radial blade lean angle (δ) is defined by

$$\tan\delta = R\frac{\partial \theta_c}{\partial R} \tag{30}$$

Similarly for the x-component of the blade force

$$F_{Bx} = -F_{B\theta}\tan\sigma + \frac{1}{2\bar{\rho}B}\frac{\partial B}{\partial x}(p_s' + p_p') \tag{31}$$

with the axial blade lean angle (σ) defined by

$$\tan\sigma = R\frac{\partial \theta_c}{\partial x} \tag{32}$$

Dissipative Force Term

A prescribed loss model is adopted in this work and we need to relate the dissipative force terms in our momentum equations to the entropy. Using the definition of rothalpy (equation (8)) the Gibbs relation can be written as

$$t\nabla s = \nabla I - \frac{1}{\rho}\nabla p - \nabla\left(\frac{\mathbf{W}^2}{2}\right) + \Omega^2\mathbf{R} \tag{33}$$

from which ∇p is eliminated by using equation (2), giving

$$t\nabla s = \nabla I - \mathbf{W}\times(\nabla\times\mathbf{W}) + 2\boldsymbol{\Omega}\times\mathbf{W} - \mathbf{F}_\tau \tag{34}$$

If we now take the scalar product of this equation with $\mathbf{W}$ and use equation (7), we arrive at the entropy/dissipative force relation

$$t\,\mathbf{W}.\nabla s = -\mathbf{W}.\mathbf{F}_\tau \tag{35}$$

Following [19], we assume that the dissipative force acts along a streamline, i.e.,

$$\mathbf{F}_\tau = F_\tau \mathbf{s} \tag{36}$$

where $\mathbf{s}$ is a unit vector in the streamwise direction. From equations (35) and (36), assuming that the perturbation terms are negligible when the resulting equation is averaged, we have

$$\tilde{F}_\tau = -\tilde{t}\frac{\partial \tilde{s}}{\partial s} \tag{37}$$

the three components of which can be written as

$$\tilde{F}_{\tau x} = -\frac{\tilde{t}}{1+\tan^2\lambda+\tan^2\beta}\frac{\partial \tilde{s}}{\partial x}\bigg|_\psi \tag{38}$$

$$\tilde{F}_{\tau R} = \tilde{F}_{\tau x}\tan\lambda \tag{39}$$

and

$$\tilde{F}_{\tau\theta} = \tilde{F}_{\tau x}\tan\beta \tag{40}$$

The loss and its gradient would in general come from a blade-to-blade program or be prescribed from an experimental correlation. The loss would include the profile loss of the blade along with shock losses if these occurred. Any account of annulus endwall boundary layers would be included by modifying the loss at the throughflow calculation stage. In

adopting the above model, the dissipative force terms in the REE (equation (26)) can be seen to be zero, but the $\tilde{F}_{\tau\theta}$ term in the circumferential momentum equation remains.

Perturbation Terms

The perturbation terms given by equations (22–24) involve velocity perturbations in all three coordinate directions. While the W''_θ and W''_x terms can readily be found from a blade-to-blade program, the W''_R terms would be more difficult, requiring an analysis such as that performed by Abdallah and Hamed [21] on a series of cross passage surfaces. We, however, have assumed that each S_1 surface is a surface of revolution so that there is no velocity component normal to the surface. This can be expressed as

$$W_R = W_x \tan\lambda \tag{41}$$

or

$$W''_R = W''_x \tan\lambda \tag{42}$$

which considerably simplifies the perturbation terms. Their form in the REE is given by

$$P_R - P_x \tan\lambda = -\widetilde{W''^2_x}\frac{\partial \tan\lambda}{\partial x}\bigg|_\psi + \frac{\widetilde{W''^2_\theta}}{R} \tag{43}$$

and in the θ momentum equation by

$$P_\theta = \frac{1}{BR\bar{\rho}}\frac{\partial}{\partial x}(BR\overline{\rho W''_\theta W''_x})\bigg|_\psi + \widetilde{W''_\theta W''_x}\frac{\partial \tan\lambda}{\partial R} + \frac{\widetilde{W''_\theta W''_x}}{R}\tan\lambda \tag{44}$$

The perturbation terms in equations (43) and (44) are found from the blade-to-blade solution flow variables that are interpolated onto x = constant lines. The mean and perturbation terms are then evaluated by numerical integration along these lines using equation (53) et seq.

The perturbation terms presented here are similar to the G functions discussed by Smith [6]. In his paper, Smith assumed that the major flow variables vary linearly across the blade-to-blade passage. Here we need no such assumption as we can evaluate these terms exactly.

By setting the velocity normal to our S_1 surface to zero, we have constrained the flow by neglecting any mixing in the spanwise direction. It is possible to expand the analysis to include a spanwise mixing model which contains the radial perturbation terms and the effects of mixing in the energy equation.

Final Form of the Equations

We have derived the equations used in the throughflow analysis under the following assumptions:

1 The flow is on surfaces of revolution and can be represented by mean and perturbation values with respect to the θ coordinate.

2 The loss terms can be modeled by a dissipative force which acts in the direction of the total flow using a prescribed loss model.

3 There are no velocity perturbations normal to the S_1 streamsurfaces.

4 The flow is adiabatic.

With these assumptions the radial equilibrium equation is

$$\frac{\sec^2\lambda}{\bar{\rho}}\frac{\partial \bar{p}}{\partial R} = -\tilde{W}^2_x\frac{\partial \tan\lambda}{\partial x}\bigg|_\psi + \frac{(\tilde{W}_x\tan\beta + \Omega R)^2}{R} + \frac{\tan\lambda}{\bar{\rho}}\frac{\partial \bar{p}}{\partial x}\bigg|_\psi + F_{B\theta}(\tan\lambda\tan\sigma - \tan\delta) + P \tag{45}$$

in which

$$P = \widetilde{W''^2_x}\frac{\partial \tan\lambda}{\partial x}\bigg|_\psi + \frac{\widetilde{W''^2_\theta}}{R} + \left(\frac{p'_s + p'_p}{2\bar{\rho}B}\right)\left(\sec^2\lambda\frac{\partial B}{\partial R} - \tan\lambda\frac{\partial B}{\partial x}\bigg|_\psi\right) \tag{46}$$

$F_{B\theta}$ is found from the θ momentum equation as

$$F_{B\theta} = \frac{\tilde{W}_x}{R}\frac{\partial}{\partial x}[(\tilde{W}_x\tan\beta + \Omega R)R]\bigg|_\psi - \tilde{F}_{\tau\theta} - P_\theta \tag{47}$$

in which

$$\tilde{F}_{\tau\theta} = -\frac{\tilde{t}\tan\beta}{1+\tan^2\lambda+\tan^2\beta}\frac{\partial \tilde{s}}{\partial x}\bigg|_\psi \tag{48}$$

and

$$P_\theta = \frac{1}{BR\bar{\rho}}\frac{\partial}{\partial x}(BR\bar{\rho}\overline{W''_\theta W''_x})\bigg|_\psi + \widetilde{W''_\theta W''_x}\frac{\partial \tan\lambda}{\partial R} + \frac{\widetilde{W''_\theta W''_x}}{R}\tan\lambda \tag{49}$$

The continuity equation takes the form

$$\delta\psi = \int_R^{R+\delta R} BR\bar{\rho}\tilde{W}_x dR \tag{50}$$

with the energy equation

$$\tilde{I} = C_p\tilde{t} + \frac{1}{2}\tilde{W}^2_x(1+\tan^2\lambda+\tan^2\beta) + \frac{1}{2}[\widetilde{W''^2_x}(1+\tan^2\lambda) + \widetilde{W''^2_\theta}] - \frac{\Omega^2R^2}{2} = I_{\text{inlet}} \tag{51}$$

and the equation of state

$$\tilde{\rho} = \tilde{p}/R\tilde{t} \tag{52}$$

On internal calculating stations we need loss and turning in common with other calculating stations, but now information regarding perturbation terms and the blade geometry is also required. The loss, turning, and perturbation terms are found from a blade-to-blade program and contribute directly to the blade force. The three-dimensional blade geometry is found from a stacking program, and includes the blade lean angles which appear as a multiplier of the blade force. The blade blockage acts chiefly to modify the continuity equation and has relatively little influence on the REE. It is through these interaction terms that a designer can examine some of the major three-dimensional effects inside a blade row.

Acknowledgment

The authors wish to thank Rolls-Royce Limited for permission to publish this paper.

References

1 Wu, C. H., "A General Theory of Three-Dimensional Flow in Subsonic and Supersonic Turbomachines of Axial-, Radial-, and Mixed-Flow Types," NACA TN 2604, 1952.

2 Krimerman, Y., and Adler, D., "The Complete Three-Dimensional Calculation of the Compressible Flow Field in Turbo Impellers," *Jnl. Mech. Eng. Sci.*, Vol. 20, No. 3, 1978, pp. 149–158.

3 Wilkinson, D. H., "Calculation of Blade-to-Blade Flow in Turbomachines by Streamline Curvature," Aeronautical Research Council R & M No. 3704, 1972.

4 Denton, J. D., "A Time Marching Method for Two- and Three-Dimensional Blade-to-Blade Flows," Aeronautical Research Council R & M No. 3775, 1975.

5 Deconinck, H., and Hirsch, C., "Finite Element Methods for Transonic Blade-to-Blade Calculation in Turbomachines," ASME JOURNAL OF ENGINEERING FOR POWER, Vol. 103, 1981, pp. 665-677.

6 Smith, L. H., Jr., "The Radial Equilibrium Equation of Turbomachinery," ASME JOURNAL OF ENGINEERING FOR POWER, Jan. 1966, pp. 1-12.

7 Silvester, M. E., and Hetherington, R., "Three-Dimensional Compressible Flow Through Axial Flow Turbomachines," *Numerical Analysis—An Introduction*, edited by J. Walsh, Ch. II, Pt. III, 1966, pp. 182-189.

8 Novak, R. A., "Streamline Curvature Computing Procedures for Fluid-Flow Problems," ASME JOURNAL OF ENGINEERING FOR POWER, Oct. 1961, pp. 478-490.

9 Frost, D. H., "A Streamline Curvature Through-Flow Computer Program for Analysing the Flow Through Axial-Flow Turbomachines," Aeronautical Research Council, R & M 3687, 1972.

10 Senoo, Y., and Nakase, Y., "An Analysis of Flow Through a Mixed Flow Impeller," ASME JOURNAL OF ENGINEERING FOR POWER, Jan. 1972, pp. 43-50.

11 Novak, R. A., and Hearsey, R. M., "A Nearly Three-Dimensional Intrablade Computing System for Turbomachinery," *Journal of Fluids Engineering*, Mar. 1977, pp. 154-166.

12 Marsh, H., "A Digital Computer Program for the Through-Flow Fluid Mechanics in an Arbitrary Turbomachine using a Matrix Method," Aeronautical Research Council R & M No. 3509, 1968.

13 Bosman, C., and El-Shaarawi, M. A. I., "Quasi-Three-Dimensional Numerical Solution of Flow in Turbomachines," *Journal of Fluids Engineering*, Mar. 1977, pp. 132-140.

14 Hirsch, C., and Warzee, G., "An Integrated Quasi-3D Finite Element Calculation Program for Turbomachinery Flows," ASME JOURNAL OF ENGINEERING FOR POWER, 1979, pp. 141-148.

15 Habashi, W. G., and Youngson, G. G., "A Transonic Quasi-3D Analysis for Gas Turbine Engines Including Split-Flow Capability for Turbofans," *International Journal for Numerical Methods in Fluids*, Vol. 3, 1983, pp. 1-21.

16 Denton, J. D., "Throughflow Calculations for Transonic Axial Flow Turbines," ASME JOURNAL OF ENGINEERING FOR POWER, Vol. 100, 1978, pp. 212-218.

17 Spurr, A., "The Prediction of 3D Transonic Flow in Turbomachinery Using a Combined Through-flow and Blade-to-Blade Time Marching Method," *Int. J. Heat and Fluid Flow*, Vol. 2, No. 4, 1980, pp. 189-199.

18 Jennions, I. K., and Stow, P., "A Quasi-Three-Dimensional Turbomachinery Blade Design System. Part II Computerized System," Submitted to the 29th ASME Gas Turbine Conference, Amsterdam, June, 1984.

19 Horlock, J. H., "On Entropy Production in Adiabatic Flow in Turbomachines," *Journal of Basic Engineering*, Dec. 1971, pp. 587-593.

20 Wennerstrom, A. J., "On the Treatment of Body Forces in the Radial Equilibrium Equation of Turbomachinery," Aerospace Research Laboratories Report No. 75-0052, 1975.

21 Abdallah, S., and Hamed, A., "The Elliptic Solution of the Secondary Flow Problem," ASME Paper No. 82-GT-242, 1982.

APPENDIX

Passage Averaging – Definitions and Consequences

The passage average of a quantity A is defined by

$$\bar{A} = \frac{\int_{\theta_p}^{\theta_s} A\,d\theta}{\theta_s - \theta_p} \tag{53}$$

with a density weighted average defined as

$$\tilde{A} = \frac{\int_{\theta_p}^{\theta_s} \rho A\,d\theta}{\int_{\theta_p}^{\theta_s} \rho\,d\theta} = \frac{\overline{\rho A}}{\bar{\rho}} \tag{54}$$

From these definitions we can see that

$$A = \tilde{A} + A', \quad \overline{A'} = 0 \tag{55}$$

and

$$A = \tilde{A} + A'', \quad \widetilde{A''} = 0 \tag{56}$$

where the prime and double prime notation has been used to denote a perturbation about the mean value. The perturbations need not be small, and indeed have not been assumed to be small in the analysis. Using these definitions, we can write the average of a simple product as

$$\overline{\rho W_\theta W_x} = \bar{\rho}\widetilde{W_\theta W_x} = \bar{\rho}\widetilde{(\tilde{W}_\theta + W''_\theta)(\tilde{W}_x + W''_x)} \tag{57}$$

$$= \bar{\rho}\tilde{W}_\theta \tilde{W}_x + \bar{\rho}\widetilde{W''_\theta W''_x} \tag{58}$$

This splitting of terms into a mean and perturbation component is adopted throughout the analysis. The mean component is the one we work with directly in the throughflow solution, while the perturbation component will be retrieved from a blade-to-blade calculation.

If we now take the $\partial(R\rho W_x)/\partial x$ term in the continuity equation, passage averaging, using Leibnitz's theorem, gives

$$\frac{1}{\theta_s - \theta_p}\int_{\theta_p}^{\theta_s} \frac{\partial}{\partial x}(R\rho W_x)\,d\theta = \frac{1}{\theta_s - \theta_p}\left[\frac{\partial}{\partial x}\int_{\theta_p}^{\theta_s} R\rho W_x\,d\theta - (R\rho W_x)_s\frac{\partial\theta_s}{\partial x} + (R\rho W_x)_p\frac{\partial\theta_p}{\partial x}\right] \tag{59}$$

which, as we are working on streamsurfaces that are surfaces of revolution (i.e., $R \neq R(\theta)$), is

$$\frac{1}{\Delta\theta}\int_{\theta_p}^{\theta_s}\frac{\partial}{\partial x}(R\rho W_x)\,d\theta = \frac{1}{B}\frac{\partial}{\partial x}(BR\bar{\rho}\tilde{W}_x) + \frac{1}{\Delta\theta}\left[(R\rho W_x)_p\frac{\partial\theta_p}{\partial x} - (R\rho W_x)_s\frac{\partial\theta_s}{\partial x}\right] \tag{60}$$

with the circumferential gap and blockage defined by

$$\Delta\theta = \theta_s - \theta_p = \frac{2\pi B}{N} \tag{61}$$

in which N is the number of blades in the row. In forming the averaged continuity equation, the last two terms in equation (60) can be combined with those from the remaining terms in equation (3) and eliminated using the condition of no flow through the blade surfaces. This can be expressed as

$$\mathbf{W}.\mathbf{n} = 0 \tag{62}$$

when $\mathbf{n}$ is the vector normal to the blade surface and is used in the form

$$W_\theta = RW_x\frac{\partial\theta}{\partial x} + RW_R\frac{\partial\theta}{\partial R} \tag{63}$$

on both pressure and suction surfaces of the blade.

For a typical term in the momentum equations we have

$$\frac{1}{\Delta\theta}\int_{\theta_p}^{\theta_s}\frac{\partial}{\partial x}(R\rho W_x W_\theta)\,d\theta = \frac{1}{\Delta\theta}\left[\frac{\partial}{\partial x}\int_{\theta_p}^{\theta_s} R\rho W_x W_\theta\,d\theta + (R\rho W_x W_\theta)_p\frac{\partial\theta_p}{\partial x} - (R\rho W_x W_\theta)_s\frac{\partial\theta_s}{\partial x}\right] \tag{64}$$

$$= \frac{1}{B}\frac{\partial}{\partial x}(BR\overline{\rho W_x W_\theta}) + \frac{1}{\Delta\theta}\left[(R\rho W_x W_\theta)_p\frac{\partial\theta_p}{\partial x} - (R\rho W_x W_\theta)_s\frac{\partial\theta_s}{\partial x}\right] \tag{65}$$

$$= \frac{1}{B}\frac{\partial}{\partial x}(BR\bar{\rho}\tilde{W}_x\tilde{W}_\theta) + \frac{1}{B}(BR\bar{\rho}\widetilde{W''_x W''_\theta}) + \frac{1}{\Delta\theta}\left[(R\rho W_x W_\theta)_p\frac{\partial\theta_p}{\partial x} - (R\rho W_x W_\theta)_s\frac{\partial\theta_s}{\partial x}\right] \tag{66}$$

Again, the last two terms of the right-hand side can be eliminated when combined with other expanded terms in the θ

momentum equation by using the no-flow condition. However, unlike equation (60), gradients of perturbation terms appear.

The only other average that needs consideration here is that of the pressure gradient terms, viz.,

$$\frac{1}{\Delta\theta}\int_{\theta_p}^{\theta_s} R\frac{\partial p}{\partial R}\,d\theta = \frac{R}{\Delta\theta}\left[\frac{\partial}{\partial R}\int_{\theta_p}^{\theta_s} p\,d\theta + p_p\frac{\partial\theta_p}{\partial R} - p_s\frac{\partial\theta_s}{\partial R}\right] \quad (67)$$

$$= \frac{R}{\Delta\theta}\left[\frac{\partial}{\partial R}\left\{\bar{p}(\theta_s-\theta_p)\right\} + p_p\frac{\partial\theta_p}{\partial R} - p_s\frac{\partial\theta_s}{\partial R}\right] \quad (68)$$

$$= \frac{R}{\Delta\theta}\left[(\theta_s-\theta_p)\frac{\partial\bar{p}}{\partial R} + \bar{p}\frac{\partial\theta_s}{\partial R} - \bar{p}\frac{\partial\theta_p}{\partial R} + p_p\frac{\partial\theta_p}{\partial R} - p_s\frac{d\theta_s}{\partial R}\right] \quad (69)$$

Combining these resulting terms ($p_s=\bar{p}+p_s'$, etc.) gives

$$\frac{1}{\Delta\theta}\int_{\theta_p}^{\theta_s} R\frac{\partial p}{\partial R}\,d\theta = R\frac{\partial\bar{p}}{\partial R} + \frac{R}{\Delta\theta}\left[p_p'\frac{\partial\theta_p}{\partial R} - p_s'\frac{\partial\theta_s}{\partial R}\right] \quad (70)$$

which is the average radial pressure gradient and the pressure perturbations, the latter being referred to as a blade force term, e.g., for the R momentum equation

$$-\frac{1}{R\bar{\rho}\Delta\theta}\int_{\theta_p}^{\theta_s} R\frac{\partial p}{\partial R}\,d\theta = -\frac{1}{\bar{\rho}}\frac{\partial\bar{p}}{\partial R} + F_{BR} \quad (71)$$

with the radial component of the blade force given by

$$F_{BR} = \frac{N}{2\pi B\bar{\rho}}\left[p_s'\frac{\partial\theta_s}{\partial R} - p_p'\frac{\partial\theta_p}{\partial R}\right] \quad (72)$$

A Quasi-Three-Dimensional Turbomachinery Blade Design System: Part II—Computerized System

I. K. Jennions
Principal Theoretical Scientist.

P. Stow
Head of Theoretical Science.

Theoretical Science Group,
Rolls-Royce Limited,
Derby DE2 8BJ, England

The purpose of this work has been to develop a quasi-three-dimensional blade design and analysis system. In Part II of the paper the computerized blade design system is presented and an example given to illustrate its use. The system comprises a streamline curvature throughflow program incorporating the analysis of Part I of this paper, a blade section stacking program, and one of a number of blade-to-blade calculation programs. The information flow between each part of the system is described and the importance of each stage in the calculation indicated. Information is transferred between programs via a data base which enables other design programs, e.g., heat transfer programs, to access the results. This modular approach enables individual design program advances to be made relatively easily. The system is flexible enough to incorporate a number of blade-to-blade programs, the one used depending on the specific application. An example of the flow through a turbine nozzle guide vane is presented. Experimental data are compared with the results from the quasi-three-dimensional system, a fully three-dimensional program and an unlinked two-dimensional system. The results from the quasi-three-dimensional system are very encouraging.

Introduction

In the design of compressors and turbines, individual nozzles, rotors, or stages are designed to perform specific tasks. So, for example, a compressor stage might be required to produce a desired increase in total pressure or a turbine stage to achieve a work output, both with some lower limits on the acceptable efficiency. Components are designed with the aid of theoretical methods and computer programs. Due to the highly complex flows encountered in turbomachines and the current speed of computers, methods for solving the full three-dimensional flow problem have only been developed to the point where they can be used on isolated blade rows in the design times available. Even so, three-dimensional design is a difficult and time consuming task. One reason for this is that three-dimensional methods currently adopted are analytic in nature and consequently must be used in a change parameter/re-analyze mode of operation. In order to aid the process and introduce three-dimensional effects into conventional blade design systems it is possible to link current two-dimensional design programs to produce quasi-three-dimensional solutions. This maintains current design options while producing a solution which is superior to that obtained using the component programs in isolation. The quasi-three-dimensional system interacts with the full three-dimensional system as shown in Fig. 1.

The two-dimensional design of individual blade rows in a multistage turbomachine follows a familiar pattern. A throughflow program (TFP) is run in order to design the annulus shape and set the blade row velocity triangles and hence performance. A blade-to-blade program (BBP) then accepts the aerodynamic information along a streamline

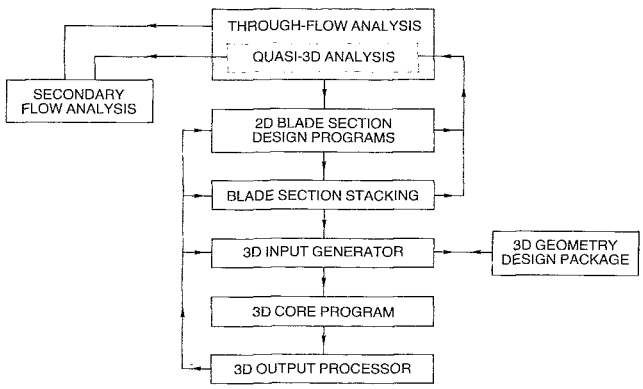

Fig. 1 Quasi-three-dimensional and three-dimensional aerodynamic design system

Contributed by the Gas Turbine Division of THE AMERICAN SOCIETY OF MECHANICAL ENGINEERS and presented at the 29th International Gas Turbine Conference and Exhibit, Amsterdam, The Netherlands, June 4–7, 1984. Manuscript received at ASME Headquarters December 19, 1983. Paper No. 84-GT-27.

through the blade row from the TFP in order that the blade sections may be designed. Finally, these sections are stacked in a section stacking program (SSP) to form the three-dimensional blade. In the traditional system, no interaction between the programs is taken into account, e.g., the choice of stack is assumed not to affect the position of the streamlines. This is clearly an approximation and it has been the purpose of the current work to quantify the interactions between these programs and to produce a system that can account for these effects.

In Part I of this paper [1] a quasi-three-dimensional throughflow analysis was developed for computing stations inside blade rows. A passage averaging technique was employed to avoid the ambiguity associated with defining the shape of the throughflow surface and to ensure a rigorously consistent coupling of the throughflow and blade-to-blade flow solutions. The calculation demands interaction terms from both the BBP and SSP, and an iterative method of solution is clearly required. The flexibility of the Rolls-Royce data base and the modular approach adopted for design programs has enabled these links to be made easily. It should be noted that this modular approach allows any one of a number of blade-to-blade programs to be used, and thereby extends the general applicability of the system.

The present paper is arranged in three main sections. The first deals with the quasi-three-dimensional computing system, its component programs and their links to the data base. The second section describes the ways in which the system can be used, while the third section presents an example of its use on a turbine nozzle guide vane.

Quasi-Three-Dimensional Computing System

The quasi-three-dimensional computing system is shown schematically in Fig. 2 and consists of three main programs (TFP, BBP, SSP) linked to the data base. The throughflow input generator is used to display and/or alter the interaction information at the beginning of each quasi-three-dimensional cycle, a cycle consisting of a TFP run, several BBP runs, and an SSP run. The component programs are now described, starting with the TFP.

Throughflow Program. In the throughflow calculation the flow through a number of stages is usually considered, with certain design targets such as stage pressure ratio, or stage work, specified as boundary conditions in order to solve the governing equations. The flow is assumed to be axisymmetric in the duct regions with a passage averaging technique used on stations inside the blade rows to make the equations of motion two-dimensional. The analysis for these internal stations has been presented, for the streamline curvature method adopted, in Part I of this paper [1] and the resulting equations for radial stations are given in the Appendix. The equations contain the following interaction terms: (*i*) relative whirl angle, (*ii*) blockage, (*iii*) perturbation terms, (*iv*) loss, and (*v*) axial and radial blade lean angles.

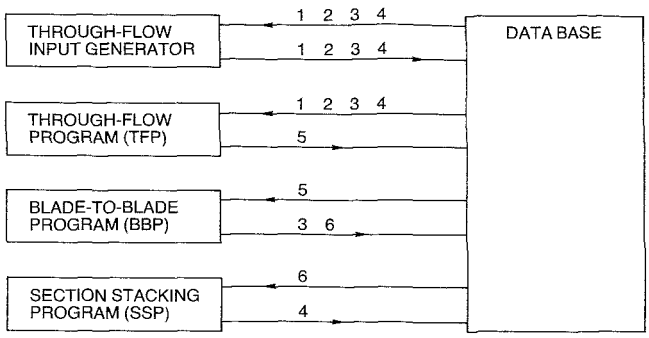

The program links are given by:

1 Annulus geometry
2 Through-flow boundary conditions
3 Relative whirl angle
Blockage
Perturbation terms
Loss
4 Axial and radial blade leans
5 Streamline radius and streamtube height
Blade-to-blade boundary conditions
6 Stream section geometry

Fig. 2 Quasi-three-dimensional computing system

The first four of these terms are found from a BBP, while the fifth is found from the SSP, as indicated in Fig. 2. With these as input, the TFP calculates the blade-to-blade streamsurfaces and their thicknesses (streamtube heights). It also calculates the flow inlet and exit conditions, i.e., Mach numbers and whirl angles, to be used as boundary conditions in the blade design.

Blade-to-Blade Program. In a section design program, the flow on one blade-to-blade streamsurface through a single blade row is considered. The streamsurface geometry from the throughflow calculation is used in order to render the equations two-dimensional, and the object of the design is to match the throughflow supplied conditions whilst satisfying any additional aerodynamic or structural conditions that may be imposed.

These design objectives can be met by using either a design or analysis blade-to-blade method. In a design method the blade surface velocity can be prescribed and the calculation produces the geometry to achieve this. In contrast, analysis methods construct the blade section to approximately satisfy the boundary conditions, the performance is examined at design and off-design, and the blade geometry is modified in order to satisfy the design targets. There are also mixed design and analysis methods that allow the specification of surface velocity over part of the blade together with the geometry over the remainder. Clearly this makes the achievement of mixed structural and aerodynamic constraints easier.

Nomenclature

B = blade blockage term
C_p = specific heat at constant pressure
F_B = blade force
F_γ = dissipative body force
I = rothalpy
$\dot{m}$ = mass flow rate
p = static pressure
P = perturbation term
R = radius from machine axis; gas constant
s = entropy
t = static temperature
T = total temperature
$\mathbf{W}$ = relative velocity vector
x = distance along machine axis
β = relative whirl angle
δ = radial blade lean
λ = hade angle
ρ = density
Ω = angular velocity
σ = axial blade lean

Superscripts

$-$ = passage average
$\sim$ = density weighted average
$/$ = perturbation about a passage average
$//$ = perturbation about a density weighted average

Subscripts

H = hub
p = pressure surface
s = suction surface
T = tip
x = axial component
θ = circumferential component
ψ = along a streamline

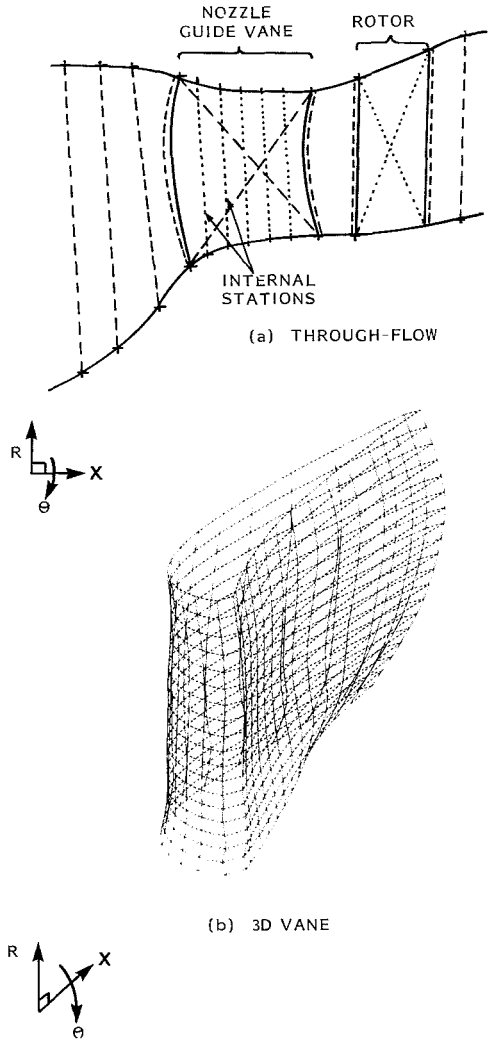

Fig. 3 Vane geometry

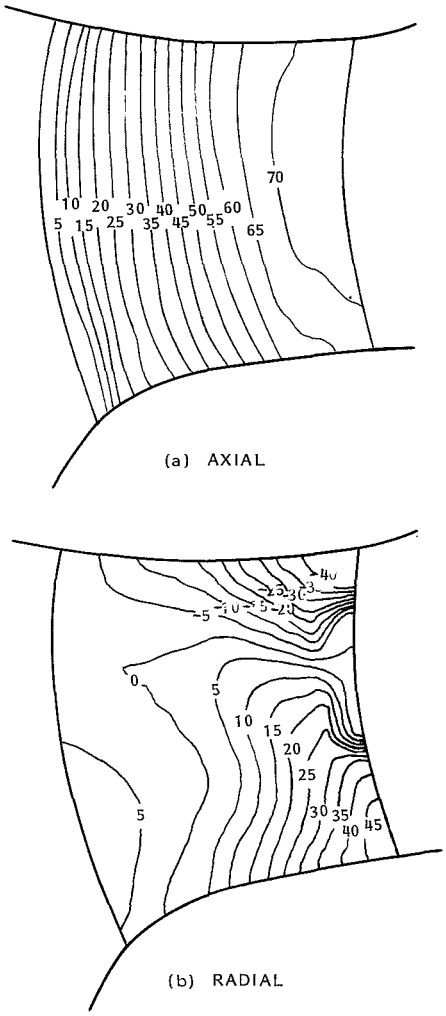

Fig. 4 Blade lean angles

Whilst the throughflow solution is always obtained using the TFP, both the methods outlined above and the different conditions at which sections are designed give rise to a number of blade-to-blade solution techniques, e.g., streamline curvature, time marching and finite element methods. All these methods are linked into the quasi-three-dimensional system.

The selected BBP is run to design a number of blade sections, which are then filed on the data base. The perturbation terms detailed in the Appendix are also filed ready for the next quasi-three-dimensional cycle.

Section Stacking Program. Blade sections from hub to tip are designed using an appropriate BBP and these are then stacked to produce the full three-dimensional blade geometry. As the blade sections have been designed in isolation, they can be positioned at any circumferential position in the annulus, subject to the blade being acceptable from stress and geometry considerations. Once the stack has been decided, the axial and radial blade lean angles are filed. These angles will affect the blade force term in equation (1) and hence the radial static pressure gradient on internal calculating stations.

Uses of the Quasi-Three-Dimensional System

There are many possible ways of running the TFP, and these have been maintained when the internal station analysis was incorporated. For example, we can run a fan to a pressure ratio and relative whirl angle, or a high pressure turbine stage to power, efficiency, and deflection, with stations inside the blade rows. In general, program usage can be broken down into two major modes, either design or analysis, which are now discussed in terms of the quasi-three-dimensional system.

The steps in a typical quasi-three-dimensional blade design calculation are as follows. Filing as shown in Fig. 2 takes place at the end of each step.

1 The annulus geometry, blade positions, and aerodynamic conditions are set up in the throughflow input generator.

2 The TFP is run to produce streamline geometry and inlet/exit aerodynamics for a BBP. If the streamline geometry (principally streamtube height) has not changed from the last cycle, then the iteration can be judged to have converged, if not continue.

3 Blade sections are designed using a BBP and the throughflow generated conditions. Iteration may be required with step 2 in order to achieve efficiencies with acceptable blade loadings.

4 The designed sections are stacked, taking account of cooling air tubes, stress considerations, etc. Blade leading and trailing edge definition set in step 1 may need to be altered if axial chords have changed.

5 Return to step 2 for the next cycle.

The choice of streamline geometry in step 2 to define convergence is somewhat arbitrary, alternative definitions in terms of appropriate design parameters can readily be used. With the design mode of the system, it is also possible to examine the effects of stack, loading distribution (both axial and radial) and loss on the converged solution.

In the analysis mode of operation the system run options

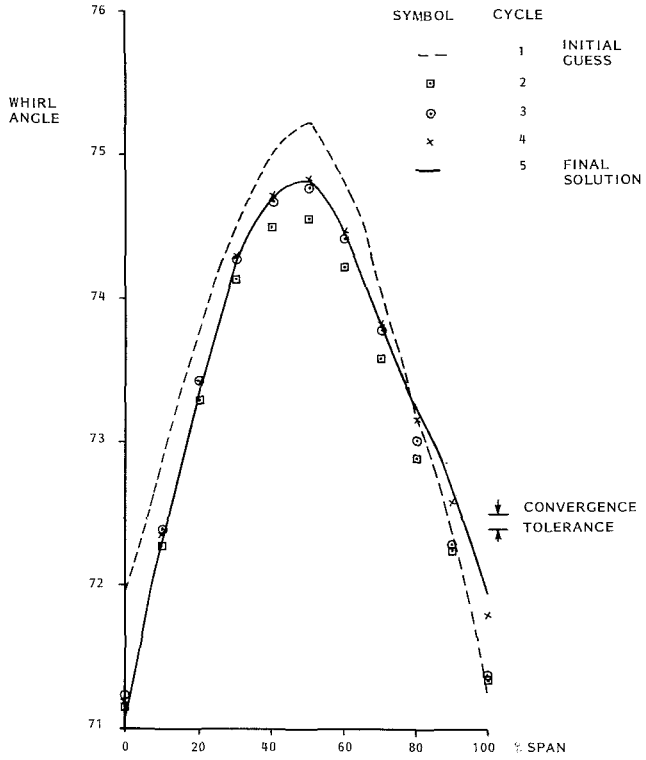

Fig. 5 Convergence of solution

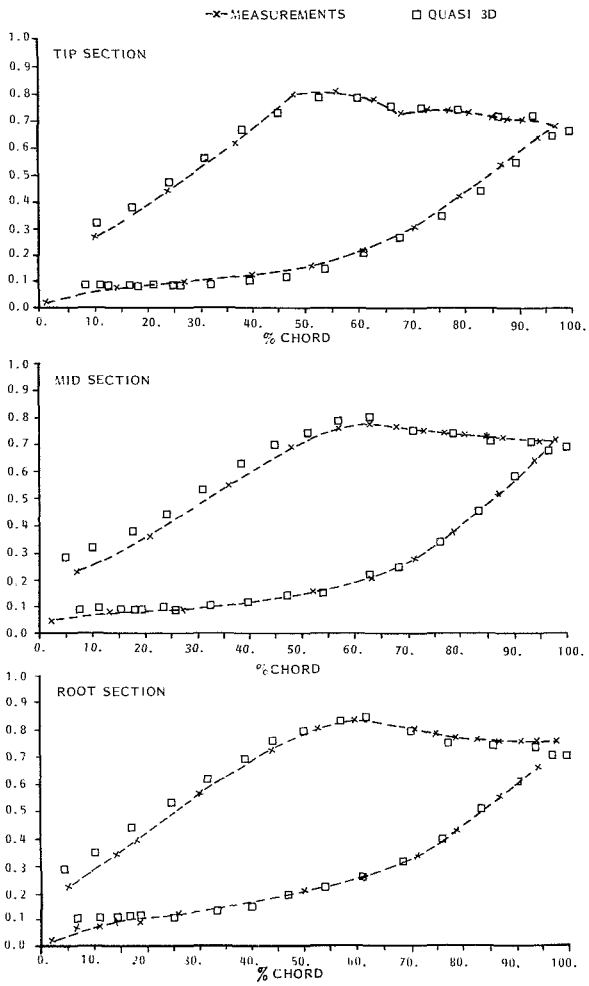

Fig. 6 Surface Mach numbers from experiment and the quasi-three-dimensional system

are not so numerous, and a typical calculation is given by the following steps. Again it is assumed that the filing shown in Fig. 2 takes place after each step.

1 Set up the annulus geometry, blade positions, and aerodynamic conditions in the input generator. The blade lean angles and the blade positions will be known from the three-dimensional geometry.

2 Run the TFP to produce streamline geometry, inlet and exit whirl angles, and Mach numbers.

3 Obtain the blade section geometry by interpolating the three-dimensional stacked geometry onto the TFP streamlines.

4 Run a BBP (for a number of sections) to the inlet conditions supplied by the TFP and a Kutta condition imposed at the blade trailing edge. This will result in an exit whirl angle that will not, in general, agree with the TFP. Convergence is then defined by the TFP and BBP whirl angles agreeing to within a prescribed tolerance.

5 Amend the whirl angle profile specified as input to the TFP from the BBP angles just produced. Return to step 2 for the next cycle.

Flow Through a Nozzle Guide Vane

The foregoing method for the analysis mode of operation has been used to compute the flow through a turbine nozzle guide vane. The throughflow geometry and the three-dimensional stacked vane, as seen by the SSP, are shown in Fig. 3. Curved leading and trailing edges are an outcome of the chosen stack, which also gives a highly convex pressure surface over the last half of the vane, as shown by the radial blade lean angles in Fig. 4. The axial blade lean contours are relatively simple, reflecting the gradual turning of the gas through the vane.

This particular vane has been rig tested at the midheight exit Mach number of 0.7, both with and without the rotor in place. Measurements of surface static pressures on the vane were taken at three different heights (20, 50, and 80 percent), and the presence of the rotor was found to make little difference to these readings. Without the rotor, it was possible to measure exit whirl angle and Mach number profiles. These results, along with the measured capacity of the vane, form the basis of our comparison with the predictions from the quasi-three-dimensional system.

For the purpose of the present investigation the flow was assumed to be lossless with no radial profiles of flow variables at inlet, and hence no attempt was made at modeling the inlet boundary layers. The initial guess of exit whirl angle was taken as the blade exit metal angle, and the TFP was run to produce a midheight exit Mach number of 0.7 by changing the inlet mass flow. This adjustment to the mass flow was made on each cycle, after the exit whirl angles had been changed from the BBP. Convergence of the system is shown in Fig. 5 and was judged to occur when the exit whirl angle changed by less than 0.1 deg between cycles.

Five cycles were needed to attain this tolerance. This is a typical number of cycles for such cases and is relatively independent of the initial guess. The quasi-three-dimensional results were produced using a streamline curvature BBP and five internal stations in the TFP. This BBP is an extensively developed and evaluated compatible mixed design and analysis mode program, only the analysis part of which is used here. The full geometry of the blade including the leading edge is used in the calculation.

Comparison of the quasi-three-dimensional and measured results is shown in Fig. 6 for the three instrumented sections. The suction surface peak Mach number and its position, along with the subsequent diffusion to the blade exit are seen to be predicted well for all sections. There is some

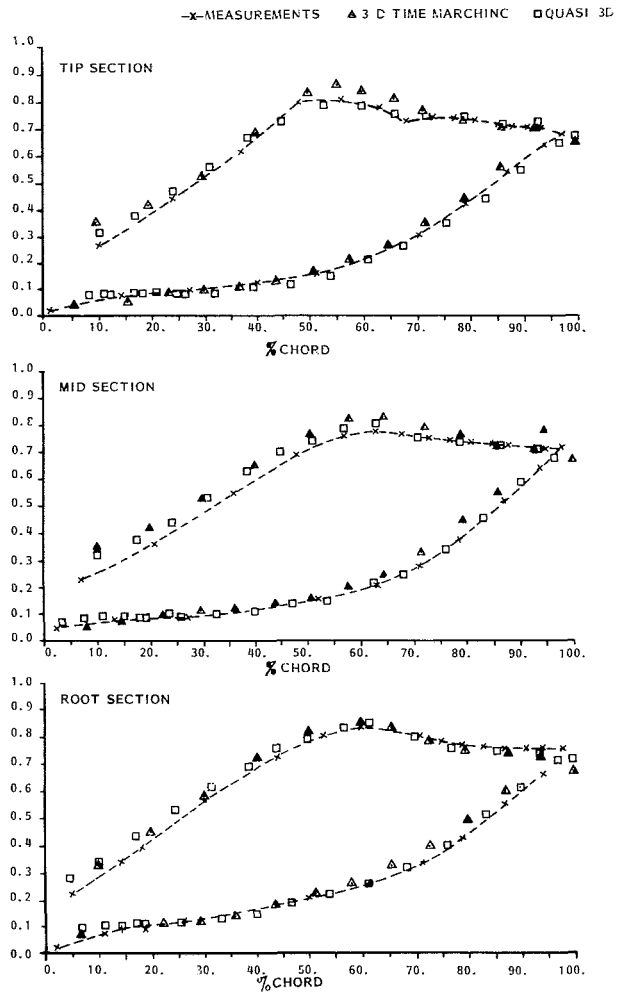

Fig. 7 Surface Mach number comparison with fully three-dimensional results

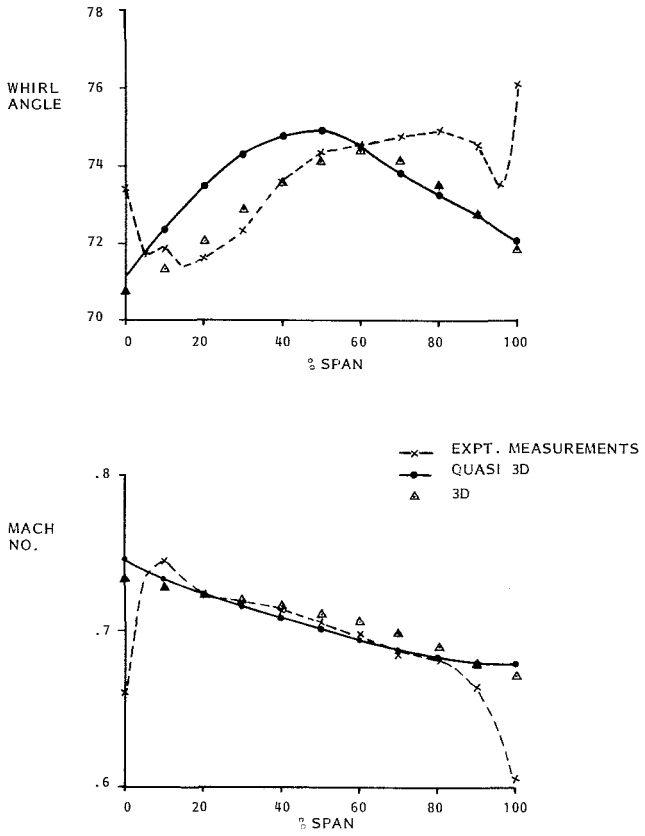

Fig. 8 Whirl angle and Mach number at blade row exit

disagreement between theory and test on the first 50 percent of the suction surface, but this can be attributed in some part to the rig having incidence on the leading edge (some swirl being present in the incoming flow) while the calculations have been run at design. The whole pressure surface is in good agreement with test. The predicted capacity ($\dot{m}\sqrt{T}/P$) of the vane was 2.7 percent higher than that measured on test. This seems to be reasonable as the blade profile boundary layers have been calculated to be worth 1.5 percent and the annulus boundary layers are probably of the same magnitude.

A fully three-dimensional inviscid time marching calculation has been performed on this vane and the results are shown in Fig. 7. The run was made using the same inlet conditions as the TFP and so takes no account of inlet boundary layers or loss generated through the row. The results are in qualitative agreement with those from the quasi-three-dimensional system. However, the three-dimensional results show higher peak Mach numbers than test or quasi-three-dimensional, and also higher Mach numbers over the last half of the pressure surface. The exit conditions from the quasi-three-dimensional and three-dimensional calculations are qualitatively very similar (Fig. 8), their deviation from the measured Mach numbers being due to the hub and tip boundary layers, which are quite pronounced.

The hub boundary layer is thinner than that at the tip due to the higher annulus curvature found on the hub. Whirl angle differences between experiment and calculations are attributed to be secondary flow generated by the endwall boundary layers, not accounted for in either the quasi-three-dimensional or three-dimensional runs. These results show that good predictions can be achieved with a fully linked quasi-three-dimensional system.

In contrast, the results from an unlinked system using the same component programs as the quasi-three-dimensional system are shown in Fig. 9, and are labelled "two-dimensional." As no internal stations have been used in the throughflow calculation, the streamtube height variation is taken to vary linearly through the row, and the streamline radius is taken to have a cubic variation matching position and slope at inlet and exit. The two-dimensional solution is obtained by using the converged quasi-three-dimensional conditions in order to run the TFP with no internal stations. The blade-to-blade geometry is obtained from the SSP using the streamline radius approximation, and the sections are analyzed in the BBP in the normal way. The two-dimensional method significantly underpredicts the peak Mach number and, on all three sections, loses any detail regarding the back suction surface diffusion. In fact, the two-dimensional solutions seem to be predicting an almost constant Mach number over the last 50 percent of the blade suction surface. This effect can be attributed, to some extent, to the fact that the streamtube heights are not necessarily compatible with the annulus geometry, an effect which would be more serious with a profiled annulus.

To conclude the above discussion, it appears that the quasi-three-dimensional system is working well (in this case) and produces results that are superior to the unlinked system, and as good as those produced by the three-dimensional method.

As well as the predictions just given, we can output the component terms of the radial equilibrium equation to give a physical insight into the dominant effects on the flow at each station. To facilitate ease of reference to the terms, the meaningful names shown under equation (1) are used. These terms are shown in Fig. 10 for the first, third, and fifth in-

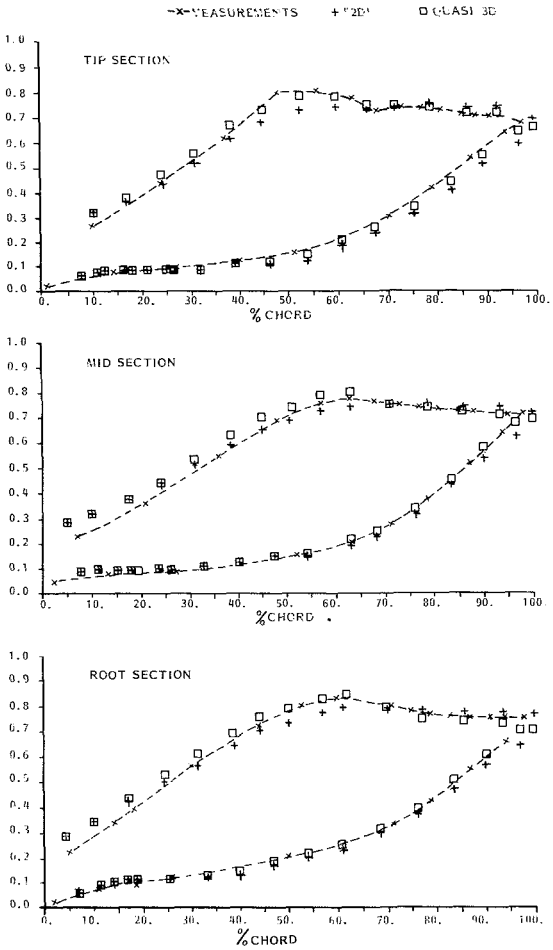

Fig. 9 Surface Mach number comparison with two-dimensional results

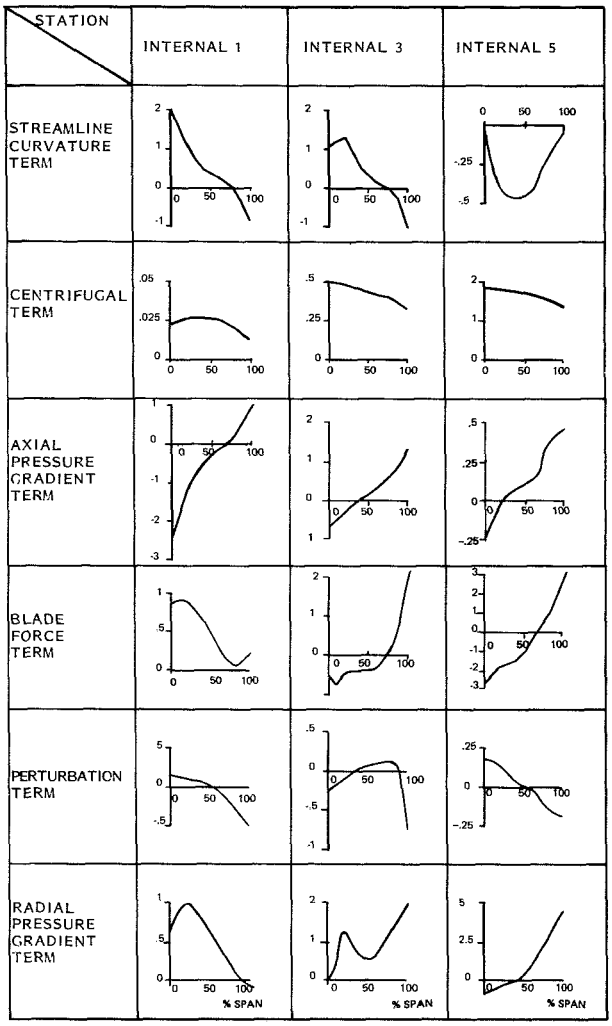

Fig. 10 Balance of REE terms through the row

ternal station, and appear in the same order as in equation (1). All the terms shown have been non-dimensionalized with respect to the maximum radial pressure gradient term on internal 1. On the first internal station the centrifugal effect does not affect the overall radial pressure gradient term significantly and the perturbation terms only have an effect near the tip. The streamline curvature terms shows high hade on the hub with smaller and opposite annulus curvature at the tip. The axial pressure gradient terms acts to counterbalance the curvature term. The main shape of the total curve therefore comes from the blade force term. Similar balances between the terms can be seen on the other two stations. On internal 3 all terms contribute significantly, whereas on internal 5 the centrifugal and blade force terms dominate.

The low streamline curvature term on the fifth internal is due to the annulus aligning itself with the machine centerline, while the axial pressure gradient ($\partial p/\partial x|_\psi$) is always positive but is affected by the hade (tan λ) to produce the observed distributions. Both of these terms can therefore be controlled by the shape of the annulus.

The centrifugal term increases as we move downstream and reflects the increase in whirl velocity, this being a term over which a designer would have little control. The blade force term is controlled by how quickly the angular momentum changes, and also by the blade lean and hade angles. On internals 1 and 3, the radial blade lean is small and plays little part, but on internal 5 it has large values. To produce a given radial pressure gradient term, it is therefore possible to select the stack of the blade in order to alter the blade force term that is significant on all the internal stations.

Conclusion

A quasi-three-dimensional blade design and analysis system has been developed both mathematically and computationally in Parts I and II of this paper, respectively. The system is arranged on a modular basis, in which the programs are linked via a data base. Possible ways of running the system both in design and analysis modes have been discussed.

The flow through a turbine nozzle guide vane has been computed using the quasi-three-dimensional system and is compared with experimental data. Close agreement was found for surface Mach numbers at hub mean and tip sections, with satisfactory results for vane capacity and exit profiles of Mach number and whirl angle. Results from a fully three-dimensional inviscid time marching method are included, as are those from an unlinked system. The latter shows the effects of approximations inherent in the unlinked approach. It is also shown that with the linked quasi-three-dimensional system it is possible to provide a physical insight into the terms contributing to the mean radial pressure gradient, and it is suggested that this can be controlled by the choice of blade stack adopted.

It is concluded that such a linked system is a valuable extension to conventional two-dimensional compressor and turbine blade design systems, enabling important three-dimensional aspects to be considered early in the design cycle, and providing a valuable link with fully three-dimensional analysis methods.

Acknowledgment

The authors wish to thank Rolls-Royce Limited for permission to publish this paper. Thanks are also due to numerous members of the turbine department who provided valuable assistance on the test case.

Reference

1 Jennions, I. K., and Stow, P., "A Quasi-Three-Dimensional Turbomachinery Blade Design System—Part I: Throughflow Analysis," submitted to the 29th ASME Gas Turbine Conference, Amsterdam, June 1984.

APPENDIX

Equations on Internal Stations

The governing equations on internal computing stations have been derived in [1]. Here they are stated for completeness and in order that the terms in the radial equilibrium equation may be identified.

Radial Equilibrium Equation

$$\underbrace{\frac{1}{\bar{\rho}}\frac{\partial \bar{p}}{\partial R}}_{\text{Radial pressure gradient}} \underbrace{= -\tilde{W}_x^2 \cos^2\lambda \frac{\partial \tan\lambda}{\partial x}\Big|_\psi}_{\text{Streamline curvature in } (R,x)} + \underbrace{\frac{(\tilde{W}_x \tan\beta + \Omega R)^2 \cos^2\lambda}{R}}_{\text{Centrifugal effect}} + \underbrace{\frac{\sin\lambda\cos\lambda}{\bar{\rho}}\frac{\partial \bar{p}}{\partial x}\Big|_\psi}_{\text{Axial pressure gradient}} + \underbrace{F_{B\theta}(\tan\lambda\tan\sigma - \tan\delta)\cos^2\lambda}_{\text{Blade force effect}} \underbrace{+P\cos^2\lambda}_{\text{Perturbation terms}} \quad (1)$$

in which

$$P = -\widetilde{W_x''^2}\frac{\partial \tan\lambda}{\partial x}\Big|_\psi + \frac{\widetilde{W_\theta''^2}}{R}$$

$$+ \frac{(p_s' + p_P')}{2\bar{\rho}B}\left(\sec^2\lambda\frac{\partial B}{\partial R} - \tan\lambda\frac{\partial B}{\partial x}\Big|_\psi\right) \quad (2)$$

θ Momentum equation

$$\underbrace{F_{B\theta}}_{\text{Blade force}} \underbrace{= \frac{\tilde{W}_x}{R}\frac{\partial}{\partial x}[(\tilde{W}_x \tan\beta + \Omega R)R]\Big|_\psi}_{\text{Change in angular momentum}}$$

$$\underbrace{-\tilde{F}_{\tau\theta}}_{\text{Dissipative body force}} \underbrace{+\ P_\theta}_{\text{Perturbation terms}} \quad (3)$$

in which

$$\tilde{F}_{\tau\theta} = -\frac{\tilde{t}\tan\beta}{1+\tan^2\lambda+\tan^2\beta}\frac{\partial \tilde{s}}{\partial x}\Big|_\psi \quad (4)$$

and

$$P_\theta = \frac{1}{BR\bar{\rho}}\frac{\partial}{\partial x}(BR\bar{\rho}\,\overline{W_\theta'' W_x''})\Big|_\psi + \widetilde{W_\theta'' W_x''}\frac{\partial \tan\lambda}{\partial R} + \frac{\widetilde{W_\theta'' W_x''}}{R}\tan\lambda \quad (5)$$

Continuity equation

$$\dot{m} = 2\pi\int_{R_H}^{R_T} BR\bar{\rho}\tilde{W}_x \partial R \quad (6)$$

Energy equation

$$\tilde{I} = C_p\tilde{t} + \frac{1}{2}\tilde{W}_x^2(1+\tan^2\lambda+\tan^2\beta) - \frac{\Omega^2R^2}{2} + \frac{1}{2}\widetilde{W_x''^2}(1+\tan^2\lambda) + \frac{1}{2}\widetilde{W_\theta''^2} \quad (7)$$

Equation of state

$$\bar{\rho} = \bar{p}/R\tilde{t} \quad (8)$$

Acknowledgment

The authors wish to thank Rolls-Royce Limited for permission to publish this paper. Thanks are also due to numerous members of the turbine department who provided valuable assistance on the test case.

Reference

1 Jennions, I. K., and Stow, P., "A Quasi-Three-Dimensional Turbomachinery Blade Design System—Part I: Throughflow Analysis," submitted to the 29th ASME Gas Turbine Conference, Amsterdam, June 1984.

APPENDIX

Equations on Internal Stations

The governing equations on internal computing stations have been derived in [1]. Here they are stated for completeness and in order that the terms in the radial equilibrium equation may be identified.

Radial Equilibrium Equation

$$\underbrace{\frac{1}{\bar{\rho}}\frac{\partial \bar{p}}{\partial R}}_{\text{Radial pressure gradient}} = \underbrace{-\tilde{W}_x^2 \cos^2\lambda \frac{\partial \tan\lambda}{\partial x}\Big|_\psi}_{\text{Streamline curvature in } (R,x)} + \underbrace{\frac{(\tilde{W}_x \tan\beta + \Omega R)^2 \cos^2\lambda}{R}}_{\text{Centrifugal effect}} + \underbrace{\frac{\sin\lambda\cos\lambda}{\bar{\rho}}\frac{\partial \bar{p}}{\partial x}\Big|_\psi}_{\text{Axial pressure gradient}} + \underbrace{F_{B\theta}(\tan\lambda\tan\sigma - \tan\delta)\cos^2\lambda}_{\text{Blade force effect}} + \underbrace{P\cos^2\lambda}_{\text{Perturbation terms}} \quad (1)$$

in which

$$P = -\widetilde{W_x''^2}\frac{\partial \tan\lambda}{\partial x}\Big|_\psi + \frac{\widetilde{W_\theta''^2}}{R} + \frac{(p_s' + p_P')}{2\bar{\rho}B}\left(\sec^2\lambda\frac{\partial B}{\partial R} - \tan\lambda\frac{\partial B}{\partial x}\Big|_\psi\right) \quad (2)$$

θ Momentum equation

$$\underbrace{F_{B\theta}}_{\text{Blade force}} = \underbrace{\frac{\tilde{W}_x}{R}\frac{\partial}{\partial x}[(\tilde{W}_x\tan\beta + \Omega R)R]\Big|_\psi}_{\text{Change in angular momentum}} \underbrace{-\tilde{F}_{\tau\theta}}_{\text{Dissipative body force}} \underbrace{+ P_\theta}_{\text{Perturbation terms}} \quad (3)$$

in which

$$\tilde{F}_{\tau\theta} = -\frac{\tilde{t}\tan\beta}{1+\tan^2\lambda+\tan^2\beta}\frac{\partial \tilde{s}}{\partial x}\Big|_\psi \quad (4)$$

and

$$P_\theta = \frac{1}{BR\bar{\rho}}\frac{\partial}{\partial x}(BR\bar{\rho}\widetilde{W_\theta'' W_x''})\Big|_\psi + \widetilde{W_\theta'' W_x''}\frac{\partial \tan\lambda}{\partial R} + \frac{\widetilde{W_\theta'' W_x''}}{R}\tan\lambda \quad (5)$$

Continuity equation

$$\dot{m} = 2\pi\int_{R_H}^{R_T} BR\bar{\rho}\tilde{W}_x \partial R \quad (6)$$

Energy equation

$$\tilde{I} = C_p\tilde{t} + \frac{1}{2}\tilde{W}_x^2(1+\tan^2\lambda+\tan^2\beta) - \frac{\Omega^2R^2}{2} + \frac{1}{2}\widetilde{W_x''^2}(1+\tan^2\lambda) + \frac{1}{2}\widetilde{W_\theta''^2} \quad (7)$$

Equation of state

$$\bar{\rho} = \bar{p}/R\tilde{t} \quad (8)$$

DISCUSSION

C. Hirsch[1]

The passage-averaged representation of the turbomachinery flow, as developed in [6, 14] of the paper and applied by the authors, is essentially based on the exact form of the averaged continuity and momentum conservation laws. This leads to the introduction of the tangential blockage factor B in the continuity equation and to the "perturbation terms" in the momentum equation. These terms appear as gradients of a stress tensor, the "secondary stress"

$$\bar{\bar{\tau}}^s = \overline{\rho \mathbf{w}'' \times \mathbf{w}''}$$

and originate from the momentum transport due to the non-axisymmetric components of the flowfield $\mathbf{w}''$ in the same way the Reynolds stresses appear in turbulence.

However, in the present paper, as well as in [6, 14], only approximate forms of the energy and entropy equations are used in the through-flow component of the Quasi-3D system. Since the authors do present a most interesting discussion of the order of magnitude of the different contributions to the radial pressure gradient, including the influence of the secondary stresses, it would be of even great interest to collect similar information for the energy and entropy equations. Applying the passage-averaging procedure as described in the Appendix, the averaged energy equation can be written, for a steady relative flow, as follows:

$$\nabla \cdot \overline{\rho \mathbf{w} I B} = 0 \quad (D1)$$

where the gradient operator acts on the two-dimensional space $(r\text{–}z)$, with the metric coefficients of the three-dimensional cylindrical coordinate system.

Explicitly, one has

$$\partial_r \overline{Br\rho w_r I} + \partial_z \overline{Br\rho w_z I} = 0 \quad (D2)$$

Introducing the density weighted, average rothalpy $\tilde{I}$, the

[1] Professor, Dept. of Fluid Mechanics, Vrije Universiteit Brussel.

energy equation becomes, taking into account the continuity equation,

$$\bar{\rho}\tilde{w}_m\partial_m\tilde{I}=-\frac{1}{B}\nabla(\overline{\rho\mathbf{w}''I''B}) \tag{D3}$$

The averaged rothalphy $\tilde{I}$ is defined by

$$\tilde{I}=\tilde{h}+\frac{\tilde{\mathbf{w}}^2}{2}-\frac{\mathbf{u}^2}{2}=\tilde{h}+\frac{\tilde{\mathbf{w}}^2}{2}-\frac{\mathbf{u}^2}{2}+\frac{\overline{\rho\mathbf{w}''\cdot\mathbf{w}''}}{2\bar{\rho}} \tag{D4}$$

The sum of the first three terms of the right-hand side are the total energy of the averaged flow $\hat{I}$, while the last term represents the averaged kinetic energy of the large scale nonaxisymmetric fluctuations $\mathbf{w}''$, $\tilde{k}$

$$\tilde{k}=\frac{\overline{\rho\mathbf{w}''\cdot\mathbf{w}''}}{2\bar{\rho}} \tag{D5}$$

Hence, one can write

$$\tilde{I}=\hat{I}+\tilde{k} \tag{D6}$$

An alternative form of the energy conservation equation for the average flow is obtained by working out the rothalpy fluctuation term I''.

From

$$I=\tilde{I}+I'' \tag{D7}$$

one has

$$I''=h''+\mathbf{w}''\cdot\tilde{\mathbf{w}}+\frac{\mathbf{w}''\cdot\mathbf{w}''}{2}-\tilde{k} \tag{D8}$$

This leads to the following form of the conservation equation for the total energy of the averaged flow, $\hat{I}$

$$B\bar{\rho}\tilde{w}_m\partial_m\hat{I}=-\nabla(\overline{\rho B\mathbf{w}''h''})-\nabla(B\overline{\rho\mathbf{w}k''})+\nabla(B\tilde{\mathbf{w}}\bar{\tilde{\tau}}^s) \tag{D9}$$

The first term on the right-hand side represents the contributions from the transport of fluctuating enthalpy by the nonaxisymmetric flow field. This term contributes to energy mixing together with the second term, which describes the transport of the kinetic energy of the nonaxisymmetric flow components

$$k''=\frac{\mathbf{w}''\cdot\mathbf{w}''}{2}$$

by the total flow field $\mathbf{w}$. The last term represents the work of the secondary stresses against the average velocity field.

In [6, 14] of the paper, the energy equation (D9) is applied with a vanishing right-hand side, assuming conservation of the total energy of the averaged flow $\hat{I}$. The authors, on the other hand, apply equation (D3) with a vanishing right-hand side, implying the conservation of the averaged total energy $\tilde{I}$.

Since these two quantities differ by the kinetic energy term $\tilde{k}$, according to equation (D6), it would be interesting to estimate the magnitude of this term for the examples treated by the authors. In addition, since the equations (D3) and (D9) show that one cannot define an average flow that satisfies all the conservation equations, a discussion of the approximations involved in using an approximate form of the energy equations would be welcome.

Another approximation applied by the authors, and also by Smith and Hirsch in [6, 14], concerns the entropy equation. Assuming, in accordance with the concept of a distributed friction force $\mathbf{F}_\tau$, that the entropy field remains axisymmetric, that is

$$s''=0 \text{ and } s=\tilde{s} \tag{D10}$$

one obtains the following form for the entropy equation

$$\bar{\rho}\tilde{T}\tilde{w}_m\partial_m\tilde{s}=-\bar{\rho}\tilde{\mathbf{w}}\cdot\mathbf{F}_\tau-(\overline{\rho\mathbf{w}''\cdot T''})\nabla\tilde{s} \tag{D11}$$

The last term on the right-hand side contributes to the redistribution of losses by the nonaxisymmetric flow components, and is generally neglected. Although this term is probably small for low-speed flows, this might not be the case anymore at higher speeds and higher blade loadings. Here also, the authors might be able to derive from their calculations some estimations of the approximations involved in neglecting this term.

An interesting aspect of the authors' work concerns the transfer of data from the blade-to-blade surfaces to the meridional surface. Two elements are essential in this transfer and are related to the deviation angles and to the losses. The authors determine the outlet angles in the blade-to-blade calculations by applying a Kutta condition at the trailing edge. This replaces the introduction of correlations. However, it is known that this leads to large uncertainties and variations in the outlet angle, especially for rounded trailing edges, depending on the way this Kutta condition is applied. A discussion of the accuracy of this procedure would be interesting, particularly with regard to the three-dimensional effects on the outlet flow angles arising from the overall three dimensionality of the flow and from secondary flow effects.

The second aspect concerns the compatibility of the axial variation of stagnation pressure inside the blade rows, as applied in the through-flow calculation and as obtained, or imposed, in the blade-to-blade calculations. Since the inviscid blade-to-blade codes assume isentropic flow conditions for continuous flows, the stagnation pressure at any chordwise position is equal to the inlet relative stagnation pressure (in absence of shock waves). This is however not the case in the corresponding position in the meridional plane. A clarification of the method used by the authors for the estimation of losses and of the way the compatibility of the total pressure variations are ensured would be most interesting.

Authors' Closure

For the vane presented in Paper II the maximum value of $\tilde{k}$ was approximately 20 percent of the dynamic energy ($\tilde{\mathbf{w}}^2/2$) of the flow. We have seen values as high as 40 percent on some rotors. The effect of this term on the temperature of the flow is, however, small, the static enthalpy being around 98 percent of the rothalpy for this rig case.

To clarify the position regarding our use of equation (D3) there are two points to be made. The first is that the only physical argument in the literature for neglecting $\tilde{k}$ is given by Sehra and Kerrebrock [R1]. They intuitively postulate that the energy of fluctuations is unavailable to the mean flow, and define their rothalpy ($\hat{I}$) in accordance with equation (D6). This would be true if the analogy between these apparent stresses and the Reynolds stresses of turbulent flow theory could be shown to be valid. We doubt that this is true, especially considering the size of the term involved and the mechanism causing the nonuniformity. Secondly, we construct our energy equation as equation (D3) to be consistent with our blade-to-blade programs. While Sehra and Kerrebrock obtain their blade-to-blade information from experiment, if we were to introduce $\hat{I}$ as constant along a streamline in the through-flow calculation, it would imply loss of energy in the blade-to-blade calculation for which we do not have a physical mechanism.

In order to examine the contribution made to the solution from the nonaxisymmetric entropy and enthalpy distributions with the required accuracy it would be necessary to run the system with a viscous blade-to-blade program. While we could do this, the computational time required to run one blade-to-blade calculation would be greater than that required to produce the example given in the paper. We have directed our efforts at producing a fast design system capable of operating in an industrial environment, these considerations dictating the use of an inviscid mainstream and coupled

boundary layer approach for the blade-to-blade analysis. While it may be possible to construct examples where s'' or h'' have some importance, it is difficult to imagine that these terms could be more important than the already ignored effects of streamsurface distortion and radial mixing. These latter effects dictate the caution needed in using the system. Components such as fans and high-pressure turbine vanes are amenable to the present approach, while multistage compressors would be viewed with much more caution.

Professor Hirsch is correct when he comments about the Kutta condition. Strictly this condition can only be applied at a sharp trailing edge but we apply the condition to blunt trailing edges in the knowledge that the answers we obtain agree with our experimental data. The condition itself, equalization of pressure or velocity, is applied in each blade-to-blade program depending on the numerical scheme employed. As we are not attempting to include secondary flow or three-dimensional wake effects into the scheme at present this treatment is adequate. If the flow being examined was felt to have these effects then a three-dimensional code would be used to examine them.

The whole subject of loss in a Quasi-3D system is deserving of far greater discussion than we have room for here. Inside Rolls-Royce we have numerous ways of including loss in our calculations. The ways depend on the physical processes to be modeled and the accuracy of our calculation/correlation procedures. However most of these ways can be put into one of two categories:

(*i*) Use the blade-to-blade program to predict the loss from boundary layers, shock waves, wakes, etc., and impose this loss on the through-flow calculation.

(*ii*) Prescribe the loss by using an outside correlation or test data. This is the procedure adopted by Wang et al. [R2].

In the latter case the blade-to-blade program accepts the prescribed loss from the through-flow by an adjustment of the streamtube contraction through the row. In this way we effectively interchange blockage and loss in the calculations.

References

R1 Sehra, A. K., and Kerrebrock, J. L., "The Effect of Blade-to-Blade Flow Variations on the Mean Flow-Field of a Transonic Compressor," AIAA Paper No. 79-1515, July 1979.

R2 Wang, Q., Zhu, G., and Wu, C. H., "Quasi-Three-Dimensional and Full Three-Dimensional Rotational Flow Calculations in Turbomachines," ASME JOURNAL OF ENGINEERING FOR GAS TURBINES AND POWER, Vol. 107, No. 2, Apr. 1985, pp. 277–285.

J. W. Railly

It would be most valuable to know the extent to which the perturbation terms in the through-flow problem solution influence the distribution of pitch-wise-averaged whirl and meridional velocities. To this end, would it be possible to make available a comparison between solutions to the (direct) through-flow problem as given in the paper and the same problem in which the perturbation terms are left out? Such a comparison should permit, in the latter case, the choice of a suitable (single) S_2 surface such as the surface (as quoted by the authors) which divides the mass flow (from the S_1 solution) into two equal parts. Alternatively, the choice of a surface which, at the trailing edge, blends into the average outlet angle of the S_1 solutions would be suitable. Blade thickness effects would be included in the usual way.

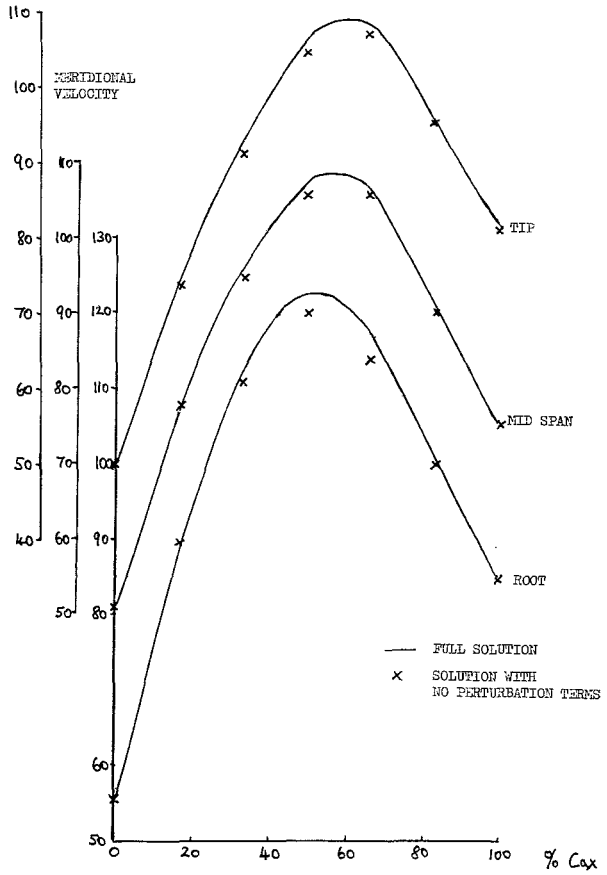

Fig. 1 Comparison of through-flow solutions with and without perturbation terms

Authors' Closure

Professor Railly has asked an interesting question to which we can only supply part of the answer here. If we were to set all the perturbation terms to zero and converge the quasi-3D system then the resulting aerodynamic variables from the BBP and TFP would not agree. This is because the blade-to-blade solution would inherently contain the perturbation terms due to its nonuniform circumferential flow, while the through-flow solution would not. We could alternatively set the perturbation terms to zero for the fully converged solution and rerun just the TFP. This would give an indication as to the value of the perturbation terms for this one step in the solution scheme. The results of doing this are shown in terms of the meridional velocity in Fig. 1, the whirl velocity showing similar trends as the whirl angle is fixed. The maximum difference between the two solutions is about 3 percent, which is considerably more than our convergence criterion. A paper the authors are at present writing should help answer Professor Railly's question, as it itemizes each perturbation term with respect to its fellows and indicates their relative importance for a vane and a rotor.

We agree that, in principle, a passage-averaged approach could well be used to test the various S_2 surfaces chosen by other authors.

Solution of Transonic S_1 Surface Flow by Successively Reversing the Direction of Integration of the Stream Function Equation

Wang Zhengming
Institute of Engineering Thermophysics,
Chinese Academy of Sciences,
Beijing, China

In the solution of the stream function equation on an S_1 relative stream surface with transonic velocities, the occurrence of two values of the density is avoided by using a method of combining simple iteration with an integration method. In this method, the direction of integration is successively reversed, i.e., the starting line for the integration is varied from iteration to iteration. The governing equations are therefore satisfied as fully as possible during each iteration, and the procedure leads to rapid convergence. The method uses nonorthogonal curvilinear coordinates and artificial compressibility. The technique can be used to calculate transonic S_1 surface flows, with either subsonic or supersonic inlet velocities. Example calculations indicate that the method is very effective.

Introduction

Because convenient iterative methods were available, solution of the transonic flow problem was first obtained by solving the potential equation. In 1971, Murman and Cole introduced type-dependent, finite difference relaxation method for the solution of the transonic small disturbance equation [1]. Afterwards, Jameson developed numerical methods to solve the full-potential equation in the transonic range, e.g., rotated difference schemes [2], fully conservative schemes [3], finite volume method [4], etc. Especially with the introduction of artificial compressibility technique [5], the calculation of the transonic potential equation was successfully simplified.

In the case of rotational flow the stream function equation is employed instead of the potential function equation, and its solution has been tried by several investigators. Hafez's scheme [6] was applied to calculate the transonic flow past an isolated airfoil. For flow past a cascade of blades, there exist some new problems. It is well known, that in the solution of the stream function equation on an S_1 surface with transonic velocities, the existence of two values of the density ρ is difficult to handle. It is also known from the calculations of some cascades that the iteration procedures often do not converge for the simple iteration method and that initial flow parameters may not be available for the integral method.

In order to overcome these difficulties, a method of successively reversing the direction of integration is suggested herein. The contradiction of two values of the density is avoided by the method of combining simple iteration with an integral method, and the initial value problem with the integral method is resolved by varying the starting line of the integration. Therefore, the governing equations are satisfied as fully as possible in the process of the iteration, and the procedure leads to rapid convergence. The method can be used in the case of transonic S_1 stream surface flow problems where the inlet velocity is either subsonic or supersonic. Example calculations indicate that the iteration converges, and the method is very efficient when proper relaxation factors and artificial density coefficients are used. In order to simplify this problem, irrotational flow is considered in this paper. If higher calculation accuracy is needed, the nonuniform entropy increase across the shock and the influence of the rotation can be considered.

Basic Equations

In [7], the basic equations governing internal flow in a turbomachine are expressed with respect to general nonorthogonal coordinates and corresponding nonorthogonal velocity components. This coordinate system has the advantage that it is body-fitted without the use of conformal mapping and that the boundary conditions can be satisfied conveniently and accurately. It has been extensively used in China for the solution of S_1 and S_2 stream surface flow (for example, see [8–12]) and is also used in the present calculation.

From [7], the momentum equation on an S_1 surface of revolution (i.e., the partial differential equation along the e^2-direction) is

Contributed by the Gas Turbine Division of THE AMERICAN SOCIETY OF MECHANICAL ENGINEERS and presented at the 29th International Gas Turbine Conference and Exhibit, Amsterdam, The Netherlands, June 4–7, 1984. Manuscript received at ASME Headquarters December 19, 1983. Paper No. 84-GT-23.

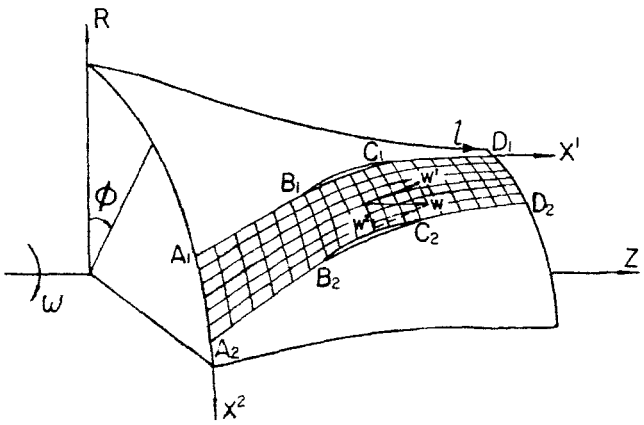

Fig. 1 S_1 surface of revolution

$$\frac{\partial}{\partial x^2}[(W^1 + W^2\cos\theta_{12})\sqrt{a_{11}}] - \frac{\partial}{\partial x^1}[(W^2 + W^1\cos\theta_{12})\sqrt{a_{22}}]$$

$$= 2\sqrt{a_{11}}\sqrt{a_{22}}\ \omega^3\ \mathrm{Sin}\ \theta_{12} + \frac{\sqrt{a_{11}}}{W^1}\left(\frac{\partial I}{\partial x^2} - T\frac{\partial s}{\partial x^2}\right) \tag{1}$$

Because the nonorthogonal curvilinear coordinates (x^1, x^2) are placed on the S_1 surface, (see Fig. 1), the basic metric tensor a_{11}, a_{22}, a_{12}, and the angle θ_{12} included by the coordinate lines may be calculated with the following basic relations

$$a_{11} = \frac{\partial 1}{\partial x^1}\frac{\partial 1}{\partial x^1} + \frac{\partial (r\varphi)}{\partial x^1}\frac{\partial (r\varphi)}{\partial x^1}$$

$$a_{22} = \frac{\partial 1}{\partial x^2}\frac{\partial 1}{\partial x^2} + \frac{\partial (r\varphi)}{\partial x^2}\frac{\partial (r\varphi)}{\partial x^2}$$

$$a_{12} = \frac{\partial 1}{\partial x^1}\frac{\partial 1}{\partial x^2} + \frac{\partial (r\varphi)}{\partial x^1}\frac{\partial (r\varphi)}{\partial x^2}$$

$$\cos\theta_{12} = \frac{a_{12}}{\sqrt{a_{11}}\sqrt{a_{22}}}$$

Where 1 is the generating line of the S_1 surface of revolution.

The definition of the stream function based on the continuity equation is

$$W^1 = \frac{\dfrac{\partial \psi}{\partial x^2}}{\rho\tau\sqrt{a_{22}}\ \mathrm{Sin}\ \theta_{12}} \tag{2}$$

$$W^2 = \frac{-\dfrac{\partial \psi}{\partial x^1}}{\rho\tau\sqrt{a_{11}}\ \mathrm{Sin}\ \theta_{12}} \tag{3}$$

Combining equation (1) with (2) and (3) gives the stream function equation in the following weak conservation form

$$\frac{\partial}{\partial x^1}\left[\frac{\sqrt{a_{22}}}{\tau\rho\mathrm{Sin}\theta_{12}}\left(\frac{1}{\sqrt{a_{11}}}\frac{\partial \psi}{\partial x^1} - \frac{\mathrm{Cos}\theta_{12}}{\sqrt{a_{22}}}\frac{\partial \psi}{\partial x^2}\right)\right]$$

$$+ \frac{\partial}{\partial x^2}\left[\frac{\sqrt{a_{11}}}{\tau\rho\mathrm{Sin}\theta_{12}}\left(\frac{1}{\sqrt{a_{22}}}\frac{\partial \psi}{\partial x^2} - \frac{\mathrm{Cos}\theta_{12}}{\sqrt{a_{11}}}\frac{\partial \psi}{\partial x^1}\right)\right]$$

$$= 2\sqrt{a_{11}}\sqrt{a_{22}}\omega\ \mathrm{Sin}\ \sigma\ \mathrm{Sin}\ \theta_{12}$$

$$+ \frac{\rho\tau\sqrt{a_{11}}\sqrt{a_{22}}\mathrm{Sin}\ \theta_{12}}{\dfrac{\partial \psi}{\partial x^2}}\left(\frac{\partial I}{\partial x^2} - T\frac{\partial s}{\partial x^2}\right) \tag{4}$$

When I and s at the inlet are uniform and the nonuniformity of the entropy increase across the shock can be neglected, equation (4) reduces to

$$\frac{\partial}{\partial x^1}\left[\frac{\sqrt{a_{22}}}{\tau\rho\mathrm{Sin}\theta_{12}}\left(\frac{1}{\sqrt{a_{11}}}\frac{\partial \psi}{\partial x^1} - \frac{\mathrm{Cos}\ \theta_{12}}{\sqrt{a_{22}}}\frac{\partial \psi}{\partial x^2}\right)\right]$$

$$+ \frac{\partial}{\partial x^2}\left[\frac{\sqrt{a_{11}}}{\tau\rho\mathrm{Sin}\theta_{12}}\left(\frac{1}{\sqrt{a_{22}}}\frac{\partial \psi}{\partial x^2} - \frac{\mathrm{Cos}\theta_{12}}{\sqrt{a_{11}}}\frac{\partial \psi}{\partial x^1}\right)\right]$$

$$= 2\sqrt{a_{11}}\sqrt{a_{22}}\omega\ \mathrm{Sin}\ \sigma\ \mathrm{Sin}\ \theta_{12} \tag{5}$$

Other flow relations needed are

$$(W)^2 = (W^1)^2 + (W^2)^2 + 2W^1W^2\mathrm{Cos}\theta_{12} \tag{6}$$

$$\frac{\rho}{\rho_i} = \left(\frac{\mathrm{I} + \frac{1}{2}\omega^2 r^2 - \frac{1}{2}W^2}{h_i}\right)^{\frac{1}{\gamma - 1}} \tag{7}$$

Nomenclature

a_{11}, a_{22} = basic metric tensor
c = artificial density coefficient
e^1, e^2 = contravariant coordinate base
h = enthalpy of gas per unit mass
I = relative stagnation rothalpy
$J,K(j,k)$ = ordinal number of calculation stations along direction x^1 and x^2
l,ϕ = orthogonal curvilinear coordinates on S_1 surface of revolution
M = Mach number
p = pressure of gas
r,ϕ,z = cylindrical coordinates
s = entropy of gas per unit mass
T = absolute temperature of gas
W = relative velocity of gas
W^1, W^2 = contravariant physical component of W
x^1, x^2 = nonorthogonal curvilinear coordinates on S_1 surface
γ = ratio of specific heat
$\epsilon_{L\psi}$ = accuracy of residual convergence
θ_{12} = angle included by the coordinate lines
λ = Laval number, $\lambda = W/a^*$, where a^* is the critical sonic velocity
ρ = density of gas
$\tilde{\rho}$ = artificial density of gas
σ = $\tan^{-1}(dr/dz)$
τ = normal thickness of stream filament
ψ = stream function
ω = angular velocity of rotor
ω_ψ, ω_ρ = relaxation factors of ψ and ρ

Superscript

(n) = nth iteration
(0) = initial value
0 = stagnation state

Subscript

i = at inlet
p = pressure surface
s = suction surface

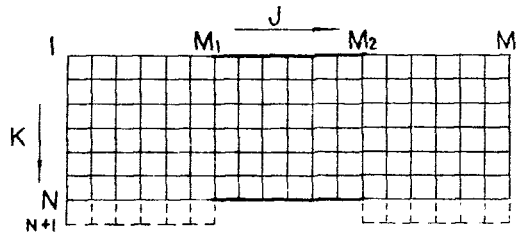

Fig. 2 Schematic calculation plane

The five equations, (2), (3), (5), (6), and (7), contain five unknown scalar quantities, ρ, ψ, W^1, W^2, W, and may be solved.

Difference Form

The corresponding difference operator of equation (5) in conservative form may be expressed by

$$L_\psi = \left[\left(\delta_{x_1}\frac{1}{\rho}\frac{\sqrt{a_{22}}}{\sqrt{a_{11}}}\frac{1}{\tau \mathrm{Sin}\theta_{12}}\delta_{x^1} - \delta_{x^1}\frac{1}{\rho}\frac{\mathrm{Cos}\theta_{12}}{\tau \mathrm{Sin}\theta_{12}}\delta_{x_2}\right)\right.$$

$$\left. + \left(\delta_{x^2}\frac{1}{\rho}\frac{\sqrt{a_{11}}}{\sqrt{a_{22}}}\frac{1}{\tau \mathrm{Sin}\theta_{12}}\delta_{x^2} - \delta_{x^2}\frac{1}{\rho}\frac{\mathrm{Cos}\theta_{12}}{\tau \mathrm{Sin}\theta_{12}}\delta_{x_1}\right)\right]\psi$$

$$- 2\sqrt{a_{11}}\sqrt{a_{22}}\omega \mathrm{Sin}\sigma \mathrm{Sin}\theta_{12} \tag{8}$$

and the difference form of the stream function equation is written simply as

$$L\psi = 0 \tag{9}$$

Figure 2 shows the corresponding schematic calculation plane. It must be indicated, that the intervals of the mesh in Fig. 1 show the increments ΔS_1, ΔS_2 of line length of the coordinates and the intervals of the mesh in Fig. 2 straight show the increments Δx^1, Δx^2 of the coordinates. They satisfy the following differential relations

$$ds_1 = \sqrt{a_{11}}dx^1, \quad ds_2 = \sqrt{a_{22}}dx^2$$

The difference expressions of all terms in expression (8) are

$$\left[\delta_{x_1}\left(\frac{1}{\rho}\frac{\sqrt{a_{22}}}{\sqrt{a_{11}}}\frac{1}{\tau \mathrm{Sin}\theta_{12}}\right)\delta_{x_1}\psi\right]_{j,k} = \frac{1}{(\Delta x^1)^2}$$

$$\cdot\left[\left(\frac{1}{\rho}\frac{\sqrt{a_{22}}}{\sqrt{a_{11}}}\frac{1}{\tau \mathrm{Sin}\theta_{12}}\right)_{j+1/2,k}(\psi_{j+1,k} - \psi_{j,k})\right.$$

$$\left. - \left(\frac{1}{\rho}\frac{\sqrt{a_{22}}}{\sqrt{a_{11}}}\frac{1}{\tau \mathrm{Sin}\theta_{12}}\right)_{j-1/2,k}(\psi_{j,k} - \psi_{j-1,k})\right]$$

$$\left[\delta_{x_2}\left(\frac{1}{\rho}\frac{\sqrt{a_{11}}}{\sqrt{a_{22}}}\frac{1}{\tau \mathrm{Sin}\theta_{12}}\right)\delta_{x_2}\psi\right]_{j,k} = \frac{1}{(\Delta x^2)^2}$$

$$\cdot\left[\left(\frac{1}{\rho}\frac{\sqrt{a_{11}}}{\sqrt{a_{22}}}\frac{1}{\tau \mathrm{Sin}\theta_{12}}\right)_{j,k+1/2}(\psi_{j,k+1} - \psi_{j,k})\right.$$

$$\left. - \left(\frac{1}{\rho}\frac{\sqrt{a_{11}}}{\sqrt{a_{22}}}\frac{1}{\tau \mathrm{sin}\theta_{12}}\right)_{j,k-1/2}(\psi_{j,k} - \psi_{j,k-1})\right]$$

$$\left[\delta_{x_1}\left(\frac{1}{\rho}\frac{\mathrm{Cos}\theta_{12}}{\tau \mathrm{Sin}\theta_{12}}\right)\delta_{x_2}\psi\right]_{j,k} = \frac{1}{\Delta x^1 \Delta x^2}$$

$$\left[\left(\frac{1}{\rho}\frac{\mathrm{Cos}\theta_{12}}{\tau \mathrm{Sin}\theta_{12}}\right)_{j+1/2,k}(\psi_{j+1/2,k+1/2} - \psi_{j+1/2,K-1/2})\right.$$

$$\left. - \left(\frac{1}{\rho}\frac{\mathrm{Cos}\theta_{12}}{\tau \mathrm{Sin}\theta_{12}}\right)_{j-1/2,k}(\psi_{j-1/2,k+1/2} - \psi_{j-1/2,k-1/2})\right]$$

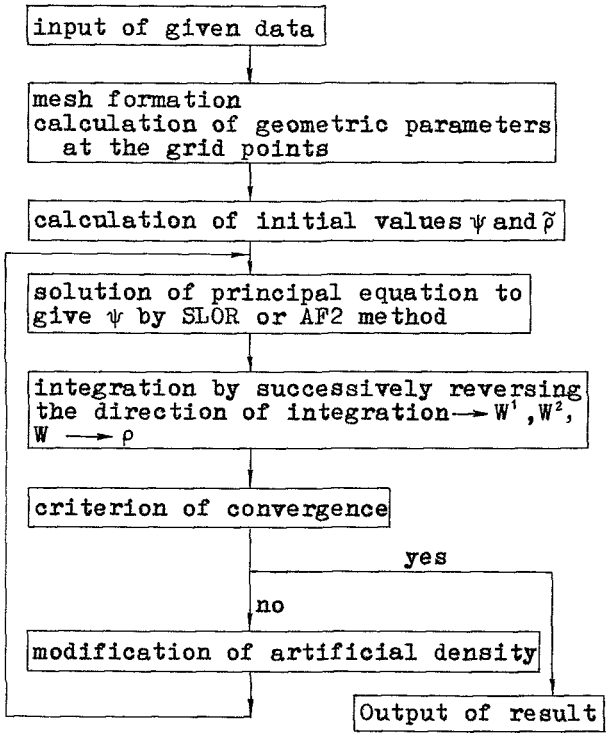

Fig. 3 Flow diagram of present method

$$\left[\delta x^2\left(\frac{1}{\rho}\frac{\mathrm{Cos}\theta_{12}}{\tau \mathrm{Sin}\theta_{12}}\right)\delta x^1\psi\right]_{j,k} = \frac{1}{\Delta x^1 \Delta x^2}$$

$$\left[\left(\frac{1}{\rho}\frac{\mathrm{Cos}\theta_{12}}{\tau \mathrm{Sin}\theta_{12}}\right)_{j,k+1/2}(\psi_{j+1/2,k+1/2} - \psi_{j-1/2,k+1/2})\right.$$

$$\left. - \left(\frac{1}{\rho}\frac{\mathrm{Cos}\theta_{12}}{\tau \mathrm{Sin}\theta_{12}}\right)_{j,k-1/2}(\psi_{j+1/2,k-1/2} - \psi_{j-1/2,k\ 1/2})\right]$$

Calculation Procedure

In order to express it clearly, the flow diagram of the iterative algorithm is shown in Fig. 3.

The process is explained in detail as follows:

***(i)* Given Data.** In order to solve the flow problem on an S_1 surface of revolution, the data which must be given are: shape of the generating line of S_1 surface of revolution, $r(Z)$; angular coordinates of the blade profile, $\phi_s(Z)$ and $\phi_p(Z)$; normal thickness of steam filament, $\tau(Z)$; uniform flow condition at the inlet, P^0, T^0, Mi, βi; flow condition at exit, p_2 or β_2; specific heat ratio, γ; and angular velocity of rotor, ω.

***(ii)* Process of Solving the Principal Equation (i.e., Process of $\tilde{\rho} \rightarrow \psi$).** With the application of the artificial compressibility technique, ρ should be replaced by $\tilde{\rho}$ in the difference form $L\psi = 0$ of the principal equation. There are a number of ways to solve this difference equation, e.g., method of decomposition of matrix into (L) and (U), line relaxation method, approximate factorization schemes AF1 or AF2 [13, 14], etc. In this paper, the line relaxation method is used. The use of AF2 method will be discussed in another paper.

When the stream function equation on an S_1 surface is solved by SLOR method, there are two possible selections: the first is line relaxation along the x^1-direction and the second is line relaxation along the x^2-direction. It is obvious that the first one is more convenient than the second. Because the coefficient matrix of the algebraic equations solved on every line is tridiagonal, it may be solved easily by Thomas's

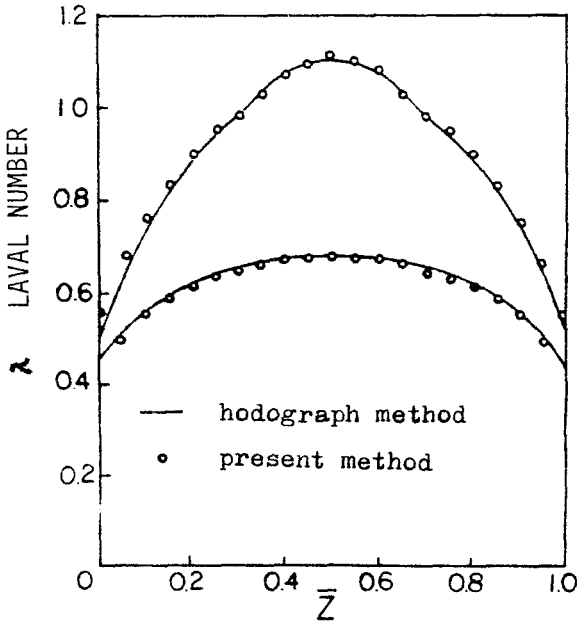

Fig. 4 Velocity distribution along blade surface

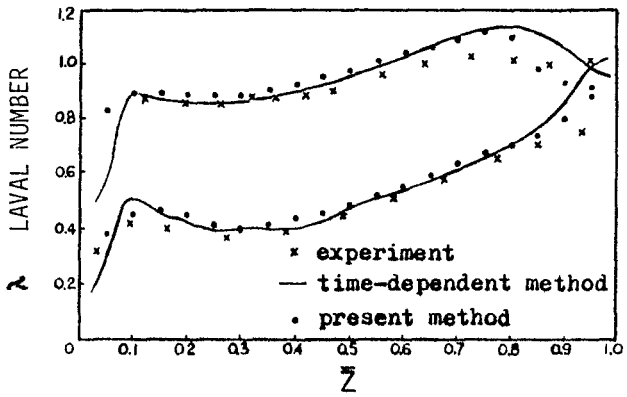

Fig. 5 Velocity distribution along blade surface

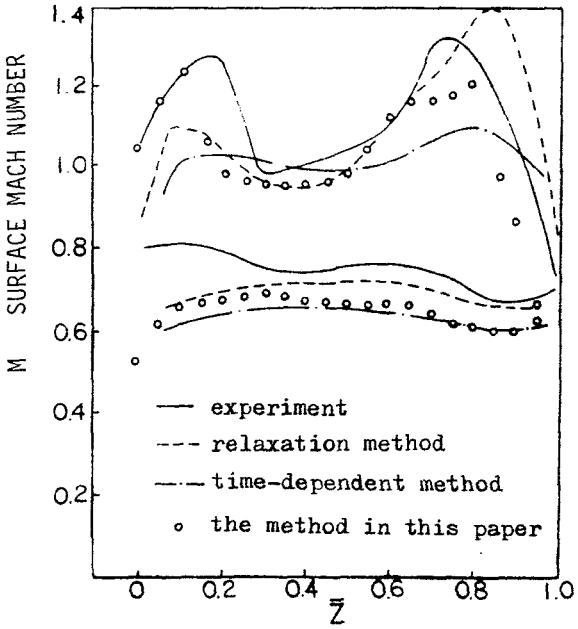

Fig. 6 Velocity distribution along blade surface

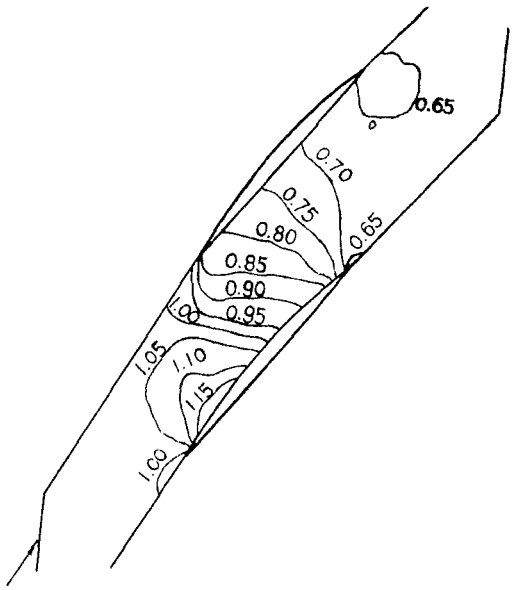

Fig. 7 Mach number contours ($M_l = 1.03$)

method. However, in the line relaxation along x^2-direction, the forms of the coefficient matrix are not the same in different regions. Although, in the internal flow area of the cascade, the matrix is tridiagonal, in the external flow area of the cascade, however, it is only approximately tridiagonal having two nonzero elements quantities in the corner region. In the solution of the equations, there is no method better than Gauss's elimination method. Therefore, in the solution of the principal equation, the line relaxation method along X^1-direction is employed in this paper.

***(iii)* Process of Calculating W^1, W^2, W and ρ.** In order to avoid the occurrence of two values of the density, it is clear that determining ρ directly from ψ is not feasible. In the present paper, the scheme of calculating W first, and ρ second, from ψ is applied. Of course, there are many variations in carrying out this process. The following discussion describes some of these methods:

1 Simple Iteration Method:

W^1 and W^2 are first calculated with the following relations obtained from the continuity equation:

$$W^1 = \frac{\dfrac{\partial \psi}{\partial x^2}}{\tau \tilde{\rho} \sqrt{a_{22}} \operatorname{Sin}\theta_{12}} \tag{10}$$

$$W^2 = \frac{-\dfrac{\partial \psi}{\partial x^1}}{\tau \tilde{\rho} \sqrt{a_{11}} \operatorname{Sin}\theta_{12}} \tag{11}$$

where, ψ is the new value and $\tilde{\rho}$ is the old value. Then, density ρ is calculated with the relation obtained from the energy equation.

In the process of solving the principal equation by simple iteration, the relation between every physical quantity in the momentum equation is not satisfied. When W^1, W^2, and ρ are calculated from new ψ, only the relations of continuity and energy equation are used. The key to convergence in the transonic stream function problem is as fully as possible, using the momentum equation in the calculation.

2 General Integration Method:

Velocity is calculated by integrating the momentum equation. But in our problem the determination of the integration constant is difficult, i.e., it is difficult to determine

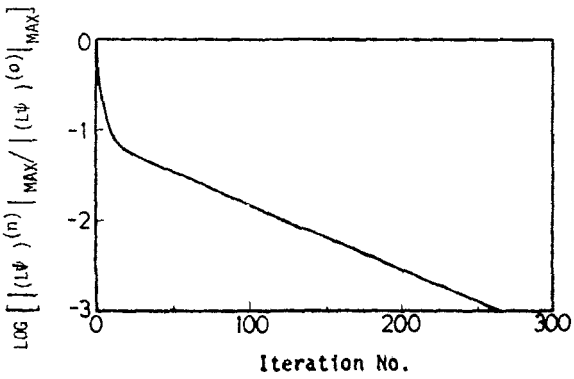

Fig. 8 Conference history of residual

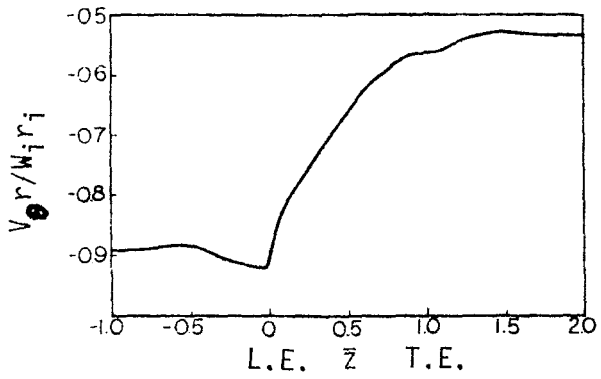

Fig. 9 $V_\theta r$ distribution along mean streamline

the flow parameters on the selected initial line. In the calculation of isolated airfoils the initial line may be selected on a boundary of uniform flow in the far field. Because the boundary conditions for cascades are different from that of isolated airfoils, another method must be found.

3 Method of Successively Reversing the Direction of Integration:

In order to overcome the difficulty that simple iteration is not convergent and to solve the difficulty that the flow parameters on the initial integral line cannot be determined by a general integration method, the calculation is made in the following manner: W^1 and W^2 on an initial integral line selected in the x^1-direction are first calculated using the expressions (10) and (11) based on the continuity equation. Then W^1 values on the other mesh lines along x^1 direction are calculated by integrating the momentum equation. Thus W^2 and W over the whole computing region may be obtained easily.

Equation (5) is changed into the following form:

$$\frac{\partial}{\partial x^2}(\sqrt{\bar{a}_{11}}W^1) = -\frac{\partial}{\partial x^1}\left[\frac{\sqrt{\bar{a}_{22}}}{\tau\bar{\rho}\mathrm{Sin}\theta_{12}}\left(\frac{1}{\sqrt{\bar{a}_{11}}}\frac{\partial\psi}{\partial x^1}-\frac{\mathrm{Cos}\theta_{12}}{\sqrt{\bar{a}_{22}}}\frac{\partial\psi}{\partial x^2}\right)\right] + \frac{\partial}{\partial x^2}\frac{\mathrm{Cos}\theta_{12}}{\tau\bar{\rho}\mathrm{Sin}\theta_{12}}\frac{\partial\psi}{\partial x^1} - 2\sqrt{\bar{a}_{11}}\sqrt{\bar{a}_{22}}\omega\,\mathrm{Sin}\sigma\,\mathrm{Sin}\theta_{12} \tag{12}$$

Then W^1 value at grid point $(j,k+1)$ is

$$(W^1)_{j,k+1} = \frac{1}{(\sqrt{\bar{a}_{11}})_{j,k+1}}\int_{(x^2)_{j,k}}^{(x^2)_{j,k+1}}\left\{-\frac{\partial}{\partial x^1}\left[\frac{\sqrt{\bar{a}_{22}}}{\tau\bar{\rho}\mathrm{Sin}\theta_{12}}\left(\frac{1}{\sqrt{\bar{a}_{11}}}\frac{\partial\psi}{\partial x^1}-\frac{\mathrm{Cos}\theta_{12}}{\sqrt{\bar{a}_{22}}}\frac{\partial\psi}{\partial x^2}\right)\right] + \frac{\partial}{\partial x^2}\frac{\mathrm{Cos}\theta_{12}}{\tau\bar{\rho}\mathrm{Sin}\theta_{12}}\frac{\partial\psi}{\partial x^1} + 2\sqrt{\bar{a}_{11}}\sqrt{\bar{a}_{22}}\omega\mathrm{Sin}\sigma\mathrm{Sin}\theta_{12}\right\}dx^2 + \frac{(\sqrt{\bar{a}_{11}})_{j,k}}{(\sqrt{\bar{a}_{11}})_{j,k+1}}(W^1)_{j,k} \tag{13}$$

After W^1 is thus calculated, W^2, W, and ρ are obtained by the following expressions

$$W^2 = -\frac{\sqrt{\bar{a}_{22}}}{\sqrt{\bar{a}_{11}}}\frac{\dfrac{\partial\psi}{\partial x^1}}{\dfrac{\partial\psi}{\partial x^2}}W^1$$

$$W=\sqrt{(W^1)^2+(W^2)^2+2W^1W^2\mathrm{Cos}\theta_{12}}$$

$$\rho=\rho_i\left(\frac{I+\frac{1}{2}\omega^2r^2-\frac{1}{2}W^2}{h_i}\right)^{\frac{1}{\gamma-1}}$$

It may be emphasized that in the process of iteration different initial integral lines must be successively selected, i.e., the direction of integration must be successively reversed. This was accomplished in this paper in the following manner: at the nth iteration the grid line $k=1$ or $k=2$ is selected as the initial integral line and integration is carried out along $+x^2$-direction, but at the $(n+1)$th iteration, the grid line $k=N$ or $k=N-1$ is taken as the initial line and integration is carried out along $-x^2$-direction. Because the direction of integration is successively reversed, the relations of the basic equations are balanced and tend to satisfy as fully as possible in the whole computed range.

***(iv)* Treatment of Artificial Density and Convergence Criteria.** The density is treated by the artificial compressibility method. The formula of calculating artificial density is

$$\tilde{\rho}_{j,k} = \rho_{j,k} - V_{j,k}\left[\frac{W^1}{W}(\rho_{j,k}-\rho_{j-1,k}) + \frac{W^2}{W}(\rho_{j,k}-\rho_{j,k-1})\right] \tag{14}$$

where

$$V_{j,k} = C\,\mathrm{Max}\left[0,\ 1-\frac{1}{M^2_{j,k}}\right]$$

*The convergence of iteration is judged by the reduction in the magnitude of the residual. It is required that the ratio between the maximum of the residual at the n*th iteration and the maximum of the initial residual is smaller than the $\epsilon_{L\psi}$ specified, i.e., the following expression must be satisfied

$$\frac{\mathrm{Max}\left|(L\psi)^{(n)}_{j,k}\right|}{\mathrm{Max}\left|(L\psi)^{(0)}_{j,k}\right|} < \epsilon_{L\psi}$$

Computed Results

Some typical cascade flows are calculated by the method presented in this paper and quite satisfactory results are obtained. The computing mesh used is slightly different in different examples. In general, there are 50 stations along the x^1-direction and 15 stations along the x^2-direction. After 200–300 iterations the accuracy of convergence $\epsilon_{L\psi}$ is about 10^{-3}. In the process of calculation it is found that the choices of the relaxation factors ω_ψ and ω_ρ and the artificial density

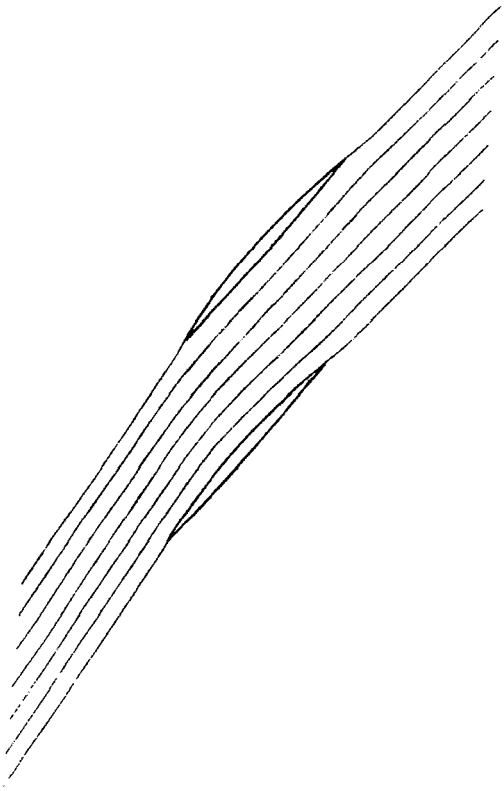

Fig. 10 Stream line distribution

coefficient C are very important for iterative convergence. Obviously, if C is chosen to be too large, the accuracy of calculation would be reduced. On the other hand, if C is chosen to be too small, the iterations would not converge. In the computer program, the artificial density coefficient automatically decreases. Calculations indicate, however, that this decrease is not limitless.

The hodograph solution of the example shown in Fig. 4 is taken from [15]. The experimental data of Fig. 5 are taken from Fig. 42(*b*) of [16], and the time-dependent method solution is taken from [17]. The experimental data of Fig. 6 are taken from [18]. The result of this paper is compared with the relaxation solution of [19].

The cascade geometry of Fig. 7 is taken from [20]. This is an example where the inlet velocity is supersonic, $M_i = 1.03$ and $p_2/p_i = 1.465$. In Fig. 7, the Mach number contours obtained by the present method are shown. The convergence history of the residual of calculating the cascade is shown in Fig. 8. Figure 9 is $V_\theta r$ distribution along the mean stream line of this cascade. Figure 10 shows streamline distributions obtained in the calculation. It may be seen from Fig. 9, that at the place where the mean stream line passes through the passage shock, the change of $V_\theta r$ is greater than other places. However, because in this example the passage shock is weak, the shock captured in the calculation is smeared over several grid lines. Therefore, the change of $V_\theta r$ at the shock is not as obvious as that obtained by a shock-fitting algorithm.

It is seen from these figures that in general, the computed results follow the experimental data better than other calculated results, although the difference with experimental data is still significant.

The difference may be attributed to (*i*) the approximation in the physical model and (*ii*) the influence of introducing the artificial density and rather coarse mesh used in the calculation.

Concluding Remarks

In this paper the transonic stream function problem is solved by the method of successively reversing the direction of integration, and improved results are obtained. The calculations indicate that problems with mulitple values of the density and iteration convergence are resolved.

In order to increase the speed and the accuracy of the convergence, the same problem is now being tried with AF2. Also in the future, the problems of entropy increase across the shock, rotational effects, and viscosity will be considered.

Acknowledgment

The author acknowledges the encouragement and guidance of Prof. C. H. Wu in carrying out this research work.

References

1 Murman, E. M., and Cole, J. D., "Calculation of Plane Steady Transonic Flow," *AIAA Journal*, Vol. 9, No. 1, 1971.

2 Jameson, A., "Iterative Solution of Transonic Flow over Airfoils and Wings," *Comm. Pure Appl. Math.*, Vol. 2, 1974.

3 Jameson, A., "Transonic Potential Flow Calculation Using Conservation Form," *Proceedings of the AIAA Second Computational Fluid Dynamics Conference*, Hartford, Conn., 1975.

4 Jameson, A., and Caughey, D. A., "Finite Volume Method for Transonic Potential Flow Calculations," *Proceedings of the AIAA Third Computational Fluid Dynamics Conference*, New Mexico, 1977.

5 Hafez, M. M., South, J. C., and Murman, E. M., "Artificial Compressibility Methods for Numerical Solution of Transonic Full Potential Equation," AIAA 11th Fluid and Pleasma Dynamics Conference, 1978.

6 Hafez, M., and Levell, D., "Numerical Solution of Transonic Stream Function Equation," AIAA 1981.

7 Wu Chung-Hua, "Three-Dimensional Turbomachine Flow Equations Expressed with Respect to Non-orthogonal Curvilinear Coordinates and Methods of Solution," Lecture notes, China University of Science and Technology, 1975; also *Proceedings of 3rd ISABE*, Munich, Germany, 1976.

8 Wu Wenquan, and Liu Cuie, "Flow-Field Matrix Solution for Direct Problem of Flow along S_1 Relative Stream Surface Employing Nonorthogonal Curvilinear Coordinates and Corresponding Nonorthogonal Velocity Components," *Journal of Engineering Thermophysics* (in Chinese), Vol. 1, No. 1, 1980.

9 Zhu Rongguo, "Flow-Field Line-Relation Solution for Inverse Problem of Flow along S_2 Relative Stream Surface Employing Nonorthogonal Curvilinear Coordinates and Corresponding Non-orthogonal Velocity Components," *Journal of Engineering Thermophysics* (in Chinese), Vol. 1, No. 1, 1980.

10 Wu Wenquan, Zhu Rongguo, and Liu Cuie, "Computational Design of Turbomachine Blades," *Journal of Aircraft*, Vol. 17, No. 5, 1980.

11 Wu Chung-Hua, and Wang Baoguo, "Matrix Solution of Compressible Flow on S_1 Surface Through a Turbomachine Blade Row with Splitter Vanes or Tandem Blades," ASME Paper 83-GT-10, to appear in ASME *Journal of Engineering for Power*.

12 Wang Qinghuan, Wu Wenquan, Zhu Genxing, Li Weihong, and Wu Chung-Hua, "Solution of Three-Dimensional Compressible Flow in an Axial-Flow Compressor Stator by the Use of S_1 and S_2 Relative Surfaces," *Journal of Engineering Thermophysics* (in Chinese), Vol. 4, No. 4, 1983.

13 Ballhaus, W. F., Jameson, A., and Albert, J., "Implicit Approximate-Factorization Schemes for Steady Transonic Flow Problems," *AIAA Journal*, Vol. 16, No. 6, 1978.

14 Holst, T. L., and Ballhaus, W. F., "Fast, Conservative Schemes for the Full Potential Equation Applied to Transonic Flows," *AIAA Journal*, Vol. 17, No. 2, 1979.

15 Hobson, D. E., "The Hodograph Method for Design of Transonic Turbine Blades," CUED/A-Turbo/TR, 40, 1972.

16 Dunavant, J. C., and Erwin, J. R., "Investigation of a Related Series of Turbine-Blade Profiles in Cascade," NACA, TN 3802, 1956.

17 Gopalakrishnan, S., and Bozzola, R., "A Numerical Technique for the Calculation of Transonic Flow in Turbomachinery Cascades," ASME Paper No. 71-GT-42, 1971.

18 Savage, M., Felix, A. R., and Emery, J. C., "High-Speed Cascade Tests of a Blade Section Designed for Typical Hub Conditions of High-Flow Transonic Rotors," NACA RM L55F07 1955.

19 Dodge, P. R., "Transonic Relaxation Methods," ASME 76-GT-63.

20 Starken, H., "Untersuchung der Stromung in ebenen Uberschall-verzogerung Gittern," DLR FB 71-99 DFVLR Institut fur Luftstrahlantriebe, 1971.

Lü Pan-Ming[1]
Research Associate.

Wu Chung-Hua
Professor and Director of
Institute of Engineering Thermophysics.

Institute of Engineering Thermophysics,
Chinese Academy of Sciences,
Beijing, China

Computation of Potential Flow on S_2 Stream Surface for a Transonic Axial-Flow Compressor Rotor

A set of conservative full potential function equations governing the fluid flow along a given S_2 streamsurface in a transonic axial compressor rotor was obtained. By the use of artificial density and a potential function/density iteration, this set of equations can be solved, and the passage shock on the S_2 streamsurface can be captured. A computer program for this analysis problem has been developed and used to compute the flow field along a mean S_2 streamsurface in the DFVLR transonic axial compressor rotor. A comparison of computed results with DFVLR L2F measurement at 100 percent design speed shows fairly good agreement.

Introduction

In recent years, along with the rapid development of computer science and calculation technique, direct computation of the three-dimensional flow field within a transonic axial compressor rotor has begun to be possible; nevertheless, huge internal storage capacity of computers and large computer time required by these three-dimensional methods precludes their applications in many cases, so there still seems to be a need for less expensive numerical calculation methods.

As early as the beginning of 1950s, a general theory of three-dimensional flow within a subsonic or supersonic turbomachine was proposed in [1]. It suggested that the three-dimensional flow in a turbomachine may be obtained by the iteration between the two-dimensional flows on blade-to-blade S_1 relative streamsurfaces and hub-to-shroud S_2 relative streamsurfaces. Since late 1960s, this theory has been applied extensively and developed further. (For example, the three-dimensional flow equations have been expressed with respect to general nonorthogonal curvilinear coordinates and corresponding nonorthogonal velocity components so that the coordinates are body-fitted and the boundary conditions can be satisfied accurately [2], and a quick convergence of the three-dimensional subsonic solution through iterative calculation between S_1 and S_2 families of streamsurfaces has been achieved [3].) Two major advantages can be expected with this method: First, the internal storage capacity of computer required will be very reasonable; and second, it is possible to do a variety of simplified quasi-three-dimensional calculations to meet different ends; hence it is especially useful for engineering applications. At the very beginning, this theory was proposed only for pure subsonic or pure supersonic flow. In recent years, however, it has also been applied to design and analysis calculations of transonic compressors and turbines by many engineers and research workers. But it should be pointed out that due to the lack of exact analysis methods for transonic flow along the arbitrary S_1 and S_2 streamsurfaces, reported calculations are confined thus far to quasi-three-dimensional calculations, and the jumps in streamsurface configuration and flow variables across the shock are neglected [4, 5].

In the past decade, the potential equation has been successively used as a basis of solving the external transonic flow fields. This paper will describe how, at IETP, CAS, the full potential equation has been used to solve the analysis (direct) problem of transonic flow on a general S_2 streamsurface. A similar work for S_1 streamsurface is given in [6]. It is hoped that these two works may be utilized to perform a successive iteration between several general S_1 flows and several general S_2 flows so that the three-dimensional flow in transonic turbomachines may be obtained. The flow is considered to be inviscid, isentropic, irrotational, and steady.

In a streamsurface analysis (direct) problem, the geometry of the streamsurface shape and the thickness of the stream sheet are to be taken from the last cycle calculation on another family of streamsurfaces. However, as a first approximation they can also be estimated from the geometry of the blade elements.

In the present paper, a new conservative potential function equation on a given S_2 streamsurface was obtained from basic equations employing nonorthogonal coordinates and corresponding nonorthogonal velocity components. This equation can be solved by the use of the artificial density technique [7, 8], and the solution process presented herein is a newly developed Φ-$\rho(\Gamma)$ iteration procedure. Based upon the foregoing solution method, an effective S_2 analysis problem computer program TRANST has been coded.

A typical example of calculation, in which the transonic flow along the mean S_2 surface in the DFVLR single-stage axial transonic compressor rotor [9] was calculated, is given herein to demonstrate the capability of the present method.

[1] Currently with the Department of Engineering Thermophysics, University of Science and Technology of China, Hefei, Anhni, China

Contributed by the Gas Turbine Division of THE AMERICAN SOCIETY OF MECHANICAL ENGINEERS and presented at the 29th International Gas Turbine Conference and Exhibit, Amsterdam, The Netherlands, June 4–7, 1984. Manuscript received at ASME Headquarters December 19, 1983. Paper No. 84-GT-30.

The calculated flow field on the midchannel hub-to-shroud S_2 streamsurface is compared with DFVLR L2F measured data.

Potential Function Equation on S_2

The governing equations for the steady relative flow of a nonviscous fluid passing through a rotor blade passage are

$$\text{continuity equation} \quad \nabla\cdot(\rho W)=0 \tag{1a}$$

$$\text{irrotational condition} \quad \nabla\times V=0 \tag{2}$$

$$\text{energy equation} \quad dI/dt=0 \tag{3a}$$

From these equations, a set of equations of the flow on the hub-to-shroud S_2 relative streamsurface can be obtained. An arbitrary curvilinear relative coordinate system x^1, x^2, and x^3, where x^1 and x^2 lie in the meridional plane, and $x^3 = \phi$, as suggested in [2], is adopted in the present analysis.

With respect to the curvilinear coordinates employed, a velocity vector can be expressed in tensor notation as follows

$$V=v^i\mathbf{e}_i=v_i\mathbf{e}^i=V^i\mathbf{u}_i=V_i\mathbf{u}^i$$

$$W=w^i\mathbf{e}_i=w_i\mathbf{e}^i=W^i\mathbf{u}_i=W_i\mathbf{u}^i$$

$$W^i=\sqrt{g_{ii}}w^i \quad W_i=\sqrt{g^{ii}}w_i \quad V^i=\sqrt{g_{ii}}v^i$$

$$V_i=\sqrt{g^{ii}}v_i \quad g_{ij}=\mathbf{e}_i\cdot\mathbf{e}_j \quad g^{ij}=\mathbf{e}^i\cdot\mathbf{e}^j$$

$$g=r^2a_{11}a_{22}\sin^2\theta_{12}$$

From equation (1a), the continuity equation for flow along an S_2 streamsurface was obtained in [2] as

$$\frac{\partial}{\partial x^1}(\tau\rho W^1\sqrt{a_{22}}\sin\theta_{12})+\frac{\partial}{\partial x^2}(\tau\rho W^2\sqrt{a_{11}}\sin\theta_{12})=0 \tag{1b}$$

where the bold partial derivative sign denotes the partial derivatives taken along the S_2 streamsurface [1]. The relation between this partial derivative and ordinary spatial partial derivative is

$$\frac{\partial}{\partial x^\alpha}=\frac{\partial}{\partial x^\alpha}+\frac{\partial\varphi}{\partial x^\alpha}\frac{\partial}{\partial\varphi} \quad \alpha=1 \text{ or } 2 \tag{4}$$

which holds for any flow variable.

It can be easily shown that an equivalent representation of equation (1a) is

$$\frac{\partial}{\partial x^\alpha}(B\rho\sqrt{g}\,w^\alpha)=0 \quad \alpha=1,2 \tag{1c}$$

From equation (2) a potential function Φ can be introduced, with

$$\nabla\Phi=V=W+U \tag{5a}$$

then

$$w^i=g^{ij}\Phi_j \quad i,j=1,2 \tag{5b}$$

where

$$\Phi_j=\frac{\partial\Phi}{\partial x^j}$$

From equation (3), it is seen that along any relative stream line,

$$I=(h-(U)^2/2)+(W)^2/2=\text{constant} \tag{3b}$$

Other useful relations are

$$p=C\rho^\kappa \tag{6}$$

$$p=R\rho T \tag{7}$$

$$n\cdot W=0 \tag{8a}$$

From equation (8),

$$W_\varphi=W_r r\frac{\partial\varphi}{\partial r}+W_z r\frac{\partial\varphi}{\partial z} \tag{8b}$$

For convenience, two auxiliary variables, local sonic velocity, a, and angular momentum of flow, Γ, are introduced

$$(a)^2=\kappa RT=(\kappa-1)\left[I-\frac{(W)^2}{2}+\frac{(U)^2}{2}\right] \tag{9}$$

$$\Gamma=V_\theta r=\frac{\partial\Phi}{\partial\theta}=\frac{\partial\Phi}{\partial\varphi} \tag{10}$$

Equations (4) and (10) lead to the following very simple transformation relation between spatial partial derivatives

Nomenclature

a_{ij} = metric tensor elements of two-dimensional x^i coordinate system
B = angular thickness of S_2 stream filament
b = thickness of S_1 stream filament
e_i, e^i = x^i coordinate base vector and reciprocal vector
G = artificial density coefficient
g = determinant of three-dimensional metric tensor
g^{ij}, g_{ij} = metric tensor elements of three-dimensional x^i coordinate system
H = absolute stagnation enthalpy of unit mass of gas
h = enthalpy of unit mass of gas
I = relative stagnation rothalpy of unit mass of gas, $(h-U^2/2)+W^2/2$
M = relative flow Mach number
$\mathbf{n}$ = unit normal vector of S_2 surface
p = pressure of gas
R = gas constant
r = radius, radial coordinate
T = temperature of gas
U = velocity of rotor at radius r
$\mathbf{u}_i, \mathbf{u}^i$ = x^i coordinate unit base vector and reciprocal vector
V = absolute velocity of gas
W = relative velocity of gas
x^i = general curvilinear coordinates
Z = coordinate along machine axis
α_Γ = relaxation factor
κ = ratio of specific heats
Γ = angular momentum of gas about z-axis, $V_\theta r$
Φ = potential function of absolute flow
θ, φ = absolute and relative tangential coordinate of the cylindrical coordinate system, respectively
$\theta_{12}, \theta_1, \theta_2$ = angle between coordinate lines x^1 and x^2, x^1 and z, x^2 and r, respectively
ρ = density of gas
τ = thickness of S_2 stream filament
ω = angular velocity of rotor blade
$\frac{\partial}{\partial x^1}, \frac{\partial}{\partial x^2}$ = partial derivatives taken along the S_2 surface

Superscript

i = contravariant component of vector

Subscript

I = reference state where the enthalpy of gas is equal to I
i = covariant component of vector
r, θ, φ, z = components along cylindrical coordinates

and stream surface partial derivatives of the potential function on S_2 streamsurface

$$\frac{\partial \Phi}{\partial x^\alpha} = \frac{\partial \Phi}{\partial x^\alpha} + \frac{\partial \varphi}{\partial x^\alpha}\Gamma \quad \alpha = 1 \text{ or } 2 \tag{11}$$

When equation (11) and (5*b*) are used, the continuity equation (1*c*) is transformed into

$$\frac{\partial}{\partial x^1}\left(C_1\rho\frac{\partial \Phi}{\partial x^1} + C_2\rho\frac{\partial \Phi}{\partial x^2} - C_3\rho\right) + \frac{\partial}{\partial x^2}\left(D_1\rho\frac{\partial \Phi}{\partial x^1} + D_2\rho\frac{\partial \Phi}{\partial x^2} - D_3\rho\right) = 0 \tag{12}$$

where

$$C_1 = B\sqrt{g}\,g^{11} \quad C_2 = D_1 = B\sqrt{g}\,g^{12} \quad D_2 = B\sqrt{g}\,g^{22}$$

$$C_3 = B\sqrt{g}\Gamma\left(g^{11}\frac{\partial \varphi}{\partial x^1} + g^{12}\frac{\partial \varphi}{\partial x^2}\right)$$

$$D_3 = B\sqrt{g}\Gamma\left(g^{12}\frac{\partial \varphi}{\partial x^1} + g^{22}\frac{\partial \varphi}{\partial x^2}\right)$$

Equation (12) is now the potential function equation in conservative form for irrotational absolute flow on an S_2 streamsurface and will be used as the principal equation in the present method.

From equations (8*a*) and (10), it can be easily shown that

$$\Gamma = r^2\left(\omega + w^1\frac{\partial \varphi}{\partial x^1} + w^2\frac{\partial \varphi}{\partial x^2}\right) \tag{13}$$

From equations (3*a*) and (6)

$$\rho = \rho_I\left\{1 - \frac{1}{2I}\left[(W)^2 - \omega^2 r^2\right]\right\}^{\frac{1}{\kappa-1}} \tag{14}$$

where state I is a reference state of gas, in which state the gas enthalpy, h_I, is just equal to the relative stagnation rothalpy of gas in the real state, I. Also

$$(W)^2 = \omega^2 r^2 + (W^1)^2 + (W^2)^2 + 2W^1W^2\cos\theta_{12} + \frac{\Gamma^2}{r^2} - 2\omega\Gamma \tag{15}$$

$$W^1 = \sqrt{g_{11}}\,w^1 = \sqrt{g_{11}}\,(g^{11}\frac{\partial \Phi}{\partial x^1} + g^{12}\frac{\partial \Phi}{\partial x^2}) \tag{16}$$

$$W^2 = \sqrt{g_{22}}\,w^2 = \sqrt{g_{22}}\left(g^{21}\frac{\partial \Phi}{\partial x^1} + g^{22}\frac{\partial \Phi}{\partial x^2}\right) \tag{17}$$

Now, equation (12) can be solved interactively together with equations (13) and (14) for three unknowns Φ, ρ, and Γ.

Difference Scheme and Artificial Density

With an arbitrary two-dimensional curvilinear coordinate system the computational domain can always be automatically transformed to a rectangle. To raise the accuracy of solution, however, any abrupt changes in the mesh spacing and in the angle between x^1 and x^2, θ_{12}, should be avoided in forming the mesh.

Now equation (12) can be discretized by the use of a central difference scheme [8]. In the x^1-direction, let $i = 1, MM$ and in the x^2-direction, $j = 1, N$.

$$\left[C_1\rho\frac{\partial \Phi}{\partial x^1} + C_2\rho\frac{\partial \Phi}{\partial x^2} - C_3\rho\right]_{i+\frac{1}{2},j} - \left[C_1\rho\frac{\partial \Phi}{\partial x^1} + C_2\rho\frac{\partial \Phi}{\partial x^2} - C_3\rho\right]_{i-\frac{1}{2},j} + \left[D_1\rho\frac{\partial \Phi}{\partial x^1} + D_2\rho\frac{\partial \Phi}{\partial x^2} - D_3\rho\right]_{i,j+\frac{1}{2}} - \left[D_1\rho\frac{\partial \Phi}{\partial x^1} + D_2\rho\frac{\partial \Phi}{\partial x^2} - D_3\rho\right]_{i,j-\frac{1}{2}} = 0 \tag{18}$$

where

$$\left(\frac{\partial \Phi}{\partial x^1}\right)_{i+\frac{1}{2},j} = \Phi_{i+1,j} - \Phi_{i,j} \tag{19}$$

$$\left(\frac{\partial \Phi}{\partial x^2}\right)_{i+\frac{1}{2},j} = \frac{1}{4}\left[\Phi_{i+1,j+1} + \Phi_{i,j+1} - \Phi_{i+1,j-1} - \Phi_{i,j-1}\right] \tag{20}$$

$$\left(\frac{\partial \Phi}{\partial x^1}\right)_{i,j+\frac{1}{2}} = \frac{1}{4}\left[\Phi_{i+1,j+1} + \Phi_{i+1,j} - \Phi_{i-1,j+1} - \Phi_{i-1,j}\right] \tag{21}$$

$$\left(\frac{\partial \Phi}{\partial x^2}\right)_{i,j+\frac{1}{2}} = \Phi_{i,j+1} - \Phi_{i,j} \tag{22}$$

At boundary grid points, the preceding formulations should be replaced by other special formulas, which will be discussed in the next section.

Equation (18) can be rearranged into the following form

$$A_1\Phi_{i,j-1} + A_2\Phi_{i,j} + A_3\Phi_{i,j+1} = A_4 \tag{23}$$

This equation can be easily solved using standard line relaxation method.

In order to introduce the necessary artificial viscosity to ensure stability and the capture of a shockwave, density $\rho_{i\pm1/2,j}$ and $\rho_{i,j\pm1/2}$ in equation (23) or (18) at supersonic grid points should be replaced by corresponding artificial density $\tilde{\rho}_{i\pm1/2,j}$ and $\hat{\rho}_{i,j\pm1/2}$, respectively.

$$\tilde{\rho}_{i+\frac{1}{2},j} = (1-\nu_{i+\frac{1}{2},j})\rho_{i+\frac{1}{2},j} + \nu_{i+\frac{1}{2},j}\rho_{i+r+1/2,j} \tag{24}$$

$$\hat{\rho}_{i,j+\frac{1}{2}} = (1-\nu_{i,j+\frac{1}{2}})\rho_{i,j+\frac{1}{2}} + \nu_{i,j+\frac{1}{2}}\rho_{i,j+s+\frac{1}{2}} \tag{25}$$

where the subscripts

$$r = \pm 1 \quad \text{when} \quad w^1_{i+\frac{1}{2},j} \lessgtr 0$$

$$s = \pm 1 \quad \text{when} \quad w^2_{i,j+\frac{1}{2}} \lessgtr 0$$

and

$$\nu_{i+\frac{1}{2},j} = \begin{cases} \text{MAX}[(M^2_{i,j}-1)G, 0] & w^1_{i+\frac{1}{2},j} \geqq 0 \\ \text{when} & \\ \text{MAX}[(M^2_{i+1,j}-1)G, 0] & w^1_{i+\frac{1}{2},j} < 0 \end{cases}$$

$$\nu_{i,j+\frac{1}{2}} = \begin{cases} \text{MAX}[(M^2_{i,j}-1)G, 0] & w^2_{i,j+\frac{1}{2}} \geqq 0 \\ \text{when} & \\ \text{MAX}[(M^2_{i,j+1}-1)G, 0] & w^2_{i,j+\frac{1}{2}} < 0 \end{cases}$$

where G is a user-specified positive constant less than 2.0.

Boundary Conditions

At the inlet boundary AB (See Fig. 1), where the flow is considered to be uniform in the circumferential direction, the radial velocity is zero, and the stagnation pressure, stagnation temperature, flow angle, and mass flow rate were specified. The radial distribution of the inlet axial velocity can be determined by the radial equilibrium condition.

Rae [10] suggested that the proper inlet computational boundary condition for a transonic axial compressor rotor (when the axial velocity component is subsonic) should be nonreflective or should be the so-called "radiation condition." However, a uniform inlet flow assumption sometimes can also lead to a convergent solution. Numerical calculation shows that the present computational scheme probably contains sufficient artificial viscosity and numerical viscosity, which effectively damped the perturbation wave reflecting and propagating backward to the computational domain in the vicinity of inlet boundary and ensured the iteration approached convergence stably.

At the computational domain's exit boundary CD, the flow is also considered to be axisymmetric; the radial velocity is also considered to be zero; and the exit circumferential velocity or alternatively the exit flow angle is specified. For the exit spanwise variation of axial velocities, the radial equilibrium condition again should be used.

With the radial distribution of axial velocity (w^1) at inlet and exit grid lines known from equation (5*b*), the Neumann condition required for solving the governing differential equation is at hand.

Boundaries AC and BD are solid walls, the boundary condition is that of flow tangency (i.e. no mass flow across the boundary) and requires the x^2 contravariant velocity component at the wall surface to be zero ($w^2=0$). This boundary condition is implemented by applying

$$(B\rho\sqrt{g}w^2)_{i,\,J+\frac{1}{2}} = -(B\rho\sqrt{g}w^2)_{i,\,J-\frac{1}{2}} \tag{26}$$

where $J=1$ or N.

Thus, at these boundaries, equation (18) becomes

$$\left[C_1\rho\frac{\partial\Phi}{\partial x^1}+C_2\rho\frac{\partial\Phi}{\partial x^2}-C_3\rho\right]_{i+\frac{1}{2},\,J} - \left[C_1\rho\frac{\partial\Phi}{\partial x^1}+C_2\rho\frac{\partial\Phi}{\partial x^2}-C_3\rho\right]_{i-\frac{1}{2},\,J} \pm 2\left[D_1\rho\frac{\partial\Phi}{\partial x^1}+D_2\rho\frac{\partial\Phi}{\partial x^2}-D_3\rho\right]_{i,\,J\pm\frac{1}{2}} = 0 \tag{27}$$

In order to calculate the value of $\partial\Phi/\partial x^2$ at the wall surface, the foregoing condition ($w^2=0$) can be used again. It leads to

$$(B\rho\sqrt{g}w^2)_{i\pm\frac{1}{2},\,J} = 0 \tag{28}$$

or

$$\left[D_1\rho\frac{\partial\Phi}{\partial x^1}+D_2\rho\frac{\partial\Phi}{\partial x^2}-D_3\rho\right]_{i\pm\frac{1}{2},\,J} = 0 \tag{29a}$$

$$\left(\frac{\partial\Phi}{\partial x^2}\right)_{i\pm\frac{1}{2},\,J} = \left(\frac{D_3}{D_2}-\frac{D_1}{D_2}\frac{\partial\Phi}{\partial x^1}\right)_{i\pm\frac{1}{2},\,J} \tag{29b}$$

Calculation Procedure

The calculation procedure consists of an iterative solution of equation (12), (13), and (14).

At the beginning of iteration, initial distribution of $\Phi^{(0)}$ should be calculated using an estimated distribution of velocities. Next, the $\Gamma^{(0)}$ is assumed to be distributed linearly along the chord. Density $\rho^{(0)}$ is calculated by the use of equation (14). Then equation (12) is solved with the line relaxation method for an improved distribution of potential function, $\Phi^{(1)}$.

Recalculation of Γ and ρ by the use of equations (13) and (14), respectively, leads to a tentative value of Γ, $\tilde{\Gamma}^{(1)}$, and new $\rho^{(1)}$. In order to make the iteration stabilized, especially in the initial period of iteration process, the new value of Γ should be properly damped. Thus

$$\Gamma^{(n+1)} = \Gamma^{(n)} + (\tilde{\Gamma}^{(n+1)} - \Gamma^{(n)})\alpha_\Gamma \tag{30}$$

where α_Γ is a relaxation factor varying from 0.2 to 0.5 initially, and increasing later step by step until it reaches a value slightly less than 1.0.

At the same time, artificial densities $\tilde{\rho}_{i\pm\frac{1}{2},\,j}$ and $\hat{\rho}_{i,\,j\pm\frac{1}{2}}$ at all supersonic grid points, calculated by equations (24) and (25), should take the place of $\rho_{i\pm\frac{1}{2},\,j}$ and $\rho_{i,\,j\pm\frac{1}{2}}$, respectively, in equation (12). Then equation (12), into which the new values of $\Gamma^{(1)}$, $\tilde{\rho}^{(1)}$, and $\hat{\rho}^{(1)}$ are substituted, is solved again. This procedure is repeated until convergence is reached.

This iteration procedure was developed from traditional $\Phi-\rho$ iteration. To distinguish it from the traditional $\Phi-\rho$ iteration, it is referred to as $\Phi-\rho$ (Γ) iteration.

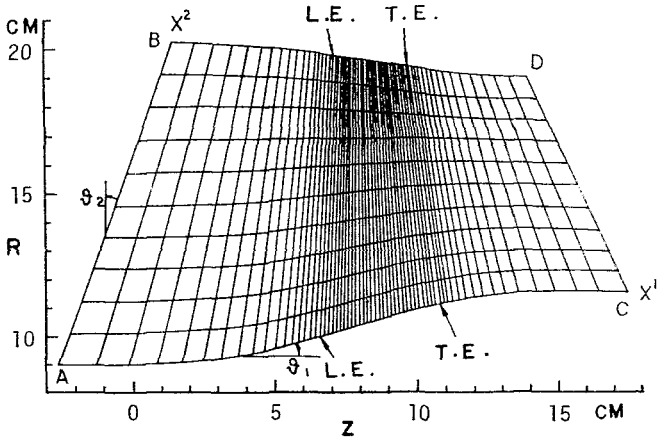

Fig. 1 Computation mesh in physical plane

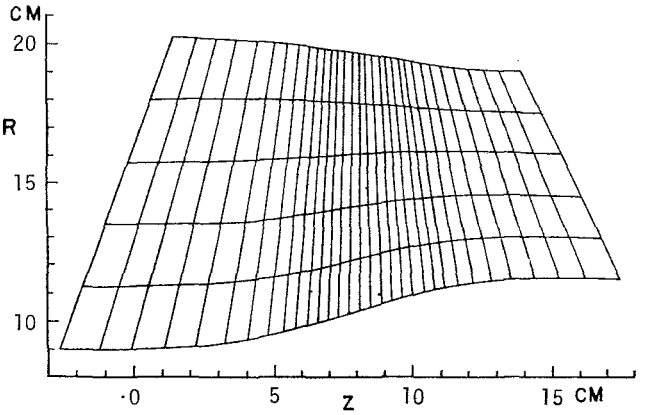

Fig. 2 Sparse grid network

Computer Program and Calculation Example

The computer program TRANST for an analysis solution of the transonic flow along an S_2 streamsurface was coded using the present method. It has mainly two applications:

1 The program TRANST can be used as a component part of the solution chain for full three-dimensional flow field in a

transonic blade row, based on the general theory of iterative solution between two families of streamsurfaces. In this case, $\partial\phi/\partial x^1$, $\partial\phi/\partial x^2$ and B are to be obtained from the S_1 calculations of the preceding cycle.

2 The program TRANST can be used alone to calculate the hub-to-shroud two-dimensional flow field. In this case, only the flow on a single representative mean (central) S_2 streamsurface is calculated.

The computational example presented here belongs to the second application. The program TRANST has been used to analyze the internal flow field of the DFVLR rotor passage, operating at 100 percent design speed and with mass flow corresponding to the point of maximum isentropic efficiency (about 89 percent). The flow channel and computational domain of this rotor are shown in Fig. 1. The measured data for this rotor have been used to define the computation condition: mass flow rate 17.3 kg/s, rotational speed of rotor 20,260 rpm, upstream stagnation temperature 288.2°K, upstream stagnation pressure 101,600 N/M^2. At the downstream boundary, whirl component of velocity V_θ is obtained from the measured isentropic efficiency and downstream total pressure. The flow calculation does not account for the wall boundary layers, only a 3 percent annulus blockage being included.

In TRANST, the calculation is carried out successively in two independent mesh networks: First, the calculation is done in a 32 × 6 sparse grid network illustrated in Fig. 2. After some 180 iterations were done, the parameters in grid points, such as Φ, Γ, ρ, etc. were linearly interpolated to the final 63×11 fine mesh network (see Fig. 1). At this fine grid system, the calculation is proceeded until the convergence criteria is met.

In TRANST, the convergence criteria require the maximum relative change in relative velocity at any grid point in the flow field

$$\epsilon = \underset{i,j}{\mathrm{MAX}} \left| \frac{W_{i,j}^{(n+1)} - W_{i,j}^{(n)}}{W_{i,j}^{(n)}} \right|$$

to be less than a prescribed tolerance. In the present example, $\epsilon < 0.4\times10^{-3}$ is specified, and the corresponding total computer time is approximately 0.6 s per grid point on an UNIVAC 1100.

In the present calculation, the thickness of the S_2 stream sheet is simply assumed to be proportional to the circumferential arc length of the flow channel and the abrupt changes in the shape of the S_2 streamsurface and in the thickness of the corresponding S_2 stream sheet across the shock are neglected.

Results of Calculation and Discussion

The projection on the meridional plane of the lines of constant relative Mach number of the flow on mean S_2 streamsurface obtained in the calculation is shown in Fig. 3. A comparison of these values with the DFVLR experimental data [9] shows that the calculated Mach numbers at the blade leading edge are approximately equal to the measured values in a pitchwise average sense, but at the trailing edge, the calculation is about 0.1 lower than the experiment because the blockage due to profile boundary layer has not been taken into account in the present calculation, and if a correction factor was introduced into S_2 stream sheet thickness, B, this discrepancy can be expected to be reduced. At the same time the shock location on the S_2 surface indicated by the calculated results is about 6–9 percent chord behind the location obtained in the experiment.

However, it is more interesting to observe the magnitudes of "abrupt" changes in the shape of the streamsurface and the thickness of stream sheet as well as in the various flow

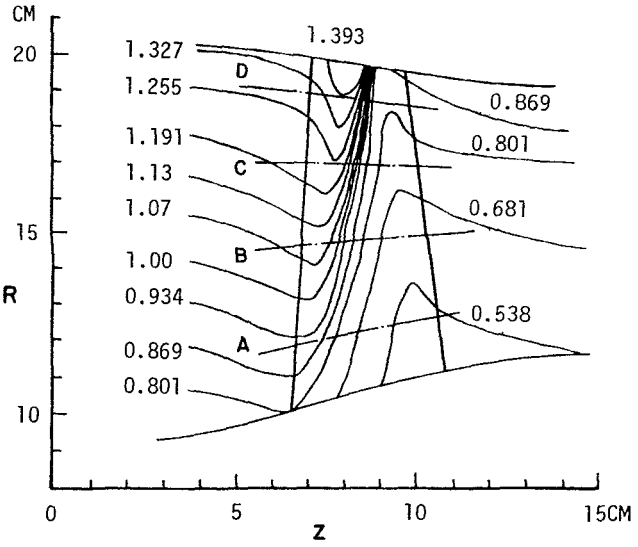

Fig. 3 Projection on meridional plane of computed Mach number contour of flow along mean S_2 stream surface

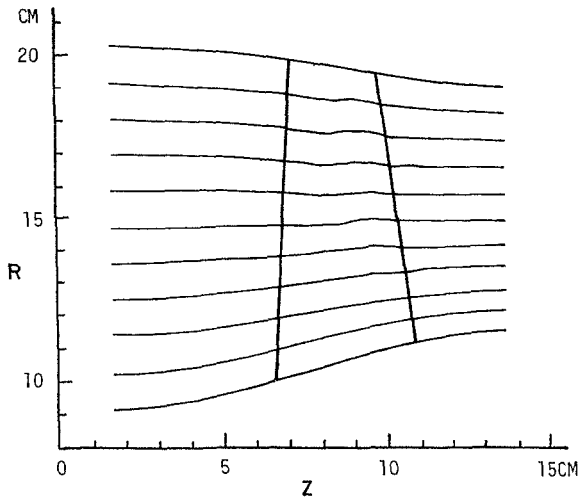

Fig. 4 Projection on meridional plane of computed streamline on mean S_2 stream surface

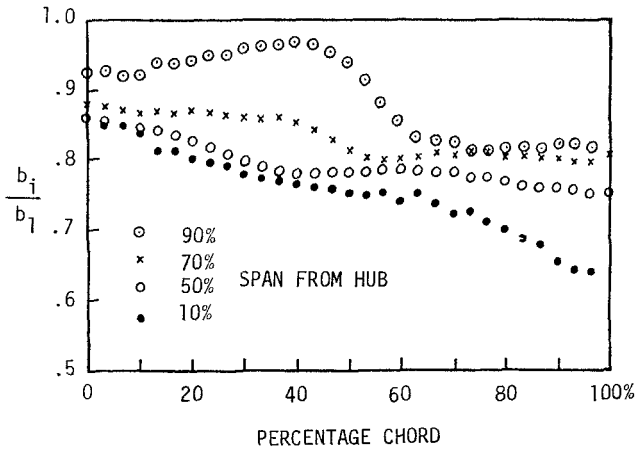

Fig. 5 Chordwise variation of computed radial thickness of S_2 stream sheets

variables "across" the shock. Figure 4 shows the projection of S_2 surface streamlines on the meridional plane. The abrupt change across the shock can be seen clearly and is, of course, more marked in the high velocity region near casing. It seems

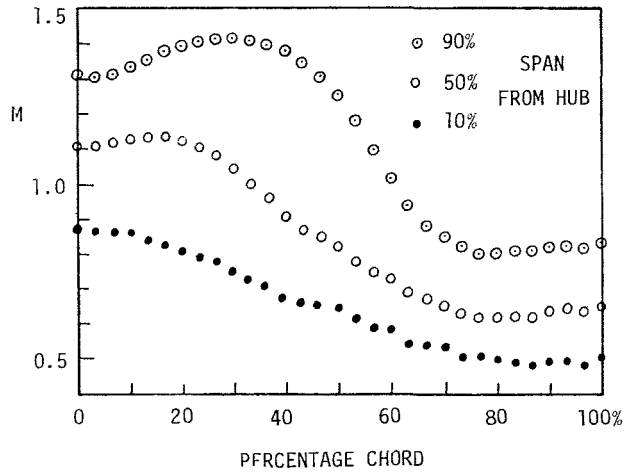

Fig. 6 Chordwise distribution of calculated Mach number on mean S_2 stream surface

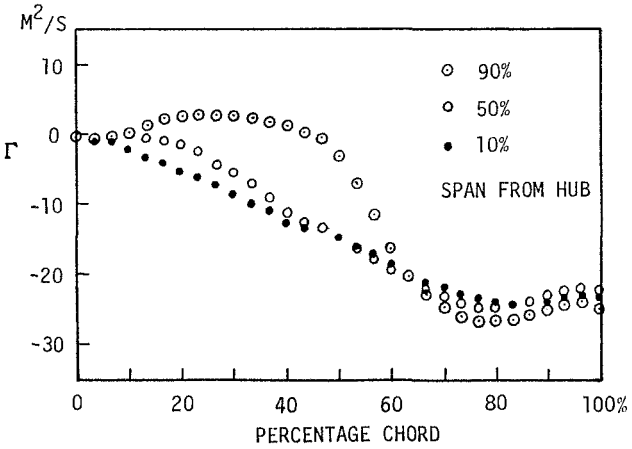

Fig. 7 Chordwise distribution of calculated angular momentum on mean S_2 stream surface

that the effect is delayed in the low-velocity region. Figure 5 shows the calculated chordwise variation of the radial distance between streamlines on S_2 surface or the relative radial thickness of S_1 stream sheets at their intersections with the mean S_2 surface. The "jump" across the shock at the high velocity is quite large and should not be neglected in an accurate transonic S_1 flow calculation.

Figures 6–7 show the calculated chordwise variation of the relative flow Mach numbers and the angular momentum, Γ. It is interesting to notice that in the upper half of the blade passage there are overturnings of the fluid across the shock as clearly indicated in Fig. 7. This phenomenon was first observed in the design calculation of the transonic compressor stage reported in [4] and was also reported in the experimental data of [11].

It may also be noted from Figs. 4–7, that the shock captured in the calculation spreads over quite a few grid points. This is typical of this type of transonic calculation.

Concluding Remarks

A numerical method has been developed for the analysis (direct) problem of steady transonic flow on a hub-to-shroud S_2 streamsurface in an axial compressor rotor. A new conservative, inviscid, full-potential transonic equation expressed with respect to general nonorthogonal coordinates and corresponding nonorthogonal velocity components is solved by the use of artificial density and a new iteration algorithm among the three variables Φ, Γ, and ρ. The arbitrary boundary shape is easily fitted by coordinate lines without coordinate transformation and the boundary conditions are accurately satisfied.

A new nonuniform grid refinement technique has been developed, which not only saves the time required to reach convergence, but also makes the initiation of the iteration process very easy.

The computer code developed was used to calculate the transonic flow along the mean S_2 streamsurface of the DFVLR transonic rotor and a quick convergence and satisfactory results were obtained.

Although the shock captured in the calculation spreads over a few grid points, it still shows clearly the "jump" in the configuration of stream sheet and in the flow variables across the shock. It also shows the overturning phenomena, which usually occurs in current design of transonic compressors. It is emphasized that for an accurate calculation of either transonic cascade flow or S_1 and S_2 surface flow, the rather large abrupt changes in the surface configuration and flow variables across the passage shock should be taken into account.

References

1 Wu, Chung-Hua, "A General Theory of Three-Dimensional Flow in Subsonic and Supersonic Turbomachines of Axial, Radial, and Mixed-Flow Types," ASME Paper No. 50-A-79; Trans. ASME, Nov. 1952, or NACA TN 2604, 1952.

2 Wu, Chung-Hua, "Three-Dimensional Turbomachine Flow Equations Expressed with Respect to Non-orthogonal Curvilinear Coordinates and Methods of Solution," Lecture Notes, China University of Science and Technology, 1975; also *Proceedings of the 3rd ISABE*, 1976, pp. 233–252.

3 Wang, Qinghaun, et al., "Solution of Three-Dimensional Compressible Flow in an Axial-Flow Compressor Stator by the Use of S_1 and S_2 Relative Surfaces," *Journal of Engineering Thermophysics*, Vol. 4, No. 4, 1983.

4 Academia Sinica, and Shengyang Aeroengine Company, "Theory, Methods, and Application of Three-Dimensional Flow Design of Transonic Axial-Flow Compressor," Research Report, 1976; *Journal of Engineering Thermophysics*, Vol. 1, No. 1, 1980, pp. 44–54.

5 Xu, Jian-Zhong, "Shock Relations in Turbomachines," *Journal of Mechanical Engineering*, Vol. 16, No. 3, 1980, pp. 61–69.

6 Chang, Gialin, and Wu, Chung-Hua, "Implicit Algorithm for Conservative Transonic S_1 Full-Potential Equation Employing Nonorthogonal Curvilinear Coordinates and Nonorthogonal Velocity Components," Paper to be presented at the Conference on Computational Methods in Turbomachinery, The University of Birmingham, Apr. 1984.

7 Hafez, M. M., South, J., and Murman, E. M., "Artificial Compressibility Methods for Numerical Solution of Transonic Full Potential Equation," *AIAA Journal*, Vol. 17, No. 8, 1979.

8 Holst, T. L., "Fast, Conservative Algorithm for Solving the Transonic Full-Potential Equation," *AIAA Journal*, Vol. 18, No. 12, 1980.

9 McDonald, P. W., et al., 'A Comparison Between Measured and Computed Flow Field in a Transonic Compressor Rotor," ASME JOURNAL OF ENGINEERING FOR POWER, No. 4, 1980.

10 Rae, W. J., and Lordi, Z. A., "A Study of Inlet Conditions for Three-Dimensional Compressor Flows," XE-6129-A-4, June 1978, Calspan Corporation.

11 Dunker, R. J., and Hungenberg, H. G., "Study of the Flow Field Behind a Transonic Axial Compressor Rotor Using Laser-Anemometry and Unsteady Pressure Measurements," AIAA 79-7034, 4th ISABE, 1979, pp. 269–276.

Transonic Cascade Flow Solved by Separate Supersonic and Subsonic Computations With Shock Fitting

Wu Wenquan
Associate Professor.

Wu Chung-Hua
Professor and Director.

Yu Dabang
Lecturer, now with Beijing Industrial University.

Institute of Engineering Thermophysics, Chinese Academy of Sciences, Beijing, China

A new method to solve the transonic flow past a plane cascade with inlet bow wave and a passage shock extending from the leading edge all the way across the flow channel is presented. In this method, different algorithms are used for supersonic and subsonic flow regions, respectively, and the aerothermodynamic relations of a connecting passage shock are satisfied. Within the supersonic region, the method of characteristics is used. For calculation of the subsonic flow, the stream function equation expressed with respect to nonorthogonal curvilinear coordinates and nonorthogonal velocity components is solved with a matrix method. By the use of Rankine-Hugoniot relations, the passage shock can be accurately determined and a definite jump of the aerothermodynamic quantities across the passage shock is obtained. All calculations involved are programmed and incorporated into a single code. The computational procedure is straightforward and simple, and the computational time is short. Some results of typical applications of this method are given in this paper. Agreement of the numerical results with the experimental data, including the location and shape of the passage shock wave, is very good.

Introduction

In the past decade, significant progress has been made in the numerical solution of transonic flow with shock waves in turbomachines. In general, these methods follow two distinct approaches: time-marching and relaxation techniques. In the former approach, the steady flow solution is obtained as an asymptotic solution to a real or pseudo-unsteady flow equation. In the latter approach, the steady transonic flow equation is solved by an iteration algorithm in a manner similar to that in the solution of an elliptic boundary value problem, employing different difference schemes in different regions, or by the recently developed artificial compressibility method. Many instructive results have been obtained, but in the former approach, the computer storage and computing time required are usually quite large; in the latter approach the entropy gradient downstream of the shock must be neglected, and in both approaches it is difficult to capture the shock clearly. The shock obtained usually is smeared over quite a few grid points and the calculated result does not agree with the experimental data over the whole flow region.

The location and shape of the shock wave in a transonic cascade are important in the design and analysis problem of the transonic cascade. It is hoped that a relatively simple method may be developed in which the location and shape of the shock wave can be accurately and clearly defined. Transonic cascade flow is characterized by the presence of adjacent regions of supersonic and subsonic flows that are separated by a passage shock wave. It is well known that method of characteristics and matrix method are efficient methods for supersonic and subsonic flow, respectively. In [1], they have been used to analyze transonic cascade flows, where the shock waves had been obtained by simple optical measurement. Quite accurate and detailed information of the flow over the whole region was provided by this method. Since detailed flow measurement by optical methods, such as the Laser two-focus method, is time-consuming and costly, simple shock photographs followed by this simple calculation do provide a practical engineering solution to the analysis or design problem of transonic cascade flow.

This method has been further developed to include the determination of the passage shock in the computing code and is presented herein.

Physical Model

Steady, inviscid transonic flow past a compressor cascade, as shown in Fig. 1, is considered in this paper. At the inlet, the flow is supersonic and its axial velocity component is subsonic. There are detached bow shock waves upstream of the blunt leading edge of blade. Except for a small subsonic flow region near the leading edge of the blade, flow downstream of the bow wave is supersonic. The bow shock wave extends across the passage, and the flow downstream of the passage shock is subsonic. Thus, the passage shock wave is a dividing boundary line between the supersonic and subsonic flow regions. This is the flow pattern considered in this paper.

Contributed by the Gas Turbine Division of THE AMERICAN SOCIETY OF MECHANICAL ENGINEERS and presented at the 29th International Gas Turbine Conference and Exhibit, Amsterdam, The Netherlands, June 4–7, 1984. Manuscript received at ASME Headquarters December 19, 1983. Paper No. 84-GT-24.

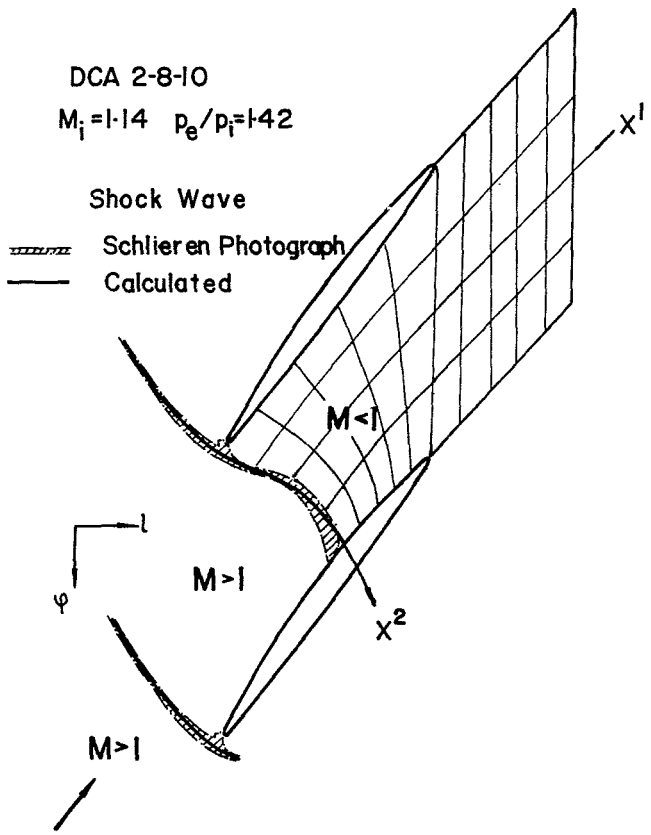

Fig. 1 Flow pattern and coordinate system used in a compressor cascade

For the cascade, when the inlet flow conditions (such as inlet Mach number, M_i, stagnation temperature and pressure, $T_i°$ and $p_i°$), and outlet flow condition (in general, the outlet flow angle, β_e, or pressure, p_e) are given, the flow pattern can be determined and is unique. For ideal fluid flow past the cascade with a sharp trailing edge, the Kutta-Joukowsky condition is that the stagnation point is at the trailing edge of the blade. For the real viscous flow and a blunt trailing edge, a generalized Kutta-Joukowsky condition may be used instead; namely, the velocities at the both blade surfaces near the trailing edge will be approximately the same [2]. This condition can be used to consider the effect of the back pressure of the cascade downstream.

Supersonic Flow Region

For the steady inviscid flow past a cascade of blades, the governing aerothermodynamic equations expressed with respect to coordinate system (φ, l), in which l is the generatrix of the surface of revolution, were given in [3]. When the flow is supersonic, there are two families of real characteristic curves, C_1 and C_2. The differential equations along the characteristic curves are

$$\frac{1}{W}\frac{dW}{dl} \mp \tan\mu \frac{d\beta}{dl} - \tan^2\mu \left[\frac{\omega^2 r \sin\sigma}{a^2} + \frac{1}{a^2}\frac{dI}{dl} + \frac{1}{\tau}\frac{d\tau}{dl} + \frac{\lambda_{2,1}\sin\sigma\cos\beta}{r(\lambda_{2,1}\cos\beta - \sin\beta)} + \frac{1}{J}\frac{N\cos\beta - M\sin\beta}{(\lambda_{2,1}\cos\beta - \sin\beta)}\right] = 0$$

where

$$\lambda_1 = (r\cdot d\varphi/dl)_1 = K/J - \sqrt{K^2 - JL}/J = \tan(\beta+\mu)$$

$$\lambda_2 = (r\cdot d\varphi/dl)_2 = K/J + \sqrt{K^2 - JL}/J = \tan(\beta-\mu)$$

$$J = 1-(W_l/a)^2, K = W_l W_\varphi/a^2, L = 1-(W_\varphi/a)^2$$

$$M = \frac{1}{a^2}\left[\left(\omega^2 r + \frac{W_l^2}{r}\right)\sin\sigma + \frac{a^2}{\tau}\frac{\partial\tau}{\partial l} + \frac{\partial I}{\partial l}\right]$$

$$N = \left[1-\left(\frac{W}{a}\right)^2\right]\left[\left(\frac{W_\varphi}{r}+2\omega\right)\frac{\sin\sigma}{W_l} + \frac{1}{W_l^2}\left(\frac{1}{r}\frac{\partial I}{\partial\varphi} - \frac{T}{r}\frac{\partial S}{\partial\varphi}\right)\right] + \frac{1}{a^2 r}\frac{\partial I}{\partial\varphi}$$

The method of characteristics solution has been programmed recently [4]. In the program, the coefficients used in the calculation are the average value between two connecting points obtained after the iteration. The convergence is very fast and usually only a few iterations are necessary. When a characteristic curve meets the blade surface, the flow direction is known from the tangency condition and the velocity is determined. The interpolations used in the calculation are made on a two-dimensional basis, so that the values interpolated are rather accurate.

In transonic computations, it is difficult to capture the bow shock waves. Approximate engineering models, however, are available for plane cascades [5–9]. They have been shown to be quite accurate for moderate supersonic Mach number range encountered in current transonic compressors. For example, for the DFVLR cascade of double circular arc blades DCA 2-8-10 [10] at inlet Mach number of 1.14, the bow shock waves laid out according to [5] agree well with the experimental data, see Fig. 2.

It is well known that there is an unique incidence angle corresponding to the inlet Mach number. Determination of the unique incidence angle is also included in the code. The calculation is started with a set of assumed values of Mach number and flow angle at the inlet and extended along the circumferential direction several pitches until the solution covering one pitch length repeats itself. Then the uniform

Nomenclature

h = static enthalpy
I = relative stagnation rothalpy
M = local Mach number
p = pressure
T = temperature
W = relative velocity
a_{ij} = basic metric tensor
β = relative flow angle
λ = slope of characteristics on surface of revolution
θ_{12} = angle included by the coordinate lines
μ = Mach angle, $\mathrm{Sin}^{-1}1/\mathrm{M}$
ρ = mass density
σ = slope of surface of revolution in meridional plane
τ = normal thickness of stream filament of revolution
ψ = stream function
ω = angular velocity of blade
(φ, l) = orthogonal coordinates on surface of revolution
(x^1, x^2) = general nonorthogonal coordinates system

Superscript

0 = stagnation state

Subscript

i = at inlet
e = at outlet
1,2 = first and second family of characteristics, respectively

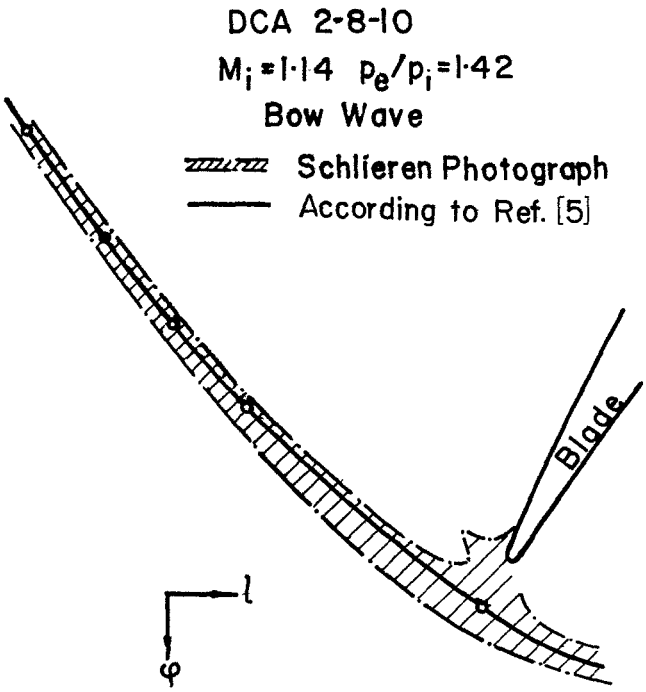

Fig. 2 Comparison between calculation and experiment for bow wave

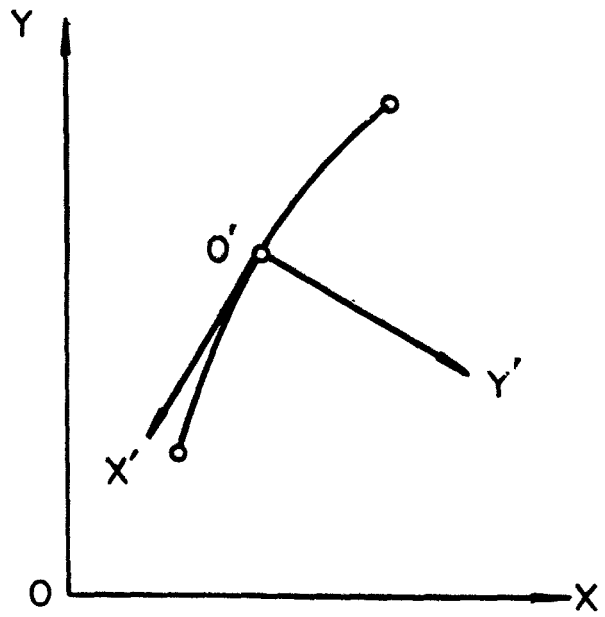

Fig. 3 Rotation of coordinate system for curve fitting

condition far upstream is determined by the use of the set of equations of continuity, momentum, and energy [11]. The inlet flow angle β_i obtained is the unique incidence for the inlet flow Mach number M_i. The unique incidence angles determined for the two inlet Mach number 1.14 and 1.34 are very close to the experimental data. For example, when M_i is 1.34, the calculated inlet flow angle is -62.8 deg, which is very close to the experimental value of -63.1 deg.

At present, experimental data are available only for plane cascade. The present calculation is thus limited to the plane cascade.

Because double circular arc profiles are often used for compressor blade sections with transonic incoming velocities, double circular arc blade profiles, which have different radii of circular arcs at the leading and trailing edge of the blade, also have been programmed in the code. Only a few geometric parameters are needed as the input data; the coordinates of the profile of the blade are calculated in the computer program.

The method of characteristics calculation is programmed as a subroutine. The result of this calculation is stored in a computer file. In this way, the supersonic flow is solved only once in the calculation, whereas the subsonic flow subroutine is repeated many times.

Subsonic Flow Region

The computer program for calculation in the subsonic flow region downstream of the passage shock works with arbitrary nonorthogonal curvilinear coordinates and corresponding nonorthogonal velocity components along the coordinate lines reported in [12, 13]. The advantages of employing this general coordinate system are that it can fit the blade boundary surfaces very well without conformal transformation, the expressions of the boundary conditions are simple and can be satisfied accurately, the spacing of grids can be chosen at will to increase the accuracy of the numerical computation, and grid pattern can be standardized. It may be noted that the velocity at the blade surface is tangent to the blade surface and coincides with the coordinate line, the component corresponding to the other coordinate line is equal to zero, the tangency condition at the solid boundary is thus satisfied exactly.

For the present calculation the use of this general nonorthogonal coordinate system is especially advantageous in that an X^2 coordinate line can be chosen to coincide with the passage shock and is also the inlet boundary of the subsonic flow region, see Fig. 1. It is especially convenient in the procedure of adjustment of the passage shock. The coordinate lines (x^1, x^2) are laid out proportionally in a chosen manner. The computational meshes are formed automatically in the code, and the size of the meshes varies gradually. In order to increase the accuracy of the curve fitting, the rotated coordinate system is used in the procedure of curve fitting, as shown in Fig. 3.

The principal equation for subsonic flow in the terms of the stream function is

$$\frac{1}{a_{11}}\frac{\partial^2\psi}{\partial(x^1)^2} - 2\frac{\cos\theta_{12}}{\sqrt{a_{11}a_{22}}}\frac{\partial^2\psi}{\partial x^1\partial x^2} + \frac{1}{a_{22}}\frac{\partial^2\psi}{\partial(x^2)^2} + \frac{J}{\sqrt{a_{11}}}\frac{\partial\psi}{\partial x^1} + \frac{K}{\sqrt{a_{22}}}\frac{\partial\psi}{\partial x^2} = \mathrm{M}$$

where

$$J = -\frac{\partial\ln(\sqrt{a_{11}/a_{22}}\tau\sin\theta_{12})}{\sqrt{a_{11}}\partial x^1} + \frac{\cos\theta_{12}\partial\ln\tau}{\sqrt{a_{22}}\partial x^2} + \frac{1}{\sin\theta_{12}\sqrt{a_{22}}}\frac{\partial\theta_{12}}{\partial x^2}$$

$$K = -\frac{\partial\ln(\sqrt{a_{22}/a_{11}}\tau\sin\theta_{12})}{\sqrt{a_{22}}\partial x^2} + \frac{\cos\theta_{12}\partial\ln\tau}{\sqrt{a_{11}}\partial x^1} + \frac{1}{\sin\theta_{12}\sqrt{a_{11}}}\frac{\partial\theta_{12}}{\partial x^1}$$

$$\mathrm{M} = \left(\frac{1}{\sqrt{a_{11}}}\frac{\partial\ln\rho}{\partial x^1} - \frac{\cos\theta_{12}}{\sqrt{a_{22}}}\frac{\partial\ln\rho}{\partial x^2}\right)\frac{1}{\sqrt{a_{11}}}\frac{\partial\psi}{\partial x^1} + \left(\frac{1}{\sqrt{a_{22}}}\frac{\partial\ln\rho}{\partial x^2} - \frac{\cos\theta_{12}}{\sqrt{a_{11}}}\frac{\partial\ln\rho}{\partial x^1}\right)\frac{1}{\sqrt{a_{22}}}\frac{\partial\psi}{\partial x^2} - 2\omega\tau\rho\sin\sigma\sin^2\theta_{12} + (\tau\rho\sin\theta_{12})^2\left(\frac{\partial\psi}{\partial x^2}\right)^{-1}\left(\frac{\partial I}{\partial x^2} - T\frac{\partial s}{\partial x^2}\right)$$

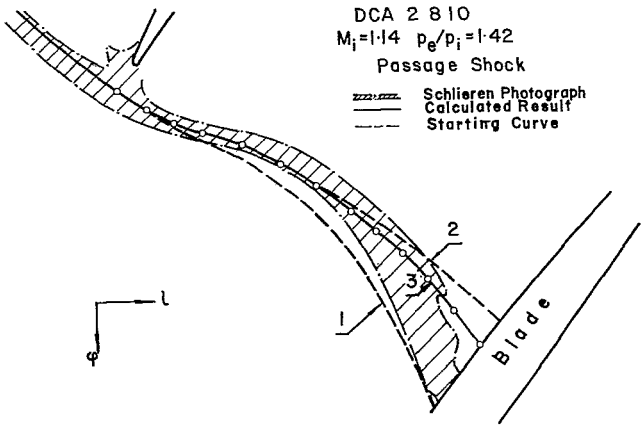

Fig. 4 Comparison between calculated and experimental passage shock

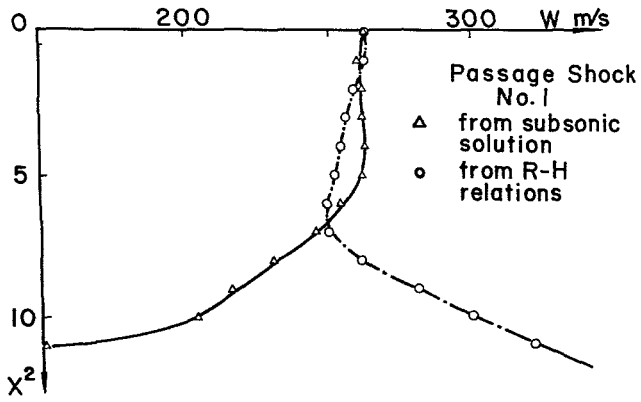

(a) Velocity W

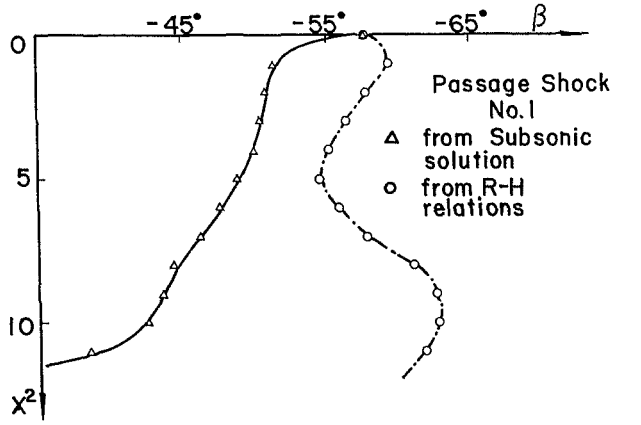

(b) Flow direction β

Fig. 5 Comparison between result calculated by R-H relations and result obtained in subsonic solution

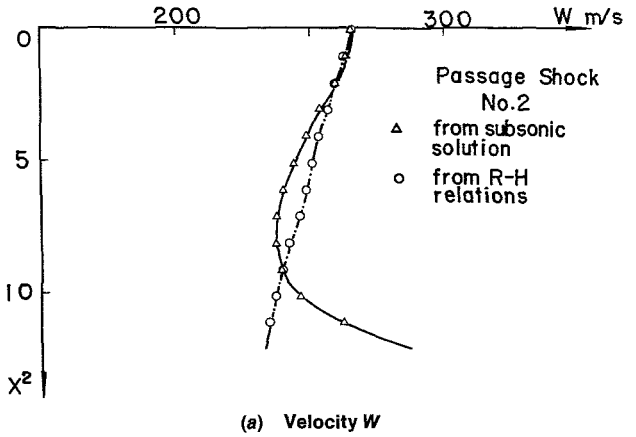

(a) Velocity W

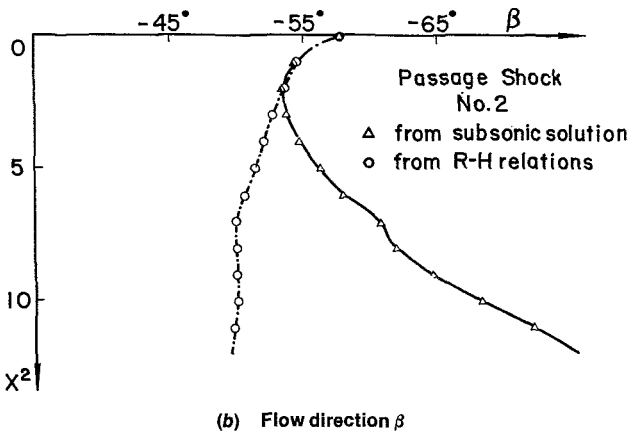

(b) Flow direction β

Fig. 6 Comparison between result calculated by R-H relations and result obtained in subsonic solution

When the fluid flows through the bow shock and passage shock, the intensities of the shock wave are different at the different points and the increases of entropy are also different. The entropy gradient term is taken into account in the calculation throughout the whole subsonic region.

The boundary conditions are:

(*i*) Dirichlet boundary condition at the boundaries of the blade surface and the passage shock. The values of the stream function along the passage shock are obtained from the calculated result of the supersonic region and are taken to be the stream function values along the inlet station of the subsonic region.

(*ii*) Periodical condition in the region downstream of the blade

(*iii*) Neumann boundary condition at the outlet station

Due to the influence of viscosity in real flow, the circulating flow past the blade cascade without separation is an approximate model. Although the solution obtained is comparable to the experimental value over most of the flow region, the effect of the separated wake, usually existing near the trailing edge of the blade, on the flow, especially on the outlet flow direction cannot be neglected. In order to determine the outlet flow angle affected by viscosity, the generalized Kutta-Joukowsky condition is used; namely, the velocities on the two blade surfaces near the trailing edge should be approximately equal. In typical applications, the difference between the outlet flow angle calculated in this way and the experimental data is less than 1 deg [14].

The derivatives in the stream function equation are replaced by central nine-point difference scheme, and the difference equation is solved by matrix method, as was done previously in the subsonic S_1 computer code [13].

Shock Fitting

To define the location and shape of the passage shock (the dividing line of the supersonic and subsonic flow regions) clearly and accurately is an important part of the present method.

According to the calculation for the supersonic flow and the assumed location and shape of the passage shock, the Mach number just upstream of the shock, M_u, and the angle included by the shock and incoming flow, α, are determined completely. Then the turning angle across the shock, δ, Mach number just downstream of the shock, M_d, and the pressure

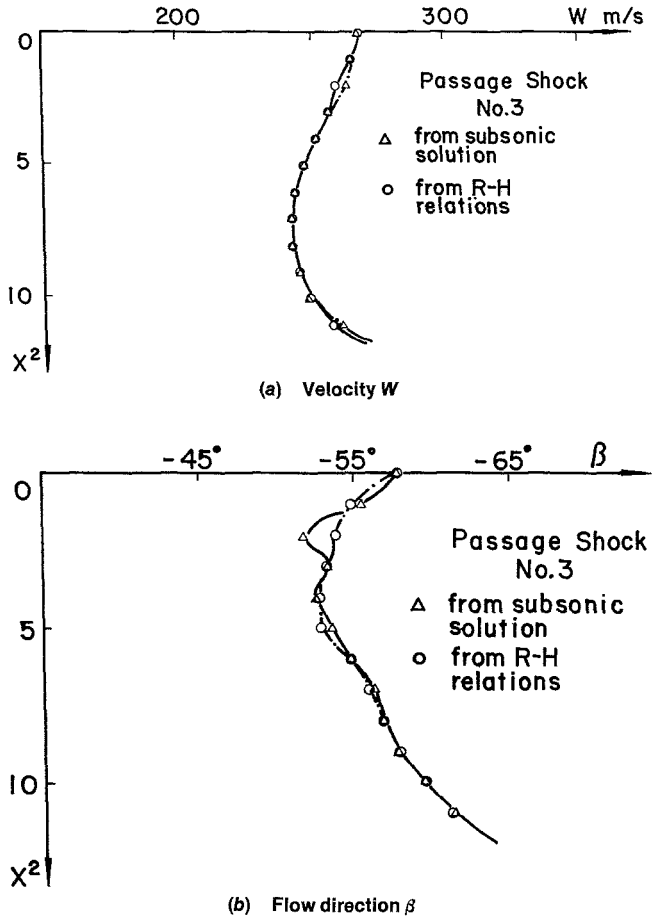

Fig. 7 Comparison between result calculated by R-H relations and result obtained in subsonic solution

ratio across the shock, p_d/p_u, density ratio, ρ_d/ρ_u, and entropy change, $s_d - s_u$, etc. are calculated by the Rankine-Hugoniot relations. If the assumed location and shape of the passage shock are correct, these calculated values of aerothermodynamic quantities just downstream of the shock and those obtained in the solution of the subsonic flow at the inlet boundary must be the same. Based upon this condition, the correct location and shape of the shock can be obtained in the following two ways:

(*i*) Manual interaction between designer and computer. Calculation is started with an assumed location and shape of the passage shock. Separate calculations for the supersonic flow and the subsonic flow regimes are performed. If the obtained results are not consistent with the Rankine-Hugoniot relations, the location and shape of passage shock are adjusted. When agreement between the two is obtained, the location and shape of the shock are the correct ones. The process of correction is indicated in Figs. 4–7. When the assumed shock marked No. 1 was used, there was a big difference between the results obtained in the subsonic solution of the stream function equation and values calculated just downstream of the shock by the Rankine-Hugoniot relations, especially velocity, W, and flow direction, β. It is obvious that the location and shape of the assumed shock No. 1 are not correct. Next, passage shock No. 2 was assumed. The agreement was similarly very poor. The correct location and shape of the passage shock finally obtained is the one labeled No. 3.

With a little experience it is not difficult to adjust the location and shape of the passage shock and the total computational time is short.

(*ii*) Automatic correction by the computer. An automatic correction process is incorporated in the code. The initial location and shape of the passage shock can be assumed rather arbitrarily. Then the location and shape will be adjusted automatically until it becomes the correct one. A typical result is shown in Fig. 8. In order to examine the ability of automatic adjustment built into the program, initial locations and shapes which are far from the correct ones and located on both sides of the correct position were intentionally specified. Both of them automatically converged to the correct one.

In the case of manual correction, because of the designer's experience and judgment, convergence time is less than that in automatic correction. However, the latter method gives higher accuracy. On the UNIVAC 1100, computer, computation time for suspersonic region with 90×20 mesh points is less than 2 min, and for subsonic region with 13×40 mesh points, computation time for each iteration is less than 1 min. To obtain the convergent result, the total computation time is about 10 min.

It is a major feature of the present method that the location and shape of the passage shock are determined accurately in the code. The correct jump of the aerothermodynamic variables of flow across the passage shock can thus be obtained.

Typical Computational Results

Two typical computations are included in this paper. The geometrical parameters of the DFVLR DCA 2-8-10 cascade, which is used in the calculations, are as follows:

chord length:	$C = 90$ mm
radius of leading edge circle/chord:	$r_l/C = 0.003$
radius of trailing edge circle/chord:	$r_t/C = 0.009$
maximum thickness of blade/chord:	$h_{max}/C = 0.06$
pitch/chord:	$t/C = 0.85$
stagger angle:	55 deg
camber angle:	10 deg

Example 1: The inlet Mach number M_i is 1.14 and the outlet/inlet pressure ratio, p_e/p_i, is 1.42. The result of calculation is shown in Figs. 1, 2, 4–7.

Example 2: $M_i = 1.34$ and $p_e/p_i = 1.62$. The passage shock wave was corrected by the two methods mentioned in the preceding section. The result of calculation is shown in Figs. 8–12.

The experimental locations and shapes of the bow wave and the passage shock are also shown in the Figs. 1, 2, 4, and 8. As usual, the bow wave and passage shock in the Schlieren photographs are not sharp curves but are smeared over a few grid points. A great part of the calculated shock wave is seen to lie within the experimental band, only a very small portion of the passage shock near the suction surface of the blade lies outside the experimental band. This difference is very likely due to the interaction between the passage shock and boundary layer over the blade surface, which was not taken into account in the calculation. It is interesting to note that the two very different passage shocks, which were assumed at the start of computation, all led to practically the same one after convergence was reached.

The distribution of streamlines and variations of a number of flow variables on the blade surfaces and along the mean streamline obtained in the calculation of second case (M_i = 1.34) are shown in Figs. 9–12. The abrupt changes in the

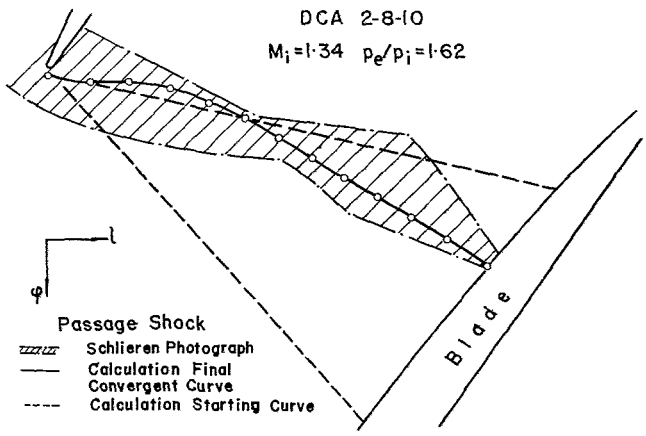

Fig. 8 Comparison between calculated and experimental passage shock

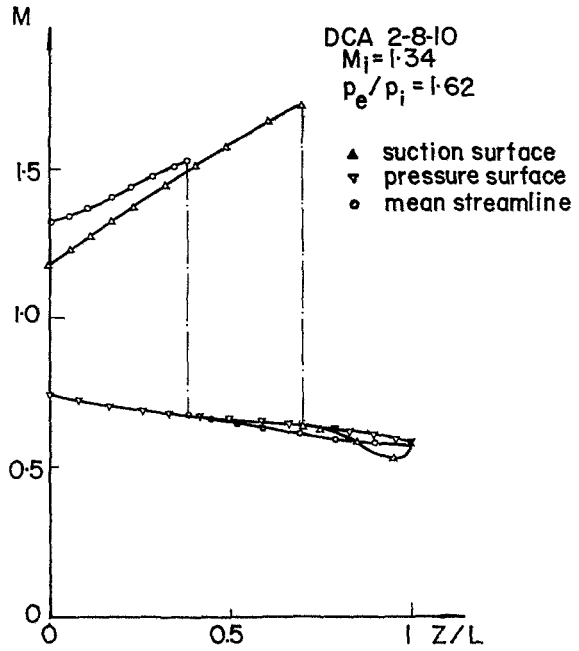

Fig. 9 Variation of Mach number on blade surface and along mean streamline

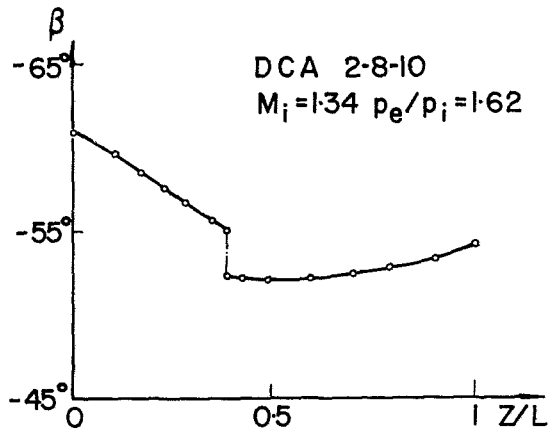

Fig. 10 Variation of flow angle along mean streamline

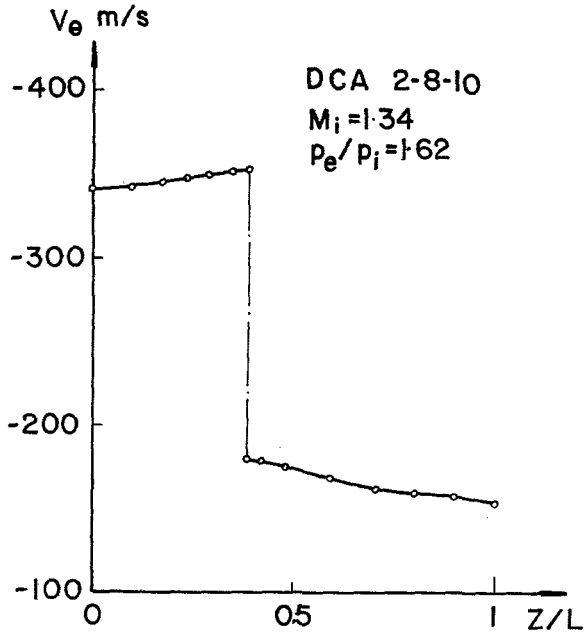

Fig. 11 Variation of V_e along mean streamline

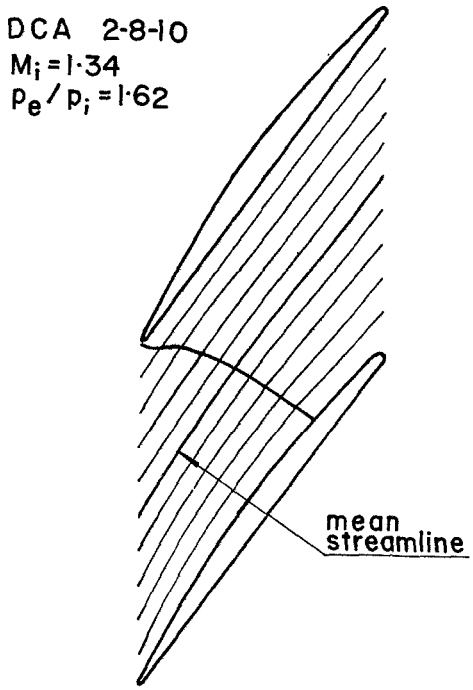

Fig. 12 Streamlines in the passage of blade

streamline direction, the flow angle, and the normal distance between streamlines (or in other words, the thickness of stream sheet) can be seen clearly in Figs. 10 and 12. It may also be noted that there is an overturning of the flow in passing the passage shock similar to the one first noticed in the design computation of CAS transonic rotor [15]. The variation of Mach number shown in Fig. 9 indicates that, in the flow, air accelerates upstream of the passage shock, and that the flow decelerates mainly through the passage shock. Figure 11 shows that the change in tangential velocity in the transonic cascade occurs mainly through the passage shock.

Concluding Remarks

A method incorporating separate computation methods, for the supersonic regime (method of characteristics) and subsonic regime (matrix method) has been developed for calculating the flow in a transonic cascade. The cascade blade

has blunt leading edge and blunt trailing edge. An empirical method is used for the location and shape of the detached bow wave, whereas the passage shock is successively corrected in the calculation until the flow quantities on the two sides of it satisfy the Rankine-Hugoniot relations. Computation for DFVLR DCA cascade with inlet Mach number of 1.14 and 1.34 takes about 10 min on a UNIVAC 1100 computer with a 90×20 mesh in the supersonic region and with a 13×40 mesh in the subsonic region.

The result of calculation by this method provides accurate detailed information about the flow through the blade cascade. The jumps of the flow variables across the shock are properly determined. From these results it may be concluded that, for an accurate determination of either direct or indirect problem of the transonic flow on an S_1 or S_2 stream surface, the jumps across the shock wave in the flow direction, stream sheet thickness, and angular momentum about the machine axis should be properly taken into account in the calculation.

The method presented can be easily applied to calculate the transonic flow in a nozzle or diffuser having an embedded shock. It may also be extended to the calculation of transonic flow on an S_1 surface of revolution or an S_2 surface with a single or two embedded shocks.

It is found that the arbitrary nonorthogonal coordinate system employed in the code for the subsonic flow region is very helpful. Not only the boundary of the blade but also the passage shock can be selected as coordinate lines. The calculation mesh can be formed proportionally and automatically. It is especially suitable in the process of correcting the passage shock. The passage shock obtained is clearly defined and agrees quite well with the experimental data.

References

1 Wu, C. H., Wu, W. Q., Hua, Y. N., and Wang B. G., "Transonic Cascade Flow With Given Shock Shapes Solved by Separate Subsonic and Supersonic Computation," Paper No. 832070, 4th annual meeting Chinese Society of Engineering Thermophysics, Xian, Oct. 1983.

2 Joukowsky, M. I., "Calculation of Flow Through a Cascade of Blades and Design of Cascade From a Given Velocity Distribution" (in Russian), *CKTI*, Vol. 27, 1954.

3 Wu, C. H., and Costelow, E. L., "A Method of Solving the Direct and Inverse Problem of Supersonic Flow Along Arbitrary Stream Filament of Revolution in Turbomachines," NACA TN 2492, 1951.

4 Liu, C. E., and Wu, W. Q., "Computer Program of Supersonic Flow Past Inlet of Cascade Section on an Arbitrary Stream Filament of Revolution and Determining Unique Inlet Flow Angle," *Journal of Engineering Thermophysics*, Vol. 1, No. 3, 1980.

5 Moeckel, W. E., "Approximate Method for Predicting Form and Location of Detached Shock Waves Ahead of Plane or Axially Symmetric Bodies," NACA TN 1921, 1949.

6 Love, E. S., "A Reexamination of the Use of Simple Concepts for Predicating the Shape and Location of Detached Shock Waves," NACA TN 4170, Dec. 1957.

7 York, R. E., and Woodard, H. S., "Flow in the Entrance Region of Supersonic Compressor Cascades," ASME JOURNAL OF ENGINEERING FOR POWER, Apr. 1976, pp. 247–257.

8 Ruan, Z. K., "Experimental Determination of Shape and Location of Bow Shock Wave Ahead of a Plane Cascade," *Journal of Engineering Thermophysics*, Vol. 4, No. 4, 1983.

9 Hua, Y. N., "An Extended Calculation of Detached Bow Wave Ahead of Plane Cascade," Paper No. 832072, 4th Annual Meeting, *Chinese Society of Engineering Thermophysics*, Xian, Oct. 1983.

10 Starken, H., "Untersuchung der stromung in ebenen Uberschall-Verzogerungsgittern," DLR FB 71-99, DFVLR Institute fur Luftstrahlantriebe, 1971.

11 Wu, Wen Quan, Zhu, Rong Guo, and Liu, Cai E., "Computational Design of Turbomachine Blades," *Proceedings of 4th International Symposium on Air Breathing Engines*, Orlando, Fla. Apr. 1979; also, *AIAA, Journal of Aircraft*, Vol. 17, No. 5, May 1980.

12 Wu, C. H., "Three-Dimensional Turbomachine Flow Equations Expressed With Respect to Non-Orthogonal Curvilinear Coordinates and Methods of Solution," Lecture Notes, China University of Science and Technology, 1975; also *Proceedings of 3rd International Symposium on Air Breathing Engines*, March, 1976, Munich, West Germany.

13 Wu, W. Q., and Liu, C. E., "Flow-Field Matrix Solution for Direct Problem of Flow Along S_1 Relative Stream Surface Employing Nonorthogonal Curvilinear Coordinates and Corresponding Nonorthogonal Velocity Components," *Journal of Engineering Thermophysics*, Vol. 1, No. 1, 1980.

14 Wu, S. L., and Wu, W. Q., "The Determination of Outlet Flow Angle for Flow Past Cascade on Arbitrary Surface of Revolution, Research Report," Institute of Mechanics, Academia Sinica, 1968 (to be published in *Chinese Journal of Engineering Thermophysics*).

15 Chinese Academy of Sciences and Shenyang Aeroengine Company, "Theory, Method and Application of Three-Dimensional Flow Design of Transonic Axial-Flow Compressor," *Journal of Engineering Thermophysics*, Vol. 1, No. 1, 1980.

has blunt leading edge and blunt trailing edge. An empirical method is used for the location and shape of the detached bow wave, whereas the passage shock is successively corrected in the calculation until the flow quantities on the two sides of it satisfy the Rankine-Hugoniot relations. Computation for DFVLR DCA cascade with inlet Mach number of 1.14 and 1.34 takes about 10 min on a UNIVAC 1100 computer with a 90 × 20 mesh in the supersonic region and with a 13 × 40 mesh in the subsonic region.

The result of calculation by this method provides accurate detailed information about the flow through the blade cascade. The jumps of the flow variables across the shock are properly determined. From these results it may be concluded that, for an accurate determination of either direct or indirect problem of the transonic flow on an S_1 or S_2 stream surface, the jumps across the shock wave in the flow direction, stream sheet thickness, and angular momentum about the machine axis should be properly taken into account in the calculation.

The method presented can be easily applied to calculate the transonic flow in a nozzle or diffuser having an embedded shock. It may also be extended to the calculation of transonic flow on an S_1 surface of revolution or an S_2 surface with a single or two embedded shocks.

It is found that the arbitrary nonorthogonal coordinate system employed in the code for the subsonic flow region is very helpful. Not only the boundary of the blade but also the passage shock can be selected as coordinate lines. The calculation mesh can be formed proportionally and automatically. It is especially suitable in the process of correcting the passage shock. The passage shock obtained is clearly defined and agrees quite well with the experimental data.

References

1 Wu, C. H., Wu, W. Q., Hua, Y. N., and Wang B. G., "Transonic Cascade Flow With Given Shock Shapes Solved by Separate Subsonic and Supersonic Computation," Paper No. 832070, 4th annual meeting Chinese Society of Engineering Thermophysics, Xian, Oct. 1983.

2 Joukowsky, M. I., "Calculation of Flow Through a Cascade of Blades and Design of Cascade From a Given Velocity Distribution" (in Russian), *CKTI*, Vol. 27, 1954.

3 Wu, C. H., and Costelow, E. L., "A Method of Solving the Direct and Inverse Problem of Supersonic Flow Along Arbitrary Stream Filament of Revolution in Turbomachines," NACA TN 2492, 1951.

4 Liu, C. E., and Wu, W. Q., "Computer Program of Supersonic Flow Past Inlet of Cascade Section on an Arbitrary Stream Filament of Revolution and Determining Unique Inlet Flow Angle," *Journal of Engineering Thermophysics*, Vol. 1, No. 3, 1980.

5 Moeckel, W. E., "Approximate Method for Predicting Form and Location of Detached Shock Waves Ahead of Plane or Axially Symmetric Bodies," NACA TN 1921, 1949.

6 Love, E. S., "A Reexamination of the Use of Simple Concepts for Predicating the Shape and Location of Detached Shock Waves," NACA TN 4170, Dec. 1957.

7 York, R. E., and Woodard, H. S., "Flow in the Entrance Region of Supersonic Compressor Cascades," ASME JOURNAL OF ENGINEERING FOR POWER, Apr. 1976, pp. 247–257.

8 Ruan, Z. K., "Experimental Determination of Shape and Location of Bow Shock Wave Ahead of a Plane Cascade," *Journal of Engineering Thermophysics*, Vol. 4, No. 4, 1983.

9 Hua, Y. N., "An Extended Calculation of Detached Bow Wave Ahead of Plane Cascade," Paper No. 832072, 4th Annual Meeting, *Chinese Society of Engineering Thermophysics*, Xian, Oct. 1983.

10 Starken, H., "Untersuchung der stromung in ebenen Uberschall-Verzogerungsgittern," DLR FB 71-99, DFVLR Institute fur Luftstrahlantriebe, 1971.

11 Wu, Wen Quan, Zhu, Rong Guo, and Liu, Cai E., "Computational Design of Turbomachine Blades," *Proceedings of 4th International Symposium on Air Breathing Engines*, Orlando, Fla. Apr. 1979; also, *AIAA, Journal of Aircraft*, Vol. 17, No. 5, May 1980.

12 Wu, C. H., "Three-Dimensional Turbomachine Flow Equations Expressed With Respect to Non-Orthogonal Curvilinear Coordinates and Methods of Solution," Lecture Notes, China University of Science and Technology, 1975; also *Proceedings of 3rd International Symposium on Air Breathing Engines*, March, 1976, Munich, West Germany.

13 Wu, W. Q., and Liu, C. E., "Flow-Field Matrix Solution for Direct Problem of Flow Along S_1 Relative Stream Surface Employing Nonorthogonal Curvilinear Coordinates and Corresponding Nonorthogonal Velocity Components," *Journal of Engineering Thermophysics*, Vol. 1, No. 1, 1980.

14 Wu, S. L., and Wu, W. Q., "The Determination of Outlet Flow Angle for Flow Past Cascade on Arbitrary Surface of Revolution, Research Report," Institute of Mechanics, Academia Sinica, 1968 (to be published in *Chinese Journal of Engineering Thermophysics*).

15 Chinese Academy of Sciences and Shenyang Aeroengine Company, "Theory, Method and Application of Three-Dimensional Flow Design of Transonic Axial-Flow Compressor," *Journal of Engineering Thermophysics*, Vol. 1, No. 1, 1980.

DISCUSSION

H. Starken[1]

In this paper a method is presented to calculate the inviscid flow through transonic compressor cascades. This is a valuable step in the development of theoretical methods to predict the real flow behavior. However, the results are still far from reality because the neglected viscous effects are dominant in the subsonic regions of transonic cascade flows. This can be clearly seen in the Schlieren picture corresponding to the flow case of Fig. 9 and shown in Fig. 13. A severe boundary layer separation is caused by the passage shock which leads to a reacceleration and a second normal shock wave. The measured blade Mach number distribution and the exit flow conditions are therefore considerably different in the calculation and the experiment as shown in Fig. 14. Therefore, I do not agree with the concluding remark of the paper: "The result of calculation by this method provides accurate detailed information about the flow through the blade cascade." Theoretical solutions in this velocity range have to account for viscosity effects in order to be reasonably accurate.

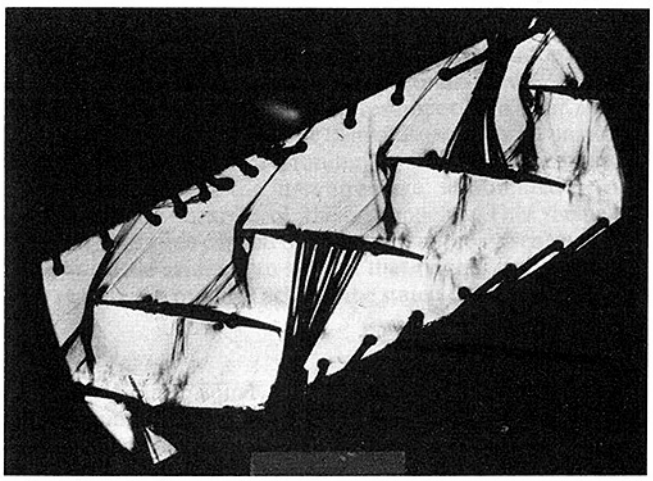

Fig. 13 Schlieren picture of the cascade DCA 2-8-10 at $M_1 = 1.34$ [10]

[1] DFVLR, Köln, Germany

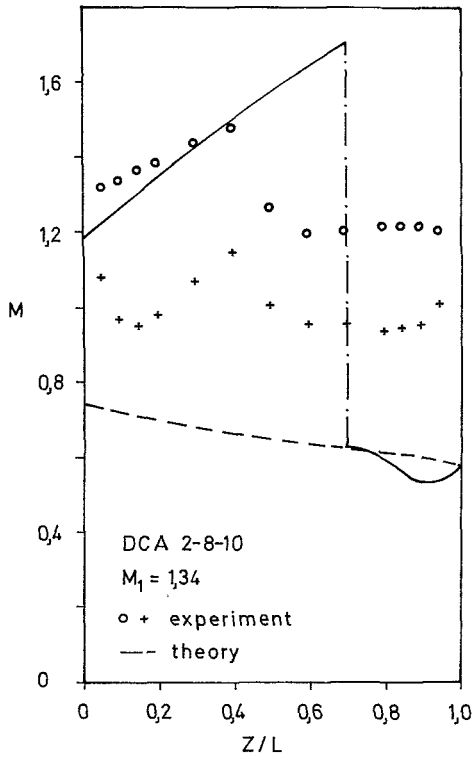

Fig. 14 Theoretical and experimental surface Mach number distribution of the DCA 2-8-10 cascade

An Inviscid Blade-to-Blade Prediction of a Wake-Generated Unsteady Flow

H. P. Hodson
Whittle Laboratory,
Cambridge University Engineering Department,
Cambridge, U.K.

This paper describes a time-marching calculation of the unsteady flow generated by the interaction of upstream wakes with a moving blade row. The inviscid equations of motion are solved using a finite volume technique. Wake dissipation is modeled using an artificial viscosity. Predictions are presented for the rotor mid-span section of an axial turbine. Reasonable agreement is found between the predicted and measured unsteady blade surface static pressures and velocities. These and other results confirm that simple theories can be used to explain the phenomena of rotor-stator wake interactions.

Introduction

Recently published experimental results (e.g. [1], [2]) have shown that the effects of blade row interactions should not be disregarded when designing axial-flow turbines and that particular attention should be given to the effects of wake-generated unsteadiness. It is desirable to be able to predict these effects, especially when the blade row of interest is a rotor, since it will always be difficult to make measurements in the rotating frame of reference.

Unsteady flows can be computed using either linearized small perturbation theories (e.g. [3]), or by marching the solution of the nonlinear equations of motion in time. In the past, linearized methods have been preferred because they are computationally more efficient. Time-marching, on the other hand, possesses a significant advantage over linearized methods of solution, that is, its ability to deal easily with large, nonlinear disturbances such as wakes and shock waves. This paper describes a time-marching calculation procedure which has been used to predict the wake-generated unsteady flow in an axial-flow turbine, thus providing further insight into the mechanisms of wake interactions.

One of the earliest attempts at predicting wake-generated unsteadiness was made by Farn and Whirlow [4]. Unfortunately, apart from stating that they solved the *inviscid* equations of motion, very little information is given. They did, however, note that the demands upon computational resources are greatly increased when, as is commonplace, the number of upstream blades is not an integer multiple of those in the blade row of interest.

Mitchell [5] has described a similar technique in which the calculation was restricted to a single blade row. The wakes were provided by imposing, at the upstream boundary, the changes of incidence and velocity which were associated with the wakes of the upstream blade row. Potential interactions were thus excluded. Because the computational domain was restricted to a single blade passage, he applied a time-dependent periodicity condition [6] upstream of the blade row. Downstream, however, he was forced to apply a time-*in*dependent periodicity condition.

Ispas et al. [7] avoided the problem of applying time-dependent periodicity conditions by extending the computational domain to include the number of blade passages over which the flow pattern repeated. Potential interactions were again excluded and, surprisingly, the flow was assumed to be isentropic. A comparison with experimental data showed that the predicted unsteady pressures were similar in magnitude but significantly different in phase to their measured counterparts.

As an alternative to the above methods, Krammer [8] describes a time-marching scheme in which the unsteady potential flow equation was coupled to a discrete vortex representation of the wake. He only considered the case of an equal number of stator and rotor blades and quantitative agreement with experimental data was only fair.

All of the schemes described in references [4] to [8] attempt to solve the inviscid equations of motion. The scheme described in this paper is also inviscid. The reasons for this are twofold. Firstly, unsteady flow computations require significantly more computational resources than their steady flow equivalents, therefore the demands made by an unsteady viscous scheme would be prohibitive. Secondly, the inviscid schemes described in the literature have, to a limited extent, been successful in spite of their simplicity. This theme of simplicity has been carried over into the author's scheme since there was little evidence to suggest that further complications were required in order to achieve the stated objective.

Equations

The two-dimensional inviscid equations of motion are solved using a finite volume scheme based upon that of Denton [9]. Following reference [9], the equations of motion are written in conservation form, for an elemental control volume ΔV and a time increment Δt to give

Contributed by the Gas Turbine Division of THE AMERICAN SOCIETY OF MECHANICAL ENGINEERS and presented at the 29th International Gas Turbine Conference and Exhibit, Amsterdam, The Netherlands, June 4-7, 1984. Manuscript received at ASME Headquarters December 27, 1983. Paper No. 84-GT-43.

Mass $$\Delta\rho = \sum_n (\rho \mathbf{u} \cdot d\mathbf{A}) \Delta t / \Delta V \quad (1)$$

x-momentum

$$\Delta(\rho u_x) = \sum_n (p dA_x + \rho u_x \mathbf{u} \cdot d\mathbf{A}) \Delta t / \Delta V \quad (2)$$

y-momentum

$$\Delta(\rho u_y) = \sum_n (p dA_y + \rho u_y \mathbf{u} \cdot d\mathbf{A}) \Delta t / \Delta V \quad (3)$$

Entropy $$\Delta(\rho s) = \sum_n (\rho s \mathbf{u} \cdot d\mathbf{A}) \Delta t / \Delta V \quad (4)$$

where $d\mathbf{A}$ is the inward normal vector representing the areas of the n surfaces of the elemental control volume. Closure of these equations is provided by the usual perfect gas relations, namely

$$p = \rho R T \quad (5a)$$

$$s - s_1 = c_p \ln(T/T_{01}) - R \ln(p/p_{01}) \quad (5b)$$

Because an equation for the conservation of entropy is used rather than one for the conservation of energy (for which an acceptable and stable scheme could not be devised [9]) the solution is ideally restricted to shock-free flows although in practice, weak shocks can be predicted without a significant loss of accuracy.

The Grid

The finite volume elements are formed by pitchwise and quasi-streamwise lines, the spacings of which do not have to be uniform. The grid is, therefore, identical to that used by Denton [9]. It is illustrated in Fig. 1. The nodes are located at the corners of the element and the fluxes of mass, momentum, and entropy through the faces of the element, as well as the pressure forces acting upon it, are determined using the average values of the flow properties which are stored at the nodes. These fluxes and forces are then used to evaluate the changes in mass, momentum, and entropy within the control volume during each time increment Δt.

The Differencing Scheme

Stability of the scheme is achieved by applying the changes in density within the control volumes to the upstream nodes of the element, with the remaining differences $\Delta(\rho s)$, $\Delta(\rho u_x)$ and $\Delta(\rho u_y)$ being sent downstream. It is also necessary to update the static pressures using the new values of density and entropy before the momentum changes are evaluated. This differencing scheme is, therefore, similar to Denton's scheme "B" [9] and as such, it permits the solution of problems where the stagnation point is located on the pressure surface with reversed flow around the leading edge. Unfortunately, it is also unstable when the axial Mach number exceeds unity.

There are two weaknesses of this basic differencing scheme. Firstly, like all explicit single-step schemes, it is first order accurate in time. However, the results of reference [2] suggest that the wake-generated unsteadiness is dominated by convected phenomena. If this is so and if the Mach numbers are low, then the errors which result from forward differencing in time will not significantly affect the solution. This is because the C.F.L. criterion will ensure that the time-scale for the transmission of convected phenomena is much greater than the length of the time step.

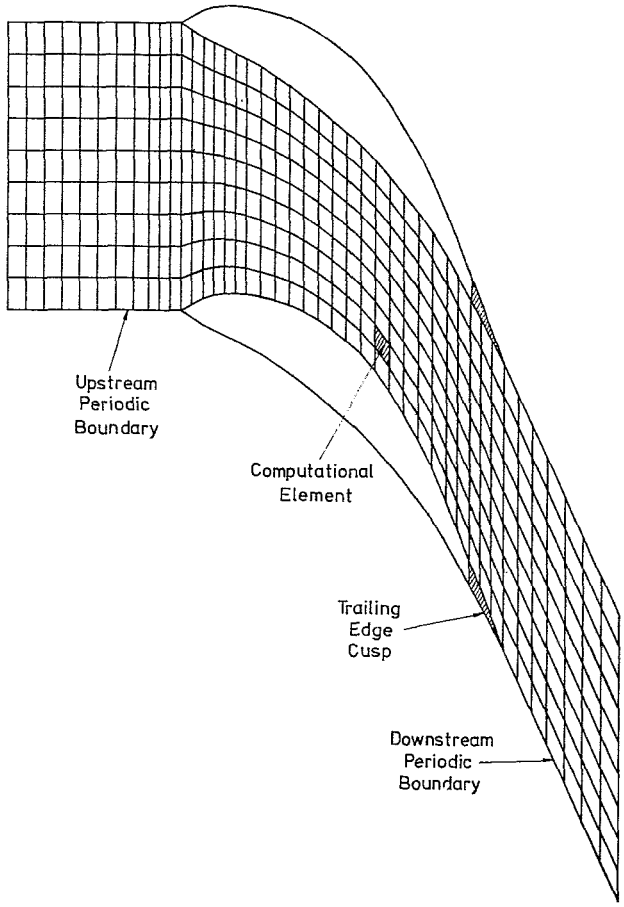

Fig. 1 Computational mesh

The second error arises because in unsteady flow, the scheme has only first order accuracy in the axial direction. Errors of the order of Δx are clearly unacceptable. They have therefore been minimized by sending only a fraction $(1-F)$ of the changes in density to the upstream nodes, with the remainder F being sent downstream. The opposite applies for the changes in ρs, ρu_x and ρu_y. The error is therefore reduced to the order of $(1-2F)\Delta x$ and the accuracy is improved so that is better than first but still less than second order. Typically, the value of F is set to 0.4.

Time-Step Limitations

As with all explicit time-marching methods, the theoretical maximum time step is related to the C.F.L. condition, which states that information (e.g. pressure waves) cannot travel

Nomenclature

a = sound speed
C = chord
c_p = specific heat capacity at constant pressure
p = pressure
R = gas constant
s = surface distance, entropy
T = temperature
t = time
u, U = velocity
U_m = mean blade velocity
V = volume
x = axial distance
y = tangential distance
ρ = density
Δ = amplitude of

Subscripts and Superscript

0 = stagnation
1 = inlet (relative)
2 = exit (relative)
∞ = free stream
le = leading edge
x = axial
y = tangential
$-$ = mean

more than one mesh spacing during one time increment. In practice, this criterion reduced to

$$\Delta t < \left| \frac{\Delta x}{a \pm u_x} \right| \quad \text{and} \quad \left| \frac{2\Delta y}{a \pm u_y} \right| \tag{6}$$

which must be satisfied for each and every element.

Boundary Conditions

To a large extent, the usual requirements regarding the application of unsteady boundary conditions at the inlet and exit planes of the computational domain have been ignored and at these boundaries, the true time dependency of the equations is modeled only approximately. This is because it appeared from an inspection of the available experimental data (e.g. [2] and [10]), that the flow field is dominated by convective rather than pressure wave-type phenomena. For this reason, the potential interactions of adjacent blade rows have also been ignored. Only wake generated unsteadiness is allowed to exist.

At the inlet boundary, the wake is assumed to have a velocity profile $U(y')$ in the wake-relative frame of reference which is given by

$$\frac{U_\infty - U(y')}{U_\infty} = \frac{(U_\infty - U)_{\max}}{U_\infty} \cdot \left[1 - \left[\frac{y'}{b}\right]^{3/2}\right]^2 \tag{7}$$

where y' is the pitchwise distance from the center-line of the wake and b is the half width of the wake. During the calculation, the wake is moved across the inlet boundary at the relative blade speed.

In steady flow calculations with subsonic inflow, it is usual to specify the stagnation pressure, stagnation temperature and relative flow angle at the upstream boundary of the computational domain. The application of the same boundary conditions in unsteady flow would mean that the velocity profile of the wake would be obtained as part of the solution and not specified as a boundary condition. In view of this, it was decided to specify, at the inlet boundary, the stagnation temperature, which is assumed to be constant in the wake-relative frame of reference, the relative flow angle and the mass-flow per unit area ρu_x. Specification of the mass flow and angle is not identical to specification of the velocity profile, but the variation in density along the inlet boundary will usually be sufficiently small so as to make this difference insignificant. The inlet boundary conditions are equivalent to having a choked blade row upstream of the computational domain. At the exit boundary of the computational domain, a constant and uniform static pressure is specified, which is equivalent to the flow exhausting into a large duct or chamber.

At the inlet and exit boundaries, it is assumed, incorrectly, that the second derivative of the flow properties is equal to zero in the axial direction. A similar assumption has been made at the blade surfaces, where the properties on the blade surface are updated using only the changes which occur within the elements adjacent to the surface. This is, of course, in addition to the imposed tangency condition, which requires that there is no flow through the surface.

A cusp is fitted to the trailing edge of the blade (see Fig. 1). This is because it is felt that a cusped trailing edge is a better approximation to the real viscous flow than is a blunt trailing edge. For simplicity no cusp is required at the leading edge.

Downstream of the blade, a slip-stream should be provided. The provision of such a contact surface requires the calculation of the position of the slip-stream (which usually forms the upper and lower periodic boundaries) at each time level, thus increasing the complexity of the scheme. In order to avoid this, the same periodicity condition is applied both upstream and downstream of the blade row. This means that vorticity can still be shed from the blade but that the vortex sheet becomes smeared over a few grid points.

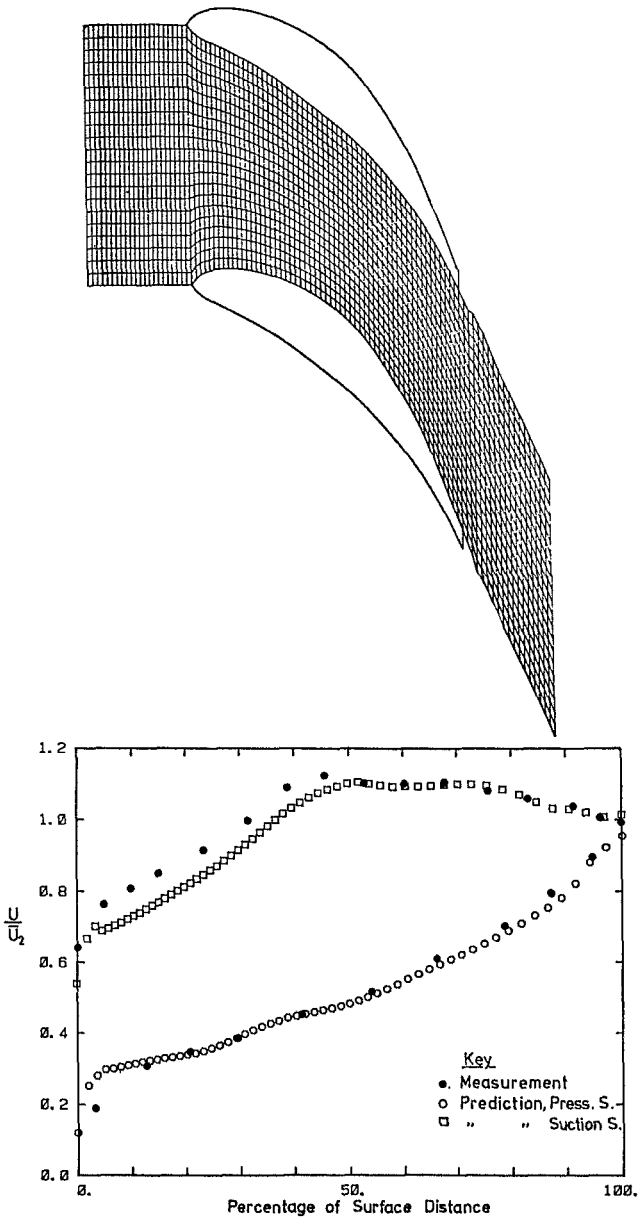

Fig. 2 Blade surface velocity distributions at the mid-span of the Cambridge no. 2 turbine rotor

Usually, the number of upstream blades will not be an integer multiple of the number of blades in the blade row of interest. The periodicity condition used in steady flow must therefore be modified. Ispas et al. [7] avoided the problem by solving the flow throughout the number of blade passages for which the flow repeated. This is extremely costly in terms of CPU memory and time. It was therefore decided to use the method described by Erdos and Alzner [6]. This involves the application of time-lagged periodic boundary conditions to the computation domain of Fig. 1. The method requires the storage of sufficient information to define the flow at one or other of the periodic boundaries at all of the time levels which occur in the wake passing cycle. It is not possible to describe the technique in detail within the space available. The reader is therefore recommended to read the excellent description of the method which is contained in reference [6].

Denton [9] has pointed out that within the blade passage, there are n quasi-stream lines and $n-1$ elements. The number of equations is therefore less than the number of unknowns and pitchwise smoothing must be applied so that the final

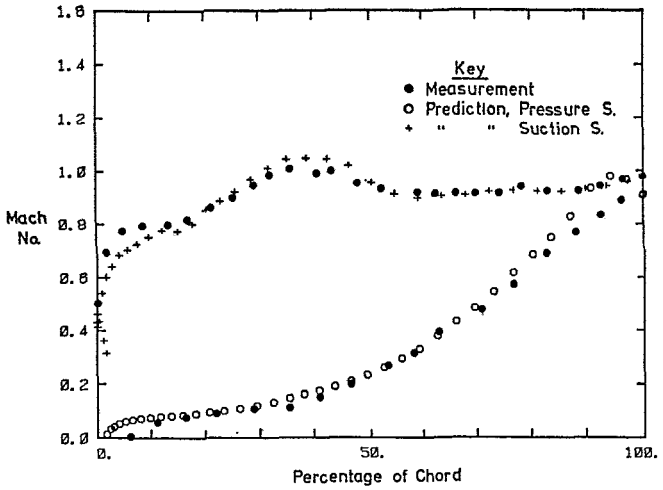

Fig. 3 Blade surface Mach number distribution for the VKI-MacDonald turbine blade

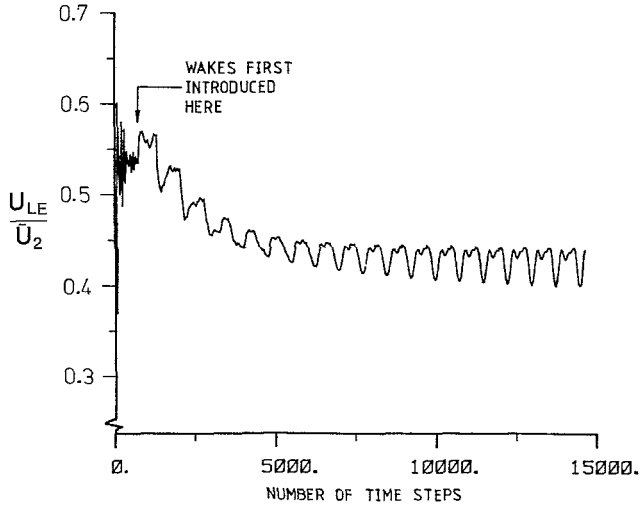

Fig. 4 Convergence of the solution to a periodic state

solution is independent of the initial guess. This smoothing has been retained in the present scheme.

Steady Flow Predictions

In order to demonstrate the accuracy of the present entropy equation scheme, several two-dimensional steady-flow solutions are presented. In calculating the steady flows, the velocity deficit in the wake was set to zero and time-independent periodic boundary conditions were applied.

Figure 2 contains a comparison between the measured and predicted surface velocity distributions of the mid-span section of a turbine rotor for which an unsteady prediction has also been made. The computational mesh is also shown. For the purpose of calculating the steady flow, this mesh is much finer than is actually required. The predicted velocity distribution is in excellent agreement with the measurements, except over the leading half of the suction surface, where there is a maximum difference in the measured and predicted values of approximately 10 percent.

Figure 3 shows a comparison between the measured and predicted Mach number distributions of the transonic turbine rotor blade which was tested by Sieverding [11] at VKI. The computational mesh consisted of 61 axial and 10 tangential grid points. The agreement between the predicted and measured values is excellent on both surfaces.

For both of the above test cases, the predicted distributions were identical to those made by the author using Denton's [9] scheme.

Artificial Dissipation of the Wakes

The numerical and artificial viscosities inherent within the numerical scheme have been used to simulate the viscous decay of the wakes. Mitchell [5] used a similar technique. It is, of course, recognized that the use of an artificial viscosity to model the viscous decay is not proper and that a cascade wake correlation might represent a better, albeit more complex, alternative.

A numerical experiment was performed during which wakes were moved across the inlet boundary of a computational domain which was an extended form of the inlet portion of the mesh shown in Fig. 2. This enabled the rate of decay of the wake to be adjusted to the value observed in the actual turbine.

An Unsteady Flow Prediction for a Turbine Rotor

The unsteady prediction which is described below was obtained for the mid-span section of the rotor of the Cambridge No. 2 axial-flow turbine. The reduced frequency ($\bar{\omega} = \omega C_x/2U_x$) of this rotor is equal to 4.5 and the flow is, therefore, unsteady in the true sense with a reduced frequency which is typical of many turbines. The velocity deficit associated with the stator wakes has been found [1] to be equal to 10.5 percent of the mean value in the rotor-relative frame of reference at a plane which is 43 percent of the rotor C_x upstream of the rotor leading edges. Further information on the unsteady flow in this turbine can be found in references [1] and [2].

The steady flow solution for this rotor has been described above. The same mesh (Fig. 2) has been used for the unsteady prediction. It consists of 94 × 22 nodes which would, for a steady flow solution, require approximately 270 kbytes on a 32 bit computer. For the equivalent unsteady problem, however, this requirement is increased to 750 kbytes because time-dependent boundary conditions must be applied.

In addition to the increased memory requirement, the application of time dependent boundary conditions means that the rate of convergence is reduced. This is because the properties at the phase-lagged periodic boundaries are only updated once every period of the imposed oscillation. The number of time steps to reach convergence is, therefore, very dependent upon the number of time steps in a wake passing period. Because of the low rotor speed this number was equal to 740 for the turbine rotor.

The time-history of the velocity at the leading edge of the suction surface has been used to indicate the rate of convergence of the solution. It is shown in Fig. 4. The initial, relatively high frequency fluctuations occur while the steady flow is computed. The wakes are then introduced and the unsteady solution develops. The much slower rate of convergence to the unsteady solution is clearly visible. In fact, it is not quite complete even after 20 periods of the wake passing frequency. At this point, however, the program was stopped since it was thought to be unrealistic to extend the computational time beyond the 141 minutes of CPU (IBM 360/165) time which had already been used.

In order to obtain a true picture of the unsteady phenomena, the steady flow solution for the mean inlet and exit conditions has been subtracted from the unsteady solution. The resulting unsteady velocity field is shown in Fig. 5. The unsteady velocities are represented by vectors, whose length is proportional to the magnitude of the unsteady velocity. For the sake of clarity, only one quarter of the points have been plotted. To aid identification of the wake regions, high and low value entropy contours have been superimposed. The solutions for the three blade passages shown in Fig. 5

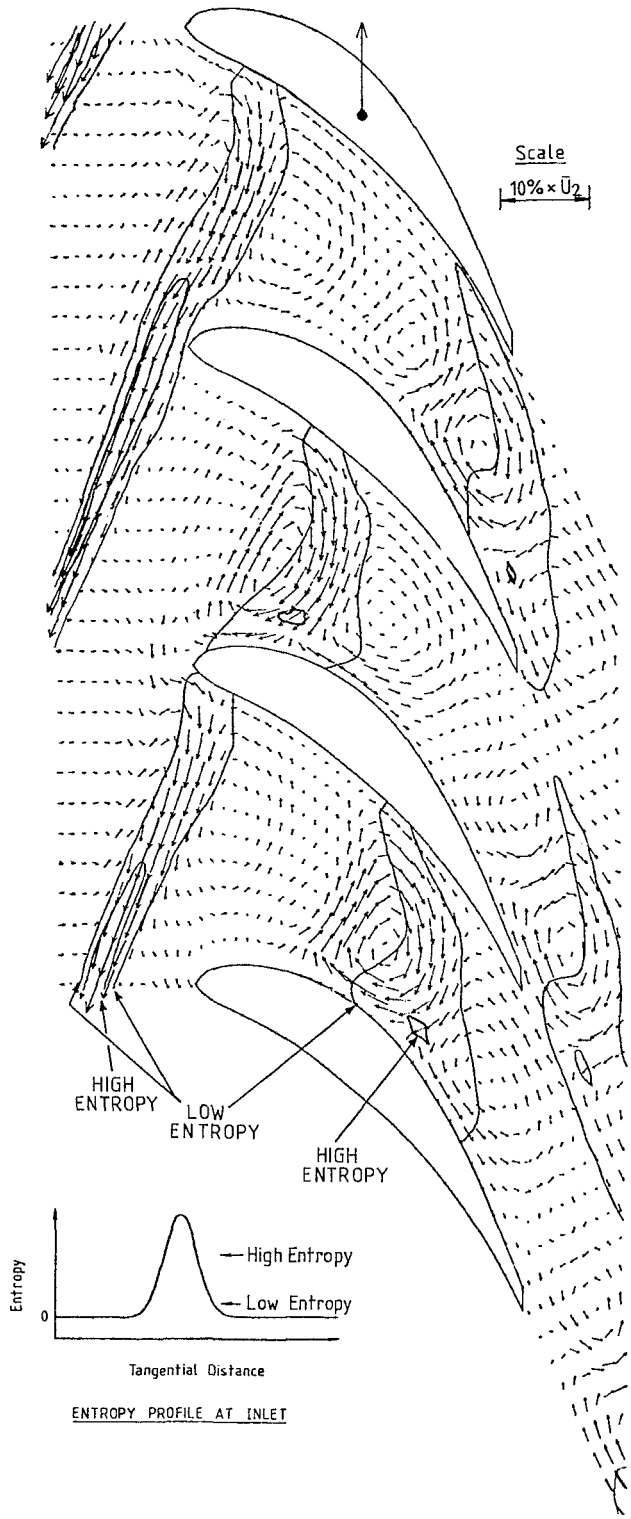

Fig. 5 Unsteady velocity vectors and entropy contours

were obtained for a single blade passage, at different time levels within the wake passing cycle. They have been combined only to aid interpretation.

Figure 5 illustrates many of the phenomena which are associated with the convection of wakes through a downstream blade row. Perhaps the most striking feature is the behavior of the wakes as "negative jets" [12] superimposed upon an otherwise steady free-stream. As a wake first moves into a rotor blade passage, it becomes bowed because the mid-passage convection velocity is much higher than that near the leading edge stagnation points. The amount of bowing will, of course, be dependent upon the suction and pressure surface velocity distributions. Once the wake has been chopped by a rotor blade, the newly formed wake segment becomes distorted. There are three reasons for this distortion. The first, which results in a broadening of the wake near the suction surface and a thinning near the pressure surface, occurs because the "negative jet" draws wake fluid away from the pressure surface and onto the suction surface. The second form of distortion results in a shearing and therefore lengthening of the wake segment. It arises as a result of the different suction and pressure surface convection velocities. A further consequence of this shearing action is that the requirement for the conservation of vorticity [13] results in a thinning of the wake as it becomes elongated. The third form of wake distortion begins as the wake first meets the leading edge of a blade, when the downstream side of the wake is accelerated over the blade surfaces and away from the upstream side, which remains in the vicinity of the stagnation point. As a result of the velocity distribution of the blade this broadening of the wake segment in the vicinity of the blade surface is much more pronounced over the leading part of the suction surface.

Figure 5 also shows that, having passed through the rotor blade row, the individual segments remain isolated from each other and, as a result, the flow onto the next stator (if one exits) would be even more unsteady than that onto the rotor since it will contain both moving rotor and upstream stator wakes. The upstream stator wakes will not, of course, move with the rotor wakes when viewed in a stationary frame. Instead, their position will fluctuate about a mean. The magnitude of the stator wake unsteadiness at the rotor exit can be estimated by examining the size of the vectors in Fig. 5. This shows that the velocity deficit remains significant even after the interaction with the rotating blade row.

The migration of the wakes towards the suction surface also results in a movement of low entropy fluid towards the pressure surface which then replaces the migrated wake fluid. This recirculating motion then results in the formation of a pair of large vortices, of opposite sign, which lie on each side of the wake. Between these main vortices, there are a pair of weaker vortices in a region which should be irrotational. The existence of these much weaker vortices is due to the effects of the numerical and artificial viscosities, the sum of which will be approximately equal to the value of the turbulent viscosity, even in the low turbulence regions between the wakes. This, therefore, demonstrates one of the consequences of using an inviscid scheme together with a simple and somewhat artificial mechanism to dissipate the wakes. A second consequence can also be seen in Fig. 5. This is that during the computation, entropy is merely dispersed whereas in the real machine, it would be produced as a result of the viscous dissipation of the wakes.

Figure 6 shows the unsteady components of the blade surface velocities. The measured [2] unsteady free-stream velocities are shown in Fig. 7. A comparison of the measured and predicted traces shows that the wave forms are very similar. The differences which do exist are thought to be due to the arbitrary definition of the "free-stream" in reference [2] as well as to deficiencies in the prediction scheme.

The shape of the wave forms in Figs. 6 and 7 are easily explained with reference to the unsteady vector plots of Fig. 5. The plateaux in the wave forms of Figs. 6 and 7 coincide with the low entropy free-stream fluid which lies between the wakes. As a wake approaches a point on the suction surface, the velocity begins to rise. It continues to do so until the center-line of the wake is very close. The velocity then falls so that once the center-line has passed, the unsteady velocity vector points upstream. As the wake recedes, the velocity then rises to the undisturbed value. On the pressure surface, as the

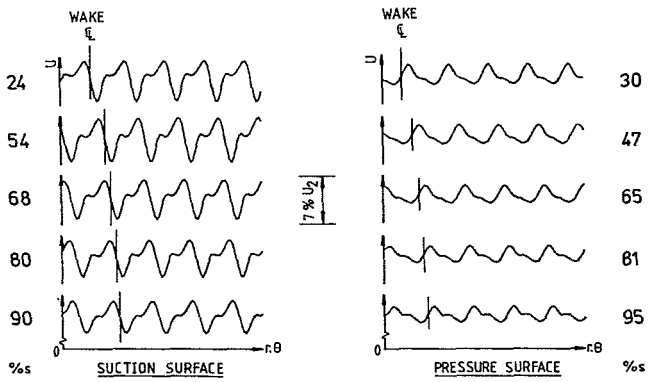

Fig. 6 Predicted unsteady blade surface velocities

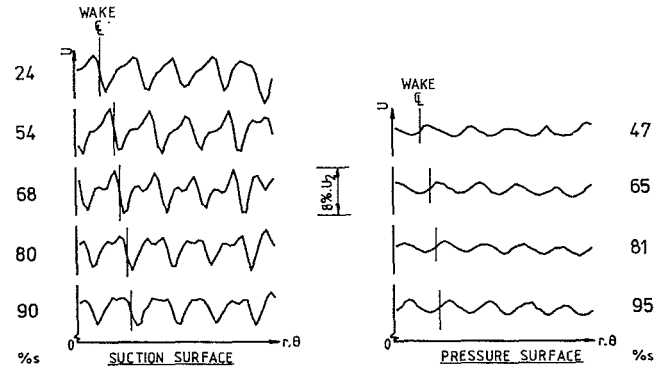

Fig. 7 Measured unsteady blade surface velocities [2]

results in Fig. 5 suggest, the velocity waveform is the mirror image of that on the suction surface.

The velocity traces of Figs. 6 and 7 show that there is a phase lag along both the suction and the pressure surfaces. Figure 8 presents the surface distributions of the amplitude and phase of the velocities at the wake-passing frequency. The measured values are also shown. The phases have been corrected so that they refer to a single blade. As expected, the suction and pressure surface disturbances are of opposite sign at the leading edge. Along the surfaces, the agreement between the predicted and measured phase distributions is excellent with the difference on the suction surface being caused by the fact that the predicted mean velocities (see Fig. 2) are lower than the measured values over the leading half of the suction surface. These phase distributions also show, as expected, that the velocity disturbances travel at a speed which is similar to that of the mean flow. The predicted suction-surface amplitudes are also in reasonable agreement with the measurements, but on the pressure surface, there is a difference. This difference is thought to be caused by the fact that in the turbine rotor the ratio of the turbulent to the mean velocity fluctuations is much higher on the pressure surface (typically 2½ times) than on the suction surface, which would presumably result in a higher rate of dissipation on the pressure surface.

The predicted surface distribution of the amplitude and the phase of the unsteady pressures, at the blade passing frequency, are shown in Fig. 9. The measured values are also shown. On the suction surface, the agreement is quite good, with the exception that over the last 25 percent of the blade surface, an upstream-travelling disturbance is predicted. This, like the high amplitude pressure fluctuations at the trailing edge, is thought to be caused by the method of application of the phase lagged periodicity condition.

On the pressure surface, there is a predicted phase shift of the pressure signal at 57 percent of the surface length, where

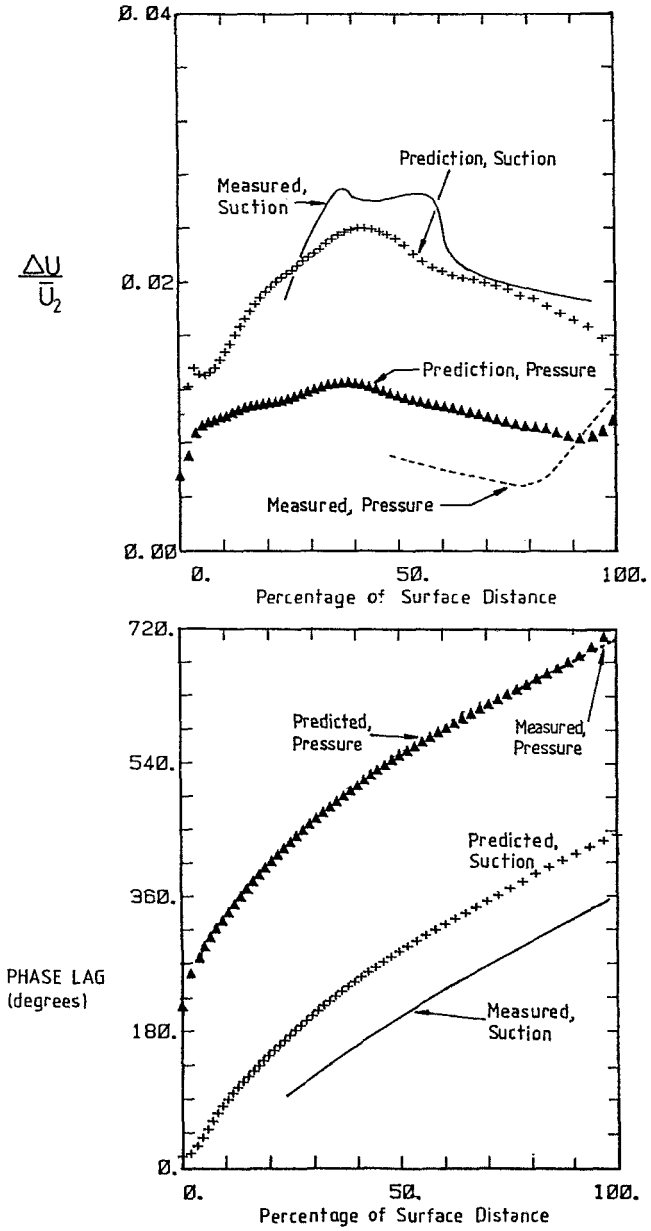

Fig. 8 Amplitude and phase of blade-surface velocities at the wake-passing frequency

the amplitude of the 1st harmonic is also zero. This is, therefore, a point where the pressure signal becomes inverted. In the measurements, there is a similar phase shift, although it occurs at 44 percent of the surface length. Unfortunately, there was no transducer at this location and it is therefore impossible to confirm that a node actually exists. However, if it does, then the agreement between the predictions and measurements is again reasonable.

It should, of course, be pointed out that a scheme such as the one described which is neither second order accurate nor one in which the boundary conditions are properly applied, is not expected to be capable of accurately predicting the unsteady pressure field.

It should also be noted that phase analyses can be misleading. For example, if convected and wave phenomena were to co-exist then the analysis would merely produce the vector sum of the two phenomena. These facts are thought to explain the complicated phase distributions which are associated with the blade surface pressure signals.

Figure 10 shows the unsteady pressure signals at the same locations as those shown in Fig. 6 for the velocities. A

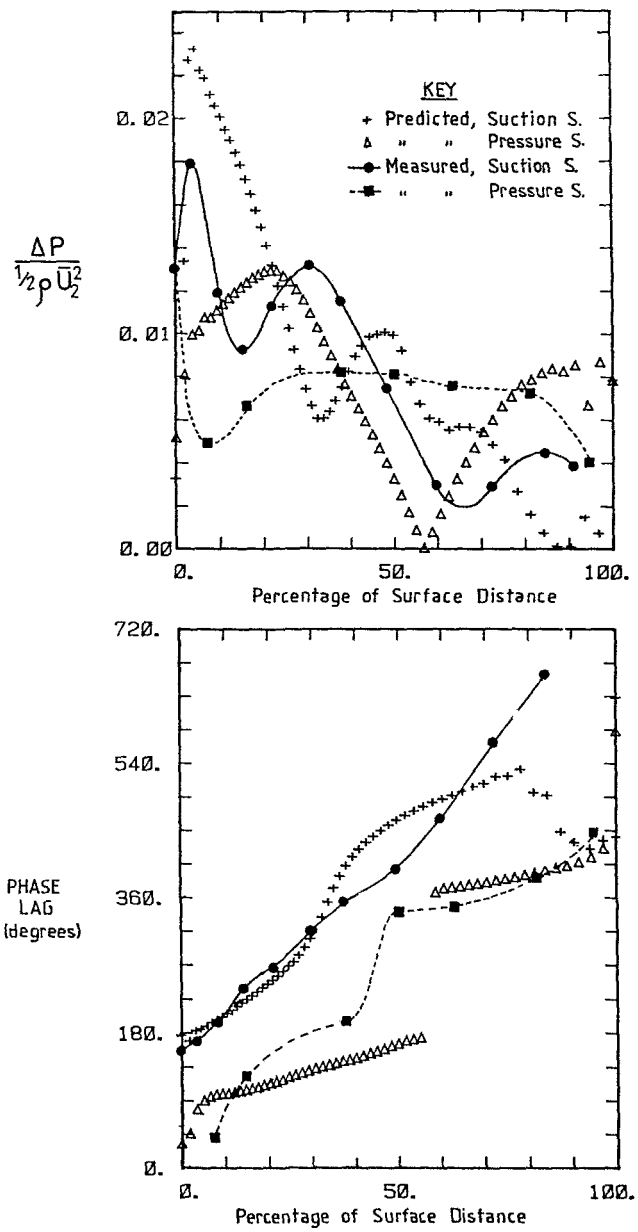

Fig. 9 Amplitude and phase of the blade-surface static pressures at the wake passing frequency

comparison of the velocity (Fig. 6) and the pressure fluctuations shows that over much of the suction surface, the point of maximum pressure is coincident with the center of the rapid decrease in velocity that is associated with the center-line of the wake. This is consistent with the behavior of the wakes as negative jets, and confirms the existence of convected pressure phenomena. If the same phenomena were to occur on the pressure surface, then the pressure minima would be expected to be coincident with the wake center-lines. Clearly, this is not so and it must therefore be concluded that on the pressure surface, the convected pressure disturbances are reduced in significance when compared with the wave-like disturbances which must also exist. These facts explain why, on the suction surface, the phase distribution of the velocity and pressure disturbances are similar whereas on the pressure surface, the pressure disturbances travel at a rate which is greater than the convection speed but less than the sound speed.

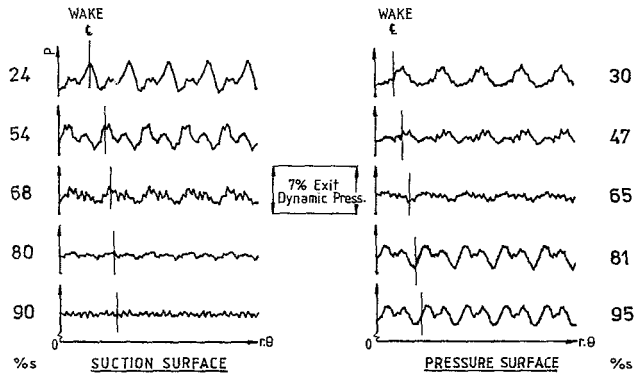

Fig. 10 Predicted unsteady blade-surface pressures

Conclusions

The wake generated unsteady flow within the rotor of an axial flow turbine has been predicted. The results confirm the existence of such phenomena as wake chopping, migration, and shearing. The agreement between the measured and predicted results also suggest that many of the phenomena associated with rotor-stator wake interactions are dominated by inviscid rather than viscous effects. It is therefore likely that an improved inviscid scheme would be sufficient to meet the current needs regarding the prediction of wake generated unsteady flows in axial machines.

Acknowledgment

The author wishes to thank Dr. J. D. Denton of the Whittle Laboratory for the supply of the computer program upon which the scheme was based and for his useful advice during its development.

References

1 Hodson, H. P., "Boundary Lyer and Loss Measurements on the Rotor of an Axial-Flow Turbine," ASME JOURNAL OF ENGINEERING FOR GAS TURBINES AND POWER, Vol. 106, No. 2, Apr. 1984, pp. 391–399.

2 Hodson, H. P., "Measurements of Wake-Generated Unsteadiness in the Rotor Passages of Axial-Flow Turbines," ASME JOURNAL OF ENGINEERING FOR GAS TURBINES AND POWER, Vol. 107, No. 2, Apr. 1985, pp. 467–476.

3 Guiraud-Vallée, D., Fenain, M., Lerat, A., Rehbach, C., Sides, J., and Vivian, H., "Numerical Studies of Unsteady Inviscid Flows at Onera," a communication presented at "Conf. on Numerical Methods in Fluid Dynamic Applications," Reading Univ., Jan. 1979.

4 Farn, C. L., and Whirlow, D. K., "Application of Time-Dependent Finite Volume Method to Transonic Flow in Large Turbines," in *Transonic Flow Problems in Turbomachinery*, Eds. Adamson, T. C., and Platzer, M. F., Hemisphere, 1977.

5 Mitchell, N. A., "A Time-Marching Method for Unsteady Two-Dimensional Flow in a Blade Passage," *Int. J. Heat and Fluid FLow*, Vol. 2, No. 4, 1980.

6 Erdos, J. I., and Alzner, E., "Computation of Unsteady Transonic Flows Through Rotating and Stationary Cascades," N.A.S.A. CR-2900, 1977.

7 Ispas, I., Grollius, H., and Gallus, H. E., "Uber den Einflub von Nachlaufdellen auf die instationäre Druckverteilung an den nachflogenden Schaufelreihen in Axialverdichtern und Axialturbinen," V.D.I.-Berichte No. 361, 1980.

8 Krammer, P., "Computation of Unsteady Blade Forces in Turbomachines by Means of Potential Flow Theory and by Simulating Viscous Wakes," ASME Paper 82-GT-198, Mar. 1982.

9 Denton, J. D., "An Improved Time Marching Method for Turbomachinery Flow Calculation," ASME Paper 82-GT-239.

10 Grant, R. J., and Johnson, C. G., "Unsteady Measurements in a Stator Blade Passage in the M.E.L. Model Turbine," C.E.G.B. Memorandum, MM/MECH/TF 261, Sept. 1980.

11 Sieverding, C., "Base Pressure in Supersonic Flow," V.K.I. Lecture Series on "Transonic Flows in Turbomachines," 1976.

12 Lefcourt, M. D., "An Investigation Into Unsteady Blade Forces in Turbomachines," ASME JOURNAL OF ENGINEERING FOR POWER, Oct. 1965, pp. 345–354.

13 Smith, L. H., "Wake Dispersion in Turbomachines," ASME *Journal of Basic Engineering*, Sept. 1966, pp. 688–690.

DISCUSSION

T. H. Okiishi[1]

The author deserves praise for this and related contributions [1, 2] to the turbomachine stage aerodynamic interaction literature. His clearly written and oral presentations are appreciated.

Recent analysis of experimental data on total-pressure loss across a compressor stage stator row indicate that chopped rotor wake segments passing through a stator row can result in significant losses along all pathlines in that stator row [14].

If a similar effect is important in turbine rotor rows, the eventual incorporation of a stator wake viscous decay model will be necessary to accurately predict turbine rotor aerodynamic performance. The measurement of stator wake influence on turbine rotor row loss is difficult at best. However, in an earlier paper [1], Hodson displayed evidence of a positive loss in the region of flow between rotor blade surface boundary layers/wakes on the suction side and negative losses outside the boundary layers/wakes on the pressure side.

[1]Department of Mechanical Engineering and Engineering Research Institute, Iowa State University, Ames, Iowa.

References

14 Okiishi, T. H.,. Hathaway, M. D., and Hansen, J. L., "A Note on Blade Wake Interaction Influence on Compressor Stator Aerodynamic Performance," ASME JOURNAL OF ENGINEERING FOR GAS TURBINES AND POWER, Vol. 107, No. 2, Apr. 1985, pp. 549–551.

Unsteady Losses in Transonic Compressors

W. F. Ng

A. H. Epstein

Massachusetts Institute of Technology, Cambridge, Mass. 02139

A newly developed probe has been used to measure the time-resolved total temperature and pressure in a transonic compressor. The investigation revealed the presence of large fluctuations in the blade-to-blade core flow occurring at a frequency of three to four times blade passing. These variations are not steady in the rotor relative frame and are thought to be caused by unsteadiness in the rotor shock system, driven perhaps by a shed vortex in the blade wake. The loss associated with this unsteadiness is calculated and the implications for stage performance are discussed.

Introduction

The design point efficiency of highly loaded transonic compressor stages has been of considerable concern over the last 20 years. Even today's highly developed stages perform at levels 5–10 percent below those suggested by first principles [1]. The stage designer must be able to predict the span-wise distribution as well as the overall stage efficiency. The test engineer must measure performance in a manner which is accurate in the context of a multistage machine and consistent among several stages, even if the absolute accuracy of the measurements may be less certain. The best loss models used in design and analysis procedures are still ultimately dependent upon empirical correlations for accurate loss estimations.

Usually, losses are both calculated and measured in the circumferential average [2]. Even in cases when the blade-to-blade flow is examined, the flow is usually considered to be steady in the rotor relative frame. We believe that these two assumptions, while often useful, are fundamentally incorrect and that their adoption may obscure the fluid physics of transonic compressors.

Over the past few years, we have been developing the measurement tools needed to explore the time-resolved blade-to-blade flows. These included high frequency response total pressure probes and combination probes capable of simultaneously measuring the time-resolved total and static pressures and two flow angles [3]. These instruments do not directly measure compressor loss, however; rather, Euler's turbine equation must be used, thus presupposing that the flow is steady and the rothalpy is constant. In order to relax this constraint, we have developed a high frequency response total temperature probe which we have used to explore the flow in a transonic compressor. The results of this investigation are presented herein.

Contributed by the Gas Turbine Division of THE AMERICAN SOCIETY OF MECHANICAL ENGINEERS and presented at the 29th International Gas Turbine Conference and Exhibit, Amsterdam, The Netherlands, June 4–7, 1984. Manuscript received at ASME Headquarters, January 12, 1984. Paper No. 84-GT-183.

Experimental Background

The flow in two low-aspect-ratio transonic compressor stages has been studied. One, a high through-flow (HTF) stage, designed at the U.S. Air Force Aero Propulsion Laboratory (AFAPL) [4], has a conventionally measured design point stage total pressure ratio of 2.06 at 88.2 percent stage adiabatic efficiency, Fig. 1. The tip speed is 457 m/s (1500 fps) at standard conditions. This 43 cm (17 in.) diameter stage was tested at AFAPL and in the MIT Blowdown Compressor Facility [5], (a short duration test tunnel). All of the data reported herein are near the design point: 100 percent speed, 28.4 kg/s, 2.065 pressure ratio. The steady-state AFAPL data were recorded with stator leading edge mounted instruments. The high frequency response data were taken at MIT with probes inserted between the stators approximately at the midspan stator leading edge station. (A comparison of total pressure measurements taken with probes ranging from 2 mm to 5 mm in diameter did not show any blockage effects due to probe insertion.)

The other stage, 51 cm (20 in.) in diameter, was designed at the NASA Lewis Research Center (LeRC) [6] and has a design point stage total pressure ratio of 1.65 at 87.0 percent adiabatic efficiency at a 430 m/s (1411 fps) tip speed, Fig. 2. Measurements on this stage were made both at MIT and on a conventional rig at NASA LeRC with and without the stators.

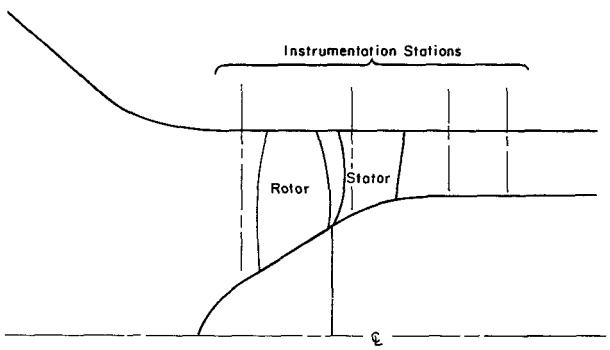

Fig. 1 Flowpath of AFAPL high through-flow compressor

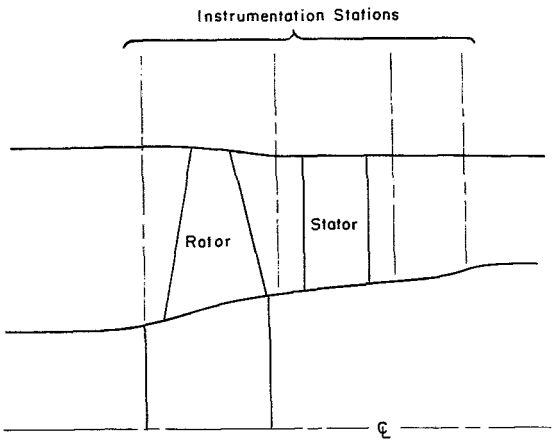

Fig. 2 Flowpath of NASA LeRC compressor

The data reported herein are for the isolated rotor at 100 percent speed, 34 kg/s, 1.68 total pressure ratio on the NASA rig.

Three instruments were used to study the time-resolved flow in these stages. Total pressure was measured with a 1.2 mm diameter, semiconductor diaphragm impact type probe with frequency response extending past 25 kHz. A four sensor, 3 mm diameter cylinder probe was used to take simultaneous measurements of total and static pressures and radial and circumferential flow angles. This is a refinement of the sphere probe reported in [7], designed to yield increased resolution in the circumferential direction at the expense of radial resolution. Its frequency response rolls off above 12 kHz.

It was necessary to develop a new instrument for this effort in order to make direct, quantitative, time-resolved measurements of the fluid temperature behind the rotor and stators of the transonic compressors. This is the dual wire aspirating probe shown in Fig. 3. It consists of two coplanar constant temperature hot wires at different overheat ratios operated in a 1.5 mm diameter channel with a choked exit so that the flow past the wires is at constant Mach number (0.2). Thus the mass flux by the wires is a function only of free stream total temperature and pressure and is not otherwise affected by changes in free stream velocity or density. The hot wires are operated in two separate constant temperature anemometer circuits, thus yielding two independent measurements from which the two unknowns, free stream stagnation temperature and pressure, can be uniquely determined. No electronic compensation or foreknowledge of the mean flow characteristics are required. Also, the diffusion of the flow in the channel reduces the dynamic structural load on the wires by a factor of 6 compared to that on an isolated hot wire at a typical rotor exit Mach number (0.6 ~ 0.8).

The probe's angular response is ±20 degrees for a 1 percent change while its frequency response extends past 20 kHz. The

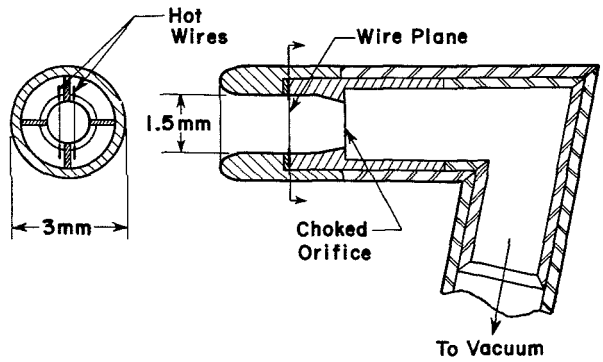

Fig. 3 Cutaway of high frequency response total temperature, total pressure aspirating probe

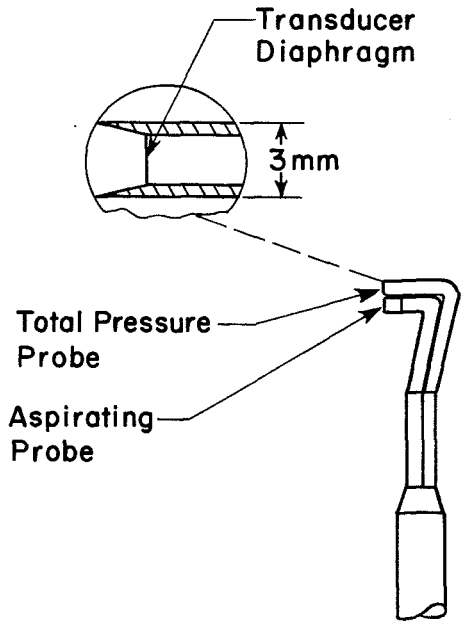

Fig. 4 Aspirating probe with "piggyback" semiconductor total pressure transducer

resolution of the instrument in the configuration used for these experiments was noise limited at 0.4 percent, 1.2°C (although it could be readily extended to 0.6°C) while the absolute accuracy was about 1 percent. As a check on proper operation, a semiconductor diaphragm total pressure impact probe was mounted "piggyback" on the aspirating probe to allow a redundant pressure measurement (Fig. 4). Further details of the dual wire aspirating probe's construction and calibration can be found in [8].

Nomenclature

a = speed of sound
C_p = specific heat at contant pressure
M = Mach number
M_{ST} = shock translational Mach number
$\bar{M}_{ST}$ = maximum shock translational Mach number
P = static pressure
P_T = stagnation pressure
r,R = radius
S = entropy
St = Strouhal numbers
T = static temperature
T_T = stagnation temperature
t = time
Θ = blade wake momentum thickness
γ = ratio of specific heats
ω = blade rotational speed
ω_{ST} = shock motion frequency
β = blade stagger angle

Subscripts

1 = conditions upstream of a shock
2 = conditions downstream of a shock
T = tangential direction
ST = shock translation
t = rotor tip

Superscripts

$'$ = relative to shock
$''$ = blade relative frame

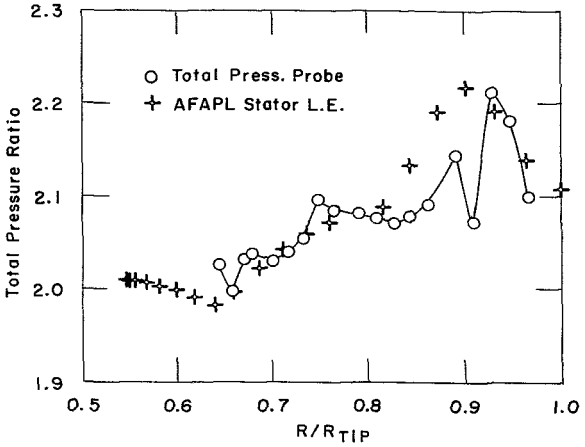

Fig. 5 Comparison of conventional measurement at AFAPL with time-average of high frequency response measurement at MIT (AFAPL rotor exit)

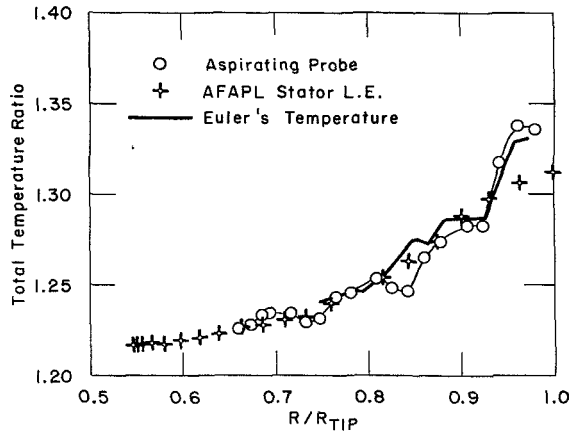

Fig. 6 Comparison of conventional measurement at AFAPL with time-average of high frequency response measurement at MIT (AFAPL rotor exit)

Experimental Observations

The outflow from the rotors and stators was surveyed both by positioning probes at fixed radii and by high speed (4 m/s) radial traverses [9]. As a first step, confidence in the overall performance of the rigs and high frequency instrumentation was established by comparing the spanwise total pressure distribution measured using conventional pneumatic instrumentation with the time-average of the measurements from high frequency response probes. Figure 5 compares the total pressure ratio measured conventionally at the stator leading edge at AFAPL versus the time-average of the high frequency response measurements. The span averaged total pressure ratios are quite comparable, 2.10 versus 2.08 (although there are small differences in the distribution which will be discussed later).

Total temperature ratio measurements on the AFAPL stage are similarly compared in Fig. 6. These are also in good agreement except near the tip where the time-average of the high frequency measurements show a greater temperature rise. From information such as the above, we conclude that the stages are operating in the same manner at similar operating points in the various facilities.

The time-resolved total pressure ratio on the LeRC rig, measured 0.5 chords downstream of the isolated rotor, is shown in detail in Fig. 7. The blade passing frequency is 5.87 kHz. Note that the details of the flow field change dramatically from blade-to-blade. They cannot be considered

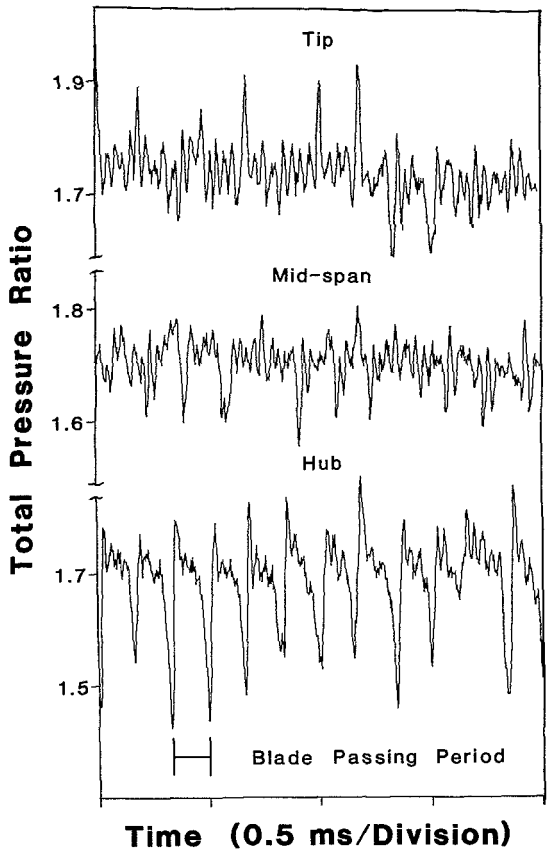

Fig. 7 Typical instantaneous total pressure ratio measured at NASA rotor exit

steady in the rotor relative frame. A striking feature is the large total pressure fluctuations in the inviscid core flow regions. These fluctuations, with a frequency of three to four times blade passing, are, near the tip, as large as the wake total pressure defect; at mid-span, on the order of 1/2 the wake defect; and diminished, although still discernible in the root region. At the tip, the amplitude of these fluctuations is 6 percent of the rotor total pressure ratio, decreasing to about 4 percent at mid-span.

In order to ascertain the influence of individual blade geometry variations, the pressure signatures of individual passages were cut from the data trace and spliced to form a continuous record of the flow in each passage as sampled by the stationary frame probes once per rotor revolution. Examination of such a trace near the tip (Fig. 8B) shows the flow to be no more repeatable in a particular rotor passage than it is in the rotor as a whole (Fig. 8A). We thus conclude that geometrical differences are small compared to other effects producing unsteadiness.

Given the time-resolved measurement, the ensemble averaged blade-to-blade flow can be calculated for either the entire rotor flow or for the spliced trace of any individual blade. The latter corresponds to information derived from conditional sampling high response probes and from typical laser anemometer (L.A.) systems. Figure 8C shows a 22 blade passing ensemble average of the blade passage of trace 8B. (A comparison between the ensemble average of all the blades in the rotor and the average of a particular blade passage revealed little difference.) A similar plot for the flow near the hub is shown in Fig. 9. Figures 8C and 9C resemble the more conventional view of the rotor blade-to-blade outflow. The wakes are regular and the core flow is relatively smooth. Unfortunately, much of the actual flow detail has been obliterated. The large fluctuations in the inviscid core, in

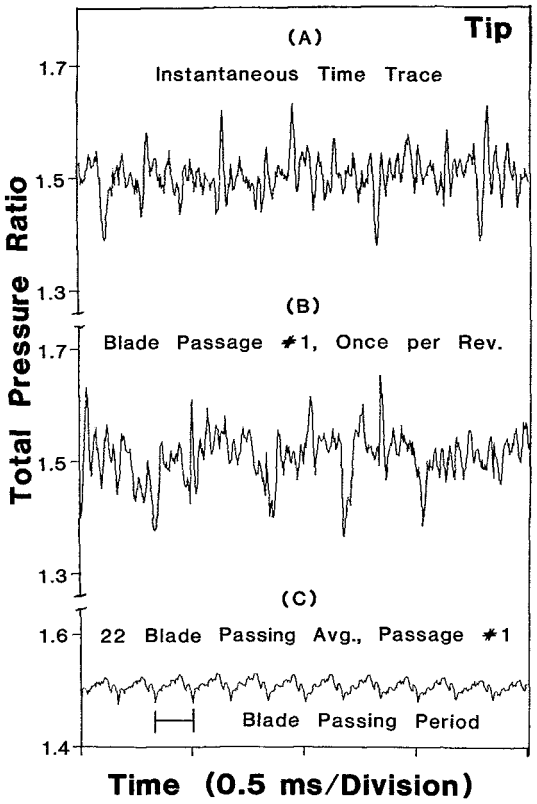

Fig. 8 NASA rotor exit pressure ratio near tip (R/R_t = 0.91) for (A) rotor as a whole, (B) an individual blade passage, and (C) ensemble average of that individual blade passage

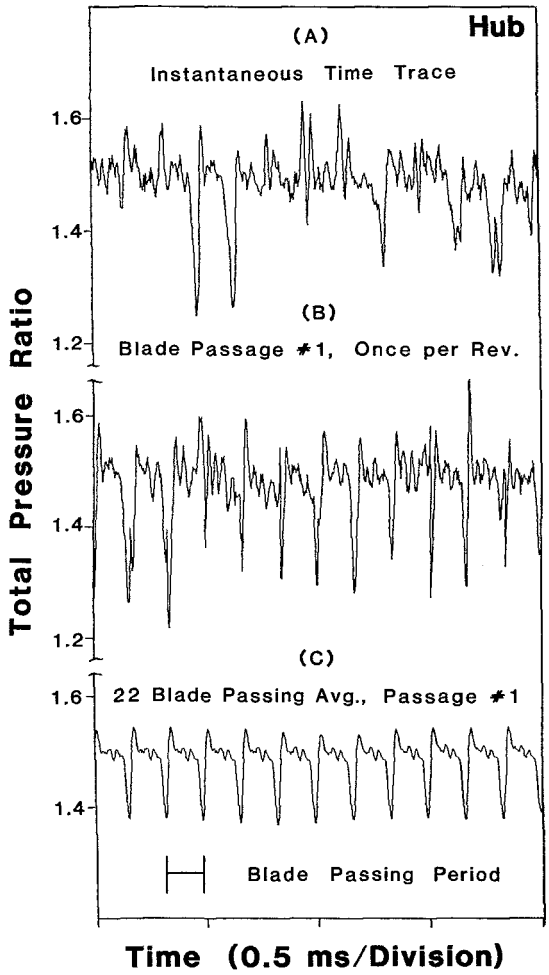

Fig. 9 Same as Fig. 8 but for hub flow (R/R_t = 0.68)

particular, are no longer in evidence. This indicates that these fluctuations are neither steady in the rotor relative frame, nor particular to individual blade passages. Thus the fluctuations would not normally be detectable by conditionally sampled data systems or laser anemometers.

The flow in the rotor is unsteady over an additional time scale as illustrated in a multi-revolution plot of total pressure ratio (Fig. 10) in the NASA Facility. This trace shows that both the mean flow in the stage and the blade-to-blade flow (as evidenced in the figure by the envelope of the wakes and other fluctuations) vary on the time scale of somewhat more than a rotor revolution. Close examination of the blade-to-blade flow shows it is changing during these low frequency oscillations but repeating in detail at similar points on succeeding cycles. This suggests that the stage behavior may be characterized as quasi-steady excursions around an average operating point. The amplitude of this disturbance is considerable (2 to 5 percent of the mean total pressure ratio) and has been observed on both stages, at MIT and at NASA LeRC, and during both isolated rotor and complete stage (rotor-stator) operation. This phenomenon is the subject of a continuing investigation and will not be further addressed in this paper except to note that when data measured at different times is compared, care was taken to do so at similar points on the low frequency cycle.

The time-resolved measurements of total temperature at the rotor outlet also show the low and high frequency fluctuations. A rapid radial traverse of both total temperature and pressure at the AFAPL rotor exit is shown in Fig. 11. This also illustrates that the total temperature fluctuations in the core flow are as large as those of the wake at tip and mid-span (which often makes the exact wake locations difficult to discern from the temperature measurement alone).

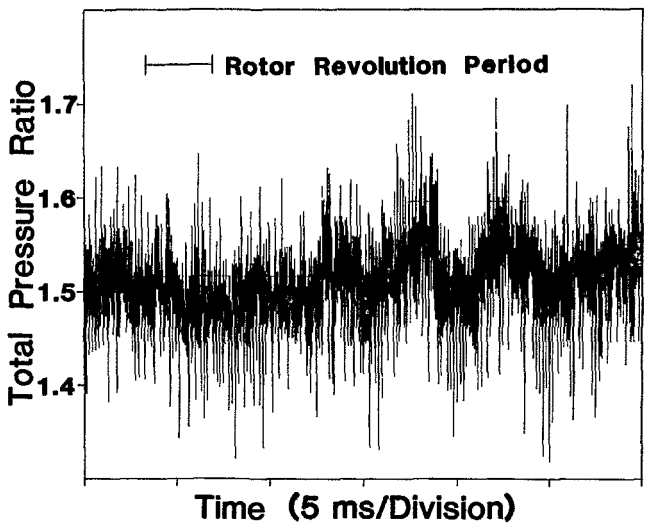

Fig. 10 Multirevolution plot of NASA rotor exit total pressure. The fine lines are the blade wakes.

Comparison of Angle and Temperature Measurements

Euler's turbine equation is often used to compute the rotor efficiency (total temperature) from measurements of the rotor outflow angles. The derivation of Euler's equation includes the assumption that the rotor relative flow is steady. Since the measurements presented herein show this not to be true in

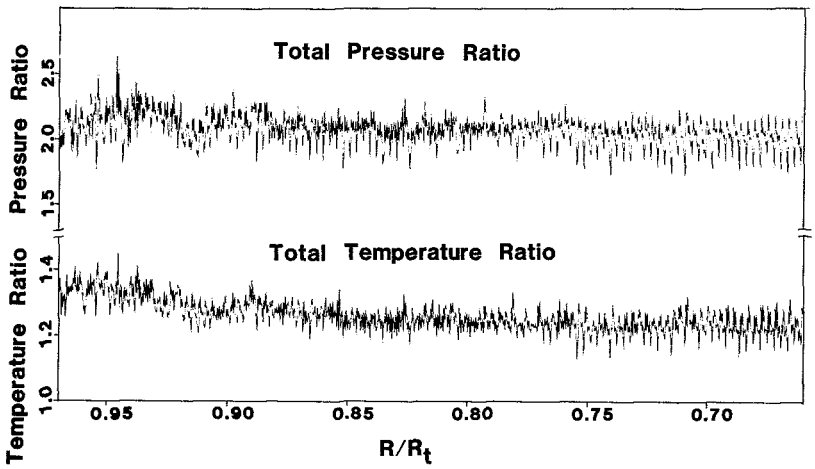

Fig. 11 A rapid radial traverse (20 ms) of the AFAPL rotor exit total temperature and pressure. The large vertical lines are the wakes.

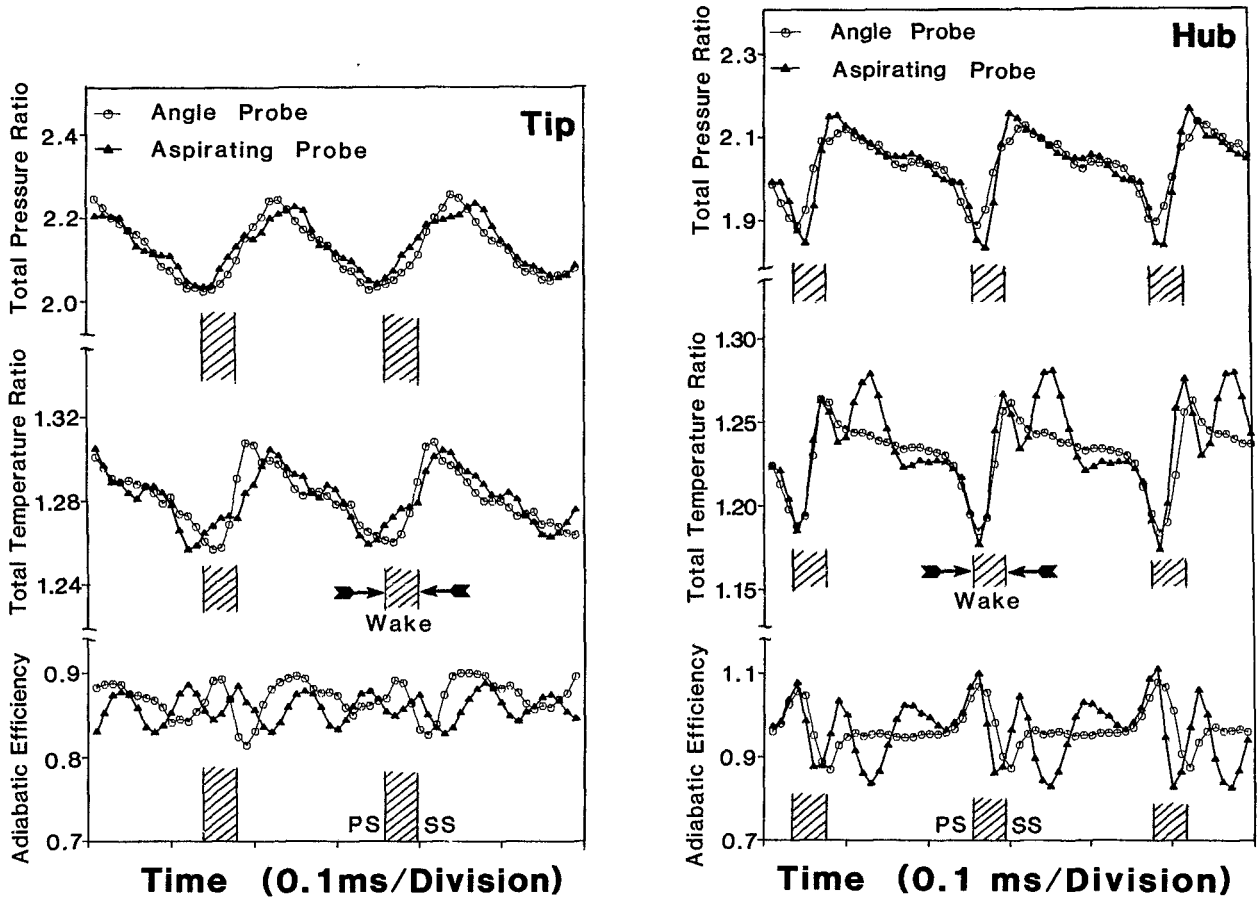

Fig. 12 Comparison of ten blade ensemble averaged measurements from the aspirating and angle probes

detail, we have compared the AFAPL rotor efficiency as measured using the total temperature probe with that computed from Euler's equation using time-resolved angle measurements made with the four-sensor cylinder probe. The two sets of measurements were made during different test runs at MIT. To avoid complications due to the aforementioned low frequency fluctuations, the two measurements are compared during similar points on the low frequency cycle as indicated by similar total pressure signatures. A detailed comparison is shown in Fig. 12. Since the measurements could not be simultaneously made on the same blade passage, ten blade ensemble averages are shown (which thus tends to smear the flow details which are unsteady in the relative frame). The agreement is quite close near the tip. Near the hub, agreement is also good except for the added detail in the core flow fluctuations from the aspirating probe measurements. This difference may be simply due to roll off of high frequency response in the angle probe. The net result is that the direct measurement shows the blade-to-blade loss to be distributed across the passage, not just concentrated in the blade wakes.

The time-averaged total temperatures were compared in Fig. 6 with the AFAPL measurements and show close agreement between the two time-resolved measurements and reasonable agreement with the conventional data. The

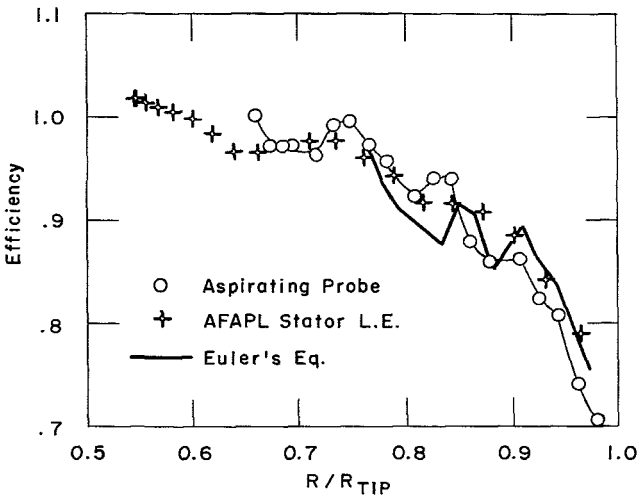

Fig. 13 Comparison of conventional measurement at AFAPL with time-average of high frequency response measurement at MIT (AFAPL rotor exit)

resultant adiabatic efficiencies are shown in Fig. 13. Overall, we conclude that even with the high degree of unsteadiness observed in these stages, Euler's turbine equation is an approximation good in time-average to one percent or better.

We note here that the high frequency response measurements from both the aspirating and angle probes show regions near the hub with adiabatic efficiencies greater than one (i.e., the change in entropy is negative). This is in agreement with the AFAPL steady state data which also show an average efficiency greater than one near the hub. In general, these regions of high efficiency are concentrated in the pressure side blade wakes. The source of this phenomenon is unclear. It cannot be explained by a misestimation of the streamlines through the rotor since the stage inflow is uniform. It could be an artifact of the measurement process or a result of heat transfer but we have yet to arrive at a satisfactory explanation for this observation.

Moving Shock Hypothesis

The large, high frequency pressure and temperature fluctuations in the rotor core flow region are quite striking in that they are not readily predicted by conventional calculations or theories. These fluctuations could be caused by variations in the inlet Mach number profile which would then result in a variation of the blade-to-blade passage shock strength. For the AFAPL stage, the variation required is 0.05 in the inlet Mach number, a level which is not inconsistent with the upstream turbulence intensity level of 4 percent measured with the laser anemometer in the NASA rig [10]. We are unable, however, to advance a plausible physical driver for the inflow variation which would result in the periodicity observed in the outflow of three to four times blade passing. Whatever the source, if this variation were steady in the rotor relative frame, it would appear in standard laser anemometer data. Ensemble averaged laser anemometer measurements on the NASA LeRC stage show the rotor exit blade-to-blade flow to be smooth, however, resembling the ensemble averaged high frequency response data of Figs. 8C and 9C. A three-dimensional, inviscid Euler calculation for the rotor also shows a smooth core flow region. More importantly, the outflow of individual blades is measured as different on successive blade revolutions (Figs. 8B and 9B). Thus the relative flow cannot be steady for an entire rotor revolution. From the above, we conclude that the variations cannot be fixed in the relative frame. How then do we explain the observed fluctuations?

These fluctuations can be simply explained if the shock system in the rotor is unsteady, i.e., if the shocks move relative to the blades. In this section we will present a simple model of the rotor passage flow with moving shocks, compare the results of the model with the data, and discuss physical mechanisms which could excite the shock system to produce the observed outflow.

We will start with the simplest physical model, a constant area channel with a uniform inlet flow whose inlet Mach number, M_1, is greater than 1. The normal shock in the passage is moving harmonically about its mean position, i.e.,

$$M(t)_{ST} = \bar{M}_{ST} \sin \omega_{ST} t \tag{1}$$

where $M(t)_{ST}$ is the Mach number (referenced to the upstream flow) at which the shock wave translates with frequency ω_{ST}, M_{ST} is the maximum translational Mach number, and t is time. Making use of coordinate transformation, the inflow Mach number relative to the shock is

$$M_1' = M_1 - M_{ST} \tag{2}$$

and the relative exit Mach number is

$$M_2' = \frac{(M_1')^2 + \left(\frac{2}{\gamma-1}\right)}{\left(\frac{2\gamma}{\gamma-1}\right)(M_1')^2 - 1} \tag{3}$$

where γ is the ratio of specific heats.

The static pressure ratio across the passage is

$$\frac{P_2}{P_1} = \frac{2\gamma}{\gamma+1}(M_1')^2 - \frac{\gamma-1}{\gamma+1} \tag{4}$$

where the subscripts 1 and 2 refer to the passage inlet and outlet, respectively.

The static temperature ratio is given by

$$\frac{T_2}{T_1} = \frac{\left[1 + \frac{\gamma-1}{2}(M_1')^2\right]\left[\frac{2\gamma}{\gamma-1}(M_1')^2 - 1\right]}{\frac{(\gamma+1)^2}{2(\gamma-1)}(M_1')^2} \tag{5}$$

The absolute frame exit Mach number is now

$$M_2 = M_2' + \sqrt{\frac{T_1}{T_2}} M_{ST} \tag{6}$$

All of the channel exit flow properties can now be calculated for given inlet conditions. The stagnation (total) pressure ratio P_T at any time can be expressed as

$$\frac{P_{T2}}{P_{T1}} = \frac{P_2}{P_1}\left(\frac{1 + \frac{\gamma-1}{2}M_2^2}{1 + \frac{\gamma-1}{2}M_1^2}\right)^{\frac{\gamma}{\gamma-1}} \tag{7}$$

and total temperature, T_T, ratio is

$$\frac{T_{T2}}{T_{T1}} = \frac{T_2}{T_1}\left(\frac{1 + \frac{\gamma-1}{2}M_2^2}{1 + \frac{\gamma-1}{2}M_1^2}\right) \tag{8}$$

Thus, the total pressure and temperature ratios can either increase or decrease depending upon the direction of the shock motion.

When the shock wave moves upstream relative to the flow, its strength is higher compared to a stationary or downstream moving wave. Since the entropy rise $(S_2 - S_1)$ across a shock is proportional to a high power of the Mach number $[(S_2 - S_1) \sim (M^2 - 1)^3$ for weak shocks], the moving shock generates

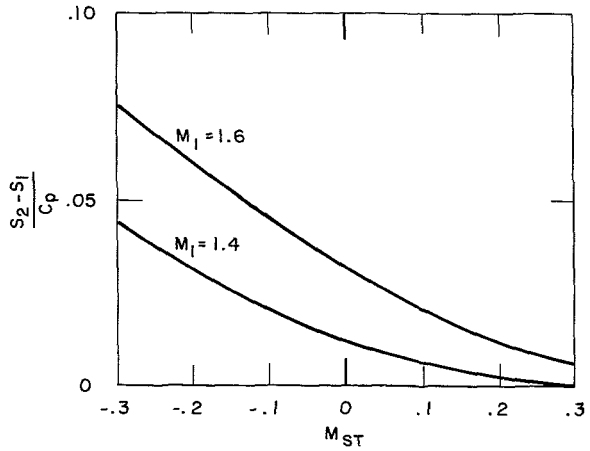

Fig. 14 Variation of moving normal shock entropy rise with shock translation Mach number

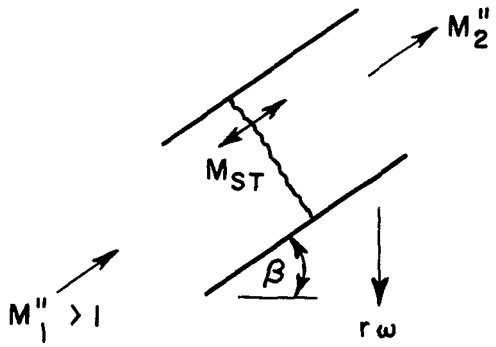

Fig. 15 Moving shock model geometry

more loss than a stationary shock at the same average Mach number. This dependence is shown in Fig. 14.

This simple model can now be modified to a compressor-like geometry by orienting the passage at a stagger angle, β, and moving it at a rotational velocity $r\omega$, where r is the radius and ω the rotational speed (Fig. 15). Defining the tangential Mach number of the blades as $M_{T2} = r\omega/a_2$, where a_2 is the outlet speed of sound, the absolute frame exit Mach number, M_2 is given by

$$M_2^2 = M_2''^2 + M_{T2}(M_{T2} - 2M_2'' \sin\beta) \tag{9}$$

where the double prime denotes the blade relative frame. The absolute frame total temperatures and pressures can now be calculated as in equations (7) and (8). The entropy rise due to the shock motion is

$$\frac{S_2 - S_1}{C_P} = \ln\frac{T_{T2}}{T_{T1}} - \frac{\gamma - 1}{\gamma}\ln\frac{P_{T2}}{P_{T1}} \tag{10}$$

A calculation for the parameters of the AFAPL stage at about mid-span is shown in Fig. 16. Note that the change in streamtube properties is a strong function of the shock translation Mach number, M_{ST}.

We can now apply this model to the measurements. With reference to Fig. 17, the solid line is the measured instantaneous exit total pressure, the dotted line is a best fit sinusoidal variation. By applying equations (2-8), the total temperature variation which would result from a moving shock producing the observed pressure pattern can be calculated. This is compared to the observed temperature variation in Fig. 18. The agreement is quite reasonable, especially considering the simplicity of the model compared to an actual three-dimensional compressor shock pattern. The shock motion necessary to produce the observed pressure and temperature pattern was calculated as 0.3 mm using equation

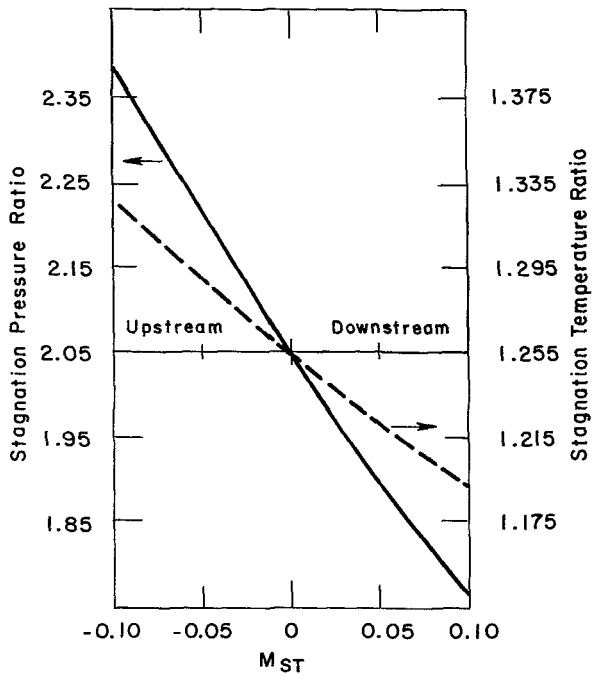

Fig. 16 Calculated rotor outflow variation due to moving shock (AFAPL rotor, $R/R_t = 0.84$)

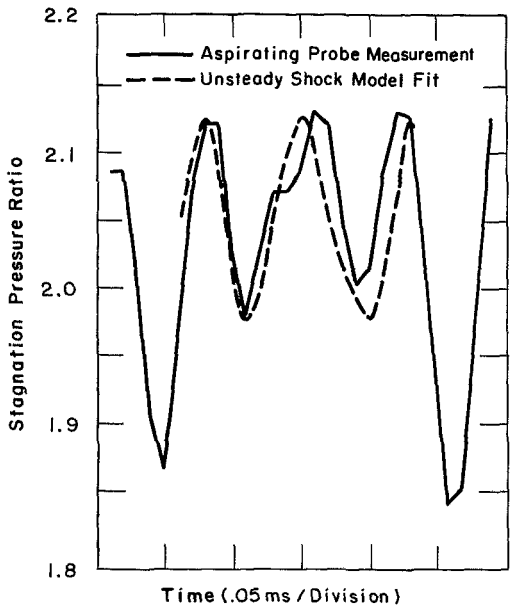

Fig. 17 Fit of moving shock model to time-resolved measurement (AFAPL rotor exit, $R/R_t = 0.84$)

(1) (varying over the span from 0.2 to 0.6 mm). This level of motion is quite plausible for essentially any shock system, not just that in a compressor.

Support for the unsteady shock hypothesis comes from data recently taken on the NASA stage by a laser anemometer operated in a data capture mode in which the instantaneous velocity at each particle occurrence is stored for analysis, not just the ensemble averaged velocity [10]. The data show a dual peak distribution near the normal passage shock locations which would be characteristic of a shock moving back and forth over the sampling point.

The unsteady shock hypothesis can also explain the observation that the core fluctuations appear larger near the suction side of the blade than near the pressure side. This

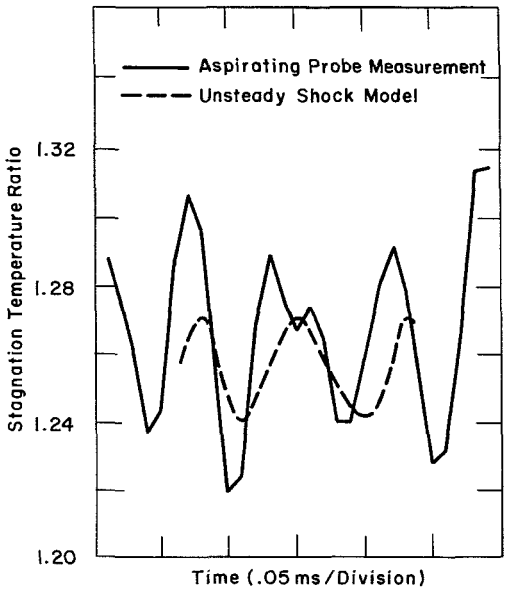

Fig. 18 Comparison of moving shock model prediction with time-resolved measurement (AFAPL rotor exit, $R/R_t = 0.84$)

comes about since the position of the shock bending around the blade leading edge from the pressure side is fairly stiff. The shock is either attached or the standoff distance is set by the leading edge radius and the approach Mach number. The suction side of the blade appears almost as a flat plate to the shock, however, which is free to move considerable distance from only a small pressure change. Recent high speed Schlieren pictures in an annular cascade support this observation [11].

The pressure and temperature variations, although uncorrelated in phase from blade passage to passage, appear within a fairly narrow frequency range, 15 kHz–20 kHz. What is physically driving the shocks in this manner? Several plausible explanations can be advanced such as a relaxation oscillation with the boundary layer. One promising mechanism is the von Karman vortex streets shed in the wakes of transonic airfoils. These vortex streets are observed to occur at Strouhal numbers [St = (freq.) × Θ/velocity] based on wake momentum thickness, Θ, of 0.15–0.20 [12], [13]. Using the model of Koch and Smith [2] to estimate the wake momentum thickness at the trailing edge (which agrees with the measured pressure defect), a shedding frequency for the AFAPL rotor at $R/R_t = 0.84$ of 15–20 kHz is calculated, quite close to the observation. The mechanism by which this shedding drives the passage shock may be as simple as a periodic change in circulation or an increase in blockage but clearly needs further calculation.

Independent of the driving mechanism, the entropy rise directly due to the moving shock can be estimated from the observed fluctuations using equation (10). This is calculated to be about 0.15 percent in stage efficiency for the AFAPL rotor for the high frequency fluctuations under discussion. Thus the direct production of entropy by the moving shocks as inferred from these measurements is not important. The influence of the resultant unsteadiness may not be simply ignored however.

Discussion—Effects of High Frequency Unsteadiness

High frequency pressure and temperature fluctuations are present at the rotor outflow whatever their cause. We now wish to examine the implications of this outflow pattern.

It is unlikely that the pressure fluctuations of the length scales observed can be efficiently recovered in the downstream

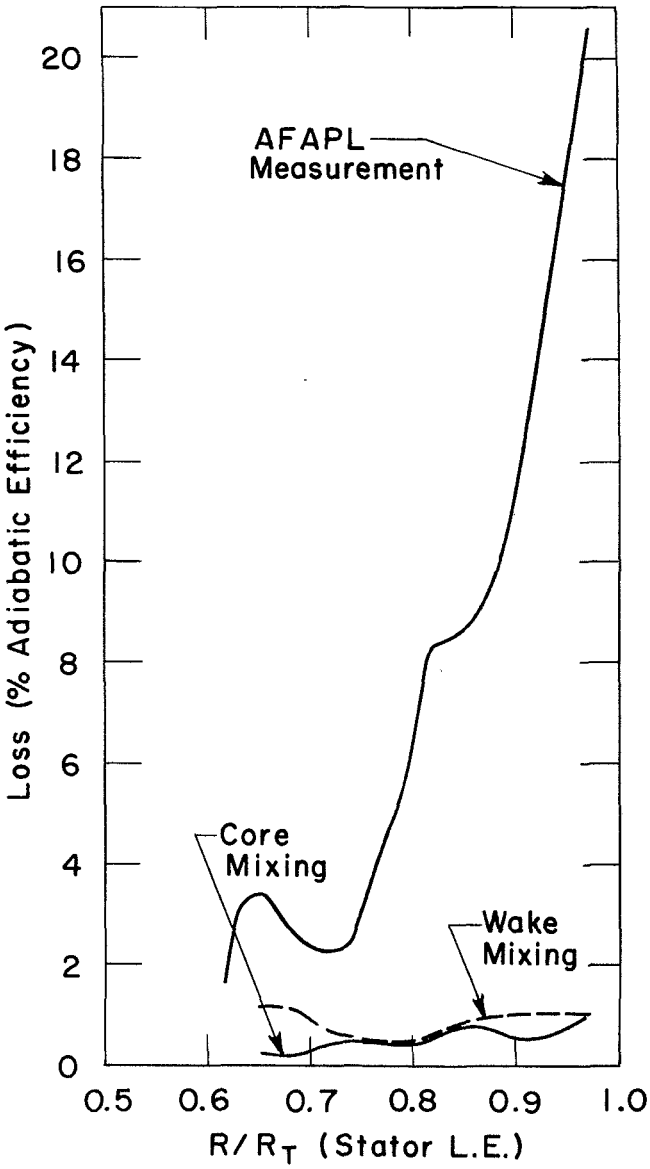

Fig. 19 Comparison of measured AFAPL rotor loss with calculated wake mixing and high frequency core mixing losses

flow. We therefore estimated the mixing losses associated with homogenizing the flowfield. This was done for a compressible flow in a straight duct, both as constant area and as constant pressure mixing with little difference in result. (A two-dimensional mixing calculation would be a better representation of the flow but has yet to be done.) The spanwise loss variation from this fluctuation mixing is compared in Fig. 19 to the loss associated with the wake mixing, and the AFAPL measured rotor loss. The unsteady loss is on the order of the wake loss and accounts for 0.5 to 1 percent in adiabatic efficiency averaged over the span.

Measurement of the flow behind the stators shows the fluctuations to have decayed by about 50 percent. Thus, they are still present as a distortion of the inlet flow to the next stage corresponding to a 5–10 percent variation of inflow Mach number. This high frequency pattern of approach Mach number will result in a variation of passage shock strength in the following rotor, producing additional total temperature and pressure fluctuations in the outflow of that stage, with an attendant increase in loss. Unless some unidentified damping mechanism is present, this pattern can propagate through a multistage compressor.

The NASA rotor is the first of a two stage design [6]. We have calculated the perturbations in the outflow of the second stage rotor which would result from the high frequency variations measured at the first stage stator exit at MIT [3]. The resultant total pressure variation is three times that at the first stage rotor exit and would result in a mixed out three point decrement in second stage efficiency. This does not include the effect of any driven shock motion similar to that in the first stage. The above implies that the performance of the second stage would be higher when tested by itself than in the two stage configuration. It also raises the question of how this additional loss should be debited.

Clearly, care must be taken when interpreting measurements made in the presence of the high frequency fluctuations. Accurate probe measurements of the time-averaged total pressure at a given axial station will not reflect the mixing loss not yet incurred. Since the phenomenon persists for several chords downstream, a probe's measurement of total pressure will change with its streamwise position. The magnitude of this effect, however, would not be more than 1 percent for the stages studied.

Concluding Remarks

A measurement of the time-resolved total temperature and total pressure in two transonic, low-aspect-ratio compressor stages has revealed the presence of large fluctuations in the blade-to-blade core flow occurring at a frequency of three to four times blade passing. These variations are not steady in the rotor frame and are thought to be caused by unsteadiness in the rotor shock system, perhaps driven by a shed vortex in the blade wake.

A simple mixing calculation shows that the high frequency unsteadiness contributes on the order of 1 percent of the rotor loss. The unsteadiness may also precipitate further nonuniformity and loss in following stages. Conventional steady-state instrumentation may give misleading results in this flow since the loss associated with the fluctuations does not appear directly at the rotor exit.

Clearly, a more sophisticated analysis that more closely models the complicated rotor flow field may influence some of the above conclusions, the exact magnitude of the losses in particular. Further work must be done to explain and verify the physical mechanisms causing the core flow fluctuations and their effects on downstream blade rows. We hope that further investigations may resolve some of these questions.

Acknowledgments

The authors wish to thank J. L. Kerrebrock who has contributed much to the inception and development of the ideas contained herein. The NASA high frequency data were taken by Mr. J. Gertz. W. T. Thompkins suggested that the shocks might be unsteady and A. J. Strazisar, E. M. Greitzer and E. E. Covert have contributed many hours to discussing these topics.

This work has been supported by the U.S. Air Force Office of Scientific Research, Dr. James Wilson, program manager.

References

1 Kerrebrock, J. L., "Flow in Transonic Compressors," *AIAA Journal*, Vol. 19, No. 1, Jan. 1981.

2 Koch, C. C., and Smith, L. H., Jr., "Loss Sources and Magnitudes in Axial-Flow Compressors," ASME JOURNAL OF ENGINEERING FOR POWER, Vol. 98, No. 3, July 1976, pp. 411–424.

3 Epstein, A. H., et al., "Time-Resolved Measurements in a Low-Aspect-Ratio Transonic Compressor Stage," ASME Paper No. 82-GT-201, 1982.

4 Wennerstrom, A. J., et al., "Investigation of a 1500 ft./sec. Transonic, High-Through-Flow, Single-Stage Axial-Flow Compressor with Low Hub/Tip Ratio," AFAPL-TR-76-92, Oct. 1976.

5 Kerrebrock, J. L., et al., "The MIT Blowdown Compressor Facility," ASME Paper No. 74-GT-47, Mar. 1974.

6 Urasek, D. C., et al., "Performance of Two-Stage Fan Having Low-Aspect-Ratio, First-Stage Rotor Blading," NASA Technical Paper 1493, 1978.

7 Kerrebrock, J. L., et al., "A Miniature High Frequency Sphere Probe," *Proc. ASME Symposium, Measurement Methods in Rotating Components of Turbomachinery*, 1980.

8 Ng, W. F., and Epstein, A. H., "High Frequency Temperature and Pressure Probe for Unsteady Compressible Flows," *Rev. Sci. Instrum.*, Dec. 1983.

9 Ng, W. F., "Time-Resolved Stagnation Temperature Measuremnt in a Transonic Compressor Stage," PhD thesis, Massachusetts Institute of Technology, Dept. of Mechanical Engineering, Oct. 1983.

10 Strazisar, A. J., "Investigation of Flow Phenomena in a Transonic Fan Rotor Using Laser Anemometry," ASME 29th Gas Turbine Conference, Amsterdam, 1984.

11 Bolcs, A., "A Test Facility for the Investigation of Steady and Unsteady Transonic Flows in Annular Cascades," ASME Paper 83-GT-34, April 1983.

12 Heinemann, H. J., et al., "V. Karman Vortices and Their Frequency Determination in the Wakes of Profiles in the Suband Transonic Regimes," IUTAM Symposium Transonicum II, Springer Verlag, Berlin/Heidelberg/New York, 1976.

13 Heinemann, H. J., and Butefisch, K. A., "Determination of the Vortex Shedding Frequency of Cascades with Different Trailing Edge Thicknesses," AGARD-CP277, 1977.

The NASA rotor is the first of a two stage design [6]. We have calculated the perturbations in the outflow of the second stage rotor which would result from the high frequency variations measured at the first stage stator exit at MIT [3]. The resultant total pressure variation is three times that at the first stage rotor exit and would result in a mixed out three point decrement in second stage efficiency. This does not include the effect of any driven shock motion similar to that in the first stage. The above implies that the performance of the second stage would be higher when tested by itself than in the two stage configuration. It also raises the question of how this additional loss should be debited.

Clearly, care must be taken when interpreting measurements made in the presence of the high frequency fluctuations. Accurate probe measurements of the time-averaged total pressure at a given axial station will not reflect the mixing loss not yet incurred. Since the phenomenon persists for several chords downstream, a probe's measurement of total pressure will change with its streamwise position. The magnitude of this effect, however, would not be more than 1 percent for the stages studied.

Concluding Remarks

A measurement of the time-resolved total temperature and total pressure in two transonic, low-aspect-ratio compressor stages has revealed the presence of large fluctuations in the blade-to-blade core flow occurring at a frequency of three to four times blade passing. These variations are not steady in the rotor frame and are thought to be caused by unsteadiness in the rotor shock system, perhaps driven by a shed vortex in the blade wake.

A simple mixing calculation shows that the high frequency unsteadiness contributes on the order of 1 percent of the rotor loss. The unsteadiness may also precipitate further nonuniformity and loss in following stages. Conventional steady-state instrumentation may give misleading results in this flow since the loss associated with the fluctuations does not appear directly at the rotor exit.

Clearly, a more sophisticated analysis that more closely models the complicated rotor flow field may influence some of the above conclusions, the exact magnitude of the losses in particular. Further work must be done to explain and verify the physical mechanisms causing the core flow fluctuations and their effects on downstream blade rows. We hope that further investigations may resolve some of these questions.

Acknowledgments

The authors wish to thank J. L. Kerrebrock who has contributed much to the inception and development of the ideas contained herein. The NASA high frequency data were taken by Mr. J. Gertz. W. T. Thompkins suggested that the shocks might be unsteady and A. J. Strazisar, E. M. Greitzer and E. E. Covert have contributed many hours to discussing these topics.

This work has been supported by the U.S. Air Force Office of Scientific Research, Dr. James Wilson, program manager.

References

1 Kerrebrock, J. L., "Flow in Transonic Compressors," *AIAA Journal*, Vol. 19, No. 1, Jan. 1981.

2 Koch, C. C., and Smith, L. H., Jr., "Loss Sources and Magnitudes in Axial-Flow Compressors," ASME JOURNAL OF ENGINEERING FOR POWER, Vol. 98, No. 3, July 1976, pp. 411–424.

3 Epstein, A. H., et al., "Time-Resolved Measurements in a Low-Aspect-Ratio Transonic Compressor Stage," ASME Paper No. 82-GT-201, 1982.

4 Wennerstrom, A. J., et al., "Investigation of a 1500 ft./sec. Transonic, High-Through-Flow, Single-Stage Axial-Flow Compressor with Low Hub/Tip Ratio," AFAPL-TR-76-92, Oct. 1976.

5 Kerrebrock, J. L., et al., "The MIT Blowdown Compressor Facility," ASME Paper No. 74-GT-47, Mar. 1974.

6 Urasek, D. C., et al., "Performance of Two-Stage Fan Having Low-Aspect-Ratio, First-Stage Rotor Blading," NASA Technical Paper 1493, 1978.

7 Kerrebrock, J. L., et al., "A Miniature High Frequency Sphere Probe," *Proc. ASME Symposium, Measurement Methods in Rotating Components of Turbomachinery*, 1980.

8 Ng, W. F., and Epstein, A. H., "High Frequency Temperature and Pressure Probe for Unsteady Compressible Flows," *Rev. Sci. Instrum.*, Dec. 1983.

9 Ng, W. F., "Time-Resolved Stagnation Temperature Measuremnt in a Transonic Compressor Stage," PhD thesis, Massachusetts Institute of Technology, Dept. of Mechanical Engineering, Oct. 1983.

10 Strazisar, A. J., "Investigation of Flow Phenomena in a Transonic Fan Rotor Using Laser Anemometry," ASME 29th Gas Turbine Conference, Amsterdam, 1984.

11 Bolcs, A., "A Test Facility for the Investigation of Steady and Unsteady Transonic Flows in Annular Cascades," ASME Paper 83-GT-34, April 1983.

12 Heinemann, H. J., et al., "V. Karman Vortices and Their Frequency Determination in the Wakes of Profiles in the Suband Transonic Regimes," IUTAM Symposium Transonicum II, Springer Verlag, Berlin/Heidelberg/New York, 1976.

13 Heinemann, H. J., and Butefisch, K. A., "Determination of the Vortex Shedding Frequency of Cascades with Different Trailing Edge Thicknesses," AGARD-CP277, 1977.

DISCUSSION

J. Moore[1]

The authors use Euler's turbine equation to compute the rotor efficiency (total temperature) from measurements of the rotor outlet flow angles. From these results they conclude "overall, . . . even with the high degree of unsteadiness observed in these stages, Euler's turbine equation is an approximation good in time-average to one percent or better." It is known, however [14], that moment of momentum is destroyed by shear stresses at the stationary shroud wall in rotors giving rise to a production of rothalpy $(h+W^2/2-\omega^2r^2/2)$ and thus locally voiding the simple application of Euler's turbine equation for steady flow. Can the authors then comment on the extent of the diffusion or convection of rothalpy radially inward from the stationary shroud wall where it is generated?

References

14 Moore, J., and Moore, J. G., "Three-Dimensional, Viscous Flow Calculations for Assessing the Thermodynamic Performance of Centrifugal Compressors—Study of the Eckardt Compressor," AGARD Conference Proceedings No. 282 of the AGARD Meeting on Centrifugal Compressors, Flow Phenomena and Performance, Brussels, May 1980.

[1]Mechanical Engineering Department, VPI&SU, Blacksburg, Virginia 24061

Authors' Closure

The use of Euler's turbine equation to compute the rotor total temperature from measurements of the rotor outflow angles rests on two assumptions: (*a*) that the flow is steady in coordinates rotating with the rotor and (*b*) that there is no exchange of energy between streamtubes (in rotor coordinates). The change in rothalpy can be due to *viscous interaction* or to *unsteadiness* in rotor coordinates. Unfortunately, we have at present no means of separating the two effects. In addition, the probes are not designed to look at flow phenomena near the tip casing. The relative size of the rotor and the probes made it impossible to look at the generation of rothalpy due to shear stresses at the tip casing from the present set of data.

Loss Reduction in Axial-Flow Compressors Through Low-Speed Model Testing

D. C. Wisler
Manager,
Turbomachinery Research
Aircraft Engine Group,
General Electric Company,
Cincinnati, Ohio 45215

A systematic procedure for reducing losses in axial-flow compressors is presented. In this procedure, a large, low-speed, aerodynamic model of a high-speed core compressor is designed and fabricated based on aerodynamic similarity principles. This model is then tested at low speed where high-loss regions associated with three-dimensional endwall boundary layers, flow separation, leakage, and secondary flows can be located, detailed measurements made, and loss mechanisms determined with much greater accuracy and much lower cost and risk than is possible in small, high-speed compressors. Design modifications are made by using custom-tailored airfoils and vector diagrams, airfoil endbends, and modified wall geometries in the high-loss regions. The design improvements resulting in reduced loss or increased stall margin are then scaled to high speed. This paper describes the procedure and presents experimental results to show that in some cases endwall loss has been reduced by as much as 10 percent, flow separation has been reduced or eliminated, and stall margin has been substantially improved by using these techniques.

Introduction

The flow in a multistage, axial-flow compressor is complex in nature because of the proximity of moving blade rows, the buildup of endwall boundary layers, and the presence of leakage and secondary flows. These regions of complex flows and associated high loss are shown in Fig. 1. With the trends over the past two decades being to higher pressure rise per stage, higher aerodynamic loadings, higher speed, and lower aspect ratio, designers of advanced components are challenged to find configurations having improved aerodynamic performance while avoiding flow separation, increased loss, and stall margin penalties. For example, assessments of loss mechanisms, such as those of [1], suggest that approximately one-half of the total loss in the rear stages of a multistage compressor is associated with the endwall boundary layers. Thus the trend toward lower aspect ratios increases the fraction of the total flow that is subjected to three-dimensional, endwall boundary layer effects, making it particularly important to devise ways to reduce endwall losses. Although analytical progress is being made, accurate experimental data are needed to determine how various types of airfoil sections, blade setting procedures, annulus wall design parameters, and vector diagram types affect compressor performance and, consequently, engine fuel usage. This paper presents a systematic procedure for reducing loss and improving performance through low-speed model testing.

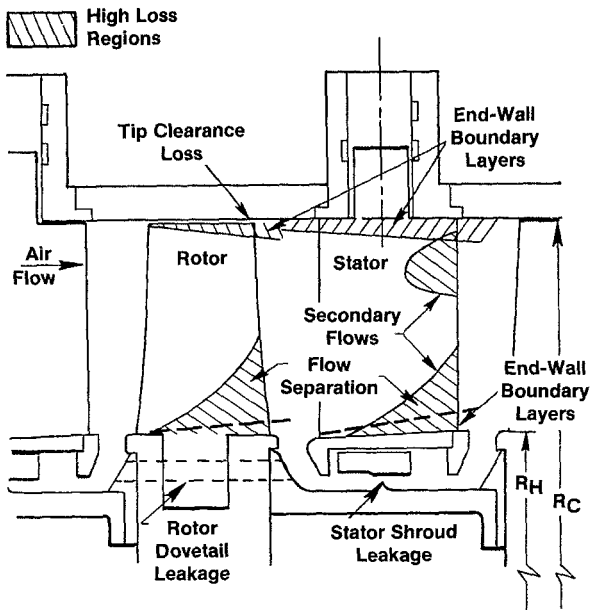

Fig. 1 High-loss regions in a multistage compressor

Modeling Concept

Basic Principles. The success of model testing depends upon aerodynamic similarity. References [2] and [3] point out that if geometrically similar bodies with the same orientation are moved through a fluid so that the similarity parameters (Reynolds number and Mach number) are equal, then the dimensionless forces on the two bodies are equal. When the

Contributed by the Gas Turbine Division of THE AMERICAN SOCIETY OF MECHANICAL ENGINEERS and presented at the 29th International Gas Turbine Conference and Exhibit, Amsterdam, The Netherlands, June 4-7, 1984. Manuscript received at ASME Headquarters January 12, 1984. Paper No. 84-GT-184.

Mach numbers of the two bodies (airfoils) being tested are different, then another level of complexity is added. In this case, the dimensionless force remains invariant with Mach number if the angle of attack, camber, and thickness of the airfoil are increased in a prescribed manner as Mach number is decreased. In isolated airfoil theory one often illustrates this geometric modeling in terms of the Prandtl-Glauert similarity rules of [2], although these rules are not used in the research described in this paper because of their restrictive assumptions. Great care must be exercised in the modeling process if meaningful results are to be achieved. Not only must geometry be modeled properly at different Mach numbers, but the airfoils must have the same scaled surface roughness and be tested in fluids of the same turbulence intensity and Reynolds numbers. Additional complexity occurs when modeling a compressor because other parameters, such as solidity and aspect ratio, must be taken into account.

Technical Approach. The low-speed model testing program for improving compressor performance involves the following systematic technical approach.

First, a low-speed, aerodynamic, model of a high-speed core compressor is designed and fabricated based on aerodynamic similarity principles. This model, which has the same solidity, aspect ratio, vector diagrams, reactions, Reynolds numbers, airfoil surface pressure distributions, clearance-to-blade height, and axial spacing-to-chord ratio as its high-speed counterpart, forms a low-speed baseline.

Second, this baseline blading is tested in a facility where high-loss regions can be located and loss mechanisms determined with much greater accuracy and much lower cost and risk than is possible in small, high-speed compressors. Tests are conducted on buildups that consists of four repeating stages to operate the blading in the multistage environment and thus properly simulate loss mechanisms.

Third, after high loss regions in the baseline are identified, configurations employing candidate ideas for improving the performance of the baseline are designed and tested. Modifications are made to the airfoil sections, the endwalls, or the vector diagrams to reduce the loss, improve stall margin, etc. Innovative ideas on the forefront of technology, such as custom-tailored airfoils and vector diagrams (including airfoil endbends), unorthodox wall geometry, and bleed and leakage schemes, are evaluated for their effectiveness in improving performance.

Fourth, improvements obtained in the low-speed testing are incorporated into the high-speed compressor where appropriate. In addition, the accurate, detailed, experimental data are used to develop and improve analytic models and design techniques for compressor.

Advantages and Disadvantages of Low-Speed Model Testing. There are three principle advantages to low-speed model testing: greater accuracy, lower cost, and lower risk. The large size and low speed of this type of research facility permit detailed, accurate probing with probe blockage effects nearly eliminated. Blades and vanes are large enough to be instrumented. Lower speed means lower stresses and therefore lower hardware and testing cost. Finally, low-speed testing provides an opportunity for exploring configurations that may have some aerodynamic risk of a performance penalty without risking the disruption of a major engine program. For example, airfoil shapes that appear promising for loss reduction may have features that will adversely affect stall margin. Since the cost of reblading and testing a high-speed, multistage compressor is so high, this will simply not be done if there is significant risk of stall margin loss. The principle disadvantage of this type of testing is that the effect of shock waves cannot be evaluated, but this is not a consideration in middle and rear stages of core compressors.

Low-Speed Modeling Procedure

In this section the procedure for obtaining a low-speed model of a high-speed core compressor is presented.

Establishing the High-Speed Conditions to be Modeled. The first step in the modeling process is to select and evaluate the high-speed condition to be modeled. The performance of the high-speed core compressor is determined either from a circumferential-average design analysis or from a data match of compressor test data that establishes vector diagram quantities and thermodynamic properties at each station in the compressor. The stages to be modeled are selected and their radius ratio, aspect ratio, and pitchline solidity are averaged. Conventional normalizing techniques for compressor stage characteristics are applied to the selected high-speed stages to establish average (target) values of pressure-rise and flow coefficients for the low-speed model. Average radial distributions of normalized rotor exit total pressure, rotor and stator loss coefficients, and stator exit swirl angles and average Reynolds numbers for the high-speed compressor

Nomenclature

A = annulus area of compressor
C = chord
D = diffusion factor

$$= 1 - \frac{V_2}{V_1} + \frac{\Delta V_\theta}{2\sigma V_1}$$

h = annulus height
$\dot{m}$ = mass flow
P = pressure (normalized pressure = $P/(1/2\,\rho U_T^2)$
ΔP = $P_2 - P_1$
r/r = radius ratio
R = radius
Re = Reynolds Number = $\rho U_T C/\mu$
S = circumferential spacing between airfoils
T = measured torque minus tare torque
U_T = tip wheel speed
V = velocity
α = absolute air angle
β = relative air angle
ϵ = blade tip clearance
η = efficiency = ψ'/ψ
μ = coefficient of viscosity
ξ = stagger angle
ρ = density
σ = solidity
ϕ = flow coefficient = $\dot{m}/\rho A U_t$
ψ' = pressure coefficient

$$[\Delta P/1/2\,\rho U_T^2]\left[1 = \frac{1}{2\gamma}\left(\frac{\Delta P}{P_1}\right) + \left(\frac{\gamma+1}{6\gamma^2}\right)\left(\frac{\Delta P}{P_1}\right)^2 + \ldots\right]$$

ψ = work coefficient = $T/(1/2\,\rho U_T^2 \phi)$

Subscripts

C = casing
H = hub
S = static conditions
t = total conditions
1 = inlet conditions
2 = discharge conditions
θ = tangential direction

Table 1 Comparison of performance parameters and vector diagram quantities for the high-speed stage 7 and the low-speed stage A baseline model

	High-Speed Stage 7	Low-Speed Model
Flow Coefficient	0.442	0.442†
Pressure Rise Coefficient	0.640	0.647†
Reaction (Pitchline)	68%	63%
Radius Ratio	0.89	0.85
Blade Tip Clearance to Height	1.28%	1.35%
Rotor Inlet Pitchline Quantities		
Relative Air Angle	59.3°	59.5°
Relative Mach Number	0.757	0.148
Wheel Speed U (M/S)	377.6	53.33
Normalized Tangential Vel.(V_θ/U)	0.815	0.815
Normalized Axial Velocity (V_z/U)	0.484	0.480
Rotor Exit Pitchline Quantities		
Relative Air Angle	46.2°	44.4°
Relative Mach Number	0.514	0.106
Wheel Speed U (M/S)	376.7	53.33
Normalized Tangential Vel.(V_θ/U)	0.469	0.472
Normalized Axial Velocity (V_z/U)	0.485	0.480
Stator Inlet Pitchline Quantities		
Absolute Air Angle	47.9°	47.6°
Absolute Mach Number	0.549	0.112
Normalized Tangential Vel.(V_θ/U)	0.523	0.528
Normalized Axial Velocity (V_z/U)	0.473	0.482
Stator Exit Pitchline Quantities		
Absolute Air Angle	21.7°	21.0°
Absolute Mach Number	0.382	0.080
Normalized Tangential Vel.(V_θ/U)	0.184	0.183
Normalized Axial Vel.(V_z/U)	0.462	0.476
Rotor Pitchline Properties		
Solidity	1.25	1.16
Aspect Ratio	1.28	1.20
Diffusion Factor	0.48	0.47
Incidence Angle	-1.5°	-8.9°
Deviation Angle	6.0°	7.8°
Camber	20.6°	31.8°
Flow Turning	13.1°	15.1°‡
Stator Pitchline Properties		
Solidity	1.67	1.58
Aspect Ratio	1.37	1.21
Diffusion Factor	0.46	0.46
Incidence Angle	-3.4°	-5.9°
Deviation Angle	6.2°	6.2°
Camber	35.8°	38.7°
Flow Turning	26.2°	26.6°

†These values were computed by using the pitchline wheel speed. Based on the rotor tip speed, the flow coefficient becomes 0.407 and the pressure coefficient becomes 0.555 as seen in the figures.

‡The additional rotor turning required for the low-speed model is evident.

stages are determined. An effective-area coefficient (blockage) is specified. The chordwise variations of Mach number (velocity) on the surfaces of the high-speed blades and vanes to be modeled are computed by using a blade-to-blade flow analysis procedure.

With this completed, the high-speed conditions to be modeled are established.

Creating the Low-Speed Vector Diagrams. The next step in the modeling process is to establish the vector diagram quantities and thermodynamic properties of the low-speed model. A circumferential-average analysis is conducted using a numerical solution of the radial-equilibrium equation, continuity equation, energy equation, and equation of state [4]. The radial distributions of normalized total pressure, loss coefficient and stator exit swirl angles determined for the high-speed compressor are input along with the annulus dimensions of the low-speed test facility, an effective-area coefficient, low-speed rotative speed, and an airflow that

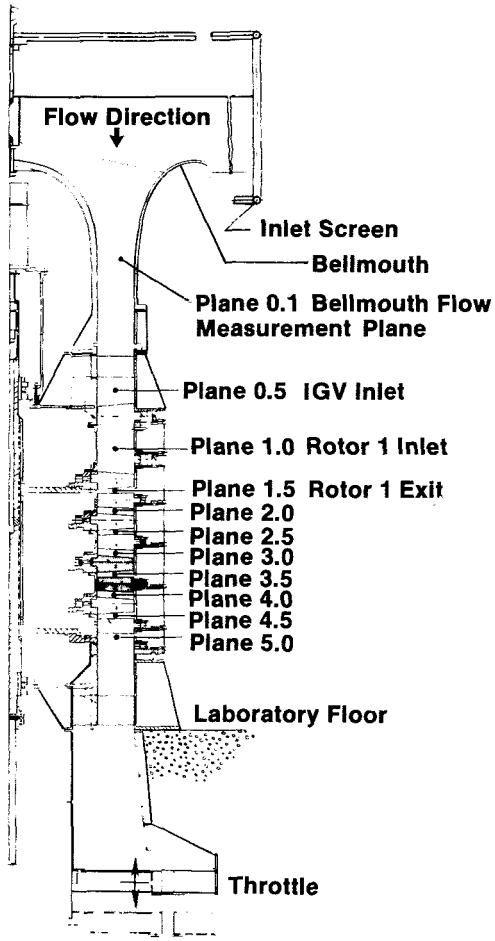

Fig. 2 Cross section of low-speed research compressor in 0.7 *r/r* configuration

matches the axial-velocity/blade-speed ratio of the high-speed compressor. The level of rotor exit total pressure is iterated until the target pressure rise coefficient is achieved. This target level may have to be slightly higher than the value of the high-speed compressor in order to produce comparable diffusion factors, because the high-speed compressor may have appreciable axial velocity diffusion, whereas the constant annulus height, incompressible flow, low-speed model will not. Also, the low-speed model may require a few degrees more rotor turning than the high-speed design in order to obtain comparable diffusion factors (needed to obtain similar blade surface velocity distributions) in the incompressible case where the axial velocity ratio is 1.0.

All vector diagram and thermodynamic information is now available for designing the low-speed airfoils.

Designing the Low Speed Airfoils. The low-speed airfoils are designed to achieve the same normalized suction surface velocity distribution as the high-speed airfoils by using the following iterative procedure. The low-speed blades are set relative to the low-speed vector diagram angles and then the incidence angles, the chordwise camber distributions, and the thickness distributions of the low-speed arifoils are modified until these airfoils achieve the same normalized surface velocity distributions as the high-speed airfoils. Generally, the low-speed airfoils require several degrees over cambering in the leading edge region and somewhat more thickness than the high-speed airfoils in order to match velocity distributions. A boundary layer analysis is conducted to locate the regions of transition and potential separation in order to verify aerodynamic similarity with the high-speed airfoil. The chord

Table 2 Listing of blading designs presented in text

Airfoil	Type
Rotor I	Baseline
Stator I	Baseline
Rotor II	Unload TE/Load LE Hub
Rotor III	Tailored Surface Boundary Layers
Rotor A	Baseline E^3
Stator A	Baseline E^3
Rotor B	Load TE/Unload LE Tip
Rotor C	Compensate for Tip Vortex, Hub-Strong P_T Profile
Stator B	Twist Gradients in Endwall

lengths and number of airfoils selected are based on the values of solidity and aspect ratio to be modeled. Testing is done at a Reynolds number equal to or nearly equal to the Reynolds number of the high-speed compressor at altitude cruise.

A typical example showing a performance comparison for a high-speed compressor and its low-speed model is given in Table 1 and [5].

Experimental Test Facility

The Low-Speed Research Compressor (LSRC) is an experimental facility that duplicates many of the essential features of a small high-speed compressor flow field in a large, low-speed machine where very detailed investigations of the flow-field can be made. The facility, shown schematically in a four-stage configuration in Fig. 2, has a constant casing diameter of 1.524-M (60.0 in.). The axis of rotation of the compressor is vertical, and flow enters from the top through a calibrated bellmouth/inlet system which filters and measures the flow. A bulletnose is inserted in the bellmouth to reduce the area of the flow measurement plane for greater measurement accuracy. After passing through the blading, the air is exhausted through a large, circular throttle plate that can be raised or lowered to change the compressor back pressure by varying the exit area. The facility is driven by a 400-hp steam turbine. Rotative speed of the compressor is controlled to within ±0.25 percent of design rpm. Power input to the compressor is determined by a strain gauge-type torquemeter in the drive shaft having an accuracy of ±0.07 percent of measured torque at the design point. All pressures are measured on pressure transducers having an accuracy of ±0.025 percent of full scale (12.45 KPa or 50 in H_2O). Overall measurement accuracies are as follows: flow coefficient and pressure coefficient are accurate to within ±0.15 percent and efficiency is accurate to within ±0.15 percent and efficiency is accurate to within ±0.15 points.

The compressor is set up in a four-stage configuration when testing models of core compressors in order to simulate the repeating stage environment. The third stage is generally the test stage for obtaining detailed internal performance and flow surveys. Overall performance, quoted as an average for the four-stage group, is based upon measured airflow, measured work input (torque and speed), and measured pressure rise from casing/hub static pressures and from mass-averaged radial distribution of total pressure obtained from pressure rakes.

The detailed performance of the blading is obtained from measurements using single-element traversing total and static pressure probes, boundary layer probes, flow-angle measuring probes, and rotating total pressure rakes read out through a slipring. Static pressure taps, located in a matrix of circumferential and radial positions on the blade and vane surfaces, provide airfoil pressure distributions and loading.

Loss Reduction and Performance Improvements

The use of low-speed model testing to reduce loss and improve the aerodynamic performance of core compressors is illustrated in the examples presented below. These examples are also listed in Table 2.

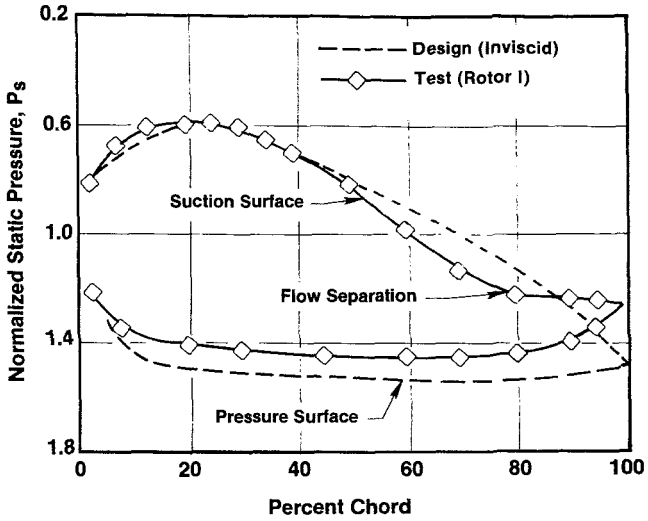

Fig. 3 Comparison of measured blade surface static pressures with design intent showing separated flow on baseline Rotor I

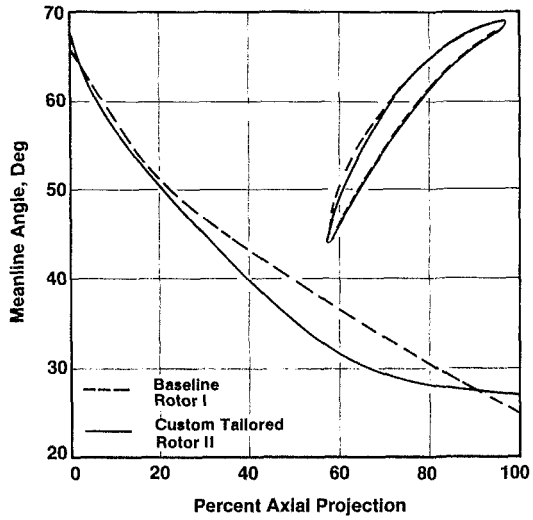

Fig. 4 Comparison of the baseline Rotor I with the "custom-tailored" Rotor II designed to reduce flow separation

Evaluating the Baseline. The performance of the low-speed baseline compressor is evaluated to locate regions of high loss and potential improvement. In this paper, two different low-speed baseline compressors are presented. Both are high-radius-ratio (r/r = 0.85), low-aspect-ratio, high-solidity compressors having shrouded stators and inlet guide vanes. Both have 54 rotor blades and 74 stator vanes in each stage.

The first baseline, called Rotor I/Stator I, is a low-speed model of Stages 4–9 of a highly-loaded, high-reaction, nine-stage core compressor. The high-speed compressor airfoil sections that were modeled have circular-arc meanlines, with double-circular-arc thickness distributions for the rotors and NACA 65-series thickness distributions for the stators. Test results showed that the low-speed design flow, pressure rise, and efficiency goals were closely meet. However, nearly 50 percent of the annulus height was affected by endwall boundary layers with indications of strong secondary flows. Also a large region of separated flow was found on the suction surface of the rotor hub at peak efficiency.

The second baseline, called Rotor A/Stator A, is a low-

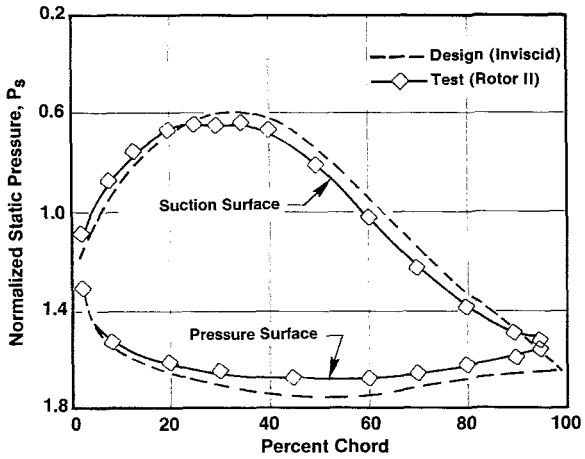

Fig. 5 Elimination of flow separation with Rotor II as shown by measurements of blade surface static pressures

speed model of Stage 7 of a preliminary design for the 10-stage, 23:1 pressure-ratio, E^3-type compressor [6]. The Stage A baseline blading was generally similar in design to the Stage I blading, except that the Rotor hub was modified as described below to avoid the separated flow found in Rotor I. A comparison of the performance parameters and the vector diagram quantities for the high-speed compressor and the corresponding low-speed model is presented in Table 2. Test results showed that the low-speed design goals were very closely met. However, that stator hub began showing evidence of flow separation with throttling, eventually causing the hub region to collapse and the pressure-flow characteristic to roll over and flatten out. Additional results are given in [7].

Custom Tailoring Airfoils. As Mach numbers and aerodynamic loading on airfoils increased and as improved cascade analysis techniques became available, designers recognized that the standard airfoil types conventionally used could often be improved upon. Consequently, in an effort to reduce loss, reduce flow separation, reduce the effects of tip leakage and secondary flow, control boundary layer growth, etc., they began to custom tailor the airfoil to the airflow by using camber and thickness distributions that are completely arbitrary (i.e., at the complete discretion of the designer). The following examples are given.

Airfoils Having Unloaded Trailing Edges and Loaded Leading Edges. The existence of separated flow on the suction surface of the baseline Rotor I hub was found experimentally. This separated flow was identified by a "flattening" of the measured static pressure distribution on the rotor suction surface as shown in comparison to design intent in Fig. 3. The meanline angle distribution and the airfoil section shape for the hub of the circular arc-type Rotor I are shown in Fig. 4. A subsequent custom tailoring of the airfoil sections near the rotor hub by uncambering (unloading or straightening) the trailing edge region, overcambering (loading) the leading edge region, and moving the maximum thickness toward the leading edge, as shown in Fig. 4, removed the separated flow, as estimated by a boundary layer analysis and as seen in Fig. 5.

The improved performance of the Rotor II configuration compared to that of the baseline is shown in Fig. 6. A significant 0.8 point increase in compressor efficiency was obtained at the design point when separated flow on the rotor hub was eliminated. Substantial increases in flow and pressure rise were also obtained because the reduction in deviation angle attendant to the removal of flow separation was larger than anticipated. This design modification was transformed to high speed and a comparable performance improvement

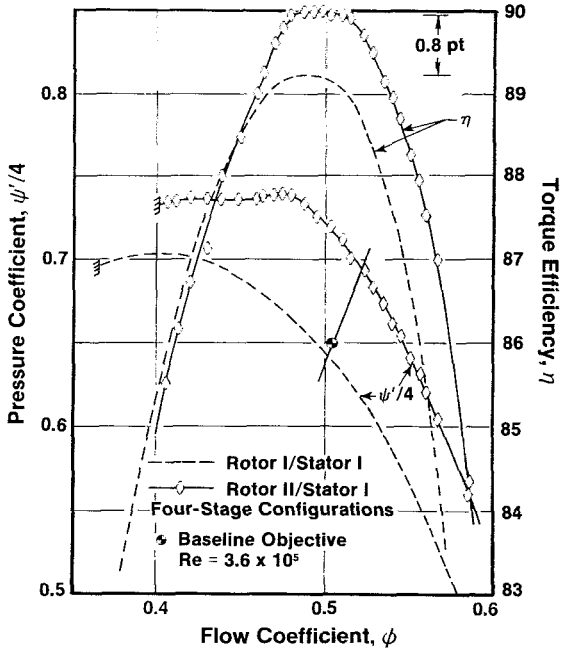

Fig. 6 Improved performance of the "custom-tailored" Rotor II relative to that of the baseline Rotor I

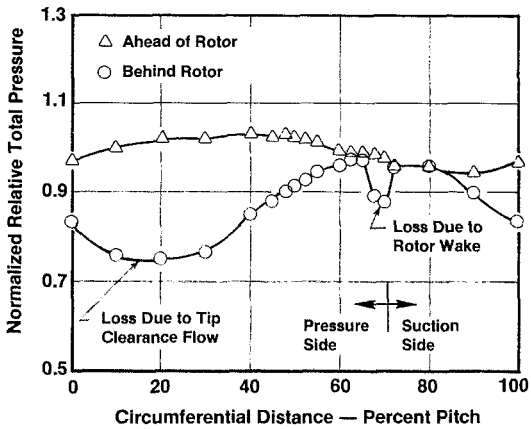

Fig. 7 Loss due to tip clearance flow compared to loss due to Rotor wake

was obtained there also. In addition, this design philosophy was incorporated into the hub sections of the baseline Rotor A, and no separated flow was observed on that rotor at the design point.

Airfoils Having Loaded Trailings Edges and Unloaded Leading Edges. Measurements of relative total pressure taken on the baseline Rotor A indicated that very small rotor wakes were present in the tip region, and a large tip-loss core, probably associated with the tip clearance flow, was located between the wakes (see Fig. 7). Similar trends have been observed by Fessler and Hartmann [8] and by Hunter and Cumpsty [9]. It was thought that the tip clearance flow might be entraining suction surface boundary layer fluid, explaining the unusually thin wakes near the tip. The rotor trailing edge region should, therefore, be able to take higher diffusion rates without separtion. Consequently, the tip meanline shape was modified to unload the leading edge by removing 4.5 deg of camber and loading the trailing edge by adding 6.0 deg of camber relative to Rotor A. The maximum thickness was moved from 50 to 60 percent chord, which gave increased trailing edge loading. This could reduce tip clearance leakage by reducing the maximum pressure difference across the rotor

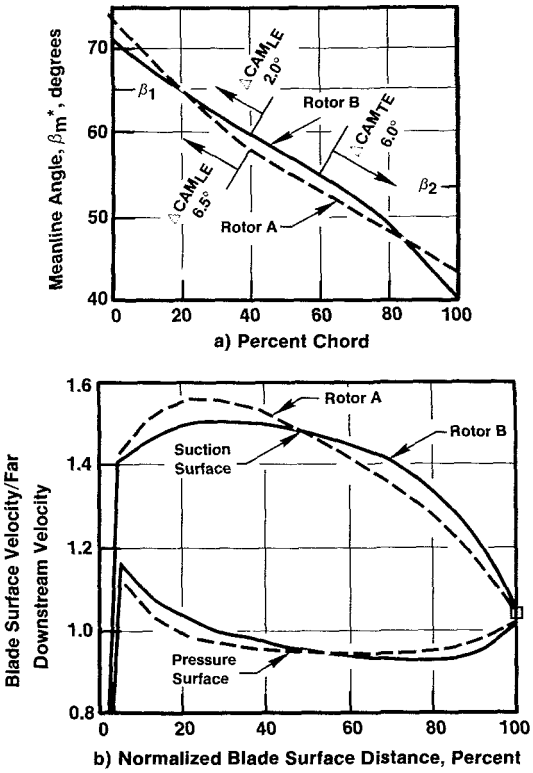

Fig. 8 Comparison of meanline angles and surface velocity distributions for Rotor B and baseline Rotor A

without undue risk of flow separation. Also, an added efficiency improvement might be expected at high speed due to the reduction in peak Mach number. The new rotor was named Rotor B, and a comparison of its meanline and surface velocities with those of Rotor A are given in Fig. 8. The loading differences between the rotors was gradually reduced radially so that the rotors were identical from the mean radial station (pitchline) to the hub.

Rotor B demonstrated an improved high-efficiency flow range and a 0.3 point improvement in efficiency at the design point compared with that of Rotor A, as seen in Fig. 9. Also, measured blade surface pressure distributions showed that the increased trailing edge loading, reduced leading edge loading, and reduced peak-suction-surface velocity were achieved.

The Rotor B-type airfoil section showed sufficient performance improvement over the baseline that its design features were transformed to high speed and incorporated into the core compressor of the NASA/GE Energy Efficient Engine (E^3).

Airfoils Having Tailored Surface Boundary Layers. Another type of custom-tailored rotor, Rotor III, was designed to have reduced profile drag by increasing the extent of laminar flow over the forward portion of the airfoil and then tailoring the turbulent diffusion over the aft portion to minimize trailing-edge values of suction surface momentum and displacement thicknesses. This approach was successfully used by Liebeck to reduce the drag of isolated airfoils [10] and was also discussed by Walker for cascades [11].

Rotor III was designed as follows. Laminar flow was promoted over the forward portion of the airfoil by continual acceleration of the flow from the leading edge to Schlichting's flat-plate instability point [12]. For the hub section, the peak suction surface velocity was moved aft from 25 percent arc length to 38 percent compared to the baseline Rotor I. At the tip, the movement was from 27 percent to 55 percent. Transition from laminar to turbulent boundary layer then followed in a region of zero velocity change. The turbulent diffusion immediately aft of the transition point was rapid at

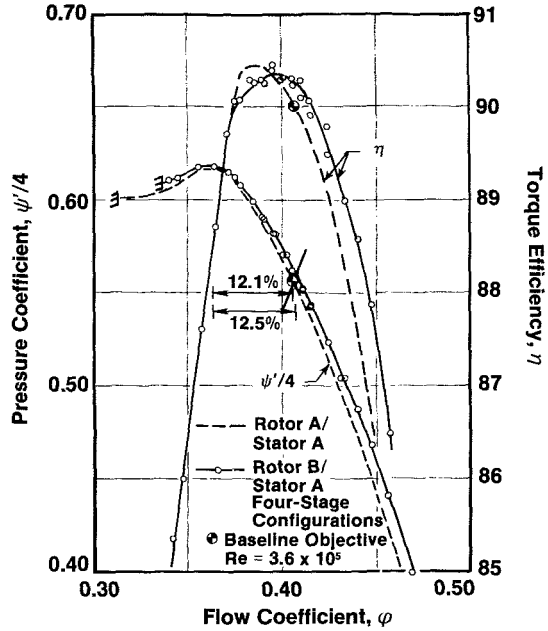

Fig. 9 Improved performance of Rotor B relative to that of Rotor A

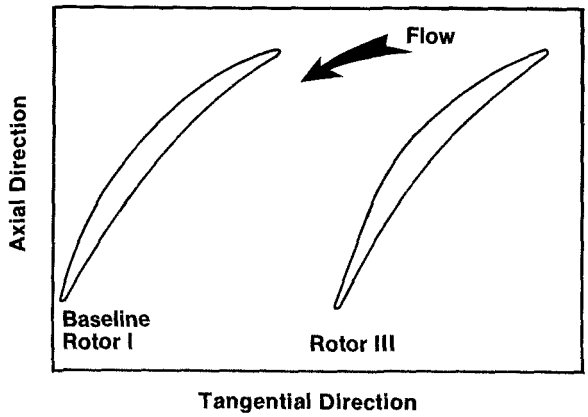

Fig. 10 Comparison of Rotor III airfoil section having tailored surface boundary layers with that of the baseline Rotor I

first, since the boundary layer was stable and capable of large amounts of diffusion without separation. As the turbulent boundary layer developed, the diffusion rate was decreased toward the trailing edge. Boundary layer calculations made on Rotor III predicted a 30 percent reduction in friction losses; this is equivalent to a gain in polytropic efficiency of 0.5 point. However, this gain depends upon maintaining laminar flow on the suction surface as intended. If transition occurs either earlier or later than intended, the profile losses increase and may be no smaller than the baseline losses. A Rotor III airfoil section generated by this technique is compared to the baseline Rotor I section in Fig. 10.

The performance of Rotor III is compared to that of the baseline Rotor I in Fig. 11. Both rotors are running with the same baseline Stator I. The improved performance of Rotor III near the design point and a 1 point improvement in efficiency demonstrated the success of the technique. The normalized blade surface static pressure measurements shown in Fig. 12(*a*) are in good agreement with design intent at the design point. The location of the peak suction surface velocity far aft on the blade and the rapid diffusion to the trailing edge are clearly shown.

However, further development of this design philosophy is needed because when this stage was throttled below the design flow, a rather abrupt reduction in flow, pressure rise and

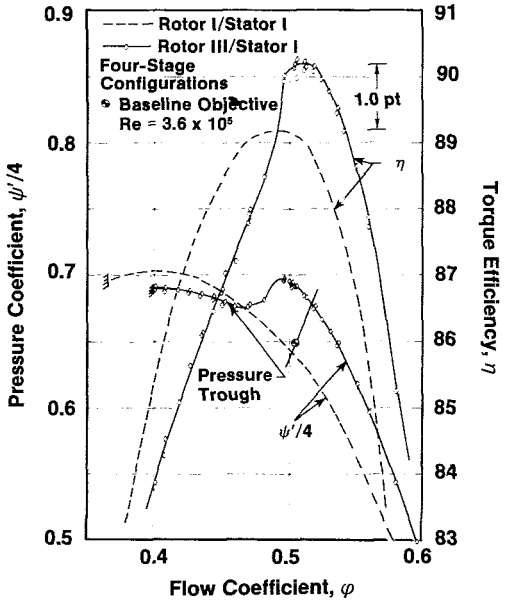

Fig. 11 Improved performance of Rotor III relative to that of Rotor I

efficiency to levels below the baseline values occurred, as shown in Fig. 11. This was produced by the sudden onset of a large region of separated flow in the hub region. The blade surface static pressure measurements in Fig. 12*b*, taken at 20 percent span in the pressure-trough region, show this substantially reduced blade loading and presence of separated flow. The multistaging effect, whereby reduced pumping due to the onset of separation in one stage raises the incidence further and compounds the problem in surrounding stages, apparently is more severe than usual with blading in which the turbulent diffusion is scheduled to just avoid separation over a substantial portion of the airfoil at the design condition. Design modifications to the airfoils were specified in which the design concept was unchanged but the trailing edge camber was reduced in order to reduce the pressure rise at the design flow. These new airfoils were tested and were found to partially relieve the abrupt flow separation, but further development is required before this type of blading is proven to be fully satisfactory in the multistage environment.

Airfoils Having Compensation for Secondary Flow/Tip Leakage Effects. Analysis of the static pressure measurements on the suction surfaces near the tips of both Rotors A and B revealed an undesirable acceleration-deceleration-acceleration of the fluid along the forward half of the suction surface as seen in Fig. 13. This was attributed to three-dimensional secondary flow and tip leakage effects. As a consequence, an innovative "tailored" airfoil shape was designed to compensate for this undesirable effect. The new rotor design, Rotor C, was based on the differences between the design intent velocity distribution and the experimentally observed one for Rotor B. The suction surface velocity was found to be less than the Rotor B design intent from 0 percent to 35 percent along the blade surface and greater than design intent from 35 percent to the trailing edge (see Fig. 13). Based on this, if Rotor C were designed in the same manner, a similar undesirable velocity distribution would probably result. Therefore, the following design approach was undertaken in the outer 20 percent of span. First, the desired velocity distribution for Rotor C was established. Then, in order to avoid the acceleration-deceleration-acceleration pattern, a "mirror image" velocity distribution was chosen which "overaccelerates" the potential flow solution relative to the desired distribution in the first 32 percent of the blade surface and "underaccelerates" it in the midportion of the blade. The

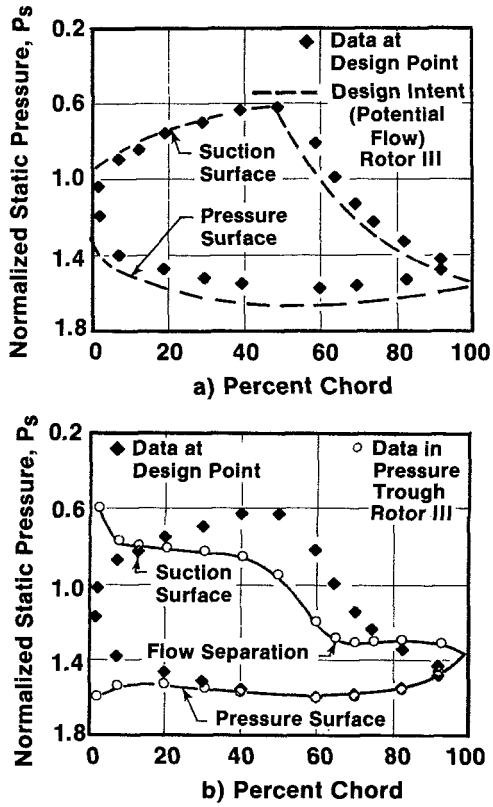

Fig. 12 Measured surface static pressure distribution for Rotor III: (a) at the design-point, (*b*) in the pressure-trough region

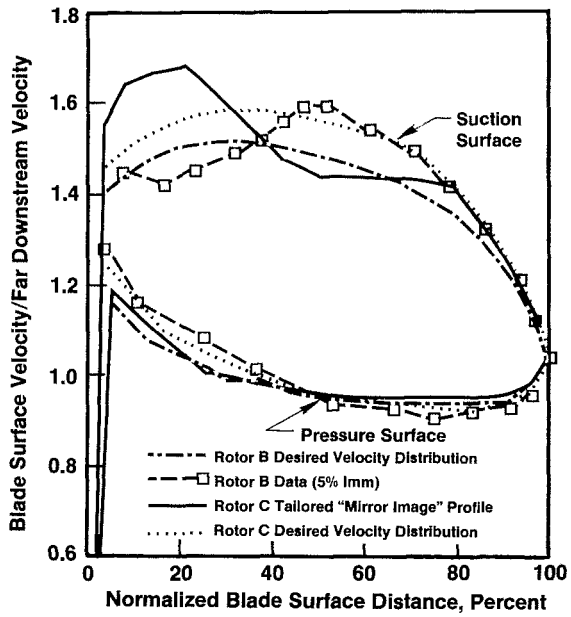

Fig. 13 Comparisons of normalized blade surface velocity distributions for the tip sections of Rotors B and C

blade was designed using this "mirror image" distribution and a two-dimensional cascade analysis by streamline curvature computer code, anticipating that the desired velocity distribution would be achieved during test after secondary flow effects are encountered. Figure 14 presents a comparison of the tip section meanline shapes of Rotors B and C. Aside from its nonconventional shape, the Rotor C tip section stagger is higher by 3.3 deg in recognition of the vector diagram changes which will be described later.

Rotor C demonstrated a small improvement in peak efficiency (0.1–0.2 point) and a very slight increase in the range

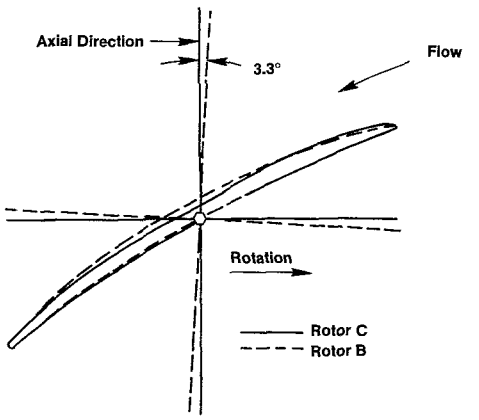

Fig. 14 Comparison of airfoil tip sections for Rotors B and C

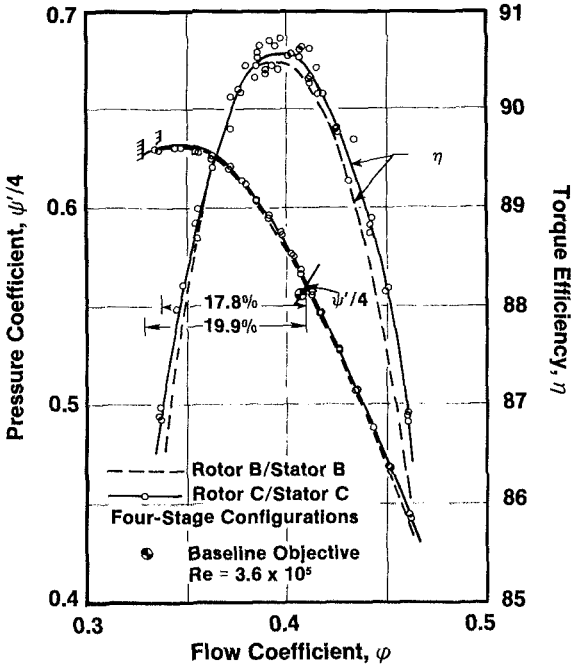

Fig. 15 Comparison of the overall performance of Rotors C and B

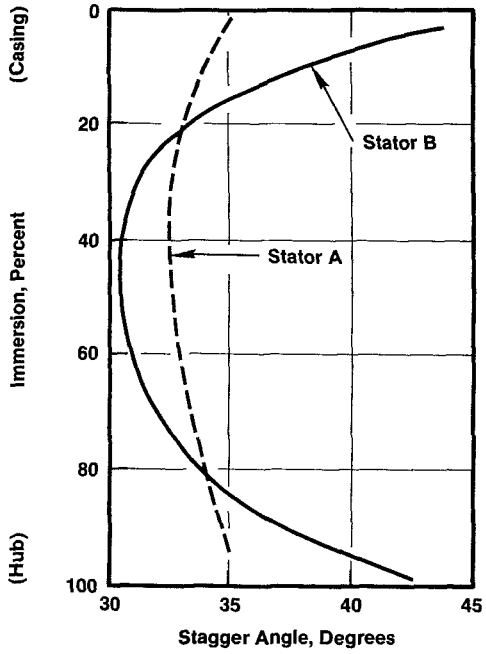

Fig. 16 Swirl distribution of Stator B compared with that of Stator A

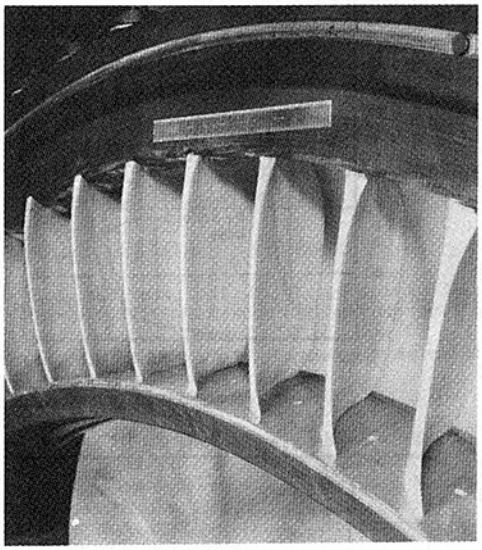

Fig. 17 Photograph of Stator B

of high efficiency operation compared with Rotor B, as seen in Fig. 15. Because of vector diagram changes, the improvement in overall performance cannot be attributed entirely to the novel rotor tip section shape, but it is thought to be a contributor. The pressure distribution on the airfoil surface in the tip region exhibited some, but not all, of the "smoothing" that was intended. The effects of secondary flow and tip leakage are still apparent. More work is needed in this area to fully compensate for tip clearance effects, but the initial results were encouraging.

Trailoring Vector Diagrams. Detailed flow measurements in the Stator A baseline blading showed regions of high swirl angles near both endwalls and regions of separated flow near the hub. In an effort to reduce losses in these areas, the vector diagrams were "tailored" to produce vane twist in the endwall region and to have a hub-strong total pressure profile.

Twist Gradient Vector Diagram. The twist gradient vector diagram incorporates higher stator exit swirl angles in the endwall regions compared to the more conventional baseline swirl distribution as shown in Fig. 16. This produces lower axial velocities (reduced flow) in the endwall region and higher axial velocities in the pitchline region relative to the baseline. The same values of pressure rise, flow coefficient, flow turning, and average stator exit tangential momentum as the baseline were maintained. The resulting stator, called Stator B, is twisted closed about 8 deg in the endwall regions but has the same incidence angles, thickness distribution, and type of meanline angle distribution as the baseline Stator A. The airfoil sections of Stator B were stacked at 30 percent chord rather than the usual 50 percent chord to reduce the acute angles where the suction surface intersects the endwalls in the leading edge region, since large acute angles would cause increased corner boundary layer growth. The appearance of Stator B, shown in Fig. 17, is considerably different from that of a more conventional stator.

Stator B demonstrated two important performance improvements over Stator A as seen in Fig. 18. First, an improvement in efficiency was obtained at every flow tested with a 0.4 to 0.5 point improvement at the design point. This implied a 10 percent reduction in endwall loss. Second, a significant improvement in the pressure-flow characteristic

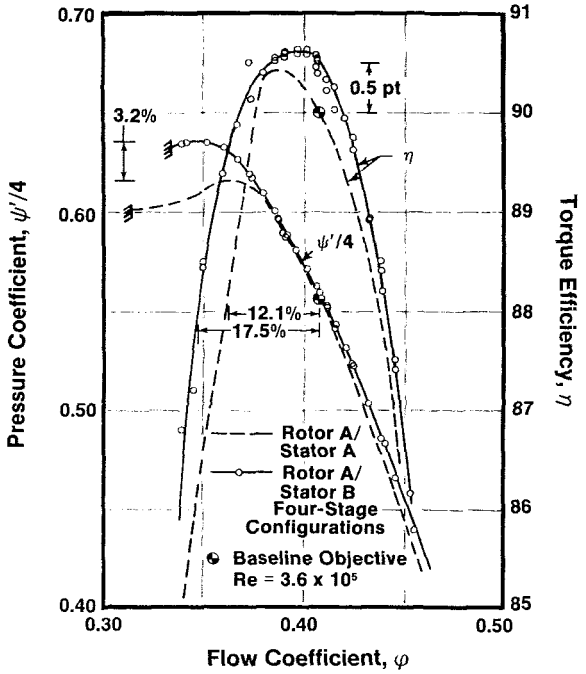

Fig. 18 Improved performance of Stator B relative to that of Stator A

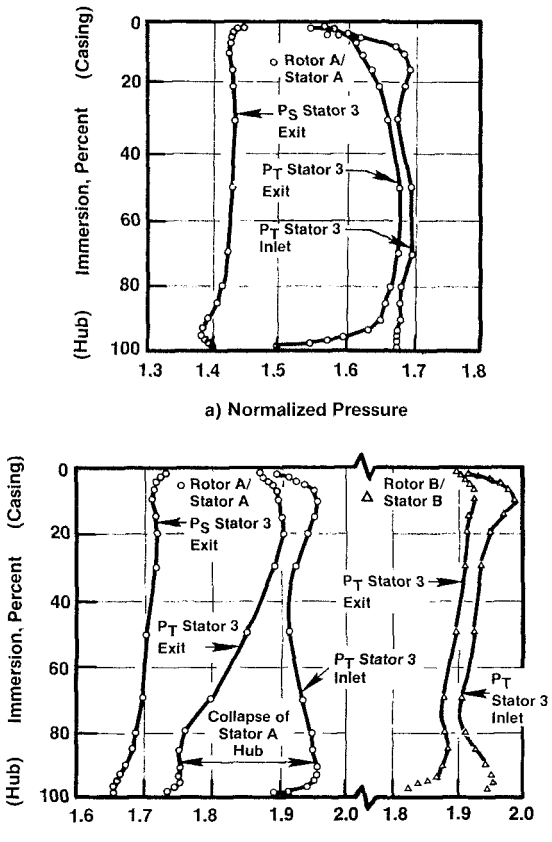

Fig. 19 Radial variation of total pressure showing (*a*) losses near endwalls at design point and (*b*) collapse of Stator A hub relative to Stator B upon throttling

was obtained from peak efficiency to stall, with an elimination of the rollover and flattening of the characteristic observed in the baseline. There is a 3.2 percent improvement in peak pressure coefficient and a 5.4 percent improvement in flow range from the design point to peak pressure. The 6 percent increase in stalling flow coefficient for Stator B is not thought to be too significant, since rear stages of this type will

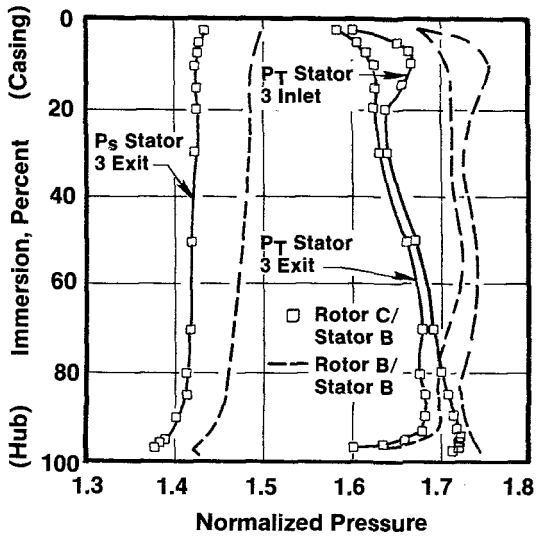

Fig. 20 Hub-strong total pressure profile of Rotor C

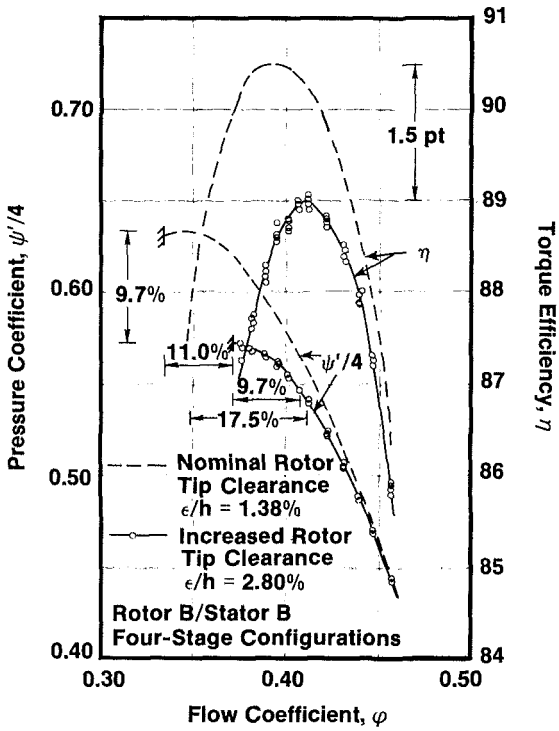

Fig. 21 Effect of increased tip clearance on overall compressor performance

probably not operate much beyond the peak pressure rise point in a high-speed compressor.

Detailed surveys of total pressure, static pressure and flow angles were taken across the annulus in order to locate and assess high-loss regions. Selected results are shown in Fig. 19, where the higher loss regions near the endwall are evident at the design point in Fig. 19(*a*). The losses in the hub region were slightly lower for the B-type vector diagram than for the baseline A-type, supporting the performance improvement observed in Fig. 18. As the compressor was throttled to peak pressure, the hub region began to weaken and, upon further throttling, collapse for the A-type vector diagram, while the hub remained stronger for the B-type. This collapse of the hub flow, shown in Fig. 19(*b*), is primarily responsible for the rollover and flattening of the baseline pressure/flow characteristic in Fig. 18.

Further evidence of the improvement in the stator hub flow using the B-type vector diagram was seen in the vane surface static pressure measurements. Stator B operates with less leading edge loading, more favorable incidence, and less flow separation than Stator A.

The twist-gradient type of vector diagram showed sufficient performance improvement over the baseline that it was incorporated into the core compressor of the NASA/GE Energy Efficient Engine (E^3).

Hub-Strong Pressure Gradient. Analyses of the Rotor B/Stator B configuration showed that further strengthing of the hub region could be beneficial. Consequently, Rotor C was designed to produce higher total pressure from pitchline-to-hub and lower total pressure from pitchline-to-tip than Rotors A and B, but with the same overall average. A radially nonconstant distribution of total pressure of ±24% of stage exit dynamic head, to help reduce hub loading, was used compared to ±9% for Rotors A and B. The significant hub strong tilt in the measured pressure distribution is apparent in Fig. 20, although no change in the hub loss coefficient was observed.

The Rotor C-type vector diagram, coupled with the blade shape change that was discussed previously, did produce a modest 0.1 to 0.2 point improvement as shown in Fig. 15.

Evaluating the Effects of Tip Clearance, Leakage, Etc. The aerodynamic efficiency of axial flow fans, compressors, and turbines is highly dependent upon the leakage flow through airfoil tip clearances, stator shroud seals, rotor dovetails, etc. An increase in the clearance produces a substantial increase in leakage, which consequently produces a substantial loss in efficiency and stall margin. Typical leakage paths are shown in Fig. 1.

The LSRC has provided valuable data showing the effects of flow leakage on compressor performance. The following example, taken from an extensive, systematic study, is given. Overall performance of the Rotor B/Stator B four-stage configuration was obtained at two levels of tip-clearance-to-blade-height ratio, 1.36 and 2.8 percent, and results are shown in Fig. 21. This increase in tip clearance costs 1.5 points in peak efficiency, 11.0 percent in stalling flow coefficient (flow range), and 9.7 percent in peak pressure rise relative to the nominal clearance. The increase in loss near the casing at increased clearance extended to 30 percent immersion in the measured profiles of relative total pressure. These are substantial penalties to pay, and designers are using innovative techniques such as active clearance control and modified wall geometry to minimize the loss in performance. Research programs have been conducted in the LSRC to evaluate modified wall geometries in the form of casing treatment [13], trenches over the rotor tip, and shroud/seal configurations.

Improving Analytical Models. Advances in analytical methods are contributing to better optimization of design parameters and to improved performance through better modeling of the flow fields in the compressor. The LSRC has contributed to this advancement by providing reliable test data for developing these models.

A stall margin correlation has been developed [14] that gives the peak pressure rise coefficient achievable in the multistage environment where stall is usually caused by flow breakdown in the endwall region. Peak recovery was found to be a function of a geometric parameter analogous to that used to correlate diffuser performance, with additional dependence on tip clearance, Reynolds number, and vector diagram type. This correlation is based upon a large amount of LSRC data, plus some other sources. Stall pressure rise data from high-speed multistage compressors and fans, corrected to the same Reynolds number an normalized clearance as the LSRC configurations, are in excellent agreement with the low-speed data and the diffuser correlation.

A preliminary design model capable of predicting the maximum efficiency potential of an axial-flow compessor has been developed [1]. The profile loss and endwall loss portions of this model were developed by using LSRC data. The efficiency of virtually all configurations could be predicted to within ±1 point using this model, and the agreement was within ±0.5 points for 70 percent of the cases, even at highspeed.

A secondary flow, spanwise mixing analysis has been developed for axial flow turbomachines [15]. Detailed measurements taken on the LSRC have provided a major source of experimental data a demonstrate the validity of the analysis.

Conclusions

Low-speed aerodynamic model testing plays a significant role in developing turbomachinery components. It often provides a lower-cost, lower-risk approach than high-speed testing. However, great care must be exercised when constructing aerodynamic models so that similarity is adequately achieved. The large number of successful examples of component development through low-speed model testing, some of which were presented in this paper, attest to the validity of the technique.

Acknowledgments

The author wishes to thank the Aircraft Engine Business Group of the General Electric Company and the National Aeronautics and Space Administration for their permission to publish this paper. Some of the research presented was sponsored by NASA under Contract NAS3-20070, Dr. Wojciech Rostafinski, Project Manager.

References

1 Koch, C. C., and Smith, L. H., Jr., "Loss Sources and Magnitudes in Axial-Flow Compressors," ASME JOURNAL OF ENGINEERING FOR POWER, Vol. 98, No. 3, July 1976, p. 411.

2 Keuthe, A. M., and Chow, C. Y., *Foundation of Aerodynamics*, John Wiley and Sons, 1976, pp. 15–18 and pp. 255–279.

3 Liepmann, H. W., and Roshko, A., *Elements of Gas Dynamics*, John Wiley and Sons, 1957, pp. 253–263.

4 Smith, L. H., Jr., "The Radial Equilibrium Equation of Turbomachinery," ASME JOURNAL OF ENGINEERING FOR POWER, Jan. 1966.

5 Wisler, D. C., *Core Compressor Exit Stage Study*, Volume 1, Design Report, NASA CR 135391, Dec. 1977.

6 Wisler, D. C., Koch, C. C., and Smith, L. H., Jr., "Preliminary Design Study of Advanced Multistage Axial Flow Core Compressors," NASA CR135133, Feb. 1977.

7 Wisler, D. C., *Core Compressor Exit Stage Study*, Volume VI, Final Report, NASA CR 16554, Dec. 1981.

8 Fessler, T. E., and Hartmann, M. J., "Preliminary Survey of Compressor Rotor-Blade Wakes and Other Flow Phenomena with a Hot-Wire Anemometer," NACA Research Memorandum RM E56A13, June 1956.

9 Hunter, I. H., and Cumpsty, N. A., "Casing Wall Boundary Layer Development Through an Isolated Compressor Rotor," ASME Paper No. 82-GT-18, 1982.

10 Liebeck, R. H., "A Class of Airfoils Designed for High Lift in Incompressible Flow," AIAA Paper No. 73–86, 1973.

11 Walker, G. L., "A Family of Surface Velocity Distributions for Axial Compressor Blading and Their Theoretical Performance," ASME Paper No. 75-GT-34, 1975.

12 Schlichting, *Boundary Layer Theory*, McGraw Hill, 1979, 7th ed., pp. 449–483.

13 Prince, D. C., Jr., Wisler, D. C., and Hilvers, D. E., Study of Casing Treatment Stall Margin Improvement Phenomena," NASA CR-134552, Mar. 1974.

14 Koch, C. C., "Stalling Pressure Rise Capability of Axial Flow Compressor Stages," ASME JOURNAL OF ENGINEERING FOR POWER, Vol. 103, Oct. 1981, p. 645.

15 Adkins, G. G., Jr., and Smith, L. H., Jr., "Spanwise Mixing in Axial-Flow Turbomachines," ASME JOURNAL OF ENGINEERING FOR POWER, Vol. 104, Jan. 1982, p. 97.

An Experimental Study of the Compressor Rotor Blade Boundary Layer

M. Pouagare
Graduate Assistant.

J. M. Galmes[1]
Research Associate.

B. Lakshminarayana
Director of Computational Fluid Dynamics Studies and Professor of Aerospace Engineering.
Fellow ASME

Department of Aerospace Engineering,
The Pennsylvania State University,
University Park, Pa. 16802

The three-dimensional turbulent boundary layer developing on a rotor blade of an axial flow compressor was measured using a minature "x" configuration hot-wire probe. The measurements were carried out at nine radial locations on both surfaces of the blade at various chordwise locations. The data derived includes streamwise and radial mean velocities and turbulence intensities. The validity of conventional velocity profiles such as the "power law profile" for the streamwise profile, and Mager and Eichelbrenner's for the radial profile, is examined. A modification to Mager's crossflow profile is proposed. Away from the blade tip, the streamwise component of the blade boundary layer seems to be mainly influenced by the streamwise pressure gradient. Near the tip of the blade, the behavior of the blade boundary layer is affected by the tip leakage flow and the annulus wall boundary layer. The "tangential blockage" due to the blade boundary layer is derived from the data. The profile losses are found to be less than that of an equivalent cascade, except in the tip region of the blade.

Introduction

Viscous and turbulence effects in the flow through turbomachinery rotor passages play a very significant role in the continued improvement in performance, design, and development of turbomachinery. The boundary layer developing on a rotor blade is mostly turbulent and three-dimensional (Fig. 1) and is significantly affected by the rotation, curvature, and pressure gradients that exist in these passages. In the front stage, where the turbulence is low, there may be a laminar and transitional boundary layer near the leading edge. The boundary layers are also affected by the presence of the annulus (tip and hub) walls. The rotor blade boundary layer is one of the least understood phenomena due to the complexities in measurement as well as analysis. The probes used should rotate with the rotor and, since the boundary layers are thin, they should be miniaturized for accurate measurement.

One of the major objectives of this investigation is to experimentally study these boundary layers, from the hub to the tip and from the leading to the trailing edge on both surfaces of the blade. This should lead to a better understanding of the effects of these boundary layers on rotor passage flow, losses, and other phenomena. The additional objective is to obtain a comprehensive set of data that can be utilized in the validation

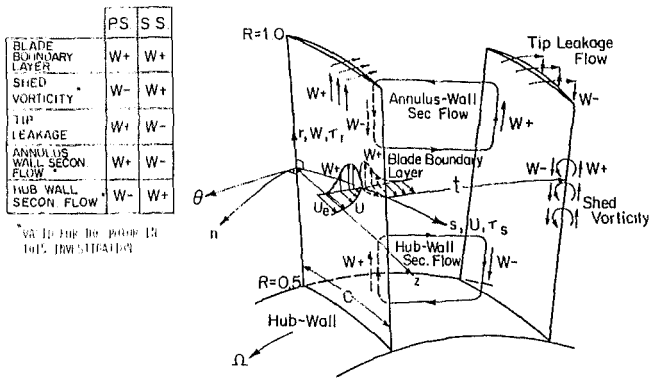

Fig. 1 Nature of blade boundary layer and notation used

of computer codes under development at The Pennsylvania State University and elsewhere for the prediction of the entire viscous flow in turbomachinery rotor passages.

The boundary layers developing at various radii are strongly coupled. Hence it is necessary to study the entire boundary layer (hub to tip on both surfaces) for a thorough understanding and interpretation of the viscous flow close to the blade surface. In earlier work [1], the blade boundary layer measurements were taken on a lightly loaded fan rotor blade at only four radial locations. Also Toyokura's et al. [2] measurements of the blade boundary layer in an axial flow compressor were carried out only at three radial locations. The present study is more comprehensive and includes measurement of 68 boundary layers on both surfaces of a compressor rotor blade.

[1] Presently at Societe Europeenne de Propulsion, Vernon, France

Contributed by the Gas Turbine Division of THE AMERICAN SOCIETY OF MECHANICAL ENGINEERS and presented at the 29th International Gas Turbine Conference and Exhibit, Amsterdam, The Netherlands, June 4–7, 1984. Manuscript received at ASME Headquarters January 18, 1984. Paper No. 84-GT-193.

Table 1 Rotor blade element details

	Radius Ratio					
	Rotor					
Radius ratio	0.5	0.6	0.7	0.8	0.9	1.0
Chord, cm	12.39	12.68	13.25	13.68	14.41	15.41
Blade spacing, cm	6.97	8.37	9.60	11.15	12.55	13.94
C_L	0.457	0.464	0.588	0.600	0.476	0.17
Max. thickness (percent of chord)	9.5	9.1	7.6	6.5	5.9	5.1
Stagger angle, deg	22.5	26.0	28.5	34.0	39.0	45.0

Experimental Facility and Measurement Technique

The Axial Flow Compressor Facility. The measurements reported in this paper were performed in the axial flow compressor facility in the Department of Aerospace Engineering at The Pennsylvania State University. A detailed discussion of the facility is given by Lakshminarayana [3]. The hub/outer annulus wall diameter ratio of the facility is 0.5, with the diameter of the outer annulus wall equal to 0.932 m. The inlet guide vane row consists of 43 blades, and the rotor of 21 blades. The distance between the IGV trailing edge and the rotor leading edge is 24.1 cm (or three chord lengths of IGV blade) at the midspan position. The performance of this compressor stage ($\psi - \phi$ curve) is given in [3]. Operating conditions for the data reported herein (except the blade pressure distribution) are as follows: flow coefficient based on tip speed, $\phi = 0.56$ (design flow coefficient); stage loading coefficient based on tip speed, $\psi = 0.486$; speed of the rotor, 1088 rpm; tip clearance 0.15–0.2 cm. The blade element details of the rotor are given in Table 1.

Rotating Probe Traverse Mechanism and Data Acquisition System. The rotating-probe traverse mechanism and the instrumentation system used in these blade boundary layer measurements are described in detail in [3]. The main feature of the rotating-probe traverse gear mechanism is a SLO-SYN motor of 0.007 Nm torque driving a 31.81 $\times$ 10^{-3}-m-dia shaft through a planetary reduction gear train. The gear train steps down the circumferential stepping from 1.8 deg/step to 0.0166 deg/step. Because of the fine step, the initial positioning of the probe can be done very accurately with maximum uncertainty of ± 0.05 mm. The probe holder, stepping motor, and probe are mounted inside the rotating hub of the machine. The motor is powered and controlled by a stationary traverse indexing device through an eight-channel brush slip-ring unit. Thus the circumferential traverse can be accomplished when the rotor is rotating. The radial and axial motions have to be accomplished manually when the rotor is stationary. The probe traverses in slots in the hub.

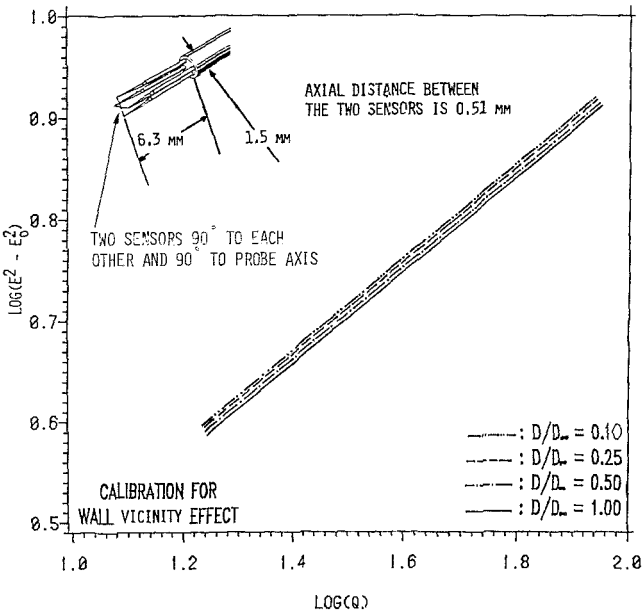

Fig. 2 Hot-wire calibration curves for wall vicinity effect

Nomenclature

B = blockage coefficient (equation (10)); constant in King's law (equation (1))
C = chord length
C_D = local drag coefficient based on local inlet dynamic head of the relative flow
C_L = local lift coefficient based on local inlet dynamic head of the relative flow (derived from measured blade pressure distribution)
C_p = pressure coefficient $(p_l - p_1)/\frac{1}{2}\rho U_1^2$
D = drag force; distance between sensor and wall
D_∞ = reference distance between sensor and wall
e = fluctuating voltage
E = voltage of the hot-wire
E_0 = voltage of the hot-wire at zero velocity
l = length of the hot wire
d = diameter of the hot wire
N = n/C
n' = exponent in the power law equation
p_l, p_1 = local and inlet static pressure
P_0 = relative stagnation pressure
Q = calibration nozzle jet velocity
R = r/r_{tip}
S = streamwise distance (s) normalized by the corresponding arc length of the blade surface measured from the leading to the trailing edge of the blade
s,n,r = streamwise, normal, and radial directions (orthogonal to each other) shown in Fig. 1. $s = 0$ at the leading edge, $n = 0$ on the blade surface, $r = 0$ at the axis of the machine
t = blade spacing
T_s, T_r = streamwise and radial turbulence intensity normalized by U_e
T_z, T_θ = axial and tangential components of turbulence intensity normalized by local relative velocity
u,v,w = fluctuating velocities in s-, n-, r-directions (Fig. 1)
V_1, V_2 = total velocity sensed by wires 1 and 2, respectively
V_z, V_θ = axial and relative tangential

Table 2 Radial and streamwise measurement locations of the blade boundary layer

R	Pressure side distance S				Suction side distance S			
0.583	0.22	0.44	0.68	0.92	0.49	0.66	0.81	0.99
0.67	0.23	0.48	0.70	0.93	0.55	0.69	0.84	0.99
0.75	0.24	0.52	0.73	0.94	0.60	0.72	0.87	0.99
0.832	0.245	0.525	0.75	0.95	0.63	0.77	0.9	0.99
0.918	0.25	0.53	0.76	0.96	0.65	0.81	0.94	0.99
0.945	0.26	0.54	0.78	0.97	0.66	0.83	0.96	
0.959	0.26	0.54	0.78	0.97	0.66	0.83	0.97	
0.973	0.27	0.55	0.79	0.98	0.67	0.84	0.98	
0.98	0.27	0.55	0.79	0.98	0.67	0.84	0.99	

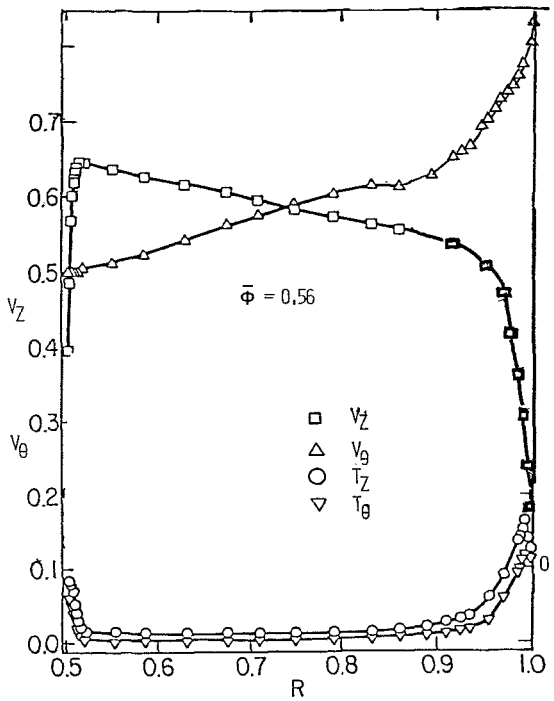

Fig. 3 Inlet axial and relative tangential velocity and turbulence intensity profiles (0.35 chords upstream of the rotor leading edge)

Measurement Technique and Corrections for Wall Vicinity Effect. All the velocity and turbulence measurements were taken with a miniature cross flow "x" wire probe (TSI model 1247), shown as an insert in Fig. 2. The sensors were 3-μm-dia platinum-tungsten wires with $l/d \approx 300$. The sensors were located in the (s–r)-plane with their axis at 45 deg to the s-axis (Fig. 1) and were traversed normal to the blade surface. The signals from each of these wires were transmitted through a slip-ring unit to two DISA 55D01 anemometers, a sum and difference circuit, and an R.M.S. voltmeter. The upper frequency response of the hot-wire system was adjusted to about 20 KHz, which was sufficient to resolve the highest turbulent frequencies of about 15 KHz encountered in this flow. Since the flow traverse was done close to the blade surface, the component of velocity in the n-direction is assumed to be small. The present configuration, together with the relevant hot-wire equations [4] provide the value of the streamwise velocity U, radial velocity W, and the respective intensities $\overline{u^2}$ and $\overline{w^2}$ in the s, n, r system shown in Fig. 1. The s-coordinate is parallel to the blade surface lying on the cylindrical plane, n is principal (outward) normal, and r is in the radial direction, as shown in Fig. 1. The coordinate system is orthogonal.

Since the measurements were taken very close to the blade surface and wire heat transfer characteristics are affected by the wall vicinity, the hot-wire probe was calibrated to derive corrections for the wall vicinity effect. The probe was calibrated in a jet, with a wall (parallel to the jet) at the exit. The distance between the wall and the probe was gradually changed from 0.5 mm to 5 mm, beyond which the change in calibration curve (see Fig. 2) was found to be negligibly small. The data includes the voltage at zero velocity (E_0) as well as the voltage (E) at various jet velocities (Q). It is clear from Fig. 2 that the exponent in King's is not affected by the wall. King's law is given by

$$E^2 - E_0^2 = BQ^\alpha \tag{1}$$

where B is a calibration constant and α is the exponent. The values of E_0 and B are affected by the wall vicinity. The correlation for the wall vicinity based on this data is given by

Nomenclature (cont.)

velocity normalized by the blade tip speed
U = streamwise relative velocity normalized by U_e
U_e = local free-stream (or edge) relative streamwise velocity
U_1 = local inlet relative velocity
U_t = blade tip speed
W = radial velocity normalized by U_e
α = exponent in King's law (equation (1))
β = relative flow angle measured from the axial direction
γ = stagger angle
δ = boundary layer thickness normalized by the local blade chord
ϵ = streamline angle in the s–r-plane
ϵ_w = limiting streamline angle
ζ = profile loss coefficient (equation (11))
δ_1, θ_{11}
δ_2, θ_{22}
θ_{21}, θ_{12} = displacement and momentum thicknesses normalized by C
ν = kinematic viscosity
ϕ = average flow coefficient (average axial velocity at the inlet of the IGV divided by the blade tip speed)
ψ = mass-averaged stagnation pressure rise coefficient normalized by $\rho U_t^2/2$

Subscripts

max = maximum values
ps,ss = pressure and suction surfaces, respectively
se = edge values in the streamwise direction
TE = trailing edge
w,e = wall and edge, respectively
z = axial direction
∞ = values at the location where there are no wall vicinity effects
0 = values at zero velocity; stagnation values
1,2 = inlet and exit of the rotor; values refer to wires 1 and 2

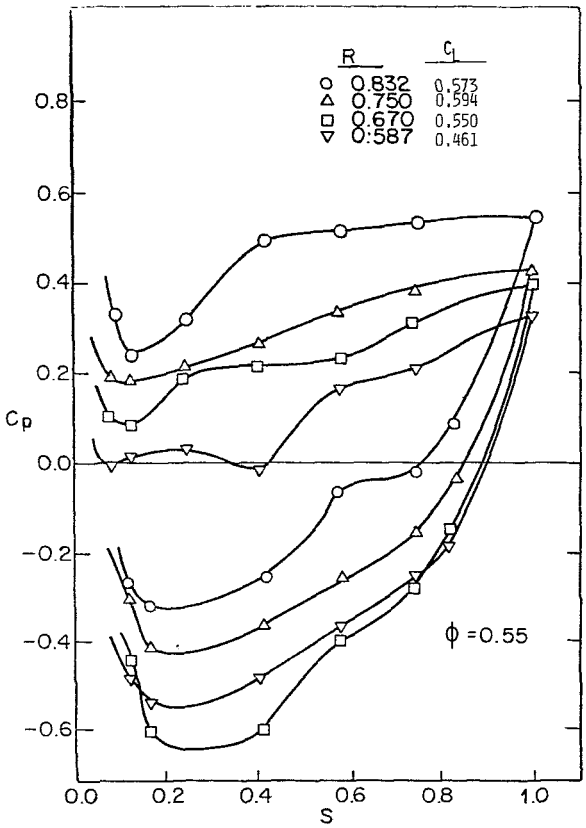

Fig. 4 Blade pressure distribution at $R = 0.587$, 0.67, 0.75, and 0.832

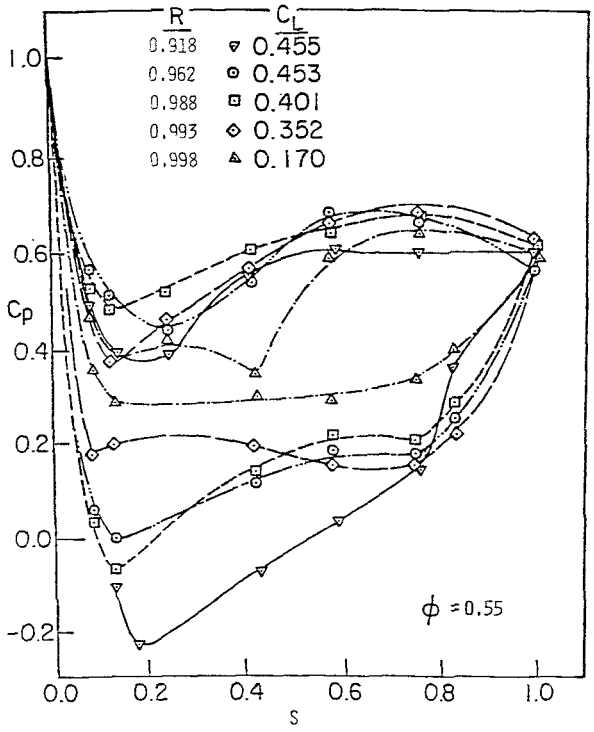

Fig. 5 Blade pressure distribution and blade lift coefficient at $R = 0.918$, 0.962, 0.988, 0.993, and 0.998

$$E_0^2 = (E_{0\infty}^2 - E_{0w}^2)\frac{D}{D_\infty} + E_{0w}^2 \tag{2}$$

where $E_{0\infty}$ is the value of E_0 at $D = D_\infty$, and E_{0w} is the voltage at zero velocity near the wall. D is the distance between the sensor and the wall. The value of $D_\infty = 5$ mm, and $D = 0.5$, 1.25, 2.5, and 5 mm. The shift in the data shows that the coefficient B is affected, and the following correlation for B is derived from this data

$$B = \hat{C}B_\infty \exp\left(-\frac{D}{D_\infty}\ln\hat{C}\right), \quad \hat{C} = 1.01 \tag{3}$$

where B_∞ is the coefficient away from the wall.

It appears, that without the corrections introduced through equations (2) and (3), there is an error of approximately 6 percent in the velocity close to the wall. These corrections (equations (2) and (3)) have been incorporated in the hot-wire equations. The values of E_{0w} and $E_{0\infty}$ were measured at the beginning and end of each measurement run. Note that the corrections were applied separately for both wires taking into account the 0.51 mm spacing between them.

Correction for Spatial Error. The two sensors of the hot-wire probe are spaced at 0.51 mm apart. In order to correct for the error introduced by this distance, the velocity that each wire senses (V_1, V_2) is plotted separately versus the true distance of each wire (N_1, N_2) from the wall. Then the streamwise and radial velocity components at some distance N_1 (the distance of the closest to the wall wire) are calculated using the value of V_1 at N_1 and the interpolated (or extrapolated) values of V_2 at the location N_1. Details of this technique and a comparison between corrected and raw data are given in [5]. The turbulence intensities cannot be corrected for the spatial error.

Experimental Results and Interpretation

The boundary layer measurements were carried out at various radial and axial locations shown in Table 2. For brevity, only typical results are given and interpreted in this paper. All the data are presented and interpreted in [5]. The radial variation of the flow properties 0.35 chords upstream of the rotor is shown in Fig. 3. The circumferential variation at this location was small (since it is about 2.5 IGV-chords downstream of IGV), and the data in Fig. 3 represent the time averages sensed by a stationary hot-wire. The hub wall boundary layer thickness and the annulus wall boundary layer thickness are about 4 percent of the blade span. In Fig. 3, the turbulence intensities are normalized by the local relative velocity, and the magnitude in the free stream is less than 2 percent.

Blade Pressure Distribution. The rotor blade static pressures at $\phi = 0.55$ are shown in Figs. 4 and 5 for various radial locations. The measuring techniques and the data are given in [6]. At the radii away from the tip (Fig. 4), there is a sudden increase in static pressure beyond $S = 0.8$ on the suction side at all radii. Near the tip (Fig. 5), there is a decrease in pressures on both surfaces from its values away from the tip. This is caused by the presence of the tip clearance. The values of the local lift coefficient (C_L) based on the local dynamic head of the inlet relative velocity are also shown in Figs. 4 and 5.

Velocity Profiles. The distribution of the streamwise and the radial velocity profiles at three chordwise locations for the five radial locations $R = 0.583$, 0.75, 0.918, 0.959, 0.98 is shown in Figs. 6 and 7 for the suction and pressure surfaces, respectively. The measured velocity profiles at all other radial and chordwise locations can be found in [5].

Streamwise Velocity Profile (U). The growth of the boundary layer and the profile shapes on the suction side (Fig. 6) are similar at $R = 0.583$ through $R = 0.918$. At these radii, the growth of the boundary is primarily controlled by the streamwise pressure gradient which is of similar magnitude at all the three radii under consideration (Fig. 4). However, at

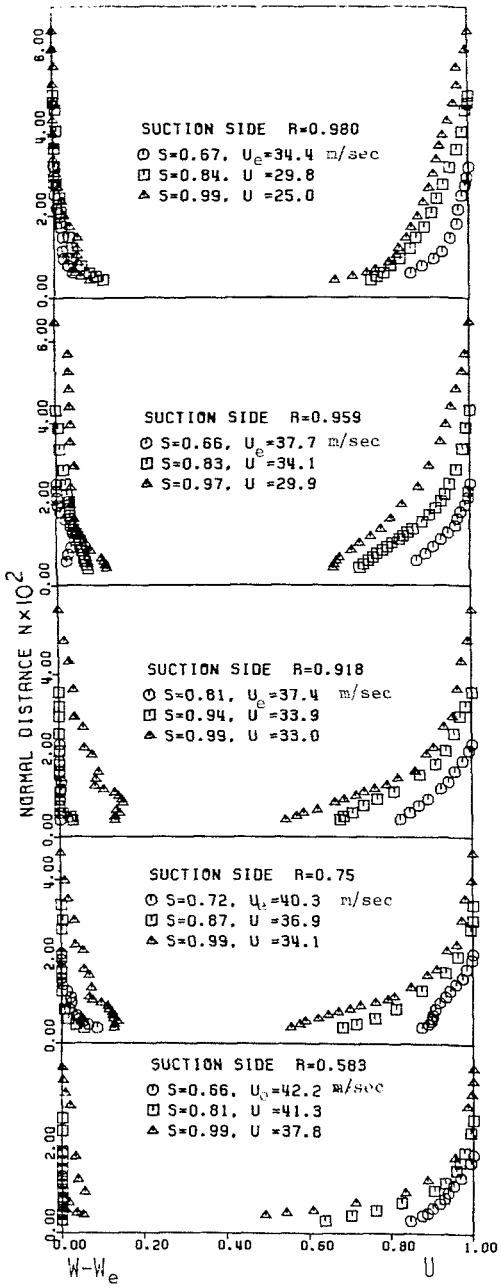

Fig. 6 Streamwise and radial velocity profiles on the suction side

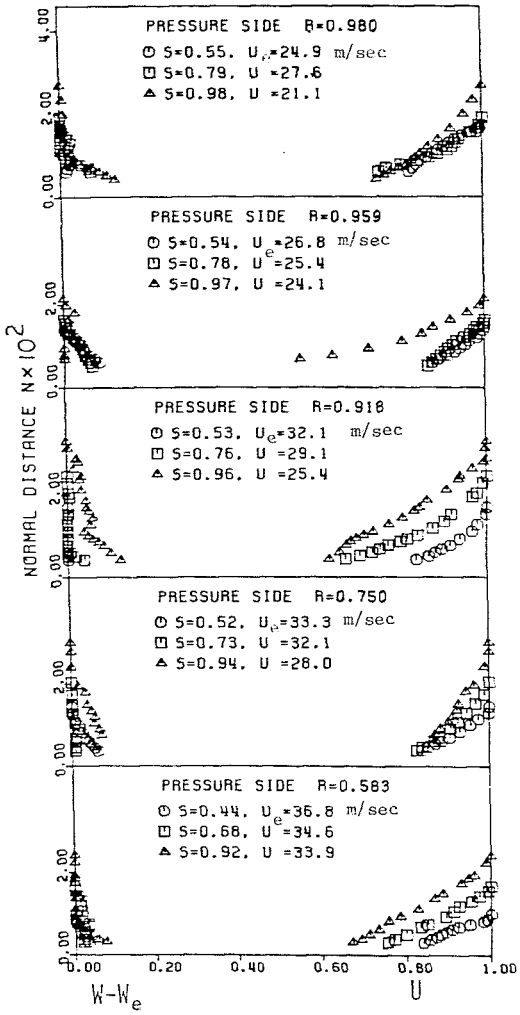

Fig. 7 Streamwise and radial velocity profiles on the pressure side

the trailing edge ($S=0.99$), the boundary layer thickness increases with radius, from 3.7 percent of chord length at $R=0.583$ to 6.0 percent of chord at $R=0.980$. Most of this increase occurs beyond the midspan region, even though the blade section loading (C_L) is decreasing radially in this region. The increase in δ can be explained by examining the three-dimensional nature of the blade boundary layer. As will be seen in a later section, the radial component of velocity in the boundary layer is outwards and its maximum value is of the order of 10 to 15 percent of the streamwise velocity. Therefore, the low momentum fluid is constantly transferred from the lower radii to the higher radii, and this causes the boundary layer to grow faster at the higher radii, even though the streamwise pressure gradients are similar in magnitude.

The endwall effects and, in particular, the tip leakage flow have a strong influence on the boundary layer growth on the suction side beyond $R=0.918$. A sudden increase of the boundary layer thickness is observed at the highest radii ($R=0.973$, 0.98); δ reaches 6.5 percent of the local blade chord length at $R=0.98$, $S=0.99$. This sudden increase of δ with radius in the tip region is not caused by the streamwise pressure gradient alone. The authors attribute this increase to the radial transport of the blade boundary layer and the tip leakage. While the tip leakage flow passes from the pressure side to the suction side, it acts to "blow" the blade boundary layer on the suction side, thus increasing its growth. As will be seen later, this effect is reversed on the pressure side.

As on the suction side, the boundary layers are similar at $R=0.583$ through $R=0.918$ on the pressure side. At the trailing edge locations, the boundary layer thickness increases with radius from 2.5 percent of chord at $R=0.583$ to 3.3 percent of chord at $R=0.918$. As on the suction side, this is again attributed to the transfer of low momentum fluid from lower to higher radii by the radial velocity.

In the tip region ($R=0.959$ to $R=0.98$), on the pressure side, the boundary layer is growing at a lower rate than at $R=0.918$. This is attributed to two factors: decreased streamwise pressure gradient on the pressure side in the tip region, and the tip leakage flow, which acts as a "suction" on the blade boundary layer preventing it from growing.

Radial Velocity Profile ($W-W_e$) At the radial locations $R=0.75$ to $R=0.918$, which are not influenced directly by the presence of the hub wall or the annulus wall, the radial velocity profiles show similar trends at all radii (Figs. 6 and

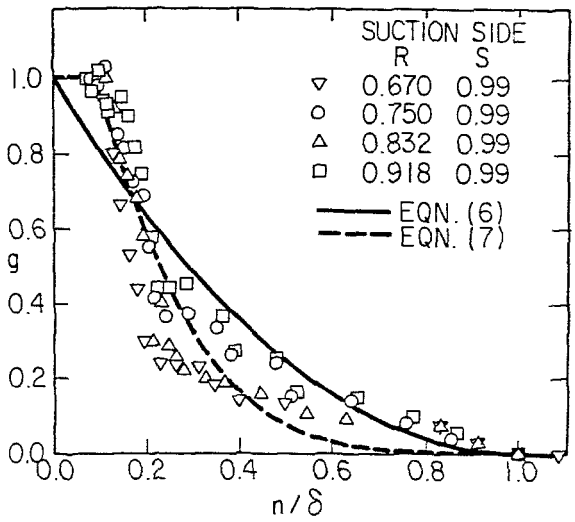

Fig. 8 Mager's representation of the radial velocity

7). On the suction side, the radial velocity starts developing beyond the midchord location and reaches its maximum value at the trailing edge location. On the pressure side, the radial velocity starts developing much earlier, approximately at the quarter-chord location [5].

The radial velocities are smaller on the suction side at the trailing edge in the tip region ($R=0.959$, 0.98) compared to the corresponding locations at lower radii ($R=0.75$ to $R=0.918$). The radial velocity in this region is influenced by the leakage flow, which induces outward radial velocity near the pressure surface and inward velocity near the suction surface of the blade (Fig. 1). These and other phenomena, such as the presence of a scraping vortex, alter the radial velocity profiles significantly. This area should be explored further, with carefully planned experiments.

Analysis of the Streamwise and Radial Velocity Profile. This section includes only a brief summary of profile analysis carried out. A complete description can be found in [5].

An attempt was made to fit the measured streamwise velocity profiles with the power law model

$$U=\left(\frac{n}{\delta}\right)^{1/n'} \tag{4}$$

It was found (see [5]) that the exponent that gave the best fit varied from 1/4 to 1/10 on the pressure side and 1/6 to 1/12 on the suction side. The power law gave poor representation of the profiles near the trailing edge locations, particularly on the suction side.

Several models have been proposed for the radial velocity profile. The crossflow profiles due to Mager [7] and Eichelbrenner [8] are based on experimental data and polynomial fit, respectively. The only model available for a rotating boundary layer is due to Anand and Lakshminarayana [9]. This model is based on an approximate solution of the radial equilibrium equation in the outer layer and is valid for a blade with large stagger angle. Hence it is not applicable to the configuration dealt with in this paper. Comparisons are made with Mager and Eichelbrenner's models and a modification to Mager's model is proposed.

Mager's Crossflow Model. Mager's crossflow model is given by

$$\tan\epsilon=\tan\epsilon_w g\left(\frac{n}{\delta}\right) \tag{5}$$

where

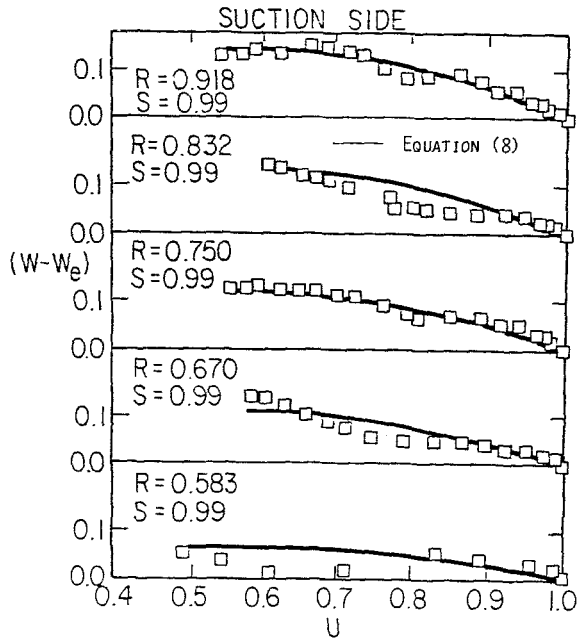

Fig. 9 Hodograph plot of velocity profiles

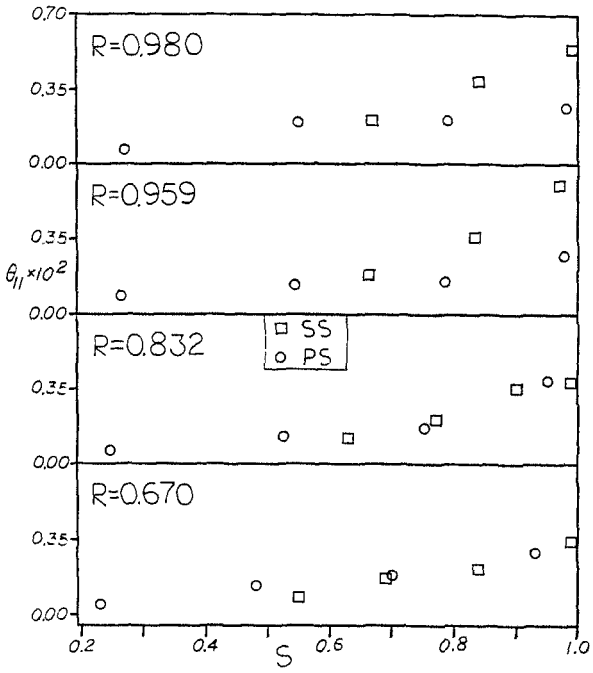

Fig. 10 Momentum thickness at various radial locations

$$g=\left(1-\frac{n}{\delta}\right)^2 \tag{6}$$

The values of g function derived from the experimental data near the trailing edge on the suction side are plotted in Fig. 8. The data are compared with the correlation due to Mager (equation (5)). None of the data agrees well with Mager's Profile. It should be noted here that the momentum integral technique, successfully used in predicting the boundary layer growth by many investigators, utilizes Mager's profile. This seems to indicate that gross effects (total radial mass flow and momentum) are predicted reasonably well by Mager's correlations, even though the profile representation is not accurate.

The data on the suction side (away from the endwalls at

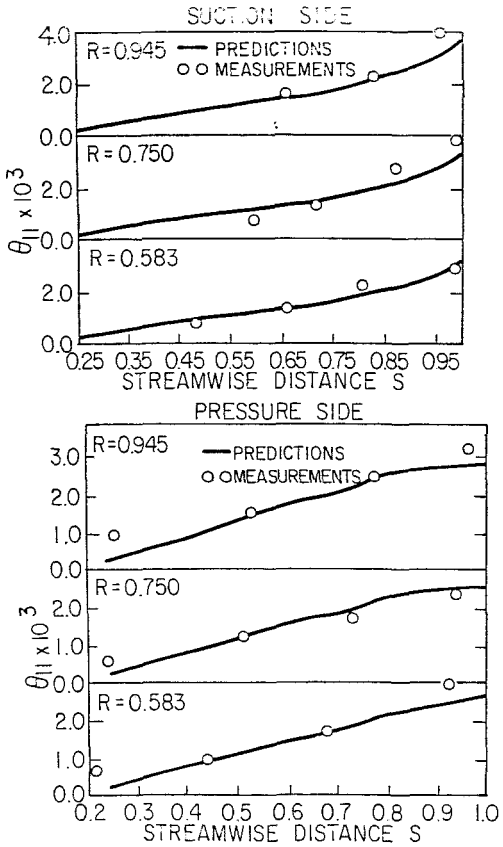

Fig. 11 Comparison between the measured and predicted momentum thicknesses

$R = 0.67$ to 0.918) seems to almost collapse into a single curve (Fig. 8). An inherent weakness of Mager's model is that it cannot represent the collateral region. A modified version which can represent the collateral region is the following

$$\frac{\tan\epsilon}{\tan\epsilon_w} = \left[1 - \left[\frac{n}{\delta} - \left(\frac{n}{\delta}\right)_c\right]\right]^m - \left[\frac{n}{\delta}\right]_c^m \quad \text{for} \quad \frac{n}{\delta} \geq \left[\frac{n}{\delta}\right]_c$$

$$\frac{\tan\epsilon}{\tan\epsilon_w} = 1 \quad \text{for} \quad \left[\frac{n}{\delta}\right]_c \geq 0 \tag{7}$$

where $[n/\delta]_c$ is the location where the collateral region starts. The exponent m can take different values.

The modified correlation (equation (7)) is shown in Fig. 8 and compared with the data. The value of $(n/\delta)_c$ is taken to be 0.1. The present set of data and previous measurements [9,10] justify this value. This correlation (with $m = 5$, $(n/\delta)_c = 0.1$) shows good agreement with the data on the suction side from $R = 0.67$ to 0.918. This seems to indicate that the correlation based on equation (7), which includes the collateral region, improves the profile representation. Further improvements should include the pressure gradient effects.

Eichelbrenner's Crossflow Model. In Eichelbrenner's [8] model, the crossflow is coupled with the streamwise flow by a fifth-order polynomial

$$W - W_e = \bar{B}U + \frac{1}{2}\bar{D}U^2 - \left(6\bar{B} + 4\bar{C} + \frac{3}{2}\bar{D}\right)U^3 + \left(8\bar{B} + 7\bar{C} + \frac{3}{2}\bar{D}\right)U^4 - \left(3\bar{B} + 3\bar{C} + \frac{1}{2}\bar{D}\right)U^5 \tag{8}$$

where

$$\bar{B} = \left(\frac{\partial W}{\partial U}\right)_w = \tan\epsilon_w, \quad \bar{C} = \left(\frac{\partial W}{\partial U}\right)_e, \quad \bar{D} = \left(\frac{\partial^2 W}{\partial U^2}\right)_w$$

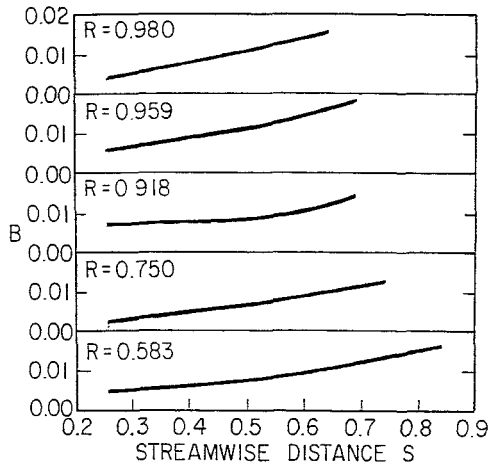

Fig. 12 Blockage coefficient at various radial locations

Assuming that a collateral region exists near the wall, D is set equal to zero.

The measurements at the trailing edge region on the suction side at radial locations $R = 0.583$ to $R = 0.918$ are plotted in the hodograph plane in Fig. 9. It can be seen that Eichelbrenner's model (equation (8)) gives good predictions. However, this model did not give good results for the profiles in the tip region (see [5]). The flow in this region is dominated by viscous effects across the entire passage, and the inviscid region is small. Eichelbrenner's expression is based on experiments in which the crossflow results from the transverse pressure gradient. This is not the case in the tip region, hence the poor agreement.

In general, Eichelbrenner's model gave better predictions than Mager's. As Mager himself noted [7], there is no physical reason to believe that g is a function of n/δ alone. On the other hand, Eichelbrenner's representation in the hodograph plane has a more physical meaning, since the crossflow is a direct result of the defect in the streamwise velocity profile.

Displacement and Momentum Thicknesses. The momentum thickness in the streamwise direction is defined by

$$\theta_{11} = \frac{1}{C}\int_0^h U(1-U)dn, \quad h > \delta \tag{9}$$

The definition and values of all the thicknesses (θ_{11}, θ_{12}, θ_{21}, θ_{22}, δ_1, δ_2) derived from the data can be found in [5]. The streamwise momentum thickness (θ_{11}) is plotted in Fig. 10 for both the pressure and suction sides. At the lower radii, $R = 0.67$ to $R = 0.832$, on both sides, θ_{11} varies almost linearly from the leading to the trailing edge. On the pressure side, in the annulus wall regions at $R = 0.980$, θ_{11} remains almost constant after the midchord location. This is because the tip leakage flow, which originates somewhere between the quarter-chord and midchord locations, has a "suction" effect on the boundary layer and thus the boundary layer does not grow. On the contrary, on the suction side in the tip region, the boundary layer grows much faster than those at the lower radii. Here the tip leakage flow has a "blowing" effect on the boundary layer.

In Fig. 11, the values of θ_{11} derived from the data are compared with the predictions based on the momentum-integral technique developed by Lakshminarayana and Govindan [11]. The predictions of θ_{11}, shown in Fig. 11, are good on both surfaces, especially for the chordwise location lying between $S = 0.4$ and $S = 0.85$. The momentum integral technique seems to underestimate θ_{11} on the pressure side for the locations nearest to the leading edge. The values at radii beyond $R = 0.945$ are not computed as it is beyond the scope

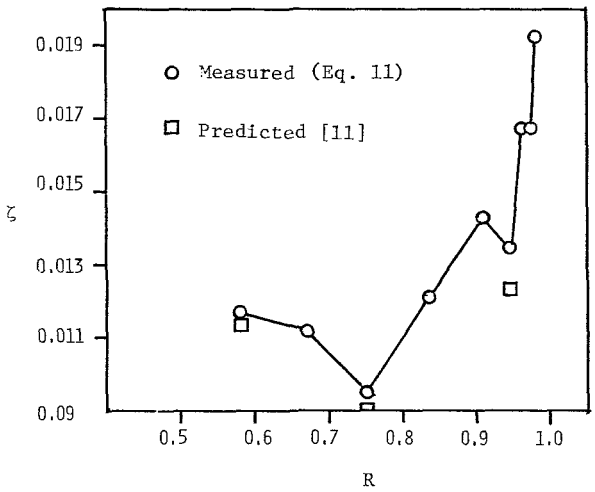

Fig. 13 Profile loss coefficient

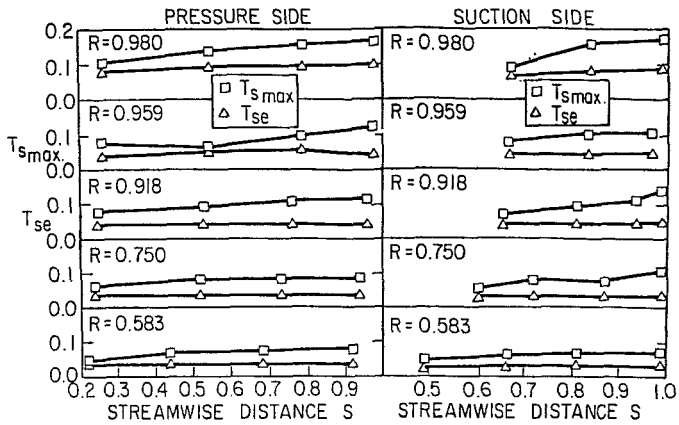

Fig. 14 Free-stream and maximum values of the streamwise turbulent intensity

of the analysis of [11], since the tip effects are not included in the analysis.

Blade Boundary Layer Blockage. The "tangential blockage" due to blade thickness and boundary layer has been widely used by designers of turbomachines. The blockage coefficient, defined in this paper, is given by

$$B = \frac{(\delta_1)_{ss} + (\delta_1)_{ps}}{\cos\gamma}\left(\frac{C}{t}\right) \tag{10}$$

It should be noted that this includes the contribution from the blade boundary layers only. Interpolating the present experimental data, the blockage B was derived at different streamwise and radial locations and is shown in Fig. 12. In this figure, the streamwise direction S is measured along the mean streamline. The blockage varies from 0.5 percent at S = 0.25 to 1.5 percent in the trailing edge region.

Profile Loss Coefficient. The aerodynamic losses at each radius can be estimated from the momentum thickness at the trailing edge by using Speidel's [12] formula

$$\zeta = \frac{P_{01} - P_{02}}{\frac{1}{2}\rho U_1^2} = \frac{2[(\theta_{11})_{ss} + (\theta_{11})_{ps}]_{TE}}{\cos^3\beta_2 \cos^{-2}\beta_1}\frac{C}{t} \tag{11}$$

The results of the above expression were compared with the loss coefficient of the corresponding two-dimensional cascade

$$\zeta_{2D} = C_D\left(\frac{C}{t}\right)\Big/\cos\beta_m \tag{12}$$

where

$$C_D = \frac{D}{\frac{1}{2}\rho U_1^2 C}; \quad \tan\beta_m = \frac{\tan\beta_1 + \tan\beta_2}{2}$$

C_D was taken from the experimental measurements of Herring et al. [13] in two-dimensional cascades. These are an approximate interpolation, as the data for an exact (as the rotor) cascade is not available. Hence these results are not presented. In the midspan region, the cascade loss coefficient was found to be 30–60 percent higher than that measured in the rotor. However, in the tip region the trend is reversed and the losses in the rotor are higher. These results are consistent with the trends expected. The boundary layer growth at lower radii should be less than that of a cascade and vice-versa at outer radii. This is caused by the radial transport of the blade boundary layer. It should be noted that the loss coefficient (ζ) includes only the blade profile loss and not the endwall boundary layer loss. The total loss coefficient is likely to be higher for the rotor near the blade tip.

In Fig. 13, the measured and the predicted [11] loss coefficients are shown. The measured flow angles along with the predicted momentum thickness were used to predict the loss coefficient. The agreement between the predicted and the measured values is very good. This shows the usefulness of the momentum integral technique as a design tool.

The present study indicates that the profile losses, away from the tip in a compressor rotor are less than or equal to the profile losses of an equivalent rectilinear cascade. This is in contrast with Hodson's [14] measurements in a turbine, where he found that the profile losses of an axial-flow turbine at midspan was 50 percent higher than that of an equivalent rectilinear cascade. The results of the present study agrees well with the findings of the theoretical and experimental investigation of Toyokura et al. [2]. They found that the growth of the boundary layer developing on a rotating blade was smaller than the one developing on an identical stationary blade.

It should be remarked here that Speidel's formula used here is based on a two-dimensional analysis and it is only an approximation for three-dimensional flows.

Maximum and Free-Stream Values of Streamwise Turbulence Intensity. The maximum and free-stream values of the streamwise intensity are plotted for the pressure and the suction sides in Fig. 14. The free-stream intensities on both the surfaces increase moderately up to $R = 0.959$, beyond which a sudden increase is observed. This shows that the blade boundary layer in this region is strongly interacting with the highly turbulent, fully three-dimensional endwall flow [15]. This flow results from the mixing of the inviscid secondary flow, annulus wall boundary layer, and tip leakage flow. A very similar trend is also found for the radial intensity T_r. The maximum intensities are comparable on both sides of the blade, except on the suction side near the trailing edge, where a large increase is observed.

The complete set of the measured turbulent intensity profiles, and a detailed interpretation of this data can be found in [5].

Conclusions

The major conclusions derived on the basis of this investigation are:

1 In regions away from the wall, the streamwise component of the boundary layer is influenced mainly by the streamwise pressure gradients. In the tip region, the boundary layer is affected by the tip clearance flow, which acts as "blowing" on the suction side and as "suction" on the pressure side of the blade.

2 The radial velocity in the boundary layer is outward at most locations and reaches its maximum value in the trailing edge region. At the radii away from the tip region, the maximum radial velocity occurs on the suction side. At the radii near the tip region, the radial velocity is approximately the same on the pressure and on the suction side of the blade. This is due to the presence of the tip leakage.

3 Mager's correlation of the radial (crossflow) velocity profile does not show good agreement with the present set of data. The modified version proposed in this paper shows better agreement on the suction side of the blade away from the annulus wall.

4 Eichelbrenner's representation of the radial velocity gives good predictions away from the tip region. It seems that the hodograph representation of the radial velocity is more promising than other correlations proposed.

5 The momentum-integral technique developed by Lakshminarayana and Govindan provides good prediction for θ_{11}. The predictions near the leading and trailing edges of the blade could be improved if the input pressure gradients in these regions were known more accurately.

6 The profile loss coefficient estimated from two-dimensional cascade experiments overestimates the losses in the midspan region of the rotor.

7 The turbulence intensities are found to suddenly increase in the tip region, where the three-dimensional effects and the leakage flow are dominant.

Acknowledgment

This investigation was carried out under the sponsorship of the National Aeronautics and Space Administration, through the Grant NSG 3266, with Dr. P. M. Sockol as the Technical Monitor.

References

1 Lakshminarayana, B., Hah, C., and Govindan, T. R., "Three-Dimensional Boundary Layer Development on a Fan Rotor Blade," *AIAA Journal*, Vol. 22, No. 1, 1984, pp. 83–89.

2 Toyokura, T., Kurokama, J., and Kimoto, Y., "Three-Dimensional Boundary Layer Flow on Rotating Blades," *Bulletin of the JSME*, Vol. 25, 1982, pp. 513–520.

3 Lakshminarayana, B., "An Axial Flow Research Compressor Facility Designed for Flow Measurement in Rotor Passages," *Journal of Fluids Engineering*, Vol. 102, Dec. 1980, pp. 402–411.

4 Klatt, F., "The X Hot-wire Probe in a Plane Flow Field," *DISA Information*, No. 8, July 1969.

5 Pouagare, M., Galmes, J. M., and Lakshminarayana, B., "An Experimental Study of the Compressor Rotor Blade Boundary Layer," PSU/TURBO 84-1, 1984.

6 Sitaram, N., and Lakshminarayana, B., "End Wall Flow Characteristics and Overall Performance of an Axial Flow Compressor Stage," NASA CR 3671, 1983.

7 Mager, A., "Generalization of Boundary Layer Momentum Integral Equations to Three-Dimensional Flows Including Those of Rotating System," NACA Technical Report 1067, 1952.

8 Eichelbrenner, E. A., "Three-Dimensional Boundary Layer," *Annual Review of Fluid Mechanics*, Vol. 5, 1973, pp. 339–360.

9 Anand, A. K., and Lakshminarayana, B., "Three-Dimensional Boundary Layer in a Rotational Helical Channel," *Journal of Fluids Engineering*, Vol. 97, No. 2, 1975, pp. 197–210.

10 Olsson, K. A. E., "Centrifugal Effect on the Boundary Layer on a Blade of an Axial Turbomachine," M.I.T., Gas Turbine Lab Report 66, Apr. 1962.

11 Lakshminarayana, B., and Govindan, T. R., "Analysis of Turbulent Boundary Layers on Cascade and Rotor Blades of Turbomachinery," *AIAA Journal*, Vol. 19, No. 10, 1981, pp. 1333–1341.

12 Speidel, L., "Berechrung der Stömungverluste Von ungestaffelten Ebenen Schaufelgittern," *Ing. Arch.*, Vol. 22, 1954, p. 295.

13 Herring, L. J., Emery, J. C., and Erwin, J. R., "Systematic Two-Dimensional Cascade Tests of NACA 65-Series Compressor Blades at Low Speeds," NACA TN 3916, 1957.

14 Hodson, H. P., "The Development of Unsteady Boundary Layers on the Rotor of an Axial-Flow Turbine," AGARD-CP-351, 1983.

15 Lakshminarayana, B., Pouagare, M., and Davino, R., "Three-Dimensional Flow Field in the Tip Region of a Compressor Rotor Passage—Part I and Part II," ASME JOURNAL OF ENGINEERING FOR POWER, Vol. 104, No. 4, Oct. 1982, pp. 760–781.

1 In regions away from the wall, the streamwise component of the boundary layer is influenced mainly by the streamwise pressure gradients. In the tip region, the boundary layer is affected by the tip clearance flow, which acts as "blowing" on the suction side and as "suction" on the pressure side of the blade.

2 The radial velocity in the boundary layer is outward at most locations and reaches its maximum value in the trailing edge region. At the radii away from the tip region, the maximum radial velocity occurs on the suction side. At the radii near the tip region, the radial velocity is approximately the same on the pressure and on the suction side of the blade. This is due to the presence of the tip leakage.

3 Mager's correlation of the radial (crossflow) velocity profile does not show good agreement with the present set of data. The modified version proposed in this paper shows better agreement on the suction side of the blade away from the annulus wall.

4 Eichelbrenner's representation of the radial velocity gives good predictions away from the tip region. It seems that the hodograph representation of the radial velocity is more promising than other correlations proposed.

5 The momentum-integral technique developed by Lakshminarayana and Govindan provides good prediction for θ_{11}. The predictions near the leading and trailing edges of the blade could be improved if the input pressure gradients in these regions were known more accurately.

6 The profile loss coefficient estimated from two-dimensional cascade experiments overestimates the losses in the midspan region of the rotor.

7 The turbulence intensities are found to suddenly increase in the tip region, where the three-dimensional effects and the leakage flow are dominant.

Acknowledgment

This investigation was carried out under the sponsorship of the National Aeronautics and Space Administration, through the Grant NSG 3266, with Dr. P. M. Sockol as the Technical Monitor.

References

1 Lakshminarayana, B., Hah, C., and Govindan, T. R., "Three-Dimensional Boundary Layer Development on a Fan Rotor Blade," *AIAA Journal*, Vol. 22, No. 1, 1984, pp. 83–89.

2 Toyokura, T., Kurokama, J., and Kimoto, Y., "Three-Dimensional Boundary Layer Flow on Rotating Blades," *Bulletin of the JSME*, Vol. 25, 1982, pp. 513–520.

3 Lakshminarayana, B., "An Axial Flow Research Compressor Facility Designed for Flow Measurement in Rotor Passages," *Journal of Fluids Engineering*, Vol. 102, Dec. 1980, pp. 402–411.

4 Klatt, F., "The X Hot-wire Probe in a Plane Flow Field," *DISA Information*, No. 8, July 1969.

5 Pouagare, M., Galmes, J. M., and Lakshminarayana, B., "An Experimental Study of the Compressor Rotor Blade Boundary Layer," PSU/TURBO 84-1, 1984.

6 Sitaram, N., and Lakshminarayana, B., "End Wall Flow Characteristics and Overall Performance of an Axial Flow Compressor Stage," NASA CR 3671, 1983.

7 Mager, A., "Generalization of Boundary Layer Momentum Integral Equations to Three-Dimensional Flows Including Those of Rotating System," NACA Technical Report 1067, 1952.

8 Eichelbrenner, E. A., "Three-Dimensional Boundary Layer," *Annual Review of Fluid Mechanics*, Vol. 5, 1973, pp. 339–360.

9 Anand, A. K., and Lakshminarayana, B., "Three-Dimensional Boundary Layer in a Rotational Helical Channel," *Journal of Fluids Engineering*, Vol. 97, No. 2, 1975, pp. 197–210.

10 Olsson, K. A. E., "Centrifugal Effect on the Boundary Layer on a Blade of an Axial Turbomachine," M.I.T., Gas Turbine Lab Report 66, Apr. 1962.

11 Lakshminarayana, B., and Govindan, T. R., "Analysis of Turbulent Boundary Layers on Cascade and Rotor Blades of Turbomachinery," *AIAA Journal*, Vol. 19, No. 10, 1981, pp. 1333–1341.

12 Speidel, L., "Berechrung der Stömungverluste Von ungestaffelten Ebenen Schaufelgittern," *Ing. Arch.*, Vol. 22, 1954, p. 295.

13 Herring, L. J., Emery, J. C., and Erwin, J. R., "Systematic Two-Dimensional Cascade Tests of NACA 65-Series Compressor Blades at Low Speeds," NACA TN 3916, 1957.

14 Hodson, H. P., "The Development of Unsteady Boundary Layers on the Rotor of an Axial-Flow Turbine," AGARD-CP-351, 1983.

15 Lakshminarayana, B., Pouagare, M., and Davino, R., "Three-Dimensional Flow Field in the Tip Region of a Compressor Rotor Passage—Part I and Part II," ASME JOURNAL OF ENGINEERING FOR POWER, Vol. 104, No. 4, Oct. 1982, pp. 760–781.

DISCUSSION

J. Moore.[2]

Dr. Lakshminarayana and his co-authors are to be complimented once again on a careful and thorough experimental study of complex three-dimensional compressor flow. In such flows it is easy to lose sight of the extent of departures from simple flow models. For example, can the authors quantify the departures of the profile boundary layer development on the pressure and suction sides of the blade from that predicted by simple two-dimensional boundary layer theory?

In his presentation of the paper in Amsterdam, Dr. Lakshminarayana showed an interesting "hill plot" of the through-flow velocity at the exit of the compressor rotor passage. This showed the boundary layers on all four walls and the velocity distribution of the potential flow. I believe the readers of this journal would find such a plot gives a useful summary of the measurements.

Author's Closure

We would like to thank Dr. J. Moore for the discussion of the paper. It is difficult to state quantitatively the departure of the blade boundary layer profile from those predicted from simple two-dimensional boundary layer theories, as this involves a knowledge of the transition and the blade pressure distribution. A detailed analysis of the boundary layer profile data [5] indicated considerable departure from the law of the wall and wake, and the power law profiles used widely in two-dimensional boundary layer practice. Furthermore, even small cross flows would substantially affect the growth of the blade boundary layer, and to a lesser extent the boundary layer profiles. In view of this, no attempt was made to compare the boundary layer profiles predicted from the two-dimensional code. A three-dimensional blade boundary layer code presently under development will be employed to compare the measured data reported in this paper.

An attempt has been made [16] to integrate all the data in this compressor rotor to derive a composite plot of the velocity distribution from blade to blade, and from hub to tip at various axial locations of the blade passage. The flow in the end wall region is measured using a three-sensor hot-wire probe, the flow in the inviscid region from a three-hole probe, and the flow in the blade boundary layer region is reported in this paper. Since they were acquired at differing axial, tangential, and radial locations, the various sets of data had to be interpolated to derive the composite flow field. Therefore these interpolated plots are meant for a *qualitative* understanding of the entire flow field and should not be used for quantitative comparison or study. Two sets of plots are given in [16]; one of these is a three-dimensional plot showing

[2]Mechanical Engineering Dept., VPI & SU, Blacksburg, VA 24061.

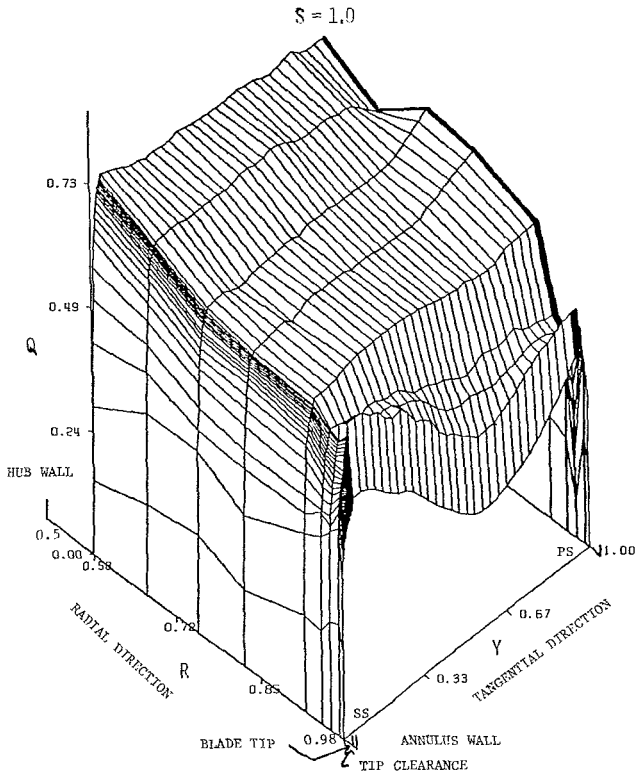

Fig. 15 Three-dimensional plot of the velocity Q at $Z = 1.0$

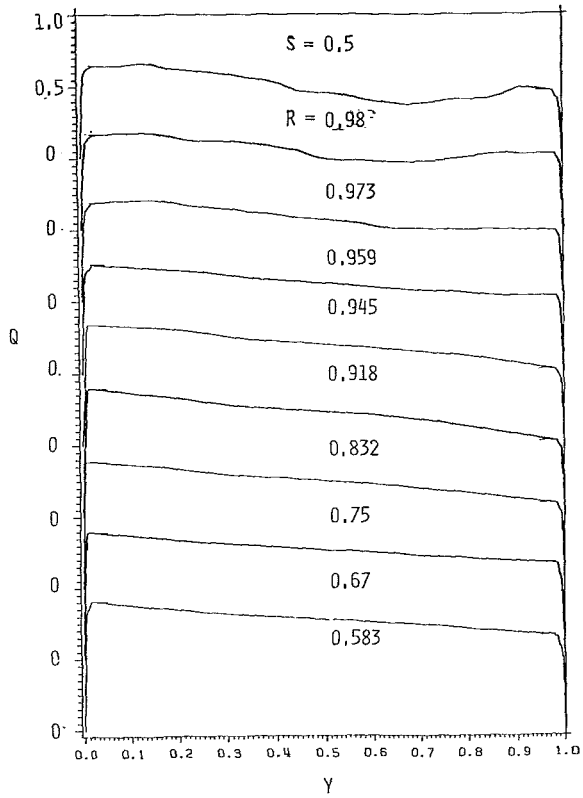

Fig. 16 Blade-to-blade distribution of Q at $Z = 0.5$

the variation of Q, which is the resultant of the axial and the tangential relative velocity normalized by the blade tip speed. A typical plot at the trailing edge ($S = 1.0$) is shown in Fig. 15 (see [16] for all other axial locations). In this plot, Y is the nondimensionalized tangential distance from the suction surface. The inviscid effects as well as the effects of annulus wall boundary layer, tip leakage flow, and the extent of the blade boundary layer are clearly revealed in this figure. The other type of plot given in [16] is a conventional plot showing the blade-to-blade variation of Q, interpolated from the three sets of data described earlier. A typical plot ($S = 0.5$) is shown in Fig. 16. The blade boundary layer growth at this axial location is relatively small as evidenced from the data presented in this paper.

References

16 Pouagare, M., and Lakshminarayana, B., "Three Dimensional Flow Field Data in a Low Speed Axial Flow Compressor Rotor Passage," NASA CR (submitted for publication), 1985.

Inlet Boundary Layer Effects in an Axial Compressor Rotor: Part I—Blade-to-Blade Effects

J. H. Wagner

R. P. Dring

H. D. Joslyn

United Technologies Research Center,
East Hartford, Conn. 06108

This paper discusses experimental data measured on the blading and downstream of an isolated compressor rotor with thick inlet endwall boundary layers. The objective of the study was to compare these results with data acquired previously with thin inlet boundary layers and to assess the impact of inlet boundary layer thickness on the secondary flow. Flow visualization results showed the powerful impact of the hub corner stall and how at the same near stall flow coefficient where with thin inlet boundary layers the blade was separated at midspan, with thick inlet boundary layers it was attached. It was also shown that while secondary flow was very weak, it did produce sufficient radial redistribution to cause an apparent negative loss at the blade root.

Introduction

Many of the complex flow phenomena that occur within and behind axial compressor rotating blade rows are not fully understood at the present time. One major factor that contributes to the complexity of the highly three-dimensional flow field is the existence of thick boundary layers on the hub and tip of the annulus. Under some situations, such as the inlet stages of a multistage compressor, the annulus boundary layer represents only a small fraction of the total incoming flow field. However, as that fraction increases to the point where the boundary layer represents a major portion of the flow field, as is the case with middle and exit stages, there is a major impact due to the effects of the three-dimensional flows that are generated.

The importance of these three-dimensional flows from a design viewpoint is inherently related to the through-flow analysis and to the blade-to-blade analysis of multistage design. An understanding of these mechanisms is necessary in order to predict the losses through blade rows generated by the airfoil boundary layers, leakage flows, passage vortices, and endwall boundary layer phenomena.

A large amount of data has been obtained from cascade studies of these effects. Secondary flow effects in compressor cascades resulting from tip leakage and inlet skewing have been studied, for example, by Lakshminarayana and Horlock [1] and by Moore and Richardson [2], respectively. Cascade studies have included measurements of three-dimensional secondary flow effects as well as flow visualization results. More recently, detailed studies have also been done in rotating rigs. Tip leakage flow visualization results were obtained in an axial flow compressor by Phillips and Head [3]. High response measurements downstream of axial compressor blade rows have been performed by many investigators including Schmidt and Okiishi [4], Reynolds and Lakshminarayana [5], and Kool, et al. [6]. Adkins and Smith [7] have presented an approximate method for the inclusion of secondary flow effects due to endwall boundary layers, tip clearance, shrouding, airfoil surface boundary layers, and wake transport in a compressor through-flow analysis. Their predictions of the radial distributions of various flow parameters and loss agree quite well with many investigators' results. Even with this large body of data, there is still a need for improved models of the endwall flows in axial compressors. Evidence of this need can be seen in the long and costly development process most new compressor designs require in order to attain their design objectives of flow, pressure rise, and efficiency.

A benchmark study to obtain detailed flow measurements within and behind an isolated compressor rotor has already been conducted at the United Technologies Research Center (see Dring et al. [8] and [9]). The test rotor was typical of a mid-compressor rotor and the test conditions were varied over a wide range of blade loading (incidence) with relatively thin inlet boundary layers on the annulus hub and tip. The objectives of that study were to document the effects of blade loading on the generation of the three-dimensional flow field in the rotor blade-to-blade passage and in the flow downstream of the rotor, and to compare the results with various analytical predictions.

The objective of the present study [10] was to extend this earlier work by investigating the three-dimensional flow field for the same rotor but with much thicker hub and tip inlet boundary layers. The bulk of the present data was acquired in the rotating frame of reference of the rotor. Surface flow visualization and fullspan surface pressure measurements were made on the rotor airfoil and fullspan surveys of the velocity and pressure fields aft of the rotor were obtained. The data were acquired over a range of rotor incidence and

Contributed by the Gas Turbine Division of THE AMERICAN SOCIETY OF MECHANICAL ENGINEERS and presented at the 29th International Gas Turbine Conference and Exhibit, Amsterdam, The Netherlands, June 4–7, 1984. Manuscript received at ASME Headquarters January 6, 1984. Paper No. 84-GT-84.

for inlet hub and tip boundary layer thicknesses typical of a middle stage rotor.

It was determined from the results that the relative unloading of the midspan region of the airfoil (due to the thicker endwall boundary layers) inhibited a fullspan separation at high loading preventing high loss fluid in the hub corner stall from being centrifuged to the tip region. Radial redistribution of high and low total pressure fluid influenced the magnitude of the spanwise distribution of loss such that there was a general decrease in loss near the hub to the extent that for the least loaded case a locally negative loss (increase in total pressure) was observed.

Background

The experimental program was performed in the United Technologies Research Center's Large Scale Rotating Rig (LSRR-2). A brief review of the facility follows; however, a more comprehensive description can be found in [11].

The facility consists of a large bellmouth entrance duct which contracts to a constant 5 ft (1.52 m) diameter. The flow passes through a system of screens to the inlet of the 0.8 hub/tip ratio isolated compressor rotor. For the present program, the rotor shaft speed was 510 rpm. The range of flow coefficient ($\bar{\phi}$) based on area averaged C_x was from 0.65 to 0.95. The airfoil true chord is 6 in. (0.15 m) and is constant with span. This results in an airfoil aspect ratio of 1.0 and a Reynolds number range (based on average inlet relative flow speed) of 4.3×10^5 to 5.0×10^5. Axial chord at midspan was 5 in. (0.13 m). Axial distances have been normalized with the rotor axial chord at midspan and are referenced from either the rotor leading or trailing edge axial locations at midspan. Rotor tip clearance varied from 2.3 percent span at the leading edge to 1.0 percent at midchord to 3.3 percent span at the trailing edge. Details of the airfoil geometry are given in detail in [10].

A system of annular screens located 342 percent of midspan axial chord upstream of the rotor was used to generate the hub and case boundary layers. Upstream wall static pressures and spanwise traverse data were acquired at Sta. 1, located 82 percent axial chord upstream of the rotor. Rotating frame traverses were performed at Sta. 2, 30 percent aft of the rotor trailing edge ([10], Fig. 2). This location was chosen because backflow (due to rotor hub corner stall) was not present at this plane, as determined previously [9], but the effects of secondary flow were still present. Downstream flow path static pressures were measured at Sta. 3 at a distance of 224 percent of midspan axial chord aft of the rotor. A rotor mounted traverse device located inside the hub was used to position the pneumatic probes used in this study. Aerodynamic results were obtained over two rotor blade pitches from 5 percent to 97 percent span. Two of the rotor blades were instrumented to acquire surface static pressures at seven spanwise locations from 4 percent to 95 percent span. These instrumented airfoils were also used for surface flow visualization using the ammonia/Ozalid technique developed by Ruden [12] and demonstrated by Dring et al. [8], Johnson [13] and Dring and Joslyn [11].

Table 1 Inlet profile integral results

Thin Inlet	δ^*(% span)	Θ(% span)	H
Hub	0.88	0.68	1.30
Tip	1.45	1.10	1.32
Thick Inlet	δ^*(% span)	Θ(% span)	H
Hub	7.8	5.3	1.47
Tip	7.9	5.3	1.49

The accuracy of the pressure measurement system was ± 2 percent of reading. Since all pressure measurements were referenced to the midspan absolute inlet total pressure the uncertainty in C_P is ± 2 percent. The uncertainty in the flow angles is ± 1 degree. During traverse testing the flow coefficient was not allowed to vary by more than ± 1/2 percent.

Discussion of the Results

The main focus of this paper is to demonstrate the impact of inlet endwall boundary layer thickness on the basic aerodynamics of an isolated compressor rotor. Where possible, results from the previous work by Dring et al. [8] with thin inlet boundary layers will be compared with the present thick inlet boundary layer results. Discussion of the results will be limited to two flow coefficients, the nominal design coefficient, $\bar{\phi}$ = 0.85, and the near stall flow coefficient, $\bar{\phi}$ = 0.65. The flow coefficient for the thin inlet boundary layer results of [8] are based on midspan C_x which, as will be seen presently, is very close to the area averaged inlet flow speed.

The inlet velocity profiles were measured at Sta. 1 at three equally spaced circumferential locations around the annulus for the four test flow coefficients ($\bar{\phi}$ = 0.65, 0.75, 0.85, and 0.95). The C_x profiles were essentially invariant with flow coefficient and had only small variations for the three circumferential locations. The standard deviation of the displacement and momentum thicknesses was 5 and 3 percent, respectively. The standard deviation of the shape factors was 2 percent. These deviations were almost entirely due to the nonaxisymmetry of the measured velocity profiles at the three circumferential locations. The average of the twelve thick inlet velocity profiles is shown in Fig. 1 with the inlet profile from the thin inlet program. Integral parameters are summarized in Table 1. Symmetry about midspan is evident in the shape as well as in the integral results. The displacement and momentum thicknesses for the thick inlet case were approximately 8 and 5 percent of the airfoil span. The boundary layer thicknesses for the hub and tip were approximately 37 percent of the span. This was a substantial increase in boundary layer thickness compared to the thin inlet conditions for the previous program where integral thicknesses were about 1 to 2 percent and boundary layer thicknesses were only 5 to 10 percent of the airfoil span. The average inlet C_x

Nomenclature

B_x = airfoil axial chord
C_P = pressure coefficient: $(P-P_{T1})/Q_{U_m}$
C_x = axial components of flow velocity
$\bar{C}_x$ = area averaged axial velocity
P = pressure
P_{T1} = inlet absolute total pressure at midspan
Q_{U_m} = dynamic pressure of wheel speed at midspan ($\frac{1}{2}\rho U_m^2$)
Q_1 = rotor inlet relative dynamic pressure
U = wheel speed
U_m = wheel speed at midspan
W = relative flow speed
X = axial distance
ρ = density
ϕ = flow coefficient: (C_x/U_m)
$\bar{\phi}$ = flow coefficient: $(\bar{C}_x/U_m)$
δ^* = displacement thickness
θ = yaw angle
θ^* = airfoil metal angle
Θ = momentum thickness
H = shape factor
h_2/h_1 = streamtube contraction

Subscripts

S = static
T = total
1,2 = station
m = midspan

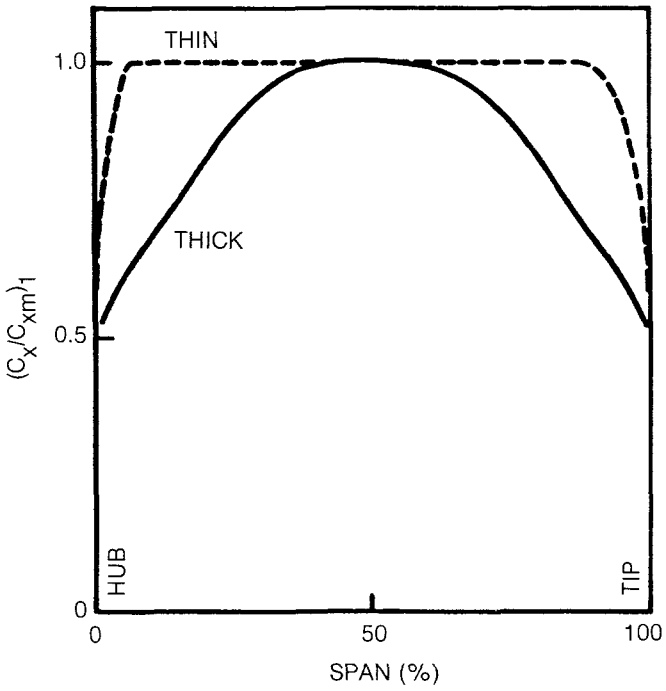

Fig. 1 Inlet velocity profiles 82 percent axial chord upstream of rotor

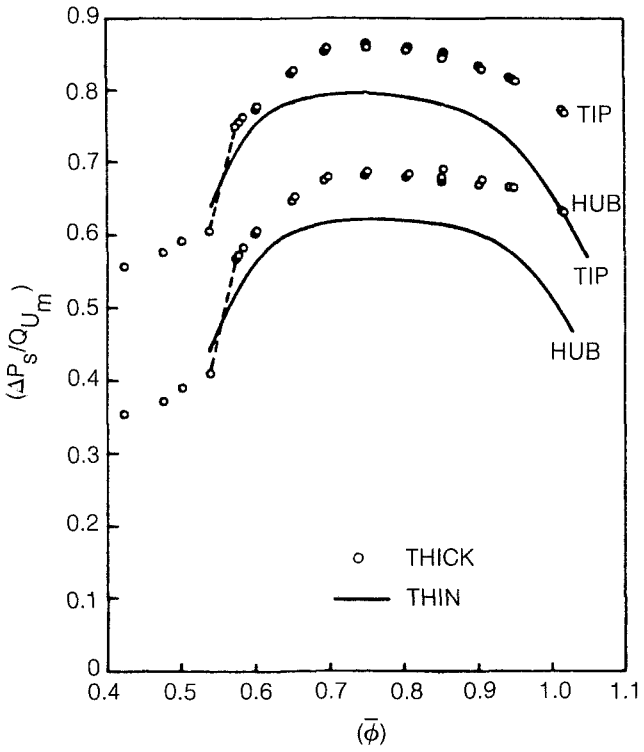

Fig. 2 Rotor static pressure rise characteristic

for the thick inlet program was 84 percent of the midspan value and compared to 98 percent from the thin inlet test. Because the flow coefficient based on the midspan flow speed for the thin inlet test is so close to the average flow coefficient, the midspan value will be used in the discussion of the results.

The rotor static pressure rise (ΔP_s) characteristic is shown in Fig. 2. The static pressure rise (from Sta. 1 to Sta. 3) has been normalized with a dynamic pressure based on midspan wheel speed. The flow coefficient is based on the area averaged inlet axial velocity at Sta. 1. Hub and tip are shown

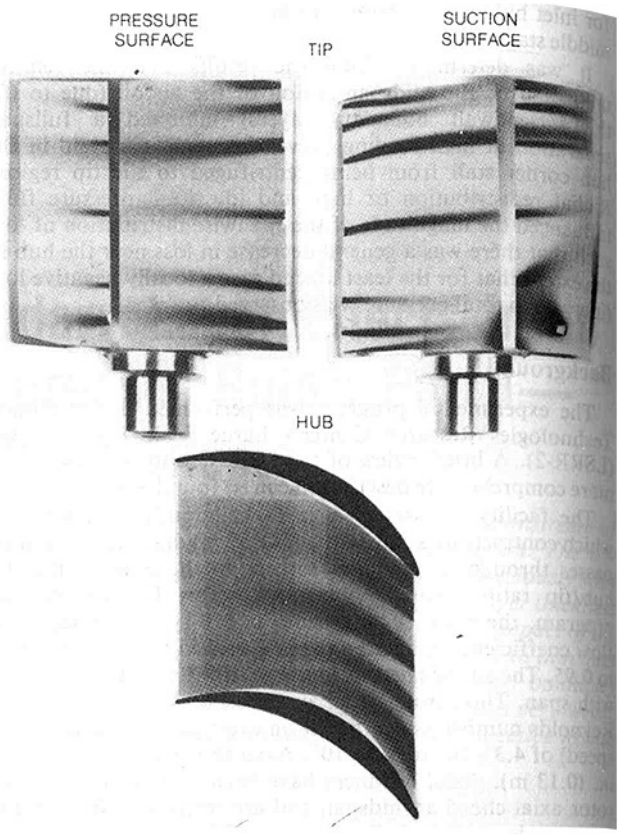

Fig. 3 Airfoil passage flow visualization, $\bar{\phi} = 0.85$

for the present thick inlet boundary layer test (as the symbols). In addition to the present data, two curves are included indicating the hub and tip static pressure rise across the rotor measured with thin inlet boundary layers. This previous data has been corrected slightly due to the different inlet reference plane locations, Sta. 1 for the present program and Sta. 0 for the previous program. The previous data has been raised by (0.015) ϕ^2 to account for the boundary layer growth between Sta. 0 and Sta. 1. The flow coefficient (ϕ) from the previous work was also corrected for flow speed based on average inlet velocity, i.e., $\bar{\phi} = 0.98\ \phi$.

Thickening of the hub and tip inlet boundary layers has increased the static pressure rise by typically 6 percent with the most pronounced increase at the higher flow coefficients. An increase in static pressure rise across a rotor due to thickened inlet boundary layers has been observed previously by Hunter and Cumpsty [14]. Stall occurred at a slightly higher flow coefficient with a more abrupt drop in pressure rise near stall. Effects of rotating stall were observed (back flow seen with tufts mounted on the hub and case between Sta. 0 and 1) for any flow coefficient below 0.57.

The airfoil and endwall flow visualization results will be discussed in detail in order to help explain many of the results that can be seen in the traverse data and in the airfoil pressure distributions. The pressure surface traces for $\bar{\phi} = 0.85$ (Fig. 3) show a slight radial outflow over most of the airfoil and especially near the hub and near the trailing edge/tip region. Tip leakage effects are noticeable on both the pressure and suction surfaces. The pressure side boundary layer is being drawn into the tip clearance region causing a relatively high velocity jet on the suction side of the airfoil which draws the suction surface tip region boundary layer radially outward. The suction surface results for $\bar{\phi} = 0.85$ show a hub corner stall region (with back-flow) extending from midchord to the trailing edge at the hub and from the hub radially outward to

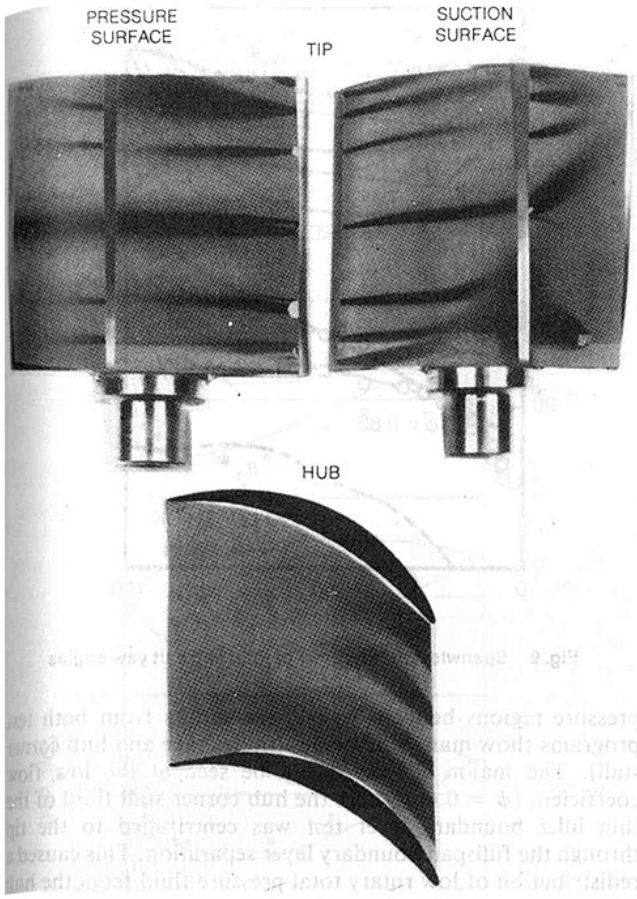

Fig. 4 Airfoil passage flow visualization, $\bar{\phi} = 0.65$

midspan at the trailing edge. The corner stall caused a radial displacement of the suction surface boundary layer.

The flow visualization results for the lowest flow coefficient (highest loading, $\bar{\phi} = 0.65$, Fig. 4) show strong tip leakage flow on both the pressure and suction surfaces of the airfoil with the most pronounced radial outflow on the pressure side. Suction side results show two back-flow regions, one near the hub, due to the hub corner stall, extending from midchord aft to the trailing edge and out to 75 percent span and one locally near the trailing edge/tip region. Radial displacement effects on the suction surface due to the corner stall blockage can be seen to extend forward to the 30 percent chord location near the hub and out to the tip at the trailing edge.

The endwall results did show slight circumferential boundary layer displacement due to secondary flow from the pressure surface to the suction surface. No evidence of a scraping vortex or a leading edge horseshoe vortex could be seen on the airfoil surface or on the endwall results.

Many similarities exist between the flow visualization results of the present program and those of the previous program with thin hub and tip inlet boundary layers. From these results it has been observed that both tests had, in general, little radial displacement of the airfoil surface boundary layer when not in the vicinity of the corner stall region or the tip. The main difference in the flow visualization results between the two tests was at the lowest flow coefficient ($\bar{\phi} = 0.65$). The effect of the thick inlet boundary layer profiles was to reduce the spanwise extent of the corner stall region by preventing a fullspan separation at the trailing edge. This reduction in extent was caused by the relative unloading at midspan due to the higher than average axial flow speed at midspan.

Contour plots of the total pressure results for the two flow coefficients (0.85 and 0.65) are shown in Figs. 5 and 6 with the

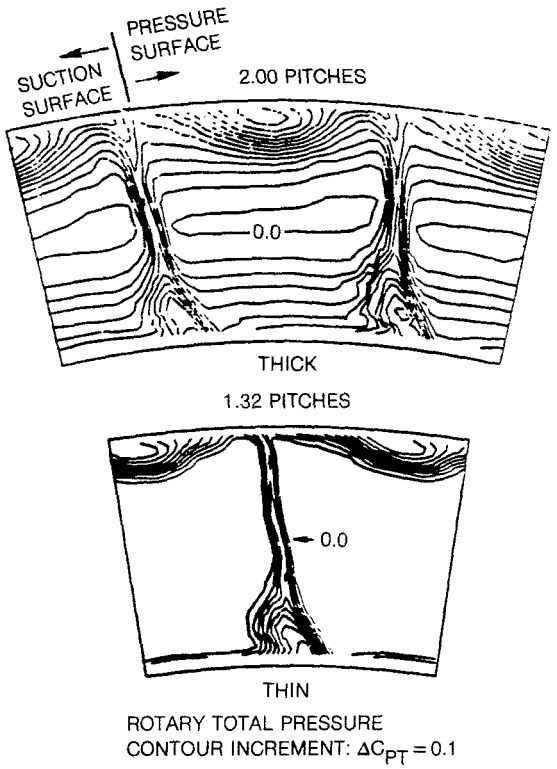

Fig. 5 Rotary total pressure contours, $\bar{\phi} = 0.85$

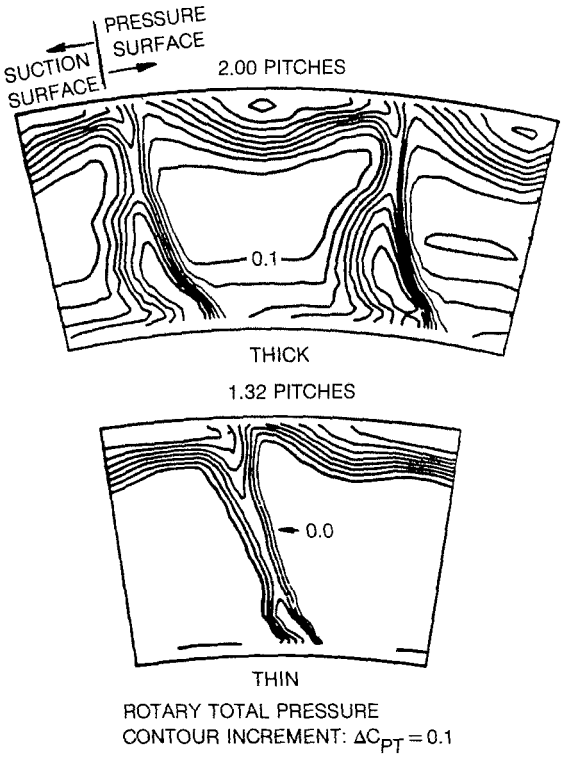

Fig. 6 Rotary total pressure contours, $\bar{\phi} = 0.65$

data from the previous thin inlet boundary layer test. All the pressures were measured relative to the inlet absolute total pressure at midspan and normalized with a dynamic pressure based on midspan wheel speed. The total pressure is presented in the form of rotary total pressure:

$$P_{T,ROT} = P_S + 1/2\rho(W^2 - U^2)$$

instead of relative total pressure. Rotary total pressure was

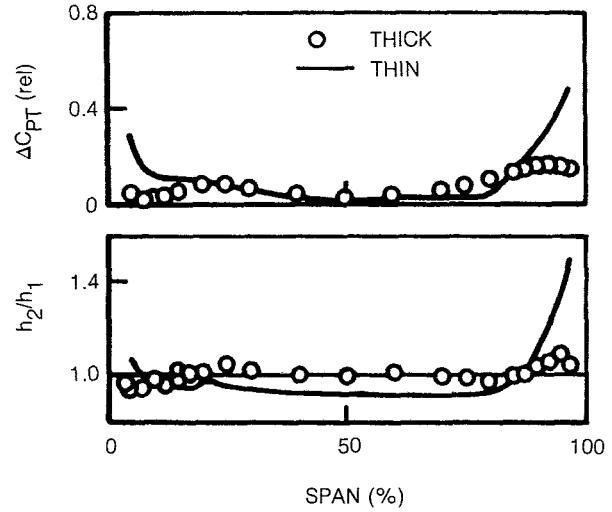

Fig. 7 Spanwise distribution of loss and streamtube contraction, $\bar{\phi}$ = 0.85

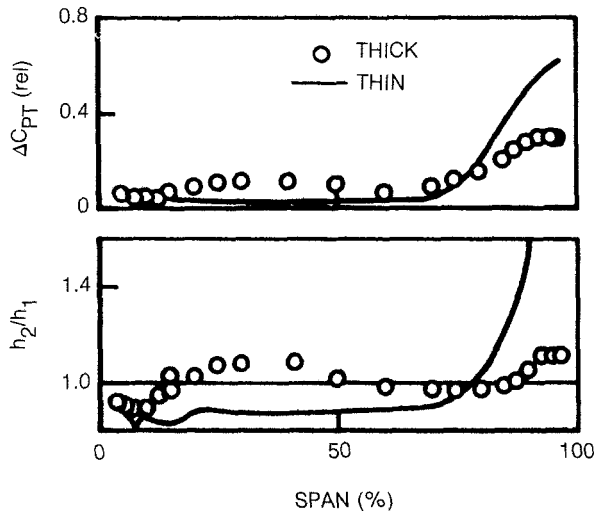

Fig. 8 Spanwise distribution of loss and streamtube contraction, $\bar{\phi}$ = 0.65

chosen for several reasons. First, rotary total pressure is the primary parameter leading to the growth of the streamwise component of vorticity in the rotating frame of reference, as discussed by Hawthorne [15]. Second, it is constant in the region between wakes for the thin boundary layer results. Lastly, by eliminating the radial variation of relative total pressure due to radial position, the contours in between wakes for the present program are due solely to the inlet C_x profile.

The results at the high flow coefficient ($\bar{\phi}$ = 0.85, Fig. 5) show the presence of a relatively thin midspan wake. A large high loss (low rotary total pressure) region is present between the wakes at the tip. A smaller high loss region is present in the airfoil wake at the hub due to the corner stall. Generally speaking, the contours in the core flow region reflect the inlet total pressure profile.

The hub corner stall for the low flow coefficient ($\bar{\phi}$ = 0.65, Fig. 6) extends out to 75 percent span. Evidence of weak secondary flow near the hub can be seen as higher total pressure fluid moves down to the hub on the pressure surface side of the airfoil wake. The midgap tip loss region affects the core flow from the tip down to 75 percent span with the core of the loss region slightly removed from the endwall.

The rotary total pressure results with thin inlet boundary layers are also presented in Figs. 5 and 6 for comparison with the present results. Except for the uniform rotary total

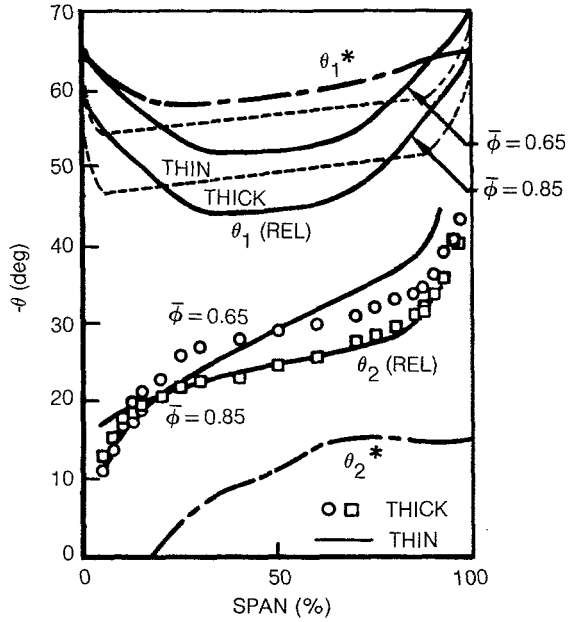

Fig. 9 Spanwise distributions of inlet and exit yaw angles

pressure regions between wakes, the results from both test programs show many similarities (tip leakage and hub corner stall). The major difference can be seen at the low flow coefficient ($\bar{\phi}$ = 0.65) where the hub corner stall fluid of the thin inlet boundary layer test was centrifuged to the tip through the fullspan boundary layer separation. This caused a redistribution of low rotary total pressure fluid from the hub to the tip. This did not happen in the present program, since, as seen in the flow visualization results, the airfoil never experienced fullspan boundary layer separation (due to a more negative incidence at midspan for the same area average flow coefficient).

Spanwise distributions of circumferentially mass averaged loss in relative (or rotary) total pressure (ΔC_{PT}(rel)), contraction ratio (h_2/h_1) and exit relative yaw angle (θ) for the two flow coefficients are shown in Figs. 7, 8, and 9. These data along with the inlet relative yaw angle are the input parameters required for any potential flow calculation. The lines shown with the data are from the previous test with thin inlet boundary layers. For all flow coefficients, the present study had higher loss in the midspan region with lower loss at the hub and tip. The tip loss increased with increased loading. However, the near hub net loss was unusually low. This is somewhat surprising in light of the monotonically increasing corner stall seen in the rotary total pressure contours (Figs. 5 and 6). The radial displacement of high total pressure fluid has significantly affected the fullspan nature of the spanwise distribution of loss. Generally, the hub and tip loss have been substantially reduced by radial displacement of high total pressure fluid into those areas with increased loss in the midspan region. This effect is most pronounced at the low flow coefficient ($\bar{\phi}$ = 0.65, Fig. 6).

Contraction ratio (h_2/h_1) results are also shown in Figs. 7 and 8. At the nominal design flow coefficient ($\bar{\phi}$ = 0.85, Fig. 7) there was contraction in the hub region (h – ratio less than 1.0) with expansion occurring from 15 to 35 percent span and from 90 percent outward. At the near stall flow coefficient ($\bar{\phi}$ = 0.65, Fig. 8) the effect of the severe hub corner stall, characterized by low loss at the hub and higher loss in the lower midspan region, can be seen as a region of expansion for spanwise locations between 20 and 60 percent while tip loss only affects the outer 10 percent. Generally speaking, regions of higher net loss are characterized by streamtube expansion (h – ratios greater than 1.0) and surrounding low

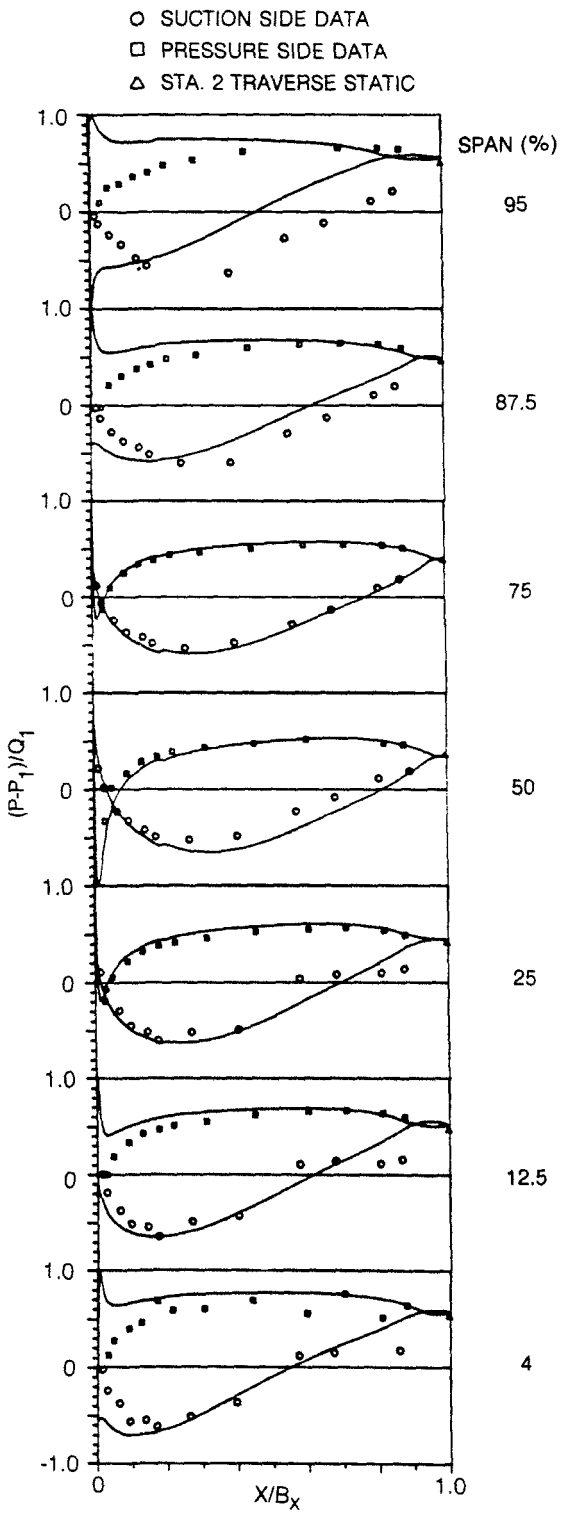

Fig. 10 Fullspan airfoil pressure distributions, $\bar{\phi} = 0.85$

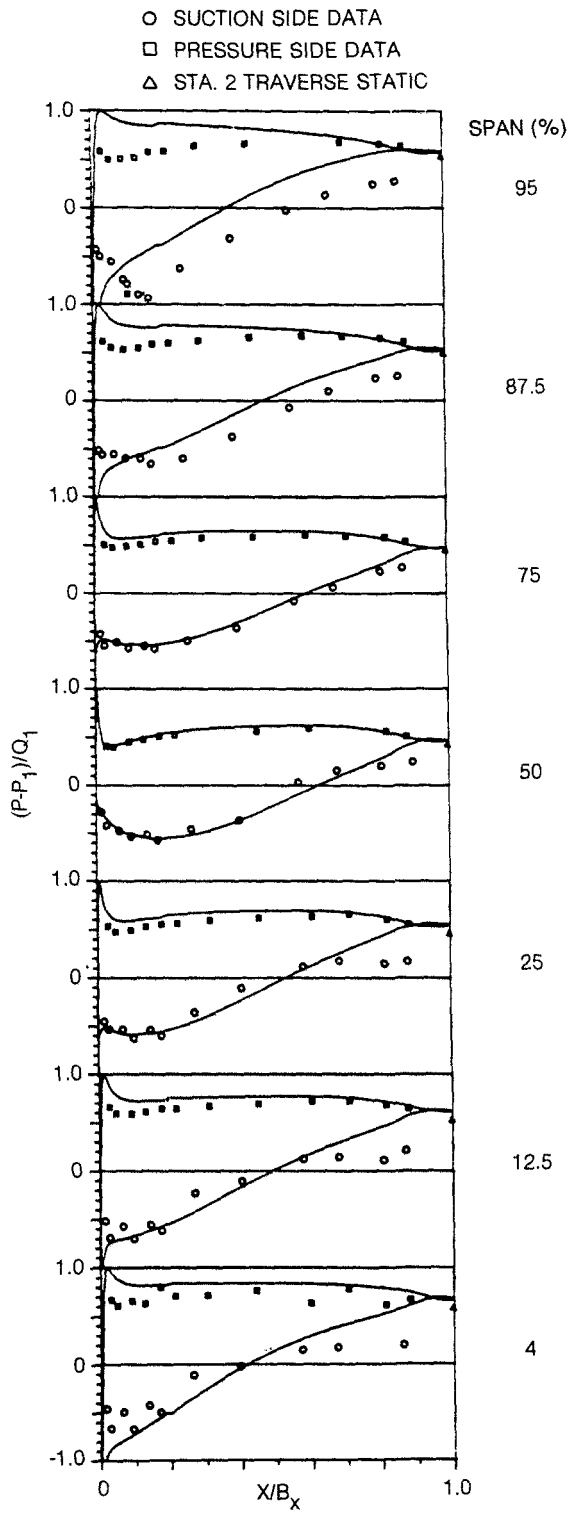

Fig. 11 Fullspan airfoil pressure distributions, $\bar{\phi} = 0.65$

loss regions by streamtube contraction (h – ratios less than 1.0).

Circumferentially area averaged rotor exit relative yaw angles (Fig. 9) are shown with the calculated relative inlet yaw angles and the leading and trailing edge metal angles (θ^*). Included with the present data are inlet and exit yaw angles from the previous program with thin inlet boundary layers. From the figure, differences in incidence, deviation, and turning between the two inlet conditions can be seen. The flow in the present program had much higher inlet angles at the hub and tip with lower inlet angles at midspan. At the low flow coefficient ($\bar{\phi} = 0.65$) the lower midspan inlet angle in the present program prevented a fullspan trailing edge separation. This prevented the low total pressure fluid in the hub corner stall from being centrifuged out to the tip as it had been in the previous program. The radial transport of the high loss low momentum fluid out of the hub corner stall region in the previous program produced a well behaved (high turning, low loss) flow condition near the hub for the low flow coefficient $\bar{\phi} = 0.65$ (see Figs. 6 and 9). In the present

program, however, the unseparated suction surface boundary layer at $\bar{\phi} = 0.65$ was qualitatively similar to the flow at higher flow coefficients but with a more severe corner stall with higher deviation (lower turning).

Summarizing these results, one can see that the total pressure contour results do not present the entire picture in regards to net mass averaged loss when the inlet rotary total pressure is as severely distorted as it is in the present program. The radial displacement of the high and low total pressure fluid significantly affects the spanwise distributions of net loss, contraction ratio, and exit flow angle.

Fullspan airfoil pressure distributions for the two flow coefficients ($\bar{\phi}=0.85$ and 0.65) are shown in Figs. 10 and 11. Rotor exit (Sta. 2) traverse static pressure data as well as computed two-dimensional potential flow results (based upon measured inlet and exit data) are shown with the measured pressure distributions. The computed pressure distributions are based on the method of Caspar et al. [16]. Pressure distributions from the previous program with thin inlet boundary layers are reported in [8, Figs. 17, 18, and 19].

The data at 75 percent span were the only results, for all flow coefficients, not significantly affected by either the hub corner stall or the tip flow. This is seen in the excellent agreement between the measured and computed results at both flow coefficients. Comparison between the measured and computed results for 87.5 and 95 percent span shows the influence of the complicated three-dimensional nature of the tip flow. From 50 percent span inward, the effects of the hub corner stall are clearly seen (especially at the low flow coefficient). For $\bar{\phi} = 0.85$ (Fig. 10) the corner stall strongly affects the suction surface flow out to 25 percent span. As flow coefficient is decreased to $\bar{\phi} = 0.65$ (Fig. 11) the effect of the hub corner stall extends to midspan. In general, the airfoil surface pressure distributions reflect the observations made from the flow visualization results. There is excellent agreement between the computed downstream static pressure and the value from the traverse results at Sta. 2 (plotted in Figs. 10 and 11 at $X/B_x = 1.0$).

Results from the previous thin inlet program are remarkably similar to those presented here. In addition, similar diagreements between the computed two dimensional and measured three-dimensional results occurred in the same locations.

Conclusions

An extensive body of experimental results has been presented which provides detailed information as to the nature of the flow over an isolated axial compressor rotor with thick hub and tip inlet boundary layers. These data provided a basis of comparison with a previous benchmark study which had thin inlet boundary layers. This additional data will be most useful in improving the blade-to-blade and through-flow analyses used in the design phases of compressor development. Specific conclusions are as follows.

1. The relative unloading of the midspan portion of the airfoil (due to incidence) inhibited a full-span separation which prevented the hub corner stall high loss flow from centrifuging to the tip as had occurred with the thin inlet boundary layer at the low flow coefficient.
2. The radial distribution of mass averaged loss was strongly influenced by the relatively weak radial displacement of rotor passage flow. Specifically, the radial redistribution consisted of the exchange of high total pressure fluid in the midspan region with low total pressure fluid near the hub.
3. Regions of high net mass averaged loss are characterized by a flow expansion ($h-$ratios greater than 1.0) surrounded by low loss regions characterized by a flow contraction ($h-$ratios less than 1.0), due to the effects of the large blockage present in the high loss regions.
4. Static pressure rise was increased by 6 percent at the design flow coefficient compared to previous results with thin inlet boundary layers.
5. For all loadings there was increased loss in the midspan region and decreased loss near the hub and tip regions relative to previous results with thin inlet boundary layers.
6. Exit relative flow angles were only weakly affected by loading, unlike the previous program which, for the lowest flow coefficient, reflected the effects of the massive transport of the hub corner stall to the tip.

Acknowledgments

The thin boundary layer isolated rotor data was acquired under Air Force contract funding under the direction of C. Herbert Law (AFWAL/POTX), project engineer, Contract Number F33615-77-C-2083. The thick boundary layer isolated rotor data was acquired under funding from NASA Lewis Research Center under the direction of Mr. Michael Pierzga, project manager, Contract Number NAS3-23157.

References

1 Lakshminarayana, B., and Horlock, J. H., "Leakage and Secondary Flows in Compresor Cascades," A.R.C.R. & M. No. 3483, Mar. 1965.

2 Moore, R. W., Jr., and Richardson, D. L., "Skewed Boundary Layer Flow Near the End Walls of a Compressor Cascade," ASME Paper No. 56-A-131, July 1956.

3 Phillips, W. R. C., and Head, M. R., "Flow Visualization in the Tip Region of a Rotating Blade Row," *Int. J. Mech. Sci.*, Vol. 22, Jan. 1980, pp. 495–521.

4 Schmidt, D. P., and Okiishi, T. H., "Multistage Axial-Flow Turbomachine Wake Production, Transport and Interaction," *AIAA Journal*, Vol. 15, 1977, pp. 1138–1145.

5 Reynolds, B., and Lakshminarayana, B., "Blade Loading and Spanwise Effects on the Near and Far Wake Characteristics of a Compressor Rotor Blade," AIAA Paper No. AIAA-80-0201, 18th Aerospace Sciences Meeting, Jan. 14–16, 1980, Pasadena, Calif.

6 Kool, P., DeRuyck, J., and Hirsch, C., "The Three-Dimensional Flow and Blade Wake in an Axial Plane Downstream of an Axial Flow Compressor Rotor," ASME Paper No. 78-GT-66, Mar. 1978.

7 Adkins, G. G., and Smith, Jr., L. H., "Spanwise Mixing in Axial-Flow Turbomachines," ASME JOURNAL OF ENGINEERING FOR POWER, Vol. 104, Jan. 1982, pp. 97–110.

8 Dring, R. P., Joslyn, H. D., and Hardin, L. W., "An Investigation of Compressor Rotor Aerodynamics," ASME JOURNAL OF ENGINEERING FOR POWER, Vol. 104, Jan. 1982, pp. 84–96.

9 Dring, R. P., Joslyn, H. D., and Hardin, L. W., "Experimental Influence of Compressor Rotor Wakes," AFAPL-TR-79-2107, Air Force Aero Propulsion Laboratory, Technology Branch, Turbine Engine Division (TBX), Wright- Patterson Air Force Base, OH 45433.

10 Wagner, J. H., Dring, R. P., and Joslyn, H. D., "Axial Compressor Middle Stage Secondary Flow Study," NASA CR-3701, July 1983.

11 Dring, R. P., and Joslyn, H. D., "Measurements of Turbine Rotor Blade Flows," ASME JOURNAL OF ENGINEERING FOR POWER, Vol. 103, No. 2, Apr. 1981.

12 Ruden, P., "Investigation of Single Stage Axial Fans," NACA RM No. 1062, April 1944.

13 Johnson, J. P., "A Wall-Trace Flow Visualization Technique for Rotating Surfaces in Air," ASME *Journal of Basic Engineering*, Dec. 1964, p. 907.

14 Hunter, I. H., and Cumpsty, N. A., "Casing Wall Boundary-Layer Development Through an Isolated Compressor Rotor," ASME Paper No. 82-GT-18.

15 Hawthorne, W. R., "Secondary Velocity in Stratified Compressible Fluids in Rotating Systems," CUED/A-Turbo/TR 63, University of Cambridge, England, 1974.

16 Caspar, J. R., Hobbs, D. E., and Davis, R. L., "Calculation of Two-Dimensional Potential Cascade Flow Using Finite Area Methods," *AIAA Journal*, Vol. 18, No. 1, Jan. 1980, pp. 103–109.

Inlet Boundary Layer Effects in an Axial Compressor Rotor: Part II—Throughflow Effects

J. H. Wagner

R. P. Dring

H. D. Joslyn

United Technologies Research Center,
East Hartford, Conn. 06108

This paper presents results of an experimental aerodynamic study conducted in the rotating frame of reference downstream of an isolated compressor rotor with both thick and thin inlet endwall boundary layers. The paper focuses on those aspects of the data having particular significance to the assumptions and application of throughflow theory. These aspects include the spanwise distributions of static pressure and blockage, and the radial redistribution of fluid as it passes through the blade row. It is demonstrated that the main contributions to total pressure loss, blockage, and the distortion of the static pressure field were due to the hub corner stall and tip leakage. This is a significant departure from previous conclusions which looked to the endwall boundary layer and to secondary flow as major loss and blockage producing mechanisms.

Introduction

The throughflow analysis is at the core of most axial compressor design systems. This is a two-dimensional (axisymmetric) calculation that requires as input, in addition to annulus geometry, a row-by-row description of the spanwise distributions of loss, deviation, and blockage (or their equivalents). The output of the calculation is a spanwise description of the absolute and relative Mach triangles at each streamwise station along the annulus. To date, however, due to a lack of sufficiently detailed experimental data, it has not been possible to assess the accuracy of such a calculation. Specifically, it has not been possible to carry out a throughflow calculation based purely on measured aerodynamic data for input and to compare the computed results directly with other measured data. It is the overall objective of a long-term research program at UTRC to generate an extensive data base that will allow one to scrutinize these analyses in detail by comparing their results with detailed experimental data obtained in both single and multistage compressor configurations (Dring, Wagner, and Joslyn [1–7]). It is expected that the benefits of this program will include an improved basis for throughflow modeling that will ultimately lead to the following: improved compressor performance, acceleration of the compressor development process, and improvement in the ability of the compressor analyst to bridge the gap between the usually sparse amount of data available from a high-speed, multistage rig test and an accurate description of the nature of the flow. To this end, the focus of the present paper (Part II) is to examine a number of aspects of the data acquired on an isolated compressor rotor with thick ($\delta \approx 35$ percent span) and thin ($\delta \approx 5$–10 percent span) inlet endwall boundary layers as to their implications for throughflow analysis.

It is the objective of the present paper to examine those aspects of the flow having particular significance to the assumptions and application of throughflow theory. These aspects include (*i*) blockage, since it is a required input to the calculation, (*ii*) the full-span static pressure field, since static pressure it has historically been used to establish the blockage, and (*iii*) radial redistribution in the flow, since radial flow violates the assumption of strip theory, which is usually [8] at the basis of throughflow analysis. This objective will be carried out by examining both aerodynamic data and trace gas trajectory data acquired in the UTRC Large-Scale Rotating Rig in the rotating frame of reference of the rotor.

The spanwise distributions of total pressure loss and deviation were discussed in Part I. In particular, it was shown how these distributions are strongly influenced by hub corner stall and tip leakage. The present paper (Part II) will analyze the spanwise distributions of blockage in the same way. Historically, blockage has been inferred from measured data by adjusting its level until reasonable agreement was obtained between measured and computed hub and tip static pressures. This is a necessary but undesirable approach, since it provides little or no information about the spanwise distribution of blockage. In the present work, and as in [4, 5, 6], because of the detailed nature of the data, blockage has been calculated directly and not inferred. It will be seen from the data that whereas the contribution of secondary flow is very small, the hub corner stall has a significant impact on both the static pressure field and the blockage.

Background

The Large-Scale Rotating Rig, its aerodynamic instrumentation, and experimental uncertainty are described in detail in Part I of this paper [7]. Data from three stations along the rig flow path will be discussed (Part I, Fig. 1). The

Contributed by the Gas Turbine Division of THE AMERICAN SOCIETY OF MECHANICAL ENGINEERS and presented at the 29th International Gas Turbine Conference and Exhibit, Amsterdam, The Netherlands, June 4–7, 1984. Manuscript received at ASME Headquarters January 5, 1984. Paper No. 84-GT-85.

inlet static pressure and the inlet velocity and trace gas concentration profile documentation was done at station 1, 82 percent of axial chord ahead of the rotor at midspan. For the thick boundary layer data, the traverse data were acquired at station 2, 30 percent of axial chord downstream of the rotor at midspan [4]. For the thin inlet boundary layer, traverse data were acquired at planes located 10, 30, 50, and 110 percent downstream of the rotor [1, 2]. The exit static pressures on the flow path hub and casing were measured at station 3, 224 percent of axial chord downstream of the rotor. Some flow path static pressure data were also acquired on the casing at station 2.

A trace gas technique was employed to document the trajectory of the inlet boundary layer fluid for the thick test. This technique has been demonstrated previously by Denton and Usui [9] and by Moore and Smith [10]. The basic concept is that a streamline trajectory can be traced by seeding the flow with a trace gas and then searching for that trace gas with a detector at downstream locations. Care must be taken that the flow is not disturbed by undesired wakes from the trace gas injector or by the injection process. Care must also be taken that the transport of the trace gas is by convection and not by molecular diffusion, as it might be for example with helium. In the past [9, 10], various hydrocarbons have been used but in the present program carbon dioxide was used as the trace gas. It has the advantages of being inexpensive, nontoxic, and nonflammable. A Nondispersive Infrared Detector (NDIR) (Beckman Model 109) was used to measure the CO_2 concentration.

The CO_2 injector consisted of a pair of 0.375-in.-dia tubes that were part of the hub and tip boundary layer thickening devices [4, 6]. The tubes had 0.015-in.-diameter holes drilled in them at 1 in. intervals around the annulus. A third injector was also used at midspan but it will not be discussed in the present paper. A Kiel probe mounted in the rotating frame traverse unit was used to sample the flow. This probe was connected to the NDIR by a rotary union. The NDIR was calibrated on-line before every traverse with a zero gas (0 ppm CO_2) and a span gas (2000 ppm CO_2). Atmospheric concentration of CO_2, i.e., the background level, was typically 300 ppm. The injector flow was set to provide a maximum local inlet concentration of typically 1000 ppm above the background value. The CO_2 flow rate through each injector was also recorded at the beginning of each traverse.

The trace gas concentration results will be presented in the form of contour plots. The values of the contours represent the difference between the measured value and the background value, normalized by the maximum difference. Although they are plotted together, the data for the hub and tip injectors were acquired separately.

Discussion

The discussion of the results will be primarily focused on the three-dimensional endwall flow mechanisms and specifically the impact that they had on the static pressure field, on the blockage, and on radial redistribution. Comparisons will be made between the thick and the thin rotor inlet endwall boundary layer tests with the rotor operating at its nominal design flow coefficient ($\bar{\phi} = 0.85$) and at a near stall condition ($\bar{\phi} = 0.65$). In Part I [7], it was pointed out that for the thick inlet boundary layer the flow coefficient is based on an area averaged value of C_x and that for the thin case it is based on the midspan value (which is very close to the area averaged value).

Flow path static pressure measurements are an important part of any compressor test. In high-speed, engine scale testing, however, these measurements are usually limited to the stationary part of the annulus (sometimes only on the casing) between adjacent blade rows and possibly at one or more circumferential locations between adjacent blades in a row. This type of data is a key element in the analytical synthesis (i.e., throughflow analysis) of the compressor aerodynamics.

The static pressure data for the present rotor with thick and thin inlet boundary layers is shown in Figs. 1 and 2, respectively. The flow path hub and tip static pressures for the far downstream location (station 3) are shown for both tests. In addition, for the thick test the tip static pressure is shown at the traverse plane (station 2). The figures also include static pressure in the flow from the circumferentially area-averaged traverse results. For the thick test (Fig. 1), data were limited to the plane 30 percent aft of the rotor trailing edge [4]. For the thin test (Fig. 2) data were taken at planes 10, 30, 50, and 110 percent aft of the rotor [1, 2]. For the plane 10 percent aft at the design flow coefficient (0.85) traverse data could not be acquired close to the hub since the backflow region of the hub corner stall penetrated back to this plane [1, 2]. For reference in examining both figures, the relative total pressure at midspan is at $C_p = +1.0$, so the normalized rotor exit relative dynamic pressure $(W/U_m)^2$ at midspan ranges in magnitude from 0.7 to 1.3.

In general, the figures indicate an increasing static pressure from hub to tip with one notable exception for the thin test (Fig. 2) at the near stall condition ($\phi = 0.65$) close to the trailing edge ($\Delta X/B_x = 0.1$). For this test, the static pressure decreased with radius from 50 to 85 percent span. Also, it can generally be seen that there is a significant overall static pressure rise as the flow moves downstream behind the rotor. This can be seen in the data from the various traverse planes for the thin case (Fig. 2). It isn't until the flow is 50 to 110 percent aft of the rotor that the traverse results begin to extrapolate to the flow path values at station 3 (224 percent aft). For the thick test (Fig. 1), the traverse data (30 percent aft) is again well below the far downstream values at station 3, but it does extrapolate well to the flow path tip static pressure measured at the traverse plane (station 2).

Although it is clear from both the thick and thin inlet boundary layer data that there is considerable diffusion due to wake mixing, the locally very low static pressures measured

Nomenclature

B_x = airfoil axial chord
C_p = pressure coefficient: $(P - P_{T1})/Q_{U_m}$
C_x = axial component of flow velocity
$C_{x,m}$ = axial velocity at midspan
$\bar{C}_x$ = area averaged axial velocity
$\bar{C}_x^a$ = circumferentially area-averaged axial component of flow velocity
$\bar{C}_x^{PT}$ = axial velocity based on circumferentially mass-averaged total and static pressures and yaw and pitch angles
$\bar{K}$ = blockage factor $(\bar{C}_x^a/\bar{C}_x^{PT})$
P = pressure
P_{T1} = inlet absolute total pressure at midspan
Q_{U_m} = dynamic pressure of wheel speed at midspan: $(1/2\ \rho U_m^2)$
U_m = wheel speed at midspan
W = relative flow speed
ΔX = axial distance
ρ = density
ϕ = flow coefficient: (C_x/U_m)
$\bar{\phi}$ = flow coefficient: $(\bar{C}_x/U_m)$

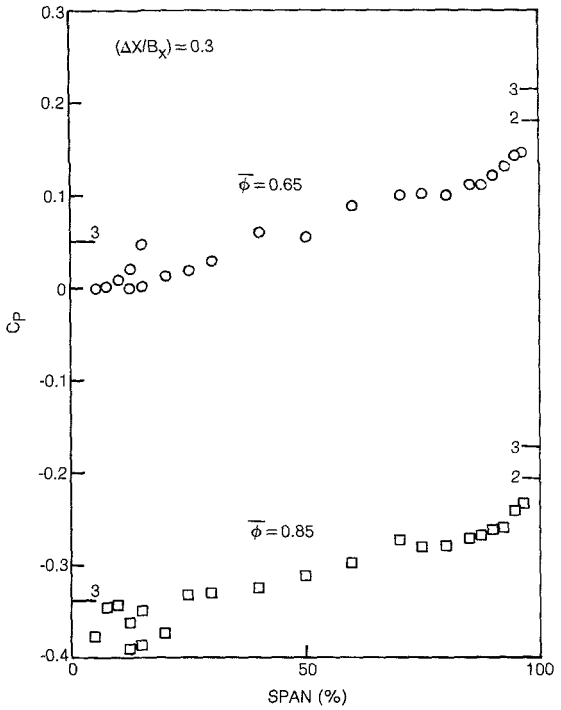

Fig. 1 Spanwise distributions of static pressure, thick inlet boundary layers

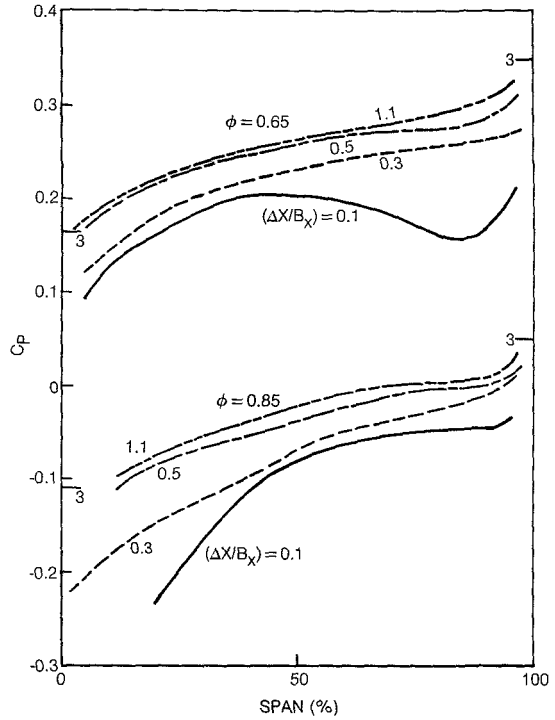

Fig. 2 Spanwise distributions of static pressure, thin inlet boundary layers

close to the trailing edge and near the hub in the thin test (Fig. 2, 10 percent aft) are particularly noteworthy. For this case, at flow coefficients from 0.75 up to and exceeding 0.95 there was a hub corner stall whose backflow region penetrated downstream to the traverse plane 10 percent aft. The corner stall caused locally very high losses and blockage and a very low static pressure. The low static pressure diffused rapidly with downstream distance (Fig. 2). At the near stall flow coefficient (ϕ = 0.65), the airfoil suction surface boundary layer separated and the hub corner stall collapsed as the high loss fluid was centrifuged out to the tip through the fullspan separation bubble [1, 2]. It can also be seen in Fig. 2 that at this condition the low static pressure region also moved out to the tip, along with the loss ([2], Figs. 15 and 16) and, as will be discussed below, the blockage. Here again, the low static pressure diffused rapidly with downstream distance. These observations about the low static pressure regions can also be seen in the contour plots of static pressure in [1] and [4]. The contour plots shown that the low static pressure regions are close to the high loss regions in both the radial and circumferential directions.

In summary, the flow path and traverse static pressure data indicate that there is considerable diffusion as the wake mixes out downstream of the rotor and also that there is a local region of low static pressure close to the rotor where the loss and, as will be seen shortly, the blockage are high. Finally, the downstream diffusion is nearly complete by a downstream distance of about 50 percent of the airfoil axial chord.

Blockage, in the present discussion, reflects the departure from axisymmetry in the flow (due to blade-to-blade effects) and it corresponds to what has been called "tangential blockage" [11]. In this sense, it accounts for the blockage due to airfoil wakes, corner stall, tip leakage, and to the extent that they depart from axisymmetry, the endwall boundary layers and secondary flows. A definition for the calculation of the blockage from the measured data has been suggested in [4], [5], and [6]. According to this definition the blockage factor ($\bar{K}$) is the ratio of the circumferentially area-averaged axial velocity to an axial velocity calculated from the circumferentially mass-averaged total and static pressures and

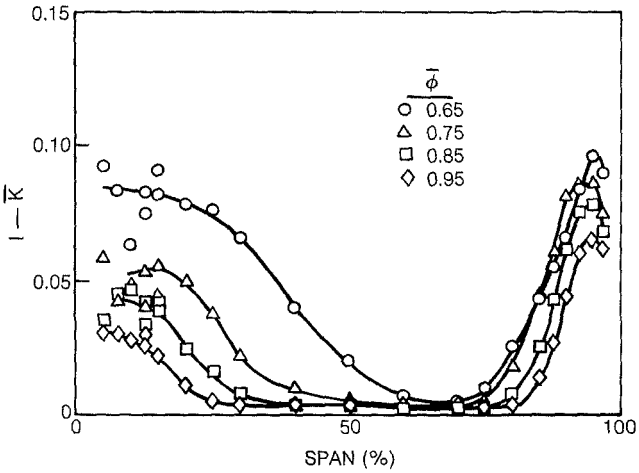

Fig. 3 Spanwise distributions of blockage, thick inlet boundary layers, $\Delta X/B_X$ = 0.3

flow yaw and pitch angles. It has been observed that the major difference between area and mass averaging has been in the total pressure. This definition results in blockage as a function of radius, and as an example, results for the thick and thin inlet boundary layer tests have been plotted in Figs. 3 and 4 for the four flow coefficients at station 2 (30 percent aft of the rotor trailing edge). By this definition, when the flow is purely axisymmetric, the blockage factor is equal to one and there is no blockage ($1 - \bar{K} = 0$). The flow is seen to approach this situation in the midspan region for both the thick and thin cases.

For the thick test (Fig. 3), there is a rapid increase in the magnitude and the spanwise extent of the blockage at the hub as the flow coefficient is reduced from 0.95 to 0.65. This trend is consistent with the growth of the hub corner stall region as seen in both the surface flow visualization and in the contour plots of rotary total pressure ([7], Figs. 3-6). Note that

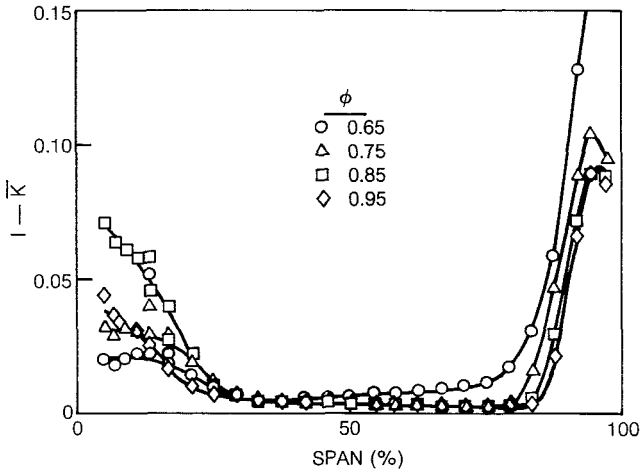

Fig. 4 Spanwise distributions of blockage, thin inlet boundary layers, $\Delta X/B_X = 0.3$

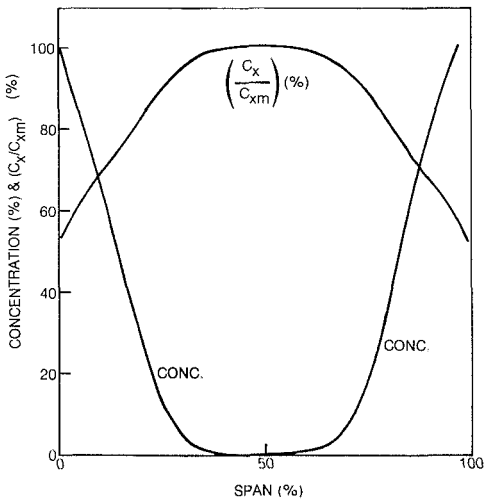

Fig. 5 Inlet velocity and trace gas concentration profiles at station 1

whereas radial redistribution of high and low total pressure fluid has caused the total pressure loss close to the hub to appear to be very low ([7], Figs. 7 and 8), the blockage, i.e., the departure from axisymmetry, increases monotonically as the hub is approached. The reason for this is that the radial distribution of total pressure loss is usually very sensitive to even weak radial redistribution of wake fluid, whereas the blockage depends on the entire pitchwise flow distribution.

In the tip region for the thick test (Fig. 3), the blockage is due to a combination of tip leakage and endwall boundary layer effects. The blockage in this region is also increasing with loading (i.e., decreasing flow coefficient) but at a much more gradual rate than at the hub.

The blockage distributions for the thin inlet boundary layers (Fig. 4) are considerably different from the thick test. As the flow coefficient was reduced the blockage at the hub reached a maximum at $\phi = 0.85$ and decreased to a minimum at 0.65. At the tip, the blockage is gradually increasing with decreasing flow coefficient. From 0.75 to 0.95, it is similar in magnitude and spanwise extent to the thick test (in spite of widely different inlet conditions). At the near stall flow coefficient of 0.65, however, the tip blockage has increased dramatically. The decrease in hub blockage and increase in tip blockage is another manifestation of the radial transport of the low total pressure fluid from the hub to the tip through the profile separation bubble at this near stall flow coefficient [1, 2].

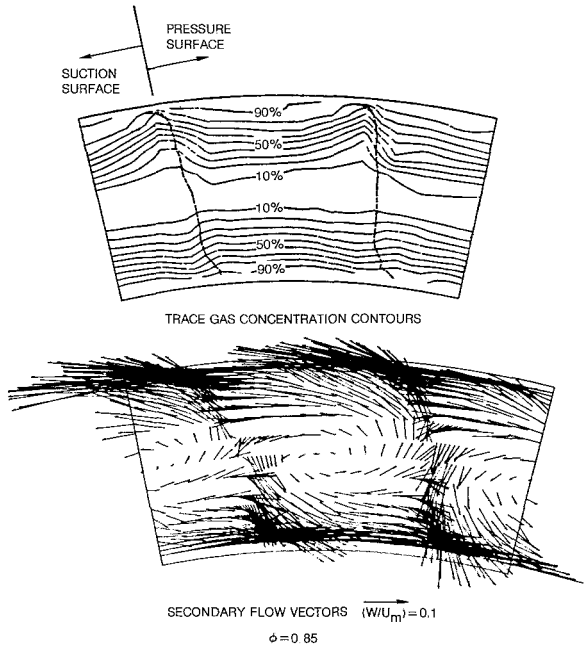

Fig. 6 Radial redistribution, thick inlet boundary layer, $\bar{\phi} = 0.85$, $\Delta X/B_X = 0.3$

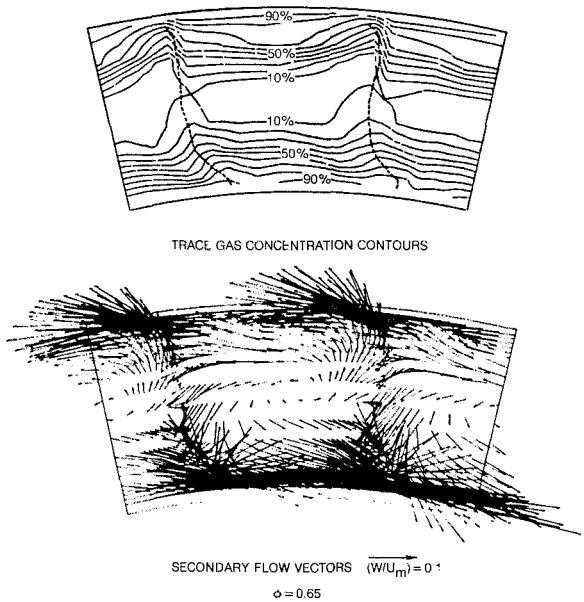

Fig. 7 Radial redistribution, thick inlet boundary layer, $\bar{\phi} = 0.65$, $\Delta X/B = 0.3$

The blockage decreases rapidly as the flow downstream of the rotor mixes out and approaches axisymmetry [6]. It is this mixing which also produces the static pressure rise as the flow proceeds downstream (Fig. 2). By equating the change in blockage to a change in axial momentum (tangential momentum being conserved), one can estimate a static pressure rise from the decrease in blockage, i.e., an increase in available annulus area. On this basis, fairly good agreement has been obtained between the blockage results (Fig. 4) and the static pressure rise with downstream distance (Fig. 2). This only indicates that the suggested definition for $\bar{K}$ is not unreasonable.

It is interesting to note that at the two highest flow coefficients (0.85 and 0.95), the spanwise blockage distributions for the thick and thin inlet boundary layer tests are very similar as to the magnitude and spanwise extent of the regions

of high blockage. This is consistent with the fact that the rotor had the same tip clearance in both cases, and with the fact that it has been observed that corner stall is insensitive to the incident endwall boundary layer thickness [5 and 12].

The remainder of this paper deals with radial transport for the test with the thick inlet hub and tip boundary layers. This will be done by examining the trace gas results and the secondary flow vectors from the aerodynamic results. The normalized inlet trace gas concentration profiles on the hub and tip are shown in Fig. 5 along with the normalized inlet velocity profile. These data were acquired at station 1, 82 percent of axial chord upstream of the rotor leading edge. This station is 260 percent of axial chord downstream of the inlet velocity and trace gas profile generator ([4], Fig. 2). The hub and tip trace gas profiles are similar in shape to the velocity defect (in terms of thickness and near linearity). Since the inlet flow to the rotor was axisymmetric, a radial-circumferential contour plot of concentration would result in axisymmetric contours. Any departure of the concentration contour results from axisymmetry at the rotor exit traverse location (station 2) would indicate some net radial transport within and/or downstream of the rotor blade-to-blade passage.

The secondary flow vectors (Figs. 6 and 7) are constructed by projecting the local velocity vectors measured in the rotating frame (at station 2) onto a plane normal to the gap averaged yaw angle measured at midspan. As an indication of their magnitude, a radial vector corresponding to $(W/U_m) = 0.1$ would give rise to a pitch angle of 6 deg.

The trace gas concentration contours and the secondary flow vectors are illustrated in Figs. 6 and 7 for the nominal and near stall flow coefficients of 0.85 and 0.65. The airfoil wake centerline is shown on the contour results by the dashed lines. At the design flow ($\bar{\phi} = 0.85$) the concentration contours indicate very little radial redistribution, except in the vicinity of the airfoil wakes. This same observation was also made in Part I [7] in regard to the absence of rotation of the Bernoulli surfaces due to secondary flow or due to the relative eddy [2]. This same absence of secondary flow has also been observed in a multistage environment [5]. The lack of secondary flow is due to the fact that in a compressor the initial streamwise vorticity in the flow due to the jump from the absolute to the rotating frame of reference, i.e., inlet skew, is of opposite sign to the streamwise vorticity generated by turning [13]. For the present configuration a rough estimate indicated that the initial vorticity dominated the vorticity generated by turning. The data show that Bernoulli surface rotation due to the relative eddy in the midspan region is also very weak. This eddy can be seen as the counterclockwise rotation in the region between the airfoil wakes in the secondary flow vector plot. The eddy is due to the axial component of the relative vorticity being equal to -2Ω when the flow in the absolute frame is irrotational. The terms contributing to this axial component of vorticity are a radial derivative of the relative tangential velocity component and a tangential derivative of the radial velocity component. The Bernoulli surface rotation is small, since the contribution of the radial velocity to the relative eddy is small in comparison to the contribution of the tangential velocity, and it is the radial velocity which causes rotation. If the absolute frame inlet flow had been irrotational, and if the rotor exit flow had been free vortex, the radial velocity due to the relative eddy would have been zero. This was actually the case for the thin boundary layer at the near stall flow coefficient [2].

Although the distortion of the concentration contours in the tip region is consistent with the secondary flow vectors, i.e., radial outflow on the suction side of the wake and radial inflow on the pressure surface side, such agreement should not be expected at all locations. The trace gas contours indicate the net radial transport between station 1 and station 2, whereas the secondary flow vectors only indicate the local rate of transport at station 2.

At the near stall flow condition ($\bar{\phi} = 0.65$), there are significant radial displacements evident in flow near both endwalls. In the tip region there is a displacement toward the tip in the region of the airfoil wake and a displacement away from the tip in the midgap region between wakes. The latter location is where most of the low total pressure fluid is concentrated at the tip (Part I, Fig. 6). At the hub there is a radial displacement toward the tip in the wake and toward the hub on the suction surface side of the wake. Here again, Bernoulli surface rotation due to secondary flow and the relative eddy is very weak. This is consistent with the contour plots of rotary total pressure (Part I, Fig. 6). The secondary flow vectors for this near stall condition are similar to the nominal design condition (Fig. 6), but with the radial flows being somewhat stronger.

When viewed on a circumferentially averaged basis, the change in the spanwise distribution of trace gas concentration across the rotor (from station 1 to station 2) was very close to what it would have been with no airfoils present, that is, a simple thickening of the concentration profiles as would occur due to boundary layer growth in the annular duct ([4], Fig. 47). This observation is valid at all four flow coefficients tested.

Conclusions

Several types of aerodynamic and trace gas concentration data have been acquired in the rotating frame of reference behind an isolated compressor rotor with thick and thin inlet endwall boundary layers. Specific aspects of the data have been examined in terms of their implications to throughflow modeling of compressor aerodynamics. These included: the spanwise distributions of static pressure and blockage, and radial transport within and downstream of the airfoil row. Specific conclusions are as follows:

1 The hub corner stall is not only a major loss-producing mechanism, but it also causes locally high blockage and low static pressure.

2 When high loss fluid is transported radially, the blockage and low static pressure go with it. This was observed to cause a local minimum in the gap averaged static pressure within the flow.

3 Blockage grew in magnitude and spanwise extent as the hub corner stall grew with increasing loading.

4 The static pressure rise downstream of the rotor corresponded closely to the decay in blockage and the approach to axisymmetry as the wakes mixed out.

5 Bernoulli surface rotation due to secondary flow and the relative eddy was very weak.

6 Although radial transport is generally weak, it is still sufficient to have a major impact on the spanwise distribution of loss.

Acknowledgments

The thin boundary layer isolated rotor data were acquired under Air Force contract funding under the direction of C. Herbert Law (AFWAL/POTX), project engineer, Contract Number F33615-77-C-2083. The thick boundary layer isolated rotor data were acquired under funding from NASA Lewis Research Center under the direction of Mr. Michael Pierzga, project manager, Contract Number NAS3-23157.

References

1 Dring, R. P., Joslyn, H. D., and Hardin, L. W., "Experimental Investigation of Compressor Rotor Wakes," AFAPL-TR-79-2107, Air Force Aero Propulsion Laboratory, Technology Branch, Turbine Engine Division (TBX), Wright-Patterson Air Force Base, Ohio.

2 Dring, R. P., Joslyn, H. D., and Hardin, L. W., "An Investigation of

Compressor Rotor Aerodynamics," ASME JOURNAL OF ENGINEERING FOR POWER, Vol. 104, No. 1, Jan. 1982, pp. 84–96.

3 Dring, R. P., "Boundary Layer Transition and Separation on a Compressor Rotor Airfoil," ASME JOURNAL OF ENGINEERING FOR POWER, Vol. 104, No. 1, Jan. 1982, pp. 251–253.

4 Wagner, J. H., Dring, R. P., and Joslyn, H. D., "Axial Compressor Middle Stage Secondary Flow Study," NASA Contract No. NAS3-23517, NASA Contractor Report 3701, July 1983.

5 Dring, R. P., Joslyn, H. D., and Wagner, J. H., "Compressor Rotor Aerodynamics," AGARD-CP-351, *Viscous Effects in Turbomachines*, June 1–3, 1983, Reference 24.

6 Dring, R. P., "Blockage in Axial Compressors," ASME JOURNAL OF ENGINEERING FOR GAS TURBINES AND POWER, Vol. 106, No. 3, July 1984, pp. 712–714.

7 Wagner, J. H., Dring, R. P., and Joslyn, H. D., "Inlet Boundary Layer Effects in an Axial Compressor Rotor, Part I: Blade-to-Blade Effects," ASME JOURNAL OF ENGINEERING FOR GAS TURBINES AND POWER, Vol. 107, No. 2, Apr. 1985, pp. 374–380.

8 Adkins, G. G., and Smith, L. H., "Spanwise Mixing in Axial Flow Turbomachines," ASME JOURNAL OF ENGINEERING FOR POWER, Vol. 104, No. 1, Jan. 1982, pp. 97–110.

9 Denton, J. D., and Usui, S., "Use of a Tracer Gas Technique to Study Mixing in a Low Speed Turbine," ASME Gas Turbine Conference, Paper No. 81-GT-86, 1981.

10 Moore, J., and Smith, B. L., "Flow in a Turbine Cascade—Part 2: Measurement of Flow Trajectories by Ethylene Detection," ASME Gas Turbine Conference, Paper No. 83-GT-69, 1983.

11 Moore, J., and Smith, B. L., AGARD Conference Proceedings No. 195 on Through-Flow Calculations in Axial Turbomachinery, 47th Meeting of AGARD/PEP, AGARD-CP-195, May 20–21, 1976.

12 Horlock, J. H., Louis, J. F., Percival, P. M. E., and Lakshminarayana, B., "Wall Stall in Compressor Cascades," ASME *Journal of Basic Engineering*, Vol. 88, Sept. 1966, pp. 637–648.

13 Moore, R. W., and Richardson, D. L., "Skewed Boundary Layer Flow Near the Endwalls of a Compressor Cascade," ASME *Transactions*, Vol. 79, Nov. 1957.

Compressor Rotor Aerodynamics," ASME JOURNAL OF ENGINEERING FOR POWER, Vol. 104, No. 1, Jan. 1982, pp. 84–96.

3 Dring, R. P., "Boundary Layer Transition and Separation on a Compressor Rotor Airfoil," ASME JOURNAL OF ENGINEERING FOR POWER, Vol. 104, No. 1, Jan. 1982, pp. 251–253.

4 Wagner, J. H., Dring, R. P., and Joslyn, H. D., "Axial Compressor Middle Stage Secondary Flow Study," NASA Contract No. NAS3-23517, NASA Contractor Report 3701, July 1983.

5 Dring, R. P., Joslyn, H. D., and Wagner, J. H., "Compressor Rotor Aerodynamics," AGARD-CP-351, *Viscous Effects in Turbomachines*, June 1–3, 1983, Reference 24.

6 Dring, R. P., "Blockage in Axial Compressors," ASME JOURNAL OF ENGINEERING FOR GAS TURBINES AND POWER, Vol. 106, No. 3, July 1984, pp. 712–714.

7 Wagner, J. H., Dring, R. P., and Joslyn, H. D., "Inlet Boundary Layer Effects in an Axial Compressor Rotor, Part I: Blade-to-Blade Effects," ASME JOURNAL OF ENGINEERING FOR GAS TURBINES AND POWER, Vol. 107, No. 2, Apr. 1985, pp. 374–380.

8 Adkins, G. G., and Smith, L. H., "Spanwise Mixing in Axial Flow Turbomachines," ASME JOURNAL OF ENGINEERING FOR POWER, Vol. 104, No. 1, Jan. 1982, pp. 97–110.

9 Denton, J. D., and Usui, S., "Use of a Tracer Gas Technique to Study Mixing in a Low Speed Turbine," ASME Gas Turbine Conference, Paper No. 81-GT-86, 1981.

10 Moore, J., and Smith, B. L., "Flow in a Turbine Cascade—Part 2: Measurement of Flow Trajectories by Ethylene Detection," ASME Gas Turbine Conference, Paper No. 83-GT-69, 1983.

11 Moore, J., and Smith, B. L., AGARD Conference Proceedings No. 195 on Through-Flow Calculations in Axial Turbomachinery, 47th Meeting of AGARD/PEP, AGARD-CP-195, May 20–21, 1976.

12 Horlock, J. H., Louis, J. F., Percival, P. M. E., and Lakshminarayana, B., "Wall Stall in Compressor Cascades," ASME *Journal of Basic Engineering*, Vol. 88, Sept. 1966, pp. 637–648.

13 Moore, R. W., and Richardson, D. L., "Skewed Boundary Layer Flow Near the Endwalls of a Compressor Cascade," ASME *Transactions*, Vol. 79, Nov. 1957.

DISCUSSION

N. A. Cumpsty[1]

In discussing a paper by Joslyn and Dring [14] I queried the appropriateness of studying a compressor with extensive regions of stall – may I ask again why so much effort is being put into the study of another apparently bad compressor? On the abovementioned paper [1] it was the stator at fault, now it seems to be the rotor – what are we to conclude? Is it the case that this compressor is designed according to Pratt and Whitney practice? Are we to assume that most compressors contain large stall patches but the instrumentation has been hitherto inadequate to spot them? This seems unlikely and it seems unlikely that performance is at its best with such large regions of stall. Would the authors care to comment on this.

References

14 Joslyn, H. D., and Dring, R. P., "Axial Compressor Stator Aerodynamics," ASME JOURNAL OF ENGINEERING FOR GAS TURBINES AND POWER, Vol. 107, No. 2, Apr. 1985, pp. 485–493.

[1] Whittle Laboratory, Cambridge University, Cambridge, U.K.

Authors' Closure

The authors share Mr. Cumpsty's concern over the occurrence of corner stall in typical compressor designs. Without the kind of detailed investigations and large-scale facilities as in the present work and in [15] the presence of large patches of corner stall could quite possibly go undetected. For this reason, the authors would like to solicit input to the literature from other researchers in order to provoke dialog on the occurrence of corner stall.

References

15 Wisler, D. C., "Loss Reduction in Axial Flow Compressors Through Low-Speed Model Testing," ASME JOURNAL OF ENGINEERING FOR GAS TURBINES AND POWER, Vol. 107, No. 2, Apr. 1985, pp. 354–363.

Surface Static Pressures in an Inlet Vortex Flow Field

W. Liu

E. M. Greitzer

C. S. Tan

Department of Aeronautics and Astronautics,
Massachusetts Institute of Technology,
Cambridge, Mass. 02139

An experimental investigation of the three-dimensional flow field associated with an inlet vortex is reported. The specific configuration investigated is an inlet, in proximity to a ground plane, in crosswind. Parametric data are presented to define the regimes of vortex formation in this configuration, as a function of inlet height to diameter ratio and inlet velocity ratio. The detailed static pressure distribution on the inlet is given for two quite different flow regimes, one with a strong inlet vortex and one with no inlet vortex. These new quantitative data are supplemented by flow visualization studies that allow an estimate to be made of the circulation around the inlet vortex. It is argued that the static pressure distributions in both cases can be clearly interpreted using the basic ideas of inlet vortex formation that were previously developed from (qualitative) water tunnel studies.

Introduction

When the inlet of a gas turbine engine, pump, or other device that creates a significant mass flow into the inlet, is situated near a surface, a strong vortex is often observed to form. This "inlet vortex" (or ground vortex as it is sometimes called) stretches from the surface into the inlet and can cause effects ranging from blade erosion due to dirt ingestion [1], to compressor surge [2].

A recent study of this phenomenon has shown that there are two fundamentally different mechanisms that are associated with the formation of this vortex [3]. The first of these, which has been recognized in a qualitative manner for some time, is the amplification of ambient vorticity, i.e., vorticity created "far upstream," due to the flow into the inlet. Calculations of the three-dimensional flow about an inlet near a ground plane showed that ambient *vertical* vorticity was concentrated in the region of the stagnation streamline from the ground surface into the inlet. The calculation procedure is described in [3] which also includes a description of flow visualization experiments that showed results in accord with these calculations.

The second mechanism, however, which had *not* been previously recognized, does not depend on the presence of ambient vorticity, nor even on the existence of a ground boundary layer. Due to this second mechanism, an inlet vortex can occur in a flow that is *upstream irrotational*, for an inlet in crosswind. In this situation, the inlet vortex will be accompanied by a variation in circulation (round the inlet) along the length of the inlet, and hence a trailing votex as well. Figure 1, which is taken from [3], shows a *schematic* of the location of the vortex lines for this inlet vortex/trailing vortex system. The circulation of the inlet and trailing vortex are roughly equal in magnitude but opposite in sign, since there is essentially no circulation round the inlet at a station far from the lip [3].

Although not indicated in the figure, it should be noted that the dimensions of the (cores of the) inlet and trailing vortices are quite different. The former is set by a balance between diffusion and convection, while the latter appears to be set by the size of the rotational region in the rear of the inlet, i.e., by the scale of the separated region on the leeward side of the inlet, which is on the order of the inlet diameter. In the present experiment, the characteristic dimensions are roughly 0.02 m and 0.3 m, respectively, i.e., more than an order of magnitude different.

Another important aspect of the phenomenon is that the flow regimes that are encountered depend on the ratio of inlet velocity to "ambient" or far upstream velocity, denoted by V_i/V_∞. For high values of this quantity (greater than fifteen,

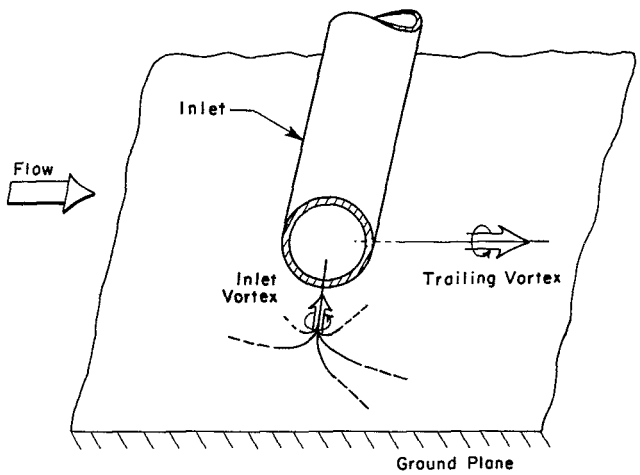

Fig. 1 Sketch of vortex lines associated with an inlet in crosswind in irrotational stream flow

Contributed by the Gas Turbine Division of THE AMERICAN SOCIETY OF MECHANICAL ENGINEERS and presented at the 29th International Gas Turbine Conference and Exhibit, Amsterdam, The Netherlands, June 4-7, 1984. Manuscript received at ASME Headquarters, January 18, 1984. Paper No. 84-GT-201.

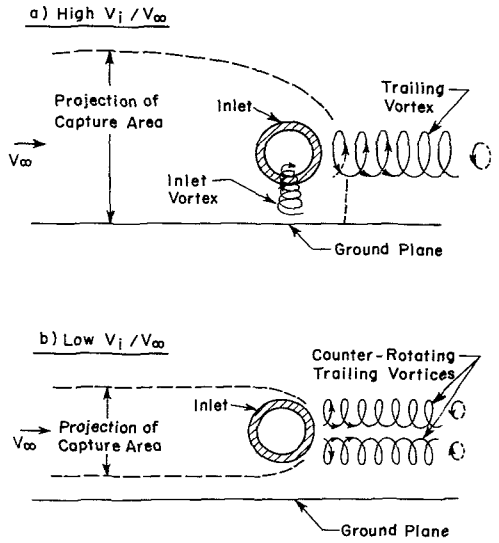

Fig. 2 Flow patterns at "high" and "low" values of velocity ratio, V_i/V_∞

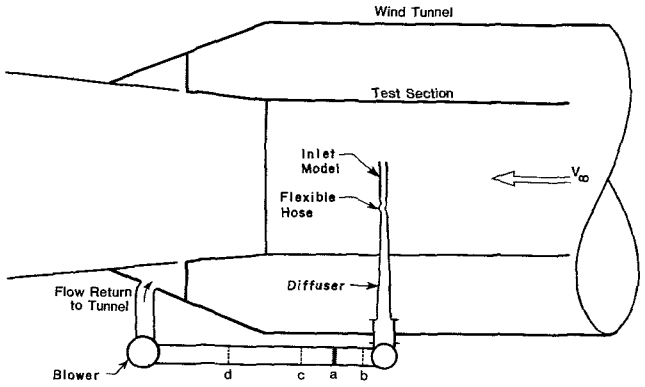

Fig. 3 Layout of blower/ducting configuration in wind tunnel (top view), inlet model setup for crosswind (90 deg of yaw) experiments; stations a, b, c, refer to honeycomb or screen flow straightener locations; d is screen used for flow measurement

say, for a typical aircraft engine configuration) an inlet vortex/trailing vortex system is formed, as described above and illustrated in Fig. 2(*a*). For lower values, however, a quite different picture is obtained with two *counterrotating* vortices trailing from the rear of the inlet, as shown in Fig. 2(*b*). Note that Figs. 2(*a*) and 2(*b*) have been drawn from the extensive observations of flow visualization experiments reported in [3]. These two different flow regimes are mentioned here, since the overall picture of the flow that they show will be helpful in the interpretation of the static pressure measurements presented below.

Both of the mechanisms of inlet vortex formation were described in detail in [3], which presented an experimental and theoretical study of inlet vortex formation and which also summarized the salient results in the existing literature on this topic. The experiments, however, were carried out in a water tunnel using hydrogen bubble flow visualization and were restricted to results of a *qualitative* nature. In particular, no *quantitative* data could be obtained on the magnitude of the velocity and pressure distributions round the inlet, nor on the strength of the vortex and the variations in circulation round the inlet. This paper thus presents the first detailed quantitative measurements of the three-dimensional flow associated with the inlet vortex. The measurements are confined to the case of an inlet in cross wind and therefore focus on the "second mechanism," which is less well understood. It will be shown that from these static pressure measurements one can infer a flow field model that is consistent with the flow seen in the water channel experiments. In addition, although the circulation was not measured directly, a rough estimate is made for the strength of the inlet vortex, based on this model.

Experimental Facility

Overall Facility Considerations. The experiments were designed to simulate an aircraft engine in near static operation in proximity to a ground plane. They were carried out in the MIT Wright Brothers Wind Tunnel. This is a closed circuit tunnel, with an elliptical test section 3.05 m in width, 2.30 m in height, and 4.6 m in length. A ground plane 2.4 m wide at a height of 0.5 m from the bottom was used in the present series of tests, giving a test section area of approximately 4.7 m^2.

The criteria for the inlet design were as follows: In simulating the actual situation, the ratio of inlet volume flow to tunnel volume flow should be much less than unity. In addition, the maximum velocity ratio (inlet velocity/ambient wind velocity) was selected (somewhat arbitrarily) to be at least 25, since this ratio must be high for vortex formation [4, 5]. For a fixed tunnel size, these criteria drive one towards a small inlet. However, the size of the inner diameter of the inlet, D, should be large enough for good resolution of the flow field inside the inlet, since the velocity field at the location of the engine face is a very important part of the problem. This dimension was therefore set at 0.15 m, giving a ratio of test section area to inlet area of approximately 240. With a 25:1 velocity ratio, this means that the maximum flow through the inlet is approximately 10 percent of the tunnel mass flow. The flow through the inlet was induced by a centrifugal fan (three stages of backward leaning blades), which was connected to the inlet with appropriate ducting. The inlet velocity and the "ambient wind" velocity could thus be controlled separately.

Due to the swirling three-dimensional flow in the inlet, under the conditions of interest in this study, the inlet mass flow was metered at a location far downstream in the ducting [6]. A layout of the inlet and ducting configuration used is shown in Fig. 3, which gives the location of the flow measurement station as well. In the configuration indicated, the experiment is set up with the inlet at 90 deg to the ambient flow (i.e., at crosswind); however, the inlet can also be placed at other angles of yaw down to zero, analogous to the conditions investigated in the water channel [3]. The maximum inlet velocity that could be obtained was approximately 120 m/s (depending on the precise orientation of the inlet and the connections used) and thus the flow can be considered incompressible for the work reported herein. Further details of the experimental facility are given in [6].

Nomenclature

C_P = static pressure coefficient, $(C_P = (P-P_{ref})/(P_t - P_{ref}))$
d = diameter of "trip wire" on inlet surface
D = inner diameter of inlet
H = inlet centerline height above ground
P = static pressure
P_{ref} = reference tunnel static pressure
P_t = total pressure
V_e = local freestream velocity around cylinder
V_i = inlet throat velocity (average)
V_∞ = ambient (far upstream) velocity
Γ = circulation
ν = kinematic viscosity

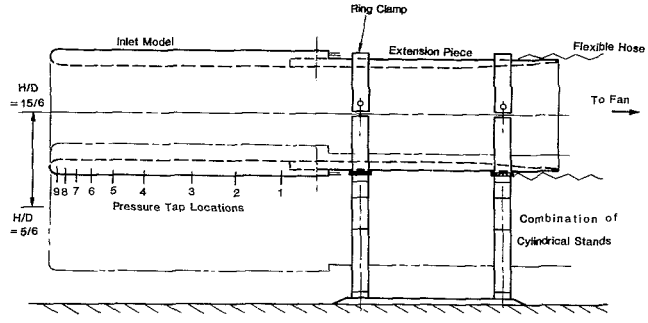

Fig. 4 Inlet model supports: numbers refer to axial locations of static pressure taps

Inlet Model. The inlet model used was a circular cylinder, with no centerbody. It was designed so that no lip separation would occur over the parameter range of interest. The design method used was the semi-empirical criterion of Boles and Stockman [7], which is based on the diffusion ratio (defined here as the ratio of the peak velocity on the inlet lip to the velocity at a station in the inlet two diameters downstream of the lip). From data on STOL inlets, it was found that diffusion ratios lower than 2.4 gave attached flow around the inlet lip at Mach numbers comparable with those in the present experiment. This diffusion ratio was calculated for different geometries using a higher-order panel method potential flow code designed for propulsion system inlets [8]. After screening several geometries, it was found that an acceptable inlet could be derived using elliptical segments, with a ratio of outer to inner diameter of 1.25. Details of the procedure, as well as of other aspects of the experiment design are also given in [6].

Two inlet models were constructed, one of plexiglass, which was used for flow visualization, and the other of aluminum, which was employed for quantitative measurements. This latter had an array of 36 static pressure taps on the outside surface, in addition to 4 on the inner surface. The taps, each 1.02 mm in dia, are arranged in four axial rows, 90 deg apart. As shown in Fig. 4, they are unequally spaced, being more heavily clustered in the region of the inlet lip. The pressure taps are connected, through tubing buried in aluminum, epoxy-filled channels in the outer surface, to a Scanivalve/pressure transducer data acquisition system. By rotating the inlet about its axis, a detailed map of the circumferential and axial distribution of the pressure can be obtained.

The inlet support system, also shown in Fig. 4, allows the ratio of the height of the inlet centerline to the inlet diameter, H/D, to be varied from 0.83 to 2.5; this covers the range of primary interest. In addition, although not shown, a fairing made of a thin walled plexiglass cylinder, with outer diameter the same as the inlet, is used around the extension piece to enclose the pressure lines leading from inlet to the pressure transducer.

Experimental Procedures and Preliminary Tests

Flow Regimes. Prior to the inlet vortex experiments, the aluminum model was put through some preliminary tests in the wind tunnel. It was found that the static pressure readings were not repeatable when the cylinder was rotated, and the measured static pressure coefficients (C_P) were more than a factor of two different than C_P distributions reported in the literature for the supercritical flow round a cylinder in a uniform stream [9, 10]. (Potential flow arguments suggest, and the data confirm, that with no net flow through the inlet, the flow round the inlet at distances more than roughly a diameter from the lip should be similar to that round a two-dimensional cylinder.)

At the range of Reynolds numbers used in the tests (4×10^4 to 1.6×10^5) one would indeed expect that the flow over the outside of the inlet would be near transition between subcritical and supercritical regimes [11] and thus that the pressure distribution would be sensitive to small irregularities on the surface. (In this regard, it is interesting to note that some of the flow visualization experiments carried out on the outer surface of the inlet showed surface flow patterns that were quite similar to those found in the study of a circular cylinder in the transition regime [11].) This point was further supported when, with the inlet at a height of 2.5 D, the tunnel velocity was raised to 22 m/s (Reynolds number = 3×10^5). At this value of Reynolds number the C_p distribution was close to the result given in [9] or [10] for supercritical flow round cylinders.

Since actual inlets are an order of magnitude larger than the model and actual ambient velocities are roughly the same as those used in the experiments, the Reynolds numbers encountered in practice are an order of magnitude larger than those which can be attained in the experiments. To obtain similar flow regimes between model and actual situation, as well as to eliminate the dependence on the local details of the surface roughness, it was thus desirable to operate the inlet in the supercritical regime. To do this, it was necessary to add a "trip" to the surface. Methods are described in the literature for doing this [12, 13], and several were tried. Of these, it was found that a "trip wire," as suggested in [12] gave the best results. For the range of tunnel speeds used, 3 to 6 m/s, using the relation $V_e d/\nu = 800$, as given in [12], a wire of $d = 2.3$ mm was chosen. The wire is attached to two rings which are embedded flush on the surface near the two ends of the inlet model. These can be rotated so that the trip wires remain always at the same orientation (plus and minus 67 deg) to the oncoming flow.

Flow Visualization Techniques. Three methods of flow visualization were used in the experiment: a surface flow technique, smoke, and tuft grids. The first of these, which has recently been developed by Langston and Boyle [14] uses the flow of ink as an indicator to record the limiting streamlines. A matrix of ink dots (from a "permanent" type marker) was laid out on a sheet of 0.076-mm mylar drafting material. A thin layer of oil of wintergreen (methyl salicylate) was sprayed, from an atomizer, evenly over the paper. The tunnel was then turned on. The wintergreen acts as a solvent to the ink, and, if gravitational forces do not have a significant component in the plane of the sheet, the latter flows in response to shear forces.

This prepared sheet was placed either on the floor below the lip of the inlet to trace the ground vortex, or wrapped around the inlet body to reveal the surface pattern. The tunnel was run for a time on the order of several minutes. After the flow over the mylar sheet showed no further changes in ink location it was removed and allowed to dry, so that the ink trace was permanently left on the mylar. An additional feature of this technique is that (low velocity) areas, where the dye does not flow very rapidly, can be resprayed in order to better define the limiting streamlines in these regions.

Wind Tunnel Flow Quality. The quality of flow in the Wright Brothers Wind Tunnel was also examined. It was found that the thickness of the ground boundary layer at the location under the inlet, i.e., δ, was approximately 0.08 m. However, this is an order of magnitude less than the characteristic dimension of the capture stream-tube area at the conditions of interest. (The latter dimension scales as $D\sqrt{V_i/V_\infty}$. For the conditions at which the static pressure measurements were taken with the "strong vortex," this is greater than 0.6 m.) In addition, based on the results reported in [3], the precise value of the ground boundary-layer

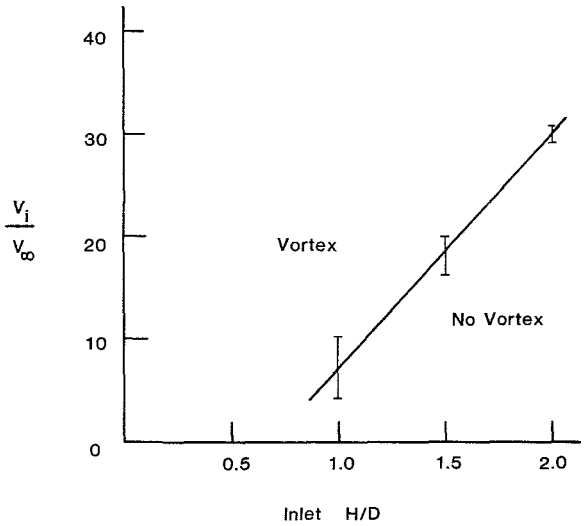

Fig. 5 Regimes of vortex formation

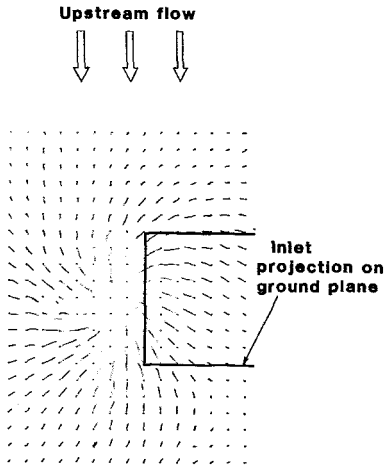

Fig. 6 Skin friction lines (on ground surface) showing inlet vortex

thickness (or, in fact, whether or not there *is* a ground boundary layer) should not have a significant effect on the phenomena described below.

Although the flow in the wind tunnel was "nominally" irrotational, a slight background swirl was measured in the test section, due presumably to the tunnel fan. However the rotation associated with this background swirl had the *opposite sense* to that in the inlet vortex. It is thus to be emphasized that the former is definitely *not* the cause of the latter. As pointed out in [3], the mechanism of inlet vortex formation is rather due to the inherently three-dimensional flow associated with an inlet/ground plane configuration in crosswind.

Results

Parametric Study of Vortex Formation. Tests were carried out using smoke visualization to determine the ratios of V_i/V_∞ at which an inlet vortex would form. The tests were run at values of H/D of 1.0, 1.5, and 2.0. The results are shown in Fig. 5. The "error bars" in the figures mark the estimated uncertainty associated with the data. The vortex observed has a sense of rotation in the clockwise direction looking into the inlet, consistent with that found in [3]. Near the vortex/no-vortex boundary, the inlet vortex is quite unsteady, and occasionally even changes direction of rotation briefly. This is suspected to be due to the (small) ambient swirl in the tunnel, which is comprised of vorticity of the opposite sense to that associated with the inlet vortex.

The results shown were obtained using the trip wire. Without the wire, it was found that although the C_P is much altered, the transition point for the various H/D does not change appreciably, and within the uncertainty of the smoke flow observations (roughly plus or minus ten percent) the onset of vortex formation is not affected by the trip wire.

Qualitative Study of the Trailing Vortex. The trailing vortex was also examined using smoke flow visualization. This vortex was seen to trail from roughly the three o'clock position at the lip (looking into the inlet). At a tunnel velocity of 3 m/s, a value of H/D of 1.5, and a velocity ratio of $V_i/V_\infty = 33$, the locus of the vortex lies on a line at about 15 deg to the axis of the tunnel, with a counterclockwise sense of rotation (as defined looking upstream). The sense of rotation could be clearly seen by placing a tuft grid downstream of the inlet.

The angle of drift (in the lateral direction) of the trailing vortex enables us to estimate the strength of its circulation. Using a simple (two-dimensional) image vortex system, one can readily demonstrate that the vortex should indeed move to the right[1] as it drifts downstream. The angle of drift of the vortex is set by the ratio of the velocity with which the vortex is convected downstream and the induced velocity with which it moves across the tunnel (due to the field of its image).

Within the context of this description, the lateral velocity of the vortex is given by

$$V_{\text{lateral}} = \Gamma/4\pi H \tag{1}$$

where Γ is the circulation round the vortex and where the center of the vortex is taken to be at the centerline of the inlet. The angle of drift is therefore approximately

$$\text{Drift angle} = \Gamma/(4\pi H V_\infty) \tag{2}$$

for small drift angles.

If we substitute the experimental values of drift angle, H, and V_∞, we find that for the conditions cited the nondimensional value of the circulation, Γ/DV_∞, is found to be approximately 5. This can be regarded as an estimate for the circulation round the trailing vortex, and hence round the inlet vortex also, for a situation that is characteristic of an actual aircraft engine at static or near static conditions.

It is to be noted that the choice of the length D in the nondimensionalization is somewhat arbitrary. Nondimensionalization can also be done using the height, H, as well, i.e., Γ/HV_∞. The choice made here is based on characterizing the magnitude of the circulation compared to that round a body of characteristic dimension D (i.e., chord for an airfoil, diameter for a cylinder, etc.). It should be emphasized that whichever the nondimensional length used, the nondimensional circulation will be a strong function of the parameters H/D and V_i/V_∞.

Surface Flow Visualization. Surface flow patterns were obtained using the wintergreen/ink spot technique. This was applied to mylar sheets placed on the ground underneath the inlet, as well as wrapped around the inlet. A result of doing the former is shown in Fig. 6, in which the projection of the inlet and the oncoming flow direction are also shown. The spiral pattern associated with the vortex can be clearly seen.

Static Pressure Distribution on Inlet. The static pressure coefficient C_P (defined as $C_P = (P-P_{\text{ref}})/(P_t-P_{\text{ref}})$) has been obtained for a value of $H/D = 1.0$ for two different situations: one in which no inlet vortex existed and one in which a strong vortex was present. Due to an apparent drift in the tunnel flow conditions at low flows, this latter could not be done at the very high velocity ratio used for the flow

[1] As defined looking upstream.

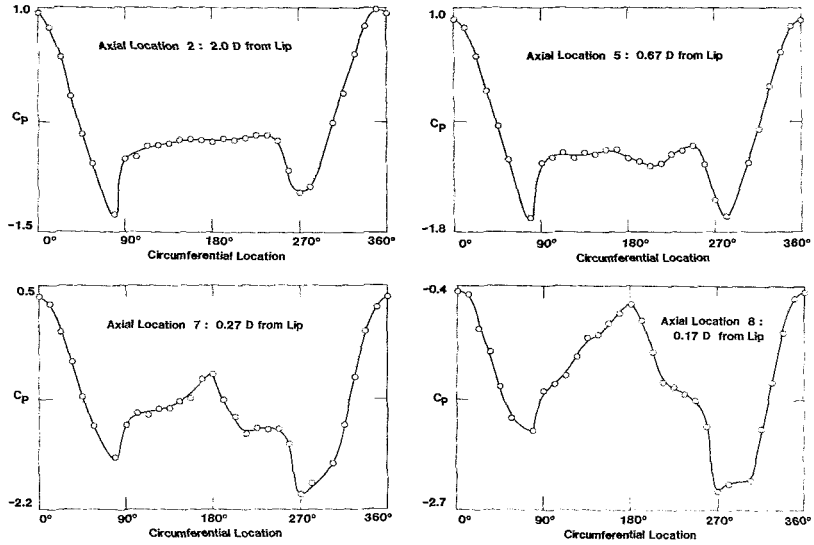

Fig. 7 Static pressure distributions on inlet with no inlet vortex present (low V_i/V_∞). Note that individual curves have different scales.

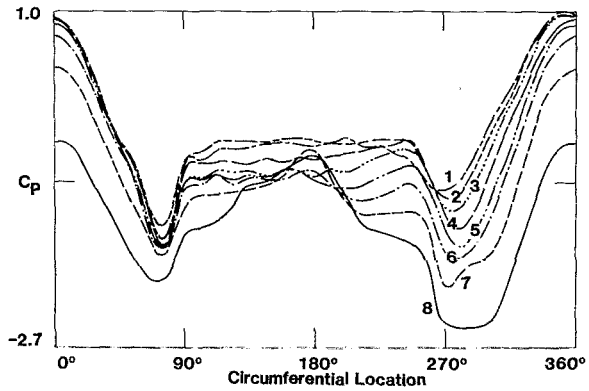

Fig. 8 Composite plot of static pressure distribution on inlet with no vortex present (low V_i/V_∞)

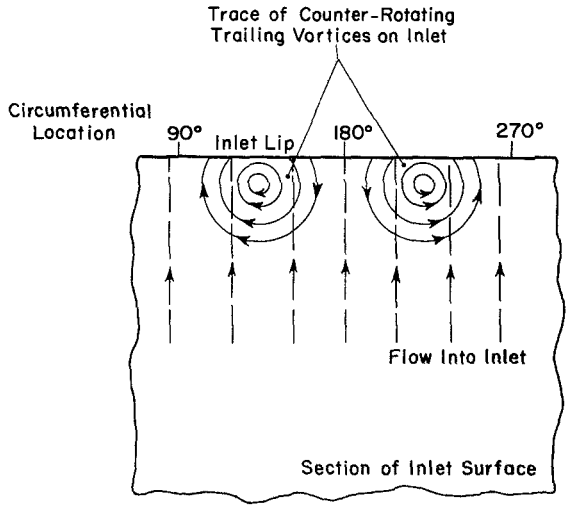

Fig. 9 Conceptual model for interaction (on inlet surface) of counterrotating trailing vortices and flow into inlet

visualization; however, the velocity ratio used was quite high enough for a strong vortex to be formed.

No Inlet Vortex ("Low" Values of V_i/V_∞). When the velocity ratio (capture ratio) was low, no inlet vortex is present. The features of this type of flow can be seen in Figs. 7 and 8, which show the C_P distribution for a value of $V_i/V_\infty = 4$. In the figures, the value of C_P versus the circumferential location is shown. The convention used is that zero degrees is the "leading edge," i.e., the upstream location on the cylinder. The angles vary in a clockwise manner looking *into* the inlet, so that 90 deg is on top, 180 deg is at the rear, and 270 deg is at the bottom. (The axial locations of the static pressure taps, along the inlet, are shown to scale in Fig. 4.)

Note that in Fig. 7, to show the details at each axial location, the different graphs are plotted on different scales, owing to the different ranges in C_p that are obtained along the inlet. (This will be even more evident in the high V_i/V_∞ case discussed below.) However, in the composite plot, Fig. 8, which shows eight axial locations, all curves are drawn to the same scale.

The plot in the upper left of Fig. 7 shows the static pressure distribution at a location 2.0 (inner) dia from the lip. There is some asymmetry due to the proximity to the ground, but the main features of the profile are similar to those of the flow round a two-dimensional cylinder. (This was also true at the 2.5 D station.)

For axial stations from 2.0 dia to 0.67 dia from the lip (stations 2 to 6) the static pressure distributions are not greatly dissimilar. As one approaches closer to the lip, however, the flow becomes much more three-dimensional. At station 7, one can see the formation of a *peak* in the static pressure distribution at the 180 deg location. This peak increases as one moves further toward the lip, as shown in the data from station 8, which is 0.17 dia from the lip. Both of these plots show a *low velocity region near the 180 deg location*. (This is also seen in Fig. 8.)

A conceptual flow field model can be developed to explain this type of static pressure distribution. At the most basic level, we can regard the overall flow as being composed of a general sink-type flow into the inlet, with (as shown in Fig. 2(*b*)) two counterrotating trailing vortices superposed on it. From the flow visualization studies in [3], the scale of the vortical region for each of these vortices was approximately half the inlet diameter, so that we can suppose that the two trailing vortices are centered at roughly 135 and 225 deg locations, i.e., somewhere in the middle between the 180 deg location and the top and bottom of the inlet, respectively.

A *sketch* of the streamlines of such a composite flow, on the unwrapped rear of the inlet (from 90 to 270 deg) is shown in Fig. 9. The solid lines show the streamlines associated with the

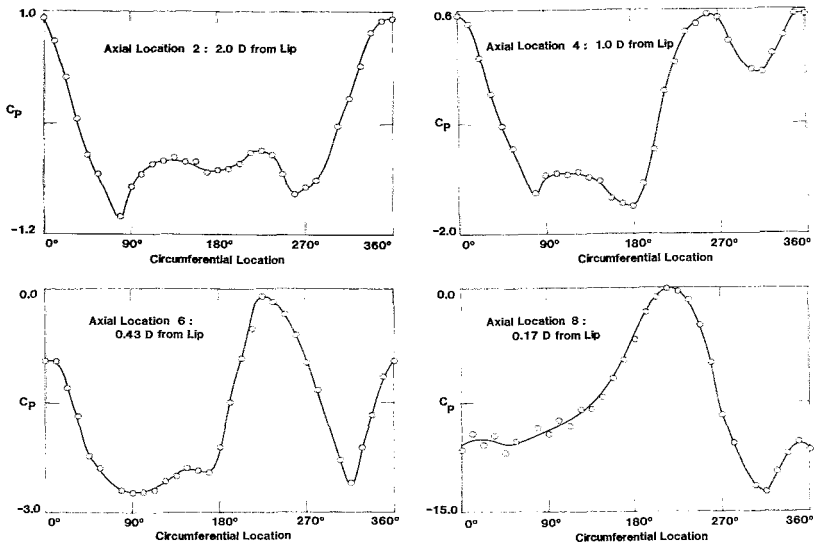

Fig. 10 Static pressure distribution on inlet with strong vortex present (high V_i/V_∞). Note that the individual curves have different scales.

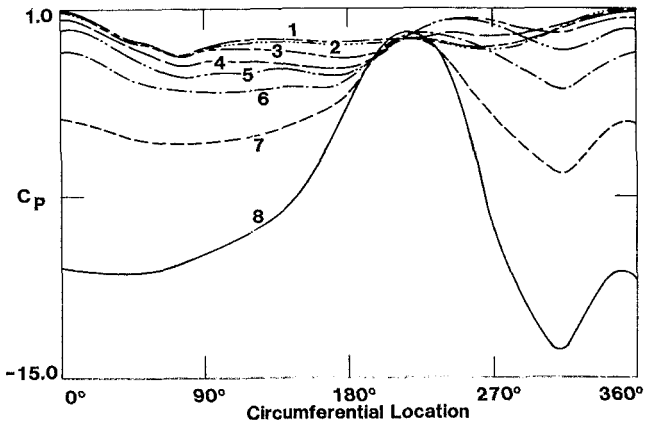

Fig. 11 Composite plot of static pressure distribution on inlet with strong vortex present (high V_i/V_∞)

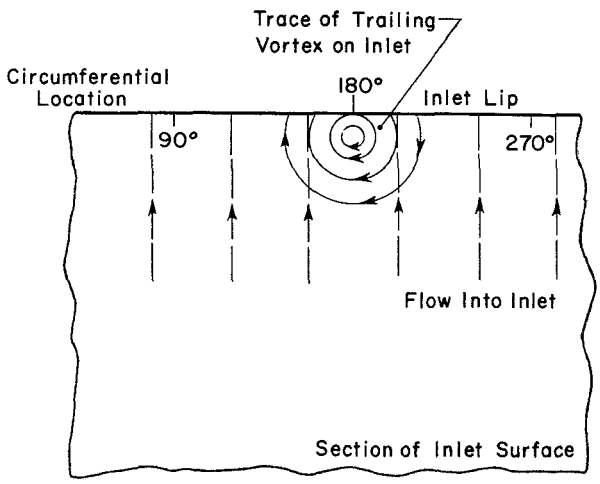

Fig. 12 Conceptual model for interaction (on inlet surface) of trailing vortex and flow into inlet at high V_i/V_∞

trailing vortices, and the dashed lines show those associated with the overall flow into the inlet; for simplicity, the latter are shown as straight lines, although it is recognized that they are not really so in actuality.

It can be seen that this type of pattern will create a low velocity (i.e., high static pressure) between the pair of trailing vortices, and a high velocity (i.e., low static pressure) region on the outer side of the pair. The C_p distribution would thus be expected to show a peak near 180 deg and two troughs somewhere near the top and bottom of the inlet.

This type of behavior is indeed clearly exhibited in the data from stations 7 and 8, which are shown in Fig. 7. The conceptual model is thus in accord with observed results. (The asymmetry between the top and bottom is due to the presence of the ground plane and can perhaps be regarded as a vestige of the much stronger asymmetry that will be seen to exist at high values of velocity ratio.)

Strong Vortex ("High" Values of V_i/V_∞). When the velocity ratio (capture ratio) was large, a strong vortex is formed. The inlet surface static pressure distribution in this case is shown in Figs. 10 and 11, where plots of the circumferential C_P distribution at different locations along the inlet are presented for a situation with strong vortex at a $V_i/V_\infty = 17$. As previously discussed, at locations far from the inlet lip, the C_P distribution has a form similar to that for a two-dimensional cylinder near a ground plane.

Due to the strong inflow, however, the region which is non-two-dimensional is considerably larger than in the no-vortex situation. As shown in Fig. 10, at a location 1 dia from the lip, there is substantial alteration from the profile at 2 dia, and as one approaches closer to the lip the distribution changes markedly. Specifically, a region of high static pressure appears at the lower rear of the inlet; this can be seen to be at roughly 260 deg at axial location 4, at 1.0 dia from the lip. For axial locations closer to the lip, the C_p plots show a peak in static pressure at the 210 deg location, indicating a region of low velocity there, as shown in the data from stations at 0.43 and 0.17 dia from the lip. (Again, the plots in Fig. 10 are not to the same scale, in order to show more detail.)

The C_p data for all eight locations are shown in Fig. 11 (these *are* all to the same scale), and it can be seen that there is a large variation from station 1 to station 8, with a strong top-to-bottom asymmetry in the regions near the inlet lip.

The basic structure of the inlet vortex/trailing vortex flow field which was provided by the flow visualization in [3] is also of use in developing a conceptual flow model to understand the observed static pressure distributions. This leads us again to regard the velocity distribution as due to the interaction of the trailing vortex and the flow into the inlet, as *sketched* in Fig. 12. From the flow visualization, it was found that, at the capture ratios that characterize a strong inlet

vortex, the center of this trailing vortex is near the lip at roughly the 180 deg location. Based on this, the figure shows an unwrapped view of the rear of the inlet (from 90 to 270 deg). The dashed lines again indicate the streamlines associated with the overall flow into the inlet, regarded as roughly axisymmetric, and represented for simplicity as straight. The solid lines show the streamlines that would be induced by the trailing vortex. It can be seen that this superposition of the two velocity fields creates velocity magnitudes which are low near the 210 deg location, and thus results in a high static pressure at this location.

Although this picture appears to explain the central feature of Fig. 10, the high static pressure near 210 deg, it does not explain why there is a localized low pressure region near 300 deg. In order to understand this latter feature, it is important to realize that the *inlet vortex* (which is at the 270 deg location) also has an influence on the velocity field.

Accounting for the respective signs of the circulation of the inlet and trailing vortex, the latter will reinforce the velocity field of the former near the 210 deg location, and this may account for the fact that the velocity at this location is quite low. Near 300 deg, however, which is close to the inlet vortex, (and far from the trailing vortex) the velocity induced by the inlet vortex is the same direction as the overall flow into the inlet, and it is this more localized effect which is thought to be evidenced in Fig. 10. The picture in the figure in fact appears to be one of a "one lobed" variation on which is imposed a much more localized variation due to the inlet vortex. The general features of the pressure distribution thus do appear to be qualitatively explained using this simple model of the inlet vortex/trailing vortex system.

Comparison of the results of the no vortex and strong vortex cases shows that as V_i/V_∞ increases, the region of low velocity near the lip is displaced clockwise. We view this as denoting *a shift of the lower trailing vortex to become the inlet vortex* accompanied with some downward motion of the upper trailing vortex as well. We hope to examine this evolution from two trailing vortices to one (trailing vortex) in the future.

Finally, we can note that the C_p distribution provides only a limited description of the complex flow field associated with the inlet vortex. Pressure distributions, however, could be used in connection with potential flow calculation procedures to gain some additional insight into the overall flow field. In particular, one may be able to use this information to determine the circulation round the inlet (hence the strength of the inlet vortex) since this is nonunique within the framework of a potential flow calculation. It is also clear that it is critical to measure the circulation round the inlet vortex, since this is an important parameter in determining the overall flow field.

Summary and Conclusions

A study has been conducted of the flow field associated with the inlet vortex. The conditions that mark the boundary between vortex/no vortex situations have been defined for an inlet at 90 deg of yaw, in a nominally irrotational free stream, at various height to diameter ratios. Smoke flow visualization was employed to show this transition. The trailing vortex of the inlet vortex system has also been studied qualitatively with smoke visualization. The static pressure distribution round the inlet model was measured for situations with a strong vortex and with no vortex present. The results for a flow with no inlet vortex show a pressure distribution which can be explained as due to the presence of two counterrotating trailing vortices. The results for a flow with a strong vortex show a high-pressure (low-velocity) region that appears to be due to the interaction of the trailing vortex/inlet vortex system with the overall flow into the inlet. Both of these pressure distributions are in accord with the basic flow field structure obtained from previous water channel studies [3].

Acknowledgments

The authors wish to acknowledge the helpful suggestions of E. E. Covert, F. H. Durgin, and P. Lorber concerning various aspects of the experimental program, the comments of M. Landahl concerning possible calculation procedures, and the assistance of Mr. Tang Guo-Cai in obtaining some of the measurements. This work was supported under Air Force Office of Scientific Research Contract F49620-82-K-0002, Dr. J. D. Wilson, Program Manager.

References

1 Younghans, J. L., and Paul, D. L., "Considerations in Inlet/Engine Integration," ch. 13 in *The Aerothermodynamics of Aircraft Gas Turbine Engines*, edited by G. C. Oates, AFAPL-TR-78-52, Air Force Aero Propulsion Laboratory, 1978.

2 Motycka, D. L., "Ground Vortex-Limit to Engine/Reverser Operation," ASME JOURNAL OF ENGINEERING FOR POWER, Vol. 98, 1976, pp. 258–266.

3 De Siervi, F., et al., "Mechanisms of Inlet Vortex Formation," *Journal of Fluid Mechanics*, Vol. 124, 1982, pp. 173–207.

4 Glenny, D. E., "Ingestion of Debris into Intakes by Vortex Action," Min. of Tech., Aero. Research Council CP 1114, 1970.

5 Motycka, D. L., Walter, W. A., and Muller, G. L., "An Analytical and Experimental Study of Inlet Ground Vortices," AIAA Paper 73-1313, 1973.

6 Liu, W., "Design and Analysis of an Experimental Facility for Inlet Vortex Investigation," M.I.T. Gas Turbine and Plasma Dynamics Laboratory Report 166, 1982.

7 Boles, M. A., and Stockman, N. O., "Use of Experimental Separation Limits in the Theoretical Design of V/STOL Inlets," AIAA Paper No. 77-878, 1977.

8 Stockman, N. O., and Farrell, C. A., "Improved Computer Programs for Calculating Potential Flow in Propulsion System Inlets," NASA TM-73728, 1977.

9 Hoerner, S. F., *Fluid-Dynamic Drag*, published by the author, 1965.

10 Roshko, A., "Experiments on the Flow Past a Circular Cylinder at Very High Reynolds Numbers," *Journal of Fluid Mechanics*, Vol. 10, 1961, pp. 345–356.

11 Humphreys, J. S., "On a Circular Cylinder in a Steady Wind at Transition Reynolds Numbers," *Journal of Fluid Mechanics*, Vol. 9, 1960, pp. 603–612.

12 Cebeci, T., and Bradshaw, P., *Momentum Transfer in Boundary Layers*, McGraw-Hill, New York, 1977.

13 Guven, O., Farrell, C., and Patel, V. C., "Surface Roughness Effects on the Mean Flow Past a Circular Cylinder," *Journal of Fluid Mechanics*, Vol. 98, pp. 673–701.

14 Langston, L. S., and Boyle, M. T., "A New Surface Streamline Flow Visualization Technique," *Journal of Fluid Mechanics*, Vol. 125, 1982, pp. 53–57.

Flutter of Swept Fan Blades

R. E. Kielb

K. R. V. Kaza

National Aeronautics and Space Administration,
Lewis Research Center,
Cleveland, Ohio 44135

The purpose of the research presented in this paper is to study the effect of sweep on fan blade flutter by applying the analytical methods developed for aeroelastic analysis of advanced turboprops. Two methods are used. The first method utilizes an approximate structural model in which the blade is represented by a swept, nonuniform beam. The second method utilizes a finite element technique to conduct modal flutter analysis. For both methods, the unsteady aerodynamic loads are calculated using two-dimensional cascade theories that are modified to account for sweep. An advanced fan stage is analyzed with 0, 15, and 30 deg of sweep. It is shown that sweep has a beneficial effect on predominantly torsional flutter and a detrimental effect on predominantly bending flutter. This detrimental effect is shown to be significantly destabilizing for 30 deg of sweep.

Introduction

A research program to develop advanced turboprops (or propfans) is currently being conducted at the NASA Lewis Research Center. As shown in Fig. 1, the blades being considered are of complex sweep, including substantial, nonuniform sweep. The primary reasons for using thin, swept airfoils are to reduce acoustic noise and to increase efficiency during high subsonic (M = .8) flight conditions. A possibly detrimental effect of sweep is on flutter. The research program at NASA has included aeroelastic experiments and development of analytical methods for predicting flutter of swept, rotating blades. For a description of some of these experiments and the analytical methods see [1–4].

It is expected that the use of advanced, swept fan blades in turbofan engines would also result in similar improvements in efficiency and noise as in advanced turboprops. However, it is not known whether it is possible to design practical, swept fan blades that have adequate flutter margin. Since the analytical methods developed for the advanced turboprop blades include unsteady cascade aerodynamic effects, they are also applicable to fan blades of turbofan engines. The purpose of the research presented in this paper is to conduct an initial study of the effect of sweep on fan blade flutter by applying the analytical methods developed for aeroelastic analysis of advanced turboprops.

Whereas a practical swept fan blade is likely to have a curved elastic axis (the locus of section shear centers), similar to the shape shown in Fig. 1, the initial parametric studies reported herein are of swept blades with straight elastic axes. This assumption simplifies the structural analysis by removing the effect of curvature. However, future research must consider additional parametric studies of the actual configurations that are likely to be used. Some effects to be studied are elastic axis-c. g. placement, transonic and three-dimensional aerodynamics, and cascade-sweep interaction.

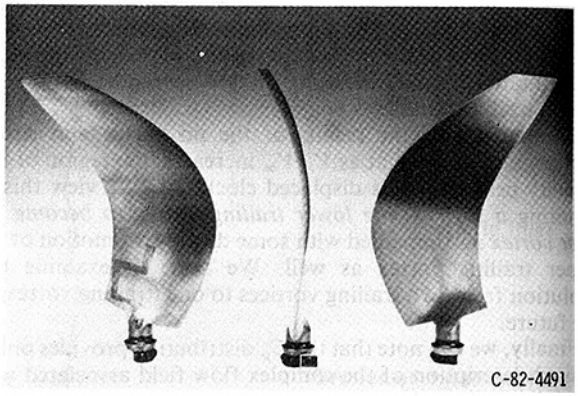

Fig. 1 Advanced turboprop shape

Theory

Two analytical methods are used in this study. The first one [1, 5] utilizes an approximate structural model in which the blade is represented by a swept, nonuniform beam (the beam must have a straight elastic axis). As previously mentioned, practical swept fan blades are likely to have curved elastic axes. Therefore, this method can only be used to study parametric trends (which is the purpose of this paper).

The second method [2, 3, 6] is an extension to the well-known finite element program NASTRAN to include cascade effects in the flutter analysis of swept blades. This method is capable of modelling blades of complex configuration, including sweep, curved elastic axis, and can also consider structural coupling between blades.

For both methods, the unsteady aerodynamic loads are calculated using two-dimensional cascade theories which are modified to account for sweep. The techniques used to account for sweep differ between the two methods and are described below. It must be mentioned that the actual flow field is complicated by three-dimensional and transonic effects, especially at the tip region. Cascade unsteady aerodynamic models, including these effects, are currently under development and are not presently available. The authors are currently conducting research in this area which will be reported in future publications. The three-dimensional

Contributed by the Gas Turbine Division of THE AMERICAN SOCIETY OF MECHANICAL ENGINEERS and presented at the 29th International Gas Turbine Conference and Exhibit, Amsterdam, The Netherlands, June 4–7, 1984. Manuscript received at ASME Headquarters January 9, 1984. Paper No. 84-GT-138.

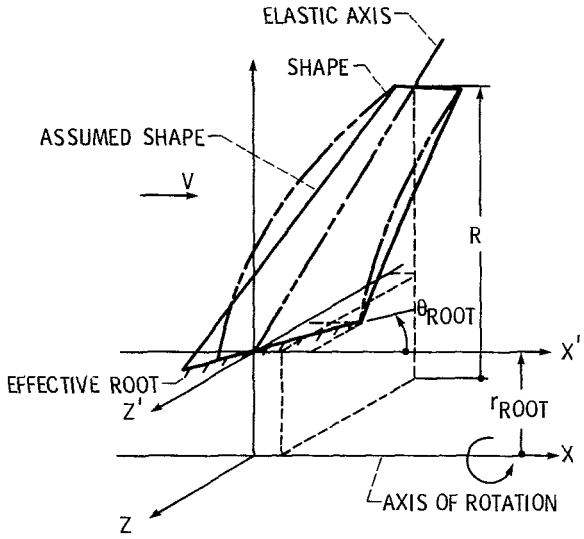

Fig. 2 Structural model-beam method

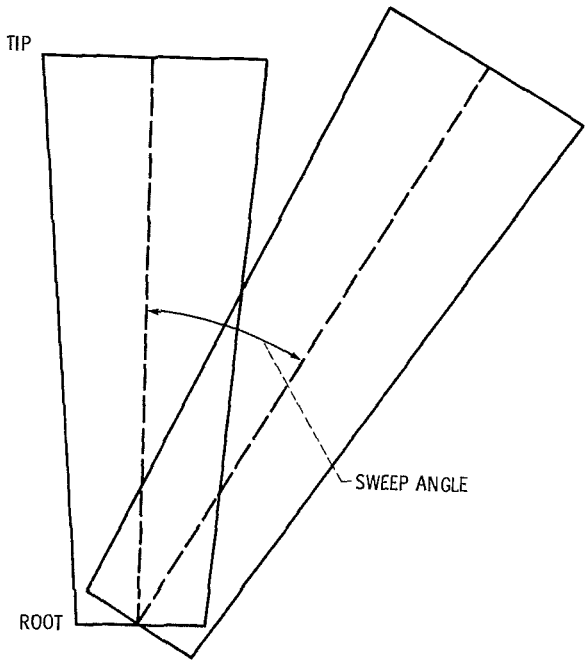

Fig. 3 Blade planforms, swept and unswept

effects are expected to be less significant for swept turbofans than for advanced turboprops because of the presence of the duct.

Beam Method. The details of the derivation of the beam method for unswept blades are given in [5]. This method was developed for pretwisted, nonuniform blades by using Hamilton's principle. The derivation of the equations has its basis in the geometric nonlinear theory of elasticity in which elongations and shears are negligible compared to unity. A general expression for foreshortening (axial shortening of the tension axis due to bending, torsion, and noncoincidence of the elastic and tension axes) is explicitly used in the formulation. This method for unswept blades was modified in an approximate manner to account for blade sweep. For simplicity, it was assumed that, although the blades are swept, the elastic axis is straight (see Fig. 2). Only the component of centrifugal load along the blade axis is considered. Also, for the flutter problem, the blade is assumed to be vibrating about its undeformed position. The use of these assumptions can

Table 1 Blade physical and material properties

Number of blades	28
Hub radius, m	0.3876
Tip radius, m	1.021
Material density, kg/m^3	4374.
Air density, kg/m^3	1.
Speed of sound, m/s	340.3
Modulus of elasticity, N/m^2	1.23×10^{11}
Shear modulus, N/m^2	4.744×10^{10}

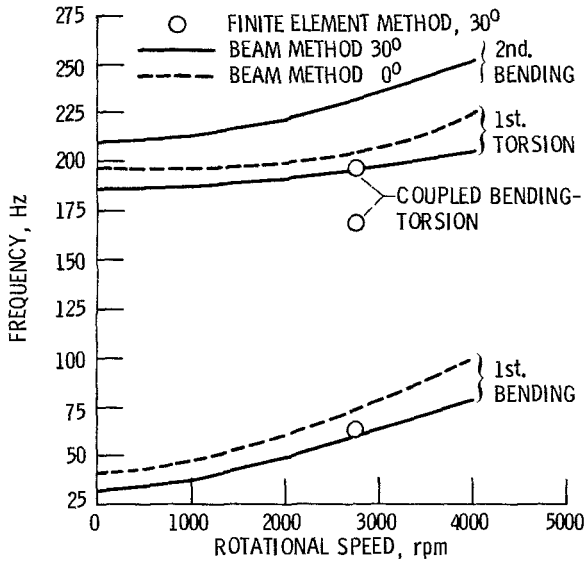

Fig. 4 Campbell diagram

result in significant errors in the prediction of higher mode flutter characteristics. For example, it is known that proper consideration of the steady-state displacements can cause the pure torsion mode (nonrotating) to change into a lower frequency, highly coupled bending-torsion mode. This modified version of the method used in [5] also has the capability to consider blade mistuning, but this is not considered herein.

Both subsonic [7] and supersonic [8] two-dimensional unsteady cascade aerodynamic theories are used. The assumed relative flow is the component normal to the elastic axes. The chord and stagger angle are also defined for sections normal to the elastic axis. The lift and moment are integrated in a stripwise manner to give a quasi-three-dimensional effect. These aerodynamic loads are corrected for sweep effects by using similarity laws. This method, used in [9, 10] for an isolated, nonrotating, swept wing, involves modification of the two-dimensional lift and moment expressions for an unswept wing. The spanwise component of flow is neglected and similarities in the vertical velocity boundary conditions for swept and unswept wings are utilized.

The space variable in the resulting coupled integro-partial differential equations of motion is eliminated by using a modified Galerkin's method. The trial functions are the uniform beam mode shapes. For all results presented in this paper two modes were used for each of three types of motion: bending in the plane of rotation, bending perpendicular to the plane of rotation, and torsion. The assumption of simple harmonic motion results in a generalized eigenvalue problem that is iteratively solved to determine the flutter boundary. Further descriptions of this analytical method can be found in [1, 5].

Finite Element Method. The detailed description of this method is given in [2, 3, 6]. For the reader's convenience a brief description follows. The method consists of three steps: (*i*) a "differential stiffness" matrix is determined from the

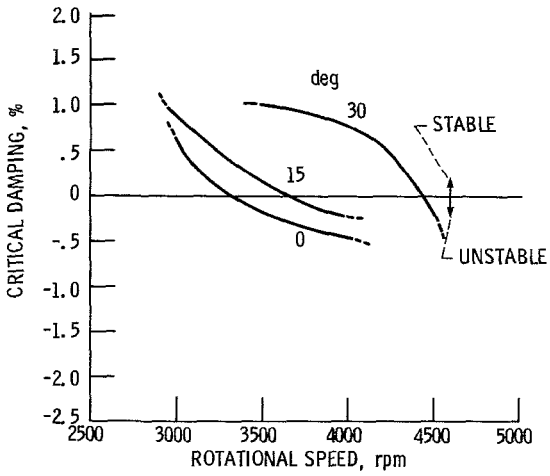

Fig. 5 Torsion mode damping, M = 0.43

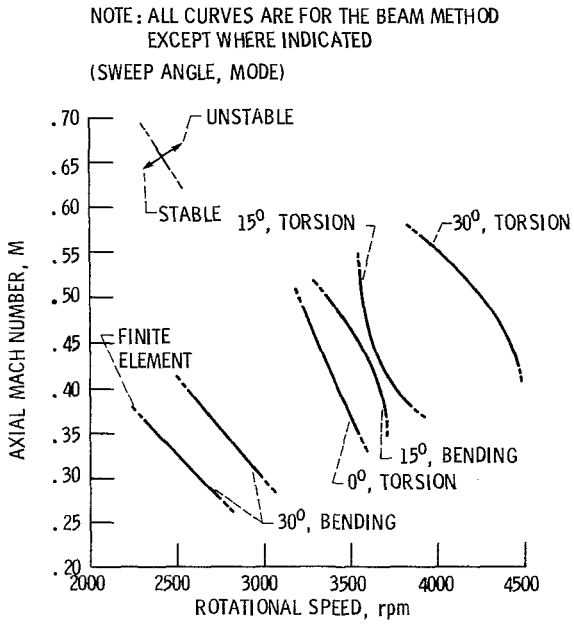

Fig. 6 Flutter boundaries

steady-state solution (by considering both centrifugal and steady aerodynamic loads and by using a Newton-Raphson iteration to determine the equilibrium position); (*ii*) by using the additional stiffness from step (*i*), a free vibration analysis is performed to determine the modal characteristics; and (*iii*) a modal flutter analysis is performed.

The two-dimensional, subsonic, cascade theory described in [11] is used to calculate the unsteady aerodynamic loads. The theories of [7] and [11] are closely related and give similar results. A supersonic aerodynamic theory including sweep effects has yet to be incorporated into this method. The subsonic unsteady aerodynamic loads are modified to account for sweep effects by considering only the component of flow normal to the local leading edge. Although this method can include steady aerodynamic loads, they are not considered herein.

In general, a blade is a surface with multiple curvature. The method to form the aerodynamic forces for such a surface is as follows. For each station a "mean surface" is constructed between chord lines (which are normal to the leading edge and not parallel to each other) for this station and the adjacent spanwise locations (inboard and outboard). The modal translations normal to this surface are then used to construct the generalized aerodynamic force matrix.

As in the beam method, a complex generalized eigenvalue problem results. The flutter boundary is determined by repeated use of the "KE-Method" [12] for different axial Mach numbers and rotational speeds. Since this computer code presently lacks supersonic unsteady aerodynamics, the relative flow Mach number (perpendicular to the local leading edge) at all stations must be less than one. This restricts the operating conditions at which this method can be used.

Results and Discussion

The baseline fan stage used for these studies is the same unswept, unshrouded advanced fan stage that was considered in [5]. This stage has 28 blades, a .38 hub-to-tip ratio, and an aspect ratio (length/hub chord) of 3.3 (unswept). The physical and material properties for the blade are listed in Table 2. In the studies to follow, the blade is modified to include a constant sweep angle while keeping the inner and outer radii constant (i.e., a constant annular flow area). Thus the swept blade is longer. In addition, the chord (defined in a direction normal to the elastic axis direction) and stagger angle have the same radial distribution as the baseline blade.

The parametric studies described in this paper are for the cases of 0, 15, and 30 deg sweep. Figure 3 shows the planform of the blade for 0 and 30 deg sweep. Because the inner and outer radii are constant, the elastic axis of the blade lengthens with increased sweep. This causes the blade natural frequencies to decrease with sweep. In [5], the unswept version of this baseline blade was studied and was found to encounter flutter in a predominantly torsion mode. In the following discussion, the modes are classified as either bending or torsion. The aeroelastic modes are actually coupled bending-torsion modes. However, for the blade considered herein, there is only weak aerodynamic coupling between the bending and torsion modes. To aid in understanding the flutter behavior, flutter boundaries will be shown for each mode even though only the most critical is of practical interest.

Beam Analysis. The section properties of the unswept blade were given in [5]. As mentioned, the swept blade is similar to the unswept one, except in length. Therefore, the section properties in planes normal to the elastic axis are the same as those listed in [5]. The blade lengths (measured along the elastic axis) are .63, .66, and .73 m for the 0, 15, and 30 deg sweep cases, respectively.

The blades were first analyzed without aerodynamic loads to find the natural frequencies of the various swept configurations. Figure 4 shows the dependence of frequency on rotational speed for 0 and 30 deg sweep. As expected, the frequency of the bending modes increases with rotational speed more than the torsional modes, and the longer, 30-deg, swept blades have lower frequencies.

The unsteady aerodynamic loads were added to investigate the flutter characteristics. In [5], it was predicted that the unswept blade would encounter torsional flutter at an axial Mach number of .43 and a rotational speed of 3330 rpm. With M = .43, the rotor speed was varied and the aerodynamic damping (percent of critical) of both the torsional and bending modes was calculated. The results for the torsional mode are shown in Fig. 5. As can be seen, sweep tends to stabilize the torsional mode. The use of 15 deg of sweep is equivalent to adding approximately .3 percent critical damping and increases the flutter rotational speed by approximately 10 percent. The use of 30 deg of sweep has a stronger effect. At 3330 rpm (the unswept blade flutter point), the added equivalent damping is approximately 1 percent. The flutter rotational speed is increased over that of the unswept blade by

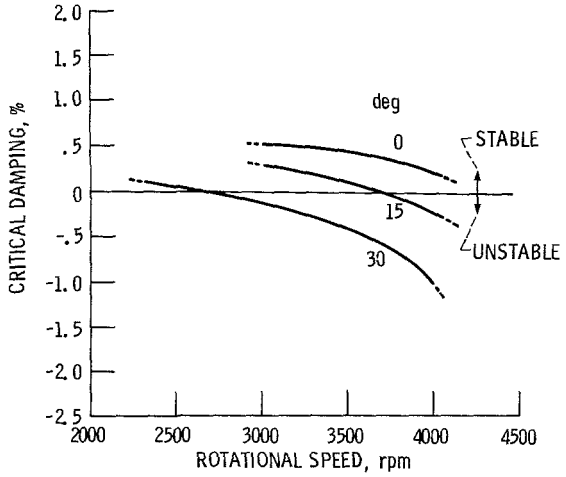

Fig. 7 Bending mode damping, M = .43

more than 30 percent. The stability calculations were repeated for other axial Mach numbers, and the flutter boundaries are summarized in Fig. 6. It is seen that increasing sweep always has a beneficial effect on the torsion mode. As mentioned, this method is questionable for this mode because of the possible errors in frequency and mode shape. Finally, it should be mentioned that the critical interblade phase angle for the torsion mode was always 77.14 deg (a 6-nodal-dia forward travelling wave).

Since the blade is pretwisted, the first bending mode of this blade is "coupled bending-bending" involving motion both in and out of the plane of rotation. It was shown in [5] that the unswept blade would not flutter in this first bending mode. The axial Mach number was fixed at .43, and the damping was predicted for a range of rotational speeds. The results, given in Fig. 7, show that, in contrast to the previous results for the torsion mode, sweep has a detrimental effect on bending mode flutter. For 15 deg of sweep the blade is predicted to flutter at 3630 rpm. At this rpm the effect of sweep is equivalent to reducing the damping by .35 percent. For 30 deg of sweep the detrimental effect is greater. The flutter rotational speed is further reduced to 2500 rpm. The stability calculations were repeated for other axial Mach numbers and the flutter boundaries, along with the torsion flutter boundaries, are shown in Fig. 6. Comparing flutter boundaries for 15 and 30 deg sweep shows the severely detrimental effect of sweep on bending flutter.

Unlike for torsion, the critical interblade phase angle for the bending modes varied with sweep, Mach number, and rotational speed. Also in contrast to the torsion mode, the critical interblade phase angle always represented a backward traveling wave. The critical interblade phase angles for the bending modes are always in the range -25.7 to -90.0 deg (2- and 7-nodal-dia backward travelling waves).

A comparison of the bending and torsion modes in Fig. 6 shows that for 15 deg of sweep, the two flutter boundaries are close together and in the stabilized direction (higher rotational speed and/or Mach number) compared to the boundary for the unswept blade. This is an overall improvement in the flutter boundary. This is not the case for 30 deg of sweep, where the torsion mode is greatly stabilized, but the bending mode is destabilized to such an extent that it lies well to the left of the unswept blade boundary. This represents an overall degradation of the blade's flutter behavior. In summary, for the three sweep angles considered, the 15 deg blade is a slight improvement over the unswept blade, and the 30 deg blade is significantly less stable.

The results described above for the bending modes are

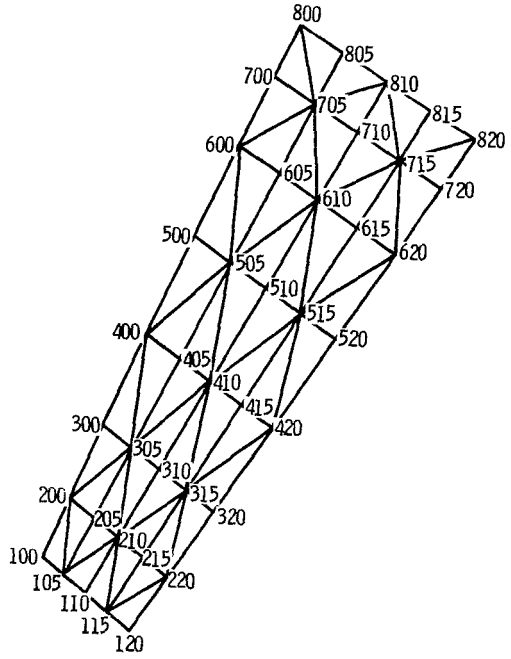

Fig. 8 Finite element model

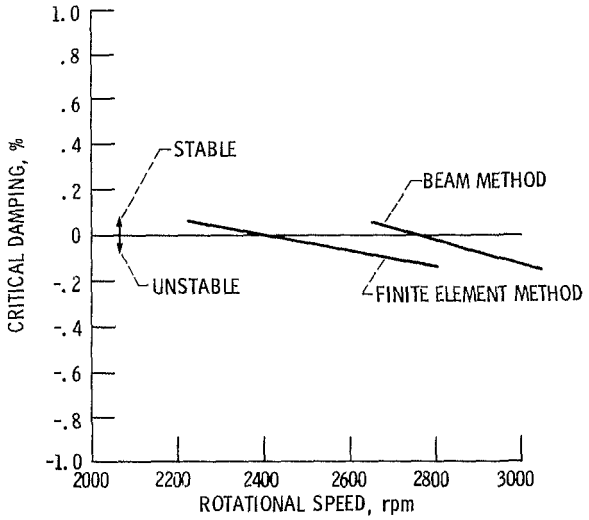

Fig. 9 First bending mode damping, M = 0.35

qualitatively in agreement with those of [13], in which the effects of sweep on fixed wing flutter are presented. In [13], it is shown that the additional coupling terms between the aerodynamic loads and displacements [8, 9] provide the mechanism to permit pure bending flutter. It appears likely that this same mechanism is the primary cause of the significant destabilizing effect on the bending modes shown herein.

Finite Element Analysis. The model, shown in Fig. 8, consisted of 40 nodes, 56 elements, and 193 active degrees of freedom. This mesh density is known to be inadequate for detailed stress information but adequate for natural frequency and the associated modal flutter analyses. The well-known CTRIA2 elements, which also have been shown to be adequate for predicting the first few natural frequencies and mode shapes of plates with moderate twist, were used [14].

The natural frequencies and mode shapes were calculated and compared with the beam analysis. The predicted frequencies at 2750 rpm are compared with the beam method results in Fig. 4. There is good agreement with the first mode

and poor agreement with the higher. This was expected since the beam analysis is questionable for low aspect ratio, platelike blades and can include the effects of steady-state displacements only approximately.

As mentioned, this method is currently limited to relative Mach numbers (normal to the local leading edge) less than 1. Therefore, high axial Mach numbers or rotational speeds cannot be currently considered. Because of the relatively low Mach number and rotational speed predicted above for the onset of flutter in the bending mode, attention is focused on bending flutter of the blade with 30 deg sweep. The axial Mach number was fixed at .35 and the rotational speed was varied. Figure 9 shows the damping versus rotational speed predicted by using the finite element method. For comparison the results are also shown for the beam method. There is fair agreement between the two methods for the first mode damping. The finite element method results are approximately .1 percent lower than those of the beam method. However, because of the relative insensitivity of damping to rotational speed, the difference in speed at which flutter will occur is more than 300 rpm. The higher modes were stable at these operating conditions and are not shown, however, it should be noted that the aerodynamic damping predictions of the two methods for the higher modes show poor agreement.

The finite element stability calculations were repeated at other operating conditions and the resulting flutter boundary is shown together with the beam results in Fig. 6. As can be seen, the first mode flutter boundary for the blade with 30 deg of sweep is similar to that of the beam method but is somewhat more unstable. Thus two independent methods predict that sweep has a significantly destabilizing effect on bending mode flutter. The finite element method cannot be presently used to predict torsion mode flutter for the 30 deg blade or for either mode of the 0 and 15 deg blade because of the restriction to subsonic relative flow.

Summary and Conclusions

The effect of sweep on fan blade flutter was studied by applying two analytical methods. An advanced fan stage was analyzed with 0, 15, and 30 deg of sweep. The major conclusions from this investigation are summarized as follows:

1 Sweep has a predominantly aerodynamic effect on fan blade flutter, which is beneficial for torsional modes and detrimental for bending modes.

2 The critical flutter mode is predominantly torsional for low sweep angles (less than 15 deg) and predominantly bending for high sweep angles.

3 With significant sweep (30 deg or more) the blades are significantly less stable than similar unswept blades.

4 The flutter modes are always found to be forward traveling waves for the torsional modes and backward traveling waves for the bending modes.

5 For the blade with 30 deg of sweep, there is fair agreement between the finite element and beam method damping predictions for the first mode and poor agreement for the higher modes.

References

1 Mehmed, O., et al., "Bending-Torsion Flutter of a Highly Swept Advanced Turboprop," NASA TM 82975, 1981.

2 Elchuri, V., and Smith, G. C. C., "NASTRAN Flutter Analysis of Advanced Turbopropellors," NASA CR 167926, Apr. 1982.

3 Elchuri, V., and Smith, G. C. C., "Flutter Analysis of Advanced Turbopropellors," *24th Structures, Structural Dynamics, and Materials Conference*, Pt. 2, Collection of Technical Papers, American Institute of Aeronautics and Astronautics, 1983, pp. 160–165.

4 Turnberg, J., "Classical Flutter Stability of Swept Propellors," 24th Structures, Structural Dynamics, and Materials Conference, AIAA Paper No. 83-0847, Lake Tahoe, Nevada, May 2–4, 1983.

5 Kaza, K. R. V., and Kielb, R. E., "Flutter of Turbofan Rotors with Mistuned Blades," *AIAA Journal*, Vol. 22, No. 11, Nov. 1984, pp. 1618–1625.

6 Smith, G. C. C., and Elchuri, V., "Aeroelastic and Dynamic Finite Element Analysis of a Bladed Shrouded Disc," D2536-941001, Textron Bell Aerospace Co., Buffalo, N.Y., Mar. 1980. NASA CR 159728.

7 Smith, S. N., "Discrete Frequency Sound Generation in Axial Flow Turbomachines," ARC-R&M-3709, British ARC, 1973.

8 Adamcyzk, J. J., and Goldstein, M. E., "Unsteady Flow in a Supersonic Cascade with a Subsonic Leading-Edge Locus," *AIAA Journal*, Vol. 16, No. 12, Dec. 1978, pp. 1248–1254.

9 Barmby, J. G., Cunningham, H. J., and Garrick, I. E., "Study of Effects of Sweep on the Flutter of Cantilever Wings," NACA TN 2121, 1950.

10 Bisplinghoff, R. L., Ashley, H., and Halfman, R., *Aeroelasticity*, Addison-Wesley, 1955.

11 Rao, B. M., and Jones, W. F., "Unsteady Airloads for a Cascade of Staggered Blades in Subsonic Flow," *Unsteady Phenomena in Turbomachinery*, AGARD-CP-177, Apr. 1976.

12 "The NASTRAN Theoretical Manual," NASA SP-221(06), 1981.

13 Cunningham, H. J., "Analysis of Pure-Bending Flutter of a Cantilever Swept Wing and Its Relation to Bending-Torsion Flutter," NACA TN 2461, 1951.

14 Kielb, R. E., Leissa, A. W., and MacBain, J. C., "Vibrations of Twisted Cantilever Plates—A Comparison of Theoretical Results," accepted for the *Int. Journal of Num. Meth. in Eng.*

A. V. Srinivasan
Manager.

D. G. Cutts
Research Engineer.

Applied Mechanics,
United Technologies
Research Center,
East Hartford, Conn. 06108

Aerodynamically Excited Vibrations of a Part-Span Shrouded Fan

The structural response of a part-span shrouded fan due to an aerodynamic excitation was measured using strain gages. The excitation was provided by means of a 4-lobed distortion screen mounted upstream of the rotor. Vibration measurements made with tuned and mistuned conditions at integral order speeds have been analyzed to determine the aeromechanical response charcteristics of the assembly. The results from the experimental investigation are presented and discussed.

Introduction

Vibration-induced fatigue failure of rotor blades is of continuing concern to the designer of aircraft engines. The emphasis on improved engine performance under the necessary constraints of minimum weight and satisfactory life requires that vibration levels in all rotor blades be kept low. Further, certain important design considerations of rotor blades require a thorough understanding of the aeromechanical characteristics of bladed disk assemblies. These design considerations include (*i*) blade life prediction that uses vibration amplitudes in its calculations, (*ii*) setting allowable frequency margins that need to be justified on the basis of the intensity of resonant stresses at integral order speeds, and (*iii*) prediction of susceptibility of the component to aeroelastic instabilities. Clearly, a successful design process depends on the reliability of the analyses that serve as the basis of design systems. Such reliability can be established only through a data base obtained through tests of components conducted under controlled environments.

An assembly of light and flexible blades with or without shrouds is prone to vibration in an operating environment. Periodically varying pressure fields from guide vanes, flow distortion due to struts or other upstream obstructions and unbalance of the rotor system are some of the principal sources of excitation that result in blade vibration response. Limiting the vibratory stresses to acceptable levels in a given design requires that the designer be able to calculate the dynamic characteristics of the assembly.

The calculation of vibratory characteristics of an assembly of blades usually relies on an important assumption; i.e., any one blade on the rotor is assumed to be identical in all respects to any other blade on the same rotor. Based on this assumption, the frequency response characteristics of a bladed disk assembly are computed. The results are used by designers to set resonant speed margins of rotors and also to determine blade flutter susceptibility. However, minor differences in

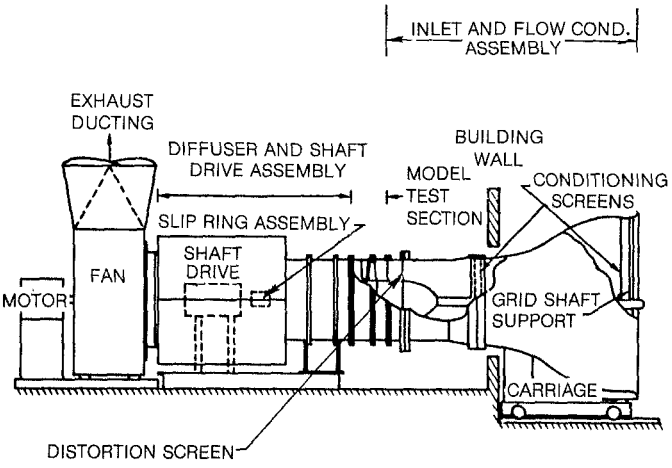

Fig. 1 The aerodynamic rig

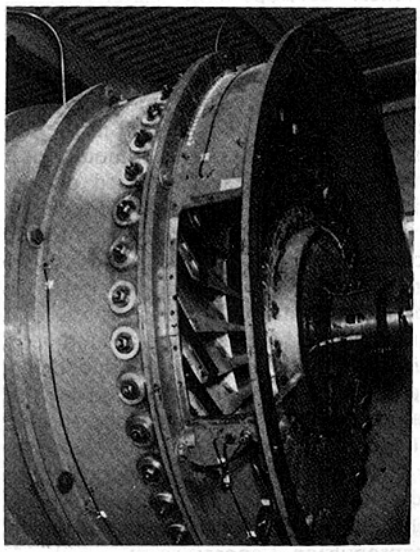

Fig. 2 Installation of the R-80 fan in the aerodynamic rig

Contributed by the Gas Turbine Division of THE AMERICAN SOCIETY OF MECHANICAL ENGINEERS and presented at the 29th International Gas Turbine Conference and Exhibit, Amsterdam, The Netherlands, June 4–7, 1984. Manuscript received at ASME Headquarters January 12, 1984. Paper No. 84-GT-172.

Table 1 Resonant frequencies for individual blades in uncoupled configuration as measured in rig B

BLADE NUMBER	1B MODE		1T MODE	
	MISTUNED	"TUNED"*	MISTUNED	"TUNED"*
	FREQUENCY-HZ	FREQUENCY-HZ	FREQUENCY-HZ	FREQUENCY-HZ
1	64.78		321.1	
2	63.53		304.7	
3	63.51		305.6	
4	65.88	63.30	322.1	311.5
5	64.09		314.9	
6	64.01		311.5	
7	64.52		315.9	
8	62.12	63.96	306.9	304.3
9	62.92		315.2	
10	64.14		303.6	
11	64.88		320.1	
12	65.29		311.4	
13	67.76	64.55	322.2	317.7
14	65.92	64.60	316.4	314.2
15	64.64		320.5	
16	65.66		315.1	
17	64.27		314.1	
18	64.88		322.2	
19	63.89		316.3	
20	64.83		309.8	
21	63.66		313.8	
22	63.48		303.8	
23	63.61		310.6	
24	67.39	63.57	320.6	315.2
25	63.21		316.1	
26	64.86		320.0	
27	64.85		318.5	
28	55.78	63.17	289.7	297.5
29	64.69		314.6	
30	63.69		319.5	
31	64.74		323.9	
32	67.74	64.50	319.6	314.7
33	66.66	63.40	318.1	315.9
34	(66.60)	62.90	(315)	320.5
35	64.62		318.1	
36	63.51		312.3	
37	64.59		306.4	
38	64.52		324.3	
39	64.31		318.9	
40	63.72		309.6	

*Results shown for modified blades only
( ) Estimated results

individual blade characteristics are inevitable, severe requirements on manufacturing tolerances notwithstanding. A phenomenon known as mistuning arises from scatter of vibrational characteristics such as, for example, a scatter in frequencies of individual blades mounted on the periphery of a rotor disk. Even a rotor with essentially no scatter in its blade frequencies develops some scatter due to nonuniform normal wear during service. Therefore, it is only the degree of mistuning that differs from one rotor to another.

For a tuned rotor, the distribution of vibratory amplitudes remains harmonic and the vibratory mode shape of the bladed-disk assembly can be described in the familiar nodal diameter/nodal circle pattern. The modes of a mistuned assembly may not exhibit such ordered patterns. The circumferential variation of vibratory amplitudes in a mistuned rotor may not bear any resemblance to a sinusoidal wave. The extent of change from an ideal, well-ordered set of modes to an arbitrary, irregular set of vibratory patterns depends upon a host of parameters, such as (*i*) extent of scatter in individual blade frequencies, (*ii*) blade location around periphery of the rotor, (*iii*) degree of mechanical and/or aerodynamic coupling, and (*iv*) mechanical damping present in the system and the nature of its distribution around the rotor due, for example, to nonuniform rubbing at shroud interfaces.

In order to obtain a data base that can serve to enhance the understanding of the mechanical and aeromechanical response characteristics of a part-span shrouded fan, the Air Force Aeropropulsion Laboratory at the Wright-Patterson Air Force Base sponsored a research effort at UTRC under Contract No. F33615-79-C-2054. Results obtained from the phase of the program in which the extremely small vibratory motions at shroud interfaces were measured have already been reported [1]. The scope of the program included (*a*) measurement of response characteristics of the fan, in vacuum, in its first and second family modes at several speeds up to 1200 rpm in both tuned and deliberately mistuned conditions, (*b*) measurement of the nature and extent of relative vibratory motion at shroud interfaces, and (*c*) characterization of the tuned and mistuned assembly in an aerodynamic environment in which the assembly is subjected to integral order, as well as nonintegral order vibration. In this paper, in the interest of space, only the integral order response measurements obtained under the influence of a 4-lobed flow-distortion screen are discussed.

The Aerodynamic Test Facility

The overall arrangement of the aerodynamic rig is shown in Fig. 1. Air enters the facility through a 12-ft-dia inlet with aluminum honeycomb inset into the face to remove crossflow effects. The inlet contracts, passing the flow through a series of fine mesh screens to reduce the turbulence level. A further contraction achieves the 5-ft o.d. of the test section. A distortion-generating section is installed upstream of the test section. The test section itself consists of an axial series of constant-diameter casings enclosing the rotor assembly and

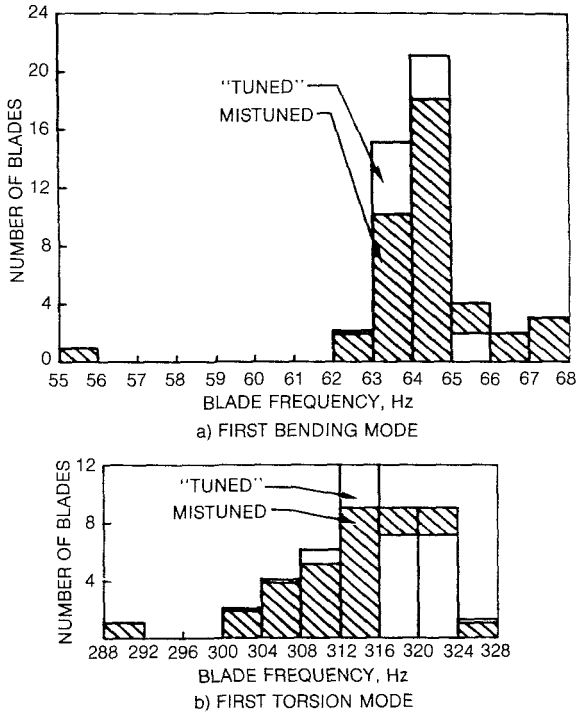

Fig. 3 Histograms of "blade-alone" modal frequencies for the "tuned" and mistuned assembly

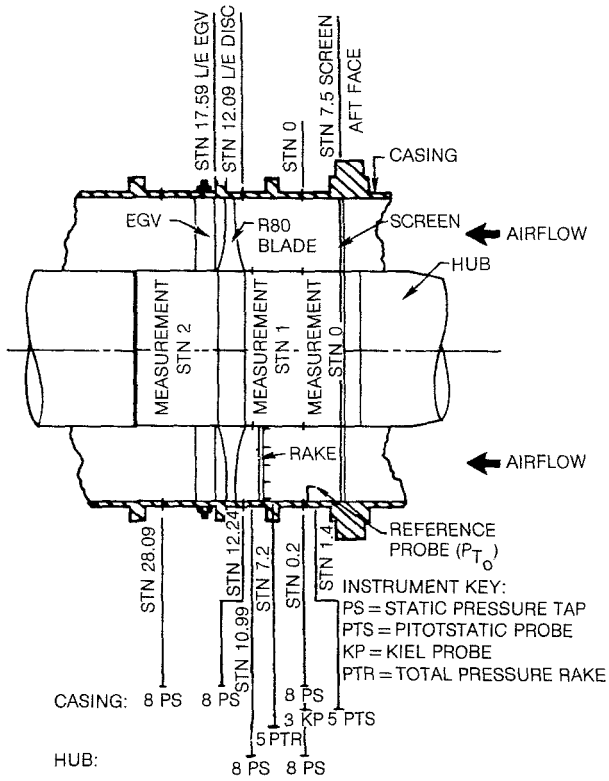

Fig. 4 Pressure instrumentation in test section

the exit guide vanes. The rotor is mounted on a drive-shaft cantilevered from two downstream bearings, providing a clean flow path to the model blading. The shaft is driven by a 200 hp d-c motor with a maximum speed of 1200 rpm and 0.1 percent accuracy on speed regulation. Downstream of the test section, the flow is decelerated by means of a dump diffuser before entering the inlet of a centrifugal fan that exhausts the air through the building roof. The fan is capable of a maximum static pressure rise of 25 in. of water and has a vortex valve mounted in its inlet face to control the axial flow rate. Axial velocities between 50 and 300 ft/s are possible with typical fan and compressor models. The rotating frame instrumentation is interfaced to stationary frame equipment through a 100-channel slip ring package mounted on the aft end of the rotor shaft.

The Test Component

The capabilities of the rig dictated the design goals for the bladed-disk assembly. Operating at 1200 rpm, the fan must develop a moderate to small pressure rise—less than 1 percent, and must have, in the speed range, modes of vibration in the first and second families that can respond under forced vibration. The final design resulted in a 60-in.-dia fan consisting of 40 blades. Each blade made of aluminum (AL6061T6) is 15 in. long with an aspect ratio of 2.5 (tip)–3.0 (root), with a part span shroud located at 47 percent span. The maximum thickness of the airfoil increases linearly towards the tip in order to bring the frequencies low enough to be excited within the speed range. The root attachment is a bolted dovetail arrangement with matching slots in a disk of 30 in. in diameter. To provide realistic loading at shroud and root interfaces, at 1200 rpm, a pretwist of 1 deg was built into the design so that on assembly, the shrouds would be loaded with about 180 lbs and the root was tightened using two axial bolts through the disk. A photograph of the assembly designated as the R-80 fan is shown, installed in the aerodynamic rig in Fig. 2.

To assess the degree of mistuning in the assembly tests were performed to measure the frequencies of the first bending

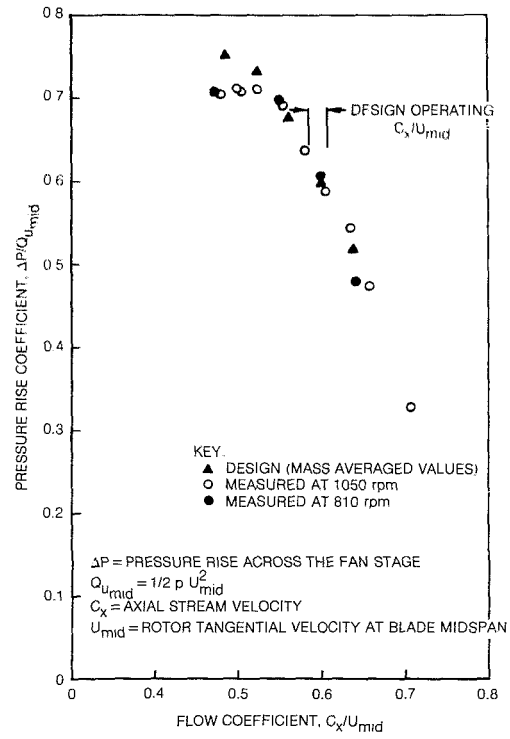

Fig. 5 R80 fan clean inlet speed line: comparison of measured values with design points

(1B) and the first torsion (1T) modes of individual blades assembled in the rotor. This was accomplished by detuning all but the test blade using lead weights, as shown in Fig. 2, and exciting the test blade with its drive crystal. The frequency at maximum response was taken as the resonant frequency. Tuning of the blades was accomplished by modifying the mass of the blade tips by drilling spanwise holes and filling with

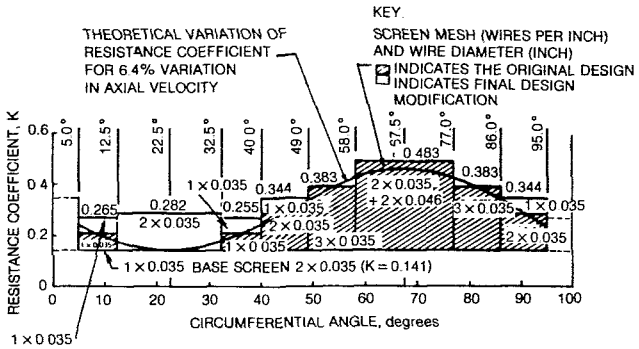

Fig. 6 Theoretical variation of resistance coefficient and corresponding overlay segment characteristics for a quadrant of the four cycle distortion screen

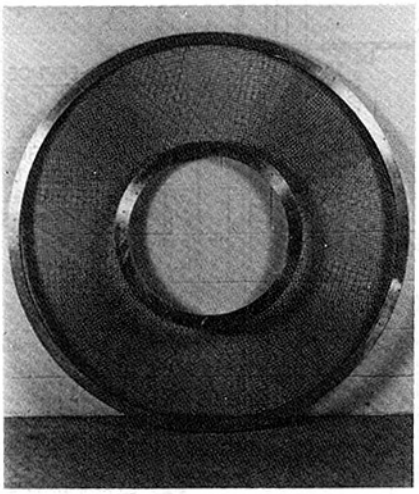

Fig. 7 The four lobe aerodynamic distortion screen

lead pellets. In this way, two configurations of tuned condition were established, i.e., the initally "tuned" condition and the deliberately mistuned condition. Table 1 presents the list of individual blade frequencies in the 1B and 1T modes measured with the fan assembly mounted in the rig for these two conditions. Figure 3 presents these frequencies in the form of histograms.

Aeromechanical Characterization of the R-80 Fan Assembly

The design of the fan was such that, within the maximum rig speed of 1200 rpm, an integral order resonance corresponding to a fourth "engine order" (4E) could be induced. Therefore, the aeromechanical characterization of the fan discussed below pertains to the aerodynamically forced vibration of the R-80 fan via distortions induced in the flow by a 4-lobed screen. Such a screen with four lobes was designed, fabricated and installed in the flow field. Velocity defects in the flow field due to the presence of the distortion screen were measured and correlated with blade strains.

Instrumentation and Calibration in Test Rig. The pneumatic instrumentation in the fixed frame of reference is concentrated at two stations upstream of the fan stage and at one downstream station as shown in Fig. 4. Eight equally spaced static pressure taps were located circumferentially in the outer casing and hub at the upstream stations and in the outer casing at the downstream station. At station 0, closest to the screen, detailed pressure measurements were made using a combination of 5 pitot-static and 3 kiel probes placed at various radial positions at 8 equally spaced circumferential locations. These measurements were used for rig calibration

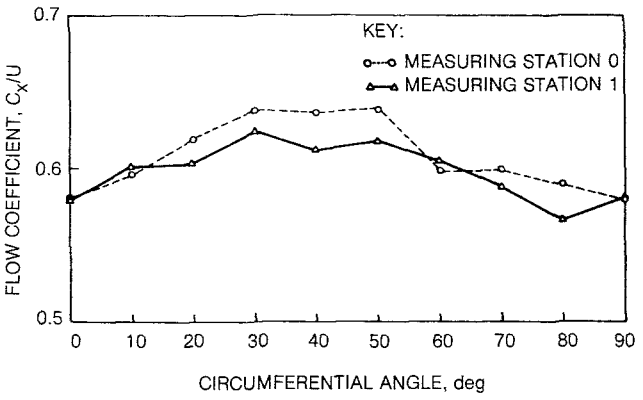

Fig. 8 Variation of average flow coefficient with circumferential angle at the two measuring stations downstream of the distortion screen

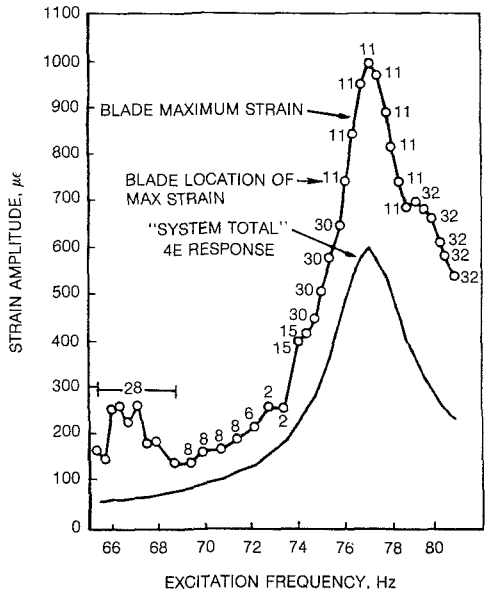

Fig. 9 Variation of "system total" 4E response and blade maximum strain amplitude of mistuned assembly due to a 4-lobed distortion in the airstream with excitation frequency

and also for screen documentation. At station 1, closest to the fan, the radial distribution of pressure was measured using a 5-element (with Gaussian spacing) total pressure rake. Measurements at this station were used to determine the inflow distortion due to the screen.

Assessment of the static pressure rise across the stage for fan performance and speed line determination utilized the pressure measurements at station 2. With the R-80 fan installed in the rig and with clean inlet conditions, initial runs were made at 810 rpm to calibrate the reference total pressure probe which was used subsequently for the control of tunnel flow conditions. Runs were also made to check for inlet distortion; no significant distortion was found. The clean inlet speedline characteristic was determined at 1050 rpm with some checkpoints also being made at 810 rpm. Results of these measurements in terms of fan static pressure rise coefficient $\Delta P/Q_{u_{\text{mid}}}$, and axial flow velocity ratio C_x/U are presented in Fig. 5. The static pressure rise was determined from outer casing wall taps at measuring stations 0 and 2, while the dynamic pressure, and hence the axial velocity C_x, were determined from a kiel probe and casing pressure tap at measuring station 0. The reference velocity is the rotor tangential velocity at blade midspan (22.5 in.). Also shown in Fig. 5 are the mass-averaged values from design computations. As can be seen, there is good agreement between

the design and measured values, except near stall. 0.525 was set as the low safe limit for axial flow coefficient. At 1200 rpm the maximum value of flow coefficient attainable was 0.7.

Aerodynamic Distortion Screen Design. During the mechanical characterization testing phase, it was shown that in the first family of modes, only a 4-nodal-dia mode could be excited. A 4-lobed distortion screen was therefore selected so that this mode could be studied in an aerodynamic environment. The objective was to design and build a screen that would produce a spatially fixed fan inflow with its axial component varying sinusoidally in the circumferential direction. In this way, only low-order (preferably the first family) modes would be excited.

The method used to design the screen is given in [2] and [3] and employed overlays of wire screens, which cause a loss in total pressure in the airstream passing through the screen. The overlay method of [3] allows a variation of total pressure to be calculated using the combined resistance coefficient of the screen. The latter is accurately predicted by summing the individual resistance coefficients of the support, or base screen, and overlay screens for a given value of loss coefficient based on Reynolds number. The design equations of [2] were programmed to allow various designs to be easily examined.

Theoretical calculations indicated that an axial flow variation of ±3 percent would produce a blade vibratory stress (at the above-shroud-maximum-thickness location) of ±5000 psi. However, this was based on the assumptions of a low aerodynamic damping (0.00124) and the location of

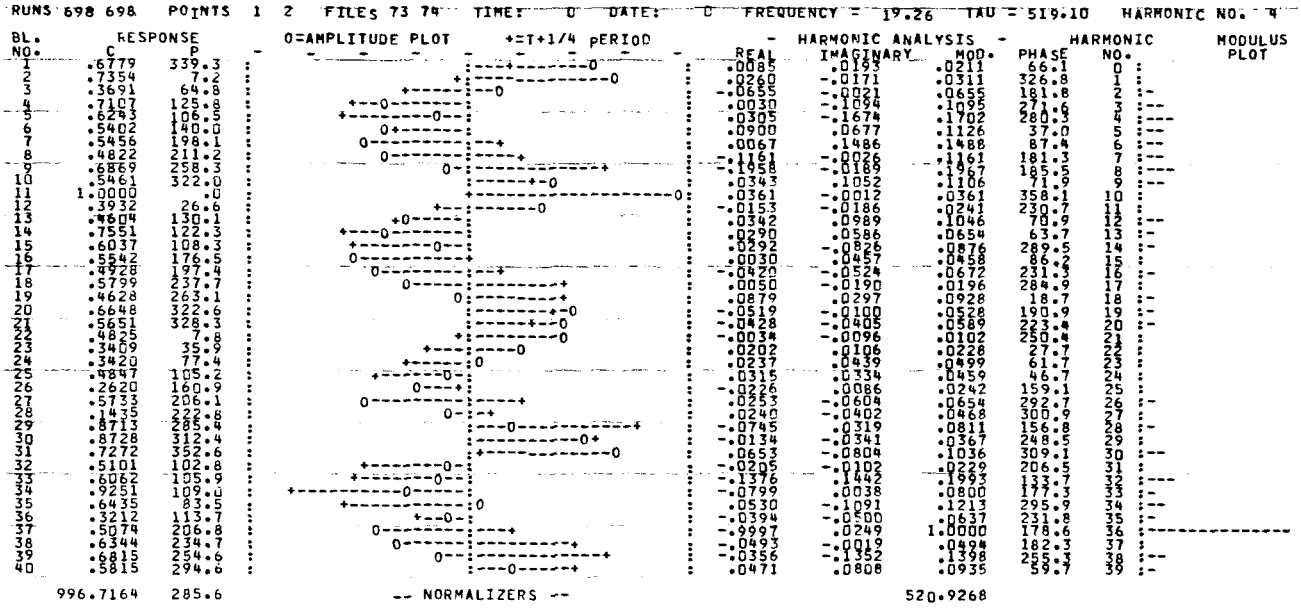

Fig. 10 Response of the mistuned assembly to the 4-lobed distortion in the airstream at an excitation frequency of 77.04 Hz (1156 rpm): peak "system total" response and maximum blade strain

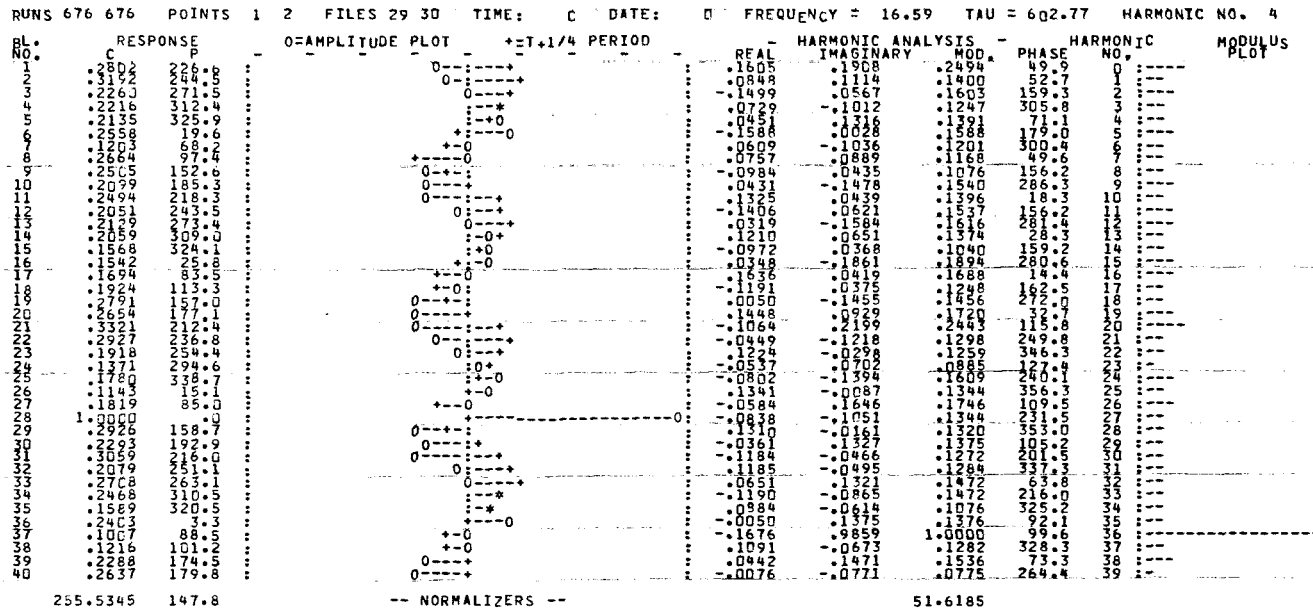

Fig. 11 Response of the mistuned assembly to the 4-lobed distortion in the airstream at an excitation frequency of 66.36 Hz (995.4 rpm): peak response of blade no. 28

distortion at the fan station. To test the influence of these assumptions, it was decided to build a trial screen and obtain data early in the test program. The distortion chosen for this screen was a 10 percent distortion, 4-lobe square wave with each high resistance region extending over a range of 45 deg. The trial screen was a temporary modification of the partially built test screen and was made by wiring onto the base screen (2 × 0.035, i.e., 2 wires per in., 0.035-in.-dia square mesh) four segments of 18 × 0.009 square mesh screen. The results obtained from this screen at rotor speeds near the integral (4E) order speed confirmed that a distortion of only 3 percent was needed to produce adequate strain in the blades. However, without going to specially made screens or varying the wire size in other ways, spray painting for instance, a distortion of 6.4 percent was found to be large enough to enable a reasonably smooth distortion variation using available materials. This design is shown in Fig. 6. The figure shows the calculated variation of resistance coefficient together with the screen mesh specifications (shown crosshatched) required to approximate the curve with eight resistance steps per lobe. This screen was found to have a distortion of approximately 5 percent at a measuring station close to the fan. However, the strain induced in the blades at the integral order speed was excessive and the screen was subsequently modified by increasing the resistance in the low resistance regions. This caused a distortion of the sinusoidal distribution but reduced the maximum distortion to usable levels. A photograph of the final screen used in this program is shown in Fig. 7. A low-melting-point alloy (Cerrobend) was used to "anchor" the stainless steel screening in the outer rim and hub. This proved to be very satisfactory and convenient.

Screen Evaluation and Distortion Measurement. The screen was evaluated at a rotor speed of 1056 rpm and an average flow coefficient (C_x/U) of 0.62. The procedure used was to rotate the screen incrementally in front of the fixed frame pneumatic instrumentation described earlier. The pressure readings were digitized and stored on tape in the form of pressure coefficients, i.e., $(P_{T_0} - P)/1/2\rho U^2$, where P is the pressure reading, P_{T_0} is the pressure at a reference probe at measuring station 0 (see Fig. 4), ρ is air density, and U is the tangential wheel speed at midblade span. Subsequent data reduction was performed to obtain the Fourier components of the variation in average axial flow coefficient (C_x/U) at each increment of angle around a quadrant of the screen. The screen is assumed to be cyclic symmetrical and hence the results for a quadrant were applied to the whole screen.

Figure 8 shows the resulting variation of axial coefficient for one quadrant around the screen at the two measuring stations 0 and 1. 0 deg is at top dead center of the rig. The strength and phase of each Fourier component at the two stations are given below.

Harmonic content of C_x/U variation

	Station 0		Station 1	
Harmonic	Amplitude	Phase (lead)	Amplitude	Phase (lead)
0	1.2195		1.1986	
4	0.0283	38.6	0.0225	37.2
8	0.0043	67.2	0.0066	26.8
12	0.0056	53.7	0.0042	10.1
Average C_x/U	0.610		0.599	
4th order distortion	4.64%		3.75%	

Integral Order Resonance. The fan assembly was subjected to forced vibration through aerodynamic excitation provided by the 4-lobed distortion screen that could, according to calculations, cause a predominantly 4E resonant vibration around 1100 rpm. The aerodynamic conditions of

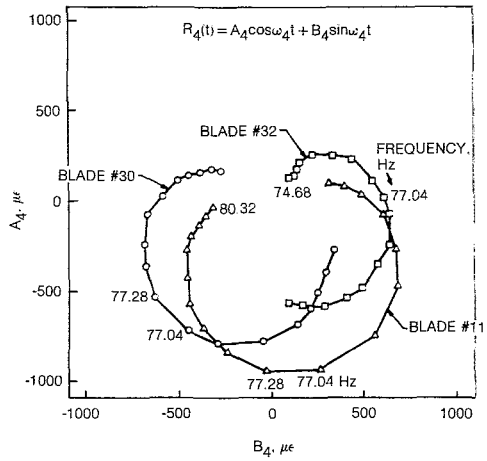

Fig. 12 Polar plots of fourth harmonic of blade response $R_4(t)$ in mistuned assembly with 4ND aerodynamic excitation. Responses shown for blades 11, 30, and 32.

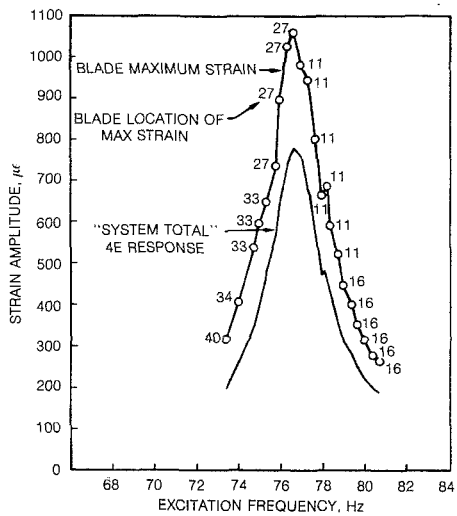

Fig. 13 Variation of "system total" 4E response and blade maximum strain amplitude of tuned system due to a 4-lobed distortion in the airstream with excitation frequency

flow were set at the design point (i.e., $C_x/U = 0.6$) and the blades were surveyed to determine the extent of vibratory strain levels experienced. The observations clearly confirmed that the assembly responded with stress levels of over ±10,000 psi even before the integral order speed could be reached. It was evident that the assembly was responding quite actively under the influence of strong aerodynamic excitations provided by the distortion screen. However, the strain levels were unacceptably large and the risks of high-frequency fatigue failures were not minimal. Therefore, it was decided to redesign the screen in order to reduce the level of distortion. The redesigned screen, as discussed earlier, was found to be adequate and resulted in stress levels of around ±10,000 psi at integral order speed. The latter was determined experimentally to be 1149 rpm for the tuned system.

A plot of maximum strain measured, in the mistuned assembly, in the region of the integral order speed is shown in Fig. 9. The different blade numbers shown indicate that the maximum strain experienced by different blades at different speeds reached a peak with blade No. 11 as the integral order speed is reached. The stick plots shown in Figs. 10 and 11 confirm that the general nature of the response mode is a 4-nodal-dia backward traveling wave, although blades No. 28 and No. 11 record a much larger strain at 66.36 Hz and 77.04 Hz, respectively. Thus the response of the assembly as a whole

is essentially characterized by the backward traveling wave, whose behavior over the frequency range around the integral order is also shown in Fig. 9 as the "system total" response. This should be viewed as the response of the assembly in a "regular system mode" and is obtained from stickplots by summing the contributions of the fundamental harmonics $(A_4 + A_{-4})$ in the present example.

The components of the fourth harmonic of the response of blades that are most active at the integral order speed (i.e., blade No. 11, No. 30, No. 32) are plotted in the form of polar plots in Fig. 12. These plots have been used to obtain an "integral order resonant frequency" of 77.1 Hz with a loss factor of .034.

Figures 13–15 show similar results obtained for the "tuned" assembly. The assembly is somewhat "better behaved" as can be observed in these figures. In this case, the resonant frequency was found to be 76.6 Hz with a loss factor of 0.026. Comparison of the responses of the tuned and mistuned assemblies shows that the blades in the mistuned assembly do not experience strains larger than those in the tuned system.

Correlation Between Measured Strain and Aerodynamic Stimulus. To correlate the distortion pattern with the strain response, it appears desirable to use an indirect method based on the Fourier series (spatial) of the distortions and the corresponding spatial harmonic analysis of the single-frequency Fourier analysis of the time series from strain gages. The amplitude of the distortion/strain correlation can then be derived from the normalization coefficients of the various harmonic analyses. The phase can be derived from the relative orientations of the spatial patterns of the distortion and strain. As an example, consider the data at 1150 rpm (see Fig. 14), where the system response is a maximum for the tuned assembly.

With reference to Fig. 16, the 4ND component of the inlet distortion provides four maxima of C_x/U at .0225 above its average value of .599, at angular positions of 37.2, 127.2, 217.2 and 307.2 deg from TDC in the direction of rotation. Each blade will encounter a varying incidence angle reaching a minimum at these locations. The response to this gust was measured and is typified by the 4ND strain response, a backward-traveling wave with an amplitude of 689 $\mu\epsilon$ and time phase of 180.4 deg relative to blade No. 1 at the moment of the timing pulse. This pulse is triggered when blade No. 24 passes the vertical at TDC. The maximum strain therefore occurs when any given blade is phased at 153 deg–180.4/4 or 107.9 deg past the vertical (also at 197.9, 287.9, and 17.9 deg).

In order to compare the phase lag in this response with that of the unsteady aerodynamic gust functions, the lag due to the dynamics of the blades must be subtracted (the blades are being driven at resonance, hence lag the gust force by a quarter cycle, 22.5 deg). The location of maximum incidence angle just before TDC is 7.8 deg, or 25.7 deg (17.9+7.8) before the closest location of maximum strain. The equivalent time lag of 102.8 deg (4×25.7) is reduced by 90 deg to 12.8 deg; this is the phase angle between the force and response due to aerodynamics alone.

The amplitude of the unsteady aerodynamic gust function requires a knowledge of the blade force to strain response relationship. This is not yet available, but some comparisons of relative gust function amplitudes for 4ND and 8ND responses can be made if theoretical corrections, as shown below, are made for amplification factors resulting from resonances.

The .013 of critical damping (i.e., 1/2 of the loss factor referred to earlier) measured for the 4ND mode, on a single degree of freedom basis, corresponds to a theoretical displacement magnification factor of 38.5. The strain amplitude of 689 $\mu\epsilon$ at resonance may therefore be reduced to 17.9 $\mu\epsilon$ (i.e., 689/38.5), which would have resulted at a frequency below resonance. The ratio of this strain to the distortion of .0225 (i.e., 17.9/.0225 = 796) is therefore proportional to the aerodynamic gust function.

A similar calculation for the mistuned assembly may be made. Using the results from run at 1156 rpm (see Fig. 10), the backward-traveling 4ND response component was 520 $\mu\epsilon$ at 178.6 deg phase. The 4ND maximum strain response is now

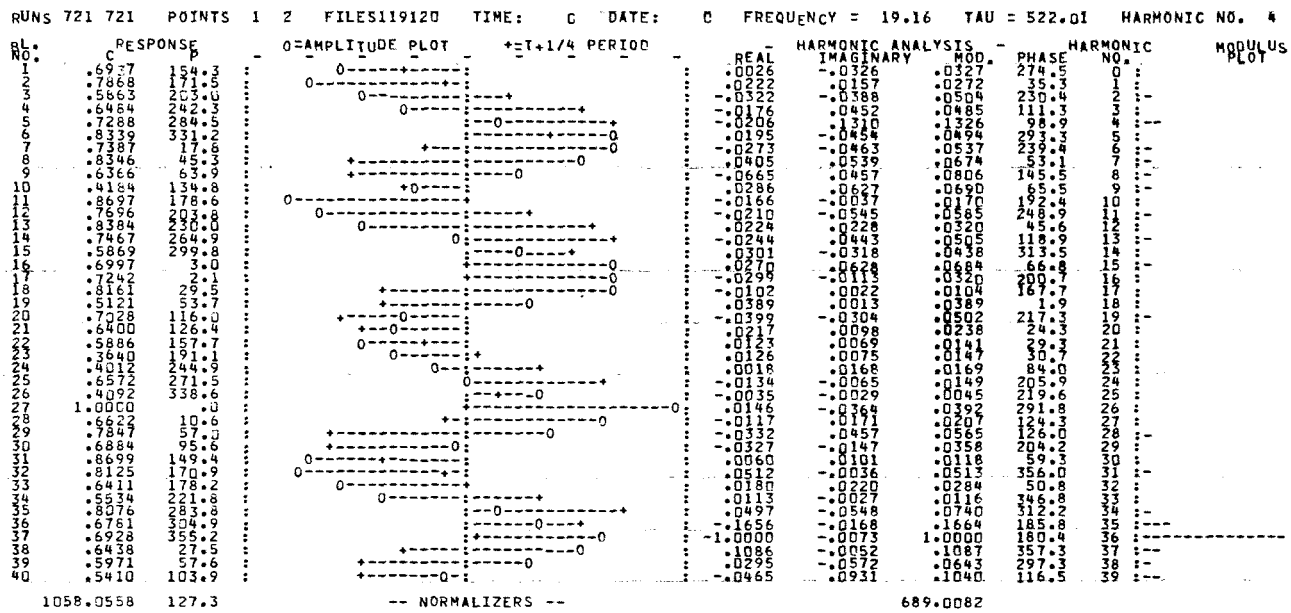

Fig. 14 Response of tuned assembly to the 4-lobed distortion in the airstream at an excitation frequency of 76.64 Hz (1150 rpm): peak "system total" response and maximum blade strain

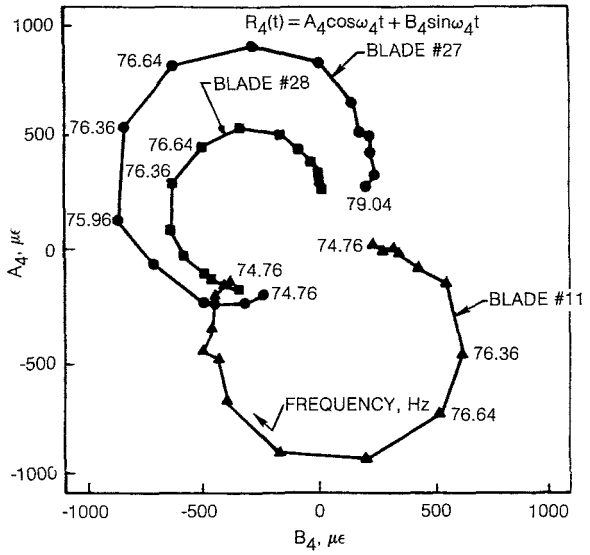

Fig. 15 Polar plots of fourth harmonic of blade response $R_4(t)$ in tuned assembly and 4ND aerodynamic excitation responses shown for blades 11, 27, and 28

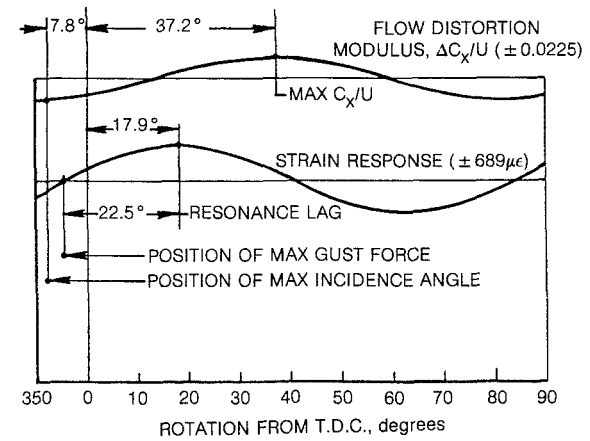

Fig. 16 Spatial position of 4ND flow coefficient and tuned assembly strain response distributions (one quadrant)

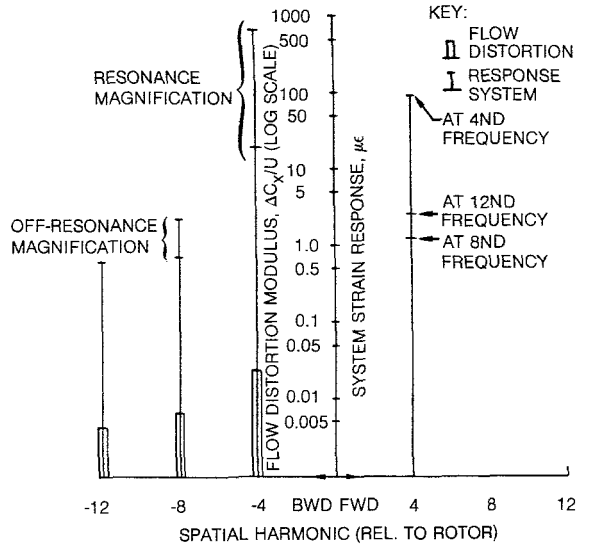

Fig. 17 Correlation between principal components of flow distortion and tuned assembly system strain response

at 108.4 deg (153–178.6/4) from the vertical, and the maximum incidence angle occurred at 7.8 deg before TDC. Hence the maximum strain at 18.4 deg (108.4–90) lags the maximum incidence angle by 26.2 deg and the temporal (gust function) phase lag is therefore 14.8 deg (4 × 26.2–90). The proportionality number that corresponds to 796 calculated above is 786 based on a critical damping factor of .017.

To compare these phase lags with that predicted by the aerodynamic gust response function for an isolated airfoil in translation, the reduced frequency is required. The reduced frequency is given by $\lambda = \omega b/(U^2 + C_x^2)^{1/2}$, where ω is the frequency, b is the semichord at midspan, U is the tangential velocity at midspan, and C_x is the axial velocity. Inserting appropriate values for the variables, the reduced frequency is found to have a value of 0.36 for the first family response. Assuming a Sears sinusoidal gust function, a lag angle of 8 deg can be expected (see Fig. 13.4 of [4] to compare with the 12.8 and 14.8 deg determined above).

The correlation of distortion and strain may be considered in terms of the harmonics of their respective circumferential distributions around the fan. The aerodynamic distortion was described earlier in terms of multiples of 4ND harmonics, and it was assumed to have cyclic symmetry. The magnitudes of the three major harmonics of the distortion are shown plotted on Fig. 17, along with the resulting harmonics of the strain response for the "tuned" system. For complete correlation, the strain response should be entirely in the backward traveling ND patterns, but as can be seen, the response includes forward traveling components (i.e., 4ND from 4ND, 8ND and 12ND excitation). In particular, the response to the 12ND excitation is mostly a forward traveling 4ND wave. This presumably is the principal feature of a mistuned second family 4ND mode, whose resonance is about 280 Hz, but which has significant 12ND content. It should be noted that although a similar response for the first family 4ND resonance was obtained for the mistuned assembly as for the "tuned," no significant higher order (8ND and 12ND) harmonics were excited.

Discussion of Results

A part-span shrouded experimental fan 60 in. in diameter was subjected to forced vibration in an aerodynamic environment. The bladed disk assembly consisted of 40 blades made of aluminum. The blades were 15 in. long and of aspect ratio varying from 2.5 (tip) to 3.0 (root). Tests were conducted at speeds not exceeding 1200 rpm. In the aerodynamic rig, the uniform flow field was interrupted by a distortion screen so that the cascade of blades experienced a forcing function of a four nodal diameter pattern in the fixed system. Responses at integral order speeds were measured on all blades for both the initially "tuned" and mistuned configurations.

The rotor had been designed such that the first family 4-nodal diameter mode would be integral with a rotor speed below the maximum speed of 1200 rpm. Under the influence of the flow distortion, the assembly response at integral order was clear and unambiguous with strong excitation levels and strong interblade coupling through the aerodynamics. For the first family, 4-nodal-dia response, the loss factor was estimated as 0.026 for the tuned system and 0.034 for the mistuned system.

A major finding from this program is that the maximum strain levels measured in the deliberately mistuned rotor are not higher than those measured in the "tuned system." The "tuned" system undoubtedly was not perfect and therefore we are comparing two mistuned systems. Nevertheless, the maximum response levels from the entire series of tests did not show the mistuned system to be in any way worse than

"tuned" system in terms of measured strains. This observation is generally at variance with the conclusions based on analytical studies reported in [5, 6, 7]. However, direct comparisons may not be valid because of the differences in the characteristics of the bladed-disk assemblies studied. For example, in the present study, the blades are shrouded, the assembly is grossly mistuned with a random distribution of blade frequencies and has no distinct twin modes in the family of modes discussed in this paper. Further, the mechanical coupling through the shrouds appears to be considerably smaller in comparison to the strong aerodynamic coupling observed.

The effort to correlate measured strains with the aerodynamic stimulus has shown an excellent correlation between the principal component of the distortion pattern and the corresponding strain pattern. In addition, multiples of the principal harmonic are present in the distortion which correlate with corresponding strain patterns measured in the assembly. However, an interesting feature of this correlation is that, in addition to backward traveling waves, forward traveling waves are also present so that the response pattern in the fixed system will not appear as a standing wave at integral order speed. Again this feature is attributed to the influence of mistuning present in the rotor.

That the response patterns of a mistuned assembly do not always follow the imposed excitation was abundantly clear in all data analyzed. Therefore, one should not be surprised if a backward traveling wave forcing function resulted in a response pattern containing a predominant forward traveling wave. It all depends on the degenerate modes of the system, their phasing and the manner in which they combine. A knowledge of the modal characteristics of the assembly is essential in order to be able to interpret data from forced vibration responses.

Acknowledgment

This research program, comprising the forced vibration testing of a part-span shrouded fan in vacuum as well as in an aerodynamic environment, was sponsored by the U.S. Air Force Aeropropulsion Laboratory at the Wright-Patterson Air Force Base under Contract No. F33615-79-C-2054. The Air Force project managers were Dr. James MacBain and Dr. William Stange.

The support provided by Dr. Larry Hardin and the permission of the sponsors to publish this paper are gratefully acknowledged.

References

1 Srinivasan, A. V., and Cutts, D. G., "Measurement of Relative Vibratory Motion at the Shroud Interfaces of a Fan," presented at the Ninth Biennial Conference on Mechanical Vibration and Noise, Dearborn, Mich., Sept. 1983.

2 Bruce, E. P., "Design and Evaluation of Screens to Produce Multicycle ±20 Percent Amplitude Sinusoidal Velocity Profiles," AIAA Paper No. 74-623.

3 McCarthy, J. H., "Steady Flow Past Nonuniform Line Grids," *Journal of Fluid Mechanics*, Vol. 19, 1964, pp. 491–512.

4 Fung, Y. C., *An Introduction to the Theory of Aeroelasticity*, Dover Publications, New York, 1969.

5 Ewins, D. J., "The Effects of Detuning Upon the Forced Vibrations of Bladed Disks," *Journal of Sound and Vibration*, Vol. 9, No. 1, 1969, pp. 65–69.

6 Srinivasan, A. V., and Frye, H. M., "Effects of Mistuning on Resonant Stresses of Turbine Blades," presented at the Winter Annual Meeting of the ASME, New York, 1976.

7 MacBain, J. C., and Whaley, P. W., "Maximum Resonant Response of Mistuned Bladed Disks," presented at the Ninth Biennial Conference on Mechanical Vibration and Noise, Dearborn, Mich., Sept. 1983.

Some Recent Advances in the Understanding and Prediction of Turbomachine Subsonic Stall Flutter

R. M. Chi
Senior Research Engineer.

A. V. Srinivasan
Manager.

Applied Mechanics Research,
United Technologies Research Center,
East Hartford, Conn. 06108

In this paper, some recent advances in the understanding and prediction of subsonic flutter of jet engine fan rotor blades are reviewed. Among the topics discussed are (i) the experimental evidence of mistuning in flutter responses, (ii) new and promising unsteady aerodynamic models for subsonic stall flutter prediction, (iii) an overview of flutter prediction methodologies, and (iv) a new research effort directed toward understanding the mistuning effect on subsonic stall flutter of shrouded fans. A particular shrouded fan of advanced design is examined in the detailed technical discussion.

Introduction

Subsonic stall flutter near the engine surge operating condition has been a major obstacle in the design of fan and compressor rotors in advanced gas turbine engines. As discussed in two earlier review papers by Jeffers and Meece [1] and Mikolajczak, Arnoldi, Snyder, and Stargardter [2], serious blade failures were caused by high cycle fatigue as a result of subsonic stall flutter. A significant increase in engine development cost is often an inevitable byproduct of stall flutter occurrences during engine testing. Lubomski [3] further provided an excellent and informative discussion on this type of aeroelastic instability, especially in terms of the engine inlet condition changes.

Extensive effort, both experimental and analytical, has been dedicated to the understanding, prediction, and even control of subsonic stall flutter. Because of the aeroelastic nature of the entire flutter phenomenon, many measurements and studies have been made in the aerodynamic as well as the structural responses during or near flutter. It is natural to consider the engine subsonic stall flutter as a flow induced vibration problem similar to the better known fixed wing stall flutter or even the heat exchanger tube flutter in power plant cross flows. However, engine subsonic stall flutter generally occurs at frequencies (and reduced frequencies as well) much higher than those of usual wing or heat exchanger tube flutter. The aerodynamic environment about jet engine rotor blades is hardly uniform or steady even when blades are experiencing no appreciable vibration. This limits the direct transfer of aerodynamic technology from the fixed wing into rotating turbomachines. In addition, engine rotor blades generally couple with each other, not only aerodynamically through the passing airstream but also mechanically through the blade root structure elements, like disk and/or spacers, and part span shrouds, if applicable.

Aerodynamically, it has not been established conclusively whether during stall flutter the relative flow is fully attached along the blade suction surface or is separated during part or the entire blade vibration cycle. However, Sisto and Perumal [4] have assumed the existence of flow separations in an attempt to model the stalled unsteady aerodynamics in a rectilinear cascade. Unfortunately, only incompressible flow was studied and no experimental verification of their theory was made.

Structurally, significant vibratory stress variations from blade to blade are usually observed in engine flutter testing. The vibratory stress variations can be attributed to the varying air flow characteristics from one blade passage to another (aerodynamic mistuning) and/or the variation of vibrational as well as geometrical characteristics from blade to blade (blade mistuning). Recently, some analytical efforts [5–7] were attempted to study the effect of blade frequency mistuning on flutter in general, though they were not directed specifically to stall flutter because of the lag in the development of unsteady aerodynamic models for stall flutter applications.

Despite the difficulty in solving the subsonic stall flutter problem, some important technological advances in understanding and predicting the sophisticated subsonic stall flutter phenomenon have been made in the past decade, and they are discussed in this paper.

Subsonic Stall Flutter Responses

During subsonic stall flutter, the rotor blade incidence angles are generally high. For example, Fig. 1 shows the variation of the blade leading edge incidence angle along the blade span for three subsonic stall flutter conditions and one stable operating condition of a high-performance engine fan. Incidence angles above 10 deg may occur for a large portion of the blade span when stall flutter occurs. This has led to the

Contributed by the Gas Turbine Division of THE AMERICAN SOCIETY OF MECHANICAL ENGINEERS and presented at the 29th International Gas Turbine Conference and Exhibit, Amsterdam, The Netherlands, June 4–7, 1984. Manuscript received at ASME Headquarters January 9, 1984. Paper No. 84-GT-151.

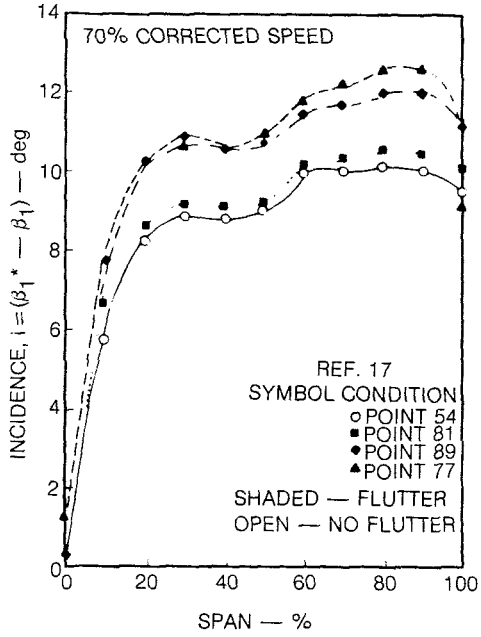

Fig. 1 Incidence across the blade span

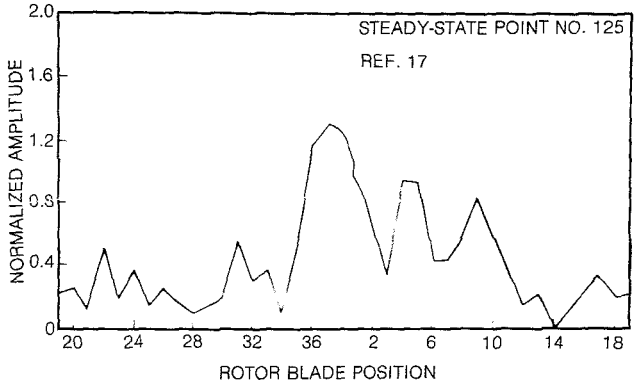

Fig. 2 Apparent tangential deflection

general belief that high blade loading associated with the high blade incidence angles is the major cause of subsonic stall flutter. Experimental measurements of the actual blade motion and the unsteady aerodynamic responses have been made during blade flutter. Representative results are discussed here.

Blade Vibratory Deflections. Using optical sensors mounted in the engine casing. Nieberding and Pollack [8], Kurkov and Dicus [9], and Kurkov [10, 11] have measured and analyzed the apparent tangential deflections of the fluttering blades. Figure 2 shows a typical circumferential distribution of the apparent tangential deflection at the fan blade tip during subsonic stall flutter. A large blade-to-blade variation in deflection amplitude was observed and attributed most likely to the inherent blade mistuning of the fan stage. Such a blade deflection pattern is commonly discussed in terms of traveling waves related to a Fourier series expansion.

To decompose the blade vibration pattern into its traveling wave components, consider the Fourier series expansion of the unsteady blade displacement $f(\theta)$

$$f(\theta)e^{i\omega t} = \left(\sum_{n=-\infty}^{\infty} S_n e^{in\theta}\right)e^{i\omega t} \tag{1}$$

where the displacement $f(\theta)$ contains both the (double) amplitude, $A(\theta)$, and the phase, $\phi(\theta)$, of all blades, i.e.,

$$f(\theta) = A(\theta)e^{i\phi(\theta)} \tag{2}$$

Note that θ is the circumferential angle and defined positive against the direction of rotor rotation, and for the entire set of blades, we write

$$\theta = (k-1)\frac{2\pi}{N_b} \qquad k = 1,2, \ldots, N_b$$

It is noted that the blades are counted in the direction of rotor rotation. Knowing the blade displacements in equation (2), one can calculate the Fourier coefficient S_n via the integral

$$S_n = \frac{1}{2\pi}\int_0^{2\pi} f(\theta)e^{-in\theta}d\theta = |Sn|\ e^{i\phi n} \tag{3}$$

or approximately

$$S_n \simeq \frac{1}{2\pi}\sum_{k=1}^{N_b} f[(k-1)\Delta\theta]e^{-in(k-1)\Delta\theta}\Delta\theta \tag{4}$$

where $\Delta\theta = 2\pi/N_b$. When the number of blades is large ($N_b \to \infty$ and $\Delta\theta \to 0$) we will have the exact Fourier coefficient. Also note that $n > 0$ for a forward traveling wave (FTW) and $n < 0$ for a backward traveling wave (BTW). In fact, the lower and upper limits in the summation in equation (1) can be replaced by $n_{\min}$ and $n_{\max}$ where

Nomenclature

A = amplitude
A_h, A_α = unsteady lift coefficients based on Carta's definition
b = airfoil half-chord
B_h, B_α = unsteady moment coefficients based on Carta's definition
c = airfoil full-chord
C = modal amplitude
C_L = lift coefficient
C_M = moment coefficient
$f(\theta)$ = unsteady blade displacement
g = structural damping
h = bending displacement
i = index or $\sqrt{-1}$
$Im\{\ \}$ = imaginary part of $\{\ \}$
k = blade number index; reduced frequency; wave number
KE = time-averaged system kinetic energy
l = reference length taken as blade tip full-chord
M_{ii} = generalized mass
n = number of nodal diameters
N = number of doublet modes
N_b = number of blades
P = perturbation pressure due to blade motion
ΔP = lower surface perturbation pressure minus upper surface perturbation pressure
q_i = generalized coordinate
$\bar{q}_n$ = modal content of n nodal traveling wave
Q_{ij} = generalized force
$Rl\{\ \}$ = real part of $\{\ \}$
s = blade pitch (leading edge distance)
S_n = n nodal diameter displacement traveling wave
t = time
V = blade-tip flow velocity
W = work done on system by external forces
x_s = flow separation point
x_{PCH} = pitching axis location
x,y,z = coordinate system in streamwise, radial, and vertical directions
α = pitching amplitude

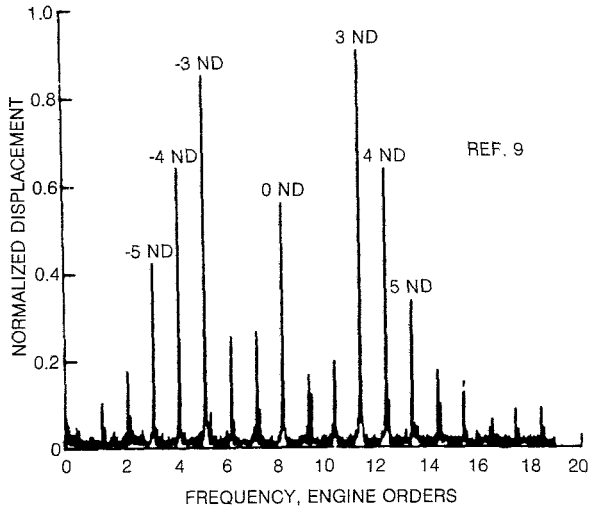

Fig. 3 Traveling wave components of blade deflections as observed by a stationary observer

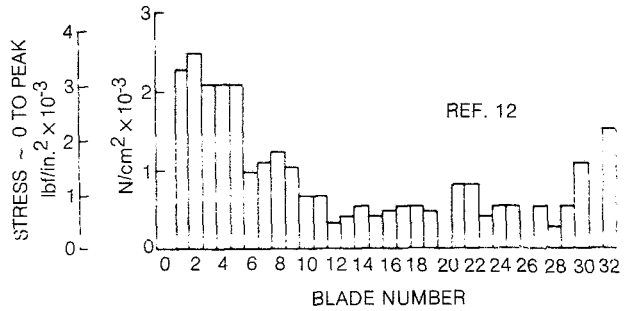

Fig. 4 Blade flutter amplitude for TS22 rotor at 67 percent speed from strain-gage measurements

$$n_{\min} = \begin{cases} 1 - N_b/2 & \text{for even } N_b \\ -(N_b - 1)/2 & \text{for odd } N_b \end{cases}$$

and

$$n_{\max} = \begin{cases} N_b/2 & \text{for even } N_b \\ (N_b - 1)/2 & \text{for odd } N_b \end{cases}$$

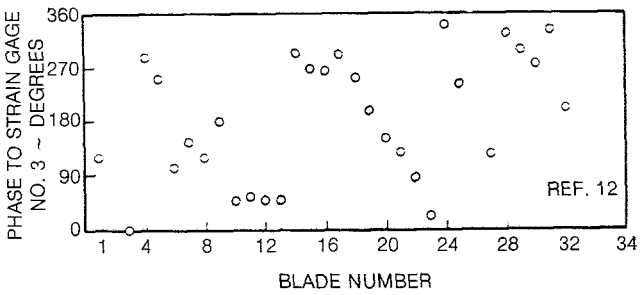

Fig. 5 Blade flutter phase angles for TS22 at 67 percent speed from strain-gage measurements

Then equation (4) becomes the exact inversion of equation (1).

These traveling waves of various nodal diameters at an identical flutter frequency are easily recognizable in the stationary references frame, because they appear at different frequencies in the stationary references frame. This can be understood by performing a Galilean transformation from the rotating coordinate θ to the stationary coordinate $\hat{\theta}$

$$\theta = \hat{\theta} + \Omega t$$

where Ω is the engine rotational speed. The stationary reference frame frequency is simply the following.

$$\omega_{\text{stationary}} = \omega_{\text{flutter}} + n\Omega$$

Figure 3 shows typical forward and backward wave amplitudes for various nodal diameters. Because of the one-per-blade sampling rate, only traveling waves of nodal diameters up to half of the number of blades are defined.

Blade Vibratory Stresses. The blade vibratory stresses during subsonic stall flutter exhibit responses similar to the tip deflections. Figure 4 shows typical stress distribution around an shrouded fan rotor. Furthermore, the interblade phase angles are shown in Fig. 5. The lack of a constant blade stress distribution and linearity in phase variation implies the existence of several traveling waves in the flutter mode. The phase measurement of the vibratory stresses is usually much more accurate than that of the blade tip deflections.

Unsteady Aerodynamic Pressures. Casing kulites have been used to measure the unsteady pressure wave contents associated with blade vibrations (see [9–12]). The measurement of unsteady pressure during flutter can be made

Nomenclature (cont.)

α_i = mean incidence angle
α_{CH} = stagger angle
β = kulite sensor circumferential offset from reference blade
δ_{STR} = structural logarithmic decrement
δ_{AERO} = aerodynamic logarithmic decrement
δ_{ij} = Kroneker delta
θ = circumferential angle in rotating frame
$\hat{\theta}$ = circumferential angle in stationary frame
λ = eigenvalue; stagger angle $\left(\equiv \frac{\pi}{2} - \alpha_{CH}\right)$
π = 3.14159 . . .
ρ = reference density taken as fluid density at blade-tip leading edge
σ_n = interblade phase angle ($2\pi n/N_b$)
τ = pitch-to-chord ratio ($\equiv s/c$)
ϕ = phase angle
Φ_i = natural mode shape function
Ω = rotor speed
ω = circular frequency
Δ = difference
$|\ |$ = absolute value

Subscript

AERO = aerodynamic
STR = structural
L = lift
M = moment
R,I = real, imaginary part
h,α = bending, torsion

Superscript

B = backward traveling wave
F = forward traveling wave

Abbreviation

BTW = backward traveling wave
FTW = forward traveling wave

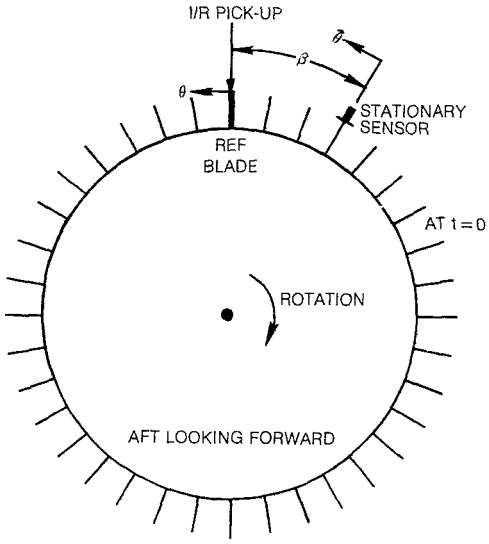

Fig. 6 Coordinate system

by stationary kulite sensors relatively easily, as opposed to rotating sensors. However, aeroelasticians are more interested in the unsteady pressure relative to the rotating reference frame. Consequently, it is required to construct rotating-reference-frame data from stationary-reference-frame data. The analysis method, shown below, in fact applies to all types of stationary sensors of which casing kulite is an example.

Consider a cascade of blades in the rotating reference frame as shown in Fig. 6. Assuming a simple harmonic flutter motion of frequency ω, the amplitudes of vibration of the blades can be considered as a periodic function of θ with a period of 2π. As discussed earlier, the blade displacement can be written in terms of the Fourier series

$$\text{displacement} = \left[\sum_{n=n_{\min}}^{n_{\max}} f_n(x) e^{in\theta} \right] e^{i\omega t} \tag{5}$$

where x is measured in the chordwise direction from the blade leading edge.

Consider a given n, then

$$\text{displacement} = f_n(x) e^{i(\omega t + n\theta)} \tag{6}$$

which is expressed in the familiar traveling wave form. In response to this displacement traveling wave, the air flow is perturbed to generate various perturbation pressure traveling waves. Similarly, the pressure wave can be written in general as the following.

$$P_n = F_n(\theta) f_n(x) e^{i(\omega t + n\theta)} \tag{7}$$

where the "transfer function" $F_n(\theta)$ is necessarily a periodic function of θ with a period of $(2\pi/N_b)$ in order to make the pressure wave form equation (7) compatible with the displacement wave form equation (6). Consequently, one can write the "transfer function" $F_n(\theta)$ in terms of the Fourier series

$$F_n(\theta) = \sum_{m=-\infty}^{\infty} F_{mn} e^{imN_b\theta} \tag{8}$$

where F_{mn} is mth spatial harmonic component of the pressure transfer function $F_n(\theta)$. Substituting equation (8) into equation (7) yields

$$P_n = \sum_{m=-\infty}^{\infty} A_{mn}(x) e^{i[\omega t + (n+mN_b)\theta]} \tag{9}$$

where

$$A_{mn}(x) = F_{mn} f_n(x)$$

Equation (9) is the most general description of a linear pressure traveling wave of nodal diameter n in the rotating reference frame expressed in terms of the angle θ measured from, say, a known reference blade surface. Again, θ is here defined positive in the direction opposite to the rotor rotation.

To transform the rotating reference frame wave from equation (9) into the stationary reference frame, one uses the "Galilean transformation"

$$\theta = \hat{\theta} + \Omega t - \beta \tag{10}$$

where

Ω = rotor speed
t = time
$\hat{\theta}$ = angle measured from a known stationary reference point, say a casing-mounted kulite transducer, positive direction taken the same as positive θ
β = the physical angle between the stationary kulite sensor ($\hat{\theta} = 0$) and the reference blade ($\theta = 0$) when $t = 0$

Also when $t = 0$, the reference blade passes the one-per-rev stationary pickup (see Fig. 6). Note that positive β is always measured when the one-per-rev pickup lies to the left of the stationary sensor.

Substituting the coordinate transformation equation (10) into the most general rotating reference frame pressure waveform equation (9), one obtains the following most general pressure waveform in the stationary reference frame characterized by $\hat{\theta}$

$$P_n = \sum_{m=-\infty}^{\infty} P_{mn}(x) e^{i(\omega_{mn} t + k_{mn}\hat{\theta})} \tag{11}$$

where

$$P_{mn}(x) = A_{mn}(x) e^{-ik_{mn}\beta} \tag{12}$$

$$\omega_{mn} = \omega + k_{mn}\ \Omega \tag{13}$$

$$k_{mn} = n + m\ N_b \tag{14}$$

It is worth mentioning that the wave number k_{mn} is not changed through coordinate transformation, but the rotating refernce frame frequency ω is being observed as the frequencies ω_{mn}, where m in general varies from $-\infty$ to $+\infty$ for a given nodal diameter n. We may call the frequency shift from ω to ω_{mn} the "generalized Doppler Shift" because of its close similarity to the familiar Doppler effect for sound waves. There is an exact correspondence if we set $m = 0$ in equations (13) and (14).

The complex amplitude $P_{mn}(x)$ in equation (11) can be written as

$$P_{mn}(x) = |P_{mn}(x)|\, e^{i\phi_{mn}(x)} \tag{15}$$

where the amplitude $|P_{mn}(x)|$ and the phase $\phi_{mn}(x)$ can be extracted from the casing kulite data. Recall that the casing kulite sensor is located at $\hat{\theta} = 0$ at all time by definition. Setting $\hat{\theta} = 0$ in the general wave form equation (11), one has the casing kulite flutter response described as a summation of various harmonics of the traveling wave of nodal diameter n.

$$P_n(\hat{\theta} = 0) = \sum_{m=-\infty}^{\infty} |P_{mn}(x)|\, e^{i(\omega_{mn} t + \phi_{mn}(x))} \tag{16}$$

The results given in Fig. 7 show the zeroth order ($m = 0$) pressure amplitude for the umbrella mode ($n = 0$), three nodal, four nodal, and five nodal forward ($n = 3, 4, 5$) and backward ($n = -3, -4, -5$) traveling waves for a shrouded fan stage during a part speed subsonic stall flutter, of which the blade tip tangential deflection pattern corresponds to Fig. 3 as discussed earlier. The traveling wave patterns for the tangential deflections and the unsteady pressure show an apparent similarity, both suggesting the important mistuned structural characteristics of the shrouded fan.

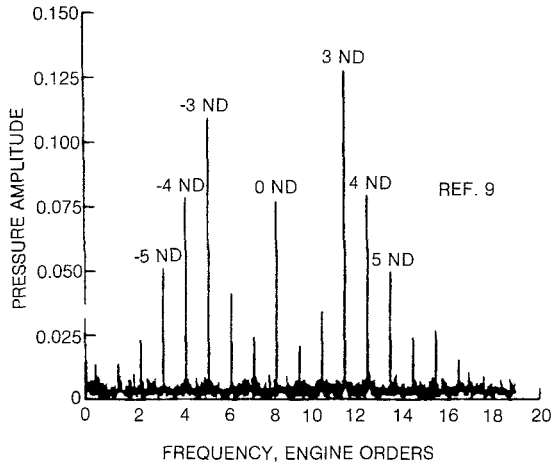

Fig. 7 Traveling wave pressure amplitudes measured by casing Kulite

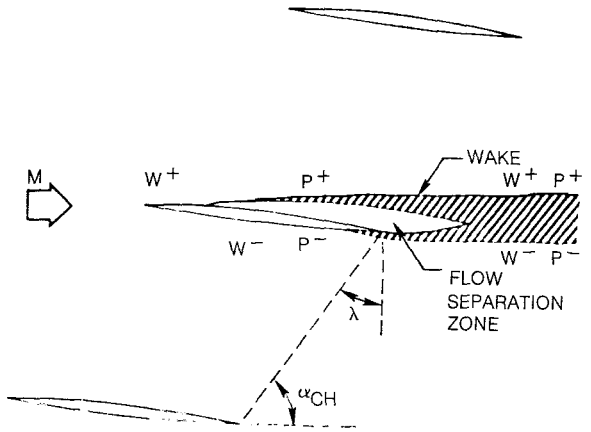

Fig. 8 Cascade geometry

The higher order ($m > 0$) pressure amplitudes at higher frequencies are not shown in Fig. 7. The number of significant terms in equation (16) depends on the extent of circumferential variation of the unsteady perturbation pressure within the blade passage. In particular, if there is a strong shock within the blade passage, one would expect to include more terms to yield a satisfactory representation of the unsteady pressure field.

Having obtained the amplitudes $|P_{mn}(x)|$ and the phases $\phi_{mn}(x)$ from the stationary kulite sensor data, one can calculate the amplitudes A_{mn} for the rotating-reference-frame wave form equation (9).

$$A_{mn}(x) = |P_{mn}(x)|\, e^{i[\phi_{mn}(x) + k_{mn}\beta]} \tag{17}$$

Note that Kurkov and Dicus [9] set $\beta = 0$ in their analysis. Substituting (17) into (9), we have the general form of the pressure traveling wave of nodal diameter n in the rotating reference frame

$$P_n = \sum_{m=-\infty}^{\infty} |P_{mn}(x)|\, e^{i[\omega t + \phi_{mn}(x) + k_{mn}(\theta+\beta)]} \tag{18}$$

from which one can calculate the amplitude and phase of the pressure wave at each circumferential location θ. Careful identification of the angle θ can further result in a reasonable estimate of the unsteady pressure on both the pressure surface and suction surface of the blade near the tip section. In practice, the surface pressure is very difficult to measure by using blade-mounted pressure transducers. Alternatively, equation (18) can be written as

$$P_n = \left\{ \sum_{m=-\infty}^{\infty} |P_{mn}(x) e^{i[\phi_{mn}(x) + mN_b\theta + k_{nm}\beta]} \right\} e^{i(\omega t + n\theta)} \tag{19}$$

where again $k_{mn} = n + m \cdot N_b$. The quantity in the large bracket { } represents a periodic function of θ with a period of $2\pi/N_b$. This means that it is an invarient for geometrically similar points in all blade passages (i.e., points that are separated by exactly one blade pitch).

Provided the blade unsteady pressures and unsteady deflections are known, one can calculate the aerodynamic work over a cycle of oscillation. This can be done by considering different nodal diameter waves separately and summing the results together (see for example [11] and [12].

Unsteady Aerodynamic Models

The application of classical subsonic unsteady aerodynamic theories, such as the theory of Smith [13], which is based on an acceleration potential, and the theory of Jones and Moore [14] based on a modified velocity potential, to real engine operating conditions has not shown any aeroelastic instabilities for either unstalled (low blade loading) or stalled (high blade loading) subsonic flows.

The apparent effect of high loading on the occurrence of subsonic stall flutter has led to the consideration of nonuniformity of the mean flow about the rotor blades due to blade cambers, thicknesses, and incidence angles in the unsteady aerodynamic modeling. Atassi and Akai [15] studied the incompressible problem analytically. Verdon and Caspar [16] studied the subsonic problem numerically. Preliminary results have shown that the blade geometry and the resultant steady flow turning can influence the unsteady aerodynamic responses significantly for an unsymmetrical double circular arc airfoil and further application of their theory to real engine blades is under active studies.

In the past several years, two other efforts have been undertaken to provide at least a near-term solution to the urgent need of a workable subsonic stall flutter design system for current engine.

One effort by Jeffers et al. [17] has resulted in a semi-empirical unsteady aerodynamic theory for high incidence stalled flow. The semi-empirical unsteady aerodynamic theory utilizes the unsteady aerodynamic test data for isolated airfoils at high incidence angles to correct the flat plate cascade unsteady aerodynamic force coefficients based on the Smith theory. This theory has resulted in a useful and conservative stall flutter design system for part-span shrouded rotor blades within certain design limits.

The other research effort by Chi [18, 19] has resulted in a separated flow unsteady aerodynamic theory that assumes flow separation as the underlying mechanism of stall flutter. In the separated flow unsteady aerodynamic theory [18, 19], the subsonic mean flow is assumed to separate at an identical and fixed point along the cord for all airfoils. The basic flow model is shown in Fig. 8. The distinction of this model from the classical attached flow model is that in the separated flow region on the airfoil the pressure is assumed given. For example, the local pressure is usually assumed equal to the free-stream pressure. Consequently, the downwash on the airfoil (representing the wake boundary motion) in the separated flow region is an unknown to be determined as part of the solution. Elsewhere on the airfoil, as in the classical attached flow theory, the downwash is known and the pressure is to be determined. As a result of the relatively simple flow model, a kernel (Green's) function approach similar to, but more general than, its classical nonstalled (nonseparated) counterpart is developed. Because of its elliptic nature, the complex mixed boundary value problem is transformed into two Fredholm integral equations. A

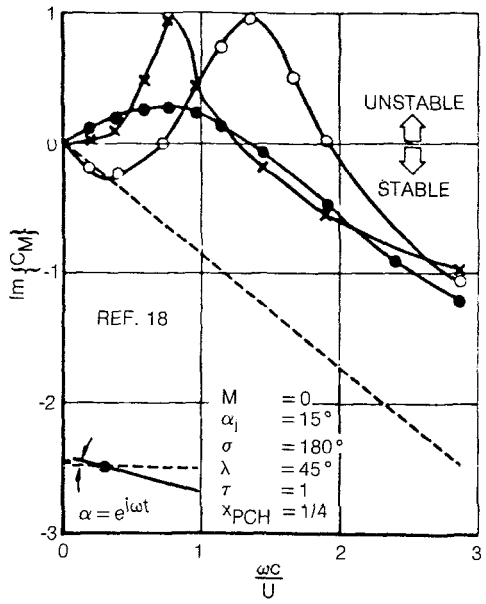

Fig. 9 Imaginary part of moment coefficient versus reduced frequency: —x— experiment [20]; —•— CHI [18]; —○— Yashima and Tanaka [20]; ···· attached flow

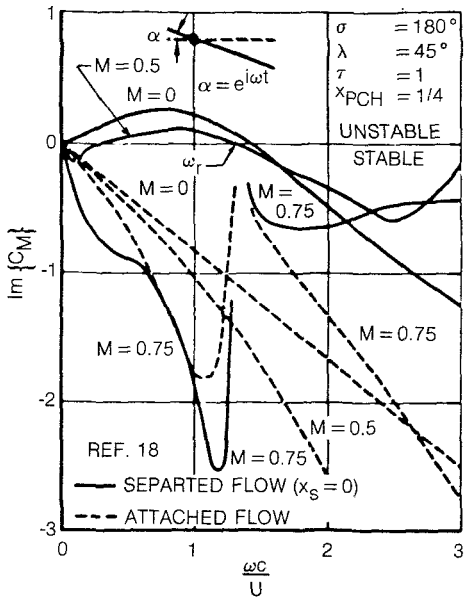

Fig. 10 Imaginary part of moment coefficient versus reduced frequency

standard collocation method is used to solve the two resultant integral equations. The solution of one integral equation yields the downwash distribution in the separated flow region. With the complete downwash now known, the other integral equation is used to solve for the pressure differential across the airfoil.

Figure 9 shows the imaginary part of the aerodynamic moment coefficient (proportional to the aerodynamic damping in pitch) versus the reduced frequency based on the airfoil full-chord and upstream flow velocity at zero Mach number. Relevant cascade parameters are stagger angle of 45 deg, solidity of 1, and interblade phase angle of 180 deg. All blades are at a mean angle of attack 15 deg and the mean flow separates at the leading edge. Airfoil thickness ratio is 4 percent. The top surface of each blade is a circular arc and the lower surface a flat plate. These parameters are chosen to match Yashima and Tanaka's experiment [20] in which an 11-blade linear cascade was forced to pitch about the quarter-chord in a water tunnel at a Reynolds number of approximately $.5 \times 10^5$. Flow visualization confirmed leading-edge flow separation occurred at a mean angle of attack 15 deg. Yashima and Tanaka's theoretical results [20], based upon a free streamline theory for incompressible flow with leading edge separation, showed torsional instabilities in the relatively low frequency range. The separated flow theory agrees reasonably well with their experimental data as shown in Fig. 9. It is noted that classical attached flow theory does not predict torsional instability at all these parameters. For subsonic Mach numbers, Fig. 10 shows the imaginary part of the moment coefficients for cascade flat plate airfoils pitching about the quarter-chord. For Mach number 0.75, a destabilizing effect of flow separation on torsional vibration is seen for superresonant conditions and the reverse is true for subresonant conditions.

Flutter Prediction Approaches

Three approaches to flutter prediction are frequently used in gas turbine engine design: (*i*) the empirical parameter correlation, (*ii*) the aerodynamic damping correlation, and (*iii*) the eigenvalue approach.

In the empirical parameter approach, one or more parameters that have been known to be influential in the type of blade instability of concern are plotted for various flutter and no-flutter points. From these correlations, empirical stability limits are generated. However, the design curves generated do not explicitly include enough important parameters that affect flutter boundaries and, therefore, can only be applied to designs of very similar geometric configurations and aerodynamic environments.

In the aerodynamic damping approach [21], the aerodynamic work done on all the rotor blades over a cycle of traveling wave harmonic oscillation is first computed by assuming that flutter occurs at one of the rotor system natural frequencies and the flutter mode shape is indentical to the corresponding natural mode shape. Then the total work done per cycle of oscillation is normalized by four times the rotor system kinetic energy to obtain the aerodynamic logarithmic decrement δ_{AERO}. Positive values of δ_{AERO} imply system stability. Negative values of $_{AERO}$ indicate system instability if the structural modal damping (which is always assumed positive) is not sufficient to overcome the negative δ_{AERO}. In equation form the aerodynamic damping is defined as

$$\delta_{AERO} = -\frac{N_b}{4}\frac{W}{KE}$$

where

N_b = number of blades
W = unsteady aerodynamic work for the one blade
KE = average kinetic energy

The unsteady aerodynamic work for one entire blade is calculated in a quasi three-dimensional "strip" analysis in which the airfoil is represented by sections of constant cross section at several radial locations. The unsteady work done at each cross section by the unsteady aerodynamic forces and moments during each vibratory cycle is obtained by calculating the product of the in-phase components of lift (L) and differential displacement perpendicular to blade chord (dh) and moment (M) and differential twist ($d\alpha$). The two-dimensional unsteady aerodynamic work per unit span is then integrated over the entire blade span to obtain the total work (W) the blade according to the following relationship

$$W = \int_{r_{root}}^{r_{tip}} (-\oint L \cdot dh + \oint M \cdot d\alpha) dr$$

In its expanded form, the unsteady aerodynamic work can

be shown to be a function of the parameters: air density (ρ), relative flow velocity (U), blade semichord (b), reduced frequency (k), unsteady lift and moment coefficients (A and B, respectively; maximum vibratory displacements of twist (C_α) and "flap" (C_h) and twist-to-flap phase angle (ϕ)

$$W=\int_{r_{\text{root}}}^{r_{\text{tip}}} \rho\ \pi^2\ b^2\ U^2k^2\{A_{hI}C_h{}^2+\{(A_{\alpha R}-B_{hR})\sin\phi + (A_{\alpha I}+B_{hI})\cos\phi\}C_\alpha C_h+B_{\alpha I}C_\alpha{}^2\}dr$$

In the eigenvalue approach [22, 23], the coupling among various twin orthogonal modes within a given nodal diameter vibration of perfectly tuned rotors is considered. The blade normal displacement Z_a is expressed by

$$Z_a(x,y,z,t)=\sum_{i=1}^{N} q_i(t)\Phi_i(x,y) \tag{20}$$

where

$\Phi_i(x,y)$ = blade natural mode shape functions
$q_i(t)$ = generalized coordinates

Due to cyclic symmetry of the engine rotor system two natural mode shapes exist for each distinct natural frequency and a given nodal diameter. The twin orthogonal mode shapes are written as sinusoidal functions in circumferential direction (θ) and are 90 deg apart in phase, i.e.,

$$C\ \sin\ (n\theta+\phi)$$
$$C\ \cos\ (n\theta+\phi)$$

where

n = number of nodal diameters
θ = circumferential angle, opposite to direction of rotor rotation
C = amplitude; varying from point on blade
ϕ = phase angle; varying from point to point on blade

These twin orthogonal modes are used in the flutter analysis. Obviously one always deals with an even number of modes for a given nodal diameter pattern.

If we take (*i*) the sine and cosine modes corresponding to the lowest (first) natural frequency as the first and second modes in the expansion equation (20); and (*ii*) the sine and cosine modes corresponding to the second natural frequency as the third and fourth modes in the expansion equation (20), etc., then we have

$$\Phi_i=\begin{cases} C_i\ \sin\ (n\theta+\phi_i) & i=1,3,\ldots,N-1 \\ C_i\ \cos\ (n\theta+\phi_i) & i=2,4,\ldots,N \end{cases}$$

Associated with each Φ_i is a natural frequency ω_i. For even i, the following relations hold:

amplitude $C_i = C_{i-1}$
phase $\phi_i = \phi_{i-1}$ $i=2,4,\ldots,N$
natural frequency $\omega_i = \omega_{i-1}$

Using Lagrange's equations, one can derive the following eigenvalue problem for simple harmonic motion of frequency, ω.

$$\sum_{\substack{j=2 \\ j=\text{even}}}^{N}\left\{\left[\left(\frac{\omega}{V}\right)^2\frac{1}{\omega_i{}^2}-\lambda\right]\delta_{ij-1}+\frac{\rho l}{M_{ii}\omega_i{}^2}Q_{ij}\right\}\bar{q}_j=0(i=\text{odd})$$

where

λ = eigenvalue = $\dfrac{1+ig}{V^2}$

g = loss factor = $\dfrac{\delta_{\text{STR}}}{\pi}$

Q_{ij} = generalized force =

$$\begin{cases} \dfrac{NB}{2l}\int\int C_i\ e^{-i\phi_i}\Delta P^F{}_j\ dx\ dy & \text{for FTW} \\ \dfrac{NB}{2l}\int\int C_i\ e^{i\phi_i}\Delta P^B{}_j\ dx\ dy & \text{for BTW} \end{cases}$$

$\Delta P_j{}^{F,B}$ = forward or backward traveling wave pressure load on reference blade due to jth mode
l = reference length
ρ = air density
δ_{ij} = Kronecher delta
M_{ii} = generalized mass of ith mode

For forward traveling waves, the blade response is

$$Z_a(x,y,t)=e^{i(\omega t+n\theta)}\sum_{j=\text{odd}}\bar{q}_jC_je^{i\phi_j}$$

and for backward traveling waves the blade response

$$Z_a(x,y,t)=e^{i(\omega t-n\theta)}\sum_{j=\text{odd}}\bar{q}_jC_j\ e^{-i\phi_j}$$

The main features of the eigenvalue approach are the following:

(*a*) As a result of the aerodynamically and structurally coupled flutter response theory, flutter frequencies and flutter modes are calculated, rather than assumed, for a given set of structural properties and steady aerodynamic characteristics. The theory also provides a basis for understanding the concurrence of both traveling wave flutter and standing wave flutter usually observed in rotating systems.

(*b*) For each set of steady-state aerodynamics and natural modes, the critical flow velocity at the airfoil tip, the critical structural damping (δ_{STR}), and the system response frequency at which flutter onset would occur are calculated for selected reduced frequencies. The reduced frequencies are selected so that the flutter modes, each of which is dominated by one of the natural modes, would have a critical flow velocity very near the test flow velocity. This enables their associated critical δ_{STR}, which by definition is equal in magnitude but opposite in sign to the aerodynamic damping δ_{AERO}, to be compared to the δ_{AERO} as calculated by the classical uncoupled method [21]. Other reduced frequencies provide a prediction of stability at additional velocities for which spanwise air densities, relative Mach numbers, incidences, etc., are maintained constant. These steady-state aerodynamic conditions represent various total inlet temperatures at constant corrected speed and flow with average total inlet pressure changed to maintain constant density.

(*c*) Plots of critical flow velocity versus critical δ_{STR} provide a clear overview of predicted bladed-disk stability. When three natural modes are considered, each reduced frequency results in three points on the V-δ_{STR} plot that represent three flutter modes with varying degrees of natural mode participation. Curve fitting the points of similar flutter modes from several reduced frequencies establishes boundaries between stable and unstable V-δ_{STR} regions (δ_{AERO} + δ_{STR} = 0). Because structural damping is assumed to be

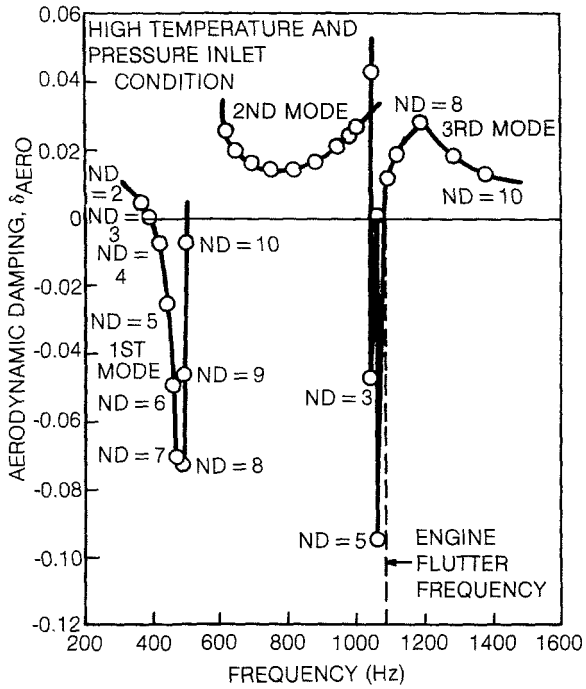

Fig. 11 Fan rotor stall flutter prediction using separated flow aerodynamics

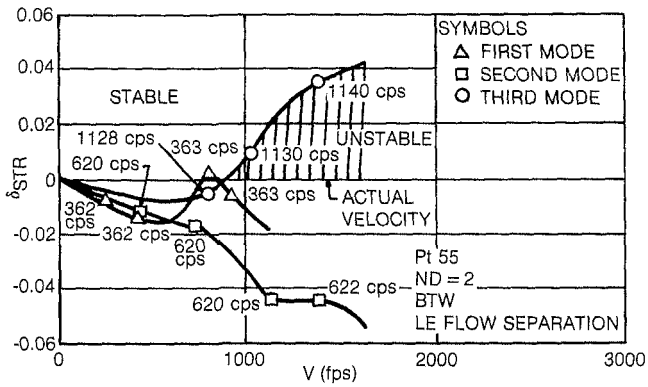

Fig. 12 V-δ_{STR} plot for first-stage fan (ND = 2)

positive, solutions on the negative δ_{STR} side imply stability. For a positive value of δ_{STR}, the curve defines either the flow velocity, above which flutter would occur, or in the case where the curve forms a "bubble," a velocity range within which flutter would occur.

Using "beam type" bladed disk vibration modes, the uncoupled aerodynamic damping correlation approach [21] and the coupled eigenvalue approach [22] have been used to correlate extensive flutter test data. Representative results are discussed below. The results discussed in this paper are all based on the separated flow unsteady aerodynamic theory, because of the very promising flutter data correlation found.

Subsonic Stall Flutter Prediction for a Shrouded Fan

A two-parameter (reduced velocity versus normalized incidence) empirical correlation of near-surge stall flutter data from ambient inlet rig testing improperly accounted for the effects of high-Mach-number, low-altitude inlet conditions, and as a result, flutter occurred at certain flight conditions during engine testing when the fan was on a normal operating line. The flutter mode changed from a 770-Hz, 2nd-bending-torsion mode in the rig tests to a 1000-Hz, above-shroud-torsion mode in the engine tests.

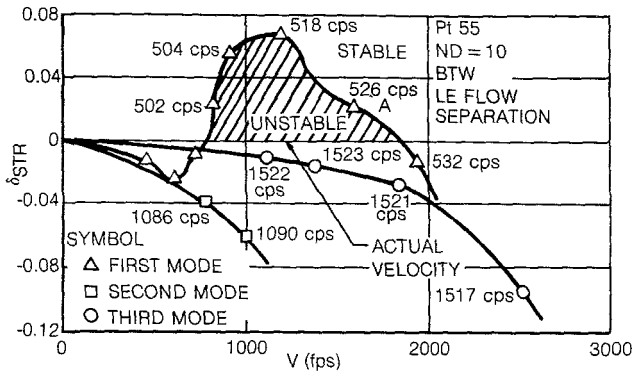

Fig. 13 V-δ_{STR} plot for first-stage fan (ND = 10)

Until the separated flow unsteady aerodynamic theory was developed recently, no analysis could predict these drastic changes in stability between the rig and engine operating conditions. A semiempirical prediction system [17] based on aerodynamic damping correlations that used an unstalled aerodynamics theory modified to reflect stalling effects generally agreed with stability trends of the torsional mode, but not those of the bending-torsion mode. The correlation results of separated flow analysis, however, are excellent. They are discussed below.

(a) Fan Rotor Engine Torsional Flutter. For the first-stage fan at high inlet temperature and pressure engine operating conditions, leading-edge flow separation was assumed to be present over the entire blade span. This assumption was necessitated by the absence of an established steady-state flow separation criterion. The intention was to probe the potential of using the analysis to establish a conservative design criteria.

As shown in Fig. 11, an above-shroud-torsion, 5-nodal-diameter (ND), third mode was calculated to be very negatively damped for backward traveling waves. This is in excellent agreement with test data, which revealed the 1000-Hz flutter mode to be comprised of several low-nodal-diameter third modes [17]. The coupling between modes within a nodal diameter was generally found to be small but occasionally quite significant. The 5-ND torsional flutter mode was calculated to contain a 5.6 percent contribution from the second mode and 2.9 percent from the first mode. The frequency was 4.5 Hz lower (−0.4 percent) than the torsional natural frequency. Other more stable nodal diameters were calculated to be more highly coupled, but the flutter frequency was rarely more than 1 percent different from the natural frequency of the dominant mode. To illustrate the flutter response based on the eigenvalue approach, we choose to discuss here the results of nodal diameters 2 and 10 in detail, because they represent two distinctly different types of flutter. The two-nodal-diameter case is essentially uncoupled single-degree-of-freedom flutter, while the ten-nodal-diameter case is strongly coupled aerodynamically.

The two-nodal-diameter, backward-traveling-wave flutter boundary is shown in Fig. 12. Because the structural damping is always assumed positive, the second-mode branch is always stable. The first-mode branch also remains stable as long as a small amount of structural damping exists. The third-mode branch becomes unstable above a fixed blade-tip flow velocity depending on the amount of structural damping. The calculated flutter mode shapes indicate essentially no mode coupling. Consequently, the flutter result is consistent with the aerodynamic damping results shown in Fig. 11. Also indicated in Fig. 12 are the flutter frequencies for selected flutter points on the V-δ_{AERO} plot.

A similar result for 10-nodal diameters is shown in Fig. 13.

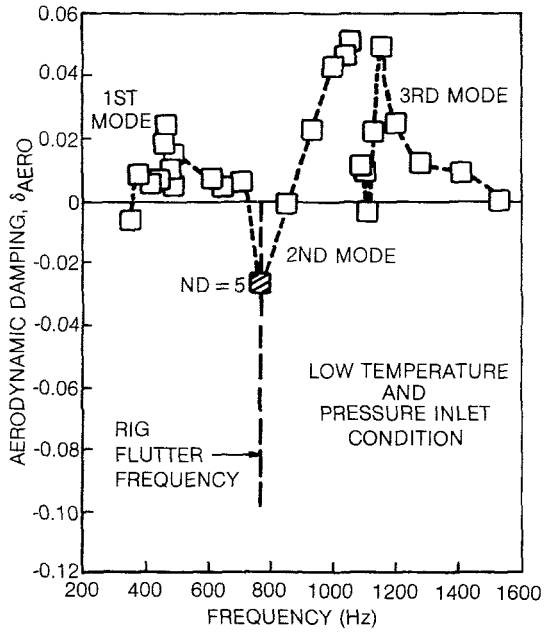

Fig. 14 Fan rotor stall flutter prediction using separated flow aerodynamics

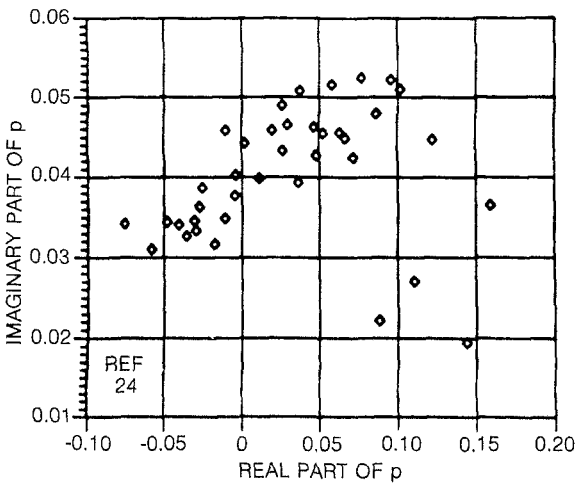

Fig. 15 Effects of mistuning on blade flutter with rigid shroud (test point 125), $S/c = 0.8134$, $\theta = 29.75$ deg, $\eta = 0.44$, $M = 0.795$, $\lambda = 1.79$, $\mu = 0.76$, $N_b = 38$

The branch labels are used to reflect the predominant mode in the flutter response. The actual flutter mode shapes are strongly coupled in this case. For example, the flutter boundary point A in Fig. 13 has the mode contents of 76 percent from the first twin modes, 14.7 percent from the second twin modes and 9.3 percent from the third twin modes. Because of the strong mode coupling during flutter, the flutter boundary is not consistent with the aerodynamic damping result shown in Fig. 11. Figure 11 shows that the 10-nodal-diameter, first-mode, backward-traveling-wave becomes stable when the structural logarithmic decrement reaches 0.008, while Fig. 13 shows stability cannot be reached unless the structural logarithmic decrement is increased above approximately 0.07. This result indicates that, if the calculated aerodynamic damping is small and negative, an equal amount of (positive) structural damping may not be adequate to stabilize the flutter mode when the mode coupling is significant during flutter. The eigenvalue flutter analysis method predicts when the mode coupling is significant and how significant it is.

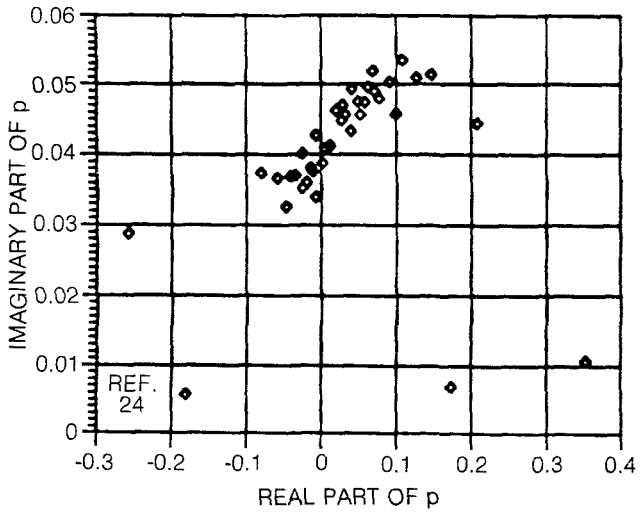

Fig. 16 Effect of mistuning on blade flutter with flexible shroud (test point 125), $S/c = 0.8134$, $\theta = 29.75$ deg, $\eta = 0.44$, $M = 0.795$, $\lambda = 1.79$, $\mu = 0.76$, $N_b = 38$, $(EI)_{Ring} = 336.74$ Nm 2, Support Spring = 139.93 N/m

***(b)* Fan Rotor Rig Second-Bending-Torsion Flutter.** When the rig stall flutter conditions were analyzed, the analysis correctly predicted the critical flutter mode to change from torsion to bending-torsion motion. As shown in Fig. 14, the 5-ND second mode was calculated to be the most negatively damped, and its frequency is very close to the measured test frequency. These stability calculations were very sensitive to flow Mach number. The results shown in Fig. 14 were actually for flow Mach numbers and velocities that were 3 percent lower than those calculated based on test data. Analysis of these lower values was attempted because of promising results for the nominal flow conditions and the conclusion that the change was within the range of normal experimental uncertainty.

These encouraging stall flutter prediction results strongly suggest that further research effort be undertaken to establish a steady flow separation criterion for a judicious application of the separated flow unsteady aerodynamic theory in subsonic flutter predictions.

Analytical Study of Mistuning Effect on Subsonic Stall Flutter

The effect of blade mistuning on subsonic stall flutter has been clearly shown in real engine testing. It is generally accepted that mild blade mistuning of a tuned bladed disk system tends to stabilize the rotor system.

Srinivasan [24] has analyzed the mistuning effect on the subsonic stall flutter margin based on a simplified blade model that assumes a single degree of freedom torsional motion and demonstrated analytically the simultaneous occurrence of traveling waves of various nodal diameters. In this analysis, an eigenvalue problem is formulated with the eigenvector defined as the force between the blade and the support structure and the eigenvalue p defined as

$$p = \frac{\omega^2 - \omega_0{}^2}{\omega_0{}^2}$$

where ω is the system response frequency and ω_0 is the averaged blade frequency. Positive values of the imaginary part of p indicate system stability and negative values indicate system instability.

Along with the mistuning study, Srinivasan further investigated the influence of shroud flexibility on stall flutter margin. Several engine torsional stall flutter incidents that occurred in the same shrouded first fan discussed earlier were

studied. It was found that the shroud flexibility tends to destablize the shrouded rotor blades. Figure 15 shows the stability margin based on a mistuned analysis by considering the above-shroud outer panel as a single-degree-of-freedom oscillator (in torsion) attached to a infinitely rigid shroud foundation. Figure 16 shows a similar result for the case of flexible shroud modeled as a ring. The stability margin is seen to decrease due to the shroud participation in the aeroelastic response. For simplicity, these results were obtained by using Smith's unsteady aerodynamic theory (which does not account for steady air loading) in calculating the aerodynamic forces. Whether this conclusion can be generalized to real three-dimensional rotor blades subject to stalled (loaded or separated) unsteady air loads remains to be seen.

Concluding Remarks

In this paper, some recent advances in the understanding and prediction of jet engine subsonic stall flutter have been reviewed. As a result of the studies reviewed in this paper, the following conclusions are made.

The development in unsteady aerodynamic theories for subsonic stall flutter prediction has been very encouraging, though further effort is needed to improve and eventually qualify the use of separated flow unsteady aerodynamic theory in the formal subsonic stall flutter prediction system. This would involve the basic task of justifying the assumption of mean flow separation during subsonic stall flutter and further development effort to establish useful flow separation criteria. Furthermore, the effects of aerodynamic shock motion and three-dimensional nature of the flow field on stall flutter, which are not considered in present aerodynamic models, have drawn increasingly more attention among workers in aeroelastic research. The eventual development of a practically useful flow model that includes flow separation, shock motion, and three-dimensionality for high subsonic flows appears promising.

For shrouded rotor stages, the fundamental understanding of shroud motion, including its flexibility and interface dynamics, requires fundamental studies. In this effort, the consideration of mistuning along with the shroud motion studies appears important.

Acknowledgments

The authors would like to thank J. D. Jeffers, II (previously) and C. E. Meece of P&WA Government Products Division, who led and contributed significantly to various subsonic stall flutter programs that resulted in a major portion of the analytical results given in this paper. The pioneering effort of A. P. Kurkov of NASA Lewis Research Center and his colleagues in flutter measurement studies is instrumental in providing valuable test data that have guided the analytical flutter prediction effort. D. A. Hilliard, M. Klein, R. Upton, D. Rimkunas, K. S. Reuschel of P&WA and G. J. Micklow previously of P&WA have been contributing significantly to the challenging subsonic stall flutter studies through various R&D programs. The excellent and pioneering research work of A. P. Kurkov of NASA Lewis Research Center and H. Stargardter of P&WA Commercial Engineering Division has constituted part of the discussion given in this paper.

References

1 Jeffers, J. D., II, and Meece, C. E., Jr., "F100 Fan Stall Flutter Problem Review and Solution," *Journal of Aircraft*, Vol. 12, Apr. 1975, pp. 350–357.

2 Mikolajczak, A. A., Arnoldi, R. A., Snyder, L. E., and Stargardter, H., "Advances in Fan and Compressor Blade Flutter Analysis and Prediction," *Journal of Aircraft*, Apr. 1975, pp. 325–332.

3 Lubomski, J. F., "Characteristics of Aeroelastic Instabilities in Turbomachinery - NASA Full Scale Engine Test Results," NASA TM-79085, 1975.

4 Sisto, F., and Perumla, P. V. K., "Lift and Moment Predictions for an Oscillating Airfoil with a Moving Separation Point," ASME Paper 74-GT-28, 1974.

5 Bendiksen, O. O., "Flutter of Mistuned Turbomachinery Rotors," ASME Paper No. 83-GT-153.

6 Kielb, R. E., and Kaza, K. R. V., "Effects of Structural Coupling on Mistuned Cascade Flutter and Response," ASME Paper No. 83-GT-117.

7 Srinivasan, A. V., and Fabunmi, J., "Cascade Flutter Analysis of Cantilevered Blades," ASME Paper No. 83-GT-129.

8 Nieberding, W. C., and Pollack, J. L., "Optical Detection of Blade Flutter," ASME Paper 77-GT-66, Mar. 1977.

9 Kurkov, A. P., and Dicus, J., "Synthesis of Blade Flutter Vibratory Patterns Using Stationary Transducers," ASME Paper 78-GT-160, Apr. 1978.

10 Kurkov, A. P., "Flutter Spectral Measurements Using Stationary Pressure Transducers," *Measurement Methods in Rotating Components of Turbomachinery*, ASME, New York, 1980, pp. 225–233; also ASME JOURNAL OF ENGINEERING FOR POWER, Vol. 103, No. 2, Apr. 1981, pp. 461–467.

11 Kurkov, A. P., "Measurement of Aerodynamic Work During Fan Flutter," NASA TM-82-652, prepared for 1981 ASME Winter Annual Meeting, Washington, D.C., Dec. 15–20, 1981.

12 Stargardter, H., "Subsonic/Transonic Stall Flutter Study," NASA CR-165256, June 1979.

13 Smith, S. N., "Discrete Frequency Sound Generation in Axial Flow Turbomachines," CVDE/A, Turbo/TR29, 1971.

14 Jones, W. P., and Moore, J. A., "Aerodynamic Theory for a Cascade of Oscillating Airfoils in Subsonic Flow," *AIAA Journal*, Vol. 14, No. 5, May 1976, pp. 601–605.

15 Atassi, H., and Akai, T. J., "Effect of Blade Loading and Thickness on the Aerodynamics of Oscillating Cascades," Paper No. 78-227, AIAA 16th Aerospace Science Meeting, Huntsville, Ala., Jan. 16–18, 1978.

16 Verdon, J. M., and Caspar, J. R., "Development of a Linear Aerodynamic Analysis for Unsteady Transonic Cascades," NASA CR-168038, Oct. 1982.

17 Jeffers, J. D., May, A., and Deskin, W. J., "Evaluation of a Technique for Predicting Stall Flutter in Turbine Engines," NASA CR-135423, Feb. 1978.

18 Chi, M. R., "Unsteady Aerodynamic in Stalled Cascade and Stall Flutter Prediction," ASME Paper No. 80/C2/Aero-1, 1980 ASME Aerospace Science Meeting, San Francisco, Aug. 1980.

19 Chi, M. R., "Lifting and Nonlifting Kernel Functions for Cascade and Isolated Airfoils," *AIAA Journal*, Oct. 1980, pp. 1265–1268.

20 Yashima, S., and Tanaka, H., "Torsional Flutter in Stalled Cascade," ASME 77-GT-72, 1977.

21 Carta, F. O., "Coupled Blade-Disc-Shroud Flutter Instabilities in Turbojet Engine Rotors," ASME JOURNAL OF ENGINEERING FOR POWER, Vol. 89, July 1967, pp. 419–426.

22 Chi, M. R., "General Flutter Theory of Turbomachine Rotor Systems," P&WA PM80-285, Apr. 15, 1980.

23 Dugundji, "Flutter Analysis of A Tuned Rotor with Rigid and Flexible Disks," MIT Gas Turbine Report, No. 146, July 1979.

24 Srinivasan, A. V., "Influence of Mistuning on Blade Torsional Flutter," NASA CR-165137, Aug. 1980.

Optimization and Mechanisms of Mistuning in Cascades

E. F. Crawley
Boeing Assistant Professor.

K. C. Hall
Hertz Fellow.

Gas Turbine and Plasma Dynamics Laboratory,
Massachusetts Institute of Technology,
Cambridge, Mass. 02139

An inverse design procedure has been developed for the optimum mistuning of a high bypass ratio shroudless fan. The fan is modeled as a cascade of blades, each with a single torsional degree of freedom. Linearized supersonic aerodynamic theory is used to compute the unsteady aerodynamic forces in the influence coefficient form at a typical blade section. The mistuning pattern is then numerically optimized using the method of nonlinear programming via augmented Lagrangians. The objective of the mistuning is to achieve a specified increase in aeroelastic stability margin with a minimum amount of mistuning. It is shown that a necessary but not sufficient condition for aeroelastic stability is that the blades be self-damped. If this condition is met, an optimized mistuning pattern can be found that achieves a given stability margin for a much lower level of mistuning than is required for the alternate mistuning pattern. However, small errors in the implementation of the optimum mistuning pattern severely reduce the anticipated gains in stability margin. These small errors are introduced by the manufacturing process and by the approximation of the optimum mistuning pattern by patterns of a few discrete blade frequencies. Alternate mistuning, which requires only two blade frequencies, is shown to be relatively insensitive to errors in implementation.

Introduction

Structural mistuning, defined as blade to blade nonuniformity in blade mass and stiffness properties, is present in all bladed disks due to manufacturing uncertainty. Despite the fact that this mistuning is known to affect both the aeroelastic stability and forced response, the aeroelastic analysis of rotors is most often performed for the tuned condition. Several authors have suggested that prescribed mistuning patterns be deliberately introduced to increase the stability of the rotor at its operating point [1–4].

The objective of this study is to develop an inverse design procedure for the optimum selection of a pattern of structural mistuning. To accomplish this, the aeroelastic equations of motion are formulated for a typical supersonic section of a high bypass ratio fan. A degree of difficulty, or cost, of mistuning is defined for each possible mistuning pattern. Using numerical optimization algorithms, the stability of the fan at its aeroelastic design point is then increased while minimizing the cost of the required mistuning. The outgrowth of this optimization is a better understanding of the underlying mechanisms of cascade flutter and the advantages and limitations of structural mistuning. Finally, an assessment of the practical applicability of mistuning to enhance the stability margin of a shroudless fan is performed. This assessment includes considerations of both manufacturing tolerances and the difficulty of maintaining the large number of blade types in inventory necessary for the optimally mistuned rotor configuration.

Contributed by the Gas Turbine Division of THE AMERICAN SOCIETY OF MECHANICAL ENGINEERS and presented at the 29th International Gas Turbine Conference and Exhibit, Amsterdam, The Netherlands, June 4–7, 1984. Manuscript received at ASME Headquarters January 18, 1984. Paper No. 84-GT-196.

Analytic Model of a Mistuned Fan

To simplify the optimization of the fan, a relatively simple aeroelastic model is used. The supersonic unstalled torsional flutter of an unshrouded fan is examined by assuming that flexible blades, each with a single torsional degree of freedom, are attached to a rigid disk. For blades with wide spacings between bending and torsional frequencies, flutter analysis using this single degree of freedom agrees well with coupled bending torsion analysis [5]. The addition of finite disk flexibility changes the details of the analysis, but does not significantly reduce the ability of mistuning to augment the cascade stability [6].

If the dynamics of the blades are represented at a typical section (Fig. 1), the flutter equations of motion expressed in individual blade coordinates are

$$[I_{\alpha i}]\{\ddot{q}_i\} + [\omega_{\alpha i}^2\ I_{\alpha i}]\{q_i\} = \{M_i^m\} \tag{1}$$

To convert the flutter equations to the form of a standard eigenvalue problem, the blades are assumed to undergo simple harmonic motion.

$$q_i = \mathrm{Re}(\bar{q}_i\ e^{j\omega t}) \tag{2}$$

The right-hand side of equation (1) represents the homogeneous, motion-dependent, unsteady aerodynamic moments acting on the blades, which can be determined from any appropriate linearized unsteady aerodynamic model (e.g., [7]). In the derivation of such models, it is assumed that the blades in the cascade undergo harmonic motion in travelling

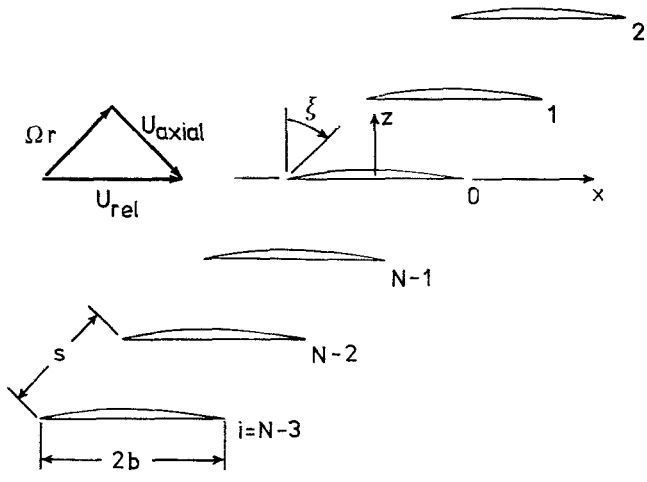

Fig. 1 Cascade geometry

waves of a single interblade phase angle. The resulting unsteady moment coefficients as a function of interblade phase angle can be converted to the more convenient influence coefficient form by a simple linear transformation. The resultant unsteady influence coefficient matrix $[L]$ is in general complex and still a function of the oscillatory frequency ω. The unsteady aerodynamic moments are expressed in this form, since it more clearly reveals the origins of the forces acting on the blades. It will be shown that this formulation simplifies the flutter equations of motion for the mistuned rotor. The unsteady moments acting on the blades are then

$$\{M_i^m\} = \pi\rho b^4\omega^2[L]\{\bar{q}_i\}e^{j\omega t} \tag{3}$$

Introducing equations (2) and (3) into equation (1) results in the complex eigenvalue problem

$$-\omega^2\left[I_{\alpha i}\right]\{\bar{q}_i\} + \left[\omega_{\alpha i}^2\ I_{\alpha i}\right]\{\bar{q}_i\} = \pi\rho b^4\omega^2[L]\{\bar{q}_i\} \tag{4}$$

If equation (4) is divided by $I_R\omega_R^2$ where ω_R and I_R are the torsional frequency and the section moment inertia of the reference blade, then the resulting nondimensional eigenvalue problem is

$$\left[(1+\delta_i)\right]\{\bar{q}_i\} = \Omega^2\left[\left[(1+\epsilon_i)\right] + \frac{1}{\mu r^2}[L]\right]\{\bar{q}_i\} \tag{5}$$

where r and μ are the section nondimensional radius of gyration and mass, and δ_i and ϵ_i are the fractional stiffness and mass mistuning of the ith blade. From equation (5), it is evident that the individual blade mistuning appears explicitly when the aerodynamic moments are expressed in influence coefficient form. This explicit appearance of blade mistuning simplifies the subsequent optimization.

If it is assumed that $[L]$ is constant and can be computed at the reference frequency ω_R, then the eigenfrequencies of equation (5) can be found. Associated with each eigenfrequency is a stability margin ζ_i, which can be interpreted as the structural damping which must be subtracted from the blades to yield pure oscillatory motion. This stability margin gives a good estimate of the actual damping ratio in lightly damped modes [8] and will be used as the figure of merit in the optimization which follows.

The Importance of Blade Self Damping

Each term in the aerodynamic influence coefficient matrix $[L]$ has a unique physical significance. The term in the first row and the second column, for example, designates the moment acting on the first blade due to the motion of the second blade. By the symmetry of the rotor, assuming that the blades are geometrically identical, this must be the same as the moment felt by the second blade due to the motion of the third. The circulant matrix $[L]$ is of the form [3]

$$[L] = \begin{bmatrix} L_0 & L_{N-1} & L_{N-2} & \cdots & L_1 \\ L_1 & L_0 & L_{N-1} & \cdots & L_2 \\ \cdot & \cdot & \cdot & \cdot & \cdot \\ \cdot & \cdot & \cdot & \cdot & \cdot \\ \cdot & \cdot & \cdot & \cdot & \cdot \\ L_{N-1} & L_{N-2} & L_{N-3} & \cdots & L_0 \end{bmatrix} \tag{6}$$

The term L_0 expresses the moment acting on any given blade due to its own motion. It will be shown that this is the

Nomenclature

b = semichord
c = chord
$\mathbf{e}$ = error in mistuning
E = root mean square of errors in mistuning
i_a = active inequality constraints
i_b = inactive inequality constraints
$I_{\alpha i}$ = moment of inertia of section of ith blade
J = Lagrangian cost function
J_a = augmented Lagrangian cost function
$1_{\beta n}$ = unsteady moment coefficient due to nth interblade phase angle travelling wave
$[L]$ = aerodynamic influence coefficient matrix
L_K = the Kth influence coefficient
M_i^m = unsteady moment acting on ith blade due to motion of blades
N = number of blades
q_i = displacement of ith blade
$q_{\beta n}$ = displacement of nth travelling wave
r = nondimensional radius of gyration
s = complex plane representation of nondimensional eigenfrequency, $s=j\Omega$
V = reduced velocity
W = weighting on inequality penalty function
β = interblade phase angle
δ_i = stiffness mistuning of the ith blade
ϵ_i = mass mistuning of the ith blade
ζ_i = stability margin of the ith eigenvalue
$\bar{\zeta}$ = required stability margin
η = inequality constraint Lagrange multiplier
θ = inequality constraint function
ϕ = objective cost function
μ = nondimensional mass of section of blade
$\omega_{\alpha i}$ = ith natural blade frequency
ω_R = reference blade frequency
Ω = nondimensional eigenfrequency
Ω_R = reference nondimensional eigenfrequency
$\tilde{\Omega}$ = perturbation of nondimensional eigenfrequency

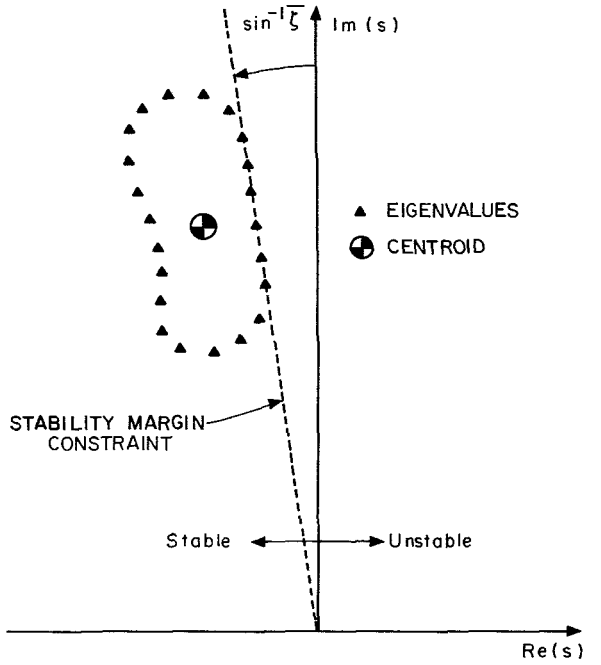

Fig. 2 s-plane interpretation of eigenvalues showing centroid and stability margin constraint

only term in the influence coefficient matrix which can provide a stabilizing influence on the rotor. To show the importance of this term, consider the problem with mass mistuning only. The eigenvalue problem is then given by

$$\frac{1}{\Omega^2}\{\bar{q}_i\} = \left[\left[(1+\epsilon_i)\right] + \frac{1}{\mu r^2}[L]\right]\{\bar{q}_i\} \tag{7}$$

where $1/\Omega^2$ represents the eigenvalues of the matrix on the right-hand side of equation (7). Making use of the matrix property that the sum of the eigenvalues of a matrix equals the trace of the matrix, we have

$$\frac{1}{N}\sum_{K=0}^{N-1}\frac{1}{\Omega_K^2} = 1 + \frac{L_0}{\mu r^2} + \frac{1}{N}\sum_{i=0}^{N-1}\epsilon_i \tag{8}$$

In the absence of mistuning and unsteady aerodynamic moments, the reference blade vibrates at the nondimensional eigenfrequency $\Omega = \Omega_R = 1$. In the presence of small amounts of mistuning and aerodynamic moments, which are small compared to the elastic and inertial moments, Ω will still be nearly equal to Ω_R. The eigenfrequency Ω can be expressed as a sum of its reference value and a perturbation $\tilde{\Omega}$ from the reference value Ω_R.

$$\Omega = \Omega_R + \tilde{\Omega} = 1 + \tilde{\Omega} \tag{9}$$

The last step in equation (9) is due to Ω_R being unity. Hence the eigenvalues of equation (7) are

$$\frac{1}{\Omega^2} = \frac{1}{1+2\tilde{\Omega}+\tilde{\Omega}^2} = 1 - 2\tilde{\Omega} + 0(\tilde{\Omega}^2) \tag{10}$$

For convenience, let $s = j\Omega$, which gives the s-plane interpretation to the eigenvalues. Substitution of equation (10) into equation (8) yields that the centroid of the eigenvalues (Fig. 2) is given approximately by

$$\begin{aligned} \mathrm{Re}(<s>) &= \frac{1}{2}\mathrm{Im}\left(\frac{L_0}{\mu r^2}\right) \\ \mathrm{Im}(<s>) &= 1 - \frac{1}{2}\mathrm{Re}\left(\frac{L_0}{\mu r^2}\right) - \frac{<\epsilon>}{2} \end{aligned} \tag{11}$$

That is, the real part of the centroid, $<s>$, depends on the imaginary part of L_0, and the imaginary part of the centroid depends on the real part of L_0 and the mean value of the mistuning.

The location of the eigenvalues in the s-plane can be considered to be distributed around the centroid. Recalling that the system will be unstable if any eigenvalue is in the right half-plane, the objective is to move the least stable eigenvalue as far to the left as possible. This can be achieved either by moving the centroid to the left, or by reducing the size of the distribution about the centroid, which pulls the rightmost eigenvalue to the left.

Interpreted in this light, equation (10) is an important result. It shows that the centroid of the eigenvalues lies in the left half-plane if and only if $\mathrm{Im}(L_0)$ is less than zero. Since a necessary condition for aeroelastic stability of the rotor is that the centroid of the eigenvalues lies in the left half-plane, it can be deduced that a necessary but not sufficient condition for stability is that $\mathrm{Im}(L_0)$ be less than zero. This is equivalent to the condition that the blades be self-damped.

The location of the centroid is set by the average value of the mass (and stiffness) of the blades and the blade self-damping term. The distribution of the eigenvalues about the centroid is controlled by the nonuniformity in the mass and stiffness of the blades and by the off-diagonal terms in the aerodynamic influence coefficient matrix (i.e., the unsteady cascade influences in the aerodynamics).

The objective of deliberate mistuning is to use the mechanism of mechanical mistuning to reduce the influence of the blade to blade aerodynamic coupling and to move the less stable eigenvalues toward the centroid. Note that no amount of mistuning will cause the centroid to move in a stabilizing direction and no amount of mistuning can increase the stability margin of the rotor beyond that given by the blade self damping.

The Mistuning Problem as a Constrained Minimization

Having established the fundamental limitations of stability enhancement by mistuning, the next step is to optimize the mistuning pattern. It has been suggested that alternate mistuning may be nearly optimum [3]. In this section, a formal definition of optimum mistuning will be presented, and a method for finding the optimum mistuning pattern will be discussed. The steps to be taken are: first, to choose an appropriate objective cost function, which is a measure of the difficulty of mistuning the rotor; second, to define the set of constraints which must be satisfied; and third, to solve this constrained minimization problem using numerical optimization techniques.

The first step is to define an objective cost function which is a measure of the difficulty of implementing any given mistuning pattern. A cost function that gives a reasonable measure of the difficulty of mistuning and is easily implemented in the optimization is

$$\phi(\epsilon) = \left\{\left(\sum_{i=0}^{N-1}\epsilon_i^n\right)\Big/N\right\}^{1/n} \tag{12}$$

where n is an even integer. This cost function strongly penalizes the blades with the largest amount of mistuning. Thus it tends to keep the required mistuning within a range which can be practically implemented. While equation (12) with $n=4$ was used throughout this study, any other well-behaved cost function could be used.

The next step is to define an appropriate set of constraints. Since the objective is to increase the stability margin of the rotor, one set of constraints requires that each mode of the rotor have a stability margin greater than or equal to some minimum stability margin $\bar{\zeta}$ (Fig. 2). This is given as N inequality constraints of the form

$$\theta_i(\epsilon) = \zeta_i - \bar{\zeta} \geq 0, \quad i = 0,1, \ldots, N-1 \tag{13}$$

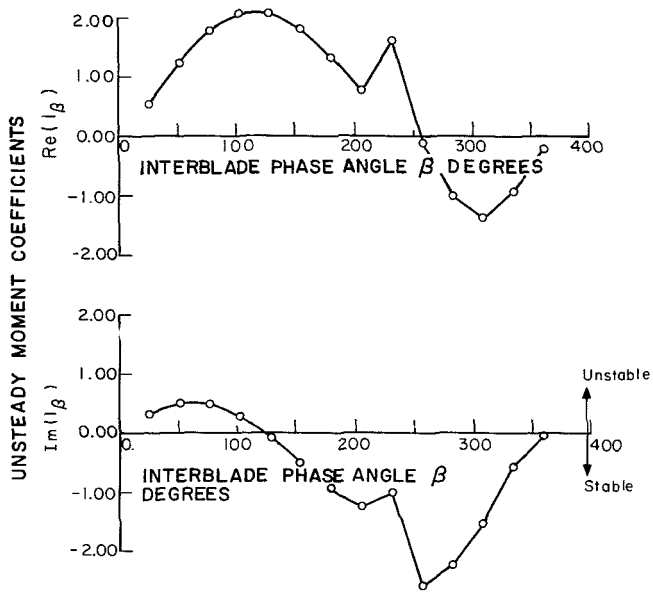

Fig. 3 Unsteady aerodynamic moment coefficients as a function of interblade phase angle

where

$$\zeta_i = -\mathrm{Re}(s_i)/|s_i| \tag{14}$$

To simplify the optimization procedure, only mass mistuning was considered. Furthermore, it was assumed that mass could be added but not removed from the blades. The additional N constraints expressed in inequality form are

$$\theta_{i+N}(\epsilon) = \epsilon_i \geq 0, \quad i = 0,1, \ldots, N-1 \tag{14}$$

At this point, the optimization statement has been completely formulated. The cost function to be minimized is a measure of the level of mistuning in the rotor while the constraints are that the rotor must meet certain minimum stability requirements and that the mistuning pattern must be of an acceptable form. The last step is to numerically compute the mistuning pattern which results in a constrained minimum. It is convenient to introduce the Lagrangian cost function as a sum of the objective cost function, plus the constraint functions multiplied by Lagrange multipliers.

$$J = \phi + \eta^T \theta \tag{15}$$

It can be shown that, except in rate circumstances known as abnormal cases, the necessary conditions for a constrained minimum are given by the Kuhn-Tucker conditions [9]

$$\left.\begin{aligned} \nabla J &= 0 \\ \eta_j \theta_j &= 0 \\ \eta_j &\leq 0 \\ \theta_j &\geq 0 \end{aligned}\right\} \; j = 0,1,2, \ldots, 2N-1 \tag{16}$$

From equation (16), it is seen that the introduction of the Lagrange multipliers causes the constrained minima to be stationary points of J. Unfortunately, these stationary points may be maxima, minima, or saddle points. Hence one may not find all the stationary points of J by searching for the minima of J. This problem may be remedied by adding a quadratic-like quantity which is zero along the constraints and positive if the constraints are violated. Hence the augmented Lagrangian cost function J_a [9] is

$$J_a = \phi + \eta^T \theta + \frac{1}{2} W \sum_{i_a} \theta_i^2 + \frac{1}{2} W \sum_{i_b} (\theta_i - |\theta_i|)\theta_i \tag{17}$$

where i_a indicates the set of active constraints (i.e., constraints with nonzero Lagrange multipliers), i_b indicates the set of inactive constraints, and W is some positive number which is large enough to insure that the augmented Lagrangian cost J_a is a minimum at the constrained minima of the objective cost function ϕ.

If the Lagrange multipliers are known exactly and W is large enough, then finding the minima of the augmented Lagrangian cost is equivalent to finding the stationary points of the Lagrangian cost J. However, if the Lagrange multipliers are known only approximately but W is very large, the minima of J_a will be approximately the stationary points of J. This is the foundation of the method known as "nonlinear programming via augmented Lagrangians."

Location of the minimum constrained cost by this method is summarized as follows: initial values of the penalty function coefficient W and the Lagrange multipliers η are chosen. The augmented Lagrangian cost function is then considered to be a function of the independent mistuning variables ϵ. This function is then minimized by an appropriate unconstrained minimization technique. The Broyden-Fletcher-Shanno (BFS) algorithm [10] was chosen because of its robust performance and fast convergence to a minimum [11]. Once the minimum of the augmented Lagrangian cost is found, the values of the Lagrange multipliers are updated by the equations

$$\text{for } \eta_{i_{\text{old}}} = 0, \quad \eta_{i_{\text{new}}} = \begin{cases} W(\theta_i - |\theta_i|) \text{ if } < 0 \\ 0 \quad \text{otherwise} \end{cases}$$

$$\text{for } \eta_{i_{\text{old}}} < 0, \quad \eta_{i_{\text{new}}} = \begin{cases} \eta_{i_{\text{old}}} + W\theta_i \text{ if } < 0 \\ 0 \quad \text{otherwise} \end{cases} \tag{18}$$

At this point, the value of the penalty function coefficient may also be increased. The Kuhn-Tucker conditions are then evaluated to determine if the necessary conditions for a constrained minimization have been met. If they have not been met, the entire process is repeated until convergence.

Results of the Aeroelastic Optimization

As an example, the optimum mistuning pattern of a high bypass ratio shroudless fan will be determined by considering the behavior at the 85 percent span. At this typical section, the relative Mach number, M, is 1.317, the reduced frequency, k, is 0.495; the stagger angle, ξ, is 58.99 deg; the solidity, σ, is 1.404; the airfoil to fluid mass ratio, μ, is 181.8; and the nondimensional radius of gyration, r, is 0.4731. The fan on which this example calculation is based has 43 blades. However, in order to reduce the amount of computation required, optimizations were performed on rotors with 12, 13, and 14 blades, but with all other geometric and aerodynamic parameters of the 43 bladed fan, including the solidity, held fixed. The unsteady moment coefficients are computed from a supersonic linearized aerodynamic model [7]. Figure 3 shows the unsteady moments predicted by this theory as a function of interblade phase angle for the 14-bladed rotor. Note that for the interblade phase angles of 26, 51, 77, and 103 deg, the imaginary part of $l_{\beta n}$ is greater than zero, implying that for the tuned rotor, these modes are unstable.

The aerodynamic moments are then transformed from the interblade phase angle form to the influence coefficient form by use of the transformation [12, 14]

$$L_K = \frac{1}{N} \sum_{n=0}^{N-1} l_{\beta n} e^{j\frac{2\pi K n}{N}} \tag{19}$$

The transformed moments are shown in Fig. 4. The term L_K expresses the influence the motion of the $(K+i)$th blade has on the ith blade. Note that $\mathrm{Im}(L_0)$ is less than zero indicating that the blades are self damped. Hence it may be possible to stabilize the rotor by mistuning. Figure 4 also reveals that the neighboring blades exert the dominant aerodynamic moments

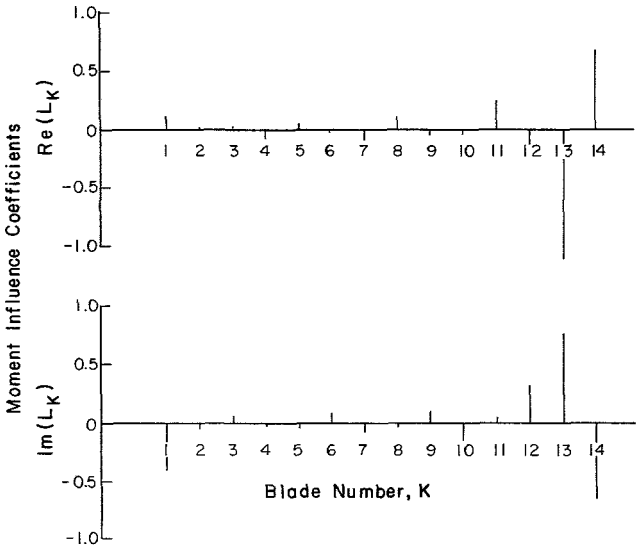

Fig. 4 Unsteady aerodynamic moment coefficients showing the influence of the $(K+i)$th blade on the ith blade (note that $L_0 = L_{14}$)

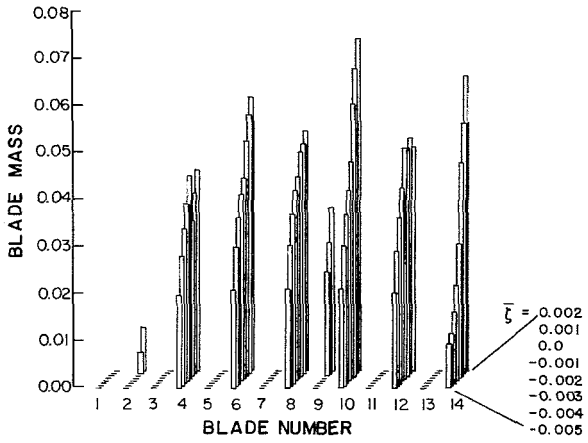

Fig. 5 Optimum mistuning patterns of 14-bladed rotor

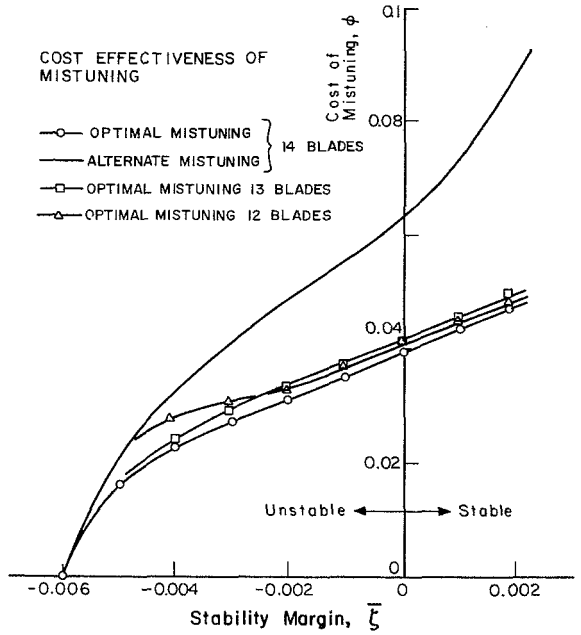

Fig. 6 Cost effectiveness of mistuning for 12-, 13-, and 14-bladed rotors

on a given blade. The aerodynamic influence matrix is therefore strongly banded.

One interpretation of equation (19) is that the aerodynamic influence coefficients L_K are exactly the Fourier coefficients of a Fourier series representation of the aerodynamic moments as a function of interblade phase angle. Said another way, L_0, the blade's self-influence, is just the average value of $1_{\beta n}$. Likewise, L_1 and L_{N-1}, the influence of the two neighboring blades on a given blade, are related to the first harmonic of $1_{,\beta n}$ as a function of β_n. Examinations of unsteady force coefficients from a number of analytic [7, 13] and experimental [14–17] sources all demonstrate the dominant influence of the few neighboring blades. It would be expected that any effective mistuning scheme would sharply reduce the influence of these adjacent blades.

Knowing the aerodynamic influence coefficients, the procedure for finding the optimum mistuning pattern was straightforward. First, initial guesses were chosen for the optimum mass mistuning pattern and the Lagrange multipliers. A constrained minimum was then found for the case in which the stability margin of all the modes was greater than or equal to -0.005. After the optimum mistuning pattern was determined for $\bar{\zeta} = -0.005$, the optimum mass mistuning was found for $\bar{\zeta} = -0.004$, using as initial guesses the optimum mass mistuning and Lagrange multipliers from the $\bar{\zeta} = -0.005$ case. The optimum mistuning patterns for the cases of $\bar{\zeta} = -0.003$, -0.002, -0.001, 0, 0.001, and 0.002 were found sequentially in an analogous way. It should be noted that at each step there are in fact many constrained minima and there is no guarantee that the local minimum found is a global minimum. The actual minimum found depends on the initial guesses for the mistuning pattern, the Lagrange multipliers, and the value of the penaltity function coefficients. While an exhaustive search for the global minimum was not performed, the local optimum patterns presented are the lowest cost local minima found in each case. Optimum mistuning patterns for stability margins larger than 0.002 could not be found as the numerical procedure failed to coverge if the required stability margin was too large.

The optimum mistuning patterns determined by this procedure for a 14-bladed rotor are presented in Fig. 5. Beginning with the case of $\bar{\zeta} = -0.005$, the pattern of mistuning is "almost alternate." The odd numbered blades have no change from their nominal mass (i.e., $\epsilon_i = 0$). The even numbered blades all have nearly equal nonzero mass mistuning, except for blade 2, which remains at its nominal mass, and blade 14, which has a mass mistuning of about half that of the other even numbered blades. This almost alternate mistuning pattern grows in magnitude for increasing $\bar{\zeta}$, but does not change in nature until $\bar{\zeta} = 0.0$. At this value of required stability margin, the mass mistuning of blade 9 becomes nonzero. At $\bar{\zeta} = 0.001$, the mass mistuning of blade 2 also becomes small but nonzero.

Notice that the mistuning patterns shown in Fig. 5 all resemble to some degree a truly alternate mistuning pattern. One might expect that the optimum mistuning patterns are not significantly more cost effective than alternate mistuning. This is not the case, however, as is shown in Fig. 6. The curves show the cost of mistuning versus the required stability margin. The optimum mistuning patterns are seen to achieve a given stability margin at a lower level of mistuning than for alternate mistuning. The similarity of the curves for 12-, 13-, and 14-bladed rotors indicate that there is no fundamental difference in the ability to optimally mistune rotors of odd, even, or prime numbers of blades.

Some insight into why optimum mistuning patterns are effective can be gained by examining the eigenvalues in the complex plane. Figures 7–9 show the eigenvalues for $\bar{\zeta} = -0.00602$ (tuned), 0.0, and 0.002. As the stability margin

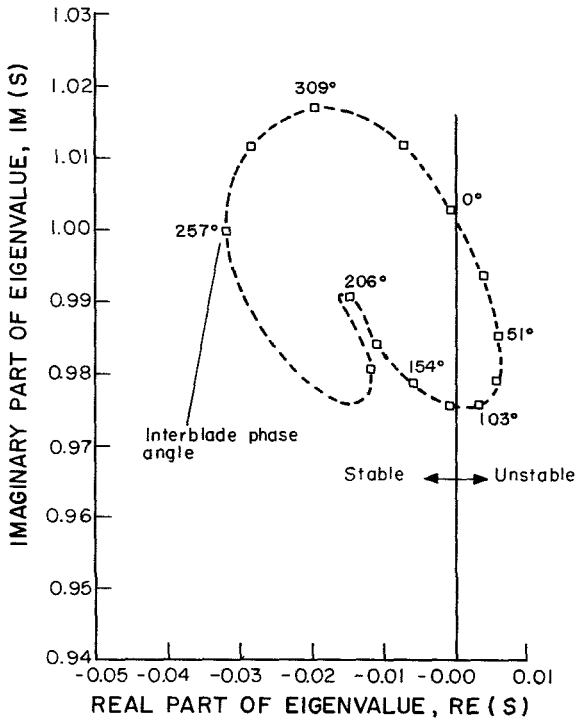

Fig. 7 Eigenvalues of tuned rotor

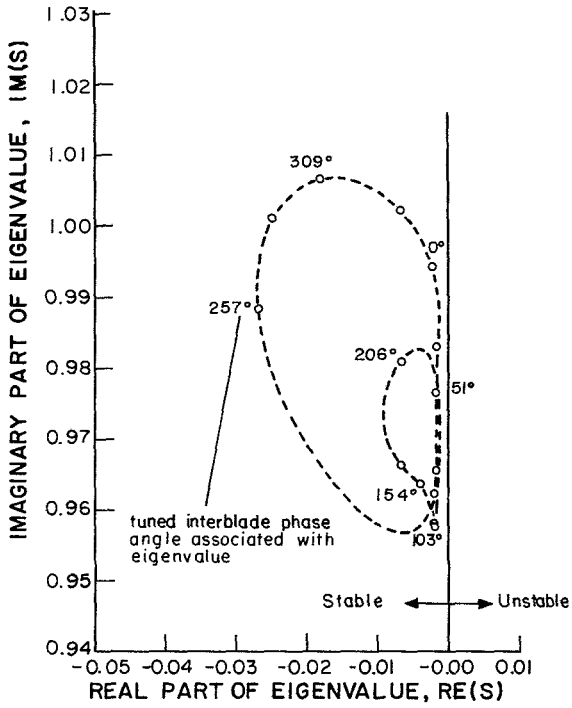

Fig. 9 Eigenvalues of optimally mistuned rotor: $\tilde{\zeta} = 0.002$

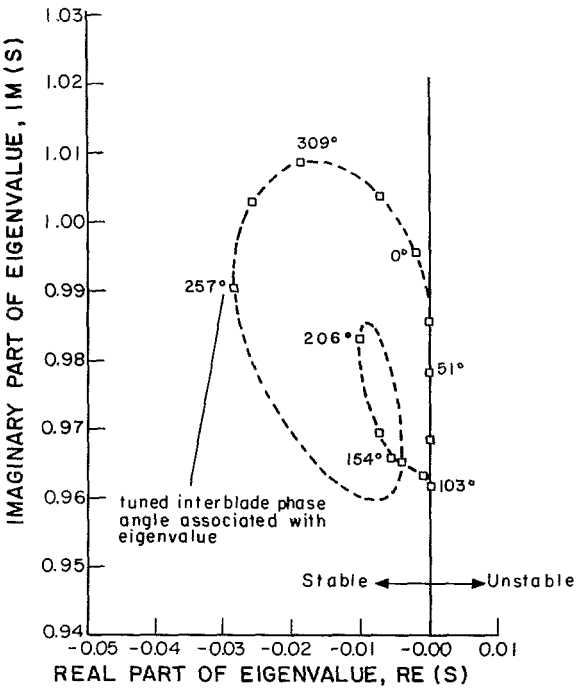

Fig. 8 Eigenvalues of optimally mistuned rotor: $\tilde{\zeta} = 0$

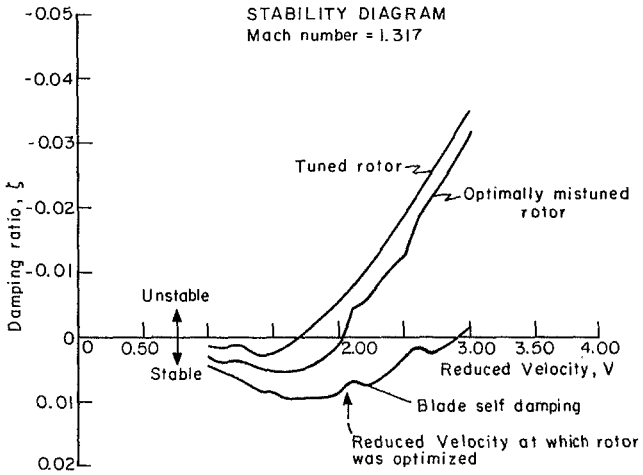

Fig. 10 "V-g" stability diagram of a mistuned rotor ($\tilde{\zeta} = 0.002$) with limiting cases

constraint is increased, an increasing number of eigenvalues lie along the constraint. In contrast, only one of the N eigenvalues of the alternately mistuned rotor will in general lie on the constraint.

Upon examination of a number of optimum mistuning patterns such as those shown in Fig. 5, certain characteristic trends become apparent. An almost alternate pattern is evident, which serves to reduce the dominant influence of the neighboring blades (Fig. 4). This almost alternate mistuning pattern is broken at several points around the rotor, as with blades 2 and 9 in Fig. 5. It is believed that this break disrupts the longer wavelength communication of signals around the rotor. Finally, a certain fine structure of the mistuned blades is evident, the details of which are dependent on the local minimum found.

Off-Design Performance of the Optimally Mistuned Rotor

The rotor thus far has been aeroelastically optimized at a single aeroelastic design point. A modified V-g diagram can be constructed which shows the negative of the stability margin (or damping ratio) of the least stable eigenvalue versus the reduced velocity of operation for a constant Mach number (Fig. 10). The upper curve in Fig. 10 shows the stability margin of the tuned rotor. For rotors which can be modeled with a single degree of freedom per blade, the tuned rotor is necessarily less stable than a mistuned rotor [3, 18]. The lower curve is the stability margin associated with the centroid of eigenvalues. Recall that this is to first order the best stability margin that can be achieved by mistuning. Hence the stability curve for the rotor that was optimally mistuned with a

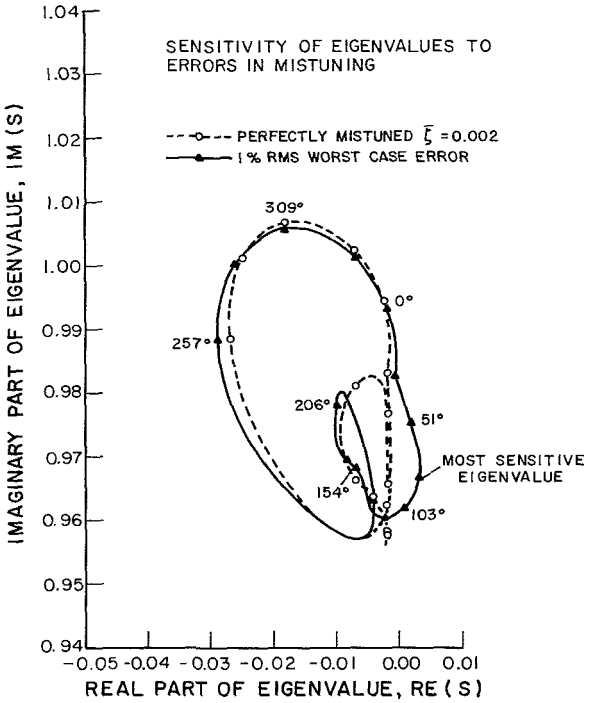

Fig. 11 Sensitivity of optimally mistuned eigenvalues to errors in mistuning

stability margin constraint of $\bar{\zeta} = 0.002$ (at the aeroelastic design point) should, and does, lie between these two curves. For this mistuning case, the flutter reduced velocity has been raised approximately 20 percent at a constant Mach number. Such an improvement could be used by the designer to reduce the chord of the blades.

An important remaining issue, which directly impacts the practical application of mistuning, is the sensitivity of the aeroelastic behavior of the rotor to errors in implementation. Although the designer may specify a certain mistuning pattern, the manufacturing process places limits on the tolerances which can be maintained. The actual mistuning pattern will be somewhat different than the optimum, and can be expressed as

$$\epsilon_i = \epsilon_{i_{\text{specified}}} + e_i \tag{20}$$

where e_i is the error in mistuning.

To investigate this problem, errors were introduced into the optimally mistuned 14-bladed rotor with a stability margin of 0.002. The procedure was to compute the worst-case arrangement of the error, which is bound to occur eventually in the assembly of a large number of rotors, and then assess the degradation of the stability margin arising from that worst case. To find the worst possible imperfectly mistuned pattern, the gradient of the stability margin, $\nabla\zeta_n$, of each of the N eigenvalues was found with respect to the mistuning variables, ϵ. The actual mistuning patterns were then taken to be

$$\epsilon_i = \epsilon_{i_{\text{specified}}} - \frac{E\sqrt{N}\nabla\zeta_n}{\|\nabla\zeta_n\|}, \quad n=0,1,\ldots,N-1 \tag{21}$$

The term $-\nabla\zeta_n/\|\nabla\zeta_n\|$ is the unit vector which indicates the pattern of error that is most destabilizing to the nth eigenvalue. The unit vector is scaled by $E\sqrt{N}$, where E is the root mean square of the mass mistuning errors. The rotor was mistuned in this fashion for each of the N eigenvalues. Of these N cases, the one with the most negative stability margin is the worst possible arrangement of the error. For an RMS scatter of 1 percent in mass mistuning, it was found that the optimally mistuned rotor's stability was reduced from 0.002 to −0.00317 (Figs. 11 and 12). Hence it is seen that the optimally mistuned rotor is very sensitive to errors in mistuning.

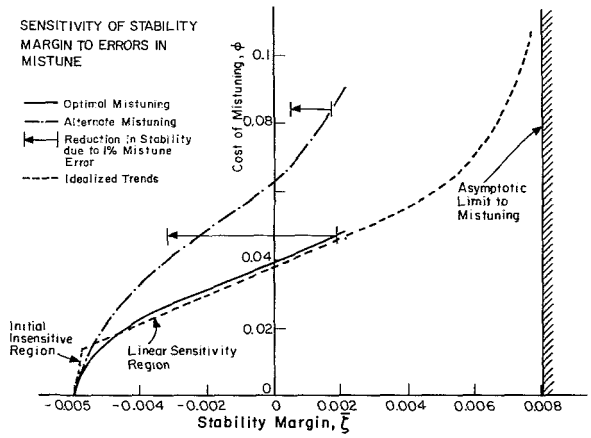

Fig. 12 Sensitivity of stability margin to errors in mistuning

This same sensitivity analysis was applied to an alternately mistuned rotor with a perfectly mistuned stability margin of 0.00171. For 1 percent RMS scatter in mass mistuning, the stability margin was reduced from 0.00171 to 0.00047 as shown in Fig. 12. This shows that although alternate mistuning is not as cost effective as optimum mistuning, it is much more robust, that is, less sensitive to errors in the implementation of mistuning.

Some insight into this difference in sensitivity can be gained by examining the idealized trends in Fig. 12. These idealized trends can be divided into three regions. For the first few percent of mistuning introduced into the tuned rotor, very little change in stability occurs. In fact, it can be shown that for the first increment of mass mistuning of blades with a single degree of freedom, no change in stability occurs [18, 19]. Since normal manufacturing tolerances result in an RMS frequency scatter of only a few percent, most of these rotors lie within the initial insensitive region. Because of this, different builds of the same production rotor have similar flutter boundaries and can be modeled as tuned in flutter analysis.

Beyond the first few percent of mistuning, the trend enters an approximately linear region of sensitivity, i.e., linearly increasing stability with increasing mistuning. In this region, the stability of the optimum pattern is more sensitive to mistuning than the alternate pattern. Eventually the asymptotic limit of stability, the stability margin of the centroid of eigenvalues, is approached and the cost per increase in stability rises sharply.

This idealized trend can be used to explain the sensitivity of the optimum patterns. Figure 12 shows that the optimum cost curve has a very shallow slope at $\bar{\zeta} = 0.002$. This implies that a small change in mistuning, if introduced correctly, can result in a large increase in stability. But for the same reason, small errors in mistuning can cause large decreases in stability. On the other hand, alternate mistuning is relatively insensitive to errors in mistuning but is not nearly optimal. Thus there is a clear design trade-off between optimality and robustness of design.

Approximations to the Optimum Mistuning Patterns

The cost function used in the optimization reflects only one of the true costs of building a mistuned rotor. The real difficulty is not only in the level of mistuning required, but also in the complexity of the mistuning pattern and the number of different blades which must be manufactured and kept in inventory. For example, the optimum mistuning pattern of the 14-bladed rotor analyzed in this study requires nine different blade frequencies. To produce realistic patterns, the optimum mistuning patterns have been approximated with patterns made up of only a few tones.

Table 1 Three tone, suboptimum mistuning patterns

		Mistuning Pattern						
Blade number	Optimum	3 a	3 b	3 c	3 d	3 e	3 f	3 g
1	0.00%	0.00%	0.00%	0.00%	0.00%	0.00%	0.00%	0.00%
2	0.94	0.00	0.00	6.00	0.00	0.00	6.00	0.00
3	0.00	0.00	0.00	0.00	0.00	0.00	0.00	0.00
4	4.27	5.00	6.00	6.00	6.00	6.00	6.00	6.00
5	0.00	0.00	0.00	0.00	0.00	0.00	0.00	0.00
6	5.81	6.00	7.00	7.00	7.00	8.00	8.00	9.00
7	0.00	0.00	0.00	0.00	0.00	0.00	0.00	0.00
8	5.09	5.00	6.00	6.00	6.00	6.00	6.00	6.00
9	3.47	5.00	0.00	0.00	6.00	6.00	6.00	6.00
10	7.05	6.00	7.00	7.00	7.00	8.00	8.00	9.00
11	0.00	0.00	0.00	0.00	0.00	0.00	0.00	0.00
12	4.76	5.00	6.00	6.00	6.00	6.00	6.00	6.00
13	0.00	0.00	0.00	0.00	0.00	0.00	0.00	0.00
14	6.26	6.00	7.00	7.00	7.00	8.00	8.00	9.00

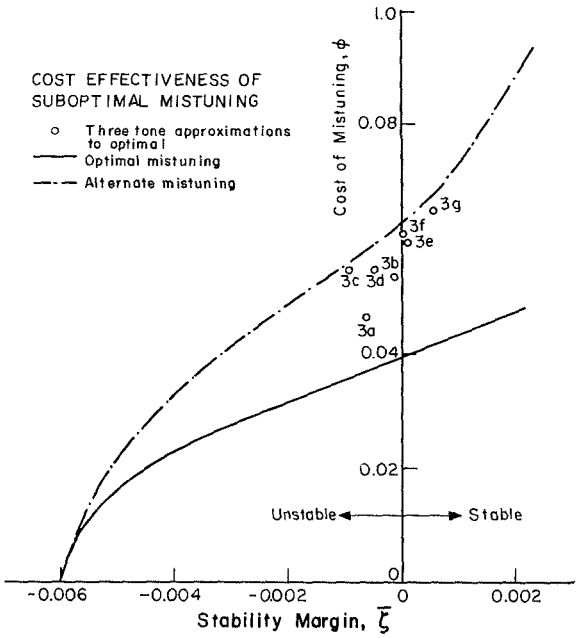

Fig. 13 Cost effectiveness of three tone suboptimum mistuning patterns

Suboptimum mistuning patterns were selected using the optimum mistuning pattern for $\bar{\zeta} = 0.002$ as a guide. Table 1 shows various suboptimum mistuning patterns that were considered, each of which uses three tones to approximate the optimum mistuning patterns. Figure 13 shows the cost of the three-tone suboptimum mistuning patterns versus the stability margin they achieved. Notice that all the suboptimum mistuning patterns have costs slightly less than the alternate mistuning pattern. The results of suboptimum mistuning patterns with two and four tones showed similar results [19]. It appears that the strength of the optimum mistuning patterns lies in the detailed structure of the patterns and not in the grosser features. Thus the very features which make the pattern difficult to implement, that is, the subtle details of the mistuning structure, also account for its optimality.

Conclusions

1 The aeroelastic eigenvalues form a pattern around their centroid. The location of the centroid is controlled by the average blade mechanical properties and the blade self-damping. The criterion that the blades be self-damped is a necessary condition for aeroelastic stability. The distribution of the eigenvalues about the centroid is due to the off-diagonal terms in the aerodynamic influence coefficient matrix, that is, by the unsteady aeroelastic influence of the neighboring blades. This pattern of eigenvalues can be modified by mistuning the rotor. Mistuning makes use of the existing damping to stabilize the rotor by decreasing the blade-to-blade aerodynamic influences.

2 An inverse design procedure has been developed which arrives at an optimum pattern of blade structural mistuning for a given increase in aeroelastic stability margin. The optimum pattern is significantly more cost effective than alternate mistuning. The success of optimum mistuning does not depend on an even number of blades being present, as similar results are found for rotors with even, odd, and prime numbers of blades. The optimum mistuning pattern has three characteristic trends: an almost alternate pattern, which is broken at several points around the rotor, and some additional fine detail. The optimum pattern was found to be sensitive to errors in mistuning, and its practical implementation using only a small number of different blade frequencies significantly diminishes the benefits of optimum mistuning.

3 Three distinct regions of mistuning influence were identified: an initially insensitive region; a region of approximately linear sensitivity; and an asymptotic region of insensitivity. Most current rotors, which are designed without deliberate mistuning, operate in the initial insensitive region. Thus they can be analyzed as tuned and the presence of small amounts of mistuning will only enhance the aeroelastic stability. In contrast, a rotor which incorporates deliberate mistuning should be designed to operate in the region of asymptotic insensitivity, i.e., with a relatively large amount of mistuning, so that small errors in mistuning will not adversely affect the flutter boundaries of rotors in service.

Acknowledgments

The authors wish to acknowledge the support of the NASA Lewis Research Center under grant NSG-3079 with Dr. John Adamczyk, Mr. Calvin Ball, and Mr. Donald Boldman serving as technical monitors. The authors also wish to thank the Fannie and John Hertz Foundation which has provided financial support to both the authors. They further wish to acknowledge the constructive interaction with Drs. A. V. Srinivasan, O. O. Bendiksen, R. E. Kielb, and K. R. V. Kaza, and the practical insight contributed by Mr. Hans Stargardter.

References

1 Kaza, K. R. V., and Kielb, R. E., "Effect of Mistuning on Bending-Torsion Flutter and Response of a Cascade in Incompressible Flow," presented at the AIAA Dynamics Specialists Conference, Atlanta, Ga., Apr. 9–11, 1981; (also NASA Technical Memorandum 81674).

2 Kielb, R. E., and Kaza, K. R. V., "Aeroelastic Characteristics of a Cascade of Mistuned Blades in Subsonic and Supersonic Flows," presented at the ASME Eighth Biennial Engineering Division Conference, Hartford, Conn., Sept. 20–23, 1981; (also NASA Technical Memorandum 82631).

3 Bendiksen, O. O., "Flutter of Mistuned Turbomachinery Rotors," ASME Paper No. 83-GT-153 presented at the ASME 28th International Gas Turbine Conference, Phoenix, Ariz., March 27–31, 1983.

4 Srinivasan, A. V., "Influence of Mistuning on Blade Torsional Flutter," NASA CR-165137, Aug. 1980.

5 Bendiksen, O. O., and Friedmann, P. P., "The Effect of Bending-Torsion Coupling on Fan and Compressor Blade Flutter," ASME Paper No. 81-GT-163 presented at the ASME International Gas Turbine Conference, Houston, Texas, Mar. 9–12, 1981.

6 Kielb, R. E., and Kaza, K. R. V., "Effects of Structural Coupling on Mistuned Cascade Flutter and Response," ASME Paper No. 83-GT-117, 1983.

7 Adamczyk, J. J., and Goldstein, M. E., "Unsteady Flow in a Supersonic Cascade with Subsonic Leading-Edge Locus," *AIAA Journal*, Vol. 16, No. 12, Dec., 1978.

8 Dugundji, J., and Bundas, D. J., "Flutter and Forced Response of Mistuned Rotors Using Standing Wave Analysis," AIAA Paper No. 83-0845, presented at the 24th AIAA/ASME/ASCE/AHS Structures, Structural Dynamics and Materials Conference, Lake Tahoe, Nev., May 2–4, 1983.

9 Pierre, D. A., and Lowe, M. J., *Mathematical Programming via Augmented Lagrangians: An Introduction with Computer Programs*, Addison-Wesley, Reading, Mass., 1975.

10 Broyden, C. G., "The Convergence of a Class of Double-rank Minimization Algorithms," *Journal of the Institute of Mathematics and Applications*, Vol. 6, 1970, pp. 76–90 and 222–231.

11 Dixon, L. C. W., "The Choice of Step Length, a Crucial Factor in the Performance of Variable Metric Algorithms," presented at the Conference on Numerical Methods for Nonlinear Optimization, University of Dundee, Scotland, June 28–July 1, 1971.

12 Srinivasan, A. V., and Fabunmi, J. A., "Cascade Flutter Analysis of Cantilevered Blades," ASME Paper No. 83-GT-129, presented at the ASME 28th International Gas Turbine Conference and Exhibit, Phoenix, Ariz., Mar. 27–31, 1983.

13 Smith, S. N., "Discrete Frequency Sound Generation in Axial Flow Turbomachines," ARC Reports and Memoranda No. 3709, Mar., 1972.

14 Samoylovich, G. S., *Nestatsionarnoye Obtekaniye i Aerouporugiye Kolebaniya Reshetok Turbomashin*, Izd-Vo Nauka, Moscow, 1969, pp. 1–444; (translated version "Unsteady Flow Around and Aeroelastic Vibrations in Turbomachine Cascades," prepared by the Translation Division Foreign Technology Division, WP-AFB, Ohio FTB-HT-23-242-70, Feb. 23, 1971.)

15 Hanamura, Y., Tanaka, H., and Yamaguchi, K., "A Simplified Method to Measure Unsteady Forces Acting on the Vibrating Blades in Cascade," *Bulletin* of the JSME, Vol. 23, No. 180, June 1980.

16 Carta, F. O., "Unsteady Gapwise Periodicity of Oscillating Cascaded Airfoils," ASME Paper No. 82-GT-286, 1982.

17 Riffel, R. E., and Rothrock, M. D., "Experimental Determination of Unsteady Blade Element Aerodynamics in Cascades," Detroit Diesel Allison report, Aug. 1980.

18 Whitehead, D. S., "Torsional Flutter of Unstalled Cascade Blades at Zero Deflection," ARC Reports and Memoranda No. 3429, 1966.

19 Hall, K. C., and Crawley, E. F., "Optimal Mistuning for Enhanced Aeroelastic Stability of Transonic Fans," MIT Gas Turbine and Plasma Dynamics Laboratory Report No. 176, Nov. 1983.

Investigation of Flow Phenomena in a Transonic Fan Rotor Using Laser Anemometry

A. J. Strazisar
NASA-Lewis Research Center,
Cleveland, Ohio 44135

Several flow phenomena, including flow field periodicity, rotor shock oscillation, and rotor shock system geometry have been investigated in a transonic low aspect ratio fan rotor using laser anemometry. Flow periodicity is found to increase with increasing rotor pressure rise and to correlate with blade geometry variations. Analysis of time-accurate laser anemometer data indicates that the rotor shock oscillates about its mean location with an amplitude of 3–4 percent of rotor chord. The shock surface is nearly two-dimensional for levels of rotor pressure rise at and above the peak efficiency level but becomes more complex for lower levels of pressure rise. Spanwise shock lean generates radial flows due to streamline deflection in the hub-to-shroud streamsurface.

Introduction

In recent years, several investigators have presented detailed internal laser anemometer flowfield measurements in transonic axial-flow compressors [1–4]. The results obtained have traditionally been used by computational fluid mechanic researchers as a data base for validation of numerical flow field solution techniques [5–9]. Internal flow field measurements will continue to be used for this purpose as computational methods evolve toward viscous-inviscid interaction schemes and eventually toward fully viscous solution schemes.

Such measurements can also be used to improve our understanding of several flow phenomena within transonic blade rows in order to improve empirical models which are still used in the blade design process. Two recent investigators [9, 10] have attempted to refine the classic Miller-Lewis-Hartman loss model based on normal shocks [11] to include effects of shock obliquity in the blade-to-blade and spanwise direction. Another recent investigation has provided evidence that the strength of the rotor passage shock may vary considerably from passage-to-passage and may be time unsteady as well [12]. Both of these phenomena can impact overall performance in that they can both cause higher loss than one would predict for a steady flow which is uniform in all passages. It may therefore be possible to improve blade row performance by understanding the origin of such effects and modifying the blade design to minimize them. Other areas of current research interest which require internal flow field data are the development of secondary flow and wake mixing models and the effect of blade row interactions on individual blade row performance.

Contributed by the Gas Turbine Division of THE AMERICAN SOCIETY OF MECHANICAL ENGINEERS and presented at the 29th International Gas Turbine Conference and Exhibit, Amsterdam, The Netherlands, June 4-7, 1984. Manuscript received at ASME Headquarters January 18, 1984. Paper No. 84-GT-199.

The NASA Lewis Research Center has undertaken a program aimed at obtaining detailed measurements within transonic blade rows which satisfy the need for internal flow field data generated by research interests in the foregoing areas. The first phase of this program involves mapping of the flow in a transonic low aspect ratio fan rotor in sufficient detail to enable accurate determination of the three-dimensional rotor shock structure and the response of the flow field to varying back-pressure conditions. Flow phenomena such as shock unsteadiness, flow periodicity, and shock-driven radial flows have also been investigated. Results obtained from these measurements are the subject of this report. Later phases of the current program include mapping of the flow field through controlled diffusion stators operating behind the fan rotor, and a study of the impact of blade row interaction on the intra-rotor flow field and the wake mixing rate.

Laser Anemometer System

The laser anemometer (LA) system used in the present investigation is a single-channel fringe anemometer that has been previously described in detail [4, 13, 14]. Optical access to the flow field is provided by a 3-mm-thick glass window which conforms to the outer flowpath contour in both the circumferential and streamwise directions. The clearance between the window and the rotor tip is 0.5 mm at design speed. The laser beams enter the test compressor in a nominally radial direction. However, the beams can be deflected off-radial to minimize regions near the blade root which are blocked from optical access by spanwise blade twist and to enable the measurement of radial velocity components. Liquid seed particles, which are nominally 1-1.4 microns in diameter, are injected into the flow through a 6-mm-dia tube located 35 cm upstream of the rotor.

The circumferential location of each velocity measurement

relative to the rotor is determined by tagging the measurement with a pulse from a variable frequency clock that is phase-locked to the rotor rotational speed. The clock frequency is set to give 50 pulses per blade passing. All measurements that occur within an interval between adjacent clock pulses are assigned to a "rotor shaft position," which is defined as the center of the interval. The blade geometry is used to calculate the rotor shaft position that corresponds to the blade suction surface at any axial, radial point within the rotor. LA measurements are obtained within a data window that starts on the suction surface of a given blade and contains 50 shaft positions blade-to-blade across 17 of the 22 rotor blades. The time required for the passing of the last five blades is used to reset the clock frequency to track rotor speed drift and to perform on-line data reduction. A typical run consists of obtaining 60,000 measurements within the data window, which yields about 70 measurements at each of the 850 shaft positions if the data are evenly distributed.

Data may be gathered in either a data-average mode or a data-capture mode. In the data-average mode, only the sum of the velocities, the sum of the velocities squared, and the number of measurements are recorded at each shaft position. Although the velocity mean and standard deviation are calculated from these three quantities, all information on the distribution of the velocities that occurred at each shaft position are lost. Since only three words of storage are required for each shaft position, a data window that is 850 shaft positions wide requires only 2550 words of storage independent of the number of measurements requested in a run. In the data-capture mode, each individual velocity measurement that occurs at a shaft position is recorded. This mode allows analysis of the distribution of the velocity measurements that occurred at each shaft position and is useful for the analysis of flow steadiness as will be shown later. However, this mode of operation requires two words of storage for each velocity measurement. A typical run in which 60,000 measurements are requested therefore requires 120,000 words of storage. The data-average mode was therefore used for most of the measurements reported here.

Laser anemometer measurement locations are shown in Fig. 1, which is a meridional view of the test rotor. Conventional pressure and temperature traverse data are obtained at stations 1 and 2 shown in the figure. LA measurements are made along conical surfaces which pass through radii corresponding to 10 percent mass flow fractions at the rotor trailing edge. These conical surfaces are generated by straight line interpolation between design streamline radii which are known at stations 1 and 2 and the blade edges. Measurement locations are distributed axially at 20 percent chord intervals from −100 percent to −20 percent chord, at −10 percent chord, at 2.5 percent chord intervals from −5 percent to 10 percent chord, at 10 percent chord intervals from 10 percent to 100 percent chord, and at aerodynamic survey stations 1 and 2. Surveys are also taken at four locations evenly spaced between the rotor trailing edge and the stator leading edge plane and at the stator leading edge plane.

Test Compressor

The test rotor for the present study is a low aspect ratio fan. The rotor design pressure ratio is 1.63 at a mass flow of 33.25 kg/s. The tip relative Mach number is 1.38 at the design tip speed of 429 m/s. The rotor has 22 blades, an aspect ratio of 1.56 (based on average span/root axial chord), an inlet tip diameter of 51.3 cm, and an inlet hub/tip radius ratio of 0.375. The rotor tip clearance at design speed is 0.5 mm. The rotor does not have a part-span shroud which is typically required to prevent flutter in fan stages of higher aspect ratio. Details of the rotor aerodynamic design are given in [15].

The results reported here were obtained from a rotor-only configuration with the stator removed. This configuration eliminates circumferential variations in the flow field induced by stationary blade rows and thus allows comparison of the measurements with numerical predictions based on circumferentially uniform upstream and downstream conditions.

The rotor design speed operating line is shown in Fig. 2 for both the rotor-only and full-stage (rotor + stator) configurations. Mass flow is measured across a calibrated orifice located far upstream of the compressor. The rotor pressure rise is calculated from mass-averaged total pressure surveys obtained at aerodynamic survey stations 1 and 2 shown in Fig. 1. Laser anemometer measurements were obtained on all nine streamsurfaces at the near stall (NS) and peak efficiency (PE) operating points. At the midrange (MR) operating condition, measurements were made on the 10, 20, 30, 40, 60, and 80 percent span streamsurfaces. Additional LA surveys were obtained on selected streamsurfaces at the choke (CH) and design flow (DF) operating points.

Note that the rotor stall point occurs at a higher mass flow in the rotor-only configuration than in the full-stage configuration. One explanation is that the presence of the stators may be suppressing the development of rotating stall within

Nomenclature

A = shock motion amplitude
CH = choke flow compressor operating point
DF = design flow compressor operating point
f = shock motion frequency
$\dot{M}$ = mass flow
M_s = shock motion Mach number
MN = Mach number component normal to the shock
MR = midrange compressor operating point
MREL = local relative Mach number component in the $Z\theta$ = plane
NS = near stall compressor operating point
P = total pressure
p = static pressure
PE = peak efficiency compressor operating point
PR = rotor total pressure ratio
$S1$ = blade-to-blade streamsurface
$S2$ = hub-to-shroud midgap streamsurface
R = radius, radial direction
t = time
u_s = shock motion velocity
x_s = shock position
Z = axial direction
Z_{s2} = streamwise distance along the midgap $S2$ streamsurface
α_s = shock lean angle in the midgap $S2$ streamsurface
α_{s1} = streamline slope in the midgap $S2$ streamsurface (positive toward the tip)
β_{rel} = relative flow angle measured from the axial in $Z\theta$ = plane
β_s = shock sweep angle in the $S1$ streamsurface
ω_s = steady state shock pressure loss coefficient
ω_u = unsteady shock pressure loss coefficient

Subscripts

ss = steady state
u = unsteady
1 = conditions upstream of a shock
2 = conditions downstream of a shock

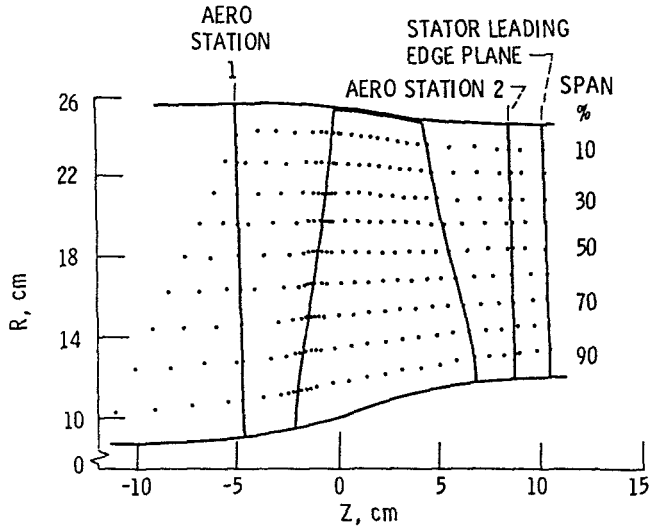

Fig. 1 Meridional view of the test fan showing laser anemometer and aerodynamic survey locations

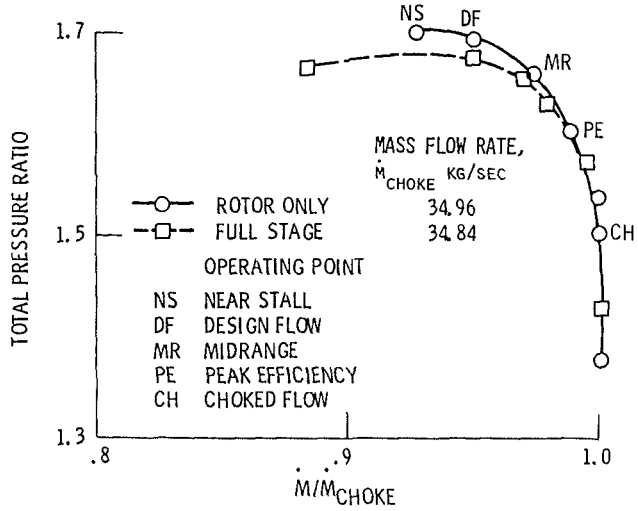

Fig. 2 Rotor design speed operating line

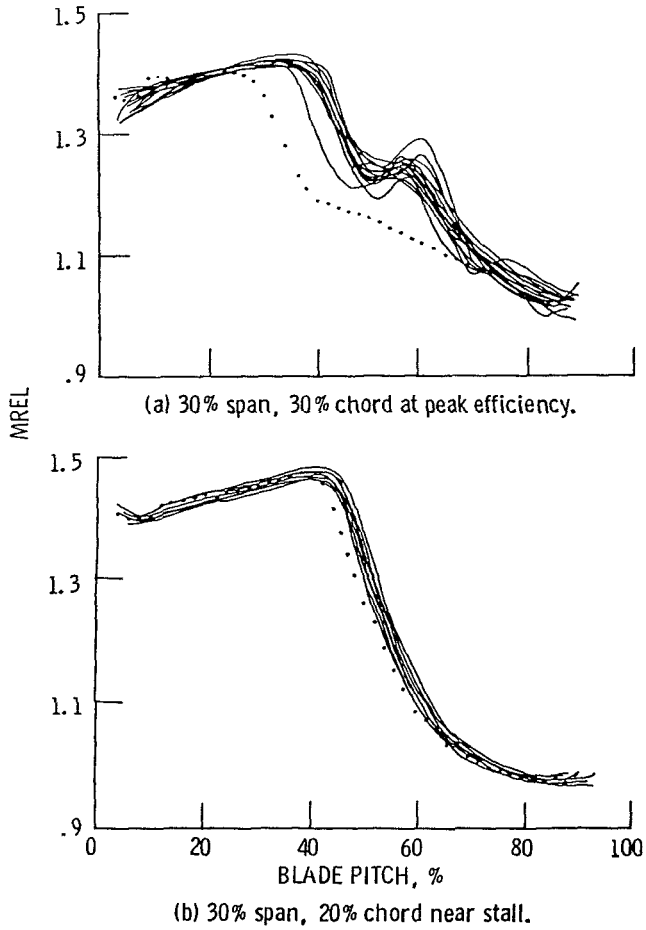

Fig. 3 Blade-to-blade distribution of relative Mach number across 17 blade passages. (. . . . passage number 12)

the rotor. A second possibility is that, in the rotor-only case, rotor stall may be triggered by a flow separation in the test rig diffuser, which is located between the rotor and throttle valve. With the stators removed, the flow entering the diffuser still contains most of the rotor exit swirl, which generates a relatively high absolute Mach number. In either case, the near-stall flow field measurements obtained in the rotor-only case may not be representative of the flow field just prior to rotor blade stall. However, the measurements obtained at the NS operating point do provide a set of data which is consistent with that obtained at other operating points along the rotor-only design speed line.

Flow Periodicity

In reporting on LA measurements obtained in a 550 m/s tip speed fan rotor with a part-span shroud, Harvey et al. [12] have shown significant nonperiodicity in the flow field at the design speed peak efficiency operating condition. Some rotor blade passages displayed nearly shock-free flow, while other passages displayed the expected normal shock characteristics. Harvey also observed that the flow was much more periodic at the design speed near stall point and at part-speed operating conditions than at the design-speed peak efficiency condition. The pattern of nonperiodic flow was frozen to the rotor, i.e., the same flow always occurred in the same blade passage, which suggests that blade geometry variations were the cause of the nonperiodicity. However, the blades were not available for inspection when the nonperiodicity was discovered. In reporting on measurements obtained in a 426 m/s tip speed unshrouded compressor rotor, the present author [4] has shown that flow field variations from passage-to-passage were on the order of 5 percent or less except for local variations around the blade leading edges.

The foregoing results prompted an investigation of both the running blade geometry and the flow field periodicity in the present fan rotor. The fan geometry at design speed was measured by focussing the LA probe volume on the blade tip. The LA system clock frequency was increased from the usual 50 cycles (shaft positions) per blade passage to 1000 shaft positions per passage, yielding a circumferential resolution of 0.008 mm between shaft positions. The position of each rotor blade was measured at 14 axial locations for 50 rotor revolutions. The results indicate a high degree of geometric uniformity within the rotor. The spacing within the blades was uniform to within 2 percent and the blades moved by less than 0.1 percent of blade spacing relative to one another during the 50 measured revolutions. The blade tip LA measurements indicated an untwist of 1.96 ± 0.04 deg compared to a finite element analysis prediction of 2.02 deg.

Blade-to-blade relative Mach number distributions across the 17 measured blades are shown in Fig. 3. In order to decrease the statistical uncertainty of these measurements at each shaft position, the total number of measurements

acquired across the 17-blade data window was increased from 60,000 to 450,000, which would yield approximately 500 measurements at each shaft position if the data were uniformly distributed. Data obtained at the peak efficiency point at 30 percent span, 30 percent chord are shown in Fig. 3(*a*). Data obtained at the near-stall point at 30 percent span, 20 percent chord are shown in Fig. 3(*b*). The peak efficiency Mach number distributions suggest a two-shock system in the rotor with a front shock inlet Mach number of 1.35 to 1.4 and a rear shock inlet Mach number of 1.25 to 1.3. Note that the two-shock system appears in all rotor passages.

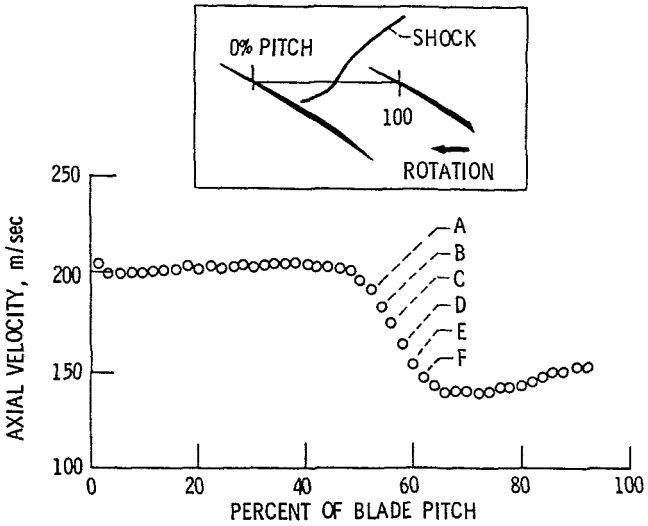

Fig. 4 Blade-to-blade distribution of mean axial velocity component at 10 percent span, 20 percent chord for the near-stall operating condition

The data indicate that the flow field in individual passages can be spatially averaged together to provide an accurate representation of the flow field in an "average" blade passage. The data also support the observation of Harvey et al. in that the flow is much more periodic near stall than at peak efficiency. The degree of periodicity within the present rotor is closer to that observed in the unshrouded NASA compressor rotor than to that observed by Harvey et al. in the shrouded fan rotor. It would therefore appear that rotor geometry variations caused by part-span shrouds might be the cause of flow field nonperiodicity. However, the higher tip speed of the shrouded fan rotor might also contribute to the observed periodicity levels.

One explanation for the increased nonperiodicity observed at peak efficiency is as follows. Choke flow operating points are often characterized by an oblique shock system in the rotor tip region. As the back pressure is raised and the mass flow decreases, the shock structure transitions to a normal shock structure. Because the flow field is at a transition point between these two shock structures near the peak efficiency operating condition, it may be most sensitive to blade geometry variations and small flow perturbations at this flow point.

An interesting feature of Fig. 3(*a*) is the flow field in passage 12, which is clearly different than all other passages at peak efficiency and which lies outside the envelope of all other blade passage Mach number distributions at midgap for the near stall condition. Blade number 12 has a strain gauge mounted at 50 percent chord, 30 percent span on the blade suction surface, which is also the point at which the rotor passage shock hits the blade surface. Analysis of flow periodicity 20 percent of chord downstream of the trailing edge at peak efficiency indicates that the suction side of the blade wake 12 also lies outside the envelope of all other blade wakes. These results demonstrate that surface-mounted instrumentation located in transonic regions of the flow field

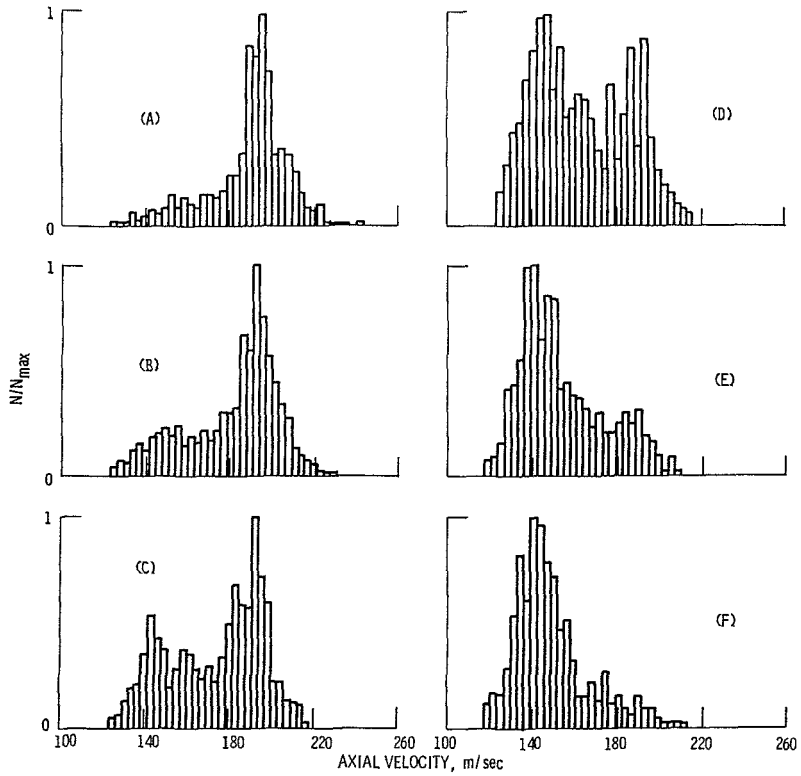

Fig. 5 Normalized distribution of axial velocity measurements at the six points shown in Fig. 4 in the vicinity of the rotor passage shock

Table 1 Shock loss as a function of shock motion for 10 percent span, 20 percent chord, near stall

Frequency (hz)	M_s	ω_u	ω_u/ω_s
0	0	.00717	1.00
500	.028	.00735	1.025
1000	.056	.00789	1.110
2500	.141	.01153	1.608
5000	.281	.02191	3.056

Shock motion amplitude = 3 mm
Inlet relative Mach number = 1.343
Steady-state shock normal Mach number = 1.171
Steady-state shock loss ω_s = .00717

can have a significant impact on individual blade performance.

Unsteady Shock Motion

Shocks have been observed to oscillate about their mean location in schlieren photos and movies taken in wind tunnels and diffusers. It is therefore reasonable to expect that the shocks in transonic compressor rotors may also display motion about a mean position. Such motion can lead to an increase in net shock loss, since the increase in loss when the shock moves upstream (thus increasing the shock inlet Mach number) is greater than the loss decrease when the shock moves downstream (thus decreasing the shock inlet Mach number).

In order to investigate shock motion in the test rotor, LA data were acquired in the data capture mode previously described. The results of one such run are shown in Figs. 4 and 5. Figure 4 is a plot of the average blade-to-blade distribution of the axial velocity component measured at the near stall operating condition at 10 percent span, 20 percent chord. Figure 5 shows the histograms of the distribution of the individual measurements that occurred in all blade passages at shaft positions *a–f* shown in Fig. 4. The ordinate of each figure is the number of measurements, N, which occurred in velocity "bins" that are 3 m/s in width, normalized by the number of measurements in the highest bin, NMAX. Since each histogram contains data from all 17 blade passages at a given shaft position, it is possible that the width of each histogram is due to passage-to-passage flow variations as opposed to time-unsteadiness of the flow. However, inspection of histograms at a given shaft position in a single passage indicates that the averaged histograms shown here are not broadened due to flow nonperiodicity.

On the upstream side of the shock (points *a*, *b*) the most probable velocity is the preshock level of 198 m/s. As one proceeds across the shock to positions *c* and *d*, the occurrence of the pre- and postshock levels of 198 m/s and 140 m/s is almost equally probable. On the downstream side of the shock the postshock level of 140 m/s is the most probable. The data suggest that the amplitude of the shock motion is on the order of 2 to 3 shaft positions on either side of the mean shock location shown in Fig. 4. This corresponds to a distance of about 3 mm (3.5 percent chord) in a direction normal to the shock. Similar amplitudes have been observed at other spanwise locations for near stall as well as peak efficiency operating conditions. In addition, analysis of peak efficiency rotor wake data 50 percent chord downstream of the blade at 10 percent span indicates that the rotor wake oscillates by about 3 to 4 shaft positions about its mean location. This wake oscillation may be driven by the shock oscillation. If this is the case, it may be possible to infer the shock oscillation frequency by measuring the wake oscillation frequency using a high response total pressure transducer.

Although only the shock motion amplitude is known, we can estimate the net increase in shock pressure loss for a given frequency by assuming a harmonic shock motion of frequency F and amplitude A in a direction normal to the shock surface. These assumptions yield

$$x_s = A \cdot \sin(2\pi \mathrm{Ft}) \tag{1}$$

$$\mathrm{M}_s = u_s/a_{\mathrm{sound}} = (2\pi \mathrm{FA}/a_{\mathrm{sound}}) \cdot \cos(2\pi \mathrm{Ft}) \tag{2}$$

$$\mathrm{MN}(t) = (\mathrm{MN})_{ss} + \mathrm{M}_s \tag{3}$$

where x_s, u_s, and M_s are the position, speed, and Mach number of the moving shock and MN(t) and MN_{ss} are the time varying and steady-state Mach number components normal to the shock surface. Note that since the shock speed, u, is controlled by the product of the shock motion amplitude and frequency, shock motions of small amplitude and high frequency are equivalent to those of large amplitude and low frequency. A shock pressure loss coefficient can be defined as

$$\omega_s = (1 - P_2/P_1)/(1 - p_1/P_1) \tag{4}$$

where P_2/P_1 is the total pressure ratio across a normal shock with an approach Mach number of MN(t) and p_1/P_1 is the static-to-total pressure ratio associated with the fan inlet relative Mach number, MREL. Shock loss coefficients calculated for various values of M_s for the shock shown in Fig. 4 are summarized in Table 1. The unsteady loss, ω_u, was calculated from a time average of equation (4). The measured value of MREL = 1.343 was used to evaluate p_1/P_1. The total pressure ratio P_2/P_1 was evaluated at the shock normal Mach number given by equation (3) using measured values of MN = 1.171 and A = 3 mm. The results indicate that for the shock motion amplitude measured in this case, a shock frequency of 1 khz can result in an 11 percent increase in net shock pressure loss compared to a stationary shock. The existence of shock motion frequencies on this order does not seem to be unrealistic when viewed from the rotor time frame. Since the rotational speed of this rotor is on the order of 250 revs/s, a shock oscillating at 1 khz would go through only about four cycles of motion per rotor revolution. Measurements of shock motion amplitude and frequency in rotors with different aerodynamic design features are clearly needed before we can determine to what extent the shock motion amplitudes measured here and the frequencies assumed here are characteristic of all transonic blade rows.

Procedure for Determining Shock Surfaces

The following sections deal with the response of the rotor shock system to varying back-pressure levels and with the three-dimensionality of the shock surface. One flow field representation often used in such discussions is a blade-to-blade contour plot of relative Mach number. While such plots provide information throughout the blade-to-blade flow field, they do not provide an accurate indication of the rotor shock location when, as is often the case, the Mach number varies along the face of the shock. In such cases there is no single mach number contour line that runs parallel to the shock. The following discussion therefore makes use of shock fronts determined from plots of the relative Mach number MREL in the blade-to-blade direction at constant chord such as Fig. 6 and from plots of MREL in the streamwise direction at constant pitch relative to the suction surface, such as Fig. 7.

Although the seed particle velocity does not accurately follow the gas velocity in the high deceleration region immediately downstream of the shock, the point at which the Mach number first begins to decrease is considered to be an accurate and consistent indicator of the shock location. The uncertainty in the shock location determined by this procedure is on the order of 2 shaft positions (4 percent of rotor pitch) in the circumferential direction and 1 percent of rotor axial chord in the axial direction. Both Figs. 6 and 7 indicate the existence of two shocks in the blade passage. The

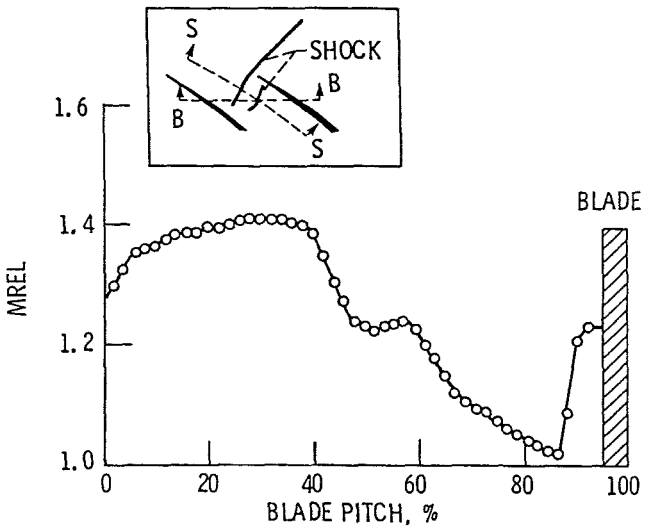

Fig. 6 Blade-to-blade distribution (view B-B) of relative Mach number at 30 percent span, 30 percent chord at peak efficiency

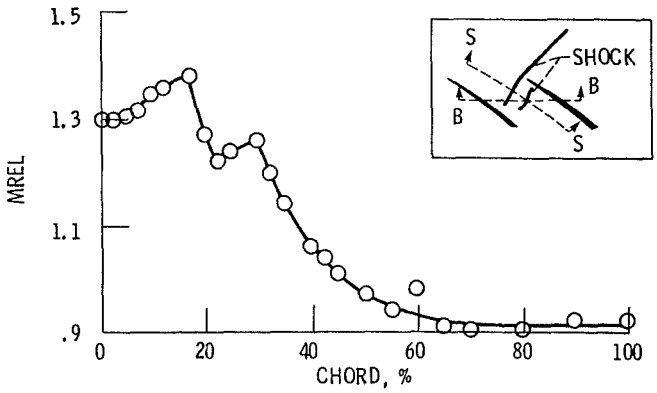

Fig. 7 Streamwise distribution (view S-S) of relative Mach number at 30 percent span, 60 percent blade pitch from the suction surface at peak efficiency

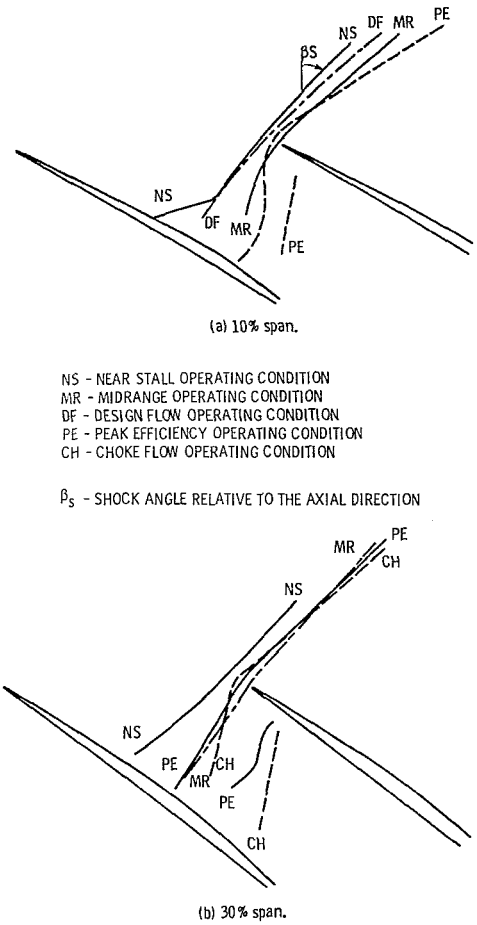

Fig. 8 Rotor shock structure at design speed for various operating conditions

second shock, which occurs only for back pressures at or below the peak efficiency level, rarely shows up as clearly in blade-to-blade plots as it does in Fig. 6. Streamwise plots of MREL were found to provide a much more sensitive indication of the second shock location. In order to improve the spatial resolution of the streamwise plots, LA surveys were taken every 2.5 percent chord from the blade leading edge to 80 percent chord on the 10 percent to 40 percent span streamsurfaces at the peak efficiency operating condition.

Shock Structure as a Function of Rotor Pressure Rise

The response of the rotor shock system to varying back-pressure levels is shown on the 10 percent and 30 percent span streamsurfaces in Fig. 8, using the operating condition labels shown in Fig. 2. In some cases the shock is not drawn all the way to the blade suction surface because the location of the shock-blade intersection point could not be determined from the data. This is due in part to the fact that data are missing at some axial survey locations and in part to the fact that the shock sometimes hits the blade between survey station locations. The bow wave angle, β_s, measured from the axial direction decreases while the passage shock angle increases with increasing pressure rise across the rotor. This flattening of the shock is consistent with an increase in the shock strength. The standoff distance between the shock and the blade leading edge decreases as the back pressure is raised from the choke flow level to the peak efficiency level. Further increases in back pressure then result in an increase in the standoff distance. For back pressure levels at and below peak efficiency a system of two oblique shocks exists. As the back pressure rises, the second shock becomes less oblique as shown at 30 percent span and then disappears before the midrange condition is reached. At 10 percent span near stall, the shock structure near the blade surface appears to be the front foot of a lambda shock. Mach number contour plots of the data in this region show a lambda-shaped grouping of Mach number contours, but a rear shock foot cannot be discerned from the data using the procedure described above for determining a shock surface location.

Three-Dimensional Rotor Shock Structure

The three-dimensionality of the rotor shock structure is displayed at the peak efficiency, midrange, and near-stall operating conditions in Fig. 9(*a–c*), respectively. The shaded blade section is the 10 percent span blade section. The intersection of each measurement streamsurface between 20 percent and 60 percent span with the suction surface of the left blade and the pressure surface of the right blade is also shown to help locate the shock with respect to the blade surface. It should be noted that the apparent lean of the shock in the spanwise direction is a strong function of the procedure used to construct a figure of this type. The blade section at each span is shown at the blade spacing appropriate for that span, i.e., BLADE SPACING $= 2 \cdot \pi \cdot$ RSLOCAL/NB, where RSLOCAL is the local streamsurface radius and NB is the

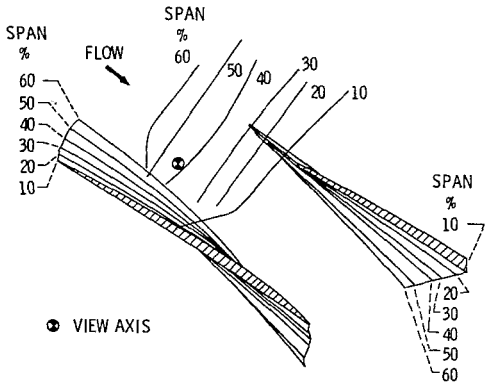

(a) Near stall (NS) operating point.

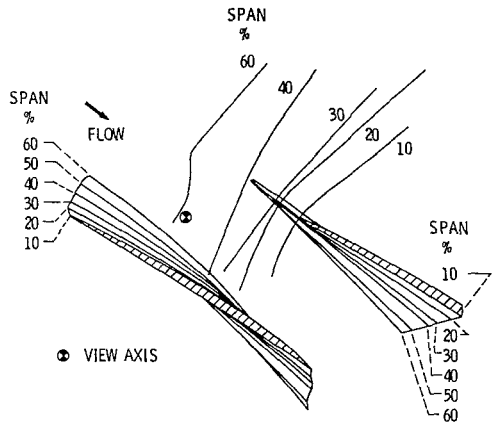

(b) Midrange (MR) operating point.

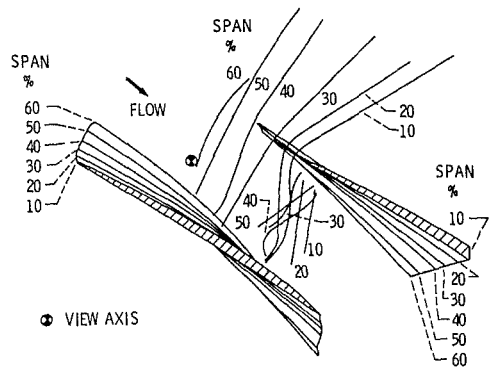

(c) Peak efficiency (PE) operating point.

Fig. 9 Spanwise rotor shock structure

number of rotor blades. In addition, the blade sections are aligned circumferentially according to their position relative to a radial line that passes through the 10 percent span streamsurface at midgap at the blade leading edge. This line, referred to as the view axis in each figure, was chosen because it passes approximately through the center of the shock surface. Viewing along this line therefore gives the least distorted two-dimensional representation of the shock surface.

The near-stall shock surface shown in Fig. 9(*a*) is nearly planar with little curvature in the blade-to-blade or *S*1 surface. The shock sweep angle in the *S*1 surface is nearly constant along the face of the shock and is independent of span as well. At the midrange flow condition the sweep angle begins to vary along the face of the shock at a given space. The bow shock sweep angle also begins to vary with span. However, the bow and passage shock surfaces are each nearly planar in themselves. At the peak efficiency condition the bow and front passage shock are no longer planar. The bow shock

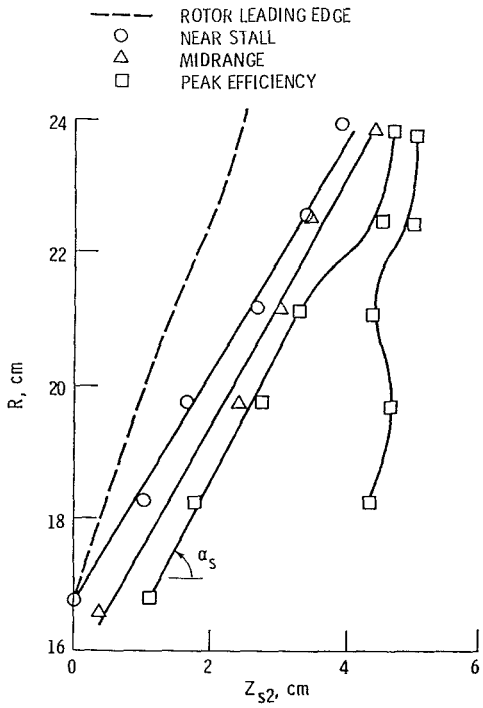

Fig. 10 Intersectioon of rotor passage shock with the midgap hub-to-shroud streamsurface

angle varies significantly with span. The passage shock angle with respect to the axial direction decreases rapidly above 30 percent span and the shock surface becomes nearly vertical above 20 percent span. The rear passage shock sweep angle and axial location above 30 percent span are quite different than those below 30 percent span. These characteristics lead to a highly complex shock structure outboard of 30 percent span.

Certain features of the results shown above agree quite well with the empirical shock models proposed by Prince [9] and Wennerstrom [10]. A normal shock appears to be a quite accurate model for the shock surface except for the outboard regions of the blade at relatively low backpressure operating conditions. Under those conditions Prince has proposed an axial front passage shock that turns near the blade suction surface so as to approach the blade normal to the surface. This model agrees quite well with the peak efficiency data. The extent to which these results are generic remains to be determined by obtaining LA data on rotors that have different design characteristics than the present rotor.

The intersection of the passage shock and the blade leading edge with the midgap meridional (or *S*2) surface is shown in Fig. 10. The abscissa, Z_{s2}, is the distance measured in the streamwise direction in the midgap *S*2 streamsurface. Note that the front shock lean angle in the *S*2 surface, α_s, is nearly independent of both span and rotor operating condition with the exception of the tip region at peak efficiency. The shock sweep angle in the *S*1 surface, β_s, the lean angle in the midgap *S*2 surface, α_s, and the design streamline slope in the *S*2 surface, α_{s1}, were combined with the inlet relative Mach number and flow angle measured in the $Z\theta$-plane (MREL, β_{rel}) to calculate the true Mach number components normal to the shock surface at midgap. The isentropic shock relations were then used to calculate the true Mach number change across the shock and the shock loss coefficient defined in equation (4). The relative Mach number and flow angle and the shock sweep angle were also used to calculate the Mach number change and loss across the shock which one would predict by neglecting streamline slope and shock lean. The

Table 2 Shock jump conditions calculated at rotor midgap for the peak efficiency operating condition

% Span	α_s	β_s	MREL	β_{rel}	α_{s1}	$(MREL)_{2D}$	$(MREL)_{3D}$	α_{s1}	$(\omega_s)_{2D}$	$(\omega_s)_{3D}$
Front shock			Preshock					Postshock		
10	81.0	3.5	1.35	61.9	−4.4	1.00	1.01	2.7	.015	.015
20	81.0	4.5	1.31	60.9	−3.2	1.01	1.02	2.6	.010	.009
30	60.0	35.0	1.36	58.9	−2.1	.76	1.06	8.7	.048	.016
40	63.0	22.0	1.32	56.7	−1.0	.83	1.07	7.1	.030	.006
50	63.0	26.0	1.22	56.0	0.3	.85	1.10	3.3	.013	.0007
60	63.0	23.0	1.16	53.2	1.6	.94	[a]	[a]	.003	[a]
Rear shock										
10	86.5	13.0	1.29	58.7	−4.6	.92	.92	−.5	.015	.016
20	86.5	9.5	1.26	57.9	−3.5	.99	.99	0.1	.007	.007
30	90.0	32.0	1.23	54.5	−2.2	.83	.83	−1.0	.017	.017
40	90.0	56.0	1.20	49.7	−1.0	.93	.93	−.3	.006	.006
50	79.0	55.0	1.12	50.0	0.3	.97	1.02	1.3	.001	.0004

[a]Three-dimensional calculations result in subsonic inlet Mach number component normal to the shock surface

results are summarized in Table 2 for the peak efficiency operating condition. Subscript two-dimensional refers to quantities calculated by neglecting shock lean and streamline slope while subscript three-dimensional refers to quantities calculated by including these effects.

As one would expect, including shock lean in the calculations results in higher postshock Mach numbers and significantly lower shock loss than calculated by neglecting the lean. Mach number changes measured across the shock by the LA are generally in better agreement with the three-dimensional calculations than with the two-dimensional calculations. Consider for example the front passage shock at 30 percent span, peak efficiency. From Table 2, we see that the shock is nearly normal to the relative flow in the *S*1 surface ($\beta_s + \beta_{REL} = 93.9$ deg), which leads to a two-dimensional-calculated postshock Mach number of .76. However, when the shock lean and streamline slope are included in the calculation, the postshock Mach number is 1.06. The Mach number measured by the LA system behind this shock is approximately 1.2 as seen in Fig. 7. There are many other examples of this type in the data in which supersonic Mach numbers measured downstream of shocks that are normal in the *S*1 surface can be explained by shock lean in the spanwise direction.

The results shown in Table 2 also indicate that the streamline slope changes across the shock due to streamline deflection toward the tip in the *S*2 surface. A limited number of radial velocity component measurements were acquired with the LA to investigate the existence of such shock-driven radial flows. These measurements require that the laser beams be deflected off-radial by rotation about an axis parallel to the compressor axis of rotation. When this is attempted inside the blade row the rotor blades block the incoming laser beams and prevent data acquisition across much of the blade pitch. Blade-to-blade radial velocity component data were therefore acquired just upstream of the rotor at −5 percent chord from 10 percent to 40 percent span at the near-stall operating condition. Postshock streamline slopes on the order of 4 to 16 deg were measured just behind the shock. After the flow reexpanded further downstream of the shock, the measured streamline slopes were on the order of 0 to −4 deg, which agree with the design levels.

Conclusion

Flow field survey data acquired with a laser anemometer have been used to investigate several features of the flow field in a transonic low aspect ratio fan rotor. The data also provide a more extensive set of flow field data on a single rotor than available in the past for use in validation of numerical flow field predictions.

Investigation of the flow field periodicity indicates that the flow becomes more periodic as the level of rotor pressure rise increases. In addition, surface-mounted instrumentation gives rise to significant flow field changes.

Laser anemometer data acquired in a time-accurate mode of operation indicate that the rotor passage shock oscillates about its mean location with an amplitude on the order of 3–4 percent of rotor chord, while the rotor wake oscillates about its mean location with an amplitude of about 4–6 percent of blade pitch. Calculation of the increase in shock loss due to shock oscillation requires that the oscillation frequency be known. Although this frequency cannot be determined from the LA data, estimates of the loss increase based on the assumption of harmonic shock motion at moderate frequencies indicates that shock motion may indeed contribute to part of the total shock loss in transonic blade rows.

The rotor passage shock is a nearly two-dimensional surface, with spanwise lean for levels of rotor pressure rise that are at or above the peak efficiency level. Under these conditions, several features of the shock structure are in agreement with recently proposed shock models. However, at pressure rise levels below peak efficiency, a two-shock system develops in the rotor with complex surface curvatures in the outboard region of the front shock and along the entire spanwise extent of the rear shock. The extent to which these results are generic remains to be determined by obtaining LA data on rotors that have different design characteristics than the present rotor.

Spanwise lean of the shock surface generates radial flows due to streamline deflection across the shock in the hub-to-shroud streamsurface. These radial flows have been measured in the present investigation at a point upstream of the rotor, but cannot be measured inside the rotor with the present optical configuration. A new configuration capable of acquiring radial flow data within the rotor blade will be used in future investigations.

Acknowledgments

The author wishes to express appreciation to Michael Pierzga, Michael Hathaway and Sue Simonyi for help with data acquisition and reduction, and to David Hobbs, David Prince and Alan Epstein for many helpful discussions.

References

1 Wisler, D. C., "Shock Wave and Flow Velocity Measurements in a High-Speed Fan Rotor Using Laser Velocimeter," ASME JOURNAL OF ENGINEERING FOR POWER, Vol. 99, No. 2, Apr. 1977, pp. 181–188.

2 Dunker, R. J., Strinning, P. E., and Weyer, H. B., "Experimental Study of the Flow Field Within a Transonic Axial Compressor Rotor by Laser Velocimetry and Comparison with Through-Flow Calculations," ASME JOURNAL OF ENGINEERING FOR POWER, Vol. 100, No. 2, Apr. 1978, pp. 279–286.

3 Weyer, H. B., and Dunker, R. J., "Dual Beam Laser Anemometer Study of the Flow Field in Transonic Compressor," *Secondary Flows in Turbomachines*, AGARD CP-214, Mar. 1977.

4 Strazisar, A. J., and Powell, J. A., "Laser Anemometer Measurements in a Transonic Axial Flow Compressor Rotor," ASME JOURNAL OF ENGINEERING FOR POWER, Vol. 103, No. 2, Apr. 1981, pp. 430–437.

5 McDonald, P. W., Bolt, C. R., Dunker, R. J., and Weyer, H. B., "A Comparison Between Measured and Computed Flow Fields in a Transonic Compressor Rotor," ASME Paper No. 80-GT-7, 1980.

6 Chima, R. V., and Strazisar, A. J., "Comparison of Two- and Three-Dimensional Flow Computations with Laser Anemometer Measurements in a Transonic Compressor Rotor," ASME JOURNAL OF ENGINEERING FOR POWER, Vol. 105, No. 3, July 1983, pp. 596–605.

7 Sarathy, K. P., "Computation of Three-Dimensional Flow Fields Through Rotating Blade Rows and Comparison with Experiment," ASME JOURNAL OF ENGINEERING FOR POWER," Vol. 104, No. 2, Apr. 1982, pp. 394–402.

8 Singh, U. K., "A Computation and Comparison with Measurements of Transonic Flow in an Axial Compressor Stage with Shock and Boundary Layer Interaction," ASME JOURNAL OF ENGINEERING FOR POWER, Vol. 104, No. 2, Apr. 1982, pp. 510–515.

9 Prince, D. C. Jr., "Three-Dimensional Shock Structure for Transonic/Supersonic Compressor Rotors," AIAA *Journal of Aircraft*, Vol. 17, No. 1, Jan. 1980, pp. 28–37.

10 Wennerstrom, A. J., and Puterbaugh, S. L., "A Three-Dimensional Model for the Prediction of Shock Losses in Compressor Blade Rows," ASME Paper No. 83-GT-216, 1983.

11 Miller, G. R., Lewis, G. W., and Hartmann, M. J., "Shock Losses in Transonic Compressor Blade Rows," ASME *Transactions*, Vol. 83, No. 3, July 1961, pp. 235–242.

12 Harvey, W. B., Hobbs, D. E., Lee, D., Williams, M. C., and Williams, K. F., "Rotor Redesign for a Highly Loaded 1800 ft/sec Tip Speed Fan, III. Laser Doppler Velocimeter Report," NASA CR-167954, Apr. 1982.

13 Powell, J. A., Strazisar, A. J., and Seasholtz, R. G., "Efficient Laser Anemometer for Intra-Rotor Flow Mapping in Turbomachinery," ASME JOURNAL OF ENGINEERING FOR POWER, Vol. 103, No. 2, Apr. 1981, pp. 424–429.

14 Powell, J. A., Strazisar, A. J., and Seasholtz, R. G., "High-Speed Laser Anemometer for Intrarotor Flow Mapping in Turbomachinery," NASA TP-1663, Feb. 1982.

15 Urasek, D. C., Gorrell, W. T., and Cunnan, W. S., "Performance of Two-Stage Fan Having Low-Aspect-Ratio, First-Stage Rotor Blading," NASA TP-1493, Aug. 1979.

Investigation of the Three-Dimensional Flow Field Within a Transonic Fan Rotor: Experiment and Analysis

M. J. Pierzga
U.S. Army Propulsion Laboratory (AVSCOM), Cleveland, Ohio 44135

J. R. Wood
NASA Lewis Research Center, Cleveland, Ohio 44135

An experimental investigation of the three-dimensional flow field through a low aspect ratio, transonic, axial-flow fan rotor has been conducted using an advanced laser anemometer (LA) system. Laser velocimeter measurements of the rotor flow field at the design operating speed and over a range of through flow conditions are compared to analytical solutions. The numerical technique used herein yields the solution to the full, three-dimensional, unsteady Euler equations using an explicit time-marching, finite volume approach. The numerical analysis, when coupled with a simplified boundary layer calculation, generally yields good agreement with the experimental data. The test rotor has an aspect ratio of 1.56, a design total pressure ratio of 1.629 and a tip relative Mach number of 1.38. The high spatial resolution of the LA data matrix (9 radial × 30 axial × 50 blade-to-blade) permits details of the transonic flow field such as shock location, turning distribution, and blade loading levels to be investigated an compared to analytical results.

Introduction

Advancement in the aerodynamic design of gas turbine engine fans, compressors and turbines have historically resulted primarily from an empirical approach. Although this approach has led to more efficient, lighter-weight engines, major new advancements in component performance will most likely not result from empiricism alone. A fundamental understanding of the complex flow phenomena which occur within advanced turbomachines is essential if significant advancements in performance are desired. As the cost of building and testing gas turbine engine components increases so does the need to reduce the number of redesigns necessary to achieve the desired performance. The need for redesigns is inherent in design systems which rely heavily on empirical correlations. There exists a need to develop design systems that rely less on empirical correlations and more on precedures which are capable of calculating those aspects of the internal flow field for which the correlations were developed. The development of these new design systems will require extensive experimental investigations of the intra-blade flow field to determine their validity.

In addressing this need, the NASA Lewis Research Center, in cooperation with the Army Propulsion Laboratory, has undertaken a program designed to increase the basic understanding of the complex internal flows of gas turbine fans and compressors. The program relies primarily on the use of nonintrusive optical techniques to evaluate the intra-blade flow field of transonic compressor blading. Concurrently, advanced computational techniques are being developed which incorporate the three-dimensional flow field effects of this class of turbomachine. A combination of experimental observation and computational experience should lead to a better understanding of these complex flows and ultimately to major strides in gas turbine design technology.

Previous researchers have presented comparisons between three-dimensional calculations and internal flow field measurements [1, 2]. They have generally found that inviscid codes model the inlet to transonic rotors quite well but tend to overpredict the deceleration through the rotor. This is usually attributed to lack of the streamline displacement effects due to boundary layer growth. Those who have added boundary layer calculations to three-dimensional analyses [3, 4] have found that the flow field is substantially altered by addition of the displacement thickness to the solid surfaces. The technique used in [3] included simple models for shock-boundary layer interaction, laminar-turbulent transition, and separation effects. The boundary-layer calculations were performed only on the blade surfaces and yielded better agreement with experimental data than did the calculations without boundary layer effects. In [4], results were shown for the same rotor analyzed in [1] and demonstrated the extent to which inclusion of a simple boundary layer model on the blades and endwalls could alter the flow field in a transonic rotor.

Contributed by the Gas Turbine Division of THE AMERICAN SOCIETY OF MECHANICAL ENGINEERS and presented at the 29th International Gas Turbine Conference and Exhibit, Amsterdam, The Netherlands, June 4–7, 1984. Manuscript received at ASME Headquarters January 18, 1984. Paper No. 84-GT-200.

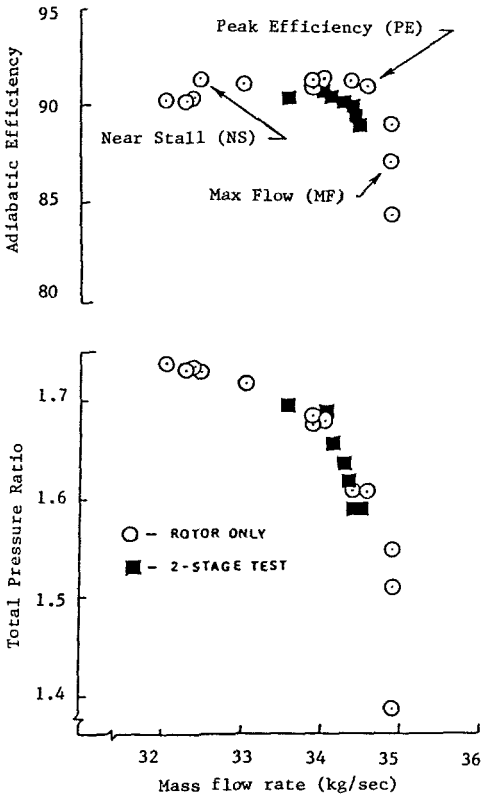

Fig. 1 Rotor performance at design speed

The focus of the present work is the investigation of a detailed set of optical measurements of an advanced transonic, axial-flow compressor flow field obtained under the current NASA/Army research program. These data, coupled with the results of an inviscid three-dimensional flow field calculation, provide the basis on which the internal flow features and trends are interpreted herein. Strazisar [5] provides a more fundamental overview of the rotor flow physics, including the three-dimensional nature of the shock fronts based on these same data.

Compressor Rotor

The research vehicle used in the present work was the first-stage rotor of a NASA Lewis designed, two-stage fan [6]. The first-stage rotor was designed as a 22 blade, low aspect ratio (1.56), damperless replacement for the original 43 blade, high aspect ratio (2.94), dampered rotor [7]. The new blading met or exceeded its design total pressure ratio and adiabatic efficiency goals of 1.629 and 0.896, respectively, when tested in the two-stage configuration. The inlet relative Mach number at the rotor tip was 1.38 at the design tip speed of 428.9 m/s and design mass flow rate of 33.25 kg/s.

The rotor was tested in the present work without inlet guide vanes or downstream stators so that blade row interactions would not be present. Figure 1 shows the measured rotor performance characteristic for a constant design speed condition. Also shown in the figure, for reference purposes, are data from the redesigned two-stage fan investigation [6]. Herein, all future reference to rotor performance will deal solely with the isolated rotor data.

The entire experimental research program conducted with the isolated rotor configuration of this low aspect ratio fan covered a range of data points from max flow (MF) to near stall (NS); however, the most detailed information was obtained at the peak efficiency (PE) and near stall points. Most of the comparisons between experiment and computation will be restricted to these two flow points.

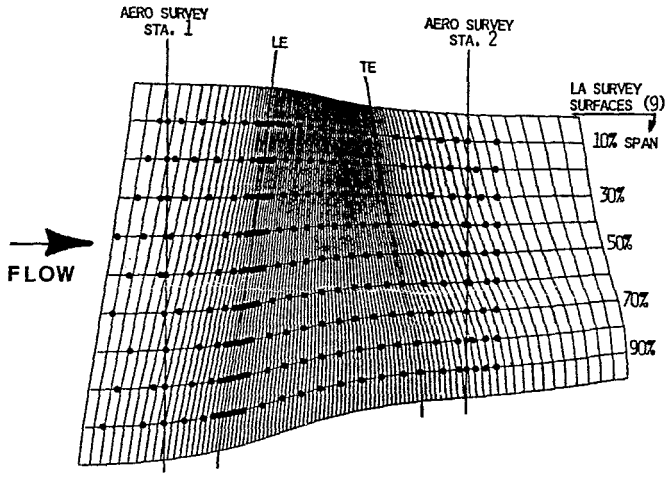

Fig. 2(a) Computational grid in the meridional plane with the LA survey locations and the standard aerodynamic instrumentation planes (note: not all axial locations were taken at the max flow condition)

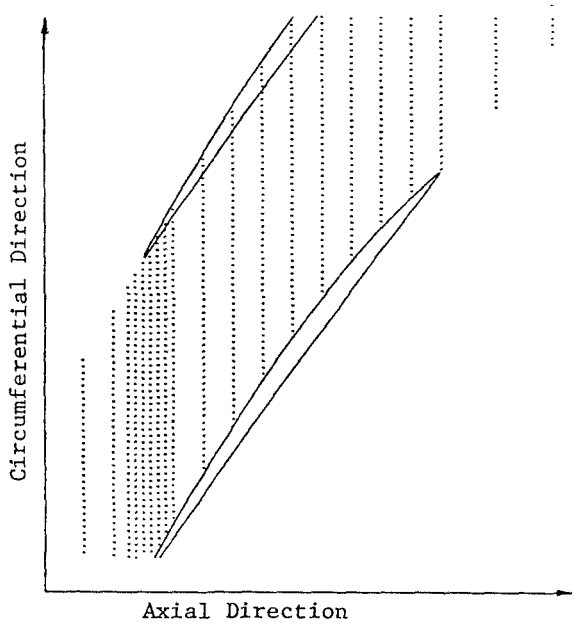

Fig. 2(b) Typical pitchwise measurements locations for the LA data at all percent span locations and flow rates

Instrumentation

A fringe laser anemometer system (LA) was the principal instrument used during the experimental evaluation program. This instrument is a single-channel, dual-beam system with an on-axis backscatter collection scheme and has been previously described in detail [8] and [9]. Data aquisition and storage were accomplished via a dedicated minicomputer, while post processing and graphical output was handled by a large central computer. Access to the compressor flow path was through a 3-mm-thick glass window which extended far enough foreward and aft of the test rotor to enable free-stream and blade wake measurements. The window curvature closely conformed to the rotor outer flow path, thereby minimizing disturbances to the tip region flow. Fluorescent seed particles, whose nominal diameter was 1-1.4 microns, were spray atomized into the flow stream through a 6-mm-dia tube located over 60 cm upstream of the rotor leading edge. In addition to LA measurements, conventional instrumentation was used to record compressor overall pressure and tem-

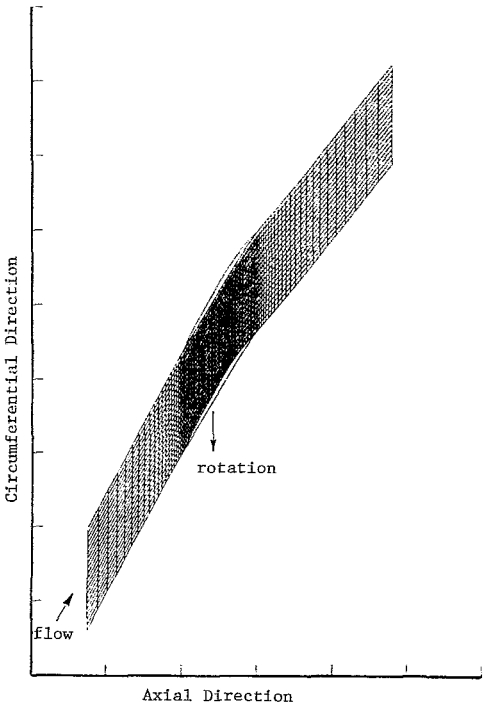

Fig. 3 Computational grid at 10 percent span from the tip

perature levels. This information was used to calculate the compressor overall performance characteristic as well as to control the on-line operating condition set point.

Data Collection

The precise rotor-relative location of each LA velocity measurement was determined using a pulse from a variable frequency oscillator that was phase-locked to the rotor rotational speed. All of the data presented herein were collected with the oscillator set at 50 pulses per blade passage and a maximum blade survey range of 17 passages. The blade geometry was used to set the first measurement position (shaft position) to coincide with the suction surface of a known blade. Since the data collection windows were equally spaced with no circumferential gaps, some data were acquired at shaft positions that were physically within the rotor blade. Data collected in these areas were handled in the off-line reduction of the data, to be discussed later. This method of surveying across a number of blade passages allowed for a larger overall data collection window as well as provided the ability to investigate passage to passage flow variations. It is not within the scope of the present work to look at such passage dependency among the data, and thus all of the blade passages were ensemble averaged to yield an "average" blade passage data set. A typical data run consisted of collecting 60,000 velocity measurements within the entire data collection window at each axial survey location. This yielded approximately 70 measurements at each of the 850 shaft positions of 1200 averages for the 50 "average" shaft positions. Time to collect the 60,000 measurements was approximately 60 s for each of the two velocity components measured at each shaft position. The two angular orientations of the LA probe volume used to obtain the velocity components was predetermined from an initial screening run at each LA survey span location and flow rate. The pitchwise-averaged flow angle at several axial stations along the survey streamsurface was obtained from this screening run. The two LA fringe orientations used in the data runs were derived by bracketing this mean flow angle by 20 deg.

The laser anemometer survey locations along with the meridional view of the computational grid used by the three-dimensional analysis code are shown in Fig. 2(*a*). The LA blade-to-blade matrix is shown in Fig. 2(*b*). LA survey locations, denoted by solid circles in Fig. 2(*a*), were axially distributed at specific locations based on the axial projection of the local chord length along design streamlines to provide data coverage at 20 percent intervals upstream, 2.5 percent intervals around the leading edge, 10 percent intervals within the blade, and five evenly spaced locations between the rotor trailing edge and the position of the stage configuration stator leading edge. Survey points were also included at the conventional instrumentation survey planes (stations 1 and 2), as shown in the figure. The radial distribution of survey points was along design streamlines that pass geometrically through desired percent span positions at the rotor trailing edge plane. This radial position designates the particular LA survey streamline such as 10 percent, 20 percent, 30 percent and so on. The nine radial immersions used in the experimental investigation were spaced at 10 percent span intervals, beginning at 10 percent from the rotor tip and coincided with nine of the three-dimensional computational planes.

Numerical Analysis

The numerical analysis of the rotor was conducted using a three-dimensional computational procedure developed by Denton [10]. This procedure was based upon a finite volume technique. The code was modified [4] to include the effects of boundary layer displacement using an injected mass technique, which allowed flow to pass through the walls in proportion to the rate of growth of the boundary layer displacement thickness. The boundary layers were calculated as if the grid lines in the streamwise direction were actual flow field streamlines. Boundary layers were calculated on both the blade surfaces and on the endwalls which were assumed to rotate with the blading. The displacement thickness was computed from the von Karman integral boundary layer equation using a constant shape factor (1.5) and constant skin friction coefficient (.005). Setting the shape factor to a constant value limits the growth of the displacement thickness in regions of sharp adverse pressure gradients and could significantly effect the results. However, increasing the complexity of the computational procedure could lead to significant increases in computer time. Thus the decision was made to evaluate the present rotor using the simplified procedure in order to assess its effect on the flow field solution.

The upstream boundary was located 1.5 times the tip axial chord upstream for the tip and 0.7 times the hub axial chord upstream for the hub. At the upstream boundary the total pressure, total temperature, absolute tangential velocity, and meridional flow angle were held constant at each spanwise grid line and assumed to be uniform in the tangential direction. The only downstream condition specified was the static pressure at the hub, and it was assumed to be constant in the tangential direction. The static pressure gradient from hub to tip at the downstream boundary was calculated assuming no curvature of the streamlines in the hub-to-shroud plane that was appropriate for this case based upon the flow path geometry. The downstream boundary was located two tip axial chords downstream at the tip and one hub axial chord downstream at the hub.

All of the solutions presented were obtained with a computational grid of 21 points blade-to-blade, 95 points in the streamwise direction with 50 points from blade leading to trailing edge (Fig. 3) and 11 points from hub-to-shroud. A large number of computational points was used in the present work so that any discrepancies between analysis and data could not be attributed to use of a coarse grid. The peak

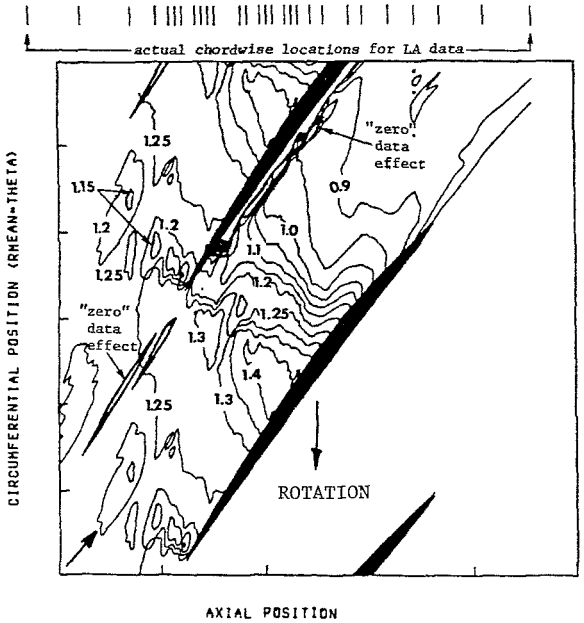

Fig. 4(a) Contour plot using "raw" data

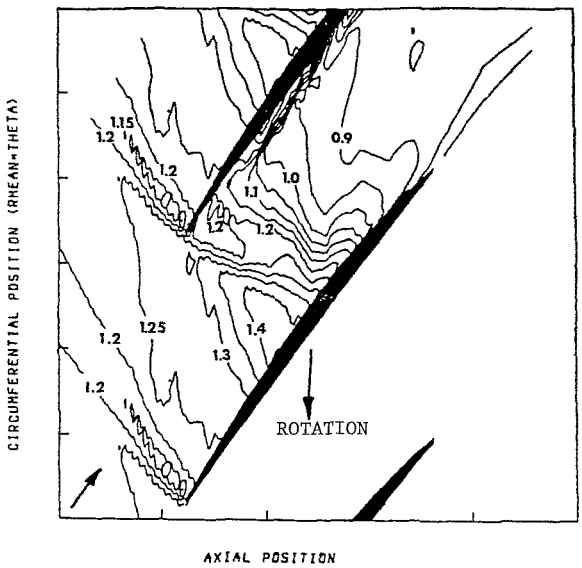

Fig. 4(c) Contour plot with data interpolated to increase the number of axial locations

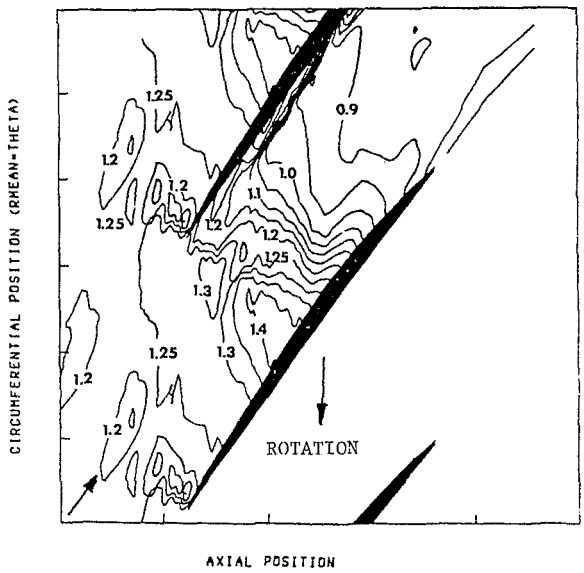

Fig. 4(b) Contour plot with all "zero" data removed

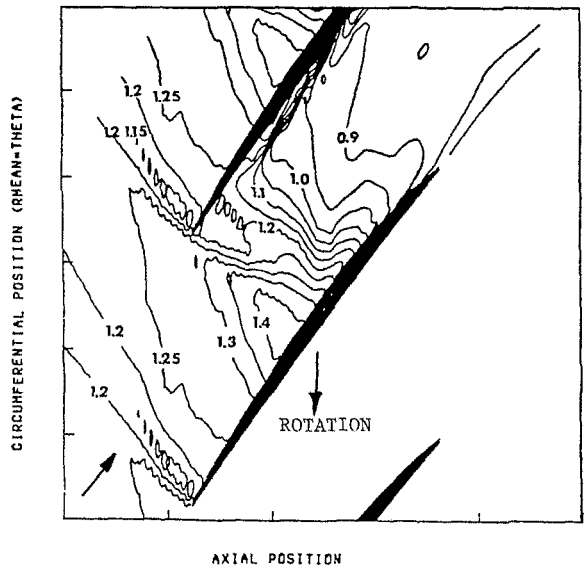

Fig. 4(d) Contour plot with final level of smoothing

efficiency point was repeated with the number of blade-to-blade points reduced from 21 to 11. The solution showed that the major difference between the coarse grid solution and the fine grid solution was a small change in location of the shock and in the relative Mach number ahead of the shock at the transonic sections. The shock also tended to be smeared slightly more with the coarse grid than with the fine grid. Evaluation of the computational method in terms of sensitivity of the code to grid size is not within the scope of the present work and is mentioned only to provide the reader with an indication of its importance for this rotor at this one flow point. The sensitivity of the solution to blade-to-blade grid spacing was not checked for the other flow conditions analyzed. Streamwise grid spacing was constant on the blading but was expanded upstream and downstream in order to isolate the boundaries from the leading and trailing edges with as few points as necessary in an attempt to capture the correct upstream wave strength and to limit the effect of a uniform circumferential pressure at the downstream boundary. In all cases multigrid ($7 \times 12 \times 3$) with a nonuniform time step was used.

The boundary-layer displacement thickness was updated every 50 time-steps, with 50 percent of the new displacement thickness added to 50 percent of the previous value. Fractional updating of the boundary layer was necessary since full correction tended to produce instability.

Convergence was assumed to occur when all the following conditions were met:

1 The maximum change in axial velocity anywhere in the flow field divided by the root-mean-square of all the absolute velocities in the flow field did not exceed .01 percent.

2 Mass flow at each streamwise grid line agreed with the inlet mass flow to within 0.3 percent.

3 Inlet mass flow did not change by more than 0.3 percent over several hundred time steps.

4 Mach numbers at four selected positions on the rotor suction surface did not change by more than 0.02 over several hundred time steps.

The foregoing conditions are rather stringent for this case and may not be required for other blade rows. The 0.01 percent restriction on axial velocity change could be relaxed to 0.02 in this case with little change in the solutions. The criterion for change in inlet mass flow rate was necessary for this blade row operating at near its peak efficiency point. For operation at lower than peak efficiency flow, small changes in mass flow rate are not as important and that condition could have been relaxed. During initial runs to establish the proper pressure ratio in order to set the peak efficiency flow, several solutions were obtained at flows very near that for peak efficiency (mass flow ratios of 0.984 and 0.998 versus the peak efficiency value of 0.992). At 10 percent span from the tip for both flows, the shock on the suction surface moved approximately 15 percent of axial chord from the position obtained at peak efficiency. For the higher flow, the shock on the pressure surface moved rearward by about 20 percent of axial chord and increased in face Mach number from about 1.23 to 1.36.

The code as described in [4] did not satisfy the boundary condition at a solid surface, requiring the velocity normal to the surface to be zero. Because of this, there are areas in the flow where the velocity does not have a zero normal component to a solid surface. This is particularly true around the leading edge of a blade and at points where a strong shock hits the solid surface. All solutions presented herein were produced with this condition at the solid surfaces. In order to check the effects on the solutions presented, the normal velocities were set at zero [11] at the solid surfaces and the flow point at peak efficiency repeated. Very little difference was found in the final solutions when judged in terms of line plots of near-blade relative Mach number and flow angles. The flow angle did conform to the blade angle at the surface but at one grid point off the blade the flow angles for the two cases with and without the zero normal velocity condition imposed were very similar. The major differences occurred at the percent span locations near the hub, where the leading edge is thick. Mach numbers on the suction surface were slightly higher than those obtained without the normal velocity set to zero. The shock location at all spanwise stations on the suction surface was the same for both cases. The numerical error in total pressure increased near the hub sections when the zero normal velocity condition was imposed.

For the computations with the boundary layers included, time steps to convergence ranged from 2486 for the peak efficiency case (where the location of the shock is very sensitive to even small mass flow changes) to 1300 at the maximum flow condition. Computation times on a Cray-1 computer were 17 and 9 min, respectively. Computation time on an IBM 370-3033 would be approximately 10 times as long. No appreciable increase in time resulted from use of the boundary layer calculations. The solution actually converged somewhat better with the boundary layer calculations than without.

Data Presentation

Due to the large quantity of experimental data collected, over 32.5 million velocity measurements per operating point, data presentation represents a major effort and concern. To compare the overall flow features observed in the experimental and analytical data, contour maps of relative Mach number are most useful. Experimental data, however, do not usually produce good quality contour maps. The background noise, nonuniform survey location spacing, problems associated with LA blade flash and data drop-out all contribute to poor quality plots. Analytical data, on the other hand, have very few of these problems as evidenced by the quality of such contour maps.

To avoid constructing contours of experimental data by hand for each flow condition surveyed, a method has been developed to "enhance" the LA data, without altering its informational content, such that it becomes suitable for computer generated contour plots. The following procedure was used to enhance the data before presentation:

1 Each blade-to-blade data window was first screened to confirm that there were at least one hundred LA measurements obtained and that the window circumferential extent did not overlap the pressure surface of a blade. If either condition was not satisfied, the recorded velocity value was set equal to zero.

2 An interpolation procedure was then used to establish values to fill the zero velocity data windows using information from adjacent survey points in both the streamwise and pitchwise directions. This method allowed information from both directions to influence the final interpolated value. Once the areas of zero velocity had been interpolated, the pitchwise data were smoothed such that a maximum change due to the smoothing was limited to 0.5 percent of the original value. This amount of smoothing removed the high-frequency noise in the data without distorting the highly desirable velocity gradient regions of the flow field.

3 These nonzero velocity data were then used to increase the streamwise data density by interpolating along preferred directions. Streamwise data density of 2.5 percent of axial chord was necessary to achieve the desired contour map quality.

4 Finally, these data were smoothed in the chordwise direction to eliminate small oscillations due to acquisition noise in the original data as well as possible peaks due to the interpolation procedure. The smoothing procedure permits a maximum change at any point of 0.5 percent of the unsmoothed value.

Figure 4 shows contours of relative Mach number for the 30 percent span immersion survey location at peak efficiency operation. Figure 4(*a*) represents a relative Mach number contour map using only the raw LA data including zero velocity values and blade interior values. Figure 4(*b*) shows the improvement that can be achieved with simple removal and replacement of "bad" data and a small amount of smoothing. Figure 4(*c*) shows the effect of increasing chordwise data density where data have been interpolated to every 2.5 percent axial chord. Finally, Fig. 4(*d*) shows the contour map which results from the screened, chordwise interpolated, smoothed data. As shown, the enhancement procedure enables reasonable contour maps to be constructed without changing the basic information found in the data that was not enhanced. This enhancement procedure, along with a four-step check similar to that shown in Fig. 4, was used to generate all of the remaining contour maps presented and to make certain that the enhancement process only clarified the contour plots and did not produce new features in the flow field.

Results and Discussions

Introduction. The data presentation initially focuses on the use of contour maps of relative Mach number to show changes in flow conditions as the rotor exit pressure was changed. Comparisons are made between the analysis code and the results obtained with the laser anemometer. Results are also presented in terms of overall pressure rise and turning as measured and predicted. Plots of relative Mach number at various flow rates and percent spans are shown to give a more detailed picture of the flow in a quantitative sense. In each line plot the analysis is compared to the LA data at comparable percent gap locations. Finally, some applications of

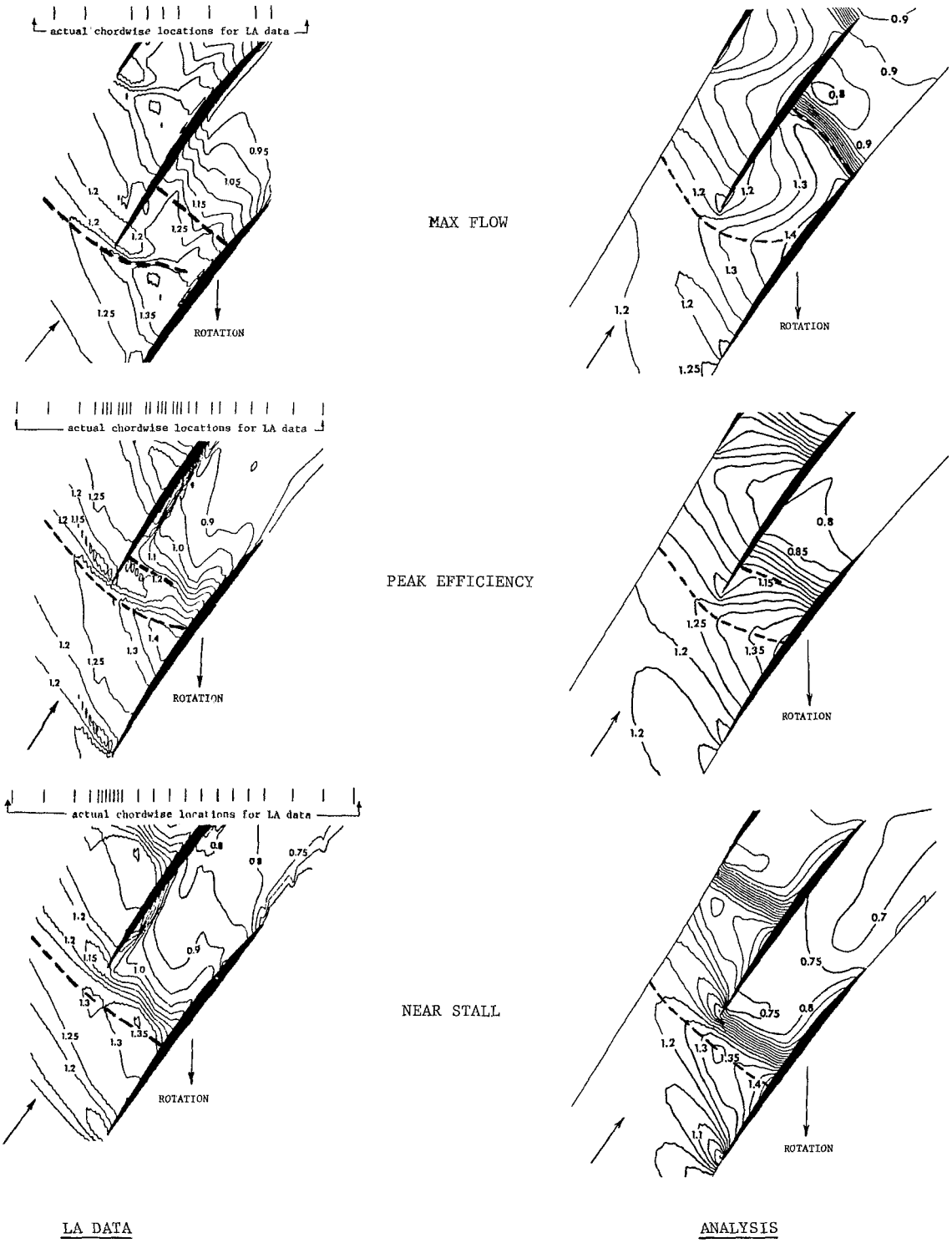

Fig. 5 Contour plots of relative Mach number at 30 percent span from the tip for max flow, peak efficiency, and near-stall flow points: comparison of LA survey results with analysis results. ---- Shock location.

the results which might have significance in the design of future compressor blading is addressed.

Mass flow rates measured in experimental facilities and calculated numerically have a degree of uncertainty associated with them such that comparison of absolute magnitudes may not match well. To compensate for this fact, all of the comparisons are made at mass flow rates that have been nondimensionalized with the maximum flow rate measured from the experiment or calculated by the analysis code as appropriate. Although this approach was taken, the agreement between the predicted maximum flow and the experimental measurement was excellent for both the runs without and with boundary layer calculations. The maximum flow predicted without boundary layers was 1.2 percent higher than the measured flow and that predicted with boundary layers was only 0.06 percent higher.

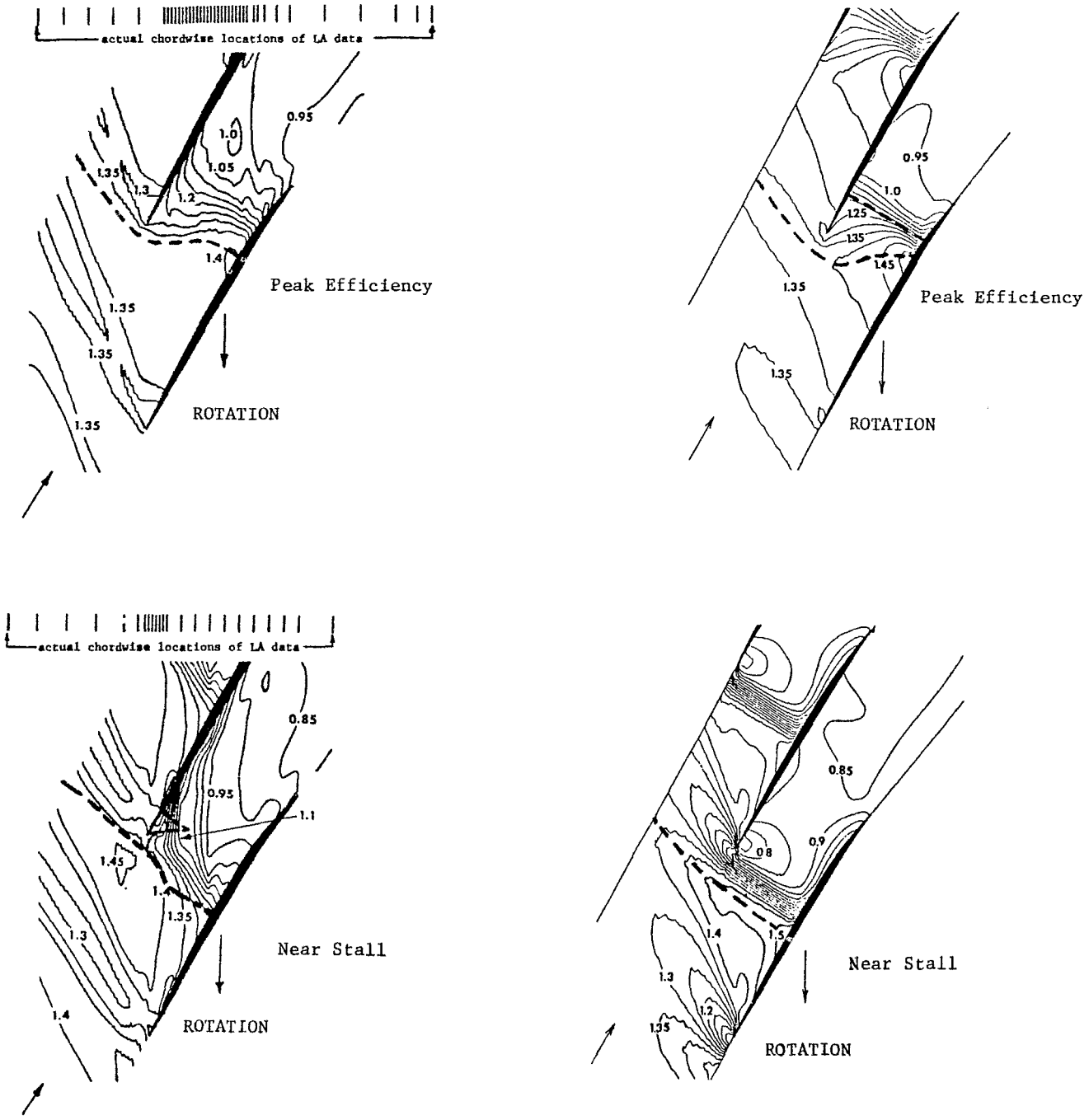

Fig. 6(*a*) Contour plots of relative Mach number at 10 percent span from the tip for the peak efficiency and near-stall flow rates: comparison of LA survey data with analysis results. – – – Shock locations.

Relative Mach Number Contours.

Thirty Percent Span. Figure 5 is a composite showing the results obtained with the laser anemometer and analysis code at 30 percent span for the three flow conditions; max flow, peak efficiency, and the near-stall point. The shock locations are shown for each flow rate in order to provide a clearer picture of the flow in the passage. Locations of the wave systems and shocks were determined by inspection of relative Mach number and relative flow angle data with respect to the streamwise direction and designating the starting point of the flow deceleration as the shock front. This was done at as many pitchwise locations as needed for the desired resolution. Experimental LA data must be interpreted in this manner due to possible seed particle lag once a high velocity gradient region is encountered. The numerical calculation actually produced shocks that were smeared over several grid points,

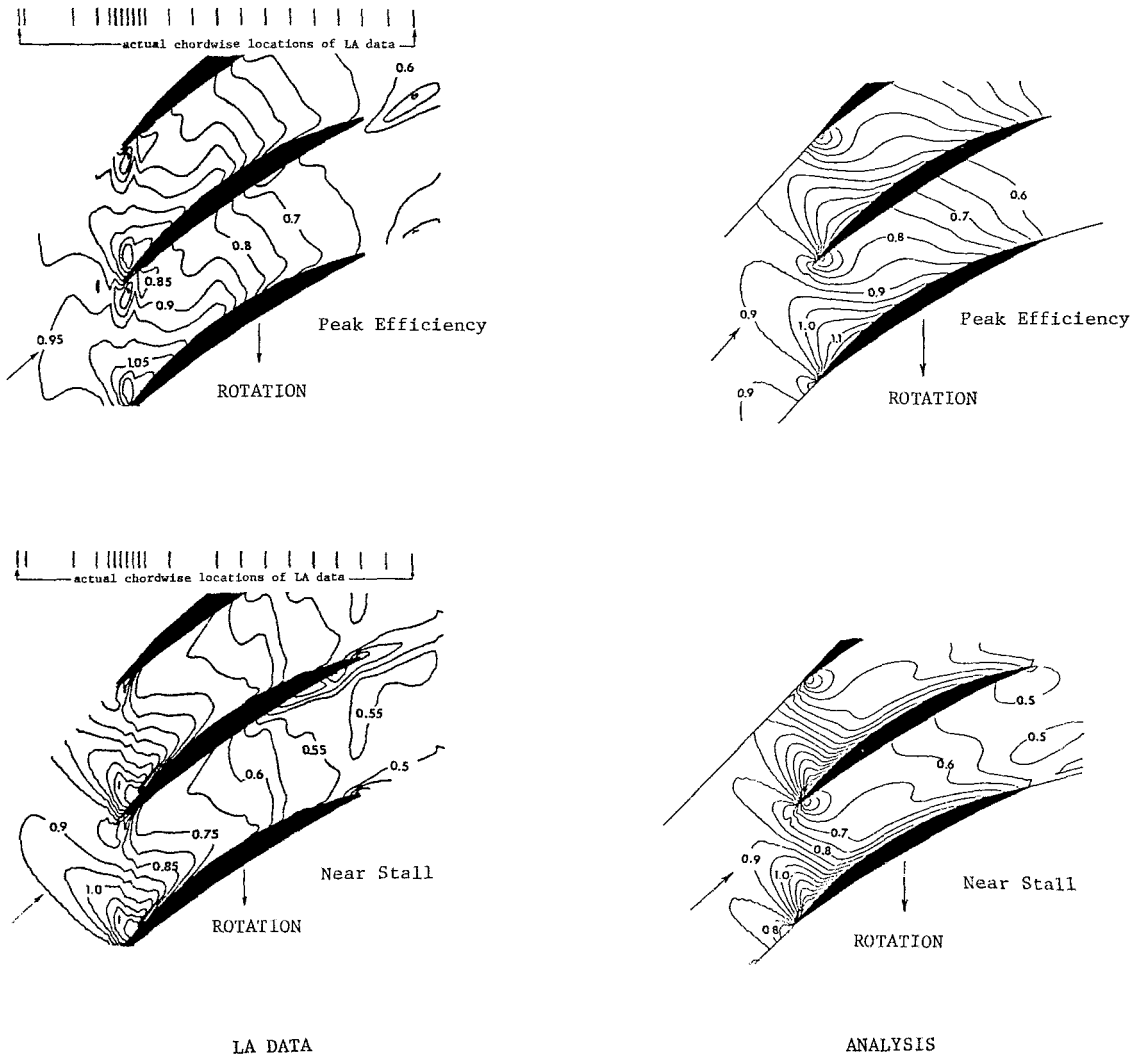

Fig. 6(*b*) Contour plots of relative Mach number at 70 percent span from the tip for the peak efficiency and near-stall flow rates: comparison of LA survey data with analysis results

and thus the actual location of the shock is between the beginning and ending of the deceleration. The grid spacing used herein was small, and the shocks were assumed to be located at the beginning of the deceleration.

The LA data in Fig. 5 show the progression from an oblique shock at max flow with supersonic flow in the aft portion of the blading, to a near normal shock followed by a second shock a peak efficiency, and finally, a single normal shock ahead of the blade leading edge at the near stall point. The peak Mach number varies from 1.4 ahead of the shock at max flow and peak efficiency to 1.35 ahead of the shock at near stall. Also shown in the figure are the results obtained with the three-dimensional analysis code. The major difference between the experiment and analysis at max flow is the location of the second shock at the exit of the passage. The peak Mach numbers upstream of the first shock are approximately equal. Although, the location of the second shock is sensitive to back pressure at the max flow condition, a 7 percent increase in back pressure was required in order to move the computed shock to the approximate position of the measured second shock. This is a large change in pressure, and it is more probable that the difference in location is a result of the constant shape factor used in the boundary layer calculations. Also, LA data in the aft portion of the rotor for the max flow condition were only taken at the 40, 60, 90, and 100 percent chord locations so that good shock definition in this region was very difficult. The Mach number at the rotor exit is less for the numerical results at this flow point than the measurements indicate (an exit Mach number of about 0.95 for the data and 0.9 for the analysis).

The agreement at the peak efficiency point between the data is much better than for the max flow case. The front shock is accurately located by the code and there is a rear shock located in approximately the same position as the measured rear shock. The second shock is shown extending from the pressure surface to about midpitch. At points closer to the suction surface, interpreting the location of the shock was more difficult, since an acceleration of the flow or a constant Mach number region was not found in the streamwise plots. However, indications of a second shock were found near the suction surface by noting changes in the Mach number gradient in the streamwise direction. This was true for both the analysis and LA data. The computed Mach number in the exit region of the blade is lower than the measured Mach number (0.8 compared to 0.9). Peak Mach number upstream of the shock is 1.4 for both the data and the analysis. The agreement between analysis and data at the near stall point is good in terms of shock location and peak Mach number. The comptured Mach number at blade exit is underpredicted (0.7 versus 0.8), as it was with the previous cases.

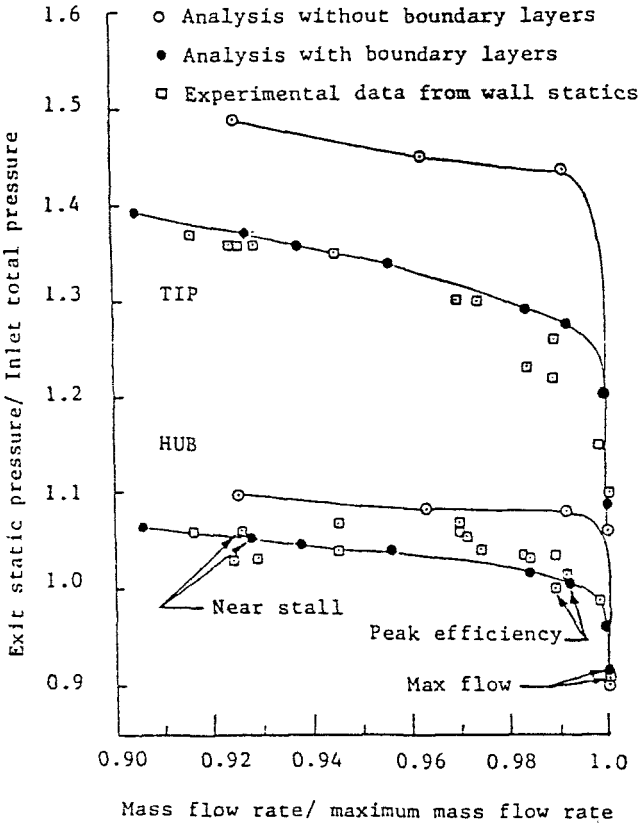

Fig. 7(*a*) Static pressure ratio across the rotor

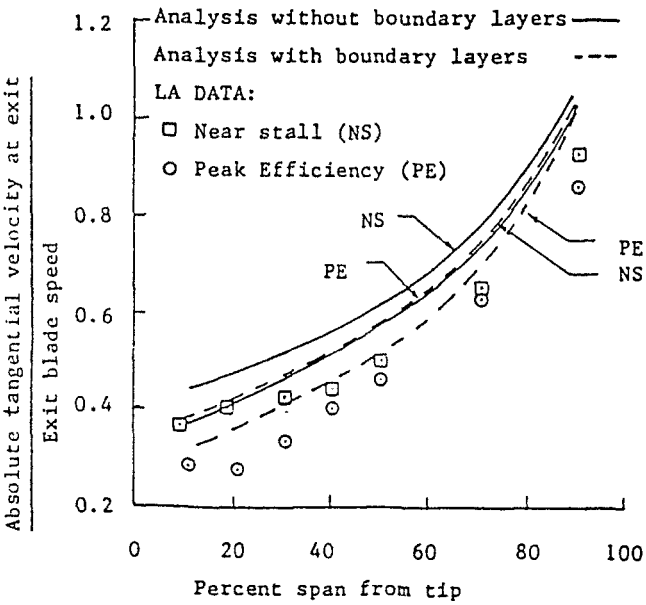

Fig. 7(*b*) Change in absolute tangential velocity at midpitch for peak efficiency and near-stall versus percent span from tip

Near Tip and Near Hub Sections. Figure 6 shows the peak efficiency and near stall flow points at the 10 percent span location (Fig. 6(*a*)) where the inlet relative Mach number is supersonic and at the 70 percent span location (Fig. 6*b*)) where the inlet relative Mach number is subsonic. Results are shown for both the experiment and the analysis. The peak efficiency LA data at 10 percent span in Fig. 6(*a*) shows a front shock that is nearly normal around the leading edge but

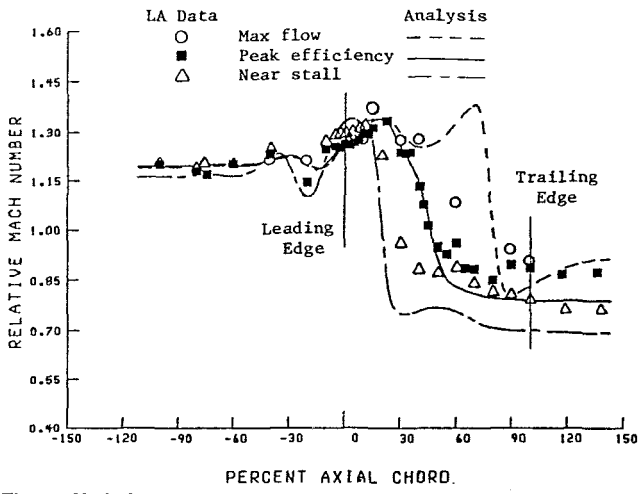

Fig. 8 Variation in relative Mach number with percent chord at midpitch for three flow points at 30 percent span from the tip

is oblique over most of the passage gap. Inspection of the streamwise and pitchwise LA data indicated that a second shock might exist. However, the data were not conclusive and thus a second shock is not indicated in the figure. A second shock was predicted by the three-dimensional analysis code at the approximate location suggested by the LA data. The high values of relative Mach number after the normal portion of the shock have been investigated by Strazisar [5] and appear to be due to the three-dimensional shock inclination in the hub-to-shroud plane.

At the near-stall point the second shock has disappeared from the analysis and only a normal shock standing in front of the blade remains. A second shock system on the pressure surface around the leading edge is indicated by the LA data. This feature appears to be necessary to guide the high incidence angle flow around the leading edge so that it can adjust to the blade surface angles. This assumption was supported by computing particle trajectories through this proposed system based on the wave angles and the measured inlet Mach number. Final pressure surface flow angles after passing through the second shock system were within a few degrees of the surface values. This phenomenon is not predicted by the analysis and may be due, at least in part, to tip region flow effects. More extensive analyses at other operating conditions and percent span locations with high incidence angles are required before a full explanation can be presented. Peak Mach numbers before the shock are, in both cases, approximately 0.1 higher for the analysis than for the data. Suction surface Mach numbers are generally higher (0.1 to 0.2) in the analysis since the viscous effects are incorporated only as a mass addition and not a momentum deficit.

Figure 6(*b*) shows maps of constant relative Mach number for peak efficiency and near stall at the 70 percent span location for both the LA data and the three-dimensional analysis results. Flow field features between the two operating conditions are very similar and agreement between the LA data, and the numerical results is quite good, although the analysis yields a slightly lower exit Mach number than experimentally verified.

Overall Performance. In Fig. 7 , an attempt has been made to provide a clear picture of how the three-dimensional analysis code compares to the experimental data on a global basis that could be useful in the design phase of a new blade row. Figure 7(*a*) shows the static pressure rise across the rotor at the hub and tip as a function of nondimensional mass flow

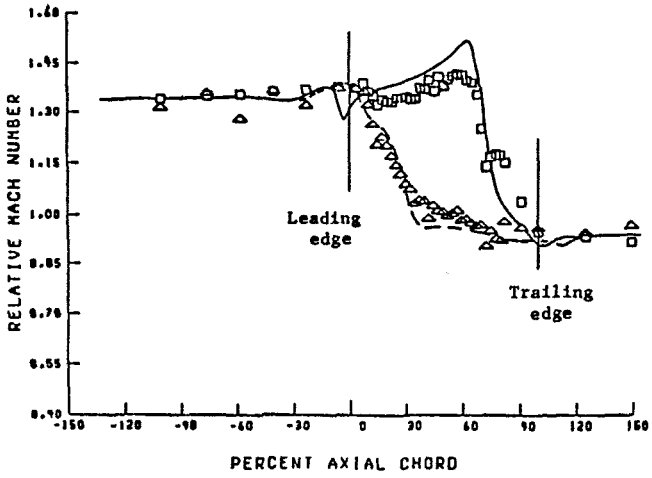

(a) 10 percent span from tip, peak efficiency

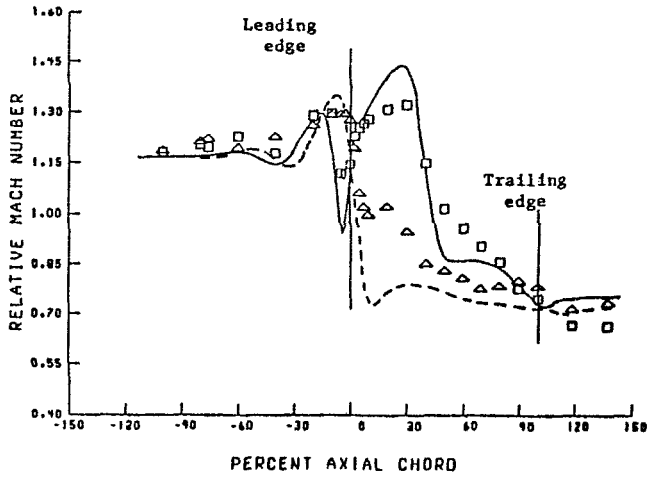

(d) 30 percent span from tip, near-stall

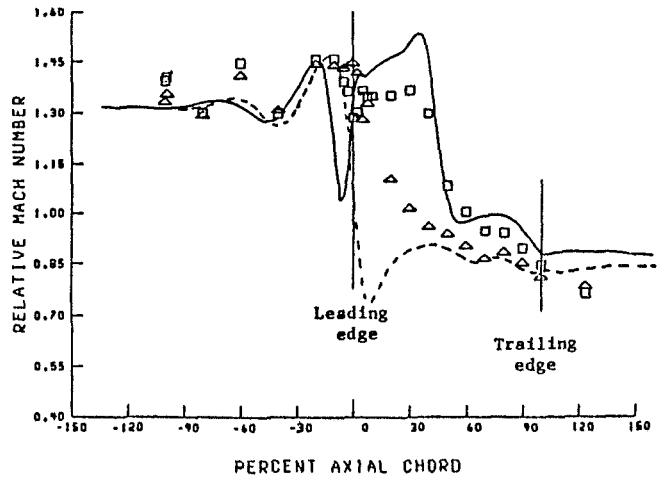

(b) 10 percent span from tip, near-stall

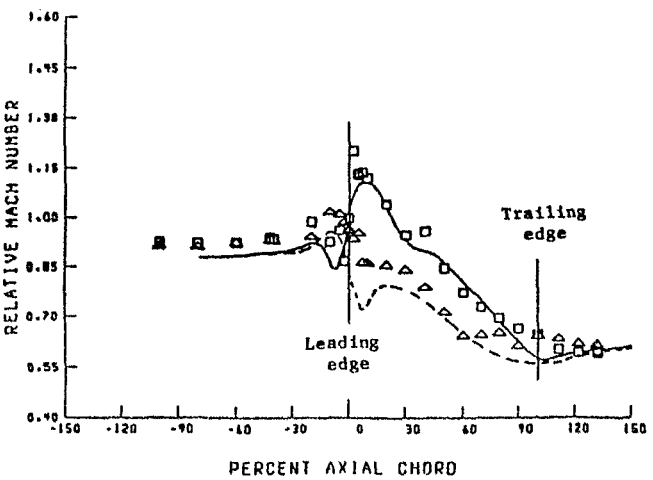

(e) 70 percent span from tip, peak efficiency

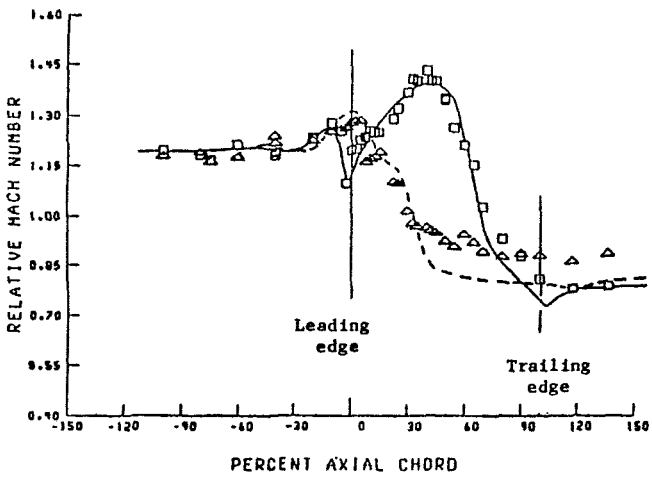

(c) 30 percent span from tip, peak efficiency

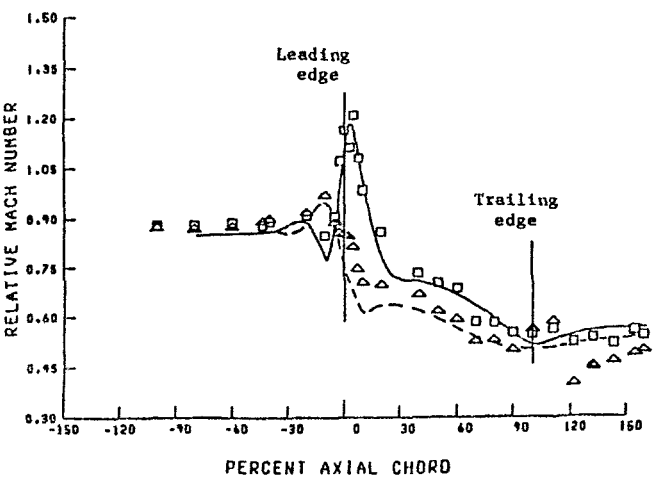

(f) 70 percent span from tip, near-stall

Fig. 9 Variation in relative Mach number with percent chord for three spanwise locations for peak efficiency and near-stall flows: □, LA data near suction surface, △ LA data near pressure surface; ___ analysis near suction surface; – – – analysis near pressure surface

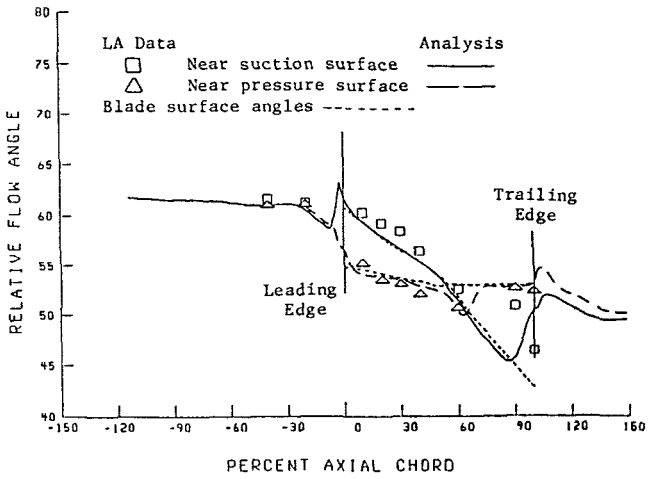

Fig. 10(*a*) Max flow point

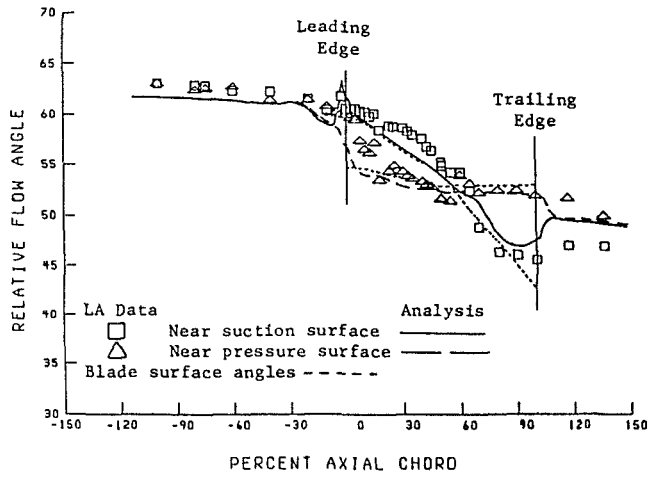

Fig. 10(*b*) Peak efficiency point

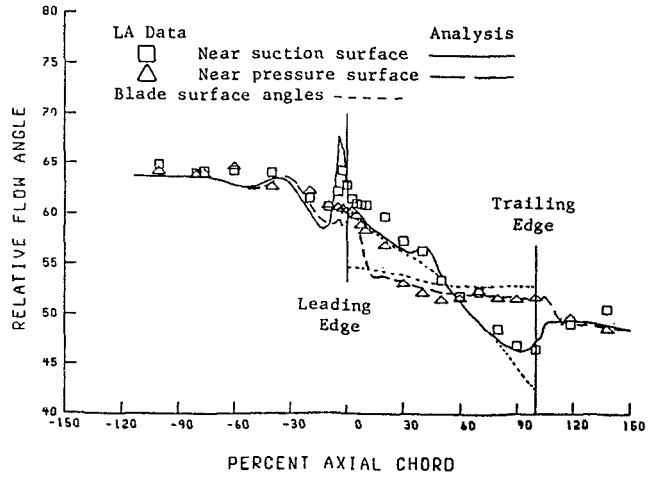

Fig. 10(*c*) Near-stall point

Fig. 10 Variation in relative flow angle with percent chord along the speed line for experiment and analysis at 30 percent span from the tip

rate. As expected, the analysis without boundary layers predicted a much higher pressure rise at both hub and tip than was measured with conventional pressure instrumentation. Excellent agreement between the measurements and the analysis with boundary layer effects is experienced over the entire speed line from max flow to near stall. Unstable operation of the rotor was experimentally observed at a mass flow ratio of about 0.89, while at a mass flow ratio of 0.906 the analysis was stable. The near-stall numerical solution was certainly aided by the restriction of a constant shape factor for the boundary layer calculations. Overall turning of the flow across the blade row at midpitch, given by rotor exit absolute tangential velocity divided by wheel speed is shown versus percent span for the peak efficiency and the near stall point in Fig. 7(*b*). Agreement between LA data and analytical results is within 30 percent at peak efficiency and less than 16 percent near-stall over the entire blade span. The pitchwise averages of the flow turning (not shown) agree within 21 percent at peak efficiency and within 15 percent for near stall. The temperature ratios across the rotor predicted by the analysis and preliminary data from standard aerodynamic survey probes (not shown) were compared at peak efficiency and found to agree within 2 percent over the entire span. This discrepancy between the LA results, analysis results, and standard aerodynamic measurements is expected to be resolved by application of high-frequency response pressure probes behind the rotor in future experiments.

Relative Mach Number at Midpitch. A more quantitative approach to comparison of the LA data and the analysis results is to look at data along the rotor midpitch line. It is precisely this type of plot that has been used to determine the shock front locations for all of the relative Mach number contour maps presented thus far. The relative Mach number along a midpitch line versus percent chord at 30 percent span for all three operating points is shown in Fig. 8. The expansion of the flow after the first shock at max flow as predicted by the analysis code leads to a strong passage shock at approximately 70 percent chord. Some indication of a second shock in the max flow LA data is evident from the peak in Mach number at 10 percent chord, plateau from 30 to 40 percent chord and subsequent deceleration from 40 to 60 percent chord. Agreement in the front shock location between the analysis and experiment is good but, as before, a low exit Mach number is predicted by the analysis. The differences in the second shock location may be due in part to insufficient LA survey locations in this region. Only one LA data point exists between the start of the computed reexpansion and the rotor exit. At peak efficiency, the two-shock system that was observed in earlier contour maps is again evident in the experimental data (shown by a plateau of Mach number from 20–30 percent chord) but not as evident in the analysis results. There is, however, a change in the gradient of computed Mach number at 40 percent chord, indicating the existence of the second shock. At percent gap locations closer to the pressure surface, the gradient change becomes more pronounced until the existence of the second shock becomes evident. Shock location and peak Mach number before the shock agree well for both peak efficiency and near stall.

Near-Blade Surface Comparisons. Generally, an important task for the blade row designer is to tailor the blade shapes so that adverse gradients that produce large growths in the boundary layer are either reduced or controlled. It is of great concern to determine how well a particular analysis code predicts the surface velocities in order to determine how much faith the designer should place in the ability to tailor the blading for low losses. Blade loading in terms of differences in relative Mach number across the channel in the pitchwise direction versus percent chord are shown in Fig. 9 for 10, 30, and 70 percent spans for both peak efficiency and near stall. The LA data are taken at the first point off the blade surface

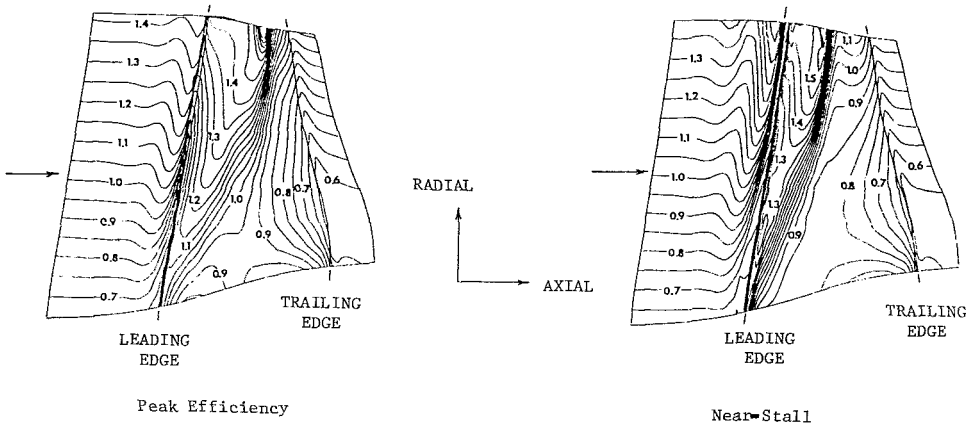

Fig. 11 Contours of suction surface relative Mach number projected on the meridional hub-to-shroud plane, analysis results

where a sufficient number of measurements were available. This was generally close to 5 and 95 percent pitch and, therefore, the analysis results were selected at these same locations. For all three spanwise locations the agreement on loading levels is reasonably good at peak efficiency. At near stall, however, the analysis yields much higher loadings at 10 and 30 percent span but is resonable at 70 percent. The major difference in the loading level results from lower computed Mach numbers on the pressure surface than measured. Suction surface agreement is generally good for both flow rates. For all percent span locations and flow points, the shock location on the suction surface is well predicted by the analysis.

Another area that is of some interest to the turbomachinery designer is the manner in which the flow is turned through the blade row. Figure 10 shows the measured relative flow angle as a function of percent chord for both the suction and pressure surfaces. The results are shown for the 30 percent span immersion location and for all three operating conditions. Also shown in the figure are the blade surface metal angles. The measured suction surface flow angles show that generally the flow follows the suction surface throughout the entire operating range. The analysis results of suction surface flow angle follow many of the same trends observed in the LA data. Flow deviations from the suction surface metal angle in the aft portions of the blade are observed both experimentally as well as analytically with the amount of deviation increasing from peak efficiency to near stall operation. The axial location at which the flow deviates from the blade changes from abut 90 percent chord at peak efficiency to about 80 percent chord near-stall. The data at max flow are too sparse to determine where the flow deviates from the blading.

The pressure surface flow angle data in Fig. 10 appear not to be as well behaved as the suction surface data. Both analytical and experimental data follow the blade surface over most of the chord, except in the leading edge region. Figure 10(*c*) indicates that the pressure surface flow angle does not adjust and start to follow the pressure surface at near stall as quickly as it did at the other conditions. It is not until about 30 percent chord that the relative flow angle matches the blade angle. The analysis also indicated that the flow does not adjust to the blading immediately at near-stall, however it adjusted more rapidly than the LA data indicates.

Analysis Results in the Meridional Plane. Figure 11 shows the nature of the shock system and how the numerical result changes from peak efficiency to near-stall. In this suction surface hub-to-shroud view, the shock inclination angle changes dramatically at radial positions between the tip and 30 percent span, while below 30 percent span, the inclination remains constant. The shock location changes from the aft portion of the blading near the tip to the front part of the blading near the hub. Overall, the Mach numbers in front of the shock increase as the operating point changes from peak efficiency to near stall. Since it is difficult to predict the point where stall will occur in the analysis, due to the use of a constant shape factor, one approach is to consider where the shock structure is strong enough to separate the boundary layer. The static pressure rise across a normal shock at a Mach number of 1.3 is generally considered sufficient to produce boundary layer separation. At the near stall flow, the Mach number contour at 1.3 penetrates to about 90 percent span from the tip and the inclination of the shock in the meridional plane decreases from that at peak efficiency. The shock is almost normal to the flow at near stall, and thus, the pressure rise across it is approaching that of a normal shock. The shock location has moved forward and occurs in front of the rotor throat. This combination could produce global separation on the blade and subsequent stall of the rotor. Information of this kind could be used for a new design to warn the designer of a potential stall condition.

Concluding Remarks

The comparisons between analytical and experimental data for a transonic, low-aspect ratio, axial-flow fan rotor have, in general, shown good agreement for all of the operating conditions presented. The overall trends in the relative Mach number contour maps indicate the very good shock capturing ability of the analysis code at all rotor span locations. The results presented have demonstrated the extent to which an inviscid Euler solver with a very simple boundary-layer correction scheme was able to predict the complex three-dimensional flow field of this transonic rotor flow field. The code predicted the maximum flow for the rotor extremely well. Results were also shown that indicate that the code may be useful in analysis of a new blade row design to insure that desired stall margin is attained. The chordwise plots of relative Mach number and relative flow angle reveal some area in which analysis and LA data deviate. Some of these conditions may be traced to the boundary layer model used.

A three-dimensional analysis technique, such as the one used herein, would probably not be used in the preliminary design of turbomachinery blading, however it may well be used to check a final configuration for design and off-design operation. This capability to compute the off-design flow field is extremely important and has shown to yield

reasonably good quantitative results for the present rotor configuration. The analysis code did not predict the multiple shock system on the pressure surface required to turn the flow parallel to the blade. This may have been due to the numerical smoothing used in the code and should be investigated further. Results concerning the intra-blade flow turning and work distribution should be useful information for compressor design systems.

As mentioned, the goal of the current NASA/ARMY research program is centered around increasing the fundamental understanding of the three-dimensional flow field of compressor blading. The material presented has been one such attempt to investigate the flow field of a particular transonic fan rotor, and as such, the results shown apply only for this case. Further work dealing with different types of blading is needed to determine how much of what was observed experimentally and computed numerically for this isolated rotor is generic to this class of turbomachine and how much was rotor specific. As more machines are investigated, questions such as blade row interactions and multistage matching should also be addressed.

Acknowledgment

The authors wish to express their appreciation to Mr. Gary Podboy for his efforts in reducing the volumes of LA experimental data and to Mr. Jong Liu for his assistance with the three-dimensional numerical analysis code.

References

1 Chima, R. V., and Strazisar, A. J., "Comparison of Two- and Three-Dimensional Flow Computations With Laser Anemometer Measurements in a Transonic Compressor Rotor," ASME JOURNAL OF ENGINEERING FOR POWER, Vol. 105, No. 3, July 1983, pp. 596–605.

2 Sarathy, K. P., "Computation of Three-Dimensional Flow Fields Through Rotating Blade Rows and Comparison with Experiment," ASME JOURNAL OF ENGINEERING FOR POWER, Vol. 104, No. 2, Apr. 1982, pp. 394–402.

3 Singh, U. K., "A Computation and Comparison with Measurements of Transonic Flow in an Axial Compressor Stage with Shock and Boundary Layer Interaction," ASME JOURNAL OF ENGINEERING FOR POWER, Vol. 104, No. 2, Apr. 1982, pp. 510–515.

4 Denton, J. D., Lecture Notes, ASME Turbomachinery Institute Course on Fluid Dynamics of Turbomachinery, July 18–27, 1983.

5 Strazisar, A. J., "Investigation of Flow Phenomena in a Transonic Fan Rotor Using Laser Anemometry," proposed paper for the ASME 29th Gas Turbine Conference and Exhibit, July 3–7, 1984.

6 Urasek, D. C., Gorrell, W. T., and Cunnan, W. S., "Performance of Two-Stage Fan Having Low Aspect Ratio First-Stage Rotor Blading," NASA TP-1493 ad AVRADCOM TR 78-49, Aug. 1979.

7 Cunnan, W. S., Stevans, W., and Urasek, D. C., "Design and Performance of a 427-Meter-Per-Second-Tip-Speed Two-Stage Fan Having a 2.40 Pressure Ratio," NASA TP-1314, Oct. 1978.

8 Powell, A. J., Strazisar, A. J., and Seasholtz, R. G., "Efficient Laser Anemometer For Intra-Rotor Flow Mapping in Turbomachinery," ASME JOURNAL OF ENGINEERING FOR POWER, Vol. 103, No. 2, Apr. 1981, pp. 424–429.

9 Strazisar, A. J., and Powell, J. A., "Laser Anemometer Measurements in a Transonic Axial Flow Compressor Rotor," ASME JOURNAL OF ENGINEERING FOR POWER, Vol. 103, No. 2, Apr. 1981, pp. 430–437.

10 Denton, J. D., "An Improved Time Marching Method for Turbomachinery Calculation," ASME Paper 82-GT-239, 1982.

11 Glassman, A. J., private communications, Lewis Research Center, Nov. 1983.

reasonably good quantitative results for the present rotor configuration. The analysis code did not predict the multiple shock system on the pressure surface required to turn the flow parallel to the blade. This may have been due to the numerical smoothing used in the code and should be investigated further. Results concerning the intra-blade flow turning and work distribution should be useful information for compressor design systems.

As mentioned, the goal of the current NASA/ARMY research program is centered around increasing the fundamental understanding of the three-dimensional flow field of compressor blading. The material presented has been one such attempt to investigate the flow field of a particular transonic fan rotor, and as such, the results shown apply only for this case. Further work dealing with different types of blading is needed to determine how much of what was observed experimentally and computed numerically for this isolated rotor is generic to this class of turbomachine and how much was rotor specific. As more machines are investigated, questions such as blade row interactions and multistage matching should also be addressed.

Acknowledgment

The authors wish to express their appreciation to Mr. Gary Podboy for his efforts in reducing the volumes of LA experimental data and to Mr. Jong Liu for his assistance with the three-dimensional numerical analysis code.

References

1 Chima, R. V., and Strazisar, A. J., "Comparison of Two- and Three-Dimensional Flow Computations With Laser Anemometer Measurements in a Transonic Compressor Rotor," ASME JOURNAL OF ENGINEERING FOR POWER, Vol. 105, No. 3, July 1983, pp. 596–605.

2 Sarathy, K. P., "Computation of Three-Dimensional Flow Fields Through Rotating Blade Rows and Comparison with Experiment," ASME JOURNAL OF ENGINEERING FOR POWER, Vol. 104, No. 2, Apr. 1982, pp. 394–402.

3 Singh, U. K., "A Computation and Comparison with Measurements of Transonic Flow in an Axial Compressor Stage with Shock and Boundary Layer Interaction," ASME JOURNAL OF ENGINEERING FOR POWER, Vol. 104, No. 2, Apr. 1982, pp. 510–515.

4 Denton, J. D., Lecture Notes, ASME Turbomachinery Institute Course on Fluid Dynamics of Turbomachinery, July 18–27, 1983.

5 Strazisar, A. J., "Investigation of Flow Phenomena in a Transonic Fan Rotor Using Laser Anemometry," proposed paper for the ASME 29th Gas Turbine Conference and Exhibit, July 3–7, 1984.

6 Urasek, D. C., Gorrell, W. T., and Cunnan, W. S., "Performance of Two-Stage Fan Having Low Aspect Ratio First-Stage Rotor Blading," NASA TP-1493 ad AVRADCOM TR 78-49, Aug. 1979.

7 Cunnan, W. S., Stevans, W., and Urasek, D. C., "Design and Performance of a 427-Meter-Per-Second-Tip-Speed Two-Stage Fan Having a 2.40 Pressure Ratio," NASA TP-1314, Oct. 1978.

8 Powell, A. J., Strazisar, A. J., and Seasholtz, R. G., "Efficient Laser Anemometer For Intra-Rotor Flow Mapping in Turbomachinery," ASME JOURNAL OF ENGINEERING FOR POWER, Vol. 103, No. 2, Apr. 1981, pp. 424–429.

9 Strazisar, A. J., and Powell, J. A., "Laser Anemometer Measurements in a Transonic Axial Flow Compressor Rotor," ASME JOURNAL OF ENGINEERING FOR POWER, Vol. 103, No. 2, Apr. 1981, pp. 430–437.

10 Denton, J. D., "An Improved Time Marching Method for Turbomachinery Calculation," ASME Paper 82-GT-239, 1982.

11 Glassman, A. J., private communications, Lewis Research Center, Nov. 1983.

DISCUSSION

D. C. Prince, Jr.[1]

This paper contains a large amount of very interesting and useful information about the aerodynamic behavior of a transonic fan rotor. I believe, however, that some aspects of this information continue to be rather mysterious, and hope that the authors will be able to expand on their discussion.

I am particularly concerned in these data about whether the laser anemometer measures enough momentum change through the rotor. Figure 7(*b*) shows that the absolute tangential velocity measured at rotor exit midpitch is substantially less than is predicted analytically. The text, however, states that the analytical prediction agrees with standard aerodynamic measurements within 2 percent over the entire span. I hope the authors can comment on whether the absolute tangential velocity measured by the LA farther downstream, perhaps at 50 percent chord downstream of the rotor exit, is the same as that measured at rotor exit, or is in better agreement with the standard instrumentation.

I also observe that the measured shock discontinuities shown at all test conditions in Figs. 5 and 6 for streamlines at 10–15 percent of the flow off both pressure and suction surfaces are nearly perpendicular to the flow direction. It seems surprising to me that the Mach number downstream of a perpendicular front is not clearly subsonic. If, as I suppose, the seed particles whose velocity is actually measured by the LA only catch up to the flow at some distance downstream of the rotor exit, it seems possible that they would also miss measuring a substantial fraction of the shock discontinuity.

A recent analysis, based on the drag of spheres at low Reynolds numbers, suggests that seed particles at 1 micron diameter could have acquired no more than 30 percent of the acceleration of the carrying air after traveling 10 percent of the axial chord downstream of a shock. The results also suggest that the seed particles might have to be as small as 0.25 microns in diameter for a reliable measurement of the shock discontinuity.

I would appreciate some discussion by the authors on the possible use of the vector momentum change across the shock discontinuities to support the identifications of shock locations and orientations. According to conventional supersonic aerodynamics the vector momentum change should be perpendicular to the shock front.

Finding that the Mach number downstream of a near-normal shock is not clearly subsonic is as troublesome in the analytical results of Figs. 5 and 6 as in the experimental results. My experience suggests that Euler solvers with highly skewed calculation grids may underestimate shock strengths, and sometimes completely suppress oblique shocks.

W. J. Calvert[2]

How well do the experimental and calculated variations of temperature rise and of blade deviation angle agree along the blade span?

[1] Consulting Engineer, General Electric Co., Cincinnati, Ohio

[2] Procurement Executive, Ministry of Defence, Royal Aircraft Establishment, England

Author's Closure

The authors wish to thank both Dr. Prince and Dr. Calvert for the time and effort spent in preparing their discussions of our paper. We feel strongly that there is a great deal of information yet to be extracted from these data.

In reference to Dr. Prince's question of momentum change across the blade row, Fig. 7(*b*) does indicate large differences in absolute tangential velocity measurements at the blade exit. The information in Fig. 7(*b*) is obtained from the LA data by stacking the streamsurface survey data taken over a period of several months. Although one would expect that as long as the operating points are carefully controlled, as they were, there should be no problem in establishing identical flow conditions over this time period. However, the turning for this blade row at the exit changes by double the amount of change in axial velocity at the exit; thus, small changes in mass flow settings produce large changes in exit tangential velocity.

To better understand the relation between LA data, standard aerodynamic data, and code results, we have reduced additional LA data which were taken at the rotor peak efficiency condition. However, instead of streamsurface surveys, the data were obtained along radial lines corresponding to the standard aerodynamic stations and the rotor leading and trailing edges. These data allow for a more direct comparison of spanwise flow quantities.

The results of comparing these data at station 2, see Fig. 2(*a*), indicate that for the peak efficiency case, the LA tangential velocity measurements agree with standard instrumentation to within 3–4 percent along the entire blade span. The analysis results, on the other hand, differ from the probe data by about 8–10 percent, and always on the high side. This result is consistent with Fig. 7(*b*) and the statement in the text which quotes a 2 percent agreement in temperature ratio between the analysis and the aerodynamic instrumentation.

This 2 percent difference in temperature ratio corresponds to about 10 percent difference in temperature rise (and thus, change in angular momentum). We would then conclude, based upon the more recent data taken with the LA as a radial survey, that the laser anemometer does measure momentum change across the rotor that is consistent with our standard instrumentation.

In addition to the station 2 data, we have also reduced LA data taken at the rotor trailing edge at various spanwise locations for peak efficiency. Comparisons of these data show that the LA relative flow angles agree within 2 degrees of the values obtained from the standard instrumentation over the blade span.

Likewise, the results of the analysis show similar agreement for relative flow angle at the trailing edge. Based on these results and in answer to Dr. Calvert's question, the LA measurements, the standard instrumentation measurements, and the analysis all yield values of relative flow angle (and thus, deviation) which are very close. The question of temperature rise can be related back to the results of tangential momentum measurements just discussed which need further study.

As Dr. Prince noted, the question of particle lag is of concern when measuring large changes such as those occurring across a shock. Dr. Prince correctly notes that the Mach numbers behind the shocks as presented appear to be too high. We made a one-dimensional calculation for the 10 percent span section of the change in conditions across the bow wave near the leading edge (the face Mach number was 1.374) and obtained an aftershock Mach number of 1.17 compared to a measured value of 1.26. Particle lag was discussed in [9]; according to the relations described therein, we calculated the distance where a 1.3 micron particle would achieve 50 percent of the expected deceleration across the shock. Using this 50 percent deceleration value, we calculated an aftershock absolute tangential velocity that agreed within 0.7 percent of the measurements at the corresponding distance downstream and normal to the shock. The LA particles were apparently prevented from attaining the expected postshock velocity farther downstream by expansion waves emanating from the suction surface. This same calculation was done at about 30 percent pitch from the pressure surface at 22.5 percent chord. This calculation neglected the effect of meridional lean on the normal shock Mach number since local lean angle was shown in [5] to be unimportant at this percent span location. Results of the lag calculations indicate that a 1.3 micron particle would attain the velocity of the aftershock air at about 40–50 percent chord.

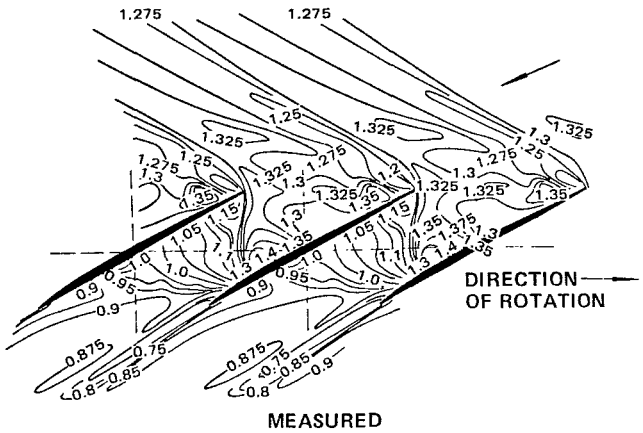

Fig. 12 Mach number distribution of DFVLR rotor at maximum efficiency [12]

We agree with Dr. Prince that immediately behind the shock near the leading edge, even small particles (less than 1 micron) will not have sufficient time to attain aftershock velocity. Indeed, most particles near the pressure surfaces immediately downstream of the shock may be impacted by the blade according to the simple shock and particle lag relations.

Data taken by DFVLR [12] also indicate higher than expected Mach numbers behind *a* (Fig. 12). The data taken by DFVLR were taken with a laser transit anemometer which can detect submicron particles so the particle lag effects should be less of a consideration than those used in the current study. With a face Mach number of about 1.3, the measurements do not indicate subsonic flow until past 50 percent chord. The consistency between our data and that by DFVLR in this area would tend to indicate that simple particle lag considerations in this very complex flow field may not be sufficient to account for the measured velocities. We agree, however, that it is a fruitful area to research.

References

12 Dunker, R. J., and Hungenberg, H. G., "Transonic Axial Compressor Using Laser Anemometry and Unsteady Pressure Measurements," *AIAA Journal*, Vol. 18, No. 8, Aug. 1980.

Holographic Measurements and Theoretical Predictions of the Unsteady Flow in a Transonic Annular Cascade

M. R. D. Davies
Whittle Laboratory.

P. J. Bryanston-Cross
CEGB Research Fellow,
Whittle Laboratory.

University of Cambridge,
Cambridge, U.K.

A series of measurements have been made on a transonic annular cascade. The cascade which represents the tip section of a compressor fan blade has an inlet Mach number of 1.18. By the use of external vibrators it is possible to vibrate the blades independently in torsion simulating different interblade phase angles in order to gain an understanding of shock movement and blade loading. The results presented are made over interblade phase angles of 180 and 135 deg at a blade frequency parameter of 0.1, based on chord. The holographic data obtained shows detail of shock movement during the cycle using a miniature holocamera located within the hub of the cascade. Unsteady sidewall pressure measurements have also been obtained over the vibration cycle. The data obtained have been compared with finite element calculations.

Introduction

The possibility of flutter in turbomachinery continues to be of concern to engine manufacturers. This, coupled with progress in predicting single blade and bladed disk vibrational modes, has provided the driving force for the development of unsteady aerodynamic moment calculations. Currently the most successful of these has been the numerical field methods as developed by Whitehead [1], and Verdon and McCune [2]. However, the published data for comparison with these techniques are sparse, mainly due to the difficulties of producing blade to blade repeatability with unsteady results. Carta's results [3], for example, are of high quality but are limited to incompressible flows. The unsteady forces generated in compressible flow are considered to be substantially different, as described by Whitehead [4]. In particular there is uncertainty as to the nature of the blade forces generated when a shock moves over the blade surface in supersonic flow. Fleeter et al. [5] for example found no effects attributable to this movement in their supersonic experiments.

In this experiment an annular cascade of blades was excited externally in a supersonic flow. Both the interblade phase angle and the vibrational amplitude were held constant by means of negative feedback. Holography was used to visualize the position of the compressor shock system at different points throughout a blade vibration cycle for two interblade phase angles. These results have been compared with both the steady and unsteady parts of Whitehead's Finsup program [1]. They have also been compared with pressure transducers situated in the hub. The comparison shows an agreement for the steady state solution. In the unsteady flow, although large, quarter span, shock movements are consistently observed over the blade cycle, they have not been seen to follow it with a constant phase angle. The size of the shock movement is, however, equal in width to shock induced unsteady peak predicted by Finsup.

Finally this is the first time holographic flow visualization has been shown to operate from within a supersonic annular cascade without the complex corrective optics associated with other optical techniques.

1 The Annular Cascade

The experimental program was carried out on an annular cascade designed by Whitehead, Watson, and Nagashima [6], then developed by Nagashima [7] and Grant [8]. The cascade was required as a versatile rig for measuring unsteady loads on turbine and compressor blades. The magnitude of these loads can be greatly affected by the acoustic properties of the cascade. An annular rather than a linear arrangement was chosen to better reproduce the acoustics of a real machine.

Figure 1 shows a section through the cascade. Axial flow is steadily accelerated to the inlet of 32 inlet guide vanes. These act as supersonic nozzles, accelerating and turning the flow onto a cascade of biconvex, double circular arc, untwisted blades, staggered at 58 deg, one span length axially downstream. The I.G.V. wakes pass between these blades. Eight equispaced static pressure tappings are available on the inner and outer walls between the two blade rows and the total

Contributed by the Gas Turbine Division of THE AMERICAN SOCIETY OF MECHANICAL ENGINEERS and presented at the 29th International Gas Turbine Conference and Exhibit, Amsterdam, The Netherlands, June 4–7, 1984. Manuscript received at ASME Headquarters, January 12, 1984. Paper No. 84-GT-174.

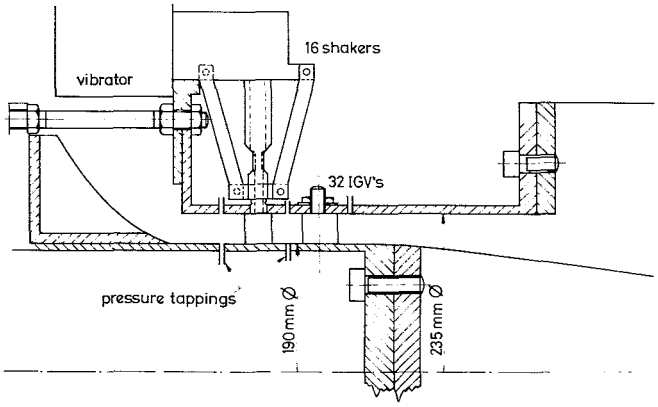

Fig. 1 General view

Table 1 Steady and unsteady cascade data

Overall Dimensions	
Tip diameter	235 mm
Hub diameter	190.5 mm
Hub/Tip ratio	0.811
Annular height	22.2 mm
Inlet Guide Vanes	
Number of blades	32
Spacing at mean diameter	20.9 mm
True chord	44.1 mm
Axial chord	36.7 mm
Stagger angle	33°
Air outlet angle	60°
Vibrating Cascade	
Number of blades	16
Spacing at mean diameter	41.8 mm
Chord	41.6 mm
Space/chord ratio	1.005
Stagger angle	58°
Thickness	4%
Type double circular arc	
Reynolds number	$4.9\times10^5-6.5\times10^5$
Blade material Aluminum allow (H15TB)	
Unsteady Data	
Frequency	160 Hz ± ½Hz
Frequency parameter	0.104–0.205
Torsional axis – mid chord amplitude of vibration	0.5° ± 0.003°
Interblade phase angle	$(2n/16)$ $(n=1.2...16)$

pressure is measured just upstream of the guide vanes in the nose of the contraction. Full steady and unsteady details of the cascade are given in Table 1.

Each one of the biconvex blades is driven independently in pure torsion about the midchord at a frequency parameter of 0.1. A lower value than ever encountered in engine blading. This independent drive allows an adjustable interblade phase angle to be set electronically; the variation of this angle around the annulus is shown in Fig. 2.

2 Unsteady Wall Pressures

Three pressure transducers were fitted flush into the inner wall of the cascade. This wall could be moved axially and tangentially relative to the blades so that the unsteady wall pressures could be measured anywhere in the blade passage. The measuring positions and dimensions are given in Fig. 3. The transducer signal was filtered of all components other than that of the blade vibration frequency. There was always a strong signal at this frequency. The background signal was pure noise although its amplitude varied considerably with Mach number and interblade phase angle. The phase of the pressure signal relative to the blade motion was also measured; this was found to be unreliable under some flow conditions and has therefore not been included.

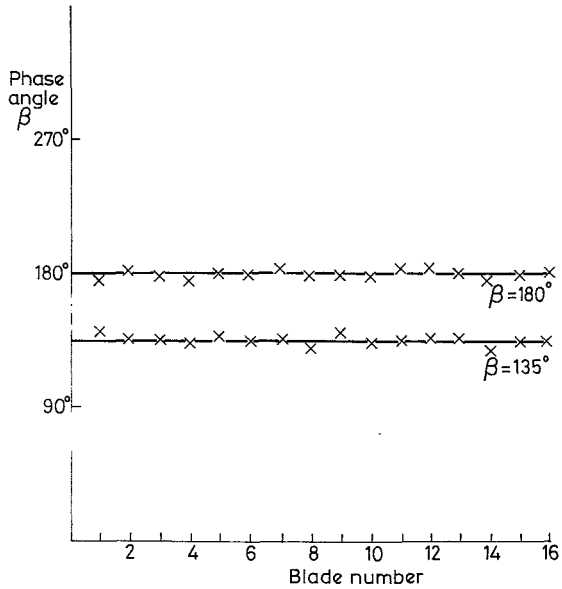

Fig. 2 Circumferential variation of interblade phase angle β

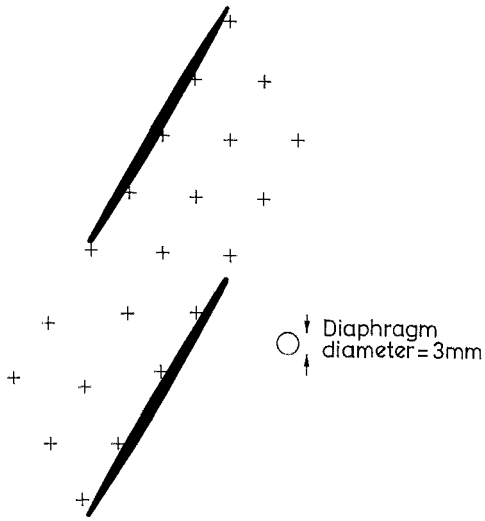

Fig. 3 Pressure transducer positions

3 Holographic Flow Visualization

The construction of the annular cascade at the Whittle Laboratory provided a formidable challenge to the application of any optical visualization technique. The only viewing window available was situated within the hub Fig. 4; and the cascade was itself enclosed within a 2-m-dia. pressure vessel. However, there was clearly a need to provide optical measurements to compare with the spatially limited number of pressure transducer measurements and with theoretical predictions.

Holographic interferometry was chosen as the flow visualization technique because it did not require the complicated corrective optics normally associated with either shadowgraphy or schlieren methods [9], when operated within an annular cascade.

It also provided a near instantaneous picture of the shock wave structure as opposed to the long sample averaging periods associated with laser anemometry [10]. Further it has also been possible to visualize some of the three-dimensional features found in the leading edge shock region. This was seen

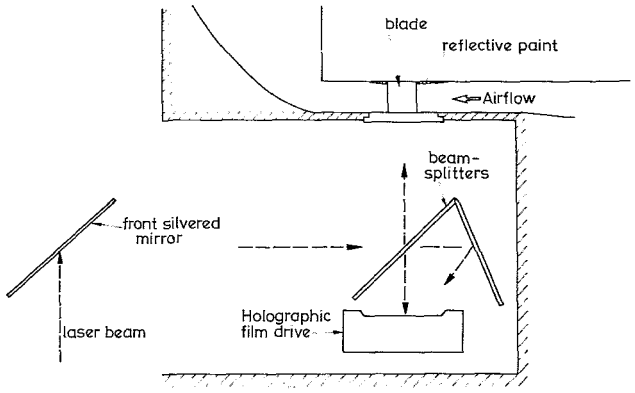

Fig. 4 Optical layout

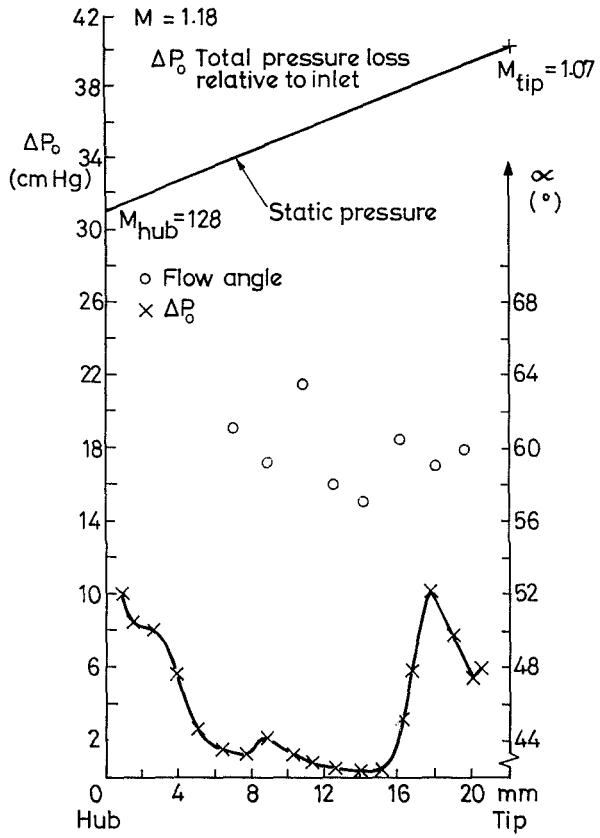

Fig. 5 Spanwise variation of P_0 and α

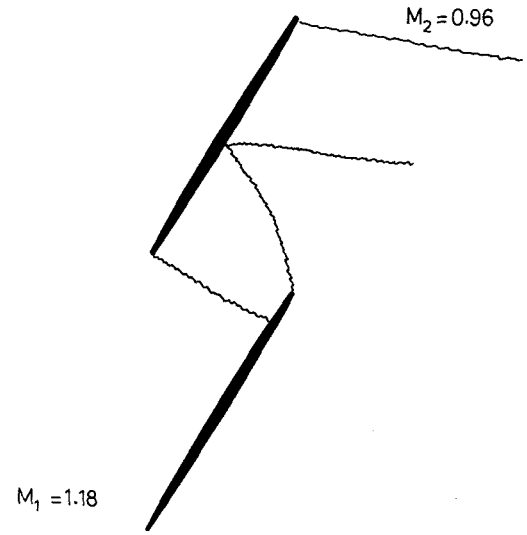

Fig. 6 Steady flow shock structure from holography

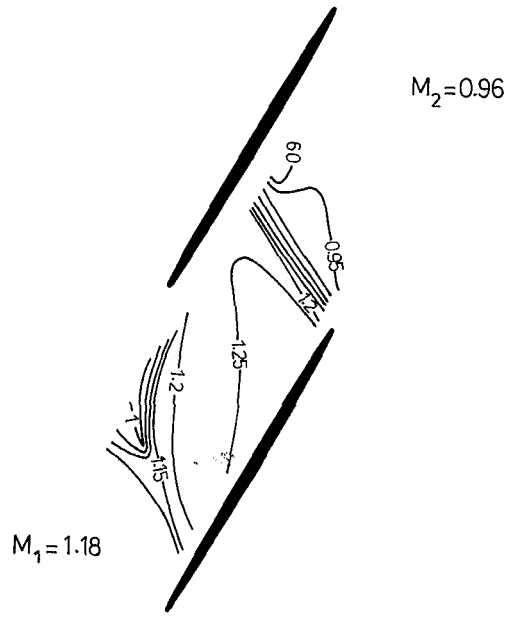

Fig. 7 Steady Mach number contours from Finsup

in some of the original holograms as a three-dimensional bowing of the shock. However in order to make the photographic reconstructions shown in Fig. 14 a large drop in image quality has been tolerated. This is the difference between being able to "look around" a three-dimensional image as opposed to viewing a two-dimensional photographic print.

The laser beam was produced by a ruby pulse laser, previously described in [11]. The beam was first collimated then projected through a perspex window in the outside pressure chamber. It was then turned through 90 deg by a front silvered 100-sq-mm mirror, which directed it inside the 120-mm-dia. hollow hub Fig. 4. Inside the hub was mounted a 70-mm automatic film drive carrying a 10e75 Agfa holotest film and two beam splitters. The first beam splitter reflected the beam through a window in the hub onto the casing on the far side of the blades. The casing wall had been painted with reflective paint, this paint which consists of very small glass beads which reflect light directly back along its original path. This removed the need for a highly polished interior surface. The reflected beam from the casing then passed back through the window and the beam splitter onto the holotest film. The second beam splitter was used to produce an internal reflection which was also directed onto the film forming a reference beam. Two laser pulses were produced separated by a short time delay (200 μs, 6 percent of the blade period). This was found adequate to visualize the shock structure around the blades. The pulses were synchronized to the blade vibration cycle using an electronic triggering system. It is noted that the 70-mm holographic film was loaded into conventional film cassettes. As a result of this it was only possible to take a sequence of 10 holograms on each film. At the end of which the rig was shut down and the holographic assembly removed from the hub to change film cassettes.

A fuller account of the theory of holographic shock visualization in supersonic flow is given in [11] to [13].

4 Program Finsup

Finsup is a field method for calculating the steady and

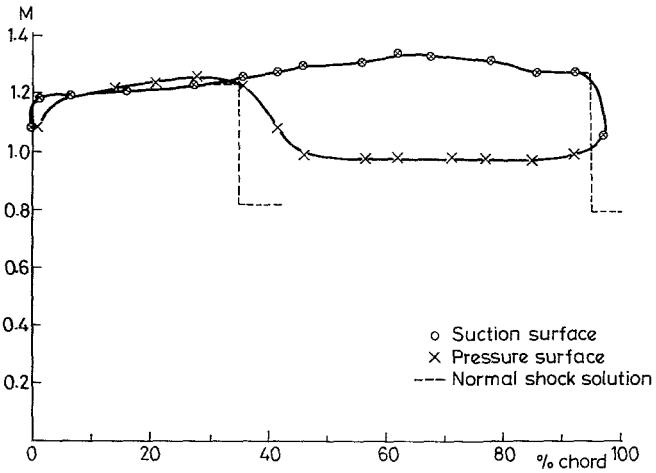

Fig. 8 Finsup prediction of the steady flow

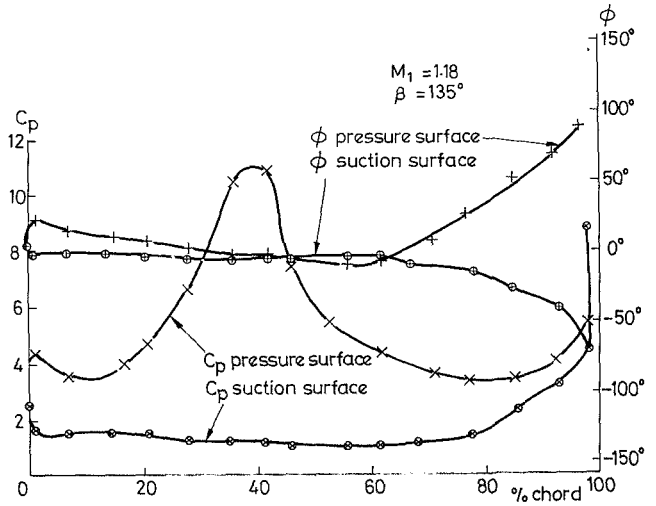

Fig. 9 Finsup's unsteady C_p and phase angle ϕ prediction around the chord

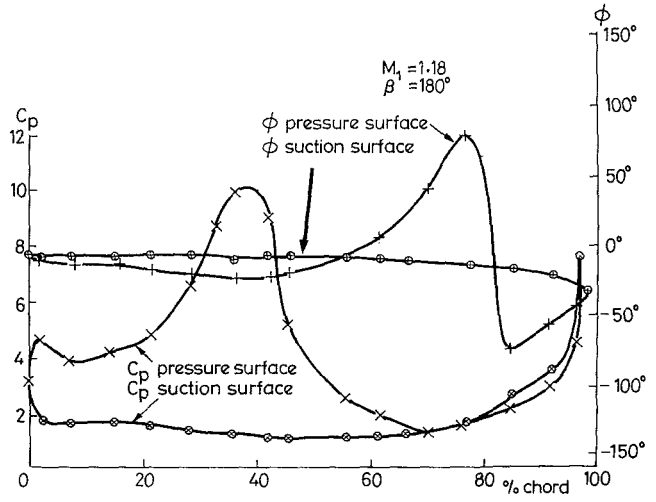

Fig. 10 Finsup's prediction of unsteady C_p and phase angle around the chord

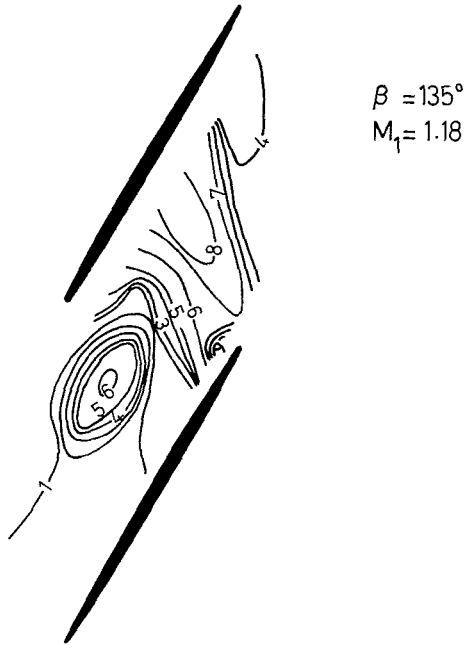

Fig. 11 Unsteady C_p amplitude contours from Finsup

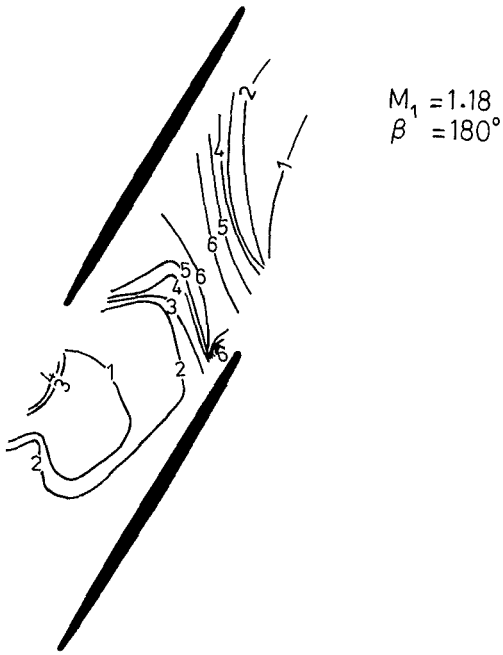

Fig. 12 Unsteady C_p amplitude contours from Finsup

unsteady flows in a blade row. It first produces a mesh of triangular finite elements between the blades, then, working from inlet and outlet flow data, the steady potential flow field is solved. A small blade vibration may now be inputed at a known frequency parameter and interblade phase angle. This will cause small flow perturbations and hence an unsteady loading on the blade. The real and imaginary components of this load are computed along with the unsteady flow field. A full description is given by Whitehead [1].

With 340 elements the program computing times are roughly 1 sec to generate the mesh, 2.0 s to calculate the steady flow and 3.5 s for each case of unsteady flows on an IBM 370/165.

5 Steady Flow

For useful comparison of experimental and theoretical unsteady results the steady flows must first be matched.

The inlet Mach number of the flow in the annular cascade is calculated from the inlet total pressure and the average of hub

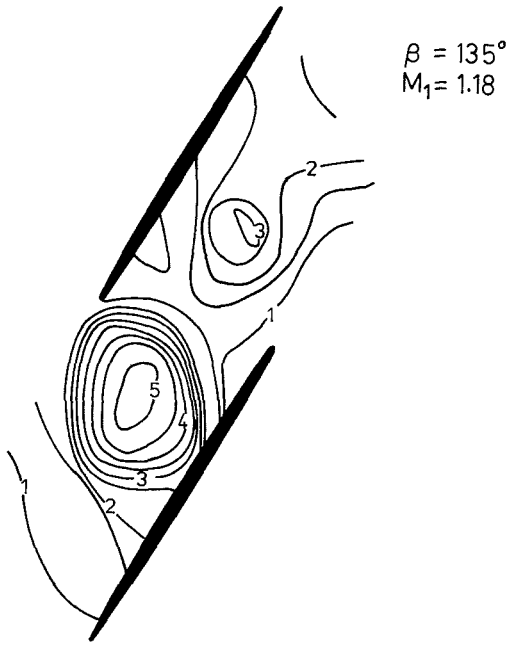

Fig. 13 Unsteady C_p amplitude contours from hub wall pressure transducers

and tip wall pressure tappings situated between the blade rows, i.e., it gives an isentropic midspan Mach number. This was kept constant at $M_1 = 1.18$ throughout the tests. Figure 5 shows the results of traversing this flow with a cobra probe. Even with the high hub tip ratio employed here, there are considerable spanwise variations. The static pressure gradient produces an isentropic Mach number variation from 1.07 to 1.28, and the total pressure traverse shows endwall boundary layers and suspected secondary flow losses. These spanwise gradients are confirmed in the holographic pictures where the leading edge shock is often seen to bow radially when it is viewed from different directions.

Figure 6 shows the steady flow shock structure reproduced from holograms. This same picture was reproduced many times and in the two adjacent passages. Therefore any shock movement will have been caused by the blade vibration. The picture shows an attached leading edge normal shock, then an oblique trailing edge shock reflected from the adjacent blade pressure surface and finally a trailing edge wave from the pressure surface. The normal leading edge shock must be weak for the flow to accelerate back up to supersonic for the trailing edge shock, the minimum upstream Mach number for a shock at that angle being 1.1. The flow must therefore be decelerated from a Mach number of 1.18 before the leading edge shock. This will occur through a series of weak upstream shocks emerging from adjacent blades. Such shocks were only ever seen in the holograms taken with vibrating blades.

The d.c. drift on the pressure transducers invalidated any steady data from them. The coarseness of the grid, see Fig. 3, and the shock smearing through the wall boundary layer would have made "shock capturing" by this method highly unlikely.

The position and strength of the shocks in program Finsup are fixed by indirectly adjusting the back pressure and inlet Mach number. Both of these parameters were known from pressure tappings. From these data Finsup produced the contours shown in Fig. 7. There is a deceleration and acceleration before the leading edge of the blade but no recognizable leading edge shock. It may have been too weak and numerically smeared to have been shown. The trailing edge shock angle is the agreement with, but reaches the

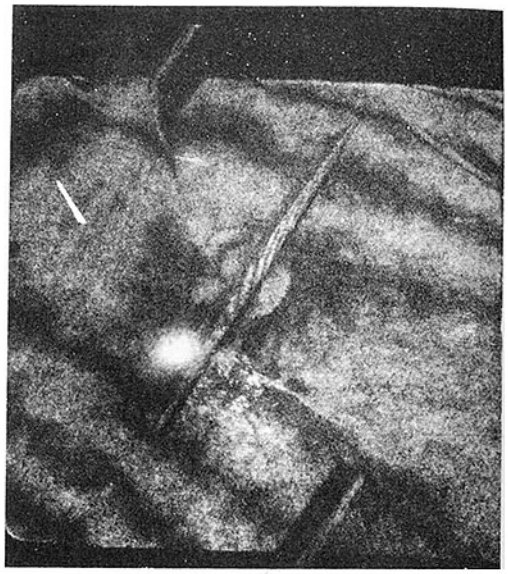

$\beta = 135$ deg position = 90 deg

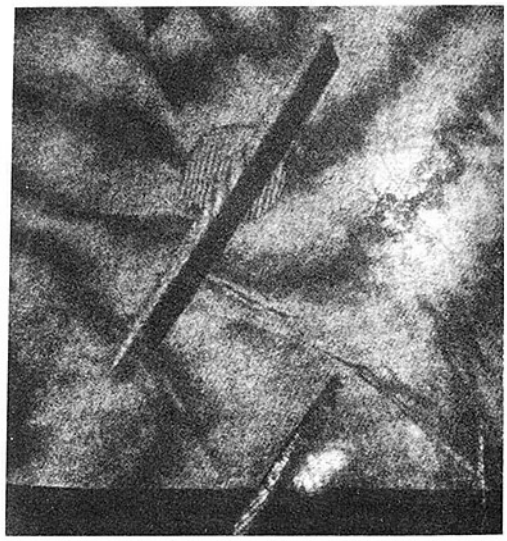

$\beta = 180$ deg position = 315 deg

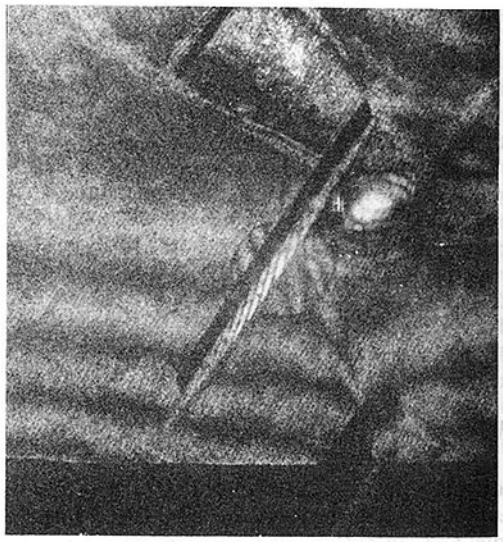

$\beta = 180$ deg position = 225 deg

Fig. 14 Holographic reconstructions

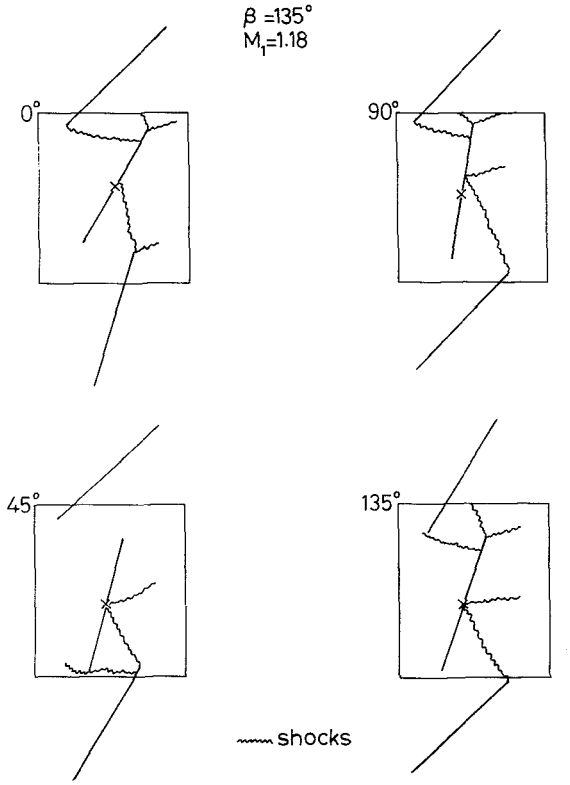

Fig. 15 Shock positions from holography

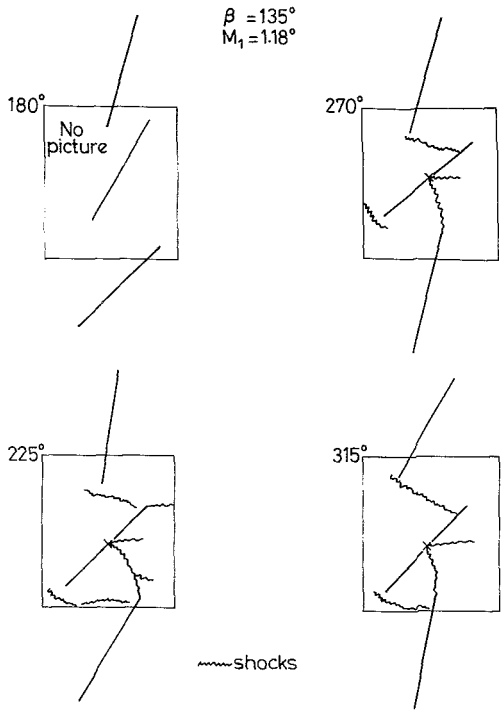

Fig. 16 Shock positions from holography

pressure surface just in front of, the shock measured by holography.

6 The Unsteady Flow

In this section the theoretical and experimental unsteady results are presented and discussed.

Theoretical Prediction. Finsup has been used to calculate the unsteady pressure amplitude coefficient

$$\left(C_p = \frac{p}{\rho_1 v_1{}^2 \alpha}\right),$$

and phase angle around the chord of the blade. Anticlockwise blade displacement is considered positive and positive phases angle refers to the pressure leading the displacement. The results, shown in Figs. 9 and 10 can be characterized as follows. Suction surface: the calculated pressure coefficient is low along the blade surface until just before the trailing edge region where the shock causes it to rise steeply. The phase is just less than zero in both cases. Pressure surface: again there is a sharp rise in C_p where the shock meets the blade surface. The phase however is small and negative on both surfaces, until 60 percent chord, where each case displays different characteristics.

Figures 11 and 12 show the pressure coefficient amplitude contours predicted by Finsup. These are for the pressures relative to the wall, not to the moving blades. For the pressure coefficients on the blade surface Figs. 9 and 10 are referred to. The trailing edge shock is again clearly seen in both plots. The center passage peak shown in Fig. 11 is not due to shock movement as no leading edge shock is predicted. It is probably a focussing of pressure waves. It will not affect the blade loading as it does not extend to either blade surface.

Comparison With Pressure Transducers. The general pattern of the unsteady contours from Finsup are corroborated by those from pressure transducer readings, Fig. 13. There is a peak corresponding to the position of the trailing edge shock but this does not extend to the blade surfaces (see Discussion). The predicted focussing of waves in center passage is completely endorsed.

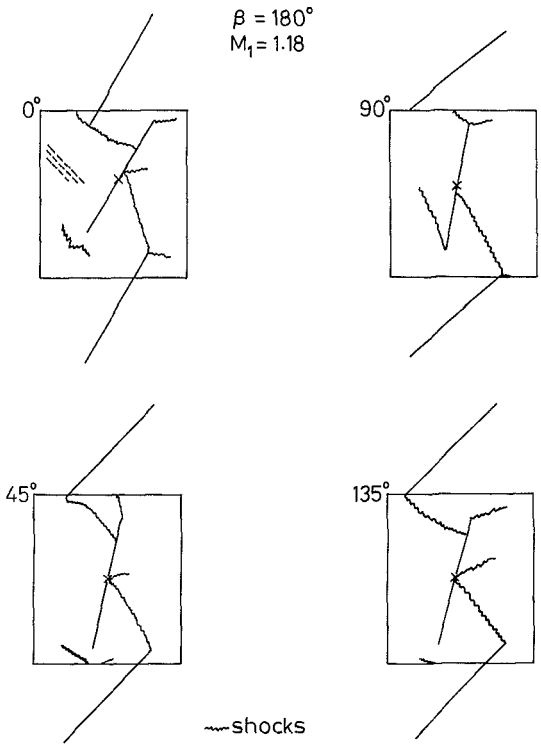

Fig. 17 Shock positions from holography

Holographic Results – Photographic Reconstructions. The reconstructions shown in Fig. 14 were made by projecting a "real" holographic image onto a photographic film. The fringes represent the density change across the shock and are

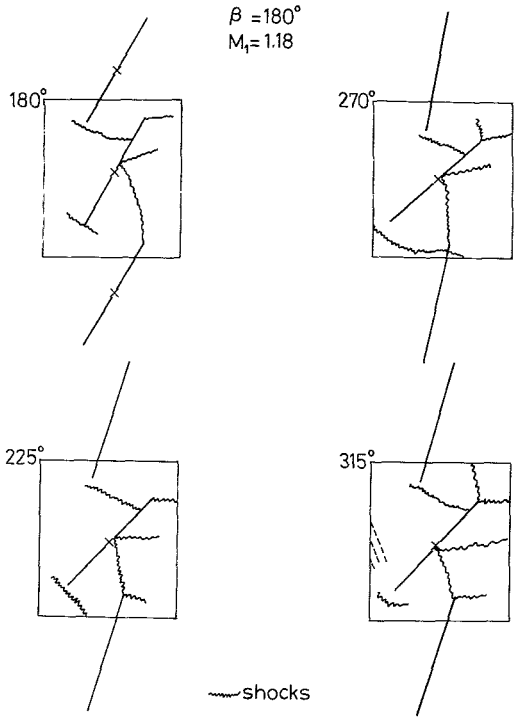

Fig. 18 Shock positions from holography

visualized either as a consequence of blade movement or flow unsteadiness vibrating the shock, as described in [13]. The reconstructions also show vibrationally formed fringes; these result from the movement of optical components (broad fringes over the whole field), and blade vibration (narrow fringe along the edge and mounting pin of the blade).

Because of the difficulty in photographing what is essentially a three-dimensional image, most of the data are presented in the form of sketches. Figures 15 to 18 show such sketches taken at 8 points throughout a blade vibration cycle, and at 2 interblade phase angles; the angle given refers to the position of the center blade. The box shows the viewing region of the hologram with the blade amplitude exaggerated to illustrate the relative blade positions. Comparison with the pictures of Fig. 14 will confirm some of the detail in the sketches. The following conclusions can be drawn:

- As stated, the shock was essentially stationary when the blades were stationary. Therefore, all the shock movement observed in the unsteady pictures is driven by the vibrating blades.
- The results were largely cylically repeatable. They were sketched from 30 frames with minor contradictions in only 2 cases.
- The trailing edge shock was always attached to the trailing edge, whereas Finsup predicts some movement in this region.
- The point of shock intersection on the pressure surface moves over 25 percent of the chord. This is the breadth of the unsteady pressure peak from Finsup – Figs. 9 and 10.
- The shock does not perform simply harmonic motion; it is however cyclical.
- The results are not quasi-steady. A leading edge shock and a trailing edge shock reflection would always be predicted whereas they are not always present.

7 Discussion

A vibrating shock wave will cause an unsteady load on a blade due to its oscillation over the blade surface and its oscillating strength. Such movements have been clearly seen in the holograms presented here. Some explanation of their non-harmonic nature may be given by the comparison with a variable geometry supersonic inlet [15]. Here the inlet may be opened, the shock swallowed, then the inlet, returned to its original position, will run shock free. This hysteresis effect may be occurring in the blade passages. The Finsup program however only calculates harmonic motion at the blade frequency so it would be impossible to predict such effects. Further evidence is inconclusive on this question. Fleeter et al. [5] were unable to either predict or measure any effects attributable to shock movement, whereas Davis and Malcolm showed clear harmonic motion over an isolated airfoil. The geometry may then be the deciding factor.

The wall pressure transducers did not conclusively pick up the shock movement. An unsteady peak was seen, Fig. 13, but only in the center of the passage. There are two possible reasons for this: tip clearance flows could have swamped the readings or, the coarseness of the grid and the shock smearing in the wall boundary layer could have made shock capturing impossible.

Figures 15 and 17 show dotted lines which depict faint traces of pressure waves, assumed to be travelling upstream. They may have been seen here because of their low velocity traveling against a nearly sonic flow. A wave traveling near the sonic speed would pass out of view between laser pulses and not be seen. This may also explain why leading edge shocks are sometimes not seen in the holograms, when at least a small shock, confined to the leading edge region, would always be predicted.

8 Conclusions

Holography has been used to visualize the shock structure around the compressor by building a small format holocamera inside the hub of the annular cascade. It has been found possible from viewing these holograms to gain detailed description of the shock structure present.

The Finsup program predicts the steady trailing edge shock structure found from holography. The leading edge shock is missed, probably owing to its weakness.

The Finsup program predicts large unsteady pressures where the shock meets the blade surfaces. These pressures are greatest on the pressure surface where they act with a small negative phase angle for $\beta = 135$ and 180 deg.

The holograms clearly show the shocks oscillating over 25 percent of the chord on the pressure surface. The oscillations are not simple harmonic motion but they are periodic.

Wall pressure transducers have been used with some success to predict the unsteady flow field in the blade passage.

Acknowledgments

The authors make grateful acknowledgment to Dr. D. S. Whitehead for the use of the program Finsup, and to Rolls Royce Ltd., for supporting the experimental work.

References

1 Whitehead, D. S., "The Calculation of Steady and Unsteady Transonic Flow in Cascades," CUED report CUED/A-Turbo/TR 118, 1982.

2 Verdon, J. M., and McCune, J. E., "Unsteady Supersonic Cascade in Subsonic Axial Flow," *AIAA Jour.*, Vol. 13, 1975, p. 193.

3 Carta, F. O., "Unsteady Gapwise Periodicity of Oscillating Airfoils," ASME Paper No. 82-GT-286, 1982.

4 Whitehead, D. S., "The Effect of Compressibility on Unstalled Torsional Flutter," CUED report CUED/A-Turbo/TR 51, 1973.

5 Fleeter, S., Novich, A. S., Riffel, R. E., Caruthers, J. E., "An Experimental Determination of the Unsteady Aerodynamics in a Controlled Oscillating Cascade," ASME Paper No. 76-GT-17, 1976.

6 Whitehead, D. S., Watson, P. J., Nagashima, T., "A Proposed Experiment to Measure Moment Coefficients for Aerofoils Oscillating in Cascade," CUED/A-Turbo/TR 46, 1973.

7 Nagashima, T., "The Vibration of Compressor and Turbine Blades in Compressible Flow," Ph.D. thesis, Cambridge University, 1974.

8 Grant, R. J., "Compressible and Unsteady Flow Through Cascades," Ph.D. thesis, Cambridge University, 1976.

9 Fabri, J., "Experimental Techniques Developed at ONERA for Advanced Compressor Testing," Communication présentée au Symposium international sur la compresseurs pour l'industrie, Prague 2–4 Oct. 1979.

10 Strazisar, A. J., and Chima, R. V., "Comparison Between Optical Measurements and a Numerical Solution of the Flow Field Within a Transonic Axial Flow Compressor Rotor," AIAA/SAE/ASME 18th Joint Propulsion Conference, June 1980.

11 Bryanston-Cross, P. J., Lang, T., Oldfield, M. L. G., Norton, R. J., "Interferometric Measurements in a Turbine Cascade Using Image Plane Holography," ASME JOURNAL OF ENGINEERING FOR POWER, Vol. 103, Jan. 1981, pp. 124, 130.

12 Decker, A. J., "Holographic Flow Visualization of Time-Varying Shock Waves," *Journal of Applied Optics*, Vol. 20, Sept. 1981, p. 3120.

13 Bryanston-Cross, P. J., "Three-Dimensional Flow Visualization," 6th Symposium on Measuring Techniques for Transonic and Supersonic Flow in Cascades and Turbomachinery Lyon, Sept. 1981.

14 Davis, S. S., and Malcolm, G. N., "Transonic Shockwave/Boundary Layer Interaction on an Oscillating Airfoil," *AIAA Journal* 79-076912, 1980, p. 1306.

15 Shapiro, A. H., *Compressible Fluid Flow*, Wiley, 1953.

A. Binder
Research Engineer.

W. Förster
Research Engineer.

H. Kruse
Head of Turbine Division.

H. Rogge
Research Engineer.

DFVLR Propulsion Institut,
Cologne, W.-Germany

An Experimental Investigation Into the Effect of Wakes on the Unsteady Turbine Rotor Flow

Detailed measurements were carried out near and within a turbine rotor using the Laser-2-Focus velocimeter. Testing was performed in a single stage cold air turbine at off-design conditions with a stator outlet Mach number of approximately 0.8. Instantaneous and averaged results of the velocity, the yaw angle, and the turbulence intensity provided information on the rotor flow field. This report describes the periodical and random unsteady effects of the stator wakes impinging on the rotor blades. In particular the constant unsteadiness contours clearly disclose the development of the wakes cut by the rotor blades. The objective of the study was to gain more insight into unsteady flow phenomena affecting losses, heat transfer, and related problems.

Introduction

By the successive arrangement of stationary and rotating blade rows, the flow in turbomachines is highly unsteady. This significantly affects boundary layer behavior [7, 13] and related problems like loss generation and heat transfer.

In subsonic flow the primary sources of the flow unsteadiness are the wake interaction and cutting, as well as potential flow interactions. Dring et al. [4] showed that in most cases both mechanisms are occurring simultaneously. The potential influence, however, is decaying much faster than the wake which may be convected several chords downstream. In addition to these periodic fluctuations, which are caused by the described blade row interactions (and which e.g., would be obtained from a phase-lock averaged hot wire probe signal), strong random fluctuations can be observed indicating high turbulence levels [8], especially in the wake.

Kerrebrock and Mikolajczak [9] showed that the lower speed within the wake produces a slip velocity which leads to a cross flow within the blade passage. By this the intersected wake parts within the rotor blades will be deformed near the suction and pressure sides [11].

Experimental verification of this flow behavior within the rotating components of turbomachines is rather complicated. The Laser-2-Focus (L2F) velocimeter, however, allows the nonintrusive measuring of the phase-lock averaged magnitude and direction of the flow vector, as well as of the velocity fluctuations parallel and perpendicular to the mean flow [15, 16]. The small measurement volume length and the high illumination intensity in the measurement volume allow measurements close to the wall and, therefore, a rather complete mapping of the interesting flow field.

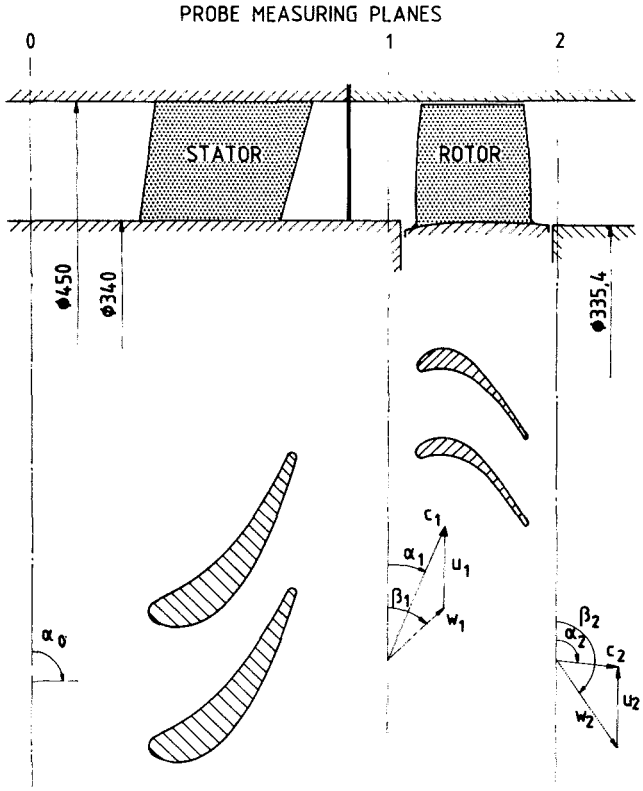

Fig. 1 Turbine geometry and vector diagrams

In the present work the L2F-measuring technique was used to take detailed flow field data near and within the rotor of a

Contributed by the Gas Turbine Division of THE AMERICAN SOCIETY OF MECHANICAL ENGINEERS and presented at the 29th International Gas Turbine Conference and Exhibit, Amsterdam, The Netherlands, June 4-7, 1984. Manuscript received at ASME Headquarters January 12, 1984. Paper No. 84-GT-178.

Table 1 Aerodynamic and geometric parameters

	Guide Vane	Rotor
Chord (mid-span)	0.0975m	0.0608m
Number	20	31
Tip diameter	0.45m	0.45m
Hub diameter (see Fig.1)	0.34m	0.34m
Hub diameter (rotor exit)	-	0.3354m
Axial gap (mid-span)	0.054m	
Hub-to-tip ratio	0.756	0.756
Inlet metal angle (mid-span)	90°	42.4°
Exit metal angle (mid-span)	21.1°	147.5°
Rotor speed (designed, T_{to} = 450 K)	8850 rpm	
Mass flow rate (designed, T_{to} = 450K, p_{to} = 4 bar)	18 kg/s	
Stage reaction ratio ($\Delta h_{rotor}/\Delta h$)	0.43	

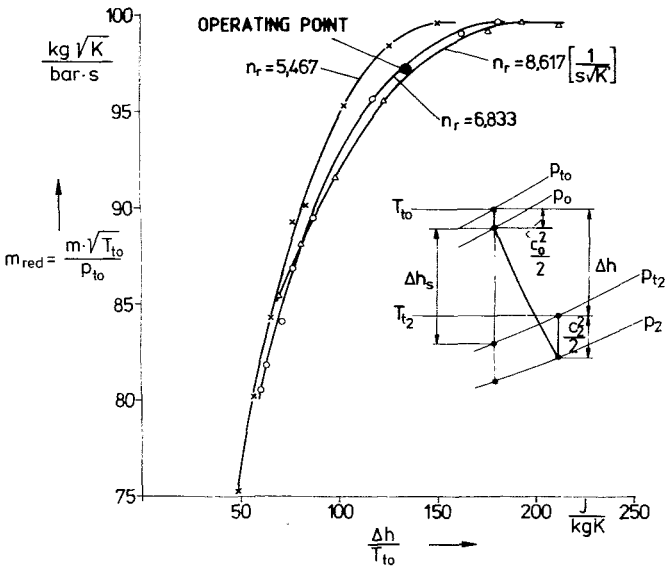

Fig. 2 Performance map

cold air turbine, with special emphasis on determining the movement of the stator wakes within the rotor blade passages.

Experimental Apparatus

The L2F measurements reported on in this paper were conducted in a 0.45-m-dia cold air turbine test facility that was designed for a maximum turbine entry temperature of 450 K and a maximum inlet pressure of 6 bar. Details on this test apparatus are documented in [2].

For the tests a transonic stage with low aspect ratio in the stator vanes and a high hub-to-tip ratio (see Table 1) was used. A cross section of the stage is shown in Fig. 1. The lower part of Fig. 1 shows a velocity vector diagram for mid-span, as well as the flow angle sign conventions used in this paper. In order to evaluate the overall performance characteristics, conventional aerodynamic measurements were carried out in the three probe measuring planes (Fig. 1). Total-pressure probes, direction probes, total-temperature probes, and five-hole probes were mounted in a radial traversing device which also allowed turning of the probes. In each probe measuring plane static pressure taps were installed at the hub and the casing walls. In order to determine the nonuniform flow field behind the stator, it was possible to rotate the upstream part of the casing together with the stator vanes and the probes of plane 0, independently of the downstream rotor casing carrying the probes of planes 1 and 2.

Test Conditions

From the performance map (Fig. 2) of the model turbine, which was obtained with conventional measurement techniques as mentioned above, the operating point for the L2F measurements was selected according to the following aspects:

- The detailed analysis of the flow field in a rotating turbine blade row with laser anemometry was a novel testing method, and little was known about problems that would be arising while measuring in the rotating blade passages. It was therefore desirable to avoid partial supersonic flow in the test section which would have presented additional difficulties in interpreting the measurement results. As the turbine stage was designed to be transonic, the actual operating point was chosen so far below the design point that an entire subsonic flow field would be expected.
- In Fig. 3 is shown the measured relative rotor inlet angle for different operating conditions. To obtain a rotor flow field similar to the design point condition, the operating point ($\bar{\beta}_1$ = 47 deg) was determined so as to get a nearly zero incidence flow ($\beta_{1_{design}}$ = 44.1 deg).

Laser Measuring Technique

The L2F velocimeter offers the opportunity to obtain information concerning the phase-lock averaged values of the two-dimensional flow vector magnitude and direction, as well as of the velocity fluctuations parallel and perpendicular to the mean flow vector, even in rotating blade passages.

The instrument provided no information on the mean velocity or its fluctuation in the spanwise direction.

Nomenclature

c = absolute velocity
c' = absolute velocity fluctuation (random part)
$\overline{c'^2}$ = mean square of c'
h = enthalpy (Δh = enthalpy drop)
m = mass flow rate
n = rotor speed
n_r = reduced rotor speed $n_r = n/\sqrt{T_{t0}}$
p = pressure
q = dynamic head (isentropic)
r = radius
T = temperature
t = time
Tu = turbulence intensity
u = rotational velocity
w = relative velocity
α = absolute flow angle (yaw)
β = relative flow angle (yaw)
ζ = total pressure loss coefficient $(p_{t0}(r) - p_{t1}(r,\varphi))/q_1$
φ = coordinate in circumferential direction

Subscripts

i = 0,1,2 number of probe measuring plane
l = longitudinal velocity fluctuation
rel = relative
t = total
tr = transverse fluctuation velocity
per = period

Superscripts

= = average over the entire measuring plane
~ = periodic fluctuation
^ = time integrated

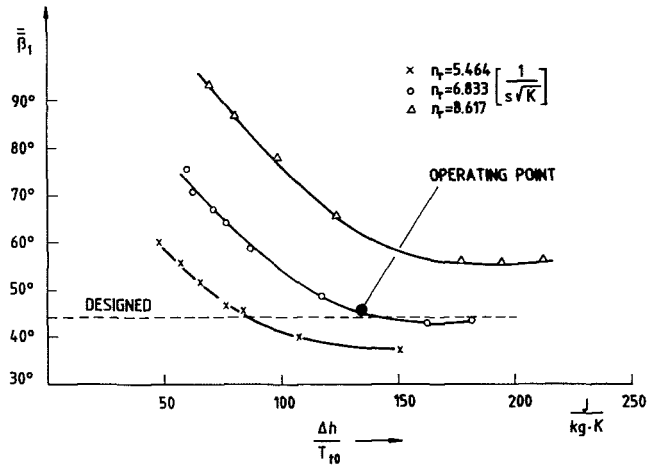

Fig. 3 Relative flow angle $\bar{\beta}_1$ of probe measuring plane 1

Details on the principles of the L2F-measuring device are well documented in [15, 16]. For the L2F-measurements the rotor casing was provided with circular windows which were located between the probe measuring planes 1 and 2. By this arrangment it was possible to measure ahead of, within, and behind the rotor blade row. The L2F device was mounted outside the test apparatus on a supporting structure which was adjustable in the axial and radial directions of the turbine rotor in order to fix the individual measuring points.

In Fig. 4 are shown the L2F-measurement locations near and within the turbine rotor, these locations being fixed in relation to the stator and thus, in the absolute frame. For the L2F-measurements reported in this paper seven axial measuring planes were chosen including two planes in front of the rotor and one plane behind the rotor. Due to the nonuniformity of the stator outlet flow it was necessary to traverse in the circumferential direction. Therefore, at each axial and radial position six equidistant measurement locations within one stator pitch were chosen. The planes (1–4) contained 11 and the planes (5–7) contained 9 radial locations.

The flow occurring in a rotor blade passage is unsteady, even for an observer moving on a blade. This unsteadiness, affecting engine performance, loss generation, and heat transfer, is mainly caused by the interaction of the moving blade row with the stator vane wakes and by potential interaction [4]. A velocity-time-record measured in a turbine in a flow field affected by the rotor would look like that shown in Fig. 5. As shown in the literature [5] such a fluctuating velocity can be divided into a periodic fluctuating velocity $\tilde{c}(t)$ and a turbulent velocity fluctuation $c'(t)$. $\tilde{c}(t)$ is the phase-locked average of $c(t)$, whereas $c'(t)$ is the random fluctuating component.

The L2F-measuring device does not allow recording of the instantaneous velocity $c(t)$ continuously like a hot wire probe which would produce a curve similar to that in Fig. 5. Instead the L2F-method uses a sampling technique: The governing electronics divide the time of each passing rotor blade period into 16 storage segments. The circumferential positions of the laser measurement volume were fixed with respect to the rotor blades by 31 trigger signals per revolution corresponding to the blade number (see [16]).

The measured events occurring during the corresponding 1/16 of each rotor period are stored in the corresponding phase-locked segment. This happens until a sufficient number of appropriate results is available in each storage segment at different angles of the focal plane.

In order to protect the L2F-photomultipliers from becoming saturated by strong radiation generated when a blade surface moves through the probe volume, the laser beams are switched out periodically so that the time of

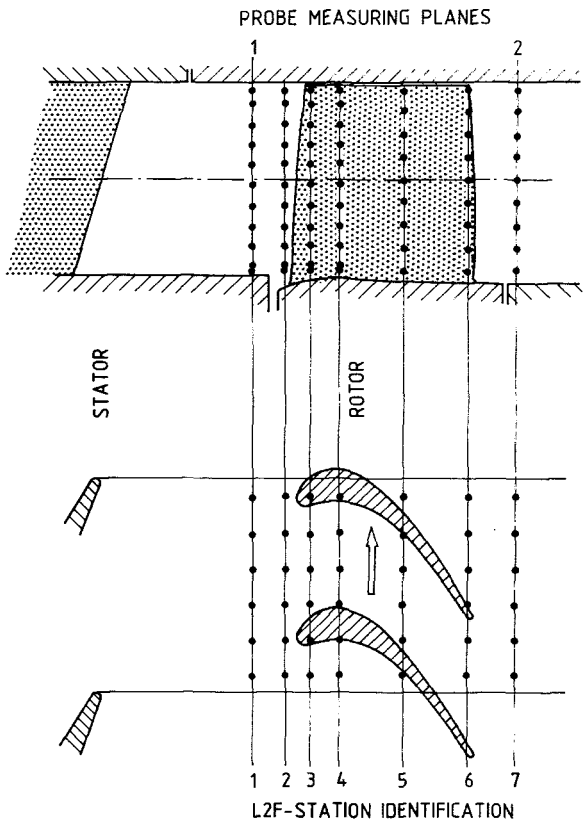

Fig. 4 L2F-locations

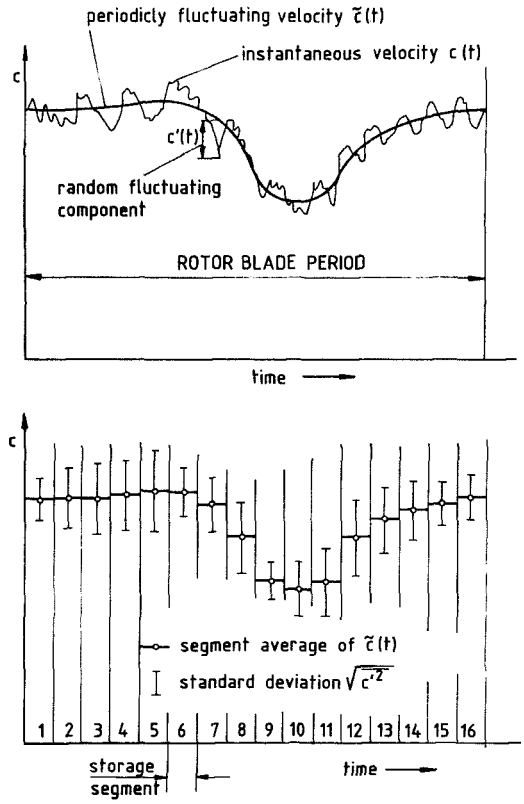

Fig. 5 Velocity record

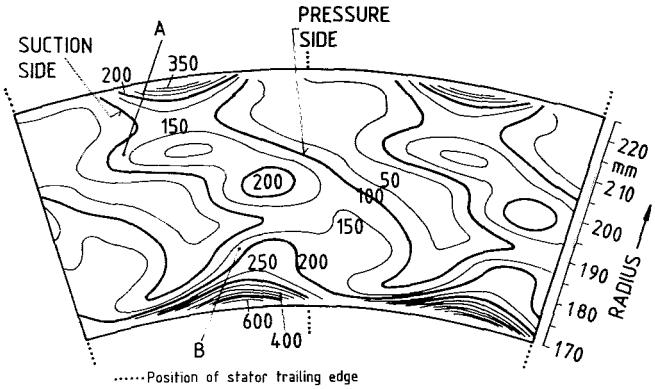

Fig. 6(*a*) Contours of time integrated mean square of random velocity fluctuation $\overline{c_f'^2}$ (L2F-plane 1, [m^2/s^2])

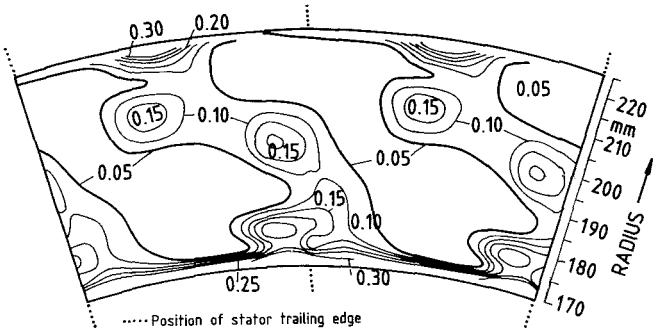

Fig. 6(*b*) Contours of total pressure loss coefficients ζ (probe-measuring-plane 1)

strongest radiation is faded out. For the results presented in this paper the maximum fade-out time corresponded to 20 percent of the rotor blade pitch (midspan, L2F-measuring plane 4). In this way only the remaining number of the 16 segments represents the blade passage.

Using all the measurements collected in that way, a statistical evaluation leads to the segment average of the velocity $\tilde{c}(t)$, the flow angle $\tilde{\alpha}(t)$, and standard deviations of velocity within each of the 16 (or less) segments of the rotor pitch. The standard deviations were defined as $\overline{c_f'^2}$ parallel and as $\overline{c_{fr}'^2}$ perpendicular to the mean velocity.

The experimental uncertainty inherent in the L2F-measurement technique was investigated in detail by Schodl [15], especially for turbomachinery applications. Using the assumptions of [15], the uncertainty in the described measurements is ±.5 deg in flow angle and ±1 percent in the absolute velocity.

Results and Discussion

In the present paper an attempt was made to identify the wakes of the stator vanes near and within the turbine rotor with the help of the distribution of the random unsteadiness levels $\overline{c_f'^2}$. There were two ways of evaluating the results based on L2F-measurements in order to identify the wakes:

First, the time-averaged mean square of the random velocity fluctuations at every stationary measuring location disclosed the wake pattern in the absolute frame without any reference to the rotor blade positions.

Second, the local and temporal correlation of individual measurements led to an instantaneous flow field pattern disclosing the wakes intersected by the rotor blades for an instantaneous rotor position in relation to the stator vanes.

Time-Averaged Results. This stationary average is defined as

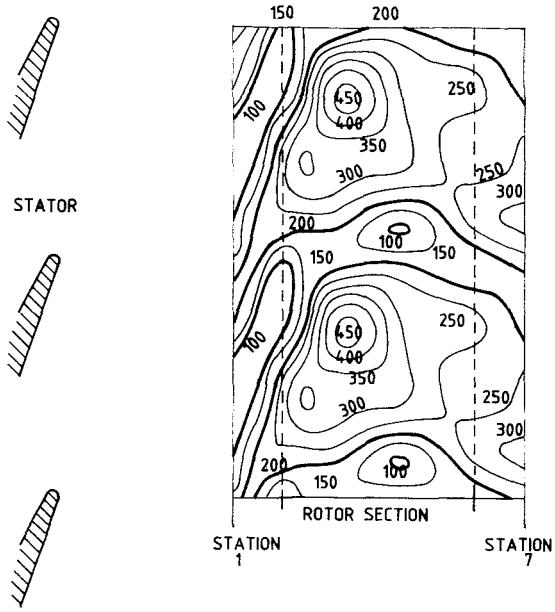

Fig. 7 Contours of time integrated mean square of random velocity fluctuation $\overline{c_f'^2}$ (midspan, [m^2/s^2])

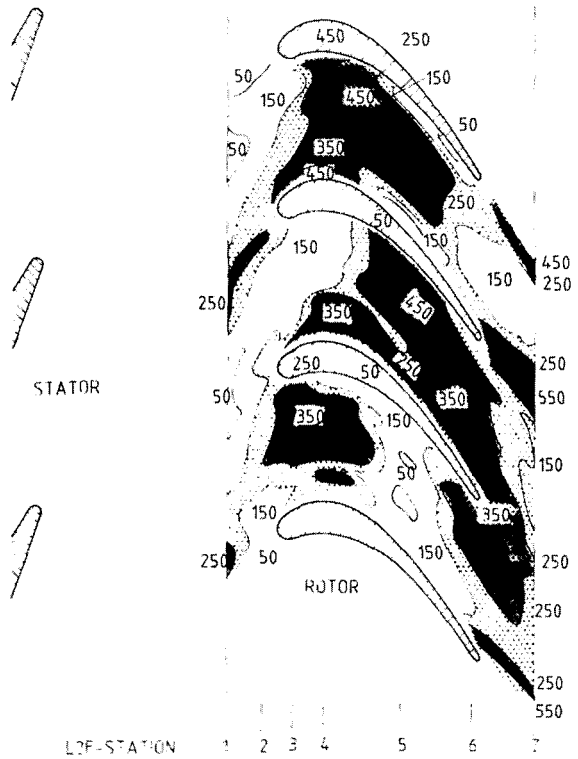

Fig. 8 Instantaneous pattern of random velocity fluctuation of $c_f'^2$ (midspan, [m^2/s^2])

$$\overline{\hat{c}_f'^2} = \frac{1}{t_{per}} \int_0^{t_{per}} \overline{c_f'^2} dt \tag{1}$$

Within the blade passages (L2F-measuring plane 3–6) the integration of the time-dependent values for each stationary measuring location was done for the time between passing of the rotor blade pressure side and the suction side; that is, for less than the total passing time of one rotor pitch t_{per}. In front of and behind the rotor the integration was extended to the total time t_{per}. Assuming the random velocity fluctuation

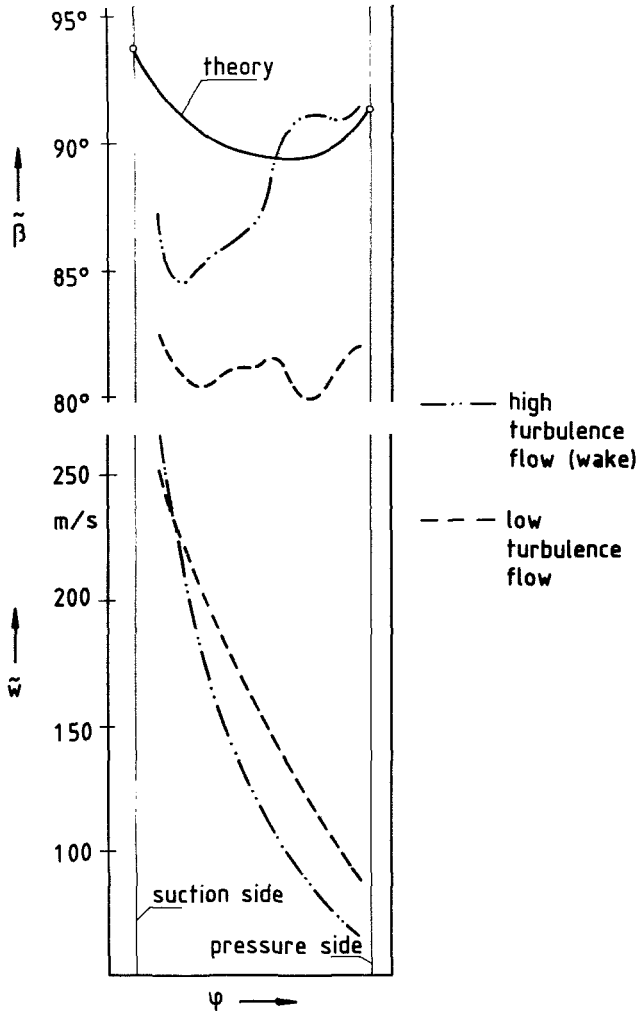

Fig. 9 Relative flow angle $\tilde{\beta}$ and relative velocity $\tilde{w}$ (L2F-plane 4)

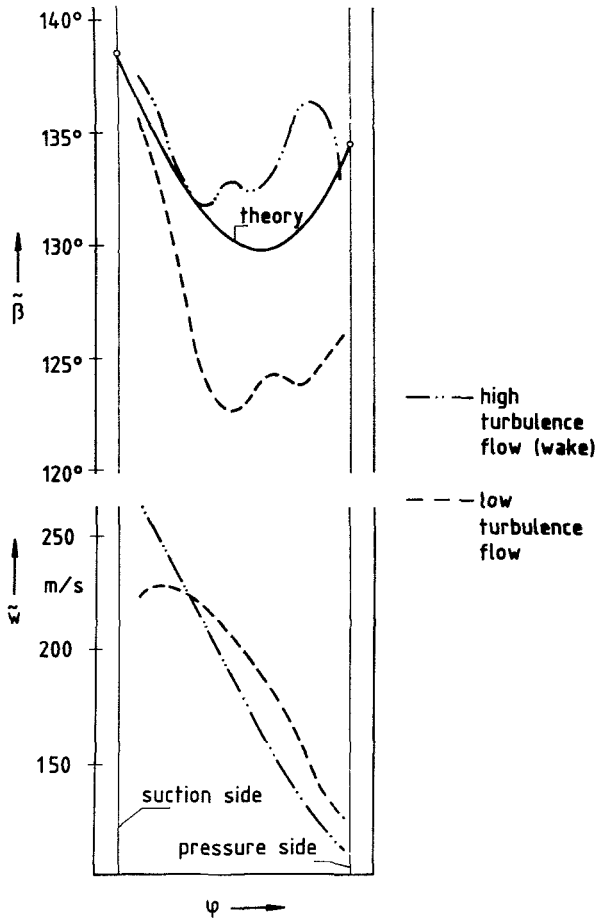

Fig. 10 Relative flow angle $\tilde{\beta}$ and relative velocity $\tilde{w}$ (L2F-plane 5)

$c'(t)$ to be statistically independent of the periodically fluctuating velocity $\tilde{c}(t)$, the local time average $\overline{c_l'^2}$ (equation (1)) in plane 1 is shown in Fig. 6(*a*).

The region showing high fluctuation is the wake. It was inclined to the radial direction due to the radial yaw angle distribution behind the stator and to the different axial distances between measuring plane and trailing edge of the stator (see Fig. 1).

The other two regions showing high fluctuation, A and B, were not caused by the wake; they were the result of secondary flows within the blade passage (see [3]). These passage vortices which had developed within the stator passage included the high-fluctuation regions accumulated near the suction side of the wake. The outer high-fluctuation region A is at a distance from the casing, whereas the inner region B is close to the hub. This was the consequence of the radial pressure gradient due to the centrifugal forces. Reduction of this gradient behind the stator required a radial flow towards the hub.

This radial flow induced a motion of the region B to the hub and separated the region A from the casing.

Within the wake there was a stronger flow towards the hub because the tangential velocity was lower.

As a consequence also, the highly fluctuating material from the wake migrated to the hub, and thus increased the high-fluctuation regions near the hub. The pattern of fluctuation contours in Fig. 6(*a*) looks like that of the total-pressure loss contours in probe-measuring plane 1 (Fig. 6(*b*)).

In Fig. 7 the distribution of the integrated random velocity fluctuation of a plane at midspan (r = 197,5 mm) is shown. The figure represents two stator blade spacings. The rotor was mounted between the two dotted lines. As the consequence of the integration procedure (equation (1)) rotor blades are not visible in this distribution.

The curved path of the regions of constant fluctuation, especially for the region of low fluctuation, indicates the turning of the absolute flow within the rotor section.

The averaged stator outlet absolute flow angle was $\bar{\alpha}_1$ = 22.4 deg (plane 1). The averaged rotor outlet flow angle (absolute flow, probe measuring plane 2) was $\bar{\alpha}_2$ = 105 deg for the test conditions. Within the region of low fluctuation there is a small increase of the fluctuating velocity. Within the wake region, however, a marked increase of random velocity fluctuation can be recognized, mainly in the first half of the chord.

Instantaneous Results. Looking at the instantaneous pattern of the mean square of the random velocity fluctuation $\overline{c_l'^2}$, in the same plane at midspan in Fig. 8, the same effect is noticeable. Each of the three rotor blade passages (arbitrarily chosen) in this figure had a different position in relation to the stator vanes because of the different blade numbers. The stator consisted of 20 blades, the rotor had 31 blades. In the figure the stator wakes intersected by the rotor blades clearly contrast with the regions of low fluctuation. (The unsteadiness level within the dotted area is more than $\overline{c_l'^2} > 150$ m^2/s^2.) As a consequence of the higher velocity near the suction side and the lower velocity near the pressure side, this region representing the wake is turned in the counterclockwise direction. Within the intersected parts of the wakes

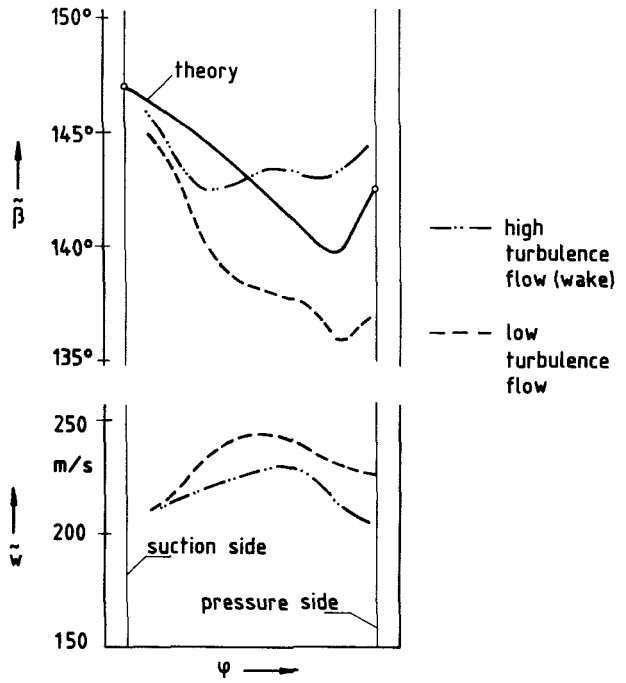

Fig. 11 Relative flow angle $\tilde{\beta}$ and relative velocity $\tilde{w}$ (L2F-plane 6)

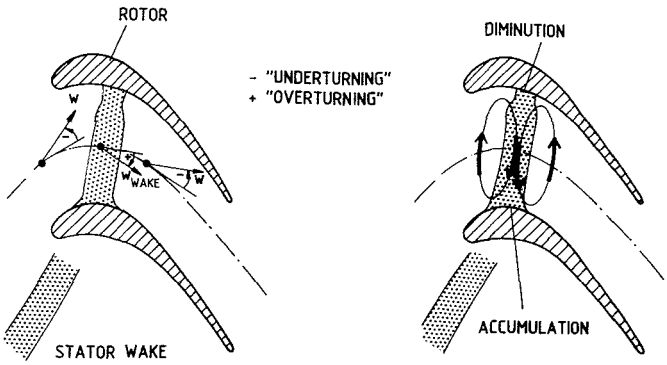

Fig. 12 Wake cutting, wake deformation and flow circulation inside the rotor

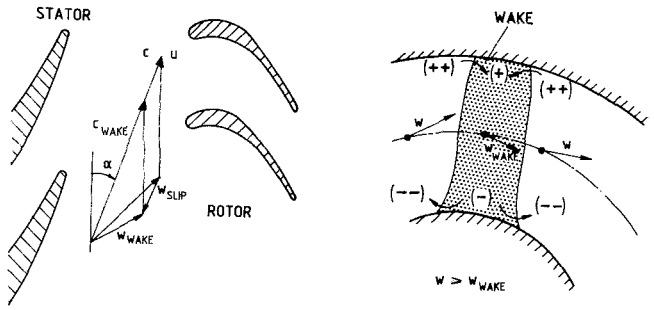

Fig. 13 Slip velocity and wake deformation

passing the rotor the random velocity fluctuation $\overline{c_l'^2}$ considerably increased, even in the middle of the rotor blade channel where the rotor blade boundary layer effects could be excluded. Just as in the aforementioned distribution of the time-averaged fluctuation, there was no noticeable increase of the instantaneous random fluctuation in the regions of lower unsteadiness between the wakes.

It is not yet possible to give a final explanation for this different behavior of the wake regions and the regions of low fluctuation passing the rotor section.

Some reasons may be assumed for the cause of such a marked increase of the velocity fluctuation in the stator wake region:

- The stator wake region of the turbine contains secondary vortices which are associated with trailing shed vorticity (see [3]). When the wake is cut by the rotor blades, the vortices may break down and consequently there would be an increase of velocity fluctuations.
- Shear layers which are associated with the wake are turned within the rotor region. This may have an effect of increasing the velocity fluctuation $\overline{c_l'^2}$.
- Within the wake region separation of rotor blade boundary layers may occur, which leads to an increasing velocity fluctuation.

Further investigation or perhaps further evaluation of the present measurements may provide more insight.

At the suction surface near the maximum thickness of the blades there were regions of high velocity fluctuations, even if no wake was passing. These regions are perhaps due to local separations at the blade suction surfaces. Another effect of the complex rotor-stator interactions was noticeable with the help of the distributions of the relative flow angle $\tilde{\beta}$ and the relative velocity $\tilde{w}$ in the axial L2F-measuring planes 4, 5, and 6 (at 50 percent blade height, r = 197,5 mm). In each of these figures (9, 10, and 11) two distinct positions of the rotor blade channel in relation to the stator were selected.

Corresponding to the wake situation the circumferential $\tilde{\beta}$-distribution in each plane altered periodically. The situations shown in the figures represent those of maximum and minimum $\tilde{\beta}$-values respectively.

Several different instantaneous positions are demonstrated in Fig. 8, which covers three rotor blade passages. In the channel on the top of the figure the wake is just passing the L2F-measuring plane 4, whereas in the intermediate channel the low-turbulence region is passing plane 4. When the stator wake (high-turbulence region) is passing, the relative velocity $\tilde{w}$ is lower than in the case of low turbulence (Fig. 9), except near the suction side.

In the relative flow angle distribution it can be seen that when the wake was passing, there were much higher values of $\tilde{\beta}$ (overturning) than in low-turbulence flow regions (underturning). In this L2F-measuring plane near the pressure side the difference in flow direction between high and low turbulence flow regions was approximately 11 deg. Near the suction side the difference was lower, and the instantaneous relative flow direction indicated separation of the flow. The velocity vector tended away from the wall, where the difference between the flow direction and the local tangent to the profile amounts to about 10 deg.

The result of a rotor potential flow calculation [10, 18] is also shown in this figure. It should be noted that there is a considerable difference between the measured instantaneous values and the potential flow.

In the downstream L2F-measuring plane 5 (Fig. 10) the velocity and flow angle distributions showed a similar behavior of the flow. In this plane the potential flow calculation was in better agreement with the measured values. Near the suction side the measured flow angle corresponded to the angle of the blade suction surface, and therefore no separation occurred in this plane as in plane 4 (previous figure). Near the pressure side the flow angle distribution within the stator wake showed a velocity vector which indicated a flow tending away from the pressure side (angle of flow greater than pressure surface angle).

When the low-fluctuation flow was passing the measuring plane, the velocity vector indicated a flow toward the pressure side (lower $\tilde{\beta}$-values). Thus, in this plane a periodical movement of wake material from the pressure side to the

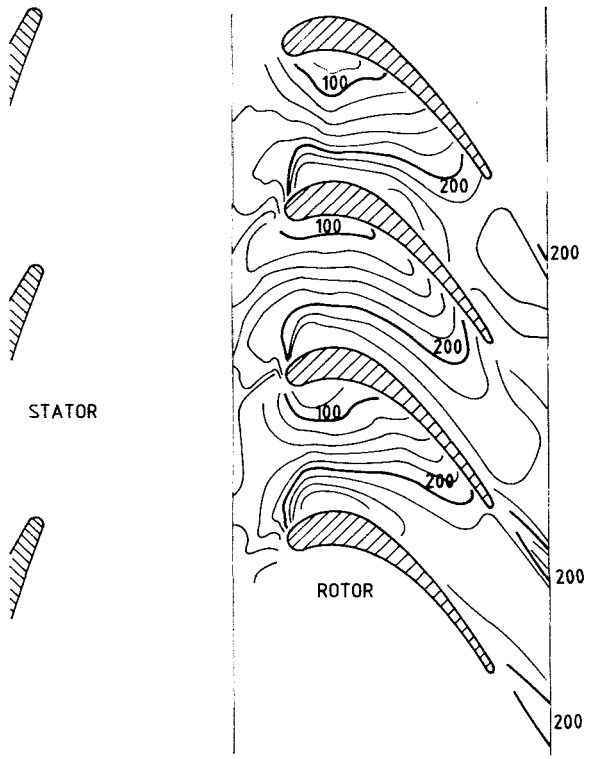

Fig. 14 Instantaneous pattern of relative velocity $\bar{w}$ (midspan, [m/s])

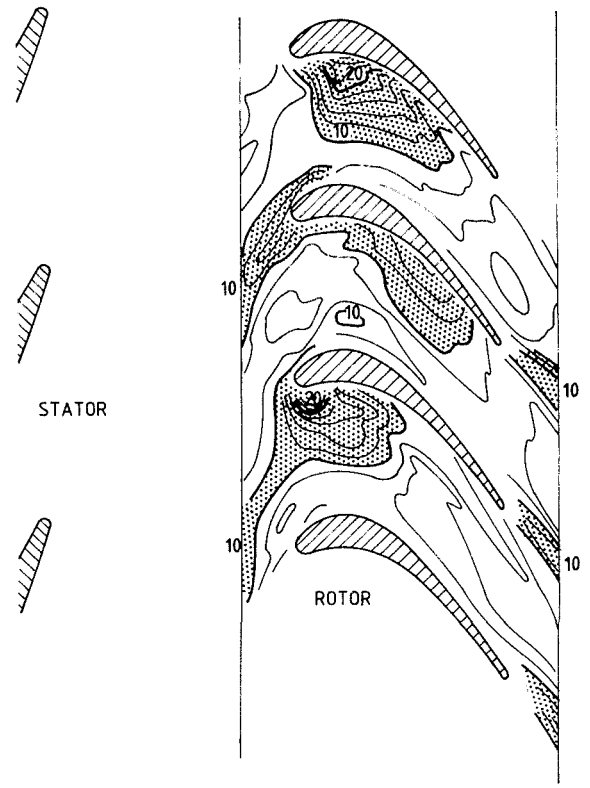

Fig. 15 Instantaneous pattern of turbulence intensity Tu_{rel} (midspan, [percent])

suction side can be assumed. Figure 11 shows the flow angle and velocity distributions of the relative flow in plane 6 for the high turbulence and the low turbulence situations. Although, measuring plane 6 was near the rotor trailing edge plane, the influence of the stator wakes is still visible in this figure. The effects are similar to those described in Figs. 9 and 10.

Figure 12 is a schematic representation emphasizing the overturning and underturning regions described in the previous figures. Within the stator wake there is an overturning relative to an assumed mean streamline, and beside the wake the measured angles indicate underturning of the flow. An observer who moves with the mean flow would see two circulating flow regions by the sides of the wake.

In the inner region of the wake this circulation coincides with a flow toward the suction side, whereas in the outer parts of the wake a movement toward the pressure side occurs.

This flow circulation leads to a deformation of the stator wake within the rotor blade channel. At the pressure side the wake is diminished, whereas, near the suction side it is extended by accumulation of wake material. The assumption of such a deformation of the wake is confirmed by means of the random velocity fluctuation contours ($\overline{c_l'^2}$ = const) at midspan (Fig. 8). As a consequence of this counter circulation, the boundary layer may tend to separate at the pressure side where the relative flow angle $\tilde{\beta}$ exceeds the blade surface angle (Fig. 10) (see [2]). Two reasons can be mentioned which give rise to the described motion causing overturning within the wake and underturning outside of it:

- Behind the stator the absolute velocity within the wake (Fig. 13) is lower than that outside of the wake. Due to this defect in absolute velocity the relative flow angle within the wake is greater than that outside of the wake (see the velocity triangle in Fig. 13, [9]). The figure shows that the static wake fluid has a slip velocity toward the suction side of the rotor. This slip velocity occurring in a turbine rotor is contrary to that occurring in compressor rotors where it is directed toward the pressure side [9].
- As shown in the velocity vector diagram the relative velocity of the wake fluid is lower than that of the other flow. The pressure gradients caused by the deflection within the rotor blade channel depend upon the flow velocity. When the wake is passing the pressure side the overpressure is lowered within the wake as a consequence of the lower velocity (Fig. 13). At the suction side the underpressure is increased while the wake is passing. These pressure differences give rise to motions from the surrounding flow into the wake at the pressure side and away from the wake into the surrounding flow at the suction side (Fig. 13).

The abovementioned circulation leading to an overturning in the wake region and to an underturning in regions of high velocity may be supported by the described exchange.

Figure 14 shows the relative flow velocity distribution at midspan (r = 197.5 mm) with the rotor in the same relative position with respect to the stator as in Fig. 8.

Due to the different positions of the rotor blade channels relative to the stator there are different distributions of the relative velocity in the blade passages. With the help of these local relative velocities and mean squares of the random velocity fluctuations $\overline{c_l'^2}$ and $\overline{c_{tr}'^2}$, the distribution of the relative turbulence intensity was formed (Fig. 15). Again, the stator wake regions can be recognized by looking at these contours of relative turbulence intensity, but one has to pay attention to the different local relative velocities used as the denominator in the turbulence intensity Tu_{rel}. Low velocities at the pressure side and high values of turbulence energy, especially in the stator wake regions, lead to extremely high turbulence intensities of more than 20 percent. The distribution of the turbulence intensity shown in this figure was calculated with the two measured components of the random velocity fluctuations. As stated before no in-

formation was obtained on the spanwise fluctuations. These spanwise fluctuations are expected to have only a small quantitative influence on the relative turbulence intensity.

Such values of turbulence intensity probably cause the rotor blade boundary layer on the pressure side to become turbulent, at least when the wake is passing [7, 12].

Summary

The Laser-2-Focus velocimeter was applied to provide data for the unsteady flow near and within the rotor of a single stage cold air turbine.

The nonuniform stator outlet flow impinging on the rotor blade row, detected with the help of the distribution of the integrated mean square of the random velocity fluctuation, indicated high turbulence levels within the wake regions and the regions associated with secondary flows.

The cutting of the stator wakes by the rotor was well demonstrated in an instantaneous flow pattern of the random velocity fluctuation. There was a marked increase of velocity fluctuation within the intersected wake, whereas outside of the wake no such effects occurred. Further investigations should be made concerning this phenomenon because no final explanation was found.

In the rotor section two counterrotating circulation regions were recognized at both sides of the stator wake. They resulted from the difference in the velocities within and outside of the wake, respectively. Inside the wake there was an overturning, and outside of it an underturning of the flow.

The high fluctuation of the flow in the wake region in connection with the low relative velocities measured near the pressure side of the rotor blade led to very high values of turbulence intensity. This high turbulence intensity could significantly affect boundary layer behavior, and thus heat transfer.

Acknowledgments

The authors wish to express their gratitude to Dr. R. Schodl for his support in L2F-measuring technique, W. Karnatschke who has done the L2F-measurements, and Mr. Tweedt for his assistance in correcting this paper.

References

1 Binder, A., and Kruse, H., "Optical Flow Measurements in a Transonic Turbine Stage," 6th ISABE, 1983, Paris.

2 Binder, A., and Rogge, H., "Messung des Leitradnachlaufes vor und im Laufrad einer Turbine," VDI-Berichte 487, 1983, pp. 201–208.

3 Binder, A., and Romey, R., "Secondary Flow Effects and Mixing of the Wake Behind a Turbine Stator," ASME JOURNAL OF ENGINEERING FOR POWER, Vol. 105, No. 1, Jan. 1983.

4 Dring, R. P., et al., "Turbine Rotor-Stator Interaction," ASME Paper No. 82-GT-3, 1982.

5 Evans, R. L., "Turbulence and Unsteadyness Measurements Downstream of a Moving Blade Row," ASME JOURNAL OF ENGINEERING FOR POWER, Vol. 97, 1974, pp. 131–139.

6 Goldman, L. J., and Seasholtz, R. G., "Laser Anemometer Measurements in an Annular Cascade of Core Turbine Vanes," NASA-Technical Paper 2018, 1982.

7 Hodson, H. P., "Boundary Layer and Loss Measurements on the Rotor of an Axial-Flow Turbine," ASME Paper No. 83-GT-4.

8 Joslyn, H. D., Dring, R. P., and Sharma, O. P., "Unsteady Three-Dimensional Turbine-Aerodynamics," ASME JOURNAL OF ENGINEERING FOR POWER, Vol. 105, Apr. 1983, pp. 322–331.

9 Kerrebrock, K. L., and Mikolajczak, A. A., "Intra-Stator Transport of Rotor Wakes and Its Effects on Compressor Performance," ASME JOURNAL OF ENGINEERING FOR POWER, Oct. 1970, p. 359.

10 Lucchi, C. W., and Schmidt, W., "Nachrechnung transsonischer Gitter," Dornier GmbH, 1979, Berichts Nr. 79/258.

11 Meyer, R. X., "The Effect of Wakes on the Transient Pressure and Velocity Distributions in Turbomachines," ASME *Journal of Basic Engineering*, Oct. 1958, pp. 1544–1552.

12 Pfeil, H., and Schröder, T., "Messungen im Nachlauf eines quer zur Strömungsrichtung bewegten Zylinders," VDI-Berichte 361, 1980, S. 17/21.

13 Pfeil, H., and Herbst, R., "Grenzschichtentwicklung bei instationärer Zuströmung," VDI-Berichte 361, 1980, S. 45/48.

14 Platzer, M. F., "Unsteady Flows in Turbomachines—A Review of Current Developments," Unsteady Aerodynamics, AGARD-CP-227 (Canada), Sept. 1977.

15 Schodl, R., "Entwicklung des Laser-Zwei-Focus-Verfahrens für die beruhrüngslose Messung der Strömungsvektoren, insbesondere in Turbomaschinen," Diss. TH Aachen, 1977.

16 Schodl, R., "A Laser-Two-Focus (L2F) Velocimeter for Automatic Flow Vector Measurements in the Rotating Components on Turbomachines," ASME *Journal of Fluids Engineering*, Vol. 102, No. 4, Dec. 1980.

17 Schodl, R., "Verfahren und Programm zur Auswertung der von einem L2F-GeschwindigkeitsmeBgerät gelieferten MeBdaten," DFVLR, Interner Bericht 325/2/1981.

18 Starken, H., Rechter, H., and Weber, A., "Verlustarme, superkritische Verdichtergitter-optimale Druckverteilung, Grenzschichtrechnung, reibungsfreie Nachrechung und experimentelle Uberprufung," DFVLR, Interner Bericht IB 325-08-83, 1983.

19 Werle, M. J., "Compressor and Turbine Blade Boundary Layer Separation," Viscous Effects in Turbomachines, AGARD-CPP-351 (Denmark), June 1983.

formation was obtained on the spanwise fluctuations. These spanwise fluctuations are expected to have only a small quantitative influence on the relative turbulence intensity.

Such values of turbulence intensity probably cause the rotor blade boundary layer on the pressure side to become turbulent, at least when the wake is passing [7, 12].

Summary

The Laser-2-Focus velocimeter was applied to provide data for the unsteady flow near and within the rotor of a single stage cold air turbine.

The nonuniform stator outlet flow impinging on the rotor blade row, detected with the help of the distribution of the integrated mean square of the random velocity fluctuation, indicated high turbulence levels within the wake regions and the regions associated with secondary flows.

The cutting of the stator wakes by the rotor was well demonstrated in an instantaneous flow pattern of the random velocity fluctuation. There was a marked increase of velocity fluctuation within the intersected wake, whereas outside of the wake no such effects occurred. Further investigations should be made concerning this phenomenon because no final explanation was found.

In the rotor section two counterrotating circulation regions were recognized at both sides of the stator wake. They resulted from the difference in the velocities within and outside of the wake, respectively. Inside the wake there was an overturning, and outside of it an underturning of the flow.

The high fluctuation of the flow in the wake region in connection with the low relative velocities measured near the pressure side of the rotor blade led to very high values of turbulence intensity. This high turbulence intensity could significantly affect boundary layer behavior, and thus heat transfer.

Acknowledgments

The authors wish to express their gratitude to Dr. R. Schodl for his support in L2F-measuring technique, W. Karnatschke who has done the L2F-measurements, and Mr. Tweedt for his assistance in correcting this paper.

References

1 Binder, A., and Kruse, H., "Optical Flow Measurements in a Transonic Turbine Stage," 6th ISABE, 1983, Paris.

2 Binder, A., and Rogge, H., "Messung des Leitradnachlaufes vor und im Laufrad einer Turbine," VDI-Berichte 487, 1983, pp. 201–208.

3 Binder, A., and Romey, R., "Secondary Flow Effects and Mixing of the Wake Behind a Turbine Stator," ASME JOURNAL OF ENGINEERING FOR POWER, Vol. 105, No. 1, Jan. 1983.

4 Dring, R. P., et al., "Turbine Rotor-Stator Interaction," ASME Paper No. 82-GT-3, 1982.

5 Evans, R. L., "Turbulence and Unsteadyness Measurements Downstream of a Moving Blade Row," ASME JOURNAL OF ENGINEERING FOR POWER, Vol. 97, 1974, pp. 131–139.

6 Goldman, L. J., and Seasholtz, R. G., "Laser Anemometer Measurements in an Annular Cascade of Core Turbine Vanes," NASA-Technical Paper 2018, 1982.

7 Hodson, H. P., "Boundary Layer and Loss Measurements on the Rotor of an Axial-Flow Turbine," ASME Paper No. 83-GT-4.

8 Joslyn, H. D., Dring, R. P., and Sharma, O. P., "Unsteady Three-Dimensional Turbine-Aerodynamics," ASME JOURNAL OF ENGINEERING FOR POWER, Vol. 105, Apr. 1983, pp. 322–331.

9 Kerrebrock, K. L., and Mikolajczak, A. A., "Intra-Stator Transport of Rotor Wakes and Its Effects on Compressor Performance," ASME JOURNAL OF ENGINEERING FOR POWER, Oct. 1970, p. 359.

10 Lucchi, C. W., and Schmidt, W., "Nachrechnung transsonischer Gitter," Dornier GmbH, 1979, Berichts Nr. 79/258.

11 Meyer, R. X., "The Effect of Wakes on the Transient Pressure and Velocity Distributions in Turbomachines," ASME *Journal of Basic Engineering*, Oct. 1958, pp. 1544–1552.

12 Pfeil, H., and Schröder, T., "Messungen im Nachlauf eines quer zur Strömungsrichtung bewegten Zylinders," VDI-Berichte 361, 1980, S. 17/21.

13 Pfeil, H., and Herbst, R., "Grenzschichtentwicklung bei instationärer Zuströmung," VDI-Berichte 361, 1980, S. 45/48.

14 Platzer, M. F., "Unsteady Flows in Turbomachines—A Review of Current Developments," Unsteady Aerodynamics, AGARD-CP-227 (Canada), Sept. 1977.

15 Schodl, R., "Entwicklung des Laser-Zwei-Focus-Verfahrens für die beruhrüngslose Messung der Strömungsvektoren, insbesondere in Turbomaschinen," Diss. TH Aachen, 1977.

16 Schodl, R., "A Laser-Two-Focus (L2F) Velocimeter for Automatic Flow Vector Measurements in the Rotating Components on Turbomachines," ASME *Journal of Fluids Engineering*, Vol. 102, No. 4, Dec. 1980.

17 Schodl, R., "Verfahren und Programm zur Auswertung der von einem L2F-Geschwindigkeitsmeßgerät gelieferten MeBdaten," DFVLR, Interner Bericht 325/2/1981.

18 Starken, H., Rechter, H., and Weber, A., "Verlustarme, superkritische Verdichtergitter-optimale Druckverteilung, Grenzschichtrechnung, reibungsfreie Nachrechung und experimentelle Uberprufung," DFVLR, Interner Bericht IB 325-08-83, 1983.

19 Werle, M. J., "Compressor and Turbine Blade Boundary Layer Separation," Viscous Effects in Turbomachines, AGARD-CPP-351 (Denmark), June 1983.

DISCUSSION

T. H. Okiishi[1]

The authors deserve commendation for their fine work on clarification of the physics of turbine stage stator/rotor flow interaction. Their use of the L2F velocimeter to track stator wake movement through the downstream rotor row is representative of the detailed flow field surveys currently possible with nonintrusive data acquisition techniques and we look forward to more results from them in the not-too-distant future.

Similar measurements to the ones discussed in this paper have been made in a compressor stage stator [20] at the DFVLR, Köln, and are being made in a fan stage stator at the NASA Lewis Research Center. Such data are complementary to turbine stage interaction studies and should be considered also.

The usefulness for design purposes of the unsteady flow aspects of row/row interaction is reasonably clear when aeromechanical or aeroacoustic concerns are considered. However, the influence of this interaction on turbomachine blade row loss is less clear. The position taken presently by most of those interested in assessing the influence of periodic flow unsteadiness on blade row loss is that most if not all of the effect is attributable to downstream row blade surface boundary layers, more specifically transition and possibly separation in these layers, being affected periodically by passing blade wake segments. A recent analysis [21] of low-speed, axial-flow compressor, and higher-speed compressor and fan stage stator data suggests that the viscous loss suffered by rotor blade wake segments as they pass through a downstream stator row is a considerable portion of the stator row loss. In other words, the row loss associated with the downstream row of a turbomachine stage consists of a combination of downstream blade boundary layer *and* upstream blade wake segment losses.

The large random velocity fluctuations associated with the turbine stator wakes passing through the rotor described in the present paper would tend to support the hypothesis that losses along all pathlines in a turbine rotor row could be considerable.

[1]Iowa State University, Department of Mechanical Engineering and Engineering Research Institute, Ames, Iowa.

References

20 Dunker, R. J., "Flow Measurements in the Stator Row of a Single-Stage Transonic Axial-Flow Compressor with Controlled Diffusion Stator Blades," in: *Viscous Effects in Turbomachines*, AGARD Conference Proceedings No. 351 (AGARD-CP-351), 1983.

21 Okiishi, T. H.,. Hathaway, M. D., and Hansen, J. L., "A Note on Blade Wake Interaction Influence on Compressor Stator Aerodynamic Performance," ASME JOURNAL OF ENGINEERING FOR GAS TURBINES AND POWER, Vol. 107, No. 2, Apr. 1985, pp. 549–551.

Measurements of Wake-Generated Unsteadiness in the Rotor Passages of Axial Flow Turbines

H. P. Hodson
Whittle Laboratory,
Cambridge University Engineering Department,
Cambridge, U.K.

This paper describes an investigation into the free-stream unsteadiness which is found in the rotor passages of axial flow turbines and which is caused by the interaction of the stator wakes with the rotor blades. The major part of this investigation was conducted at the midspan of the rotor of a large-scale, single-stage air turbine. Measurements are presented of the unsteady free-stream velocities and blade surface pressures. These are supplemented by further results which were obtained during a flow visualization experiment in a small-scale water turbine. It is shown that the unsteadiness is dominated by the convected phenomena associated with the passage of the wakes through the rotor.

Introduction

The unsteady interaction of the rotating and stationary blade rows in axial-flow turbomachines is known to affect many aspects of their performance including blade loading [1], stage efficiency [2], heat transfer [3], stall margin [4], and noise generation [5]. It is, therefore, surprising that very little information is available concerning the mechanism of the interactions, particularly with regards to axial-flow turbines. The interaction between the rotor and stator blades can, of course, be divided into two parts; these are the potential and wake interactions. This investigation is concerned with wake-generated interactions in axial flow turbines.

One of the earliest studies of the convection of a wake over a downstream blade was carried out by Meyer [6], who, using thin aerofoil theory, obtained a solution for the interaction of a wake with a moving, uncambered aerofoil. Lefcourt [7] later extended Meyer's analysis to include the effects of the wake and blade thicknesses. There are, of course, considerable differences between the flow over an isolated and lightly loaded aerofoil and that through a turbomachine blade row. For example, Smith [8] has noted that in turbomachines, the circulation of the blades results in a shearing of the wake segments as they convect through the blade passages.

Some of the first detailed experimental data regarding wake interactions were provided by Kerrebrock and Mikolajczak [9], who observed that the circumferentially nonuniform stagnation temperature profile at the exit of a compressor stator could be explained using the ideas put forward in [6] to [8]. Similar conclusions can be drawn from the results of Adachi and Murakami [10] and Weyer and Dunker [11] who, in independent studies, measured the velocity field within the passages of compressor stators. Wagner et al. [12] and Zierke and Okiishi [13] have also discovered that in axial compressors, simple convective theories can be used to explain the interactions of the blade wakes as they progress through the downstream stages.

Unfortunately, there are very few experimental data on the convection of wakes in axial turbines. It is, therefore, impossible to determine the extent to which the aforementioned theories can be applied in such machines. This paper describes an investigation of stator-rotor wake interactions in axial-flow turbines.

Experimental Apparatus

Two very different axial turbines were used during this investigation. The first was a large-scale, low-speed, single-stage air-driven turbine within which rotating-frame measurements of the velocities and blade surface static pressures have been made. The second was a small-scale, low-speed, water-driven turbine in which flow visualization was used to study the stator wake-rotor interaction. In both machines, the stator-rotor axial gap (see Tables 1 and 2) was such that potential interactions were insignificant.

The importance of the reduced frequency parameter $\bar{\omega}$ is well known in connection with unsteady flows. In this case it is probably useful to define an "average" reduced frequency parameter

$$\bar{\omega} = \frac{\omega C_x}{2U_x}$$

which, on substitution of the appropriate parameters (see Tables 1 and 2) is equal to 4.5 for the air turbine and 4.7 for the water turbine. The flow through the turbine rotors is, therefore, unsteady in the true sense with a reduced frequency which is typical of those found in modern axial turbines.

Air Turbine. The large single-stage Cambridge No. 2 Turbine (Fig. 1) is particularly suitable for detailed flow investigations (see, for example, [14–17]). The stage is a free-

Contributed by the Gas Turbine Division of THE AMERICAN SOCIETY OF MECHANICAL ENGINEERS and presented at the 29th International Gas Turbine Conference and Exhibit, Amsterdam, The Netherlands, June 4–7, 1984. Manuscript received at ASME Headquarters January 12, 1984. Paper No. 84-GT-189.

Table 1 Air turbine information

	Stator	Rotor
Reynolds number	4.2×10^5	3.15×10^5
Stage loading, $\Delta h_0/U_2^2$	–	1.0
Rotational speed (rpm)	–	530
Inlet axial velocity (m/s)	17.95	–
Flow coefficient	–	0.495
Blade inlet angle (deg from axial)	0.0	0.0
Blade exit angle (deg from axial)	65.0	−65.0
Chord (mm)	152.4	114.3
Pitch-chord ratio	0.742	0.698
Aspect ratio	1.5	2.0
Blade number	36	51
Mean radius (m)	0.647	0.647
Stagger (deg)	44.5	44.5
Rotor stator axial gap (mm)	–	81.5
Reduced frequency ($\omega C_x/2U_x$)	–	4.5

Table 2 Water turbine information

	Stator	Rotor
Reynolds number	4.7×10^5	4.7×10^5
Stage loading, $\Delta h_0/U_m{}^2$	–	1.0
Rotational speed (rpm)	–	500
Inlet axial velocity (m/s)	1.04	–
Flow coefficient	–	0.51
Blade inlet angle (deg from axial)	0	0
Blade exit angle (deg from axial)	63	−63
Chord (mm)	21	21
Pitch-chord ratio	0.97	0.97
Aspect ratio	0.55	0.55
Blade number	12	12
Mean radius (mm)	38.8	38.8
Stagger (deg)	45	45
Rotor-stator axial gap (mm)	–	11.1
Reduced frequency ($\omega C_x/2U_x$)	–	4.7

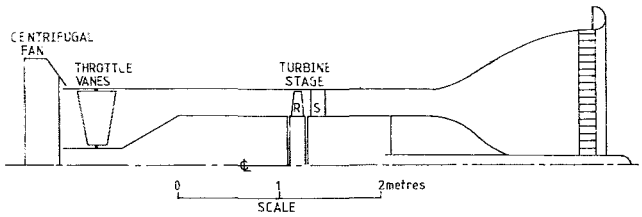

Fig. 1 Cambridge No. 2 Turbine

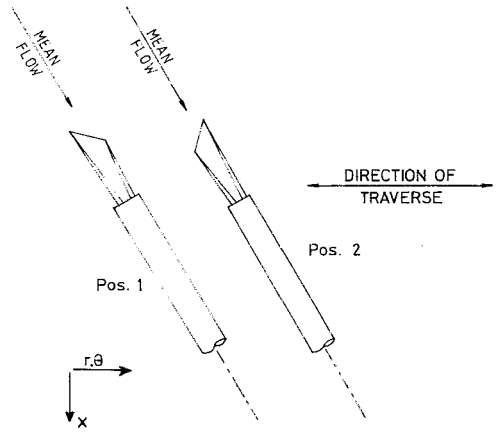

Fig. 2 Orientation of hot wires for velocity measurements

vortex design with zero exit swirl and a high degree of reaction. Although such a design is conservative, the uniform and axial velocity at inlet to the stage means that with the conditions for radial equilibrium satisfied, there is no curvature in the meridional plane. The midspan flow may therefore be regarded as two-dimensional.

All the measurements described in this paper were made at the rotor midspan radius with the turbine operating at the design condition of zero exit swirl. Further information on both the geometry and the operating conditions can be found in Table 1 and references [14–17].

Rotating-Frame Anemometry. The time-dependent velocity field within the rotor passage has been investigated by circumferentially traversing hot-wire anemometers at the midspan radius using a computer controlled traverse mechanism. High quality slip rings were used to connect the hot-wires and the traverse mechanism to the stationary frame instrumentation.

Because the radial velocity was known to be small [15], a two-dimensional adaptation of the single sensor technique [18] was used to measure the velocity field. To do this, DISA 45 degree hot-wire probes (Type 55P12) were placed in first one and then the other of the positions shown in Fig. 2. The corrected cosine law of Champagne et al. [19] was then used to determine the magnitude and direction of the flow vector. A check upon the accuracy of this method was provided by traversing a third hot wire (DISA type 55P10) whose sensor was aligned with the radial direction. This probe was also used to provide a measure of the turbulence levels. A similarly aligned hot wire has also been used to traverse the blade surface boundary layers [17].

Rotor Blade-Surface Static Pressure Measurements. The rotor midspan blade surface pressures were measured using 19 miniature strain gauge type pressure transducers. These transducers (Gaeltec type 3Ea/b) had a diameter of 3 mm. They were therefore mounted just below the blade surface in cavities which were connected to the surface via small diameter holes. The arrangement is shown in Fig. 3. Slip rings were again used to connect the transducers to the stationary frame instrumentation.

In view of the transducers' high frequency response (> 10 kHz) and the relatively high resonant frequency of the cavities (typically > 5 kHz) when compared with the blade passing frequency of 318 Hz, the dynamic and static calibrations of the measurement system were assumed to be equal. The validity of this assumption was confirmed when, after doubling the diameter of the pressure tappings, the measurements were repeated and no discrepancies observed.

Phase-locked-averaging [20] over 100 revolutions has been used, throughout this investigation, to enhance the periodic

Nomenclature

BPF = blade passing frequency
C_x = axial chord
h_0 = stagnation enthalpy
i = incidence
P = static pressure
r = radius
rms = root-mean-square
U = velocity
u' = random velocity fluctuation
U_x = axial velocity
U_m = mean blade velocity
x = axial distance
ρ = density
ω = frequency
$\bar{\omega}$ = reduced frequency
Δ = amplitude of, change in

Subscripts

1 = rotor inlet (relative)
2 = rotor exit (relative)

Superscripts

− = mean
~ = phase-locked average

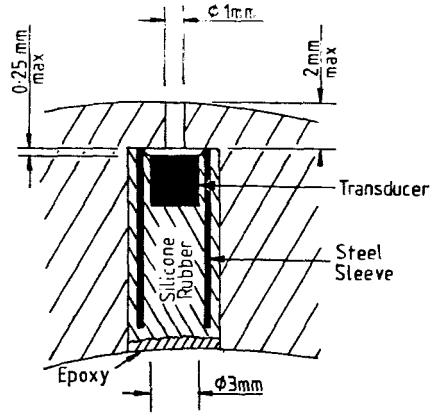

Fig. 3 Mounting of pressure transducers in blade surface

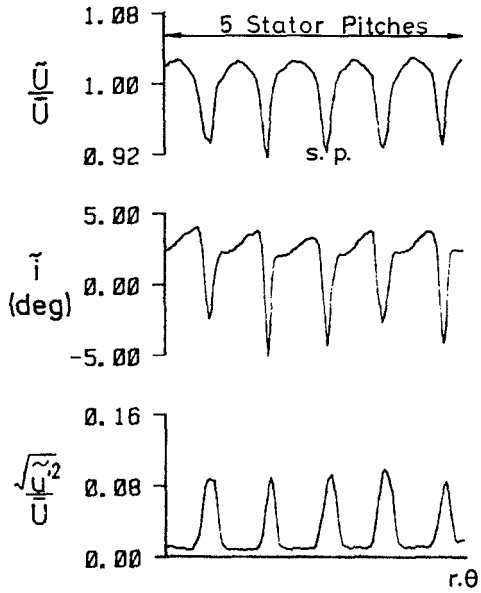

Fig. 4 Rotor-relative in-flow at 43 percent C_{x_s} downstream of stator trailing edges

variations within the transducer signals. The results of the velocity measurements are, for example, presented in the form of the ensembled mean,

$$\tilde{U}(j) = \sum_{n=1}^{100} U(j,n)/100$$

the ensembled root mean square of the random fluctuations,

$$\sqrt{\tilde{u}'^2(j)} = \sqrt{\sum_{n=1}^{100} (U^2(j,n) - \tilde{U}^2(j))/100}$$

the time mean,

$$\bar{U} = \sum_{j=1}^{J} \tilde{U}(j)/J$$

the root mean square of the periodic fluctuations,

$$\sqrt{\tilde{U}^2} = \sqrt{\sum_{j=1}^{J} (\tilde{U}^2(j) - \bar{U}^2)/J}$$

and the mean level of the random fluctuations,

Table 3 Stator wakes at 43 percent Cx_s downstream of stator trailing edges

Profile loss coefficient [14]	0.0140	Absolute Frame of Reference
δ^*/pitch	0.0090	
θ/pitch	0.0071	
$H = \delta^*/\theta$	1.27	
$(\tilde{U}_{max} - \tilde{U}_{min})/\bar{U}$	0.021	
Mean incidence (deg)	2.1	Rotor Relative Frame of Reference
Incidence variation (deg)	7.5	
$(\tilde{U}_{max} - \tilde{U}_{min})/\bar{U}$	0.105	
$\sqrt{\tilde{u}'^2}/\bar{U}$	0.041	
$\sqrt{\tilde{u}'^2}/\bar{U}$ max	0.095	
$\bar{U}/\tilde{U}_2$	0.447	

$$\sqrt{\tilde{u}'^2} = \sqrt{\sum_{j=1}^{J} \tilde{u}'^2(j)/J}$$

where j represents the jth point in the nth sample of phase-locked data.

Water Turbine. The single-stage axial-flow water turbine was manufactured by Techquipment of the U.K. It is a 50 percent reaction design and has a blade geometry which is very similar to that of the large-scale air turbine described above. Further information on the water turbine can be found in Table 2.

The turbine has a transparent casing and it can therefore be used for flow visualization studies. During the experiments, drafting ink was injected through a 0.75-mm-dia backward facing pitot which was placed within the wake of a stator blade. Because the illumination was provided by a stroboscope, the photographs show only the phase-locked-average of the interactions.

Results and Discussion

Air Turbine. By mounting hot wires upon the rotor so that they would traverse the stator exit flow field at the mid-span radius, it was possible to determine the levels of periodic and random unsteadiness contained within the rotor-relative inflow.

The results of a traverse at 43 percent C_{x_s} downstream of the stator trailing edges are summarized in Table 3 and shown in Fig. 4. Significantly, they show that within the stator wakes, there is a reduction in incidence of 7.5 deg and in velocity of 10.5 percent. They also show that the stator wakes are turbulent, with a maximum rms level equal to 9.5 percent of the mean velocity and a mean rms which is equal to 4.1 percent. It is acknowledged that the above variations, while they are significant, are not necessarily as large as those which can occur in designs where the rotor-stator gap is much smaller.

It should, perhaps, be noted that because the axis of the wire used to measure the rms levels in this turbine was aligned with the radial direction, the rms only contains information about the streamwise fluctuations. The rms is, therefore, only a measure of the turbulence level, If, however, the turbulence is assumed to be isotropic, then the turbulent kinetic energy is approximately equal to 1.5 times the square of the rms value.

In a previous publication [17], the author has described a series of measurements of the rotor blade surface boundary layers using a radially-aligned single-sensor hot wire. In this

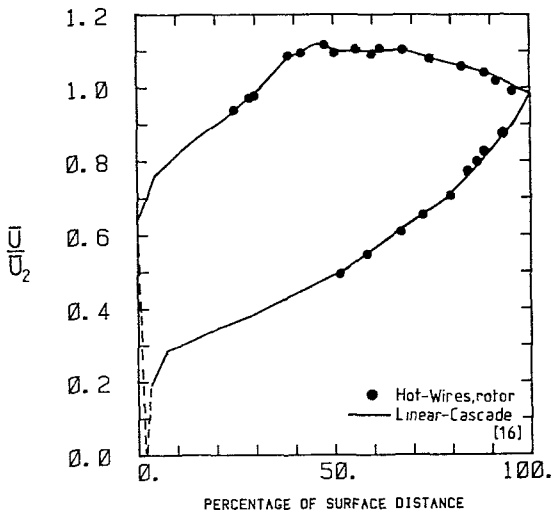

Fig. 5 Blade surface velocity distribution

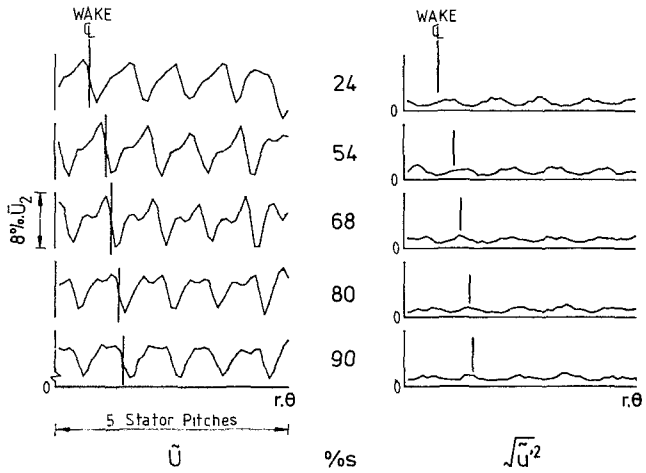

Fig. 6 Unsteady blade surface velocities on the suction surface

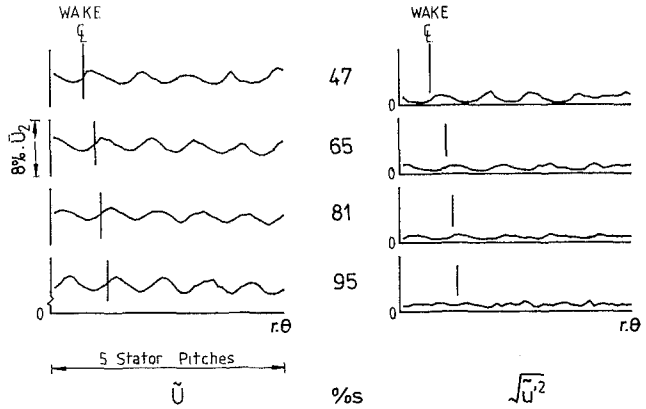

Fig. 7 Unsteady blade surface velocities on the pressure surface

paper, the so-called blade-surface free-stream velocities, which were measured during that investigation, are described in detail. The location of these velocities is *arbitrarily* defined as the distance from the surface which is 10 percent greater than the distance at which the maximum velocity first occurred. The time averaged blade-surface velocity distribution is shown in Fig. 5 together with the results of a linear cascade test [16] in which the blade geometry was equal to that of the rotor midspan.

Some of the phase-locked-averages of the blade-surface

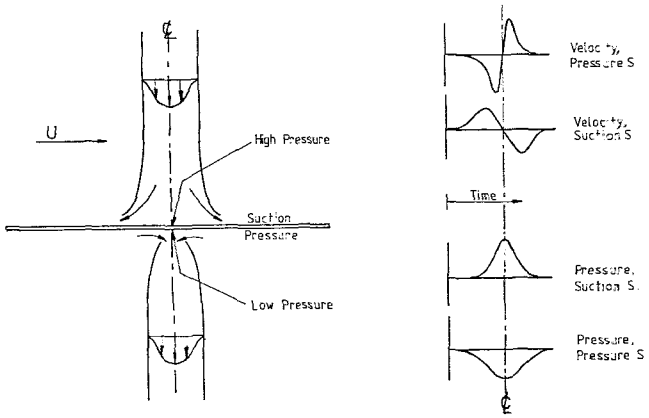

Fig. 8 Representation of wake as a "negative jet"

free-stream velocities are shown in Figs. 6 and 7. For clarity, only the fluctuating portions of the velocity signals are shown.

On the suction surface (Fig. 6), the velocity signal is characterized by a plateau or slow increase, at about the mean value, which is then followed by a rapid increase up to the maximum value, a rapid fall from the maximum to the minimum and, finally, another rapid increase up to the plateau or region of less rapid increase. Toward the rear of the suction surface, this characteristic wave form becomes distorted and the separation of the wakes, as indicated by the rms levels, becomes less well defined.

On the pressure surface (Fig. 7), the amplitude of the velocity fluctuations is less than that on the suction surface whereas the amplitude of the rms fluctuations is approximately the same. In the case of the velocity waveform, the signal is the mirror image of that which occurs on the suction surface with the exception that the separate portions are less well defined. Just as on the suction surface, the pressure surface waveforms become less well defined towards the trailing edge.

The characteristic shapes of the velocity fluctuations which have been noted in Figs. 6 and 7 can be explained using the model of Lefcourt [7]. Figure 8 is based upon that model. It shows the velocity and pressure time-histories at points on the suction and pressure surfaces of a flat plate during the passage of a wake or "negative jet." The similarity between these signals and those shown in Figs. 6 and 7 is self-evident although, in contrast to the simple model, the pressure surface velocity variations are less than those near the suction surface. It should be noted that the negative jet depicted in Fig. 8 will persist within the rotor passage, even when it has been chopped by the rotor blades, because of the inertia of the fluid. Interestingly, and contrary to expectations, the results of Figs. 6 and 7 show that the peak levels of free stream turbulence do not always coincide with the apparent centerlines of the wakes (as suggested by the model of Lefcourt [7]) just as the minimum rms values do not always coincide with the velocity plateaux which indicate the inter-wake regions of the flow.

The blade-surface distributions of the mean levels of the periodic and random velocity unsteadiness are presented in Figs. 9 and 10, respectively. They show that over the rear of both surfaces, the kinetic energy associated with the periodic and random fluctuations is largely conserved. However, a comparison of Figs. 9 and 10 shows that the level of periodic unsteadiness on the suction surface is approximately 2½ times that on the pressure surface, whereas the mean level of free-stream turbulence is only slightly greater. In addition, the energy contained within the turbulent fluctuations is greater than that contained within the periodic fluctuations on the pressure surface, while on the suction surface, the opposite

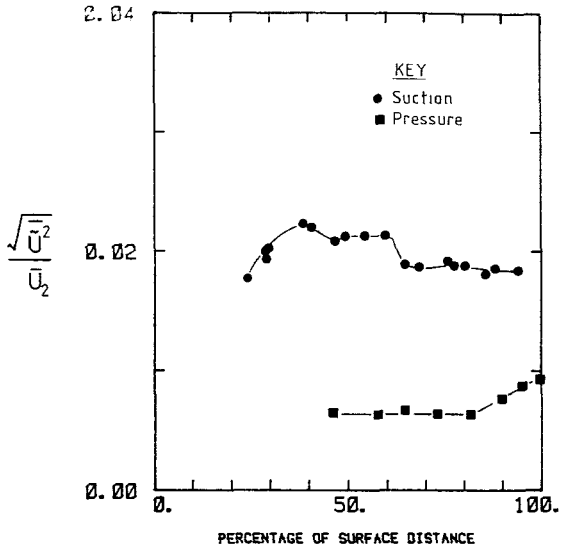

Fig. 9 Mean periodic unsteadiness – velocity

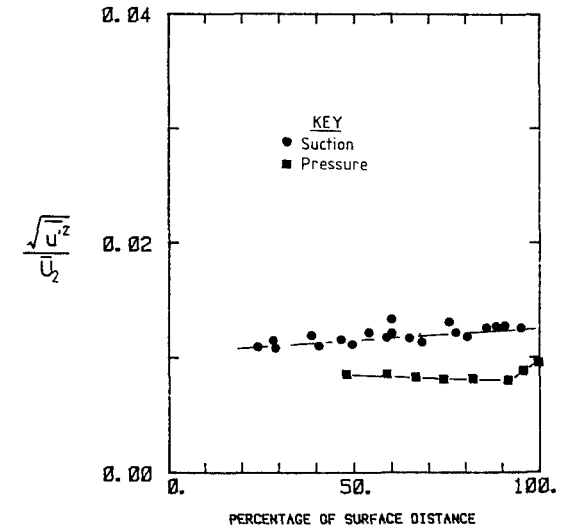

Fig. 10 Mean random unsteadiness – velocity

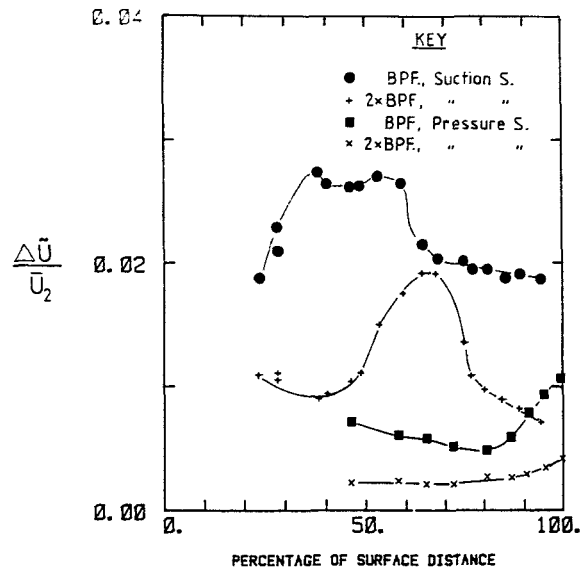

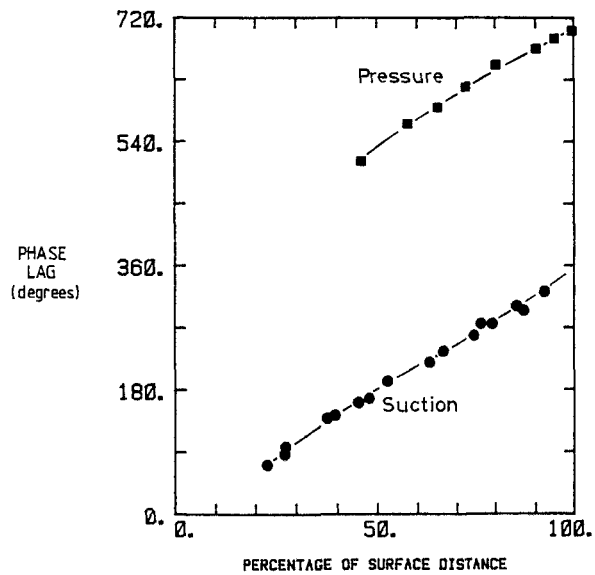

Fig. 11 Amplitude and phase of the blade surface velocities

occurs. Clearly, these differences are important with regard to the development of the blade surface boundary layers [17].

A closer inspection of Fig. 10 reveals that the mean level of free-stream turbulence on the suction surface increases along the surface at about the same rate as it falls on the pressure surface. Thus, it appears that the "negative jet" is responsible for transporting the high turbulence wake fluid away from the pressure surface towards the suction surface of the passage. The effects of this migration have also been noted by the author in measurements of the rotor relative exit stagnation pressure profile [16]. It is also possible that this transportation of the wake fluid explains why the level of periodic unsteadiness is much less on the pressure than on the suction surface.

The phase-locked-averages of the free-stream velocities (i.e., Figs. 6 and 7) show that because there are no potential interactions, it is the blade passing frequency and its harmonics which dominate the periodic unsteadiness. Figure 11 shows the amplitude and phase distributions of the blade-surface velocities at the blade passing frequency. The velocity measurements were, in fact, made on either side of a blade passage. The phases, however, have been corrected so that they apply to a single blade. It should be noted that phase lags of more than 360 deg could be determined because of blade-to-blade differences in the wakes and that the phase reference was provided by the once-per-revolution trigger pulse which was used to start the phase-locked data acquisition.

The phase relationships which are predicted for disturbances which travel at the local convection velocity (see Fig. 5) and the sound speed are shown in Fig. 12. At the leading edge, the phase difference between the suction and pressure surface disturbances has been set to 180 deg in accordance with the model of Meyer [6]. A comparison of these predicted (Fig. 12) and measured phase distributions (Fig. 11) shows that the suction surface disturbances travel at the local convection speed whereas the pressure surface velocity fluctuations, which are much smaller, appear to travel at a speed which is closer to the mean convection speed.

Unfortunately, the blade surface static pressure measurements provided only limited information. In particular, mean values could not be determined because it was impossible to compensate for the thermal drift of the transducer output. Furthermore, the transducer output signals unexpectedly contained large amplitude harmonics of the rotational frequency. These harmonics occurred as a result of

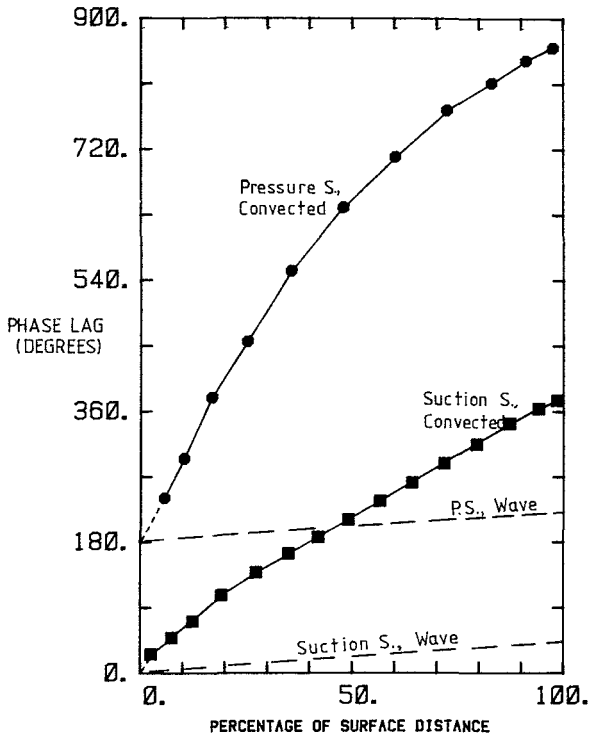

Fig. 12 Predicted phase distributions for convected and pressure wave type disturbances

blade vibrations being sensed by the transducer via distortion of their bodies and/or acceleration of their diaphragms. Fortunately, however, they did not occur at the blade passing frequency and it was therefore possible to determine the amplitude and phase distributions at this frequency, which is clearly the most important with respect to the generality of these results.

The distributions of the amplitude and phase of the surface static pressures of the blade-passing frequency are shown in Fig. 13. On the suction surface, the amplitude associated with this frequency is greatest at 5 percent of the surface length, after which there is a general decrease, with local maxima at 30 and 83 percent of the surface length. On the pressure surface, the amplitude is almost constant. Near the trailing edge the amplitudes on each surface are almost equal.

The distributions of the amplitude of the surface static pressure of second harmonic of the blade passing frequency have also been plotted in Fig. 13. Near the leading edge of the suction surface, the amplitude of this harmonic is approximately equal to 1/16th of that of the fundamental whereas near the trailing edge, it is almost equal. On the pressure surface, the amplitude of the second harmonic is typically equal to 1/8th of that of the fundamental.

The distributions of the amplitude of the first harmonic are, in fact, quite similar to those observed by Dring et al. [22] and Grant and Johnson [21] on the second stage stators of axial turbines. They are very different from the monotonic decays which have been observed (e.g., [23]) in axial compressors.

It is interesting to compare the magnitudes of the pressure and velocity fluctuations at the blade passing frequency. This can be done if the latter are converted into dynamic pressure fluctuations, when it is found that on the suction surface, especially towards the rear, the velocity fluctuations are much more significant. On the pressure surface, however, the velocity and pressure fluctuations are of equal strength. The

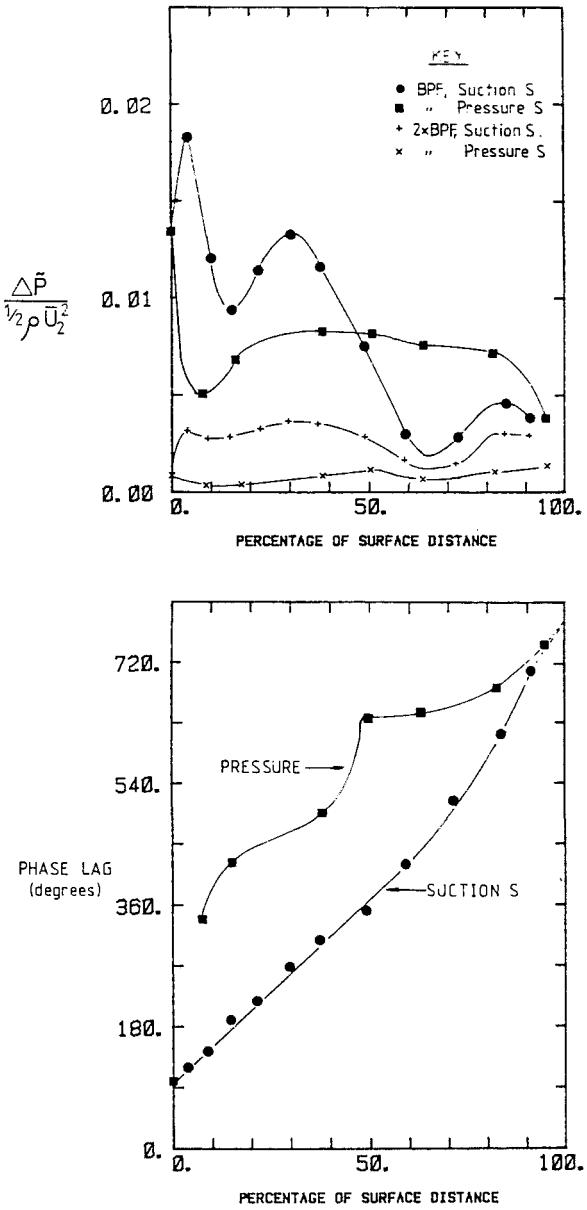

Fig. 13 Amplitude and phase of the blade surface velocities

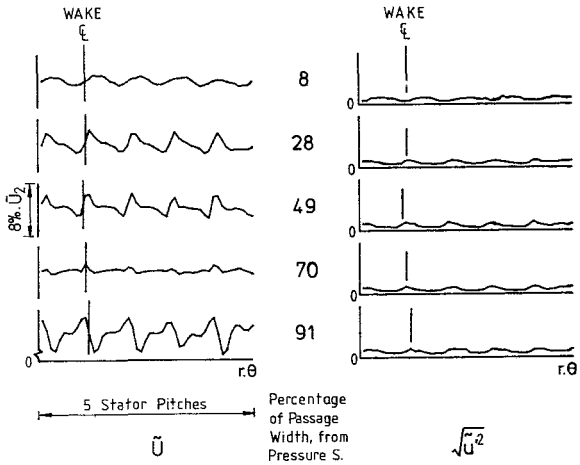

Fig. 14 Unsteady velocities across the blade passage at 82 percent C_{x_r}

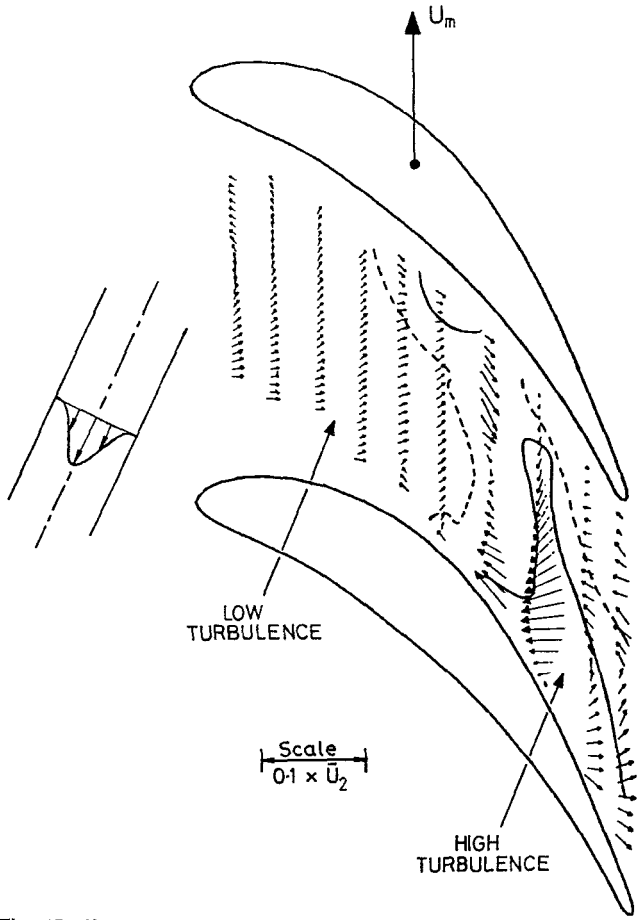

Fig. 15 Unsteady velocity vectors and rms contours in the rotor passage

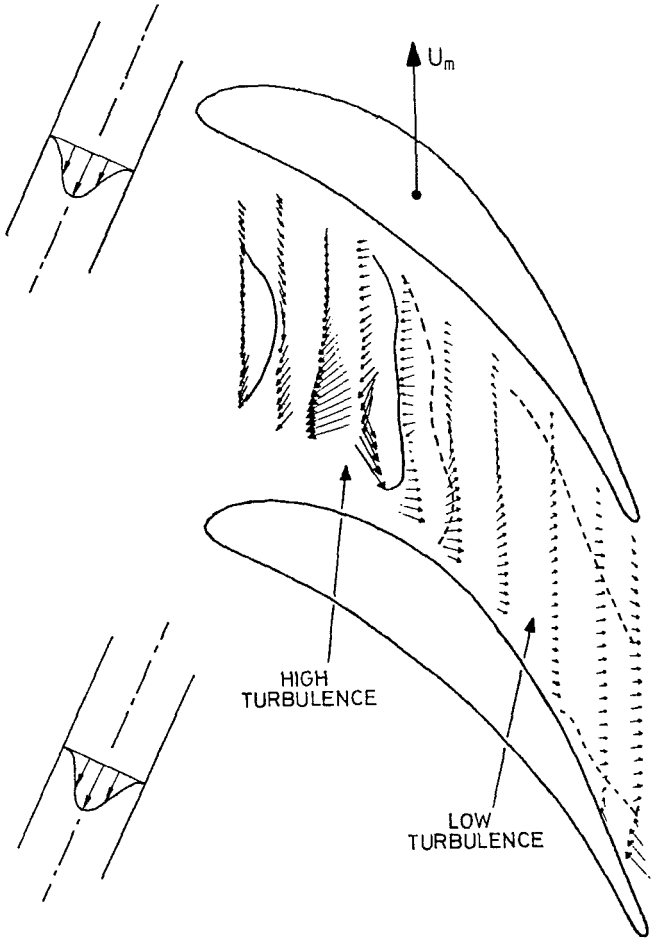

Fig. 16 Unsteady velocity vectors and rms contours in the rotor passage (one-half cycle later than Fig. 15)

significance of this with respect to the development of the blade surface boundary layers is already known [17].

The phase distributions of the first harmonic of the pressure fluctuations are also shown in Fig. 13. The phase reference is the same as that used in Fig. 11 for the velocities. Figure 13 shows that near the leading edge, there is a 180 deg phase difference between the suction and pressure surface signals which is caused by the simultaneous unloading of the suction surface and loading of the pressure surface as the wakes interact with the leading edge. Near the trailing edge, the phase difference reduces to zero which, since the amplitudes of the suction and pressure surface signals are approximately equal there, suggests that the Kutta condition is probably valid at the blade passing frequency whereas at the second harmonic, it is apparently not. It is also found, by comparing Figs. 11 and 13, that the velocity and pressure fluctuations are all in phase at the trailing edge.

The actual variation of the phase of the pressure disturbances along the two surfaces is not understood. On the suction surface, for example, the signals appear to travel at approximately 70 percent of the mean convection speed. On the pressure surface, the distribution is much more complicated. It should, perhaps, be pointed out that phase analyses can be misleading. If, for example convected and pressure wave phenomena were to coexist, then the analysis would merely produce the phase angle of the vector sum of the two phenomena. This may help to explain the distributions which have been observed.

The existence of "convected" pressure disturbances is not, in fact, uncommon, nor is it unexpected in the present situation. Other workers, for example, Fleeter et al. [23] have observed similar phenomena in axial compressors and, in the results of references [21] and [24], such disturbances can also be observed.

Having found that the blade surface velocity fluctuations can be explained with reference to simple theories, but that the pressure fluctuations could not, it was decided to traverse the flow within the rotor passage in order to obtain further information about the unsteady flow field. In all, ten sets of circumferential traverses were made. An analysis of each set showed that qualitatively, they were identical.

The velocity and rms traces which were obtained at different tangential locations within the passage at 82 percent C_{x_r} are shown in Fig. 14. The differences which exist between the suction and pressure surfaces have already been discussed with reference to the "negative jet" model of references [6] and [7]. Apparently, as Fig. 14 shows, the distortion of the wake, which is caused by the interaction of the wake with the blade surface, extends only a short distance from the suction surface whereas it extends a long way from the pressure surface. At 70 percent of the passage width, the velocity fluctuations are very small, which suggests that the distortions of the wake "cancel" each other in midpassage. Because, however, the turbulence level is unsigned, there is no such "cancellation" of the rms and the nature of the periodic turbulence variations remains unchanged across the passage.

In order to obtain a true picture of the unsteady phenomena within the rotor passage, the time-mean velocity measurements were subtracted from the phase locked averages. The results are presented in Figs. 15 and 16 in the form of unsteady velocity vector plots at two equally spaced time levels within the wake passing cycle. For the purpose of identifying the wake regions, high ($0.012 \times \bar{U}_2$) and medium ($0.008 \times \bar{U}_2$) value rms contours have been superimposed.

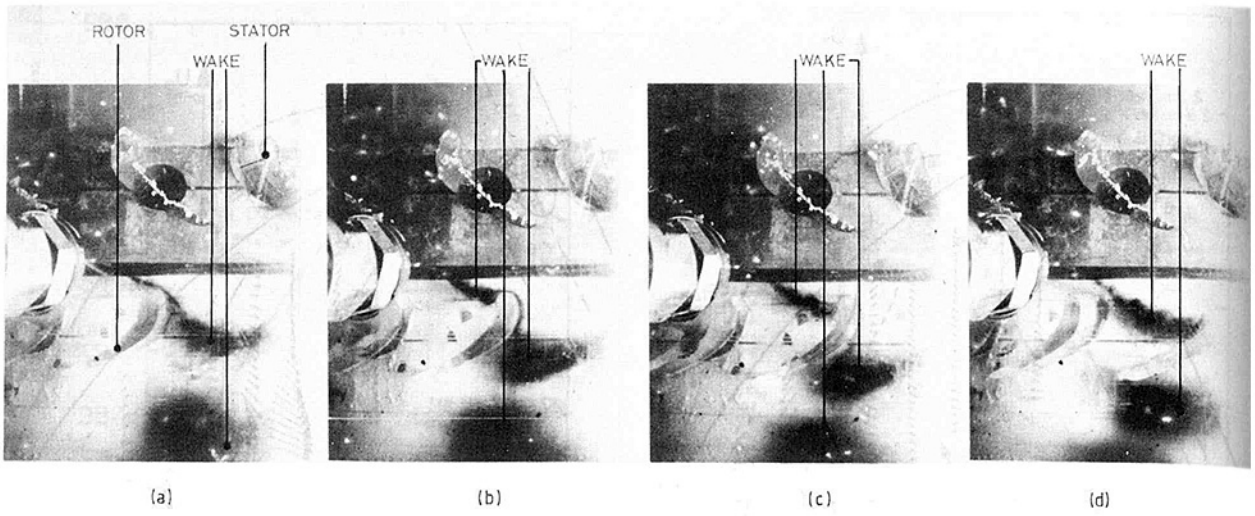

Fig. 17 Stator wake and rotor blade interactions in the water turbine

Figure 15 confirms the existence of several of the phenomena which have been discussed above. The most striking feature is the behavior of the wake segments as negative jets, with high loss fluid being convected toward the suction surface. Low loss fluid is transported toward the pressure surface in order to replace the migrated wake fluid. A pair of vortices, of opposite rotation, is thus formed, with one placed on each side of the wake.

In Fig. 16, the wake shown in Fig. 15 has almost disappeared from the blade passage and a new wake segment has entered. As in the previous figure, the new wake behaves as a negative jet and its associated vortices are already established.

The recirculatory motion which has already been noted will result in a broadening of the wake near the suction surface and a thinning near the pressure surface. In addition to this distortion, a second phenomenon exists which will add to the wake segment broadening on the suction surface whilst suppressing the wake segment thinning on the pressure surface. This phenomenon begins at the leading edge, where the leading portion of the wake accelerates along the surfaces away from the trailing portion which remains in the vicinity of the stagnation point. By the time the trailing portion has reached the blade surface, the leading portion has moved further away and the wake, in the region of the surfaces, becomes even wider. It is only over the rear portion of the suction surface, where there is some diffusion, that a small reduction in width might occur. Because the velocity gradient is much lower over the leading part of the pressure surface than over the leading part of the suction surface, this stretching of the wake segment will be less pronounced on the pressure surface.

Another feature which is clearly evident in Figs. 15 and 16 is the large amount of distortion which the centerline of the wake has undergone. This distortion takes the form of a reorientation together with a bowing, in the downstream direction, of the wake segment. Both of these phenomena arise as a result of the cross-channel variations in the convection velocity. The reorientation of the segment, which is particularly visible, is to be expected since, as Fig. 12 showed, a fluid particle will convect along the suction surface at about twice the rate of one which convects along the pressure surface. The bowing of the segment is more visible in Fig. 16. This is because it is in the region of leading edges, that the differences between the midpassage convection velocity and the blade surface velocities are at their greatest.

A further comparison of Figs. 15 and 16 shows that in the center of the passage, the wake width reduces as the segment is sheared. This, as Smith [8] points out, probably occurs as a consequence of the need to conserve vorticity as the length of the segment increases during the reorientation. A further consequence of the wake segment reorientation can be seen in Figs. 6 and 7, where it was noted that the characteristic shapes of the velocity waveforms became distorted towards the rear of the blade surfaces.

Water Turbine. Figure 17 contains some of the results of the flow visualization experiment carried out in the water turbine. The sequence of photographs shows the movement of a wake through a rotor blade row during one wake passing cycle. The phenomena of wake bowing (Fig. 17(*a*)), shearing (Fig. 17(*b*)), chopping (Fig. 17(*c*)), and migration (Fig. 17(*d*)) can all be seen.

The results of Fig. 17 also show that the stator wake, after its passage through the rotor, is no longer a single entity. Instead, it consists of individual segments which lie between the wakes of adjacent rotor blades once they have convected through the blade row. As a result of the interaction, the flow onto a subsequent stator row would contain both rotor and 1st-stator wake generated unsteadiness. The stator wake segments do not, of course, rotate with the rotor wakes as they are convected downstream. Instead, they convect with the stationary frame flow. In axial compressors, a similar phenomenon has been observed (e.g. [12] and [13]).

Conclusions

Wake interactions are already known to affect the performance of axial turbines. The results of this investigation show that wake generated unsteadiness of the midspan of the rotor of a single-stage turbine can be explained using the simple, inviscid theories of wake chopping, migration, bowing and shearing.

In the case of multistage turbines, it is likely that these theories will also be adequate even though, as the results of the flow visualization here show, the unsteady flow will increase in complexity after each blade row.

Acknowledgment

The author wishes to thank the members of the Whittle Laboratory who assisted in the investigation, especially Dr. J. D. Denton and Dr. P. Bryanston-Cross. The financial assistance of the C. E. G. B. is also gratefully acknowledged.

References

1 Moses, H. L., and O'Brien, W. F., Jr., "The Chord-Wise Pressure Distribution on a Rotating Axial Flow Compressor Blade," Presented at 2nd Int. Symp. on Air Breathing Engines, Sheffield, Mar. 1974.

2 Lopatitskii, A. O., et al., "Energy Losses in the Transient State of an

Incident Flow on the Moving Blades of Turbine Stages," *Energomashinostroenie*, Vol. 15, Aug. 1969.

3 Kuhl, W., and Koschel, W., "Turbine Flow Phenomena and Their Effect on the Rotor Blade Heat Transfer," Presented at Int. Symp. on Applications of Fluid Mech. and Heat Trans. to Energy and Environmental Problems, University of Patras, Patras, Greece, June 29th–July 3rd, 1981.

4 Carta, F. O., "An Experimental Study on the Aerodynamic Response of a Subsonic Cascade Operating Near Stall," Project SQUID Technical Report UTRC-2-PU, July 1976.

5 Gallus, H. E., Grollius, H., and Lambertz, J., "The Influence of Blade Number Ratio and Blade Row Spacing on Axial-Flow Compressor Stator Blade Dynamic Load and Stage Sound Pressure Level," ASME JOURNAL OF ENGINEERING FOR POWER, July 1982, pp. 633–641.

6 Meyer, R. X., "The Effects of Wakes on the Transient Pressure and Velocity Distributions in Turbomachines," ASME *Journal of Basic Engineering*, Oct. 1958, pp. 1544–1552.

7 Lefcourt, M. D., "An Investigation Into Unsteady Blade Forces in Turbomachines," ASME JOURNAL OF ENGINEERING FOR POWER, Oct. 1965, pp. 345–354.

8 Smith, L. H., "Wake Dispersion in Turbomachines," ASME *Journal of Basic Engineering*, Sept. 1966, pp. 688–690.

9 Kerrebrock, J. L., and Mikolajczak, A. A., "Intra-Stator Transport of Rotor Wakes and Its Effect on Compressor Performance," ASME JOURNAL OF ENGINEERING FOR POWER, Oct. 1970, pp. 359–368.

10 Adachi, T., and Murakami, Y., "The Dimensional Velocity Distribution Between Stator Blades and Unsteady Force due to Passing Wakes," *JSME*, Vol. 22, No. 170, Aug. 1979, pp. 1074–1082.

11 Weyer, H., and Dunker, R., "Flow Measurements in Stator Rows Behind a Transonic Axial Compressor," AGARD-CP-351, Copenhagen, June 1983.

12 Wagner, J. H., Okiishi, T. H., and Holbrook, G. J., "Periodically Unsteady Flow in an Imbedded Stage of a Multistage, Axial-Flow Turbomachine," ASME JOURNAL OF ENGINEERING FOR POWER, Vol. 101, Jan. 1979, pp. 42–51.

13 Zierke, W. C., and Okiishi, T. H., "Measurement and Analysis of Total-Pressure Unsteadiness Data From an Axial-Flow Compressor Stage," ASME JOURNAL OF ENGINEERING FOR POWER, Vol. 104, Apr. 1982, pp. 479–488.

14 Hunter, I. H., "Endwall Boundary Layer Flows and Losses in Axial Turbomachines," Ph.D. thesis, Cambridge 1979.

15 Denton, J. D., and Usui, S., "Use of a Tracer Gas Technique to Study Mixing in a Low-speed Turbine," ASME Paper 81-GT-86, 1981.

16 Hodson, H. P., "Boundary Layer and Loss Measurements on the Rotor of an Axial-Flow Turbine," ASME JOURNAL OF ENGINEERING FOR GAS TURBINES AND POWER, Vol. 106, Apr. 1984, pp. 391–399.

17 Hodson, H. P., "The Development of Unsteady Boundary Layers on the Rotor of an Axial Flow Turbine," AGARD-CP-351, Copenhagen, June 1983.
Analysis of Rotor Wakes," *Aero-Quart.*, Nov. 1972, pp. 285–300.

19 Champagne, F. H., Sleicher, C. A., and Wehrman, O. H., "Turbulence Measurements with Inclined Hot Wires, Part 1" *J.F.M.*, Vol. 28, No. 1, 1967, pp. 153–175.

20 Gostelow, J. P., "A New Approach to the Experimental Study of Turbomachinery Flow Phenomena," ASME JOURNAL OF ENGINEERING FOR POWER, Vol. 99, 1977, pp. 97–105.

21 Grant, R. J., and Johnson, C. G., "Unsteady Measurements in a Stator Blade Passage in the M.E.L. Model Turbine," CEGB Memorandum, MM/MECH/TF 261, Sept. 1980.

22 Dring, R. P., Joslyn, H. D., Hardin, L. W., and Wagner, J. H., "Turbine Rotor-Stator Interaction," ASME JOURNAL OF ENGINEERING FOR POWER, Vol. 104, Oct. 1982, pp. 743–750.

23 Fleeter, S., Bennett, W. A., and Jay, R. L., "The Time-Variant Aerodynamic Response of a Stator Row including the Effects of Airfoil Camber," ASME JOURNAL OF ENGINEERING FOR POWER, Vol. 102, Apr. 1980, pp. 334–343.

24 Ispas, I., Grollius, H., and Gallus, H. E., "Uber den Einflub von Nachlaufdellen auf die instationare Druckverteilung an den nachflogenden Schaufelreihen in Axialverdichtern und Axialturbinen," VDI-Berichte No. 361, 1980.

Incident Flow on the Moving Blades of Turbine Stages," *Energomashinostroenie*, Vol. 15, Aug. 1969.

3 Kuhl, W., and Koschel, W., "Turbine Flow Phenomena and Their Effect on the Rotor Blade Heat Transfer," Presented at Int. Symp. on Applications of Fluid Mech. and Heat Trans. to Energy and Environmental Problems, University of Patras, Patras, Greece, June 29th–July 3rd, 1981.

4 Carta, F. O., "An Experimental Study on the Aerodynamic Response of a Subsonic Cascade Operating Near Stall," Project SQUID Technical Report UTRC-2-PU, July 1976.

5 Gallus, H. E., Grollius, H., and Lambertz, J., "The Influence of Blade Number Ratio and Blade Row Spacing on Axial-Flow Compressor Stator Blade Dynamic Load and Stage Sound Pressure Level," ASME JOURNAL OF ENGINEERING FOR POWER, July 1982, pp. 633–641.

6 Meyer, R. X., "The Effects of Wakes on the Transient Pressure and Velocity Distributions in Turbomachines," ASME *Journal of Basic Engineering*, Oct. 1958, pp. 1544–1552.

7 Lefcourt, M. D., "An Investigation Into Unsteady Blade Forces in Turbomachines," ASME JOURNAL OF ENGINEERING FOR POWER, Oct. 1965, pp. 345–354.

8 Smith, L. H., "Wake Dispersion in Turbomachines," ASME *Journal of Basic Engineering*, Sept. 1966, pp. 688–690.

9 Kerrebrock, J. L., and Mikolajczak, A. A., "Intra-Stator Transport of Rotor Wakes and Its Effect on Compressor Performance," ASME JOURNAL OF ENGINEERING FOR POWER, Oct. 1970, pp. 359–368.

10 Adachi, T., and Murakami, Y., "The Dimensional Velocity Distribution Between Stator Blades and Unsteady Force due to Passing Wakes," *JSME*, Vol. 22, No. 170, Aug. 1979, pp. 1074–1082.

11 Weyer, H., and Dunker, R., "Flow Measurements in Stator Rows Behind a Transonic Axial Compressor," AGARD-CP-351, Copenhagen, June 1983.

12 Wagner, J. H., Okiishi, T. H., and Holbrook, G. J., "Periodically Unsteady Flow in an Imbedded Stage of a Multistage, Axial-Flow Turbomachine," ASME JOURNAL OF ENGINEERING FOR POWER, Vol. 101, Jan. 1979, pp. 42–51.

13 Zierke, W. C., and Okiishi, T. H., "Measurement and Analysis of Total-Pressure Unsteadiness Data From an Axial-Flow Compressor Stage," ASME JOURNAL OF ENGINEERING FOR POWER, Vol. 104, Apr. 1982, pp. 479–488.

14 Hunter, I. H., "Endwall Boundary Layer Flows and Losses in Axial Turbomachines," Ph.D. thesis, Cambridge 1979.

15 Denton, J. D., and Usui, S., "Use of a Tracer Gas Technique to Study Mixing in a Low-speed Turbine," ASME Paper 81-GT-86, 1981.

16 Hodson, H. P., "Boundary Layer and Loss Measurements on the Rotor of an Axial-Flow Turbine," ASME JOURNAL OF ENGINEERING FOR GAS TURBINES AND POWER, Vol. 106, Apr. 1984, pp. 391–399.

17 Hodson, H. P., "The Development of Unsteady Boundary Layers on the Rotor of an Axial Flow Turbine," AGARD-CP-351, Copenhagen, June 1983. Analysis of Rotor Wakes," *Aero-Quart.*, Nov. 1972, pp. 285–300.

19 Champagne, F. H., Sleicher, C. A., and Wehrman, O. H., "Turbulence Measurements with Inclined Hot Wires, Part 1" *J.F.M.*, Vol. 28, No. 1, 1967, pp. 153–175.

20 Gostelow, J. P., "A New Approach to the Experimental Study of Turbomachinery Flow Phenomena," ASME JOURNAL OF ENGINEERING FOR POWER, Vol. 99, 1977, pp. 97–105.

21 Grant, R. J., and Johnson, C. G., "Unsteady Measurements in a Stator Blade Passage in the M.E.L. Model Turbine," CEGB Memorandum, MM/MECH/TF 261, Sept. 1980.

22 Dring, R. P., Joslyn, H. D., Hardin, L. W., and Wagner, J. H., "Turbine Rotor-Stator Interaction," ASME JOURNAL OF ENGINEERING FOR POWER, Vol. 104, Oct. 1982, pp. 743–750.

23 Fleeter, S., Bennett, W. A., and Jay, R. L., "The Time-Variant Aerodynamic Response of a Stator Row including the Effects of Airfoil Camber," ASME JOURNAL OF ENGINEERING FOR POWER, Vol. 102, Apr. 1980, pp. 334–343.

24 Ispas, I., Grollius, H., and Gallus, H. E., "Uber den Einflub von Nachlaufdellen auf die instationare Druckverteilung an den nachflogenden Schaufelreihen in Axialverdichtern und Axialturbinen," VDI-Berichte No. 361, 1980.

DISCUSSION

G. J. Walker[1]

This paper makes a useful contribution to the limited literature on wake-generated unsteadiness in axial turbomachinery. The complementary flow visualization study in a water turbine of similar geometry is especially valuable.

The general features of the stator wake transport through the turbine rotor passages are broadly similar to those of a compressor rotor wake transported through a following stator as reported by Lockhart [25] and Lockhart and Walker [26]. In particular, there is agreement on the migration of wake fluid explaining the different level of periodic unsteadiness on pressure and suction surfaces of the downstream blades. There are, however, some significant differences in detail between the compressor and turbine flows due to opposite senses of:

(*a*) the incidence variation as the wake is chopped by the downstream blades;

(*b*) the rotation of chopped wake segments relative to the axial direction; and

(*c*) the direction of wake fluid migration relative to the pressure and suction surfaces of the downstream row.

The extent of wake shearing also differs in accordance with the different stage geometry and blade loading of the compressor and turbine.

In relation to experimental technique the author comments that phase-locked averaging was used "to enhance the periodic variations within the transducer signals." It is worthwhile stressing that this is only true for signals bearing a constant phase relationship to the wake passage. Periodic signals not locked in phase relative to the wake passage (as could occur with vortex shedding from a blade trailing edge, for example) would be lost by phase-locked averaging with respect to the wakes; these periodic signals would then be erroneously identified as random fluctuations. For this reason, the discusser considers it essential to observe the transducer output over a single revolution while experimental data are being acquired, in order to avoid this possible source of error (as indeed the author must have done in relation to the fluctuating pressure measurements mentioned later in the paper).

It is not clear why the random velocity unsteadiness on the pressure and suction surfaces should decrease and increase respectively at about equal rates with their average remaining essentially constant. The variation in the passage-averaged turbulence level should also depend on the rates of turbulence dissipation and production, which are influenced by the acceleration and distortion of the wake fluid as well as its convection. The constant passage-averaged time-mean random unsteadiness shown in Fig. 10 therefore appears coincidental. Stress should rather be laid on the fact that the pressure and suction surface unsteadiness curves of this figure diverge, and it is agreed that this is predominantly due to convection of fluid within the wakes.

The discusser also queries the apparent inference from Figs. 6 and 7 that there are no potential interactions because "it is the blade passing frequency and its harmonics which dominate the periodic (velocity) unsteadiness." Any fluctuations due to relative motion of the pressure fields of neighboring rows should also produce fluctuations at these frequencies; but because they propagate at a different velocity their phase relative to that of the convected wake disturbances should alter with position along the rotor blade surface. Such relative phase changes would alter the shape of the unsteady velocity disturbances along the blade surfaces and might therefore provide a partial explanation of the phenomena observed in Figs. 6 and 7.

Potential interactions may also arise from viscous effects such as the convection of a wake over the leading edge of a downstream blade. The incidence variations associated with

[1]Mechanical Engineering Department, University of Tasmania, Hobart, Australia

wake chopping cause fluctuations in the blade surface pressure, resulting in:

(*a*) pressure fluctuations at the blade passing frequency which propagate from the leading edge at sonic velocity relative to the fluid; and

(*b*) changes in shape of the wake velocity disturbance near the leading edge.

The latter effect was noted in the axial compressor studies of Lockhart [25] and may have contributed to the characteristic differences in unsteady velocity fluctuations shown in Figs. 6 and 7 of the present paper. Such phenomena might better be termed potential-viscous interactions to distinguish them from purely potential interactions.

In conclusion, some additional information is sought regarding the unsteady rms contours shown in Fig. 15. There is an isolated region of high turbulence (exceeding 0.012 $\bar{U}_2$) on the rotor blade pressure surface at about 50 percent chord which apparently indicates a local boundary layer thickening or a local region of turbulent boundary layer flow. Is this generated impulsively at the blade leading edge due to the negative incidence associated with wake chopping, or is it rather due to prolonged effects of wake-boundary layer interactions as the stator wake is convected over the rotor blade surface?

References

25 Lockhart, R. C., "Some Unsteady Flow Phenomena Downstream of an Axial Compressor Stage," M. Eng. Sci. Thesis, University of Tasmania, Australia, Sept. 1973.

26 Lockhart, R. C., and Walker, G. J., "The Influence of Viscous Interactions on the Flow Downstream of an Axial Compressor Stage," *Proc. 2nd Int. Symp. on Air-Breathing Engines*, Sheffield, U.K., Mar. 1974.

J. M. Sanz[1]

E. R. McFarland

N. L. Sanger

T. F. Gelder

R. H. Cavicchi

National Aeronautics and Space Administration,
Lewis Research Center,
Cleveland, Ohio 44135

Design and Performance of a Fixed, Nonaccelerating Guide Vane Cascade That Operates Over an Inlet Flow Angle Range of 60 Deg

A unique set of wind tunnel guide vanes are designed with an inverse design code and analyzed with a panel method and an integral boundary layer code developed at the NASA Lewis Research Center. The fixed guide vanes, 80 ft long with 6-ft chord length, were designed for the NASA Ames 40 × 80/80 × 120 ft Wind Tunnel. Low subsonic flow is accepted over a 60 deg range of inlet angle from either the 40 × 80 leg or the 80 × 120 leg of the wind tunnel, and directed axially into the main leg of the tunnel where drive fans are located. Experimental tests of 1/10-scale models were conducted to verify design calculations.

1 Introduction

To expand testing capabilities, an 80 × 120 ft leg has recently been added to the National Aeronautics and Space Administration's Ames Research Center 40 × 80 ft wind tunnel (AWST [1]). This new leg joins the original tunnel circuit at a 45 deg angle just upstream of the drive fans. At this juncture, a cascade of guide vanes is required to turn the flow 45 deg from the new leg into the original circuit for axial inflow to the drive fans. However, no air turning is desired for operation in the 40 × 80 mode when the new leg is closed off. It is obviously impractical to alternately install and remove guide vanes depending on the operating mode.

The guide vane design goals were mechanical simplicity and ruggedness to lessen cost and expedite operations, and low aerodynamics losses to minimize energy consumption. Low losses were desired not only at the two operating points with inlet air angles of 0 and 45 deg but also over an extended range from about −5 to +55 deg. This was to accommodate expected spatial nonuniformities inherent in the flow approaching the guide vanes, particularly for the 80 × 120 operation. In this mode, large models with vortex wakes are located just upstream of the vanes. The NASA Lewis Research Center has experience in designing airfoils in cascade not only with conventional techniques but also with computational fluid dynamics codes it has recently developed. Therefore, it proposed some guide vane designs for Ames' consideration.

The Lewis aerodynamic design studies considered three different concepts. One was the use of classical 65-series airfoil cascade data. A review of these data (NACA TR1368, [2]) indicated that less than one-half of the desired 60 deg inlet air angle range was possible with low loss with a single row of airfoils. A two-row design was developed that would do the job but the first row required a setting or stagger angle in the 40 × 80 mode different from that in the 80 × 120 mode. Another design utilized a single row of 20 percent thick airfoils, the forward segment of which could be pivoted to match the oncoming flow direction. The third and clearly most desirable design concept was a single row of fixed airfoils capable of accepting the flow with low losses at both modes of operation.

The purposes of this report are (*i*) to describe the

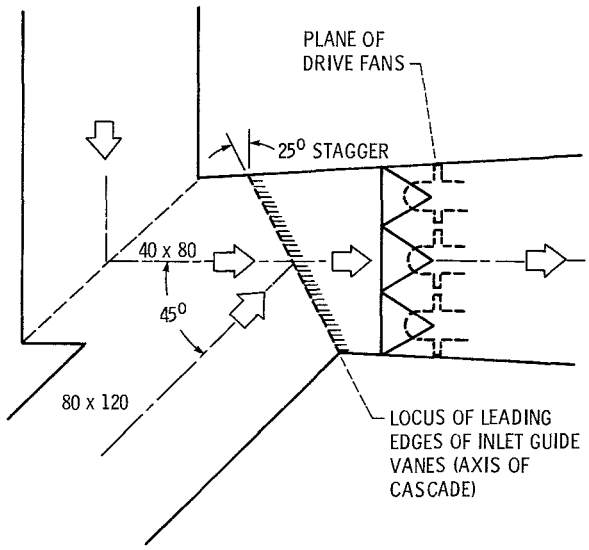

Fig. 1 Schematic of the junction of the NASA Ames 40 × 80/80 × 120 foot wind tunnel

[1]Research Scientist at NASA Lewis Research Center, Cleveland, Ohio, employed by the Universities Space Research Association.

Contributed by the Gas Turbine Division of THE AMERICAN SOCIETY OF MECHANICAL ENGINEERS and presented at the 29th International Gas Turbine Conference and Exhibit, Amsterdam, The Netherlands, June 4–7, 1984. Manuscript received at ASME Headquarters January 5, 1984. Paper No. 84-GT-75.

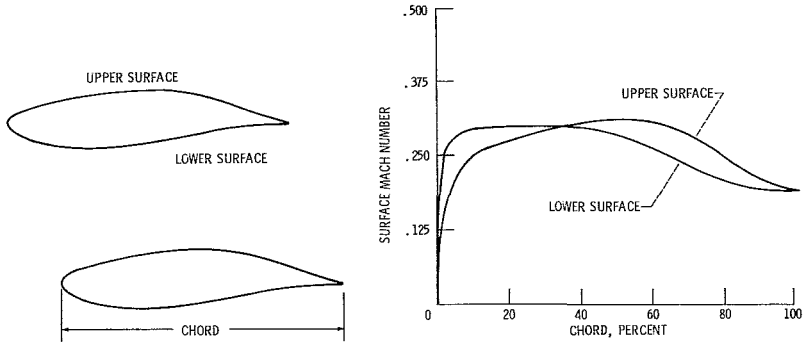

Fig. 2 Lewis No. 1 design

aerodynamic design process for a single row of fixed turning vanes that could operate over an inlet flow angle range of 60 deg with low loss, and (*ii*) to present experimental data of the performance of these vanes and compare these results with design predictions.

There were three computational fluid dynamics codes utilized in the design and off-design analysis of the guide vanes, all developed at the Lewis Research Center. The airfoil in cascade was designed with a recently developed inviscid, inverse design code with a boundary layer correction [3, 4]. The off-design analysis of the resulting cascade was made by another recently developed inviscid, blade-to-blade, panel method code [5]. An integral boundary layer code [6] was used in conjunction with the panel analysis.

The final designs were built and tested by the Ames Research Center in 0.10-scale size. Tests were conducted over an inlet air angle range from -5 to $+60$ deg at the design inlet Mach number of about 0.2. Because of Reynolds number effects, all analysis calculations were repeated for comparison with the scale-model test results.

2 The Design Problem, Procedure and Predictions

A schematic of the junction of the 40 × 80 and 80 × 120 wind tunnel legs at the Ames Research Center is shown in Fig. 1. The axis of the cascade of guide vanes shown in this figure is staggered at an angle of 25 deg to the plane of the drive fans. The problem at hand was to find a set of vanes capable of receiving the flow from either leg without the need of moving parts. In other words, find a cascade with acceptable losses in a range of inlet air angle operation of about 60 deg and with the 25 deg stagger angle shown.

For the low subsonic speed involved (Mach number of 0.2) an airfoil with a very blunt leading edge appeared most appropriate to maximize the low loss range of inlet flow angle. NACA 65-series airfoils are relatively blunt and have been used successfully for many years to provide low losses over wide ranges of inlet flow angles and for inlet Mach numbers of 0.6 or less. In reviewing the 65-series cascade data [2], which is for a maximum thickness/chord of 0.10 and a maximum blade solidity of 1.50, it can be seen that less than half the required inlet air angle range of 60 deg was obtainable with low loss in a single row of airfoils.

The inverse design code has the capability of producing more arbitrary shapes with thick leading edges, if so desired. The technique has the additional advantage of being able to input the surface velocity distribution directly. This allows control of the velocity diffusion to eliminate the boundary layer separation, thus maximizing turning and minimizing loss. Also, the new design code in the subsonic regime provides solutions very quickly; thus a large number of differing shapes can be explored in a short time. The capability of designing with blade solidities of as high as 2.0 was another encouraging feature in its use. To obtain 60 deg of inlet air angle range of operation in nonaccelerating flow with little or no separation would obviously require relatively high solidities. Thus it was clear that the best chance of achieving the design objectives with a single row of airfoils was with the inverse design method.

Lewis No. 1 Design. Use of the inverse design code requires the input of a surface velocity distribution and three design parameters that control the solidity, the inlet Mach number, and the inlet air angle at the design point. In the search for a single cascade of fixed geometry capable of receiving the flow at both modes of operation, various design inlet air angles could be tried. Nevertheless, because low losses were desired in the 40 × 80 leg, the first design, designated Lewis No. 1, was optimized for the 40 × 80 leg with incidence angle (oncoming air angle relative to mean camber line at leading edge) near zero and with essentially zero turning. However, the vane shape was highly asymmetric because of the 25 deg of stagger angle of the cascade, which results in an inlet air angle of approximately -25 deg, relative to a normal to the cascade axis. All inlet and exit air angle values in this report are relative to the drive fan axes for a more convenient reference (Fig. 1).

The design surface Mach number distribution and blade geometry are shown in Fig. 2. The input surface Mach number distribution reflects the necessary asymmetry. This fixed geometry guide vane has a solidity of 1.64, and maximum thickness/chord of 0.209. It was designed assuming a Reynolds number of 6 million (full-scale operation).

In the design code the input surface velocity distribution is chosen to tailor the blade geometry according to the design philosophy. The maximum thickness to chord ratio, the leading edge curvature, and the trailing edge thickness can be controlled with this input speed distribution. In the case at hand, the main concern is range of operation and a thick blade with a blunt leading edge was designed. Continuous flow acceleration to a peak velocity near 55 percent chord on the upper surface was specified to provide more incidence angle range for off-design operation. This peak velocity was higher than that required for a fixed inlet flow angle and diffusion from this peak results in relatively higher losses. If only the 40 × 80 mode with 0 deg inlet air angle was to be considered, a much thinner body with less diffusion could be designed. The criteria in this case were not to optimize loss at the design point, but to have a wide range of operation with acceptable losses.

The panel method code was used to analyze the designed airfoil. This code was particularly well suited for the task, because it can readily accept arbitrary blade shapes and quickly solve the flow field at different off-design conditions. Compressible flow effects are approximated in this analysis code, but the method is accurate for the low-speed flow being considered in this design. Figure 3 shows the analysis results

of the Lewis No. 1 design in the 80 × 120 mode with an inlet air angle of 45 deg.

Due to Reynolds number differences, boundary layer calculations were performed for both the full-scale and 0.10-scale cases. The boundary layer was treated differently for these cases to reflect actual testing conditions.

In the full-scale wind tunnel, tests are often run on full-scale airplanes with engines running. Buildup of soot and other contaminants on guide vane surfaces is likely, and it is anticipated that these contaminants will cause tripping of the boundary layer to turbulent flow near the leading edge. Boundary layer calculations for the full-scale guide vanes were therefore forced turbulent near the leading edge. In some cases this tripping is probably unrealistic in regions of acceleration, but in such cases the calculations should provide conservative estimates of performance.

The boundary layer calculations for the 0.10-scale model vanes were made by letting a laminar boundary layer develop in a natural fashion from the leading edge. This approach was taken because it proved difficult to properly simulate the tripping in the scale model tests. Consequently, no tripping was attempted and the calculations were then conducted to compare with the test. In all cases, the steepness of the surface velocity gradients caused the laminar boundary layer to separate rather than pass through natural transition (zero skin friction predicted in Cohen-Reshotko laminar boundary layer method, see [6]). The boundary layer was reattached as turbulent using an initial momentum thickness equal to the value at separation (conservation of momentum), and an incompressible form factor of 1.4 (equilibrium layer). If the Reynolds number based on momentum thickness for the initial turbulent boundary layer using this method was less than 320, then the momentum thickness was increased to a value corresponding to 320 (Preston, 7).

The results of the calculations for inlet air angles of 0 and 45 deg are presented in Fig. 4 and are plotted as incompressible form factor against percent of chord. Only the turbulent portion of the calculation is plotted. Turbulent boundary layer separation is assumed to occur when the incompressible form factor exceeds 2.0.

Loss coefficients (total pressure loss over inlet dynamic head) were estimated based on the boundary layer calculations using the method of Speidel [8, 9], which incorporates a simple model for calculating loss with separated boundary layers. No loss calculations were attempted for inlet angles greater that 45 deg because at those very high angles the surface velocity gradients are high and turbulent boundary layer separation is likely over 20 to 25 percent of the blade surface. The loss model was not constructed for such extreme conditions and should not be relied on for exact predictions. It was calculated for the 45 deg inlet angle only to provide an approximate guide for comparing trends. Based on these calculations, losses estimated for the full-scale blading were 0.036 in the 40 × 80 mode, and 0.043 for the 45 deg inlet angle in the 80 × 120 mode. For the 0.10 scale model, the corresponding estimated losses were 0.038 and 0.097, respectively. Regardless of Reynolds number effects, the loss levels appeared acceptable for a fixed geometry design

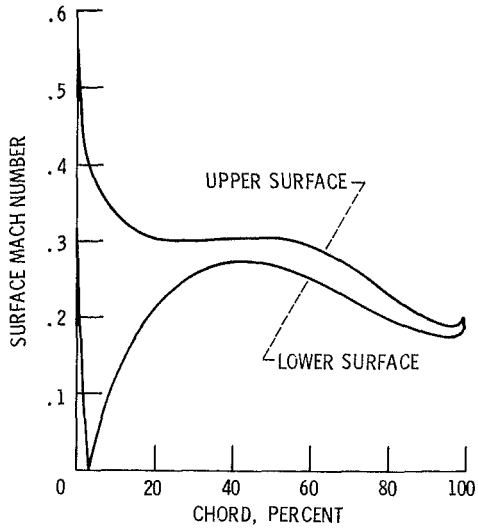

Fig. 3 Analysis of Lewis No. 1 design operating in 80 × 120 mode, inlet air angle of 45 deg

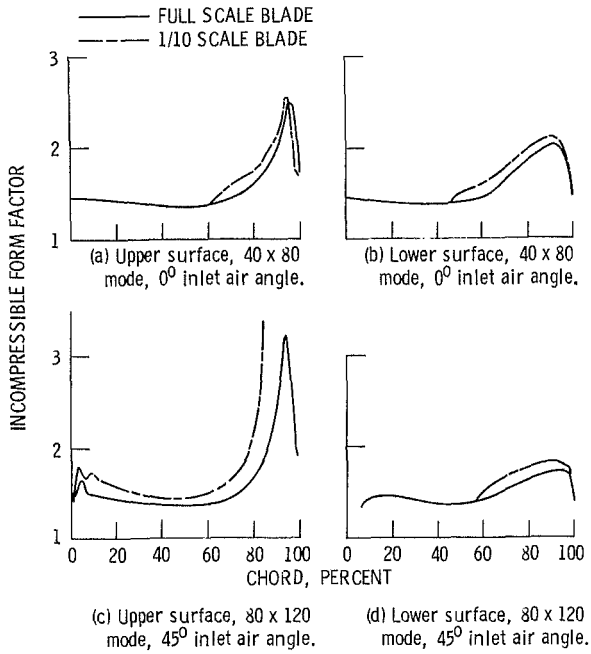

Fig. 4 Theoretical boundary layer performance for Lewis No. 1 in both operating modes

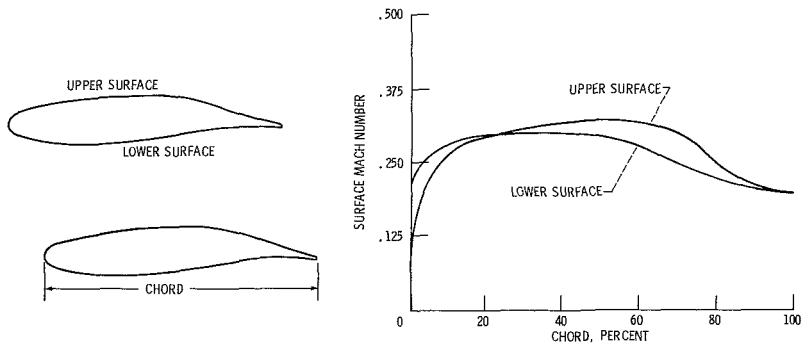

Fig. 5 Lewis No. 3 design

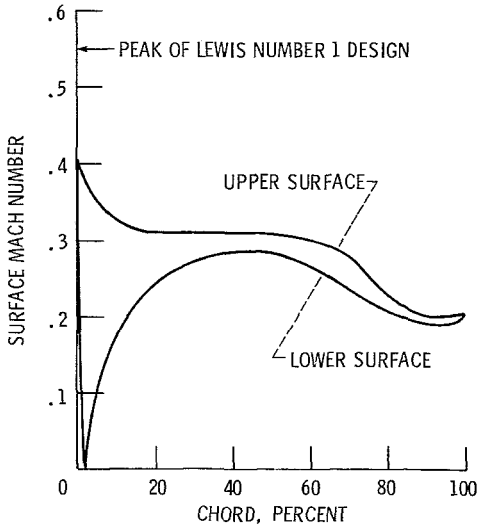

Fig. 6 Analysis of Lewis No. 3 design operatinig in 80 × 120 mode, inlet air angle of 45 deg

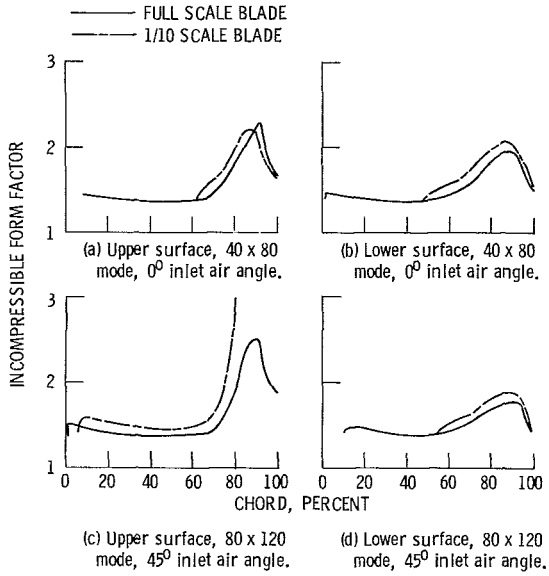

Fig. 7 Theoretical boundary layer performance for Lewis No. 3 in both operating modes

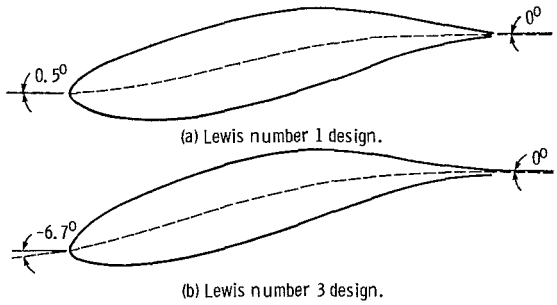

Fig. 8 Blade shapes and mean camber lines for two designs with edge angles relative to driven fan axes

operating over the required wide operating incidence angle range. Thus a hinged version of this guide vane known as the Lewis No. 2 design was not pursued.

Lewis No. 3 Design. Although the concept of a fixed geometry was proved viable in initial experimental tests of the Lewis No. 1 design at inlet air angles of 0 and 45 deg, its losses at 55 deg were unacceptable (see section 4). To increase the overall operating range, a compromised design point was pursued. This would result in some negative incidence angle of the flow in the 40 × 80 mode, but still acceptable losses, and correspondingly a lower incidence angle in the 80 × 120 mode. A few degrees of blade camber and a modest increase in solidity were deemed necessary for such a design.

To increase the range in this mode of operation, two options were available. The first one would be to increase the solidity of the cascade, with the subsequent reduction of the peak velocity near the leading edge on the upper surface. This option should keep nearly the same performance in the 40 × 80 mode. The second option available was to design the blade with both a higher solidity and a few degrees of turning in such a way that the flow would have some negative incidence in the 40 × 80 mode, but still acceptable losses, and correspondingly a lower incidence angle in the 80 × 120 mode.

The inverse design code was again used in this compromised design point approach to design a new blade following this second alternative. The new blade, the Lewis No. 3 design, is shown in Fig. 5. It has a solidity of 1.94 and a maximum thickness/chord of 0.19. At nominal conditions, the vane will receive the flow from the 40 × 80 leg with a negative incidence of 6.7 deg, and in the 80 × 120 mode it will receive it with 38 deg of positive incidence. This combined with the higher solidity was expected to increase the low loss range of operation in the 80 × 120 mode at the expense of some increase in losses in the 40 × 80 mode. The panel code analysis in the 80 × 120 mode with an inlet air angle of 45 deg is shown in Fig. 6. The reduction in the peak suction surface Mach number on the upper surface from the Lewis No. 1 design is indicated.

The reduction in peak upper surface Mach number is considered essential for stable, high inlet angle operation. The very steep velocity gradients at the leading edge of the Lewis No. 1 design (80 × 120 mode) present a distinct danger of completely stalled flow at high inlet angle. The calculated loss of 0.043 for the full-scale version of that blade assumes an unstalled condition, i.e., laminar separation and turbulent reattachment near the leading edge. Since, even with this assumption, the last 15 percent of the upper surface boundary layer is separated, the calculated loss of 0.043 should be viewed more as an estimate than an exact prediction. Clearly, using an integral boundary layer method to calculate loss for blades having incidence angles of 45 deg and substantial boundary layer separation, should only be done to compare similar designs and indicate trends.

Boundary layer calculations for the Lewis No. 3 blade are shown for inlet air angles of 0 and 45 deg in Fig. 7. Differences between Lewis No. 1 (Fig. 4) and Lewis No. 3 boundary layer behavior occurred principally on the upper surface. For the 40 × 80 mode the Lewis No. 3 upper surface boundary layer shows earlier separation. This is due to the more adverse pressure gradient that results from compromising the 40 × 80 design as previously discussed. A loss of 0.042 was calculated for the 0.10 scale (laminar boundary layer at leading edge); a loss of 0.042 was also calculated for the full-scale blade assuming a turbulent boundary layer beginning near the leading edge.

In the 80 × 120 mode at a 45 deg inlet air angle (Fig. 7(*c*) and (*d*)) losses of 0.093 and 0.052 were calculated for the 0.10-scale and full-scale blades, respectively. At inlet angles greater than 45 deg, the loss was increasingly controlled by the extent of a laminar separation bubble at the leading edge. It is not feasible to incorporate this quantitatively into the simple loss model used, so no loss estimates are made for inlet angles greater than 45 deg. A summary of these losses and the implications for the full-scale performance are presented, and will be discussed, in section 4.

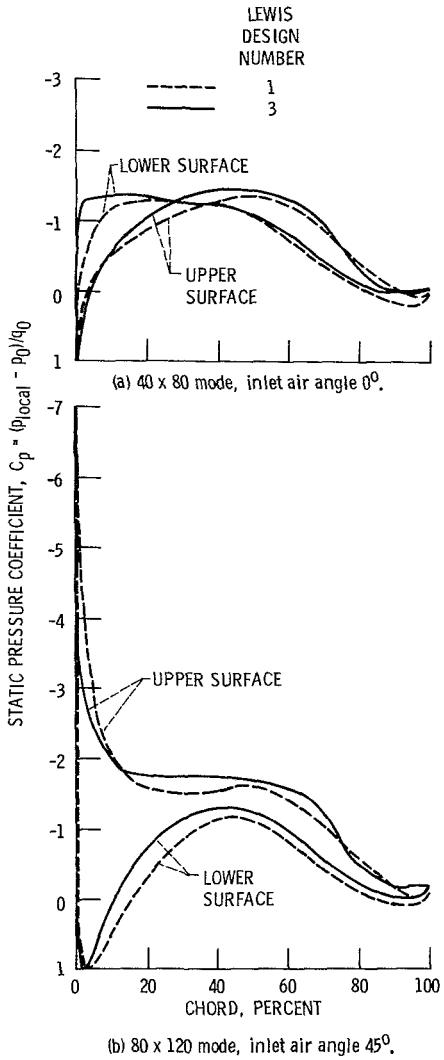

Fig. 9 Comparison of theoretical surface pressure distributions for Lewis No. 1 and No. 3 designs in both operating modes

In Fig. 8, the shapes for the Lewis No. 1 and Lewis No. 3 designs are shown along with their mean camber lines and their edge angles relative to the drive fan axes. The camber line for Lewis No. 1 is S-shaped with both ends aligned with the drive fan axes. Thus the incidence angle would be near 0 deg in the 40 × 80 operating mode, and near 45 deg in the 80 × 120 mode. The camber line for Lewis No. 3 differs from No. 1 mainly near the leading edge. Most of the upsweep to become aligned with the drive fan axes has been removed resulting in a nonoptimum incidence angle of −6.7 deg in the 40 × 80 mode and one near 38 deg in the 80 × 120 mode. The camber line at the trailing edge is aligned with the drive fan axes for both modes. In Fig. 9, the surface pressure distributions for both designs are compared in both modes of operation.

3 Test Facility, Models and Instrumentation

The experimental verification of the vane set design was conducted at and by the Ames Research Center (Norman et al. [10]). The test facility is an open-loop wind tunnel with rectangular cross section in which a cascade of 0.10-scale vanes with aspect ratio of 5 was tested. There was no tunnel wall boundary layer control and no tailboards to improve vane wake periodicity. A schematic of the test facility is shown in Fig. 10.

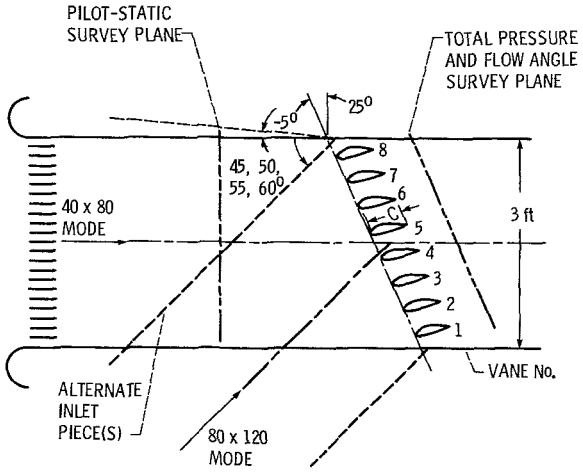

Fig. 10 Schematic of 0.1-scale test facility

The inlet flow angle into the cascade was set at seven different values (−5, 0, 5, 45, 50, 55, and 60 deg) by alternate inlet pieces. The cascade test section consisted of eight vanes plus the flat tunnel walls. Three vanes (nos. 4 to 6, Fig. 10) were instrumented with static pressure taps, 15 on the upper and 14 on the lower surface. Static pressure taps were also located on all four tunnel walls to verify that the vane set and not the tunnel walls were turning the flow.

Total pressure surveys were made upstream and downstream of the cascade (see Fig. 10). These surveys at midspan were used to calculate the pressure loss coefficient for the vane set. About 25 locations across each blade gap and all blade gaps were utilized to determine the average exit total pressure. More than half of these locations were within the blade wake. In addition, the flow angle at the cascade exit was measured to determine if the vane set over-or-under turned the flow.

It should be noted that all design calculations necessarily assumed two-dimensional and periodical flow. The purpose of the experimental tests, on the other hand, was to simulate conditions in the actual wind tunnel. Since no wall boundary layer control was desired, the degree to which flow approached two-dimensionality depended upon the aspect ratio. The aspect ratio is reasonably large, both for the scale-model and four the full-size tunnel.

The Lewis No. 1 and No. 3 vanes were designed at a Reynolds number of 6 million, which is the full-scale wind tunnel operational Reynolds number. The 0.10-scale test cascade operates with a Reynolds number of 600,000. In this context, the test results should be looked upon as a conservative estimate of the full-scale performance. Boundary layer calculations were performed at both Reynolds numbers and the calculations, in all cases, predict an improvement in the full-scale model with respect to the results for the 0.10-scale model.

Boundary layer transition and separation locations were determined by oil flow visualization techniques. Their interpretation can be very subjective, but they do provide a qualitative check on boundary layer calculation methods, and therefore on the design philosophy. Of more direct interest and relevance is the measure of blade section loss.

4 Experimental Results and Comparisons With Predictions

The 0.10-scale model experimental and theoretical results for the Lewis No. 1 design will be discussed first, followed by that for the Lewis No. 3 design. A summary of the losses in total pressure from the boundary layer analysis of Lewis No.

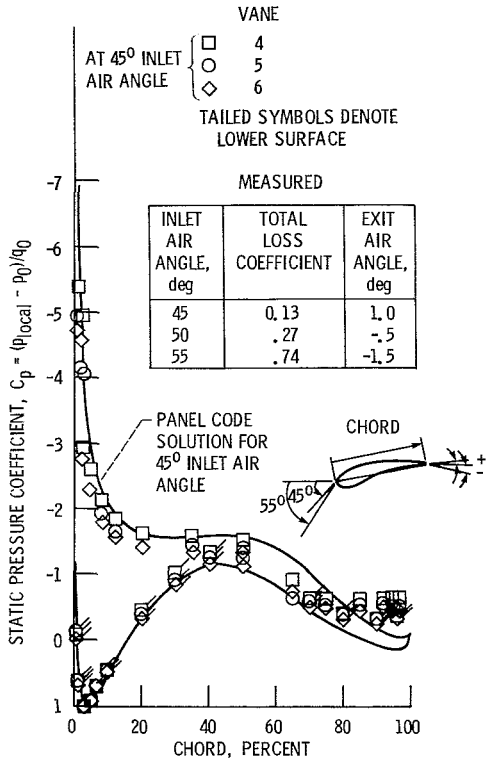

Fig. 11 Experimental surface pressure distributions compared to theoretical for Lewis No. 1 design in the 80 × 120 operating mode

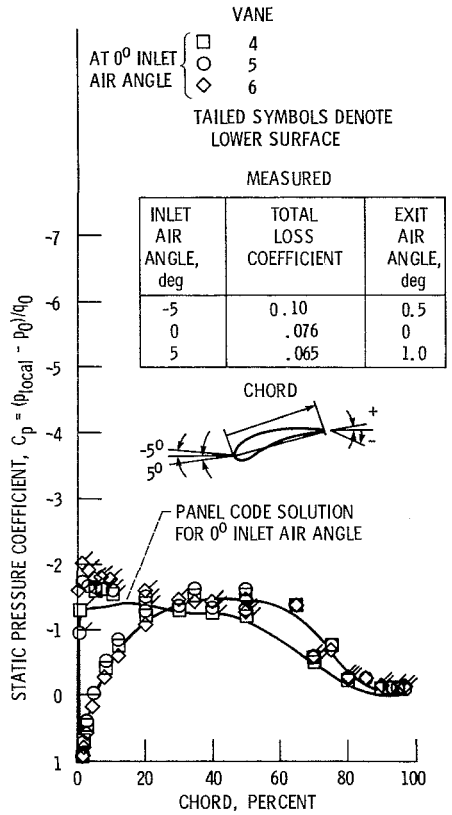

Fig. 12 Experimental surface pressure distributions compared to theoretical for Lewis No. 3 design in 40 × 80 operating mode

3 for both scale-model and full-size blades concludes this section. There, comparisons with the scale-model data are discussed along with implications for the full-scale performance.

Lewis No. 1 Design.

40 × 80 Mode. There were no surface pressure taps available for the initial tests of the Lewis No. 1 design. However at an inlet air angle of 0 deg, the measured loss coefficient was only 0.029, an excellent level. This compares favorably with a predicted value of 0.038 from Speidel's loss calculation method [8]. The measured exit air angle was −2 deg (overturned), which matches the design value.

80 × 120 Mode. The chordwise distribution of static pressure coefficient, C_p, is shown in Fig. 11 for an inlet air angle of 45 deg. Measurements on the upper and lower surfaces of three adjacent vanes are indicated as is the panel code prediction. There is a good match between the data and the prediction over the forward half-chord. The flattening out of the data on the upper surface over the aft one-third chord is indicative of boundary layer separation. This was in fact confirmed by oil flow visualization tests, which indicated that the turbulent boundary layer separated near 64 percent chord on the upper surface. There was no oil flow evidence of turbulent layer separation on the lower surface.

As tabulated in Fig. 11 for an inlet air angle of 45 deg, the measured total pressure loss coefficient was 0.13. This loss is higher than desired but acceptable in these scale-model (low Reynolds number) tests. The exit air angle was very good, within 1 deg of that desired.

Also tabulated in Fig. 11 are the loss coefficients and exit air angles for inlet air angles of 50 and 55 deg. The loss coefficient increased sharply, to 0.27 and 0.74 at these inlet angles. Such loss levels are not acceptable and the Lewis No. 3 design was developed specifically to improve on this off design performance at 50 and 55 deg. Oil flow visualization indicated the entire upper surface was in reverse flow at 55 deg.

Lewis No. 3 Design.

40 × 80 Mode. The C_p distribution is shown in Fig. 12 for an inlet air angle of 0 deg. There is a good match between the data and the prediction except over the forward 20 percent chord on the lower surface. Here there are increasingly more negative C_p values peaking near the leading edge. This is similar to what a more negative inlet air angle than 0 might show on the lower surface, but there is not a corresponding change in the C_p data on the upper surface. The effect of this unexplainable early peak was a higher than expected loss coefficient of 0.076. The oil flow visualization results and the C_p data do not indicate any turbulent boundary layer separation on either surface, and the oil flow on the lower surface did not show a change in character of the boundary layer.

The boundary layer calculation for the lower surface, however, predicted transition at 47 percent chord and possible turbulent separation at 81 percent chord, depending upon how conservatively the critical incompressible form factor is selected. But oil flow visualization showed no change in character of the boundary layer over the entire lower surface. This would be consistent with an early transition to a turbulent boundary layer due to the high negative pressure coefficient and a turbulent layer extending over the entire lower surface. An early transition to a turbulent boundary layer would produce a larger boundary layer thickness at the trailing edge and, consequently, a higher loss than anticipated and close to the level measured. Also tabulated in Fig. 12 is the performance at inlet air angles of −5 and 5 deg where the loss coefficients are 0.10 and 0.065, respectively.

80 × 120 Mode. The chordwise distribution of C_p is shown in Fig. 13 for an inlet air angle of 45 deg. Again there is a good match between the data and the prediction over the forward half-chord. There also is a modest delay in the flattening out of the data on the upper surface compared to

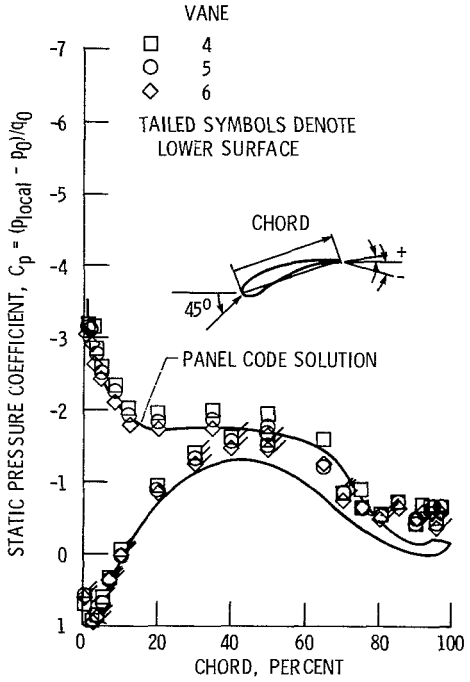

Fig. 13 Experimental surface pressure distributions compared to theoretical for Lewis No. 3 design in the 80 × 120 operating mode with inlet air angle of 45 deg. Total loss coefficient, 0.12; exit air angle, 1.5 deg

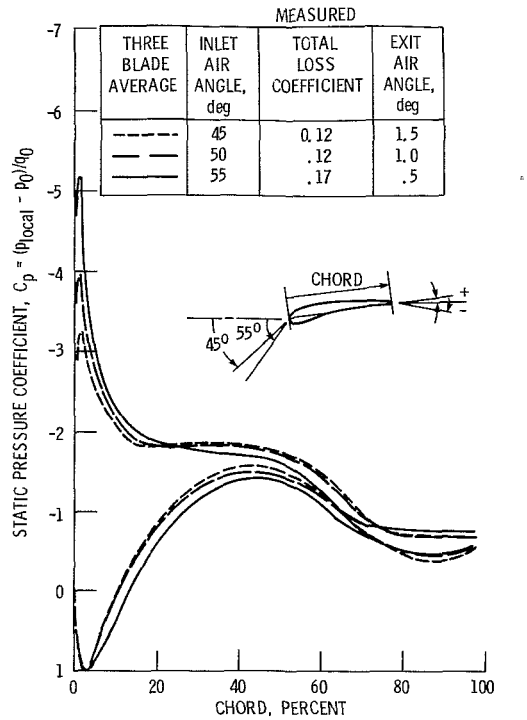

Fig. 14 Comparison of experimental surface pressure distributions for Lewis No. 3 design at three inlet air angles in the 80 × 120 operating mode

the Lewis No. 1 results (Fig. 11). This, too, was confirmed by oil flow visualization tests which indicated that the turbulent boundary layer separated near 69 percent chord on the upper surface, further aft than the Lewis No. 1 results. There was no oil flow evidence of turbulent layer separation on the lower surface.

As stated in Fig. 13 (45 deg inlet air angle), the measured loss coefficient was 0.12, about 10 percent less than for the Lewis No. 1 design. The change in C_p minimum from −5.4 for Lewis No. 1 (Fig. 11) to −3.2 for Lewis No. 3 (Fig. 13) has reduced the adverse pressure gradient on the upper surface. This in turn has decreased the boundary layer growth and reduced the losses. The exit air angle of 1.5 deg for Lewis No. 3 was also good.

The improved off-design response of the Lewis No. 3 design in the 80 × 120 mode is shown in Fig. 14. Here experimental C_p distributions (faired lines from discrete data points for clarity) for inlet air angles of 50 and 55 deg are shown along with the 45 deg value just discussed. Loss coefficients and exit air angles for these varied inlet angles are also tabulated.

The pressure gradient on the upper surface becomes more adverse as inlet air angle is increased. However, this effect is primarily in a region near the leading edge. There is little difference in C_p over the remaining chord between the 50 and 45 deg inlet angle cases and loss levels are the same, 0.12. This is less than half the loss for Lewis No. 1 at 50 deg (Fig. 11).

At 55 deg, the loss for Lewis No. 3 was 0.17 compared to 0.74 for Lewis No. 1. Although not shown on Fig. 14, the loss at 60 deg for Lewis No. 3 was 0.29. In all cases, the exit air angle was close to axial as desired. Oil flow visualization indicated turbulent layer separation near 70 percent chord for 45, 50, and 55 deg for Lewis No. 3. This is a reasonable agreement with the start of flattening of the upper surface C_p curves.

Summary of Losses in Total Pressure for Lewis No. 3 Design. There are three parts to Table 1 summarizing the Lewis No. 3 performance results as follows: (*a*) 0.10 scale experimental, (*b*) 0.10-scale theoretical, and (*c*) full-scale theoretical. The chordwise locations of transition from laminar to turbulent boundary layer and turbulent layer separation are given along with loss coefficients. This information is organized by operating mode, inlet flow angle, and blade surface.

40 × 80 Mode. There is a significant difference in the measured loss coefficient of 0.076 from that predicted of 0.042 for the 0.10-scale model. This is believed due to the premature transition on the lower surface near the leading edge instead of at the 47 percent chord location predicted. The premature transition is due directly to the difference in lower surface pressure distribution between measurement and calculation. The reason for the difference in pressure distribution is not evident. The predicted loss for the full-scale operation is the same as for the 0.10 scale model. This is coincidental since the assumed transition locations are considerably different, and the Reynolds numbers differ.

80 × 120 Mode. A comparison of the experimental with the theoretical results for the 0.10-scale model in the 80 × 120 mode indicates the experimental separation location on the upper surface for the turbulent layer is about 70 percent compared to theoretical values of 76 percent, irrespective of inlet air angle from 45 to 55 deg. Also, there is agreement that no turbulent layer separation occurs before the trailing edge on the lower surface. Corresponding comparisons of transition locations generally agree within about 10 percent. Prediction of loss coefficient with the Speidel method is not accurate when significant regions of boundary layer separation exist (incompressible form factor > 2.0). Such separation does occur for all operation in the 80 × 120 mode. However, to indicate the trend, a loss coefficient of 0.093 is presented for the minimum air angle of 45 deg in the 80 × 120 mode and is about 20 percent less than the measured value of 0.12.

Of greater significance is the predicted loss at this condition for the full-scale application. Here, because of the beneficial

Table 1 Summary of losses in total pressure for Lewis No. 3 design

			(a) 0.1 – scale experimental			(b) 0.1 – scale theoretical			(c) full-scale theoretical		
			Percent chord		Loss	Percent chord		Loss	Percent chord		Loss
Operating mode	Inlet flow angle, degs.	Blade surface	Trans.	Turb. sep.	coeff.	Trans.	Turb. sep.	coeff.	Trans.	Turb. sep.	coeff.
40 x 80	0	Upper	66	100	0.076	62	80	0.042	Forced	85	0.042
		Lower	Near L.E.	100		47	81		Near L.E.	100	
80 x 120	45	Upper	No visual	69	0.12	5	76	0.093		82	0.052
		Lower	59	100		53	100			100	
	50	Upper	1, small bubble	72	0.12	1	76	-----		82	-----
		Lower	59	100		53	100			100	
	55	Upper	1, 1/4-inch bubble	69	0.17	1	76	-----		82	-----
		Lower	37–59	100		53	100			100	

effects of a much thinner boundary layer with a tenfold increase in chord Reynolds number and the resulting movement of separation further aft (see Table 1(*c*)), the loss is reduced by almost a factor of 2. Note also this full-scale calculation is made with an early trip to turbulent flow which may not occur on both surfaces. Although the actual magnitude of the loss reduction due to scale may not be as high as 100 percent, the trend to a lower loss value in full scale is believed reliable. Thus the full-scale loss coefficient in the 80 × 120 mode for inlet angles of 45 and 50 deg is expected to be less than 0.10 and that at 55 deg less than 0.15.

5 Summary

A fixed geometry low-speed guide vane set has been designed with an inverse design code, analyzed with panel method and integral boundary layer codes and tested at 0.10 scale. The set is to operate in two different modes in the 40 × 80/80 × 120 foot NASA Ames wind tunnel which requires inlet air angles from about − 5 to +55 deg. In both modes, the exit flow is aligned with the axes of the drive fans.

The experimental tests were conducted on a cascade of 0.10-scale models with a chord-based Reynolds number of 600,000. Measured losses in total pressure (expressed as percent of inlet dynamic head) were 17 percent or less over a range of inlet air angles from −5 to +55 deg while the exit air angles remained within 1.5 deg of axial. Losses are expected to be even less in the full-scale application because of the positive influence of higher Reynolds number.

6 Acknowledgment

Many people, too numerous to mention, from two NASA laboratories contributed to the design and experimental evaluation of the new guide vanes. The authors wish to acknowledge the efforts of members of the Low-Speed Aircraft Research Branch and Low-Speed Wind Tunnel Investigations Branch from NASA Ames Research Center; and members of the Fan and Compressor Branch and Computational Fluid Mechanics Branch from NASA Lewis Research Center.

References

1 "NASA Doubling Size of Ames Wind Tunnel," *Aviation Week and Space Technology*, Vol. 114, No. 15, Apr. 13, 1981, p. 57.

2 Emery, J. C., et al., "Systematic Two-Dimensional Cascade Tests of NACA 65-Series Compressor Blades at Low Speeds," NACA TR-1368, 1958.

3 Sanz, J. M., "Design of Supercritical Cascades with High Solidity," *AIAA Journal*, Vol. 21, No. 9, Sept. 1983, pp. 1289–1293.

4 Sanz, J. M., "Improved Design of Subcritical and Supercritical Cascades Using Complex Characteristics and Boundary Layer Correction," NASA CR-168166, May 1983.

5 McFarland, E. R., "Solution of Plane Cascade Flow Using Improved Surface Singularity Methods," ASME JOURNAL OF ENGINEERING FOR POWER, Vol. 104, No. 3, July 1982, pp. 668–674.

6 McNally, W. D., "Fortran Program for Calculating Compressible Laminar and Turbulent Boundary Layers in Arbitrary Pressure Gradients," NASA TN D-5681, May 1970.

7 Preston, J. H., "The Minimum Reynolds Number for a Turbulent Boundary Layer and the Selection of a Transition Device," *Journal of Fluid Mechanics*, Vol. 3, Part 4, Jan. 1958, pp. 373–384.

8 Speidel, L., "Berechnung der Stomungsverluste von ungestaffelten ebenen Schaufelgittern," *Ingenieur-Archiv*, Vol. 22, 1954, pp. 295–322.

9 Sanger, N. L., "Two-Dimensional Analytical and Experimental Performance Comparison for a Compressor Stator Section with D-Factor of 0.47," NASA TN D-7425, Oct. 1973.

10 Norman, T. R., Horne, W. C., and Hall, L. P., "The Aerodynamic Performance of Several Guide Vane Cascades for Internal Flow Systems," Proposed NASA TM, 1984.

Axial Compressor Stator Aerodynamics

H. D. Joslyn

R. P. Dring

United Technologies Research Center,
East Hartford, Conn. 06108

Axisymmetric, through-flow calculations, currently the "backbone" of most multistage turbomachinery design systems, are being pushed to their limit. This is due to the difference between the complex, three-dimensional flows that actually occur in turbomachinery and the two-dimensional flow assumed in this type of analysis. To foster the development of design analyses that account more accurately for these three-dimensional effects, there is a need for detailed flow field data in a multistage environment. This paper presents a survey of the initial results from a detailed experimental study of the aerodynamics of the second stage of a large scale, two-stage axial compressor. Data were acquired over a range of flow coefficients. The data presented here are for the second stator and include airfoil and endwall flow visualization, and radial-circumferential traverse measurements presented in the form of fullspan contour plots of total pressure. Also presented are the spanwise distributions of total and static pressures, axial velocity, air angles, and blockage. The effect of increased loading on the growth of the hub corner stall and its impact on these parameters is discussed.

Introduction

Although through-flow analyses have been the foundation of compressor design for many years, it has not been possible to make a detailed comparison of computed results with a benchmark data base. The reason for this situation is the lack of a data base for multistage compressors that can provide measured values for all of the input parameters required by the calculation [1]. In addition to mass flow and rotational speed, the input data must include a row by row description of the spanwise distributions of total pressure loss, deviation, and blockage (or their equivalent). With this input, detailed comparisons could be made between the measured and computed velocity triangles and the total and static pressures and temperatures.

Since 1977 the United Technologies Research Center Large Scale Rotating Rig (LSRR) has been committed to providing such a data base for a variety of axial compressor configurations. To date, these have included an isolated rotor with thin and thick inlet boundary layers [2–6], and most recently a two-stage compressor where detailed data have been acquired throughout in the second stage. A comparison of the flow over the two isolated rotor configurations and the second stage rotor of the two-stage model has been presented in [7]. Although data were acquired over a range of flow coefficients, this comparison was limited to the nominal design flow coefficient for each rotor. As a continuation of this effort, the present paper provides a detailed description of the flow over the second stage stator of the two-stage compressor. The description includes data taken at three flow coefficients: a high flow case ($\phi = 0.55$), the nominal design flow case ($\phi = 0.51$), and a near stall case ($\phi = 0.45$). The data presented include airfoil and endwall surface flow visualization, and fullspan radial-circumferential traverse measurements of the total and static pressures and the flow yaw and pitch angles. The data were used to calculate the spanwise distribution of blockage according to a definition suggested in the earlier papers on the rotor data [7, 8].

The stator data presented support the conclusions made earlier, based on the rotor data, that corner stall is the dominant endwall mechanism influencing total pressure loss, deviation, blockage, and that the endwall boundary layers and secondary flow are of lesser importance. Of particular significance is the fact that at near stall conditions ($\phi = 0.45$) the stator hub corner stall caused a local blockage of 40 percent and through this it had a major influence on the spanwise distribution of static pressure at the stator exit traverse plane.

Experimental Facility and Instrumentation

The United Technologies Research Center Large Scale Rotating Rig (LSRR) is 5 ft (1.52 m) in diameter and can run at speeds up to 900 rpm. The inlet flow is from ambient air and the flow through the facility is essentially incompressible. More detailed descriptions of the rig and its data acquisition system are available in [3, 9]. The airfoil geometry and the aerodynamic test conditions for the two-stage compressor second rotor and stator are summarized in Table 1. The second stage stator was shrouded at both the hub and the tip and had a 4 in. (0.102 m) chord. Its inlet conditions were determined by the flow leaving the second stage rotor. Data were acquired at flow coefficients of 0.55 (high flow), 0.51 (design flow), and 0.45 (near stall). Rotating stall occurred at

Contributed by the Gas Turbine Division of THE AMERICAN SOCIETY OF MECHANICAL ENGINEERS and presented at the 29th International Gas Turbine Conference and Exhibit, Amsterdam, The Netherlands, June 4–7, 1984. Manuscript received at ASME Headquarters, January 6, 1984. Paper No. 84-GT-90.

Table 1 Second stage geometry and design flow conditions

Tip diameter	5 ft (1.52 m)	
Hub/tip ratio	0.8	
C_x	78 (f/s) (24 m/s)	
N	650 (rpm)	
ϕ	0.51	
$(\Delta X_{RS}/B_x)$*	0.50	
Airfoil row	Rotor	Stator
Number of airfoils	44	44
Span/B	1.50	1.50
(τ_m/B)*	0.96	0.96
(Tip Clearance)/B	0.039	N/A
Stagger (deg.)*	47.1^0	55.8^0
Camber (deg.)*	35.3^0	40.5^0
Re (W_x or C_x, B)*	3.0×10^5	2.6×10^5
$(\Delta X_{RC}/B_x)$*	0.25	0.18

*at midspan

$\phi = 0.44$. These flow coefficients were based on the area average axial velocity (C_x) and the wheel speed at midspan (U_m).

The technique used to obtain the airfoil and endwall surface flow visualization has been demonstrated and discussed previously in [2–5, 7, 9]. Briefly, it consisted of seeping a small amount of ammonia out of the airfoil and endwall surface static pressure taps. The ammonia caused a dark blue streak line to form on Ozalid paper attached to the surfaces downstream of the pressure taps.

The rotating frame radial-circumferential traverse system, described in [3], was used to obtain the rotor exit (stator inlet) data. The device can traverse circumferentially over two airfoil pitches and radially from hub to tip. For the present program, data were acquired from 5 percent span to 97 percent span. The traverse plane was located midway between the rotor trailing edge and the stator leading edge. This location (25 percent axial chord aft of the rotor trailing edge) was chosen because of mechanical constraints, i.e., the two-stage rotor-stator axial gap.

Stator exit radial-circumferential traverse data were acquired in the stationary frame at a plane 18 percent axial chord downstream of the stator trailing edge. This was accomplished with the stationary frame radial-circumferential traverse system described in [10]. Probes were mounted in the traverse device located external to the rig. They entered the flow path through sealed slots in the casing and could be traversed circumferentially over two airfoil pitches and radially from hub to tip (5 percent to 97.5 percent span).

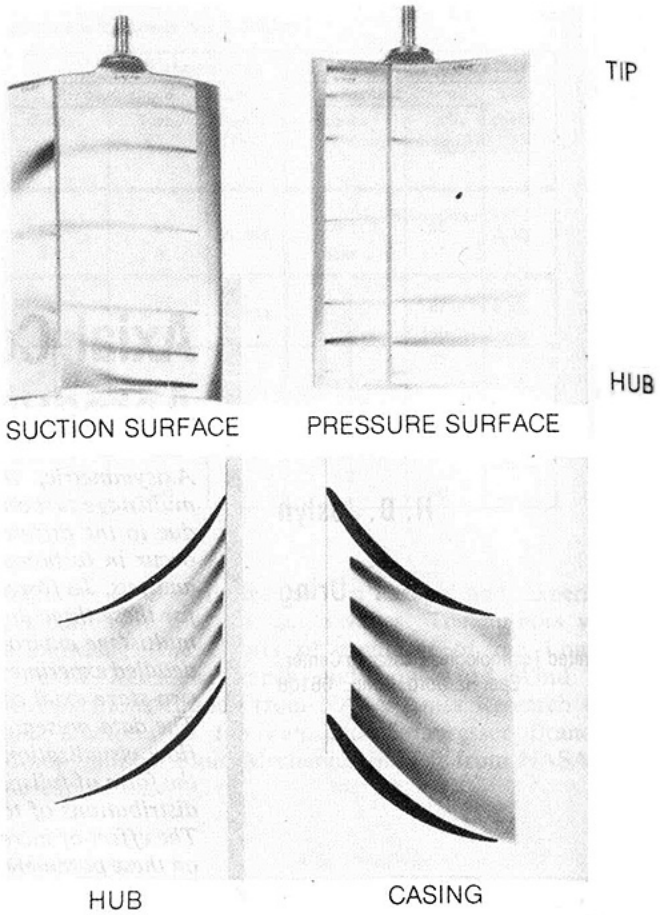

Fig. 1 Second stage stator flow visualization, $\phi = 0.55$

The traverse probes used in both the relative frame and absolute frame were United Sensor five hole pneumatic probes (USC-F-152). These probes were modified to include a cobra probe for traversing very close to the hub in the relative frame and close to the tip in the absolute frame. The probe tip diameter (D_p) was small relative to the stator and rotor midspan pitch ($D_p/\tau_m = 0.024$). A detailed description of this type of probe and its calibration can be found in [2, 4]. Data were acquired at approximately 20 radial locations and at typically 50 circumferential locations per plane of data. Measurement locations were concentrated at the hub and tip endwall regions and in the airfoil wakes. All pressure

Nomenclature

B = airfoil true chord
B_x = airfoil axial chord
C = absolute flow speed
C_p = pressure coefficient $(P\text{-}P_{TO})/Q_{U_m}$
C_x = axial component of flow velocity
$\bar{K}$ = blockage factor
N = rotational speed
P = pressure
Q_{U_m} = dynamic pressure based on midspan wheel speed: $(1/2\ \rho\ U_m^2)$
U_m = wheel speed at midspan
X = axial distance
α^* = stator airfoil metal angle
α = yaw angle (from axial, positive in direction of rotor rotation)
γ = pitch angle (from axial, positive toward tip)
ϕ = flow coefficient: C_x/U_m
ρ = fluid density
τ = pitch or gap
ΔX_{RS} = axial gap between second rotor and second stator
ΔX_{RC} = axial gap between airfoil trailing edge and traverse plane

Subscripts

h = hub
m = midspan
S = static
T = total
0 = compressor inlet
1 = stator inlet
2 = stator exit

Superscripts

a = area average (pitchwise)
m = mass average (pitchwise)
$-$ = pitchwise average

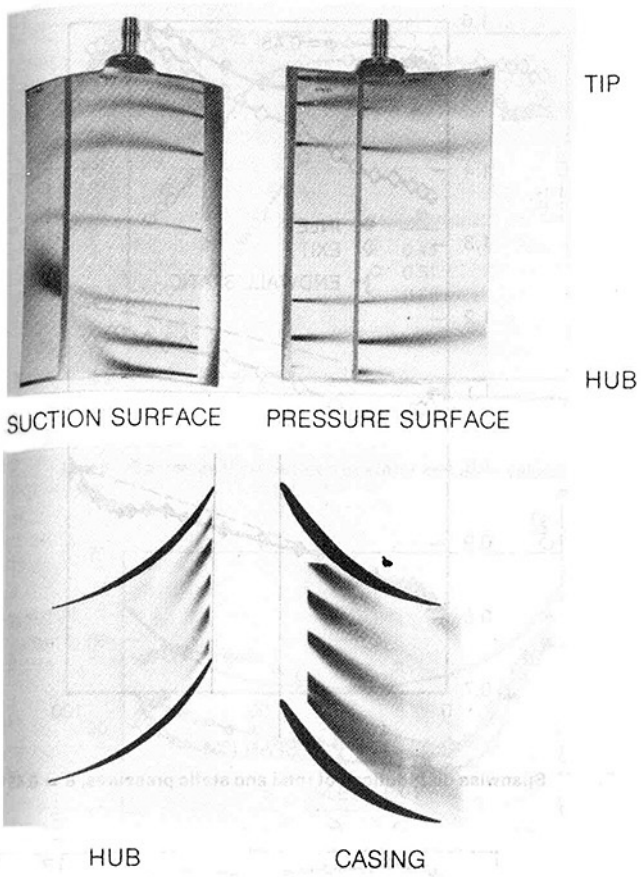

Fig. 2 Second stage stator flow visualization, $\phi = 0.51$

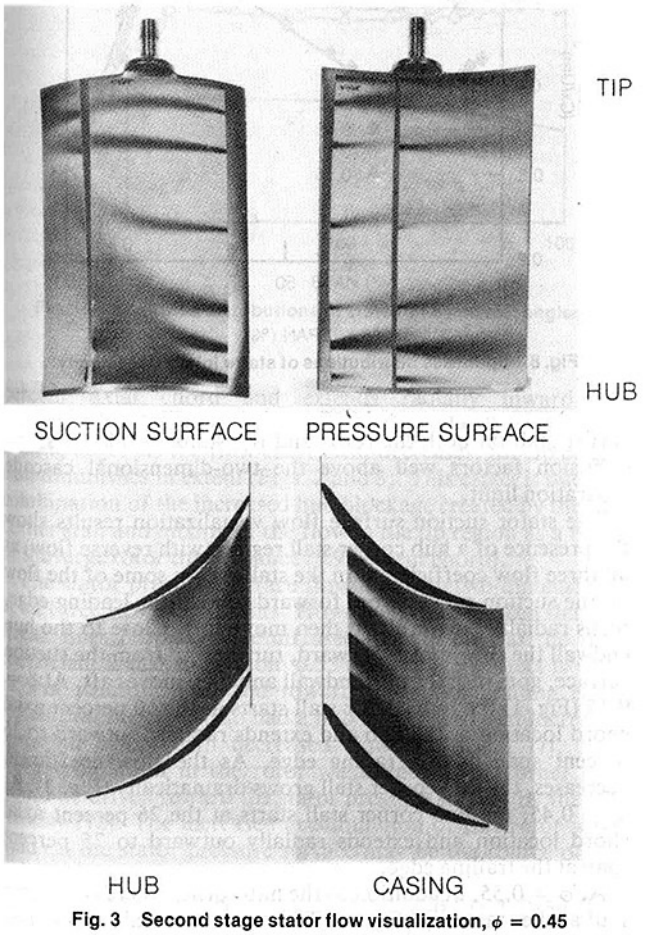

Fig. 3 Second stage stator flow visualization, $\phi = 0.45$

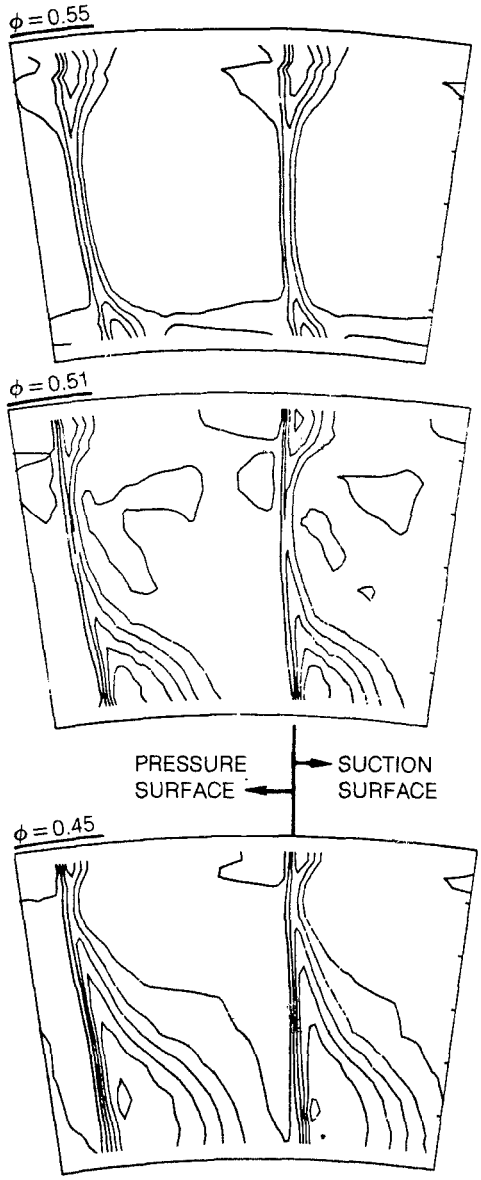

Fig. 4 Second state stator exit total pressure contours, $\Delta CPT = 0.1$

measurements were referenced to the inlet stationary frame total pressure at midspan. All flow angles were measured from axial.

The accuracy of the pressure measurement system was ± 2 percent of reading. Since all pressure measurements were referenced to the midspan absolute inlet total pressure the uncertainty in C_p is ± 2 percent. The uncertainty in the flow angles is ± 1 degree. During traverse testing the flow coefficient was not allowed to vary by more than $\pm 1/2$ percent.

Results

Surface Flow Visualization. The first indication of the influence of corner stall on the three dimensionality of the stator flow field is seen in the flow visualization results obtained at the three flow coefficients (Figs. 1, 2, and 3). Results were obtained on the suction and pressure surfaces of the second stator as well as on the hub and outer casing (tip) endwalls.

Based purely on two-dimensional diffusion factor considerations [11], one would not expect the stator to be stalled (even at the near stall flow coefficient) except for very close to

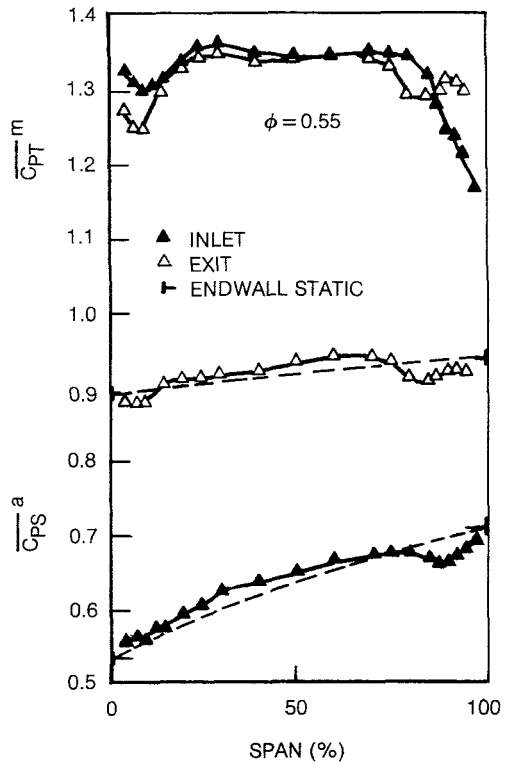

Fig. 5 Spanwise distributions of total and static pressures, $\phi = 0.55$

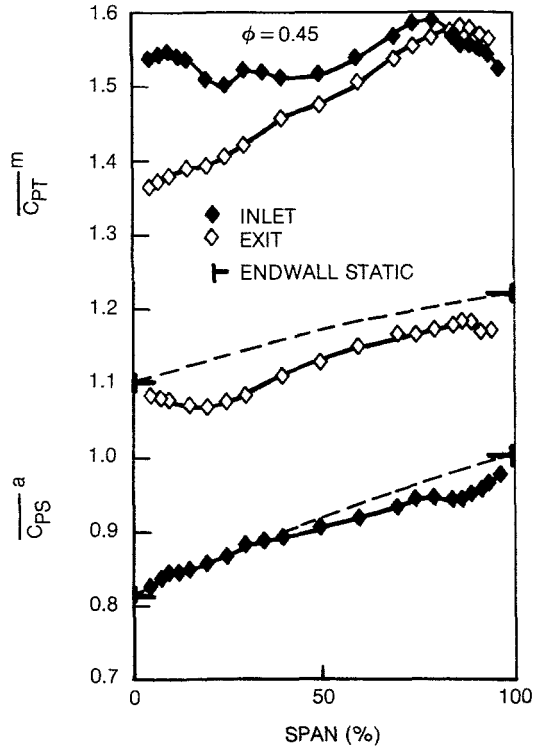

Fig. 7 Spanwise distributions of total and static pressures, $\phi = 0.45$

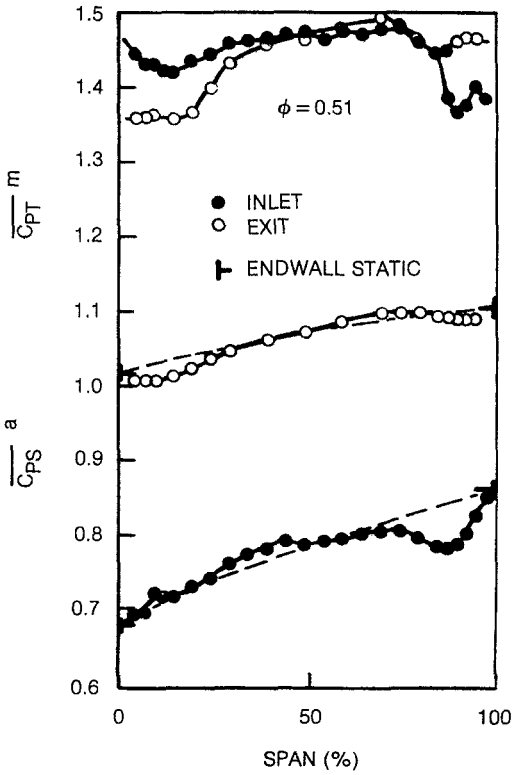

Fig. 6 Spanwise distributions of total and static pressures, $\phi = 0.51$

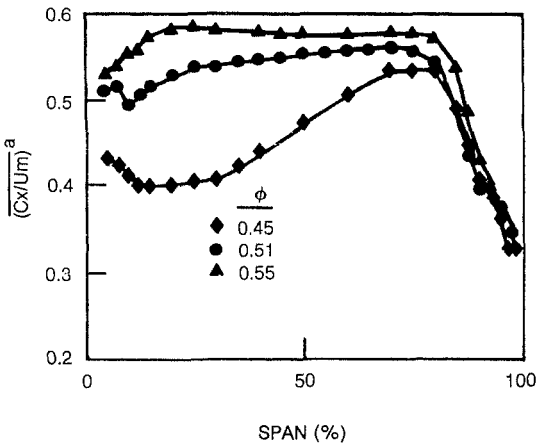

Fig. 8 Spanwise distributions of stator inlet axial velocity

the endwalls. The presence of a corner stall on the rotor has been previously reported [7] for the design flow coefficient ($\phi = 0.51$). It will be shown below that the rotor hub corner stall is responsible for increased incidence and hence loading on the stator. This leads to severe separation on the stator suction surface-hub endwall region. The combined effects of the hub corner stall on both the rotor and the stator results in stator diffusion factors well above the two-dimensional cascade separation limit.

The stator suction surface flow visualization results show the presence of a hub corner stall region (with reverse flow) at all three flow coefficients. In the stall region some of the flow on the suction surface goes forward toward the leading edge, turns radially outward and then moves aft. Close to the hub endwall the flow moves forward, turns away from the suction surface, goes into the hub endwall and then moves aft. At $\phi = 0.55$ (Fig. 1) the hub corner stall starts at the 60 percent axial chord location at the hub and extends radially outward to 36 percent span at the trailing edge. As the flow coefficient decreases, the hub corner stall grows dramatically (Fig. 3). At $\phi = 0.45$, the hub corner stall starts at the 26 percent axial chord location and extends radially outward to 75 percent span at the trailing edge.

At $\phi = 0.55$, in addition to the hub corner, there is a corner stall at the stator tip (Fig. 1). This tip corner stall starts at 74

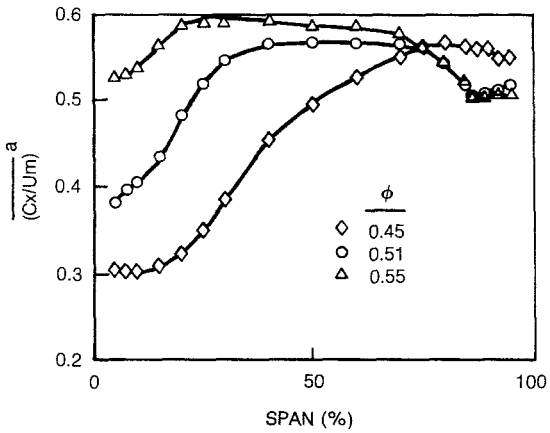

Fig. 9 Spanwise distributions of stator exit axial velocity

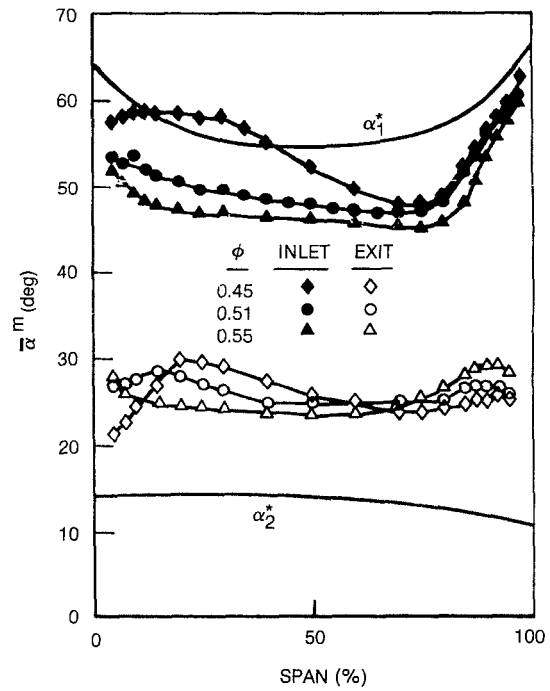

Fig. 10 Spanwise distributions of stator inlet and exit angles

percent axial chord and extends radially inward approximately 30 percent span from the tip endwall at the stator trailing edge. As the flow coefficient decreases, the tip corner stall diminishes in extent (Figs. 2 and 3). This effect is due to a combination of the increased hub blockage created by the hub corner stall and mixing of the flow in the tip region as a result of the large rotor tip clearance (3.9 percent chord).

The stator pressure surface flow is nearly two-dimensional at all three flow coefficients. However, it can be seen that the streak lines become more diffused (spread out) as the flow coefficient is decreased from 0.55 to 0.45. This effect is most evident near the hub and toward the stator trailing edge. Recall that the rotor also had a hub corner stall that increased in radial extent with decreased flow coefficient [7]. Low momentum fluid in the rotor wake due to the corner stall would be driven toward the stator pressure surface by the slip velocity [12]. The increased accumulation of this rotor wake fluid on the stator pressure surface may be the source of the increased spreading of the streak lines there.

At all three flow coefficients, the hub and tip endwall flow visualization results show no significant evidence of inlet boundary layer skewing or cross flow toward the suction surface due to secondary flow. The corner stall, however, does force the endwall flow away from the suction surface as seen in the flow visualization on the hub endwall and on tip endwall near the trailing edge. In general, there is very little turning toward the suction surface indicated by the endwall flow visualization. On the tip endwall, there is a slight deflection toward the pressure surface as the flow proceeds through the passage.

In summary, the dominant feature seen in the stator flow visualization is the suction surface-hub corner stall. As the flow coefficient is decreased, the hub corner stall region grows and the tip corner stall region contracts. The hub and tip endwall flow is dominated by the blockage due to corner stall as opposed to skew at the inlet or secondary flow toward the suction surface in the passage. On the hub endwall there is no significant evidence of turning toward the suction surface due to secondary flow. In general, the endwall flow is displaced slightly toward the pressure surface. The impact of corner stall on the total pressure loss, deviation, and blockage will be seen below in the radial-circumferential traverse results.

Total Pressure Contour Results. Detailed radial-circumferential measurements of the total and static pressures and the flow direction (yaw and pitch) were made at the stator inlet plane (25 percent axial chord ahead of the stator leading edge) and at the stator exit plane (18 percent axial chord aft of the stator trailing edge). The total pressure was measured relative to the rig inlet stationary frame total pressure at midspan. This pressure difference has been normalized with a dynamic head based on midspan wheel speed. Contour plots of the total pressure results at the stator exit plane are shown in Fig. 4 for each of the three flow coefficients. The periodicity of the flow over two stator pitches is excellent. There is a lack of any significant boundary layer development on either the hub or tip endwall and the total pressure is relatively constant outside of the wake and corner stall regions.

At $\phi = 0.55$, the low total pressure regions are confined to the wakes and to the hub and tip regions adjacent to the suction surface. These low total pressure regions in the airfoil wakes near the hub and tip are the result of corner stall (Fig. 1). Lowering the flow coefficient to 0.45 results in a spanwise and pitchwise growth of the hub corner stall region. The low total pressure region extends radially to approximately 70 percent span at the trailing edge and gapwise to nearly a full pitch near the hub. The size of the low total pressure region at the tip is greatly reduced as the flow coefficient is lowered. These variations in spanwise extent are consistent with the flow visualization results (Figs. 1 through 3).

In summary, as with the flow visualization results, the stator exit total pressure contours point to the corner stall as the major mechanism affecting the flow in the endwall regions of the stator flow field.

Circumferentially Averaged Results. Radial-circumferential traverse results that have been circumferentially averaged include the stator inlet and exit absolute total and static pressures, axial velocity, and yaw angle (Figs. 5 through 10). Except for the static pressure and axial velocity data which were area averaged, all the traverse results presented were mass averaged over two airfoil pitches. The stator inlet data, shown by the solid symbols, were calculated from measurements acquired in the rotating frame of reference. This was done to minimize unsteady effects due to the passing of rotor wakes. In general, however, results obtained from measured stationary frame data and stationary frame results calculated from rotating frame data at this axial station were in excellent agreement. The calculation procedure was as follows. From the flow properties measured at each radial-

circumferential location in the rotating frame, the corresponding stationary frame properties were calculated. At each radial position the resulting circumferential distributions were then averaged over two pitches to produce spanwise distributions of stator inlet properties. The open symbols (Figs. 5 through 10) denote the stator exit data which was acquired in the stationary frame of reference.

The circumferentially averaged total and static pressure results for all three flow coefficients are presented in Figs. 5, 6, and 7. The differences between the inlet (solid symbols) and exit (open symbols) total pressure distributions represent the stator loss. At $\phi = 0.55$ (Fig. 5), high loss regions are seen to be located near the hub and near the tip (75 to 87 percent span). These loss regions are due primarily to the hub and tip corner stall. In the region between 87 percent span and the tip, the loss appears to be negative. This apparent negative loss (total pressure rise) is due to the radial redistribution through the stator passage of the stator inlet total pressure profile. The radial redistribution is driven by the rotor tip leakage flow that resulted from the relatively large rotor tip clearance [7].

Lowering the flow coefficient results in an increase in the magnitude and radial extent of the hub endwall loss region (Figs. 6 and 7). At the 0.51 flow coefficient (Fig. 6) the hub loss region extends to nearly 35 percent span. This is consistent with the flow visualization results (Fig. 2) and total pressure contour results (Fig. 4) and is due to the growth of the stator hub corner stall. In the region between 50 and 85 percent span, the stator loss is slightly negative (1.4 percent). A region of increased apparent negative loss also occurs between 85 and 100 percent span. At $\phi = 0.45$ (Fig. 7), the hub loss has grown significantly as one would have expected from the flow visualization and total pressure contour results. Here again, however, between 85 percent span and the tip, there is a region of apparent negative loss. At the lower coefficients, $\phi = 0.51$ and 0.45, the region of apparent negative loss near the tip results from the redistribution of the stator inlet total pressure profile. In addition to mixing due to the rotor tip leakage flow, relatively small radial shifts of the axisymmetric stream surfaces between the stator inlet and exit and increased radial flows in the stator wakes also contribute to the redistribution of the inlet total pressure profile and result in regions of locally negative loss.

In summary, the stator hub corner stall is seen to be the major source of stator loss at all three flow coefficients. Decreased flow coefficient results in hub corner stall growth and an increase in loss. Regions of apparent negative loss are a result of the radial redistribution of the stator inlet total pressure profile due to the mixing produced by the relatively large rotor tip clearance, radial shifts in axisymmetric stream surfaces, and increased radial flows in the stator wakes at the lower flow coefficients.

The stator inlet and exit static pressure traverse results are also shown in Figs. 5, 6, and 7 along with the measured flow path hub and tip endwall static pressures. These flow path endwall static pressures were obtained by averaging 21 measured static pressures evenly distributed on both the hub and tip endwalls over two stator pitches with 10 additional static pressures evenly distributed around the model annulus at both the hub and tip endwalls. In general, the traverse results extrapolate well to the measured hub and tip endwall static pressures. Also shown by the dashed lines are the spanwise static pressure distributions calculated by assuming a free-vortex variation between the hub and tip values.

At all three flow coefficients, the traverse data display local maxima and minima and in some cases significant offsets in level that would not be expected based solely on the endwall static pressures and the interpolated free-vortex distributions. The depression in measured stator inlet static pressure seen in the outermost 20 percent span at all three flow coefficients is due to the high loss and blockage associated with the rotor tip leakage. This effect was seen earlier in the isolated rotor results of [2–6]. The most dramatic difference between the interpolated free-vortex distributions and the measured traverse distributions occurs at the stator exit at $\phi = 0.45$ where the entire spanwise distribution of measured stator exit static pressure is significantly below the free-vortex distribution. This is due to the increased loss and blockage associated with the stator hub corner stall.

The blockage due to the stator hub corner stall also had an impact on the stator exit hub to tip endwall static pressure difference. As the flow coefficient was decreased from 0.55 to 0.45 the difference between hub and tip endwall static pressure increased by a factor of nearly two and one-half. This increase in hub to tip static pressure difference resulted in a significant change in the radial inflow observed in the stator wake traverse data. At the stator exit at midspan, the ratio of the maximum radial (inflow) velocity to the axial velocity in the stator wake increased from 0.04 at $\phi = 0.55$ to 0.22 at $\phi = 0.45$.

In summary, regions of low static pressure appear to be associated with regions of high loss and blockage, e.g., at the rotor tip and stator hub. Blockage due to the stator hub corner stall has a major impact on the hub to tip static pressure difference and on the radial flows in the stator wakes. Finally, using endwall static pressures to infer spanwise distributions of static pressure can lead to significant errors in the deduced velocity triangles due to the local blockage effects.

Area averaged stator inlet and exit axial velocity profiles are presented in Figs. 8 and 9. At all three flow coefficients, the inlet axial velocity at the outermost 15 percent span is low due to the loss and blockage caused by the relatively large rotor tip clearance [7]. As the flow passes through the stator, the axial velocity defect at the tip is filled in by radial mixing. It is this mixing process that primarily accounts for the increase in stator exit total pressure and the apparent negative loss at the tip (Figs. 5, 6, and 7).

In both the stator inlet and exit axial velocity profiles, the effect of hub corner stall on the rotor and on the stator is evident to varying degrees and is dependent upon the flow coefficient. The rotor hub corner stall results in low axial velocities in the hub region at the stator inlet (Fig. 8), whereas the stator hub corner stall results in even lower axial velocities in the hub region at the stator exit (Fig. 9). At $\phi = 0.55$, the stator inlet and exit axial velocity profiles are nearly identical except at the tip region. This difference at the tip is due to the large rotor tip clearance and the resultant mixing due to the rotor tip leakage flow. Decreasing the flow coefficient results in a significant radial displacement of flow away from the stator hub. This is due to the growth of the stator hub corner stall and is evident in the difference between the stator inlet and exit axial velocity profiles at $\phi = 0.51$, and 0.45 (Figs. 8 and 9). By assuming the flow through the stator passage stayed within axisymmetric stream surfaces, the maximum radial displacement between the inlet and exit stream surfaces was calculated from the traverse data to be 7 percent of the span at $\phi = 0.45$. The maximum local stream surface radial displacement at $\phi = 0.51$ and 0.55 was calculated to be 4 percent and 2.5 percent, respectively.

The fullspan area average of the stator inlet and exit axial velocity distributions (Figs. 8 and 9) calculated from the traverse data agree to within a standard deviation of 1.7 percent with the nominal model inlet test flow coefficients ($\phi = 0.55, 0.51, 0.45$). This indicates a good overall continuity check on the data and, along with the measured wall static pressures, indicates a high level of experimental accuracy on all measured pressures and flow angles.

The second stator inlet and exit metal angles (α^*) and the mass averaged inlet and exit yaw angles (α^m) are presented in Fig. 10. The mass averaged stationary frame stator inlet yaw

angles were calculated from the rotating frame traverse measurements made at the rotor exit as discussed previously. The mass averaged exit yaw angles were calculated from the stationary frame traverse measurements made at the stator exit. Mass averaging reduces the influence of separated flow and the low speed, nearly axial flow that results from the hub corner stall. From Fig. 10, the variation in incidence and deviation with flow coefficient can be seen.

The stator is basically operating at negative incidence at all three flow coefficients. In general, as the flow coefficient is reduced, the inlet flow angle increases over the entire span. The increase in the midspan region is due to the opposing influences of the reduced flow coefficient and the increased rotor deviation, the former being dominant. The increased stator inlet angle near the hub region at $\phi = 0.51$ and 0.45 is due primarily to the rotor hub corner stall. At the near stall flow coefficient ($\phi = 0.45$) the effect of the rotor hub corner stall on inlet angle is more pronounced than at the design flow coefficient. This is due to the rapid growth of the rotor hub corner stall as the flow coefficient was reduced to $\phi = 0.45$. The blockage associated with this hub corner stall resulted in a significant reduction in the rotor exit (stator inlet) axial velocity in the hub region as seen in Fig. 8. The rotor deviation also increased nearly five degrees. The opposing influences of reduced rotor exit axial velocity and increased rotor deviation at the near stall flow coefficient result in the large increase in stator inlet angle seen in Fig. 10. Of the two factors contributing to the change in stator inlet angle at the hub region, the positive contribution due to reduced axial velocity has a greater influence than the negative contribution due to increased rotor deviation. The increase in stator inlet angle at $\phi = 0.45$ in turn increases the stator loading and triggers the rapid growth of the stator hub corner stall as seen in the flow visualization and total pressure contour data results (Figs. 3 and 4).

Between 75 percent span and the tip endwall, the stator inlet angle increases rapidly with span. The flow angle distributions in this region for all three flow coefficients are nearly the same, although that for $\phi = 0.55$ is nearly five degrees lower than the other two. The spanwise increase in stator inlet angle near the tip is due primarily to the rapid drop in C_x in the rotor tip region (Fig. 8). These results are very similar to those of reference [13].

At the stator exit, the deviation is positive 10 to 15 degrees. Reducing the flow coefficient increases the deviation and the exit flow angle over most of the span. Near the hub at the reduced flow coefficients, $\phi = 0.51$ and 0.45, the exit flow angle exhibits trends one might attribute to secondary flow. Going from the midspan toward the hub, the exit angle increases above the midspan level, reaches a maximum, then decreases. This trend is due to the very low speed, nearly axial flow associated with the hub corner stall and not secondary flow. Near the tip, the flow angle decreases with reduced flow coefficient. This is due to the contraction of the tip corner stall (Fig. 3) and hence lower tip blockage at the lower flow coefficient.

In summary, rotor hub corner stall has a major impact on the stator inlet angle profile due to its effects on the rotor exit axial velocity. Rotor tip leakage results in a region of low C_x and this governs the stator inlet angle profile in the tip region. Finally, stator corner stall growth at the hub and contraction at the tip have a major influence on the stator exit angle profile.

Blockage. Through-flow analyses are axisymmetric calculations of the radial distributions of mass averaged quantities. The concept of blockage has been introduced by compressor analysts to account for both endwall boundary layers (endwall blockage) and nonaxisymmetric effects (tangential blockage) [1]. Endwall blockage is included explicitly in the present fullspan data since it was acquired close to the hub and casing. Tangential blockage has been calculated from the measured traverse results. References [7] and [8] have suggested a definition of tangential blockage as the ratio of the circumferentially area averaged axial velocity to the axial velocity calculated from the circumferentially mass averaged total and static pressures and the circumferentially mass averaged flow angles. For incompressible flow this ratio, $\bar{K}$, can be expressed as follows:

$$\bar{K} \equiv (\bar{C}_x^u / \bar{C}_x^{P_T}) = f(r)$$

where

$$\bar{C}_x^{P_T} \equiv (\sqrt{(\bar{P}_T^m - \bar{P}_S^m)/1/2\rho}) \cos \bar{\alpha}^m \cos \bar{\gamma}^m$$

$$= \sqrt{\bar{C}^2}^m \cos \bar{\alpha}^m \cos \bar{\gamma}^m$$

All of the parameters in this definition are available from the traverse data at each radius. Note, however, that this definition also permits one to calculate blockage from hot-wire or laser velocimeter data down-stream of airfoil rows as well as within blade-to-blade passages. This blockage reflects all departures from axisymmetry from hub to tip including corner stall, profile wakes and tip leakage. As these effects mix out the blockage decreases to zero [8]. Results for all three flow coefficients are shown in Fig. 11 for the stator exit traverse plane. The major contribution to the blockage came from the total pressure. In general, the area and mass averages of static pressure and the yaw and pitch angles were nearly equal.

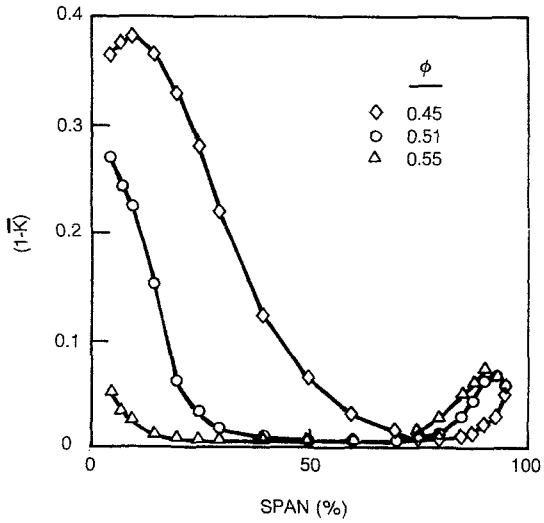

Fig. 11 Spanwise blockage variation with flow coefficient

At $\phi = 0.55$, the higher levels of blockage in the hub and tip regions are nearly evenly distributed about midspan and are of the same order of magnitude. This is consistent with the observations made previously about the hub and tip corner stall at this flow coefficient in reference to Figs. 1 and 5. As the flow coefficient is decreased, blockage due to the stator hub corner stall increases in magnitude and spanwise extent. At the tip region, however, the level of blockage decreases in magnitude and spanwise extent as the flow coefficient is decreased. This is consistent with the flow visualization and total pressure contour results which show that the tip corner stall contracts as the flow coefficient is reduced. At the design point, $\phi = 0.51$, the maximum stator hub blockage is nearly ten times greater than the rotor hub blockage ([7], Fig. 12). At $\phi = 0.45$, the blockage created by the stator hub corner stall reaches a maximum of nearly 40 percent and it extends out to nearly 70 percent span. At the 0.55 and 0.51 flow coefficients, the midspan blockage is very small (less than 1 percent).

The blockage due to the stator hub corner stall also has a

significant impact on the measured stator exit hub to tip static pressure difference. As the flow coefficient is decreased, the hub blockage increases as does the static pressure difference. As mentioned earlier the stator exit endwall static pressure difference increases by nearly a factor of 2.5 as the flow coefficient is decreased from 0.55 to 0.45 (Figs. 5 through 7). There are two primary effects causing this. First, at any given radius in the region near the hub but outside of the corner stall, the flow velocity is considerably greater than it would be without the blockage due to the corner stall. This high velocity flow results in a local reduction in static pressure. Second, the large loss associated with the corner stall results in a reduced static pressure in the stall region [6].

Using the stator inlet and exit traverse data, spanwise distributions of stator two-dimensional diffusion factor ([11], p. 204) for all three flow coefficients were calculated. Although application of the diffusion factor to such a highly three-dimensional flow is questionable, it is included in the present discussion to provide some perspective to the designer. It was found that the diffusion factor distributions exhibit the same trends with flow coefficient as does the blockage. Regions of high diffusion factor coincide with regions of high blockage. The blockage on both the rotor and stator hub contribute to the increase in stator diffusion factor. Blockage due to the corner stall on the rotor results in an increase in stator diffusion factor through an increase in stator incidence. Stator hub blockage increases the diffusion factor through a reduction in stator exit axial velocity.

In summary, corner stall is the major source of blockage in the stator exit flow and increases rapidly with decreasing flow coefficient. Blockage has a major impact on the stator exit static pressure field. Stator diffusion factor variations with flow coefficient correspond to spanwise blockage distributions.

The flow exiting the first stator was in all respects very similar to the flow leaving the second stator. The major difference was that the magnitude of the corner stall on the first stator was significantly less than on the second stator. Thus, although the flow fields were qualitatively similar, the loss, deviation and level of blockage were all somewhat lower on the first stator.

Conclusions

This paper has presented some of the initial results of a detailed experimental study of the aerodynamics of the second stage of a large scale, two-stage axial compressor. The specific second stage stator data presented include airfoil and endwall surface flow visualization, contour plots of total pressure at the stator exit, and the spanwise distributions of the circumferentially averaged stator inlet and exit total and static pressures, axial velocity, flow angle, and the calculated blockage. Corner stall was the primary three-dimensional feature of the flow and it had a dominant impact on loss, deviation and blockage. Through these parameters, it also has a strong impact on the spanwise distributions of static pressure and axial velocity. Lowering the flow coefficient resulted in a dramatic growth of the stator hub corner stall. This resulted in local values of blockage up to 40 percent. In contrast, the tip corner stall was seen to diminish as the flow coefficient was reduced.

The radial redistribution of high and low total pressure fluid through the stator passage and in the downstream flow resulted in spanwise loss distributions which were locally negative. This radial redistribution was due in part to radial flows generated in the stator passage by the corner stall and by the mixing of the rotor tip leakage flow.

At the near stall flow coefficient, $\phi = 0.45$, the rotor hub corner stall resulted in a significant increase in the stator inlet angle. This increased inlet angle was a major contributor to the growth of the stator hub corner stall. The rotor hub corner stall, through its impact on stator inlet angle, also accounted for most of the increase in stator diffusion factor in the hub region. It is believed that the additive influence of corner stall on downstream airfoil rows through its impact on axial velocity and deviation may be one of the more important mechanisms leading to the "repeating stage" [14] type of flow field.

Acknowledgments

The two-stage second stator data was acquired under Pratt & Whitney Aircraft Commercial Products Division and United Technologies Research Center Corporate funding.

References

1 AGARD Advisory Report No. 175, Propulsion and Energetics Panel Working Group 12 on Through-Flow Calculations in Axial Turbomachines, AGARD-AR-175, Oct. 1981.

2 Dring, R. P., Joslyn, H. D., and Hardin, L. W., "Experimental Investigation of Compressor Rotor Wakes," AFAPL-TR-79-2107. Air Force Aero Propulsion Laboratory, Technology Branch, Turbine Engine Division (TBX), Wright-Patterson Air Force Base, Ohio.

3 Dring, R. P., Joslyn, H. D., and Hardin, L. W., "An Investigation of Compressor Rotor Aerodynamics," ASME JOURNAL OF ENGINEERING FOR POWER, Vol. 104, Jan. 1982, p. 84–96.

4 Wagner, J. H., Dring, R. P., and Joslyn, H. D., "Axial Compressor Middle Stage Secondary Flow Study," NASA Contract Number NAS3-23157, NASA Contractor Report 3701, July 1983.

5 Wagner, J. H., Dring, R. P., and Joslyn, H. D., "Inlet Boundary Layer Effects in an Axial Compressor Rotor: Part I—Blade-to-Blade Effects," ASME JOURNAL OF ENGINEERING FOR GAS TURBINES AND POWER, Vol. 107, No. 2, Apr. 1985, pp.374-380.

6 Wagner, J. H., Dring, R. P., and Joslyn, H. D., "Inlet Boundary Layer Effects in an Axial Compressor Rotor: Part II—Throughflow Effects," ASME JOURNAL OF ENGINEERING FOR GAS TURBINES AND POWER, Vol. 107, No. 2, Apr. 1985, pp.381-386.

7 Dring, R. P., Joslyn, H. D., and Wagner, J. H., "Compressor Rotor Aerodynamics," AGARD-CP-351, Viscous Effects in Turbomachines, June 1-3, 1983, Reference 24.

8 Dring, R. P., "Blockage in Axial Compressors," ASME JOURNAL OF ENGINEERING FOR GAS TURBINES AND POWER, Vol. 106, No. 3, July 1984, pp. 712-714.

9 Dring, R. P., and Joslyn, H. D., "Measurements of Turbine Rotor Blade Flows," ASME JOURNAL OF ENGINEERING FOR POWER, Vol. 103, No. 2, Apr. 1981, pp. 400-405.

10 Joslyn, H. D., Dring, R. P., and Sharma, O. P., "Unsteady Three-Dimensional Turbine Aerodynamics," ASME JOURNAL OF ENGINEERING FOR POWER, Vol. 105, No. 2, Apr. 1983, pp. 322-331.

11 "Aerodynamic Design of Axial-Flow Compressors," NASA SP-36, 1965, p. 204.

12 Kerrebrock, J. L., and Mikolajczak, A. A., "Intra-Stator Transport of Rotor Wakes and Its Effects on Compressor Performance," ASME JOURNAL OF ENGINEERING FOR POWER, Oct. 1970, p. 359.

13 Adkins, G. G., and Smith, L. H., Spanwise Mixing in Axial-Flow Turbomachines," ASME JOURNAL OF ENGINEERING FOR POWER, Vol. 104, Jan. 1982, p. 97-110.

14 Smith, L. H., Jr., *Casing Boundary Layers in Multi-Stage Axial Flow Compressors, Flow Research in Blading*, L. S. Dzung, ed., Elsevier, Amsterdam, 1970, p. 275.

significant impact on the measured stator exit hub to tip static pressure difference. As the flow coefficient is decreased, the hub blockage increases as does the static pressure difference. As mentioned earlier the stator exit endwall static pressure difference increases by nearly a factor of 2.5 as the flow coefficient is decreased from 0.55 to 0.45 (Figs. 5 through 7). There are two primary effects causing this. First, at any given radius in the region near the hub but outside of the corner stall, the flow velocity is considerably greater than it would be without the blockage due to the corner stall. This high velocity flow results in a local reduction in static pressure. Second, the large loss associated with the corner stall results in a reduced static pressure in the stall region [6].

Using the stator inlet and exit traverse data, spanwise distributions of stator two-dimensional diffusion factor ([11], p. 204) for all three flow coefficients were calculated. Although application of the diffusion factor to such a highly three-dimensional flow is questionable, it is included in the present discussion to provide some perspective to the designer. It was found that the diffusion factor distributions exhibit the same trends with flow coefficient as does the blockage. Regions of high diffusion factor coincide with regions of high blockage. The blockage on both the rotor and stator hub contribute to the increase in stator diffusion factor. Blockage due to the corner stall on the rotor results in an increase in stator diffusion factor through an increase in stator incidence. Stator hub blockage increases the diffusion factor through a reduction in stator exit axial velocity.

In summary, corner stall is the major source of blockage in the stator exit flow and increases rapidly with decreasing flow coefficient. Blockage has a major impact on the stator exit static pressure field. Stator diffusion factor variations with flow coefficient correspond to spanwise blockage distributions.

The flow exiting the first stator was in all respects very similar to the flow leaving the second stator. The major difference was that the magnitude of the corner stall on the first stator was significantly less than on the second stator. Thus, although the flow fields were qualitatively similar, the loss, deviation and level of blockage were all somewhat lower on the first stator.

Conclusions

This paper has presented some of the initial results of a detailed experimental study of the aerodynamics of the second stage of a large scale, two-stage axial compressor. The specific second stage stator data presented include airfoil and endwall surface flow visualization, contour plots of total pressure at the stator exit, and the spanwise distributions of the circumferentially averaged stator inlet and exit total and static pressures, axial velocity, flow angle, and the calculated blockage. Corner stall was the primary three-dimensional feature of the flow and it had a dominant impact on loss, deviation and blockage. Through these parameters, it also has a strong impact on the spanwise distributions of static pressure and axial velocity. Lowering the flow coefficient resulted in a dramatic growth of the stator hub corner stall. This resulted in local values of blockage up to 40 percent. In contrast, the tip corner stall was seen to diminish as the flow coefficient was reduced.

The radial redistribution of high and low total pressure fluid through the stator passage and in the downstream flow resulted in spanwise loss distributions which were locally negative. This radial redistribution was due in part to radial flows generated in the stator passage by the corner stall and by the mixing of the rotor tip leakage flow.

At the near stall flow coefficient, $\phi = 0.45$, the rotor hub corner stall resulted in a significant increase in the stator inlet angle. This increased inlet angle was a major contributor to the growth of the stator hub corner stall. The rotor hub corner stall, through its impact on stator inlet angle, also accounted for most of the increase in stator diffusion factor in the hub region. It is believed that the additive influence of corner stall on downstream airfoil rows through its impact on axial velocity and deviation may be one of the more important mechanisms leading to the "repeating stage" [14] type of flow field.

Acknowledgments

The two-stage second stator data was acquired under Pratt & Whitney Aircraft Commercial Products Division and United Technologies Research Center Corporate funding.

References

1 AGARD Advisory Report No. 175, Propulsion and Energetics Panel Working Group 12 on Through-Flow Calculations in Axial Turbomachines, AGARD-AR-175, Oct. 1981.

2 Dring, R. P., Joslyn, H. D., and Hardin, L. W., "Experimental Investigation of Compressor Rotor Wakes," AFAPL-TR-79-2107. Air Force Aero Propulsion Laboratory, Technology Branch, Turbine Engine Division (TBX), Wright-Patterson Air Force Base, Ohio.

3 Dring, R. P., Joslyn, H. D., and Hardin, L. W., "An Investigation of Compressor Rotor Aerodynamics," ASME JOURNAL OF ENGINEERING FOR POWER, Vol. 104, Jan. 1982, p. 84–96.

4 Wagner, J. H., Dring, R. P., and Joslyn, H. D., "Axial Compressor Middle Stage Secondary Flow Study," NASA Contract Number NAS3-23157, NASA Contractor Report 3701, July 1983.

5 Wagner, J. H., Dring, R. P., and Joslyn, H. D., "Inlet Boundary Layer Effects in an Axial Compressor Rotor: Part I—Blade-to-Blade Effects," ASME JOURNAL OF ENGINEERING FOR GAS TURBINES AND POWER, Vol. 107, No. 2, Apr. 1985, pp.374-380.

6 Wagner, J. H., Dring, R. P., and Joslyn, H. D., "Inlet Boundary Layer Effects in an Axial Compressor Rotor: Part II—Throughflow Effects," ASME JOURNAL OF ENGINEERING FOR GAS TURBINES AND POWER, Vol. 107, No. 2, Apr. 1985, pp.381-386.

7 Dring, R. P., Joslyn, H. D., and Wagner, J. H., "Compressor Rotor Aerodynamics," AGARD-CP-351, Viscous Effects in Turbomachines, June 1-3, 1983, Reference 24.

8 Dring, R. P., "Blockage in Axial Compressors," ASME JOURNAL OF ENGINEERING FOR GAS TURBINES AND POWER, Vol. 106, No. 3, July 1984, pp. 712-714.

9 Dring, R. P., and Joslyn, H. D., "Measurements of Turbine Rotor Blade Flows," ASME JOURNAL OF ENGINEERING FOR POWER, Vol. 103, No. 2, Apr. 1981, pp. 400-405.

10 Joslyn, H. D., Dring, R. P., and Sharma, O. P., "Unsteady Three-Dimensional Turbine Aerodynamics," ASME JOURNAL OF ENGINEERING FOR POWER, Vol. 105, No. 2, Apr. 1983, pp. 322-331.

11 "Aerodynamic Design of Axial-Flow Compressors," NASA SP-36, 1965, p. 204.

12 Kerrebrock, J. L., and Mikolajczak, A. A., "Intra-Stator Transport of Rotor Wakes and Its Effects on Compressor Performance," ASME JOURNAL OF ENGINEERING FOR POWER, Oct. 1970, p. 359.

13 Adkins, G. G., and Smith, L. H., Spanwise Mixing in Axial-Flow Turbomachines," ASME JOURNAL OF ENGINEERING FOR POWER, Vol. 104, Jan. 1982, p. 97-110.

14 Smith, L. H., Jr., *Casing Boundary Layers in Multi-Stage Axial Flow Compressors, Flow Research in Blading*, L. S. Dzung, ed., Elsevier, Amsterdam, 1970, p. 275.

DISCUSSION

N. A. Cumpsty[1]

The authors have produced data which users can be certain is accurate and carefully obtained. What the user or reader is less sure about is the usefulness of the compressor used. The compressor stator is heavily stalled at the root, even at the design flow coefficient, $\phi = 0.51$; is it useful to put so much

[1] Whittle Laboratory, Cambridge University, Cambridge, U.K.

effort into studying a compressor, or a blade row, which is so poor? How far can we generalize from these results? Are the authors indicating that this is a good compressor – little information is given for the basis of the design, but is one to assume that the design conforms with the practice of the sponsors, Pratt and Whitney?

S. J. Gallimore[2]

The authors have presented some interesting and detailed data on the flow through a stator blade row. Their final conclusion is that corner stall could be an important mechanism leading to the "repeating stage" condition. However, there is no discussion elsewhere in the paper to suggest how this arises and the point is not obvious to me and to those with whom I have discussed it. Although Smith [14] does mention that local regions of separated flow are admissible in a repeating stage, this is not equivalent to establishing it as a cause of this type of flow field. Perhaps the authors could expand on their conclusion and give details of the mechanisms by which they expect corner stall to set up the repeating stage condition.

Authors' Closure

The authors would like to thank Mr. Cumpsty and Mr. Gallimore for the questions they have raised. The objectives of the experiments were both to describe the detailed nature of the flow field and to present the results in a way that would enable analysts to assess the accuracy of their predictions. It is not clear, however, that the presence of corner stall in this compressor causes it to be atypical. The suction surface corners of the present stator were stalled, as was the hub suction surface corner of the upstream rotor [7]. Corner stall has been observed on an isolated rotor over a wide range of incidence and inlet boundary layer thickness [2–7]. It has also been seen to occur on high solidity rotors and stators [15]. For the purposes of analytical assessment the presence of the corner stall necessitates an accurate representation of blockage (Fig. 11). Had the stator blockage been as low as that of the rotor ([7], Fig. 12) it would be more difficult to determine whether it was being modeled accurately.

Since the establishment of a "repeating" stage condition is generally considered to require more than two stages, all one can say relative to the present data is by what mechanism the flow is deteriorating in the direction of a repeating stage. The radial distributions of the circumferentially area-averaged axial velocity at the first stator exit (not shown) and at the second stator exit (Fig. 9) are monotonically deteriorating at the hub. Our observation was that the mechanism leading to this deterioration in the present experiment was the corner stall and not the endwall boundary layer.

[2] Whittle Laboratory, Cambridge University, Cambridge, U.K.

References

15 Wisler, D. C., "Loss Reduction in Axial Flow Compressors Through Low-Speed Model Testing," ASME JOURNAL OF ENGINEERING FOR GAS TURBINES AND POWER, Vol. 107, No. 2, Apr. 1985, pp. 354–363.

Comparison of Controlled Diffusion Airfoils With Conventional NACA 65 Airfoils Developed for Stator Blade Application in a Multistage Axial Compressor

H. Rechter

W. Steinert
DFVLR, Köln, West Germany

K. Lehmann
MTU München, West Germany

In their transonic cascade wind tunnel, DFVLR has done measurements on a conventional NACA 65, as well as on a controlled diffusion airfoil, designed for the same velocity triangle at supercritical inlet condition. These tested cascades represent the first stator hub section of a three-stage axial/one-stage radial combined compressor developed by MTU with the financial aid of the German Ministry of Research and Technology. One aspect of this project was the verification of the controlled diffusion concept for axial compressor blade design, in order to demonstrate the capabilities of some recent research results which are now available for industrial application. The stator blades of the axial compressor section were first designed using NACA 65 airfoils. In the second step, the controlled diffusion technique was applied for building a new stator set. Both stator configurations were tested in the MTU compressor test facility. Cascade and compressor tests revealed the superiority of the controlled diffusion airfoils for axial compressors. In comparison to the conventional NACA blades, the new blades obtained a higher efficiency. Furthermore, a closer matching of the compressor performance data to the design requirements was possible due to a more precise prediction of the turning angle.

Introduction

A combined axial-radial research compressor was developed and built by MTU financially supported by the German Ministry of Research and Technology. The main design parameters of this compressor are:

- A total pressure ratio of 13.32
- A mass flow of 3.69 kg/s
- Three axial stages and one radial stage

These were chosen with respect to its operation as a part of medium sized jet engines with a propulsive power of around 1000 kW. Figure 2 shows the longitudinal cross section of the complete compressor test rig, including the inlet and the exit air collecting chamber.

The general objective of this project was to develop and to demonstrate the capabilities of some new technological concepts in compressor aerodynamics and materials. In addition, it was expected that the experimental investigation of this compressor would promote the physical understanding of mechanisms and phenomena occurring in highly loaded turbomachines.

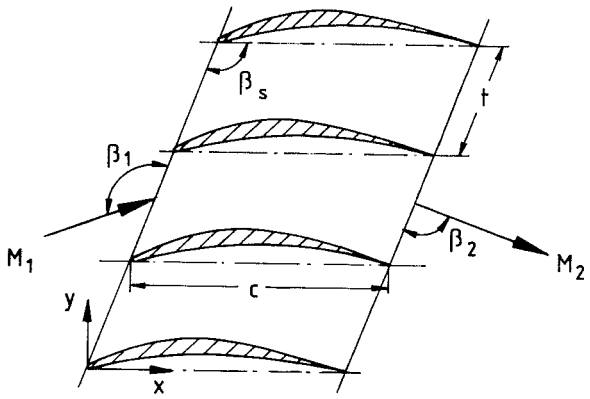

Fig. 1 Cascade notation

As far as the compressor aerodynamics is concerned, the following design goals were specified:

- minimizing the number of compressor stages, thus obtaining an engine of small dimension

Contributed by the Gas Turbine Division of THE AMERICAN SOCIETY OF MECHANICAL ENGINEERS and presented at the 29th International Gas Turbine Conference and Exhibit, Amsterdam, The Netherlands, June 4–7, 1984. Manuscript received at ASME Headquarters January 19, 1984. Paper No. 84-GT-246.

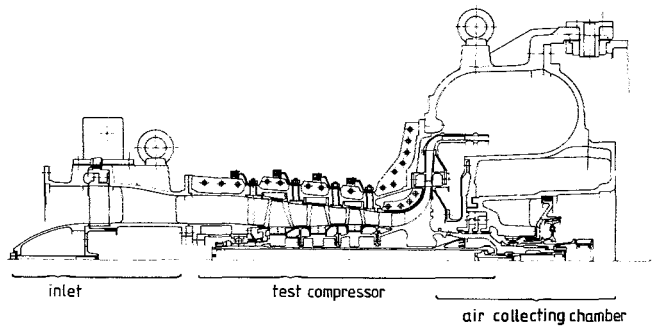

Fig. 2 Longitudinal cross section of the complete compressor test rig

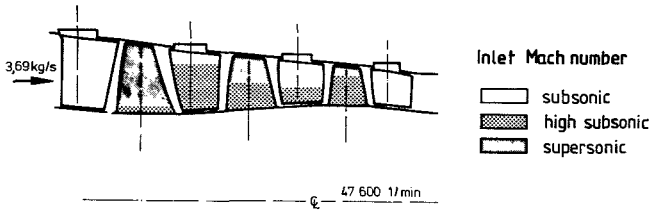

Fig. 3 Meridional view of the axial compressor blading

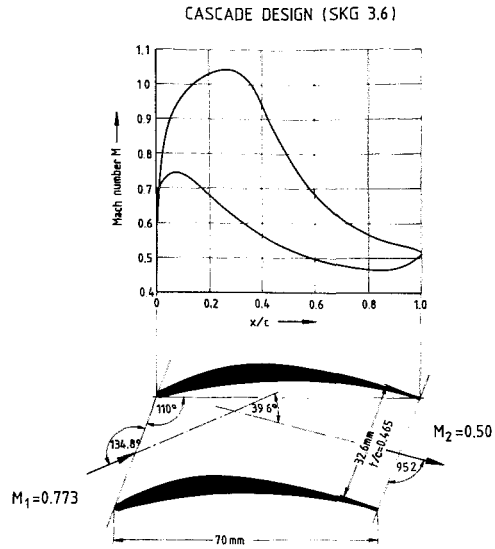

Fig. 4 Design Mach number distribution and blades of the controlled diffusion cascade SKG 3.6 ($\Omega = 1.1$, $D_{01} = 0.478$)

- high total pressure ratio
- high aerodynamic loading
- high efficiency with a sufficient off-design operating range

In order to meet these goals, it was decided to apply the controlled diffusion technique to the stator blade design of the axial compressor section and to compare it to the conventional blade design.

This part of the project was done in cooperation with DFVLR and with the help of E. Schmidt from the University of Stuttgart. In the first step, cascade tests were performed using conventional NACA 65 blades, as well as controlled diffusion blades under flow conditions representative for the hub section of the first stage. In the second phase of this investigation, an alternative set of blades was designed, consisting of controlled diffusion airfoils in each section applicable to subsonic inlet conditions. Blade number and chord remained unchanged for this new set. Figure 3 shows a meridional view of the axial compressor, indicating the various inlet Mach numbers of the blade sections throughout the flow path. With both types of blading, an extensive test program was conducted, studying not only the complete axial-radial assembly, but also the axial and the radial section in separate test stands.

This paper summarizes the results of the basic cascade tests and shows the performance map of both axial compressor sets in comparison. More detailed information about the entire compressor research program, including the nonaerodynamic aspects, can be found in [1].

Cascade Investigations

Cascade Design. Two supercritical cascades were developed for the near-hub section of the first axial compressor stator. The airfoils were derived by means of two different techniques. For the design of the first cascade MTU superposed a conventional NACA 65 thickness distribution to a circular arc camberline, taking into account empirical loss and deviation angle correlations.

The second cascade (SKG 3.6) was designed by means of Schmidt's method (see [2]). It allows the calculation of the cascade and airfoil geometry based on a blade pressure or Mach number distribution, which is optimized with respect to boundary-layer considerations and thus provides a controlled diffusion on the blade surfaces, and it also includes the effect of the axial velocity density ratio (AVDR). This method has already been used for several previous cascade designs, and it has been verified by extensive cascade testing (see [3] and [4]).

The following investigations aim to compare the controlled diffusion airfoil to a conventional blade being operated under the same flow conditions.

Figure 4 shows the Mach number distribution, which was chosen as the design input for the controlled diffusion cascade SKG 3.6. It also shows a blade passage of the designed cascade configuration with the nominal flow data. The main characteristics of the specified Mach number distribution may be summarized as follows:

- On the suction surface the sonic velocity is exceeded shortly after the flow has passed the nose region, forming a small supersonic bubble up to 35 percent of chord. The maximum Mach number is 1.05.
- Boundary-layer calculations for the suction side Mach number distribution revealed laminar-turbulent transition at about 30 percent of chord, shortly after the peak Mach number. From peak Mach number to outlet Mach number the diffusion is controlled in order to avoid boundary layer separation in the rear part of the airfoil.

Nomenclature

c = chord length
D_{01} = diffusion factor

$$D_{01} = 1 - \frac{w_2}{w_1} + \frac{1}{2}\,\frac{t}{c}\,\frac{\Delta w_u}{w_1}$$

$\dot{m}$ = mass flow
M = Mach number
p = static pressure
p_t = total pressure
t/c = gap to chord ratio
T_t = total temperature
w = velocity
x/c = relative blade coordinate
y/c = relative blade coordinate
β = flow angle
β_s = stagger angle
η = efficiency
Θ = flow turning angle
π_t = total pressure ratio
ω = total pressure loss coefficient $\omega = (p_{t1} - p_{t2})/(p_{t1} - p_1)$
Ω = axial velocity density ratio (AVDR)

Subscripts

1 = inlet plane
2 = outlet plane
u = circumferential direction

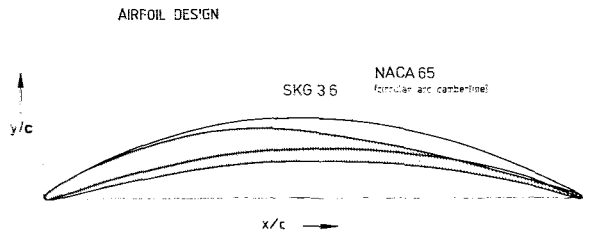

Fig. 5 Comparison of the controlled diffusion airfoil (SKG 3.6) and the conventional NACA 65 airfoil

The following design flow conditions were specified for both cascades:

- An inlet Mach number of 0.773, implying a supercritical cascade design,
- A flow turning of 39.6 deg
- A gap-to-chord ratio of 0.465
- An axial velocity density ratio (AVDR) of 1.1

The diffusion factor was calculated as 0.478.

Both airfoils in their final shapes are presented in Fig. 5. The NACA 65 airfoil has a constant curvature over the whole chord length. The SKG 3.6 airfoil, however, has very little curvature in its rear part, which looks similar to a thin flat plate. The flow turning is accomplished primarily in the front portion of the airfoil. The rear portion provides guidance for the cascade outlet flow. This portion, however, appeared to be too thin after the first boundary layer calculations. In order to avoid further design calculations, the SKG 3.6 blade was simply thickened up linearly to the NACA blade's trailing edge value beginning at 50 percent of chord.

Test Results. Both cascades were tested in the DFVLR transonic cascade tunnel. The cascade models consisted of 6 blades with a chord length of 70 mm and a span of 167 mm. At first, the measured Mach number distribution of the SKG 3.6 cascade was compared to the design distribution (see Fig. 6), and the best agreement was obtained when the experimental inlet flow angle was increased by 1 deg and the inlet Mach number was slightly below design. These differences are assumed to be due to the upstream influence of the stream tube contraction caused by the side wall boundary layer between measurement and cascade leading edge plane. The performance comparison is therefore made at a so-called "design" inlet flow angle of $\beta_1 = 135.8$ deg, which is different from the initial blade design inlet angle of $\beta_1 = 134.8$ deg. Figure 6 shows some differences in the nose region (suction peak on the pressure side), near the blade trailing edge on both sides (higher surface Mach numbers), and on the suction side near the calculated transition point. The following explanation is given for these deviations.

The airfoil's nose region could not be calculated by Schmidt's method, it had to be finished off "by hand." In the meantime, this shortcoming of the calculation procedure has been overcome. The deviation at the transition point is assumed to be due to a laminar separation bubble.

The higher surface Mach numbers near the blade trailing edge were caused by the blade thickening in this region, which had to be applied for mechanical reasons, as previously mentioned. But in spite of these deviations, it must be emphasized that the desired flow turning of 39.6 deg was almost achieved for the design flow conditions.

The Mach number distribution of the conventional NACA 65 airfoil was not known in advance. It had to be obtained by means of the cascade tests. Figure 7 shows a result of the design conditions in comparison to the SKG 3.6 cascade. The distributions look similar on the suction side, and they are nearly identical on the pressure side. On the suction side of the

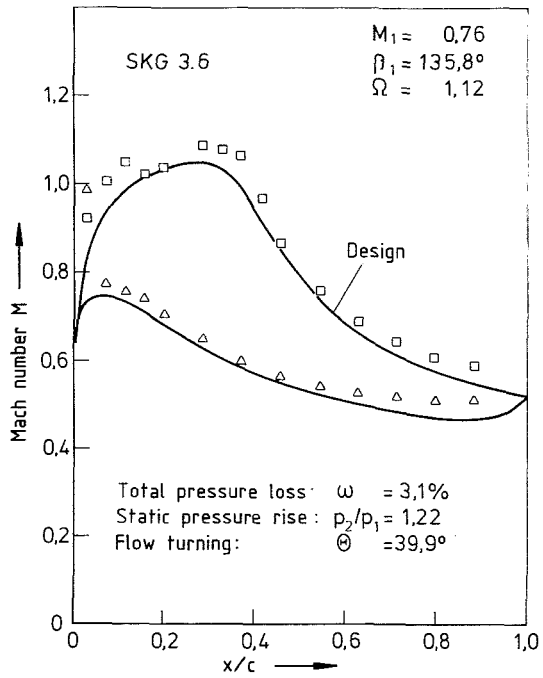

Fig. 6 Comparison of the measured and the prescribed Mach number distribution for the SKG 3.6 cascade

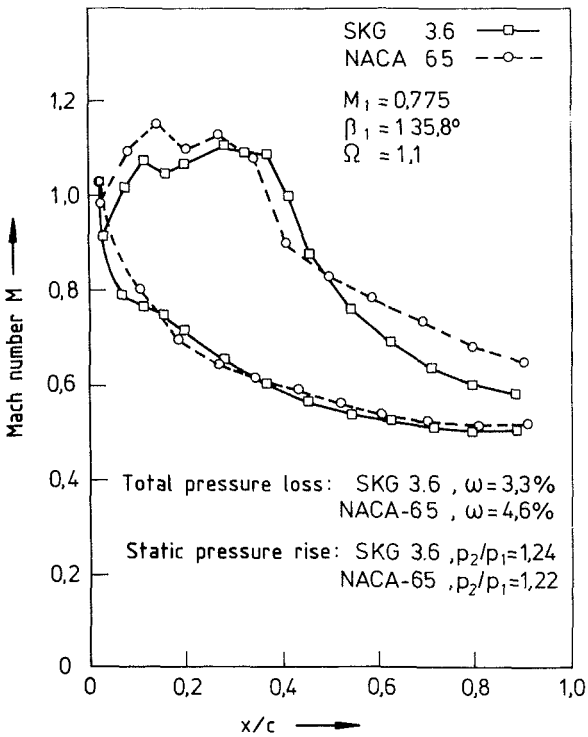

Fig. 7 Comparison of the measured blade surface Mach number distributions

NACA 65 blade, however, a kink can be observed in the Mach number curve at 40 percent of chord. From this point up to the trailing edge, the surface Mach numbers of the NACA 65 blade are higher than those of the SKG 3.6 cascade. The steep drop in the NACA 65 blade's Mach number from the peak value to the 40 percent value might be interpreted as a shock wave, terminating the supersonic bubble and causing a boundary layer thickening. This mechanism may then be responsible for the higher losses of the NACA 65 airfoil as compared to the SKG 3.6 cascade.

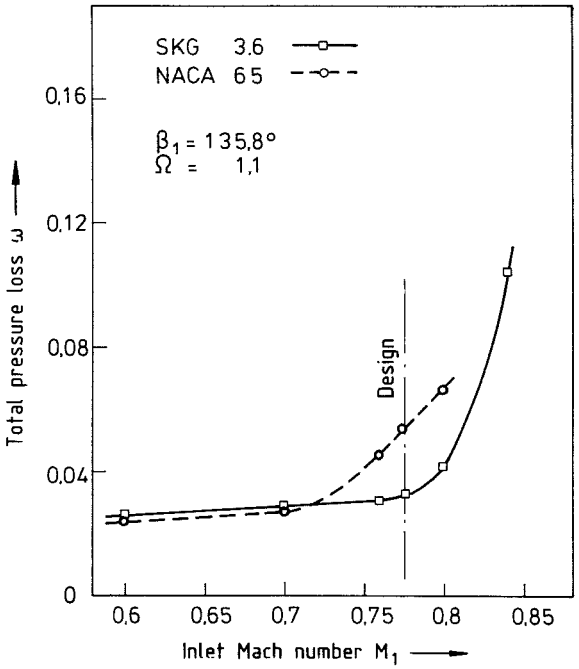

Fig. 8 Comparison of the cascade losses with varying inlet Mach number

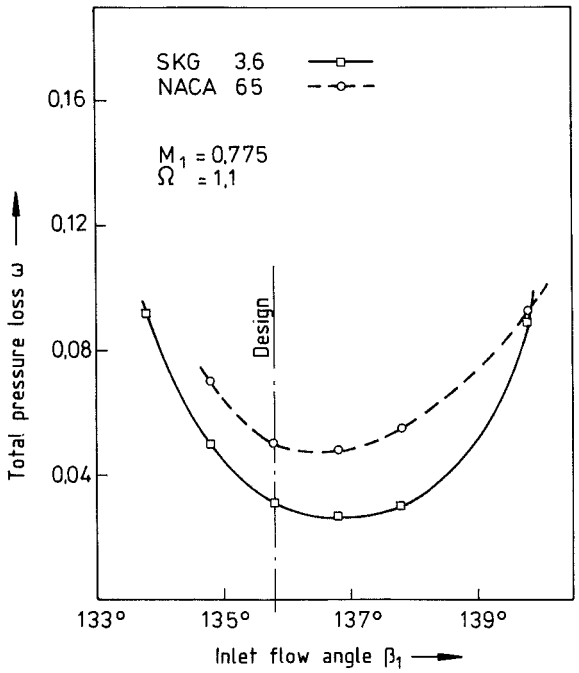

Fig. 9 Comparison of the cascade losses with varying inlet flow angle

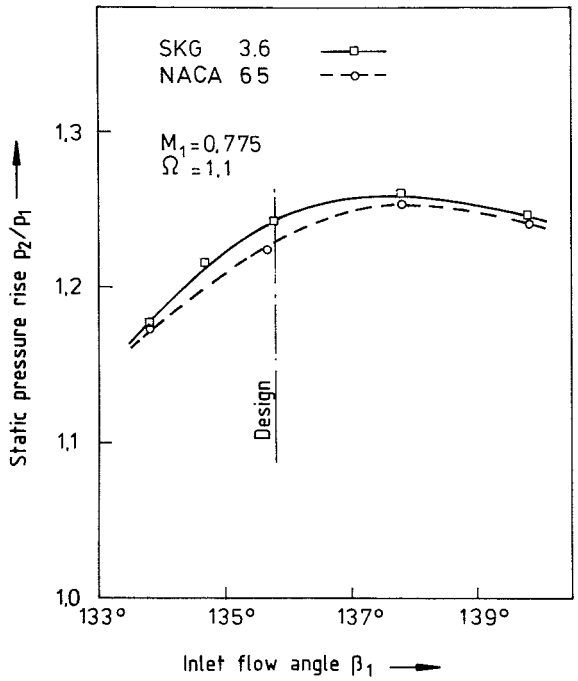

Fig. 10 Static pressure rise of the cascades with varying inlet flow angle

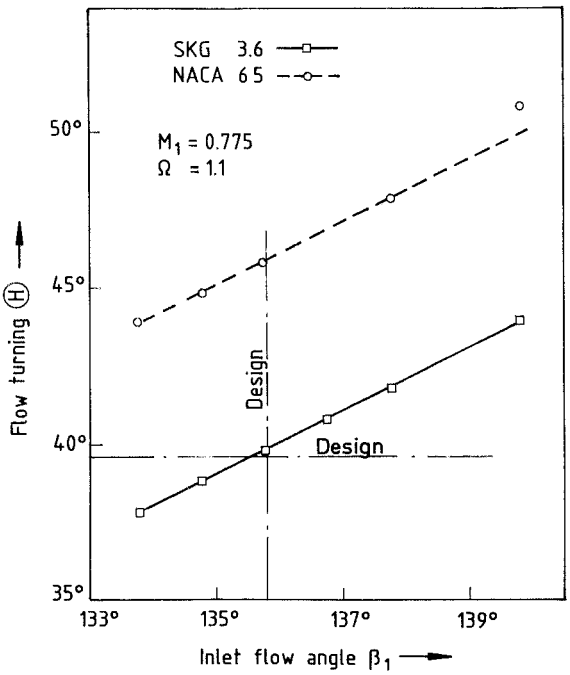

Fig. 11 Flow turning angle of the cascades with varying inlet flow angle

The total pressure loss coefficients variations for various inlet Mach numbers are presented in Fig. 7. Up to a value of 0.7, the same losses were obtained for both cascades. Beyond this value, however, different loss characteristics could be observed. The losses of the conventional airfoil increased, whereas the losses of the SKG 3.6 blade remained low up to the design inlet Mach number of 0.77. But if the design point was exceeded, they increased sharply.

In Fig. 9, the loss characteristics for inlet flow angle variations are shown. The low loss incidence range was quite small for both cascades, namely on the negative side, which means that the design point was near to choking. This is also partly confirmed by the SKG 3.6 suction peak in the nose region of the pressure side Mach number distribution (see Figs. 6 and 7). Nevertheless, the comparison of both cascades again revealed the superiority of the SKG 3.6 blade, which had a considerably lower loss level and a slightly increased operating range. The static pressure rise of both cascades is compared in Fig. 10. Slightly higher values could be obtained with the SKG 3.6 blade.

The measured flow turning was found to be completely different for these cascades (see Fig. 11). Whereas the SKG 3.6 cascade came quite close to the desired design value of 39.6 deg, the conventional cascade obtained a value of about 45 deg. This discrepancy is attributed to the shortcomings of

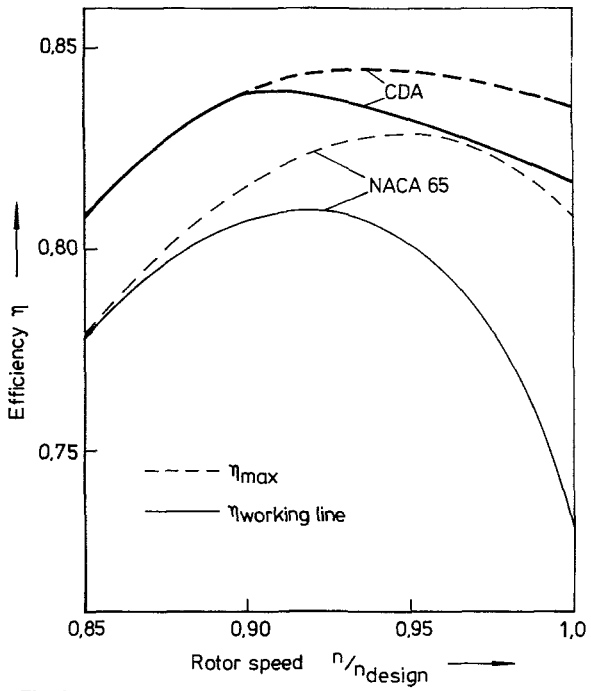

Fig. 12 Axial compressor efficiency with varying rotor speed

the deviation angle correlations which were used for the conventional design procedure.

In summarizing the cascade tests, one can say that the compared sections seem to have been designed for different flow conditions. But this was unintentional. The wrong prediction of the air turning for the NACA 65 section brought about a higher loading resulting in unfavorable loss characteristics, which made this section appear unsuitable for the specified design conditions. The SKG 3.6 section, however, met the design goal, thus demonstrating the superiority of the controlled diffusion technique.

Compressor Investigations

Design Considerations. Two alternative sets of stator bladings were designed and built for the axial section of the compressor, one using conventional NACA 65 profiles and the other being equipped with custom tailored controlled diffusion airfoils. The velocity triangles of the various blade sections were the same for both designs, and Schmidt's method was used to derive the controlled diffusion blades.

All three axial stages of the compressor were intended to operate as transonic stages. Therefore, most of the rotor sections had supersonic inlet Mach numbers. Because only cascades with subsonic inlet flow conditions up to Mach numbers of about 0.9 can be calculated by means of Schmidt's method, the controlled diffusion concept could not be applied to the rotor blades. According to the given inlet Mach numbers (see Fig. 3), it was restricted to the stator blades. Both stators therefore were tested with the same rotor configuration, consisting of a wedge type MTU profiled blading in the first stage, which had high supersonic inlet Mach numbers and a standard DCA blading in the second and third stage with moderate supersonic or high subsonic inlet Mach numbers.

Test Results. The research compressor was tested under atmospheric conditions in the MTU compressor test facility. The test results of the axial compressor section are summarized in Fig. 12.

The efficiency curves show a considerable improvement for the compressor with the controlled diffusion stators, especially at higher rotational speeds. At 95 percent rotational speed, the maximum efficiency of the compressor using the stators designed for controlled diffusion was 84.4 percent in comparison to 82.9 percent of the compressor with the conventional stators.

In addition, it can be seen that the differences in efficiency are much larger on the engine working line. This result is due to the more precise turning angle prediction by the controlled diffusion technique. The NACA 65 blades, however, resulted in an overturning of the flow which was clearly demonstrated by the cascade experiments (Fig. 10).

Conclusions

The cascade test results revealed the superiority of the controlled diffusion concept in achieving the prescribed design data, namely, the flow turning. Due to this more precise prediction of the turning angle, better aerodynamic characteristics were obtained:

- The losses were lower, and the static pressure rise was even slightly higher.
- The low loss range was extended to higher inlet Mach numbers.
- The operating range with respect to inlet flow angle was increased.

The results of the compressor tests confirm that this advanced cascade design concept contributes considerably to improve the compressor. Two advantages of the new design concept are obvious:

- The more precise prediction of the flow turning for the various blade sections results in more accurate projected compressor operating conditions.
- The lower cascade losses, namely, for high inlet Mach numbers, result in an improvement of the compressor efficiency.

References

1 Weiler, W., "Neue Technologien fur Verdichter von Luftfahrttriebwerken," *Luftfahrtforschung und Luftfahrttechnologie*, 2. BMFT-Statusseminar, 1980.

2 Schmidt, E., "Computation of Supercritical Compressor and Turbine Cascades with a Design Method for Transonic Flows," ASME JOURNAL OF ENGINEERING FOR POWER, Vol. 102, Jan. 1980.

3 Rechter, H., Schimming, P., and Starken, H., "Design and Testing of Two Supercritical Compressor Cascades," ASME Paper No. 79-GT-11.

4 Dunker, R., Rechter, H., Starken, H., and Weyer, H., "Redesign and Performance Analysis of a Transonic Axial Compressor Stator and Equivalent Plane Cascades with Subsonic Controlled Diffusion Blades," ASME Paper No. 83-GT-208.

Printed in U.S.A.

A Discussion of the Factors Affecting Surge in Centrifugal Compressors

R. L. Elder

M. E. Gill

School of Mechanical Engineering,
Cranfield Institute of Technology,
Cranfield, Bedford, U.K.

The process of surge in a centrifugal compressor has been studied and found to be dependent on a number of complex and often interrelated factors. A major factor defining surge in high-speed, vaned diffuser designs appears to be the flow in the semivaneless space. By developing work initiated by others it has been possible to propose some explanation of previously presented apparently conflicting data. In addition, a more complex mathematical model capable of assessing additional factors is proposed. Using this model good agreement with experimental surge has been obtained. This model takes into consideration pressure losses in the impeller, diffuser, and collector, and by using this model it was possible to identify the stalling elements that are responsible for overall compressor instability.

1 Introduction

The tendency for centrifugal compressors to exhibit flow instabilities and surge at low flow rates limits their operating range. Narrow operating ranges result in poor acceleration characteristics for a gas turbine engine and can prevent operation at maximum efficiency which may lie at or close to the surge line.

The literature describes a considerable amount of work carried out in an attempt to understand and to identify the causes and processes that give rise to flow instabilities [1–5]. During the experimental studies undertaken as part of those investigations the flow condition prior to and during surge has been studied and various criteria for surge proposed. In the main, however, these have not proven to be universally successful and this fact, together with some real progress in the understanding of axial flow compressor surge [6–8] has prompted this current work. These advances in axial flow technology have been gained by modeling the dynamics of stage interaction and although the techniques have illustrated a degree of sensitivity (making them difficult to use at the design stage of a compressor development programme), they have illustrated a capability of closely representing the surge process.

This paper attempts to present some further thoughts on the surge process including a summary of what appear to be the most significant factors. Also presented is a surge model (based on ideas from the axial flow work mentioned above) which attempts to quantify the factors causing surge providing some additional insight to the surge process.

Contributed by the Gas Turbine Division of THE AMERICAN SOCIETY OF MECHANICAL ENGINEERS and presented at the 29th International Gas Turbine Conference and Exhibit, Amsterdam, The Netherlands, June 4–7, 1984. Manuscript received at ASME Headquarters, January 18, 1984. Paper No. 84-GT-194.

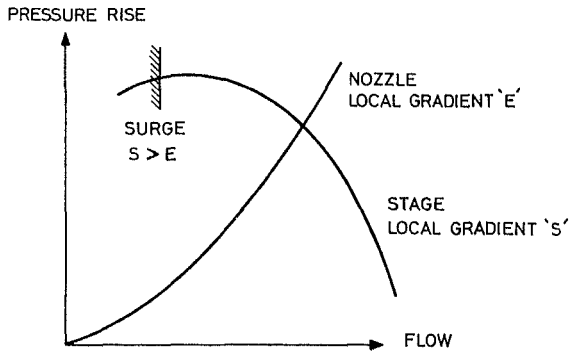

Fig. 1 Simple stability criteria

2 Parameters Affecting Compressor Stability

The following parameters have been observed to affect the surging of centrifugal compressors:

(i) Gradient of compressor pressure rise characteristic and the limited aerodynamic performance range of each component.
(ii) Inducer incidence.
(iii) Impeller blade backsweep and inlet swirl.
(iv) Number of diffuser and impeller vanes.
(v) Pressure recovery within the semivaneless-space (SVS) and incidence on the diffuser vane leading edge.
(vi) Diffuser channel pressure recovery and collector type.
(vii) Casing treatments.

A glance at the above headings will suggest that many of the features involved in centrifugal compressor design play a part in determining compressor surge. Indeed the surging of compressors is most complex and it may help to define the most significant processes if the above topics are considered separately.

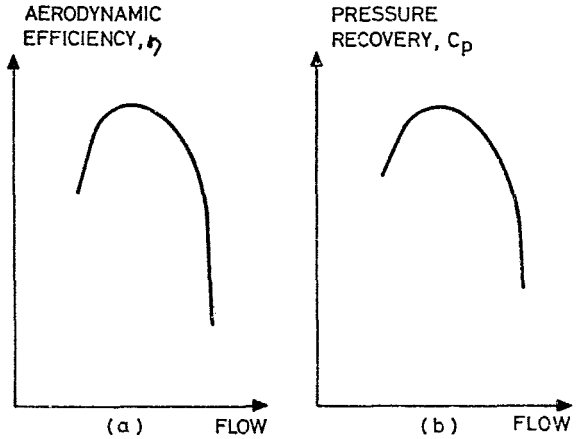

Fig. 2 Aerodynamic range of a compressor or its components

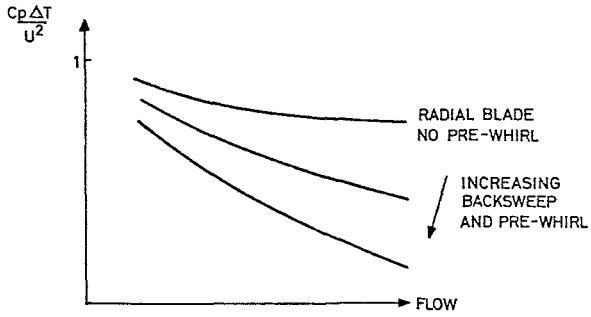

Fig. 3 Effect of backsweep and prewhirl on impeller work input

2.1 Slope of Compressor Pressure Rise Characteristic and Component Aerodynamic Range. For a simple compression system consisting of a compressor, ducting, and a throttle, Howell [9] showed, using a small perturbation analysis, that a condition for compressor stability is:

$$S<E$$

where, Fig. 1, S is the gradient of the compressor characteristic and E the gradient of the nozzle characteristic.

Howell's analysis is presented for an axial flow machine but a precisely similar analysis, with the same result, can be developed for the centrifugal compressor. It has also been argued that in many rig conditions the compressor and nozzle are sufficiently decoupled such that a better stability criteria is

$$S<0$$

That is, the compressor will surge at the peak of the pressure rise characteristic (for the analysis here we will not distinguish total from static pressure). For low-speed axial and centrifugal compressors this condition closely represents the real situation.

The cause of the peaking of a pressure rise characteristic can be illustrated by considering the isentropic efficiency relation:

$$\frac{P_2}{P_1}\left[\frac{\eta\Delta H}{C_p T_1}+1\right]^{\gamma/\gamma-1} \quad (1)$$

Clearly the peak occurs where the product of (η ΔH) is maximum. Both efficiency (η) and enthalpy rise (ΔH) can vary with flow in the following manner:

(i) It is an unfortunate fact of nature that compressors have a restricted efficiency range, Fig. 2(*a*), with losses at off design flows due to high incidences, thick boundary layers, and separation.

(ii) Enthalpy change with flow is generally a design variable being a primary function of backsweep and inlet swirl. Enthalpy-flow relations with higher negative gradient (more backsweep and/or inlet swirl) clearly tend to reduce the flow rate at which the product ($\eta\Delta H$) is a maximum and generally introduce greater stability.

The above argument on overall compressor stability can be extended and inferred to the individual components of the compressor (i.e., impeller, diffuser, etc.). That is;

(i) Each component has a pressure rise characteristic, either governed by an efficiency relation, similar to Fig. 2(*a*) (causing the pressure rise characteristic of the component to peak in the manner discussed above) or a pressure recovery characteristic similar to Fig. 2(*b*) (again the characteristic shows a peak).

(ii) The analysis presented by Howell shows that a positive gradient on the pressure rise characteristic of the compressor is a required condition for compressor surge and it is now proposed to extend this to suggest that any component operating at a point on its pressure rise characteristic, with a positive gradient, is potentially unstable (i.e, stalled components cause potential instability).

(iii) Whether the compressor as a whole is caused to surge by the stalled component depends largely on the interaction between stalled and nonstalled components.

2.2 Inducer Incidence. The performance of the inducer is sensitive to incidence and inducer stall will develop if the incidence is too high (as this causes increasing losses with reduced flow). Inducer stall is clearly more dominant if the diffuser causes the inducer to be matched near stall. There

Nomenclature

A = throughflow area
A_g = geometric throat area of channel diffuser
A_w = wetted surface area of semivaneless space
C_p = specific heat at constant pressure
C_v = specific heat at constant volume
E = gradient of nozzle characteristic
E_{net} = net energy (including losses) added to airflow
F_{net} = net rate (including drag, etc.) at which momentum is added to airflow
ΔH = compressor total head enthalpy rise
N_I = number of impeller blades (including splitters)
$N/\sqrt{\theta}$ = corrected rotor rotational speed (rpm)
P = pressure
S = gradient of compressor pressure rise characteristic
SVS = semivaneless space of the vaned diffuser (region between vane leading edge and throat)
T = temperature
U = impeller blade velocity at tip
U = absolute flow velocity (in surge model)
V = volume
W = airflow rate
PRC = pressure rise coefficient in the semivaneless space
γ = ratio of specific heats
δ = $P/14.7$
θ = $T/288$
λ = eigenvalue
η = isentropic efficiency
ρ = density

Subscripts

s = static condition
T = total head condition
1 = inlet conditions
2 = outlet conditions

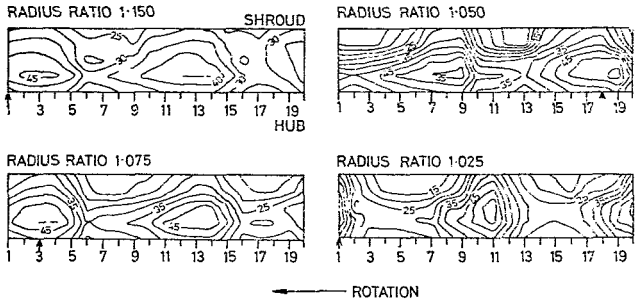

Fig. 4 Radial velocity contours for the flow exhausting from a backswept impeller with raked blade form

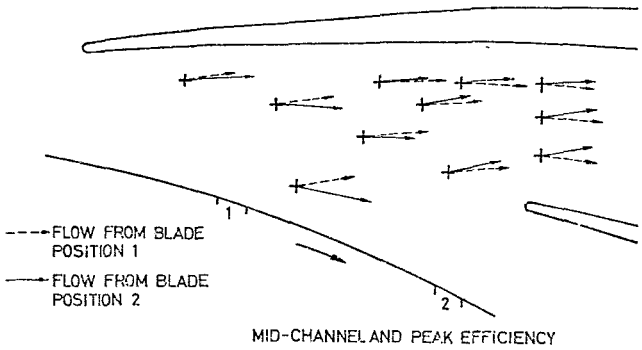

Fig. 6 Velocity vectors in the SVS region at two rotor positions

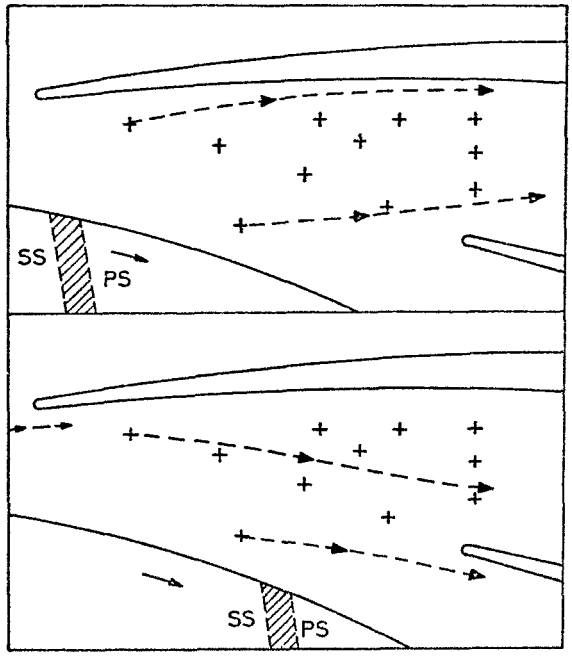

Fig. 5 Flow trajectories in the SVS

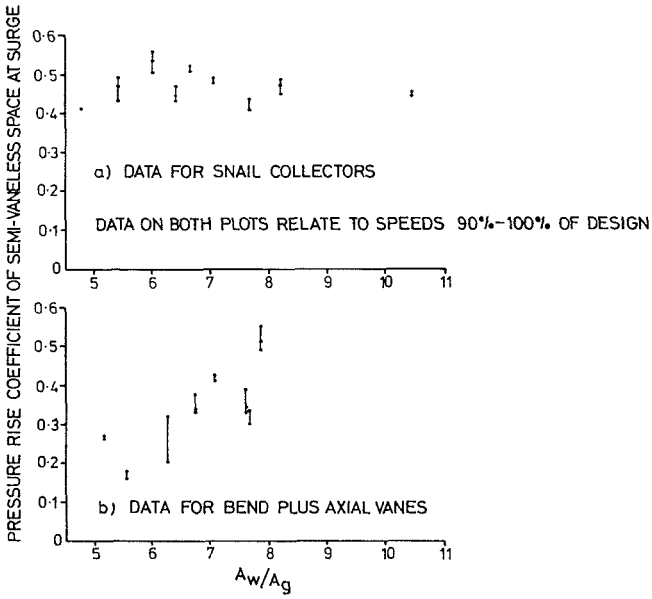

Fig. 7 Surge data from reference [5]

are, however, many instances where mild inducer stall can be tolerated, as can stall of the front stages of a multistage axial compressor. Indeed, the analogy between the inducer and the front stages of the axial machine can be taken further, since, during low-speed operation of a high-pressure ratio machine, it is inducer stall that is more likely to occur. This is a result of low compression in the impeller which results in subsequent throttling in the diffuser due to the higher meridional velocities and lower incidence than would occur at design speed. This throttling in the diffuser region causes low velocities and stalling in the inducer region.

2.3 Impeller Backsweep and Inlet Swirl. The use of inlet swirl and impeller backsweep can both provide a basic improvement in the pressure loss against flow characteristic. This arises because inlet swirl tends to reduce the inlet Mach number and backsweep improves general blade loading. In addition, due to their effect on the Euler equation, both have the effect of increasing the gradient of the $\Delta H/U^2$ characteristic, Fig. 3.

For a similar, or improved, efficiency relation (Fig. 2(*a*)) this tends to decrease the flow at which $\eta\Delta H$ is a maximum, equation (1), and thereby the flow at which the impeller characteristic peaks (stalls).

The advantages of improved blade loading and additional stability have caused blade backsweep to become commonly adopted. The use of inlet guidevanes at moderate inlet Mach numbers is not generally approved because of cost, noise, and icing considerations.

2.4 Number of Impeller and Diffuser Vanes and Flow in the Vaneless Space. It is commonly the case that, for a given rotor at a given speed, surge occurs at a higher flow when the rotor is followed by a vaned diffuser than when it is followed by only a vaneless space. This is partcularly true at high rotational speeds and it is therefore usually concluded that the surge instability is associated with the vaned diffuser. At lower speeds, 50 percent design and lower, vaned and vaneless builds tend to surge at flows closer to one another, when it appears probable that stalling of the inducer could be the driving mechanism for surge.

Various investigations have suggested that the ratio of impeller to diffuser vane number had a bearing on compressor flow range. The philosophy behind the argument, (Rodgers and Sapiro [10] and Came and Herbert [5]), concerns the scale of the wake emerging from the impeller compared to the width or pitch of the vane passage (a small wake and large diffuser vane pitch being desirable). The argument can be extended to suppose diffusers with large blade pitches are less likely to become blocked with high incidence wake flow. Flow leaving the impeller is known to be severely distorted, with large hub to shroud and transient blade to blade variations, and these flows are now being defined with the aid of laser anemometry systems, Elder, Forster, and Gill [11]. The distorted flow has not been found to mix out before the

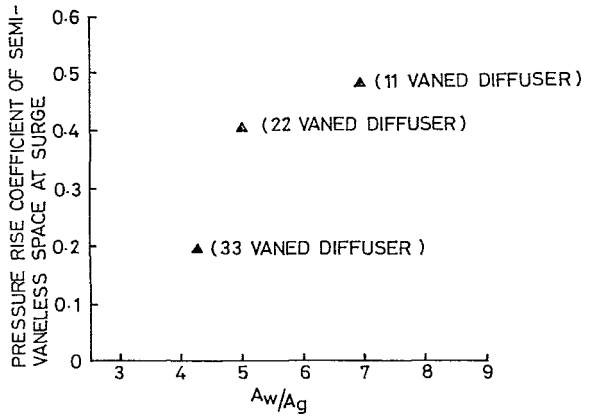

Fig. 8 Pressure rise coefficient in the semivaneless space for a 16 vaned impeller operating with vaned diffuser and snail (or scroll) collector

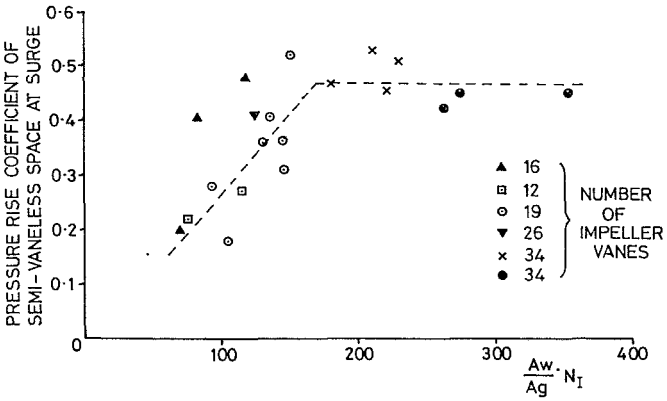

Fig. 9 Revised correlation for SVS pressure recovery at surge

station at which it is usual to site the diffuser leading edge, Fig. 4. Figures 5 and 6 show the transient flow at the diffuser inlet and the flow switching occurring in the semivaneless space as the rotor blade passes. The qualitative effects of this phenomenon are considered in more detail in the next section. The flows are discussed in greater detail in [12]. The vaneless space serves both to reduce the diffuser inlet Mach number and "settle" the flow before encountering the diffuser vane leading edge. The disadvantage of a large vaneless space is the increased boundary layer growth, up to the diffuser throat, and a penalty an overall radial size. A vaned diffuser design must, therefore, be a compromise between these effects.

The importance of rotating stall in the vaneless space and its prediction (Abdelhamid [13]) to the structural integrity of the compressor is most important. The authors feel, however, that since the frequency of surge and rotating stall oscillations are separated often by more than an order of magnitude, rotating stall cannot be the major mechanism for induction of surge. Rather, it is the effect of the stall (whether rotating or not) on the component pressure rise characteristic (Fig. 2), which can lead to instability of the system. The greatest evidence for this is the success of surge prediction models, as presented later in this note, which do not include any "rotation" effects of stall.

2.5 Pressure Recovery in the Semivaneless Space and Incidence on Diffuser Vane Leading Edge. Several authors, e.g., Kenny [1], Dean [14], Japikse [15], and Toyama et al. [16] suggest that vaned diffuser stall is caused by a breakdown in flow in the semivaneless space and Kenny suggested that

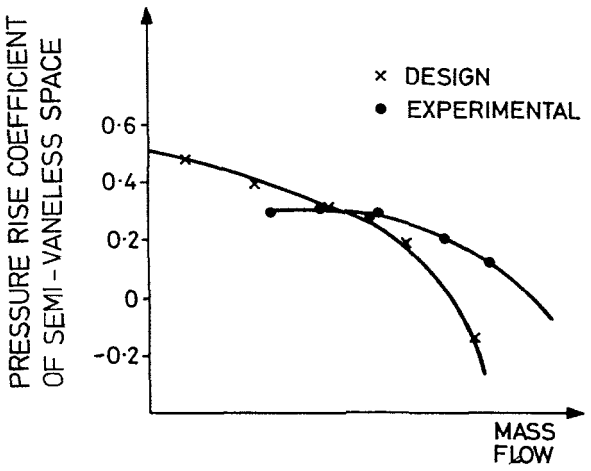

Fig. 10 Comparison of experimental and predicted SVS pressure recovery

there is a critical value ot the pressure rise coefficient of the semivaneless space of the diffuser, (PRC), at surge.

It is widely agreed that the diffuser inlet region is most sensitive and critical for surge and although various models have been proposed for the mechanism of flow breakdown in this region, Dean and Young [4], and references [1], [14], [15], and [16] above, none have accounted satisfactorily for all factors known to affect the process. Came and Herbert [5] and Baghdadi and McDonald [17] develop the argument further, suggesting that the critical pressure rise coefficient is a function of the diffusion length from diffuser inlet to throat.

Came and Herbert [5] suggest that a suitable parameter for defining the diffusion is the ratio 'wetted surface area of the semivaneless space/geometric throat area' ($=A_w/A_g$). These authors studied the relationship between this parameter and the value of PRC at surge, Fig. 7. The result is presented in two parts because there appeared to be different relationships for compressors where the collector was of the snail type and those where the collector included a radial to axial bend.

General comments on the relation are that at higher values of wetted area a value of PRC of 0.5 is typical. In the case of collectors that include a radial to axial bend the value of PRC at surge reduces at smaller wetted area, whereas for those compressors with scroll collectors, this does not appear to happen. It is argued that the larger values of wetted area, which physically infer a larger distance between the leading edge and throat (both for diffusion and the decay of distorted flow profiles) permits a larger value of PRC to be achieved before serious flow breakdown.

Came and Herbert present little explanation for the reason for the separate relations presented for the scroll and radial to axial bend collector systems. The authors of the present paper present still further confusing information in the form of Fig. 8 which shows PRC (calculated in the same way as for Fig. 7) rising with A_w/A_g for a scroll type collector (compare 7(*a*)).

The authors feel that a major parameter being neglected in the above discussion is the scale of any distortion entering the diffuser (relative to the diffuser geometry). Such scale will be largely determined by the number of impeller blades and if an influence coefficient, N_I, (= number of impeller blades, including splitters) is introduced and the data of Figs. 7 and 8 are replotted on the basis of $A_w/A_g \cdot N_I$ a much closer unique relation is obtained, Fig. 9. There is still considerable scatter, but this is to be expected as the correlation is crude and takes no account of blade backsweep, matching, or factors discussed in this paper.

It is perhaps interesting to discuss the usefulness of such a correlation as a design aid. Ultimately, if PRC could be

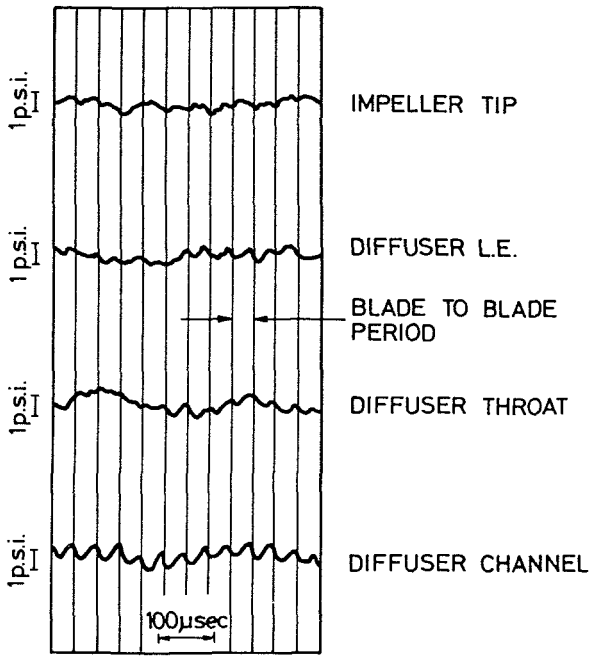

Fig. 11 Static pressure within the diffuser

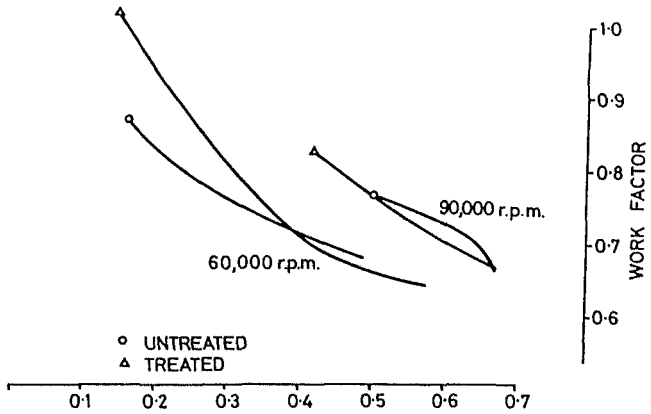

Fig. 12 Effect of casing treatment on work done factor ($\Delta H/U^2$)

defined, then surge flow could be assessed from a design program prior to compressor testing. A typical predicted range for PRC is shown in Fig. 10 together with experimental data. Clearly the design program does not describe the stall process but this is hardly surprising because it takes no account of the complexities shown in Figs. 5 and 6. Even an estimate of PRC at the design stage, however, would be of considerable interest. For a particular computed value of $(A_w/A_g \cdot N_I)$ the correlation shown in Fig. 9 would provide a range of values PRC which when translated on to the relationship shown in Fig. 10 would lead to a large uncertainty in compressor flow range.

Any discussion on this subject should refer to the Baghdadi experiment [2, 17] in which evidence is provided to suggest that rotor blade wakes have no effect on PRC at surge. This can be tolerated in the correlation proposed here because approximate calculations of the correlation variable, $(N_I \cdot A_w/A_g)$, Fig. 9, suggest that the Baghdadi compressor operated above the knee in the correlation and therefore PRC at surge is not increased by increasing the number of impeller blades. If it is assumed that the simulated swirl profile is approximately equivalent to an impeller with a very large number of blades the reported result would be expected.

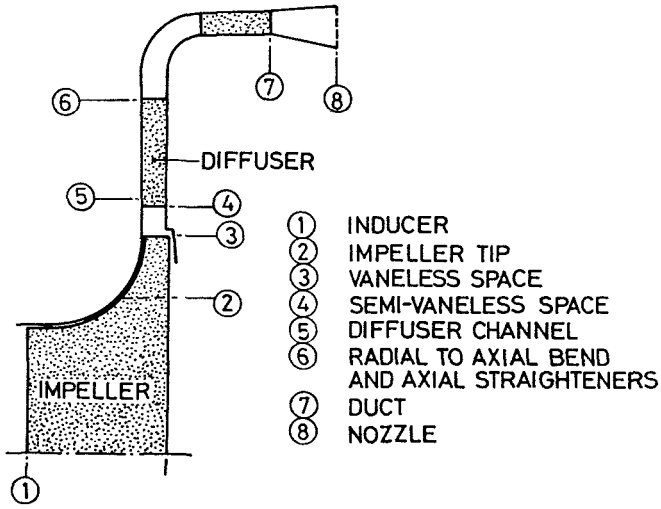

Fig. 13 Elements considered in modelling compressors with vaned diffusers

Diffuser leading edge incidence has been introduced as a factor affecting surge, e.g., Reeves [3]. There is considerable conflicting evidence, however, on this factor and laser anemometry measurements have shown that incidence on the vane leading edge fluctuates considerably due to the jet and wake exhaust from the impeller. While incidence does not appear to be a good correlation parameter on its own, PRC is very dependent upon it, and it can therefore be argued that the effect of diffuser incidence is partly implied in the correlation discussed above.

A further factor shown to affect flow range, Baghdadi and McDonald [17] and Galvas [18], is that of diffuser leading edge Mach number. In general, it would appear that higher Mach numbers provide lower off-design tolerance, i.e., Fig. 2(*b*) becomes less broad. This is yet another factor that will produce scatter in the correlation shown in Fig. 9.

2.6 Diffuser Channel and Collector Type. The diffuser channel performance takes the typical form of Fig. 2(*b*) where large losses are incurred toward choke and stall.

The failure of the channel recovery performance toward surge may be attributed to the deterioration of the inlet flow and increased throat blockage.

This provides the channel with the capability of stall and the inducement of surge. The range of adequate performance will depend on the many parameters well known to designers and the region of operation will depend on impeller-diffuser matching.

The design of channel diffuser has traditionally been achieved using relatively simple steady flow concepts. Detailed studies of fluctuating pressures, however, suggest that the flow switching which occurs at the leading edge, Fig. 5, can cause the flow in the diffuser channel to oscillate, Fig. 11. During studies of the flow in high-speed compressors such results were found to be typical where the time averaged statics indicated steady recovery down the channel.

Some investigators, Came and Herbert [5], also suggest that the collector can affect surge. This would appear perfectly feasible as the collector is an aerodynamic component having a pressure recovery-flow relationship. (For the purpose of discussion here it is assumed that the collector does not impose a distortion on the impeller.) The discussion is restricted to surge inception as distinct from post stall behavior where it is well known, Greitzer [19], that the downstream dynamics play a very large part in defining the system behavior.

The analogy with the multistage axial compressor can again be cited, where surge at high speed coincides with stall of the

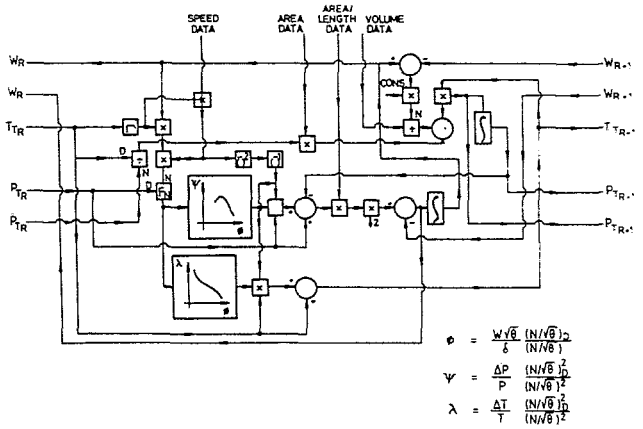

Fig. 14(a) Simplified model for an element

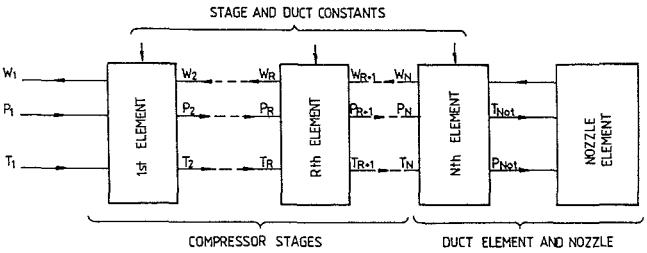

Fig. 14(b) Application of the model to a compression system

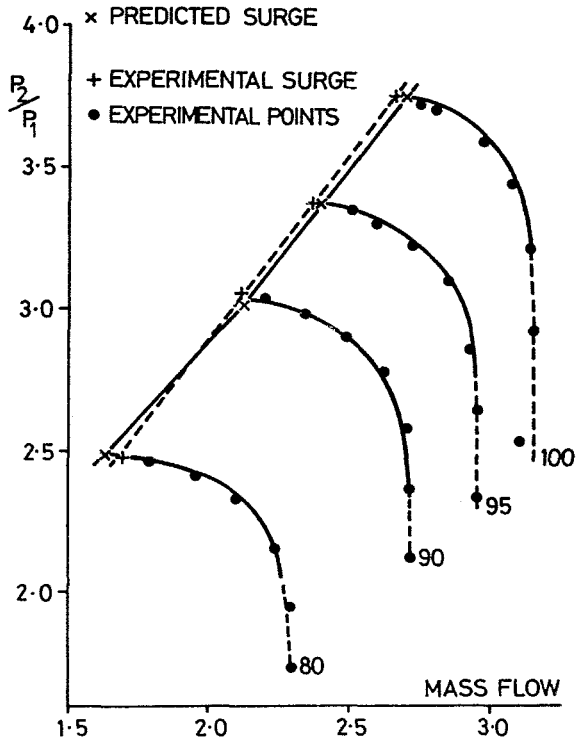

Fig. 15 Surge prediction for a centrifugal compressor

last stage, in that if a stall-prone delivery system is present, this could in principle be the critical element in producing surge.

2.7 Casing Treatments. Casing treatments are known to affect the operating range of centrifugal compressors, Jansen et al. [20], Macdougal and Elder [21]. Simplistically, there are three methods whereby they can achieve this:

(*a*) By improving the basic width of the efficiency contour, Fig. 2(*a*), by improving the flow mechanism.

(*b*) By permitting some recirculation which progessively increases toward surge such that the work done ($\Delta H/U^2$) increases more rapidly toward surge. This causes $\eta\Delta T$ and the pressure rise to peak at a lower mass flow, equation (1).

(*c*) To improve the outlet flow conditions permitting downstream components to operate more efficiently.

Initial studies (21), indicate that (*b*), Fig. 12, can be very much present. It is suggested, therefore, that a major influence of Casing Treatments is to raise the gradient of $\Delta H/U^2$ in much the same way as additional backsweep. The other factors are not discounted but the effect of these are more difficult to locate.

3 Surge Model

The foregoing discussion provides some explanation of surge and the factors that cause it, but fails to quantify the various parameters involved and the effects of their interaction. For these reasons and because some background work on predicting surge in axial flow machines existed, Corbett and Elder [8], it was proposed that a dynamic model be constructed which could both estimate the stalling tendency of the various regions of the compressor and the dynamic interaction between them.

In this model the meridional flow through the compressor is considered. By dividing the compressor into the elements shown in Fig. 13, the principles of conservation of mass, energy, and linear momentum are applied to the flow.

The conservation equations, in their integral form are:

Continuity:

$$\int_1^2 \frac{\partial \rho}{\partial t}\, dV = W_1 - W_2 \tag{2}$$

Linear Momentum:

$$\int_1^2 \frac{\partial}{\partial t}(\rho \mathbf{U}) dV = [W\mathbf{U} + p_s\mathbf{A}]_1 - [W\mathbf{U} + p_s\mathbf{A}]_2 + \mathbf{F}_{\text{net}} \tag{3}$$

Energy:

$$\int_1^2 \frac{\partial}{\partial t}[\rho(C_v T_s + U^2/2)] dV = C_p[(T_T W)_1 - (T_T W)_2] + E_{\text{net}} \tag{4}$$

where F_{net} is the effective force acting within the element (blade forces, loss drags, etc) and E_{net} must account for the rate of energy transfer to the airstream.

The application of these equations to the centrifugal compressor differs from that to multistage axial compressors [8] in that certain approximations have to be changed.

In the multistage axial compressor, each stage is taken as an element, and equations (2–4) applied across the stage. This allowed two assumptions to be made, firstly that the flow direction at element boundaries is approximately axial (and hence the problem is one-dimensional) and secondly that interstage Mach numbers are relatively low (and the momentum equation can be considerably simplified).

To realistically model the meridional path through the centrifugal compressor, (Fig. 13), where flow direction is initially axial, is turned to radial at impeller tip and may be returned to axial after the diffuser, the three components of the linear momentum equations are considered. By combining these in an appropriate manner, the order of the problem can be returned to that of the axial compressor case. The assumption of low Mach numbers at element boundaries made for the axial compressor is obviously not valid for the

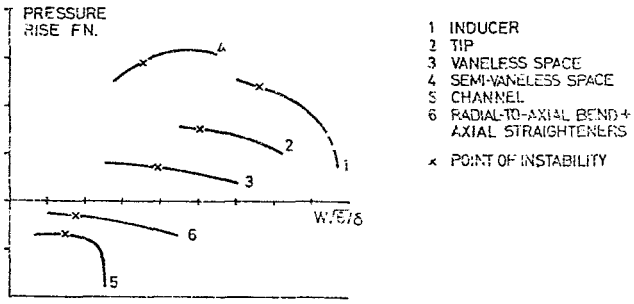

Fig. 16 Element characteristics for the compressor shown in Fig. 15

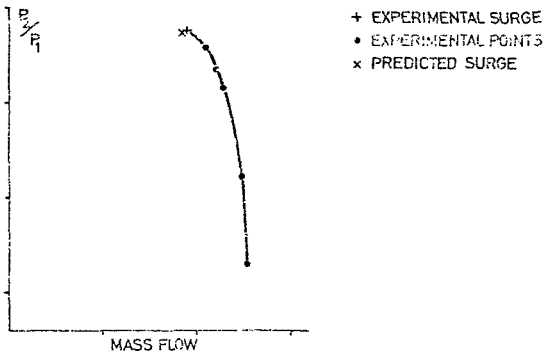

Fig. 17 Surge prediction for a medium pressure ratio machine

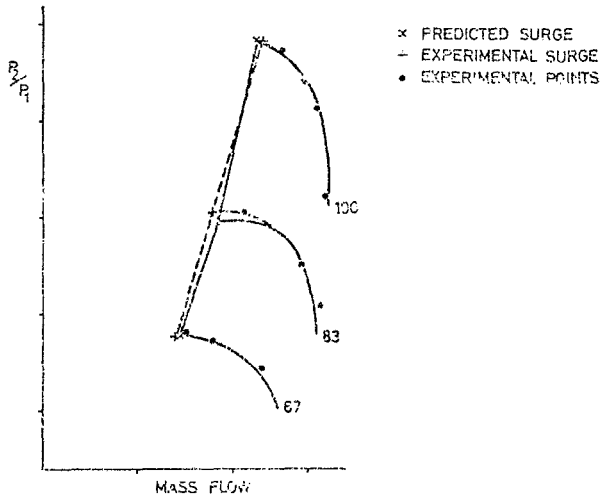

Fig. 18 Surge prediction for a vaneless build

centrifugal compressor, especially at the impeller tip. Hence the simplification made previously to express the momentum equation in terms of total pressures is now more complicated, and both static and total pressures appear in the final form of the momentum equation.

Including these simplifications discussed above equations (2–4) now present two major difficulties: firstly the evaluation of the integral terms which requires the distribution of variables (to be integrated) between station 1 and 2, and secondly, the definition of E_{net} and F_{net}.

For steady flows the terms E_{net} and F_{net} can be defined quite simply by putting the L.H.S. of equations (2–4) to zero (i.e., no transient terms). In this manner the steady state forms of F_{net} and E_{net} can be defined from experimental or design data and the argument can be extended such that F_{net} and E_{net} can be expressed (usually graphically) in the unique form:

$$(F_{net})_{ss} = f_1(W\sqrt{\theta}/\delta, N/\sqrt{\theta})$$
$$(E_{net})_{ss} = f_2(W\sqrt{\theta}/\delta, N/\sqrt{\theta}) \quad (5)$$

Where the element does not contain any rotating component the factor $N/\sqrt{\theta}$ is not required and E_{net} can be taken as zero. Equation (5) defines F_{net} and E_{net} for steady flow in terms of inlet flow conditions. It is now assumed that each element of the compressor responds in a quasi-steady manner such that equations (2–4) are valid when F_{net} and E_{net} are replaced by their "steady-state" equivalents, the instantaneous values of F_{net} and E_{net} being obtained from equation (5) using the instantaneous inlet flow conditions. Hence the terms E_{net} and F_{net} are replaced with known terms, albeit with frequency limitations.

The definition of terms under the integral between stations 1 and 2 has been achieved by assuming a linear distribution between the stations. This reduces the equations from a partial differential form to an ordinary differential form which can much more readily be solved.

Further simplifying assumptions are made to facilitate a solution. These include neglecting certain Mach number terms and the dynamic terms on the L.H.S. of the energy equation, (past experience has suggested that this term has little effect on stability). It is also assumed that pressure and density transients are isentropically related.

The system has now been reduced to a set of nonlinear ordinary differential equations that can be solved by computer simulation techniques, Elder [22].

A simpler technique that has been employed for the centrifugal compressor is to linearize the equations and perform a small perturbation analysis. The resulting equations are only valid for small perturbations from the steady-state conditions, but they can be used to define the stability of the system, i.e., whether the perturbation will increase in size or decay. The technique is applied such that the various elements, Fig. 13, are stacked to operate at their respective conditions. Figure 14(*a*) shows how the computations for each element are completed and Fig. 14(*b*) the manner in which the variables existing between elements are transferred. In this manner parameters computed from the equations for one element become the input parameters to adjacent elements. The nozzle section shown is a special element and an appropriate characteristic relating the nozzle flow to pressure ratio and area has to be used.

The time-dependent solution of the linear equations resulting from the small perturbation analysis is a linear combination of terms of the type $A_i \exp(\lambda_i t)$ where λ_i is the ith eigenvalue of the system. In general, λ_i, are complex and the presence of any λ_i with a positive real part corresponds to a solution that increases with time. Hence, the system is said to be unstable if any eigenvalue exists with a positive real part. The objective is to associate this numerical instability with test compressor surge conditions.

The results of such an analysis are shown in Fig. 15, where the compressor was divided into the elements shown in Fig. 13, and the data for F_{net} and E_{net} obtained experimentally. The agreement with experimental surge is encouraging and the element pressure characteristics, shown in Fig. 16 suggest the stalling element to be the semivaneless space, closely followed by the channel diffuser.

Figure 17 shows another result for a higher pressure ratio machine and Fig. 18 the result for a vaneless build where it was noted that stall occurred within the vaneless diffuser.

Only a brief description of the models is presented here but in general results were found to be encouraging. Difficulties have been encountered, however, particularly where the system characteristics have been uncertain and in general higher pressure ratio compressors were found to be more difficult to model than those operating at lower pressure ratios. It is interesting to note that all element characteristics

used were continuous without the abrupt changes shown by Jansen [20]

An area of direct application of such models is in the study of the effects of parametric changes on the system. In such studies the effect of scroll type collectors was investigated. These studies suggested that in the case considered, the collector type had little influence on surge, the collector losses being small and generally sufficiently remote from the surge inducing process in the SVS. This supposes that no circumferential distortion was imposed by the collector system.

In the case of the high-speed, vaned diffuser configurations considered it was always the SVS region which prompted surge. This would agree with the many observations already quoted. In this context it is suggested that the correlation shown in Fig. 9 is a correlation of situations in which SVS stall was sufficiently severe to promote surge. If another element of the compressor (impeller or channel diffuser, etc.) effects the surge process, e.g., by stalling (as commonly suggested and as indicated by the model) then the operation of that element should effect PRC at surge. This is probably a reason for scatter shown in Fig. 9.

It is not proposed therefore that there is any fundamental qualitative disagreement between the correlation and the dynamic model – only that there is difference in the degree of sophistication.

4 Conclusions

The process of surge in a centrifugal compressor has been studied and found to be dependent on a number of complex and often interrelated factors.

A major factor for surge in high-speed, vaned diffuser designs was the flow in the semivaneless space. By developing work initiated by others it has been possible to propose a simple criterion for the pressure recovery within the semivaneless space at surge. Considerable scatter exists in the correlation which, it is proposed, arises from its simplicity.

In addition a more complex mathematical model capable of assessing additional factors is proposed. Using this model good agreement with experimental surge has been obtained. This model takes into consideration pressure losses in the impeller, diffuser and collector, and by using this model it was possible to identify the stalling elements that are responsible for overall compressor instability.

5 Acknowledgments

The authors would like to thank the many persons who have contributed to the project. The people involved are too numerous to mention but the organizations include, Holset Engineering, Imperial Chemical Industries, National Gas Turbine Establishment, Plessey Aerospace, and Rolls Royce.

References

1 Kenny, D. P., Lectures on the Radial Compressor, Von Karman Institute, Brussels, May 1972.

2 Baghdadi, S., "The Effect of Rotor Blade Wakes on Centrifugal Compressor Diffuser Performance—A Comparative Experiment," ASME *Journal of Fluids Engineering*, Mar. 1977, pp. 45–52.

3 Reeves, G. B., "Estimation of Centrifugal Compressor Stability with Diffuser Loss Range System," ASME *Journal of Fluids Engineering*, Mar. 1977, p. 76–83.

4 Dean, R. C. Jr., and Young, L. R., "The Time Domain of Centrifugal and Pump Stability and Surge," ASME *Journal of Fluids Engineering*, Mar. 1977, pp. 53–63.

5 Came, P. M., and Herbert, M. V., "Design and Experimental Performance of Some High Pressure Ratio Centrifugal Compressors," AGARD, Conference Proceedings No. 282, Paper 15, 1980.

6 Kuhlberg, J. F., Sheppard, D. E., King, E. O., and Baker, J. R., "The Dynamic Simulation of Turbine Engine Compressors, AIAA 5th Propulsion Joint Specialist Conference, Paper 69–486, June 1969.

7 Willoh, R. G., and Seldner, K., "Multistage Compressor Simulation Applied to the Prediction of Axial Flow Instabilities," NASA TM X-1880, Sept. 1969.

8 Corbett, A. G., Elder, R. L., "Mathematical Modelling of Compressor Stability in Steady and Unsteady Flow Conditions," AGARD Conference Proceedings No. 177, Paper 12, Sept. 1973.

9 Howell, W. T., "Stability of Multi-stage Axial Flow Compressors," *The Aeronautical Quarterly*, Nov. 1964, Vol. 15, pp. 328–356.

10 Rodgers, C., and Sapiro, L., "Design Considerations for High Pressure Ratio Centrifugal Compressors," ASME Paper 72-GT-91, 1972.

11 Elder, R. L., Forster, C., and Gill, M. E., "Initial Findings during Studies of the Flow Within a High Speed Impeller Using a Transit Anemometer," Fourth International Conference on Photon Correlation Techniques in Fluid Mechanics, Stanford University, Aug. 1980.

12 Elder, R. L., Forster, C., and Gill, M. E., "Flow in Vaned and Vaneless Builds of Centrifugal Compressor Stages," Contract Report, Cranfield (Restricted Data), Dec. 1982.

13 Abdelhamid, A. N., "Analysis of Rotating Stall in Vaneless Diffusers of Centrifugal Compressors," ASME Paper 80-GT-184, Mar. 1980.

14 Dean, R. C. Jr., "Fluid Dynamics Design of Advanced Centrifugal Compressors," Lecture Note. Von Karman Institute, Lecture Series 50, May 1972.

15 Japikse, D., "The Influence of Diffuser Inlet Pressure Fields on the Range and Durability of Centrifugal Compressor Stages," AGARD Conference Proceedings, No. 282, Paper 13, 1980.

16 Toyama, K., Runstadler, P. W. Jr., and Dean, R. C. Jr., "An Experimental Study of Surge in Centrifugal Compressors," ASME *Journal of Fluid Engineering*, Mar. 1977, pp. 115–131.

17 Baghdadi, S., and McDonald, A. T., "Performance of Three Vaned Radial Diffusers with Swirling Transonic Flow," ASME *Journal of Fluids Engineering*, June 1975, p. 155.

18 Galvas, M. R., "Fortran Program for Predicting Off-Design Performance of Centrifugal Compressor," NASA Technical Note TN D-7487, 1973.

19 Greitzer, E. M., "Surge and Rotating Stall in Axial Flow Compressors. Part I and II," ASME JOURNAL OF ENGINEERING FOR POWER, Apr. 1976, p. 190.

20 Jansen, W., Carter, A. F., and Swarden, M. C., "Improvements in Surge Margin for Centrifugal Compressors," AGARD Conference Proceedings, No. 282, Paper 19, 1980.

21 MacDougal, I, and Elder, R. L., "The Improvement of Operating Range in Small High Speed Centrifugal Compressors using Casing Treatments," I. Mech. E. Conference Proc. *Turbocharging and Turbochargers*, 1982.

22 Corbett, A. G., and Elder, R. L., "Stability of an Axial Flow Compressor with Steady Inlet Conditions," *Journal of Mechanical Engineering Science*, Vol. 16, No. 6, 1974, pp. 377–385.

A Theoretical Model for Rotating Stall in the Vaneless Diffuser of a Centrifugal Compressor

P. Frigne
CERAC, CH-1024
Ecublens, Switzerland

R. Van den Braembussche
von Karman Institute
for Fluid Dynamics,
B-1640 Rhode Saint
Genèse, Belgium

A theoretical model for rotating stall in the vaneless diffuser of a centrifugal compressor is presented. It consists of a time-evolutive calculation of the strong interaction between the inviscid flow core and the unsteady boundary layers along the walls. It is shown that, depending on the diffuser geometry and the diffuser inlet flow angle, a transient perturbation of the outlet static pressure will generate a rotating flow pattern, if the periodicity of this perturbation corresponds to the experimentally observed number of cells. The relative rotational speed and the phase relation between the velocity and the flow angle variations are also in agreement with experimental data.

Introduction

Different types of subsynchronous rotating self-excited flow oscillations can occur in centrifugal compressors with a vaneless diffuser.

It has been shown experimentally [1] that distinction can be made between three groups of rotating stall patterns, depending on the origin of the destabilization process. Group I consists of diffuser-induced instabilities which can be detected only downstream of the impeller. Typical are the low relative propagation speed, varying between .10 and .20, and the moderate amplitude of the velocity fluctuations. Groups II and III are respectively due to an "abrupt" and "progressive" destabilization of the flow in the impeller, and the generated flow oscillations can be detected both up- and downstream of the impeller. This study is limited to diffuser rotating stall defined by Group I.

Several theories have been presented in the literature to explain the diffuser rotating stall phenomenon [2–8]. All these theories are restricted to the calculation of a stability limit for the diffuser flow. None allows for a continued calculation under unsteady operating conditions. For the inviscid models [3, 8], the amplitude of the oscillations would increase to infinity as the equations of motion have been linearized. The three-dimensional boundary layer models [4–7] are only valid for steady and axisymmetric flows.

In contrast to all previous approaches, the theoretical model presented here consists of a real nonlinear time-evolutive calculation of the diffuser rotating stall phenomenon.

Contributed by the Gas Turbine Division of THE AMERICAN SOCIETY OF MECHANICAL ENGINEERS and presented at the 29th International Gas Turbine Conference and Exhibit, Amsterdam, The Netherlands, June 4–7, 1984. Manuscript received at ASME Headquarters January 18, 1984. Paper No. 84-GT-204.

Basic Hypothesis

In spite of the simple geometry, the flow in a vaneless diffuser of a centrifugal compressor reaches a high level of complexity:

- At the impeller discharge a strong distortion exists both in axial and tangential direction, resulting in asymmetric and unsteady inlet conditions for the diffuser.
- Due to the adverse pressure gradient, a three-dimensional boundary layer separation is likely to occur when the inlet flow angle reaches a critical value.
- The inviscid flow core is reaccelerated by the obstruction of the wall boundary layers, which in turn are affected by the dynamic behavior of the inviscid flow. For this reason, this viscous-inviscid interaction should be considered as a strong one.
- At some distance downstream of the diffuser inlet, the boundary layers will merge and fully developed flow exists.
- If the diffuser is discharging into a scroll-type outlet collector, a tangential static pressure gradient exists at off-design conditions, which creates an important flow distortion.

Many simplifications have to be made in order to obtain a model which can be solved mathematically. The basic hypothesis is that the dynamic characteristics for the oscillatory flow motion are produced by the inviscid flow core. The boundary layers along the diffuser walls act as destabilizing influences. In this way, the necessary conditions to generate self-excited oscillations are fulfilled, namely the presence of both a source of excitation and a response system. Diffuser rotating stall is then generated as a two-dimensional, unsteady and strong interaction between the inviscid flow field and the wall boundary layers. This interaction occurs through a variation in space and time of the diffuser aerodynamic blockage.

In the following chapters, we will discuss separately the different components of the model for diffuser rotating stall. First the unsteady equations of motion for the inviscid flow field in a vaneless radial diffuser are derived. In order to

account for the dynamic boundary layer blockage, the free section height is variable in time and space. The inlet conditions of the inviscid flow field require the development of a model for the impeller response to the downstream pressure fluctuations, which is done in a following chapter. The free-flow section is calculated from an unsteady integral boundary layer theory. As a test case, the strong interaction with a one-dimensional external flow field is investigated.

In a last chapter, the extension to a two-dimensional external flow field is realized by applying the theory of the one-dimensional strong interaction along instantaneous streamlines. The validity of the model is then shown by some test calculations.

The Inviscid Flow Field With Dynamic Contraction

Equations of Motion. The inviscid flow core in a vaneless radial diffuser can be analyzed in a cylindrical coordinate system by means of the two-dimensional, incompressible and unsteady Euler equations, with dynamic contraction terms to account for the unsteady boundary layer blockage effects.

The obstruction due to momentum deficit is taken equal to the obstruction due to the displacement thickness. With the previous assumptions, it can be shown that the inviscid flow can be described by the following set of equations

$$(S_1)\begin{cases} \text{Vorticity transport equation:} \\ \dfrac{\partial \zeta}{\partial t} + V_R \dfrac{\partial \zeta}{\partial R} + \dfrac{V_\theta}{R}\dfrac{\partial \zeta}{\partial \theta} + D\zeta = 0 \qquad (1) \\ (S_2)\begin{cases} \text{Vorticity definition equation:} \\ \dfrac{\partial V_\theta}{\partial R} - \dfrac{1}{R}\dfrac{\partial V_R}{\partial \theta} + \dfrac{V_\theta}{R} = \zeta \qquad (2) \\ \text{Continuity equation:} \\ \dfrac{\partial V_R}{\partial R} + \dfrac{1}{R}\dfrac{\partial V_\theta}{\partial \theta} + \dfrac{V_R}{R} \\ = -\dfrac{1}{h}\left(\dfrac{\partial h}{\partial t} + V_R \dfrac{\partial h}{\partial R} + \dfrac{V_\theta}{R}\dfrac{\partial h}{\partial \theta}\right) \qquad (3) \end{cases} \end{cases}$$

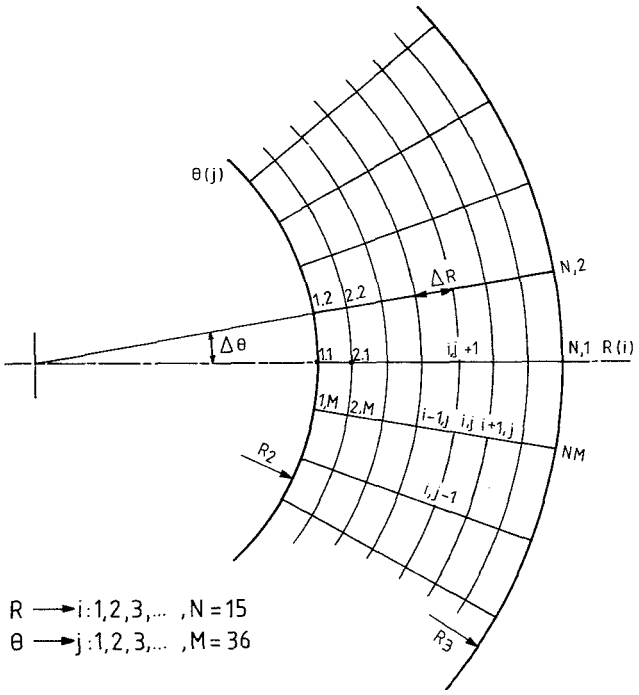

Fig. 1 Discretized computational domain in a radial vaneless diffuser

The dilatation term, D, in the vorticity transport equation represents the divergence of the velocity vector and is equal to the left-hand side of the continuity equation.

Numerical Analysis. The set (S_1) is of mixed hyperbolic elliptic nature. It consists of the hyperbolic vorticity transport equation (1) and an elliptic set (S_2) with characteristic directions $\pm J/R$. The system (S_1) cannot be written in a time-evolutive form and, consequently, no direct time-marching procedures are possible.

It is solved by an integration in time of the vorticity transport equation, while at each time level the velocity field is calculated from the elliptic set (S_2). Iterations will be required to achieve equilibrium for each time step as the coefficients of the vorticity transport equations are determined by the solution of (S_2) and the right-hand side of (S_2) depends on the

Nomenclature

b = vaneless diffuser width
C_F = wall friction coefficient
C_E = entrainment coefficient
DF = impeller diffusion factor
H = form factor (δ^*/θ)
H_1 = form factor ($(\delta - \delta^*)/\theta$)
h = free-stream section height
J = imaginary unit
L = length of the impeller blades
m = tangential periodicity of rotating flow oscillation
p = static pressure
p_0 = total pressure
R = radius
s = distance along streamline
t = time
T = period
u_1 = external longitudinal velocity
V = absolute velocity
W = relative velocity
α = absolute flow angle, from radial
β = relative flow angle, from radial
δ^* = displacement thickness
ζ = vorticity
θ = momentum thickness
λ = relaxation parameter
ρ = density
τ = relaxation time or time constant
ω_s = angular speed of the rotating stall pattern
Ω = angular speed of the impeller

Coordinates

R = radial direction
θ = tangential direction
s = coordinate along streamline

Subscripts

$i = 1, \ldots, N$ = discretization index in R-direction
$j = 1, \ldots, M$ = discretization index in θ-direction
k = time index
0 = inlet plenum
1 = impeller inlet
2 = impeller outlet = diffuser inlet
3 = diffuser outlet
ss = steady state

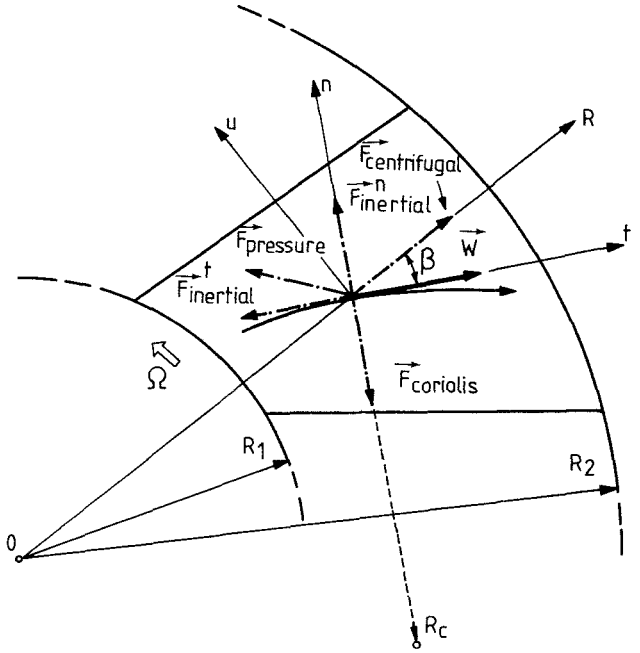

Fig. 2 Dynamic equilibrium of forces acting on an elementary flow volume in a radial impeller

solution of the vorticity transport equation and also on the boundary layer response.

The computational domain is discretized as shown in Fig. 1. It is periodic in tangential direction, and a periodicity condition has to be introduced for all variables.

The Vorticity Transport Equation. It has been shown [9] that numerical stability at the inlet boundary of the diffuser can only be achieved if the vorticity transport equation is discretized with an implicit scheme. The following fully implicit scheme is unconditionally stable

$$\zeta_{i,j}^{k+1} = \zeta_{i,j}^{k} - \frac{\Delta t}{2\Delta R} V_{R_{i,j}}^{k+1} \left(\zeta_{i+1,j}^{k+1} - \zeta_{i-1,j}^{k+1} \right)$$

$$- \frac{\Delta t}{2R_i \Delta\theta} V_{\theta_{i,j}}^{k+1} \left(\zeta_{i,j+1}^{k+1} - \zeta_{i-1,j}^{k+1} \right) - \Delta t D_{i,j}^{k+1} \zeta_{i,j}^{k+1} \qquad (4)$$

However, the accuracy is only of first order in time. Therefore, the time step Δt is limited by numerical viscosity effects.

For our implicit scheme, all variables $\zeta_{i,j}^{k+1}$ at the new time level $k+1$ must be solved simultaneously. Equation (4) represents thus a set of $(N-1)M$ equations with as many variables. For reasons of computer memory and convergence, the iterative solution method of Southwell (SOR) has been used.

The Elliptic Set (S_2). The set of first-order partial differential equations (S_2) can be written in canonical form

$$L(w) = A\frac{\partial w}{\partial R} + B\frac{\partial w}{\partial \theta} + C \bullet w + D = 0 \qquad (5)$$

with

$$w = \begin{pmatrix} V_R \\ V_\theta \end{pmatrix}$$

The elliptic nature of this system requires a discretization with central differences.

If this scheme is solved with a SOR-type iterative method, no convergence will be obtained. It can be shown [9] that this would be equivalent to the explicit Euler scheme, which is always unstable.

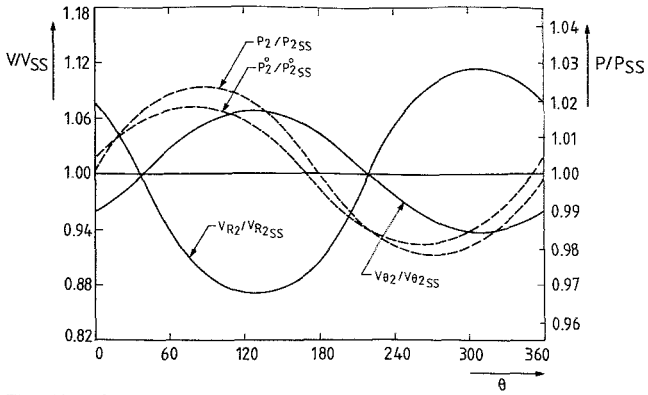

Fig. 3(a) Impeller response to a sinusoidal distortion of the outlet static pressure

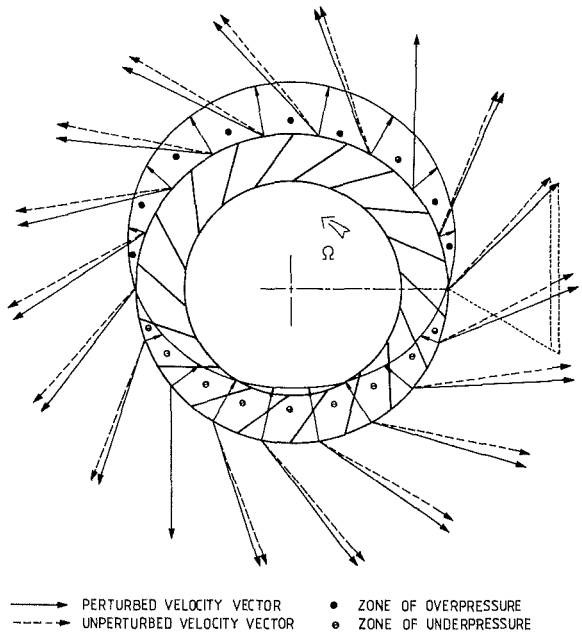

Fig. 3(b) Impeller response to a sinusoidal distortion of the outlet static pressure

Wirz [10] has developed a three-step relaxation scheme, which can be applied to a set of first-order elliptic equations. The system (5) is then transformed into

$$\frac{\partial \tilde{w}}{\partial t} + L(w) = 0; \quad \frac{\partial \hat{w}}{\partial t} + L(\tilde{w}) = 0;$$

$$\frac{\partial w}{\partial t} + \lambda^2 L(\tilde{w}) + \frac{1}{\tau}(w - \hat{w}) = 0 \qquad (6)$$

with

$\tilde{w}, \hat{w}$ = auxiliary variables, with the same boundary conditions as w
λ = relaxation parameter
τ = relaxation time

The stability limits of the three-step relaxation scheme are calculated in [9]. From the reciprocal rate of convergence, defined by Young [11], one can show that this scheme has a second-order convergence rate.

The Impeller Response

The impeller response to downstream pressure fluctuations is calculated assuming incompressible, inviscid and two-dimensional flow in a plane orthogonal to the impeller axis. The different forces acting on an elementary flow volume in a

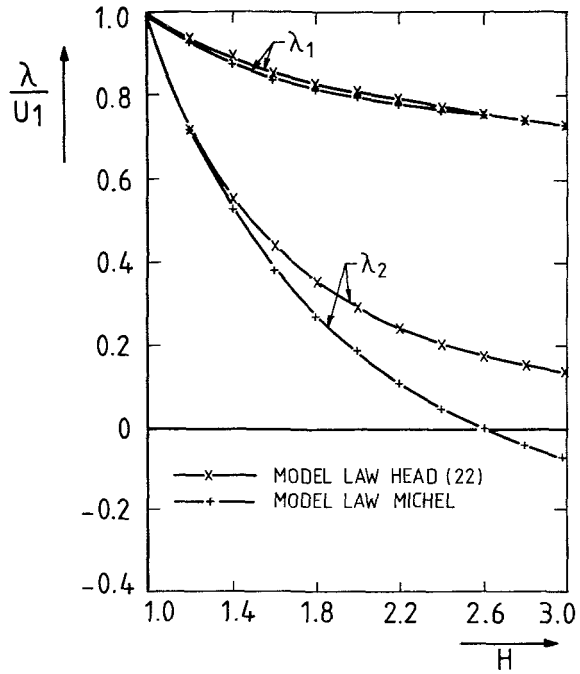

Fig. 4 Comparison of the influence of different closure relations on the characteristic directions of the hyperbolic system (23)

relative reference frame are shown in Fig. 2. The equilibrium in a direction tangent to a streamline can be expressed as

$$\frac{1}{\rho}\frac{\partial p}{\partial s} = \Omega^2 R\cos\beta - \frac{1}{2}\frac{\partial W^2}{\partial s} - \frac{\partial W}{\partial t} \tag{7}$$

This equation is integrated over the pitch and span of the blade passage, and only the global transfer function between inlet and outlet of the impeller is considered. However, circumferential variations are taken into account if the wavelength of these variations is significantly larger than the blade pitch.

For a radial impeller with straight blades and no slip effects, the transfer equation in the absolute reference system is given by

$$\frac{\partial V_{R_2}}{\partial t} + \frac{U_2}{R_2}\frac{\partial V_{R_2}}{\partial \theta} = \frac{2DF\cos\beta_2}{L(1+DF)}\left(U_2 V_{\theta_2} - U_1 V_{\theta_1} + \frac{p_1^0 - p_2}{\rho} - \frac{V_{R_2}^2 + V_{\theta_2}^2}{2}\right) \tag{8}$$

If the distribution of the outlet static pressure p_2 is imposed, the evolution of the radial velocity component V_{R_2} can be determined from a time-evolutive integration of equation (8). This integration has been performed with a single step explicit Lax-Wendroff scheme [12]. However, for the complete diffuser rotating stall model, an implicit formulation will be required.

The tangential velocity component V_{θ_2} is calculated from the velocity triangle at the impeller outlet assuming a constant relative flow angle.

As an example, the impeller response to a stationary sinusoidal distortion of the outlet static pressure is calculated. Figure 3(*a*) gives the steady-state solution of the distribution of the pressure and velocity components. Figure 3(*b*) shows the perturbed and unperturbed velocity vectors. It can be seen that, due to inertia effects, a phase shift of approximately 30 deg is created between the neutral point of the pressure distortion and the neutral velocity vector.

The Dynamic Boundary Layer Obstruction Theory

The Entrainment Theory for Unsteady Turbulent Boundary Layers.

Limited computer memory and computational time impose an integral approach. Further assumptions are

- Incompressibility
- Two-dimensional turbulent boundary layers
- Local similarity [13]
- One parameter family velocity profiles

According to Schlichting [14], the unsteady form of the boundary layer momentum integral equation is

$$\frac{\partial u_1 \delta^*}{\partial t} + u_1^2\left(\frac{\partial \theta}{\partial s} + \frac{1}{u_1}\frac{\partial u_1}{\partial s}(H+2)\theta - \frac{1}{2}C_F\right) = 0 \tag{9}$$

with $u_1(s,t)$ = external velocity.

An auxiliary equation is required to determine the evolution of the form factor $H = \delta^*/\theta$. The entrainment approach is well suited to describe the mass transfer by turbulent mixing between boundary layers and inviscid flow field. Cousteix et al. [15] propose the following expression for the unsteady entrainment equation

$$\frac{1}{u_1}\frac{\partial \delta}{\partial t} + \frac{1}{u_1}\frac{\partial}{\partial s}(u_1(\delta - \delta^*)) = C_E \tag{10}$$

For the wall friction coefficient C_F, the Ludwieg-Tillmann relation is used

$$C_F = -.246 R_\theta^{-.268} 10^{-.678H} \tag{11}$$

The entrainment coefficient is determined from a correlation, which is based on experimental data of Schubauer and Klebanoff [16]:

$$C_E = \frac{.0335H - .0248}{2.61 - .61H} \tag{12}$$

To determine the solutions completely, a closure relation is still required, which gives the form factor $H_1 = (\delta - \delta^*)/\theta$ in function of H. The model law of Head [17] has been selected

$$H_1 = \frac{2H}{H-1} \tag{13}$$

By combining equations (9, 10, 13) the complete unsteady boundary layer problem can be transformed into a first-order partial differential system

$$(S_3)\frac{\partial}{\partial t}\begin{bmatrix}\theta\\ \delta^*\end{bmatrix} + A\frac{\partial}{\partial s}\begin{bmatrix}\theta\\ \delta^*\end{bmatrix} = B\frac{\partial u_1}{\partial t} + C\frac{\partial u_1}{\partial s} + D \tag{14}$$

The characteristic directions of this system are

$$\lambda_{1,2} = \left.\frac{ds}{u_1 dt}\right|_{1,2} = \frac{H+1}{4H^2}\left((H+1) \pm (H-1)\sqrt{1 + \frac{4H}{(H+1)^2}}\right) \tag{15}$$

Figure 4 shows the characteristic directions in function of H. They are always real and positive and the system is therefore hyperbolic. Information will always be carried downstream.

Flow separation cannot be predicted. This is mainly due to the simplified wall friction law (11) and closure relation (13). A better approximation could be obtained with the closure relation of Michel et al. [18].

The corresponding characteristic directions are also shown in Fig. 4. In this case, a singularity will occur in the solution of (S_3) for $H = 2.4$, as the eigenvalue becomes negative. This can only be overcome if an inverse solution technique is used, which, however, would increase significantly the complexity of the problem and has therefore not been considered.

The One-Dimensional Unsteady Interactions.

The calculation procedure for the strong interaction of the unsteady boundary layers and the inviscid flow core is first

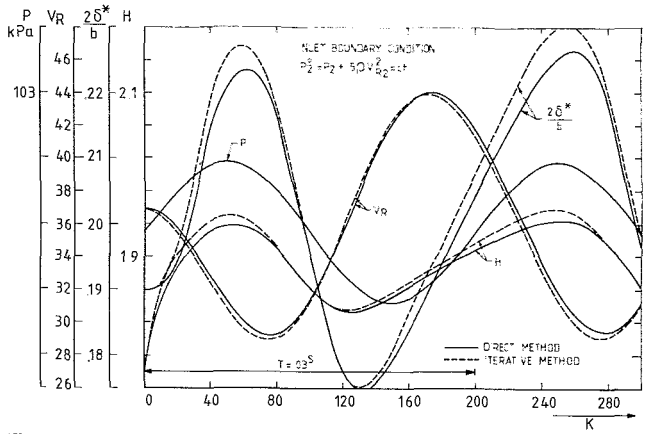

Fig. 5 Evolution of the flow characteristics at the outlet of a vaneless radial diffuser for a one-dimensional strong interaction calculation

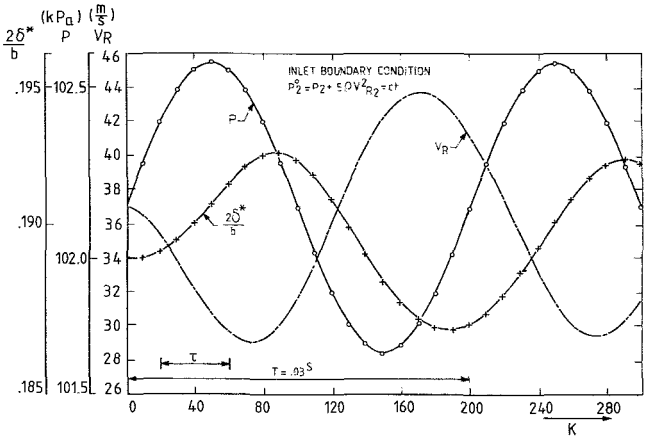

Fig. 6 Evolution of the flow characteristics at the outlet of a vaneless radial diffuser for a one-dimensional quasi-unsteady interaction calculation

tested with a simplified model of a one-dimensional radial flow in a radial vaneless diffuser. The calculation is performed for a given unsteady outlet static pressure with a constant total pressure at the inlet. The wall boundary layers are described by (S_3). For the inviscid radial flow field, the equations reduce to

$$(S_1')\quad \begin{cases} \dfrac{\partial V_R}{\partial R}+\dfrac{V_R}{R}=-\dfrac{1}{h}\left(\dfrac{\partial h}{\partial t}+V_R\dfrac{\partial h}{\partial R}\right) & \text{(continuity)} \quad (16) \\ \dfrac{\partial V_R}{\partial t}+V_R\dfrac{\partial V_R}{\partial R}=-\dfrac{1}{\rho}\dfrac{\partial p}{\partial R} & (R\text{-momentum}) \quad (17) \end{cases}$$

The coupling relations are

$$h=b-2\delta^*;\quad u_1=V_R;\quad s=R-R_2$$

Both systems (S_1') and (S_3) have to be solved simultaneously. From the numerical point of view, this implies that the right-hand side forcing terms of the discretized systems have to be expressed implicitly.

The advantage of this simplified, one-dimensional model is the existence of a direct method of solution. This direct method cannot be extended towards a two-dimensional strong interaction problem but it does allow the verification of the iterative method used for the complete model. For the iterative method, both the inviscid flow system (S_1') and the unsteady boundary layer system (S_3) are conserved in their original form. The solution requires several iteration cycles to achieve equilibrium between viscous and inviscid components. The complete procedure is described in [9].

For the direct solution method, the momentum equation (17) and the boundary layer system (S_3) are recombined into a time-evolutive partial differential system with only $\partial p/\partial R$ as a forcing term

$$(S_3')\quad \frac{\partial}{\partial t}\begin{pmatrix}\theta\\ \delta^*\\ V_R\end{pmatrix}+A\frac{\partial}{\partial R}\begin{pmatrix}\theta\\ \delta^*\\ V_R\end{pmatrix}=B\frac{\partial p}{\partial R}+D \qquad (18)$$

Two characteristic directions of this system are identical to (S_3). The third one is: $\lambda_3 = V_R$. The system (S_3') is hyperbolic, as all eigenvalues are real and different and can be integrated with the method of characteristics.

The forcing term $\partial p/\partial R$ is determined from a compatibility equation which is derived from the continuity equation (16)

$$\frac{\partial p}{\partial R}=f\left(\frac{\partial \theta}{\partial R},\frac{\partial \delta^*}{\partial R},\frac{\partial V_R}{\partial R}\right) \qquad (19)$$

As the forcing terms are expressed implicitly, an iteration procedure is required here to achieve equilibrium between the system (S_3') and the compatibility equation.

Figure 5 compares the results of the direct and the iterative solution for the one-dimensional problem. The outlet static pressure is fluctuating sinusoidally with a period $T = .03^S$ and an amplitude equal to 20 percent of the local dynamic pressure. The results of both methods are in excellent agreement and confirm the validity of the iterative method. It also appears that:

- No phase shift exists between δ^* and H.
- Both δ^* and H are characterized by an asymmetric wave shape.
- The minimum (maximum) obstruction is preceding the maximum (minimum) external velocity.

These observations are in agreement with the measurements of Houdeville et al. [19] of the unsteady boundary layer behavior under a pulsating flow field with an adverse pressure gradient. This agreement could only be obtained because a fully unsteady boundary layer method was used. The importance of these unsteady terms becomes apparent if one tries to predict the boundary layer response to the inviscid flow field fluctuations with a first-order modeling of a steady boundary layer method

$$\tau\frac{\partial h}{\partial t}+h=h_{ss}\left(V_R,\frac{\partial V_R}{\partial R}\right) \qquad (20)$$

Figure 6 shows the results for the same model problem.

From a comparison with Fig. 5, one can see that the fluctuation of V_R reaches the same level, but that the amplitude of δ^* fluctuations is one order of magnitude smaller.

The form factor H was found to remain almost constant and the typical phase relation between V_R and δ^* could not be predicted.

Global Model for Diffuser Rotating Stall

The Two-Dimensional Unsteady Strong Interaction. The inviscid flow field in a vaneless radial diffuser is described by the system (S_1). The free-flow section h is determined by the unsteady boundary layer system (S_3) and is found by applying the one-dimensional strong interaction theory along instantaneous streamlines.

For a chosen diffuser inlet flow angle, α_2, first a steady-state and axisymmetric solution is determined. From this, the homogeneous outlet static pressure, $P_{3_{ss}}$, is derived.

The time-evolutive calculation is started by imposing a transient sinusoidal distortion of the diffuser outlet static pressure p_3 with a tangential periodicity, m. This perturbation increases and decreases during a period T and vanishes af-

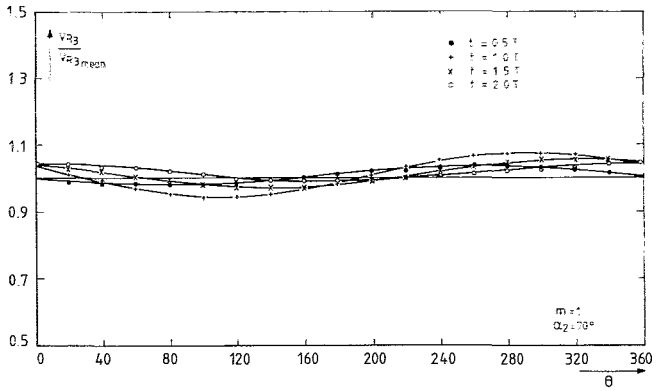

Fig. 7(a) Time-evolutive behavior of the radial velocity distribution at the diffuser outlet

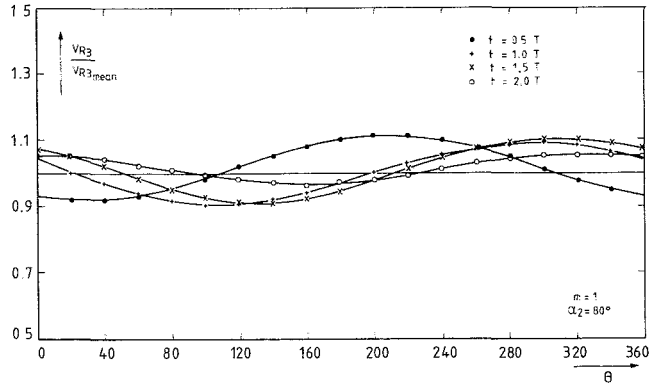

Fig. 7(b) Time-evolutive behavior of the radial velocity distribution at the diffuser outlet

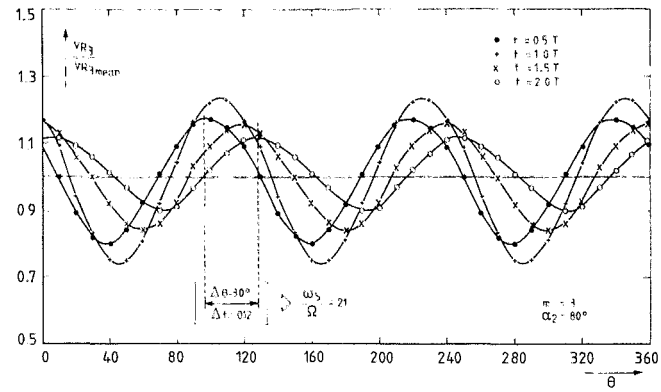

Fig. 7(c) Time-evolutive behavior of the radial velocity distribution at the diffuser outlet

terwards. One examines, by a time-evolutive integration of (S_1) and (S_3), for which conditions a rotating flow pattern is created in the vaneless radial diffuser.

The global system is solved for the following boundary conditions:

- At the outlet of the vaneless diffuser, a substitution of the given static pressure p_3 (θ, t) in the tangential momentum equation yields the tangential velocity V_{θ_3} as a boundary condition for (S_2).
- The static pressure at the diffuser inlet p_2 (θ, t) results from an integration of the radial momentum equation from the outlet to the inlet of the diffuser. The system (S_4) gives then the impeller response to this pressure distribution p_2 (θ, t) in terms of the velocity components V_{R_2} and V_{θ_2} at the inlet of the diffuser.
- V_{R_2} is imposed as a boundary condition for (S_2).
- V_{θ_2} is substituted in the vorticity definition equation (2),

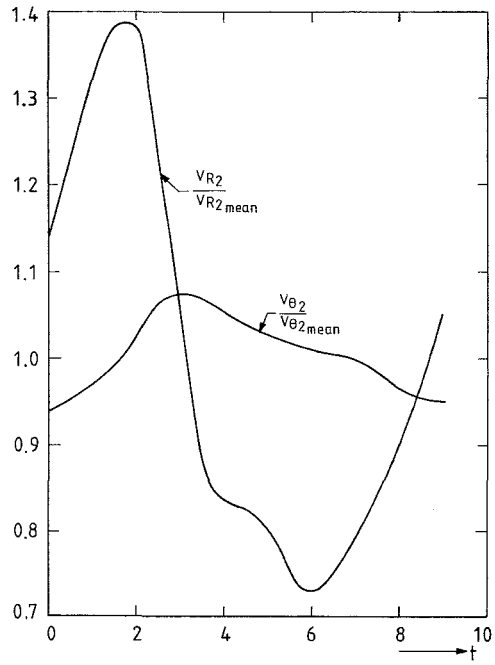

Fig. 8 Evolution of the radial and tangential velocity components in a regime of diffuser rotating stall (experimental data [20])

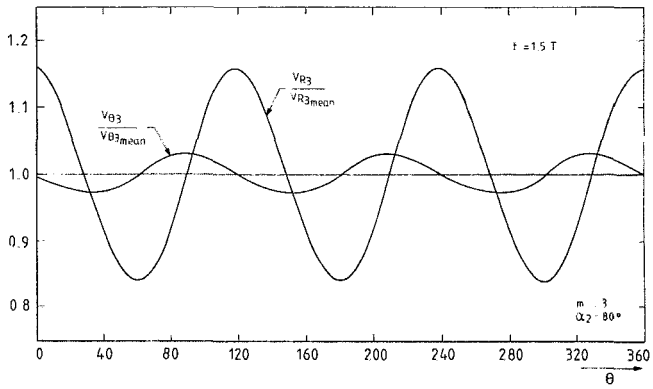

Fig. 9 Calculated phase shift between the radial and tangential velocity components in a regime of diffuser rotating stall

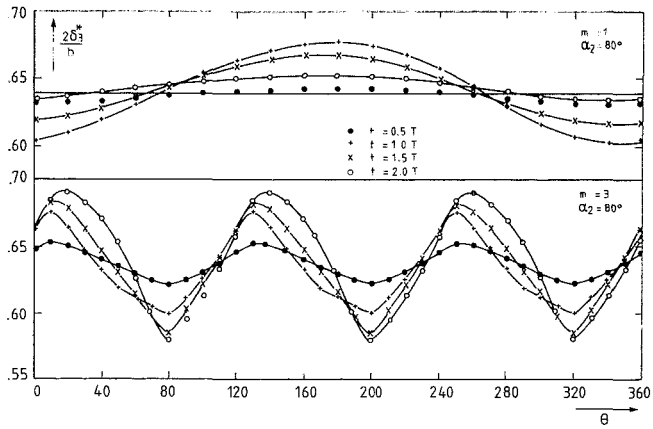

Fig. 10 Comparison of the evolution of the boundary layer obstruction at the diffuser outlet for a stable and an unstable mode of diffuser rotating stall

from which the upstream boundary condition ζ_2 for the vorticity transport equation (1) can be calculated.

- At the diffuser inlet, arbitrary values for the displacement thickness δ^* and the form factor H are imposed as boundary conditions for (S_3).

Results. The calculations are performed for the centrifugal compressor of [1] for which experimental data about rotating stall are available. The compressor is equipped with a vaneless diffuser with a radius ratio of 1.62 and a rotor outlet width to radius ratio of .077.

Figure 7(*a*) shows the evolution of the radial velocity distribution at the diffuser outlet for an inlet flow angle $\alpha_2 = 70$ deg and periodicity $m = 1$. It appears that the amplitude of the velocity fluctuations is decreasing rapidly. Therefore the flow is stable. This observation is in agreement with the experimental data of [1] as no rotating stall was detected for $\alpha_2 = 70$ deg.

The calculations are repeated for $\alpha_2 = 80$ deg, and $m = 1$ (Fig. 7(*b*)). Again the flow field is stable. This is still in agreement with the measurements, as for $\alpha_2 = 80$ deg only diffuser rotating stall with three cells was detected.

However, if a transient static pressure distortion with periodicity $m = 3$ is imposed, the calculated flow field response is quite different (Fig. 7(*c*)):

- The amplitude of the velocity fluctuations is significantly larger.
- The decrease of the amplitude in time is reduced.
- The velocity oscillations start to propagate in the tangential direction with a relative rotational speed $\omega_s/\Omega = .21$.

The measured value of the relative rotational speed in [1] amounts to .184 at $\alpha_2 = 80$ deg.

From the experiments of Ligrani and Van den Braembussche [20], one can calculate that the phase shift between the fluctuating velocity components in a regime of diffuser rotating stall is equal to 90 deg (Fig. 8).

Figure 9 shows the calculated velocity components at the diffuser outlet at time level $t = 1.5T$. The phase shift is equal to 90 deg and, as the oscillations are propagating in the positive θ-direction, the radial velocity is preceding the tangential one, which also corresponds to Fig. 8.

Moreover, agreement exists also with respect to the relative amplitudes of the velocity fluctuations.

Figure 10 compares the evolution of the boundary layer obstruction $2\delta^*/b$ at $\alpha_2 = 80$ deg for the modes $m = 1$ and $m = 3$:

- For $m = 1$, the maximum obstruction is reached at $t = .5T$, and decreases afterwards.
- For $m = 3$, however, the amplitude of the obstructions is still increasing when the outlet pressure perturbation has already disappeared. At $t = T$, the oscillation starts to propagate in the tangential direction with the same rotational speed as the velocity fluctuations.

It is also important to mention the influence of the inlet flow obstruction and the form factor, which were assumed to be constant, respectively, $2\delta^*/b = .03$ and $H = 1.7$. These values in fact should be recalculated continuously in function of the time-varying conditions at the impeller outlet. Due to this restricted interaction, the flow oscillations are rapidly disappearing at the diffuser inlet. This, together with numerical viscosity effects, is likely to be responsible for the progressive attenuation of the flow oscillations through the diffuser.

Conclusions

A theoretical model for the physical mechanism of rotating stall in a radial vaneless diffuser has been presented. It consists of a time-evolutive calculation of the two-dimensional and unsteady interaction between the inviscid flow field and the boundary layers along the diffuser walls.

It has been shown that a transient perturbation of the static pressure distribution at the outlet of the diffuser will induce a rotating flow oscillation if:

- The absolute inlet flow angle α_2 has reached a critical value.
- The periodicity of the perturbation corresponds to the experimentally observed value.

Although the generated flow oscillations are not completely self-sustained, the present results clearly demonstrate the validity of this diffuser rotating stall model.

Following characteristics of the numerically generated rotating stall are in agreement with the experiments:

- The relative tangential propagation speed ω_s/Ω of the rotating flow oscillation
- The stall cell number m
- The phase relation between the radial and the tangential velocity components
- The amplitude relationship between these velocity components

References

1 Frigne, P., and Van den Braembussche, R., "Distinction Between Different Types of Impeller and Diffuser Rotating Stall in a Centrifugal Compressor With Vaneless Diffuser," ASME JOURNAL OF ENGINEERING FOR GAS TURBINES AND POWER, Vol. 106, No. 2, Apr. 1984, pp. 468–474; Paper No. 83-GT-61; also VKI Preprint 1982-39.

2 Rodgers, C., "Impeller Stalling as Influenced by Diffusion Limitations," ASME *J. Fluids Engrg.*, Vol. 99, No. 1, Mar. 1977, pp. 84–97.

3 Jansen, W., "Rotating Stall in a Radial Vaneless Diffuser," ASME *J. Basic Engrg.*, Vol. 86, No. 4, Dec. 1964, pp. 750–758.

4 Jansen, W., "Steady Fluid Flow in a Radial Vaneless Diffuser," ASME *J. Basic Engrg.*, Vol. 86, No. 3, Sept. 1964, pp. 607–619.

5 Senoo, Y., Kinoshita, Y., and Ishida, M., "Asymmetric Flow in Vaneless Diffusers of Centrifugal Blowers," ASME *J. Fluids Engrg.*, Vol. 99, No. 1, Mar. 1977, pp. 104–114.

6 Senoo, Y., and Kinoshita, Y., "Influence of Inlet Flow Conditions and Geometries of Centrifugal Vaneless Diffusers on Critical Flow Angle for Reverse Flow," ASME *J. Fluids Engrg.*, Vol. 99, No. 3, Mar. 1977, pp. 98–103.

7 Senoo, Y., and Kinoshita, Y., "Limits of Rotating Stall and Stall in Vaneless Diffuser of Centrifugal Compressors," ASME Paper No. 78-GT-23.

8 Abdelhamid, A. N., "Analysis of Rotating Stall in Vaneless Diffusers of Centrifugal Compressors," ASME Paper No. 80-GT-184.

9 Frigne, P., "Theoretische en experimentele studie van de subsynchrone zelfgeexciteerde stromingsoscillaties in radiale turbocompressoren," Ph.D. thesis, Rijksuniversiteit Gent, June 1982.

10 Wirz, H. J., "Relaxation Methods for Time-Dependent Conservation Equations in Fluid Mechanics," *Computational Fluid Dynamics*, AGARD LS 86, Paper 4, Apr. 1977.

11 Young, D., "Iterative Method for Solving Partial Difference Equations of Elliptic Type," *Am. Math. Soc. Transact.*, Vol. 76, No. 1, 1954, pp. 92–111.

12 Roache, P. J., *Computational Fluid Dynamics*, Albuquerque, N.M., Hermosa Publishers, 1972.

13 Papailiou, K. D., "Turbulent Boundary Layers," *VKI CN*, Vol. 87, Feb. 1972.

14 Schlichting, H., *Boundary Layer Theory*, McGraw-Hill, New York, 1979.

15 Cousteix, J., Le Balleur, J. C., and Houdeville, R., "Calcul des couches limites turbulentes instationnaires en mode direct ou inverse, ecoulements de retour inclus," *La Recherche Aerospatiale*, No. 3, 1980, pp. 147–157.

16 Schubauer, G. B., and Klebanoff, P. S., "Investigation of Separation of Turbulent Boundary Layers," NACA TR 1030, 1951.

17 Head, M. R., "Entrainment Approach to Turbulent Boundary Layers," *Turbulent Boundary Layers*, VKI LS 5, Mar. 1968.

18 Michel, R., Guemard, C., and Durant, R., "Application d'un schema de longueur de melange a l'etude des couches limites turbulentes d'equilibre," ONERA NT 154, 1969.

19 Houdeville, R., and Cousteix, J., "Couches limites turbulentes en ecoulement pulse avec gradient de pression moyen defavorable," *La Recherche Aerospatiale*, No. 1, 1979, pp. 33–48.

20 Ligrani, P. M., Van den Braembussche, R., and Roustan, M., "Rotating Stall Measurements in the Vaneless Diffuser of a Radial Flow Compressor," ASME Paper No. 82-GT-257; also VKI Preprint 1981-24.

Y. Kinoshita
Research Associate.

Y. Senoo
Professor.
Mem. ASME

Research Institute of Industrial Science,
Kyushu University 86,
Kasugashi, Fukuoka 816, Japan

Rotating Stall Induced in Vaneless Diffusers of Very Low Specific Speed Centrifugal Blowers

The limit of rotating stall was experimentally determined for three very small specific speed centrifugal blowers. The impellers were specially designed for stall-free at very small flow rates, so that the cause of rotating stall could be attributed to the vaneless diffusers. Experimental results demonstrated that the blowers did not stall until the flow coefficient was reduced to very small values, which had never been reported in the literature. The critical flow coefficient for rotating stall agreed very well with the prediction based on a flow analysis and a criterion for rotating stall in vaneless diffusers developed by the authors.

Introduction

At chemical plants, gas is compressed to a very high pressure level for the purpose of chemical reaction. In oil fields gas at a very high pressure level is required for reinjection into oil wells. For these applications, multistage centrifugal compressors are popular. When the flow rate is reduced beyond a certain limit for these high pressure compressors, violent vibration is induced, and it is not safe to operate them.

It is commonly considered that the vibration is caused by rotating stall induced in the vaneless diffuser and many studies have been continued to make clear the critical flow rate for rotating stall, number of stall cells and the propagating speed of stall cells [1-10]. In this paper, the critical inlet flow angle to the diffuser at which rotating stall just begins in the vaneless diffuser is called the critical flow angle. The critical flow angles in the literature are spread in a wide range from 6 to 20 deg, and no relation is apparent between the critical flow angle and the geometry of the diffuser.

Rotating stall can be induced in the impeller as well as in the vaneless diffuser [11]. Once rotating stall is observed in a compressor or in a blower, it is not easy to identify whether rotating stall is originally induced in the impeller or in the diffuser. It is suspected that in some of the data in the literature rotating stall was not induced in the vaneless diffuser but in the impeller. Furthermore, in some cases, since the vaneless diffuser was followed by a scroll or a collector the flow was not axisymmetric at off-design conditions, and the circumferential distortion of flow in the vaneless diffuser might have modified the critical flow angle. Therefore, in order to relate the critical flow angle to the diffuser geometry, as the first step it is advisable to limit the data to those which satisfy the following two conditions. One is that there is no apprehension that rotating stall is induced in the impeller at the small flow rate where rotating stall is observed in the diffuser, and the other is that axisymmetry of flow is not distorted by the downstream structure.

Regarding very narrow vaneless diffusers, there are not much data that satisfy these requirements. Certainly, ordinary compressors with good efficiency have wide or moderate diffusers where the ratio b/r_i is larger than 0.05. However, the last stage of a multistage centrifugal compressor sometimes has a very narrow diffuser and the ratio b/r_i can be as small as 0.01.

In the present paper, impellers with very narrow exit width were specially designed so that they would not stall even at a very small flow rate. By using these impellers, the rotating stall limits of very narrow diffusers were experimentally determined and the results were compared with the prediction based on the criterion for rotating stall in [3].

Experimental Apparatus and Instrumentation

Experiments were made on blowers with parallel wall vaneless diffusers I, I′, and II. In all of these blowers the radius of the impeller was $r_i = 150$ mm, and the exit of the diffuser was opened to the atmosphere so that axisymmetry was secured for the flow unless rotating stall was induced. The vaneless diffusers I and I′ had an identical width of $b = 0.0257\, r_i$, but had different exit radii of $r_e = 1.40\, r_i$ and $1.67\, r_i$. The diffuser II had a width of $b = 2.3$ mm $= 0.0153\, r_i$, and the exit radius of $r_e = 1.40\, r_i$. The experiment was made keeping the shaft speed at 4755 rpm.

In order to avoid impeller-stall at the critical flow rate, the impellers were specially designed so that the incidence angle was almost zero and the exit/inlet relative velocity ratio w_2/w_1 was about unity at the flow rate. For that purpose, it was necessary to make the inlet radius of the impellers as small as 36 mm. The impellers I and II were closed type, and the exit width was identical to the width of the respective diffusers.

Contributed by the Gas Turbine Division of THE AMERICAN SOCIETY OF MECHANICAL ENGINEERS and presented at the 29th International Gas Turbine Conference and Exhibit, Amsterdam, The Netherlands, June 4-7, 1984. Manuscript received at ASME Headquarters January 18, 1984. Paper No. 84-GT-203.

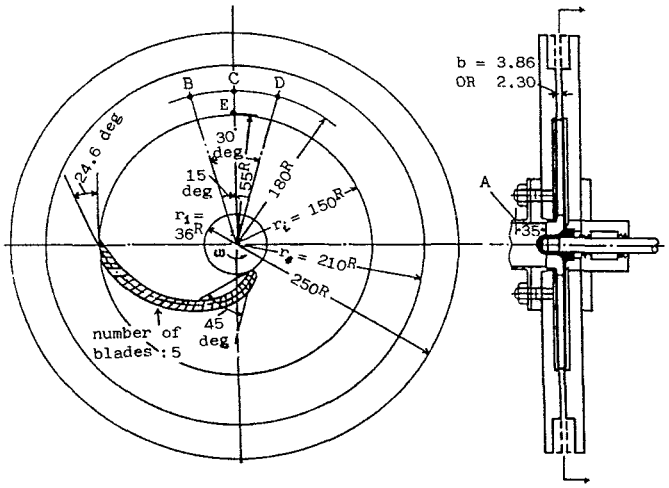

Fig. 1 Test blower and measuring points

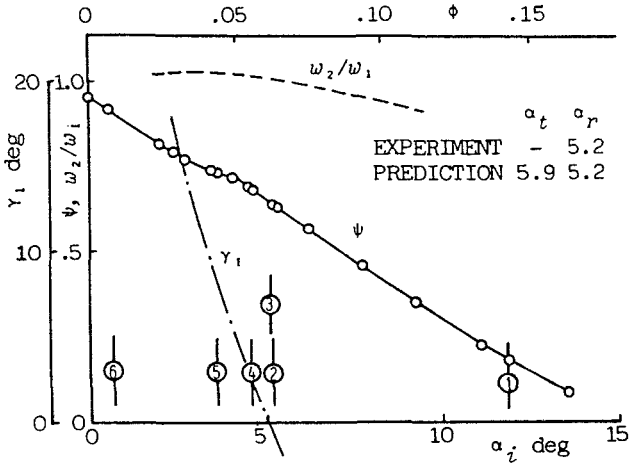

(a) Diffuser I (b/r_i = 0.0257 and r_e/r_i = 1.40)

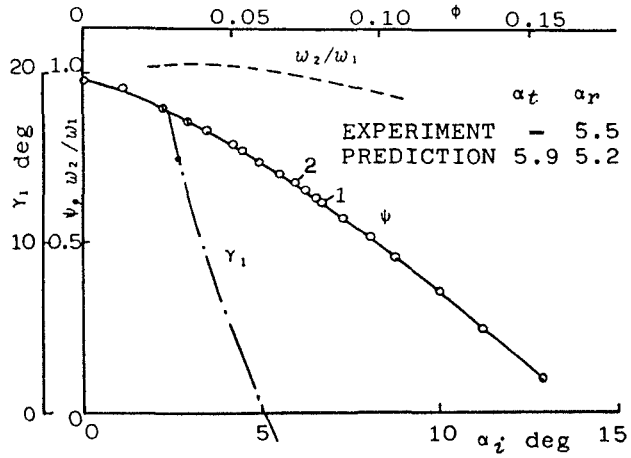

(b) Diffuser I′ (b/r_i = 0.0257 and r_e/r_i = 1.67)

Fig. 2 Pressure coefficient, incidence angle to impeller blades, and exit/inlet relative velocity ratio of impeller versus flow coefficient and inlet flow angle to diffuser

Fluctuations of velocity and pressure were measured at five stations A, B, C, D, and E indicated in Fig. 1. A was located 35 mm upstream of the impeller; B, C, and D were on the diffuser wall at a radius of 1.2 r_i, while E was located at a radius of 1.033 r_i. In the cases of the diffusers I and I′, a probe of a hot-wire velocimeter was inserted at the middle of the diffuser width so that the wire was parallel to the impeller axis. In the case of the narrow diffuser II, in order to avoid the disturbance due to the probe, a hot-film sensor was installed so that the film was flush with the diffuser wall.

The circumferential variation of pressure in the diffuser was measured at radii of 1.03 r_i, 1.2 r_i, and 1.3 r_i, and it was recognized that the maximum circumferential variation of the time-mean static pressure was less than 2 percent of the local dynamic pressure at any flow rate.

Experimental Results and Discussions

Characteristic Curves of the Blowers. The characteristic curves of the blowers with diffusers I, I′, and II are respectively presented in Figs. 2(*a*), 2(*b*), and Fig. 3 as full lines. The ordinate is the pressure rise coefficient ψ, while the abscissa is the mean flow angle α_i at the diffuser inlet. The flow coefficient ϕ is also indicated on the abscissa together with the flow angle. α_i was evaluated from the mean radial and tangential velocity components.[1] The flow rate of the blower was measured with an orifice flow meter, and the tangential component of the velocity at the impeller exit was calculated based on the blade angle, the flow coefficient and the Wiesner's slip coefficient [12]. The gradient of the characteristic curves was monotonic up to zero flow and surging was not observed at any flow rate.

[1]The probable errors are 0.02 for the flow coefficient, 0.025 for Wiesner's slip factor and 2 deg for the blade angle. As a combination of these errors the probable error of the flow angle α_i is evaluated to be 0.2 deg.

Fluctuations of Velocity and Pressure.

(*a*) *Diffuser I* (b/r_i = *0.0257 and* r_e/r_i = *1.40*). Four lines in each of six pictures in Fig. 4 indicate the fluctuation pressure or velocity at four positions at one of six different flow rates that are indicated in Fig. 2(*a*). That is, P_A line and P_C line in the picture demonstrate the pressures at positions A and C in Fig. 1, while V_B and V_D lines indicate the output signals of the hot-wire probes at B and D that were made proportional to the velocity. Comparing V_B lines or V_D lines

Nomenclature

b = diffuser width
b_2 = exit width of impeller
Δp = pressure rise across compressor
r = radial position
v_{r2} = radial component of velocity at impeller exit
u_2 = tip speed of impeller
w_2/w_1 = ratio of exit/inlet relative velocities of impeller
α_i = mean flow angle at diffuser inlet, measured from circumferential direction
α_r = α_i at which rotating stall begins
α_l = α_i at which reverse flow begins
γ_1 = incidence angle to impeller blades
ρ = fluid density at impeller exit
ϕ = flow coefficient of blower ($= v_{r2}/u_2$)
ψ = pressure coefficient of blower ($= \Delta p/\frac{1}{2}\rho u_2^2$)
σ = wave frequency of stall cells

Subscripts

e = exit of diffuser
i = inlet of diffuser

at different flow coefficients in the six pictures, variation of the flow pattern with respect to the inlet flow angle is apparent. There is no clear difference in the velocity signals V_B between the condition No. 1 (α_i = 11.8 deg) and the condition No. 2 (α_i = 5.2 deg). When the flow rate is reduced slightly further from the condition No. 2 to the condition No. 3 and the inlet flow angle to the diffuser is reduced by 0.1 deg, a periodic fluctuation in the velocity signals V_B and V_D is recognized, although the pressure coefficient ψ is hardly influenced by the change of the flow rate. From the foregoing results, it is determined that the critical flow angle in the diffuser I is α_r = 5.2 deg.

The incidence angle γ_1 to the impeller-blades varies with the flow rate as shown by a chain line in Fig. 2(*a*) and the ratio of exit/inlet relative velocities w_2/w_1 of the impeller is related to the flow rate as shown by a dotted line. These curves show that at the critical flow angle α_r, γ_1 is -0.5 deg and w_2/w_1 is 1.0 for the impeller. Therefore, it is not conceivable that the impeller was the cause of rotating stall, and it is concluded that rotating stall was induced in the vaneless diffuser.

The period of velocity fluctuation at the critical condition No. 3 was 13.0 ms. Since the phase difference of the two signals observed at positions B and D, which were located 30 deg apart, was 3.25 ms, it was concluded that three stall cells were rotating at an angular velocity of 149.5 radian per second. The angular velocity of the propagating stall cells was about 1/3 of the angular velocity of the impeller. The amplitude of the velocity fluctuation was about 1/3 of the time mean velocity at the stations. The pressure pickups at

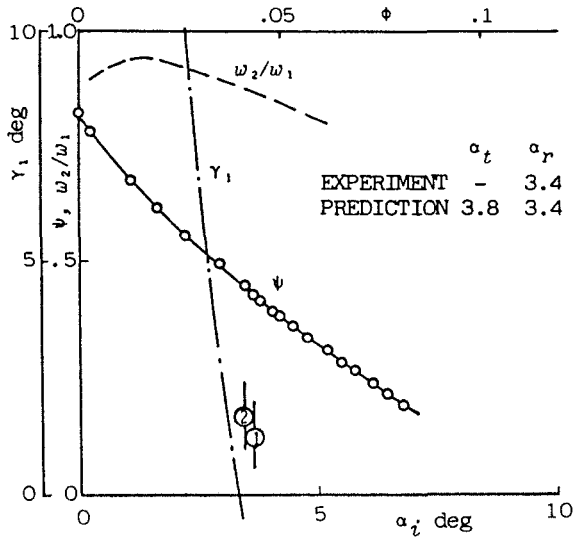

Diffuser II (b/r_i = 0.0153 and r_e/r_i = 1.40)

Fig. 3 Pressure coefficient, incidence angle to impeller blades, and exit/inlet relative velocity ratio of impeller versus flow coefficient and inlet flow angle to diffuser

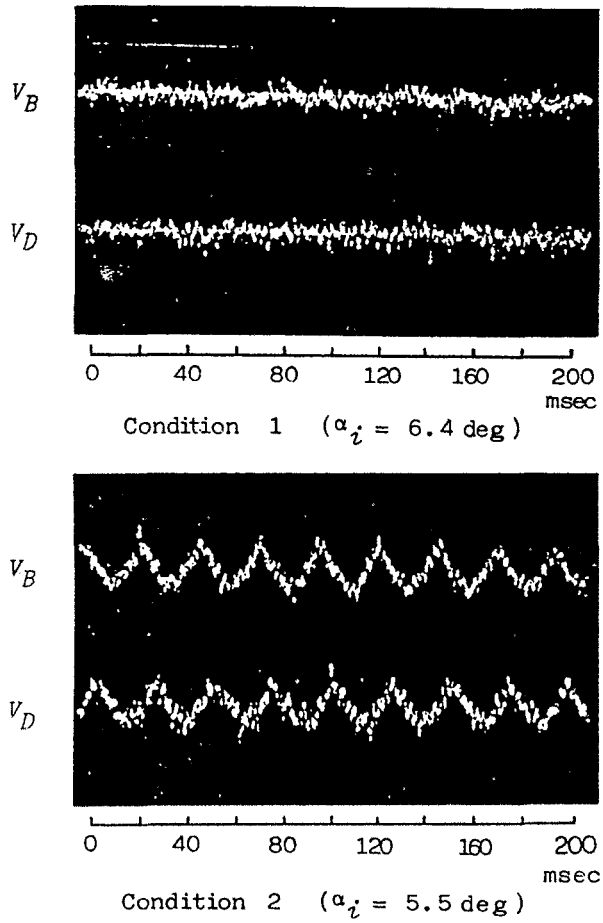

Fig. 4(*b*) Velocity in diffuser I′ (b/r_i = 0.0257 and r_e/r_i = 1.67)

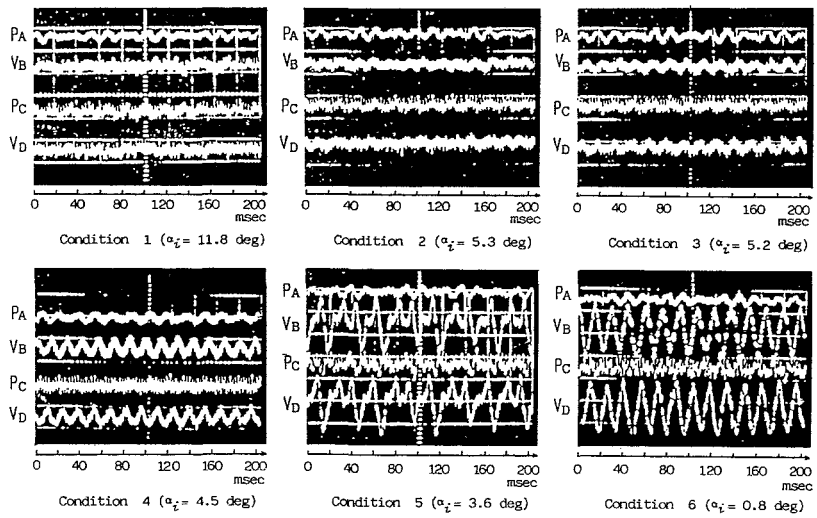

Fig. 4(*a*) Velocity and pressure at six flow rates in diffuser I (b/r_i = 0.0257 and r_e/r_i = 1.40)

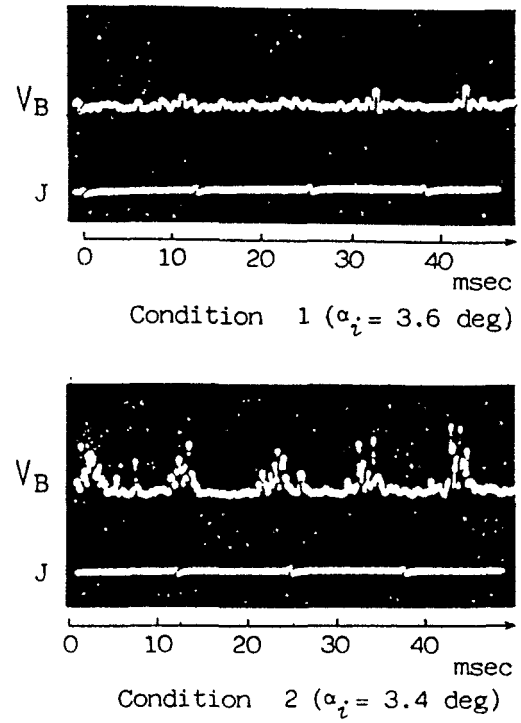

Fig. 5 Velocity in diffuser II (b/r_i = 0.0153 and r_e/r_i = 1.40)

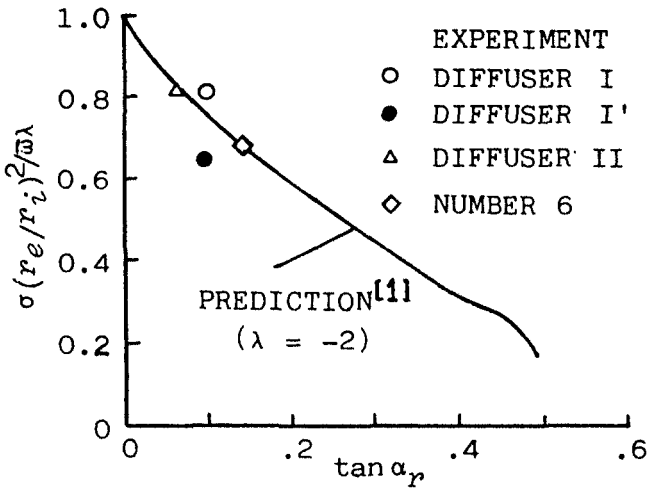

Fig. 6 Relation between propagating speed parameter and flow angle at diffuser inlet

positions A and C were not sensitive enough to show sizable variation due to propagation of stall cells.

(*b*) *Diffuser I'* (b/r_i = 0.0257 *and* r_e/r_i = 1.67). The V_B line and V_D line in each of two pictures in Fig. 4(*b*) are the output signals of hot-wire probes similar to Fig. 4(*a*). These signals demonstrate clearly that rotating stall occurred at α_i = 5.5 deg, which is close to the critical flow angle α_r = 5.2 deg observed in the diffuser I. The incidence angle γ_1 to the impeller blades is shown by a chain line and the exit/inlet relative velocity ratio is indicated by a dotted line in Fig. 2(*b*). At the critical flow angle, they are −1.0 deg and 1.0, respectively. It is not conceivable that the impeller was the cause of rotating stall, and it is concluded that rotating stall was induced in the vaneless diffuser.

The period of velocity fluctuation was 25.4 ms at the rotating stall condition and the phase difference of two signals V_B and V_D was 5.4 ms. Therefore, it was concluded that three stall cells were rotating at 82.4 radian per second. The angular velocity of the propagating stall cells was about 1/6 of the angular velocity of the impeller.

(*c*) *Diffuser II* (b/r_i = 0.0153 *and* r_e/r_i = 1.40). The velocity signal at position B is presented in Fig. 5 for two flow rates that are specified in Fig. 3. Each pulse of the J line indicates one rotation of the impeller. The velocity signal V_B demonstrates clearly that rotating stall occurred at α_i = 3.4 deg. The ψ-ϕ characteristic curve in Fig. 3 is smooth at the flow rate and the pressure coefficient ψ is hardly influenced by rotating stall. The chain line and the dotted line show that at the critical condition of rotating stall α_r = 3.4 deg, the angle of incidence γ_1 is −1.5 deg and the exit/inlet relative velocity ratio w_2/w_1 is 0.87. Therefore, it is concluded that rotating stall was not induced in the impeller, but it was induced in the vaneless diffuser.

The period of velocity fluctuation was 13.6 ms at the rotating stall condition. The propagating speed of stall cells was about 1/4 of the impeller speed, providing that there were three stall cells similarly to the cases of the diffusers I and I'.

Discussion of Test Results. In the present tests the radius ratio r_e/r_i was increased from 1.40 to 1.67 and as a result critical flow angle was increased by 0.3 deg. (For reference, there is a report [7] in which variation of the radius ratio from 1.40 to 1.60 increased the critical flow angle by 2.5 deg in the case of a diffuser of b/r_i = 0.116.) On the other hand, the variation of the diffuser width from 0.0257 r_i to 0.0153 r_i resulted in decrement of the critical flow angle as much as 1.6 deg. More discussions will be made in the next chapter regarding the critical flow angle.

According to a theoretical analysis [1], the propagating velocity of stall cells is proportional to $(r_i/r_e)^2$, and a parameter $\sigma(r_e/r_i)^2/\bar{\omega}\lambda$ is proposed to express the propagating speed σ/λ of stall cells, where σ is the wave frequency, $\bar{\omega}$ is the angular velocity of flow at the diffuser inlet, and λ is the number of stall cells. The experimental values of $\sigma(r_e/r_i)^2/\bar{\omega}\lambda$ at the critical conditions are plotted in Fig. 6 for the three diffusers together with the data in [3]. The full line is the predicted relation [1]. Fair agreement is observed between experimental data and the prediction.

Predction on Critical Flow Angle

Based on an analytical method in [13], the reverse flow zone along the wall is calculated for various values of the inlet flow angle α_i, assuming that the flow is uniform and the boundary layer is very thin at the inlet to the vaneless diffuser. The results are presented as the curves in Figs. 7 and 8 where the abscissa is the mean inlet flow angle to the diffuser and the ordinate is the radial position of diffuser. The left-hand side of the curve is the reverse flow zone. That is, in the case of Fig. 7 for diffusers I and I', if the mean inlet flow angle is larger than 5.9 deg, there is no reverse flow zone. At this flow angle, the wall streamline becomes tangential at a certain radius. This inlet flow angle is expressed as α_t. If the inlet flow angle is less than α_t, the vertical line passing through the inlet flow angle in Fig. 7 intersects with the curve at two points which indicate the reverse flow zone.

The critical flow angle for rotating stall in the diffusers was experimentally determined, and it was expressed as α_r. In the case of diffuser I, the critical flow angle α_r was 5.2 deg which is 0.88 time the estimated α_t. In the case of diffuser I', α_r was 5.5 deg and the ratio α_r/α_t is 0.93. In the case of diffuser II, as demonstrated in Fig. 5, α_r was 3.4 deg, while the predicted value of α_t is 3.8 deg as shown in Fig. 8. The ratio α_r/α_t is again 0.88. The value 0.88 agrees with the value reported in [3] based on several diffusers with the diffuser-width larger

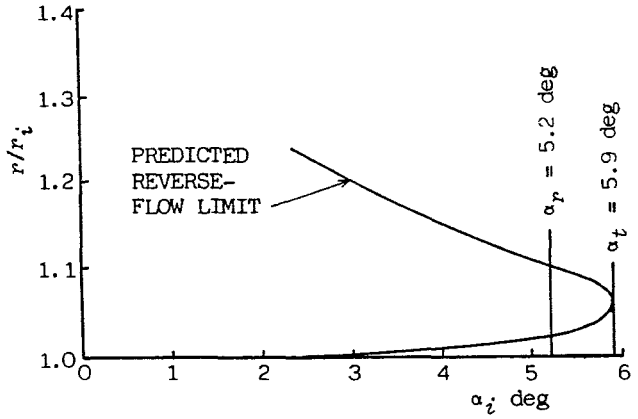

Fig. 7 Predicted reverse flow zone along walls: Diffuser I and I′ (b/r_i = 0.0257)

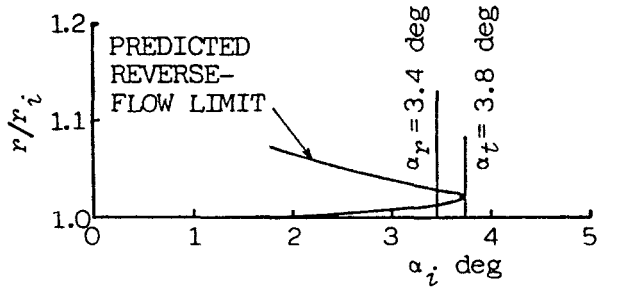

Fig. 8 Predicted reverse flow zone along walls: Diffuser II (b/r_i = 0.0153 and r_e/r_i = 1.40)

than 0.056 r_i. These three examples demonstrate that the criterion for rotating stall, $\alpha_r = 0.88\ \alpha_t$, is applicable to various diffusers with the width ratio from 0.0153 to 0.13.

The criterion that $\alpha_r = 0.88\ \alpha_t$ and the flow analysis in [13] to evaluate α_t are applied to diffusers with various value of the width ratio, and the predicted critical flow angles are indicated in Fig. 9 as a full line. For comparison, the foregoing three experimental data are plotted together with the data in [3]. Good agreement is observed in the entire range of diffuser width ratio.

Review of Experimental Data for Rotating Stall in the Literature

Critical conditions for rotating stall in vaneless diffusers reported in the literature have been collected in [8], and the data are reproduced in Fig. 10 together with new data numbers 17′ [10], 18, and 19 [9], as well as the three data obtained in the present experiment.

These experimental data are scattered considerably and no trend is apparent. A few reasons are conceivable why the data are scattered. In some cases, since the vaneless diffuser was followed by a scroll or a collector, the flow was not axisymmetric at an off-design flow rate, and the circumferential distortion of flow in the vaneless diffuser might have modified the critical mean inlet flow angle.

Another reason is that the way to determine the flow angle at the diffuser inlet was not consistent among these data. Certainly, in some of the experimental data, the flow angle was determined as $\tan^{-1}(\bar{v}_{r2}/\bar{v}_{\theta 2})$, where $\bar{v}_{r2}$ was evaluated from the flow rate and $\bar{v}_{\theta 2}$ was estimated from the input torque or the temperature rise. In other cases, such as numbers 18 and 19, the flow angle was directly measured in the passage near the inlet of the diffuser. Since the flow very near the impeller is periodic due to the influence of the impeller-blades, it is not easy to measure the mean velocity $\bar{v}$

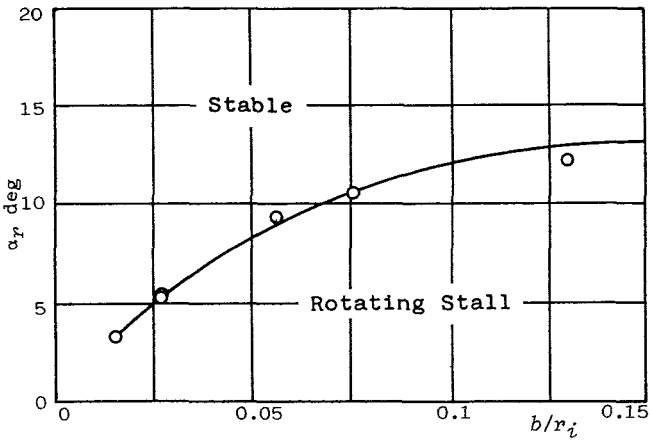

Fig. 9 Critical inlet flow angle for rotating stall in diffusers versus diffuser width b/r_i

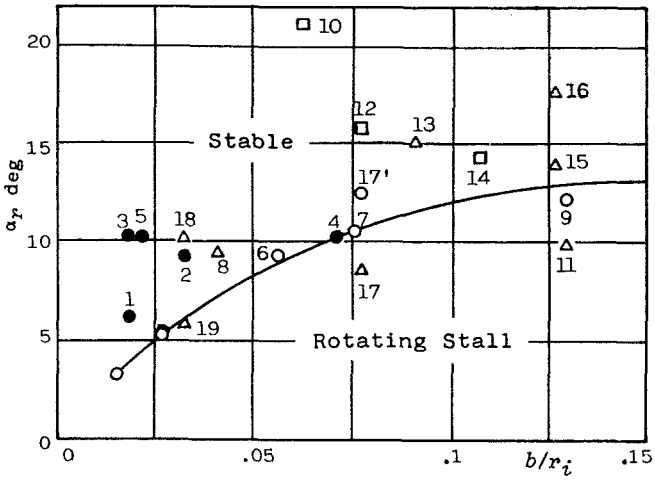

Fig. 10 Critical inlet flow angle for rotating stall in the literature [8]

accurately. If the flow is measured somewhere away from the impeller to avoid the periodicity, the boundary layer grows along the diffuser walls and the distortion of the inlet velocity profile is magnified. The flow angle at the middle of the diffuser passage can be larger than the mean flow angle by a few degrees in cases of narrow diffusers. Therefore, it might be different from the critical mean flow angle obtained by other methods by a few degrees. In the present paper, the flow angle was determined as $\tan^{-1}(\bar{v}_{r2}/\bar{v}_{\theta 2})$ where $\bar{v}_{r2}$ was evaluated from the flow rate and $\bar{v}_{\theta 2}$ was estimated from Wiesner's slip factor [12]. Wiesner's slip factor is not always the most accurate way to estimate the tangential velocity component at the exit of impeller, but it is simple and consistent, and it gives fairly accurate values.

Another possible reason for the scattering is that some erroneous data based on impeller-stall might have been included in the literature. If an impeller is stalled, the pressure rise across the impeller is probably reduced and the characteristic curve shows anomaly at the critical flow rate. Concerning the flow in vaneless diffusers, the radial pressure gradient in the diffuser is mostly balanced by the centrifugal force acting on the swirl flow. Since the time mean value of the wall friction force is not changed much by rotating stall, the mean angular velocity and the pressure rise in the vaneless diffuser are not sensitive to rotating stall and the characteristic curve is relatively smooth at the critical condition, providing that the performance of the impeller is not deteriorated by rotating stall in the vaneless diffuser. Therefore, if the characteristic curve has a kink or a peak pressure at the critical flow rate, it may be assumed that the

impeller is stalled and rotating stall observed at that condition is attributed to the impeller. In Fig. 10, those data that are judged as impeller stall based on the shape of the characteristic curves are indicated as triangular marks.

According to [10], rotating stall induced in the impeller contains strong harmonics in the velocity signal while rotating stall induced in the vaneless diffuser has an isolated frequency and weak harmonics; consequently, the signal may be used to judge the source of rotating stall. Applying this criterion to the published pressure signals in [4, 5], numbers 10, 12, and 14 in Fig. 10 are suspected as rotating stall induced in the impeller, and they are indicated as square marks.

Number 17 in Fig. 10 was once regarded [8] as the diffuser stall condition, but later experiments were repeated [10], and the new result is indicated as number 17′ in Fig. 10. Probably the data number 17 should be replaced by the data number 17′.

In cases of multistage centrifugal compressors with very narrow vaneless diffusers, the shaft diameter is made large to increase the critical speed. As a result, the inlet eye diameter of the impeller is unduely large as a low specific speed impeller. At a small flow rate the inlet relative velocity approaches the circumferential velocity of the blade-leading edge, which is about one-half of the tip speed for these impellers. On the other hand, since the mean relative velocity inside the impeller is approximately proportional to the flow rate, it is very small compared with the inlet relative velocity when the flow rate is little or when the absolute flow angle at the impeller exit is small. Because of the unduely large deceleration of the relative velocity in the impeller, it is very likely that the flow separates from the blade surface and the impeller is stalled.

If an impeller has blades with large backward leaning angle, the pressure versus flow rate characteristic curve may keep a negative gradient, even if the impeller is stalled at a small flow rate and the performance of the impeller is somewhat deteriorated. As a result, it is usually possible to operate the compressor stably, including the stall condition of the impeller. Because of the stable characteristics of the impeller, in cases of industrial centrifugal compressors an impeller designed for a large flow rate is sometimes combined with a narrow vaneless diffuser. In these cases, the impeller-blades are stalled at a flow coefficient which is not so small for the diffuser. In cases of numbers 5, 12, 13, 14, 15, and 16 in Fig. 10, the diffuser is narrower than the exit width of the impeller, and it may be possible that rotating stall occurred in the impeller before it does in the vaneless diffuser.

At least the data indicated in Fig. 10 as open circles were obtained under the acceptable condition, and the prediction indicated in the figure as a full line agrees well with those experimental data. When a vaneless diffuser is followed by a scroll or a collector as the last stage of a multistage compressor, the flow is not axisymmetric at an off-design condition, and the critical flow angle may be changed. This problem is left for a future study.

Conclusions

1 In the case of a very narrow diffuser with $b/r_i = 0.0153$, rotating stall was not observed until the mean inlet flow angle was reduced to 3.4 deg from the circumferential direction as predicted.

2 The critical flow angle for rotating stall was influenced little by modification of the exit/inlet radius ratio in the tested very narrow vaneless diffuser.

3 The critical inlet flow angle can be predicted correctly for very narrow diffusers as well as for wide diffusers.

4 The propagating speed of stall cells induced in vaneless diffusers agreed fairly well with the prediction [1].

5 In cases of small specific speed blowers, the impeller may stall before the vaneless diffuser stalls unless a special care is taken for designing the impeller.

References

1 Jansen, W., "Rotating Stall in a Radial Vaneless Diffuser," ASME *Journal of Basic Engineering*, Vol. 86, No. 4, 1964, pp. 750–758.

2 Tsurusaki, H., and Imaichi, K., "Experimental Study on Rotating Stall of Centrifugal Impeller" (in Japanese), *Turbomachinery*, Vol. 5, No. 2, Feb. 1977, pp. 14–24.

3 Senoo, Y, and Kinoshita, Y., "Limits of Rotating Stall and Stall in Vaneless Diffuser of Centrifugal Compressors," ASME Paper No. 78-GT-19, Apr. 1978.

4 Abdelhamid, A. N., Colwill, W. H., and Barrows, J., F., "Experimental Investigation of Unsteady Phenomena in Vaneless Radial Diffusers," ASME JOURNAL OF ENGINEERING FOR POWER, Vol. 101, No. 1, 1979, pp. 52–60.

5 Abdelhamid, A. N., and Bertrand, J., "Distinction Between Two Types of Self Exited Gas Oscillations in Vaneless Radial Diffusers," ASME Paper No. 79-GT-58, 1979.

6 Hisatani, M., "Rotating Stall in Vaneless Diffusers of Centrifugal Compressors" (in Japanese), JSME Paper No. 730-15, Oct. 1979, pp. 299–302.

7 Abdelhamid, A. N., "Effect of Vaneless Diffuser Geometry on Flow Instability in Centrifugal Compression System," ASME Paper No. 81-GT-10, Mar. 1981.

8 Van Den Braembussche, R. A., Frigne, P., and Roustan, M., "Rotating Nonuniform Flow in Radial Compressors," VKI PREPRINT 1980-14, Apr. 1980.

9 Ligrani, P. M., Van Den Braembussche, R., and Roustan, M., "Rotating Stall Measurements in the Vaneless Diffuser of a Radial Flow Compressor," ASME Paper No. 82-GT-257, May 1982.

10 Frigne, P., and Van Den Braembussche, R., "Distinction Between Different Types of Impeller and Diffuser Rotating Stall in a Centrifugal Compressor With Vaneless Diffuser," ASME JOURNAL OF ENGINEERING FOR GAS TURBINES AND POWER, Vol. 106, No. 2, Apr. 1984, pp. 468–474.

11 Lenneman, E., and Howard, J. H. G., "Unsteady Flow Phenomena in Rotating Centrifugal Impeller Passage," ASME JOURNAL OF ENGINEERING FOR POWER, Vol. 92, No. 1, Jan. 1970, pp. 65–72.

12 Wiesner, F. J., "A Review of Slip Factors for Centrifugal Impellers," ASME JOURNAL OF ENGINEERING FOR POWER, Vol. 89, No. 4, 1967, pp. 558–572.

13 Senoo, Y., Kinoshita, Y., and Ishida, M., "Asymmetric Flow in Vaneless Diffusers of Centrifugal Blowers," ASME *Journal of Fluids Engineering*, Vol. 99, No. 1, 1977, pp. 104–114.

impeller is stalled and rotating stall observed at that condition is attributed to the impeller. In Fig. 10, those data that are judged as impeller stall based on the shape of the characteristic curves are indicated as triangular marks.

According to [10], rotating stall induced in the impeller contains strong harmonics in the velocity signal while rotating stall induced in the vaneless diffuser has an isolated frequency and weak harmonics; consequently, the signal may be used to judge the source of rotating stall. Applying this criterion to the published pressure signals in [4, 5], numbers 10, 12, and 14 in Fig. 10 are suspected as rotating stall induced in the impeller, and they are indicated as square marks.

Number 17 in Fig. 10 was once regarded [8] as the diffuser stall condition, but later experiments were repeated [10], and the new result is indicated as number 17′ in Fig. 10. Probably the data number 17 should be replaced by the data number 17′.

In cases of multistage centrifugal compressors with very narrow vaneless diffusers, the shaft diameter is made large to increase the critical speed. As a result, the inlet eye diameter of the impeller is unduely large as a low specific speed impeller. At a small flow rate the inlet relative velocity approaches the circumferential velocity of the blade-leading edge, which is about one-half of the tip speed for these impellers. On the other hand, since the mean relative velocity inside the impeller is approximately proportional to the flow rate, it is very small compared with the inlet relative velocity when the flow rate is little or when the absolute flow angle at the impeller exit is small. Because of the unduely large deceleration of the relative velocity in the impeller, it is very likely that the flow separates from the blade surface and the impeller is stalled.

If an impeller has blades with large backward leaning angle, the pressure versus flow rate characteristic curve may keep a negative gradient, even if the impeller is stalled at a small flow rate and the performance of the impeller is somewhat deteriorated. As a result, it is usually possible to operate the compressor stably, including the stall condition of the impeller. Because of the stable characteristics of the impeller, in cases of industrial centrifugal compressors an impeller designed for a large flow rate is sometimes combined with a narrow vaneless diffuser. In these cases, the impeller-blades are stalled at a flow coefficient which is not so small for the diffuser. In cases of numbers 5, 12, 13, 14, 15, and 16 in Fig. 10, the diffuser is narrower than the exit width of the impeller, and it may be possible that rotating stall occurred in the impeller before it does in the vaneless diffuser.

At least the data indicated in Fig. 10 as open circles were obtained under the acceptable condition, and the prediction indicated in the figure as a full line agrees well with those experimental data. When a vaneless diffuser is followed by a scroll or a collector as the last stage of a multistage compressor, the flow is not axisymmetric at an off-design condition, and the critical flow angle may be changed. This problem is left for a future study.

Conclusions

1 In the case of a very narrow diffuser with $b/r_i = 0.0153$, rotating stall was not observed until the mean inlet flow angle was reduced to 3.4 deg from the circumferential direction as predicted.

2 The critical flow angle for rotating stall was influenced little by modification of the exit/inlet radius ratio in the tested very narrow vaneless diffuser.

3 The critical inlet flow angle can be predicted correctly for very narrow diffusers as well as for wide diffusers.

4 The propagating speed of stall cells induced in vaneless diffusers agreed fairly well with the prediction [1].

5 In cases of small specific speed blowers, the impeller may stall before the vaneless diffuser stalls unless a special care is taken for designing the impeller.

References

1 Jansen, W., "Rotating Stall in a Radial Vaneless Diffuser," ASME *Journal of Basic Engineering*, Vol. 86, No. 4, 1964, pp. 750–758.

2 Tsurusaki, H., and Imaichi, K., "Experimental Study on Rotating Stall of Centrifugal Impeller" (in Japanese), *Turbomachinery*, Vol. 5, No. 2, Feb. 1977, pp. 14–24.

3 Senoo, Y, and Kinoshita, Y., "Limits of Rotating Stall and Stall in Vaneless Diffuser of Centrifugal Compressors," ASME Paper No. 78-GT-19, Apr. 1978.

4 Abdelhamid, A. N., Colwill, W. H., and Barrows, J., F., "Experimental Investigation of Unsteady Phenomena in Vaneless Radial Diffusers," ASME JOURNAL OF ENGINEERING FOR POWER, Vol. 101, No. 1, 1979, pp. 52–60.

5 Abdelhamid, A. N., and Bertrand, J., "Distinction Between Two Types of Self Exited Gas Oscillations in Vaneless Radial Diffusers," ASME Paper No. 79-GT-58, 1979.

6 Hisatani, M., "Rotating Stall in Vaneless Diffusers of Centrifugal Compressors" (in Japanese), JSME Paper No. 730-15, Oct. 1979, pp. 299–302.

7 Abdelhamid, A. N., "Effect of Vaneless Diffuser Geometry on Flow Instability in Centrifugal Compression System," ASME Paper No. 81-GT-10, Mar. 1981.

8 Van Den Braembussche, R. A., Frigne, P., and Roustan, M., "Rotating Nonuniform Flow in Radial Compressors," VKI PREPRINT 1980-14, Apr. 1980.

9 Ligrani, P. M., Van Den Braembussche, R., and Roustan, M., "Rotating Stall Measurements in the Vaneless Diffuser of a Radial Flow Compressor," ASME Paper No. 82-GT-257, May 1982.

10 Frigne, P., and Van Den Braembussche, R., "Distinction Between Different Types of Impeller and Diffuser Rotating Stall in a Centrifugal Compressor With Vaneless Diffuser," ASME JOURNAL OF ENGINEERING FOR GAS TURBINES AND POWER, Vol. 106, No. 2, Apr. 1984, pp. 468–474.

11 Lenneman, E., and Howard, J. H. G., "Unsteady Flow Phenomena in Rotating Centrifugal Impeller Passage," ASME JOURNAL OF ENGINEERING FOR POWER, Vol. 92, No. 1, Jan. 1970, pp. 65–72.

12 Wiesner, F. J., "A Review of Slip Factors for Centrifugal Impellers," ASME JOURNAL OF ENGINEERING FOR POWER, Vol. 89, No. 4, 1967, pp. 558–572.

13 Senoo, Y., Kinoshita, Y., and Ishida, M., "Asymmetric Flow in Vaneless Diffusers of Centrifugal Blowers," ASME *Journal of Fluids Engineering*, Vol. 99, No. 1, 1977, pp. 104–114.

DISCUSSION

R. Van den Braembussche[1]

The authors have made several important contributions to a better understanding of the flow in vaneless diffusers and the data presented in this paper are an additional step in the confirmation of their theoretical prediction, for which they must be congratulated.

However, I want to comment on some of the experimental points which are left on Fig. 9. Most of the points on Fig. 10 have been refused because they should not correspond to diffuser rotating stall. Several arguments were used for this. Points 8, 11, 13, 15, 17, 18, and 19, indicated by an open triangle, are refused because the critical flow angle corresponds to a kink in the pressure rise curve or to peak pressure rise. However, the performance curve corresponding to point 6 (Fig. 4(*a*) of [3]) and point 9 (Fig. 7 of [3]) also show a kink in the pressure rise curve at critical flow. It is not clear why these points are left on Fig. 9, and if they are also taken off, only three points are left to compare with the theory.

Measurements of Abdelhamid [14] have shown that diffuser rotating stall can result in a kink in the performance curve (Fig. 3 of [14]) and that these instabilities can be removed by a throttling of the diffuser outlet. We are therefore not convinced that a kink in the pressure rise curve is a sufficient condition to conclude for impeller rotating stall.

[1]Associate Professor, von Karman Institute, Rhode-Saint-Genèse, Belgium.

At the time we made the comparison shown on Fig. 10, there were not many criteria available to distinguish between impeller and diffuser rotating stall. We therefore based our judgments on the published information and our own observation. However, we still think that there are many arguments to accept that the unstable conditions given on that figure are due to diffuser rotating stall.

For points 1, 2, 3, and 5 rotating stall is observed on the negative slope side of the pressure rise curve without any discontinuity.

For points 2 and 5 the rotational speed of the cells is in agreement with the theory of Jansen [1]. This could not be checked for all the points because of an uncertainty in the number of stall cells.

Impeller rotating stall has a strong upstream influence. A hot film probe installed in the inlet channel of point 5 did not show any low-frequency perturbation before surge occurred.

Points 1, 2, 3, and 5 are obtained with impellers with 65 to 68 deg backward lean angle, similar to point 9, for which it was mentioned in [3] that this would prevent the impeller from stalling.

The discrepancy between experiments and predicton of points 12, 13, 14 and 6, 7, 8 can be explained by diffuser inlet flow distortion. Each series of data is obtained with one impeller and three diffusers of different width. It is quite possible that the sudden contraction at diffuser inlet creates a diffuser inlet flow distortion. The theory [15] predicts a 3 to 7 deg change in critical flow angle due to inlet distortion.

For the other points the discrepancy between theory and experiments was explained in [8] as a Reynolds number influence, based on experimental observations. The pairs of data 1, 3 and 18, 19 are obtained with the same impeller and diffuser combination but at different Reynolds number, corresponding to a different pressure level. The theory does not predict a direct Reynolds number influence on diffuser stability but it could be that lower Reynolds numbers result in higher flow distortion at impeller exit, and therefore also influence diffuser stability.

One should not conclude from this that we have any doubt about the validity of this theory. On the contrary, the data shown in this paper prove that a very good agreement is obtained when the experimental diffuser inlet flow is close to uniform as assumed by the theory. As a conclusion, I would suggest that when using this prediction, one has to care more about diffuser inlet flow perturbations due to impeller flow, diffuser inlet geometry, or leakage flow.

References

14 Abdelhamid, A., "Control of Self-Excited Flow Oscillations in Vaneless Diffuser of Centrifugal Compression Systems," ASME Paper No. 82-GT-188.

15 Senoo, Y., and Kinoshita, Y., "Influence of Inlet Flow Conditions and Geometries of Centrifugal Vaneless Diffusers on Critical Flow Angle for Reversed Flow," ASME *Journal of Fluids Engineering*, Vol. 99, No. 1, 1977, pp. 93–103.

8 Also published in AGARD CP 282, Paper No. 12.

Author's Closure

Several reasons are conceivable for scattering of experimental data in Fig. 10. A distorted velocity distribution across the diffuser width at the inlet and a circumferentially distorted boundary condition at the diffuser exit due to the scroll are some of them. In addition, it is suspected that data of rotating stall in the impeller may be erroneously included.

In the process of deducing a relationship between variables regarding a few experimental data, a single erroneous datum can upset the whole relationship; on the other hand, the relationship is hardly misled by lack of a datum. Therefore, in the present research it is important to limit the experimental data to only very reliable ones and the data should be consistently presented.

At a small flow rate impeller blades must be stalled as it will be mentioned later. Stall of impeller blades does not always mean incipience of rotating stall in the impeller, but in many cases rotating stall is induced at the critical flow rate of impeller stall. Therefore, each of the data in Fig. 10 was examined to determine whether it was safe for impeller stall. If a datum satisfied one of conditions of possible impeller stall, it was not adopted in Fig. 9 unless the information on the experiment convinced the authors that the impeller was not stalled. The conditions of possible impeller stall are explained in the text for respective experimental points.

Rotating stall in a vaneless diffuser hardly changes the mean intensity of swirl in the diffuser unless local reverse flow occurs at the diffuser exit, and the pressure-flow rate characteristic curve does not have anomaly at the critical condition. Therefore, if anomaly is observed in the characteristic curve at the critical flow rate of rotating stall, it is at once suspected that the rotating stall is induced in the impeller. However, if the asymmetric reverse flow, which is induced by the rotating stall in the vaneless diffuser, reaches the diffuser exit, the mean pressure rise in the diffuser becomes less and anomaly appears in the characteristic curve. Therefore, at the critical condition where the characteristic curve has anomaly the incidence angle and the deceleration ratio at the inlet of the impeller are examined as a rule. If the impeller is safe for stall, it is assumed that the rotating stall is induced in the vaneless diffuser.

The mean velocity in the throat between blades at the inlet of the impeller is proportional to the flow rate. At a small flow rate the velocity is very low, and unless the circumferential velocity at the impeller inlet is very small, the deceleration rate from the impeller inlet to the throat is too large for the boundary layer to flow along the blade surface and rotating stall may be induced. However, an impeller with blades of large backward leaning angle has a characteristic curve with a steep negative gradient, and it can run stably even at the small flow rate and the impeller stall is not apparent in the performance.

In other words no impeller can work without separation of flow near the leading edge of the blades when the flow rate is reduced to less than 1/2 or 1/3 of the zero incidence flow. If a wide impeller is used for a test of a narrow vaneless diffuser, when the flow rate is reduced the impeller likely stalls before the rotating stall occurs in the vaneless diffuser. Therefore, the critical data of vaneless diffusers which were tested with an impeller wider than the diffuser width should be examined carefully to determine whether the impeller is the cause of rotating stall.

The difference in the critical flow angles of points 1 and 3 indicates the influence of a change of Reynolds number. The flow at the impeller exit and the flow in the vaneless diffuser are influenced by Reynolds number to a certain degree, but probably the effect of Reynolds number on the decelerating zone at the impeller inlet is the most serious, and at a low Reynolds number laminar separation and rotating stall in the impeller may result at a relatively large flow rate.

Points 18 and 19 show that the critical flow angle was modified by 4 deg by a change of Reynolds number, but according to [9], the critical flow coefficient was identical for the two cases. It is presumed that the velocity distribution was distorted axially or circumferentially depending upon the Reynolds number and that the flow angle was measured at the middle of the diffuser passage. In this paper data are handled on the basis of uniform inlet flow, and if the critical flow angles of points 18 and 19 are evaluated on this basis, the two points must be identical because of the identical flow coefficient.

Because of the above reasons, many of data in Fig. 10 were tentatively withheld in Fig. 9 which indicates the critical conditions of rotating stall in vaneless diffusers. If the experimental

conditions are disclosed and it becomes clear that the impellers were not the cause of the rotating stall, those data should be adopted in Fig. 9.

It is hoped that experiments on rotating stall in vaneless diffusers in the future will be carried out using impellers which are safe for stall at a flow rate less than the critical flow rate of the vaneless diffusers, and the critical flow rate of the impeller should be clearly noted. Using those reliable data, the influences of various parameters on the critical flow angle of vaneless diffusers will be clarified.

Influence of a Closely Coupled Throttle on the Stalling Behavior of a Radial Compressor Stage

J. W. Railly
Professor.
Mem. ASME

H. Ekerol
Research Fellow.

Department of Mechanical Engineering,
University of Birmingham, U.K.

On the basis of the classical discussion of the stability of compressor blade rows, a treatment is given of the stability of a stage consisting of a radial impeller followed by a vaned radial diffuser with a small radial gap between them. At the exit of the diffuser a radial array of adjustable vanes serves either to throttle the flow or to offer no resistance. In the latter case, throttling takes place by means of restrictions at inlet situated well upstream. The theory demonstrates that instability in the former case can only occur at the point of static instability, i.e., when the stage pressure characteristic slope becomes so positive that the throttle pressure characteristic is tangential to it. With the conventional throttling arrangement, instability is predicted as expected, when the stage characteristic has zero slope. Experimental confirmation of these predictions was obtained from tests on a slow speed radial compressor stage employing the above arrangement at exit, dischanging to atmosphere. When the vanes were used for throttling no rotating stall appeared but with throttling situated remotely from the stage a vigorous rotating stall mode developed.

Introduction

Although many studies have been made of the stability of axial and, to a lesser extent, of radial compressors, relatively little attention has been paid to the influence of the up- or downstream boundary condition of the stage. Thus, in the case of axial stages with small blade height (or isolated cascades) the usual boundary conditions are either, (i) the presence of an infinite parallel annulus stretching up- and downstream of the stage, termed BCI, or, (ii), the imposition of a uniform pressure field at stage exit (by releasing the flow into a space large in volume compared with the stage) termed BCII. An exception to this is the work of Greitzer [1] who investigated the influence of a diffuser at the exit of an axial stage by replacing the diffuser by a few "step" changes in area of a parallel annulus. He demonstrated that a change took place in the slope of the characteristic at the point of instability (in the direction of negative slope).

The difficulty which is introduced to the theory if a more general treatment of the problem is attempted is that the flow downstream of the stage contains vorticity which is convected along the streamlines. Thus, for example, if a short annular diffuser is installed after the stage and then truncated by a throttle or a dump diffuser, the full equations for the stream-function and the vorticity transport have to be solved. This general problem, again for axial blade rows of small blade height, h, may be tackled numerically using the methods of Takata and Nagano [2] provided the blade rows are replaced by semi-actuator disks, i.e., by rows within which the flow is constrained to travel along a given direction which is not a function of the peripheral coordinate. Downstream of an axial stage, for a parallel annulus, the stream function and vorticity transport equations (appropriate to incompressible flow) are:

$$\nabla^2\psi = \zeta \tag{1}$$

$$\frac{D\zeta}{\partial t} = 0 \tag{2}$$

For a nonparallel annulus of constant mean radius, equation (1) should be replaced by:

$$\frac{\partial}{\partial x}\left(\frac{1}{h}\frac{\partial\psi}{\partial x}\right) + \frac{\partial}{\partial y}\left(\frac{1}{h}\frac{\partial\psi}{\partial y}\right) = \zeta \tag{3}$$

in which the (small) blade height h depends only upon x the axial direction.

The numerical solution of equations (2) and (3) would, in the general case, present a considerable amount of computation and will not be considered here. In Greitzer's treatment, the vorticity was assumed to be transported along the mean flow, for each parallel section, thus linearizing the problem. Even so, the amount of analysis was quite large.

In the case of radial annulus (which would need to be considered in the event of a large radial clearance between impeller and diffuser) the analysis work is even greater, for then the mean flow is an equiangular spiral.

For this reason the present theoretical treatment avoids the complexities of the foregoing analysis by considering only the

Contributed by the Gas Turbine Division of THE AMERICAN SOCIETY OF MECHANICAL ENGINEERS and presented at the 29th International Gas Turbine Conference and Exhibit, Amsterdam, The Netherlands, June 4–7, 1984. Manuscript received at ASME Headquarters, January 12, 1984. Paper No. 84-GT-190.

case when the radial clearance between impeller and diffuser vane inner diameter is small. In the experimental rig it is 9.7 percent of impeller radius. Furthermore the investigation will discuss the stability, employing, in the first place, the boundary condition at exit, BCII, and in the second place a third boundary condition, termed BCIII, namely, the immediate throttling of the flow leaving the diffuser, i.e., without a radial annular gap. The disposition of the "throttling vanes" may be seen in Fig. 1. Since these are all adjustable they may either be set to assist the diffusion process (as shown) or turned to throttle the flow. The radial clearance at the various setting angles may be judged from Fig. 1.

Downstream of the throttle vanes, the pressure is assumed to have the uniform value, p_4. The pressure drop characteristic of these vanes may be written in terms of the radial velocity component, C_{r_3}, as follows:

$$p_3 - p_4 = \frac{1}{2}\rho C_{r_3}^2 k_T \tag{4}$$

where k_T is the resistance coefficient of the throttle. Since p_4 is uniform then, after differentiation:

$$\frac{\partial p_3'}{\partial \theta} = k_T \rho \bar{C}_{r_3}\left(\frac{\partial u_3}{\partial \theta}\right) \tag{5}$$

where u_3, the perturbation from the mean velocity, $\bar{C}_{r_3}$, has been assumed to be small. Equation (5) is now the new boundary condition at exit from the stage, BCIII.

To produce boundary condition, BCII, the vanes are set as shown in Fig. 1 and the pressure field downstream of the diffusers p_3, is uniform.

A theoretical analysis of the stability of this type of stage will be presented on the basis of small disturbance theory similar to that developed by Stenning and Kriebel (reference [4]) and Fabri (reference [5]). The analysis is simplified greatly by virtue of the assumption of negligible radial clearance between rotor and stator and by the assumption of a large number of blades in the impeller and diffuser. The importance of this last assumption will be discussed in the next section.

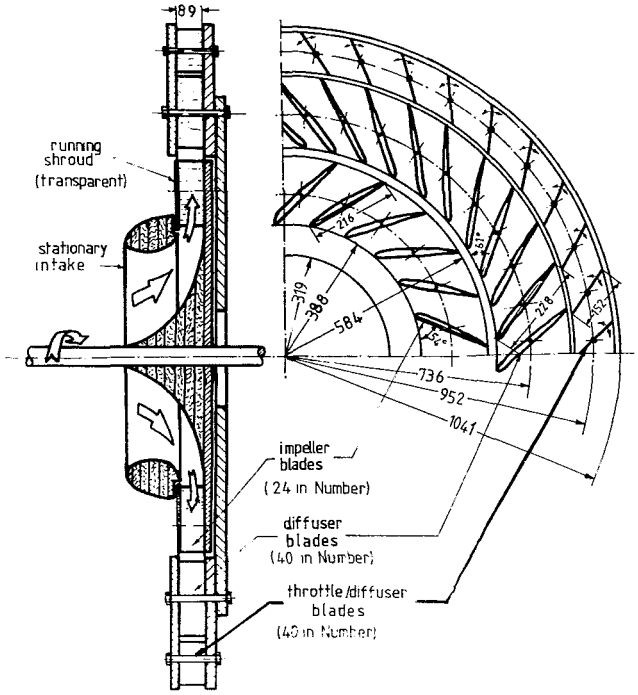

Fig. 1 Experimental machine

The stalling behavior of the stage shown in Fig. 1 was studied experimentally by measuring the pressure rise to the diffuser exit, just ahead of the array of throttle vanes, as a function of the compressor mass flow. In the first case, all the throttling was obtained by successively closing the throttle vanes and in the second case the throttle vanes were set in the "open" position as in Fig. 1 and throttling was achieved by

Nomenclature

A = area (m^2)
C = absolute velocity (m/s)
E,F,K,L,M = coefficients
G_n,H_n = complex functions
$g_{1,n},g_{2,n}$ = respectively, real and imaginary parts of G_n
$h_{1,n},h_{2,n}$ = respectively, real and imaginary parts of H_n
H = total head, (m^2/s^2)
h = absolute disturbance energy, annulus height
I = pressure term (rathalpy)

$$\left(I = \frac{p}{\rho} + \frac{W^2}{2} - \frac{\Omega^2 R^2}{2}\right)$$

T = resistance coefficient of the throttle
L = length (M)
$\mathcal{L}$ = Laplacian operator
n = wave number
p = static pressure (N/m^2)
p_0 = total pressure, (N/m^2)
R = radius (m)
r,θ = polar coordinates
t = time, (s.)
u,v = perturbation velocities in radial and tangential directions respectively, (m/s.)
W = relative velocity (m/s.)
x,y = Cartesian coordinates
Z = number of blades, impedance
χ = loss coefficient
α = absolute flow angle
β = relative flow angle
β_2' = blade angle at the tip
ϕ_1 = mass flow coefficient, $(Cr_1/\Omega R_1)$
ψ = stream function, time function in perturbation potential
ψ_{3T} = total to static pressure coefficient
λ = slip factor
ν = rotor radius ratio
ν_d = diffuser radius ratio
Ω = rotational speed of the rotor
ρ = density of the air
ξ = coefficient defined in equation (15)
η = slope of the pressure characteristic
ζ = vorticity

Subscripts

r = radial direction
R = the rotor
θ = tangential direction
S = stator
1 = generally rotor inlet
2 = generally rotor exit (or stator inlet)
3 = stator exit

Superscripts

R = relative; rotor
$\bar{\ }$ = time-average quantity
$'$ = perturbation quantity

the installation of a cylindrical structure, ahead of the intake, having a diameter about equal to the inner diameter of the impeller vanes and a length about equal to the radius. Around this structure were wound layers of fine gauze and the reduction in mass flow was effected by increasing the number of layers.

Theoretical Development

A schematic view of the radial stage is shown in Fig. 2. As described above, the abbreviations BCI, II and III related to three possible exit boundary conditions of which only the latter two will be discussed. BCII is achieved by effectively eliminating the restriction at diffuser exit and using the restriction at inlet for flow control while in the case of BCIII, the inlet throttle is absent. Before the present analysis on the radial stage was carried out a similar analysis (reference [3]) had been applied to an axial stage of 50 percent reaction which simplified the analysis. In that case the inlet to the rotor was assumed to be an infinite annulus with height equal to the height of the rotor and stator blading (which was small compared with the radius), thus permitting the assumption of a two-dimensional flow. The boundary condition upstream of the rotor for the radial stage is less easy to model since the flow accelerates quite sharply around the intake. However, since the whole analysis is of necessity quasi-two-dimensional it was assumed that the intake to the stage could be represented by a parallel annulus of mean height equal to the axial width at impeller entry and a radius, R_1. The flow ahead of the impeller was therefore the irrotational solution in terms of axial coordinate, x, and azimuthal angle, θ. At impeller entry the axial components from this solution become radial components while the tangential are unchanged.

The remaining difficulty for the solution concerns the clearance between impeller and diffuser. In the present experiment it is 9.7 percent of impeller radius; hence it is reasonable to assume that velocity and total head at diffuser entry are those at the impeller exit.

Within the impeller and the diffuser it is assumed that the flow direction relative to the blades, except at entry, does not vary with θ. In the case of the impeller, the relative velocity vector at exit is obtained by combining the apparent relative vector (at angle β_2') with a constant slip velocity, $\lambda\Omega R_2$ in order to try and take account of the change in effective relative outlet angle with flow that occurs in the actual flow.

Throughout the analysis, density is held constant and therefore the results can apply only to slow speed machines with negligible storage capacity.

Starting with the diffuser, the equation of motion is integrated along the blade centerline with respect to length, dl, giving

$$\frac{2\pi R_2}{Z_s}\left(\int_0^{ls}\frac{dl}{A_n}\right)\frac{\partial C_{r_2}}{\partial t}=H_2-H_3-x_s\frac{1}{2}C_2^2 \tag{6}$$

where C_{r_2} is radial velocity at radius R_2 just after entry at radius R_2, where A_n is normal passage width and x_s is the diffuser loss coefficient. This equation is then differentiated with respect to θ noting that each quantity will be written as the sum of a steady and a fluctuating component. For example, H_3 is written as follows:

$$H_3=\frac{\bar{p}_3}{\rho}+\frac{p_3'}{\rho}+\frac{1}{2}C_{r_3}^2\sec^2\alpha_3 \tag{7}$$

which, after differentiation and elimination of second order terms becomes

$$\frac{\partial H_3}{\partial\theta}=\frac{1}{\rho}\frac{\partial p_3'}{\partial\theta}+\nu_d^2\Omega R_2\phi_1\nu\sec^2\alpha_3\left(\frac{\partial u_1}{\partial\theta}\right) \tag{8}$$

in which u_1, is the disturbance in radial velocity at rotor entry, being simply related to the disturbance at eixt through the

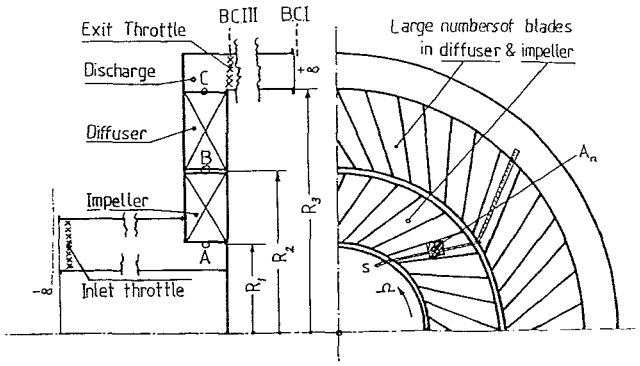

Fig. 2 Idealized machine and boundary conditions for the linearized analysis

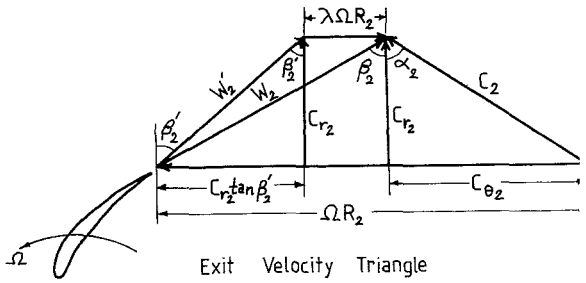

Fig. 3 Flow parameters at rotor tip

radius ratio (this being permissible since the impeller-diffuser radial clearance is small and the flow direction within impeller or diffuser (relatively) does not vary). Similarly the equation for H_2 may be shown to be given by:

$$\frac{\partial H_2}{\partial\theta}=\frac{1}{\rho}\frac{\partial p_2'}{\partial\theta}$$

$$+\nu\Omega R_2[\phi_1\nu^2\sec^2\beta_2'-(1-\lambda)\tan\beta_2']\left(\frac{\partial u_1}{\partial\theta}\right) \tag{9}$$

where λ is the slip factor (being the ratio of slip velocity to tip speed) which is maintained constant throughout the present analysis. Integrating the equation of motion within the impeller along the blade centerline the result is:

$$\frac{2\pi R_1}{Z_R}\left(\int_0^{l_R}\frac{dl}{A_n}\right)\left(\frac{\partial C_{r_1}}{\partial t}\right)=I_1-I_2-\chi_R\frac{1}{2}W_1^2 \tag{10}$$

Differentiating with respect to θ and noting that

$$I=\frac{p}{\rho}+\frac{W^2}{2}-\frac{\Omega^2R^2}{2}=H^{(R)}-\frac{\Omega^2R^2}{2}$$

and that

$$\left(\frac{\partial}{\partial t}\right)_{\text{Relative}}=\left(\frac{\partial}{\partial t}\right)_{\text{Absolute}}+\Omega\left(\frac{\partial}{\partial\theta}\right),\quad F_R=\int_0^{l_R}\frac{dl}{A_n}$$

it follows that:

$$2\pi\nu R_2\left(\frac{F_R}{Z_R}\right)\frac{\partial}{\partial\theta}\left[\left(\frac{\partial u_1}{\partial t}\right)+\Omega\left(\frac{\partial u_1}{\partial\theta}\right)\right]$$

$$=\frac{\partial H_1^{(R)}}{\partial\theta}-\frac{\partial H_2^{(R)}}{\partial\theta}-\frac{\partial}{\partial\theta}\left(\chi_R\frac{1}{2}W_1^2\right) \tag{11}$$

In terms of disturbance absolute energy, h_1, at entry to the impeller

$$\frac{\partial H_1^{(R)}}{\partial\theta}=\frac{\partial h_1}{\partial\theta}-\nu\Omega R_2\frac{\partial v_1}{\partial\theta} \tag{12}$$

where v_1 is the disturbance tangential velocity.

To find $H_2^{(R)}$ at exit, refer to Fig. 3 for the velocity triangle from which it may be shown, again to the first order, that

$$\frac{\partial H_2^{(R)}}{\partial\theta} = \frac{1}{\rho}\frac{\partial p_2'}{\partial\theta} + \nu\Omega R_2(\nu^2\phi_1\sec^2\beta_2' + \lambda\tan\beta_2')\left(\frac{\partial u_1}{\partial\theta}\right) \tag{13}$$

The treatment of the loss term must include the dependence of χ_R upon Cot β_1 (the assumed steady-state dependence) as well as the dependence of $\mathrm{Cot}\beta_1$ on both radial and tangential velocity disturbances.

Hence, making use of the velocity triangle at inlet to the impeller the loss term becomes

$$\frac{\partial}{\partial\theta}\left(\chi_R\frac{1}{2}W_1^2\right) = \left(\frac{\partial\chi_R}{\partial\mathrm{Cot}\beta_1}\right)\nu\Omega R_2(1+\phi_1^2)\left(\frac{\partial u_r}{\partial\theta}\right)$$
$$+\left(\frac{\partial\chi_R}{\partial\mathrm{Cot}\beta_1}\right)\phi_1(1+\phi_1^2)\left(\frac{\partial v_1}{\partial\theta}\right)+\chi_R\nu\Omega R_2\left(\phi_1\frac{\partial u_1}{\partial\theta}\right.$$
$$\left.-\frac{\partial v_1}{\partial\theta}\right) \tag{14}$$

again, to the first order.

A similar treatment of the loss term of the diffuser row is carried out in which $\mathrm{Cot}\alpha_2$ is written in terms of the radial velocity disturbance, u_3, noting that

$$\overline{\mathrm{Cot}\alpha_2} = \xi = (\nu^2\phi_1)/[(1-\lambda)-\nu^2\phi_1\tan\beta_2'] \tag{15}$$

It then follows that

$$\frac{\partial}{\partial\theta}(\mathrm{Cot}\alpha_2) = \left(\frac{\xi}{\phi_1}\right)\nu\Omega R_2[1+\xi\tan\beta_2']\left(\frac{\partial u_1}{\partial\theta}\right) \tag{16}$$

Combining equations (6), (8), and (9), for the diffuser to eliminate H_2 and H_3 and obtaining the velocities in terms of the radial disturbance velocity at impeller entry the following equation is obtained:

$$\nu R_2 E_1\frac{\partial}{\partial t}\left(\frac{\partial u_1}{\partial\theta}\right) = \nu\Omega R_2[F_1 - K_1 - \chi_s F_1$$
$$-\frac{1}{2}\chi_s' L_1 M_1]\left(\frac{\partial u_1}{\partial\theta}\right)+\frac{1}{\rho}\frac{\partial p_2'}{\partial\theta}-\frac{1}{\rho}\frac{\partial p_3'}{\partial\theta} \tag{17}$$

where

$$E_1 = 2\pi\left(\frac{F_s}{Z_s}\right),\quad F_1 = \nu^2\phi_1\sec^2\beta_2' - (1-\lambda)\tan\beta_2'$$

$$K_1 = \nu_d^2\phi_1\sec^2\alpha_3,\quad L_1 = \frac{(1-\lambda)^2}{\nu^2} - 2\phi_1(1-\lambda)\tan\beta_2'$$
$$+\nu\phi_1^2\sec^2\beta_2'$$

$$M_1 = \left(\frac{\xi}{\phi_1}\right)(1+\xi\tan\beta_2')$$

Combining equations (11), (12) and (13) for the impeller, the result is:

$$\nu R_2 E_2\left[\frac{\partial}{\partial t}\left(\frac{\partial u_1}{\partial\theta}\right)+\Omega\left(\frac{\partial^2 u_1}{\partial\theta^2}\right)\right] = \left(\frac{\partial h_1}{\partial\theta}\right)_{\mathrm{Abs}}$$
$$-\nu\Omega R_2 F_2\left(\frac{\partial u_1}{\partial\theta}\right)-\nu\Omega R_2 K_2\left(\frac{\partial v_1}{\partial\theta}\right)$$
$$-\frac{1}{\rho}\frac{\partial p_2'}{\partial\theta} \tag{18}$$

where

$$E_2 = 2\pi\left(\frac{F_R}{Z_R}\right),\quad F_2 = \nu^2\phi_1\sec^2\beta_2' + \lambda\tan\beta_2' + \chi_R\phi_1$$
$$+\frac{\chi_R'}{2}(1+\phi_1^2)$$

$$K_2 = 1-\chi_R+\frac{1}{2}\chi_R\phi_1(1+\phi_1^2)$$

In order to relate h_1, u_1, and v_1 at the impeller entry the assumption introduced above is made, namely, that the impeller inlet is connected to an infinite parallel annulus of radius R_1. At the junction, the axial components of velocity in the annulus equal the radial velocity components at impeller entry. Since the flow at entry is irrotational, it may be assumed that the potential function is given by:

$$\phi = \Sigma e\frac{nx}{R_1}e^{in\theta}\psi(t) \tag{19}$$

which corresponds to sinusoidal disturbances of wavelength $2\pi R_1/n$, where n is an integer. The disturbance potential is related to energy, h_1, as follows:

$$\frac{\partial\phi}{\partial t} = h_1$$

hence the following substitution may be made, for a single term of equation (19).

$$u_1 = \left[-\frac{\partial\phi}{\partial x}\right]_{x=0} = -\frac{n}{R_1}e^{in\theta}\psi(t) = -u_n e^{in\theta}$$

together with similar relationships for v_1 and their derivatives with respect to θ. Equations (17) and (18) contain pressure p_2' which would disappear on subtraction. It is convenient at this point to consider a pressure disturbance, $\delta p'$ to be imposed which will remain after subtraction of equation (17) from equation (18). This procedure was used by Fabri [5]. This corresponds to the presence of the pressure difference, $\delta p'$, in between rotor outlet and stator inlet.

The resulting equation will contain the function of time, $\psi(t)$ and its derivatives and if the Laplace transformation of the equation is carried out then $\psi(t)$ will be replaced by its transform. Thus, for the velocity, u_n,

$$\tilde{u}_n = \mathfrak{L}(u_n) = \mathfrak{L}\left[-\frac{n}{R_1}\psi(t)\right] = -\frac{n}{R_1}\tilde{\psi}(t)$$

and

$$\mathfrak{L}\left(\frac{\partial\psi}{\partial t}\right) = s\tilde{\psi}_n$$

since the initial condition is the uniform steady state.

The resulting equation still contains the pressure, p_3'. In the case when the flow is immediately released to a large plenum p_3' would be identically zero. In the presence of a throttle just downstream p_3' is obtained from equation (5). After manipulation of the various terms the following result is obtained

$$\tilde{u}_n = (\delta p/\rho)/Z_n \tag{20}$$

where Z_n, the "impedance", is given by

$$Z_n = SG_n + H_n$$

Let $g_{1,n}$, $g_{2,n}$ by the real and imaginary parts of G_n, and $h_{1,n}$, $h_{2,n}$ be the real and imaginary parts of H_n then:

$$g_{1,n} = -\nu R_2\left[E_1+E_2+\frac{1}{n}\right] =$$
$$-\nu R_2\left[2\pi\left(\frac{F_R}{Z_R}+\frac{F_s}{Z_s}\right)+\frac{1}{n}\right] \tag{21}$$

$$g_{2,n} = 0 \tag{22}$$

$$h_{1,n} = -\nu\Omega R_2\left\{\tan\beta_2' + \chi_R\phi_1 + \frac{\chi_R'}{2}(1+\phi_1^2)\right.$$
$$\left.+\chi_s[\nu^2\phi_1\sec^2\beta_2' - (1-\lambda)\tan\beta_2'] + \frac{\chi_s'}{2}\left[\frac{(1-\lambda)^2}{\nu^2}\right.\right.$$

$$-2\phi_1(1-\lambda)\tan\beta_2' + \nu^2\phi_1^2\sec^2\beta_2'\Big]\left(\frac{\xi}{\phi_1}\right)(1+\xi\tan\beta_2')$$

$$+\nu_d^2\phi_1\sec^2\alpha_3 + k_T\nu_d^2\phi_1\Big\} \tag{23}$$

$$h_{2,n} = -\nu\Omega R_2\left\{2\pi\left(\frac{E_R}{Z_R}\right)n + (1-\chi_R) + \frac{1}{2}\chi_R'\phi_1(1+\phi_1^2)\right\} \tag{24}$$

The solution of the system, equation (20), is clearly of the form

$$u_n = \left[-\frac{n}{R_1}\psi(t)\right] = \frac{(\delta p_n/\rho)}{G_n}e^{-(H_n/G_n)t} \tag{25}$$

Depending upon the real and imaginary parts of H_n and G_n the solution will represent a damped or amplified oscillatory solution. The condition of zero damping (the real part zero) i.e., $h_{1n}=0$, is then found as follows since

$$\mu = 0 = \frac{h_{1,n}}{g_{1,n}}, \quad \text{i.e., } h_{1,n} = 0$$

and the speed of propagation from

$$\omega = \frac{h_{2,n}}{g_{1,n}} = \Omega\Big[2\pi\left(\frac{F_R}{Z_R}\right)n + (1-\chi_R) + \frac{\chi_R'}{2}\phi_1(1+\phi_1^2)\Big]\Big/\Big[2\pi\left(\frac{F_R}{Z_R}+\frac{Es}{Z_s}\right)+\frac{1}{n}\Big]$$

Hence the above relationship for h_1 may be examined for this condition.

It is convenient at this point to introduce the steady stage pressure rise characteristic, ψ_{3T} as dependent upon ϕ_1. The slope of this characteristic may be shown to be

$$\eta = \frac{\partial\psi_{3T}}{\partial\phi_1} = -2\nu^2\Big\{\tan\beta_2' + \chi_R\phi_1 + \frac{\chi_R'}{2}(1+\phi_1^2) + \chi_s[\nu^2\phi_1\sec^2\beta_2' - (1-\lambda)\tan\beta_2'] + \left(\frac{\chi_s'}{2}\right)\Big[\frac{(1-\lambda)^2}{\nu^2} - 2\phi_1(1-\lambda)\tan\beta_2' + \nu^2\phi_1^2\sec^2\beta_2'\Big]\left(\frac{\xi}{\phi_1}\right)(1+\xi\tan\beta_2') + \nu_d^2\phi_1\sec^2\alpha_3\Big\} \tag{26}$$

In the event that k_T is zero, comparing equations (23) and (26) shows that instability occurs when the characteristic slope, η is zero, irrespective of the values and gradients of the losses on rotor and stator.

When k_T is nonzero, it is evident that η may take positive values at the point of zero damping, as may be seen by comparing equation (26), with $h_{1,n}$ equal to zero, with equation (23). All the terms of (23) except the last are identical to those of (26) so that the slope of the characteristic for the condition of zero damping becomes:

$$\eta_0 = \left[\frac{\partial\psi_{3T}}{\partial\phi_1}\right]_{\mu=0} = 2k_T\nu^2\nu_d^2\phi_1 = 2K_T\phi_1 \tag{27}$$

This result has a very simple outcome in the case when all the throttling of the compressor takes place at the restriction and when p_0 at inlet is P_a, although the compressor here is serving no useful function, since the entire pressure rise is destroyed at the throttle.

The throttle "pressure characteristic" referred to the impeller inlet radius in terms of flow coefficient, ϕ_1 (non-dimensionalized by tip speed), obeys a square law as follows:

$$\psi_{TH} = K_T\phi_1^2 \tag{28}$$

and it is clear, by differentiation of this result with respect to flow, that the throttle curve slope is equal to the stage

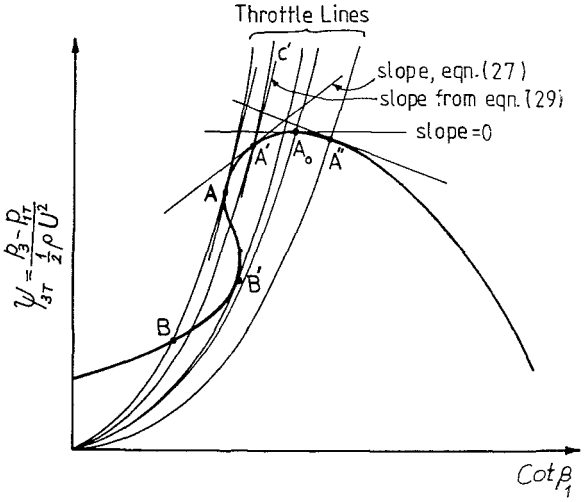

Fig. 4 Hypothetical performance map of the compressor

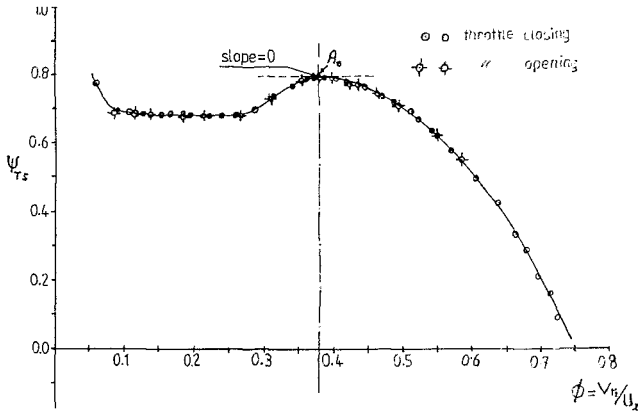

Fig. 5 Stage performance with close-couple throttling

characteristic slope, η_0, above for the same ϕ_1 value, (and hence also ψ_{3T}-value). This situation is depicted in Fig. 4 where a hypothetical characteristic is drawn and throttle lines for various K_T values are superimposed. It is clear that the point of zero damping, point A, corresponds exactly with the onset of static instability, (which is the situation for all points for which the characteristic slope exceeds the throttle value). At this point the throttle curve just touches the characteristic. The region to the left of A as far as B′ is a region which gives rise to static instability. In a situation in which throttling also occurs at some other location, say, far upstream, where the throttle coefficient (referred to ϕ_1) is K_F, then the overall throttle characteristic is given by

$$\psi_{TH} = (K_T + K_F)\,\mathrm{Cot}^2\beta_1 = (K_T + K_F)\phi_1^2 \tag{29}$$

At the point of instability, the slope of the stage characteristic is still given by equation (27), hence the difference between the slope of the combined throttle and that of the characteristic, $\Delta\eta$, is

$$\Delta\eta = 2K_F\mathrm{Cot}\beta_1 = 2K_F\phi_1 \tag{30}$$

Referring to Fig. 4, at the point A', the above result is the difference between the slope of the resistance line A′C′ and the characteristic slope at A′. In the case of a more complex boundary condition (as for example a finite length of annulus downstream of the diffuser) it is clear that the point of instability will be between point A and point A_0, at zero slope. The exact determination presents quite a lot of computation as mentioned above.

The case dealt with by Greitzer [1], namely the addition of an annular diffuser at exit may also be understood by changing the sign on the resistance coefficient, K_T, which then

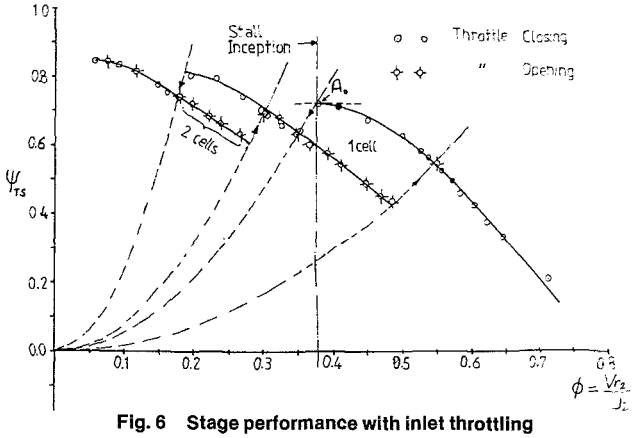

Fig. 6 Stage performance with inlet throttling

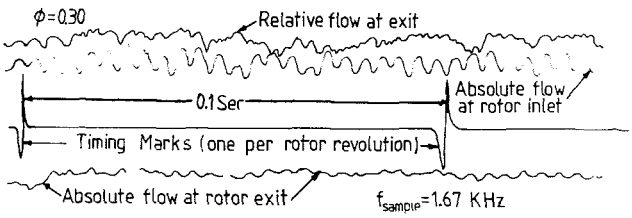

Fig. 7 Sampled hot-wire signals with close-coupled throttle

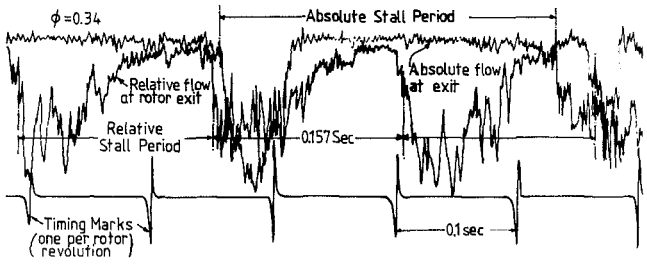

Fig. 8 Sampled hot wire signals with inlet throttle

becomes the pressure recovery coefficient of a "dump" or "short" diffuser. The resulting slope of the compressor stage characteristic based on p_3 would then be negative at instability but the condition for instability for the system, stage plus diffuser, is zero slope, as would be expected.

Experimental Evidence

The sequence of presentation perhaps ought to present the experimental result first, since the evidence in regard to stalling behavior on a (radial) stage was obtained first. Reference to Fig. 1 shows that throttling with unrestricted intake) was effected on the compressor stage shown by means of a circular array of adjustable throttle vanes. When the stage was tested the pressure characteristic shown in Fig. 5 was obtained and at no point was rotating stall observed although there was evidence of disturbed flow downstream of each rotor blade. Figure 7 shows a hot-wire trace taken just downstream of the impeller at a point to the left of A_0 on the characteristic in Fig. 5: no rotating stall is evident. The shape of the characteristic demonstrates, on the basis of the above theory, that nowhere does a throttle line intersect at the required slope (namely, that corresponding to static instability which would be the rotating stall limit for this throttle location).

The stage was then tested by arranging gauzes ahead of the rotor which were sufficiently far ahead not to influence the rotor behavior and the throttle vanes were open. The resulting pressure characteristic is as shown in Fig. 6 which exhibits the usual discontinuities associated with various regimes of rotating stall, the latter being evident from hot-wire measurements taken at rotor exit as shown in Fig. 8. It is evident that the condition of zero slope is obeyed in this case which would correspond with throttling far removed from the machine.

Conclusions

It is evident that the boundary condition imposed on a compressor stage by the installation of a throttle close to the last row has an inhibitory influence upon the onset of instability. Intuitively this might be explained by the hypothesis that as the flow through a blade row starts to fall off, instead of a uniform back pressure being present and tending to hasten this process, the close proximity of the throttle results in a local loss of pressure so allowing the blade row to carry on pumping at that point.

Further evidence in support of the above theory may be drawn from a recent study by Abdelhamid [6] in which the influence upon the onset of rotating stall in a radial machine arising from the insertion of a restrictor near the outer diameter of the vaneless diffuser was studied. An improvement in the stall margin was found the more exit was restricted although the effect upon efficiency at higher mass flows resulted in reduced efficiency. It is also likely that in this latter experiment the influence of the restrictor would be more "far-seeking" since the element involved, being a vaneless diffuser, would be rather sensitive to the upstream influence of the restrictor.

A further point arising from the analysis, as is evident from equation (23), is that instability of the stage depends only upon the overall pressure coefficient slope and not upon the slopes or values of the losses of the individual components. An investigation, referred to by Greitzer [7], carried out by Dussourd et al. further amplifies this last point. Thus a more "stable" characteristic (aimed at surge inhibition) may be achieved by the addition of closely-coupled resistances to make the combined slope of the stage characteristic negative.

Acknowledgments

The authors are indebted to the University of Birmingham. The paper is published by permission of the Director of the National Engineering Laboratory of the Department of Industry and Trade who provided support for the research programme. It is Crown Copyright.

References

1 Greitzer, E. M., "Coupled Compressor Diffuser Instability," *J. of Aircraft*, Vol. 14, pp. 233–238.

2 Takata, H., and Nagano, S., "Nonlinear Analysis of Rotating Stall," ASME JOURNAL OF ENGINEERING FOR POWER, Oct. 1972, pp. 279–293.

3 Railly, J. W., and Ekerol, H., "Influence of Throttle Position on the Stalling Behaviour of a Radial Compressor Stage," Research Report No. 174, July 1982, Mech Eng Dept., University of Birmingham, U.K.

4 Stenning, A. H., and Kriebel, A. R., "Stall Propagation in a Cascade of Airfoils," *Trans. ASME*, Vol. 80, May 1958, pp. 777–790.

5 Fabri, J., "Growth of a Perturbation in an Axial Flow Compressor," ASME JOURNAL OF ENGINEERING FOR POWER, Vol. 101, Jan. 1979, pp. 87–94.

6 Abdelhamid, A. N., "Control of Self-Excited Flow Oscillations in Vaneless Diffuser of Centrifugal Compression Systems," ASME Paper No. 82-GT-188.

7 Greitzer, E. M., "The Stability of Pumping Systems—The Freeman Scholar Lecture," ASME *Journal of Fluids Engrg.*, Vol. 103, June 1981, pp. 193–242.

8 Dussourd, J. L., Pfannebecker, G. W., and Singhania, S. K., "An Experimental Investigation of the Control of Surge in Radial Compressor Using Close Coupled Resistances," ASME *Journal of Fluids Engrg.*, Vol. 99, Mar. 1977, pp. 64–76.

Performance Characteristics of Shrouded and Unshrouded Impellers of a Centrifugal Compressor

H. Harada
Ebara Corporation,
Fujisawa, Japan

The overall performance of shrouded and unshrouded identical impellers of a centrifugal compressor were tested and compared. A closed loop test stand with Freon gas as the working fluid was employed for the experiments. The inlet and outlet velocity distributions of both impellers were measured using a three-hole cobra probe and a hot-film probe to determine the velocity distribution and unsteady flows due to wakes and inlet stall.

Introduction

Both shrouded and unshrouded impellers are widely used in centrifugal compressors. The high-pressure, single-stage impellers used for turbochargers and gas turbine compressors are unshrouded because of the high stress requirements and the problems of machining and precision casting. Senoo et al. [1] report that the performance with unshrouded impeller is affected by the clearance between the casing and the impeller, especially in the region where there is a large reduction in relative velocity in the impeller channel.

Multistage compressors requiring high reliability for industrial use and gas processing are widely used with shrouded impellers. However the performance difference between shrouded and unshrouded impellers in centrifugal compressors has, up to now, come under little investigation. Howard et al. [2–3] have measured the effect on internal flow caused by a shroud in a 9-in. diameter clear plastic impeller both with and without a shroud, using the hydrogen bubble method and a hot film probe. They reported that with unshrouded impellers the secondary flow in the impeller channel varies from the pressure side of the blade to the suction side due to leakage across the clearance, and that the presence of a shroud affects stall conditions at partial capacity. However, since the rotational speed was as low as 140 rpm, their study did not discuss the overall performance difference between shrouded and unshrouded impellers.

In the study covered by this paper, the overall performance of shrouded and unshrouded backward impellers was compared. The circumferential Mach number of the tested impeller was varied up to unity, and a three-hole cobra probe and hot-film probe were used to measure the velocity distribution and unsteady flow at the impeller inlet and outlet.

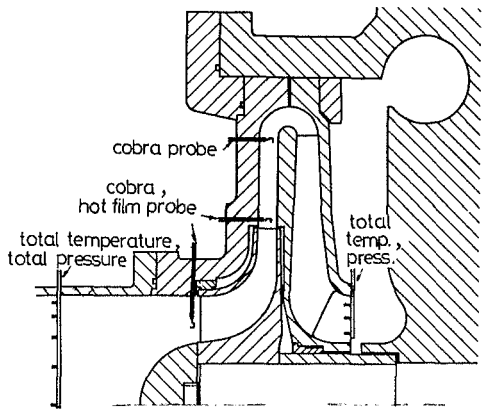

Fig. 1 Shrouded impeller cross section

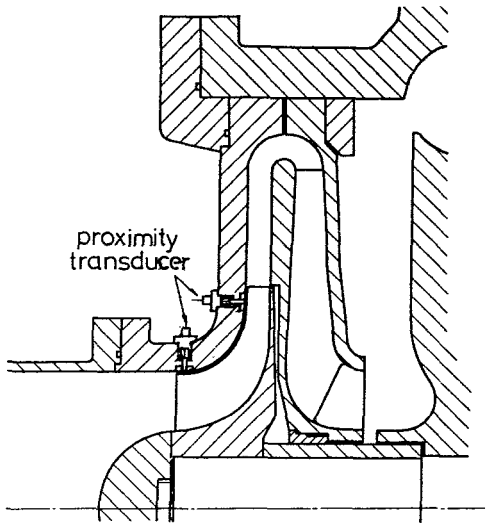

Fig. 2 Unshrouded impeller cross section

Contributed by the Gas Turbine Division of THE AMERICAN SOCIETY OF MECHANICAL ENGINEERS and presented at the 29th International Gas Turbine Conference and Exhibit, Amsterdam, The Netherlands, June 4–7, 1984. Manuscript received at ASME Headquarters December 27, 1983. Paper No. 84-GT-46.

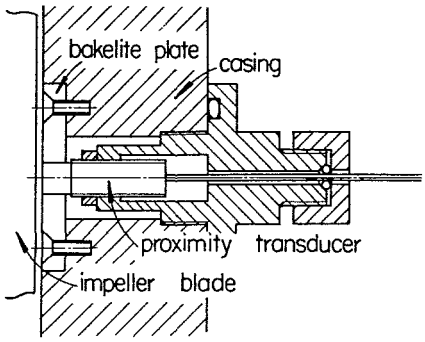

Fig. 3 Noncontacting eddy current proximity transducer

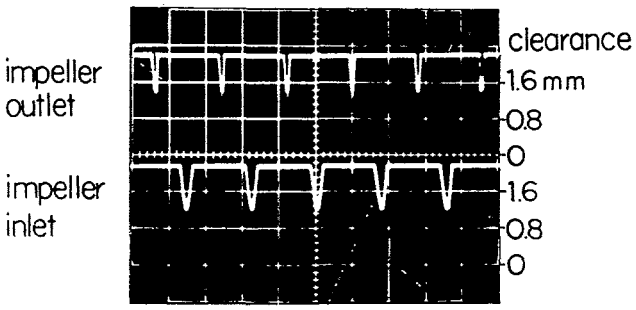

Fig. 4 Output of the proximity transducer

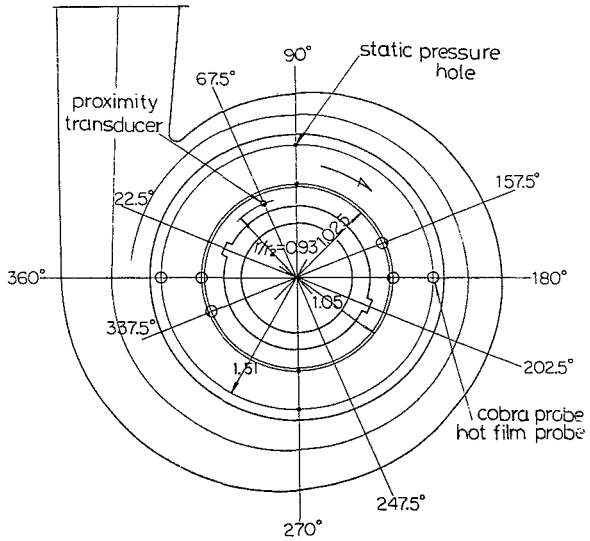

Fig. 5 Measuring position of probes

Apparatus

To test with circumferential Mach numbers up to unity, Freon gas was used in a closed loop to enable a reduction in rotating speed and input power to the compressor. An induction motor was employed to drive the compressor through a step-up gearbox and the compressor speed was changed from 1000 to 6000 rpm by a fluid coupling connected between the motor and the gearbox. Duct layout and dimensions were per ASME-PTC10-1965. Flow rate was measured by a D-1/2D tapped orifice. To determine when the system had become thermodynamically stable, the energy balance between the compressor input power and the output heat was monitored. Input power was measured by a torque meter with a speed counter installed on the high-speed shaft, and rejected heat from the gas cooler was determined from the cooling water heat gain. When both energy values coincided within a predetermined range, the system was considered to be stable. Prior to the tests, the loop gas was analyzed by a gas chromatograph to determine the air content. Compressor performance was corrected according to the results of the analysis. System pressure was kept slightly higher than atmospheric pressure to prevent air leakage into the loop. An automatic data processing device using a minicomputer was used for real-time performance calculations.

Experimental Method

Pressure measurements were carried out using semiconductor pressure transducer with a ±0.2 percent F.S. accuracy. The transducers were calibrated before testing, using a weight-type reference gauge. C-C thermocouples were used for measuring fluid temperatures. These were calibrated using quartz thermometer of ±0.001°C accuracy dipped into a constant temperature bath kept within ±0.03°C. All calibration data were stored on a minicomputer memory disk and were used for real time calculations from measured values.

A single stage compressor with an overhanging shaft and parallel wall vaneless diffuser was used for the study.

To avoid the uneven peripheral pressure distribution in the diffuser cased by a volute-type collector casing, a return channel was installed after the diffuser as shown in Fig. 1, and the compressor stage was defined as the stage from the inlet of the impeller to the outlet of the return channel. In order to check the axisymmetry of the flow, the data were taken at each two points on the same radius of inlet and outlet of the diffuser, and found them almost same.

The dimensions of the tested impeller are shown in Table 1.

Table 1

d_2	=	570 mm
b_2	=	30 mm
β_2	=	45 deg
Z	=	19

Initially, the shrouded impeller shown in Fig. 1 was tested, then the shroud was machined off to give an unshrouded impeller with an identical shape to the shrouded one. This unshrouded impeller was then fitted with a new front casing cover with the same shroud contour as shown in Fig. 2 and retested.

Nomenclature

a = velocity of sound, m/s
b = width, mm
c = absolute velocity, m/s
d = diameter, mm
f = frequency, Hz
i = number of stall cells
Mu_2 = circumferential Mach number, u_2/a_0
n = compressor rotating speed, Hz
Q = flow rate
r = radius, mm
u = circumferential velocity, m/s
x = length, mm
z = number of blades
β = blade exit angle referenced to tangential, deg
η = efficiency, percent
ψ = head coefficient

Subscripts

0 = stagnation condition at the impeller inlet
1 = impeller inlet
2 = impeller outlet
3 = diffuser inlet
4 = diffuser outlet
m = radial
u = tangential

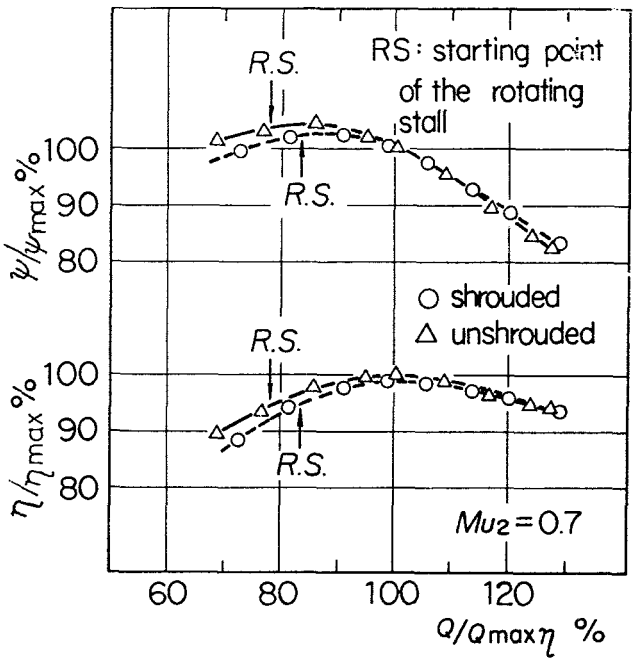

Fig. 6 Performance diagram

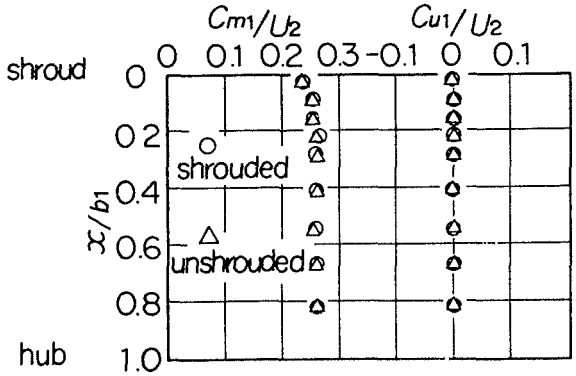

Fig. 7 Inlet velocity distribution ($Q/Q_{max\eta} = 1$)

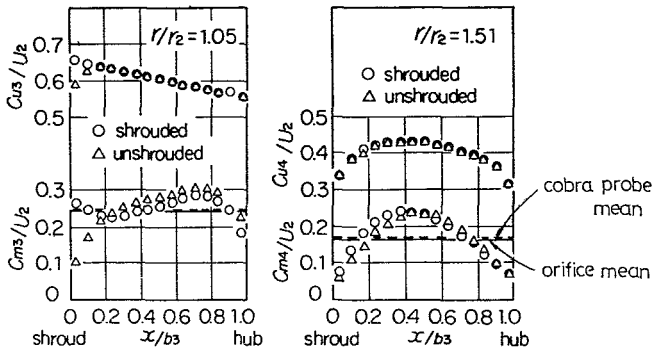

Fig. 8 Diffuser velocity distribution ($Q/Q_{max\eta} = 1$)

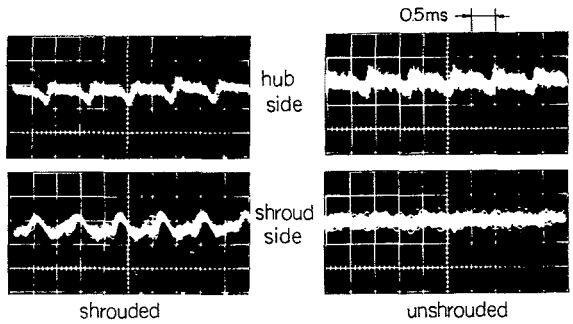

Fig. 9 Velocity fluctuation at the diffuser ($Q/Q_{max\eta} = 1$)

Generally, compressor performance with an unshrouded impeller is strongly affected by the casing-impeller clearance at the blade tip. The clearance between casing and impeller tip was designed as 1 mm, in order to avoid the contact with each other during operation.

Though the clearance is correctly set on assembly, it may change during operation due to disk deformation under rotating stress and temperature rise. Therefore, a non-contacting eddy current proximity transducer was attached to the front cover near the impeller inlet and outlet to measure the running clearance. Figure 3 shows details of the attached transducer. To eliminate signal interference due to the magnetic effect of the steel casing, the sensing probe was mounted in a bakelite plate with an o.d. 6 times that of the probe. The output voltage of the transducer was recorded by an oscillograph as shown in Fig. 4.

Tip clearance readings near the impeller outlet are shown at the top of the figure and tip clearance readings near the inlet are shown at the bottom. During operation the tip clearance at the outlet was 1.4 mm and 1.2 mm at the inlet. The ratio of inlet tip clearance to impeller inlet blade span was 0.016. Figure 5 shows the location of static pressure holes and velocity sensing probes. The velocity distribution at inlet and outlet of the impeller was measured by use of cobra probes. The unsteady flow was also measured with hot-film probes. Output of the hot film probe was recorded in a data recorder, and the frequency spectrum was analyzed. In the unshrouded impeller test, the output of the proximity sensor was used for counting the blade passing pulse to synchronize it with hot-film probe measurements. However, in the case of the shrouded impeller, small pieces of optical tape were attached to the compressor coupling at positions corresponding to the blade positions, and the pulses were detected by a photoelectric pickup.

Experimental Results

Figure 6 shows in dimensionless values the overall performances of the shrouded and unshrouded impellers at $Mu_2 = 0.7$. The 100 percent value coincides with the maximum efficiency point of the unshrouded impeller. At flow rates greater than maximum efficiency flow rates, little difference in performance was observed between the two impellers. However, at lower flow rates the shrouded impeller showed inferior performance to the unshrouded one.

Figure 7 shows the inlet velocity distribution at a flow rate near maximum efficiency. The measurements were made using the cobra probe positioned 10 mm upstream from the unshrouded impeller inlet and 15 mm upstream, in the case of the shrouded impeller. There was no difference in the inlet velocity distribution of the two impellers, and the flow had no tangential velocity components.

Figure 8 shows the measured velocity distribution obtained by traversing the cobra probe across the diffuser width at the same flow rates as shown in Fig. 7. The left figure corresponds to the location of $r/r_2 = 1.05$ and the right figure at $r/r_2 = 1.51$. The upper plots in each figure show the tangential velocity component divided by the circumferential velocity of the impeller, and lower plots show the same ratio with the radial velocity component. The horizontal coordinate shows the position across the diffuser width. The solid line in the figure indicates the mean velocity calculated from weight flow measured by the orifice and dashed line indicates the

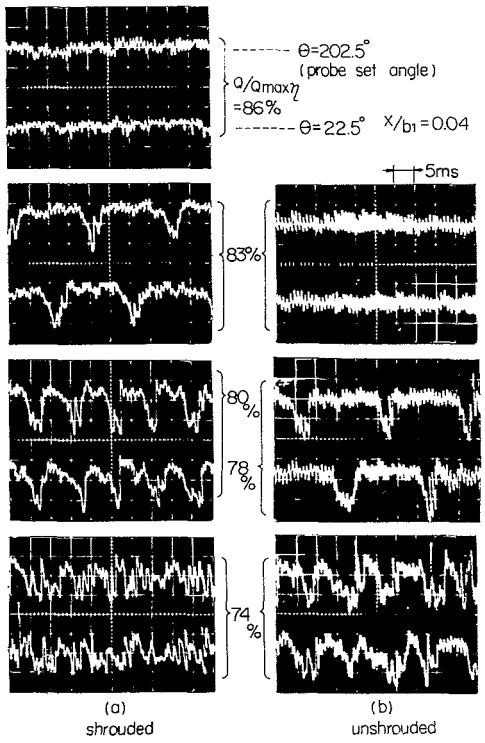

Fig. 10 Velocity fluctuation at impeller inlet

integral mean value measured by cobra probe. These values were nearly the same on both impeller.

This figure shows that the main difference in the velocity distributions of both impellers occurs at the outlet, immediately after the impeller, on the shroud side.

Figure 9 shows the flow fluctuations measured by the hot-film probe at the diffuser inlet ($r/r_2 = 1.025$) to indicate the aspect of blade wake. The probe was faced close to the flow direction, and the flow rate was about the same as in Fig. 8. The left figure is for the shrouded impeller and the right is for the unshrouded. The hub side velocity at $x/b_3 = 0.93$ is shown above, and the shroud side at $x/b_3 = 0.03$ is shown below. This figure indicates that near the sound side the shrouded impeller has larger velocity fluctuations between the blades than the unshrouded one, whereas near the hub wall there is little difference between them.

From the velocity distributions shown in Fig. 8 and the velocity fluctuations shown in Fig. 9, it can be deduced that in the unshrouded impeller, the secondary flow in the impeller channel differs from that of the shrouded impeller channel due to leakage from the pressure side to the suction side of the blade across the casing-blade tip clearance, as pointed out by Howard et al. Measurements in Figs. 8 and 9 were taken at maximum efficiency conditions at the outlet of the impeller. It is, however, well known that when the flow becomes excessively low, rotating stall occurs. Thus to investigate this phenomena, measurements were taken by installing a hot-film probe at the same location as the cobra probe and traversing it in the radial direction across the impeller inlet. The number of stall cells generated at the impeller can be calculated by the following equation

$$i = \frac{360}{\theta}\left(\frac{t_0}{t}\right)$$

where:

θ = set angle between two probes
t = period of revolution of rotating stall
t_0 = time difference of rotating stall passing through two probes.

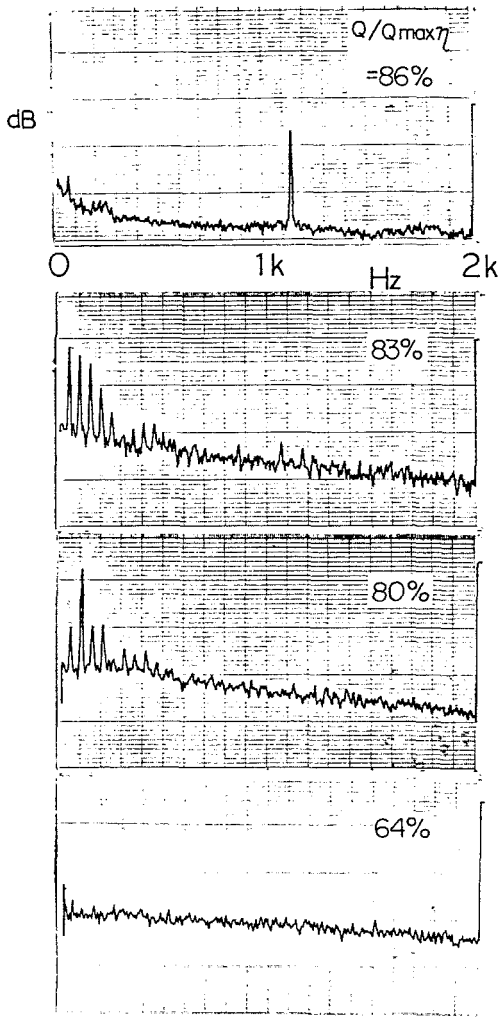

Fig. 11 Frequency analysis of inlet fluctuation of shrouded impeller

Figure 10(*a*) shows the results of measurements when the flow rate was gradually reduced down stall conditions. Figure 10(*b*) shows the same measurements with the unshrouded impeller.

With the shrouded impeller, when $Q/Q_{\max\eta}$ was larger than 83 percent, only blade passing fluctuations were observed. However, when $Q/Q_{\max\eta}$ reached 83 percent, a rotating stall occurred with one cell. When the flow rate was further decreased to 80 percent, the number of stall cells increased to two. Further reduction in flow rate showed, no more major periodic fluctuations. In the case of the unshrouded impeller, no rotating stalls were observed at the flow rate corresponding to the rate at which rotating stalls started in the shrouded impeller. When the flow rate reached 78 percent, a rotating stall with one cell occurred. When the flow was further lowered, the number of stall cells increased to two at 74 percent flow rate. Thus the author found that the shrouded impeller had inferior overall performance to the unshrouded impeller in the lower flow region and that the rotating stall took place at larger flow rates than in the case of the unshrouded impeller, resulting in a narrower stable range. Also, it was found that the outlet flow from the impeller to the diffuser in the large flow rate condition (83–100 percent $Q_{\max\eta}$) differed near the shroud site between the two types of impeller due to leakage across the casing-impeller clearance.

Figure 11 shows the results of the frequency spectrum analysis with the shrouded impeller flow fluctuation at

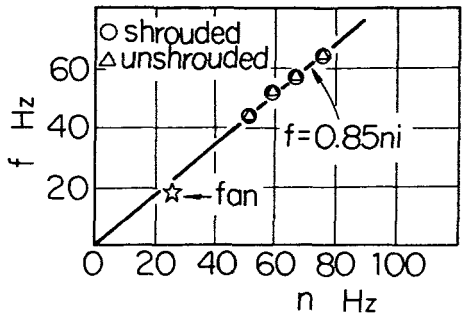

Fig. 12 Rotating stall frequency f at impeller inlet a function of impeller frequency n

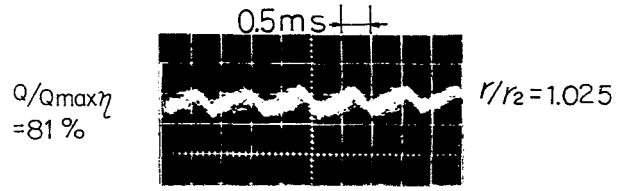

Fig. 13 Velocity flucation at the diffuser

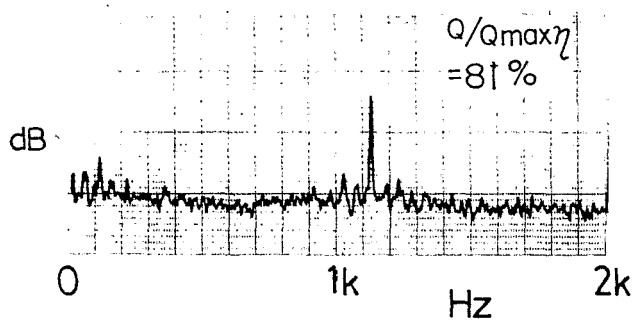

Fig. 14 Frequency analysis in case of Fig. 13

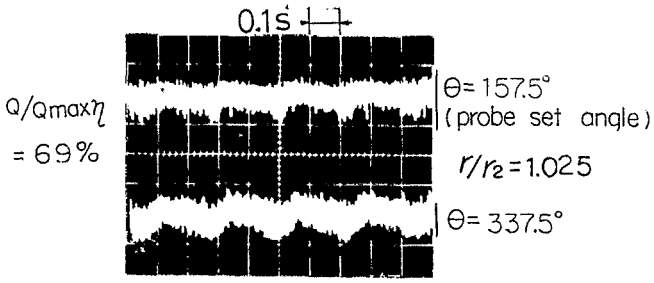

Fig. 15 Velocity fluctuation at the diffuser

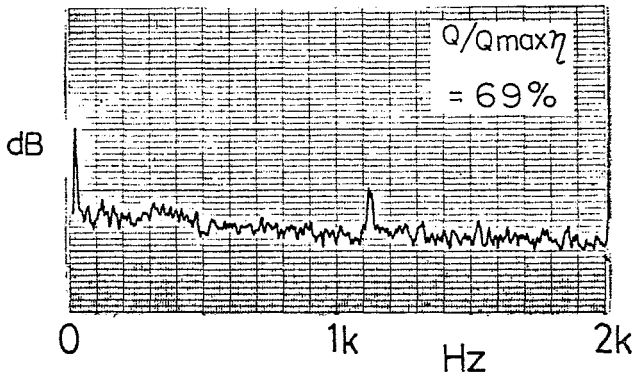

Fig. 16 Frequency analysis of velocity fluctuation at the diffuser

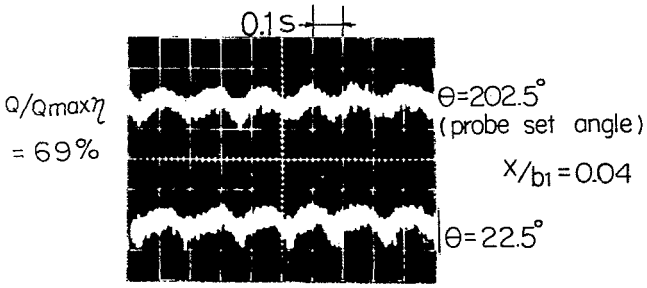

Fig. 17 Velocity fluctuation at the impeller inlet $Mu_2 = 1.0$

various flow rates. The figure indicates that when $Q/Q_{max\eta}$ is 86 percent, only the blade passing frequency is conspicuous; at 83 percent, 52 Hz and it's harmonics appear; at 80 percent, 104 Hz is distinguished. When the flow decreases below this, the discrete frequencies disappear.

Figure 12 shows the rotating stall frequency in relation to the impeller rotating speed when the number of stall cells is one. This figure shows that the rotating stall frequency is not affected by the presence of a shroud cover and is in proportion to the rotational speed of the impeller. The rotating stall frequency was 85 percent of the impeller rotating speed. The ☆ mark in this figure shows the results of a similar experiment conducted with a low-pressure fan. [5].

The flow fluctuation at low flow rate was measured at inlet of the diffuser. Figure 13 shows the result of shrouded impeller measured by the hot-film probe at the shroud side ($x/b_3 = 0.03$) of the diffuser inlet ($r/r_2 = 1.025$). In this case the flow rate $Q/Q_{max\eta}$ was 81 percent and the rotating stall of the impeller inlet occurred; however, the flow fluctuation having the same frequency as the impeller rotating stall did not appear.

Figure 14 shows the frequency spectrum analysis of the above case obtained by the hot-film probe. This figure indicates only the blade passing frequency is conspicuous.

Figure 15 shows another result obtained by the symmetrical position of the same radius of the diffuser inlet at the flow rate 69 percent.

Figure 16 shows the same results of the frequency spectrum analysis. This figure indicates the frequency of the diffuser flow fluctuation was 4 Hz and this value was much smaller than the frequency of the impeller rotating stall. The starting flow rate of this flow fluctuation at the diffuser was nearly the same for both shrouded and unshrouded impeller.

The frequency of the flow fluctuation at the diffuser was almost the same as both impellers, but they increased as the flow becomes lower.

In case of higher rotating speed of impeller than Mu_2 nearly 0.8, stall in the diffuser occurred ahead of inlet stall and at the same time the fluctuation with the same frequency appeared at the impeller inlet, too. Furthermore, this fluctuation at the impeller inlet was superimposed by stall frequency of the impeller as flow becomes lower.

Figure 17 shows the flow fluctuation at the impeller inlet in case of $Mu_2 = 1$.

Conclusion

A shroud on a centrifugal impeller affects the internal flow through the impeller. A shrouded impeller has inferior overall performance in the lower flow region compared with an identical unshrouded one and also has a narrower stable range, because rotating stall takes place at a higher flow rate. The rotating stall frequency occurring in the impeller is not affected by the presence of a shroud and is in proportion to the rotational speed of the impeller. The rotating stall frequency of the tested impeller was 85 percent of the impller rotating speed.

Acknowledgments

The author wishes to express his sincere thanks to Mr. S. Yosomiya for his helpful discussions and to Mr. T. Kashiwakura for his assistance in conducting the experiments.

References

1 Ishida, M., and Senoo, Y., "On the Pressure Losses due to the tip Clearance of Centrifugal Blower," ASME JOURNAL OF ENGINEERING FOR POWER, Vol. 103, No. 2, Apr. 1981.

2 Lennemann, E., and Howard, J. H. G., "Unsteady Flow Phenomena in Rotating Centrifugal Impeller Passages," ASME JOURNAL OF ENGINEERING FOR POWER, Vol. 92, No. 1, Jan. 1970.

3 Howard, J. H. G., and Kittmer, C. W., "Measured Passage Velocities in a Radial Impeller With Shrouded and Unshrouded Configurations," ASME JOURNAL OF ENGINEERING FOR POWER, Vol. 97, No. 2, Apr. 1975.

4 Mizuki, S., Ariga, I., and Watanabe, I., "A Study of the Flow Mechanism Within Centrifugal Impeller Channels," ASME Paper No. 75-GT-14.

5 Suzuki, S., Ugai, Y., and Harada, H., "Noise Characteristics in Partial Discharge of Centrifugal Fans," *JSME Bulletin*, Vol. 21, No. 154, April, 1978.

6 Kammer, H., and Rautenberg, M., "An Experimental Investigation of Rotating Stall Flow in a Centrifugal Compressor," ASME Paper No. 82-GT-82.

7 McAnally, III, W. J., and Goodrum, J. D., "Shrouded Impeller Test Program," Ad-784 133, Jul. 1974.

H. Hayami
Professor.

Y. Senoo
Professor.

Research Institute of Industrial Science,
Kyushu University 86,
Kasugashi, Fukuoka 816, Japan

H. Ueki
Research Associate,
Faculty of Engineering,
Nagasaki University,
Nagasaki 852, Japan

Flow in the Inducer of a Centrifugal Compressor Measured With a Laser Velocimeter

The flow field in the inducer of a high-pressure-ratio centrifugal compressor has been measured with a laser-2-focus velocimeter (L2FV) at two flow rates that were on each side of the apparent inducer-stall limit at 70 percent speed. The limit was determined based on the pressure pattern between inducer blades along the shroud. The measured time-mean velocity distribution is compared with the prediction based on an inviscid quasi-three-dimensional flow analysis and the viscous effects are clarified. Furthermore, the nature of flow unsteadiness is discussed on the basis of the L2FV data. Using the observed data it is concluded that the inducer works well even at the apparent inducer-stall condition.

Introduction

Surging of a compressor system is quite critical, and it is usually related to deterioration of the compressor performance, which is based on stall of the impeller and/or the diffuser. Since the compressor of a gas turbine is forced to operate at low mass flow rates at a part-speed during starting, the incidence angle to the inducer is large and it is presumed that the inducer is stalled, but in cases of centrifugal compressors a high efficiency and an almost ordinary pressure rise are usually achieved. Therefore, there must be two types of stall: real stall with deterioration of the compressor performance and apparent stall without deterioration of the performance. For understanding of compressor surge limit, it is quite important to investigate the latter and to clarify the difference between the two types of flow pattern.

In the present paper, the flow field in the inducer has been measured with a laser-2-focus velocimeter (L2FV) at two flow rates: a normal operating condition and a small flow rate where the inducer was apparently stalled without deterioration of the impeller efficiency. The measured time-mean velocity distribution is compared with the prediction based on an inviscid quasi-three-dimensional flow analysis. Furthermore, the nature of the flow unsteadiness in the impeller is discussed on the basis of detailed analysis on the L2FV data.

Experimental Apparatus

A high-pressure-ratio centrifugal compressor [1] with a vaneless diffuser was tested in a closed loop with Freon R-12 gas at about 12,500 rpm, which was 70 percent of the design speed. The diameter of the test impeller was 280 mm and the inducer diameter was 172 mm. The impeller had 16 main blades and 16 splitter blades; the direction of the blades was radial at the impeller exit. Gas flowed to the inducer from a plenum chamber through a straight suction pipe of length 760 mm after the contraction by a factor of 7.7. The displacement thickness of the inlet boundary layer was about 1.1 mm. The outer diameter of the vaneless diffuser was 560 mm, and it was connected to a collector. The meridional profile of the test compressor is shown in Fig. 1, and the test impeller is shown in Fig. 2.

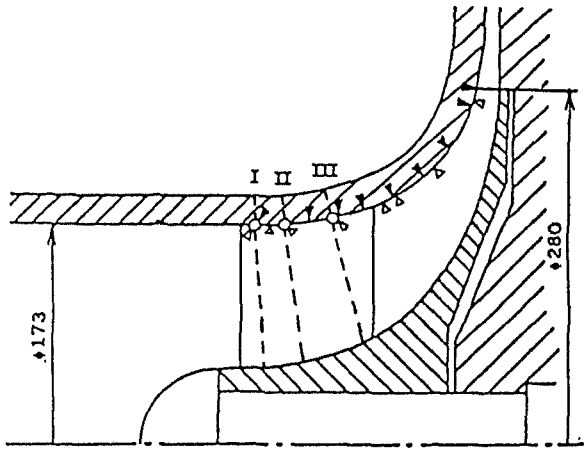

I,II,III: Location of L2FV measurement
▼ : Location of time-mean pressure taps
Δ : Location of pressure transducers

Fig. 1 Meridional profile of test compressor

In addition to securing conventional test data for impeller characterisitics, the time-mean pressure was measured at 9 points along the shroud, and the time variation of pressure as

Contributed by the Gas Turbine Division of THE AMERICAN SOCIETY OF MECHANICAL ENGINEERS and presented at the 29th International Gas Turbine Conference and Exhibit, Amsterdam, The Netherlands, June 4–7, 1984. Manuscript received at ASME Headquarters January 5, 1984. Paper No. 84-GT-74.

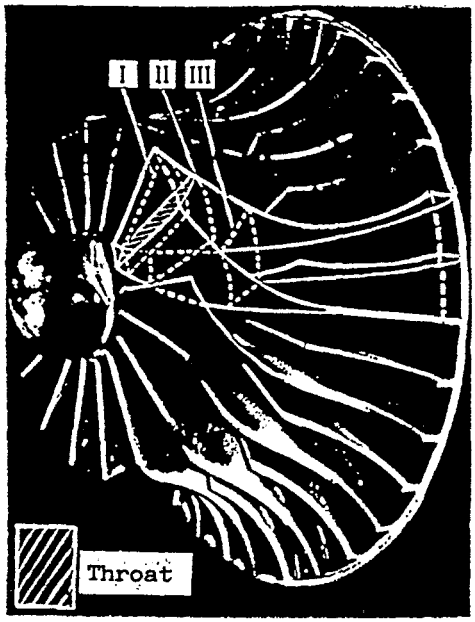

Fig. 2 Test impeller

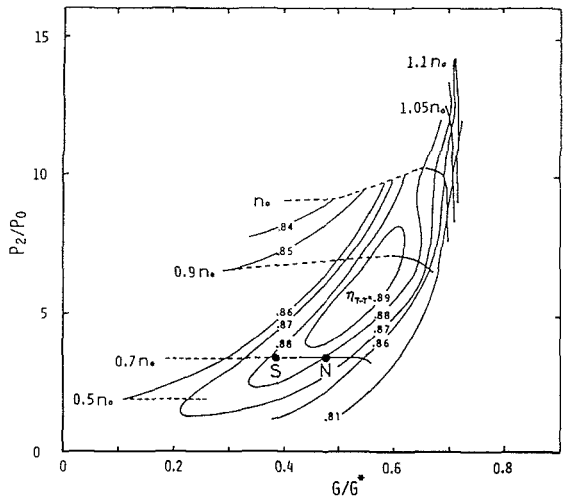

Fig. 3 Characteristics of impeller

the impeller blades passed by was measured using high frequency-response pressure transducers at several points along the shroud. These points are indicated in Fig. 1. Furthermore, the flow field in the impeller passage was investigated using a L2FV at three optical measurement sections: I, II, and III, illustrated in Fig. 1 and in Fig. 2 as dotted lines. These locations were selected on the basis of the observed contour of isobars along the shroud surface [1].

A L2FV system was initiated by Thompson [2] and Tanner [3], and it has been developed by Schodl [4]. A L2FV system has various advantages comparing with a LDV system such as a higher S/N ratio and an easier signal processing for measurement of high-speed flow, and it has been often applied to the flow in high-speed rotating impellers [5–8]. The L2FV system in the present experiment is similar to the one presented by Schodl, and the details have been reported in [8].

A L2FV is based on the principle of aligning the direction of the two spatially separated foci to the flow and measuring the time-of-flight of particles traveling between the two foci. Thus for a given distance between the two foci, s, the velocity, C, is evaluated from the time-of-flight, t, as $C=s/t$. The distance between the two foci, s, is about 0.5 mm, and the focus diameter, d, is about 10μm. The ratio of d to s is only about 1/50. In cases of high turbulent flow, a small value of d/s reduces probability of a particle passing through the two foci successively. Furthermore, a small value of d/s increases probability of false time-of-flight data, due to two foci being passed through by different particles successively. One of the special features of a L2FV system is that two foci act as a kind of narrow band filter for flow angle. The angle interval of the equivalent filter corresponds to d/s. Therefore, it is possible to discuss on the nature of flow unsteadiness using a two-dimensional probability distribution of time-of-flight that is obtained by changing the setting angle of the two foci little by little around the mean flow angle.

Concerning seeding particles, agglomerates about 2μm in mean diameter, based on SiO_2 powder of 0.04 μm diameter, were used. In order to confirm the fidelity of particles' motion to flow, the sedimentation velocity of particles were measured. The mean sedimentation velocity was 0.153 mm/s. This implies that the amplitude ratio of the particles' motion to the oscillating flow with a blade passing frequency of about 3.3 kHz is 0.95. The bulk density of agglomerates was guessed as about 1000 kg/m^3 from the mean sedimentation velocity and the mean diameter. The particles were supplied through a fine L-type tube of 5-mm-dia located in a plane 300 mm upstream of the leading edges of the impeller blades. The location of the tube opening was adjusted in the plane so that many particles passed through the measuring point. It should be noted that the concentration of particles was controlled below 3*10^9 particles per m^3 to reduce false time-of-flight data.

Results and Discussions

The characteristic curves of the test impeller are presented in Fig. 3, which were obtained in the case that the impeller exit was directly surrounded by a collector with a large cross-sectional area [1]. In the present case with a vaneless diffuser, the available stable mass flow range was narrower but the total pressure ratio[1] and the efficiency of the impeller were identical to those without the vaneless diffuser.

[1] The total pressure P_2 was estimated using the measured static pressure at the impeller exit and the velocity, which was evaluated as follows. The circumferential component of the velocity was estimated assuming a slip factor of 0.91, and the radial component was calculated from the flow rate which was measured with an orifice flowmeter.

Nomenclature

B = blockage factor
b = meridional impeller channel width
C = absolute velocity
C_m = meridional velocity component
G = mass flow rate
G^* = choked mass flow rate in suction pipe
m = meridional length along shroud
m_i = m at impeller exit
n_0 = design corrected speed
P_0 = total pressure at suction plenum chamber
P_2 = total pressure at impeller exit
p = shroud static pressure
W = relative velocity
z = distance from shroud casing
η_{T-T} = total-to-total polytropic efficiency

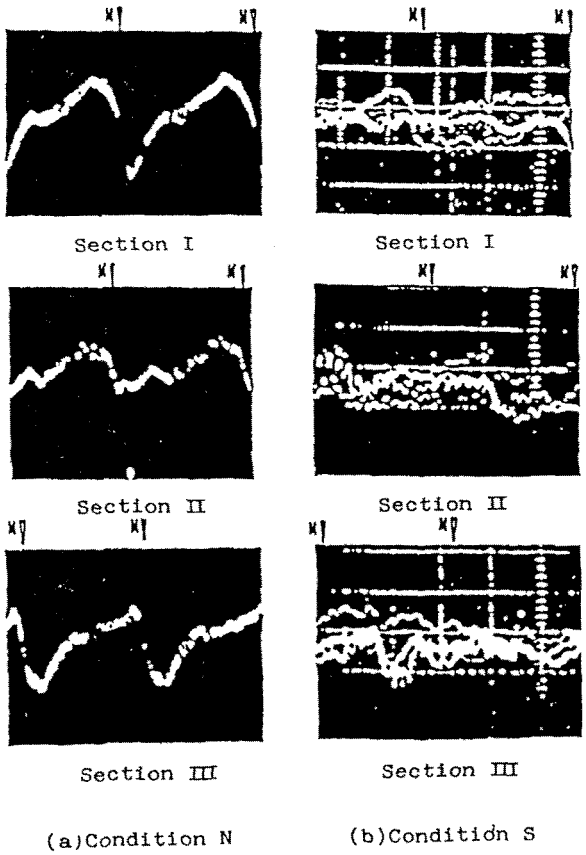

Fig. 4 Shroud static pressure variation between blades

The solid-line portions of the impeller characteristic curves are the range where the inducer worked well, while the dotted-line portions are the range where the inducer was apparently stalled and at the left-hand extremities of the characteristic curves the system of the test compressor fell in surge. The apparent inducer-stall was judged from the shroud static pressure variation between inducer blades. At a part speed, even if the inducer was apparently stalled, the dotted-line was almost horizontal and the compressor operated stably without surge over a wide mass flow range and furthermore the polytropic efficiency of the impeller was hardly deteriorated, as shown in Fig. 3.

Two operating points in the present measurement are indicated in Fig. 3 with N and S corresponding to the conditions without and with apparent inducer-stall, respectively. The static pressure variations between blades along the shroud are shown in Fig. 4. Pressure increases upward in the picture and time goes from the left to the right, or the blades move toward left. In principle, pressure should increase smoothly from the suction side of the blade to the pressure side of the adjacent blade. At the condition N, although an abnormal pressure gradient appears at the middle of the blade pitch, a fairly high pressure-difference is observed across the blade; that is, the blade acts normally. On the other hand, at the condition S pressure fluctuates irregularly and the blade apparently exerts no force on the gas, and it is judged as an apparent inducer-stall condition. However, the variation of the shroud static pressure at the impeller exit had no special feature.

Blockage Factor and Meridional Velocity Profile. At the condition N, the time-mean shroud static pressure was measured at 9 points and the ratio of the measured static pressure at each of 9 points to the total pressure in the plenum chamber are plotted in Fig. 5 with circles. A dotted line in the figure represents the predicted pressure distribution based on

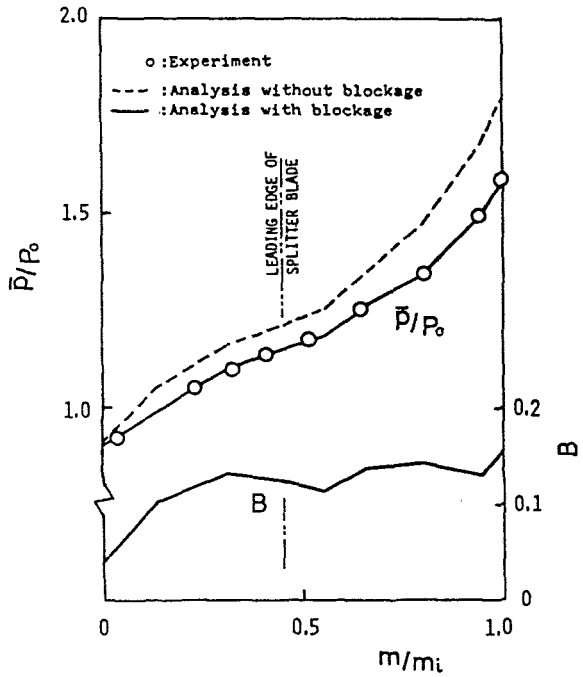

Fig. 5 Distribution of shroud static pressure and blockage factor

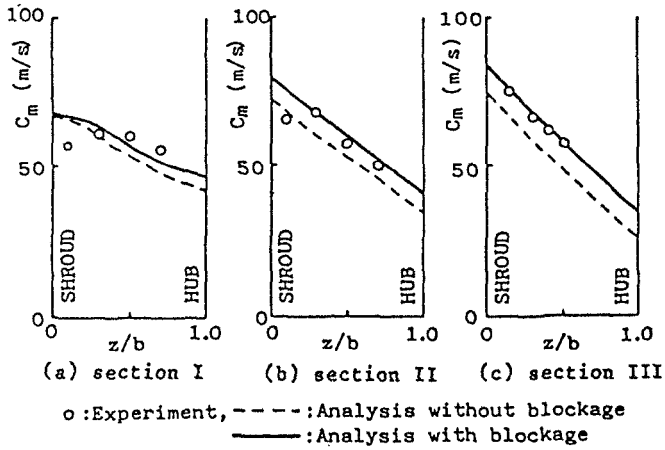

Fig. 6 Distribution of meridional velocity component at the middle between blades, condition N

the inviscid quasi-three-dimensional analysis [9]. They do not fit the circles. The discrepancy is due to the blockage effect of the boundary layer development along the surfaces of the hub and the shroud as well as the blades.

The blockage distribution along the shroud streamline can be adjusted so that the analytical pressure distribution agrees with the experimental time-mean shroud static pressure distribution from the inlet to the exit of the impeller, where the spanwise distribution of the blockage factor is assumed constant following [10]. The distribution of the blockage factor and the shroud static pressure based on the calculation including the blockage are shown in Fig. 6 as solid lines. The blockage factor B increases abruptly just downstream of the leading edge, due to the boundary layer development on the inducer blade surface, and it further increases a little bit to the impeller exit. The blockage factor at the impeller exit is 0.15[2], and the value is not large comparing with [10].

[2] In the present paper the effective flow area does not include the clearance between the blade tip and the shroud. If the area corresponding to the clearance is added as the effective flow area, the blockage factor of 0.15 in the text is increased to 0.20.

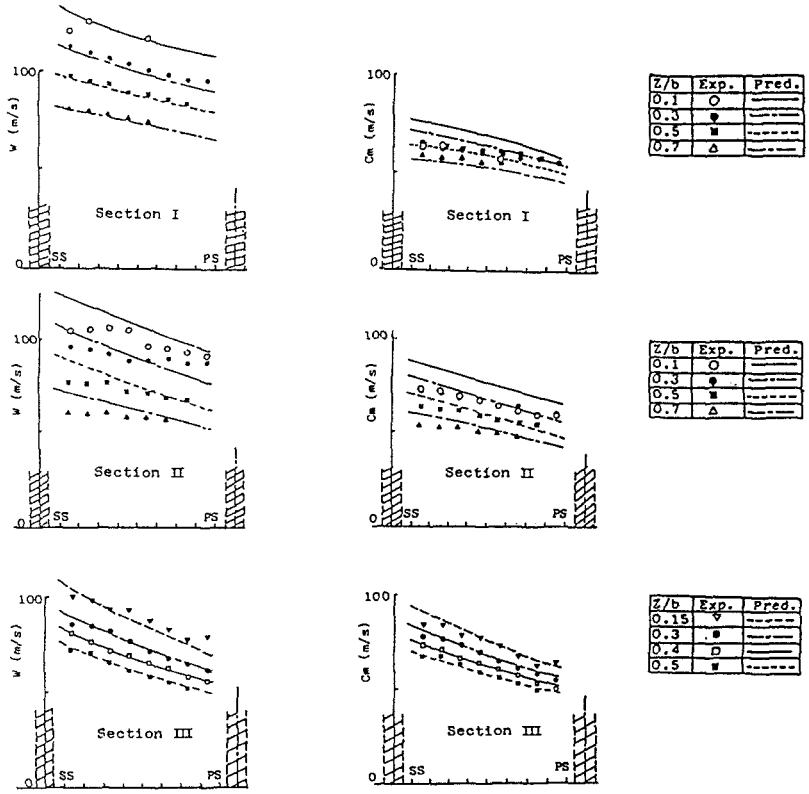

(a) Relative velocity (b) Meridional velocity component

Fig. 7 Velocity distribution between blades, condition N

The distribution of the absolute velocity[3] from the shroud to the hub was measured at three sections with the L2FV, and the data of the meridional velocity component at the middle of a blade pitch are plotted in Fig. 6 as circles. Dotted lines in the figure represent the predicted velocity distribution based on the inviscid quasi-three-dimensional analysis [9]. The distribution of the calculated meridional velocity component, considering the aforementioned boundary layer blockage, is superimposed upon Fig. 6 as solid lines. They agree well with the experimental data, except at the section I.

Figure 6 shows that the increment of the blockage is larger from the section I to II than that from the section II to III. According to the relative Mach number distribution along the shroud (Fig. 8 in [1]), the deceleration of the relative velocity is the largest from the leading edge to the throat, and it is supposed that boundary layer develops more rapidly between the sections I and II than it does between the sections II and III.

Time Mean Flow.

Flow at Normal Operating Condition. The distributions of (*a*) the relative velocity and (*b*) the meridional velocity component between blades at the condition N are shown in Fig. 7. The meridional velocity component varies linearly between blades, and the value at the middle between blades is almost equal to the blade-pitch mean value. The experimental results at the section III agree well with the prediction except at the corner of the shroud surface and the blade suction surface. However, at the section II, the gradient of distribution of the meridional velocity component between blades is somewhat smaller than that of the prediction, although the agreement between the measured midblade pitch

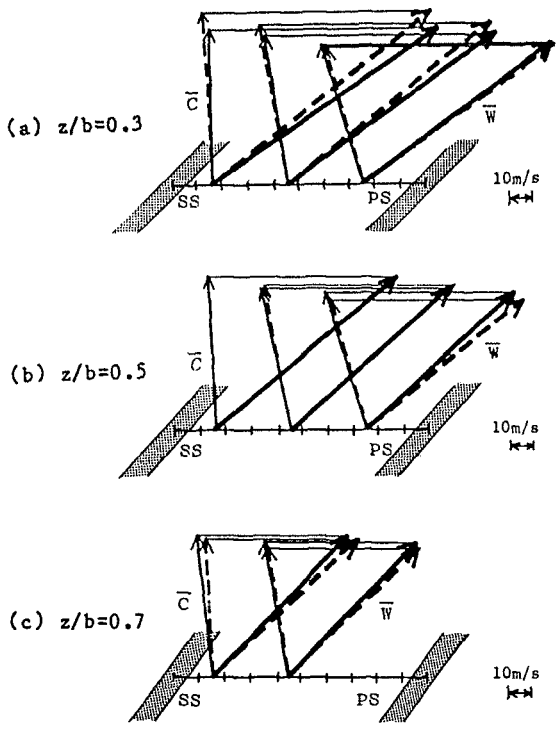

Fig. 8 Velocity triangles, section I, condition N——: Experiment, ------: Analysis

[3]For the confidence coefficient of 0.9, the confidence intervals of mean absolute velocity and mean flow angle were ±0.4% of the velocity and ±0.5 deg respectively in the case of 232 samples at the condition N, while the confidence intervals vary according to the intensity of fluctuation as well as the number of samples. At the worst case of the condition S, they were ±1.3% and ±0.8 deg respectively using 158 samples.

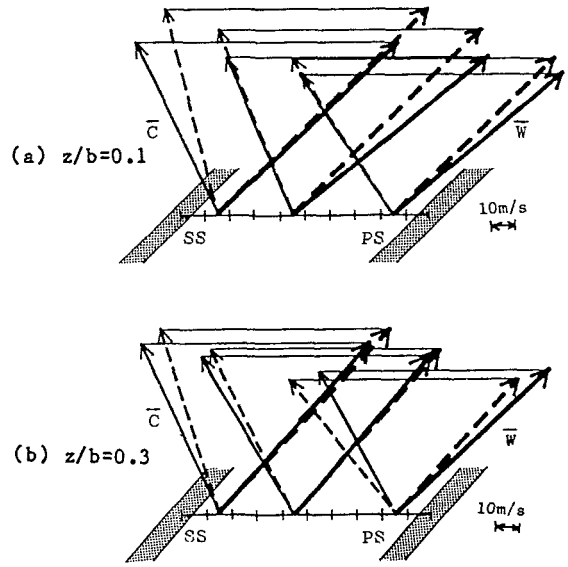

Fig. 9 Velocity triangles, section II, condition N——:Experiment, -----: Analysis

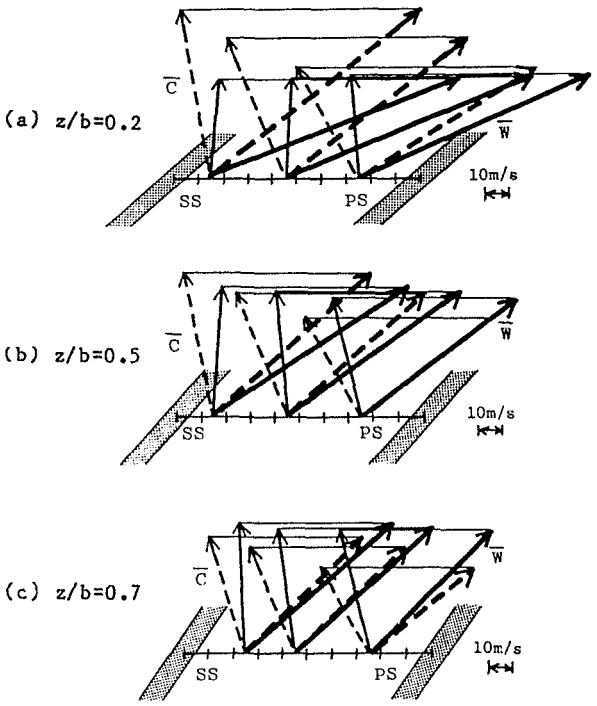

Fig. 10 Velocity triangles, section I, condition S——: Experiment, ------: Analysis

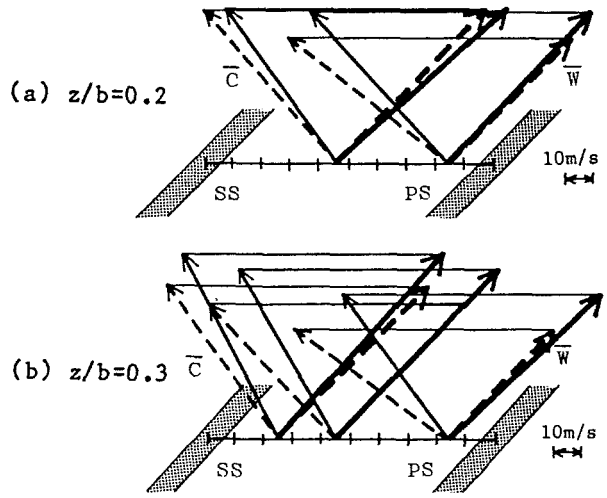

Fig. 11 Velocity triangles, section II, condition S——:Experiment, -----: Analysis

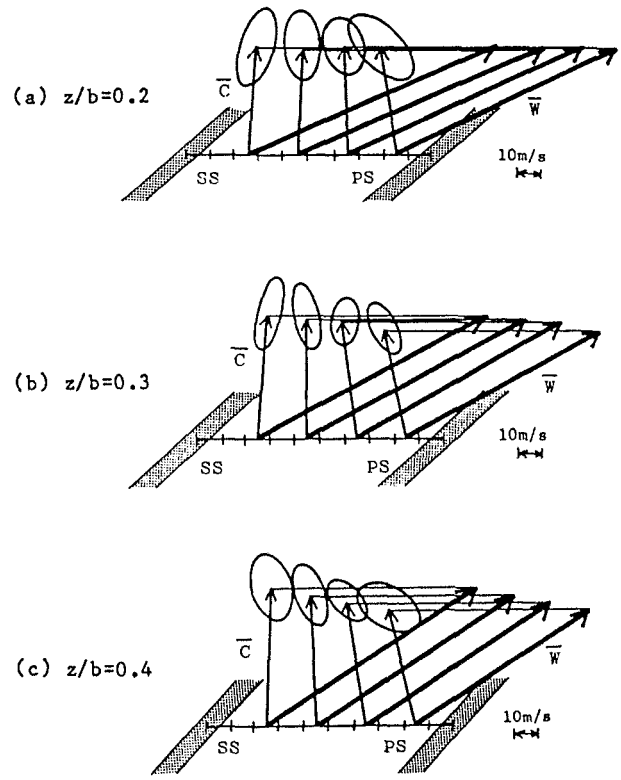

Fig. 12 Velocity triangles and 3σ contour of flow fluctuation, section I, condition S——: Experiment, ----: Analysis

value of the meridional velocity component and the predicted one including blockage effect is not so bad at the section II, as shown in Fig. 6.

Concerning the distribution of the relative velocity (Fig. 7(*a*)), the experimental results agree well with the prediction at the whole section III, except for a spot at the middle of the blade pitch on the depth ratio line $z/b=0.15$, where a little step is recognized in the relative velocity distribution. Also at section I, the experimental results agree well with the prediction, although data are sparse at $z/b=0.1$. At section II, however, an evident step in the velocity distribution is recognized at the middle of the blade pitch at $z/b=0.1$. Similar step is recognized at a large value of z/b in a less degree. The location of the step in the relative velocity distribution at sections II and III corresponds to the location where an abnormal pressure gradient appeared between blades in Fig. 4(*a*). The step in the velocity distribution and the step in the pressure distribution must be closely related to each other.

Figures 8 and 9 show the velocity triangles between blades at the sections I and II, respectively, where the measurement points are the root points of each velocity triangle arrows. Since the L2FV is stationary and the secured data are absolute velocity vectors illustrated as fine arrows in the figure, the relative velocity vector illustrated as heavy arrows in the figure is found by vectorian subtraction of the blade speed from the absolute velocity vector. The predicted inviscid velocity triangles, including the blockage effect, are also illustrated in the same figure as dotted lines. Agreement is satisfactory. The direction of the relative flow, derived from

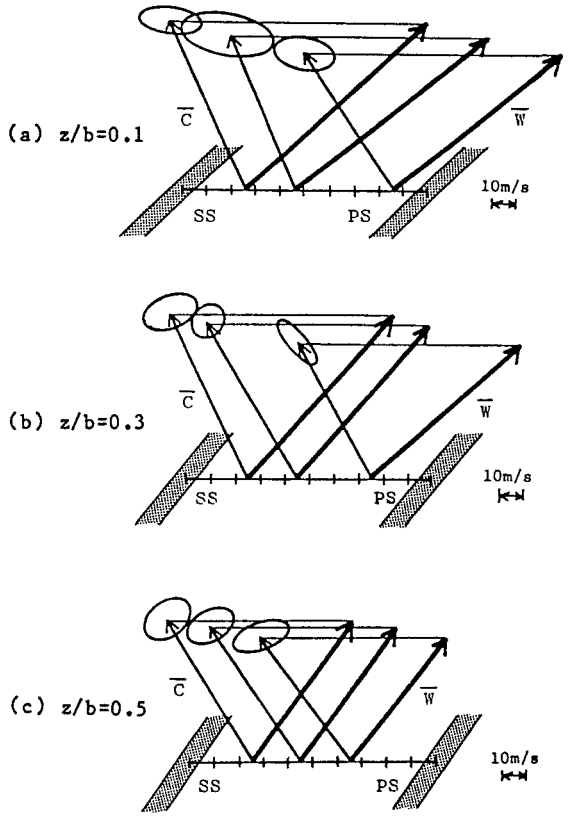

Fig. 13 Velocity triangles and 3σ contour of flow fluctuation, section II, condition N——: Experiment, -----: Analysis

the absolute velocity vectors, nearly agrees with the direction of the blade. This fact further demonstrates good accuracy of the present experimental results.

Velocity Vectors at Condition S. The velocity triangles at the sections I at the condition S, where the inducer is apparently stalled, are drawn in Fig. 10. The dotted lines are the velocity triangles based on the prediction disregarding blockage effect [9], because there is no way to estimate the blockage factor properly for the flow between stalled blades. That is, the dotted line triangles do not show the predicted velocity vectors of the stalled flow but of the ideal flow, and they are utilized to show the difference between the ideal flow and the real flow at the apparent inducer-stall.

At $z/b=0.2$ near the shroud surface, the measured meridional velocity component is particularly small and the measured relative flow angle is much smaller than the ideal relative flow angle. On the contrary, at $z/b=0.7$ near the hub in Fig.10(*c*), the meridional velocity is large to cover the loss of flow rate near the shroud, and the measured relative flow angle is almost equal to the ideal one. In either case, however, the absolute flow is hardly deflected. This implies that the inducer blades hardly work on gas or the inducer is nearly stalled in the section I, since the circumferential component of the absolute velocity is given by the blade loading at the inducer portion.

The velocity triangles at the section II are shown in Fig. 11. From the abnormal shroud static pressure variation between blades (Fig. 4(*b*)), it was assumed that the inducer was fully stalled at the section II. However, Fig. 11 shows that the measured relative flow angle agrees well with the ideal flow between blades, and a fair deflection of absolute velocity is achieved at both $z/b=0.2$ and 0.3. It is surprising that the stall region near the shroud did not extend to the depth of $z/b=0.2$ at the section II, while the stalled region spread deeply in the impeller passage at the section I. The foregoing flow behavior may be explained as follows.

Generally speaking internal flow in diffusers has less tendency to be separated from the walls than external flow along walls and airfoils against equivalent adverse pressure gradient [11]. Since the major portion of a centrifugal impeller downstream of the throat forms channels and gas is accelerated there at a part speed due to insufficient compression [1], the flow downstream of the throat is stabilized and gas flows smoothly without separation from walls.[4] On the other hand, upstream of the throat the flow separates from the inducer blade at a low mass flow due to a large incidence to blades.

In Fig. 2, the section I is mostly located upstream of the throat, which is shown as the shaded portion, and the section II is located downstream of the throat. Observing the section I more carefully, it is noticed that the blade portion upstream of the throat is shorter as the depth from the shroud is increased and the section I is inside a channel near the hub, since the blade angle at the inducer blade leading edge is varied radially and the spacing between blades is reduced with the depth.

Keeping in mind the foregoing argument and carefully reexamining the velocity triangles at the section I (Fig. 10), it is noticed that agreement of the relative flow angle between the real flow and the ideal flow is not observed at all at $z/b=0.2$, agreement is observed nearly half portion near the blade pressure surface at $z/b=0.5$ and the whole blade pitch at $z/b=0.7$. That is, the separated region is roughly located upstream of the impeller throat.

In conclusion, even though the inducer appeared fully stalled based on the shroud static pressure variation, stall of the inducer is limited in a small region near the leading edge, i.e. so-called "semi-opened" region, and very near the shroud surface, and the flow in the major part of the inducer, and the impeller passage is normal and stable. The shroud static pressure variation does not represent the flow in the inducer and it cannot be utilized as the criterion regarding inducer stall, although the pressure distribution between blades supplies useful information at normal operating conditions [1, 12–14].

In [15], it is reported that compressor surge of a typical centrifugal compressor occurs only when both components, the inducer and the diffuser, are stalled. If each of the inducer-stall and the diffuser-stall causes deterioration of the compressor performance, the performance of the compressor system must be deteriorated by the first occurence of either one of the stalls. According to the present study, however, at low mass flow rates at part speeds, the inducer-stall is only superficial, and the inducer and the impeller works well. Therefore, it is quite understandable that the compressor can operate stably until the diffuser stalls.

Flow Unsteadiness in Inducer. It is important to clarify the flow behavior in the impeller passage regarding not only the time-mean flow field but also the flow unsteadiness. Generally, a L2FV is hardly applied to measurement of turbulent flow due to large volume of measurement, i.e., 0.3–0.5 mm between the two foci. In cases of a large-scale turbulence or flow fluctuation, however, the measurement volume may be sufficient to observe the fluctuating flow field on the basis of two-dimensional probability distribution of time-of-flight obtained with a L2FV [8].

Flow Fluctuation at Condition S. From a two-dimensional-probability distribution of time-of-flight, the mean value and the standard deviation σ are evaluated at each setting angle of

[4] At the design speed or at high speeds, gas is considerably decelerated in the impeller as it is designed due to sufficient compression, and the flow downstream of the impeller throat is not stabilized at inducer-stall conditions.

the two foci and the range of three times σ can be drawn at the tip of the velocity vector in the velocity triangle. They are shown in Fig. 12 at the section I at the condition S. The shape of the 3σ contour is an ellipse, and closer to the shroud surface the area of the 3σ ellipse is larger, and at any depth ratio the area of the ellipse and the direction of the major axis vary between blades. The ellipse is the largest near the blade suction surface, and the direction of the major axis almost coincides with the direction of the absolute velocity. This implies that the flow unsteadiness in the inlet suction pipe is directly observed in this region. Away from the blade suction surface the ellipse rotates the major axis and the major axis is almost perpendicular to the blade near the blade pressure surface. At the middle of the blade pitch, the magnitude of the major axis is reduced and the ellipse becomes close to a circle, which implies an isotropic fluctuation. Closer to the blade pressure surface the ellipse increases the length of the major axis again.

In [16], the flow near the inducer inlet of a centrifugal impeller has been measured with a LDV, and two stable velocity vectors were simultaneously recognized at a point at a condition near the surge limit. One of the two directions of the relative velocity vectors agreed with the blade and the other indicated fully separated flow from the blade surface, and the vectorian substraction of two relative velocity vectors was roughly in the axial direction near the blade suction surface. It is presumed that rotating stall was generated at the inducer and the two types of flow appeared alternately: one was an unstalled flow and the other was a stalled flow with a low axial velocity. There is some similarity in the variation of the velocity vector and the present observed data; however, two distinct types of flow were not observed in the present data. No time-sequential data can be obtained with the L2FV and the frequency of the flow fluctuation is not evident.

Concerning the 3σ ellipse near the blade pressure surface, the major axis of the ellipse is perpendicular to the blade and it is twice the length of the minor axis. The fluctuation may be caused by variation of the boundary layer thickness, that is, the thickness of the boundary layer along the blade pressure surface varies considerably due to the fluctuation of the pressure gradient.

Flow Fluctuation at Condition N. Figure 13 shows the velocity triangles and the 3σ ellipse measured at the section II at the condition N where the inducer works well. At $z/b=0.3$ and 0.5, the ellipse at the middle of a blade pitch is small and the shape of the ellipse resembles a circle, so that the flow fluctuation is almost isotropic.

On the contrary, at $z/b=0.1$, the major axis of the ellipse is in the circumferential direction, and this tendency was not observed at any other depth. If the radial component of the flow fluctuation is large near the shroud and if gas moves radially conserving the angular momentum, a large fluctuation of the circumferential velocity component is accompanied with a large fluctuation in the radial velocity component. The radial fluctuation cannot be verified since the radial component of velocity cannot be measured with the L2FV. However, it is presumed that strong radial fluctuation is very likely. According to Fig. 6(*b*), the measured meridional velocity component is quite small compared to the prediction at $z/b=0.1$ near the shroud surface. The low velocity is caused by the tip clearance of blades. The shear layer near the shroud surface and various kinds of secondary flow in the layer may be the causes of the radial fluctuation of the velocity vector.

Conclusions

A high-pressure-ratio centrifugal impeller was tested at 70 percent design speed and the flow field in the inducer was measured with a laser-2-focus velocimeter (L2FV). At a normal flow rate without inducer stall, the measured time-mean velocity distribution agreed well with the prediction based on an inviscid quasi-three-dimensional flow analysis including the blockage effect due to boundary layer development.

At a low flow rate, the shroud static pressure between blades varied violently and the inducer was apparently stalled. However, according to the measurement with the L2FV, flow separation is limited only in the semi-opened region near the inducer inlet, and the flow at the throat and downstream was stable along the blade, except very near the shroud. Therefore, the stable compressor operation was possible without deterioration of efficiency.

The distribution of flow fluctuation in the impeller passage is presented from the two-dimensional probability distribution of time-of-flight at the apparent inducer-stall condition as well as at the normal conditions.

References

1 Senoo, Y., Hayami, H., Kinoshita, Y., and Yamasaki, H., "Experimental Study on Flow in a Supersonic Centrifugal Impeller," ASME JOURNAL OF ENGINEERING FOR POWER, Vol. 101, No. 1, Jan. 1979, pp. 32–41.

2 Thompson, D. H., "A Trace Particle Fluid Velocity Meter Incorporating a Laser," *Journal of Science Inst. (J. Phys. E)*, Series 2, Vol. 1, 1968, pp. 929–932.

3 Tanner, L. H., "A Particle Timing Laser Velocity Meter," *Optics and Laser Technology*, June 1973, pp. 108–110.

4 Schodl, R., "A Laser-Dual-Beam Method for Flow Measurements in Turbomachines," ASME Paper No. 74-GT-157, 1974.

5 Eckardt, D., "Detailed Flow Investigations Within a High-Speed Centrifugal Compressor Impeller," ASME *Journal of Fluids Engineering*, Vol. 98, Sept. 1976, pp. 390–402.

6 Eckardt, D., "Flow Field Analysis of Radial and Backswept Centrifugal Compressor Impellers, Part 1: Flow Measurements Using a Laser Velocimeter," *Performance Prediction of Centifugal Pumps and Compressors*, ASME New York, 1979, pp. 77–86.

7 Dunker, R. J. Strinning, P. E., and Weyer, H. B., "Experimental Study of the Flow Field Within a Transonic Axial Compressor Rotor by a Laser Velocimetry and Comparison With Through-Flow Calculations," ASME JOURNAL OF ENGINEERING FOR POWER, Vol. 100, No. 2, Apr. 1978, pp. 279–286.

8 Hayami, H., Ueki, H., and Senoo, Y., "Flow Measurements Using a Laser-2-Focus Velocimeter in a High-Pressure Ratio Centrifugal Impeller," ASME *Engineering Application of Laser Velocimetry*, 1982, pp. 111–116.

9 Senoo, Y., and Nakase, Y., "An Analysis of Flow Through a Mixed Flow Impeller," ASME JOURNAL OF ENGINEERING FOR POWER, Vol. 94, No. 1, Jan. 1972, pp. 43–50.

10 Pampreen, R. C., "A Blockage Model for Centrifugal Compressor Impellers," ASME JOURNAL OF ENGINEERING FOR POWER, Vol. 103, No. 4, Oct. 1981, pp. 698–707.

11 Senoo, Y., and Nishi, M., "Prediction of Flow Separation in a Diffuser by a Boundary Layer Calculation," ASME *Journal of Fluids Engineering*, Vol. 99, No. 2, June 1977, pp. 379–389.

12 Bammert, K., and Rautenberg, M., "On the Energy Transfer in Centrifugal Compressors," ASME Paper No. 74-GT-121, 1974.

13 Eckardt, D., "Instantaneous Measurements in the Jet-Wake Discharge Flow of a Centrifugal Compressor Impeller," ASME JOURNAL OF ENGINEERING FOR POWER, Vol. 97, No. 3, July 1975, pp. 337–346.

14 Senoo, Y., Kinoshita, Y., Hayami H., Hara, K., Ishiuchi, T., and Kobayashi, H., "Pressure at Shroud and Flow in a Supersonic Centrifugal Impeller," 1977 Tokyo Joint Gas Turbine Congress, GTSJ, JSME, and ASME, Paper No. 42, 1977.

15 Yoshinaka, T., "Surge Responsibility and Range Characteristics of Centrifugal Compressors," 1977 Tokyo Joint Gas Tubine Congress, GTSJ, JSME, and ASME, Paper No. 46, 1977.

16 Flueckinger, G., and Melling, A., "Flow Instability at the Inlet of a Centrifugal Compressor," ASME JOURNAL OF ENGINEERING FOR POWER, Vol. 103, No. 2, Apr. 1981, pp. 451–456.

The Effects of Reynolds Number on the Efficiency of Centrifugal Compressor Stages

M. V. Casey
Head Radial Compressor Development Group,
Thermal Turbomachinery Division,
Sulzer-Escher Wyss, Ltd.,
Zurich, Switzerland

An analysis of the friction losses in a centrifugal compressor stage is used to suggest a new form of correction equation for the effect of Reynolds number on efficiency. This equation relates the effect of Reynolds number to the surface roughness, the impeller outlet width ratio and the work input coefficient. Systematic tests on a wide range of compressor stages are used to calibrate the single empirical coefficient in the equation. Despite its simplicity this equation provides more accurate predictions of the Reynolds number effects than existing empirical methods.

Introduction

Although the influence of Reynolds number on the performance of turbomachinery has received considerable attention in the literature, our understanding of this phenomenon is patchy and uncertain. This uncertainty is especially acute in the field of process centrifugal compressors, where, for example, the two most widely adopted performance test codes (ASME PTC-10 [1] and VDI 2045 [2]) still use different definitions of the Reynolds number to characterize the performance of a centrifugal machine. In his recent excellent review paper, Wiesner [3] pointed out that ". . . there is no universal acceptance of the proposition that a Reynolds number effect is applicable to centrifugal compressors."

The need for a better understanding of the effects of Reynolds number has increased because of two recent trends. First, the range of application of centrifugal compressors has been extended to include many processes in the chemical and petroleum industries where extremely high pressures and low flow volumes are needed. In such applications the Reynolds number of a typical stage in the machine may be more than 200 times the Reynolds number of the original prototype stage tested in a test stand. For the narrow stages ($b_2/D_2 < 0.03$) that are used in these machines the effect of the Reynolds number is very large, Fig. 1, and cannot be neglected if an accurate and reliable prediction of performance is needed.

Second, increased competition between compressor manufacturers has made it essential to predict the performance of a machine as accurately as possible. The customer's acceptance tests are more accurate and more detailed than ever before and the financial penalties for not reaching the guaranteed power are becoming increasingly severe. An exact understanding of the effects of Reynolds number is essential for the design of multistage compressors.

The main purpose of this paper is to present a new Reynolds number correction equation that can be used in the aerodynamic design of multistage compressors. For the design of such machines the performance characteristics of each stage are known for certain fixed values of the Reynolds number, usually for those values corresponding to the pressure and gas used during the measurement of the stage in a test stand. In the actual machine, the Reynolds number depends on the size of the compressor, the operating con-

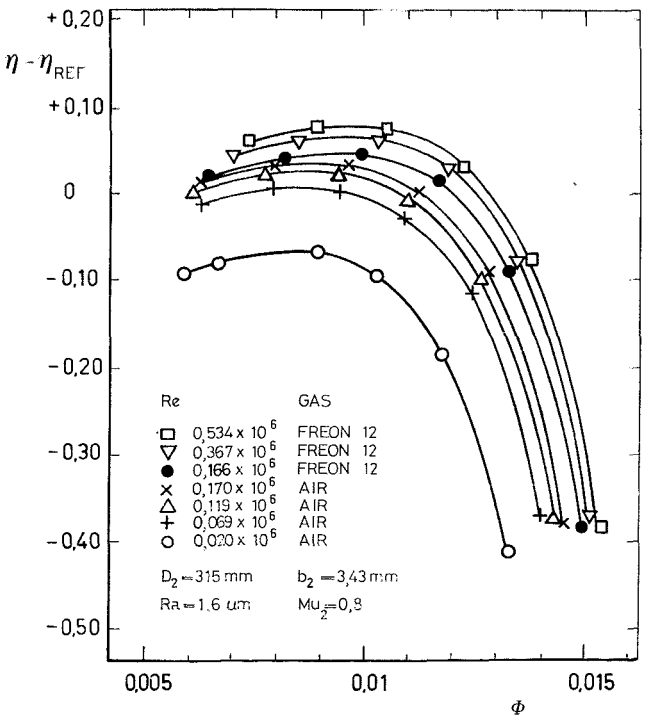

Fig. 1 Effect of Reynolds number on a typical narrow compressor stage

Contributed by the Gas Turbine Division of THE AMERICAN SOCIETY OF MECHANICAL ENGINEERS and presented at the 29th International Gas Turbine Conference and Exhibit, Amsterdam, The Netherlands, June 4-7, 1984. Manuscript received at ASME Headquarters January 19, 1984. Paper No. 84-GT-247.

ditions, and the type of gas used. The characteristic curves of each stage must be corrected to the appropriate Reynolds number before being combined to calculate the characteristics of the machine.

The correction equation suggested in this paper relates the effect of Reynolds number in a compressor stage to the effect of Reynolds number on the friction factor of an appropriately defined equivalent pipe flow. In all cases, the equivalent pipe flow is turbulent and the friction factor is a function of both Reynolds number and relative surface roughness. The correction equation can, theoretically at least, be used to correct for changes in size or surface roughness.

Correction Equations

The Need For A New Approach. The subject of this paper has been extensively discussed in the turbomachinery literature. The paper by Wiesner [3] lists many references that go as far back as Moody in 1925. Most of the published methods are variations on the well-known empirical formula

$$\frac{1-\eta}{1-\eta_{\text{ref}}} = a + (1-a)\left[\frac{\text{Re}_{\text{ref}}}{\text{Re}}\right]^n \tag{1}$$

Early work concentrated on finding a suitable constant value of both the Reynolds ratio exponent, n, and the Reynolds independent loss fraction, a, that fitted the available data. More recent work has used this basic approach, but better correlations have been obtained where the values of n and a have been made functions of other parameters (including Reynolds number). There is no general agreement on suitable values of n and a, and a wide range of possible values is given in the literature.

Part of the reason for the unusually wide variation in parameter a is clearly due to its not having been satisfactorily defined. It is conventionally defined as that fraction of the total losses that is not a function of the Reynolds number, and this gives rise to three problems in the determination of a. First, the ratio of the Reynolds-number-dependent losses to the total losses clearly changes as the Reynolds number is varied. The value of a can then only be a constant at a specified Reynolds number. Few authors in the past have appreciated this difficulty, and it is seldom made clear in the literature for which Reynolds number the value of a is defined. Second, in order to define the value of a, it is necessary to know the exact value both of the Reynolds-dependent losses and of those losses that are independent of the Reynolds number. As a consequence of this, any inaccuracy in estimating those losses that do not change with the Reynolds number can lead to errors in the Reynolds number correction method. Finally, the value of parameter a changes when the Reynolds independent losses are changed. So, for example, if the leakage loss over the cover disk of a shrouded impeller is reduced by improving the design of the labyrinth seals, then a different value of a is needed. It is clear, then, that the values of a derived for one type of compressor are unlikely to be universally valid for other types. The different values of a given by various authors in the literature are usually the result of using different data obtained from different types of impeller stage for the correlations.

The value of exponent n given in the literature also varies considerably from author to author. The main reasons for this are probably that the effects of relative roughness are usually neglected and that different authors are satisfied with different levels of agreement between the predictions and the experiments. There is, however, one recent development with this type of formula that is clearly related to the physics of the flow. This is the use of an exponent n that decreases with increasing Reynolds number (as used by Wiesner [3], Wachter and Woehrl [4] and in unpublished work by Casey [5] and Simon [6]). In a compressor, as in many other instances of turbulent flow, the effect of Reynolds number becomes progressively weaker as the Reynolds number increases. This physical law can only be included in equation (1) if n is made a function of Reynolds number.

It can be seen that equation (1) is inadequate for a general Reynolds number correction equation for centrifugal compressor stages. The predictions of this equation are sensitive to assumptions made about the Reynolds independent losses, and the important physical behavior associated with the Reynolds number is not an inherent property of the equation but can only be obtained by suitable "juggling" with exponent n.

The recent work of the ICAAMC Committee [7] and the similar work done by Simon and Buelskaemper [8] have eliminated the problems with exponent n by using an equation of the form

$$\frac{1-\eta}{1-\eta_{\text{cr}}} = a + (1-a)\frac{\lambda}{\lambda_{\text{cr}}} \tag{2}$$

where λ is the pipe flow friction factor. The Reynolds number effects and their relationship to the relative roughness are then automatically taken account of in the value of the pipe flow friction factor, an idea that was first proposed by Kotzur [9]. However, the problems with the structure of the formula and the choice of a suitable value of parameter a still remain.

There is a clear need for a new approach in which a simple and reliable theoretical loss model is used to provide a more

Nomenclature

a = Reynolds number independent loss fraction
a_1 = velocity of sound at impeller inlet, m/s
b_2 = impeller blade outlet width, m
c = coefficient in correction equation
c_d = dissipation coefficient
D_2 = impeller outlet diameter, m
D_h = hydraulic diameter ($D_h = 4*$ area/perimeter), m
h = specific enthalpy, J/kg
k_s = equivalent sand roughness, m
Mu_2 = tip speed Mach number ($\text{Mu}_2 = U_2/a_1$)
n = exponent in equation (1)
Ra = arithmetical centerline roughness, m
Re = Reynolds number ($\text{Re} = U_2 b_2/\nu_1$)
s = length of flow path, m
U_2 = impeller tip speed, m/s
V = volume flow rate, m^3/s
W = mean relative flow velocity, m/s
β_2 = impeller outlet angle, o
ζ = Reynolds independent losses
η = polytropic efficiency
λ = pipe flow friction factor
μ_0 = impeller work input coefficient
μ_y = pressure coefficient
ν_1 = kinematic viscosity, (inlet total conditions), m^2/s
ϕ = flow coefficient ($\phi = V_1/U_2 D_2^2$)

Subscripts

c = calculated
cr = critical Reynolds number
f = friction
m = measured
ref = reference conditions
1 = impeller inlet conditions
2 = impeller/stage outlet conditions

realistic structure for the correlation equation. The basis of this approach is a relatively simple sensitivity analysis that can be used to determine the sensitivity of the efficiency of a radial compressor to changes in the Reynolds number, or, in other words, the rate of change of efficiency with Reynolds number, $d\eta/d\mathrm{Re}$. In the following sections, a suitable equation for a sensitivity analysis is obtained from an estimate of the hydraulic losses in a radial compressor stage. The losses that are independent of the Reynolds number have, by definition, no effect on the sensitivity of the efficiency to Reynolds number and are, therefore, conveniently neglected in the analysis.

Dissipation Loss Model. The flow mechanisms leading to inefficiency in centrifugal compressors are poorly understood. It is, however, clear that the Reynolds-number-dependent losses are basically frictional in nature. A useful method of estimating the effect of such frictional losses has been proposed by Traupel [10] and has been successfully applied to radial compressors by Schroeder [11] and Wachter and Woehrl [4]. In Traupel's method, the energy loss caused by friction is calculated from the energy dissipation in the flow. The enthalpy loss per unit mass, dh_f, associated with the entropy production along a small element of the flow path is given by

$$dh_f = 2c_d \frac{W^2}{D_h} ds \tag{3}$$

where ds is an increment in the flow path length at a point where the mean velocity relative to the surface is W, the local hydraulic diameter is D_h and the local dissipation coefficient is c_d. The total enthalpy loss due to friction, Δh_f, is given by the integration of equation (3) along the whole flow path of the machine.

An exact integration of equation (3) for a compressor stage would be very difficult and would lead to a result of limited validity. This is because the local velocities and dissipation coefficients must first be estimated and are very uncertain. In fact, an exact integration is unnecessary, since a useful result can be obtained purely by considering the order of magnitude of the terms in the equation. For this purpose, an equivalent pipe flow that has roughly the same friction losses as the compressor is defined.

Equivalent Pipe Flow. For a typical industrial compressor stage, the following approximations are made:

(*a*) The complete flow path length is roughly twice the impeller outlet diameter

$$ds \approx 2D_2 \tag{4}$$

(*b*) The mean flow velocity in the compressor relative to the adjacent surfaces of the machine (that is, relative velocity in the moving parts and absolute velocity in the fixed parts) is roughly half the impeller tip speed

$$W \approx U_2/2 \tag{5}$$

(*c*) The mean hydraulic diameter is roughly twice the impeller tip outlet width

$$D_h \approx 2b_2 \tag{6}$$

(*d*) The mean value of the dissipation coefficient can be related to the friction factor, λ, of a fully developed turbulent pipe flow by

$$c_d \approx \lambda/4 \tag{7}$$

The effects due to local flow diffusion or acceleration, rotation, secondary flows, mixing, and to the shape of the channel are neglected. The friction factor of a turbulent pipe flow is a function of the Reynolds number and the relative roughness, and is given by the Colebrook-White formula (Moody [12])

$$\frac{1}{\sqrt{\lambda}} = 1.74 - 2\log_{10}\left(2\frac{k_s}{D_n} + \frac{18.7}{\mathrm{Re}\sqrt{\lambda}}\right) \tag{8}$$

(An intrinsic equation that gives essentially similar results has recently been published by Haaland [13].)

(*e*) The Reynolds number used in equation (8) is that defined by the mean velocity and mean hydraulic diameter. For the compressor flow, we obtain a characteristic Reynolds number as

$$\mathrm{Re} = \frac{WD_h}{\nu_1} \approx \frac{(U_2/2)(2b_2)}{\nu_1} = \frac{U_2 b_2}{\nu_1} \tag{9}$$

(*f*) The characteristic relative roughness needed in equation (8) is given by the equivalent sand roughness of the compressor surfaces, k_s, divided by the mean hydraulic diameter, D_h. It is generally accepted that the best way of defining the surface roughness of a machined surface is to use the arithmetical centerline average Ra (DIN 4762 [14]). Ra denotes the average roughness from the centerline of the peaks and troughs. It is known as the centerline average (CLA) in the UK and as the arithmetic average (AA) in the USA. The equivalent sand roughness k_s of a machined surface varies between one and three times the Ra-value (Grein [15]), and in this paper the value

$$k_s \approx 2\mathrm{Ra} \tag{10}$$

is assumed, where Ra is the mean surface roughness of the stage. Thus the characteristic relative roughness of the compressor stage can be taken as

$$\frac{k_s}{D_h} = \frac{2\mathrm{Ra}}{2b_2} = \frac{\mathrm{Ra}}{b_2} \tag{11}$$

The approximations given in (*a-f*) above define an equivalent pipe flow that has a characteristic friction factor similar to the compressor flow. There are two main justifications for using the turbulent flow in a pipe instead of the turbulent flow over a flat plate to provide the appropriate friction factor. First, the main interest in and application of a Reynolds number correction method is for those compressors with narrow outlet width ratios, these being the most sensitive to Reynolds number effects. Simple boundary layer growth calculations for such compressors suggest that the boundary layers on the side walls can easily become so thick that they grow together and merge in the center of the channel. In fact, the velocity profile measurements by Senoo [16] in the vaneless diffusers of impeller stages with an outlet width ratio of $b_2/D_2 = 0.03$ show clearly that the boundary layers merge. There is no doubt that the resulting flow has more in common with the fully developed pipe flow than with the undisturbed flow over a flat plate. Second, it is clear that the success of the ICAAMC correction method to correlate measurements on multistage compressors by means of pipe flow friction coefficient is not purely fortuitous and that the flow in narrow compressor stages really exhibits some of the characteristics of a fully developed pipe flow.

Efficiency Correction Equation. If the foregoing equations are substituted into equation (3) and integrated along the flow path, the enthalpy loss due to friction in the flow channels is found to be

$$\Delta h_f \approx \frac{1}{8(b_2/D_2)} \lambda U_2^2 \tag{12}$$

Because order of magnitude approximations have been used with this equation it is by no means exact. Additional error arises because the disk friction losses of the impeller, which are also a function of the Reynolds number, have not been taken into account. The disk friction losses in typical process compressor stages are small and in the worst case (an impeller with a narrow outlet width) are less than a quarter of the

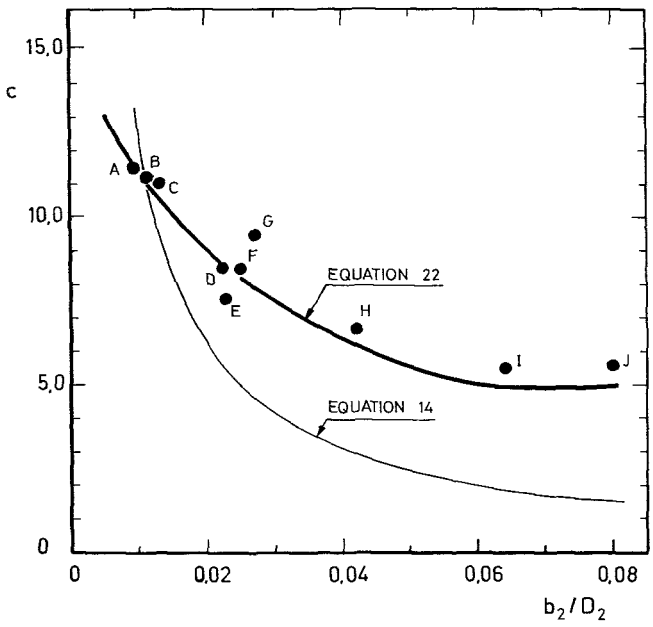

Fig. 2 The function $c = f(b_2/D_2)$

hydraulic losses. Because of this, it is reasonable to consider the friction factor given by equation (8) as representing the disk friction losses and equation (12) as representing the total Reynolds number dependent losses in the compressor stage.

Equation (12) shows that the friction losses in the stage are directly proportional to the friction factor of the equivalent pipe flow. It cannot be expected, however, that such a simple semi-quantitative analysis will give the exact value of the constant of proportionality. In order to make equation (12) more realistic, it is assumed that an equation of the form

$$\Delta h_f = c\lambda U_2^2 \tag{13}$$

provides the total Reynolds number dependent losses in a compressor stage, where

$$c = f(b_2/D_2) \approx \frac{1}{8(b_2/D_2)} \tag{14}$$

The uncertainty resulting from the approximate analysis is thereby incorporated into a single parameter c. This is taken to be a function of the impeller outlet width ratio, as suggested by the analysis, and must be empirically determined (Fig. 2).

The work input into a compressor stage is given by

$$\Delta h = \mu_0 U_2^2 \tag{15}$$

where μ_0 is the work input coefficient. The adiabatic stage efficiency can now be calculated as

$$\eta = \frac{\Delta h - \Delta h_f}{\Delta h} = 1 - \frac{c}{\mu_0}\lambda \tag{16}$$

This equation is the basis of the sensitivity analysis. A change in the friction factor of the equivalent pipe flow, $\delta\lambda$, brought about by a change in Reynolds number gives rise to the following change in stage efficiency

$$\delta\eta = -\frac{c}{\mu_0}\delta\lambda \tag{17}$$

This equation shows that for a given stage the change in efficiency with Reynolds number is directly proportional to the change in the friction factor of the equivalent pipe flow. The constant of proportionality depends on the outlet width ratio and on the work input coefficient of the stage. Equation (17) has been derived by consideration of the adiabatic efficiency. For typical process compressor stages with low-pressure ratios, it is also valid when the polytropic efficiency is used.

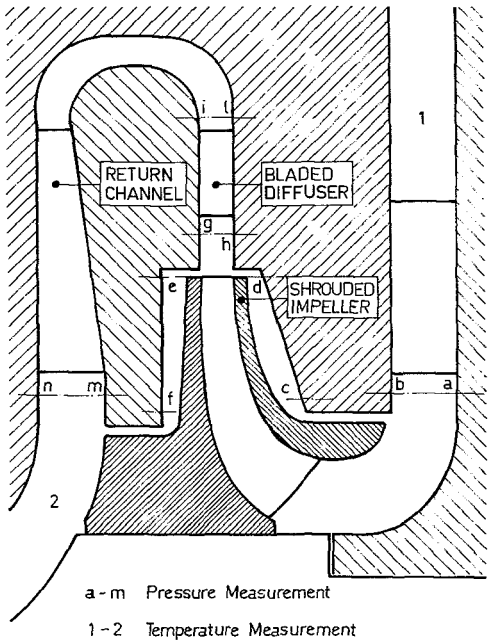

Fig. 3 Typical stage from a multistage compressor

Head and Work Coefficient Correction Equations. No general theory for the variation of the head and work coefficients with Reynolds number has been found. The equations proposed by the ICAAMC working group [7] are accepted here as being the most reasonable approximations available. Roughly half of the improvement in efficiency with Reynolds number appears as an increase in head coefficient and the remainder appears as a reduction in work input. Near to the optimum point we obtain

$$\frac{\mu_y}{\mu_{y\text{ref}}} = 0.5 + 0.5\frac{\eta}{\eta_{\text{ref}}} \tag{18}$$

and

$$\frac{\mu_0}{\mu_{0_{\text{ref}}}} = 0.5 + 0.5\frac{\eta_{\text{ref}}}{\eta} \tag{19}$$

Flow Coefficient Correction Equation. The ICAAMC working group suggested that the variation in flow coefficient could be approximated by

$$\frac{\phi}{\phi_{\text{ref}}} = \sqrt{\left(0.5 + 0.5\frac{\eta}{\eta_{\text{ref}}}\right)} \tag{20}$$

If the further assumption is made that the ratio η/η_{ref} does not greatly differ from unity, then, on expanding the term under the square root

$$\frac{\phi}{\phi_{\text{ref}}} = 0.75 + 0.25\frac{\eta}{\eta_{\text{ref}}} \tag{21}$$

This is the proposed flow coefficient correction equation for use with the present method.

Analysis of Measurement Data

Measurements. Systematic measurements of the effect of Reynolds number carried out at Sulzer-Escher Wyss during the last 15 years have been used in this analysis. Measurements of the effects of Reynolds number on 10 different compressor stages have been made during development work on new impeller types. Each stage was typical of the stages used in multistage process compressors and comprised a shrouded impeller, a bladed diffuser, a return bend, and a return channel, Fig. 3.

The stages covered a range of outlet width ratios from

Table 1 Data of the stages analyzed

Stage	Outlet width ratio b_2/D_2[-]	Impeller outlet angle β_2[o]	Impeller outlet diameter D_2[mm]	Mean stage roughness Ra[μm]	Work coefficient μ_0[-]
A	0.0090	55.5	315.0	1.6	0.86
B	0.0109	57.0	315.0	1.6	0.82
C	0.0129	59.0	315.0	1.6	0.83
D	0.0223	57.0	315.0	1.6	0.74
E	0.0226	58.1	315.0	2.2	0.80
F	0.0249	48.0	315.0	1.6	0.72
G	0.0270	56.4	315.0	1.6	0.75
H	0.0422	48.0	450.0	6.3	0.64
I	0.0640	90.0	450.0	6.3	0.87
J	0.0802	65.0	450.0	6.3	0.71

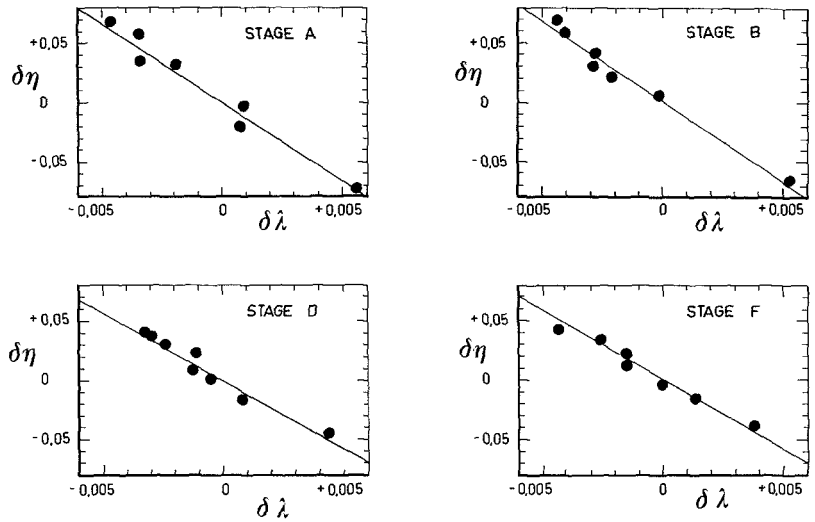

Fig. 4 Variation of efficiency with friction factor for stages A, B, D, and F

$b_2/D_2 = 0.009$ to $b_2/D_2 = 0.08$, and a range of blade outlet angles from $\beta_2 = 48$ deg to $\beta_2 = 90$ deg, Table 1. The stages were measured in one of two closed circuit test stands, "INN" and "TICINO," and the Reynolds number was varied by changing the pressure of the gas in the circuit and the test gas. All the measurements were made at a tip speed Mach number of $Mu_2 = 0.8$, the inlet temperature of the gas being adjusted by a heat exchanger in the test circuit.

The inlet and outlet pressures of the stage were measured by piezoresistive pressure transducers at several points around the circumference of the stage, the inlet and outlet temperatures by resistance thermometers; the volume flows through the stage by the use of a calibrated nozzle in the test loop. For all the measurements, the power absorbed by the stage was measured directly by a load cell taking the reaction of the moment of the freely mounted motor. The highest standards of calibration and accuracy were used with all instrumentation.

In all the experiments the power input from the direct measurement of the torque was compared with the power input determined from the thermodynamic measurements. No measurement point was accepted until equilibrium was attained and the difference between the two power measurements was less than 1 percent. In this way, it was possible to ensure that the maximum error in the efficiency was ± 1 percent.

Variation of Efficiency With Friction Factor. A comparison of the measured optimum efficiency of stages A to J and the calculated friction factor of the equivalent pipe flow convincingly confirms the linear relationship predicted by equation (17). The maximum deviation of the measurement points from a simple linear relationship is about 1 point of efficiency. This is roughly comparable with the expected accuracy of the measurements.

The results of this comparison for stages A, B, D, and F are shown in Fig. 4. In each case, the deviation in efficiency and the friction factor from reference values is plotted. For each stage, the reference value of the friction factor has been calculated as the value obtained when the stage is tested in air at standard temperature and pressure. The corresponding reference value of the efficiency has been chosen so that the scatter of the measurement points is minimized.

Determination of the Function $c = f(b_2/D_2)$. The method of least squares has been used to determine the straight lines that provide the best fit between the measurements of efficiency and the calculated values of the friction factor. These lines are plotted in Fig. 4. According to equation (17), the slopes of these lines are given by $-c/\mu_0$, and this allows the value of c for each stage to be determined. The values of c so determined are plotted in Fig. 2 as a function of the outlet width ratio of each stage. The results define a very clear curve for function c and an empirical equation for this function is given by

$$\begin{aligned} c &= 15.5/(1+35b_2/D_2) \quad \text{for } b_2/D_2 \le 0.06 \\ c &= 5.0 \qquad\qquad\qquad\quad \text{for } b_2/D_2 \ge 0.06 \end{aligned} \tag{22}$$

The fact that an unequivocal curve is defined by this analysis shows that the very simple approximations made in the analysis were justified. And, as is shown in Fig. 2, the values of c obtained from the measurements are in remarkably good agreement with the very simple equation for c suggested by the order of magnitude analysis.

The values of c given by equation (22) are valid for the industrial compressor stages used in this study. For other

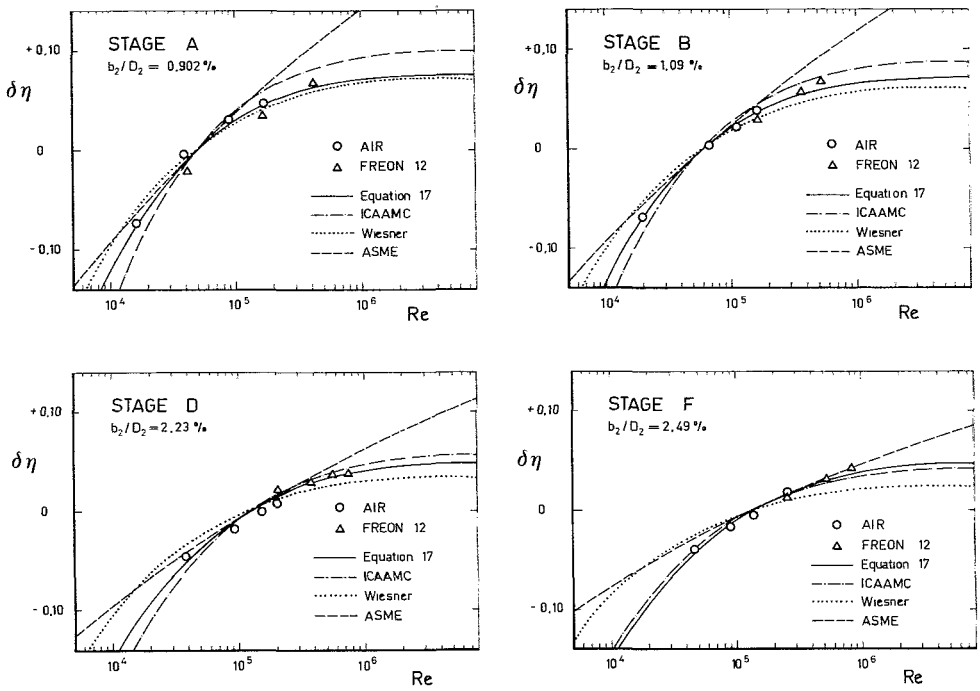

Fig. 5 Change in efficiency with Reynolds number of stages A, B, D, and F

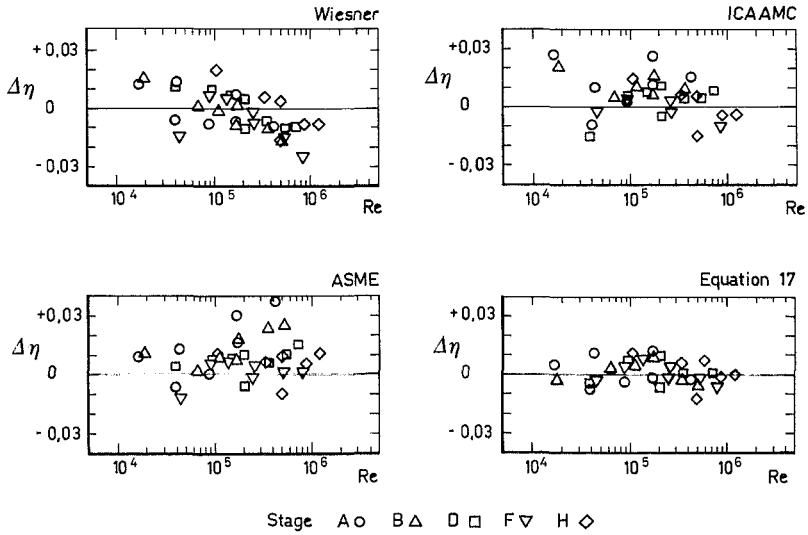

Fig. 6 Deviation between calculated and measured efficiency with different correction methods

types of compressor stage, for example, those with an unbladed diffuser or with a volute, slightly different values of c may have to be used. For such stages the same method may be adopted to determine the function of c from the measurement data.

Applications of Correction Equations

Effect of Reynolds Number. Figure 5 shows the change in efficiency with Reynolds number for stages A, B, D, and F. The predictions of equation (17) using the values of c given by equation (22) are excellent. It is clear from the very good agreement with measurements that this new correction method is extremely accurate and reliable.

Also plotted in Fig. 5 are the predictions of Wiesner's method [3], the ICAAMC method [7] and the ASME PTC-10 method [1]. A further comparison between the predictions of the different Reynolds number correction methods is shown in Fig. 6, where the deviation of each measurement point of the stages A, B, D, F, and H from the predicted value of the efficiency using the different Reynolds correction procedures has been plotted. The deviation is defined as

$$\Delta\eta = \eta_c - \eta_m \tag{23}$$

where η_c is the calculated efficiency and η_m the measured efficiency. The present method has the smallest deviation of about ± 1 point of efficiency and the measurement data are equally distributed about the line $\Delta\eta = 0$, showing that the method is consistently accurate. The error of ± 1 point is of the same order of magnitude as the possible errors in the measurements of the efficiency. The results with the ICAAMC method have more scatter (± 2 points) and are also fairly evenly distributed about $\Delta\eta = 0$. The Wiesner method has similar scatter to the ICAAMC method (± 2 points) but clearly tends to underestimate the efficiency at high Reynolds number. The largest errors ($+4 - -1$ points) are found with

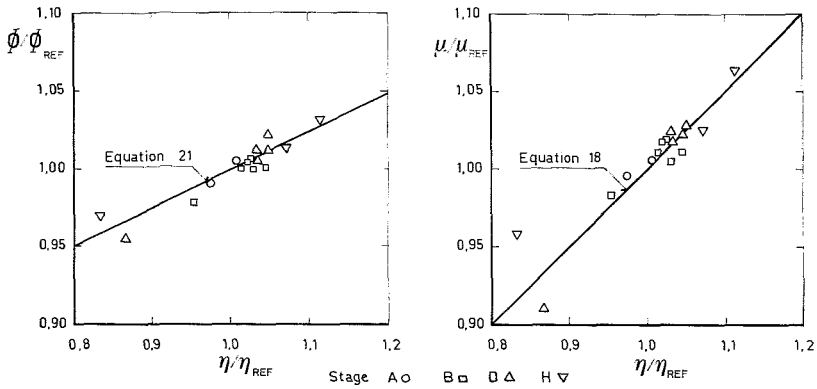

Fig. 7 Variation of head and flow coefficients

the ASME method. This method clearly overestimates measured efficiency, especially at high Reynolds number, and would appear even worse if measurements at higher Reynolds number were available.

Figure 7 shows the agreement between the measurements on stages A, B, D, and H and predictions of equations (18) and (21) for the head and flow coefficients.

Effect of Impeller Size. A prediction of the variation of efficiency with impeller diameter for stages with different outlet width ratios is plotted in Fig. 8, where the reference values are for an impeller with $D_2 = 315$ mm, $\mathrm{Ra} = 1.6$ μm and $\mu_0 = 0.7$. The curves are valid for air at standard temperature and pressure, and a tip speed Mach number of $\mathrm{Mu}_2 = 0.8$. They agree well with experience of the effect of impeller size on efficiency.

Effects of Surface Roughness. Experience has shown that equation (17) is not reliable when used to correct for the effect of surface finish on efficiency. Errors arise because the calculated change in friction factor associated with a change in surface roughness can be inaccurate for the following reasons. First, equation (17) uses a single value of Ra to represent the roughness of the whole stage. It is often the case, however, that different parts of the stage have different surface roughnesses. Even on machined surfaces with the same nominal surface finish, there may be small differences in roughness at different points or in different directions. It is, therefore, extremely difficult to ascribe a unique Ra value that accurately represents the roughness of the whole stage. Second, the conversion of the Ra roughness value into the equivalent sand roughness, k_s, (using equation (10)) is very crude. It does not take into account the effect of the shape of the roughness elements and can lead to considerable error (see Strscheletzky [17]).

It is pertinent to ask why these errors do not also make equation (17) unreliable as a Reynolds number or size correction method. The main reason is considered to be that the predicted change in friction factor associated with a change in the roughness is extremely sensitive to the value of roughness that is used. The change in friction factor for Reynolds number or size variation, on the other hand, is not as sensitive to the roughness value used. Provided, therefore, that a reasonable estimate of the mean roughness is available, then the errors in the Reynolds number or size correction method will be small. It should, in addition, be noted that because the values of the function c have been calibrated from measurements, errors arising from a slightly inappropriate value of Ra have been eliminated.

Discussion of Results

Equation (17) has many advantages over the more popular equation (1). It is simpler and has a sounder theoretical foundation. The way in which the change in efficiency is

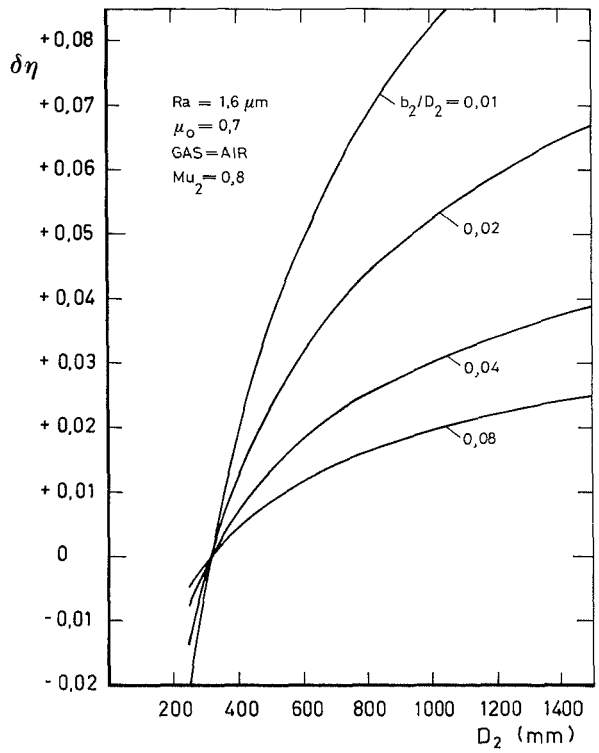

Fig. 8 Prediction of effect of impeller diameter on efficiency

related to both the work coefficient and the outlet width ratio is made very clear and is not hidden in empirical coefficients with little or no significance. The improved structure of equation (17) ensures that the effect of Reynolds number is uncoupled from the effects of the Reynolds independent losses. The effect of Reynolds number is not determined by adjusting the values of the coefficients but is taken from the well-known and reliable pipe flow equations. The effect of the relative roughness is automatically included in the pipe flow friction factor and no further adjustment of empirical constants is needed to take its effect into account. Equation (17) has only one empirical coefficient that needs to be derived from measurement data, and there is a very straightforward technique for calibrating it. Finally, equation (17) is also valid for changes in efficiency caused by changes in size, provided the appropriate changes in the friction factor are considered.

One disadvantage of the method given in this paper is that the assumptions made for its derivation are only valid for single-stage compressors. Equation (17) cannot, therefore, be used to calculate the variation of efficiency in a multistage machine. This limitation could be overcome if a suitable way of defining the mean friction factor of a multistage machine

could be found and if a simple approximation for the integration of equation (3) along the whole flow path were possible. It is not clear, however, how such an averaging procedure could be made generally applicable to all multistage compressors.

An obvious alternative method is to consider each stage of a multistage machine separately. If we neglect any effects caused by a change in the matching of the stages, this results in the following equation

$$\delta\eta = \frac{\Sigma - (cU_2{}^2\delta\lambda)_i}{\Sigma(\mu_0 U_2{}^2)_i} \tag{24}$$

where the value of $cU_2{}^2\delta\lambda$ is calculated for each individual stage i and the effect on the efficiency of the machine is summed over all the stages. The usual approximation that is made with correction methods for multistage machines is to take the first stage as representing the whole machine, such that only data for the first stage are needed in the correction equation. Equation (24) has the considerable disadvantage that data from every stage is needed.

It is interesting to note that the ICAAMC correction equation, equation (2), can be derived directly from equation (17). If the Reynolds independent losses are denoted by ζ, then the equation for the efficiency, equation (16), becomes

$$\eta = 1 - \frac{c}{\mu_0}\lambda - \zeta \tag{25}$$

If this equation is rewritten for conditions at the critical Reynolds number where no further change in efficiency occurs, then, after some manipulation, the ICAAMC correction equation can be obtained, where

$$a = \frac{\zeta}{\zeta + (c/\mu_0)\lambda_{cr}} \tag{26}$$

This provides a very clear definition of the Reynolds-number-independent loss fraction for a single-stage machine.

The ICAAMC working group [7] have shown that equation (2) can be used to correlate data on the effect of Reynolds number from several major compressor manufacturers. The group recommended that the value of $a = 0.3$ should be used to correct the performance of multistage compressors for variation of Reynolds number between workshop tests and specified process conditions. It is clear from equation (26) that a constant value of a cannot be exact for all machines. There is, however, a need for a simple equation for use with multistage compressors and the ICAAMC method represents the most sensible compromise that can be made.

The fact that such useful results can be obtained from this simple approach is mainly because losses in narrow impeller stages are primarily friction losses, which are well modeled by the equations for the fully developed turbulent pipe flow. This approach is not generally valid for those types of turbomachines where the sources of loss are more diverse. In these cases, the individual losses must be identified, the appropriate Reynolds number defined, and the separate losses corrected using the relevant Reynolds number correction equation.

Conclusions

The main conclusions of this paper are:

- The effect of Reynolds number on the friction losses of narrow compressor stages is similar to its effect on the friction factor of a fully turbulent pipe flow.
- The most appropriate definition of Reynolds number for a centrifugal compressor stage is given by $\mathrm{Re} = U_2 b_2/\nu_1$.
- An equivalent pipe flow that has a characteristic friction factor representative of the mean flow in a compressor stage can be defined by means of the following equation

$$\frac{1}{\sqrt{\lambda}} = 1.74 - 2\log_{10}\left(2\frac{\mathrm{Ra}}{b_2} + \frac{18.7}{\mathrm{Re}\sqrt{\lambda}}\right)$$

- For a single-stage compressor, the change in efficiency with Reynolds number can be reliably predicted from

$$\delta\eta = -\frac{c}{\mu_0}\delta\lambda$$

where $\delta\lambda$ is the change in friction factor of the equivalent pipe flow for a change in Reynolds number, and c is a function of the impeller outlet width ratio. The value of c for the industrial compressor stages considered in this study is given by equation (22).

- For multistage compressors, the change in efficiency with Reynolds number can be calculated by applying the above equation separately to each stage. The equations proposed by the ICAAMC working group [7] are, however, much simpler to use and have been calibrated for use with multistage machines. The ICAAMC equations can be derived from the method presented in this paper.

Acknowledgments

The author wishes to thank Sulzer-Escher Wyss, Ltd., for permission to publish this work, his colleagues in the Turbocompressor Development Department for many useful discussions, and the staff of the Sulzer Fluid Mechanics Laboratory for the care and attention devoted to the measurements.

References

1 ASME Power Test Codes, "Compressors and Exhausters," PTC-10, 1965.

2 VDI Compressor Regulations, "Acceptance and Performance Test on Dynamic and Positive Displacement Compressors," VDI 2045, 1973.

3 Wiesner, F. J., "A New Appraisal of Reynolds Number Effects on Centrifugal Compressor Performance," ASME JOURNAL OF ENGINEERING FOR POWER, Vol. 101, July 1979, pp. 384–396.

4 Wachter, J. and Woehrl, B., "Auftwertungen des Wirkungsgrades von Turbomaschinen der radialen Bauart in Abhängigkeit von Reynoldszahl und Geometrie," *Pfleiderer-Tagung*, VDI 424, 1981, pp. 19–28.

5 Casey, M., Unpublished work submitted to the ICAAMC working group on Reynolds number, June 1981.

6 Simon, H., Unpublished work submitted to the ICAAMC working group on Reynolds number, June 1981.

7 Strub, R. A., "Influence of the Reynolds Number on the Performance of Centrifugal Compressors," Final Report of the Working Group of the Process Compressor Subcommittee of the International Compressed Air and Allied Machinery Committee (ICAAMC), Zurich, Oct. 1982.

8 Simon, H. and Buelskaemper, A., "On the Evaluation of Reynolds Number and Relative Surface Roughness Effects on Centrifugal Compressor Performance Based on Systematic Experimental Investigations," ASME JOURNAL OF ENGINEERING FOR GAS TURBINES AND POWER, Vol. 106, No. 2, Apr. 1984, pp. 489–501.

9 Kotzur, J., "Analyse und Umrechnung von Radialverdichter-Kennlinien," Rohr Universität Bochum, Dec. 1978.

10 Traupel, W., *Thermische Turbomaschinen*, Vol. 1, 2d ed., Springer-Verlag, Berlin, 1966, pp. 139–140.

11 Schroeder, J., "Abschätzen der Strömungsverluste im Optimalpunkt einer Radialverdichterstufe mit Hilfe von Dissipationskoeffizienten," VDI 193, 1973.

12 Moody, L. F., "Friction Factors for Pipe Flow," ASME *Transactions*, Nov. 1944, pp. 671–684.

13 Haaland, S. E., "Simple and Explicit Formulae for the Friction Factor in Turbulent Pipe Flow," ASME *Journal of Fluids Engineering*, Vol. 105, Mar. 1983, pp. 89–90.

14 DIN Standards, DIN 4762.

15 Grein, H., "Some Considerations on the Surface Roughness of Wetted Components of Large Hydraulic Machines," *Escher Wyss News*, Vol. 1, 1975.

16 Senoo, Y., et al., "Asymmetric Flow in Vaneless Diffusers of Centrifugal Blowers," ASME *Journal of Fluids Engineering*, Vol. 99, Mar. 1977, pp. 104–114.

17 Strscheletzky, M., "Neuere Erkenntnisse über viskose Unterschichten an rauhen Wänden," Fortschr.-Ber. VDI-Z., Reihe 7, Nr. 43, 1976, ISBN 3-18-144307-7.

Journal of Engineering for Gas Turbines and Power

Technical Briefs

A Note on Blade Wake Interaction Influence on Compressor Stator Row Aerodynamic Performance

T. H. Okiishi,[1] M. D. Hathaway,[2] and J. L. Hansen[1]

Introduction

When one blade row of a turbomachine moves past another, important potential and viscous flow interaction effects occur. A number of researchers (e.g., [1-12]) support the notion that the wakes from an upstream row of blades will be severed and transported as "segments" by an adjacent downstream row of blades as illustrated, for example, by the sequence of stop-action sketches in Fig. 1. An interesting observation about the measured total pressure drop across a variety of compressor and fan stator rows seems explainable in terms of this particular wake interaction phenomenon. Our remarks are confined to compressor and fan stator flows without shocks. It would be of interest to know if the conclusions reached in this note are applicable to turbine rotor rows and to flows with shocks.

Observed Behavior and Proposed Explanation

Some compressor-stator inlet and exit time-averaged, total-head data are compared in Fig. 2. These data were acquired by traversing a cobra probe (see [13] for probe geometry and calibration details) circumferentially over one stator blade pitch at midspan in the first stage of a low-speed, axial-flow compressor (see Fig. 3) operating at design flow [13].

The data of Fig. 2 indicate a total-head loss for *all* pathlines through the stator row. Viscous loss due to stator-surface boundary layer flows is expected in the stator wakes (at, for example, point A in Fig. 1). Current shockless blade-element loss models focus on these surface boundary layers exclusively. In addition to the stator *wake* loss, however, the data of Fig. 2 can be interpreted to indicate that a significant amount of the stator *row* loss occurs in the region between adjacent blade-surface boundary layers. A pressure-measuring instrument positioned at point B in Fig. 1 would periodically sense chopped rotor wake segment pressures. If these chopped rotor wakes experience total-pressure loss due to viscous dissipation and interaction with the stator boundary layers as they move through the stator row, an average total-head loss will be registered at point B over time.

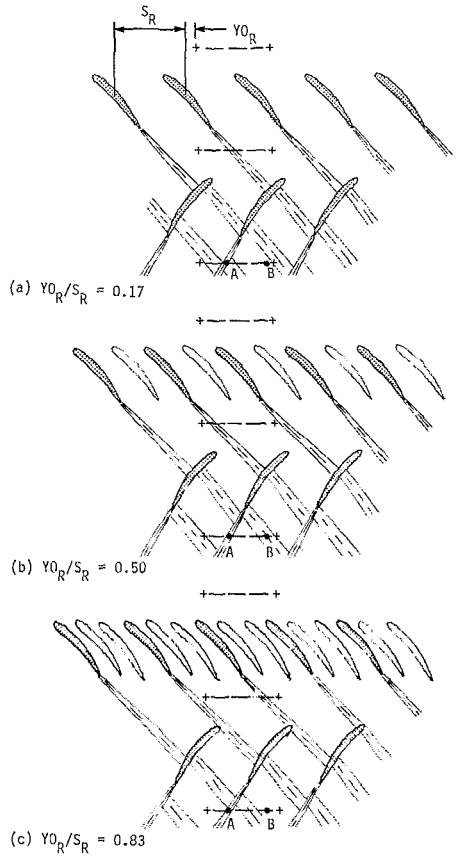

Fig. 1 Compressor stage rotor/stator interaction sequence of events

The time-averaged, stator row midspan, blade-element loss coefficient, $\bar{\omega}^*$, associated with the data of Fig. 2 is 0.059. The portion of this loss related to the region of flow between adjacent blade-surface boundary layers is 0.024 or 41 percent of the entire amount by area in the coordinate plane shown.

Similar data were calculated for the same operating condition at proximate span locations in the same compressor stage. The results are presented in Fig. 4. The stator blade wake loss is only a fraction of the entire stator blade row loss throughout the midspan portion of the compressor annulus.

Consistent results were noted for this compressor stage at near maximum efficiency operation [14]. Further, a survey of some NASA Lewis Research Center data indicated similar trends for most of a set of 12 compressor middle stage con-

[1]Department of Mechanical Engineering and Engineering Research Institute, Iowa State University, Ames, Iowa
[2]U.S. Army Propulsion Laboratory (USAVSCOM), NASA Lewis Research Center, Cleveland, Ohio

Contributed by the Gas Turbine Division for publication in the JOURNAL OF ENGINEERING FOR GAS TURBINES AND POWER. Manuscript received by the Gas Turbine Division September 4, 1984.

*$\bar{\omega}$ is defined as the ratio of the difference in circumferentially area-averaged total pressure across the stator row for a specific-span stream sheet and 1/2 the product of fluid density and absolute fluid velocity squared at the stator inlet.

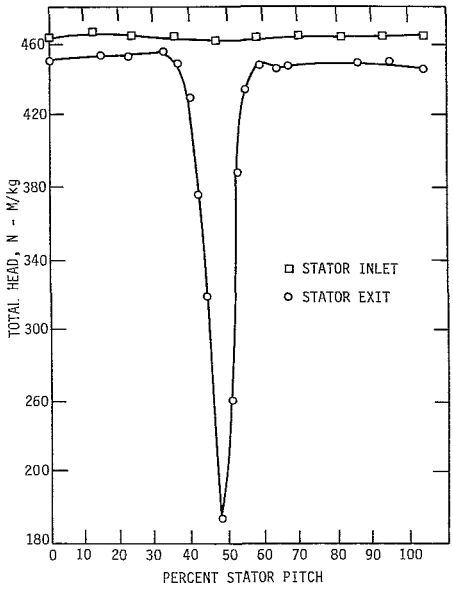

Fig. 2 First-stage stator upstream and downstream total-head values at midspan for design point operation

figurations described in [15] and for a transonic fan stage just recently tested, all at maximum efficiency operation.

Discussion

Several important questions related to the abovementioned observations deserve comment. Is it possible that a higher than true average total pressure was observed ahead of the stator associated with Fig. 2 because of probe blockage, flow unsteadiness, and/or pressure transducer drift? Is the additional viscous mixing of the rotor wake segment fluid while in transit through the stator row physically able to produce the relatively large amount of loss implied? How does the measured stator *wake* loss compare with predicted values? Can the suggested modeling be used nearer to annulus end walls? Is this phenomenon observable in a second or latter stage of a multistage turbomachine? These questions are responded to for the data of Fig. 2 in the following paragraphs.

Probe blockage behind the rotor was minimal (0.07 percent by area for 30 percent immersion; 0.20 percent for 70 percent immersion). Shroud static pressure did not vary as the probe was immersed across the rotor exit. Based on probe geometry and flow conditions, the guidelines of [16, 17] indicated that true time-averaged total-pressure recording could be expected. As mentioned in [13], a Kiel probe was used to verify the total-pressure readings acquired behind the rotor with the cobra probe. Furthermore, the pressure transducer involved was frequently calibrated and checked for drift during all tests (see [13]).

Calculations using the code of [18] indicate that for conditions similar to the ones at hand the mixing loss theory of [19] would predict only about 10 percent more rotor wake loss between measurement station and infinity (complete mix-out condition) in the absence of interaction with a stator row. On the other hand, in a related experiment involving the chopping and passage of moving cylinder wakes by a stationary cascade of blades [20], the measured "additional losses" of the cascade due to wake segment influence were comparable to the amounts noted for Fig. 2. Additional losses were ascertained to increase with increase in reduced frequency (more wake segments per second) and to decrease with increase in axial gap between moving cylinders and stationary cascade. It appears that some of the rotor wake segment loss observed in the stator row is due to an interaction influence not experienced when a downstream row of blades is absent. These different aspects, rotor wake dissipation and interaction, of the stator row loss deserve more thorough study.

A comparison of the measured stator *wake* loss, $\bar{\omega}_{sw}$, with values calculated with the inviscid-viscous interaction, blade-to-blade flow code of [18], $\bar{\omega}_{\text{code}}$, and using the loss coefficient of Fig. 203 of [21], $\bar{\omega}_{\text{SP-36}}$, is shown below:

$$\bar{\omega}_{sw} = 0.035$$

$$\bar{\omega}_{\text{code}} = 0.028$$

$$\bar{\omega}_{\text{SP}-36} = 0.016$$

The interaction of rotor wake segments with the stator surface boundary layers results in higher than predicted stator wake loss values. Experiments are presently underway to study this effect in more depth.

The wake chopping and interaction model proposed presently is restricted to the midspan region of flow where radial migration and other secondary flow components are

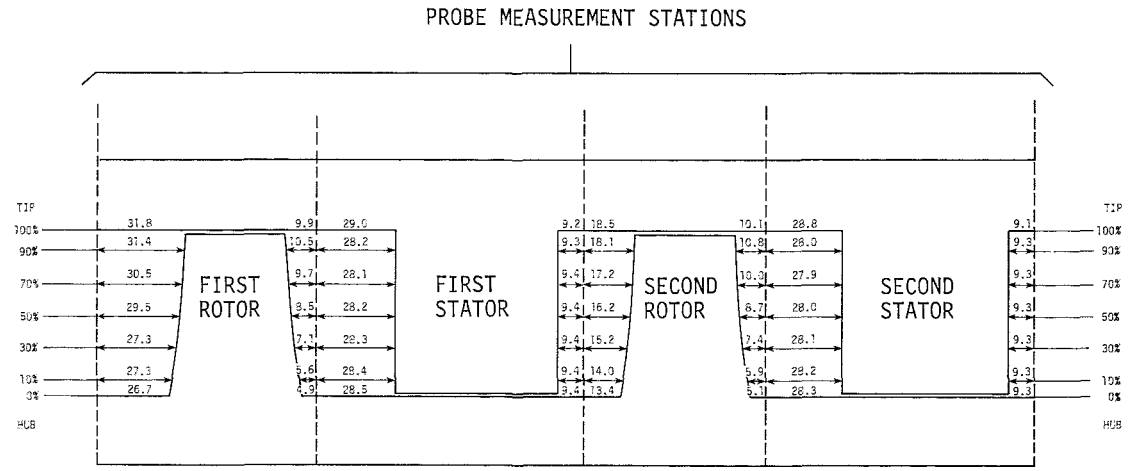

Fig. 3 Schematic showing axial location of probe measurement stations relative to adjacent blade rows (dimensions in mm) in low-speed, two-stage compressor

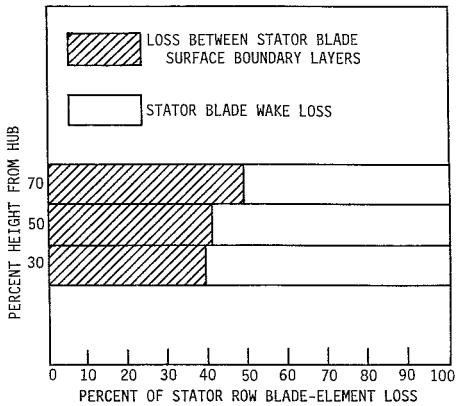

Fig. 4 First-stage stator blade element loss proportions at different spanwise positions for design point operation

minimal. Also, caution is urged if the model is to be used further downstream in a multistage machine. Sorting out the different loss components in embedded stages of a multistage machine is very difficult to do because of the presence there of a larger number and variety of wake segments from the different upstream rows involved.

Conclusions

The measured midspan loss of total pressure of a compressor or fan stage stator row under normal shockless operating conditions is relatable to stator surface boundary layers (stator wakes), the chopped rotor wakes passing through the stator row, and the interaction between these flows. An appreciable portion of the stator row loss can occur in the blade-to-blade region between the edges of blade-surface boundary layers. The interaction between rotor blade wake segments and stator-blade-surface boundary layers appears to result in much higher losses than expected in the stator wake and in the region of flow between stator boundary layers/wakes if interaction effects were ignored.

Acknowledgments

We are grateful to the Air Force Office of Scientific Research (Contract F49620-83-K-0023) and the National Aeronautics and Space Administration (Grant NAG 3-356) for support of research leading to the ideas expressed in this note. We also acknowledge the influence for good of our laboratory colleagues and of the reviewers of this note. In particular, we are indebted to J. David Stampfli and Elmer C. Hansen for their help in obtaining code results according to [18].

References

1 Meyer, R. X., "The Effect of Wakes on the Transient Pressure and Velocity Distributions in Turbomachines," *Transactions of the ASME*, Vol. 80, 1958, pp. 1544–1552.

2 Lefcort, M. D., "An Investigation Into Unsteady Blade Forces in Turbomachines," ASME JOURNAL OF ENGINEERING FOR POWER, Vol. 87A, 1965, pp. 345–354.

3 Smith, L. H., Jr., "Wake Dispersion in Turbomachines," ASME *Journal of Basic Engineering*, Vol. 88, 1966, pp. 688–690.

4 Kerrebrock, J. L., and Mikolajczak, A. A., "Intra-Stator Transport of Rotor Wakes and Its Effect on Compressor Performance," ASME JOURNAL OF ENGINEERING FOR POWER, Vol. 92, 1970, pp. 359–368.

5 Brandone, B., and Bernard, P., "Visualization par Analogie Hydraulique de l'Ecoulement dans une Grille d'Aubes Plane Mobile," *La Recherche Aerospatiale*, Vol. 141, No. 1971–2, 1971, pp. 125–128.

6 Lockhart, R. C., and Walker, G. J., "The Influence of Viscous Interactions on the Flow Downstream of an Axial Compressor Stage," in: *Proceedings of the Second International Symposium on Air Breathing Engines*, London, Royal Aeronautical Society, 1974.

7 Fleeter, S., Jay, R. L., and Bennett, W. A., "Rotor Wake Generated Unsteady Aerodynamic Response of a Compressor Stator," ASME JOURNAL OF ENGINEERING FOR POWER, Vol. 100, 1978, pp. 664–675.

8 Wagner, J. H., Okiishi, T. H., and Holbrook, G. J., "Periodically Unsteady Flow in an Imbedded State of a Multistage, Axial-Flow Turbomachine," ASME JOURNAL OF ENGINEERING FOR POWER, Vol. 101, 1979, pp. 42–51.

9 Adachi, T., and Murakami, Y., "Three-Dimensional Velocity Distribution Between Stator Blades and Unsteady Force on a Blade Due to Passing Wakes," *Bulletin of the JSME*, Vol. 22, 1979, pp. 1074–1082.

10 Gallus, H. E., Lambertz, J., and Wallman, Th., "Blade-Row Interaction in an Axial-Flow Subsonic Compressor Stage," ASME JOURNAL OF ENGINEERING FOR POWER, Vol. 102, 1980, pp. 169–177.

11 Dunker, R. J., "Flow Measurements in the Stator Row of a Single-Stage Transonic Axial-Flow Compressor with Controlled Diffusion Stator Blades," in: *Viscous Effects in Turbomachines*, AGARD Conference Proceedings No. 351 (AGARD-CP-351), 1983.

12 Hodson, H. P., "Boundary Layer and Loss Measurements on the Rotor of an Axial-Flow Turbine," ASME JOURNAL OF ENGINEERING FOR GAS TURBINES AND POWER, Vol. 106, 1984, pp. 391–399.

13 Hathaway, M. D., and Okiishi, T. H., "Aerodynamic Design and Performance of a Two-Stage, Axial-Flow Compressor (Baseline)," Iowa State University Engineering Research Institute Technical Report TCRL-24, Ames, Iowa, Dec. 1983.

14 Tweedt, D. L., and Okiishi, T. H., "Stator Blade Row Geometry Modification Influence on Two-Stage, Axial-Flow Compressor Aerodynamic Performance," Iowa State University Engineering Research Institute Technical Report TCRL-25, Ames, Iowa, Dec. 1983.

15 Britsch, W. R., Osborn, W. M., and Laessig, M. R., "Effects of Diffusion Factor, Aspect Ratio, and Solidity on Overall Performance of 14 Compressor Middle Stages," U.S. NASA Technical Paper 1523, 1979.

16 Kronauer, R. E., and Grant, H. P., "Pressure Probe Response in Fluctuating Flow," in: *Proceedings of the Second U.S. National Congress of Applied Mechanics*, ASME, New York, 1954.

17 Krause, L. N., Dudzinski, T. J., and Johnson, R. C., "Total Pressure Averaging in Pulsating Flows," NASA TMX-68128, 1972.

18 Hansen, E. C., Serovy, G. K., and Sockol, P. M., "Axial-Flow Compressor Turning Angle and Loss by Inviscid-Viscous Interaction Bade-to-Blade Computation," ASME JOURNAL OF ENGINEERING FOR POWER, Vol. 102, 1980, pp. 28–34.

19 Lieblein, S., and Roudebush, W. H., "Theoretical Loss Relations for Low-Speed Two-Dimensional-Cascade Flow," U.S. NACA Technical Note 3662, 1956.

20 Yurinskiy, V. T., and Shestachenko, I. Ya., "Losses in an Impulse Turbine Cascade in an Unsteady Flow," *Fluid Mechanics Soviet Research*, Vol. 3, 1974, pp. 22–27.

21 Johnson, I. A., and Bullock, R. O., eds., "Aerodynamic Design of Axial-Flow Compressors," U.S. NASA SP-36, 1965.

Journal of Engineering for Gas Turbines and Power

Discussion

Prediction of Stiffness and Damping Coefficients for Centrifugal Compressor Labyrinth Seals[1]

H. A. Noe and N. G. Wagner.[2] The paper presented is an interesting contribution to the state of the art of predicting the dynamic behavior of labyrinth seals. In our investigations dealing with this subject we have likewise found that – similar to the formulation in the paper presented – it is essential for a realistic model that the whole flow region be separated into jet-flow and core-flow regions and to consider the turbulent momentum exchange in the shear flow region. We also found that the mixing factor β strongly depends upon details of the labyrinth geometry. However, we feel that some points in the paper have not been clearly expressed and should be discussed as follows.

The Reynolds number Re has been calculated at the flow conditions at the labyrinth entrance in order to evaluate the wall shear stress in the whole labyrinth. As the velocity and the viscosity of the medium in the labyrinth can vary widely from inlet to outlet, the Re number should be calculated specifically for each chamber. We found that the abovementioned simplification may result in errors of up to 20 percent with respect to the wall friction coefficient. Furthermore it would appear to be more correct to describe the friction at the counterface of the tips of straight-through labyrinths by the equations for a rotating cylinder rather than by a "tube-flow" model.

The formulation of the leakage flow $\tilde{\dot{m}} = \bar{\dot{m}} + \tilde{\dot{m}}(\phi,t)$ in equation (19) should be replaced by the axial velocity in the gap $c_{ax} = c_{ax}(\phi)$, because no axial mass flow can exist only at one single discrete point. A mass flow – here the axial leakage flow – is always bound at least to an infinitesimal area. Setting $c_{ax}(\phi) = \bar{c}_{ax}(1 + \epsilon k \cos\phi)$ (ϵ = relative eccentricity, k = unknown coefficient, ϕ = angle) and integrating $\dot{m} = \int_0^{2\pi} \rho c_{ax}(\phi)\ \alpha(\phi)\ Rs(\phi)d\phi$ (ρ = density, α = local contraction coefficient, R = radius, s = gap width) leads to a mass flow as a function of the coefficient k. Comparing this mass flow equation with the St. Venant equation (which contains $\alpha(\phi)$ and carry-over factor $\zeta(\phi)$) results in an equation for determining k including mass conservation for each gap. This analysis shows further on that the leakage of straight-through labyrinths in the eccentric case differs from the concentric case. This is confirmed by experimental data [18, 19].

We regret that the authors have not explained how they obtained the coefficients of the variables in equation (19). If a formulation similar to equation (20) is used for the variables $\tilde{w}_i(\phi,t)$, $\tilde{w}_m(\phi,t)$ $\tilde{m}(\phi,t)$, and $\tilde{p}(\phi,t)$ – which is obviously necessary – a system of equations with 16 unknowns will result from this whereby only 5 equations for the solution would be available. We feel that some further assumptions or simplifications, which are not mentioned, have been made.

The change of sign for the cross-coupling stiffness in Fig. 9 is explained by the influence of the shaft rotation at low inlet swirl. This is in conflict with the results shown in Fig. 12, where the cross-coupling stiffness does not become negative despite low inlet swirl and high shaft speed.

The excellent agreement between the predicted and measured stability limits shown in Fig. 15 appears to be very impressive. This is particularly the case considering the fact that several important influencing factors must have been active during the tests. It would therefore be of very great interest to know some more details about the configuration of the rotor systems tested. Additional information, for instance about the

- critical speed ratios
- rotor speed
- type of bearings and shaft-end seals
- type and location of labyrinth seals (with or without "inlet swirl brakes"?)
- gas density

would provide a much more informative picture.

In contrast to the results reported by the authors in Fig. 15 we have observed much larger discrepancies between actual and predicted stability limit, although we used a prediction method for the stiffness and damping coefficients which seems to be very similar to that described by the authors. With our model we found a quite reasonable agreement between calculated and measured pressure distributions in the chambers of labyrinth seals of various geometries and for various inlet flow conditions. However, applying the theoretically derived coefficients in the prediction routines for rotor dynamics (e.g., determining log decrements for the eigenvalues to be considered) often results in unrealistic lowering of the stability limits of turbocompressor rotors (e.g., expressed as "critical pressure" and/or "critical" rotor speed) and do not agree with results obtained in practice. Accordingly, in line with our experience, we consider that the theoretically derived "dynamic" labyrinth coefficients have to be calibrated by empirical test data to a large extent until more sophisticated prediction methods for the labyrinth coefficients are available.

In the paper presented the authors claim that they have solved the problem in a rather pure theoretical manner. If so, we would like to congratulate them on their success; but, at the same time, we would greatly appreciate their demonstrating the alleged quality of their prediction results in Fig. 15 in more detail.

[1] By H. R. Wyssman, T. C. Pham, and R. J. Jenny, published in the October 1984 issue of the JOURNAL OF ENGINEERING FOR GAS TURBINES AND POWER, Vol. 106, No. 4, pp. 920–926.

[2] Mannesman Demag, Duisburg, Germany

References

18 Kearton and Keh, "Leakage of Air Through Labyrinth Glands of Staggered Type," *Proc. Inst. Mech. Eng.*, Vol. 166, 1952, pp. 180–195.

19 Benckert, *Versuchsauswertung aus FVV-Vorhaben*, No. 139, 179.

solution. This is the main advantage of the present method of solving full three-dimensional method. Moreover, the deviation of the S_1 surface from a surface of revolution is readily available in the full three-dimensional calculation and directly indicates the amount of secondary flow involved in that particular blade design.

References

1 Wu, C.-H., "A General Theory of Three-Dimensional Flow in Subsonic and Supersonic Turbomachines of Axial-, Radial-, and Mixed-Flow Types," ASME Paper No. 50-A-79, 1950 (Trans. ASME, Nov. 1952), or NACA TN 2604, 1952.

2 Wu, C.-H., "Matrix and Relaxation Solutions that Determine Subsonic Through-Flow in an Axial-Flow Gas Turbine," NACA TN 2750, 1950.

3 Wu, C.-H., and Brown, C. A., "Method of Analysis for Compressible Flow Past Arbitrary Turbomachine Blades on General Surface of Revolution," NACA TN 2470, 1951.

4 Novak, R. A., "Streamline Curvature Computing Procedures for Fluid-Flow Problems," ASME JOURNAL OF ENGINEERING FOR POWER, 1967.

5 Marsh, H., "A Digital Computer Program for the Through Flow Fluid Mechanics in an Arbitrary Turbomachine, Using a Matrix Method," ARC R&M 3509, 1968.

6 Frost, D. H., and Smith, D. J. L., "A Streamline Curvature Computer Program for Analyzing the Subsonic Compressible Flow Past a Cascade of Aerofoils," NGTE Report R. 327, ARC Paper No. 35346, 1973.

7 Smith, D. J. L., "Computer Solutions of Wu's Equations for Compressible Flow Through Turbomachines," NASA SP-304, *Fluid Mechanics Acoustics and Design of Turbomachinery*, Part I, 1974, pp. 43–74.

8 Hirsch, C., "Finite Element Method for Throughflow Calculations," AGARD-CP-195, 1976.

9 Bosman, C., and El-Shaarawi, M. A. I., "Quasi-Three-Dimensional Numerical Solution of Flow in Turbomachines," ASME Paper No. 76-FE-23, 1976.

10 Novak, R. A., and Hearsey, R. M., "A Nearly Three Dimensional Intrablade Computing System for Turbomachinery," ASME *Journal of Fluids Engineering*, Mar. 1977.

11 Academia Sinica, Shenyang Aeroengine Company, "Theory, Method and Application of Three-Dimensional Flow Design of Transonic Axial-Flow Compressor," *Journal of Engineering Thermophysics*, Vol. 1, No. 1, 1980 (in Chinese).

12 McDonald, P. W., Bolt, C. R., Dunker, R. J., and Weyer, H. B., "A Comparison Between Measured and Computed Flow Field in a Transonic Compressor Rotor," ASME Paper No. 80-GT-7, 1980.

13 Zhu, G., Ge, M., and Wu, C.-H., "Three-Dimensional Subsonic Flow Through a Stator by Use of a Central S_2 Stream Surface and Several S_1 Surfaces of Revolution," *Journal of Engineering Thermophysics*, Vol. 4, No. 2, 1983 (in Chinese).

14 Wu, C.-H., "Three-Dimensional Turbomachine Flow Equations Expressed with Respect to Non-Orthogonal Curvilinear Coordinates and Methods of Solution," Lecture Notes, China University of Science and Technology, 1975, or *Proceedings of 3rd ISABE*, 1976, pp. 233–252.

15 Wu, W.-Q., Zhu, R.-G., and Liu, C.-E., "Computational Design of Turbomachine Blades," *J. Aircraft*, Vol. 17, No. 5, May 1980.

16 Wu, C.-H., and Zhu, G., "Determination of the Appropriate Upstream and Downstream Conditions in Rotating Cascade Experiment and Calculation of Arbitrary S_1 Stream Surface for an Embedded Blade Row," *Journal of Engineering Thermophysics*, Vol. 4, No. 1, 1983 (in Chinese).

17 Wu, C.-H., and Wolfenstein, L., "Application of Radial-Equilibrium-Condition to Axial-Flow Compressor and Turbine Design," NACA TR 955, 1950.

18 Wu, C.-H., "Fundamental Aerothermodynamic Equations for Stationary and Moving Coordinate Systems: Action of Viscous Forces and Physical Significance of Viscous Terms," *Journal of Mechanical Engineering*, Vol. 13, No. 4, Dec. 1965 (in Chinese) or *Engineering Thermophysics in China*, Vol. 1, No. 1, 1980, Rumford Pub. Co., U.S.A.

19 Members of the Compressor and Turbine Research Division, "Aerodynamic Design of Axial-Flow Compressors," NACA RM E56B03, 1956.

20 Wu, W.-Q., and Liu, C.-E., "Flow-Field Matrix Solution for Direct Problem of Flow Along S_1 Relative Stream Surface Employing Non-Orthogonal Curvilinear Coordinates and Corresponding Non-Orthogonal Velocity Components," *Journal of Engineering Thermophysics*, Vol. 1, No. 1, 1980 (in Chinese).

21 Zhu, R.-G., "Flow-Field Line-Relaxation Solution for Inverse Problem of Flow Along S_2 Relative Stream Surface Employing Non-Orthogonal Curvilinear Coordinates and Corresponding Non-Orthogonal Velocity Components," *Journal of Engineering Thermophysics*, Vol. 1, No. 1, 1980 (in Chinese).

DISCUSSION

I. K. Jennions[1]

Firstly I would like to take this opportunity to congratulate Professor Wu and his colleagues on their recent publication of so many interesting papers; we look forward to developments of the S_1/S_2 approach. The present paper puts the original ideas of Wu [1] into practice to form both quasi-three-dimensional and fully three-dimensional numerical solution procedures, which are demonstrated on two examples.

With all quasi-three-dimensional solution procedures involving the use of an S_2 surface one has the question of how the surface is defined, and also what approximations are inherent with the approach. The authors have chosen their S_2 surface to be a streamsurface defined by the locus of the $\psi = 50$ S_1 streamlines. Other authors have defined their S_2 surface as a mean cambersurface [22], or the locus of S_1 mass-averaged streamlines [9]. It is not clear considering these choices how the S_2 surface should be defined and what effect this definition would have on the answers. A technique that avoids this problem is passage averaging [23, 24, 25], where the through-flow solution is calculated for the mean flow properties and no S_2 surface needs to be introduced. What is also not clear is the way in which the present paper defines and uses B_i, and consequently any assumption that may be made in the continuity equation. A discussion from the authors as to the choice of S_2 surface and the assumptions that are made in their method would be most welcome.

Example 1 is the design of a two-stage axial compressor for which the losses are taken from a previous experiment on a similar machine. The objective of a design, once the primary goals of pressure ratio, etc., have been met, is to perform the process efficiently. This involves understanding loss mechanisms and changing the design to increase efficiency. The example does not address this question and would be more easily understood as an analysis of an existing machine.

For the same example, Fig. 6 shows some confusion between convergence of the iterative scheme and consistency between the S_1 and S_2 solutions, which can be illustrated as follows. Convergence is most easily defined as being achieved when a chosen parameter of the system does not change by a significant amount from one iteration to the next. This parameter could be the streamtube contraction through the row, the blade exit angle, or the Mach number. For a quasi-three-dimensional calculation on a turbine rotor, performed in a similar way to that described in [26], Fig. 12 shows the change in rotor exit angle with iteration. The exit angle is calculated in the blade-to-blade program using a Kutta condition on the trailing edge. The angle is then transferred to the through-flow program for the next iteration. Convergence, as defined by the change in the exit angle from one iteration to the next, is seen to be rapid. This, however, does not ensure consistency between the through-flow and blade-to-blade solutions, a measure of which can be obtained from Fig. 13. Here the maximum value of $|(Ms_1 - Ms_2)/Ms_2|$ is 0.016, where it is stressed that this is a more severe test case (>100 deg turning) than that presented by the authors. All quasi-3D methods will possess a residual value of $|(Ms_1 - Ms_2)/Ms_2|$ due to passing averaged variables from one program to another with the inevitable interpolations. What one needs to achieve is consistency between the solutions to an acceptable level for design purposes.

[1]Principal Theoretical Scientist, Theoretical Science Group, Rolls-Royce Ltd., P.O. Box 31, Derby DE2 8BJ, England

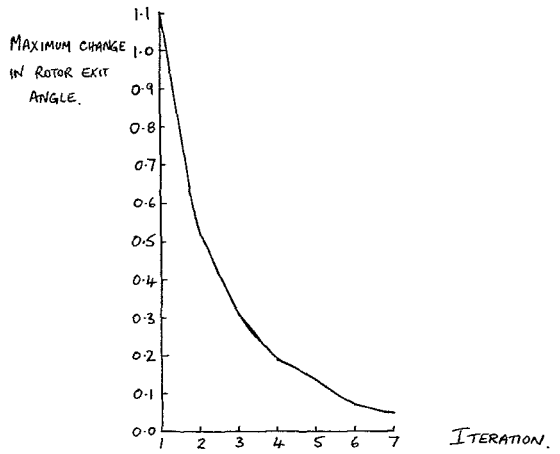

Fig. 12 Change in rotor exit angle with iteration

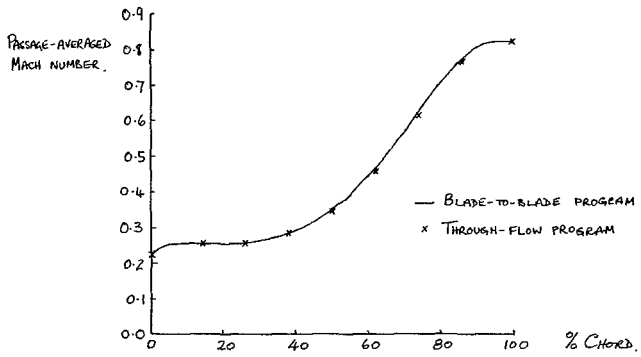

Fig. 13 Midheight section Mach numbers

Finally, it is not obvious from the paper how the authors treat conditions just downstream of the trailing edge for the fully three-dimensional solution. On a twisted S_1 surface the normal repeat condition cannot be applied as the suction and pressure surfaces are at different radial heights. If the repeat condition were to be applied properly then the S_1 calculations could not be performed in isolation. One possible treatment would be to solve for the flow with the blade in the center of the solution domain with the repeat condition applied between blade midpassage locations.

References

22 Senoo, Y., and Nakase, Y., "An Analysis of Flow Through a Mixed Flow Impeller," ASME JOURNAL OF ENGINEERING FOR POWER, 1972, pp. 43–50.

23 Smith, L. H., Jr., "The Radial Equilibrium Equation of Turbomachinery," ASME JOURNAL OF ENGINEERING FOR POWER, Jan. 1966, pp. 1–12.

24 Hirsch, C., and Warzee, G., "An Integrated Quasi-3D Finite Element Calculation Program for Turbomachinery Flows," ASME JOURNAL OF ENGINEERING FOR POWER, 1979, pp. 141–148.

25 Jennions, I. K., and Stow, P., "A Quasi-Three-Dimensional Turbomachinery Blade Design System: Part I—Through-Flow Analysis," ASME JOURNAL OF ENGINEERING FOR GAS TURBINES AND POWER, Vol. 107, No. 2, Apr. 1985, pp. 301–307.

26 Jennions, I. K., and Stow, P., "A Quasi-Three-Dimensional Turbomachinery Blade Design System: Part II—Computerized System," ASME JOURNAL OF ENGINEERING FOR GAS TURBINES AND POWER, Vol. 107, No. 2, Apr. 1985, pp. 308–316.

T. Katsanis[2] and E. McFarland[2]

The authors are to be congratulated for preparing a fine paper. In the interest of brevity, our discussion will be confined to raising questions about specific details.

The distinction between the matrix method and the relaxation method is not clear, since the relaxation method is used to solve matrix equations. Would you clarify this distinction?

The explanation of the flow calculation on a general S_1 surface does not appear complete. When the S_1 surface is a surface of revolution, periodic boundary conditions are used upstream and downstream of the blade row. However, when the S_1 surface is not a surface of revolution, the flow is not periodic on the surface upstream and downstream of the blade row. How is this problem handled?

In a three-dimensional flow, S_1 and S_2 surfaces become highly distorted, and may even be doubled back over themselves. It does not seem practical to use this scheme for a fully three-dimensional flow. In any event, the question remains as to how close a solution obtained by this method would come to a solution obtained by a three-dimensional Euler code such as Denton's.

A discussion by the authors of the limitations of their three-dimensional method would be appreciated. It is quesionable, for instance, whether the method could calculate a flow with a strong passage vortex.

Work similar to this has been done previously using the finite element method, and reported in [27].

References

27 Krimerman and Adler, "The Complete Three-Dimensional Calculation of the Compressible Flow Field in Turbo Impellers," *Journal of Mechanical Engineering Science*, Vol. 20, 1978.

[2]NASA-Lewis Research Center, Cleveland, Ohio

Note: The Author's Closure to the discussion by I. K. Jennions appears on p. 553.

(*continued from p. 285*)

Author's Closure

1 The Definition and Role of Central (Mean) S_2 Surface in the Quasi-3D Solution Procedure

1 Firstly, I would like very much to emphasize that, since the first publication of Wu's work on 3D turbomachine flow, in his 2D flow solution along an S_1 or S_2 surface and his theory of 3d Solution based on the iterative solution between flows on S_1 and S_2 surfaces, he always works definitely on calculation for a number of physical surfaces (either S_1 or S_2 surfaces). The definitions of S_1 and S_2 surface were clearly given in his first publication [28] and remain unchanged throughout his later development and all his computer codes.

2 Secondly, depending on particular situations, the shape of the S_1 or S_2 surface may either be given at the beginning of calculation or obtained at the end of the solution of the other surface flow. For instance, in S_1 calculation, usually the geometry of the S_1 stream sheet (i.e., the shape of the central stream surface plus the thickness variation of the sheet) is given and calculation is made to obtain the flow in the stream sheet (i.e., along its central stream surface).

On the other hand, the conception of the S_2 surface is especially useful for the optimum design of hub and casing contours and 3D blade design. For this type of application, the shape of the hub/tip shape and the variations of $V_\theta r$ of gas flow along central S_2 surface[3] and of its thickness[4] are specified by the designer and calculation is made to obtain the complete flow variation along the central S_2 surface and also the shape of this central S_2 surface (please see Figs. 3, 4, 5, 9 of [28], Fig. 15 of [29], and Figs. 1, 4 of [30]). Perhaps I should mention that this latter feature of Wu's S_2 solution was often overlooked by some readers. It seems to us that the phrase "quasi-3D solution" has been used by different people with different meanings. Some people seem to call his solution based on one S_2 surface flow and several S_1 surface flows a "quasi-3D solution." We use this phrase to refer to the converged solution of iterative calculation between the central S_2 surface flow and several S_1 surface flows. We believe this latter usage is the right one. The former one should be called "approximate quasi-3D solution."

Of course, in the quasi-3D solution, S_1 surfaces are usually approximately taken to be surfaces of revolution.

Therefore, in our quasi-3D blade design solution, the following procedure is taken:

1 Calculation of the central S_2 surface (called S_{2m} surface or central S_2 surface) for a prescribed design variation of hub-tip contours, $V_\theta r$, and stream sheet thickness is carried out. From the solution, the shape of the central S_2 surface and the streamline variation on the surface and the corresponding lines on the meridional plane are obtained. These latter lines are revolved around the axis of the turbomachine to form S_1 surfaces of revolution.

2 Certain blade sections are chosen on several S_1 surfaces and direct-problem solutions are obtained. (The blade section may also be designed by some method such as the mean-streamline method [31]). The variations of $V_\theta r$ and S_2 stream sheet thickness for the mean streamlines of these S_1 surfaces serves as new input values for the second calculation of the S_{2m} or central S_2 surface.

3 The above process is repeated until converged solution is obtained.

[3] In the sense that this S_2 surface lies in the central part of the blade passage

[4] In the first approximation, this is estimated by the blade thickness variation (with correction at the leading and trailing edges)

2 Full 3D Solution (Direct Problem)

In the method presented in the original paper, the blade designed by the quasi-3D solution described in the preceding section is followed right away by a full 3D direct solution. In the latter calculation, corresponding streamlines obtained in the several S_1 surface-of-revolution solution give the shapes of several S_2 surfaces, including the ones which coincide with the blade suction and pressure surface, respectively. In turn, the corresponding streamlines obtained in the several S_2 solutions give the geometry of several general (i.e., twisted and not surface of revolution any more) S_1 surfaces.

Converged solution of the iterative calculation between these two families of flow surfaces gives the full 3D solution.

It may be emphasized again that we in China always follow this original concept of S_1 and S_2 flow surfaces as first put forth in [28]. There is no ambiguity in the definition of either S_1 or S_2 surface, there is no approximation involved in the employment of S_2 surface, and there is no need for obtaining some kind of circumferentially averaged flow properties or passage-averaging procedure. Indeed we feel a kind of disappointment that this clear-cut application of physically real S_{2m} or "central" S_2 surface concept as originally put forth in [28] was overlooked or not well understood by quite a number of readers in other countries.

3 Consideration of Flow Losses in Blade Design

The present paper does not include the physical analysis of flow losses, or a method to reduce losses, but rather a way to include in the blade design process the overall effect of various kinds of losses, which are likely to exist in the type of blades to be designed, in order that the blade designed in this way will give the required performance (not only pressure ratio but also efficiency).

The paper does present a new finding in the 3D design calculation: In the S_1 calculation, entropy values consistent with those in the S_2 calculation must be used.

4 Convergence of the Iterative Process

The physical meaning of the convergence criterion

$$\left| \frac{(Ms_1 - Ms_2)}{Ms_2} \right| < \epsilon$$

we used to indicate the convergence of iterative process between S_1 and S_2 stream flow calculations is clear. In fact, the crux of Wu's theory of two families of stream surfaces is to simplify a 3D flow solution into two 2D solutions on S_1 and S_2 stream surfaces. Therefore, the result of convergence has to be given by the final equality of solutions at the same position obtained from S_1 and S_2 calculation, respectively. This is the reason that we choose this convergence criterion. Furthermore, the convergence processes of many computations we performed have shown that convergences of other flow variables, such as the streamsheet contraction in passing through the blade row, the blade exit angle, or the Mach number, had also been achieved, so long as the criterion mentioned above was fulfilled.

5 Boundary Condition Downstream of Blade Trailing Edge

The boundary condition just downstream of the trailing edge for the full 3D solution can only be approximately treated in the inviscid solution because the existence of trailing vortex cannot be considered in the inviscid model. But the twist of the S_1 stream surface is adequately considered in the full 3D solution. Just upstream of the blade leading edge and

just downstream of the trailing edge, the Dirichlet boundary condition was used in the computer code. The values of stream function on the two boundary lines of the flow domain were directly given in the calculation. Far upstream and downstream of the blade, the periodic condition is considered, i.e., identical values of any parameters have been maintained at the corresponding positions on the two boundary lines of the flow domain downstream of the trailing edge or upstream of the leading edge. (These corresponding positions have the same axial and radial coordinates.)

References

28 Wu Chung-Hua, "A General Theory of Three-Dimensional Flow in Subsonic and Supersonic Turbomachines of Axial, Radial, and Mixed-Flow Types," *Trans. ASME*, Nov. 1952; NACA TN 2604, 1952.

29 Wu Chung-Hua, "Matrix and Relaxation Solutions That Determine Subsonic Through-Flow in an Axial-Flow Gas Turbine," NACA TN 2750, 1950.

30 Wu Chung-Hua, "Subsonic Flow of Air Through a Single-Stage and a Seven-Stage Compressor," NACA TN 2961, 1953.

31 R. Cai, "A Summary of Developments of the Mean-Streamline Method in China," ASME JOURNAL OF ENGINEERING FOR GAS TURBINES AND POWER, Vol. 106, No. 2, Apr. 1984, pp. 300–305.